VOLUME 2

PROCEEDINGS

ELEVENTH INTERNATIONAL CONFERENCE ON THE BEARING CAPACITY OF ROADS, RAILWAYS AND AIRFIELDS

Edited by

Inge Hoff, Helge Mork and Rabbira Garba Saba

CRC Press
Taylor & Francis Group

ELEVENTH INTERNATIONAL CONFERENCE ON THE BEARING CAPACITY OF ROADS, RAILWAYS AND AIRFIELDS, VOLUME 2

Proceedings of the 11th International Conference on the Bearing Capacity of Roads, Railways and Airfields – Volume 2 comprises the second part of contributions to the 11th International Conference on Bearing Capacity of Roads, Railways and Airfields (2022). In anticipation of the event, it unveils state-of-the-art information and research on the latest policies, traffic loading measurements, in-situ measurements and condition surveys, functional testing, deflection measurement evaluation, structural performance prediction for pavements and tracks, new construction and rehabilitation design systems, frost affected areas, drainage and environmental effects, reinforcement, traditional and recycled materials, full scale testing and on case histories of road, railways and airfields. This edited work is intended for a global audience of road, railway and airfield engineers, researchers and consultants, as well as building and maintenance companies looking to further upgrade their practices in the field.

PROCEEDINGS OF THE ELEVENTH INTERNATIONAL CONFERENCE ON THE BEARING CAPACITY OF ROADS, RAILWAYS AND AIRFIELDS, 28-30 JUNE 2022, TRONDHEIM, NORWAY

Eleventh International Conference on the Bearing Capacity of Roads, Railways and Airfields, Volume 2

Edited by

Inge Hoff & Helge Mork

Norwegian University of Science and Technology, Trondheim, Norway

Rabbira Garba Saba

Norwegian Public Roads Administration, Trondheim, Norway

CRC Press
Taylor & Francis Group
Boca Raton London New York Leiden

CRC Press is an imprint of the
Taylor & Francis Group, an **informa** business

A BALKEMA BOOK

CRC Press/Balkema is an imprint of the Taylor & Francis Group, an informa business

Typeset by Integra Software Services Pvt. Ltd., Pondicherry, India

Library of Congress Cataloging-in-Publication Data

A catalog record has been requested for this book

Published by: CRC Press/Balkema
Schipholweg 107C, 2316 XC Leiden, The Netherlands
e-mail: enquiries@taylorandfrancis.com
www.routledge.com - www.taylorandfrancis.com

Volume 1:
ISBN: 978-1-032-12044-7 (Hbk)
ISBN: 978-1-032-12068-3 (Pbk)
ISBN: 978-1-003-22288-0 (eBook)
DOI: 10.1201/9781003222880

Volume 2:
ISBN: 978-1-032-12049-2 (Hbk)
ISBN: 978-1-032-12070-6 (Pbk)
ISBN: 978-1-003-22289-7 (eBook)
DOI: 10.1201/9781003222897

Volume 3:
ISBN: 978-1-032-12052-2 (Hbk)
ISBN: 978-1-032-12074-4 (Pbk)
ISBN: 978-1-003-22291-0 (eBook)
DOI: 10.1201/9781003222910

Eleventh International Conference on the Bearing Capacity of Roads, Railways and Airfields, Volume 2 – Hoff, Mork & Saba (eds)

Table of contents

Eleventh International Conference on the Bearing Capacity of Roads, Railways and Airfields, Volume 2 – Hoff, Mork & Saba (eds)

Preface

Bearing capacity is not an easy term to define. It is used to express the traffic load a pavement structure can withstand without showing severe damage. It is not a measure of the ultimate structural strength that will cause a failure state for a single vehicle if exceeded. The ultimate strength of a pavement is normally significantly higher than the bearing capacity. For rehabilitation projects, the bearing capacity is becoming more and more important, and it is a challenging task for an engineer to determine the remaining bearing capacity of a structure and how this capacity could be further utilized.

This conference is the eleventh in the series started in Trondheim 1982 and arranged at four-year intervals under the title Bearing Capacity of Roads and Airfields, BCRA. At the sixth conference in Lisbon, Portugal, railway tracks was added as the third important component. The acronym is since then BCRRA. The conference has been organized at five cities in addition to Trondheim (1982, 1990, 1998, 2005 and 2013): Plymouth, UK (1986), Minneapolis, USA (1994), Lisbon, Portugal (2002), Champaign, USA (2009) and Athens, Greece (2017).

The BCRA/BCRRA conferences have contributed to creating and sharing knowledge in this area through more than 2000 papers and an even higher number of participants in the conferences.

The organizing committee would like to express gratitude to all that have participated in making this conference possible.

Inge Hoff
Chair of the organizing committee

Eleventh International Conference on the Bearing Capacity of Roads, Railways and Airfields, Volume 2 – Hoff, Mork & Saba (eds)

Organizing committee

Inge Hoff, *Norwegian University of Science and Technology (NTNU), Trondheim, Norway*
Helge Mork, *Norwegian University of Science and Technology (NTNU), Trondheim, Norway*
Rabbira Saba, *Norwegian Public Roads Administration (SVV), Trondheim, Norway*
Leif Bakløkk, *Norwegian Public Roads Administration (SVV), Trondheim, Norway*

Policies on the bearing capacity of roads, railways and airfields

Eleventh International Conference on the Bearing Capacity of Roads, Railways and Airfields, Volume 2 – Hoff, Mork & Saba (eds)

The relationship between surface crack features and bearing capacity of the pavement

Nakamura Hiroyasu
Research Institute, NIPPO Corporation, 6-70 Mihashi Nishi-ku Saitama-shi,, Saitama, Japan

Kameyama Shuuichi
Hokkaido University of Science, 7-15-4-1 Maeda Teine-ku Sapporo, Hokkaido, Japan

Sakuraba Akira
TAIRIKUKENSETSU Corporation, 1-1-2 Hoshigauraminami Kushiro, Hokkaido, Japan

Kawabata. Shinichirou
Hokkaido University of Science, 7-15-4-1 Maeda Teine-ku Sapporo, Hokkaido, Japan

Tomiyama Kazuya
Kitami institute of Technology, 165 Koen-cho Kitami, Hokkaido, Japan

ABSTRACT: In Japan, a road surface characteristics measuring vehicle has been used for pavement inspection since the 1970s. At the present time, about 60 road surface characteristics measuring vehicles are used in Japan. There are three inspection items: cracks, rutting, and roughness. Cracks are evaluated by the ratio of the area of cracks with a width of 1 mm or more, but the length and width are not used. FWD is used to evaluate the structure of cracked areas. However, the relationship between these inspection items and FWD has not been clarified. Therefore, in order to manage the pavement efficiently, a new method for evaluating cracks was examined. Using a measuring vehicle that can acquire cracks with a width of less than 1 mm, the shape of the cracks were arranged. The shape of the crack focused on the width, intersection, length, and area. The measurement was performed in four sections having different types of cracks. As a result, there was no relationship between the conventional crack evaluation method and FWD, but a correlation was confirmed between the crack length and the FWD deflection.

Keywords: pavement, rack, bearing capacity, FWD, minute cracks

1 INTRODUCTION

Infrastructure built in Japan during the period of rapid economic growth from 1954 to 1975 is now rapidly aging. For example, it is estimated that the percentage of road bridges at least 50 years old will double over the next decade from about 27% in 2019 to about 52% in 2029[1)]. It has been pointed out that if government finances remain in their current constrained condition, it may be difficult to secure sufficient funds for the maintenance, management, and renewal of such infrastructure.

DOI: 10.1201/9781003222897-1

Following the collapse of ceiling plates in the Sasago Tunnel on December 2, 2012, an intensive inspection was conducted in February 2013 to confirm the safety of roadway stock and prevent injury to third-parties. Subsequently, in June 2013, the Road Act was amended to mandate relevant inspection standards and to establish a government-directed proxy system for repair work. In March 2014, a ministerial ordinance on periodic inspections, together with a public notice of same, was promulgated. And thus, from July 2014 onward, all bridges and tunnels have been subject to a regime of detailed visual inspection once every five years. Inspection items for bridges include cracking of decks and piers, and the degree of damage is evaluated by close visual inspection of the presence, shape, and length of such cracks. Inspection items for tunnels include cracking at the tops of lining arches and portals, and if such cracks are found, their location, length, and width (W) are measured using the same general procedures as those for bridges.

To extend the service life of roadways in Japan through effective maintenance, the government instituted a set of maintenance inspection guidelines in October, 2016[2) 3)4)]. Since that time, inspections have been carried out in accordance with these guidelines[5)]. The guidelines set targets for the service life of national roadways considered to be particularly susceptible to wear (e.g., those paved with asphalt). It is important to promptly repair and restore roadways that have exceeded control values ahead of their target service life (i.e., sections of roadway within "area d" in Figure 1)[6)].

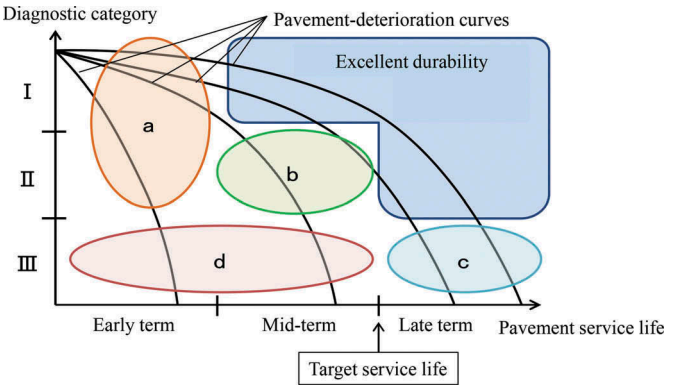

Figure 1. General categories of pavement inspection and diagnosis[6)].

The guidelines stipulate that inspections be conducted visually or by using measurement equipment. For equipment-based inspections, road surface condition measurement vehicles (RSCMVs)[7)] that photograph the road surface are widely used. These vehicles are used to check for surface cracks and ruts and to determine the International Roughness Index value of the road. A surface crack can begin as a single line and progress to a tortoise-shell pattern. Therefore, among the three inspection items, cracking is considered to be the most strongly related to the structural integrity of the pavement. Furthermore, cracks can provide a conduit for rainwater to seep into the interior of the road, which can lead to potholes[8)] and weakening of the roadbed and road base[9)]. It is thus critically important to properly assess road surface cracking and take suitable action.

In Japan, crack ratio[10)] is used as an index for assessing cracks in asphalt pavement. This ratio is determined by the method shown in Figure 2. The roadway surface is overlain with a grid consisting of 0.5 × 0.5-m squares having an area of 0.25 m^2. Then, the proportion of squares containing a crack of $W \geq 1$ mm is calculated. Using this approach, the crack rate can be easily determined. When a single crack is found in a 0.25 m^2 square, the area of the crack is taken to be 0.15 m^2, whereas if two or more cracks are found, their area is taken to be 0.25 m^2. However, if more than two cracks are found, the assessment is the same, and

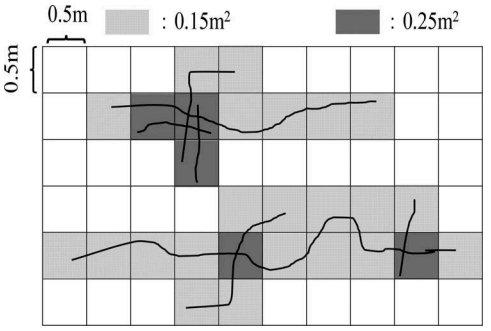

Figure 2. Method for calculating the crack ratio of asphalt pavement.

information such as crack length, shape, and complexity is not used. Also, as stated above, only cracks of $W \geq 1$ mm are counted; narrower ones are not, even though rainwater may also seep through such cracks and similarly weaken the road base or roadb ed. This is because, when RSCMVs first appeared in the 1970s, inspection capabilities were restricted by the low camera resolution and limited data processing capabilities of the day. However, now that photographic and data processing technology is considerably more advanced, it is possible to analyze pavement cracking to a much higher level of detail.

In this research, we utilized a vehicle-mounted measurement system consisting of a high-resolution line laser and a newly developed crack detection program. We measured not only conventional cracks $W \geq 1$ mm, but also microcracks (MCs) of $W < 1$ mm. The measured cracks were classified into six categories according to width: < 1 mm (Category 1); 1–2 mm (Category 2); 2–3 mm (Category 3); 3–4 mm (Category 4); 4–5 mm (Category 5), and >5 mm (Category 6). Crack characteristics, including number of intersections/branches, crack length, and crack area, were obtained. We then clarified the relationships between these characteristics and the crack ratio as well as among the crack characteristics. We also conducted falling-weight deflectometer (FWD) tests in order to investigate the relationships between crack characteristics and pavement load-bearing capacity.

2 INVESTIGATION OVERVIEW

(1) Sections investigated

For this study, a private toll road (10 km long) was chosen for investigation. This road is closed from 7PM to 7AM, so no traffic restrictions were necessary during that time, and we were free to conduct our investigation without any particular impediments. The surface layer of this section of road is a dense-graded asphalt mixture having the same pavement configuration over its entire length; the average asphalt thickness was 15 cm. The intended California Bearing Ratio (CBR) of the roadbed is not known because no record remains from its initial construction; however, the roadway has a heavy vehicle traffic classification of N2. For this study, we chose four 100-m sections with different surface-layer ages (Table 1). Section 1 had the shortest service life (6 years), and Section 4 had the longest (21 years). Sections 2 and 3 rest entirely on fill, whereas Sections 1 and 4 both have a boundary between the cut and fill.

Table 1. Service life and road earthwork performed on inspected sections.

Inspection section	Service life (roadway surface)	Roadway earthwork
Section 1	6 years (repaired in 2013)	Front 35 m: fill Back 65 mm: cut
Section 2	15 years(repaired in 2004)	All fill
Section 3	9 years(repaired in 2010)	
Section 4	21 years (repaired in 1998)	Front 10 m: cut Back 90 m: fill

(2) Investigation method

In Japan, RSCMVs are used to perform annual inspections of roadway surface conditions[11]. For the test results to be considered reliable, the resolution for detecting W was set at ≥ 1 mm. However, through the action of rainwater, even MCs of $W < 1$ mm can lead to weakening of the road base and roadbed. Thus, in this study, we used a measurement vehicle equipped with a high-resolution (0.5-mm length, 0.25-mm width) line laser like those used to inspect for cracks in tunnel walls[12), 13), 14)]. The device can detect cracks of $W < 1$ mm by using the line laser camera to capture the road surface, as shown in Photo 1.

Photo 1. Road surface crack inspection by the test vehicle.

In general, road cracking tends to oc cur at the outer wheel position (OWP) and the inner wheel position (IWP) of the road. However, because the line laser camera installed on our test vehicle cannot scan both at the same time, we directed our roadway imaging at the OWP, specifically a 1.638-m swath of roadway centered on the OWP. In Japan, the crack ratio is assessed for 100-m sections of roadway. However, the longer the assessment length, the more difficult it is to identify specific damage locations because the features within are averaged out. For the purposes of our survey, we first obtained images of roadway sections 100 m long and 1.638 m wide. Then, we divided the images into 10 sections of 10 m each and determined the crack ratio and other indices.

Also, because cracking on a roadway surface is considered to be closely related to the overall structural integrity of the pavement, we simultaneously carried out FWD measurements. The FWD is a device that uses multiple sensors, including one placed at the center load plate, to measure the surface deflection that occurs when a weight is dropped onto the pavement surface. We took such measurements at 5-m intervals at the OWP over the entire length of the investigated sections.

(3) Crack assessment method

To extract crack data from images taken by the test vehicle, we developed Pave-CAD, a dedicated software program that runs on top of computer-aided design (CAD) software and handles manually traced vector data. Figure 3 shows the process for calculating crack characteristics. First, the acquired road surface image is displayed (Figure 4).

Then, W is manually measured using CAD measurement commands. In the case of an unbranched crack, W is measured at the halfway point between the two ends. In the case of a branched crack, W is measured at the halfway point between a given end point and branch point (or between two branch points). Next, the cracks were classified by W into categories 1 to 6, as shown in Table 2, and each category was assigned a color using a CAD tracing function. By performing this operation for all cracks in the image, we generated a development diagram (Figure 5) stratified by W category. From this, we can extract the crack ratio and characteristics for each W category.

In this study, Category 1 was defined as $W < 1$ mm. However, we needed to know the degree to which Pave-CAD is capable of detecting such fine cracks. So we randomly selected 75 cracks of $W < 1$ mm in Section 4, which was found to have the greatest diversity of W on

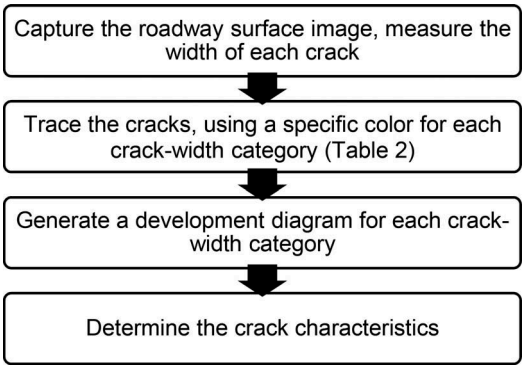

Figure 3. Procedure for calculating crack characteristics by Pave-CAD.

Table 2. Crack categories.

Category (i)	Crack width	w_i
1	$W < 1$ mm	0.81 mm
2	1 mm $\leq W < 2$ mm	1.50 mm
3	2 mm $\leq W <$ 3mm	2.50 mm
4	3 mm $\leq W < 4$ mm	3.50 mm
5	4 mm $\leq W < 5$ mm	4.50 mm
6	5 mm $\leq W$	5.50 mm

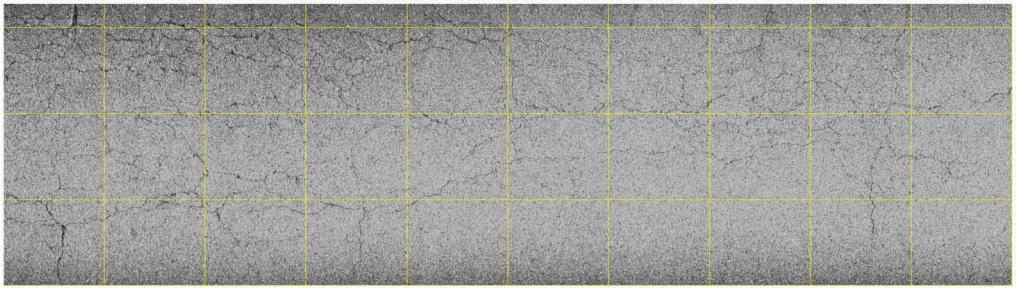

Figure 4. Acquired road surface image.

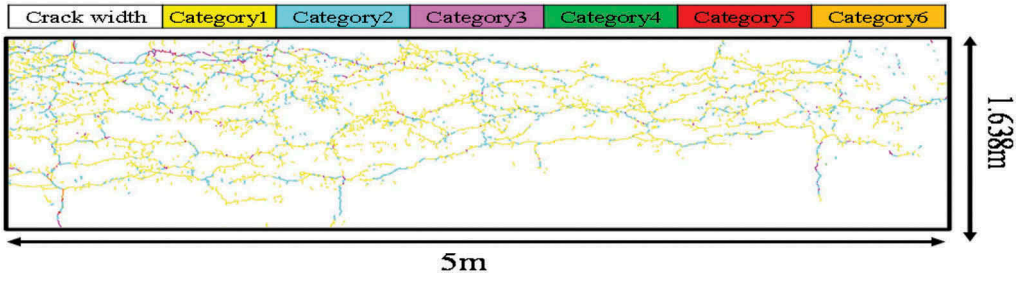

Figure 5. Development diagram stratified by crack width.

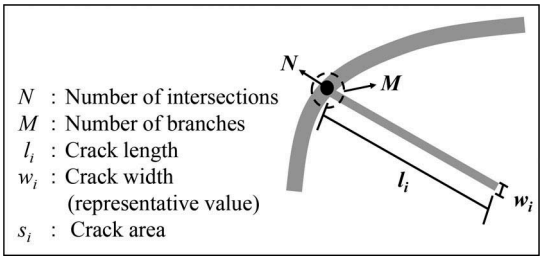

Figure 6. Crack characteristics.

visual inspection. Among these cracks, the smallest had a W of 0.650 mm and the average W was 0.814 mm. From this, we determined that our method can detect cracks having a W of 0.650 mm or more.

As shown in Figure 6, we extracted a number of crack characteristics from the development diagrams, including the number of intersections (N; in Figure 6, $N = 1$) and the number of branches (M; in Figure 6, $M = 2$). The crack length (l_i) and crack area per square meter (s_i) were also determined. The crack area (s_i) was calculated as the product of the crack length (l_i) and the representative W (W_i) (Table 2); that is, $s_i = l_i \times W_i$. Furthermore, we calculated the total crack length (L) as the sum of crack lengths li in the 10-m sections of categories 1–6 ($L = \Sigma li$), whereas the total crack area (S) was calculated as the sum of all crack areas si ($S = \Sigma si$).

(4) Assessment of pavement load-bearing capacity

FWD measurements were performed to assess the load-bearing capacity of pavement within the sections under investigation. We then corrected the obtained deflection data for load (49 kN) and temperature (20°C)[15]. In addition to deflection immediately below the FWD load plate D_0 (μm), which is a widely used indicator of overall pavement load-bearing capacity, we also employed the elastic coefficient of asphalt mixture E_1 (MPa) as calculated by Equation (1), the roadbed CBR (%) as estimated by Equation (2), and the residual equivalent thickness T_{A0} (cm) obtained from Equation (3).We took FWD measurements at two locations in each 10-m road surface image and used the averaged values.

$$E1 = \frac{2,352\left(\frac{D0-D200}{103}\right)-1.25}{h1} \tag{1}$$

E_1: Elastic coefficient of the asphalt mixture layer (MPa)
D_0: Deflection at the centerline of the load plate (μm)
D_{200}: Deflection at 200 mm from the centerline of the load plate (μm)
h_1: Thickness of the asphalt mixture layer (cm)

$$CBR = \frac{1,000}{\mathrm{D1500}} \tag{2}$$

CBR: Roadbed CBR (%)
D_{1500}: Deflection at 1,500 mm from the centerline of the load plate (μm)

$$T_{A0} = -25.8 \log \frac{D_0 - D_{1500}}{10^3} + 11.1 \tag{3}$$

T_{A0}: Residual equivalent thickness (μm)
D_0: Deflection at the centerline of the load plate (μm)
D_{1500}: Deflection at 1,500 mm from the centerline of the load plate (μm)

3 ANALYSIS OF CRACK CHARACTERISTICS

Crack ratios inclusive of MCs within the sections under investigation are shown in Figure 7. The W distribution for each section is shown in Figure 8. In Section 1, MCs vary markedly, from 20% to 80%, with Category 1 cracks (W < 1 mm) accounting for about 70% of the total. It should also be noted that some locations have many cracks and others have only a few. Because the conventional crack ratio assessment method targets cracks of $W \geq 1$ mm, the

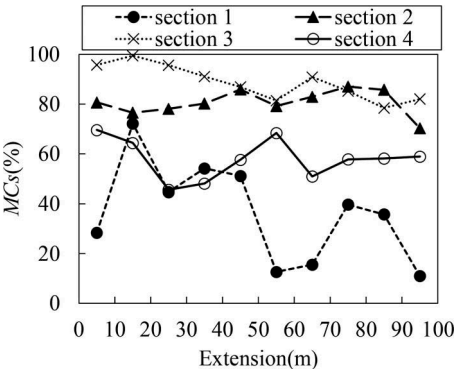

Figure 7. Variation in microcracks (MC) in the investigated sections.

degree of cracking may be substantially underestimated. About 80% of the cracks in Section 2 are MCs and there is little variation, indicating that the cracks are relatively uniform throughout the section. About half of the cracks have a $W < 1$ mm. If we were to use the conventionalmethod to measure the same stretch (W ≥ 1 mm), the crack ratio would be roughly half, or 40%. More than 80% of the cracks in Section 3 are MCs, and cracks occur over nearly the entire surface. Most these cracks are $W < 1$ mm. Using the conventional method, the degree of cracking in this section would be greatly underestimated. That is, the method would not adequately express the situation as it actually is on the road surface. However, in Section 4, the percentage of MCs with $W < 1$ mm is small at 20%, so there would be little deviation from the actual situation even with the conventional m ethod. Figure 8 and Table 1 show that as the service life of the surface layer increases, the percentage of MCs (W < 1 mm) decreases as the cracks grow wider.

Table 3 shows the relationships between MCs and several crack characteristics. The strongest correlation was found for total crack length L, despite the low R^2 value of 0.36. As

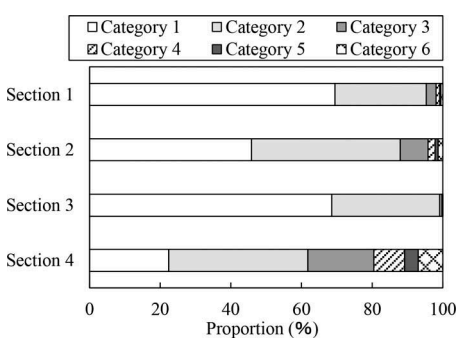

Figure 8. Proportion of crack-width categories in the investigated sections.

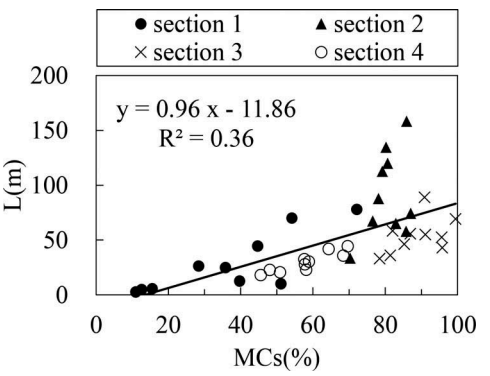

Figure 9. Relation between MCs and L.

shown in Figure 9, there was a tendency for L to increase with the number of MCs. However there was much variation, and so a clear relationship could not be confirmed.

The relationships among crack characteristics obtained in this study are shown in Table 4. The R^2 value fo r number of intersections N vs. the number of branches M was 1.00, but this is because about 95% of the cracks in the surveyed sections had two branches.

Table 3. Correlations (R^2) between MCs and crack characteristics.

	No. of intersections N	No. of branches M	Total crack length L	Total crack area S
MC	0.09	0.09	0.36	0.20

Table 4. Correlations (R2) between crack characteristics.

	Total crack length L	Number of intersections N	Number of branches M	Total crack area S
L		0.72	0.71	0.72
N			1.00	0.63
M				0.62
S				

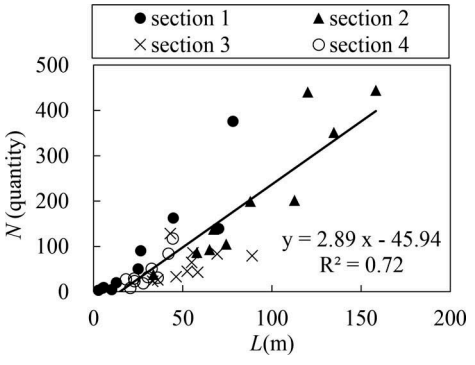

Figure 10. Relationship between L and N.

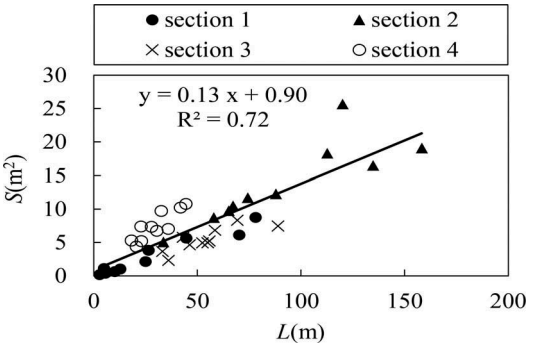

Figure 11. Relationship between L and S.

Otherwise, we found strong correlations among total crack length L, number of intersections N, number of branches M, and total crack area S. The relationship between L and N is shown in Figure 10, and that between L and S is shown in Figure 11. Because both N and S tended to increase linearly as L increased, we chose crack length as the representative characteristic for this study.

4 RELATION BETWEEN CRACKING AND PAVEMENT LOAD-BEARING CAPACITY

The relationship between MCs, which is the crack ratio inclusive of MCs with $W < 1$ mm as determined by the mesh method, and the pavement load-bearing capacity is shown in Table 5.

R^2 values of the deflection immediately below the FWD load plate D_0 and the residual equivalent thickness T_{AO} are about 0.4, whereas those of the asphalt mixture layer modulus of elasticity E_1 and the roadbed CBR are even lower. As for the relationship between MCs and D_0, which has a high R^2 value in Table 5, D_0 tended to increase with increasing MCs, but there was much variation and so no clear relationship could be confirmed (Figure 12). In this study, road surface cracking is categorized according to W (Table 2), and thus crack ratios can be determined as a function of differences in the W under evaluation. Figure 13 shows the R^2 values of crack ratio and D_0 when all cracks are included (W_{all}) and when the applicable W is increased in 1-mm increments. We can see that the R^2 value decreases substantially as the W of the target crack increases. This suggests that in this field of study, it is necessary to measure cracks of $W < 1$ mm.

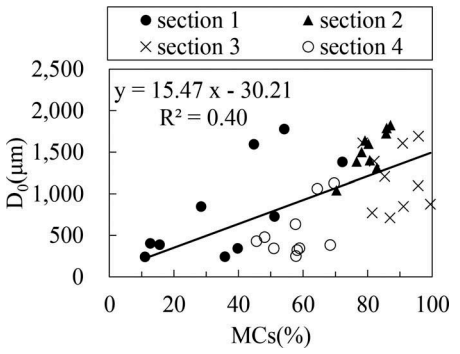

Figure 12. Relationship between MCs and D_0.

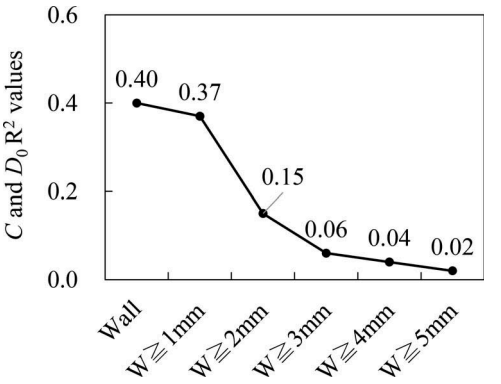

Figure 13. Relationship between crack width and R^2 correlation of crack ratio C and deflection at centerline of FWD load plate D_0.

Table 5. Correlations (R^2) between MCs and load-bearing capacity.

	D_0	E_1	CBR	T_{A0}
MC	0.40	0.23	0.05	0.44

Table 6 shows the relationship between pavement load-bearing capacity and crack characteristics for all cracks, including MCs with $W < 1$ mm. The R^2 value for total crack length L is higher than that of the other characteristics, and the correlation between L and D_0 is high.

Table 6. Correlations (R^2) between crack characteristics and load-bearing capacity.

	D_0	E_1	CBR	T_{A0}
Total crack length L	0.55	0.27	0.10	0.49
Number of intersections N	0.33	0.13	0.08	0.29
Number of branches M	0.33	0.13	0.08	0.29
Total crack area S	0.32	0.27	0.02	0.35

The relationship b etween L and D_0 is shown in Figure 14. D_0 tends to increase linearly with total crack length L, and there is little variation. Figure 15 shows the R^2 of L and D_0 as W is increased in 1-mm increments. It should be noted that the R^2 values for $W \geq 1$ mm are much

lower than those for W_{all}. From this, it is considered that total crack length (including MCs of $W < 1$ mm in addition to the cracks of $W \geq 1$ mm typically included in such analyses) is a better crack-assessment index that reflects the load-bearing capacity of the pavement.

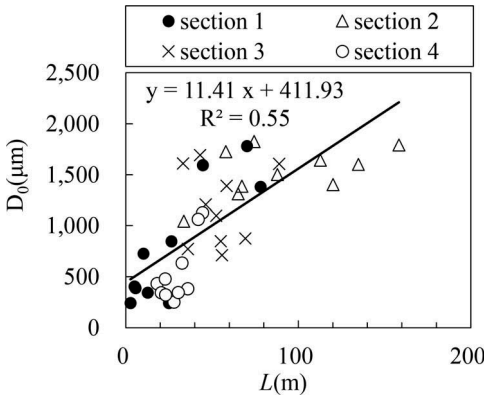

Figure 14. Relationship between L and D_0.

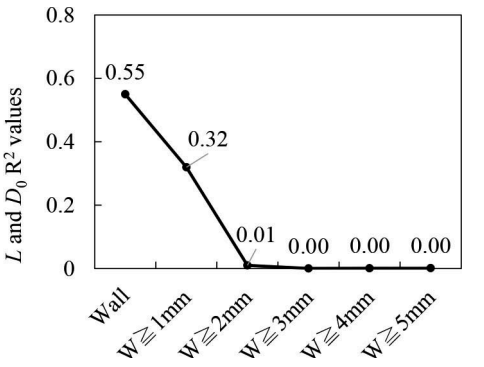

Figure 15. Relationship of L and D_0 R^2 values with crack width.

5 SUMMARY

In this research, we utilized a high-resolution line laser to detect MCs ($W < 1$ mm). Making use of our newly dev eloped Pave-CAD software, we categorized cracks by W, determined the crack characteristics (number of intersections/branches, crack length, and crack area), and determined the crack ratio inclusive of MCs as well as the relationships among crack characteristics. We also conducted FWD tests to investigate the relationships between crack characteristics and pavement load-bearing capacity.

The findings of this study are as follows.

- Using a vehicle-mounted high-resolution line laser, we were able to detect cracks of $W < 1$ mm.
- We found almost no relationship between MCs and crack characteristics (number of intersections/branches, crack length, and crack area). However, there were strong correlations among total crack length L, number of intersections N, number of branches M, and total crack area S.
- We could not confirm a relationship between MCs and D_0. However, the R^2 value between total crack length L and D_0 was 0.54. When the W analyzed was limited to ≥ 1 mm, the R^2 value decreased. Therefore, by including MCs in our calculation, we can appropriately express the load-bearing capacity of the pavement.
- It is preferabl e to assess cracks of not only $W \geq 1$ mm, but also MCs of $W < 1$ mm and to use total crack length L rather than crack ratio as the assessment index.
- We did not find a relationship between cracking and pavement load-bearing capacity when considering only cracks of $W \geq 2$ mm. Therefore, we intend to collect data on thicker cracks in future research.

REFERENCES

1) Ministry of Land, Infra structure, Transport and Tourism: Current status of aging, issues of aging countermeasures (in Japanese) http://www.mlit.go.jp/road/sisaku/yobohozen/torikumi.pdf

2) Ministry of Land, Infrastructure, Transport and Tourism Road Bureau: Pavement inspection guidelines (in Japanese) http://www.mlit.go.jp/road/sisaku/yobohozen/tenken/yobo3_1_10.pdf
3) Satoshi Muto, Kazuyuki Kubo, Masayuki Yabu: Formulation of pavement inspection guidelines (in Japanese), Pavement, Vol.52, No.1, pp.11–15, 2017.1
4) Ministry of Land, Infrastructure, Transport and Tourism: Status report (paving) regarding the formulation of inspection guidelines (in Japanese) http://www.mlit.go.jp/common/0011 70942.pdf
5) Ministry of Land, Infrastructure, Transport and Tourism Road Bureau: Annual Road Maintenance Report (in Japanese) http://www.mlit.go.jp/road/sisaku/yobohozen/pdf/h30/R1_03maint.pdf
6) Japan Road Association: Pavement management guidelines based on pavement inspection guidelines (in Japanese)
7) Ministry of Land, Infrastructure, Transport and Tourism: Test results of measurement technology for road surface properties (in Japanese) http://www.mlit.go.jp/common/001267623.pdf
8) Kimio Maruyama, Ryuji Abe, Masayuki Kumagai: Examination of the actual condition and mechanism of pavement potholes that occur during the snowmelt season (in Japanese)
9) Kenji Hashizume, Kazuaki Hashimoto, Yukio Akashi, National Nail: Proposal of Pothole Occurrence Prediction Method Due to Deterioration of Drainage Paveme nt Deeper than Base Layer (in Japanese), Pavement Engineering Papers, Vol.70, No.3 pp. I_17-I_24, 2014
10) Japan Road Association: Road Survey/Test Method Handbook (2019 Edition) (in Japanese) [Volume 1], pp.215–225
11) Public Works Research Center Homepage: http://www.pwrc.or.jp/houkokusyo.html
12) Tetsuo Ito, Koji Baba, Hiromichi Jouma, Isamu Yoshitake, Koji Nakagawa: Evaluation of peeling risk by investigating crack morphology of tunnel lining concrete (in Japanese), JSCE Proceedings, No.763/VI-63, pp. 87–93, 2004.6
13) Yoshiyuki Shigeta, Toshiyuki Tobita, Katsumi Kamemura, Masato Shinshi, Isamu Yoshitake, Koji Nakagawa: Evaluation method of soundness of lining concrete considering the direction of cracks (in Japanese), JSCE Proceedings F, Vol.62, No.4, 628–632, 2006.10
14) Tetsuo Ito, Koji Baba: Tunnel lining concrete measuring vehicle using laser (in Japanese), mechanization of construction No, 632, 14–19, 2002, 10
15) Road Management Technology Center: Let's utilize it! FWD, 2005

Eleventh International Conference on the Bearing Capacity of Roads, Railways and Airfields, Volume 2 – Hoff, Mork & Saba (eds)

Plate load testing - Effects of in-situ conditions, test procedure and calculation method

H. Andresdottir
Sweco Norge AS, Stavanger, Norway

H. Mork
Department of civil and environmental engineering, Norwegian University of Science and Technology, Trondheim, Norway

ABSTRACT: The plate load test is commonly used to determine the bearing capacity of unbound granular materials. It is widely used in road construction, and the test is mandatory as final documentation of compaction quality of unbound layers of pavements in Norway. The test is sensitive to field conditions and test execution, and several Norwegian contractors struggle to meet requirements for the test results despite repeated compaction efforts. This paper aims to assess the effects of in-situ road conditions, the superstructure materials and the test procedure and calculation method on the results of plate load tests. A case study and a field test were conducted. The case study compared four different road construction sites in Norway based on results from semi-structured interviews, collected results of plate load tests and field observations. Additional interviews and plate load test results from other road construction sites were also considered, although not for direct comparison in the case study. The field test applied two test procedures (Norwegian and Swedish) and two plate sizes (300 and 600 mm) on three superstructure layers (frost protection, subbase, and interlocking layers). The results of all tests were calculated using three calculation methods; the Swedish method, the Norwegian method, and a modified Norwegian method. The interview results indicate that crushed asphalt and/or insulation materials in the superstructure, moisture content and time from compaction to testing are the most influential factors on the plate load test results, although this should be verified with further testing. The field test results suggest that the interlocking material is important to fulfil the requirements for the E_2/E_1 value. The use of different test procedures and calculation methods showed significantly different results in some but not all cases and should therefore be investigated further. Other comparisons were largely inconclusive, likely due to limited number of tests.

Keywords: Plate load test, bearing capacity, superstructure, compaction, road construction

1 INTRODUCTION

As with any investment, maximizing the service life of road structures is of great interest to society. One of the factors that influence the service life is the road's bearing capacity, which is greatly influenced by the quality of compaction (Mork, 2018). In order to ensure an adequate pavement life, national standards and guidelines define a minimum level of compaction of superstructure materials. The static plate load test (PLT) is one of the oldest and most commonly used tests to determine the quality of compaction of granular materials (Briaud, 2013).

DOI: 10.1201/9781003222897-2

The theory behind the test and its execution is generally similar wherever the test is performed, although each country determines its own test procedure, calculation method and minimum test result requirements. The PLT has been the compaction quality test of choice for the Norwegian Public Roads Administration (NPRA) since at least the 1980s, with both test procedure and corresponding requirements only changing slightly throughout the years (Statens vegvesen, Vegdirektoratet, 1980, 1984). However, the test only recently became mandatory as a final documentation of the compaction quality of granular pavement layers for Norwegian roads (Statens vegvesen, Vegdirektoratet, 2018a). Although the PLT has been used with the same test procedure and requirements for decades in Norway, some contractors have recently experienced difficulties in reaching the required test values (Brcic, 2018, Folkedal and Bryn, 2018). The reasons for these difficulties are unknown in most cases and have, to our knowledge, not been studied to any significant extent. The following research questions have therefore been posed: 1) Which in-situ factors affect the results of a PLT? 2) In what way do the superstructure materials and their in-situ conditions affect the results of a PLT? 3) In what way do the test procedure and the associated calculation method affect the results of a PLT? This paper is based on the work of the main author´s Master´s thesis at the Norwegian University of Science and Technology (NTNU) written in 2019 with financial contribution from the NPRA, and seeks to answer the posed research questions by studying PLTs conducted at construction sites in Norway.

2 THEORY

The PLT is performed by applying incremental loads on a circular steel plate placed on the material being tested, while measuring the corresponding settlements (Shukla and Sivakugan, 2011). The loads and settlements are used to calculate the material's modulus of elasticity, using equations based on Boussinesq's formula, given in equation (1). However, Boussinesq's formula assumes the loads are applied to a homogeneous, isotropic and linearly elastic half space (Verruijt, 2018), which is not true for the materials in a pavement.

$$s = \frac{1}{E} \cdot f \cdot \left(1 - \nu^2\right) \cdot p \cdot R \tag{1}$$

Here, s is the settlement at the centre of the plate [m], f is the stress distribution factor [], ν is the material's Poisson's ratio [], E is the material's modulus of elasticity [N/m^2], p is the applied loading pressure on the plate [N/m^2] and R is the plate's radius [m] (Ullidtz, 1987, 1998). The stress distribution factor varies based on the load distribution beneath the plate. For road construction, the load is generally assumed to be evenly distributed, making f = 2 (Monnet, 2015, Timoshenko and Goodier, 1970). Assuming the load is applied relatively fast, so water in the material does not drain during the test, the Poisson's ratio can be assumed to be 0,5 (Briaud, 2013), thus simplifying and rearranging Boussinesq's formula to equation (2).

$$E = \frac{3}{2} \cdot \frac{p}{s} \cdot R \tag{2}$$

Equation (2) is usually used as a basis for calculating the modulus of elasticity from PLT measurements, although the interpretation and use of the equation differs from one national standard to another. This will be discussed in section 2.2.

Boussinesq's formula can also be used to estimate how the stress and strain change with depth and distance from the centre of the plate during loading, thus also demonstrating the depth limits of a PLT. The stress below the centre of the plate is proportional to the plate's diameter, as well as the applied load, while also being inversely proportional to the depth from the plate to the point of interest (Das, 2010). The strain below the plate, however, is also dependent on the Poisson's ratio and the modulus of elasticity (Ullidtz, 1998). As expected, the changes in stress and strain are also inversely proportional to the horizontal distance from

the plate centre (Ahlvin and Ulery, 1962), resulting in the PLT mostly measuring the response of the volume of material closest to the plate.

To further complicate the change in stress and strain in pavements during a PLT, pavements are generally layered, constructed of materials with different properties. The change in stress and strain is therefore also dependent on the ratios between the different materials' moduli of elasticity, as well as the thickness of the layers. Thus, for layered structures with stiffer materials atop more elastic materials, the change in stress decreases more rapidly in the top layers, decreasing the effects of the load on the lower layers of the structure (Acum and Fox, 1951, Fox, 1948, Burmister, 1965, 1966).

2.1 *Plate load test in the field*

As previously mentioned, the assumptions of Boussinesq's formula do not apply to layered materials, and the basic theory is thus not directly applicable to PLTs conducted on pavements. This does not mean that it is unreasonable to apply the theory, but rather that the PLT results can be affected by more factors than the equation's input parameters. The factors can vary and be difficult to establish, but recent research has tried to identify which factors influence the PLT results and to what extent.

The size of the plate was identified in one study as a possible affecting factor, where larger plates lead to larger settlements. Other studies have found that the plate size has a limited effect on the PLT results (Araújo et al. 2017). Both findings are, however, inconclusive and not easily transferable, due to the limited number of tests in the studies. The use of levelling materials could also have an effect on the PLT results. Specifically, this applies to the use of gypsum plaster, as some studies have found that its use results in higher E values compared to tests without levelling materials (Barnard and Heymann, 2015, Fladvad, 2012). This is especially apparent for the E_1 values, as the E vaules become more similar with increased compaction (Fladvad, 2012). However, the limited number of cases makes these results difficult to transfer to other situations, and more research is needed to draw substantial conclusions. The grain size distribution of the tested materials has been found to affect the results of PLTs, where open-graded materials with low fines content give higher E_2 values compared to more well graded materials (Choi et al., 2018). However, this claim also requires more testing due to the limited number of tests.

The transferability of any PLT results to other PLTs is also questionable, as studies have found that the plastic deformation and the compaction of the material during the test make the results dependent on the loading history of the material (Dasaka et al., 2014, Adam et al., 2009). This means that the results are affected by both the maximum load applied during the test, as well as each of the loading increments, not only in magnitude, but also consistency and duration (Dasaka et al., 2014). Due to this dependency on the load history and other in-situ factors, it can be argued that the modulus of elasticity determined by the PLT is not a pure material parameter (Adam et al., 2009), and the test results are highly dependent on the test procedures. For a meaningful comparison of PLT results, it is therefore essential that the PLTs are conducted in the exact same manner (Dasaka et al., 2014, Adam et al., 2009).

2.2 *National standards and guidelines*

The requirements for PLTs conducted on Norwegian pavements are defined in NPRA handbooks N200 and R211, which describe the result requirements and test procedure, respectively. The latest versions of the handbooks were published in 2021, although the PLT requirements have not changed from the 2018 versions (Statens vegvesen, Vegdirektoratet, 2014a, 2014b, 2018a, 2018b, 2021a, 2021b). As the cases discussed in section 3 used the 2014 and 2018 versions, only those two versions of the handbooks will be discussed here. The PLT was first defined as the only method for final documentation of compaction quality for granular materials in superstructures in 2014 (Statens vegvesen,Vegdirektoratet, 2014a).

The Norwegian test procedure described in R211 uses equation (3) to calculate the modulus of elasticity (Statens vegvesen, Vegdirektoratet, 2014b).

$$E = \frac{3}{4} \cdot \frac{\Delta p}{\Delta s} \cdot D \tag{3}$$

Here, E is the material's modulus of elasticity for the loading cycle in question [MPa], Δp is the difference between two measurements of loading pressure on the plate [kN/m^2], Δs is the difference between the two corresponding measurements of settlement in the centre of the plate [mm], and D is the plate's diameter [m]. The test plate should have a 0,3 m diameter, and a thin levelling layer of gypsum plaster must be used. The load is applied in two loading cycles, each of which has five loading steps; 50, 180, 300, 420 and 600 kN/m^2, during which the load should be kept constant until the changes in settlement have ceased or until the settlement is 0,02 mm/min or less. The load is removed slowly before the second loading cycle is performed. The measured loading pressures and settlements from both loading cycles are plotted in a load pressure-settlement diagram. The results are used to calculate the modulus of elasticity for each loading cycle, E_1 and E_2, using equations (4) and (5) as input values for equation (3) (Statens vegvesen, Vegdirektoratet, 2014b).

$$\Delta p = p_2 - p_1 \tag{4}$$

$$\Delta s = s_2 - s_1 \tag{5}$$

Here, Δp is the difference between two loading pressure measurements [kN/m^2], p_2 is the loading pressure corresponding to 70 % of the maximum applied load for the first loading cycle, and the last load step where the relationship between loading pressure and settlement can be approximated by a straight line for the second loading cycle [kN/m^2], p_1 is the loading pressure corresponding to 30 % of the maximum applied load [kN/m^2], Δs is the difference between two settlement measurements [mm], s_2 is the settlement corresponding to p_2 [mm] and s_1 is the settlement corresponding to p_1 [mm] (Statens vegvesen, Vegdirektoratet, 2014b). In the 2018 version of R211, the use of a levelling material is omitted, and an additional loading step of 500 kN/m^2 has been added (Statens vegvesen, Vegdirektoratet, 2018b). The Norwegian PLT result requirements are defined for single measurements, and all PLTs must fulfil the requirements for the road section to be approved. The required values are similar in the 2014 and 2018 versions of N200 (Statens vegvesen, Vegdirektoratet, 2014a, 2018a).

The requirements for PLTs conducted on pavements in Sweden are defined in the Swedish Transport Administration documents TDOK 2013:0530 and TDOK 2014:0141, which describe the result requirements and test procedure, respectively (Trafikverket, 2014, 2017).

The Swedish procedure is based on the German standard DIN 18134 (Trafikverket, 2014), and permits the use of three plate sizes, though only a 0,3 m plate diameter should be used for pavements (Trafikverket, 2014). As the field test discussed in section 3 includes plates of both 0,3 m and 0,6 m diameter, requirements for both sizes will be discussed here. Only the test procedures for the 0,3 m diameter plate is described in the Swedish documents, so values for 0,6 m diameter plates are supplemented with the suggested values in the German standard (Deutsches Institut Für Normung, 2012). The Swedish procedure permits the use of fine levelling sand, but does not require it. The loading steps are seven and should be kept constant for at least 1 min (2 min for the first loading step) or until changes in settlement have ceased. The loading steps are as follows for the two plate sizes; 80, 160, 240, 320, 400, 450 and 500 kN/m^2 for the 0,3 m diameter plate (Trafikverket, 2014) and 20, 40, 80, 120, 160, 200 and 250 kN/m^2 for the 0,6 m diameter plate (Deutsches Institut für Normung, 2012). Off-loading is performed in three steps; 50%, 25% and 0% of the maximum load. The last load step is omitted for the second loading cycle. The measured loading pressures and settlements from each loading cycle are plotted in a graph and approximated with a second degree polynomial function, equation (6), whose constants a_1 and a_2 are used in equation (7) to calculate the modulus of elasticity for each loading cycle (Trafikverket, 2014).

$$s(\sigma_0) = a_0 + a_1\sigma_0 + a_2\sigma_0^2 \tag{6}$$

Here, $s(\sigma_0)$ is the approximated settlement under the centre of the plate [mm], σ_0 is the average normal loading pressure below the plate [MN/m^2], and a_0, a_1 and a_2 are constants determined by the method of least squares.

$$E = 1,5 \cdot R \cdot \frac{1}{a_1 + a_2\sigma_{1max}} \tag{7}$$

Here, E is the material's modulus of elasticity for the loading cycle in question [MPa], R is the plate's radius [mm], a_1 and a_2 are the constants of equation (6), and σ_{1max} is the maximum normal loading pressure of the first loading cycle [MN/m^2] (Trafikverket, 2014).

The Swedish requirements are defined for single measurements, as well as for a set of either 8 or 5 measurements. The requirements for the E_2 value are defined for the average of the set of E_2 values and are calculated based on the standard deviation of the set. The requirements for the ratio E_2/E_1 are defined for each point, although only n – 1 of the measurements must fulfil that requirement. All of the measured points must, however, reach a minimum value for E_2 to be considered a valid measurement (Trafikverket, 2017).

3 METHODS

Several research methods were chosen to attempt to answer the posed research questions. An inductive case study, studying the results of PLTs conducted at four different road construction sites in Norway, was used to compare PLT results conducted under different conditions. Additional interviews with experienced test performers were conducted to identify suspected influential factors to PLT results, and files containing measurements from PLTs were collected to compare three different calculation methods. Finally, a field test was conducted to compare the effect of superstructure materials and plate size.

The cases were chosen based on responses to a recruitment e-mail sent to contractors and road owners of ongoing Norwegian road construction projects. The sites included in the case study are all of those that responded, where the planned performance of PLTs correlated with the limited time frame of the study. To include both qualitative and quantitative data, and to increase the credibility of the results, three different methods were chosen to collect data; interviews, in-situ observations and a collection of data files.

The data files collected were mainly load and settlement measurements of PLTs conducted on the site, but additional information such as in-situ conditions during the PLTs were also collected. The data was requested during an in-person meeting and handed over as a hard copy or digital files sent by e-mail. The measurements were used to calculate the E values using three calculation methods:

- Norwegian method 1 (NOR1), using equation (3) and measurements for the last load step as input values to calculate E_2
- Norwegian method 2 (NOR2), using equation (3) and measurements for the second to last load step as input values to calculate E_2
- The Swedish method (SWE), using equation (7).

Where possible, additional in-situ observations were conducted, either during on site PLT measurements or by general field observations. The information was noted down during or directly after the observations, and used as supplementary information when analysing the PLT results or the interview data.

Representatives from the contractor and/or road owners of the four cases were interviewed using a semi-structured interview. The interviewees were recruited as part of the recruitment process for the general case study, and the interviews were conducted privately in the interviewee's place of work or at a neutral setting. Key elements of the transcript were identified using keywords relevant to the research questions.

Site 1 is a tunnel project in former Hordaland county, with a 22/120 mm crushed rock subbase and a 0/32 mm crushed asphalt interlocking layer (Ak). There are two tunnels, one of which has

deep trenches (Tunnel 1), but both tunnels have a humid climate and relatively stable temperatures above freezing. Site 2 is an upgrade project of an urban road with high traffic volumes in former Østfold county, and is mainly constructed on existing pavements and established urban areas. The pavement has a subbase of 22/120 mm crushed rock and an interlocking layer of 0/32 mm Ak. Site 3 is a new motorway project in relatively undisturbed and greatly varying terrain in former Aust-Agder county. The pavement has a subbase of 22/120 mm crushed rock and an interlocking layer of 0/32 mm crushed rock (Fk). Site 3 changed mid construction from the 2014 to the 2018 version of the Norwegian handbooks, while the other sites used the 2014 version during the entire construction period. Site 4 is a motorway upgrading project in former Hedmark county, where the road is constructed upon the existing pavement or on its side terrain. The pavement has a frost protection layer of 0/250 mm crushed rock, a subbase of 22/120 mm crushed rock and an interlocking layer of 0/32 mm Ak. A section of the site has problematic subsoil, and an alternative superstructure, containing an insulation layer of XPS boards, was used there to eliminate the need for subsoil replacement.

As a supplement to the case study, additional interviews were conducted with experienced performers of PLTs in Norway. The interviews were conducted similarly to the interviews of the case study, except case specific questions were generalized. Additional PLT measurements were also obtained for sites outside of the case study (site 5 to 10), which were collected and treated similarly as the measurements of the case study.

In collaboration with the NPRA and Skanska AS, a field test was conducted in the spring of 2019 at the site of the road project Rv. 3/Rv. 25 Løten-Elverum in former Hedmark county. A total of 24 PLTs were conducted using two plate sizes and two test procedures, 0,3 m diameter according to the 2018 version of R211, and 0,6 m diameter according to DIN 18134. Three different superstructures were tested; 1) a frost protection layer of 0/300 mm crushed rock, 2) a subbase of 22/120 mm crushed rock on top of superstructure 1), and 3) an interlocking layer of 0/32 mm Fk on top of superstructure 2). Four PLTs of each plate size were conducted on each of the superstructures. The measurements from these PLTs were treated in the same manner as the measurements collected in the case study.

4 RESULTS

The results of the case study interviews are extensive and out of the scope of this paper, and will therefore not be discussed in detail. The most important influential factors mentioned by the interviewees were the moisture in the superstructure, the time between compaction and testing, the use of Ak, the fines content of the interlocking layer, the grain size and distribution of the subbase, and the use of light-weight materials. All test performers used the automatic calculations of the load-settlement measuring software to determine the E values, and some were not aware of the existence of different calculation methods. Most sites used Norwegian and Swedish test procedures and calculation methods almost interchangeably, and some even used a plate diameter of 0,6 m, though not for final documentation. Many of the contractors and road owners had an agreement on the minimum number of approved PLTs before paving was permitted. All available information for site 2 was obtained through documents, as no interviews were conducted for this site. The documents suggest that the subbase material may have been coarser than the conventional 22/120 mm material.

The calculated values from PLT measurements of the case study are provided in Figure 1. The statistical significance of the difference between calculation methods is presented in Table 1. Five results from site 2 are omitted as they were performed after additional compaction efforts. Measurements S4-M1 to S4-M5 at site 4 were conducted on a superstructure with XPS, while measurements S4-M6 to S4-M11 were conducted where there was no XPS. The statistical significance of the difference between E values using different test procedures, plate sizes, superstructure materials, and a comparison of sites based on possibly influential factors is presented in Table 2.

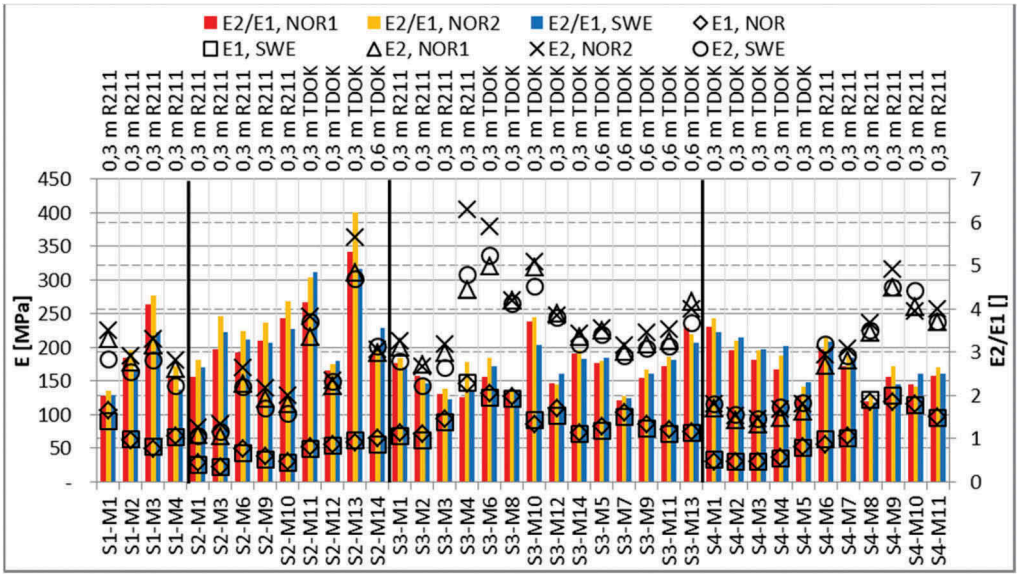

Figure 1. Calculated PLT results of the case study, using Norwegian method 1 and 2 and the Swedish method described in section 3. The number after S refers to site number, the number after M refers to measurement number at each site.

As for the case study interviews, the additional interviews are too extensive for the scope of this paper, and will not be discussed in detail. In addition to the influential factors for PLTs identified in the case study interviews, the additional interviewees also mentioned the standard of work at the construction site, the strictness of the Norwegian requirements, and the changes made to other requirements in the handbooks, e.g. regarding the grading curve of the subbase materials. Additionally, the interviewees regarded the lack of consequences for not fulfilling the PLT requirements as lack of incentive for contractors to change work procedures to reach adequate results.

Figure 2 presents the calculated PLT results for the additional measurements obtained outside of the case study. Due to limited number of tests and insufficient information about the construction sites, only the calculation methods are compared for these tests. The statistical significance of the difference between E values using different calculation methods is presented in Table 1.

The calculated results for the PLTs conducted during the field test are presented in Figure 3. Point P11C is omitted from the presented results due to an error in the measuring equipment that lead to the measurements not being registered. The statistical significance of the difference between E values using different calculation methods is presented in Table 1. The statistical significance of the difference between E values using different test procedures, plate sizes, superstructure materials, as well as a comparison of sites based on possibly influential factors is presented in Table 2.

5 DISCUSSION

As already established, the PLT is based on theoretical assumptions that don't apply for pavements. The test only measures the response of the material at the top of the superstructure, and thus gives limited indication on the compaction quality of lower layers. The effect of a PLT also decreases rapidly with horizontal distance, and the test consequently only measures compaction quality at a single point. Other methods are likely more suited to indicate the evenness

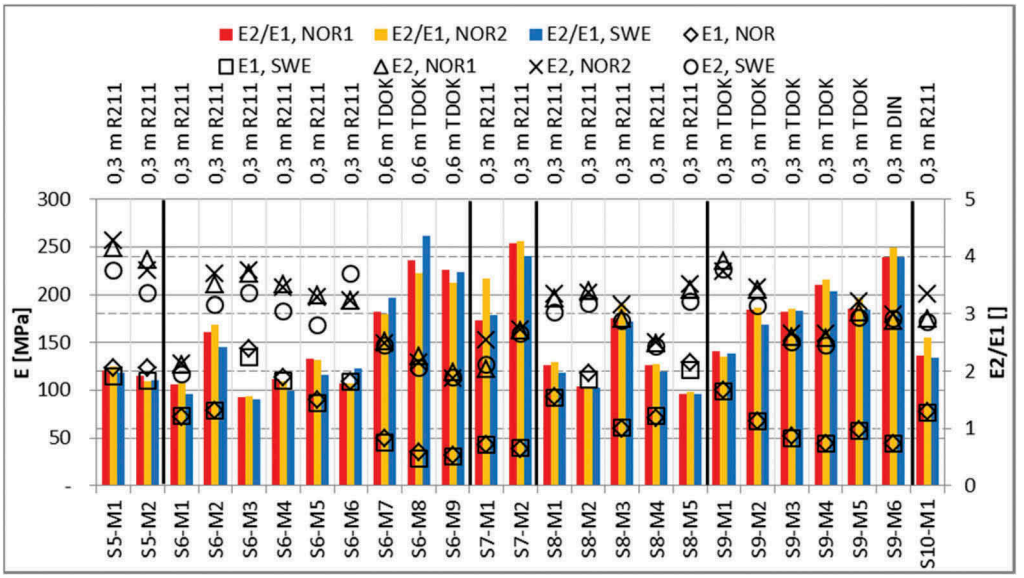

Figure 2. Calculated PLT results from sites outside of the case study, using Norwegian method 1 and 2 and the Swedish method described in section 3. The number after S refers to site number, the number after M refers to measurement number at each site.

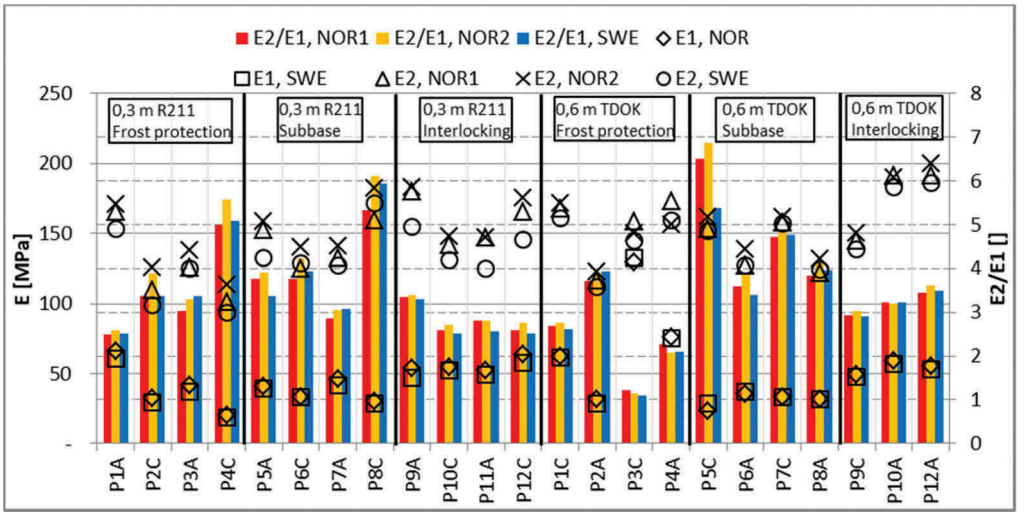

Figure 3. Calculated PLT results from the field test, using Norwegian method 1 and 2 and the Swedish method described in section 3. The number in the point name refers to the column number, and the end letter refers to the row name of the test grid.

of compaction over an area, and it thus seems counterintuitive that the PLT is chosen as the only available method for final documentation of compaction quality.

Even though the Norwegian requirements and procedure for PLTs have not changed much for decades, requirements for other elements of the construction process that can affect PLT results have been changed, such as the requirements for the grading curve of the subbase material. Furthermore, the slight changes to the Norwegian PLT procedure that have been

Table 1. An overview of the statistical significance of the difference between calculation methods at a 95 % confidence level.

	Site	1	2		3			4		5	6		7	8	9	Field test						
	Procedure / Comp.: Calculation method	0,3 m R211	0,3 m R211	0,3 m TDOK	0,3 m R211	0,3 m TDOK	0,6 m TDOK	0,3 m R211*	0,3 m TDOK**	0,3 m R211	0,3 m R211	0,6 m TDOK	0,3 m R211	0,3 m R211	0,3 m TDOK	Frost prot.	0,3 m R211	Subbase	0,3 m R211	Interlocking	0,3 m R211	Frost prot.	0,6 m TDOK	Subbase	0,6 m TDOK	Interlocking	0,6 m TDOK
E_1	NOR vs SWE	○	●	○	○	○	●	○	○	○	○	○	○	○	○	●		○		●		○		○		●	
E_2	NOR1 vs SWE	●	○	○	○	○	○	○	●	○	○	○	○	●	●	●		○		●		●		○		●	
	NOR2 vs SWE	●	●	●	○	○	●	○	○	○	○	○	○	●	●	●		●		●		○		●		●	
	NOR1 vs NOR2	●	●	○	○	○	○	●	●	○	○	○	○	○	○	●		●		○		○		●		○	
	● = Statistically significant difference at a 95 % confidence level																										
	○ = No statistically significant difference at a 95 % confidence level																										

*Conducted on a superstructure without XPS
**Conducted on a superstructure with XPS

Table 2. An overview of the statistical significance of the difference between test procedures and in-situ conditions at a 95 % confidence level.

	Calculation method	E_1		E_2		
Site	Comparison:	NOR	SWE	NOR1	NOR2	SWE
2	0,3 m R211 vs 0,3 m TDOK	●	●	○	○	○
3	0,3 m R211 vs 0,3 m TDOK	●	●	●	●	●
3	0,3 m TDOK vs 0,6 m TDOK	○	○	○	○	○
3	0,3 m R211 vs 0,6 m TDOK	○	●	○	○	○
4	0,3 m R211* vs 0,3 m TDOK**	●	●	●	●	●
3/4	**Fk** (Site 3, 2014) vs **Ak** (Site 4*)	○	●	○	○	●
3/4	**Fk** (Site 3, 2018) vs **Ak** (Site 4*)	○	○	○	○	○
1/4	**Moist Ak** (Site 1, Tunnel 2) vs **Dry Ak** (Site 4*)	○	○	○	○	●
1/4	**Moist Ak** (Site 1, Tunnel 1) vs **Dry Ak** (Site 4*)	○	●	○	○	○
1/3	**Moist Ak** (Site 1, Tunnel 2) vs **Dry Fk** (Site 3,2014)	○	○	○	○	○
1/3	**Moist Ak** (Site 1, Tunnel 1) vs **Dry Fk** (Site 3,2014)	○	○	○	○	○
1/3	**Moist Ak** (Site 1, Tunnel 2) vs **Dry Fk** (Site 3,2018)	○	○	○	○	○
1/3	**Moist Ak** (Site 1, Tunnel 1) vs **Dry Fk** (Site 3,2018)	○	○	○	○	○
2/4	**Coarse subbase** (Site 2 R211) vs **Normal subbase** (Site 4 R211*)	●	●	●	●	●
Field test	Frost protection layer: 0,3 m R211 vs 0,6 m TDOK	○	○	○	○	○
	Subbase: 0,3 m R211 vs 0,6 m TDOK	○	○	○	○	○
	Interlocking layer: 0,3 m R211 vs 0,6 m TDOK	○	○	○	○	○
	0,3 m R211: Frost protection vs Subbase	○	○	○	○	○
	0,6 m TDOK: Frost protection vs Subbase	○	○	○	○	○
	0,3 m R211: Frost protection vs Interlocking	○	○	○	○	○
	0,6 m TDOK: Frost protection vs Interlocking	○	○	○	○	○
	0,3 m R211: Subbase vs Interlocking	●	●	○	○	○
	0,6 m TDOK: Subbase vs Interlocking	●	●	○	○	○
	● = Statistically significant difference at a 95 % confidence level					
	○ = No statistically significant difference at a 95 % confidence level					

*Conducted on a superstructure without XPS
**Conducted on a superstructure with XPS

made can also affect the results, especially the change in use of gypsum plaster levelling material. Additionally, the E_2 results from the Norwegian calculation method are dependent on the

test performer's interpretation of linearity. The method is relatively easy to understand, but it is vulnerable to small errors in the four measurements used to calculate the E values. An error in measured settlement as small as 0,01 mm for one measurement can determine the difference between an adequate or an inadequate PLT result. As all PLTs must fulfil the Norwegian requirements, a single settlement error of 0,01 mm can thus determine if an entire road section is deemed acceptable or not. The Swedish calculation method is less susceptible to small errors in measurements as it is based on an approximation of all measurements. Most contractors in Norway work by a deviance acceptance system approved by the road owner, as it is generally considered unrealistic for all PLTs to fulfil the requirements. To ensure that all pavements are constructed with the same level of deviance from requirements, it might be more appropriate to define in the handbooks what is an acceptable deviation. Strict requirements and no deviation tolerance could lead to cases of data manipulation and/or underreporting, although this seems unlikely with current routines, as there are often little to no consequences for not fulfilling PLT requirements.

In the field, the calculation method is generally decided by the load-settlement measuring software. Consequently, results are often calculated using different methods. The software usually uses either Norwegian method 1 or a variation of the Swedish method, and the interpretation factor of the Norwegian procedure is thus omitted. Multiple test procedures are also used in the field, making comparison of results difficult. As there can be a statistically significant difference between results using different calculation methods or test procedures, it is essential that test performers use the correct procedure when comparing PLT results to requirements. Only results from PLTs performed using the Norwegian test procedure and calculation method should be compared to the Norwegian requirements.

6 CONCLUSION

Multiple in-situ factors were identified as possible culprits to inadequate PLT results. The ones most often mentioned in the interviews were high moisture content in the superstructure, short time between compaction and testing and the use of Ak and insulation or light-weight materials in the superstructure. None of the factors have been confirmed to affect the results in this study, and further testing is required in order to test these claims.

The field test measurements suggest that the use of an interlocking layer leads to higher E_1 values compared to measurements conducted directly on the subbase, regardless of the plate size. No statistically significant difference was found for E_2 values conducted on the interlocking layer compared to directly on the subbase, suggesting that the interlocking layer is important for keeping the E_2/E_1 values below the maximum limit. The comparison of different superstructure materials in the case study is generally inconclusive, probably due to the limited number of tests. The E values at site 2 were significantly lower than at site 4, potentially due to the larger grain size in the subbase, although other factors can also have affected the results. At site 4, the E values for PLTs conducted on superstructures containing XPS were significantly lower than for superstructures without XPS, although the difference might also be linked to the use of two different test procedures.

The number of comparable PLT results in the study is restricted by the limited number of tests conducted under similar conditions with the same test procedure and plate size. The difference between results from the different calculation methods is statistically significant for some cases, but not all. The same can be said for the three test procedures (Norwegian 0,3 m diameter, and Swedish 0,3 m and 0,6 m diameter). This suggests that there are more factors that affect the results than the calculation method and test procedure alone, although it is also possible that this stems from inconsistency in the test performance.

The research questions posed are quite broad and not easily answered. Further research is therefore needed in order to answer them sufficiently. A recommendation for future studies on the topic includes analysing the effect of moisture content in the superstructure, as well as the time between compaction and testing. Comparing the effect of using Ak or Fk in the superstructure is also recommended, specifically determining if the moisture

content and time between compaction and testing affects the materials differently. Additionally, a further analysis of the difference between calculation methods and test procedures is recommended. Finally, studying the effect of insulation or light-weight materials in the superstructure on PLT results is also recommended.

The PLT is an important quality assurance test for the compaction of Norwegian pavements. The test results give a certain indication to the quality of compaction of the granular superstructure materials, thus giving an indication of the pavement's bearing capacity and service life. To limit the need for untimely road reconstruction, it should therefore be a priority to ensure that the national PLT requirements are adequate and realistic, and that these are fulfilled on the construction sites. Solving the challenges with fulfilling PLT requirements is thus an important step in optimizing the use of society's resources, and should be prioritized in further research.

REFERENCES

Acum, W. E. A. and Fox, L. 1951. *Computation of Load Stresses in a Three-Layer Elastic System*. Géotechnique, 2, 293–300.

Adam, C., Adam, D., Kopf, F. and Paulmichl, I. 2009. *Computational validation of static and dynamic plate load testing*. Acta Geotechnica, 4, 35–55.

Ahlvin, R. G. and Ulery, H. H. 1962. *Tabulated values for determining the complete pattern of stresses, strains, and deflections beneath a uniform circular load on a homogeneous half space*. Highway Research Board Bulletin.

Araújo, D. A. M., Costa, C. M. L. and Costa, Y. D. J. *Dimension effect on plate load test results*. World Congress on Civil, Structural, and Environmental Engineering, 2017 Barcelona, Spain. Avestia Publishing.

Barnard, H. F. T. and Heymann, G. 2015. *The effect of bedding errors on the accuracy of plate load tests*. Journal of the South African Institution of Civil Engineering, 57, 67–76.

Brcic, H. 2018. *Komprimeringskontroll*. Teknologidagene 2018. Trondheim: Statens vegvesen.

Briaud, J. L. 2013. *Geotechnical Engineering: Unsaturated and Saturated Soils*. Hoboken, New Jersey, USA: John Wiley and Sons, Inc.

Burmister, D. M. 1965. *Influence diagrams for stresses and displacements in a two-layer pavement system for airfields. Part 1*. In: U. S. Dept of the Navy and Columbia Univ New York Dept of Civil Engineering and Engineering Mechanics (eds.). Defense Technical Information Center.

Burmister, D. M. 1966. *Influence diagrams for stresses and displacements in three-layer pavement systems for airfields. Part 2*. In: U. S. Dept of the Navy and Columbia Univ New York Dept of Civil Engineering and Engineering Mechanics (eds.). Defense Technical Information Center.

Choi, Y. J., Ahn, D., Nguyen, T. H. and Ahn, J. 2018. *Assessment of field compaction of aggregate base materials for permeable pavements based on plate load tests*. Sustainability (Switzerland), 10, 1–13.

Das, B. M. 2010. *Principles of Geotechnical Engineering, SI edition*. 7th ed. Stamford, USA: Cengage Learning.

Dasaka, S. M., Jain, A. and Kolekar, Y. A. 2014. *Effect of Uncertainties in the Field Load Testing on the Observed Load-Settlement Response*. Indian Geotechnical Journal, 44, 294–304.

Deutsches Institut Für Normung. 2012. *Soil - Testing procedures and testing equipment - Plate load test, English translation of DIN 18134: 2012-04*[Online]. Berlin, Germany: Deutsches Institut für Normung. Available: http://insitutest.com.au/wp-content/uploads/2015/02/Determining-thedeformation-and-strength-characteristics-of-soil-by-the-plate-loading-test-DIN18134-2012.pdf [Accessed 18. December 2018].

Fladvad, M. 2012. *Kontinuerlig komprimeringskontroll*. Master's thesis, NTNU.

Folkedal, L. A. and Bryn, N. 2018. *Komprimeringskontroll - Erfaringer fra E39 K10 Svegatjørn - Rådal*. Teknologidagene 2018. Trondheim: Veidekke.

Fox, L. 1948. *Computation of Traffic Stresses in a Simple Road Structure*. D.S.I.R., Road Res. Tech. Paper No. 9.

Monnet, J. 2015. *In situ tests in geotechnical engineering*. Hoboken, NJ: Wiley.

Mork, H. 2018. *Bereevne for eksisterande veg*. Notat 991. Norge: Institutt for veg- og jernbanebygging, NTNU.

Shukla, S. K. and Sivakugan, N. 2011. *Site Investigation and in situ Tests*. In: Das Braja, M. (ed.) Geotechnical engineering handbook. Florida, USA: J. Ross Publishing, Inc.

Statens Vegvesen, Vegdirektoratet 1980. *018 Vegbygging*. Oslo: Vegdirektoratet.

Statens Vegvesen, Vegdirektoratet 1984. *015 Feltundersøkelser*. Oslo: Statens vegvesen.

Statens Vegvesen, Vegdirektoratet 2014a. *N200 Vegbygging*. Oslo: Statens vegvesen.

Statens Vegvesen, Vegdirektoratet 2014b. *R211 Feltundersøkelser*. Oslo: Statens vegvesen.
Statens Vegvesen, Vegdirektoratet 2018a. *N200 Vegbygging*. Oslo: Statens vegvesen.
Statens Vegvesen, Vegdirektoratet 2018b. *R211 Feltundersøkelser*. Oslo: Statens vegvesen.
Statens Vegvesen, Vegdirektoratet 2021a. *N200 Vegbygging*. Oslo: Statens vegvesen.
Statens Vegvesen, Vegdirektoratet 2021b. *R211 Feltundersøkelser*. Oslo: Statens vegvesen.
Timoshenko, S. P. and Goodier, J. N. 1970. *Theory of elasticity*. 3rd ed. New York: McGraw-Hill.
Trafikverket 2014. *TDOK 2014: 0141Bestämning av bärighetsegenskaper med statisk plattbelastning*. Trafikverket.
Trafikverket 2017. *TDOK 2013: 0530Obundna lager för vägkonstruktioner*. Trafikverket.
Ullidtz, P. 1987. *Pavement analysis*. Amsterdam: Elsevier.
Ullidtz, P. 1998. *Modelling Flexible Pavement Response and Performance*. Lyngby, Denmark: Polyteknisk Forlag.
Verruijt, A. 2018. *An Introduction to Soil Mechanics*. Cham, Switzerland: Springer International Publishing: Imprint: Springer.

Case histories of roads, railways and airfields

Eleventh International Conference on the Bearing Capacity of Roads, Railways and Airfields, Volume 2 – Hoff, Mork & Saba (eds)

Improving the bearing capacity and all-weather trafficability of Australian soils

A.B. McCallum & J. Yeaman
School of Science, Technology and Engineering, University of the Sunshine Coast, Sippy Downs, Queensland, Australia

M. Farrar
Quantum Ground Stabilisation Pty Ltd, Norman Park, Queensland, Australia

E. Urbaez
Pavement Management Services Pty Ltd, Warana, Queensland, Australia

ABSTRACT: Queensland is a large state in Australia with a wet/dry climate that supports soil types known as vertosols, that are extremely active. A research program was initiated between University of the Sunshine Coast and industry (Quantum Ground Stabilisation Pty Ltd (QGS) and Pavement Management Services Pty Ltd (PMS)) to assess the efficacy of soil stabilisation products to enhance traditionally problematic vertosols. Tested products were shown to improve bearing capacity and inhibit water movement within treated pavements; additionally, back-analysis showed an increase in pavement modulus with time. QGS products appear to improve the trafficability of problematic vertosol soils in Queensland; further assessment is recommended to validate these findings.

Keywords: Trafficability, bearing capacity, soil stabilization, modulus

1 INTRODUCTION

The state of Queensland, Australia, is large and diverse. It is nearly five times the area of Japan, seven times the area of Great Britain and two and a half times the size of Texas. A large portion of the state is dominated by what is known colloquially as "Black Soil", technically "Vertosols" (Figure 1).

Vertosols can be black or grey, in colour, and are characterized by:

1. widespread cracking when dry,
2. commonly form a hummocky relief called gilgai,
3. very high soil fertility,
4. large water holding capacity,
5. good bearing capacity when dry, and
6. impassable when wet.

The climate of Queensland is frequently described as two seasons, "wet" and "dry", with occasional cyclones bringing heavy rain in what is colloquially known as "the Knock-'em downs", torrential rain causing wide spread flooding.

DOI: 10.1201/9781003222897-3

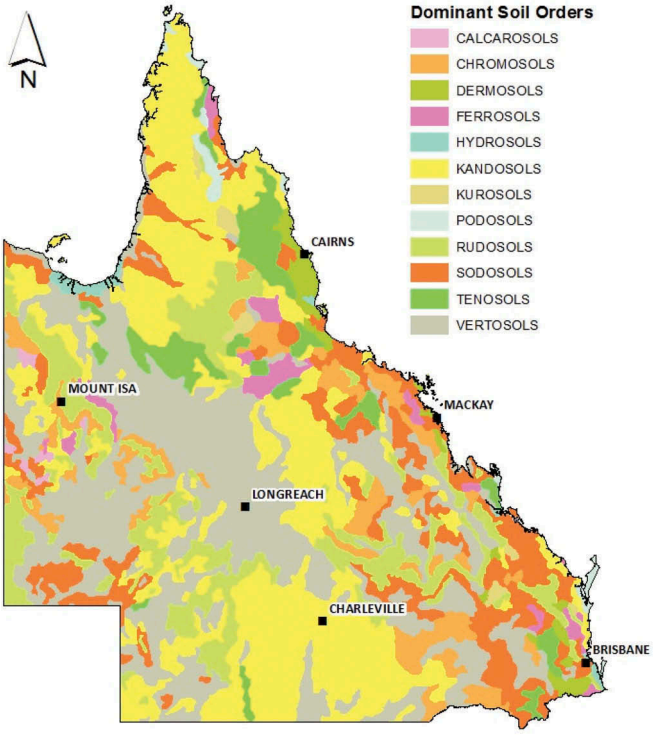

Figure 1. Dominant soil types across Queensland (Queensland Government, 2013).

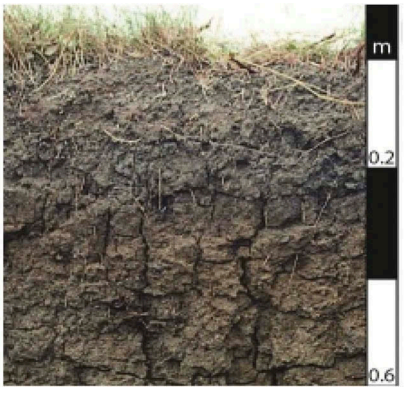

Figure 2. An example of vertosol soil, to a depth of 0.6 m from Beaudesert, Queensland (Queensland Government, 2013).

Central Queensland is currently amidst a construction boom, with major projects underway in road, rail and hard standing (wind and solar farms). It is within this context that the University of the Sunshine Coast (USC) in association with Quantum Ground Stabilisation (QGS) and Pavement Management Services (PMS) initiated research to understand the efficacy of soil stabilisation products for in situ improvement of the all-weather accessibility and bearing capacity of this marginal group of soils. This work provides a foundation for

QGS to seek accreditation for their products under the Transport Infrastructure Product Evaluation Scheme (TIPES) administered by the Australian Road Research Board (ARRB).

In this study, we outline the claims of the QGS products and summarise work undertaken to assess the efficacy of these products in improving the bearing capacity and all-weather trafficability of Australian soils.

2 CLAIMS OF THE QUANTUM PRODUCTS

The Quantum System is a chemical substance which breaks up the soil-adhering water film, leading to an irreversible agglomeration of fines, thus substantially reducing the capillary rise of water within unbound granular materials. This allows better compaction of the treated soil and increases required density under traffic when compared with untreated soil (Quantum (Australia), 2021). Quantum products in both liquid and powder form were used. The liquid product claims the following characteristics (Quantum (Australia), 2021):

1. improves compactability by changing the water absorption characteristics of the soil,
2. reduction of water absorption by reducing the capillary activity,
3. reduced water permeability,
4. Optimum Moisture Content (OMC) of treated soil is lower and the density is higher, and
5. a strong reduction in swelling and shrinking behaviour.

The dry, inorganic powdered product claims the following characteristics (Quantum (Australia), 2021):

1. prevents the treated soil from water ingression by closing the capillaries, and
2. water absorption capacity is reduced, restricting the swelling behaviour of the soil.

The Quantum System claims advantages over traditional cement and lime additives (Quantum (Australia), 2021) including:

1. absence of curing time; dress, heavy roll and immediately useable,
2. mixed soil can be stored for unlimited time and remain fully effective,
3. environmentally safe and compatible, and
4. easy to apply in the field.

The following characteristics are additionally claimed by the Quantum System (Quantum (Australia), 2021):

1. enhances bearing capacity of natural gravels and soils for road making purposes;
2. it is not a cementing agent, thus is not prone to shrinkage, it can be reworked, and it can be stockpiled;
3. it improves bearing capacity by increasing material strength and reducing permeability;
4. it works with any type of soil because it activates the cohesive forces of the soil and substantially and lastingly reduces the influence of water;
5. it modifies the soil permanently and is used in-situ or via premixing;
6. it enables reduction of wearing-course thickness;
7. it has been proven globally (Switzerland etc.) for more than forty years; and
8. construction practice and application rates are invariable.

For optimum results, Quantum (Australia; 2021) suggest that the parent material should be composed of one third gravel, one third sand and one third silt and clay, to generate material with the following characteristics (Table 1):

Table 1. Particle Size Distribution characteristics of optimum parent material.

AS Sieve Size (mm)	Minimum % Passing	Maximum % Passing	PSD Category
37.5	100	100	Gravel
19	80	100	
9.5	55	90	
4.75	40	70	Sand
2.36	30	55	
0.425	12	30	Silt and Clay
0.075	5	20	

Additionally, the following criteria should ideally be met:

- Lower Liquid Limit > 25,
- Lower Plastic Limit > 18,
- Plasticity Index >10,
- Free from deleterious substances,
- Free from excess organic matter, and
- Free from high concentrations of sulphate ions.

Where in-situ soils diverge from the preferred one third each clay, gravel and sand, the capillary rise of the parent material can be assessed in-house by the so-called "Brick Test" to determine the need for any additional components.

3 STUDIES CONDUCTED TO ASSESS PRODUCT EFFICACY

Efficacy of the Quantum products was assessed over a five year period from 2015 through 2019 at University of the Sunshine Coast and proximate field locations, in various scenarios.

Fitzpatrick (2015)
In 2015, Fitzpatrick examined the effect of the Quantum group of products with three local subgrade materials:

- Image Flat quarry overburden,
- Obi Obi Quarry overburden, and
- Moy's Pocket 2.3 road base.

He studied sample Resilient Modulus after compaction at OMC, testing three samples of each material under repeat loading of 90 min duration in accordance with AS1289.6.8.1 (1995). Results (Table 2) were inconclusive, largely because of equipment malfunctioning; but, they did demonstrate that for best results, some mechanical stabilisation is required and that equal components of gravel, sand and clay should be adopted for optimum results.

Table 2. Average Resilient Modulus under repeated load for three un/treated materials.

Material	Untreated modulus (MPa)	Treated modulus (MPa)
Image Flat overburden*	646	538
Obi Obi subgrade	471	637
Moy's quarry overburden *	494	318

*No gravel component.

Fitzpatrick's findings drove the recommendation to insist on a minimum of a Queensland Main Road Type 2.5 subbase as the requisite gradation curve (Figure 3), for use in road bearing capacity and all-weather access improvement.

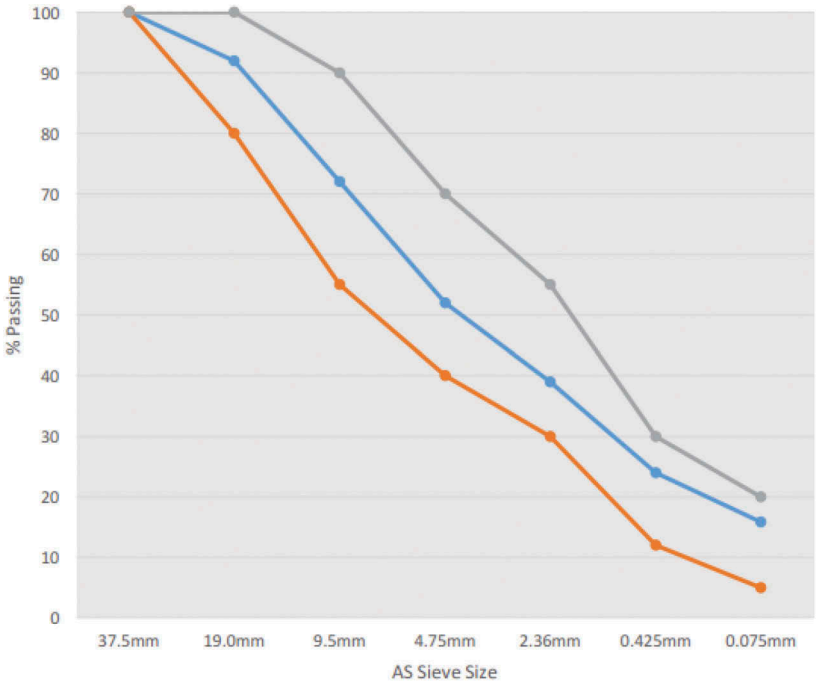

Figure 3. Recommended grading curves for optimum performance whilst utilizing Quantum liquid and powdered soil additive. Desired (blue), maximum (grey) and minimum (red) preferred curves are shown.

Curran (2016)

In 2016 Curran attempted to build on the Fitzpatrick (2015) study by undertaking a field trial at Bracalba Quarry operated by Brisbane City Council. To enable material cost comparison, an area of 240 m^2, treated to a depth of 250 mm was compared to a 400 mm thick untreated section of the same area. The parent material was a quarry overburden with the following properties (Table 3).

Table 3. Particle Size Distribution for parent material, Bracalba Quarry field trial (Curran, 2016; unpublished).

AS Sieve	Min	Max	% Passing Particle Distribution	Particle Distribution	PSD Category
37.5 mm	100	100	100		Gravel
19.0 mm	80	100	81	41	
9.5 mm	55	90	59		
4.75 mm	40	70	42		Sand
2.36 mm	30	55	30	24	
0.425 mm	12	30	18		
0.075 mm	5	20	11.5	12	Clay

Atterberg Limits for the parent material are also shown (Table 4):

Table 4. Soil characteristics of parent material, Bracalba Quarry field trial (Curran, 2016; unpublished).

Attribute	Min	Max	Value
Lower Liquid Limit		40	31
Lower Plastic Limit		14	18
Plastic Index		7.5	13.6
Linear Shrinkage	Not specified	5.8	
CBR		7.4	
@ Moisture Content		10.7%	

The finished in situ product was tested for bearing capacity using a Dynatest Falling Weight Deflectometer owned and operated by Pavement Management Services (PMS). Capillary rise in the material was monitored by in situ soil moisture equipment supplied by Pacific Data Systems (Figure 4).

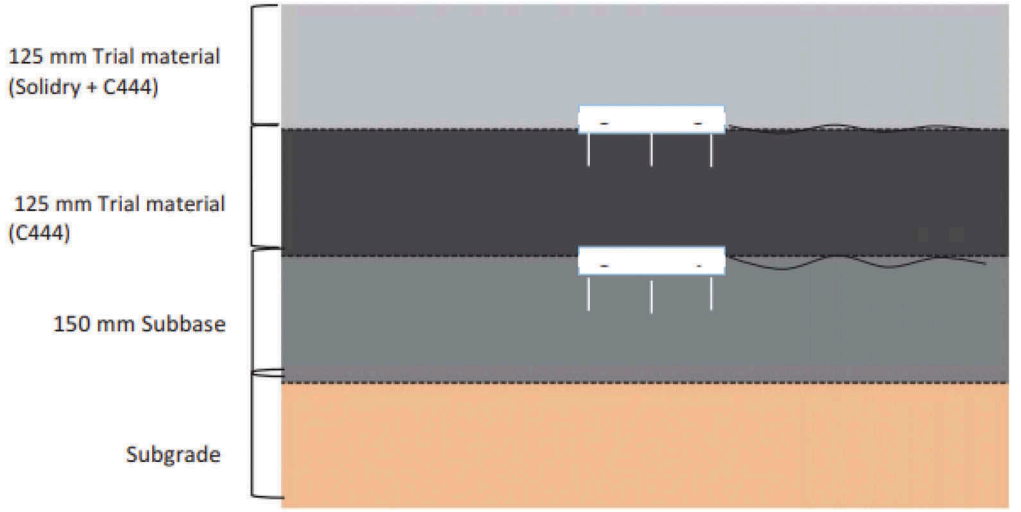

Figure 4. Schematic depiction of soil moisture gauge position within test pavement (Curran, 2016). Note: Solidry is the historical name for the powdered soil additive, the new name is QPF; C444 is the historical name for the liquid soil additive, the new name is QLF.

This equipment is designed to measure moisture content for agricultural purposes, so laboratory calibration was undertaken against known moisture contents of the parent material so that moisture content could be reported as engineering units. Moisture gauges recorded material dielectric and electrical conductivity as well as temperature. Data were recorded every 15 min and transmitted daily to an external computer repository. Site rainfall was also recorded.

Additive application rates, computed by Quantum Ground Stabilisation were:

- Liquid: 0.2 l/m^2, and
- Powder: 1% to 2% of dry weight i.e. 2 to 4 kg/m^2.

The test site was boxed out to a depth of 250 mm and a mixing pad established in the proximity. An initial 52 tonnes of the parent material were then spread on the mixing pad and 45 litres of liquid additive was applied evenly across the sample. Mixing was then conducted by a power harrow in five passes.

The material was then transported to the test site, graded and compacted with a pad foot compactor. Another 52 tonnes were then placed on the mixing pad and the powder additive spread at the rate of one 5 kg bag to 6 m^2 of material along with 45 litres of the liquid additive. This material was added to the test site making a final depth of 250 mm fully compacted. The same material (untreated) was placed adjacent to the test site to a depth of 400 mm. Thus, the trial would be comparing 250 mm of treated material against 400 mm of untreated material.

Resilient moduli from the two sites were then determined using a Falling Weight Deflectometer over a five-month period (Table 5); tests were conducted in accordance with ASTM E2835 - 11 (2015). Rainfall and soil moisture for the period were also compared (Figure 5).

Table 5. Resilient moduli for treated and untreated material at Bracalba Quarry over a five-month period.

	Mean Resilient Modulus (MPa)	
Days since installation	Treated (250 mm)	Untreated (400 mm)
14	279	572
41	475	523
90	721	516
158	823	424

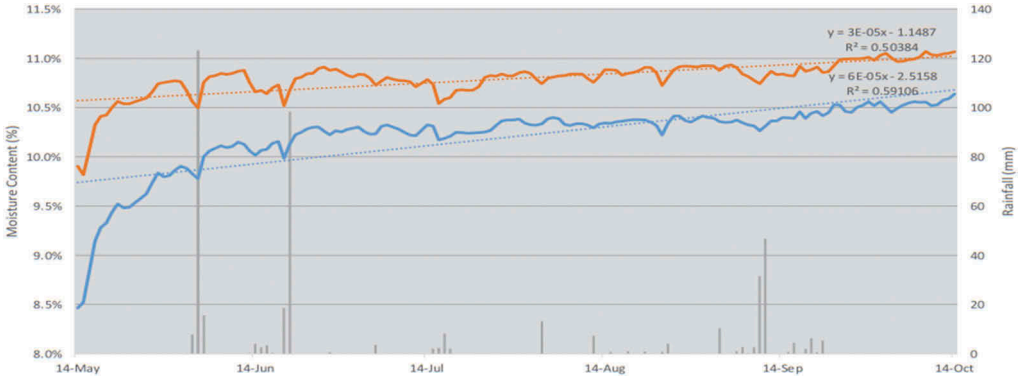

Figure 5. Variation in rainfall (vertical bars) and daily average soil moisture over the period 16 May to 14 Oct. 2016 at the Bracalba Quarry field site. Sensor 1 (red line) is at 125 mm depth; Sensor 2 (blue line) is at 250 mm depth (Curran, 2016).

The moisture content of both layers appears to remain reasonably consistent even after rainfall in excess of 100 mm.

Curran's field research suggested that low quality granular material treated with the Quantum products could attain high modulus values and that the products serve to effectively 'waterproof' the materials enabling bearing capacity sustainment after rainfall.

Callanan (2018)

Callanan (2018) furthered Curran's work by examining more temporally-extensive pavement data from the Bracalba Quarry field site. He utilised a Falling Weight Deflectometer to calculate parameters necessary for resilient modulus estimation by back calculation, using the ELMOD6 pavement software (Dynatest, 2016). These parameters were compared with in situ moisture and laboratory CBR data, to verify the claims of the Quantum products.

At an initial visual inspection in July 2018 (Figure 6), Callanan assessed that the road was in 'good' condition, exhibiting no visible defects or signs of degradation, with minimal erosion; subsequently, no temporal surface variation was evident over a three-month period.

Callanan noted the following maintenance activities: a water truck was used for dust suppression, spraying approximately $2L/m^2$ 5-10 times daily, depending on weather conditions, and grading occurred at approximately two-week intervals, where 26 mm greenstone scalps were added for protection and cover, partially acting as the recommended asphalting layer, temporarily altering the road structure.

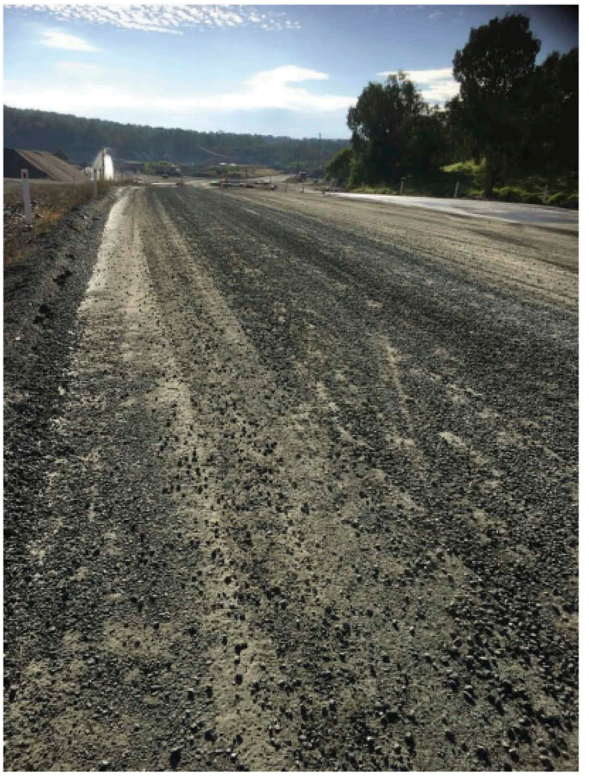

Figure 6. Treated section of road pavement facing North West in July 2018 showing no visible defects. Pavement is 10 m wide (Callanan, 2018).

Deflection testing was undertaken on 23 August 2018, 866 days after initial pavement construction (Table 6).

Table 6. Average Resilient Modulus under repeated load for un/treated pavement out to 866 days.

Days since installation	Mean Resilient Modulus (MPa)	
	Treated (250 mm)	Untreated (400 mm)
14	279	572
41	475	523
90	721	516
158	823	424
866	1127	727

In situ pavement moisture content was compared with rainfall data obtained from the Bureau of Meteorology weather station at Wamuran, approximately 10 km from site. Average moisture content for layer one (125 mm below surface) and layer two (250 mm below surface) in September 2016 was 10.4% and 9.9% respectively. In September 2018, the moisture levels sat at 10.5% and 10.45% for layers two and one respectively. Moisture content of both layers fluctuated over time, however, layer two showed a greater increase (Figure 7).

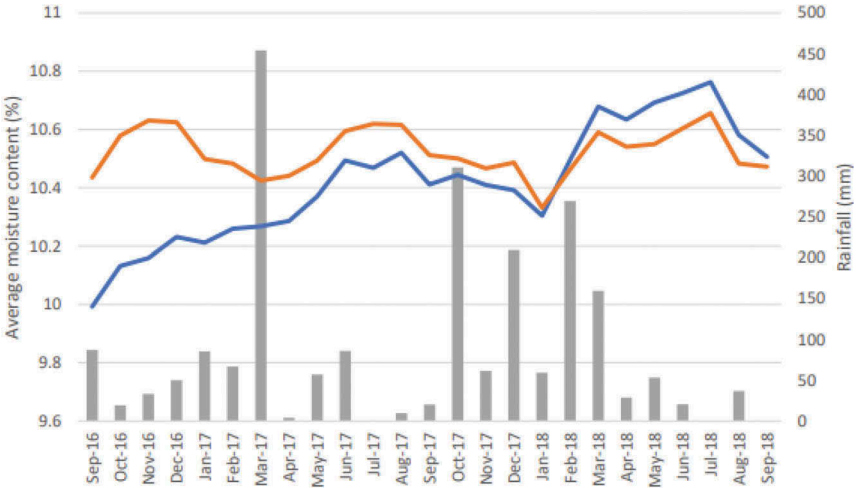

Figure 7. Pavement layer monthly average moisture content and monthly rainfall totals (vertical bars) from September 2016 to September 2018. Sensor 1 (red line) is at 125 mm depth; Sensor 2 (blue line) is at 250 mm depth (Callanan, 2018).

These moisture readings show an increase from the type 2.5 material's optimum moisture content of 8.6%. Pavement moisture content increases after significant rainfall but a delay is evident. Further evidence of this delay in pavement moisture increase after heavy rainfall can be found by comparing monthly data (Figure 8).

Although the Quantum system does not completely inhibit water infiltration into the treated unbound granular material, the effects of moisture do not appear to reduce its stiffness (Table 8).

Callanan conducted CBR testing on Type 2.5 granular unbound material (road-base) sourced from Hanson quarry Ferny Grove and a gravelly brown/dark silt composite soil, said

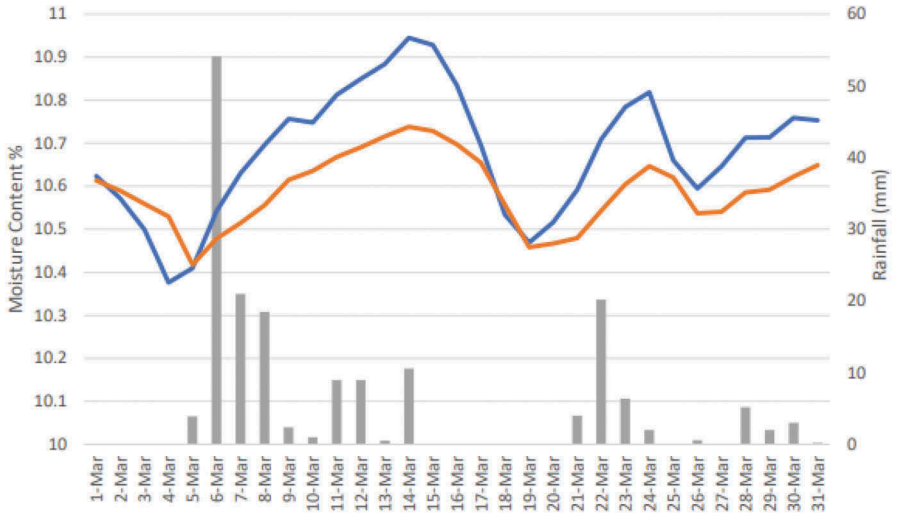

Figure 8. Pavement layer monthly average moisture content versus daily rainfall totals (vertical bars) for March 2018. Sensor 1 (red line) is at 125 mm depth; Sensor 2 (blue line) is at 250 mm depth (Callanan, 2018).

to contain a high percentage of coal dust and ash, sourced from a Queensland Railway site; soaked and un-soaked samples of each material with and without additive were tested.

Each sample was compacted in accordance with AS1289 – Methods of testing soils for Engineering purposes at OMC and left to cure in a sealed container for a four-day period before testing; results are shown (Table 7).

Table 7. CBR results for treated and untreated materials (Callanan, 2018).

Source	CBR		Percent Increase
	Control	Treated with additive	
Ferny Grove Quarry type 2.5 gravel	16	210	>1000%
Gravelly Silt – dark brown- Queensland Rail	42	78	>150%
Lower liquid limit	48	48	
Lower plastic limit	41	41.6	
Plasticity Index	7.0	6.4	
Linear Shrinkage	3.4	3.0	

CBR is seen to increase substantially, particularly in the ideal type 2.5 gravel.

Brooks (2019)

Brooks (2019) built upon the work of Curran (2016) and Callanan (2018) by conducting shear box and unconfined compression testing on material treated with the stabilisation system. Over thirty samples with various product concentrations were assessed qualitatively and quantitatively. This work was designed to simulate how materials may behave under the shear stresses induced within a roundabout.

The granular material selected was a type 2.3 road base, based on the recommendations for the base and subbase layers of unbound pavement material in a typical Queensland pavement structure (TMR MRTS05 2018); material was sourced from Hanson Construction Materials,

Glasshouse Mountains. Prior to treatment and testing base granular material characteristic were assessed by Douglas Partners (Tables 8 and 9).

Table 8. Particle Size Distribution for Hanson Quarry Type 2.3 material.

AS Sieve Size	Minimum	Maximum	% Passing	Particle distribution	PSD Category
37.5	100	100			Gravel
19.0	80	100	100	23	
9.5	55	90	97		
4.75	40	70	70		Sand
2.36	30	55	55	62	
0.425 mm	12	30	30		
0.075 mm	5	20	15	15	Clay

Table 9. Desirable physical characteristics of Hanson Quarry Type 2.3 material to obtain optimum stabilization results.

Attribute	Minimum	Maximum	Value
Lower Liquid Limit	25	50	23.2
Lower Plastic Limit	18	25	18.6
Plasticity Index	10	25	4.6
Linear Shrinkage	3	12	Not reported
CBR%			108
Dry Density			2.05
Optimum Moisture Content			10.6

Test samples were prepared following the standards outlined in Part 4D Stabilised Materials of the Austroads Guide to Pavement Technology. Liquid additive was applied at application rates of 0.8 and 0.4 l/m^3 and powder additive was applied at a rate of 40 kg/m^3 and 20 kg/m^3. Mixing commenced after both components of the stabilisation system were added to the soil; mixing was conducted using a small shovel. Water was applied during mixing to obtain the OMC specified by Douglas Partners. Stabilised soil was then placed into sample boxes for compaction and curing.

Consistent compaction of stabilised material was conducted using a wooden mallet; each sample was hit a total of 10 times, at similar forces. Samples were then cured for seven days. Sample shear strength was then assessed using a direct shear box apparatus. Eighteen tests were performed at normal forces of 20, 40 and 60 kPa, at a displacement rate of 5 mm/min (Table 10).

Table 10. Average material parameters derived from shear box test of material treated at various percent of Quantum stabilization system.

Additive Concentration	Internal Friction Angle	Cohesion (kPa)
0%	25.83	60.30
50%	41.63	263.05
100%	49.41	311.83

After curing, additional cylindrical samples were then trimmed to obtain a length-to-diameter ratio of approximately 2:1, to enable nine unconfined compression strength tests at 0, 50% and 10% of recommended soil stabilisation amounts to be conducted, in accordance with ASTM D2166/D2166-16 (Table 11).

Table 11. Unconfined Compressive Strength and Shear Strength for Type 2.3 Hanson Material.

Additive Concentration	Average Compressive Strength (kPa)		Average Shear Strength (kPa)	
		% improvement		% improvement
0%	95.70		47.85	
50%	224.56	227	112.28	233
100%	299.86	313	155.28	313

Brooks (2019) concluded that the percentage improvement in strength characteristics of the material treated with the stabilisation system, far exceeded the 50% improvement in strength (particularly unconfined compressive strength) required for TIPES accreditation.

4 SUMMARISED RESULTS FOR TESTING FROM 2015 THROUGH 2019

All results obtained to date were then compared with the TIPES requirements (Table 12).

Table 12. Comparison of characteristics of stabilized materials with TIPES accreditation requirements, over the period 2015 to 2019.

		Criteria		Test Results		
Property	Standard	Threshold Value	% increase	Untreated	Treated	% increase
Maximum dry density	AS 1289.5.4.2		5.0	2.218	2.168	nil
Optimum moisture content	AS 1289.5.4.2		0.5	7.8	8.0	nil
Bulk Mass	RMS T133	10	50	Not tested		
Rate of mass loss	RMS T186	2.0	50	Not tested		
Permeability	AS 1289.6.7.1	$3.0x10^{-7}$		$3*10^{-9}$	$2*10^{-1\circ}$	1000
Absorption (%)	AS 5101.5	2.0	50	Not tested		
Swell (%)	AS5101.5	1.5	300	-0.5	0	
Capillary rise (%)	AS 5101.5	25	50	Not tested		
California Bearing Ratio (%)	AS 1289.6.1.1	15 - 80	50	16	210	1300
Indirect tensile resilient modulus (MPa)	AS 2891.13.1	1000-2000	50	284	1127	400
Unconfined compressive strength (MPa)	AS 5201.4	1.5 – 3.0	50	0.2	1.8	300
Liquid Limit		>25				
Plastic Limit		>18	Parent Material			
Plasticity Index		>10				

These data suggest that test results meet or exceed material threshold requirements across most tested material properties.

5 CONCLUSIONS

Over the period 2015 to 2019 Quantum stabilisation products were assessed, both in the laboratory and in the field. It is clear from these studies that the addition of both the liquid and solid additive, to a variety of Australian soils, can have a beneficial effect in improving the bearing capacity and inhibiting the movement of water within a pavement. Back-analysis showed an increase in modulus over time.

From these analyses, optimal parent material characteristics can be specified. The base material should have equal components of Gravel, Sand and Silty Clay and a Plastic Index in excess of 10; optimal material characteristics and Particle Size Distribution are tabulated (Tables 13 and 14).

Table 13. Optimal parent material characteristics.

AS Sieve Size	Minimum	Maximum	% Passing	PSD Category
37.5	100	100		
19.0	80	100	100	Gravel
9.5	55	90	97	
4.75	40	70	70	Sand
2.36	30	55	55	
0.425 mm	12	30	30	Silt
0.075 mm	5	20	15	Clay

Table 14. Ideal Particle Size Distribution for parent material.

Attribute	Minimum	Maximum
Lower Liquid Limit	25	Not yet specified
Lower Plastic Limit	18	
Plasticity Index	10	
Linear Shrinkage	3	

Whilst at this time, not all attributes required by TIPES accreditation have been tested, results suggest that the bearing capacity and all-weather accessibility of roads will be improved by the application of Quantum additives in liquid and powder form to materials meeting the requirement of TMR 2.5 (A2 or E4) grading with high Liquid and Plastic Limits. Quantum additives now need to be assessed via the TIPES Stage 3 accreditation to confirm their efficacy for improving the bearing capacity and all-weather accessibility of soils for roadworks, particularly in the Queensland Black Soil country.

ACKNOWLEDGEMENTS

Thank you to Mr Bernhard Black at University of the Sunshine Coast for supporting these research activities. Thank you to an anonymous reviewer whose helpful comments assisted in improving this manuscript.

REFERENCES

ASTM International, 2015. *E2835 – 11: Standard Test Method for Measuring Deflections using a Portable Impulse Plate Load Test Device*.

Australian Road Research Board, 2019. *TIPES Guide for Applicants – Supplement Non-Traditional Chemical Stabilisation Binders*.

Australian Standard, 1995. *AS1289.6.8.1: Soil strength and consolidation tests - Determination of the resilient modulus and permanent deformation of granular unbound pavement materials*.

Brooks, R., 2019. *Investigation into the improvement of soil shear properties using a soil stabilisation method*, University of the Sunshine Coast 4th year Engineering thesis (unpublished).

Callanan, S., 2018. *Further Investigations into the Efficacy of a Soil Stabilisation Product for use within Australian Pavement Design*, University of the Sunshine Coast 4th year Engineering thesis (unpublished).

Curran, H., 2016. *Waterproofing of natural materials to improve bearing capacity*, University of the Sunshine Coast 4th year Engineering thesis (unpublished).

Dynatest, 2016. *ELMOD pavement analysis software*, Version 6, https://dynatest.com/elmod/

Fitzpatrick, S., 2015. *Developing a Procedure to Test New Innovative Additives for Soil Stabilisation*, University of the Sunshine Coast 4th year Engineering thesis (unpublished).

Queensland Government, 2013. *Common Soil Types*, webpage, https://www.qld.gov.au/environment/land/management/soil/soil-testing/types

Roads and Maritime Services, 2012. *T133: Durability of road materials modified or stabilised by the addition of cement*, New South Wales Government, Australia.

Roads and Maritime Services, 2012. *T186: Erodibility of stabilized road construction materials*, New South Wales Government, Australia.

Eleventh International Conference on the Bearing Capacity of Roads, Railways and Airfields, Volume 2 – Hoff, Mork & Saba (eds)

Asphalt reinforcement: A proven economic and ecological asphalt rehabilitation method

Andreas Elsing & Fabiana Leite-Gembus
HUESKER Synthetic GmbH, Gescher, Germany

Thomas Mielke
HUESKER Synthetic, Scandinavia

ABSTRACT: Asphalt reinforcement products manufactured using polyester fibres have successfully been applied in pavement rehabilitation for more than 40 years. Their outstanding performance has helped to increase maintenance periods, which provides a substantial financial cost saving but also a very positive ecological effect, in form of a reduction in the use of exhaustible resources and reduced traffic disruption.

This performance history impressively highlights the application of asphalt reinforcement.

A number of factors which influence the performance of an effective asphalt reinforcement have been identified. Recent research has focused on a couple of these influence factors which are summarized in this paper.

1. Surface characteristics of the raw material and their effect on the in-situ activated tensile strength
2. Elongation underneath the asphalt layer during dynamic loading and the influence on lifetime expectation

A cost comparison between the rehabilitation methods is given as well as a detailed description of the calculation of CO2 emissions.

Keywords: Asphalt reinforcement, Long term bonding strength, CO2 savings

1 INTRODUCTION

Asphalt reinforcement has been used worldwide for many years to delay or prevent reflective cracks in asphalt layers. Using asphalt reinforcement can clearly extend the fatigue life and therefore the maintenance intervals of rehabilitated asphalt pavements. Currently there are a number of different products and systems of different raw materials (e.g. Polyester, Glass, Polypropylene…) available in the market. It is not disputed that all these systems have a positive effect, however there are essential differences in the behaviour and effectiveness of such systems.

2 PAVEMENT FAILURE DUE TO REFLECTIVE CRACKING

Cracks appear in asphaltic pavements due to external forces, such as traffic loads and temperature variations. The temperature influence and the dynamic loading over time leads to the binder content in the asphalt becoming brittle. High stresses at the bottom of a pavement,

DOI: 10.1201/9781003222897-4

from external dynamic loads, such as traffic, can cause cracks which propagate from the bottom to the top of a pavement (bottom-up cracking). In order to delay the propagation of those cracks into the new layers an asphalt reinforcement of high tenacity Polyester can be installed. The reinforcement increases the resistance of the overlay against high tensile stresses and distributes them over a larger area, thereby reducing the risk of local overstressing which would result in cracks.

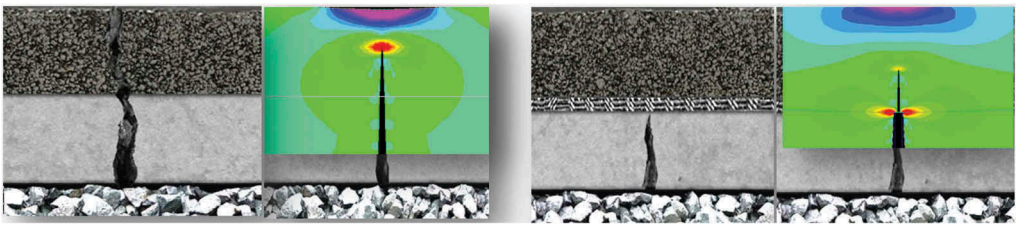

Figure 1. Simulated stress distribution with FE-Method, without (left) and with reinforcement (right) (Montestruque, 2002).

3 MOBILIZATION OF TENSILE FORCES

Typically the testing procedures, to determine the tensile strength and elongation (e.g. ISO EN 10319:2015), of Asphalt reinforcements are undertaken in "air" and not embedded in asphalt. An asphalt reinforcement improves the stress-strain properties of an asphalt pavement by adding tensile strength into the asphalt system. However, other properties (other than the in air measured reinforcement stiffness) are influencing the performance of an asphalt reinforcement and that asphalt/reinforcement interface bond is an important influence factor in transferring tensile forces into reinforcement on the contact surface. The performance of an asphalt reinforcement should ideally be determined as a composite, with asphalt and reinforcement considered together. Many tests have been performed in the past decades to demonstrate the performance of asphalt reinforcement produced with high tenacity Polyester fibres. The aim of such tests was to replicate, as close as possible, the installed in-service composite behaviour in laboratory conditions, whilst also trying to qualify the important parameters which influence the behaviour of an asphalt reinforcement.

3.1 *Bond stiffness*

De Bondt, 1999, published "Anti-Reflective Cracking Design of (Reinforced) Asphaltic Overlays", which was the last phase in his Ph.D. program and a 5 year research project at the Delft University of Technology. De Bondt determined the relevance and influence of different parameters on reflective cracking in asphalt overlays, and performed comparative investigations on different commercially available products in the market at that time. He found that one of the most important parameters is the bonding of the reinforcement to the asphalt, he defined as 'bond stiffness'. De Bondt determined the equivalent bond stiffness in reinforcement pull-out tests on asphalt cores taken from a trial road section. Parts of the results are presented in Figure 2`, for full details the reader may refer to the full publication. De Bondt determined that the equivalent bond stiffness of a polyester reinforcement was by far the most effective of all products investigated. The importance of the bituminous coating for flexible grids has a significant influence. De Bondt found that in flexible grids like a polyester reinforcement the stresses were transmitted via direct adhesion between strands and asphalt – hence the coating plays a vital part to the ultimate performance.

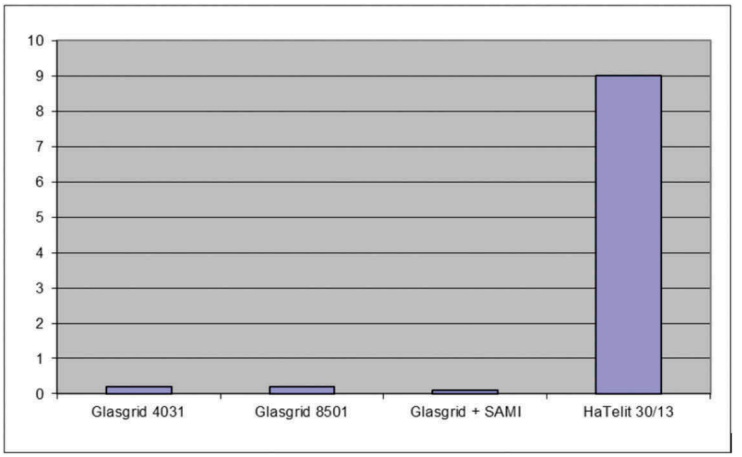

Figure 2. Equivalent bond stiffness (ceq,rf in N/mm/mm²) of different investigated products.

By using finite element models, De Bondt calculated the improvement factors for reinforcements based on material stiffness (EArf) and pull-out stiffness (ceq,rf). With a product stiffness of ~900 N/mm and a pull-out stiffness (ceq,rf) of about 9, the polyester reinforcement achieves an improvement factor of 3.5 in the simulation compared to a control section. (i.e. achieves a number of load cycles 3.5 times the number of cycles for the control section without reinforcement before reflective cracks reappear). From this research it is evident, that a good bonding of the reinforcement to the asphalt is very important for the performance of asphalt reinforcement. The combination of high reinforcement stiffness (Polyester) and high bond stiffness (Bitumen impregnation) create a high improvement factor for the overlay life of an asphalt pavement.

3.2 *Bonding strength*

To mobilize tensile forces in the reinforcement a good bonding between the asphalt layer and the integrated reinforcement is essential. Based on the German guideline ZTV Asphalt-StB 07/13 the shear force within the testing procedure according to Leutner should not be lower than 15.0 kN between the binder course and the surface layer.

Figure 3. Drill core with reinforcement (after testing).

Table 1 shows the results of drill cores tested at the University RWTH Aachen, 2018. These exemplary results show that the bonding strength is not significantly influenced by a bitumen coated Polyester grid.

Table 1. Comparison of shear forces of unreinforced drill cores and HaTelit reinforced drill cores acc. to Leutners method.

	without reinforcement		with reinforcement	
Temperature[°C]	mean value shearing force[kN]	mean value shearing distance[mm]	mean value shearing force[kN]	mean value shearing distance[mm]
20°C	26,1	3,9	24,9	3,8

3.3 *Fibre surface structure*

A Study on Geosynthetic-Reinforced Asphalt Systems, was published by Luming, 2018. This research presents a study on various aspects relevant to geosynthetic-reinforced asphalts. Section II of this thesis presents the experimental research that was conducted using overlay testing involving geosynthetic-reinforced asphalt specimens. The standard overlay test has been designed to evaluate crack propagation in asphalt concrete using a fatigue loading mechanism that induces tensile and shear stresses. The experimental study presented in Section II adopted this test to evaluate the effectiveness of the different interlayers in retarding the reflective cracking from an old asphalt into a new overlay. The asphalt specimens were tested in the standard overlay test along with geosynthetic-reinforced asphalt specimens. In addition, an image acquisition system was used to track propagation of cracks during overlay tests, see Figure 4.

Figure 4. Test set up for shear fatigue test.

Four types of reinforcement were tested. Each reinforcement had the same mesh size and the same coating to eliminate a couple of potential variables and to provide a better understanding of the influence of the raw material. Polyester (PET), Glass fiber and Polyvinyl alcohol (PVA) were tested.

Table 2. Tested asphalt reinforcement from different raw materials.

	Reinforcement 1	Reinforcement 2	Reinforcement 3	Reinforcement 4
Raw material	PVA	PET	Glass	Glass
Tensile-strength[kN/m]	50	50	50	100

Results and conclusions from this tests.

Parts of the results are presented here, for full details the reader may refer to the full publication, Luming, 2018. With the opening and closing of the simulated existing crack, the cross-crack initiates and propagates from the tip of the simulated crack towards the top surface of the asphalt concrete. Overall, the reinforced asphalt specimens showed better fatigue performance than the unreinforced asphalt concrete. The PVA and PET fibres are more compatible with the asphalt concrete than the glass fibre, thus they can better interact with the asphalt specimen at later fatigue life. The normalized load of the PVA reinforcement at the end of phase 4 was the highest, indicating the best performance of this material in enhancing the shear resistance of the asphalt concrete over fatigue life. The PET reinforcement shows second best results, close to them of PVA. The performance of the glass fibre reinforced specimens was not as good as the polymer reinforced specimens in terms of retarding the load decline. This could be attributed to the varied compatibility of the reinforcement with the asphalt concrete. PVA and PET consist of polymer fibres which are more compatible with the asphalt concrete in the stiffness of the materials than the glass fibre.

4 ELONGATION INFLUENCING THE LIFETIME

4.1 *Function of fatique*

The textbook definition of fatigue theory states that fatigue cracking initiates at the bottom of the flexible layer due to repeated and excessive loading, and it is associated with the tensile strains at the bottom of the HMA layer (Huang, 1993). The fatigue cracking in cracked pavements can be significantly delayed, by reducing the tensile strains at the bottom of a flexible asphalt layer (Figure 5).

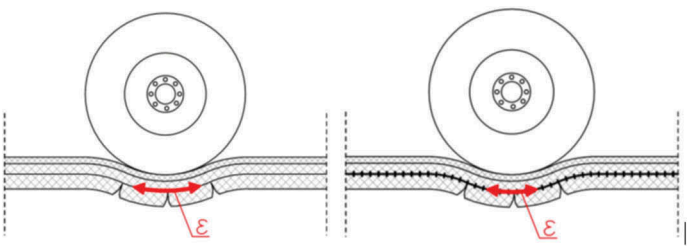

Figure 5. Schematic view of the fatigue cracking mechanism in pavement cross section without and with reinforcement.

According to the function of fatigue:

$$N_f = k_1 (1/\varepsilon_t)^{k_2}$$

N_f = allowable load repetitions of a pavement (until failure occurs)
k_1 = coefficient of fatigue
k_2 = exponent of the fatigue function
ε_t = elongation on the bottom of the asphalt layer [%]

From specialist literature the value mentioned for the coefficient factor of fatigue k1 is 2.0 × 10-12. For k_2, the exponent of fatigue function, is 5.0. At a vertical deformation of 0.5mm during a loading cycle an elongation of 0.0001% is measured below the asphalt layer. A small reduction in the elongation below the asphalt layer already has significant effects on the allowable loading cycles. Detailed figure are presented in Table 3.

Table 3. Calculated loading cycles until failure occurs.

Reduction of elongation	Elongation[ε_t]	Loading cycles[N_f]	Improvement Factor
Reference	ε=0,000100%	2.00×10^8	-
-5%	ε=0,000095%	2.99×10^8	1.5
-10%	ε=0,000090%	3.99×10^8	2.0
-20%	ε=0,000080%	6.10×10^8	3.0

4.2 *Effects of an asphalt reinforcement on the function of fatigue*

In a diploma thesis by Höptner, 2010, the benefits of asphalt reinforcement in road rehabilitation by using a modified rutting simulator have been investigated. The aim of this research was to analyze the influence of an asphalt reinforcement on reducing the deformation in pavements. The setup has been prepared according to realistic pavement design. The pre-cracked specimens have been located on an elastic rubber foundation which simulates the base course (Figure 6). The force has been applied by a rubber wheel. For the test set up a standard asphalt design has been chosen, with a 60mm binder course (AC 16 B S) and a 40mm surface course (SMA 8 S). The specimen was prepared in a roller sector compactor. In the first step the binder layer (including the simulated crack) was prepared.

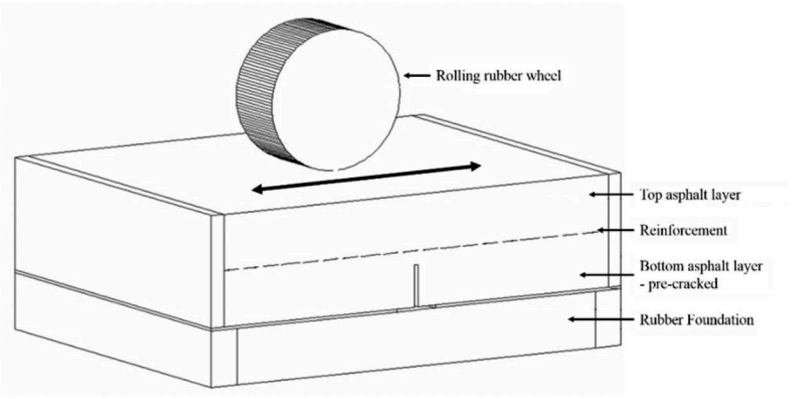

Figure 6. Test set-up cyclic loading test (schematic).

After preparing the binder course (including a simulated crack) specimens with and without reinforcement were produced. The reinforced specimen was impregnated with a bituminous emulsion (C67B4-OB) in accordance with the installation guideline of the producer of the asphalt reinforcement (Figure 7).

A force of 700N has been applied onto the specimen by a rolling rubber wheel, which is equivalent to a 10 t axle load. Two identical asphalt specimens have been produced, with, and without polyester reinforcement. The deformation from loading cycle 50.000 to the end of the testing at

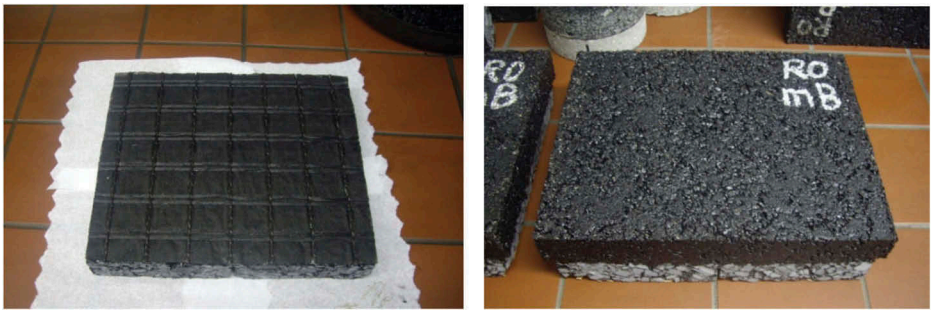

Figure 7. Pre cracked specimen with asphalt reinforcement.

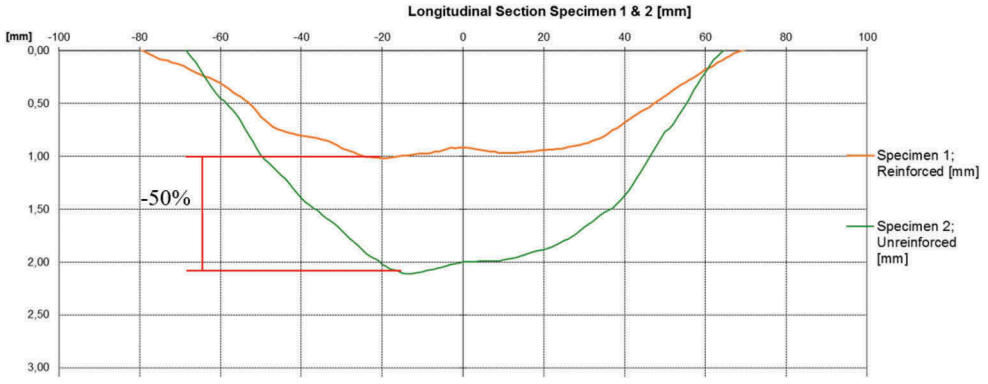

Figure 8. Deformation with and without Polyester reinforcement of an asphalt specimen between 50.000 and 60.000 loading cycles.

60.000 loading cycles was, without reinforcement, 2.1mm. The measured deformation with reinforcement, only was 1.0mm. This results in a reduction of 50% in deformation. (Figure 8).

5 ECONOMICAL AND ECOLOGICAL ASSESSMENT

5.1 *Executed project – district road "Rosenstraße", Ochtrup, Germany*

The Rosenstrasse in Ochtrup leads directly to the border crossing to the Netherlands and is therefore characterised by an extremely high volume of trucks. More technical details of the project can be found in (Elsing and Schröer 2005). The project started already in 1996 and from the very beginning on, the project was scientifically monitored and independently evaluated (TÜV Rheinland, LGA Bautechnik, 2009). The Rosenstrasse was repaired over its entire carriageway width due to substance damage in the form of net cracks. Both the binder course and the base course were also extremely cracked and in very poor condition. The service life for a full lining was assumed to be 15 years. For financial and time reasons, it was decided not to mill out the base and binder courses and to lay the asphalt reinforcement directly onto the binder course after milling off the surface course. This was to prevent the existing cracks from quickly penetrating into the new surface course and thus extend the rehabilitation interval. During execution, the asphalt reinforcement was laid according to the installation instructions and then covered with 5 cm asphalt concrete 0/11. The assumptions made at that time were verified and the durability of the road was evaluated. After 15 years the road was in excellent condition. No cracks were found along the entire length. The

adhesive bond according to Leutner was still 24 kN (Quiel, 2013). After 15 years, the road condition can be regarded as equivalent to a full rehabilitation with changing all existing cracked asphalt layers. Until today, after 23 years, the road is in perfect condition and no rehabilitation had to be carried out. In this way, sustainable renovation costs could be avoided. The use of asphalt reinforcement has proven to be a successful rehabilitation measure in its entirety.

5.2 *Cost comparison of this project*

Lying on the conservative side, only the costs of maintaining the cracked binder course were considered in this rehabilitation project. In the case of the asphalt reinforced version, the material costs of the reinforcement and the costs of installing the reinforcement are incurred. The cost of milling the binder course, the material costs of the new binder course and its paving and compaction are saved. The direct cost savings for the selected reinforced version were > 34% in 1996.

5.3 *Cost comparison in general*

A current comprehensive analysis of the costs of various rehabilitation methods was carried out on the basis of a bachelor thesis (Claußen, 2019). This included the pricing of a fictitious construction site in the Wismar (East part of Germany) area. The rehabilitation method of replacing the binder course and surface course was compared with the method of replacing the surface course using an asphalt layer, as described in the example above. In the conventional variant, 4 cm of surface course and 6 cm of binder course are to be milled out and placed again. In the reinforced version, only the surface is milled off and the asphalt reinforcement is laid on top of the existing cracked binder. The costs for the conventional variant are € 144,591.3 for 5000 m² and € 84,711.3 for the reinforced variant. Also on the basis of this example a saving of 41% of the costs can be determined.

International experience shows that the percentage of the direct cost savings are also in the range of 35% - 40%, although the prices for building materials, transport and labour vary considerably. More roads could therefore be rehabilitated for the same investment.

5.4 *CO_2 savings*

The CO_2 emissions were idendified on the basis of a concrete road maintenance measure. A detailed description of the calculation of CO_2 emissions is given in (Brzuska, 2019). The result shows that more than 60 % of the CO_2 emissions were caused solely by the production of asphalt mixes and the associated processes. The reason for the high CO_2 emissions during the production of asphalt mix is the high energy consumption. A simplified transfer of the results of this construction measure to the Rosenstrasse construction measure mentioned above gives a good estimate of the CO_2 savings for this renovation option. Here, 6 cm of binder course was retained and the asphalt reinforcement was laid on top of it. Comparison: Conventional method - replacement of binder course and surface course - with the method - laying asphalt reinforcement on the binder course. Conservatively, only the CO_2 emissions resulting from the saving of the mix for the binder course are taken into account. The CO_2 emissions resulting from the production of the base course from (Brzuska, 2019), were also assumed to be on the conservative side for the production of the binder course. CO_2 emissions caused by the arrival and departure of employees, the transport of construction machinery, the extraction and transport of asphalt granulate required for the production of mixes were not taken into account. This alone results in a CO_2 saving of 24.3 t CO_2 per rehabilitated road kilometer. Another aspect that contributes significantly to CO_2 savings is the reduction of construction time. This means that the road can also be opened to traffic earlier, leading to a reduction in traffic jams caused by the construction site. In North Rhine-Westphalia for example, 50 % of all traffic jams are caused by construction sites.

6 SUMMARY

The use of asphalt reinforcement has proven to be a successful rehabilitation measure in its entirety. Placing the reinforcement directly on the cracked binder instead of replacing all asphalt layers is a highly cost-effective and environmentally friendly solution. Less CO_2 is caused and due to the faster construction time, traffic jams are reduced which additionally saves CO_2.

The use of asphalt reinforcements reduces the rehabilitation intervals significantly. In order to reach the longest possible service life of the pavement the reinforcement needs to be robust against mechanical damage during installation and compaction of the asphalt and the later dynamical loading. Additionally the reinforcement must have a direct mobilization of tensile forces in the asphalt system, and should not reduce the bonding strength between the asphalt layers. As described in the paper polymer raw materials such as PET and PVA show an extreme high mobilization of tensile forces and combined with a bitumen coating the bonding strength is nearly undisturbed and this together ensures a maximum long service life.

REFERENCES

Bondt, de, A.H., 1999. *Anti-Reflective Cracking Design of (Reinforced) Asphaltic Overlays*, Ph.D.-thesis, Delft, Netherlands.

Brzuska, A., 2019. *Emissionen beim Bauen*, in German, *Emissions during construction*, Asphalt & Bitumen, Germany.

Claußen, O., 2019. Bachelor – Thesis, *Wirtschaftslichkeitbetrachtung zur Bauweise mit Asphalteinlagen unter Berücksichtigung von ökologischen Aspekten*, Wismar, Germany.

Elsing, A. and Schröer, S., 2005. *Experience from more than 30 years of asphalt reinforcement with polyester grids*, 15th International Road federation World Meeting, Bangkok, Thailand

Höptner, A., 2010. *Nachweis der Wirksamkeit von Asphaltbe-wehrungsgittern zur Verhinderung von Reflexionsrissen*, Diplom Thesis, Dresden University of Applied Sciences, Dresden.

Huang, Yang H. 1993. *Pavement Analysis and Design*, Prentice Hall, New Jersey, USA.

Montestruque, G. E. 2002. *Contribuição para a Elaboração de Método de Projeto de Restauração de Pavimentos Asfálticos Utilizando Geossintéticos em Sistemas Anti-Reflexão de Trincas* (in portuguese). Ph.D.-thesis, Technological Institute of Aeronautics, São José dos Campos, Brazil.

Quiel, M., 2013. *Einsatz von Asphalteinlagen im Asphaltstrassenbau*. Master Thesis, Münster University of Applied Sciences, Münster, Germany.

RWTH Aachen University, 2018. CERTIFICATE No.: 1808991, *Testing of the layer bond of drill cores with and without reinforcement*, Germany

TÜV Rheinland LGA Bautechnik, 2009. Test report BBV 0913526, *Zustandserfassung und –bewertung der Rosenstraße in Ochtrup und Erstellung eines Vergleichs des Zustands der Fahrbahn vor und nach der Sanierung mit einem Asphaltgitter*, Germany

Yang, L., 2018. *A Study on Geosynthetic-Reinforced Asphalt Systems*, Massterthesis, University of Texas, Austin, USA.

Eleventh International Conference on the Bearing Capacity of Roads, Railways and Airfields, Volume 2 – Hoff, Mork & Saba (eds)

Impact of extreme robust hydraulic bound base course made by cold recycling in situ on performance and homogeneity of reconstructed pavement from bearing capacity point of view

Z. Boros, J. Komacka & F. Bucek
STRABAG – TPA, Bratislava, Slovakia

ABSTRACT: A new approach in terms of common procedures (used not only in Slovakia) was implemented in the reconstruction of a deteriorated cement concrete pavement. The hydraulically bound layer with the robust final thickness of 40 cm was made by technology of cold recycling in situ from the concrete slab, base, and subbase layers. This layer formed the basis for new asphalt layers. Testing and comprehensive evaluation of bearing capacity of reconstructed pavement by FWD proved significantly increase in bearing capacity of pavement. The analysis also confirmed the used technology of recycling is suitable to achieve high stiffness of homogenized recycled layer and ensure acceptable homogeneity.

Keywords: Pavement, reconstruction, recycling, base, course, FWD, bearing capacity

1 INTRODUCTION

Flexible and semi-rigid pavements dominate on the Slovak road network. Only a few sections with cement concrete pavement can be found on some roads. Generally, these pavements are more than 40 years old, they have un-dowelled joints and plenty of various defects that negatively affect safety and driving comfort. Unfortunately, these sections form a part of first-class roads with the high traffic intensity. The unsatisfactory condition of the pavements of these sections needed to be addressed by rehabilitation. Therefore, a comprehensive diagnostic work was carried out, including verification of the bearing capacity. The Society for Quality Assurance and Innovation (TPA) have taken a part on these activities. In 2014, TPA handled the engineering geological and hydrological survey, bearing capacity diagnostic, the pavement design, and the design of reconstruction technology of first of such a project from 4 investigated a 2 realised total cases in Slovakia (the roads in 2014: I/62 and I/75; I/50; I/65; in 2019: I/13 - Boros, Soták). The details relating to the reconstruction of the section on the road I/65 are presented in following chapters.

2 PAVEMENT CONDITION AND DIAGNOSTICS

The pavement of the section corresponded to a jointed unreinforced concrete pavement. The maintenance of pavement was insufficient and joints between the slabs were not regularly resealed. It allowed water penetration into the pavement structure and the accelerated degradation of the pavement. The change in moisture content had the negative effect on properties of layers and subgrade under the cement concrete slab. Due to this, in combination with the

DOI: 10.1201/9781003222897-5

load, gradual vertical shifts between the plates and the "pumping" effect occurred and plenty of longitudinal and transverse cracks were formed (Figure 1). A major danger was some parts of the broken pavement not only shifted vertically as a heavy vehicle passed, but even rotated into a perpendicular position.

Figure 1. Example of distress of pavement (first class road I/65).

The FWD Dynatest 8000 was used to detect the pavement bearing capacity. In view of the high degree of damage of the pavement and the obvious need for its reconstruction, a step approximately of 100m (with 50 m shift in lanes) was chosen in agreement with the contracting authority. The measurements in this step were taken at the center of slab in undamaged (unbroken) sites. The measurements were not taken at edges and joints because the transfer at the joints (the co-action of slabs) was irrelevant for the intended purpose. Deflections generated by load force of 75 kN were measured at 9 sensors spaced from the center of load plate at 0, 200, 300, 450, 600, 900, 1200, 1500 and 1800 mm.

The surface moduli calculated from the measured deflections varied significantly along the section (Figure 2). It confirms inhomogeneity of pavement bearing capacity. Considering the cement concrete pavement, a lot of low values (below 1000 MPa) resulting from the deflection at the center of load (D1 in Figure 2) can be observed. It means, the functionality of some cement concrete slabs (load transfer to its surroundings) is limited.

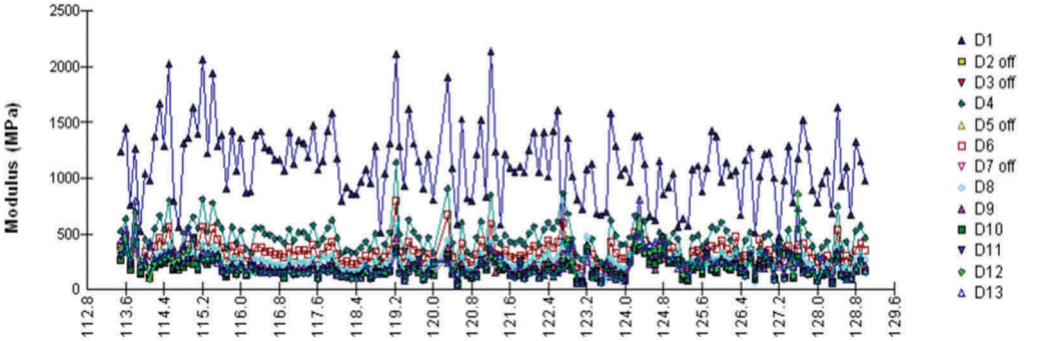

Figure 2. Surface moduli along the section of the road I/65.

The plot of surface modulus for various distances of FWD sensors (Figure 3) also demonstrates variability of properties of pavement layers. The top two images show a pavement with an undamaged, functional cement concrete slab. The smooth surface modulus curve (top left) also documents undamaged underlying layers and subgrade. The damaged part of the pavement just below the cement concrete slab can be assumed from the course on the top right. The bottom two images are characteristic of a site with a damaged cement concrete slab. On the left, there is the course corresponding to undamaged base and subbase layers. The bottom right image is typical for both damaged cement concrete slab cover and underlying layers.

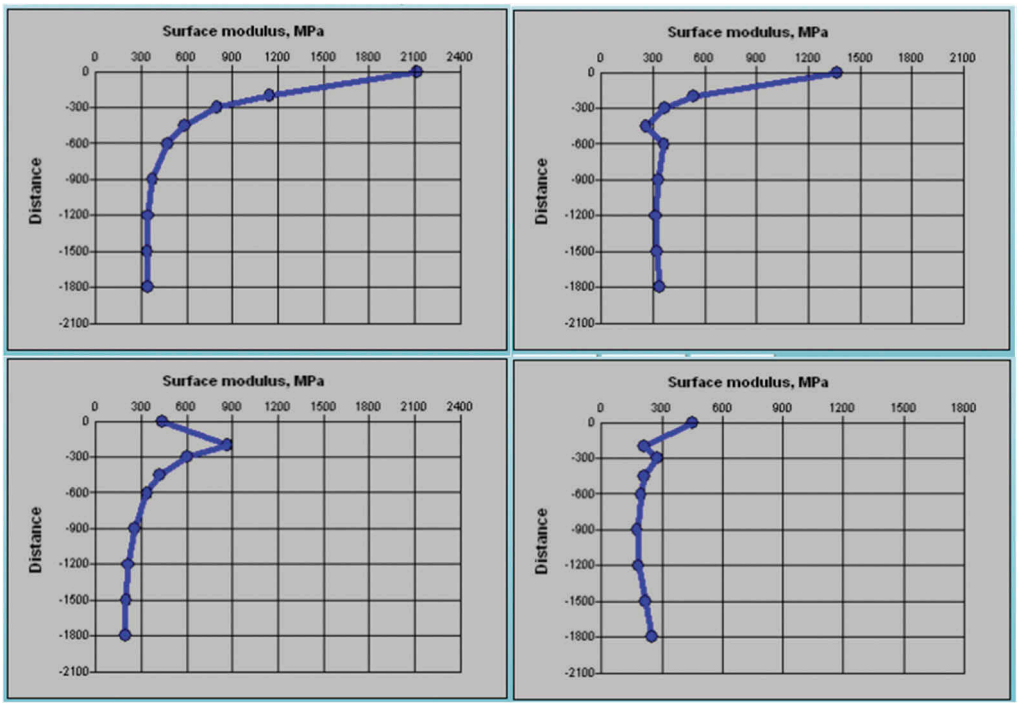

Figure 3. Example of variability of surface modulus at test points.

The evaluation of the bearing capacity showed a high degree of inhomogeneity of the cement concrete pavement in the diagnosed section. The remedy of the unsatisfactory pavement condition by local repair of the unsatisfactory parts was rejected and a total reconstruction of the pavement was proposed. Moreover, the decision of client was to change the type of pavement and build an asphalt pavement for the design period of 20 years.

3 DESIGN OF RECONSTRUCTION

The TPA Ltd prepared the design of new pavement respecting all conditions defined in Slovak pavement design method (TP 033, 2008). Traffic intensity, climate and hydrogeological conditions, subgrade bearing capacity were considered in the design process.
As the bearing capacity evaluation proved good parameters of subgrade, the aim of design process (Figure 4) was to preserve the original subgrade. Therefore, a reconstruction method was sought that would ensure this. The decision fell on recycling in situ of cement concrete slabs, base, and a part of subbase. This solution would make it possible to eliminate damaged areas of the cement concrete surfacing and maximize the reuse of existing pavement materials. and homogenization. The result of design was the hydraulically bound "homogenisation" base

layer (HMG) with the total thickness of 400 mm. It consists of mixed pavement materials (fragmented and crushed cement-concrete slabs of surfacing, and other materials of existing base and subbase course up to the depth of 400 mm – the middle part of Figure 4), new crushed aggregate (fraction 32 mm), and a slow-hardening hydraulic binder.

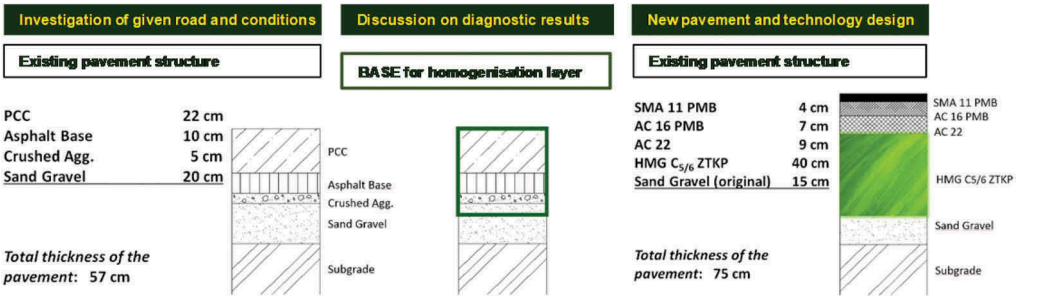

Figure 4. The design process of the "Homogenisation Layer".

When designing the pavement, it was assumed, the "homogenization" layer would have parameters corresponding to CBGM $C_{5/6}$. Because the HMG layer is not a standard layer, the special technical-qualitative conditions were elaborated for its design and construction. The final design (right part of Figure 4 and Table 1) included all considerations of the designer as well as the requirements of the client. The pavement composition met the client's requirements for a service life of 25 years under the expected traffic load of 76.6 million equivalent standard axle loads (ESAL).

Table 1. Pavement structure (simplified, without tack coats, type of binder etc.).

Pavement layer		Layer thickness [cm]
Stone mastic asphalt	SMA 11 PMB	4
Asphalt concrete - binder course	AC 16 bin PMB	7
Asphalt concrete - base course	AC 22 base PMB	9
Homogenisation hydraulically bound layer	CBGM $C_{5/6}$ (HMG)	40
Gravel sand (original)		15

4 PROCESS OF RECONSTRUCTION

The technological process of reconstruction was carefully planned not only in terms of the proper setting of the construction machinery, the dosage of the combined binder or the additional aggregate fraction to guarantee the resulting mechanical parameters of the HMG type base layer, but also in terms of minimizing traffic restrictions. In practice, the possibility of road reconstruction in full and half profile was verified.

The Figure 5 shows the individual steps of the technological process of reconstruction: 1. breaking the slabs using a "guillotine"; 2. crushing the parts of CC slabs; 3. crushed material accumulated before spreading; 4. detailed view of the spread material; 5 HMG layer after milling, adding the binder, water and compacting; 6. the result.

5 PERFORMANCE AND PARAMETERS OF NEW PAVEMENT

The measurements by FWD Dynatest 8000 before and after the reconstruction were used to assess the change in performance of pavement. Due to the difference in load forces (75 kN before and 50 kN after reconstruction) the surface modulus of pavement was used as a parameter for a comparison instead of deflections.

Figure 5. Brief overview of the reconstruction process in half road profile.

It is clear from the example in Figure 6, the values of the surface modulus after the reconstruction are higher comparing to those before the reconstruction. It is also interesting, the chosen technology focused on preserving of existing subgrade has served its purpose. It can be stated based on the surface modulus calculated from the deflections measured by the sensor spaced in 1800 mm from the load centre (the farthest FWD sensor is generally used for assessing bearing capacity of subgrade). As it can be seen in Figure 7 the surface modulus calculated from the deflections measured after reconstruction are higher in the comparison to those resulting from the deflection before reconstruction.

The surface modulus E0 of the reconstructed pavement in Figure 6 indicate a variability in the total stiffness of pavement. A closer analysis of the reasons for this variability is possible by evaluating the parameters characterizing the stiffness of individual parts of the pavement. Three parameters were used for this purpose:

- the central deflection D0 that relates to the total stiffness of the pavement;
- the deflection D 1800 characterizing the stiffness of subgrade;
- and the Structure Bearing Index (SBI) representing the stiffness of pavement structure itself; it was calculated as:

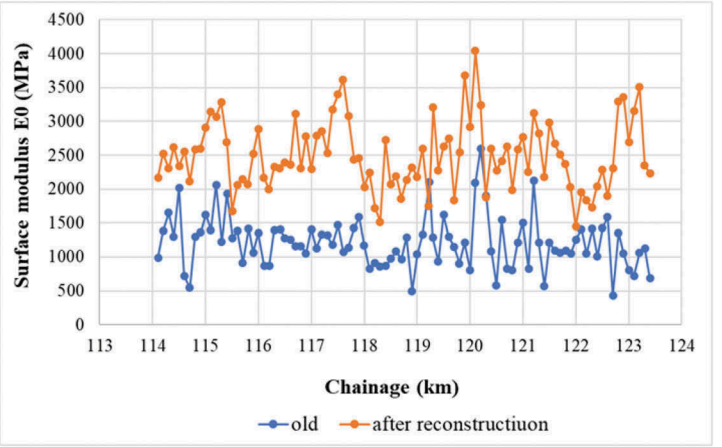

Figure 6. Surface modulus E0 of pavement before and after reconstruction.

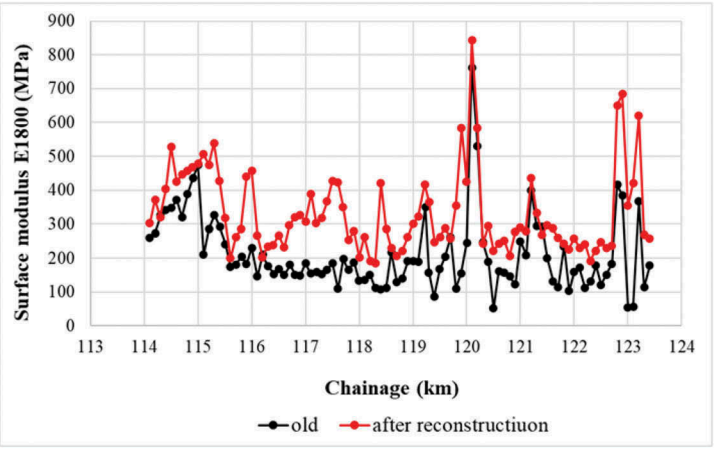

Figure 7. Surface modulus E1800 of pavement before and after reconstruction.

$$\mathrm{SBI} = (\mathrm{D0} - \mathrm{D1500}) \tag{1}$$

where D0 is the central deflection (μm) and D1500 is a deflection measured at the distance of 1500 mm (μm).

The mentioned parameters along the section are presented in Figure 8. The correlation analysis (Figure 9) proved the subgrade stiffness (deflection D 1800) is a less important factor influencing the change in central deflection D0 because the higher value of the coefficient of determination R^2 was determined for the relationship between D0 and SBI.

The SBI index expresses the stiffness of the pavement itself after filtering out the stiffness (bearing capacity) of the subgrade. The various indices characterizing the stiffness of individual parts of pavement can be used to analysis reasons of SBI index variability. The Surface Curvature Index (SCI300) and Base Curvature Index (BCI) were used in this case. The SCI300 is obviously used for an assessment of asphalt layer(s) stiffness. They were calculated as:

$$\mathrm{SCI300} = \mathrm{D0} - \mathrm{D300} \tag{2}$$

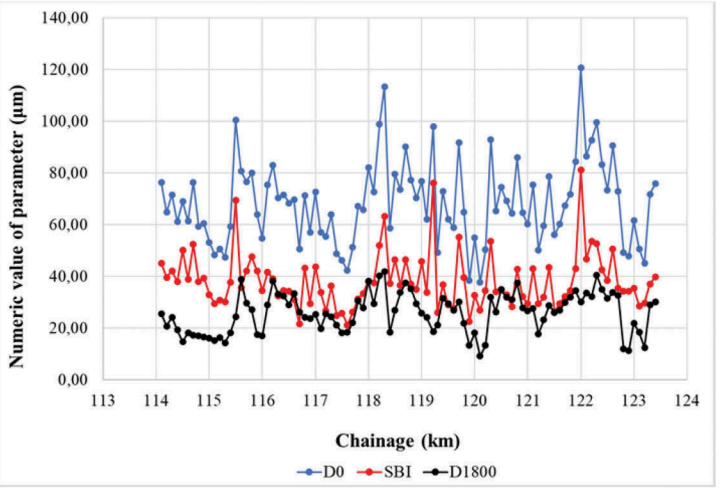

Figure 8. Values of parameters characterizing the total stiffness of pavement.

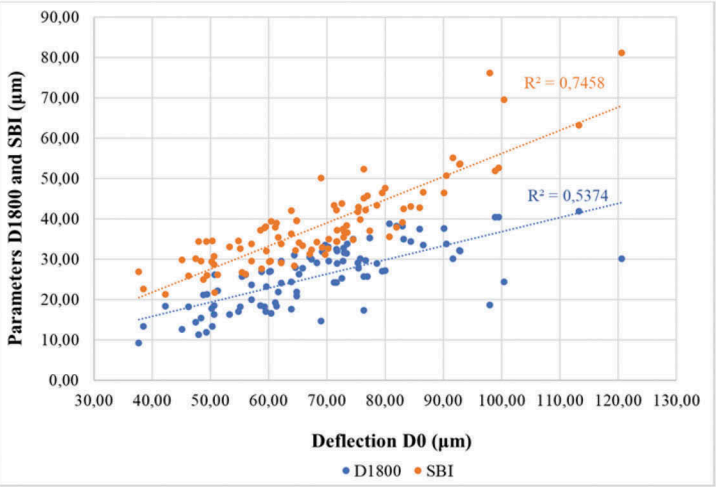

Figure 9. Correlation between the central deflection and parameters of other parts of pavement.

$$\mathrm{BCI450/1200} = \mathrm{D450} - \mathrm{D1200} \tag{3}$$

where D0 is the central deflection (μm), D450 and D1200 are deflections measured at the distance of 450 mm and 1200 mm respectively (μm).

The regression analysis confirmed a visual impression from the variability of SBI, SCI300, and BCI450/1200 along the section (Figure 10). The coefficient of determination R^2 has for the relationship between SBI and SCI300 the value of 0.455. The higher value of R^2 (0.855) for the relationship between SBI and BCI450/1200 could be perceived as confirmation of the greater influence of the homogenized (recycled) layer on the overall stiffness of the pavement structure.

All previously presented parameters were used to evaluate the bearing capacity of the reconstructed pavement based on criterions valid in Slovakia for the semi-rigid pavement (TP 031, 2008). As it can be seen in Table 2, the maximum values of all parameters are well below the limits required for the evaluated type of pavement. The average values resulting from the statistical evaluation (Figure 11) confirm the very good performance of the recycled pavement from the bearing capacity point of view.

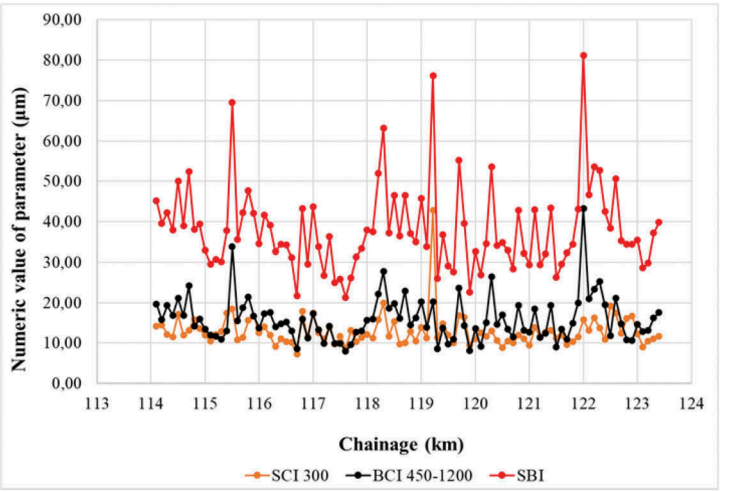

Figure 10. Values of SBI parameter and its components.

Table 2. Evaluation of bearing capacity of reconstructed pavement.

Parameter	Required limit ()	Maximum value ()	Average value ()
D0	170	121	69
SCI300	80	43	13
BCI450/1200	150	44	38
D1800	100	42	26

The homogeneity of the reconstructed pavement is another interesting topic. Coefficient of variation (CV) resulting from averages values and standard deviations of individual bearing capacity parameters of recycled pavement (Figure 11) is slightly above 0.2 for D0. Considering the kind of evaluated data, the acceptable variability and homogeneity can be stated from the viewpoint of total bearing capacity of reconstructed pavement. The CV oscillating around 0.3 (SBI, D1800, and SCI300) can be also considered as acceptable. Interesting fact is the CV for SBI is lower than CV of two possible components (SCI300 and BCI450/1200). It can be supposed the stiffness of asphalt and homogenized layer is combined along the section in such way that the final stiffness of pavement structure itself has lower variability than its two components.

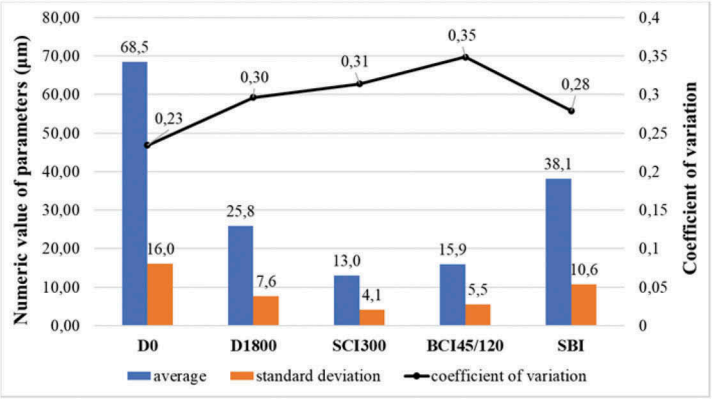

Figure 11. Statistical characteristics of bearing capacity parameters.

Although the overall evaluation confirmed the very good bearing capacity of the reconstructed pavement, it was also verified, if the modulus of elasticity of the homogenized layer considered in the design process of the new pavement was achieved. The design value of the modulus of elasticity for a layer corresponding to $CBGM_{C5/6}$ is 1200 MPa in the Slovak regulation concerning the design of flexible and semi-rigid pavements (TP 033, 2008). As some level of inhomogeneity was identified using the previously presented parameters, the division of the section into homogeneous sub-sections was carried out. The division was performed by the sum line method, the values of which were calculated as

$$S_1 = x_1 - \bar{x} \tag{4}$$

$$S_{i=2}^{n} = x_i - \bar{x} + S_{i-1} \tag{5}$$

where S_1 is the first value, S_i is the value at a point i, $x_{1,i}$ are values of used parameter at individual points and $\bar{x}$ is the average value of used parameter on whole section. The sum lines were calculated for the parameters D0, D1800, SCI300 and BCI450/1200 (Figure 12). Subsections were defined based on the shape of the sum line for the BCI450/1200 index as it was considered as the most suitable for characterizing the stiffness of the homogenized layer.

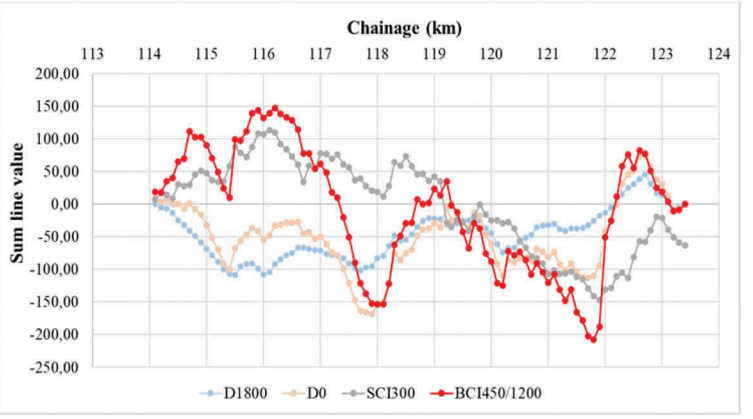

Figure 12. Sum lines of bearing capacity parameters.

After the subsections were determined, the average value of the deflection curve was calculated for each subsection. This was the input for the back-calculation of the elastic moduli using the CANUV computer program (Čelko and Komačka, 1998, Komačka and Čelko, 1996). It is one of the programs listed in COST 336 (European Commission, 2005) and has been routinely used by the Slovak Road Administration since 1996. As it can be seen in Figure 13, the elastic moduli of the homogenized layer vary in the individual subsections. Nevertheless, they all have a much larger value than the design value of 1200 MPa. The average value of elasticity modulus resulting from the back-calculation is about 4900 MPa with the coefficient of variation of 0.29 (less than for BCI450/1200 index in Figure 11). Based on this, it can be stated, the used technology of recycling succeeded in achieving stiffness of layer supposed in the design process, and acceptable homogeneity.

6 CONCLUSIONS

Various challenges from technical, technological, economic, and ecological aspects related to the design of the reconstruction of the road I/65. The possibility to make the 40 cm thick layer consisting of mix of crushed cement concrete slabs, added aggregate and hydraulic binder was

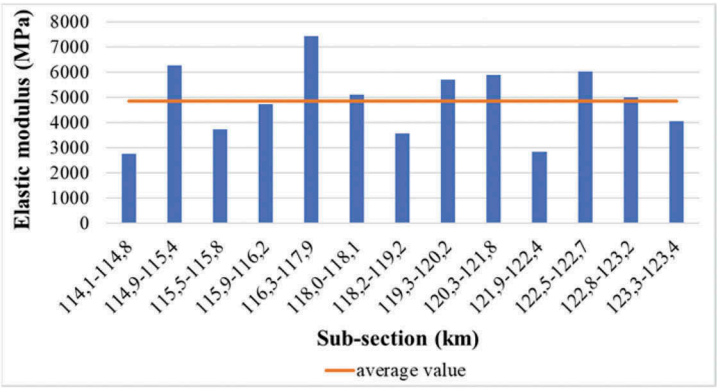

Figure 13. Elasticity modulus of homogenized layer in sub-sections.

practically verified from technological point of view. A careful selection of machinery with sufficient performance enabled a quick reconstruction. This kind of reconstruction is a green solution that significantly reduces the carbon footprint in comparison with the reconstruction based on the use of new raw materials. Moreover, the lower consumption of raw materials brings also economic benefit. The implementation of the very thick subbase layer with hydraulic binder is cost-effective also from the long-term performance of pavement. The relatively small investment added on the beginning brings approximately the doubled operating performance of final solution. The measurements by FWD proved significantly increase in bearing capacity of pavement. The analysis also confirmed the used technology of recycling is suitable to achieve high stiffness of homogenized recycled layer and ensure acceptable homogeneity.

The success of implementation of proposed technical solution for the reconstruction of the road I/65 is another in a series of similarly successful implementations carried out in Slovakia since 2015.

REFERENCES

Boros, Z., 2014a. *Pavement Diagnostics, Background for Reconstruction of Concrete Roads in Bratislava and Trnava* Region *(I/62, I/75). Measurement and Evaluation of Pavement Bearing Capacity by FWD*. Technical report. TPA, 2014.

Boros Z., 2014b. *Pavement design proposal of reconstruction of cement-concrete pavements in the region of Bratislava and Trnava (I/62, I/75)*. Technical report. TPA, 2014.

Boros Z., 2014c. *Road reconstruction design. Reconstruction of the road I/65 Turčianske Teplice - Príbovce, km 113,500 - km 129,000. Removal of the emergency state*. Technical report. TPA, 2014.

Čelko, J. and Komačka, J., 1998. *Analysis of the pavement bearing capacity on the deflection bowl basis*. V. International conference on the Bearing Capacity of Roads and Airfields. Trondheim, 1998, Volume I, pp. 609–617.

European Commission. *COST 336 The use of Falling Weight Deflectometers in Pavement Evaluation*. Final Report of the Action. 2. ed. Luxembourg: Office for Official Publications of the European Communities, 2005.

Komačka, J. and Čelko, J., 1996. *CANUV - computer program for analysis of the pavement bearing capacity on the deflection bowl basis*. Studies of University of Transport and Communications in Žilina, Civil Engineering Series, Volume 19, pp. 63–70, ES VŠDS Žilina, 1996.

Soták J., 2014. *Engineering geological survey of reconstruction of cement-concrete pavements in the region of Bratislava and Trnava (I/62, I/75)*. Technical report. TPA, 2014.

TP 031 *Measurement and evaluation of bearing capacity of asphalt pavements using FWD Kuab. Technical conditions*. Slovak Ministry of Transport, Post and Telecommunication, 2008.

TP 033 *Design o flexible and semirigid pavements. Technical conditions*. Slovak Ministry of Transport, Post and Telecommunication, 2008.

Eleventh International Conference on the Bearing Capacity of Roads, Railways and Airfields, Volume 2 – Hoff, Mork & Saba (eds)

Impact of climate change on railway construction, maintenance and safety in the United Kingdom

Nicholas DeVinne, Robert DeBold & Michael C. Forde
University of Edinburgh, UK

Carlton L. Ho
University of Massachusetts, Amherst, USA

ABSTRACT: Extreme weather has a harmful effect on railway performance, and climate change is causing this to increase. Major impacts include track failures in heat, overhead line collapse in winds, earthworks failure due to rainfall, or washout due to flooding. More than 1.5 million delay minutes are caused each year by extreme weather, alongside extended line closures. Climate trends show a tendency for an increase in extreme weather, with up to a 600% increase in extreme rainfall events in some UK regions since 1931. The UK railway network is inadequately prepared for the impacts of changing weather patterns. To maintain the performance of the railways, climate trends must be accurately identified and linked to their effects on railway infrastructure. Through this process, the areas of the UK, and the infrastructure assets that will experience the greatest risk, can be identified. With overall risk identified, targeted intervention measures can be organized and applied where necessary to maintain required resilience. Without adapting to the changing climate, railways in the UK will continue to deteriorate in performance and experience increasingly frequent infrastructure failures. Responding to climate change's effects on the railways will reduce disruption and damage to the railways, providing benefits through reduced delays and maintenance cost across the UK. Using climate data from the Meteorological Office of the past and current regional temperatures and precipitation data were used to evaluate the impact on the construction, maintenance, and safety of railway infrastructure.

Keywords: railroad, infrastructure, climate change, precipitation, temperature, delays

1 INTRODUCTION

Weather effects have a significant impact on the safety, resilience, and performance of railway operations. Currently, severe weather is responsible for around 20% of all delays on the UK rail network, representing an average of 1.5 million train delay minutes annually (Office of Rail and Road 2020) As a result, Network Rail pays out direct financial compensation to train companies of £50-100 million each year (Network Rail 2017), with even higher costs associated with repairs. For each incident of weather-related failure on the network, not only must the network be repaired, but the failures also result in indirect costs through lost time and decreased local connectivity.

Due to the ongoing effects of climate change, impacts to the railway network will become more frequent and damaging, resulting in even higher costs to the railways and

DOI: 10.1201/9781003222897-6

economy. Climate trends in the UK are leading most significantly to higher temperatures and higher precipitation. It is not only overall annual precipitation that is increasing, but also the frequency and intensity of extreme storms. Extreme rainfall events are now 60% more frequent than the preindustrial baseline (Rail Accident Investigation Branch 2020). Increasing weather intensity leads directly to increased risk to the railways and will increase the percentage of delays and disruption caused by weather. Although there is significant research into climate change, there is less research into the specific impact on transportation infrastructure, and even less on the appropriate adaptations in response. The direct links between changing weather patterns and risk to the railways has been insufficiently modelled, both in the UK and worldwide (Rail Safety and Standards Board 2016 (Wang, et al. 2020. Further research will make the network more resilient in response to the impacts of climate change.

Through better knowledge of the potential risks, UK railways can be made more resilient in the face of a changing climate. With the overall risks identified, the intensity of that risk for each aspect affecting the railways can be modelled spatially across the railway network. This will allow the combination of all relevant identified risk factors to develop a combined climate risk level assessment for each section of the railways. Additionally, the relative severity of any potential impacts to a certain section of the network (i.e., the traffic intensity on a section, and thus the overall disruption that would be caused) can be modelled to modulate the identified risk. After an overall risk level has been identified for each section of the network, appropriate investment in modifications and resilience improvements can be standardized and more efficiently implemented.

By improving the infrastructure of the railways, benefits will be gained not only for the passengers through reduced delays, but also for the infrastructure manager and the wider economy. Even if the infrastructure is unable to withstand extreme weather events, having a better understanding of those events will allow more efficient recovery from failure. More reliable data on the probability and impact of climatic effects on the railways will enable a targeted response by Network Rail, where the most vulnerable assets are improved before failure. For the wider economy, reduced railway disruption and closures would result in decreased 'lost time' cost. Responding to the growing threat of climate change is necessary across the UK and worldwide. Major incidents on the UK railway network are already relatively frequent, and will become more likely in the coming decades due to continued climate change impacts.

Discrete examples of infrastructure failures are not evidence of a wider impact of climate change. However, the growing frequency with which the railways are affected by weather shows the necessity of responding effectively to climate change. The most recent major incident in Scotland occurred on August 12, 2020. As a result of extreme precipitation, two separate incidents occurred (Haines 2020).

On the line from Edinburgh to Glasgow via Falkirk High, the adjacent canal overtopped, cascading large volumes of water onto the railway line. The associated damage resulted in a kilometer of track washed out and the railway remaining closed for a month (Dalton 2020). On the same day, a landslip at Stonehaven caused a derailment, resulting in fatal injuries to the driver and two other passengers. Here, the railway was closed for more than 2 months, with total incident cost over £10 million (McCartney 2020).

The incident which most affected the wider push for climate resilience on the UK railways was the two-month closure of the Cornish main line following heavy storms in 2014. With no diversionary routes, the entire south-west of England was cut off from the rest of the network. Overall cost to the economy has been estimated at £1.2 billion. That total cost considers losses to businesses due to lack of travel, impact of delayed time, etc. Although the direct infrastructure repair cost is important to consider, the largest impacts of railway closures are indirect (BBC News 2015) (Kennedy 2020).

Impacts to railway networks from climatic effects are not limited to the UK. For example, with increased global temperatures, railways laid in historically cold regions are at risk. The

Qinghai-Tibet railway in China is laid mainly on permafrost, which destabilizes if unfrozen. As the temperature increases, the railway is more susceptible to failure (Xiong, et al. 2015).

Susceptibility of UK railway earthworks to fail is often linked to their age (Haines 2020). However, newly constructed earthworks can also fail. In March 2020, a significant landslip occurred on the LGV Est in France (Poingt 2020).

Currently, the impact of climate changes on the transportation infrastructure of the UK has not been sufficiently modelled. Climate data shows clear trends in increasing maximum temperatures as well as increasing precipitation and extreme rainfall events, which both have an impact on the performance of the railways. The link between these climatic changes and the resilience of the UK railways must be further studied to identify likely impacts. Overall climate risk to specific assets can then be calculated. With that risk identified, appropriate responses can then be implemented to ensure continued performance.

Network Rail has recently published a final report on their task force investigation into earthworks management as a result of the Stonehaven derailment. This includes a lengthy review into the failure dynamics of earthworks and identifies pore water pressure in the earthworks as the main factor influencing failures. Additional factors of slope angle and historic vegetation management practices are also significant, but water management processes are the most important (Network Rail 2021). By further expanding on this knowledge of the factors influencing failure, the evolution in those influencing processes as a result of climate change can be quantified, and thus the spatial risk across the network identified.

2 EVIDENCE OF CLIMATE TRENDS AND ASSOCIATED PERFORMANCE IMPACTS

2.1 *Global climate change*

With years of research, there is clear evidence of globally increasing temperatures. The average global temperature has been increasing, with the average trend since then estimated at 0.65 to 1.06° C since 1850 (Committee on Climate Change 2016). Increasing temperatures are seen across the whole UK. The overall temperature increase is still on the order of 1 degree Celsius since 1910, suggesting a sharper trend of temperature increase for the UK.

Temperatures in the UK are expected to continue increasing throughout this century, even under the most optimistic emission scenarios, with two projected scenarios of UK temperatures to 2100 as RCPs (Representative Concentration Pathways) (Met Office Hadley Centre 2019). RCP 2.6 represents the most optimistic emissions scenario, and RCP 8.5 the most pessimistic (Intergovernmental Panel on Climate Change 2014). Actual temperature response will likely be between these two extremes. Thus, the likely temperature increase with respect to a 1910 baseline is around 3 degrees Celsius by 2100.

Due to global temperature increases, average sea levels have risen around 1.4 mm annually since 1900. However, this has increased to nearly 3 mm annually in recent decades. By 2100, average global sea level rise will be on the order of 0.4-0.8 m. Such an increase will have strong implications for coastal areas (Met Office Hadley Centre 2019). With rising sea levels, not only will the lowest lying littoral areas be submerged, but coastal flooding effects and wave surges will have an impact on a larger area. This will result in more impacts to railways following the coastline, which are common in the UK, especially in Cornwall and Wales.

Additionally, weather patterns are changing. Extreme weather events bringing elevated precipitation (above the 90^{th} percentile) have increased worldwide (Intergovernmental Panel on Climate Change 2012). Precipitation trends for all regions of the UK since 1931 have been analyzed to identify changes both in overall precipitation and the incidence of extreme

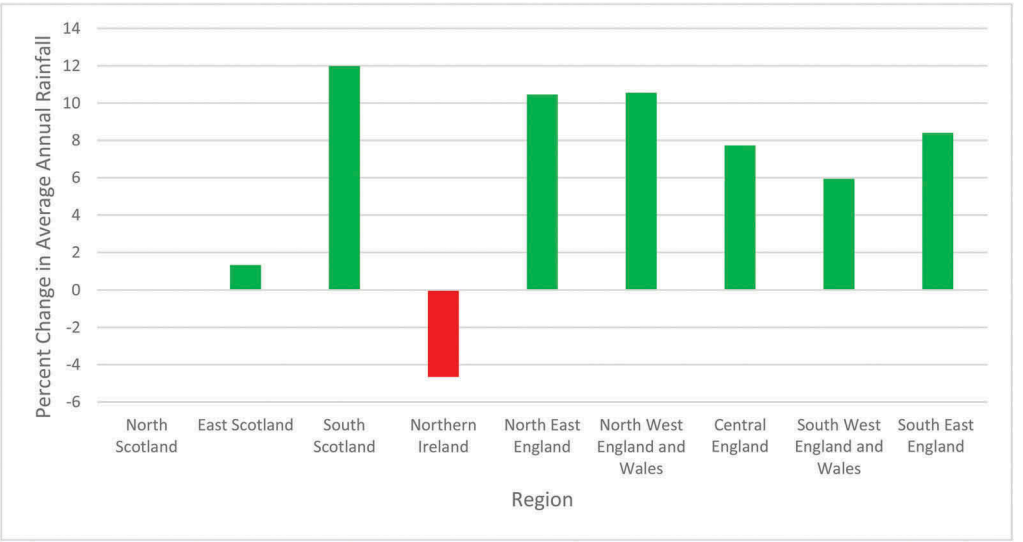

Figure 1. Percentage change in 20-year average annual rainfall by UK region from 1931 to 2019 (Data from Met Office Hadley Centre).

precipitation events. Figure 1 shows the percentage increase in annual average precipitation levels by region graphically from 1931 to 2019.

All UK regions apart from Northern Ireland have experienced increases in annual rainfall levels since 1931, with most seeing an increase of around 8-10%. North and East Scotland have seen the smallest increases in overall rainfall levels. However, Northern Ireland's railways are managed separately from the rest of the UK, so are excluded from this study. Thus, all regions under the control of Network Rail have experienced some level of rainfall increase since 1931, with these trends expected to continue to 2050/2100 (Network Rail 2015).

Additionally, the trends in extreme rainfall levels have been studied to give an idea of the evolution in the relative severity of rainfall events by region. Figures 2-5 show the identified regional trends in precipitation data overlaid onto the UK regions (Met Office Hadley Centre 2020). Regions shaded in red experienced decreases, regions in green increases, with regions in white being stable.

Shown in Figure 2, all regions experienced large increases in total annual rainfall except North and East Scotland and Northern Ireland, with the largest increase in South Scotland (12%). Shown in Figure 3, the average daily maximum rainfall (the largest amount of precipitation on any one day throughout the year) increased in all regions except North Scotland and Northern Ireland. Here, the largest increase was North East England (28%), revealing an increase in severity of extreme rainfall events. Figures 4 and 5 identify the change in occurrence of high-percentile rainfall events (days with rainfall above 30mm and 35mm respecticely). Again, increases were experienced across almost every region (apart from North Scotland). Here, the percentage changes are more extreme, with North East England experiencing a 600% increase in the average number of days with rainfall above 35mm. Regions that previously did not regularly experience extreme rainfall events are now seeing greatly increased occurrence of them.

Climate change is clearly affecting the UK, and will continue to do so. All regions of the UK are experiencing increasesing temperatures as well as changes to precipitation. Rainfall is not just increasing, but is also occuring with greater intensity. Much sharper increases are seen in the rate of occurrence of extreme rainfall levels rather than than the rate of change for overall annual rainfall. While each of these effects has impacts on railway infrastructure, the more extreme rainfall events are more likely to cause failures.

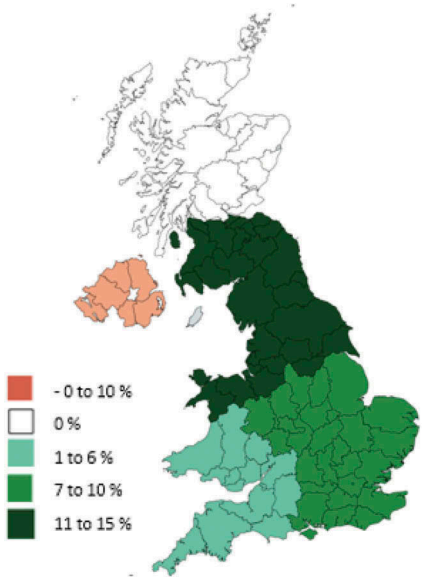

Figure 2. Percentage change in average annual rainfall by region (Data from Met Office Hadley Centre).

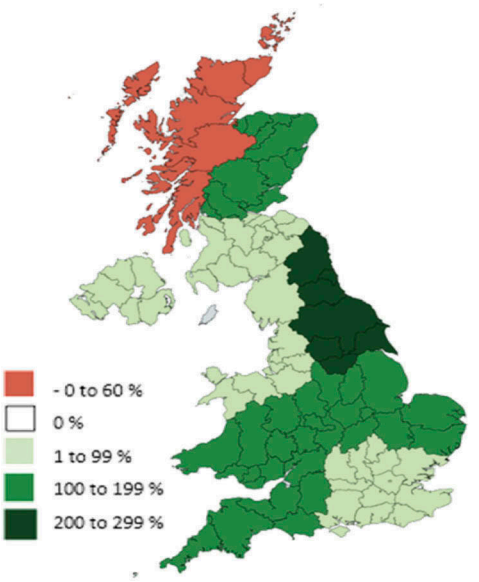

Figure 3. Percent change in average annual number of days with rainfall above 30mm by region (Data from Met Office Hadley Centre).

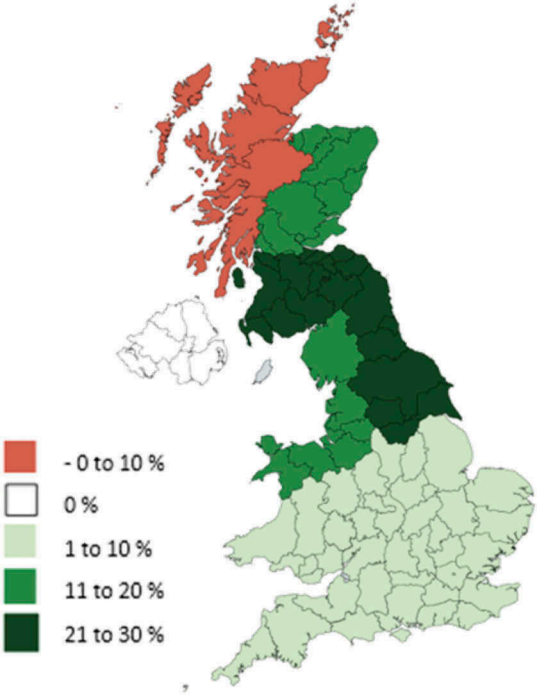

Figure 4. Percent change in average maximum daily rainfall by region (Data from Met Office Hadley Centre).

2.2 *Climate change's effects on the railways*

Climatic changes in the UK will result in varied effects on the railways, linked to an increase in extreme weather, both on the upper and lower bounds. Often, both extremes will have adverse effects to the railways. For example, the UK is expected to experience an increase in both extreme heat in the summer and extreme cold in the winter. Higher temperatures can result in rail buckling, elongation, and resulting sag of overhead line equipment. Lower temperatures can result in ice accumulation on overhead electrification, leading to damage and dewirements.

Similarly, both higher and lower rainfalls (as identified in Figures 2-5 above) result in increased risks to the railways. High intensity rainfall can result in increased probability of landslips and earthworks failure. Equally, lower rainfall can also lead to earthworks failure, by desiccation and shrinkage (Network Rail 2018).

All major identified risks to the railways, along with their triggering climatic effect and associated infrastructure asset, are summarized in Table 1 (Network Rail 2015). Most effects to the railways are linked to the changes in temperature and precipitation. Precipitation changes are linked both direct risk to earthworks as well as to increased incidence of flood hazard. Climate change will result in continually greater impacts to the performance of the UK railways without additional interventions to reduce the impact of these changes.

Scottish railways are exposed to even higher risk with respect to changes in precipitation due to local soil characteristics. Figure 6 shows the distribution of clay soil types cross the UK. Across Scotland, glacial till, or "boulder clay," with large plastic fines content makes up a large percentage of the ground. The granular material content reduces the plastic capacity of the soil, reducing its capacity to absorb excess water. With limited permeability, there is greater chance of flooding and failure (Network Rail 2018).

With increases in extreme weather, wind gusts will also become more frequent, bringing risks to damage of overhead lines. Future changes to the railway network will thus create additional points of failure. Under the UK government's plans to decarbonize the railway network by 2040 (2035 in Scotland), much additional overhead electrification is planned to be installed. Covering around 12,000 track kilometers, this will more than double the extent of overhead electrification in the UK, thus increasing the potential for failures (Network Rail 2020). While this is not now an insurmountable issue, the risk level must be addressed numerically with respect to electrification designs to ensure risk levels do not increase drastically as a result of electrification growth.

2.3 *Current impact on UK railways*

Extreme failures are the most visible impacts of the climate on the railway, but much more widespread impact is caused by smaller and more frequent weather impacts. Figure 7 shows the total cost of compensation paid out by Network Rail to train operators for weather-related delays between 2006 and 2016. The two categories of incident causing the most delays are flooding and extreme winds, with snowfall and adhesion issues third and fourth, respectively. All these categories, most notably flooding and wind, are expected to increase with climate change. Any increase in incidence of delay-triggering events will result not only in further delays to passengers but also higher costs (Network Rail 2017).

This compensation cost does not include the actual repair costs from any damage caused, nor the indirect costs due to lost time. Overall annual delay minutes linked to severe weather are on an increasing trend, as shown in Figure 8. It should be noted that the data scatter is quite high, but that there is still a definite increasing trend. Delay minutes have increased by an average of 7200 minutes per quarter since 2014 to reach a total of 1,174,559 minutes throughout 2019-2020 (Office of Rail and Road 2020). Estimated cost to the economy due to lost time and productivity from these delays is on the order of £122 million for 2019-2020 (BBC News 2008). This is in addition to the approximately £60 million in direct compensation

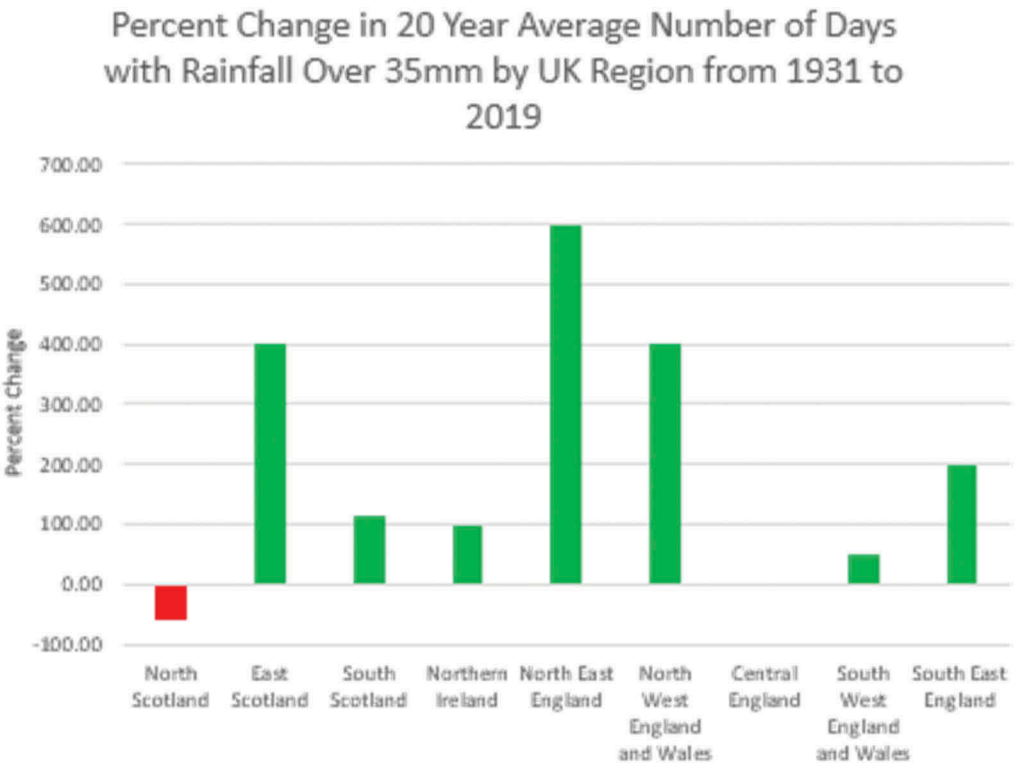

Figure 5. Percent change in average annual number of days with rainfall above 35mm by region (Data from Met Office Hadley Centre).

cost by NR, giving an annual financial impact from severe weather on the order of £200 million, again excluding any repair costs.

This is even more pronounced in Scotland, where the percentage of delays caused by severe weather is one of the highest in the UK. Figure 10 shows the average percentage of delay minutes caused by severe weather by operator, with the national average shaded in red and ScotRail in yellow. With Scottish regions experiencing some of the largest increases in maximum daily rainfall (South Scotland up 25%, East Scotland up 20%) [Figure 3 above] and annual days with extreme rainfall above 35 mm/day (South Scotland up 112%, East Scotland up 400%) [Figure 5 above], operational performance in Scotland will be even more affected by the changing climate.

2.4 *Effects on earthworks integrity*

Earthworks, which includes embankments, rock cuttings, and soil cuttings, make up more than half of the overall length of the UK railway network. They are thus the largest and most vulnerable collection of assets in the face of the changing climate. With soil cuttings and embankments constructed mainly of permeable material, significant shrink-swell (change in volume induced by changing soil saturation) occurs in heavy rains, resulting in a high rate of failures. Figure 11 shows the importance of rainfall as a factor in predicting earthworks failures across the UK rail network. During the periods in which there were more severe storms, the number of earthworks failures was equally higher. Similarly, for 30-day periods in which the total rainfall exceeded 300 mm, the rate of failure increases exponentially. This increase is less pronounced for rock cuttings, but the trend of increasing failures with increasing rainfall is still clear (Rail Safety and Standards Board 2020).

Increasing rates of failure likely in the coming decades due to increasing rates of extreme precipitation as a result of climate change. Precipitation data from across all UK regions has

Table 1. Risks to the railways posed by climate change (Adapted from Network Rail, 2015).

Temperature extremes and rate of change	Track	Buckles, derailments, reduced maintenance opportunities
	Switches and Crossings	Frozen and snow-blocked points, failure of equipment
		equipment
Low Temperature Extremes	Third Rail and Overhead Lines	Ice and snow build-up, contact failure
	Buildings	Slip/trip/fall risk to passengers and staff
	Level Crossings	Icy roads leading to vehicle incursions
Flooding Increases	All	Closure of line due to floods, Failure of inundated equipment, loss of access to assets, scour of embankments
Change in River Flows	Bridges	Asset failure via scour of riverbed material and accumulation of debris
Increased Rainfall	Earthworks	Landslip and Earthworks failure
Decreased Rainfall	Earthworks	Desiccation of earthworks
High Winds	Overhead Lines	Risk of failure from fallen trees and debris
Sea Level rise and storm surges	Coastal assets	Closure of track due to inundation, structural failure, increased wave overtopping and ingress into rolling stock
Seasonal Changes	Vegetation	Changes in tree growth rates impacting leaf fall effects
Lightning	Lineside Equipment	Asset failure
Extreme Weather	Staff	Poor working conditions

been analyzed using Met Office data, with local rainfall totals averaged across the regions to produce daily average precipitation totals. As identified in section 2.1 above, both average maximum daily rainfall totals have increased significantly for almost all observed regions.

However, for earthworks failures, the more significant factor is prolonged exposure to intense precipitation, which destabilizes the soil matrix and leads to collapse. To assess the trend in the probability of these intense rainfall totals, the 30 previous days' precipitation totals were summed for each day across the time series. Annual average 30-day totals as well as the number of 30-day periods in which the total rainfall fell within the high-risk categories from Figure 11 (200-300mm and >300mm) were then calculated using a 20-year average to minimize annual variation.

The results of this analysis are shown in Figures 12-14 below. As shown in Figure 11, the annual average precipitation per 30-day period has increased for every UK region except Northern Ireland, with most regions experiencing increases around 10 percent. The greatest increase was for South Scotland (12.5 percent), reflecting an increased risk from climate change in this region. Figure 13 shows the percentage increase in the number of 30-day periods per year in which the rainfall total was between 200 and 300mm. Significant increases were experienced across half of UK regions between 1931 and 2019, with only South East England sharply decreasing, falling by 26%. North West England and Wales experienced the largest

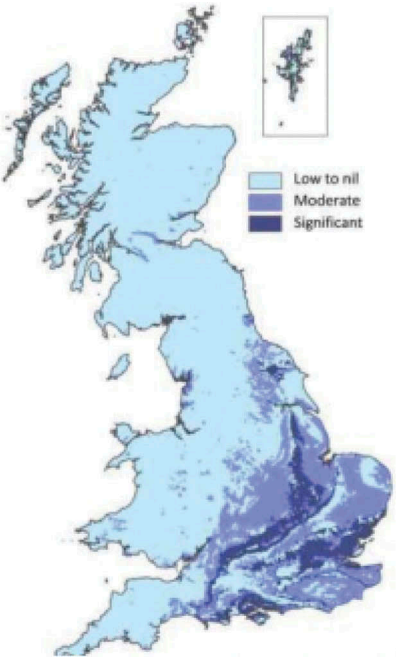

Figure 6. Potential shrink-swell of clay soils in the UK (adapted from British Geological Survey) (Network Rail 2018).

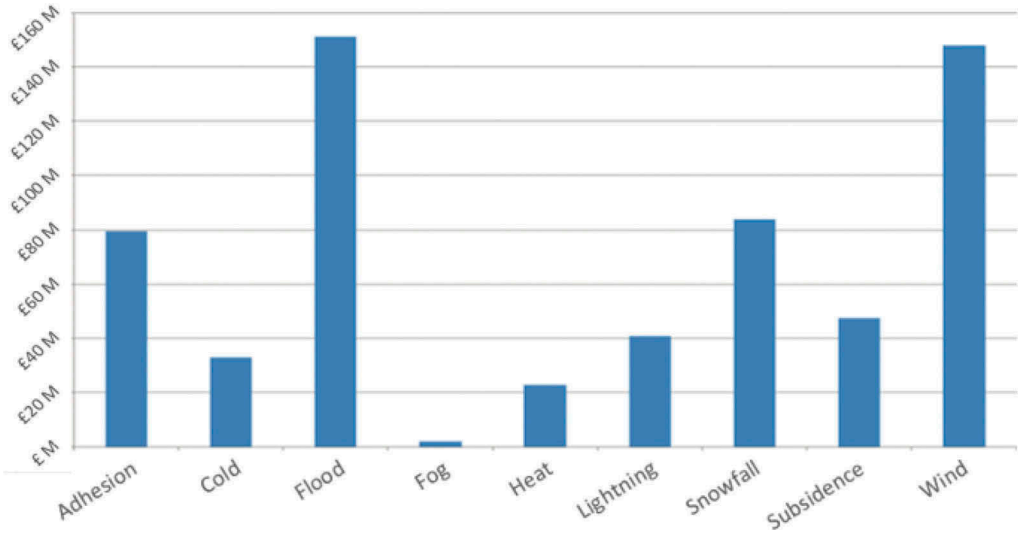

Figure 7. Total compensation cost paid by NR due to weather-related delays from 2006 to 2016 divided by triggering event (Data from Network Rail, 2017).

increase, with 258% more 30-day periods in 2019 (9.3 in 2019 vs 2.6 in 1931). South Scotland also experienced large growth, at 36% (40.7 vs 29.9 periods per year). The percentage increase in incidence for the most extreme precipitation (greater than 300mm in a 30-day period) is shown in Figure 14. Most regions are absent, having either no change, or never experiencing this level. However, South Scotland experienced an increase of over 1900% (3.05 vs 0.15 periods per year) (Met Office Hadley Centre 2020).

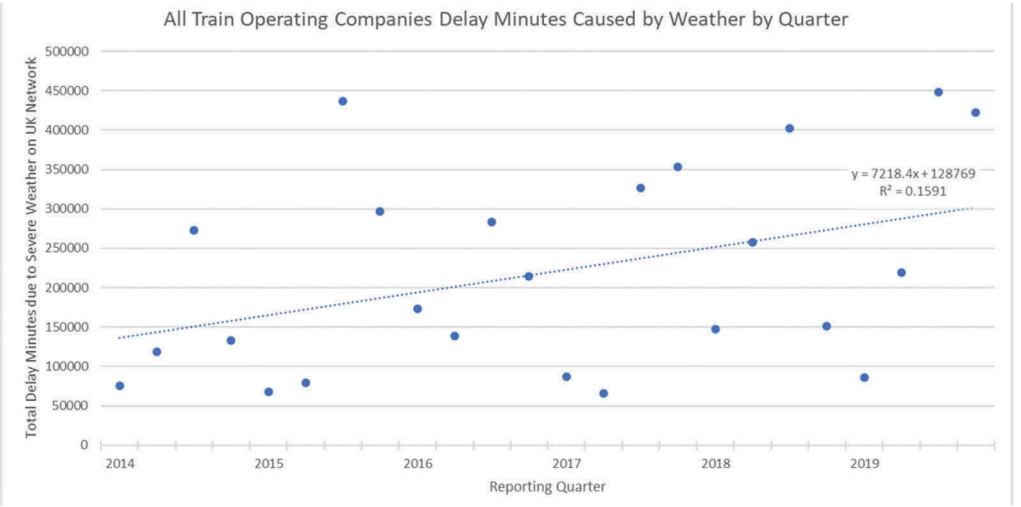

Figure 8. Trend in total delay minutes caused by severe weather on the UK railway network by quarter, 2014-2020 (Data from ORR, 2020).

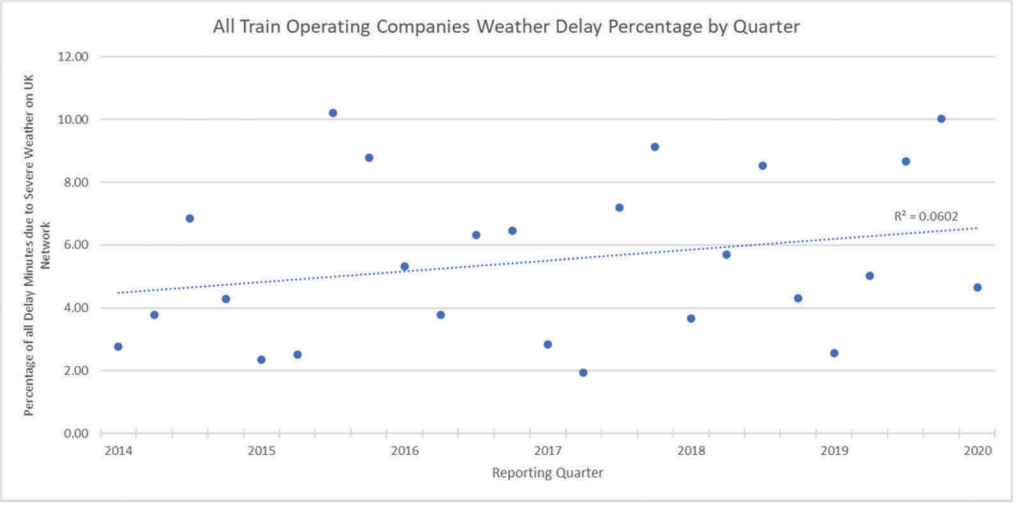

Figure 9. Trend in percentage of total delay minutes caused by severe weather on the UK railway network, 2014-2020 (Data from ORR, 2020).

Extreme changes in the typical precipitation experienced in a region like this, especially where the historical levels were near zero, must be considered when identifying the future risks for earthwork assets. The trends shown across 30-day rainfall level suggest that more extreme long-term precipitation periods are increasing across all regions, bringing increased failure risk. As earthworks failures are often sudden and can be catastrophic, as with the Stonehaven incident in Scotland in 2020, methods of addressing this increased risk must be identified.

Reducing this accident risk requires a two-fold approach. Firstly, the stability of earthworks can be improved or maintained to ensure that failures do not occur. However, this is much harder to do for natural assets than for bridges/permanent way, as they are more variably affected by climactic effects. Earthworks are inherently difficult both to monitor and repair, considering the heterogeneous nature of them. Additionally, having mainly been constructed with the original railways in the 19th century, there is limited if any information about the

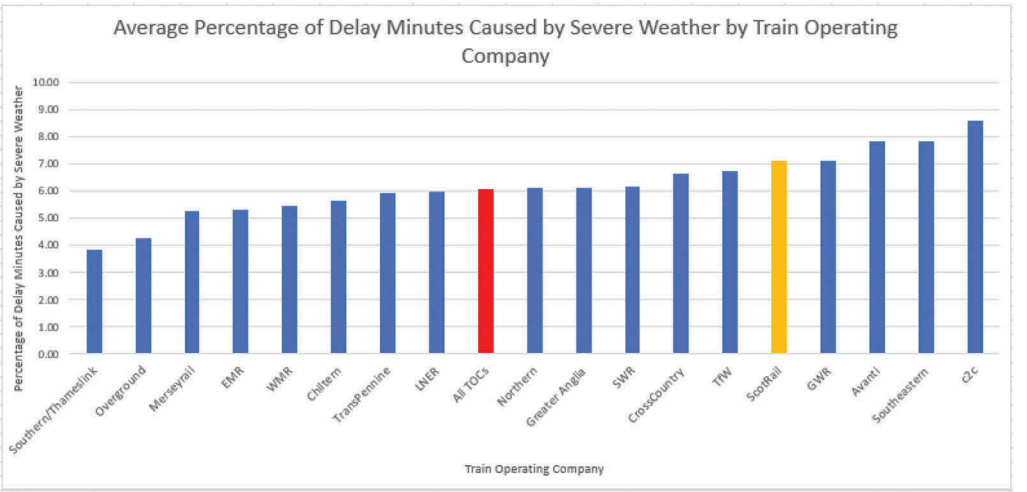

Figure 10. Average percentage of overall delay minutes experienced by train operating companies triggered by severe weather (Data from ORR, 2020).

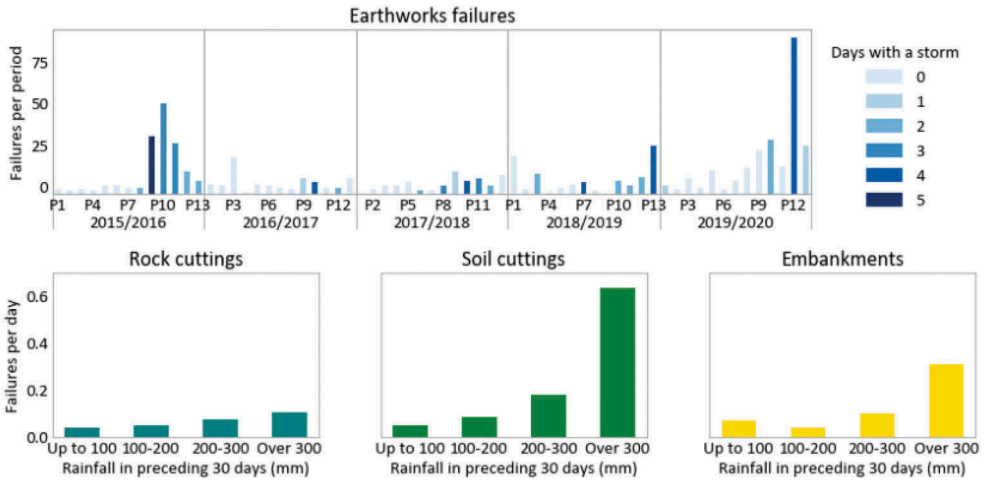

Figure 11. Top: Rate of earthworks failures per period with respect to days with a storm per control period. Bottom: Rate of earthworks failures per day with respect to rainfall in preceeding 30 days. (Data from RSSB, 2020).

underlying soil and rock types. Most embankments were constructed by simple end-tipping, meaning material was brought to the end of a growing embankment, dumped off the side, and the process repeated. This process leads to unknown and uneven soil parameters within the embankment and creates varied hazards for the future (Network Rail 2018)..

2.5 *Effects on surface water flooding*

Resulting from changes to precipitation patterns, the hydrological response of rivers and groundwater will also change. Since the 1960s, river flows have increased in the north and west of the UK, mostly in higher areas, with autumn flow levels having increased across the whole of the UK. Not only have average flows increased, but also the maximum magnitude of flows as well as the duration of those events, with these trends expected to continue.

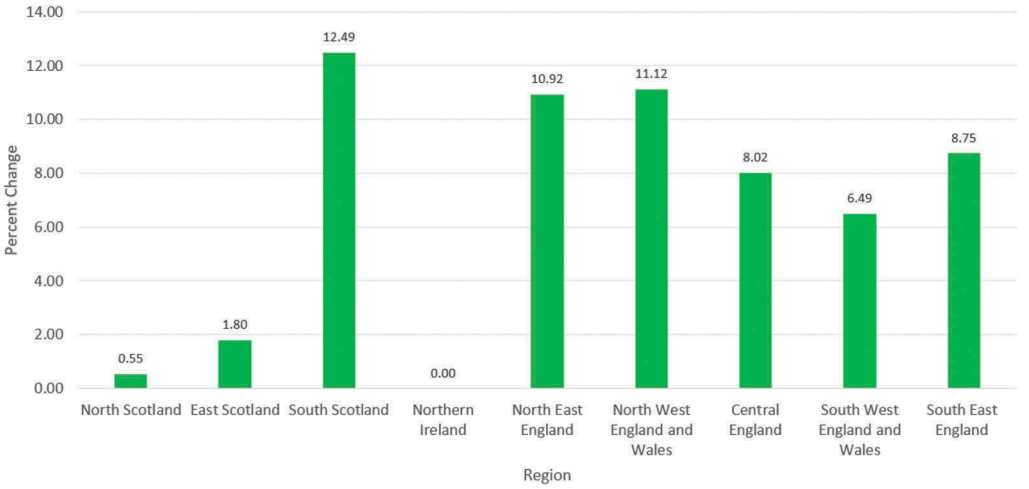

Figure 12. Percentage change in the annual average precipitation experienced in each 30-day period averaged with the previous 20 years between 1931 and 2019 across UK regions. (Data from Met Office Hadley Centre).

Using the UKCP scenarios, estimated the change in magnitude of 20-year return period floods across the UK to 2070 has been found to be between 11% and 68%, with an average estimated change around 30-40%. Trends in groundwater levels, also affecting flooding by affecting the permeability level of a floodplain, have not been extensively studied in the UK, but may also have an impact in the future (Watts, et al. 2015).

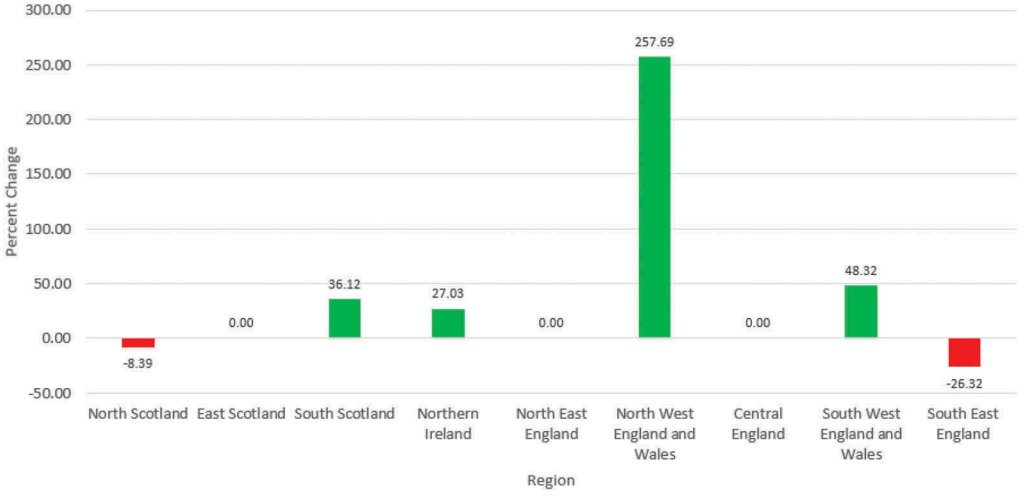

Figure 13. Percentage change in the annual average number of 30-day periods in which the total precipitation for that period was between 200 and 300 mm averaged with the previous 20 years between 1931 and 2019 across UK regions. (Data from Met Office Hadley Centre.

Future river flow levels have been modelled according to estimated climate trend scenarios to identify the likely magnitude of change versus current flow levels. Overall expected change in river flows varies substantially both by season and region of the UK. Across most of the UK, the largest increases in river flow are expected during the winter months, with some areas experiencing expected increases of up to 60%. In contrast, summer flows are expected to

decrease across most regions (UK Centre for Ecology and Hydrology 2020). This increased river flow levels and flood magnitudes will result in increased surface water risk to the railways. Looking at flooding risk to rail infrastructure itself, the Scottish Environmental Protection Agency has identified areas of flood risk according to low, medium, and high probability floods. The length of railway lines which are subject to surface or river flooding risk across the central belt of Scotland, indicate an extensive risk across even just a small area.

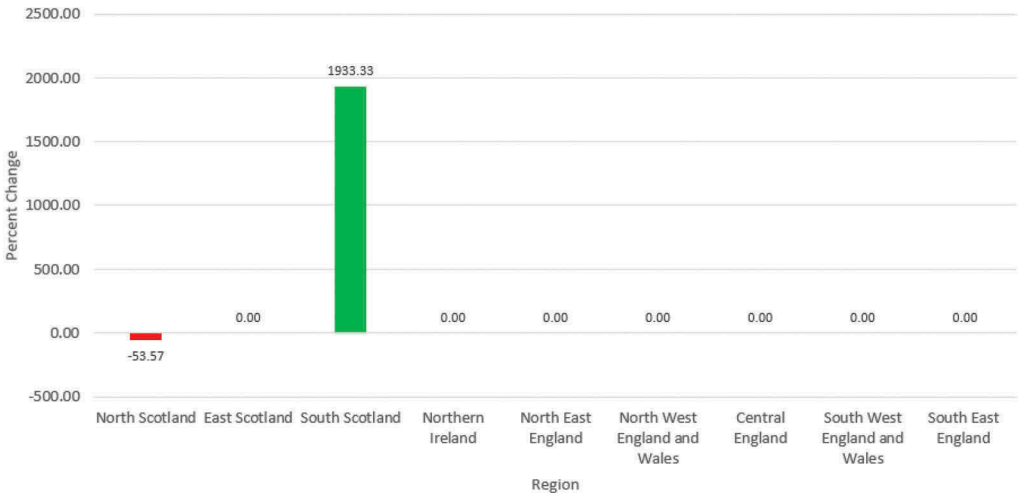

Figure 14. Percentage change in the annual average number of 30-day periods in which the total precipitation for that period was greater than 300 mm averaged with the previous 20 years between 1931 and 2019 across UK regions. (Data from Met Office Hadley Centre, 2020).

River flooding is one of the most financially and materially damaging impacts to the railway network, resulting in line closures as well as expensive repairs. Railway track performance before, during, and after a flooding event was measured by researchers at Heriot-Watt University, with results indicating a significant increase in maximum settlement. Settlement up to 65 mm was observed during compaction after flooding, versus only 8 mm in an unsaturated state. Where cyclic loading (as with trains passing over a section of track) is combined with oversaturation of soil, the subgrade is prone to form a slurry, which can result in fouling of ballast as well as deterioration of track geometry, leading to failure and derailments (Hasnayan, et al. 2017).

To combat flood damage, the Austrian railway operator commissioned the use of strategic flood risk management via the flood damage model RAIL (Railway Infrastructure Loss). Under this model, the expected flood damage as well as the linked maintenance repair costs were estimated across the network for floods with a return period of 30, 100, and 300 years.

In order to apply the model across the catchement area, detailed maps of the water depth at affected sections were used. The railway network across the catchment basin was then subdivided into lengths of 100 meters and the number of exposed sections for different classes identified for floods of 30, 100, and 300 year return periods (Kellermann, Schonberger and Thieken 2016) (Kellerman, et al. 2015).

Murphy et al, (2016), investigated applying a similar model of flood estimation to the UK network. With flooding resulting in significant damage and disruption, having more accurate modelling of the risks and probability of occurrence would allow both better preparedness as well as targeted intervention. In their model, local rainfall predictions are combined with historical river basin response to develop hydraulic models for flood inundation. This allows the accurate modelling of water depth levels across complex topographical areas. Use of forecasting methods like these would allow more proactive mitigation measures and aid in closure decision-making processes (Murphy, et al. 2016). Using this information, areas with the

highest damage cost probability combined with the lowest return period flood could be prioritized for infrastructure modification.

Modifications to the precipitation patterns across the UK because of climate change will likely lead to increased occurrence of high magnitude flooding events, especially across the winter months. This will result in increased damage and disruption to the railway network without intervention. By combining precipitation estimates with historical river flow data, the areas with the highest probability of flooding can be identified, with the associated damage costs estimated and the highest priority areas identified.

River flooding is one of the most financially and materially damaging impacts to the railway network, resulting in line closures as well as expensive repairs. Railway track performance before, during, and after a flooding event was measured by researchers at Heriot-Watt University, with results indicating a significant increase in maximum settlement. Settlement up to 65 mm was observed during compaction after flooding, versus only 8 mm in an unsaturated state. Where cyclic loading (as with trains passing over a section of track) is combined with oversaturation of soil, the subgrade is prone to form a slurry, which can result in fouling of ballast as well as deterioration of track geometry, leading to failure and derailments (Hasnayan, et al. 2017).

To combat flood damage, the Austrian railway operator commissioned the use of strategic flood risk management via the flood damage model RAIL (Railway Infrastructure Loss). Under this model, the expected flood damage as well as the linked maintenance repair costs were estimated across the network for floods with a return period of 30, 100, and 300 years.

In order to apply the model across the catchement area, detailed maps of the water depth at affected sections were used. The railway network across the catchment basin was then subdivided into lengths of 100 meters and the number of exposed sections for different classes identified for floods of 30, 100, and 300 year return periods (Kellermann, Schonberger and Thieken 2016) (Kellerman, et al. 2015).

Murphy et al, (2016), investigated applying a similar model of flood estimation to the UK network. With flooding resulting in significant damage and disruption, having more accurate modelling of the risks and probability of occurrence would allow both better preparedness as well as targeted intervention. In their model, local rainfall predictions are combined with historical river basin response to develop hydraulic models for flood inundation. This allows the accurate modelling of water depth levels across complex topographical areas. Use of forecasting methods like these would allow more proactive mitigation measures and aid in closure decision-making processes (Murphy, et al. 2016). Using this information, areas with the highest damage cost probability combined with the lowest return period flood could be prioritized for infrastructure modification.

Modifications to the precipitation patterns across the UK because of climate change will likely lead to increased occurrence of high magnitude flooding events, especially across the winter months. This will result in increased damage and disruption to the railway network without intervention. By combining precipitation estimates with historical river flow data, the areas with the highest probability of flooding can be identified, with the associated damage costs estimated and the highest priority areas identified.

2.6 *Effects on vegetation management*

Finally, the changing climate in the UK is likely to have an impact on the disruption caused by vegetation at the lineside. Trackside vegetation already causes significant disruption, mainly during leaf-fall season. This is due to the falling leaves, which when crushed by repeated passes train wheels and combined with water form an oily film which reduces the adhesion between wheel and rail. Not only is this dangerous and leads to potential signal or platform overruns, but it also results in extensive delays (Network Rail 2018).

Additionally, high winds lead to downed branches, with associated risk to overhead lines. With such an extensive network, lineside vegetation clearance is a significant issue. Overall, Network Rail is responsible for over 52,000 hectares of land and 6.3 million trees, with additional impact from vegetation on adjacent third-party land. Prior to the 1960s, before more stringent

environmental rules were put into place, complete burning, and clearance of the lineside was standard practice. Since then, the rate of incidents has grown steadily. The impact of vegetation management failures is significant on performance of the railway. Nearly 2000 cancellations were caused in 2017 due to tree strikes, while leaf fall results in an economic impact of nearly £300 million each year. There is a clear need to improve the current practices of managing lineside vegetation, with Figure 15 showing the growth in overall annual incidents relating to tree/branch strikes on the UK network between 2009 and 2017: (Varley 2018) Due to ongoing climate change, bringing increased storm frequency and higher wind gust speeds, the frequency of tree strikes will likely continue increasing if nothing is changed with respect to the current state of lineside vegetation.

Additionally, increased temperatures, associated with an increase in vegetated volume growth, will increase the impacts relating to leaf-fall. According to historical forest plots dating back to the 1870s, the main tree species in Central Europe have experienced increasing rates of vegetation growth. Tree growth rates have increased by up to 77% since 1960 due to increasing temperatures. (Madrigal-Gonzalez, et al. 2018) (Pretzsch, et al. 2014) (Committee on Climate Change 2017). With vegetation growth projected to increase with increasing temperatures across the UK, potential impact due to adhesion issues and downed branches will increase without appropriate mitigation

2.7 *Inadequate response to climate threat*

Despite overwhelming evidence of the increase in risk to railway infrastructure, there is a lack of clear strategy in the UK to meet this threat. Numerous studies have identified those risks,

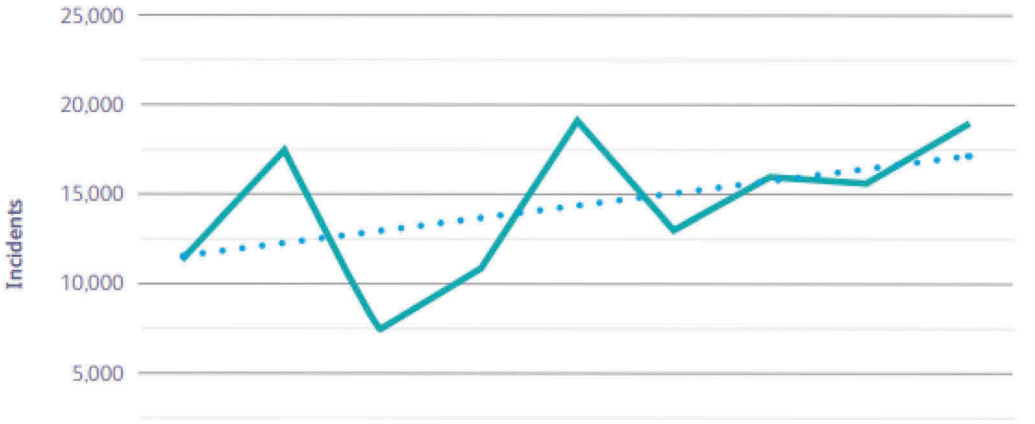

Figure 15. Annual reported incidents involving trees or branches across the UK network (Data from Varley, 2018).

but quantitative recommendations for adaptation and response are limited. An independent report published in 2014 exposed the inadequacy of Network Rail's climate response. Most of Network Rail's priorities for mitigating climate change are investigatory, with the company "not. . .actively preparing adaptation plans" (Dora 2014). Similar assessments of Network Rail's lack of preparedness are given in 2016 by the Institution of Civil Engineers and most recently in 2020 by Wang et. al., identifying an overall paucity of widespread adaptation. Climate resilience for the transportation industry is defined as "the capacity of the transportation system to anticipate, absorb, accommodate, or recover from the effects of a climate event in a required period and cost of recovery" (Intergovernmental Panel on Climate Change 2012). However, responses to climate change are mainly reactionary, with little in the way of improving readiness for future impacts. There is a focus on "day-to-day concerns at the expense of anticipation and transversality" (Depoues 2017).

In the UK, most infrastructure changes occur largely because of extreme events which exceeded the threshold of coping. The Dawlish Sea Wall, for example, has been subject to extensive maintenance throughout the years, yet no actual improvements were carried out prior to the 2014 storms despite evidence of increasing risk (Morris and Baker 10 Nov 2010). Even after the collapse in 2014, the sea wall was repaired with little modifications until a project in 2019. That project, improving only the sea wall, is costed at over £80 million, compared with the £100 million estimated in 2010 for an entire alternative route (Morris and Baker 10 Nov 2010) (Network Rail 2019).

Despite good effort by Network Rail, the increased pace of climate change is leading to increasing performance impacts on the railway. While reactionary measures have been largely sufficient previously, the traditional way of working will no longer be sustainable within the coming decades. As the effects from climate change continue to grow, the need for wider adaptation measures becomes greater. A new strategy is thus required to ensure the continued performance of the railways in the UK.

While the need for adaptation is clear, with overall average damage cost resulting from climate events expected to increase by 75% to 2050 (Doll, et al. 2014), the methods of achieving that adaptation are far less so. Potential future risks must be fully analyzed, their impacts (both economic and human) calculated, and the interventions necessary to minimize that risk considered. However, there is often incomplete data to carry out an accurate and complete risk assessment (Wang, et al. 2020).

3 CONCLUSIONS

Global Climate change has shown to have a direct influence on world temperature. The United Kingdom is experiencing similar increases in temperature on the order of 1 degree Celsius in all its countries. In addition, the annual precipitation and storm severity has also in creased with the exception of in Northern Ireland. This has a direct impact on the operation and maintenance of the British railroad system.

The direct impact of increased temperature, precipitation, and storm intensity includes impact to track structure, electrification, buildings, level crossing bridges, earthworks, vegetation, and coastal assets. Climate change has had a measurable effect in the following ways:

1. The increase in storm and storm severity has resulted in an increase in train delays. This has been particularly due to flood and high winds. Overall, delay times as a result of severe weather have increased over the period from 2014-2019 with an average increase of 7,200 min/yr.
2. The increase in the storm intensity and duration has resulted in an increase in disruptions due to the loss of earthwork integrity, failure in soil cuttings, failures of embankments, and to a lesser degree, failure in rock cuttings.
3. Increased surface water flooding that resulted from the increase in precipitation and storm severity increased the likelihood that rail infrastructure would impact the track system by increasing ballast fouling, and deteriorating the track geometry.
4. Increased storm severity resulted in an increased need for vegetative management and response. Storm severity will cause high winds and soft soil conditions that resulted in more downed trees and branches.

An ever-greater increase in adverse conditions will results from climate change. More work needs to be done to make the system of railroads in the United Kingdom more resilient to the increased temperatures and precipitation. In spite of the efforts made by Network Rail, the increases in adverse climate that is anticipated in the coming years will put a strain on the system and need to be addressed in a proactive way.

ACKNOWLEDGEMENTS

The research presented in this report was supported by the University of Edinburgh EPSRC Innovation Acceleration Account PIV047.

REFERENCES

Armstrong, John, and John Preston. 2016. "Adapting Railways to Provide Resilience and Sustainability." *Engineering Sustainability* 170 (ES4).

BBC News. 2008. *800,000 train delays cost '£1bn'*. Accessed December 1, 2020. http://news.bbc.co.uk/1/hi/uk/7295682.stm#:~:text=BBC%20NEWS%20%7C%20UK%20%7C%20800%2C000%20train%20delays%20′cost%20%C2%A31bn'&text=Rail%20passengers%20faced%20800%2C000%20delays,%C2%A31bn%20in%20lost%20time.

BBC News. 2015. *Dawlish Rail Line: Closure 'Costs Economy up to £1.2bn'*. Accessed October 29, 2020. https://www.bbc.co.uk/news/uk-england-devon–31140192.

Cedilnik, Gregor, Ryan Hunt, and Gareth Leed. 2018. "Advances in Train and Rail Monitoring with DAS." Lausanne: The Optical Society.

Chatfield, C. 1983. *Statistics for Technology*. London: Chapman-Hill.

Committee on Climate Change. 2016. "UK Climate Change Risk Assessment 2017 Synthesis Report: Priorities for the Next Five Years."

Committee on Climate Change. 2017. "UK Climate Risk Assessment 2017, Chapter 3: Natural Environment and Natural Assets."

Dalton, Alastair. 2020. "Edinburgh-Glasgow Rail Main Line Faces Two-Month Flood Damage Closure." *The Scotsman*. Accessed November 12, 2020. https://www.scotsman.com/news/transport/edinburgh-glasgow-rail-main-line-faces-two-month-flood-damage-closure–2946024.

Dawson, David A. 2012. *The Impact of Sea-Level Rise on the London-Penzance Railway Line*. University of Plymouth.

Depoues, Vivian. 2017. "Organisational Uptake of Scientific Information About Climate Change by Infrastructure Managers: the Case of Adaptation of the French Railway Company." *Climatic Change* 143 (3): 473–486.

Doll, Claus, Christian Trinks, Norbert Sedlacek, Verena Pelikan, Tina Comes, and Frank Schultmann. 2014. "Adapting Rail and Road Networks to Weather Extremes: Case Studies for Southern Germany and Austria." *Natural Hazards* (72): 63–85.

Dora, John. 2014. *A Climate Change Report Card for Infrastructure*. John Dora Consulting Limited.

Eleye-Datubo, A. G., A. Wall, and J. Wang. 2008. "Marine and Offshore Safety Assessment by Incorporative Risk Modeling in Fuzzy-Bayesian Network of an Induced Mass Assignment Paradigm." *Risk Analysis* 28 (1).

Haines, Andrew. 2020. *Resilience of Rail Infrastructure: Interim Report to the Secretary of State for Transport Following the Derailment at Carmont, near Stonehaven*. Network Rail.

Hasnayan, M Menan, W John McCarter, Peter Woodward, David Connolly, and Gerard Starrs. 2017. "Railway subgrade performance during flooding and the post-flooding (recovery) period." *Transportation Geotechnics* 57 (68).

He, Zuyuan, Qingwen Liu, Xinyu Fan, Dian Chen, Shuai Wang, and Guangyao Yang. 2018. "FIber-Optic Distributed Acoustic Sensors (DAS) and Applications in Railway Perimeter Security." *Advanced Sensor Systems and Applications* 8.

Ho, Carlton L, and Scott B Miles. 1997. "Deterministic Zonation of Seismic Slope Instability: An Application of GIS." *Spatial Analysis in Soil Dynamics and Earthquake Engineering* (67): 87–102.

Huabin, Wang, Liu Gangjun, Xu Weiya, and Wang Gonghui. 2005. "GIS-based landslide hazard assessment: an overview." *Progress in Physical Geography* 29 (4): 548–567.

Intergovernmental Panel on Climate Change. 2012. *Changes in Climate Extremes and their Impacts on the Natural Physical Environment*. Cambridge, UK: Cambridge University Press.

Intergovernmental Panel on Climate Change. 2014. "Climate Change 2014 Synthesis Report." Geneva.

Kellerman, P, A Schobel, G Kundela, and A H Thieken. 2015. "Estimating Flood Damage to Railway Infrastructure: the Case Study of the March River Flood in 2006 at the Austrian Northern Railway." *Natural Hazards and Earth System Sciences* (15): 2485–2496.

Kellermann, Patric, Christine Schonberger, and Annegret H. Thieken. 2016. "Large-scale Application of the Flood Damage Model RAilway Infrastructure Loss (RAIL)." *Natural Hazards and Earth System Sciences* (16): 2357–2371.

Kennedy, Catherine. 2020. "Dawlish Sea Wall Plans Approved to Protect Rail Link." *New Civil Engineer*.

Koks, E, J Rozenburg, M Tariverdi, M Vousdoukas, S Fraser, J Hall, and S Hallegatte. 2019. "A global multi-hazard analysis of road and railway infrastructure assets." *Nature Communications* 10 (1): 1–11.

Kramer, Steven. 1996. "Probabilistic Seismic Hazard Analysis." In *Geotechnical Earthquake Engineering*, 117–139. Upper Saddle River, NJ: Prentice Hall.

Madrigal-Gonzalez, Jaime, Enrique Andivia, Miguel A. Zavala, Markus Stoffel, Joaquin Calatayud, Raul Sanchez-Salguero, and Juan Ballesteros-Canavos. 2018. "Disentangling the Relative Role of

Climate Change on Tree Growth in an Extreme Mediterranean Environment." *Science of the Total Environment* 642: 619–628.
McCartney, Scott. 2020. "Stonehaven Train Crash: Work Starts to Fix Tracks After Derailment." *The Scotsman*.
Met Office Hadley Centre. 2020. *HadUKP Observation Data*. Accessed October 27, 2020. https://www.metoffice.gov.uk/hadobs/hadukp/data/download.html.
Met Office Hadley Centre. 2019. "UKCP18 Science Overview Report."
Met Office. 2020. *Historic Station Data*. Accessed November 25, 2020. https://www.metoffice.gov.uk/research/climate/maps-and-data/historic-station-data.
Morris, Anne Marie, and Norman Baker. 10 Nov 2010. "House of Commons Debates (Hansard)." UK House of Commons. col: 136WH-138WH.
Murphy, Alexandra, Ben Gouldby, Steven Cole, Robert Moore, and Helen Kendall. 2016. "Real-time flood inundation forecasting and mapping for key railway infrastructure: a UK case study." E3S Web of Conferences.
National Research Council. 2010. *Informing an Effective Response to Climate Change*. Washington, DC: The National Academies Press.
Network Rail. 2021. "A Review of Earthworks Management." Task Force Report.
Network Rail. 2018. *Autumn on the Railway*. Accessed November 16, 2020. https://www.networkrail.co.uk/stories/autumn-on-the-railway/.
Network Rail. 2015. "Climate Change Adaptation Report 2015." *Network Rail*. Accessed October 27, 2020. https://www.networkrail.co.uk/wp-content/uploads/2019/05/Climate-Change-Adaptation-Report-2015-FINAL.pdf.
Network Rail. 2019. "Dawlish Sea Wall." Accessed December 9, 2020. https://www.networkrail.co.uk/running-the-railway/our-routes/western/south-west-rail-resilience-programme/dawlish-sea-wall/.
Network Rail. 2018. *Earthworks Technical Strategy*. Network Rail.
Network Rail. 2014. "Route Weather Resilience and Climate Change Adaptation Plans: Scotland."
Network Rail. 2020. "Traction Decarbonisation Network Strategy: Interim Programme Business Case."
Network Rail. 2017. "Weather Resilience and Climate Change Adaptation Strategy 2017–2019." January 27. https://safety.networkrail.co.uk/wp-content/uploads/2017/02/NR-WRCCA-Strategy-2017-2019.pdf.
Office of Rail and Road. 2020. "Passenger Rail Performance." September 17. Accessed November 15, 2020. https://dataportal.orr.gov.uk/statistics/performance/passenger-rail-performance/.
Office of Rail and Road. 2020. "Passenger Rail Usage." March 12. Accessed December 4, 2020. https://dataportal.orr.gov.uk/statistics/usage/passenger-rail-usage/.
Peng, Fei, Han Wu, Xin-Hong Jia, Yun-Jiang Rao, Zi-Nan Wang, and Zheng-Pu Peng. 2014. "Ultra-Long High-Sensitivity Φ-OTDR for High Spatial Resolution Intrusion Detection of Pipelines." *Optics Express* 22 (11): 13804–13810.
Poingt, Marie-Helene. 2020. *Apres le Deraillement du TGV Strasbourg-Paris, des Questions sur les Glissements de Terrain qui Affectent les Liaisons Ferroviaires*. Accessed November 23, 2020. https://www.ville-rail-transports.com/ferroviaire/un-tgv-strasbourg-paris-deraille-suite-a-un-affaissement-de-terrain/.
Power, Christopher, Juliet Mian, Tim Spink, SImon Abbott, and Michael Edwards. 2016. "Development of an Evidence-Based Geotechnical Asset Management Policy for Network Rail, Great Britain." Advances in Transportation Geotechnics.
Pretzsch, Hans, Peter Biber, Gerhard Schutze, Enno Uhl, and Thomas Rotzer. 2014. "Forest Stand Growth Dynamics in Central Europe Have Accelerated Since 1870." *Nature Communications* (5).
Rail Accident Investigation Branch. 2020. "Resilience of Rail Infrastructure: Interim Report to the Secretary of State for Transport Following the Derailment at Carmont, near Stonehaven." September 1. Accessed October 27, 2020. https://assets.publishing.service.gov.uk/government/uploads/system/uploads/attachment_data/file/928593/resilience-of-rail-infrastructure-interim-report.pdf.
Rail Safety and Standards Board. 2020. "Infrastructure Asset Integrity 2019–2020." September 09. Accessed February 09, 2021. https://www.rssb.co.uk/-/media/Project/RSSB/RssbWebsite/Documents/Public/Public-content/Improving-Safety-and-Health/ashr/2019-20-Infrastructure-Asset-Integrity.pdf.
Rail Safety and Standards Board. 2016. "Tomorrow's Railway and Climate Change Adaptation: Final Report." June. Accessed October 27, 2020. https://www.sparkrail.org/Lists/Records/DispForm.aspx?ID=23276.
Schenato, Luca, Luca Palmieri, Matteo Camporese, Silvia Bersan, Simonetta Cola, Alessandro Pasuto, Andrea Galtarossa, Paolo Salandin, and Paolo Simonini. 2017. "Distributed Optical FIbre Sensing for Early Detection of Shallow Landslides Triggering". *Scientific Reports* 7.

Scottish Environmental Protection Agency. 2021. *Flood Risk Management Maps*. Accessed February 27, 2021. https://map.sepa.org.uk/floodmap/map.htm.

Seyram, Aguadze. 2020. *A Petri-Net Approach to Pavement Degradation and Maintenance Modelling for Pavement Asset Management*. Nottingham: University of Nottingham.

Sinha, Dhiraj, and Omkar. 2018. "Object Drop Detection on Railway Track Through Rayleigh Wave Sensing Using Laser Vibrometer." *IEEE Transactions on Vehicular Technology* 67 (10): 9158–9172.

Transport Scotland. 2020. *Building a Greener Railway: Lineside Vegetation Management for Nature and People in Scotland*. Scottish Government.

UIC - International Union of Railways. 2020. *Railway Statistics - Synopsis*. Paris: Railisa.

UK Centre for Ecology and Hydrology. 2020. *Future Flows: River Flow Changes by Season*. Accessed November 11, 2020. https://www.ceh.ac.uk/future-flows-river-flow-changes-season.

University of Arizona. n.d. "Standard Normal Table." Accessed March 20, 2021. https://www.math.arizona.edu/~rsims/ma464/standardnormaltable.pdf.

Varley, John. 2018. *Valuing Nature - A Railway for People and Wildlife*. Network Rail.

Wang, Tianni, Zhuohua Qui, Zaili Yang, Timothy Nichol, Delia Dimitriu, Geoff Clarke, Daniel Bowden, and Paul T Lee. 2020. "Impact Analysis of Climate Change on Rail Systems for Adaptation Planning: A UK Case." *Transportation Research* D.

Watts, Glenn, Martin Kernan, Richard Battarbee, Jerry Knox, and John Bloomfield. 2015. "Climate change and water in the UK - past changes and future prospects." *Progress in Physical Geography* 39 (1): 6–28.

Wiesmeyr, Christoph, Martin Litzenberger, Markus Waser, Adam Pipp, Heinrich Garn, Gunther Neunteufel, and Herbert Doller. 2020. "Real-Time Train Tracking from Distributed Acoustic Sensing Data." *Applied Sciences* 10 (2).

Xiong, ZhiWen, YongPeng Yang, ZhaoRong Zhu, XiangQing Zhao, and HanCheng Cai. 2015. "Effect of Climate Change and Railway Embankment on the Degradation of Underlain Permafrost." *Sciences in Cold and Arid Regions* 7 (5).

Yang, Zaili, Steve Bonsall, and Jim Wang. 2008. "Fuzzy Rule-Based Bayesian Reasoning Approach for Prioritization of Failures in FMEA." *IEEE Transactions on Reliability* 57 (3): 517–528.

Yuan, Wei, Shuang-Ye Wu, Shugui Hou, Zhiwei Xu, and Huayu Lu. 2019. "Normalized Difference Vegetation Index-Based Assessment of Climate Change Impact on Vegetation Growth in the Humid-Arid Transition Zone in Northern China During 1892-2013." *International Journal of Climatology* 39 (15): 5583–5598.

Zarei, Esmaeil, Nima Khakzad, Valerio Cozzani, and Genserik Reniers. 2019. "Safety Analysis of Process Systems Using Fuzzy Bayesian Network (FBN)." *Journal of Loss Protection in the Process Industries* 57 (January): 7–16.

Eleventh International Conference on the Bearing Capacity of Roads, Railways and Airfields, Volume 2 – Hoff, Mork & Saba (eds)

Digital twin optimization framework for earthworks production optimization and management

M. Amândio, M. Parente & J. Moutinho
BUILT CoLAB, Porto, Portugal

A. Gomes Correia
ISISE – Institute for Sustainability and Innovation in Structural Engineering. University of Minho, Guimarães, Portugal

ABSTRACT: Since any earthworks construction is typically susceptible to unpredictable occurrences (i.e., equipment malfunction, unfavourable atmospheric conditions), execution plans devised during design and planning phases require constant adjustments and/or reorganization of the on-site workflow in order to keep the optimal status of resource usage (i.e., excavators, dumper trucks, graders, compaction rollers). Bearing this in mind, this paper describes a developed optimization framework which is tailored to support decision-making throughout all project phases. These include not only bidding, design, and planning phases by providing the user with resource usage solutions, including the corresponding costs and durations, but also during construction phase. The latter encompasses the constant monitoring of resources and reassessment of their allocation to tasks, which is paramount in the context of increasing productivity and company competitiveness. Indeed, this construction phase resource monitoring, which leverages on smart sensor technologies, allows the system to respond to variations in productivity or work rate of construction equipment and production teams, providing suggestions for minor alterations in the allocation of these resources when necessary. The output of these optimization and re-optimization cycles takes into account several customizable factors simultaneously – multi-objective optimization – namely construction costs, construction durations, and carbon emissions, ultimately resulting in individual equipment allocation corresponding to the optimal distribution of resources throughout the construction project. Previous results for a highway construction case-study based on historical activity log databases (i.e., not including sensorization monitoring), indicate that reductions of about 20% in both construction costs and durations can be achieved.

Keywords: Earthworks, resource allocation, optimization, smart sensors, digital twin

1 INTRODUCTION

Several processes in construction are characterized by high uncertainty and variability that significantly affect the productivity of construction operations, and earthworks construction is no exception. With the increasing competition within the construction sector, companies and designers are looking to take advantage of new technologies to support the design and planning of more complex projects. Yet, currently most designers still rely on intuition and experience to plan and manage construction processes, together with rudimentary and

DOI: 10.1201/9781003222897-7

human-based productivity estimation tools and methodologies (SETRA and LCPC, 2000; Parente et al., 2016).

Nowadays, artificial intelligence techniques such as machine learning algorithms can provide accurate estimates concerning the productivity of construction equipment that have been shown to outperform conventional estimation methods, such as those provided in manufacturer's handbooks (Gomes Correia et al., 2013; Jassim et al., 2017; Kassem et al., 2021). Combined with remote monitoring and dynamic optimization technologies, these feature the potential to tackle the uncertainty and volatility inherent to construction worksite environments, preventing the exclusive reliance on engineers' intuition and experience. Additionally, since any earthworks construction is typically susceptible to unpredictable occurrences (i.e., equipment malfunction, unfavourable atmospheric conditions), execution plans devised during design and planning phases require further adjustments and/or reorganization of the on-site workflow in order to keep the optimal status of resource usage (i.e., excavators, dumper trucks, graders, compaction rollers) (Parente et al., 2018).

Thereby, this paper features a solution for a digital production optimization system which integrates resources and processes with AI techniques and real-time monitoring of mechanical equipment productivity. Bearing this in mind, this paper describes a developed optimization framework which is tailored to support decision-making throughout all project phases. These include not only bidding, design, and planning phases by providing the user with resource usage solutions, including the corresponding costs and durations, but also during construction phase. The latter encompasses the constant monitoring of resources and reassessment of their allocation to tasks, which is paramount in the context of increasing productivity and company competitiveness. Indeed, this construction phase resource monitoring, which leverages on smart sensor technologies, allows the system to respond to variations in productivity or work rate of construction equipment and production teams, providing suggestions for minor alterations in the allocation of these resources when necessary. The output of these optimization and re-optimization cycles takes into account several customizable factors simultaneously – multi-objective optimization – namely construction costs, construction durations, and carbon emissions, ultimately resulting in individual equipment allocation corresponding to the optimal distribution of resources throughout the construction project.

This paper is organized as follows. Section 2 briefly describes several relevant technologies and works relevant for the topic at issue. Section 3 presents the system architecture, workflow and application to a past construction case-study, featuring an optimization and re-optimization cycle as a response to an unexpected change in the productivity of some construction equipment. Finally, some conclusions are drawn in Section 4, together with future directions.

2 TECHNOLOGIES FOR PRODUCTION OPTIMIZATION IN EARTHWORKS

Though lacking in real-world applications, optimization-based resource management systems can be divided into predictive or reactive optimization systems, depending on their target phase of application within a construction project. On the one hand, predictive optimization is typically associated with pre-construction phases, namely bidding, design and planning, as it tends to be based on past experience, either in the form of construction guides and regulations (e.g., SETRA and LCPC, 2000), or of the own accumulated experience of the planner. This category includes the larger part of the systems found in the literature, with applications ranging from vertical alignment of highway trajectories (Miao et al., 2009) and cut/fill volumes distribution (Nassar and Hosny, 2012) during bidding and design phases, to fleet selection (Marzouk and Moselhi, 2002) and allocation (Parente et al., 2016) during planning phase.

On the other hand, reactive optimization advocates maximum flexibility concerning the constant adjustment of the initial plan as a response to more volatile environments or the possibility of unpredictable occurrences. In construction, reactive approaches are the more recent of the two, accompanying current technological advancements and trends, such as sensorization, digitalization and Construction 4.0. As such, fewer systems can be found in the literature

that fall within this paradigm (Moselhi and Alshibani, 2009; Montaser and Moselhi, 2014; Parente, 2018).

These systems are often combined or supported by other technologies, such as machine learning (ML) models (Gomes Correia et al., 2013; Jassim et al., 2017; Kassem et al., 2021), or remote monitoring sensorization frameworks (Parente, 2018; Salem and Moselhi, 2020). Whereas ML can typically be employed during all project phases on account of its potential when associated with large amounts of data (i.e., both past or current construction data), remote monitoring frameworks are normally associated with the construction phase, supporting optimization systems by providing real-time information on construction activities, and prompting reactive re-optimization cycles as a response to predetermined conditions or occurrences.

3 DIGITAL TWIN OPTIMIZATION SYSTEM FRAMEWORK

3.1 *System architecture*

The proposed system is envisioned to leverage on concepts such as artificial intelligence, optimization, sensorization, digitalization, Industry 4.0 (Parente et al., 2020) and Digital Twins to support decision making in earthwork construction projects. Figure 1 depicts the interactions between each platform that compose the system, namely Interface, Monitorization, Production and Optimization platforms.

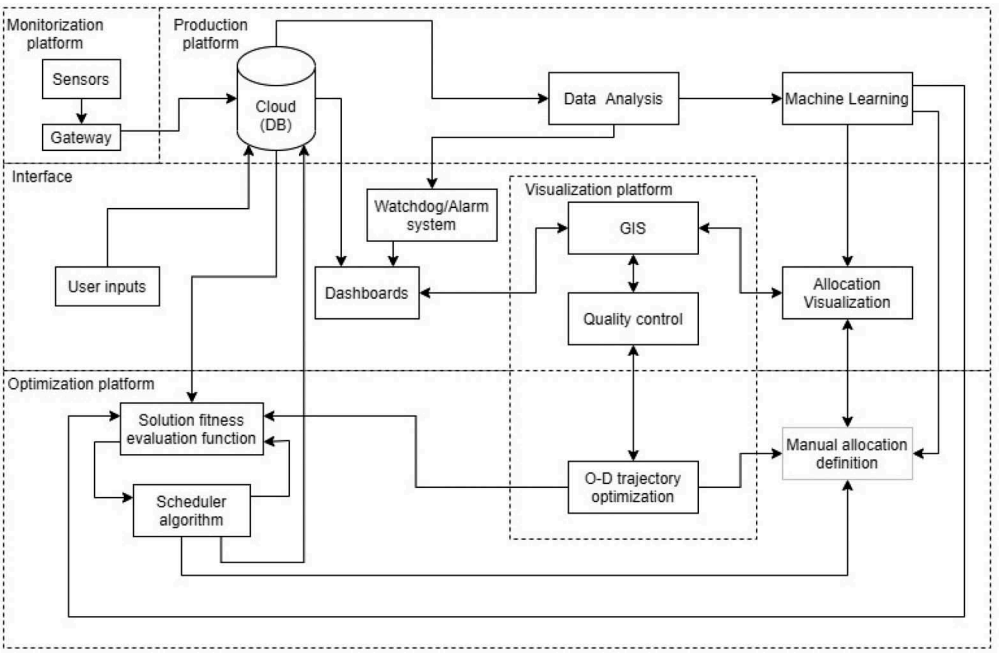

Figure 1. System architecture.

In general terms, the Production platform is responsible for compiling and maintaining all databases, not only including the static data regarding production teams and equipment specifications, as well as historical data, but also the dynamic data retrieved from in-situ sensors. On the one hand, the static data can be used for estimating the productivity of the available

production teams, both by leveraging on teams/equipment specifications/guidelines and by adopting predictive machine learning models on past data concerning similar construction projects, if such data is available. On the other hand, the dynamic sensor-based data comprises the basis for the constant comparison of the actual performance of production teams with their estimated productivity and costs. Should the actual monitored activity mismatch the originally planned performance, the "watchdog" alarm system will instantly provide the user with notifications regarding the issue and its location, which, in turn, can be used to prompt the optimization platform to suggest adjustments in view of returning performance to optimal values.

Together with the Visualization platform, which aims to provide a visual support to the decision makers, complemented by a sensor-based digital model of the construction site supported by geographic information system (GIS) spatial data, these platforms provide the Optimization platform with the information it requires to perform the optimal allocation of resources throughout the construction site. The Visualization platform is additionally directed towards synthesizing and visually representing data from active entities (i.e., active production resources) according to geolocation sensor data, as well as results from the quality control monitoring sensors.

In turn, the optimization platform aims to find different optimal trade-off solutions (i.e. Pareto-optimal solutions) for the allocation of production teams throughout the construction site and the tasks that comprise the project. The adopted multi-objective approach may address the minimization of any combination of goals, such as global construction durations, costs, or other mathematically determinable aspects, such as carbon emissions. This imparts the system with a higher flexibility, as several different optimal solutions are presented to the decision-makers, which are then free to select the one that best fits their restrictions and goals. Solutions also take into account that the optimum production team allocations are not static over time, meaning that as teams complete their work in one front, they are immediately reassigned to other work fronts. Moreover, team productivity in sequential tasks is also synchronized, thus preventing productivity bottlenecks and guaranteeing that production resources are used at their maximum efficiency.

3.2 *Internet of things framework for monitorization platform*

Considering that the activity in this type of construction projects typically go hand in hand with several instances of unpredictable occurrences (i.e., equipment malfunction, atmospheric conditions, changes in the estimated productivity of equipment), a constant adjustment or reorganization of the resources is required in order to keep the optimal status of resource usage. Traditionally, this is achieved by informed guesswork, supported by the experience of the decision-making team. Alternatively, the proposed monitorization platform allows for the real-time extraction of resource and environmental measurements depicted in Annex I.

The technological part of the system is composed by two different sensing systems: a fixed one that is on the site(s) and a moving one that is installed in the machines. These two systems communicate, via a mobile network operator or a private long range low power communication technology, with the cloud-based infrastructure that manages the whole optimization platform. Depending on the specificity of the application, several physical variables can be extracted directly (via sensors) or indirectly (via other cascading ML estimations) from this Internet of Things (IoT) framework:

- Geolocation, speed, slope and status: Monitoring the location of trucks provides, distance, speed, acceleration, estimated times of arrival, both for the decision-making team and for the excavation and spreading teams. Additionally, this information keeps updates on the status of the vehicle, assessing its efficiency ratio by tracking idle and working periods, as well as prompting an alarm under predefined conditions (e.g., excessive idle time as a result of malfunction). Finally, interactions between teams (i.e., excavator loading truck) can also be logged over time, together with the location of each transported batch of geomaterial as a result of georeferenced and timestamped unloading/spreading data. These variables are

acquired with the use of sensors such as Global Navigation Satellite System (GNSS) receivers, accelerometers, and gyroscopes.

- Weight: As one can easily infer, the weight of the geomaterial loaded in each bucket is directly related to the productivity of excavator teams. Concurrently, the productivity of the transportation equipment (e.g., trucks, dumpers) is a function of the transported geomaterial weight per trip/hour. In addition, cross-referencing this data with fuel consumption can provide useful insight concerning the effect of the former on the latter by resorting to ML analyses. To acquire the weight, different strategies are employed depending on the machine type of machine. For instance, in excavators, hydraulic sensors and rotary encoders are used to calculate the bucket load and detect each loading cycle. In trucks it is via a linear encoder, connected between the chassis and the cargo container that measures suspension deformation (that is directly related with the truck load). Conversely, the vehicle's Controller Area Network (CAN) bus can also be used to extract this type of information, but it is not always possible to do it. It depends on the vehicle's age, technological advancements or simply truck manufacturer's open policies.
- Fuel consumption: Bearing in mind that fuel consumption comprises a significant part of the cost of work operations, its monitoring comprises an essential step towards assessing the viability and the efficiency of resource usage. This can be achieved either by leveraging on available CAN interfaces in more recent equipment (with the limitations mentioned before), or alternatively by estimating it using physical variables measured by sensors and a proprietary estimation system with a prediction model implemented and developed by some of the authors.
- Environmental conditions: Since environmental humidity and temperature can have a significant influence on the effectiveness of compaction, a weather station can be installed on the corresponding equipment to support the process, as well as to support decision making concerning the employment frequency of water trucks. The fixed sensing system comprises a thermometer, and hygrometer, and atmospheric sensor (for weather forecasting and storm quick detection) and an anemometer to evaluate wind condition.

Concerning the transmission of the aforementioned sensor data to a cloud (Annex II) where everything is compiled, processed and manipulated (e.g., for predictive or optimization purposes), long-range communication protocols are an ideal solution, since *in-situ* equipment can be spread over large areas and/or in remote locations. Yet, since each production resource/team typically includes several simultaneously active sensors of different types producing large amounts of data, which may be spread out throughout each active entity, long-range radio communication is not efficient. Because of that, the proposed framework adopts a short-range sensor network integrated in each machine or equipment, allied to the implementation of a gateway. The latter features the capability to communicate both with several sensor acquisition modules, by resorting to short-range communication protocols, and with the cloud, using a long-range communication protocol (Annex II). Furthermore, while a gateway can be included in each heavy machine, an interesting alternative solution consists of including a gateway that encompasses groups of sensors installed in different machines that work in close proximity (e.g., excavator teams active on the same work front). This allows for a reduction in the number of adopted gateways, which, in turn, minimizes investment, hardware, maintenance, setup dimension, and communication costs.

3.3 *Production optimization and management workflow*

Annex III depicts the workflow of the system from Design and Planning Phase through to Construction Phase, as well as the actions performed by each group of entities in each step. The entities are named "Construction Site", which includes the active human teams or heavy machinery together with the data gathering information system if available (e.g sensors, laserscan, or other methods); "Decision Makers", which concerns the designers, engineers and contractors which participate in the decision-making process regarding the construction project;

and "Decision Support System", which corresponds to the previously described system architecture (Figure 1).

The beginning of this the process is characterized by the input of project-related data by the decision makers. These inputs include: (i) a BIM-type model (if available, or alternatively any other format that includes information on the activities, tasks to complete and work front locations); (ii) a list of all available production resources and their specifications; (iii) restrictions associated with the project (e.g., deadline, budget); and (iv) optionally, historical data of past similar construction works. Should the latter be available, ML models can be used to predict the productivities of resources based on their performance in past similar activities, which enhances the accuracy of the teams' productivity values in these early stages. Ensuing these inputs, an initial offline predictive optimization is carried out, which outputs to the decision makers a set of equally optimal solutions of resource allocations to choose from, as further detailed in Section 3.4. Note that the design and planning phase in this workflow specifically concerns the decision-making process which is carried out preceding construction, including project bidding, project design, and project planning phases. Thus, the resulting schedules correspond to offline plans based on predictions and estimations supported by the aforementioned technologies.

Conversely, following the beginning of construction phase, the availability of information originated from the active production teams and associated sensorization/IoT framework allows the system to reassess the initial schedules that resulted from design and planning phases, which can be adjusted to better fit reality. These subsequent optimization runs are supported by the machine learning models, which are increasingly accurate as the construction develops, since the data corresponding to the daily activities can be added to the prediction models' training databases. At the start of any construction phase, resources are allocated throughout the construction site according to what was determined during the planning phase's optimization process. Meanwhile, while construction activities are ongoing, the information regarding the productivity of resources will be collected by means of the IoT framework. As this new data is fed into the system, it reassesses the optimal status of the resource allocation, which can be the object of discussion by the decision-making team. Should the decision lean towards updating the current resource allocation configuration, a re-optimization cycle is carried out to obtain a new set of optimal solutions, triggering a new discussion and selection process for a new solution.

3.4 *Case study results*

Two of the major benefits of this system are the possibility of detecting changes in the productivity of an undergoing earthwork project and consequently react to those changes by making decisions regarding new resource allocations that can reduce the impact in the objectives (primarily cost and time). Therefore, to test the proposed framework a simulation of the construction phase was carried out based on real data of the earthworks of a Portuguese highway construction project.

The simulation focused on an isolated set of work fronts of the project, comprised of five embankment fronts supplied by four excavation fronts, with associated material processing volumes ranging from approximately 5000 m^3 to 15000 m^3. The original duration of the works corresponded to approximately three weeks of activity. The available resources to execute this construction project were rollers (5), bulldozers (8), excavators (12) and trucks (22), with some variability in the models and, consequently, in the productivities as well (Parente et al., 2016).

As previously mentioned, preceding the start of the construction phase, the multi-objective optimization system is capable of outputting a set of equally optimal solutions of resource allocation for the whole project to the decision makers choose from. Figure 2 depicts the results obtained with the implementation of the well-known non-dominated sorting genetic algorithm II (NSGA-2) by resorting to the mco package (Mersmann, 2014) in R environment, while Figure 3 corresponds to a detailed view of a single solution (S19). Each solution

represents a resource allocation and is identified by a unique set of objective values, i.e., cost, duration and RAD (Re-Allocation Disruption). This third objective is related with the "cost" of re-allocating any kind of equipment to a different front during construction phase. In other words, the value of RAD increases linearly with the number of times that the allocated resources change work fronts (i.e., as a result of completing their work in the previous front) throughout the development of the construction project. Thus, by minimizing the RAD as a third optimization objective, the setup time associated with reorganizing the equipment fleet during construction phase is also optimized.

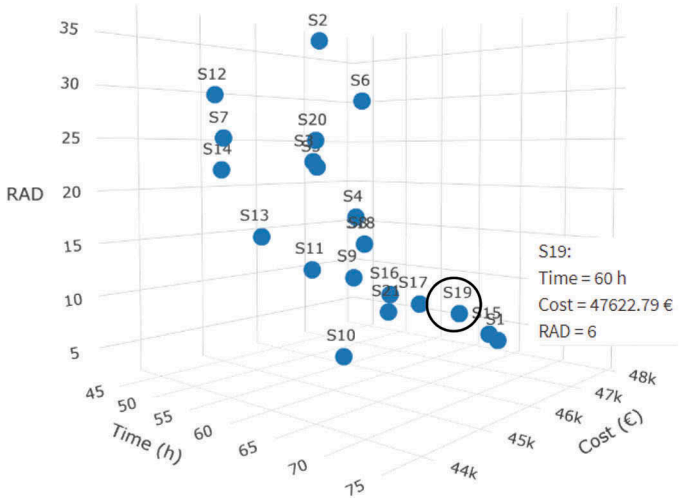

Figure 2. Pareto front that resulted from optimization during design and planning phase.

Supposing that, at some point during construction phase, the rate of one type of rollers decreases (e.g., as a consequence of working with a different geomaterial type than originally expected), the system would alert the decision makers of this change alongside with its effects to the objective values. Since this decrease in equipment rate causes the current allocation solution to no longer be optimal, the construction project would take longer, and subsequently be more expensive than what was originally planned. At this point, the decision maker can prompt the system to re-optimize the resource allocation taking into consideration the new work conditions (Figures 4 and 5).

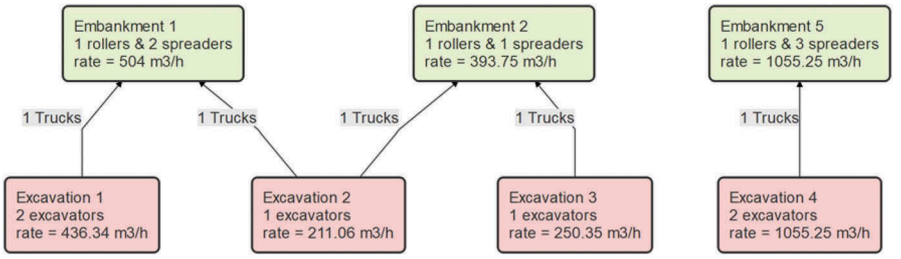

Figure 3. Resource allocation corresponding to solution S19.

As an example, 5 rollers of two different types were available in this project (Table 1). Evidently, the productivity of each type differs depending on the type of soil, as depicted on Table 1 and according to the Guide des Terrassements Routiers (GTR) compaction guide

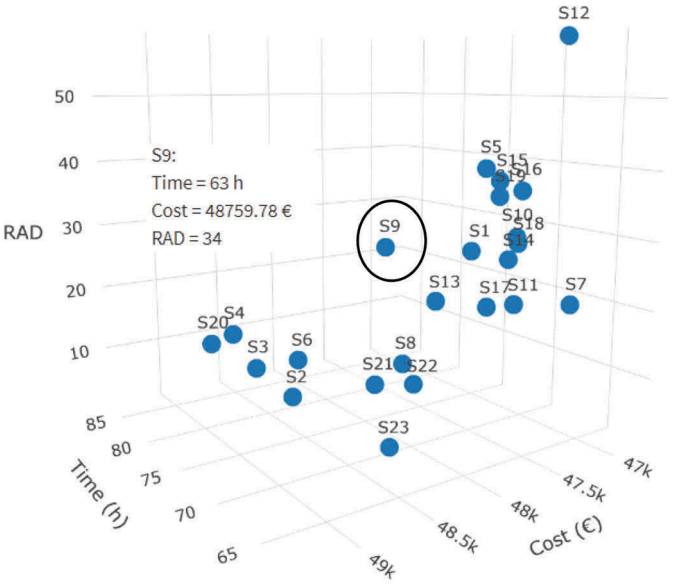

Figure 4. Pareto front that resulted from the re-optimization during construction phase.

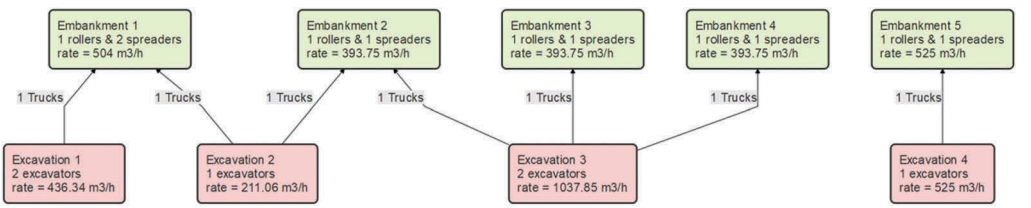

Figure 5. Resource allocation corresponding to solution S9 of re-optimization.

(SETRA and LCPC, 2000). Assuming, as mentioned above, that the rate of roller type V4 decreases to match the values of Table 2, the rate of embankment front 5 in the first phase of the project (Figure 3) would drop to approximately half, causing the increase in cost and duration shown in Table 3. Ensuing the re-optimization cycle, a re-allocation solution can be selected which mitigates the effects of this unpredictable occurrence. Hence, Figure 4 depicts the results of the re-optimization solution, while Figure 5 represents the resource allocation from the solution S9 adopted after the re-optimization. Note that the RAD values in the re-allocated pareto front (Figure 4) take into account not only the amount of times the equipment move to other work fronts during the solution itself, but also the disruption introduced in the currently adopted solution (S19) when compared with the new solutions. In other words, the points with a lower RAD in Figure 4 correspond to solutions which are closer to the currently active solution S19, as less equipment must be moved to other work fronts to achieve the transformation of solution S19 into one of these solutions.

Table 1. Roller rates during design phase.

Roller type	Soil A1	Soil C2A1
V3	614.25	393.75
V4	1055.25	683.55

Table 2. Roller rates during construction phase.

Roller type	Soil A1	Soil C2A1
V3	614.25	393.75
V4	525	300

Ultimately, it was demonstrated that the theorized system can help decision makers react to unpredictable occurrences such as equipment malfunction or rate drops as evidenced by the results of the simulation of a case study. For this case study, after an unexpected event occurred, the system was nonetheless capable of finding a set of solutions that would improve the original plan. One of those optimal solutions (S9), identified in Table 3, would minimize the construction duration while maintaining a similar cost to the original solution at the expense of equipment re-allocation. In Annexes IV and V the resource schedules can be consulted for both the solution of the design phase and the new re-optimized solution, respectively.

Table 3. Objective values.

	Predicted values from ptimization during planning	Effect of a random unpredictable occurrence	Values associated with the re-optimization
Time (h)	60	76	63
Cost (€)	47622.79	64688.58	48759.78
RAD	6	-	34

4 CONCLUSIONS

The focus of this work was to explore the advantages of a digital twin framework for earthworks capable of minimizing the effects of negative unpredictable occurrences. This can be attained from the integration of IoT and optimization tools, which allow for a continuous real-time monitoring of production teams, leading to a broader support to management and decision making. On the one hand, machine learning and optimization techniques can be used during design phase to attempt to optimize objectives, such as cost and duration, based on predicted data. On the other hand, the IoT framework allows to adapt the design phase solution to new unpredictable conditions during construction phase in real-time.

Even though the system is specifically tailored for earthwork construction, it could also be applied to constructions that strongly rely on heavy mechanical equipment, among which one can highlight road and railway construction, pavement maintenance and rehabilitation, dam construction, or tunnel construction. Thus, the proposed framework presents itself as an important tool to enhance the construction industry through digitalization, accompanying current Construction 4.0 and sustainability in construction trends.

Future work will focus on developing the IoT framework and implementing equipment sensorization on a real ongoing large-scale railway construction project, in order to test the developed Digital Twin framework in a real construction scenario.

ACKNOWLEDGMENTS

This work is supported by European Structural and Investment Funds in the FEDER component, through the Operational Competitiveness and Internationalization Programme (COMPETE 2020) and Lisbon Regional Operational Programme (ROP Lisbon) [Project n.º 046123; Funding Reference: POCI-01-0247-FEDER-046123 and LISBOA-01-0247-FEDER-046123]; and by the European Social Fund (ESF), through the North Portugal Regional Operational Programme (Norte 2020) and Lisbon Regional Operational Programme (Lisboa 2020) [Funding Reference: NORTE-06-3559-FSE-000176 and LISBOA-05-3559-FSE-000014]. This work is also supported by the European Social Fund (ESF), through the North Portugal Regional Operational Programme (Norte 2020) [Funding Reference: NORTE-06-3559-FSE-000176].

REFERENCES

Gomes Correia, A.; Cortez, P.; Tinoco, J.; Marques, R. (2013). Artificial Intelligence Applications in Transportation Geotechnics, Geotechnical and Geological Engineering, 31(3),861–879

Jassim, H.S.H.; Lu, W.; Olofsson, T. (2017). "Predicting Energy Consumption and CO2 Emissions of Excavators in Earthwork Operations: An Artificial Neural Network Model." Sustainability, 9, 1257.

Kassem, M., Mahamedi, E., Rogage, K., Duffy, K., & Huntingdon, J. (2021). Measuring and benchmarking the productivity of excavators in infrastructure projects: A deep neural network approach. Automation in Construction, 124(January), 103532

Marzouk, M., and Moselhi, O. (2002). "Selecting Earthmoving Equipment Fleets Using Genetic Algorithms." Proceedings of the 2002 Winter Simulation Conference, E. Yucesan, C.-H. Chen, J. L. Snowdon, and J. M. Charnes, eds., Montreal, Canada, 1789–1796.

Mersmann, O., Trautmann, H., Steuer, D., et al. (2014). Package "mco": Multiple Criteria Optimization Algorithms and Related Functions.

Miao, K., Li, L., Yang, X.-L., and Huo, Y.-Y. (2009). "Ant colony optimization algorithm for vertical alignment of highways." ASCE Geotechnical Special Publication, (189), 99–108.

Montaser, A., & Moselhi, O. (2014). Truck + for Earthmoving Operations. Journal of Information Technology in Construction, 19(September), 412–433.

Moselhi, O., and Alshibani, A. (2009). "Optimization of earthmoving operations in heavy civil engineering projects." Journal of Construction Engineering and Management, 135(10),948–954.

Nassar, K., and Hosny, O. (2012). "Solving the Least-Cost Route Cut and Fill Sequencing Problem Using Particle Swarm." Journal of Construction Engineering and Management, 138(8),931–942.

Parente, M.; Gomes Correia, A.; Cortez, P. (2016) "Metaheuristics, data mining and geographic information systems for earthworks equipment allocation", Advances in Transportation Geotechnics III, vol. 143, pp. 506–513

Parente, M.; Gomes Correia, A.; Figueira, G.; Mehrsai, A. (2018). "Towards improving earthworks production from an Industry 4.0 perspective: the role of remote information technologies and dynamic optimization techniques", Proceedings of 7th Transport Research Arena (TRA 2018), Vienna, Austria

Parente, M.; Figueira, G.; Amorim, P.; Marques, A. (2020). "Production scheduling in the context of Industry 4.0: review and trends", International Journal of Production Research, pp. 1–31.

Salem, A.; Moselhi, O. (2020). "AI-Based Cloud Computing Application for Smart Earthmoving Operations". Canadian Journal of Civil Engineering 48(3),312–327

SETRA, and LCPC (2000) Guide des Terrassements Routiers - Réalisation des Semblais et des Couches de Forme.

ANNEX I – EARTHWORKS PROCESS OVERVIEW, INCLUDING PROPOSED SENSORIZATION FRAMEWORK

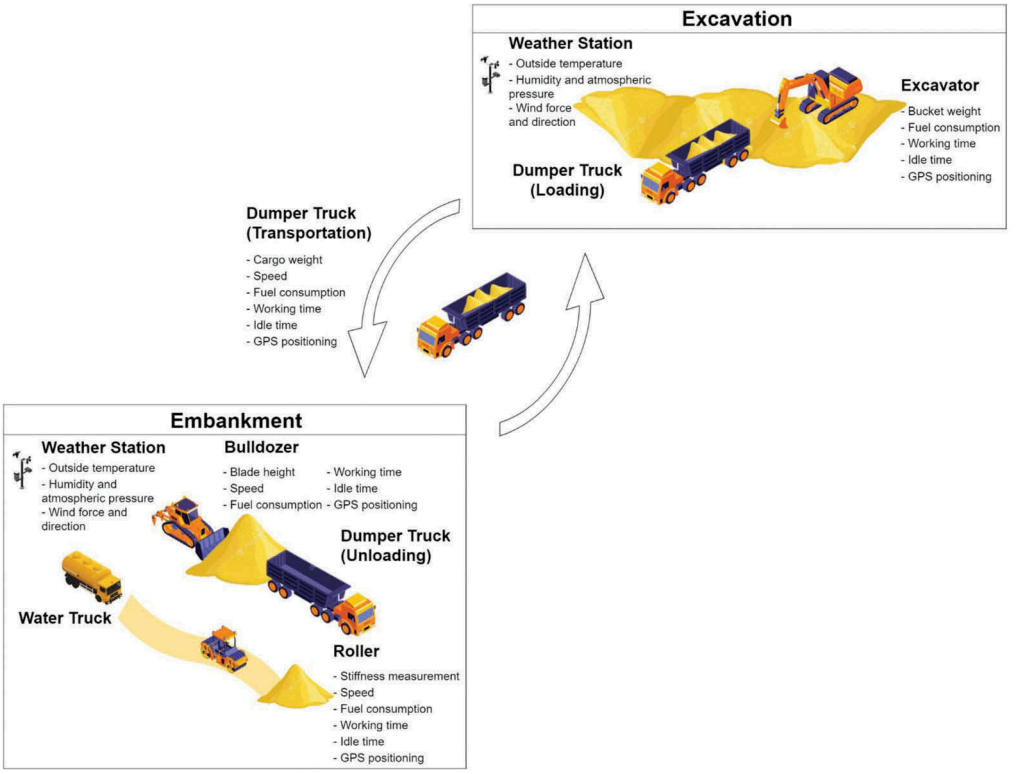

ANNEX II – IOT FRAMEWORK ARCHITECTURE

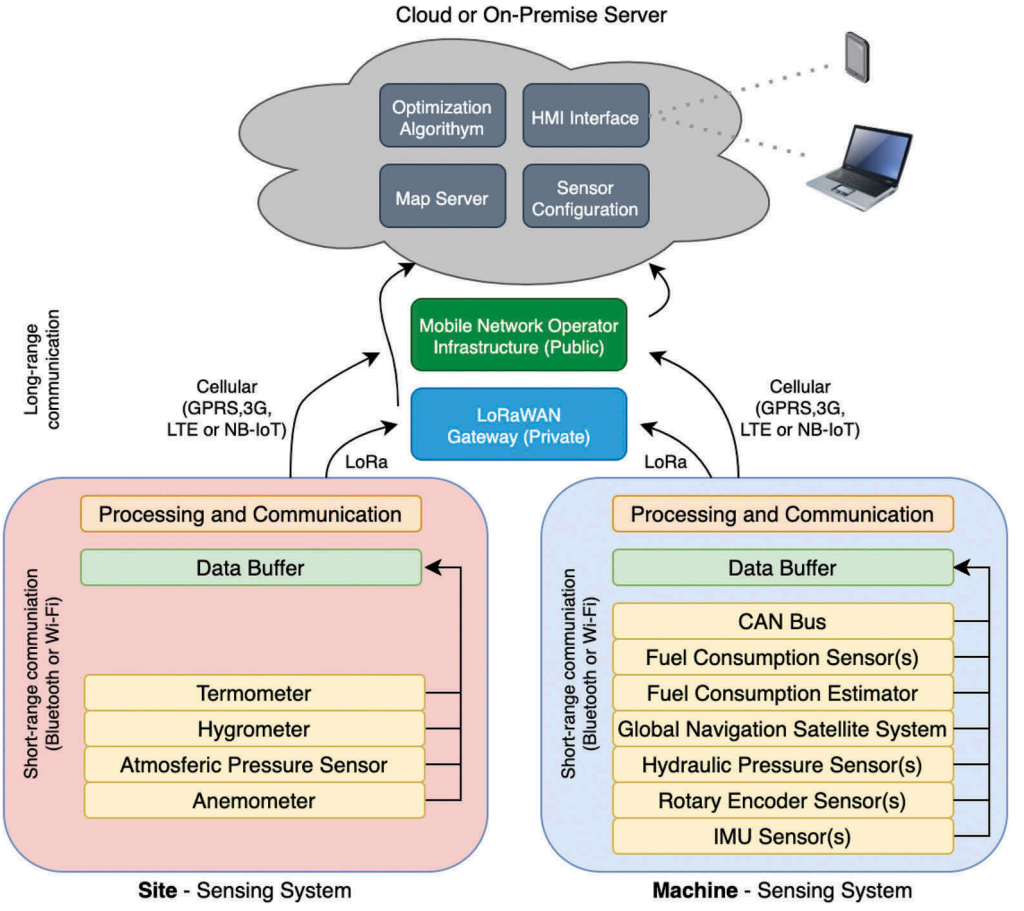

ANNEX III – PRODUCTION OPTIMIZATION AND MANAGEMENT WORKFLOW

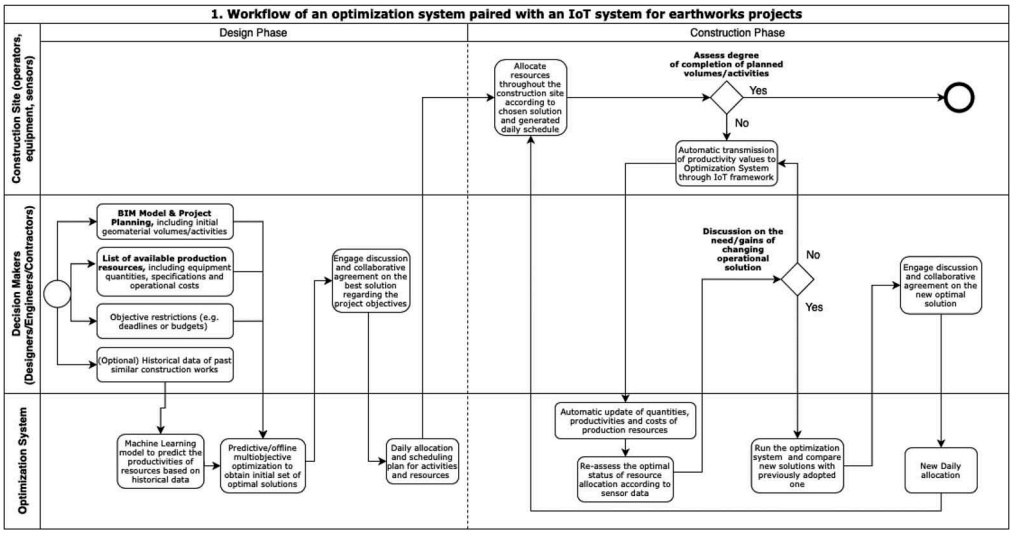

ANNEX IV – RESOURCE SCHEDULES OF SOLUTION OBTAINED IN DESIGN PHASE

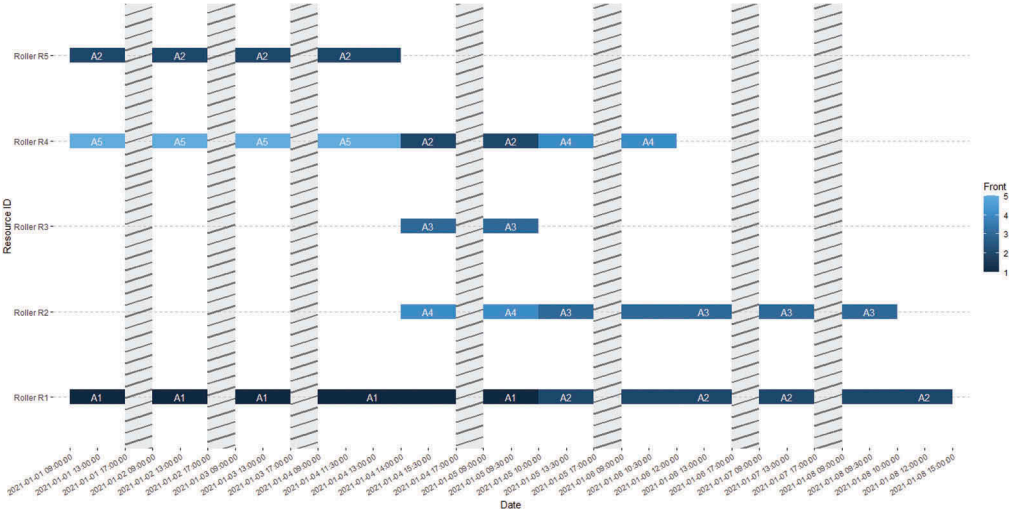

Figure IV.1: Rollers Schedule

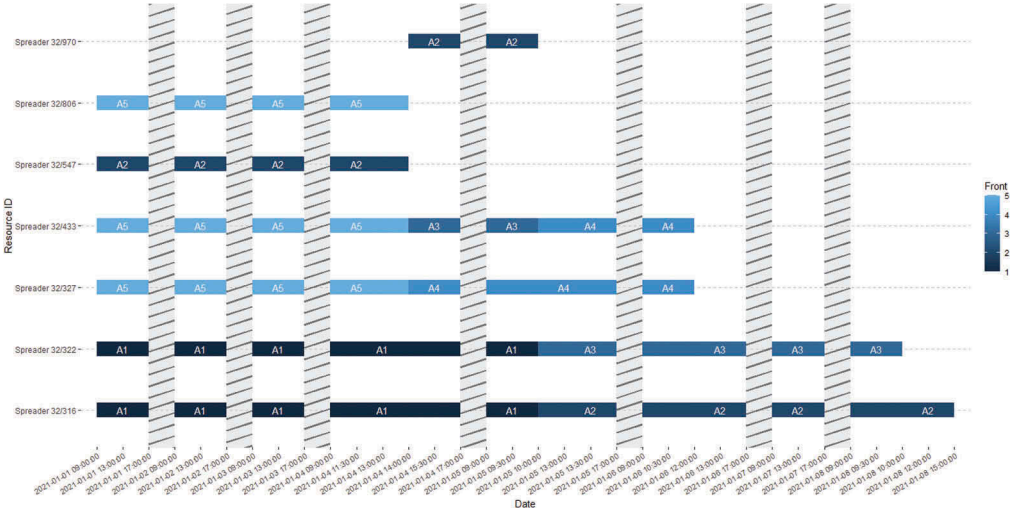

Figure IV.2: Bulldozers Schedule

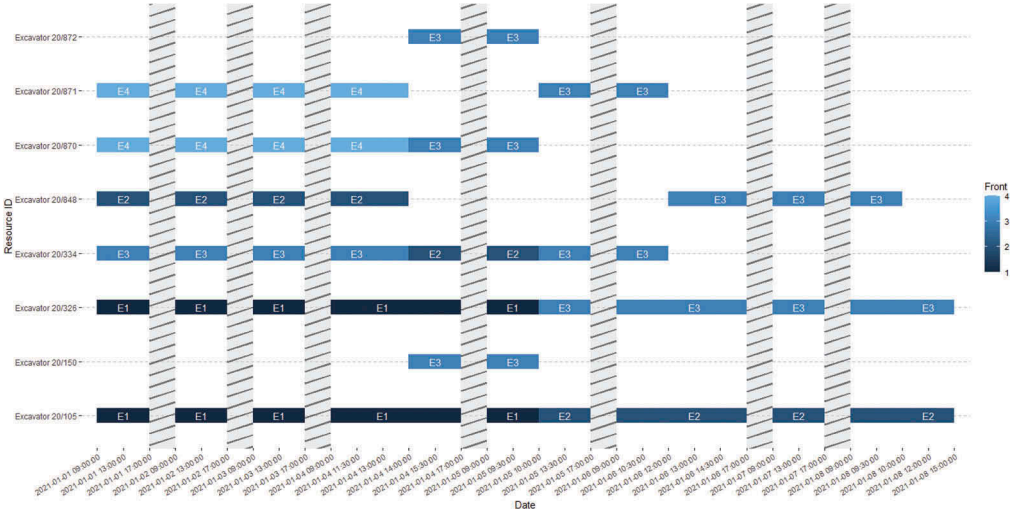

Figure IV.3: Excavators Schedule

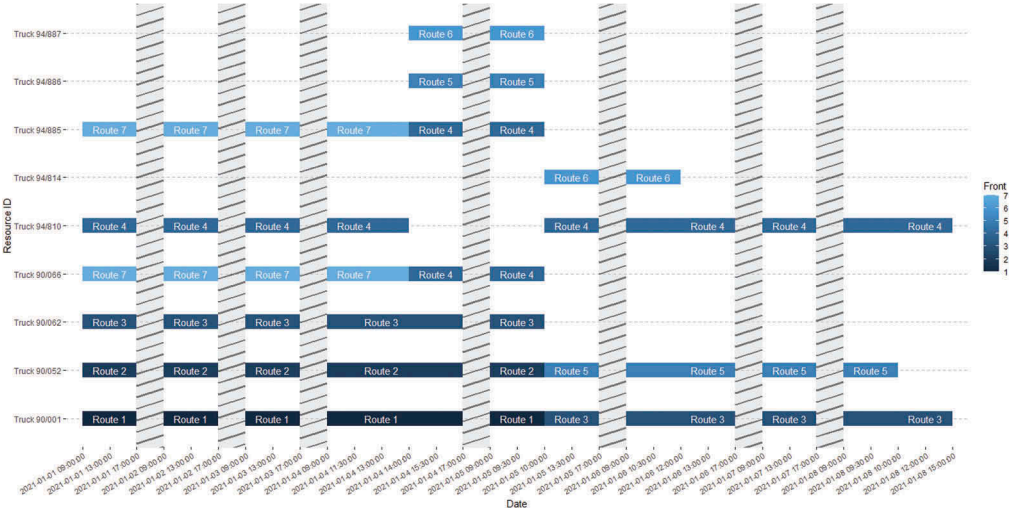

Figure IV.4: Trucks Schedule

ANNEX V – RESOURCE SCHEDULES OF RE-OPTIMIZED SOLUTION

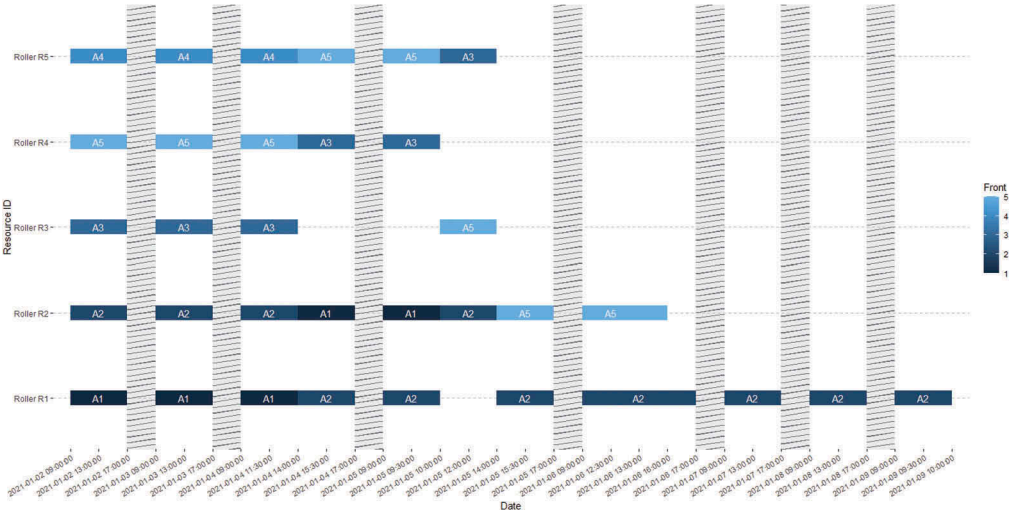

Figure V.1: Rollers Schedule

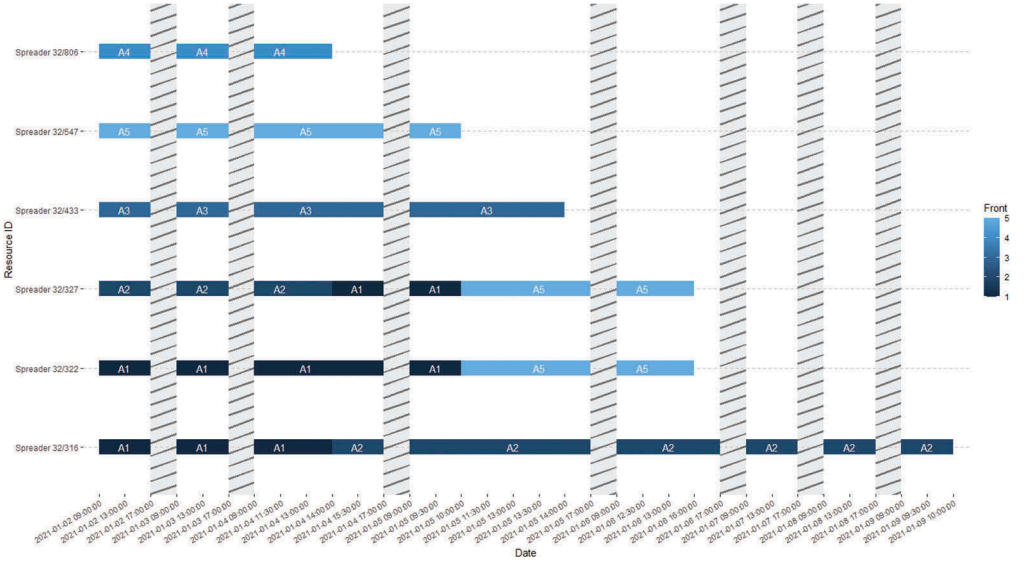

Figure V.2: Bulldozers Schedule

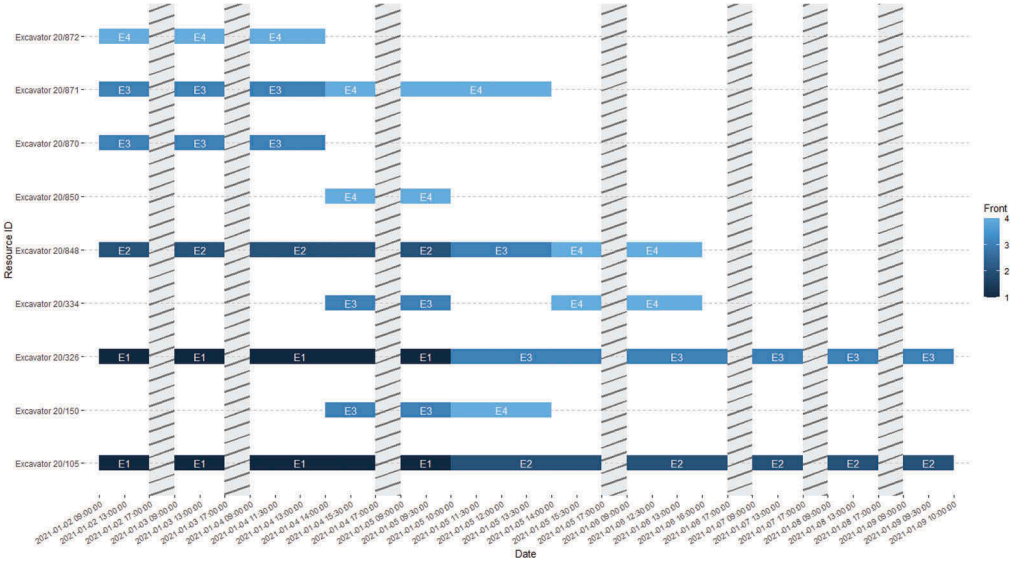

Figure V.3: Excavators Schedule

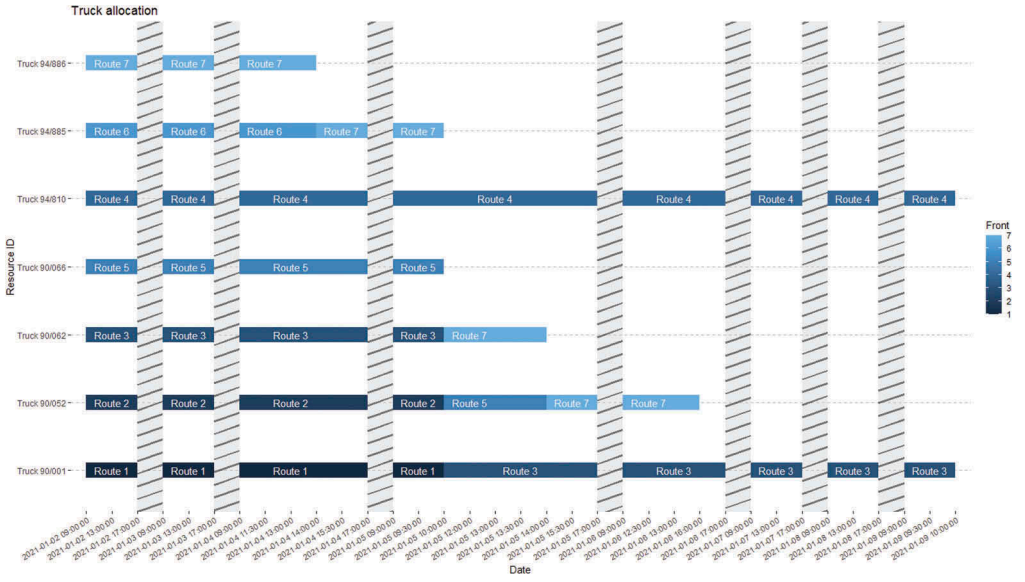

Figure V.4: Trucks Schedule

Eleventh International Conference on the Bearing Capacity of Roads, Railways and Airfields, Volume 2 – Hoff, Mork & Saba (eds)

A feasibility study of reduction of cross-section size of railway tunnels in relation to construction costs and environment emissions

B.K. Moe & A. Lau
Department of Civil and Transport Engineering, Norwegian University of Science and Technology, Trondheim, Norway

ABSTRACT: In this study, the required cross-section size of railway tunnels from the technical viewpoint of civil- and railway engineering was investigated and compared to the cross-section sizes of the Norwegian technical regulations on railway tunnels. The reduction potential of the cross- sections was investigated with regards to its effect on the CO^2-emissions and cost in the construction phase of railway tunnel projects. Cross-section measurements of two tunnels on Gardermoen-line was obtained and further demonstrated and analyzed to investigate the reduction potential in relation to today's technical standards and newer tunnel projects in development. A simplified computational model for cost and CO^2-emission from the building phase was established to investigate the effect of cross-section reduction on the cost and CO^2- emissions, where the analyzed data from Gardermoen-tunnels were used as input parameters. It was found that the areas for evacuation, fixed installations and the track construction was the parts within the cross sections with the highest reduction potential, because of the possibility of combining the evacuation- and installation area and using ballast-less track. The reduction potential was found to be in the magnitude of $10m^2$. Giving a reduction in construction cost of about 4000 kr/m, a reduction of CO^2-emissions of about 500 kg CO^2 pr unit length and a reduction in the cost related to the CO^2-emissions of 900 kr pr unit length. Through the study it was found that today's design method is in small degree suitable for optimization of tunnel cross section size. Because of the great reduction potential found in the project, in addition to several factors related to the complexity of railway tunnels which makes the design process challenging.

Keywords: Railway tunnels, Cross-section size, Reduction potential, Cost and environment, CO^2-emission

1 INTRODUCTION

The design of railway tunnels in Norway is done according to the technical regulations (Bane Nor, 2021a) and are highly interdisciplinary. Where the designers' task is to provide sufficient space and favorable placement of the different components in the railway cross-section to ensure safe and efficient operations and maintenance on the line. The knowledge and calculations related to which component that occupy which part of the tunnel cross-section to stop potential collisions of objects is presented with the use of contours within the cross-section that are related to different components and their placement and space requirements. Examples of these contours are structure gauges, loading gauges, construction gauges (Løhren, 2019) (Bane Nor, 2020a). In addition to different contours for the

DOI: 10.1201/9781003222897-8

cross-section related to the construction (Bane Nor, 2020a). The contours geometrical shape and size and the contours placement within the cross-section are based on empirical studies, experienced knowledge, geometrical calculations, and safety margins. In addition, the accuracy in which the contours envelopes an objects related to a given contour varies according to the accuracy of the geometrical calculations and the safety margins (Anderson, 2014) (Iwniki, 2006). There are several fixed components with space requirements related to safety, maintenance, and operation in the cross-section. These components have contours on both sides of the track against the lining and a contour for the catenary system in the tunnel roof.

The construction, design and dimensions of the track construction presented in (Bane Nor, 2021b), (Profillidis, 2014), (Chandra & Agarway, 2007) and (Esveld, 2001) discusses the design and dimensions of the track construction. It has been made obvious that a ballast-less track will be favourable for maintenance, operations and most importantly requires smaller tunnel cross-section, even though the initial investment- and construction costs often are higher. (Pen & Powrie, 2016) and (Esveld, 2001) discuss the engineering design of ballasted tracks and has shown that the ballast shoulder, ballast slope and ballast foundation under track superstructure normally have bigger dimensions than what is required from a technical viewpoint. This is also the case for (Bane Nor, 2021b), in which the technical regulation gives a minimum requirement for shoulder width of 400 mm, when 400 mm is shown to be more than sufficient from a technical viewpoint.

In building railway tunnels the designer's choice of tunnel concept in the design phase is a decisive factor for further choices related to the technical and practical solutions of the tunnels and ultimately the choice of construction method for the building phase (Bane Nor, 2020b). The choice of tunnel concept is based on several criteriums, such as: geology condition, geotechnical condition, safety, operation, and maintenance. After that or in parallel, the design of the tunnel will be evaluated with different variables such as: tunnel length, traffic volume, speed, construction cost, lifespan, and various technical solutions. The great number of variables in addition to the fact that the advantages and disadvantages of the different tunnel concepts in many cases are inversely proportional resulting in challenging situation in which there are no obvious choice as there will be advantages and disadvantages with all the different tunnel concepts (Bane Nor, 2020c).

In Norway there are two main construction methods used for construction of railway tunnels, drill and blast, and tunnel boring machine (TBM). According to (Baklien & Moi, 2018) there are advantages and disadvantages with both methods and the choice of construction method is therefore made carefully based on many of the same parameters as for the tunnel concept. Generally, the cost and construction time is considered the main factors to evaluate in addition to environment, maintenance, and the lifespan of the project. TBM is connected to high investments-costs but have an even and high-quality production and cause little degree of disturbances to the nearby environment. It is considered cost-efficient for longer tunnels. Drill and blast requires lower investment-costs but and is a cost-efficient solution for short tunnels. However, the downside is the technique produces high amount of disturbance during construction to the nearby environment and there are more uncertainties connected to the quality and evenness of the production. A lot of development has been achieved in the past years in improving both the construction methods, for example by improving material quality, producing lower CO^2- emissions, and developing machines with higher efficiency. These are mainly achieved by creating higher degree of digitalization and atomization of the working environment.

The aim of this study is to study is to investigate the possibility of cross-section reduction of railway tunnels within the limitations of the technical regulations, and further to study effect of tunnel cross-section reduction on the costs and emissions connected to construction and CO^2- emissions in the building phase of railway tunnels.

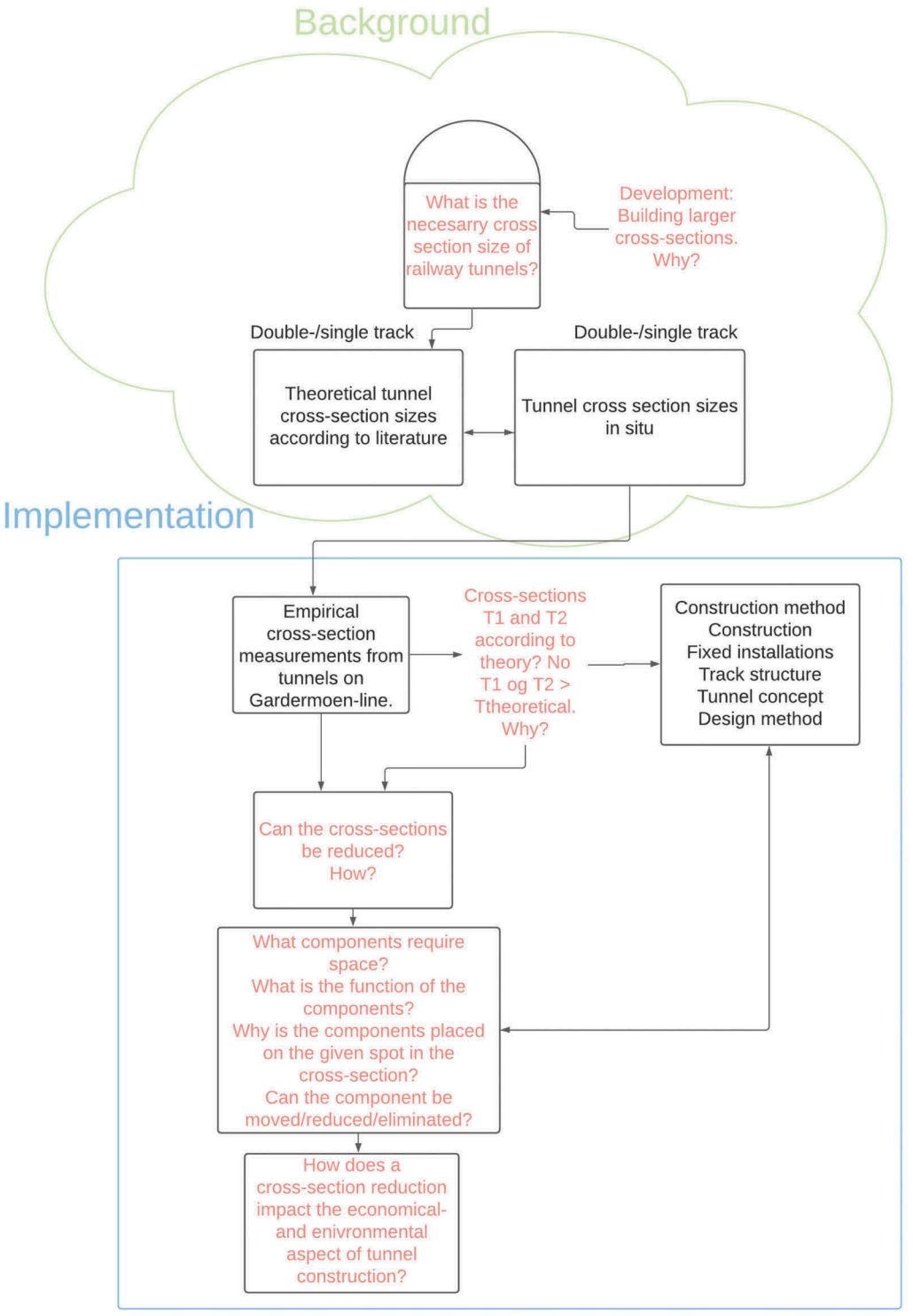

Figure 1. Illustration of the systematic approach of this study.

2 METHOD

To achieve the aim of the study, a systematic approach is adopted, see Figure 1. First, field work on the Gardermoen-line was conducted on the Rashølet single-track tunnel and Bekkedalshøgda double-track tunnel. Observations and then followed by a distance- and geometrical measurements was done using a laser meter, scale and a camara. The observations and measurements were connected to the components in the tunnel cross-sections and their fixed positions in the cross-sections related to other tunnel components and the tunnel lining. Distance- and geometrical measurements were conducted of the components, their space requirements in relation to the lining. The lining was used as a reference line in the x-plane and the formation layer by the lining was used as a reference line in the z-plane. The quality of the measurements could not be assessed properly, but it is assumed that the data quality was sufficient for the nature of the study conducted.

After that, the measurements were imported into Autocad to construct models of the tunnel cross-sections based on the field-measurements. As a precondition for the models the centreline of the track construction coincided with the centreline of the tunnels. The track construction was further modelled using geometrical calculations of the track geometry using the design rules of (Bane Nor, 2021b). In addition to the tunnel cross-section from the field-measurements, simplified models of cross-sections presented in (Bane Nor, 2020d) was constructed as a basis for comparison.

Then, the modelled cross-sections from the Gardermoen-line were compressed in the same way as the optimal cross section from (Bane Nor, 2020e). The cross-sections were analysed with respect to finding the critical components for the cross-section size. While working on this part, the components functions, space requirements and placement in the cross-sections were thoroughly investigated in respect to the railway-, civil- and electrical engineering technical requirements, in addition to taking other design criteria, such as: safety, maintenance and operation into account, to optimize the cross-sections by changing the placements of-, changing the geometry of- or eliminating the critical components.

After that, the cross-sections were compared according to Table 1 with the explanations for why the given comparisons are appropriate, to investigate the similarities/differences and consequently the potential for cross-section reduction of future projects. The comparisons were made in Autocad by using overlapping layers and functions.

Table 1. Overview of the tunnel cross-sections for comparison with a given explanation.

Tunnel1	Tunnel2	Tunnel3	Explanation
Rashølet	Rashølet (reduced)	IC-single track	Compare tunnel with reduced version and a new project to investigate the cross section of single tunnels over time
Bekkedalshøgda	Bekkedalshøgda (reduced)	IC-double track	Compare tunnel with reduced version and a new project to investigate the cross section of double tunnels over time
IC-double track	IC- double track optimal (Bane Nor 2020i)		Investigate original and optimal cross section size
IC- single track	IC- double track		Discuss choice of tunnel concept

From this work the size of the cross-section reduction potential was collected for further analysis in a simplified model for construction cost and environmental impact. The model can be reviewed from the following link. The model used the geometrical formulas (1) and (2) for the cross-section size (T), based on the radius (r) of the cross-section. Further model documentation is presented in (Tunheim et. Al, 2021).

$$T(r) = \frac{1}{2}r^2(4+\pi) \tag{1}$$

$$T^{-1}(r) = \sqrt{\frac{2T}{4+\pi}} \tag{2}$$

The model was used to calculate the construction costs and CO^2-emissions for reduced cross-sections compared to the original cross-sections used as reference cross-sections. The model was used with the standard concervative parameters for the different variables in the model to give a sufficient basis for comparison.

3 RESULTS AND DISCUSSION

In the attempt to compress the cross-section size of the tunnels on the Gardermoen-line the fixed installations one the tunnels were investigated. It was found that critical components in the Bekkedalshøgda double track tunnel was the cables casing connected to the switch in the tunnel, shown in Figure 2, the track structure were some of the components had bigger dimensions than what was recommended from the technical regulations, in addition to what has been shown from the literature is necessary dimensions of the track structure. The installation- and evacuation zone had otherwise when not taking the cabal basin into account, smaller dimensions than what is designed for newer tunnels due to the zones functioning as one zone with both installation and evacuation and the evacuation-way being the required 800 mm instead of the nowadays recommended 1200 mm. From the Rashølet single track tunnel the evacuation zone was the critical component and otherwise the track structure was constructed according to regulations.

Figure 2. Cables casing (left) connected to the switch (right).

It was found that the reduction potential of the Rashølet single track tunnel was insignificant, and that the reduction potential was high for the Bekkedalshøgda double track tunnel. The reduction potential of Bekkedalshøgda double track tunnel was further investigated by investigating the critical components in respect to the technical regulations. Figures 3 and 4 shows different attempts to optimize the cross-section of the installation zone of Bekkedalshøgda double tracked tunnel by changing the placement-, geometry and eliminating the critical component (cables casing) within the limits of the technical requirements also showing the potential for horizontal length reduction of the tunnel which was further computed into potential tunnel cross-section reduction shown in Figure 7.

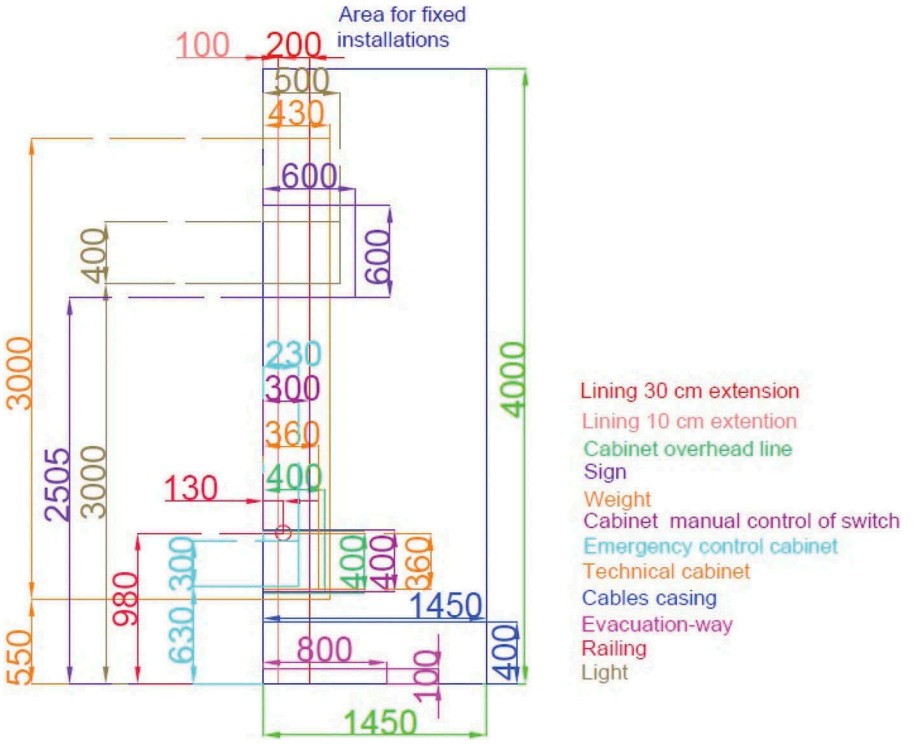

Figure 3. Installation zone of Bekkedalshøgda tunnel.

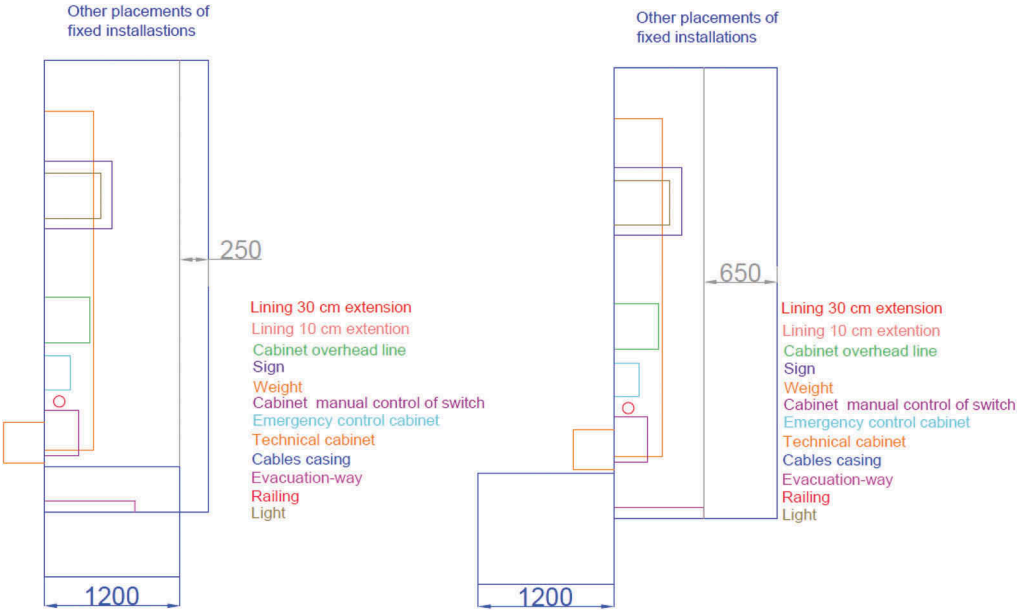

Figure 4. Different attempts to optimize the cross-section of the installation zone by changing the placement-, geometry and eliminating the critical component.

During the comparison of the tunnel cross-section presented in this study it was found that the newer projects were designed using ballast-less track, a design measure suitable for reducing the cross-section size according to the literature. The newer tunnels were designed using bigger and separate evacuation- and installation contours beyond what is necessary size according to the regulations, here the newer projects should look towards the older tunnels that utilizes the evacuation zone for installation as well compressing the cross-section size. It was found that some of the reason increased installation- and evacuation contours was due to the increased focus on safety and maintenance the last years to reduce downtime of the line. It should be discussed further if it the extra costs related to an increased cross-section is justifiable by the arguments of maintenance, safety, and operation stability.

Further the tunnels in this study were both double-track and single-track tunnels. The literature presents the choice of tunnel concept as a function of several parameters to be a challenging process. The single tracked tunnels in this study had an area range of [53-59 m^2], while the double tracked tunnels had an area range of [114-83 m^2]. Area-wise by exclusively looking at the cross-sections of the main tunnels this study shows that there is little potential savings by choosing a double track tunnel rather than choosing two single tracked tunnels. This study can not say anything conclusive about the choice of tunnel concept but there is another phenomenon related to the tunnel concept that has been found in little degree discussed in the literature and regulations related to the train's movements in the tunnels.

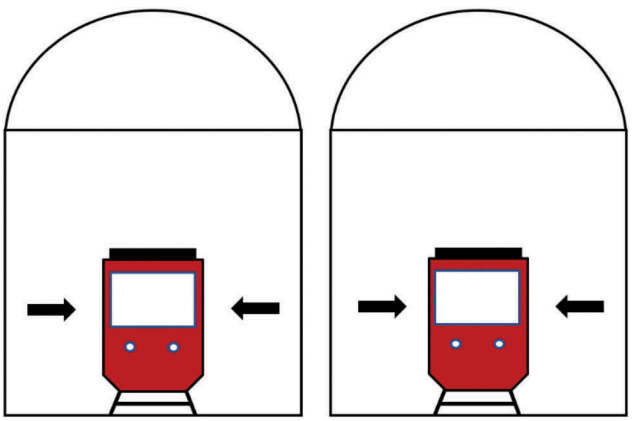

Figure 5. Illustrates forces related to the pressure in two single tracked tunnels.

Figure 5 illustrates two single tracked tunnels where a train is entering the tunnel portal. Trains at high-speed experiences aerodynamic forces in terms of pressure- and suction forces as the train is breaking through the air. At the tunnel entrance the breaking of the air is limited by the tunnel walls creating high pressure forces lateral to the train, illustrated by the arrows in the figure. For a single tracked tunnel, these forces do not represent a challenge for the train-movement as the forces are equalizing each other, as illustrated. For a double tracked tunnel the same phenomenon is experienced as illustrated in Figure 6, with a much higher pressure force coming from the right handside of the train in the tunnel. The lateral pressure forces are not equal for a double track tunnel and leads to a lateral displacement of the wheelsets of the train altering the train-movements on the track from a stable train-movement to a sinusoidal motion on the track and further create severe vibrations in the train. The instability of the train- movement due to lateral displacements of the wheelset is

caused by the nature of the wheel- rail interaction with the wheelset having a conicity creating a steering motion on the track. The steering motion enables the wheelset to steer with a deviation from the equilibrium position towards both sides of the track starting an oscillating motion with the geometry of a sinusoidal curve initiated by the initial lateral displacement that on a straight track with high speed will increase and cause vibrations in the train.

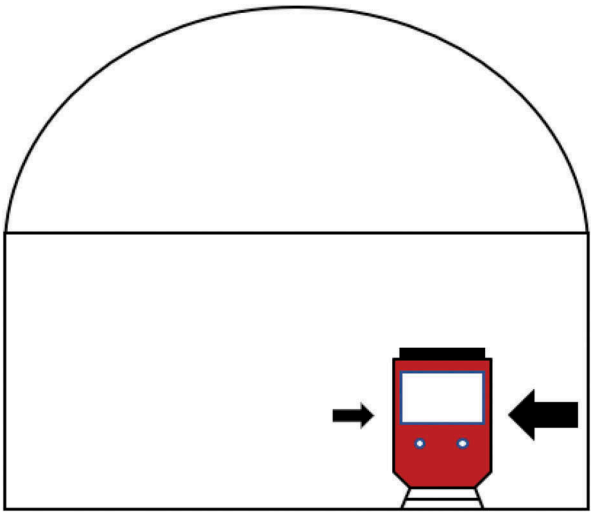

Figure 6. Illustrates the pressure forces in a double tracked tunnel.

This oscillating movement have been observed in newer double tracked tunnels causing severe vibrations on the trains. The problem has led to the need of reducing the speed on the lines and conducting early maintenance and countermeasures. By evaluating this phenomenon with the following challenges as a parameter in the choice of tunnel concept one could potentially save a lot of troubles and costs connected to maintenance and operational difficulties. As shown in this study the area-wise potential cost-savings during construction is little directly related to the tunnel concept, and it should be evaluated whether these potential construction-cost savings are sufficiently higher than the potential maintenance- and operational costs that could be triggered by the tunnel concept choice of double tracked tunnels.

Results from the model calculation of the cross-sections presented in Table 1 are presented in Figure 7, where the blue column present CO^2-emissions, the orange show CO^2 costs, and the gray show construction costs. Note that Rashølet single-track tunnel is not presented in the diagram as it was found that the reduction potential was too small to be significant. The model used for the calculations represent several simplifications and consequently there are uncertainty connected to the results, but the results are believed to be of the correct magnitude and are therefore suitable to illustrate the magnitude of the savings related to costs and CO^2 for a given cross-section size reduction for a drill and blast tunnel. From Figure 7 it is observed a reduction in cross-section size in a magnitude of 10 m^2 giving a reduction of construction costs in the magnitude of 4000 kr/m. For the CO^2- emissions a cross-section size reduction of 10 m^2 correspond to a reduction in the magnitude of 500 kg CO^2 pr unit length and the cost connected to these emissions are in the magnitude of 900 kr per unit length.

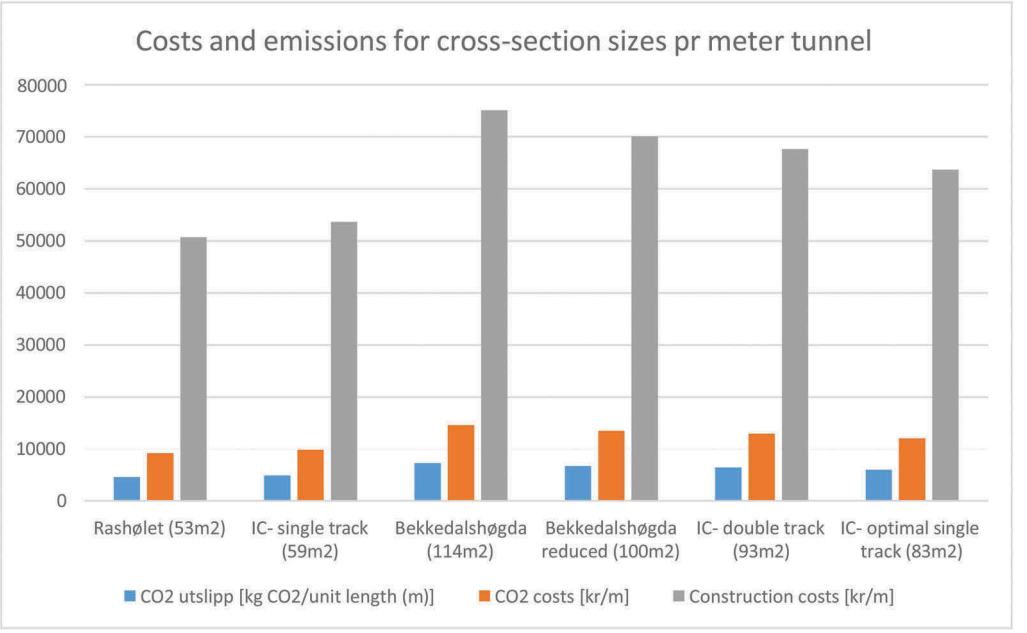

Figure 7. Costs and emissions for different cross-section sizes.

The results presented in Figure 7 is dependent on the length of the tunnel. Consequently, the longer a given tunnel is, the higher will the potential savings be. In Figure 8 this is illustrated by using the cross-section size reduction in the magnitude of 10 m^2 with the corresponding results from Figure 7. One can observe that a tunnel length of 100 meter has significantly lower costs and CO^2 emissions than a tunnel with the length of 1 km. At 1 km the construction costs will be in the magnitude of 4000000 kr, the cost related to CO^2 emissions will be in the magnitude of 900000 kr and the CO^2-emissions in itself will be in the magnitude of 50000 kg CO^2, which represent significant potential savings. It should also be noted that as the simplified computational model was used using conservative parameters, it is not unreasonable to assume that a further development of the model in addition to using more realistic parameters would give even higher potential savings.

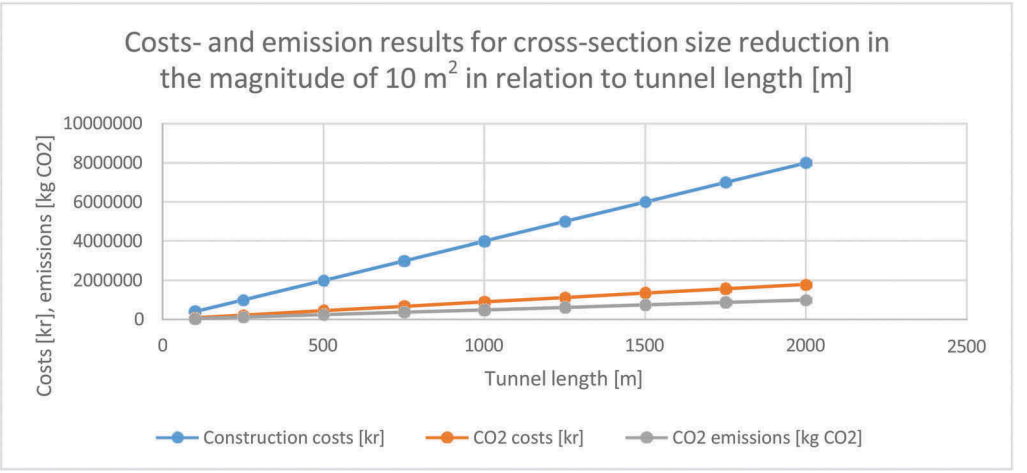

Figure 8. Costs- and emissions results for cross-section size reduction in the magnitude of 10 m^2 in relation to tunnel length.

From this study it was found that documentation of the designing process for the different tunnels have been lacking in relation to designing choices, calculations, and parameters from the requirements. A lot of the design choices was found to be based on empirical data and experience disguised in the documentation as "professional assessment". It was also found that the regulations and requirements where very comprehensive and could in many ways counteract the measures done in attempting to optimize tunnel cross-sections. Design of railway tunnels are highly interdisciplinary, and this was found to be one of the challenges in the optimalization work as the engineers from the different technical subjects regards the components in the tunnel cross-sections related to their subjects as the most important and thus the components deserving most space for easy installation, operation, and maintenance. Leading to the different technical subjects contributing to counteract the optimalization processes. Awareness of the total reduction potential of the tunnel cross-sections, could be an important measure for the different technical disciplines within railway engineering to motivate for optimalization-thinking within all the technical fields.

4 CONCLUSION

Todays design method for railway tunnels was found to in little degree contribute to optimalization of tunnel cross-sections due to the complexity and the interdisciplinary nature of the design field. The different technical disciplines were found to in many ways counteract the optimalization work by demanding bigger space for their components. It was further found that awareness of the total reduction potential of the tunnel cross-sections in relation to the construction costs and CO^2-emissions, could be an important motivational tool for optimalization-thinking.

It was found that the evacuation- and installation zone were the spaces in the tunnel cross-sections with highest reduction potential, in addition it was found that choosing ballast less tracks as the track structure gives a smaller cross-section. The reduction potential of the evacuation- and installation zone was connected to the combining of the zones giving a smaller cross-section.

The study found that the cross-section reduction in the magnitude of 10 m^2 was possible for the different tunnel configurations. Giving a reduction of construction costs in the magnitude of 4000 kr/m, while the costs connected to the CO^2- emissions corresponded to a magnitude of 500 kg CO^2/unit length (m). The costs connected to the CO^2- emissions for the same cross-section reduction was in the magnitude of 900 kr/unit length (m). It was further found that these numbers would be substantial by taking the tunnel length into account.

REFERENCES

Anderson, E., Berg, M. & Stichel, S., 2014. *Rail Vehicle Dynamics*. Kompendium. KTH. Stockholm: Avd. för Spårfordon.

Baklien, M. & Moi, V.,2018. 'Fordeler og begrensninger for TBM kontra konvensjonell driving av E39-tunnel under Romsdalsfjorden', Masteroppgave. NTNU i Trondheim. Available from: https://ntnuopen.ntnu.no/ntnu-xmlui/handle/11250/2563263 Viewed: 2020–12–11.

Bane Nor, 2020a. *Teknisk Regelverk – Profiler og minste tverrsnitt*. Available from: https://trv.banenor.no/wiki/Underbygning/Prosjektering_og_bygging/Profiler_og_minste_tverrsnitt. Viewed: 2021–02–28.

Bane Nor, 2020b. *Kriterier for valg av tunnelkonsept*. Available from: https://www.jernbanekompetanse.no/wiki/Kriterier_for_valg_av_tunnelkonsept. Viewed: 2020–12–03.

Bane Nor, 2020c. *Veileder for valg av tunnelkonsept*. Available from: https://trv.banenor.no/wiki/Veileder_for_valg_av_tunnelkonsept Viewed: 2020–12–03.

Bane Nor, 2020d. *Teknisk Designbasis for Intercity*. Available from: https://www.banenor.no/contentassets/54b785617e5f40cd83c885f66434f677/teknisk-designbasis.pdf. Viewed: 2020–10–31.

Bane Nor, 2020e. '*Fellesprosjektet Ringeriksbanen og E16 (FRE16) - TK-00 Generell, Vurdering av redusert tverrsnitt - Aerodynamisk analyse, Jong -Sunnvollen*'. FRE- 00-A-30118. Bane Nor: Oslo.

Bane Nor, 2021a. *Teknisk Regelverk*. Available from: https://trv.banenor.no/wiki/Forside. Viewed: 2021–02–26.
Bane Nor, 2021b. *Teknisk Regelverk – Overbygning*. Available from: https://trv.banenor.no/wiki/Overbygning. Viewed: 2021–06–13
Chandra, S. & Agarway, M., 2007. *Railway Engineering*, India: Oxford University Press.
Esveld, C., 2001. *Modern Railway Track*, The Netherlands: MRT-Productions.
Iwniki, S., 2006. *Handbook of Rail Vehicle Dynamics*, New York: CRC Press – Taylor Francis Group.
Løhren, A. H., 2019. «Structure gauge/loading gauge», *TBA4225 Jernbaneteknikk grunnkurs*, Tilgjengelig fra: https://ntnu:blackboard:com/ultra/courses/
Pen, L. & Powrie, W., (2016). 'Contribution of base, crib, and shoulder ballast to the lateral sliding resistance of railway track: a geotechnical perspective', *Proceedings of the Institution of Mechanical Engineers Part F Journal of Rail and Rapid Transits* **225**(2), 113–128. DOI: 10.1177/0954409710397094.
Profillidis, W., 2014. *Railway Management and Engineering*, Surry: Ashgate Publishing Limited.
Tunheim, V., Suvalija, I., Bævre, J. T., Leinan, M.-G., Bakka, & Bekkevold, N., 2021. 'Økonomisk og miljømessig modell for tverrsnittsreduksjon av jernbanetunneler', Rapport. NTNU *TBA4853 EiT - Punktlig og Effektiv Jernbane*.

Design for bearing capacity in frost affected areas

Eleventh International Conference on the Bearing Capacity of Roads, Railways and Airfields, Volume 2 – Hoff, Mork & Saba (eds)

Optimizing the effective particle diameter of crushed rock materials to mitigate the effect of convection in a pavement structure

J. Côté
Department of Civil Engineering, Laval University, Québec, Canada

N. Missaoui
Stantec, Québec, Canada

ABSTRACT: It is common practice in Norway to use crushed rock in road structures. Recent regulations allowed a large variation of the particle size distribution in this layer. This paper focuses on the influence of effective particle size of crushed rock materials on heat transfer in pavements based on pavement structure thermal modelling using a partial differential equation solver. The normal temperature for the 1980 – 2010 period in various regions of Norway, as well as the coldest year (extreme conditions) were used together with the factor N as surface conditions of a typical pavement structure. The crushed rock was modelled using various values of effective particle diameter (d_{10}), a material characteristic that significantly affects thermal properties of coarse materials. Along with temperature distributions, maximum frost depths were computed and expressed according to the climatic data of each site studied and as a function of the effective particle diameter. The results showed that d_{10} had a significant effect on frost depth mainly during the coldest winters as a result of increased heat transfer owed to natural convection. The results obtained also made it possible to establish a critical d_{10} value to minimize convection as a function of the mean annual air temperature, providing a simple tool to road designers for selecting the materials for subbase and frost protection layer (FPL).

Keywords: Heat transfer, Convection, Frost Penetration, Pavement, Crushed rock, Effective particle diameter d_{10}

1 INTRODUCTION

Freezing periods in Nordic countries are generally rather severe with temperatures reaching as low as -25 ° C. Earth-made infrastructures such as pavements may experience freezing of soil pore-water that can lead to the formation of ice lenses in frost susceptible soils. This in turn can cause frost heaving. During the spring thaw, melting of the ice lenses in subgrade soil can bring water content to values exceeding liquid limit and to the loss of consistency, thus reducing the effective resistance of the pavement structure, loss of bearing capacity and severe damages (Doré & Zubeck, 2009).

Heat transfer in soils is generally governed by conduction (Johansen, 1975). Figure 1 shows the variation of the maximum freezing depth as a function of the freezing index (FI, °C days) for Norway, the Province of Quebec in Canada, and the United States. Conduction is the sole heat transfer mechanism involved. The results show that the maximum frost depths follow a fairly narrow empirical square root function of FI (eq. [1]). Scattering of data is owed to variations in pavement structures and materials affecting average values of thermal

DOI: 10.1201/9781003222897-9

conductivity (λ) and latent heat of fusion (L_s). Eq. [1] adopts the same mathematical form as Stefan's solution for phase change.

$$\text{Frost Depth} = 0.053 \times \sqrt{FI} \rightarrow \underbrace{\sqrt{2\lambda/L_s} \times \sqrt{FI}}_{\text{Stefan}} \tag{1}$$

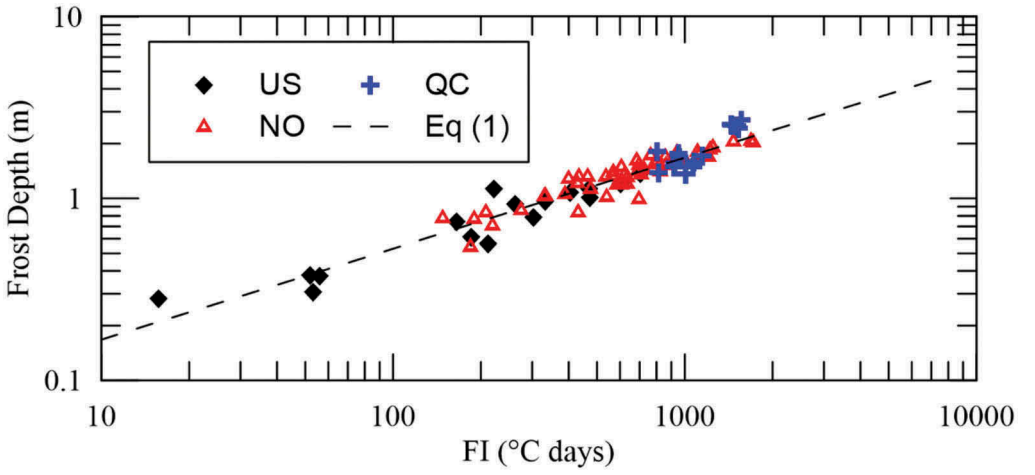

Figure 1. Frost depth in pavement as a function of the freezing index in Norway, Québec and the United States (redrawn from Côté 2009).

Figure 1 shows that frost can extend down to 2 m in Norway. Road and railway structures can be up to 2.4 m thick to reduce frost action in subgrade soils. Over the past decades, construction practices has shifted towards increased use of crushed rock to reduce consumption of natural sand or gravel. It is known that the presence of very coarse materials in embankments can promote convection and radiation heat transfer (Fillion et al. 2011 and Côté et al. 2011). This can ultimately lead to increased frost depths (Loranger 2019) if the effective particle diameter d_{10} (diameter for which 10% of all particles are smaller) is large enough. However, most of the classifications (frost susceptibility, thermal conductivity, etc.) of the current specification is based on the Frost i Jord project (Heiersted et al. 1976) and do not account for the use of coarser rock materials. Consequently, severe frost heave problems have been observed in pavement and railway structures (Aksnes 2013, Loranger et al. 2017) where the subbase and frost protection layer (FPL) were made of coarse crushed rock.

This paper aims at establishing the effect of particle size on the maximum frost depths in typical pavement structures in several location in Norway. Numerical modelling of heat transfer involving conduction, convection and radiation were performed for a pavement structure in various regions of Norway using 30-year average temperatures as well as the temperatures of coldest winter for the 1980-2010 period. The paper first presents the model (basic equation, pavement structure and material properties) used to compute temperature distributions and frost depth. Typical results are then presented followed by the analysis of data that allowed the determination of critical effective particle size (d_{10}) to avoid convection and radiation. This study is part of the "Frost Protection of Roads and Railways" project lead at NTNU.

2 NUMERICAL MODEL

Coupled heat transfer accounting for phase change is mathematically expressed as:

$$C_v \frac{\partial T}{\partial t} + \overrightarrow{V_a}\, C_a \vec{\nabla} \mathrm{T} = \nabla.\left(\lambda_{eff} \nabla T\right) + L_f \frac{\partial \theta_i}{\partial t} \tag{2}$$

where t is time (s), T is the temperature (°C) C_v and λ_{eff} are the volumetric heat capacity (J m^{-3} K^{-1}) and the effective thermal conductivity of the material (W m^{-1} °C) of the porous media, respectively, C_a is the volumetric heat capacity of air and V_a is the Darcy velocity vector for air flow considering the Oberbeck-Boussinesq approximation (see Goering and Kumar 1996), L_f is the latent heat of fusion of water (3.33×10^6 MJ m^{-3}) and θ_i is the volumetric ice content.

The full mathematical development can be found in Missaoui (2020). The pavement structure is presented in Figure 2 (and referring to Table 1) and comply with Handbok N200 (2014). FlexPDE® was used to model the 2D domain where road centerline is on the left of Figure 2. The surface temperature is taken as the average daily air temperature (T_{air}), obtained from the Meteorological Institute of Norway, and corrected with the N factor. A value of N of 1 was taken for the freezing season and 2 for the other seasons (Lunardini 1981). A zero heat flux value was imposed on the three other sides. Air convection could only occur within the subgrade and FPL (same d_{10}) and air flow was not allowed across the boundaries.

$$T_s = N \times T_{air} \tag{3}$$

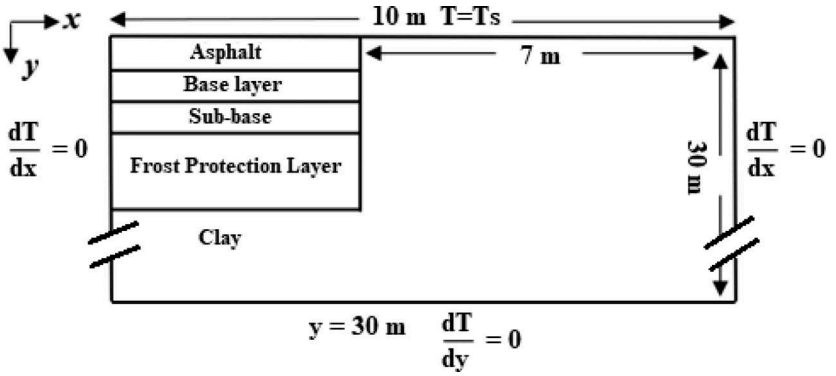

Figure 2. Pavement structure and imposed boundary conditions.

2.1 *Material properties*

As shown in Figure 2, the structure is composed of an asphalt layer, a base layer, a subbase layer, a FPL and finally a layer of clay. The subbase layer and the FPL are made of coarse crushed rock. Table 1 gives the material properties for each layer. The thermal conductivities for the asphalt, base layer subgrade soil were measured (Rieksts 2018, Loranger 2019) or established from the Côté and Konrad model (Côté and Konrad 2005, Rieksts 2018). Heat capacity, effective thermal conductivity, intrinsic permeability, and frozen and unfrozen water contents (eqs [4 – 9]) are described below.

While the porosity of subbase and FPL influences both the intrinsic permeability and the effective thermal conductivity, it does not significantly vary in the field for coarse and poorly graded (low coefficient of uniformity c_u) materials. Its influence is fairly limited (Missaoui 2020) in the context of the present study. Therefore, only d_{10} will be optimize herein.

Table 1. Properties of the used materials.

	Asphalt	Base layer	Subbase layer	Frost protection layer	Clay
Thickness (cm)	5	17	50	168	27.6
Porosity	0.07	0.29	0.42	0.36	0.45
ρ_d (kg/m^3)	2400	1980	1623	1780	1460
w (%)	0.005	0.040	0.010	0.031	0.286
θ_{tot}	0.012	0.079	0.024	0.056	0.450
λ_u (W/m°C)	1.45	1.46	eq. [5]	eq. [5]	1.19
λ_f (W/m°C)	1.45	1.26			1.70

2.2 *Soil property models*

2.2.1 *Heat capacity of all soils*

The volumetric heat capacity of porous media (static = no flow) can be expressed by eq. [4] that neglects the insignificant effect of air.

$$C_v = (1-n)C_s + \theta_w C_w + \theta_i C_i \tag{4}$$

where n is the porosity, θ_w and θ_i are respectively the volume fractions of liquid water and ice. C_w, C_i *and* C_s are the heat capacities of liquid water (4.18 MJ/m^3 °C), ice (1.90 MJ/m^3 °C) and soil particles (average = 2.10 MJ/m^3 °C), respectively.

2.2.2 *Thermal conductivity of crushed rock*

Because radiation flows within pore air in the same direction as conduction it can be assessed in the form of Fourier's law through the diffusion approximation. As a result, the effective thermal conductivity λ_{eff} of coarse and mostly dry crushed rock can be expressed as the sum of the contribution of pure conductivity λ_c (Côté and Konrad 2009) and equivalent radiant conductivity λ_r (Argo and Smith 1953) as follows:

$$\lambda_{eff} = \lambda_c + \lambda_r = \frac{(k_{2p}\,\lambda_s - \lambda_f)(1-n) + \lambda_f}{1 + (k_{2p} - 1)(1-n)} + 4\frac{\varepsilon}{2-\varepsilon} d_{10}\sigma T^3 \tag{5}$$

where λ_s and λ_f are the thermal conductivity of the solid (2.7 W m^{-1} °C^{-1}) and fluid (air: 0.024 W m^{-1} °C^{-1}), respectively, and n is the porosity, ε is particle surface emissivity (no units, taken equal to 0,9), σ is the Stephan-Boltzmann constant (5.67×10^{-8} Wm^{-3}K^{-4}) and T is the mean porous medium temperature (K). The empirical structure parameter κ_{2p} is given as a function of the fluid to solid thermal conductivity ratio (Côté and Konrad 2009).

$$\kappa_{2p} = 0.29\left(15\lambda_s/\lambda_f\right)^{\beta} \tag{6}$$

where β is an empirical parameter accounting for material structure. With a λ_s/λ_f ratio lower than 1/15, the empirical value of β for crushed rock material is 0.54. As temperature increases, the effect of the λ_r term in eq. [5] becomes more and more important.

2.2.3 *Intrinsic permeability*

The intrinsic permeability (m^2) controls the air flows and thus heat flow in coarse materials. The relationship of (Chapuis 2004) which is a function of the porosity n and the effective diameter d_{10}, was used in this study as validated by Côté et al. (2011) and Rieksts (2018) for coarse rock. As mentioned earlier, only d_{10} will be varied and n will remain constant.

$$K = 1.25 \times 10^{-4}\left[\left(d_{10}^2 n^3\right)/(1-n)^2\right]^{0.7825} \quad (7)$$

2.2.4 *Frozen and unfrozen water content*

The pores of soil are filled with, liquid water, ice, and air. The total volumetric water content θ_{tot} is the sum of the liquid θ_w and the solid (ice) θ_i water content:

$$\theta_{tot} = \theta_w + \theta_i \quad (8)$$

The water content in the soil is related to the soil pressure head according to the soil water retention curve (WRC). Integrating the "freezing-drying" assumption from the Clausius-Clapeyron equation within the Van Genuchten (1980) WRC model, yields an expression of volumetric liquid water content θ_w in frozen soils as a function of temperature (T):

$$\theta_w(T) = \theta_r + (\theta_s - \theta_r) \times \left\{1 + \left[\left(-\alpha L_f / g\ T_0\right)(T - T_0)\ \right]^n\right\}^{(1/n-1)} \quad (9)$$

where θ_r is the residual water content and θ_s is the saturated water content, i.e., the porosity of the soil, g is the acceleration of gravity, L_f is the latent heat of fusion of water and α [m^{-1}] and n [-] are adjustment parameters that reflect the inverse of the air entry value and the particle size distribution, respectively.

2.3 *Selection of representative regions*

Norwegian climate varies considerably from one region to another. Typically, coastal areas have relatively mild winters and fairly cool summers. Interior lands are characterized by cold winters with abundant snow and hot and dry summers, especially in the east of the country. To account for these climate features, six regions were selected, namely: Finnamark, Nordland, Sør-Trøndelag, Hedmark, Oppland and Hordaland, and the climate data were extracted from Eklima.no. Two scenarios of climatic conditions will be evaluated for the frost penetration modelling: 1) the 30-year normal temperatures (1980-2010) and 2) extreme conditions taken as the coldest year during this 30-year period as summarized in Table 2. Published monthly average temperatures are interpolated to generate daily values for a full year temperature cycles.

Table 2. Summaru of normal and extreme climatic data (1980-2010, Eklima.no).

	Alt. (m)	Lat. (°)	Long. (°)	$MAT_{30\ years}$ (°C)	$FI_{30\ years}$ (°C.d)	MAT_{ext} (°C)	FI_{ext} (°C.ds)
Finnmark	10	70.39	28.19	-0.1	1346	-2.2	1955
Sor-Trøndelag	628	62.57	11.37	0.8	1110	-1	1775
Oppland	639	60.91	9.28	1.89	870	0.07	1495
Hedmark	240	61.16	11.44	2.75	923	0.71	1660
Hordaland	48	60.28	5.22	7.15	0	5.78	239
Nordland	33	67.28	14.45	5.15	105	4.55	285

MAT = mean annual air temperature, FI = freezing index.

3 RESULTS OF FROST DEPTH COMPUTATIONS

The temperatures were computed within the pavement structure for a conditioning period of 30 years using the climate normals. The results for the last year cycle were recorded for the

first modelling scenario and for the second, another cycle was modelled but with the extreme conditions. Two-dimensional temperature distributions within the pavement structure were analysed to establish frost progression in time among others at each region for both scenarios.

3.1 *Scenario 1: Normal conditions*

Figure 3 shows the evolution of frost depth for the region of Finnmark (normal conditions) for d_{10} equal to 90 mm (red) as well as d_{10} equal to 30 mm (black). It clearly illustrates that when d_{10} is higher, the maximum frost penetration is higher, highlighting the effect of convection and

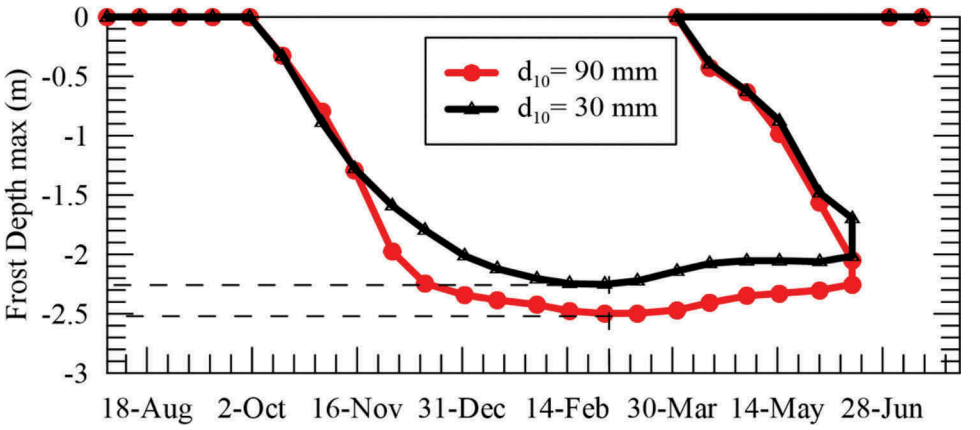

Figure 3. Evolution of the freezing depth for the Finnmark region, for d_{10}= 90 mm and d_{10}= 30 mm in normal condition.

radiation. Maximum frost depths are recorded on the first of March for both cases with values equal to 2.25 m (stays within pavement structure) and 2.49 m (extends within subgrade) for d_{10} = 30 mm and d_{10} = 90 mm respectively.

The variations of the maximum freezing depth are illustrated as a function of the MAT (Figure 4a) and the FI (Figure 4b, *notice the log scales*) for normal data for effective particle diameter varied from d_{10} = 30 mm to d_{10} = 110 mm. These results show that the maximum frost depth decreases linearly with increasing $MAT_{30years}$ (Figure 4a) and increases with increasing $FI_{30years}$ (Figure 4b). The maximum frost depth is obtained in Finnmark, reaching a value of 2.55 m for a d_{10} = 110 mm and the minimum value is obtained in Hordaland with 0 m for d_{10} = 30 mm. Figure 4 also shows the effect of d_{10} on frost penetration into the soil. In fact, for a given region, the greater d_{10} is, the greater the frost penetration into the soil is. However, this effect is rather small for normal conditions (less than 15% in the colder regions) as also revealed from the fairly good agreement between the numerical results and eq. [1] in Figure 4b.

3.2 *Scenario 2: Extreme conditions*

Similar results to those of scenario 1 were obtained for scenario 2 with extreme conditions as shown in Figure 5. As expected, much greater frost depths were obtained and the effect of d_{10} proves to be much more important especially in the colder regions as shown by the departure form eq. [1] as d_{10} increases. For example, in Finnmark and Sør-Trøndelag where values of MAT_{ext} are -2.2°C and -1 °C, respectively, the frost propagates down to the natural soil (depth > 240 cm) for all d_{10}. The computed frost depths of Finnmark (oval in Figure 5a) varies from about 3.1 m for a d_{10} of 10 mm and 20 mm to 4.5 m for d_{10} of 90 mm, which is more than a 40% increase (110 mm not shown). These results therefore show that convection and radiation begin to significantly influence frost dept in Finnmark for d_{10} values above

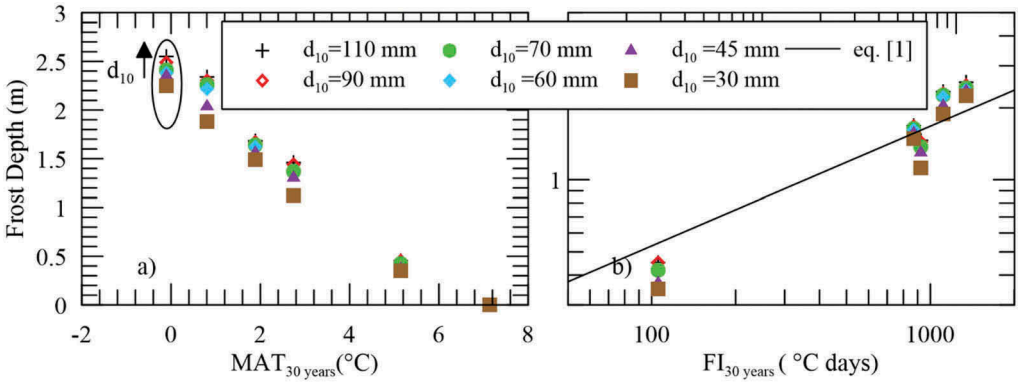

Figure 4. Variation of the maximum freezing depth according to a) MAT and b) FI under normal conditions.

20 mm. In Oppland where the MAT_{ext} = 0.07 ° C, the frost depths vary much less, as a function of d_{10}, with values from 2.2 mm to 2.5 mm and with d_{10} values equal or lower than 45 mm maintaining frost depth above the subgrade soils (< 2.4 m). The results clearly show that d_{10} has a significant influence on the heat transfer and thus frost depth, particularly in colder conditions.

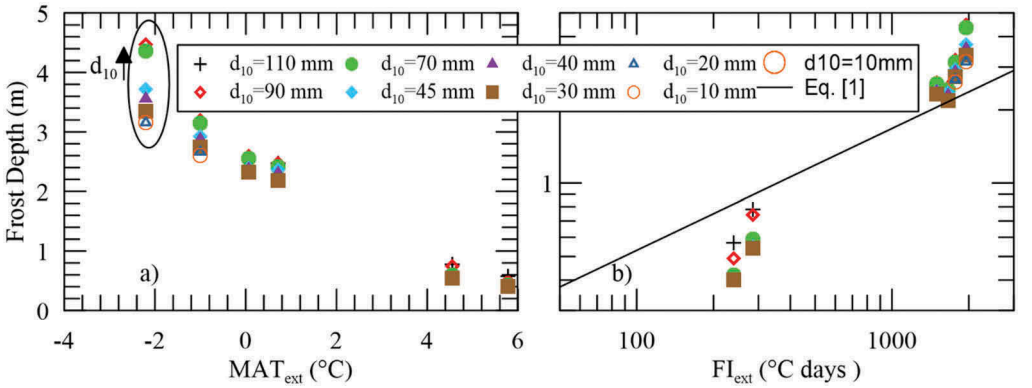

Figure 5. Variation of the maximum freezing depth depending on extreme climatic data.

4 EFFECT OF EFFECTIVE DIAMETER ON THE INITIATION OF CONVECTION

Taken separately, convection and radiation contribute differently to heat transfer when couple to conduction. Radiation heat transfer increases with increasing d_{10} and with increasing temperatures. Which means that for a given d_{10}, radiation is slightly more important in the warm season than in the cold season thus contributing to accumulate a little more heat in summer than what is lost in the winter. On the other hand, natural convection is a phenomenon only present when subsurface materials are warmer than the surface itself. So, provided that d_{10} is large enough, convection heat transfer is only present in winter promoting heat loss and greater frost depths while it does not provide extra heat input in the summer to compensate. So, from a material selection point of view, convection is the heat transfer mechanism to consider when attempting to minimize frost depths in pavement structures.

Indeed, many studies on embankments made of coarse materials have shown that heat transfer in summer is dominated by thermal conduction (and radiation), while in winter, it is controlled by thermal convection (Goering and Kumar 1996, Goering et al. 2000, Lebeau and Konrad 2008).

The results of this study clearly show that convection can be activated, and its intensity is governed by permeability which in turn is a greatly influenced by d_{10}. In order to be able to estimate the critical d_{10} for which the convection is activated, further analyses are performed using the Rayleigh number (Ra, eq. 10) that characterizes the intensity of convection. It is known that convection can only be initiated above a Ra_{crit} value of $4\pi^2$ (Schubert and Straus 1979).

$$Ra = \left(K\,\rho_f C_f \beta g H^2 \nabla T\right) / \left(\mu\,\lambda_{eff}\right) \tag{10}$$

where K and λ_{eff} are the intrinsic permeability (m^2, ep. [7]) and the equivalent conductivity ($W.m^{-1}.K^{-1}$, eq. [5] of the porous medium, respectively, ρ_f is the density of the fluid ($kg.m^{-3}$), C_f is the heat capacity of the fluid ($J.m^{-3}.K^{-1}$), β is the coefficient of thermal expansion (K^{-1}), g is the acceleration of gravity ($m.s^{-2}$), H is the height of the porous medium (m), ∇T is the temperature gradient imposed between the ends of the porous medium ($K.m^{-2}$), μ is the dynamic viscosity ($kg.m^{-1}.s^{-1}$).

Figure 6 shows examples of the variation of computed Ra values as a function of the d_{10} for a) Finnmark and b) Hedmark. The critical d_{10} is directly obtained by interpolation at $Ra_{crit} = 4\pi^2$ as shown in Figure 6. For Finnmark, $d_{10crit\ ext}$ = 47.3 mm and $d_{10crit\ normal}$ = 61.6 mm. As expected, this shows that in extreme condition convection is activated, with an d_{10} smaller than that in normal condition. For example, in Finnmark, the critical diameters are $d_{10crit\ ext}$ = 47.3 mm and $d_{10crit\ normal}$ = 61.6 mm, respectively. Similar analyses were carried out for all regions and results are summarized in Figure 7.

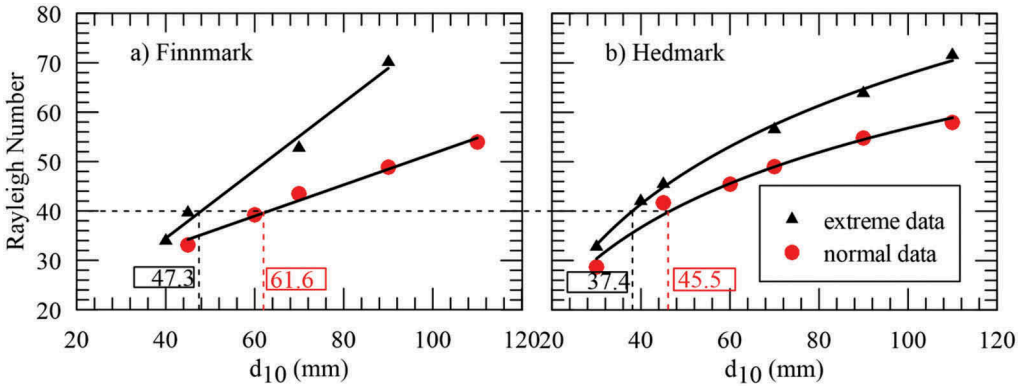

Figure 6. Variation of the Rayleigh number as a function of the effective diameter d_{10}.

Figure 7a illustrates the variation of $d_{10\ crit}$ as a function of the extreme and normal MAT for the four colder of the studied regions. The results show that $d_{10\ crit}$ is inversely proportional to MAT. This may seem counter intuitive, however, it is simply explained by the fact that colder regions accumulate less heat in the summer that warmer regions, resulting in smaller thermal gradients during winter in the colder regions and thus requiring greater permeabilities (greater d_{10}) to initiate convection. The same $d_{10\ crit}$ results are also plotted as a function of the FI for normal and extreme conditions in Figure 7b. The results show similar trend, but proportional this time, between $d_{10\ crit}$ FI. Indeed, higher values of FI require a greater critical d_{10} for it to initiate convection. Figure 7 readily allow to obtain critical d_{10} as a function of MAT or FI of a given site to consider the effect of convection on heat transfer and to reduce frost penetration into the soil.

The data for the extreme conditions can be used to determine a maximum d_{10} value that can be allowed to minimize convection effect and thus frost penetration as illustrated by the dashed blue line shown on Figure 7. As already mentioned above, smaller value of $d_{10\ crit}$ are

obtained for extreme conditions compared to normal conditions. The proposed criterion is caped at a minimum value of 40 mm as the computation results of Figure 5 showed that above average

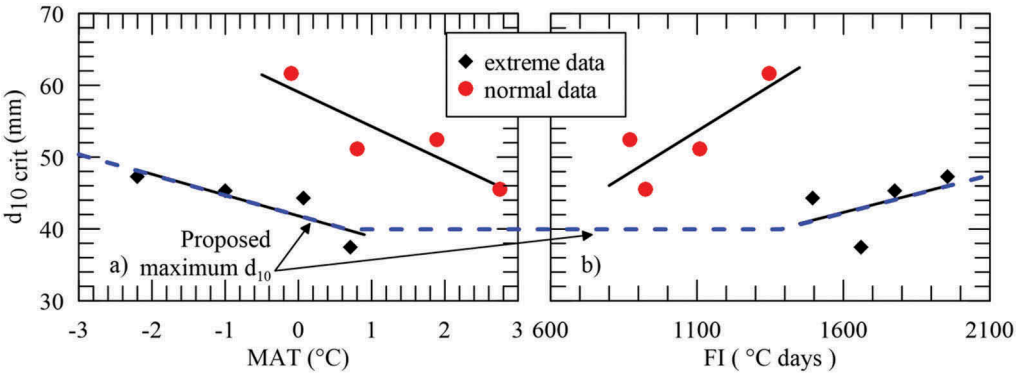

Figure 7. Variation of the critical effective diameter as a function of a) MAT et b) FI.

annual temperature of –1°C (or FI < 1500 °C days), frost will not extend in the subgrade soil and also because the effect of d_{10} is very limited even if convection may be initiated.
Future field work could include validation from temperature measurements to verify if critical thermal gradients required to generate convection are reached or not. Solving eq. [10] for ∇T leads to an expression of critical gradient:

$$\nabla T_{crit} = \left(Ra_{crit}\ \mu\ \lambda_{eff}\right) / \left(K \rho_f\ C_f \beta\ g\ H^2\right) \tag{11}$$

This allows to independently compute the ∇T_{crit} as a function of d_{10} when eq [5] (λ_{eff}) and [7] (K) are substituted in eq [11]. For the example given here, the porosity is 0.40 and all other parameters are constants at T = -5 ° C (the average winter temperature in the frost protection layer): ρ_0 is equal to 1.316 kg/m^3, β is equal to 3.76 X 10^{-3} K^{-1} and μ is equal to 16.9 × 10^{-6} kg/ms. Note that d_{10} is expressed in meters (m). With these values, eq. [11] reduces to:

$$\nabla T_{crit} = 0,04\ d_{10\ crit}^{-1,56} - 3.7 \times 10^{-5}\ d_{10\ crit}^{-0,56} \tag{12}$$

The last term of eq. [12] is insignificant and thus a simplified version is obtained:

$$\nabla T_{crit} = 0,04\ d_{10\ crit}^{-1,56} \tag{13}$$

The theoretical ∇T_{crit} values of Eq. [13] are shown by the black line in Figure 8. The ∇T_{crit} were also assessed from numerical modelling for several d_{10}, ranging from 10 mm up to 110 mm. The results for Finnmark in extreme conditions (red dots) and Hedmark in normal conditions (blue diamonds) are shown in Figure 8 and agree fairly well with eq. [13] showing that ∇T_{crit} can be related directly to $d_{10\ crit}$ independently of the climate conditions. Eq.[13] can therefore be used for first assessment of critical gradients and if known, the parameters of eq. [11] can adjusted for more accuracy. The good agreement between theoretical and numerical results of Figure 8 also supports the relevance of the numerical model used in this study.

5 CONCLUSION

Within the last decades, Norway has seen a major transition to using crushed rock materials for road and railway construction instead of natural materials such as sand or gravel. However, in coarse rock materials, natural air convection can greatly enhance heat transfer leading to increased frost penetration in pavement structures. Freezing front may reach frost susceptible subgrade soils and unexpected differential heaving may be observed along with surface deformation and damage. This paper aimed at establishing the effect of d_{10} on frost propagation to help select the coarser materials while minimizing frost depths.

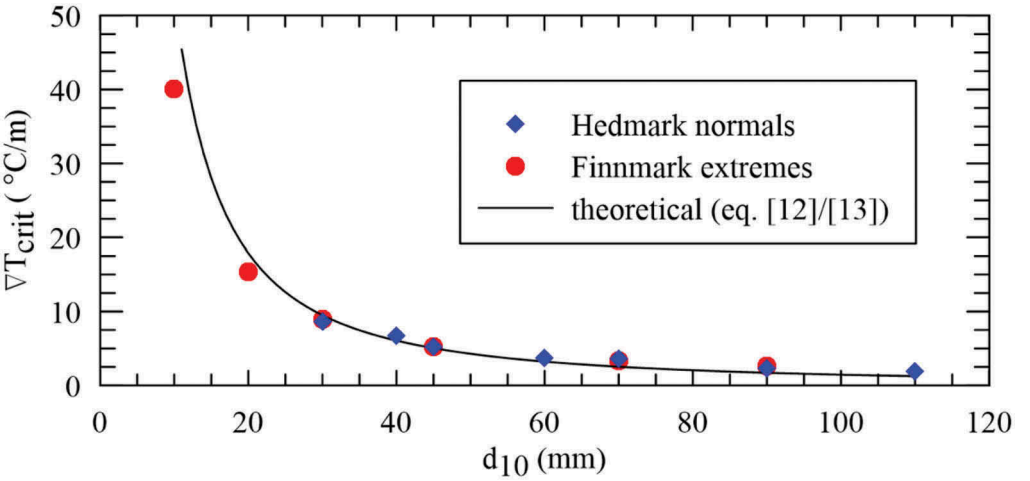

Figure 8. Variation of ∇T_{crit} as a function of d_{10}.

The results of this study allowed the development of a method to optimize the effective particle diameter d_{10} of crushed rock materials to limit the effect of convection. A numerical model has been developed to estimate the maximum freezing depth and express it according to the climatic data of a given site. The 30-years temperature normals for the 1980–2010 period for various representative regions of Norway, as well as the temperatures of coldest year (extreme conditions) were used to perform numerical modelling of heat transfer involving convection among other heat transfer mechanisms within a representative pavement structure. The results made it possible to characterize the effective critical diameter d_{10} from which convection is active for the normal 30-year data as well as for the extreme data. Analysis of the numerical results led to the development of empirical relationships to estimate the critical d_{10} based on climate data.

Based on the results of the modelling with extreme conditions, it was established that a maximum effective particle diameter of 40 mm can be used in the warmer region and that the maximum d_{10} value can be increased up to close to 50 mm in the colder regions. A theoretical relationship between the critical effective particle diameter and the critical thermal gradient to be expected in the field for convection to occur has also been developed allowing for simple verification along with pavement structure temperature data.

REFERENCES

Aksnes, J. (2013). New frost design specifications in Norway. Workshop on "Pavement design in cold regions" held together with the 9th BCRRA conference in Trondheim June 2013

Argo, W. Smith, J. (1953). Heat transfer in packed beds. Chemical Engineering Progress, 49: 443–451.

Chapuis, R. P. (2004). Predicting the saturated hydraulic conductivity of sand and gravel using effective diameter and void ratio. Canadian Geotechnical Journal, 41(5) 787–795.

Côté, J., Konrad, J.-M. 2005. A generalised thermal conductivity model for soils and construction materials. Canadian Geotechnical Journal, 42: 443–458.
Côté, J. (2009). Heat transfer in geotechnical engineering: Recent developments. 33rd Colloquium, 62nd Canadian Geotechnical Conference, Halifax, unpublished.
Côté, J., Konrad, J.-M. (2009). Assessment of structure effects on the thermal conductivity of two-phase porous geomaterials. International Journal of Heat and Mass Transfer, 52: 796–804.
Côté, J., Fillion, M.-H., and Konrad, J.-M. (2011). Intrinsic permeability of materials ranging from sand to rock-fill materials using natural air convection tests. Canadian Geotechnical Journal, 48 (6): 679–690.
Doré, G., & Zubeck, H. (2009). Cold Regions Pavement Engineering. McGraw-Hill.
Fillion, M.-H., Côté, J., & Konrad, J.-M. (2011). Thermal radiation and conduction properties of materials ranging from sand to rock-fill. Can. Geotech. Journal, 532–542.
Goering, D. J., Instanes, A., & Knuden, S. (2000). Convective heat transfer in railway embankment ballast. In proceedings of the International Symposium on Ground Freezing and Frost Action in Soils, Louvain-la-Neuve, Belgium,. Edited by J.-F. Thimus. Balkema, Rotterdam, the Netherland, 11–13.
Goering, D.-J. and Kumar, P. (1996). Winter-time convection in open-graded embankments. Cold Regions Science and Technology, 24(1),57–74.
Handbok N200 (2014). Vegbygging (Road construction). Statens vegvesens håndbokserie. Norway.
Heiersted, R. S., Refsdal, G., Saeterdal, R., & Torgersen, S. (1976). Sikring mot teleskader. Norges teknisk-naturvitenskapelige forskningsråd og Statens vegvesens utvalg for frost i jord.
Johansen, O. (1975). Thermal conductivity of soils. Ph.D. thesis, University of Trondheim, Trondheim, Norway. US Army Corps of Engineers, Cold Regions Research and Engineering Laboratory Hanover, N.H. CRREL Draft English Translation 637.
Lebeau, M., & Konrad, J. M. (2008). Natural convection of compressible and incompressible gases in undeformable porous media under cold climate conditions. Computers and Geotechnics.
Loranger, B. Kuznetsova, E., Hoff, I., Aksnes, J. and Skoglund, K.A. (2017). Evaluation of Norwegian gradation based regulation for frost susceptibility of crushed rock aggregates in roads and railways. Bearing Capacity of Roads, Railways and Airfields, ed. Loizos et al. Taylor and Francis Group, London.
Loranger, B. (2019). Frost Depth and Frost Protection Capacity of Crushed Rock Aggregates Based on Particle Size Distribution. 18th International Conference on Cold Regions Engineering and 8th Canadian Permafrost Conference, August 18–22,2019, Quebec City, Quebec, Canada.
Lunardini, V.-J. (1981). Heat transfer in cold climates, Van Nostrand Reinhold Company.
Missaoui, N. (2020). Optimisation du diamètre effectif d_{10} des matériaux de protection contre le gel pour limiter l'effet de la convection dans une structure de chaussée en Norvège. Québec Canada: Université Laval.
Rieksts, K. (2018). Heat Transfer Characteristics of Crushed Rock and Lightweight Aggregate Material, Ph.D. Thesis, Norwegian University of Technology, Trondheim, Norway.
Schubert, G., & Straus, M.-J. (1979). Three-dimensional and multicellular steady and unsteady convection in fluid-saturated porous media at high Rayleigh numbers. Journal of Fluid Mechanics, 94 (1),25–38.
Van Genuchten, M. T. (1980). A closed-form equation for predicting the hydraulic conductivity of unsaturated soils. Soil Sci. Soc. Am. J., 44, 892–898.

Eleventh International Conference on the Bearing Capacity of Roads, Railways and Airfields, Volume 2 – Hoff, Mork & Saba (eds)

Freeze-thaw influence on the water retention capacity of silty sand subgrades

J.H.C Everton & D. Saliko
Division of Building Materials, ABE/BYV, Royal Institute of Technology/KTH, Stockholm, Sweden
Pavement Technology, Swedish National Road and Transport Research Institute - VTI, Linköping, Sweden

S. Erlingsson
Division of Building Materials, ABE/BYV, Royal Institute of Technology/KTH, Stockholm, Sweden
Pavement Technology, Swedish National Road and Transport Research Institute - VTI, Linköping, Sweden
Faculty of Civil Engineering and Environmental Engineering, University of Iceland, Reykjavik, Iceland

ABSTRACT: Fine-grained materials are associated with a higher water retention capacity due to their higher surface energy in comparison with coarser materials. That characteristic is connected to why fine-grained materials also yields more suction when drying. In addition, seasonal variation of the water table subjects fine-grained subgrades to different moisture contents, varying the suction built in the subgrade, consequently affecting its mechanical characteristics. As fine-grained materials are frequently frost susceptible, they can cause issues to the whole pavement cross-section related to Freeze-Thaw (F-T) actions, widely known as frost heave and thaw weakening. This study will seek to investigate if subsequent cycles of closed-system F-T can permanently alter the unsaturated behaviour of fine-grained materials, using as background their Soil Water Retention Capacity obtained using a pressure plate apparatus. Such issues may become more common with permafrost areas being subjected to freeze and thaw cycles due to climate change or extraordinary events creating the circumstances to F-T where it is currently not observed. Two silty sands with low plasticity were tested, and the results show a reduced water retention capacity (WRC) after closed-system F-T cycles. Considering that matric suction changes the state of stress of soils, the findings suggest an impact in the resilient modulus (M_r) not only seasonally, as it is well established, but also after seasonal freezing and thaw events.

Keywords: Swrc, unsaturated soils, subgrade, cold regions pavement structures, freeze-thaw

1 INTRODUCTION

Subgrades in frost susceptible regions follow the same principia as in non-frost susceptible regions regarding water protection. Such that one of the purposes of the pavement structure resting on top of the subgrade is to protect it from water infiltration; the other functions are to protect it from high vertical and shear stresses. Therefore, considering the lower permeability of the surface layer, one can say that the subgrades in frost regions are also situated in the intermediate vadose zone, where a two-phase of continuous water and air coexist, at least for parts of the year.

An important contrast, however, from non-frost-susceptible regions is the formation of ice lenses (depending on the frost susceptibility of the soil) during the winter, in a process known as ice segregation, where water is drawn up to the freezing front due to a cryosuction effect.

DOI: 10.1201/9781003222897-10

Then, this water in excess thaws and saturate the soil during the spring until it gradually dissipates, depending on the soil's permeability and external conditions.

Whereas in non-frost-susceptible regions, the mechanism of energy dissipation allows for evapotranspiration (Doré and Zubeck, 2009), which means the moisture content stabilises, reaching a steady-state condition (Zapata, 2018), where the subgrades will be mainly in the unsaturated condition, for most of the year unless during raining events where water can reach the pavement structure transversally, or axially, in case the surface has aged and cracks have developed.

Due to the high surface energy and swelling-prone property of fine-grained materials, unfrozen water bounded to the grains – known as adsorbed water – is observed even when temperatures are well below the freezing point (Andersland & Ladanyi, 2004), which means the ice crystals grown bigger within the pores until the adsorbed water freezes, potentially displacing the grains. In the spring, the unfrozen water saturates the subgrade, causing what is known as thaw weakening – reducing the pavement's bearing capacity. The literature and experience show that the bearing capacity of such pavements slowly returns to previous levels when the water is drained. In other words, suction will increase as water drains, increasing the mechanical characteristics of the subgrade.

However, some studies suggest that F-T cycles can cause particles to break up, changing the particle size distribution, which coupled with the ice expansion, that can cause a void ratio's increase or pore geometry change, can affect the Soil Water Retention Capacity (SWRC) of the subgrades (Ren & Vanapalli, 2019; Yao et al., 2020).

1.1 *Subgrades soils in frost regions*

Natural materials used as subgrade can suffer excessive permanent deformation if not adequately protected from high stresses and water infiltration. Consequently, it can fail to provide the necessary support for the asphalt layer, with shear stresses causing strains that exceed the fatigue resistance of such layer, resulting in cracking.

In cold regions, however, another challenge is added to protecting the subgrade, which is related to frost problems. To provide adequate protection to the subgrade, one design option is to have a thicker pavement structure to isolate or minimise the subgrade's exposure to the freezing front and its consequences, as explained before. The freezing index (FI) of the region, type of subgrade material, and natural water content are variables that will affect the frost depth ($\bar{x}$), that is, the depth the frost penetrates the ground during the winter season. There is more than one model to equate the frost depth, but Stefan Solution (Eq. 1) gives a good estimation, and the parameters are relatively simple to obtain. It relates the freezing index, the latent heat of fusion (L) and the heat conductivity (k_f), both of which are a function of the material and the water content (Andersland and Ladanyi, 2004).

$$\bar{x} = \sqrt{\frac{2k_f}{L} \cdot FI} \tag{1}$$

Other strategies to prevent frost problems include changing the subgrade material to one less susceptible to frost and, alternatively, providing drainage layers to remove water from the system so that it is not attracted to the freezing fringe. Nevertheless, the soil heterogeneity along a road section and different water contributors makes it hard to have full control of the freezing process within the subgrade, and so the pavement structure should resist some level of differential frost heave (Andersland and Ladanyi, 2004).

Another design method for cold region pavements accounts for a weakened subgrade when thawing during the spring (Andersland and Ladanyi, 2004). Thawing can occur even when no frost heaving occurs, which is related to the thawing speed and the material's permeability. An example of such an issue is clay, which combines high matric suction with low permeability, making the conditions for ice segregation difficult and, therefore, frost heave less severe. However, the entrapped water in a clay subgrade layer will significantly reduce the bearing capacity during thawing (Christopher et al., 2006).

In order to adequately estimate a pavement service life based on one of the design strategies mentioned above, we need to know the material's mechanical properties to verify if they can

sustain the stresses that will be yielded in the structure due to traffic and environmental conditions. In that regard, in a mechanistic-empirical (M-E) method, the strains of interest are the horizontal tensile strain at the bottom of the bounded layer and the vertical strain at the top of the subgrade to assess fatigue cracking and rutting, respectively. Finally, the layers corresponding to the pavement structure are evaluated in terms of their combined accumulated strain throughout the pavement design life against the backdrop of the maximum permissible rutting and fatigue cracking (Doré and Zubeck, 2009).

This research aims at contributing to the scholar on the M-E method by verifying the impact that freeze-thaw cycles have on the SWRC of subgrades and potentially in its mechanical characteristics. For that purpose, two silty sand subgrades with different fines content, from the region of Östergötland in Sweden, will have their SWRC determined.

2 CHARACTERISING UNSATURATED SUBGRADES

The so-called Soil Water Characteristic Curve (SWCC), which relates suction and moisture content, is a fundamental relationship to understanding the behaviour of unsaturated soils better. In fact, there is more than one curve describing the relationship of suction and moisture content for each soil, and it is conditioned to whether the soils are experiencing drying or wetting, to its initial dry density and its initial degree of saturation (Walshire et al., 2019). Therefore, some authors suggest calling such a relationship, obtained from one's experiment, as Soil Water Retention Capacity (SWRC) as it was originated with a particular set of boundary conditions.

Authors have identified that soils show a hysteresis behaviour when drying and wetting; that is, the relationship between suction and water content is different if the soil starts fully saturated or from a dry state. Those curves are known as main drying and main wetting curve. Previous research has shown that the obtained relationship would fit within the main curves for tests initiated from fully saturated to fully dry (residual saturation) (Fredlund et al., 2012).

The SWRC can be used to estimate unsaturated soil property functions (USPF), e.g. permeability, shear strength and volume change. Although those are empirical relationships, the results show a good fit with tests specifically designed to test those properties (Fredlund et al., 2012). The estimation of USPFs are related to the drying branch of the SWRC (Fredlund et al., 2012), coupled to that, most previous studies focused on desorption tests. Therefore, for comparison and repeatability with previous studies, this study focused on the drying SWRC.

The initial dry density is another parameter for a SWRC, and for naturally occurring materials such as subgrades, they are usually at least mechanically stabilised, i.e., they are compacted to a maximum dry density at an optimum moisture content (OMC).

In this study, two silty sands were tested, and Table 1 presents the index properties obtained before the sample preparation for the suction experiments. According to the Unified Soil Classification System (USCS), both soils are classified as Silty Sand material (SM), and according to tests performed on the material with 39% fines (Kuttah, 2020), it has a plasticity index of less than 4%, resulting in low plasticity soil. The material with 17% fines was deemed nonplastic.

In light of this, the results of this study will be interpreted according to SWRC for incompressible soils, where the gravimetric SWRC (*w-SWRC*) can be converted into volumetric (*θ-SWRC*) and degree of saturation (*S-SWRC*) relationships without the need to obtain shrinking parameters (Fredlund, 2019).

Table 1. Index properties of the tested soils.

Soil Classification	Passing sieve 0,063mm (%)	Max. Dry unit weight (g/cm^3)	Optimum Moisture cont. (%)	Specific gravity (-)	Liq. Lim. LL (%)	Pl. lim. PL (%)	Pl. Index PI (%)
SM	17,40	1,902	8,7	2,65	-	-	-
SM	39,00	2,083	8,5	2,64	18[1]	14,30[1]	3,70[1]

[1] Results obtained from (Kuttah, 2020) from tests conducted in the same material.

Therefore, after establishing the boundary conditions, a SWRC to characterise unsaturated subgrades could be obtained in the laboratory.

2.1 *SWRC testing*

There are at least two well-described methods to measure the relationship between suction and moisture content, one artificially imposes a pressure in the specimen to force water out and is known as the axis translation technique; the other measures water tension in a specimen as it dries (Briaud, 2013; Fredlund et al., 2012). Their use will depend on the suction range of interest, the type of soil and the time frame available. The particle size distribution plays a significant role in the consolidation time between different pressure targets, i.e., the rate of water release from the soil for a given suction.

For the suction level experienced in subgrade soils, a pressure plate apparatus, which employs the axis translation technique, suffices the requirements considerably faster when compared with the filter paper, which employs the other method described above. This research was conducted using a pressure plate apparatus, namely SWC-150 Fredlund SWCC Device (*Figure 1*). This apparatus can apply and sustain up to 1500 kPa of air pressure in a cell chamber, and the consolidation time between applied pressures vary from several hours to days, whilst the filter paper varies from two to five days (Erlingsson et al., 2009).

Matric suction (ψ) is emulated using the SWC-150 by increasing the pore air pressure (u_a) while keeping the pore water (u_ω) at atmospheric pressure. For in situ conditions, matric suction is yielded with negative water pressures while the air pressure is kept at atmospheric level; the outcome is that the same matric suction from the field can be yielded in the laboratory (2). Furthermore, field conditions are attained in metastable conditions, where water can remain in liquid state even with negative pressure; however, if such conditions were applied in the laboratory, a cavitation process would occur, and water readings would not be meaningful (Marinho et al., 2008). Therefore, in the axis translation technique, the air pressure is intentionally higher than the atmospheric pressure to fall into a stable condition (*Figure 2*), controlling the formation of bubbles in the water reservoir below the ceramic stone seen in *Figure* 1a.

$$\psi = (u_a - u_w)_{in\ situ} = (u_a - u_w)_{axis\ translation} \tag{2}$$

Figure 1. SWC-150 Device. a) Bottom plate with the HAE ceramic stone installed into its recess b) specimen mounted on top of the ceramic stone and chamber cell positioned c) enclosed pressure chamber with top plate.

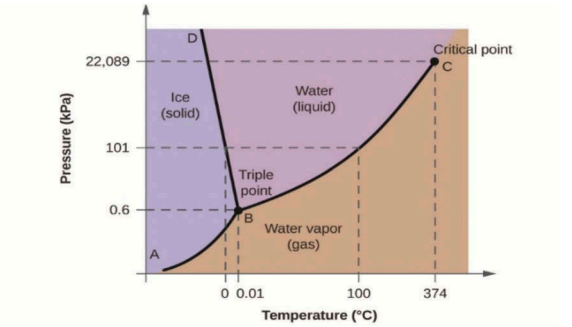

Figure 2. The phase diagram of water under stable conditions (licensed under CC BY).

2.2 *Testing preparation*

In the SWC-150 device, a metal ring is used as a sample holder, and it has a height of 32mm and 51mm in diameter. The samples were compacted to modified Proctor energy (2,7 MJ/m^3) using a rammer compactor seen in *Figure 3a* (Walshire et al., 2019).

A total of 4 samples (*Figure 3b*) for each soil were prepared at OMC and, using the same compaction effort, sealed with plastic foil to retain moisture and later subjected to cycles of freeze and thaw. *Figure 3c* shows one of the two batches with samples identified from 0 to 5 F-T cycles of 48h for each cycle (24h Freezing at -20 °C and 24h thawing at +20 °C). These temperatures and time-span were calculated in order to completely freeze and thaw the water within the sample, aiming at creating an accelerated F-T process and they find resonance in recently published papers (Ding et al., 2020; Ren & Vanapalli, 2019; Yao et al., 2020).

The method used to subject the samples to F-T is known as closed-system and it differs from an open-system, as in the latter, the sample has access to a water source throughout the freezing process. The closed-system method with three-dimensional freezing was adopted due to the practicality it offers in comparison with an open-system with uniaxial freezing imposition, which would require a distinct experimental setup. The issue revolves about preparing a smaller recompacted sample, suitable to be tested in the SWC apparatus, and yet providing access to a water source while imposing freezing uniaxially during F-T cycles.

Even though the closed-system could be seen as a simplification from field conditions, for soils with lower permeability (as low as a $k \ll 1x10^{-7} cm/s$), the frost penetration rate is often greater than the rate in which water reaches the freezing front, thus having access to water would be indifferent in this case, as the water source would freeze as well and the moisture movement to the freezing front would be restricted (see Wong & Haug, 1991). Furthermore, as material heterogeneity is expected in naturally occurring materials as subgrades, both closed-system and open-system can be seen as representations that may be expected to a certain extent in the field (Wong & Haug, 1991).

Hence, due to the nature of materials used in this study and the sampling setup, a closed-system with triaxial F-T was considered adequate to acquire a better understanding of possible effects of F-T to material's properties.

Before being tested in the SWC device, as shown in *Figure 1,* the samples were saturated at least overnight after being subjected to closed-system F-T cycles. A sample is shown in *Figure 3d*, where it is resting on top of a porous stone to regulate the flow of water and with a filter paper separating them to avoid material loss. The SWRC was determined as per ASTM D6836-16 (ASTM, 2016).

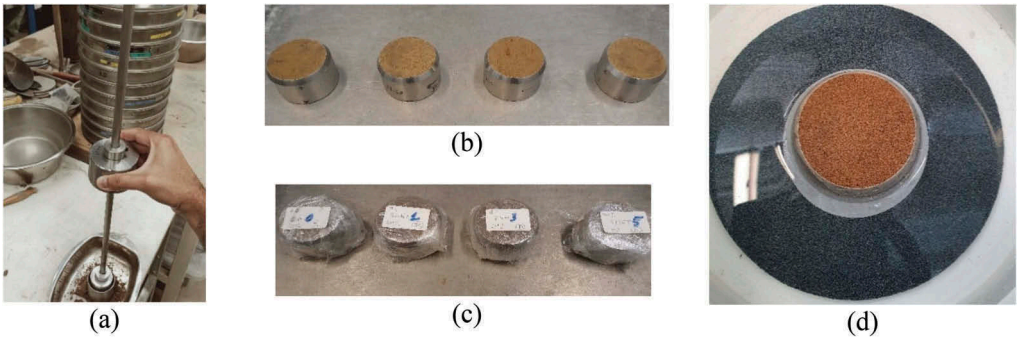

Figure 3. Sample preparation. a) Rammer compactor for small samples b) compacted samples at maximum optimum content c) conditioned samples for freeze and thaw cycles, from 0 to 5 cycles (NFT0 to NFT5) d) saturation process, before the sample is subjected to desorption in the SWC-150.

2.3 *SWRC modelling*

There are many available models to fit experimental data into continuous functions to describe the suction and water content relationship. Two of the most used ones were used in this study: the Van Genuchten 1980 (4) and the Fredlund and Xing 1994 (5). A third equation is presented by Brooks and Corey 1964 (3) and it was tested due to its ability to represent sharp air entry values (McCartney, 2007), observed in the SM with 17% fines.

$$\text{Brooks and Corey (1964)}\ \theta(\psi) = \theta_r + (\theta_s - \theta_r).(\psi/\psi_{AEV})^{-\lambda_{BC}} \tag{3}$$

$$\text{Van Genuchten (1980)}\ \theta(\psi) = \theta_r + (\theta_s - \theta_r).\left[1 + (\alpha.\psi)^N\right]^{-\left(1-\frac{1}{N}\right)} \tag{4}$$

$$\text{Fredlung Xing (1994)}\ \theta(\psi) = C(\psi).\left\{\theta_s/\left[ln\left(e + \left(\psi/a_f\right)^{n_f}\right]^{m_f}\right\}\right. \tag{5}$$

$$C(\psi) = 1 - ln[1 + (\psi/\psi_r)]/ln\left[1 + \left(10^6/\psi_r\right)\right] \tag{6}$$

Where for Brooks and Corey, ψ is the matric suction, θ_s is the saturated volumetric water content, θ_r is the residual volumetric water content, and λ_{BC} is a fitting parameter. For the Van Genuchten model, the first part is similar to the previous model, but instead of a power-law function, a hyperbolic function is introduced, where α is related to the inverse of the Air Entry Value (AEV) and N is a dimensionless fitting parameter. Finally, for Fredlund and Xing model, a_f is related to the AEV, n_f is related to the pore-size distribution (McCartney, 2007) and is a rate of desorption after the AEV (Zapata, 2018), whereas m_f is related to the residual water content (Zapata, 2018) and represents the model skew (McCartney, 2007).

Statistical analysis was used to assess the model fits of the data. The analysis was based on the sum of squares of errors (SSE) resulting from the difference between the measured and curve fitted results. Table 2 shows that Fredlund and Xing demonstrate good agreement with the measured data, except for one of the tests, which Van Genuchten described better (NFT5). It is worth mentioning that the correlation coefficient (R^2) shows a strong relationship between the model parameters and the calculated result for all models. For comparison and repeatability, the Fredlund and Xing 1994 model was adopted to perform the subsequent analysis.

Table 2. Curve fitting statistics for the silty sand with 17% fines.

	NFT0		NFT1		NFT3		NFT5	
Model	SSE	R^2	SSE	R^2	SSE	R^2	SSE	R^2
Fredlund & Xing	**1,968**	**0,996**	**1,827**	**0,997**	**0,767**	**0,999**	5,790	0,989
Van Genuchten	35,928	0,930	32,120	0,944	25,203	0,955	**4,495**	**0,992**
Brooks & Corey	43,651	0,890	36,498	0,922	46,561	0,899	35,520	0,916

3 ANALYSIS AND DICUSSION

Tests in the SM material with 17% fines (*Figure 4*) showed that the AEV was not particularly influenced by the F-T cycles, with the a_f ranging from 7,16 kPa for 0 F-T to 6,91 kPa for 5 F-T; but increasing and decreasing in the interval. On the other hand, the rate of desorption once the AEV was reached, n_f, changed significantly, decreasing from 36,53 to 9,75 in the same comparison. The fitting parameter m_f increased from 0,18 to 0,41 and it can be seen that it is proportionally inverse to the residual water content. Thus, the higher the m_f, the lower the residual water content. Finally, the residual suction decreased from 80 kPa to 30 kPa in 5 cycles of F-T. These results suggest some shift in the unsaturated behaviour of this material, where the same water content yielded less suction with the increase of the number of F-T cycles.

Figure 5 presents the results for the material with 39% fines. The a_f results suggest an increasing trend in the AEV, ranging from 12,95 kPa to 15,07 kPa from 0 to 5 F-T cycles, respectively. The desorption rate n_f increased from 4,51 to 25,50, and the residual water parameter m_f ranged from 0,21 to 0,19; whereas the residual suction decreased from 750 kPa to 150 kPa in 5 F-T cycles. A similar conclusion can be made in comparison to the other soil, that less suction is yielded with the same water content as F-T cycles increases, although the results show a sharper contrast from the first cycle of F-T, in line with previous studies.

The increased AEV may find resonance in the frost penetration theory depicted in Stefan solution (1), where the frost depth increases with falling air temperatures during winter, meaning the pore water starts to freeze from closer to the surface downwards, consequently reducing the availability of unfrozen water. One of the effects is an overall reduction in pore size, which increases the AEV (Noh et al., 2012); and the other is that the menisci between pore water and grain particles are more tensioned, yielding more suction and possibly attracting more water to the freezing front.

Such effect could change the balance in the vadose zone, shown in *Figure 6*, and the water in the capillary fringe – corresponding to the region below the AEV – could be pulled upwards. In other words, ψ_{AEV} can be different among unfrozen and frozen soils of the same type, bulk density and initial water content (Noh et al., 2012; Ren and Vanapalli, 2019).

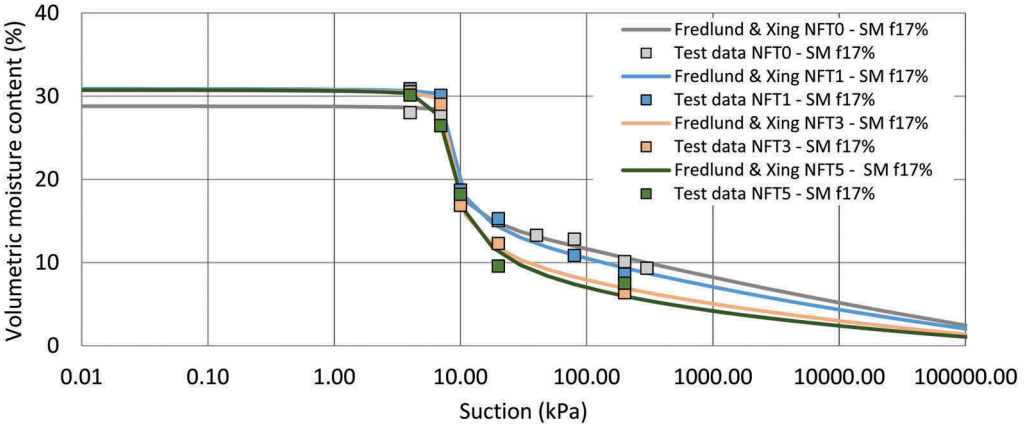

Figure 4. SWRC for silty sand with 17% fines, compacted to 95% modified Proctor energy.

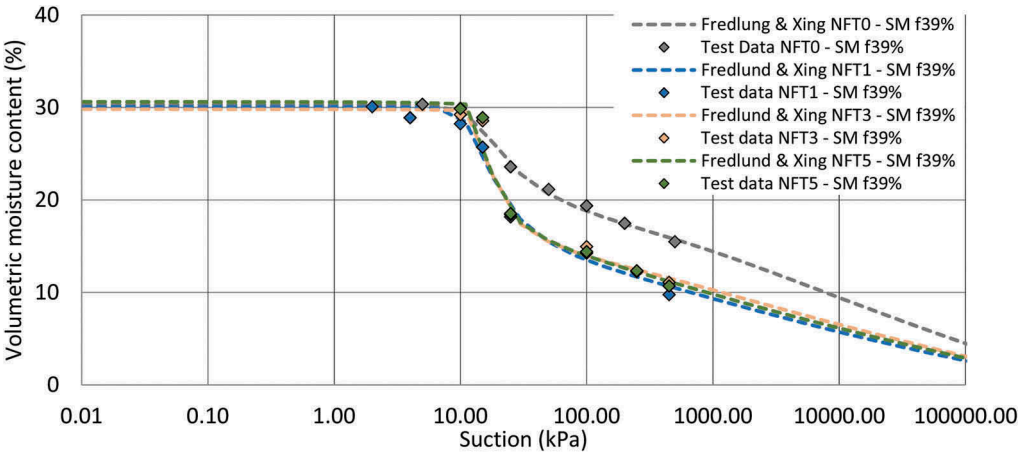

Figure 5. SWRC for a silty sand with 40% fines, compacted to 95% modified Proctor energy.

Table 3. Model parameters using Fredlund & Xing SWCC curve fitting model.

F-T cycles | soil	ψ_r (kPa)	a_f (kPa)	n_f (-)	m_f (-)	SSE (-)	R^2 (-)
0 F-T | SM *f=17%*	80	7,16	36,53	0,18	1,97	0,996
1 F-T | SM *f=17%*	47	7,42	25,90	0,23	1,83	0,997
3 F-T | SM *f=17%*	47	7,29	19,10	0,32	0,77	0,999
5 F-T | SM *f=17%*	30	6,91	9,75	0,41	5,79	0,989
0 F-T | SM *f=39%*	750	12,95	4,51	0,21	0,83	0,996
1 F-T | SM *f=39%*	450	12,18	5,76	0,31	5,32	0,990
3 F-T | SM *f=39%*	350	15,16	22,67	0,19	1,51	0,996
5 F-T | SM *f=39%*	150	15,07	25,50	0,19	0,75	0,998

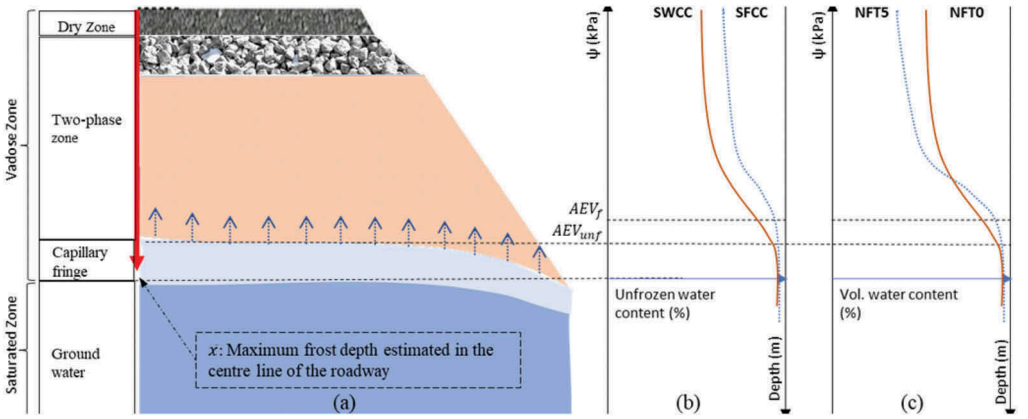

Figure 6. A) Vadose zone below a pavement structure b) idealised suction and unfrozen water content relationship from cryo-SWCC and SFCC studies c) idealised SWRCs representing data compiled in the present study.

Cryo-SWCC (Noh et al., 2012) and Soil-Freezing Characteristic Curve (SFCC) (Ren and Vanapalli, 2019) studies suggest the increase in AEV (*Figure 6b)* when comparing a single thawing sample with an unfrozen sample, but no permanent change is discussed. In the current study, SWRC model parameters were obtained from samples tested at room temperature after being subjected to F-T cycles, and they show a trend for WRC reduction. *Figure 6c* shows idealised SWRCs based on the data compiled in the study, and they differ from *Figure 6b* in the sense that they suggest a permanent shift in the SWRC post F-T cycles.

4 CONCLUSION

The studies on F-T of subgrades are needed to better understand the impacts on their mechanical characteristics. The results from the current study are limited to two silty sands with low plasticity; and the results conclude that 1) there is a reduction in WRC with increasing number of F-T cycles; 2) the contrast between the null sample (NFT0) and the other is higher with increased fines content.

More pronounced results would be expected if the samples had access to water during the cycles of freeze and thaw because then the freezing and thawing would be coupled with drying and wetting cycles. In addition, if freezing were imposed uniaxially, it would generally cause water movement to the freezing front, which creates a non-uniform degree of compaction within a sample (Wong and Haug, 1991). However, as this study was conducted imposing freezing triaxially, it is not expected significant water movement, thus no ice segregation, but rather ice crystals formation within particle's pores.

Other than its own properties, as the SWRC, a subgrade will likely be affected by F-T cycles by different degrees according to the layers' thicknesses above it and their thermal conductivity, not to mention water availability within the system. It is out of the scope of the present study to verify all those implications. It does, however, exemplify that there are many nuances for how freezing is imposed in the field, and in the present study, given the sample's size (32mm), triaxial freezing was considered adequate.

Previous studies suggest that the effects of F-T cycles stabilise between 6 and 7 cycles, but due to time constraints, the number of samples was limited. In future studies, it will be aimed to increase the number of samples to verify such stabilisation effect. Furthermore, the present study established a difference in how much suction is yielded in samples with the same water content for a different number of F-T cycles, and as suction changes the stress state of the soil, it impacts the resilient modulus (Doré and Zubeck, 2009). The result from the current study merits a further investigation to assess the extension of the impact in the Mr. including a setup to allow uniaxial freezing and thawing of samples in an open-system.

ACKNOWLEDGMENT

This work was sponsored by the Swedish Transport Administration (Trafikverket).

REFERENCES

Andersland, O. B., & Ladanyi, B. (2004). *Frozen ground engineering* (2nd ed). Wiley;ASCE.

ASTM. (2016). *Test Methods for Determination of the Soil Water Characteristic Curve for Desorption Using Hanging Column, Pressure Extractor, Chilled Mirror Hygrometer, or Centrifuge* (No. D6836-16). ASTM International. https://doi.org/10.1520/D6836-16

Briaud, J.-L. (2013). *Geotechnical Engineering: Unsaturated and Saturated Soils*. Somerset: John Wiley & Sons, Incorporated.

Christopher, B. R., Schwartz, C., & Boudreau, R. (2006). *Geotechnical aspects of pavements*. FHWA. https://www.fhwa.dot.gov/engineering/geotech/pubs/05037/

Ding, L., Han, Z., Zou, W., & Wang, X. (2020). Characterizing hydro-mechanical behaviours of compacted subgrade soils considering effects of freeze-thaw cycles. *Transportation Geotechnics*, *24*, 100392. https://doi.org/10.1016/j.trgeo.2020.100392

Doré, G., & Zubeck, H. K. (2009). *Cold regions pavement engineering*. ASCE Press;McGraw-Hill.
Erlingsson, S., Baltzer, S., Baena, J., & Bjarnason, G. (2009). Measurement techniques for water flow. In A. Dawson (Ed.), *Water in road structures* (pp. 45–67). Springer.
Fredlund, D. G. (2019). State of practice for use of the soil-water characteristic curve (SWCC) in geotechnical engineering. *Canadian Geotechnical Journal*, *56*(8), 1059–1069. https://doi.org/10.1139/cgj-2018-0434
Fredlund, D. G., Rahardjo, H., & Fredlund, M. D. (2012). *Unsaturated soil mechanics in engineering practice*. John Wiley & Sons, Inc.
Kuttah, D. (2020). *Development of a simple field method for measuring permanent deformations in silty sand subgrade* (VTI rapport 1086A; p. 46). VTI. http://vti.diva-portal.org/smash/record.jsf?pid=diva2%3A1557654&dswid=6775
Marinho, F. A. M., Take, W. A., & Tarantino, A. (2008). Measurement of Matric Suction Using Tensiometric and Axis Translation Techniques. *Geotechnical and Geological Engineering*, *26*(6), 615–631. https://doi.org/10.1007/s10706-008-9201-8
McCartney, J. S. (2007). *Determination of the hydraulic characteristics of unsaturated soils using a centrifuge permeameter* [PhD Thesis, The University of Texas at Austin]. http://citeseerx.ist.psu.edu/viewdoc/download?doi=10.1.1.822.6593&rep=rep1&type=pdf
Noh, J.-H., Lee, S.-R., & Park, H. (2012). Prediction of Cryo-SWCC during Freezing Based on Pore-Size Distribution. *International Journal of Geomechanics*, *12*(4), 428–438. https://doi.org/10.1061/(ASCE)GM.1943-5622.0000134
Ren, J., & Vanapalli, S. K. (2019). Comparison of Soil-Freezing and Soil-Water Characteristic Curves of Two Canadian Soils. *Vadose Zone Journal*, *18*(1), 1–14. https://doi.org/10.2136/vzj2018.10.0185
Walshire, L., Taylor, O.-D., & Berry, W. (2019). *Laboratory measure of SWCC for a poorly graded fine sand*. Engineer Research and Development Center (U.S.). https://doi.org/10.21079/11681/33676
Wong, L. C., & Haug, M. D. (1991). Cyclical closed-system freeze–thaw permeability testing of soil liner and cover materials. *Canadian Geotechnical Journal*, *28*(6), 784–793. https://doi.org/10.1139/t91-095
Yao, Y., Luo, S., Qian, J., Li, J., & Xiao, H. (2020). Soil-Water Characteristics of the Low Liquid Limit Silt considering Compaction and Freeze-Thaw Action. *Advances in Civil Engineering*, *2020*, 1–13. https://doi.org/10.1155/2020/8823666
Zapata, C. E. (2018). Empirical Approach for the Use of Unsaturated Soil Mechanics in Pavement Design. *PanAm Unsaturated Soils 2017*, 149–173. https://doi.org/10.1061/9780784481677.008

Drainage and environmental effects

Eleventh International Conference on the Bearing Capacity of Roads, Railways and Airfields, Volume 2 – Hoff, Mork & Saba (eds)

New expressions for waterflow in coarse road and rail track materials

I. Campos-Guereta, A. Dawson & N. Thom
Nottingham Transportation Engineering Centre, Faculty of Engineering, The University of Nottingham, Nottingham, UK

ABSTRACT: Water has a major influence on the mechanical response of geomaterials and hence on the roads, railways or taxiways built on them. Water flow is usually modelled by solving the Richards equation with appropriate hydraulic conductivity functions and water retention curves for the soil. When materials are unsaturated, this approach means that water flow will be based on capillary concepts. In finer materials this is a good approach, but for coarser, open-graded, materials such as some granular road bases, some sub-bases and railway ballast, gravity forces have a significant influence on the pore water distribution and a notable impact on water flow, while the capillary term is much less significant. In order to get a general expression for both coarse and fine materials new formulations for the hydraulic properties and for the Richards equation are presented and discussed. A new expression for the unsaturated hydraulic conductivity is suggested, dividing the capillary term and the gravity term and including them in a slightly modified form into the Richards equation. The new expression is applied to an existing physical model for the unsaturated waterflow on coarse glass beads. The results are compared and discussed.

Keywords: Coarse aggregates, unsaturated, Richards equation, waterflow, gravels, ballast, drainage

1 INTRODUCTION

Waterflow, pore pressures and water content are variables of major importance in soil mechanics. A general soil is in a variable saturation state, so it can be fully saturated, dry or semi-saturated. Most of existing literature relating to unsaturated soils refers to sand gradations and smaller, but few references exist that apply to coarse materials.

Expressions to solve unsaturated waterflow are usually founded on assumptions that are only applicable to finer soils. Thus, when applied to coarser materials these formulations start to be without a sound logical derivation and inapplicable.

The most frequently applied equation to solve variably saturated waterflow on soils is the Richards' Equation (Richards 1931), it states that the rate at with the water content changes in a differential volume of soil is equal to the waterflow entering and leaving the boundaries of that volume, with the waterflow being calculated by the Darcy equation. The mixed form for the Richards equation is given by Eq. (1), where θ is the volumetric water content, h the piezometric pressure, z the vertical coordinate, and $\overline{\overline{K}}$ the permeability tensor [L·T-1].

$$\frac{d\theta}{dt} = \overline{\nabla} \cdot \left(\overline{\overline{K}}(h) \cdot \overline{\nabla}(\mathrm{h} + \mathrm{z}) \right) \tag{1}$$

DOI: 10.1201/9781003222897-11

The piezometric pressure is, in part, dependent on the suction in the soil. So, to solve the mixed form of the Richards' Equation, the relationship between the volumetric water content and suction is needed, and it is defined by the soil water retention curve (SWRC) which gives the volumetric water content for each known suction in the soil $\theta(h)$, which is considered as a constitutive property of the soil. SWRCs are usually expressed in term of some algebraic expressions depending on a certain number of parameters determined empirically (Campos-Guereta, Dawson, and Thom 2021; Brooks and Corey 1964; van Genuchten 1980).

Permeability is usually defined in terms of the permeability of the soil when it is saturated, multiplied by a relative permeability when it is partially saturated: $k(h) = k_{sat} \cdot k_r(h)$. The value of the relative permeability is usually estimated from the selected water retention curve by the method proposed by Mualem (1976). Mualem assumed a capillary approach in which the soil pores could be simplified by a distribution of cylindrical tubes, with a pore size distribution that could be estimated from the water retention curve by applying the capillary rise equation of Young-Laplace. From the pore size distribution, he estimated the probability that two pores of different diameter were connected. With the permeability assigned to each of those pairs he was able to estimate the relative permeability of the soil establishing that the first pores to be completely filled in a capillary flow were the smaller ones, coarser ones becoming progressively filled as the degree of saturation increased. The final relative permeability was the expected value for the pair's permeability at a given pore diameter divided by the total expected permeability involving all possible pairs of diameters in the soil for the whole pore size distribution. This value was multiplied by a tortuosity factor that he assumed to be a power of the relative saturation of the soil, obtaining Eq.2 for the relative permeability, where S_r is the relative saturation, F_{V_p} the cumulative pore size distribution, r_p the pore radius and $r_p(S_r)$ is the inverse of the pore size distribution. Mualem (1976) noticed that the best fit for the exponent '*l*' was ½.

$$K_r(S_r) = S_r^l \left[\frac{\int_{r_{p,min}}^{r_p} r_p \cdot \frac{dF_{V_p}}{dr} dr_p}{\int_{r_{p,min}}^{r_{p,max}} r_p \cdot \frac{dF_{V_p}}{dr_p} dr_p} \right]^2 = S_r^l \left[\frac{\int_0^{S_r} r_p(S_r) dSr}{\int_0^1 r_p\ (\mathrm{S_r}) dSr} \right]^2 \tag{2}$$

2 CHARACTERISTICS OF UNSATURATED FLOW IN COARSE MATERIALS

A usual way to calculate the variably saturated water-flow is to solve Richards' Eq. (1) by using Eq. (2) and using an algebraic expression of the water retention curve of the soil like the one given by van Genuchten (1980), fitted to a physical or empirical estimation of the curve as in the method proposed by Campos-Guereta, Dawson, and Thom (2021).

This approach implies that a soil with a relative saturation $S_r = 0$ begins with a residual water content θ_{res}, with this residual water content distributed in the soil in the form of pendular rings between grains and also in the form of pores fully saturated but with no connection to the external boundary so that they cannot be drained. Also the presence of residual water content in a very thin layer adhered to the grain surface is present but its thickness is of only some Angstroms (Dullien 1991). When a soil having a residual water content is progressively wetted, the assumption is that the first pores to be filled will be the smallest which, when completely filled, will then permit saturation of the next coarser ones.

This approach implies the following assumptions, first: there is a water connection between all pores making possible the water to fill the smaller pores, and second: the pores, when filled are fully filled before the next coarser one is filled.

For the first assumption to be valid the pendular rings have to be connected between each other so the water can go from (unsaturated) coarser pores to smaller pores, or it's necessary to assume that the adhesion layer has a big enough conductivity to be able to achieve a fast transport of water between pores or wait a long time for an equilibrium to be reached with vapor pressure in all pores.

For the second assumption, for the pore to be able to be fully filled, the water weight in the pore body must be supported by the tension of water in the pore-throat.

For fine materials, these two assumptions are almost certainly valid as the weight of water in the pendular rings and on the pore-bodies is very small when compared with the forces of the water tension supporting the pendular rings and the volume of water in the pore bodies; but, for uniform coarse aggregates (e.g. ballast or rockfills) they are untenable.

3 LIMITATION FOR THE PORES TO BE FULLY FILLED

In the following explanation a uniform coarse aggregate will be simplified to nearly spherical shapes of the grains. The aggregate will have a porosity that will depend on the energy of compaction. The minimum packing density will be given by a cubic packing (packing density of $\pi/6$) and a maximum packing given by a tetrahedral close packing (packing density of $\pi/\sqrt{18}$), and usually near to a random packing (packing density around 0.56).

The final arrangement of spheres could be considered as a mix of cubic packings and tetrahedral packings, where the pore bodies can be of the form given the sphere pack or a tetrahedral pack (Figure 1).

Figure 1. Cubic packing (left) showing pore volume (right).

In a cubic packing the volume of the pore, $V_{p,cub}$, is calculated by Eq. (3) as the difference of the volume of a cube with side $2 \cdot r_g$ and a sphere of radius r_g.

$$V_{p.cub} = \frac{4(6-\pi)}{3} r_g^3 \tag{3}$$

The weight of water inside the pore body must be supported by the surface tension in the top pore throat and the surface tension in the bottom pore throat (Figure 2). The force is equal to the breakthrough force in the pore throat. The pore throat may be simplified to an inscribed circle in section, with a pore radius of $r_{p.cub}$ as given by Eq. (4) (see the arrowed line in the left parts of Figure 2):

$$\left(r_g + r_{p.cub}\right)^2 = 2r_g^2 \rightarrow r_{p,cub} = \left(\sqrt{2} - 1\right) r_g \tag{4}$$

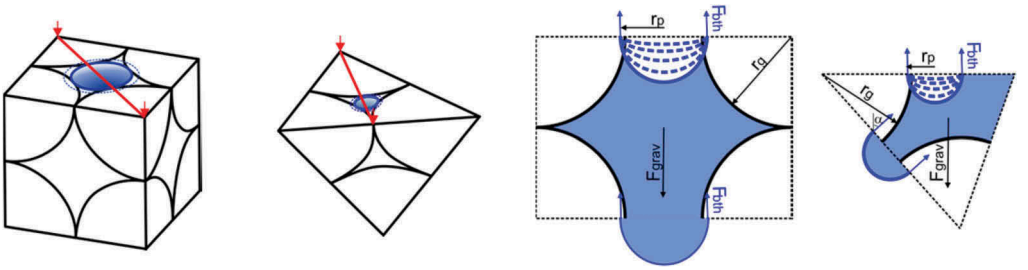

Figure 2. Equilibrium of capillary and gravity forces on a single water filled pore.

The breakthrough force, F_{bth}, supporting the pore body volume will be given by the maximum surface tension at the perimeter of the inscribed circle (Eq. (5)) where τ is the surface tension of water and θ the water-grain contact angle.

$$\mathrm{F_{bth.cub}} = 2\pi \mathrm{r_{p.cub}} \tau \cos\theta = 2\left(\sqrt{2}-1\right)\pi \mathrm{r_g} \tau \cos\theta \tag{5}$$

The maximum grain size at which pores fully-filled with water will self support in a single pore body will be then the equilibrium of the two breakthrough force (one on the top section and one in the bottom section) and the water weight in the pore body, Eq. (6):

$$2 \cdot \mathrm{F_{bth.cub}} = \mathrm{F_{grav}} = \rho_{\mathrm{w}} \mathrm{g}\ \mathrm{V_{p.cub}} \rightarrow \rho \mathrm{g} \frac{4(6-\pi)}{3} \mathrm{r_g^3} = \ 4\left(\sqrt{2}-1\right)\pi \mathrm{r_g} \tau \cos\theta \tag{6}$$

Considering the properties of the water: density = $\rho_w = 1000 kg/m^3$, $\tau = 0.072 N/m$, $\theta = 0$ and $g = 9.81 m/s^2$, the maximum grain radius to support water in the pore is $\boldsymbol{r_g = 3.16 mm}$.

In the case of a tetrahedral packing, the pore radius on breakthrough, $r_{p.tetr}$, is defined by a triangle with 3 circles on each vertex, and the inscribed breakthrough circumference is (see arrowed line in left parts of Figure 2):

$$r_{p.tetr} = \frac{2}{3}\sqrt{(2r_g)^2 - r_g^2} = \left(\frac{2}{\sqrt{3}} - 1\right) r_g \tag{7}$$

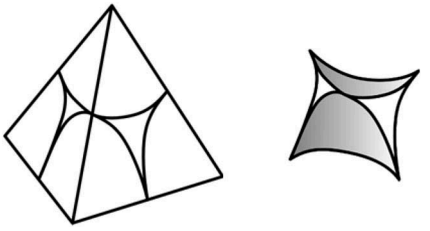

Figure 3. Tetrahedral packing (left) showing pore volume (right).

The volume of the pore body in a tetrahedra with sides $2r_g$, $V_{p.tetra}$, will be equal to the volume of the tetrahedra minus the volume of $1/6^{\mathrm{th}}$ of the sphere of radius r_g.

$$V_{p.tetra} = \frac{(2r_g)^3}{6\sqrt{2}} - \frac{\frac{4}{3}\pi r_g^3}{6} = \frac{2}{9}\left(3\sqrt{2} - \pi\right) r_g^3 \tag{8}$$

In a tetrahedra the base will have a vertical breakthrough supporting force but the other 3 faces will have a force with an angle of $\alpha_{tetra} = \mathrm{acos}1/3$. The maximum grain size that supports the water in the pore body will be approximately equal in this case to the equilibrium between the breakthrough forces and the water weight in the pore:

$$3\ F_{bth.tetr} \cos\alpha_{tetra} + F_{bth.tetr} = V_{p.tetra} \rightarrow r_g = \frac{3\sqrt{\frac{(4\sqrt{3}-6)\pi}{9\sqrt{2}-3\pi}}\sqrt{\tau \mathrm{Cos}[\theta]}}{\sqrt{g\rho}} \tag{9}$$

Considering the properties of the water as before, the maximum grain radius to support water in the pore is $\boldsymbol{r_g = 7.63 mm.}$ Therefore, for grains radius over 7mm we can assume that

the pores would only be partially filled in an unsaturated waterflow, and capillary flow would be negligible as there should not be interconnected pores that need to be filled.

4 LIMITATION FOR STABLE PENDULAR RINGS

In the same way, assuming two spherical particles, when the soil is totally dry and begins to wet, pendular rings start to appear at particle contacts in which the surface tension forces in the contact grain-water will be in equilibrium with the capillary pressure, ΔP, that is going to be dependent on the curvature of the liquid by the Youngs-Laplace equation, where r_{c1} and r_{c2} are the curvature radii at one point of the pendular ring between the two spheres:

$$\Delta P = \tau\left(-\frac{1}{r_{c1}} + \frac{1}{r_{c2}}\right) \tag{10}$$

In common soils with small grain sizes, where the gravity forces can be neglected, the curvatures $1/r_{c1}$ and $1/r_{c2}$ are assumed to be constant, and therefore the shape of the pendular rings are trivial. However, when gravity forces take part, then the pressure varies with height so that the curvature will change with height, and in that case Eq. (10) needs to be replaced by a differential equation.

Heris, Hamed Mosavian, and White (2009) analyzed the shape of the pendular rings with a maximum volume subjected to gravity forces between a couple of vertical spheres. They assumed that the value of r_{c1} could be assumed constant but that r_{c2} will change with height. In this way they obtained the solution for the shape of the pendular rings given by Eq. (11).

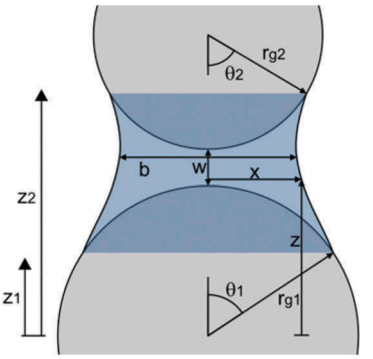

Figure 4. Liquid bridge between two particles vertically aligned (Heris, Hamed Mosavian, and White 2009).

$$X - X_1 = \int_{Z_1}^{Z_2} \frac{dY}{\sqrt{\frac{1}{\left(\frac{\alpha}{2}(Z-Z_1)^2+\beta(Z-Z_1)-\cos\theta_1\right)^2}-1}} \qquad \begin{aligned} R_g &= \tfrac{r_{g2}}{r_{g1}} \\ X_1 &= \sin\theta_1 \\ X_2 &= R_g\sin\theta_2 \\ Z_1 &= \cos\theta_1 \end{aligned} \qquad \begin{aligned} Z_2 &= R_g(1-\cos\theta_2) + W + 1 \\ W &= \tfrac{w}{r_{g1}} \\ \alpha &= \tfrac{(\rho-\rho_a)gr_{g1}^2}{\tau} = \tfrac{N_{cap}}{4} \\ \beta &= \tfrac{r_{g1}}{r_{c1}} + \tfrac{\Delta P_0 r_{g1}}{\tau} \end{aligned} \tag{11}$$

For two spheres of the same size both in touch one to another, Heris, Hamed Mosavian, and White (2009) solved Eq. (11) for the maximum water content of the pendular rings in the case of two particles of the same grain size in contact. They evaluated the main parameters in Figure 4 and fitted to equations in Table 1.

Table 1. Parameters in Figure 3 for spheres of same radius, r_g, in contact (Heris, Hamed Mosavian, and White 2009).

$\theta_1 = a + \left(\frac{b}{1+\left(\frac{N_{cap}}{c}\right)^d}\right)$	$a = 0.43495617$ $b = 2.6853361$ $c = 5.252405$ $d = 0.7621725$	$\theta_2 = a + \left(\frac{b}{1+\left(\frac{N_{cap}}{c}\right)^d}\right)$	$a = 0.30992848$ $b = 2.8383259$ $c = 1.2548094$ $d = 0.58595614$

Considering a uniformly graded coarse soil with sphere particles, the spheres will be arranged in a mixture of cubic and tetrahedral packings. For cubic packings, in order to get a capillary flow, the pendular rings need to be stable and in contact so the water can flow from higher pressure head to lower pressure head. To be in contact, the stable pendular ring in its maximum capacity showed in Figure 4 must have angles θ_1 and θ_2 higher than 45°, and with the densest packing (tetrahedral packing) the angle need to be higher than 30º.

By applying the expressions in Table 1, the angles θ_1 and θ_2 for the maximum volume of the liquid bridges are given by Figure 5 for different grain sizes. Therefore, for a cubic packing the grain size to get $\theta_1 = 45°$ is **2.16cm** and to get $\theta_2 = 45°$ it is **1.20cm**; for a tetrahedral packing the grain radius to get $\theta_1 = 30°$ is **5.70cm** and to get $\theta_2 = 30°$ is **2.60cm**. In this way, when the soil is near the residual water content, full capillary flow is possible when soil particles radii are below 2.1cm, and partially possible when below **5.7cm**.

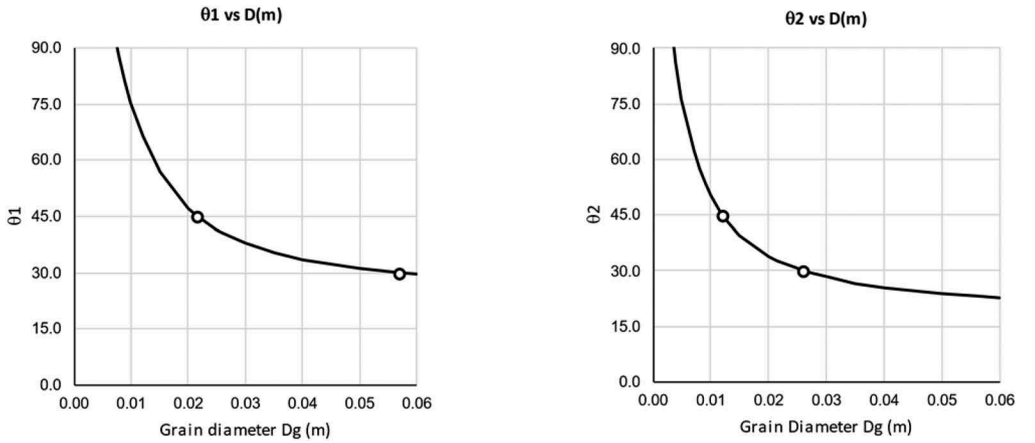

Figure 5. Angles $\theta_1$and θ_2 for the maximum water content in a liquid bridge of two particles of the same size in contact. Points represent values for angles 45º and 30º for cubic and tetrahedral packings respectively.

5 WATER FLOW ON COARSE MATERIALS

The general conclusion of Section 3 and 4 is that a coarse soil with a loose packing and a grain radius of about 3mm won't be able to retain water on the pore bodies and by the action of gravity, the water will drain. In the case of a soil with maximum packing, this will happen for a grain radius of about 7.5mm. This effect can also happen in a soil with smaller grains (if the same analysis is performed but considering not only one pore filled by water but several, then the weight of water to be supported increases (F_{grav}) while the supporting capillary forces increase less (F_{bth})). The pore body won't be fully filled by water but partially saturated and the water will be retained in pendular rings in a residual state after the waterflow. The amount of water retained in coarse soils means that the water in the form of pendular rings won't be connected with each other for a grain radius of 1.2cm for loose packings and for grain radius of 2.1cm for highly compacted soils. All of that assuming spherical shapes of the grains.

Therefore, it can be expected that a coarse soil's waterflow will behave in a different manner from that in finer soils of sand size. For soils of grain radius over 2.1cm, no capillary flow should be expected through the soil voids.

The hydraulic properties of finer soils will usually have a water retention curve in which the soil can be in a partially saturated state where the amount will depend on the value of the pore pressure. There will be a residual saturation that will depend on the volume of water contained within those pendular rings and also will depend on the water content of the pore bodies that are not hydraulically connected to soil boundaries. With water content over this residual water content, water will be redistributed, depending on the pressure head, by a capillary flow.

If a coarse material is subjected to a water flow, without the possibility of a capillary flow, the water will tend to fill the pendular rings and the pore bodies but, as concluded in Sections 3 and 4, by the action of gravity, the water will tend to drain downwards to fill lower pore bodies and pendular rings.

Many physical predictions of permeability are based on the capillary approach (Childs and Collis-George 1950). Probably the most commonly-applied expression to estimate the saturated permeability, based on the abstraction of the soil by a bundle of pore tubes, is the Kozeny-Carman Equation (Kozeny 1927; Carman 1938, 1956), and a popular expression to estimate the relative permeability is due to Mualem (1976). Mualem built a relationship for relative permeability considering a probabilistic distribution of each pair of pores in contact, assuming that the permeability of the pair was equal to the permeability of smaller pore (Eq (2)).

In his analysis, Mualem considered that there was a capillary flow in the soil, so the water in each pore tube, will flow to the smaller pores until filled, as the suction in smaller pores is higher than in the larger ones. So the permeability is computed considering sufficient of the smaller pores to be totally filled to match the relative saturation of the soil, until all the flow is done in a fully saturated soil when all the pores are filled.

Considering a uniform soil where its pore size distribution could be simplified to a line in a log plot of the pore size distribution, with a minimum pore size $R_{p.min}$ and a maximum pore size $R_{p.min}$, then the pore size distribution is given by:

$$r_p[\mathrm{S}_r] = \left(\frac{R_{p.max}}{R_{p.min}}\right)^{S_r} \tag{12}$$

Then, including Eq. (12) into Eq. (2), the relative permeability will be:

$$k_r(S_r) = \frac{\left(\left(\frac{R_{p.max}}{R_{p.min}}\right)^{S_r} - 1\right)^2 R_{p.min}^2 S_r^{\,1}}{\left(R_{p.max} - R_{p.min}\right)^2} \tag{13}$$

If, also, a uniform distribution of pores is considered ($R_{p.max} \approx R_{p.min}$), then:

$$\lim_{R_{p.\max} \to R_{p.\min}} k_r(S_r) = S_r^{2+l} \tag{14}$$

Therefore, the permeability in a soil with a uniform distribution of pores, and considering the Mualem (1976) expression to estimate the relative permeability is given by:

$$k(S_r) = k_{sat} S_r^{2+l} \tag{15}$$

However, Eq. (15) assumes that the permeability is calculated considering that each of the increasingly saturated pores are fully filled by water. But, it has already been demonstrated that, in a coarse soil, the water inside a pore void is not able to be supported by capillary forces, therefore it is not strange to make an hypothesis that (if we consider a coarse material having uniform pore sizes) under a waterflow in the vadose zone, the pores can be considered

partially saturated when the water is flowing, as it has been stated that the full saturation of the pore is not stable under gravity forces. The same approach done by several capillary based theories can be taken in this case, assuming that the pores have a cylindrical shape with diameters equal to the pore diameters. In this case, we will assume that the water flows on the grain surfaces, therefore if a cylindrical tube is assumed, then the water will flow on the cylindrical walls. In a first approach, a vertical tube will be assumed as indicated in Figure 6.

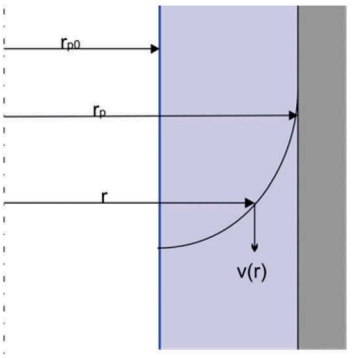

Figure 6. Water flow in a partially saturated cylindrical pore tube in a coarse material.

Considering a cylindrical symmetry and considering a section at radius coordinate r, the shear stress at r,Eq. (16) (left), will be equal to the weight of the falling liquid (at a radius below r) Eq. (16) (right).

$$\tau_1(r) = \mu \frac{\mathrm{d}v(r)}{dr};\ \tau_2(r) = \frac{\rho g \pi \left(r^2 - {r_{p0}}^2\right) h}{2\pi r h} \tag{16}$$

The equality between the two previous equations leads to an ordinary differential equation whose solution is Eq. (17).

$$v\left(r, \mathrm{r_{p0}}, r_p\right) = \int_r^{r_p} \tau_2(r)/\mu \ \mathrm{d}r = -\frac{g\rho\left(r^2 - r_p^2 + 2\ r_{p0}^2 \ln\frac{r_p}{r}\right)}{4\mu} \tag{17}$$

And the mean velocity:

$$\bar{v}\left(r_{p0}, r_p\right) = \frac{\int_{r_{p0}}^{r_p} 2\ \pi\ r \mathrm{v}\, \mathrm{d}\, r}{\int_{r_{p0}}^{r_p} 2\ \pi\ r\, \mathrm{d}\, r} = \frac{g\rho\left(r_p^4 - 4 r_p^2 r_{p0}^2 + 3\ r_{p0}^4 + 4\ r_{p0}^4 \ln\frac{r_p}{r_{p0}}\right)}{8\left(r_p^2 - r_{p0}^2\right)\mu} \tag{18}$$

The relative saturation S_r is equal to the volume of water divided by the volume of the pore:

$$S_r = \frac{\pi\left(r_p^2 - \mathrm{r_{p0}^2}\right)}{\pi R^2} \rightarrow r_{p0} = r_p\sqrt{1 - S_r} \tag{19}$$

The mean velocity can be expressed in terms of the relative saturation by substituting Eq (19) into Eq. (18).

$$\overline{v}(S_r) = \frac{g r_p^2 \rho \left(S_r(-2 + 3S_r) - 2(-1 + S_r)^2 \ln[1 - S_r] \right)}{8 S_r \mu} \tag{20}$$

Eq. (20) expresses the mean velocity of the water. The specific waterflow will be the amount of water crossing a unit area of soil and is, therefore, given by Eq. (21).

$$\overline{q}(S_r) = \overline{v}(S_r) \cdot S_r = \frac{g\ n\ r_p^2 \rho \left(S_e(-2 + 3S_r) - 2(-1 + S_r)^2 \ln(1 - Sr) \right)}{8\mu} \tag{21}$$

With this equation, for a saturated soil, the permeability will be the limit when $S_r \to 1$, which is similar to the Kozeny-Carman expression without Taylor considerations related to the porosity change (it has an additional $e^3/(1 + e)$ term multiplying k_{sat}):

$$k_{sat} = \frac{g\ n\ r_p^2 \rho}{8\mu} \tag{22}$$

and Eq. (21) can therefore be expressed in the following form:

$$\overline{q}(S_r) = k_{sat} \left(S_r(-2 + 3S_r) - 2(-1 + S_r)^2 \ln(1 - S_r) \right) \tag{23}$$

Pores in a random inclination:

The previous equations have been developed assuming that the pores are distributed vertically, but in a real soil the tubes can have any inclination from 0 to $\pi/2$ in a vertical plane. So, here it is assumed that, as a first approximation, the inclination of the pores will have the same probability from 0 to $\pi/2$, which is the case for an isotropic soil. In real soils, load history, compaction and shape of grains can lead to different probabilities in the inclinations, so an extension to a general soil could be performed if the probability of the direction of pores were known for every direction.

In this case, if the acceleration of gravity in a 2D space is g, vertically downwards, then, if the pore has an angle, α, from the vertical, the acceleration to which the water is subjected has a modulus of $g \cdot \cos\alpha$, and will have horizontal and vertical components of $g \cdot \cos\alpha \cdot \sin\alpha$ and $-g \cdot \cos\alpha \cdot \cos\alpha$, respectively. The mean velocity calculated in the plane of flow will then be:

$$\overline{v_x}(\alpha, S_r) = \overline{v}(S_r) \cdot \cos\alpha \cdot \sin\alpha;\ \overline{v_z}(\alpha, S_r) = -\overline{v}(S_r) \cdot \cos\alpha \cdot \cos\alpha \tag{24}$$

As α has the same probability at all angles from 0 to $\pi/2$, then the mean values for each component are:

$$\overline{v_x}(S_r) = \frac{\int_0^{\pi/2} \overline{v_x}(\alpha, S_r) \mathrm{d}\alpha}{\int_0^{\pi/2} \alpha\, \mathrm{d}\alpha} = \frac{4}{\pi^2}\ \overline{v}(S_r);\ \overline{v_z}(S_r) = \frac{\int_0^{\pi/2} \overline{v_z}(\alpha, S_r) \mathrm{d}\alpha}{\int_0^{\pi/2} \alpha \mathrm{d}\alpha} = \frac{2}{\pi}\ \overline{v}(S_r) \tag{25}$$

Thus, the specific waterflow in horizontal and vertical directions is given by:

$$\overline{q_x}(S_r) = \frac{4}{\pi^2}\ \bar{q}(S_r);\ \overline{q_z}(S_r) = \frac{2}{\pi}\ \bar{q}(S_r) \tag{26}$$

6 UNIDIMENSIONAL VERTICAL FLOW IN A COARSE MATERIAL

If we consider now a system in which no horizontal flow is possible (i.e. a vertical cylindrical tube with an specific waterflow on the top, q_z), then the previous equation could be simplified avoiding the horizontal terms (by symmetry there won't be horizontal variation in the saturation so $\frac{\mathrm{d}S_r}{\mathrm{d}x} = 0$.

The vertical waterflow can be obtained by applying Eq.s (22), (23) and (26).

$$\overline{q_z}(S_r) = \frac{2}{\pi}\ \bar{q}(S_r) = \frac{2}{\pi} \cdot \mathrm{k_{sat}} \cdot \Big(S_r(-2 + 3S_r) - 2(-1 + S_r)^2 \ln(1 - S_r)\Big) \tag{27}$$

so that:

$$\frac{\mathrm{d}q_z}{\mathrm{d}S_r} = \frac{8}{\pi} \cdot \mathrm{k_{sat}} \cdot (S_r - (S_r - 1)\ln(1 - Sr)) \tag{28}$$

If using the Richards equation for vertical flow in the form of $n\frac{\mathrm{d}S_r}{\mathrm{d}t} = -\frac{\mathrm{d}q_z}{\mathrm{d}z}$, and including the obtained expression for unsaturated vertical waterflow q_z, then the change in time and in the height of the water-column is given by Eq. (29).

$$n\frac{\mathrm{d}S_r}{\mathrm{d}t} = -\frac{\mathrm{d}q_z}{\mathrm{d}S_r} \cdot \frac{\mathrm{d}S_r}{\mathrm{d}z} = -k_{sat} \cdot 4 \cdot (S_r - (S_r - 1)\ln(1 - Sr)) \cdot \frac{\mathrm{d}S_r}{\mathrm{d}z} \tag{29}$$

If, instead, considering that the pore tubes are partially saturated, it is considered that some of the pores are fully saturated (specifically an amount equal to S_r) and remaining pores unsaturated, then the relative permeability is given by Eq. (14) and unidimensional flow in an uniform coarse material is represented by a simpler equation:

$$n\frac{dS_r}{dt} = -\frac{dq_z}{dS_r} \cdot \frac{dS_r}{dz} = -k_{sat} \cdot 2.5\, S_r^{1.5} \cdot \frac{dS_r}{dz} \tag{30}$$

Therefore, two approaches for the vertical flow in a column of an uniform coarse material are described, one given with Eq. (29) in with it is assumed that the same volume of water flows in every pore with each pore void being partially saturated, and the other approach, given by Eq. (30), in which water flows only in percentage of pores each of which is fully saturated (while the other pores carry no water).

7 VALIDATION WITH A REAL CASE

Reinson, Fredlund, and Wilson (2005) designed an experiment to observe the water flow through a coarse porous media (Figure 7). The experiment consisted in a column 1100mm high with a diameter of 100mm filled with 12mm glass beads with a porosity of 61%. Steady state flow was established for a period of 2h. Videographic data were collected using 3 infiltration rates: 0.630, 0.150 and 0.024 mm/s. A dye was applied and video images were taken when the dye reach 30, 50 and 170mm from the top, and the time was registered. The collected data are summarized in Table 2.

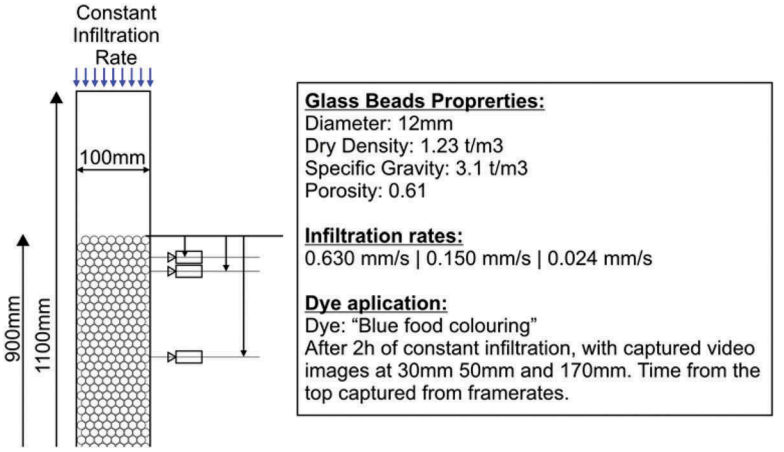

Figure 7. Lucite column to measure unsaturated hydraulic conductivity of glass beads (Reinson, Fredlund, and Wilson 2005).

Table 2. Seepage velocity measurements based on digital videography was given by the following table (Reinson, Fredlund, and Wilson 2005).

Flux velocity (infiltration rate) $v_{flux}(m/s)$	Range of measured velocity using digital videography $v_{seep}(m/s)$	Estimated volumetric water content $\theta_w = v_{flux}/v_{seep}(\%)$	Estimated degree of saturation $S = \theta_w/n(\%)$
0.000630	0.045-0.058	1.40-1.10	2.00
0.000150	0.014-0.040	1.10-0.38	0.91
0.000024	0.0018-0.003	1.30-0.80	1.60

Saturated permeability if calculated with Kozeny-Carman expression is as follows:

$$k_{sat} = \frac{1}{180} \cdot \frac{g\,\rho}{\mu} \mathrm{S}_g^2 \cdot \frac{n^3}{(1-n)^2} = \mathbf{11.71}\boldsymbol{m/s} \tag{31}$$

Yet Reinson, Fredlund, and Wilson (2005) recorded a saturated permeability of 0.055 m/s, a very significantly lower value. But when high Reynolds numbers are found for a waterflow, permeability is not constant and decreases when the Reynolds number, i.e. the water velocity, increases. And because of that it is not unexpected to measure such small permeability when compared to the value from Kozeny-Carman expression.

Considering that, in coarse materials, turbulency cannot usually be neglected, Forchheimer (1901) proposed an expression where, for very small velocities, turbulency can be neglected with only laminar effects acting but for high velocities, permeability reduces due to turbulence and inertial effects. Forchheimer (1901) expression can be reshaped in the form of the Darcy's Law, and related to the permeability on very small velocities (calculated with Kozeny-Carman for example: $1/\alpha = k_{koz}$) with Eq (32).

$$v = \frac{1}{\alpha + \beta v} \cdot i \rightarrow k_{sat} = \frac{1}{\alpha} \cdot \frac{1}{1 + \frac{\beta}{\alpha} v} = k_{koz} \cdot \frac{1}{1 + \frac{\beta}{\alpha} v} \tag{32}$$

Engelund proposed the values of β/α as in Eq. (33). β_0 and α_0 are two constants depending on the soil, with a typical value for β_0/α_0 of $1/500$ (Ferdos, Wörman, and Ekström 2015).

$$\alpha = \alpha_0 \frac{(1-n)^3}{n^2} \frac{\nu}{gD_g^2} \; ; \; \beta = \beta_0 \frac{1-n}{n^3} \frac{1}{gD_g} \rightarrow \; \frac{\beta}{\alpha} = \frac{1}{n(1-n)^2} \cdot \frac{D_g}{\nu} \cdot \frac{\beta_0}{\alpha_0} \tag{33}$$

With these considerations turbulent flow, that cannot be neglected in coarse materials, i.e. when waterflow reaches a high Reynolds number, can be considered by including the factor $1/\left(1+\frac{\beta}{\alpha}v\right)$ from Eq.s (32) and (33) to multiply the permeability computed by previously derived expressions of waterflow. The gradient at which Reinson, Fredlund, and Wilson (2005) measured permeability the saturated permeability of 0.055 m/s is not known, but considering it to be near 1 m/m (from the geometry of the permeameter) then the waterflow velocity is $v = 0.055 m/s$, and the saturated permeability is calculated in $k_{sat} = k_{koz} \cdot 1/\left(1+\frac{\beta}{\alpha}v\right) = 11.71 \cdot 0.0656 = 0.77 m/s$ still too high compared with the measured value but within one order of magnitude.

The results included in Figure 8 shows that the assumption considered in this paper (that all the pores would be partially saturated) is only valid at very small specific flow rates, at higher flow rates in general, the pores appear to be fully saturated and therefore the relative permeability can be represented by the Mualem formula applied to a uniform pore size distribution. With very small flow rates and therefore very low saturation, water can be distributed over the voids, but at higher flow rates and still very low saturation that configuration seems to become unstable and waterflow seem to be better described by Mualem's assumption. However, this conclusion is only based on three tests, and more checks are still needed. Also, some investigations are needed about which velocity to consider when considering turbulent effects. In this case the mean velocity on the whole section is considered but the velocity in isolated pores could also be considered, in which case permeability would be smaller.

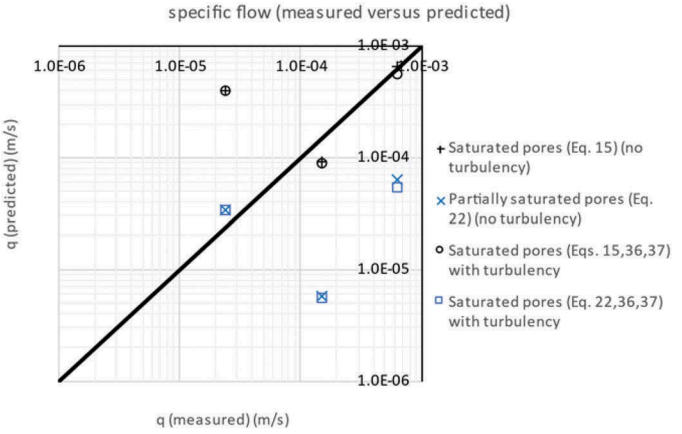

Figure 8. Specific flow calculated considering that some percentage of pores (S_r) become fully saturated (Eq. 15), or that every pore is saturated at a percentage (S_r) (Eq 22), considering turbulent effects and without that consideration; and compared to measured values.

8 CONCLUDING COMMENTS

An analytical and idealized model of the water flow in a partially saturated uniform coarse grained soil has been developed from first principles of water films, albeit those on spherical particles. It may be applicable to drainage media – e.g. associated with roads, rail tracks and

behind bridge abutments. Using data of an idealized physical model presented by Reinson, Fredlund, and Wilson (2005), it has been shown that the new derivation likely could be of used when flow rates are very low (and hence the granular material a long way from saturation) but that the classical Kozeny-Carman/Mualem approach would be better at moderate saturations and flow rates.

REFERENCES

Brooks, R. H., and Arthur T. Corey. 1964. 'Hydraulic Properties of Porous Media', *Hydrology Papers, Colorado State University*.

Campos-Guereta, Ivan, Andrew Dawson, and Nicholas Thom. 2021. 'An alternative continuous form of Arya and Paris model to predict the soil water retention curve of a soil', *Advances in Water Resources*, 154: 103968.

Carman, Philip Crosbie. 1938. 'Determination of the specific surface of powders I. Transactions', *J. Soc. Chemical Industries*., 57: 225–34.

Carman, Philip Crosbie. 1956. 'Flow of gases through porous media', *Butterworths Scientific Publications, London*.

Childs, E. C., and N. Collis-George. 1950. 'The Permeability of Porous Materials', *Proceedings of the Royal Society A: Mathematical, Physical and Engineering Sciences*, 201: 392–405.

Dullien, F. A. L. 1991. *Porous Media: Fluid Transport and Pore Structure* (Academic Press).

Ferdos, Farzad, Anders Wörman, and Ingvar Ekström. 2015. 'Hydraulic Conductivity of Coarse Rockfill used in Hydraulic Structures', *Transport in Porous Media*, 108: 367–91.

Forchheimer, P. 1901. 'Wasserbewegung durch Boden', *Zeitschrift des Vereines Deutscher Ingenieuer*, 45.

Heris, S. Zeinali, M. T. Hamed Mosavian, and E. T. White. 2009. 'Capillary holdup between vertical spheres', *Brazilian Journal of Chemical Engineering*, 26: 695–704.

Kozeny, J. 1927. *Uber kapillare leitung der wasser in boden*.

Mualem, Yechezkel. 1976. 'A new model for predicting the hydraulic conductivity of unsaturated porous media', *Water Resources Research*, 12: 513–22.

Reinson, Jeff R., Delwyn G. Fredlund, and G. Ward Wilson. 2005. 'Unsaturated flow in coarse porous media', *Canadian Geotechnical Journal*, 42: 252–62.

Richards, L. A. 1931. 'Capillary Conduction of Liquids through Porous Mediums', *physics*, 1: 318–33.

van Genuchten, Martinus Th. 1980. 'A closed-form equation for predicting the hydraulic conductivity of unsaturated soils', *Soil Science Society of America Journal*, 44: 892–98.

Eleventh International Conference on the Bearing Capacity of Roads, Railways and Airfields, Volume 2 – Hoff, Mork & Saba (eds)

Laboratory evaluation of diesel damage on asphalt surfaces

I. Artamendi, B. Allen & N. Leake
Aggregate Industries, Hulland Ward, Derbyshire, UK

H. Rahman & H. Carrol
National Highways (formerly Highways England), Birmingham, UK

C. Vicente
Kier Highways, Manchester, UK

ABSTRACT: This laboratory study assessed the suitability of the road surface hardness device, the wheel tracking machine and the pendulum tester to quantify the impact of diesel spillage on an asphalt surface. A Stone Mastic Asphalt (SMA) surface course mixture, typically used in the UK road network, was used in the study. Asphalt specimens were prepared in the laboratory using a roller compactor. Diesel was then poured on to the surface of the asphalt specimens at different levels, 2, 4, 6 and 8 l/m^2. Surface hardness measurements were carried out at 20 °C on asphalt specimens with various diesel spillage levels. Wheel tracking tests, on the other hand, were performed at 45 °C on asphalt specimens conditioned for 2 and 24 h at various diesel spill levels. Skid resistance measurements were taken when the surface of the asphalt specimen was dry, after wetting the asphalt specimen with water and after pouring diesel on to the asphalt surface. Results indicated that although the road hardness probe was able to provide some measure of the softening of the asphalt surface as a result of diesel damage, it could not provide a clear indication on the evolution of the damage with time or volume of diesel spilled. Wheel tracking data, on the other hand, provided valuable information of the effect of diesel on asphalt deformation. Moreover, skid resistance measurements using the pendulum tester showed a dramatic loss of skid resistance of the asphalt surface after a diesel spill.

Keywords: Diesel spillage, asphalt, surface hardness, deformation, skid resistance

1 INTRODUCTION

The spillage of diesel on the road network is considered an important safety, environmental and economic issue. Diesel spillages are known to reduce friction between the tyre of the vehicle and the road surface and, therefore, to increase the risk of accidents. This is particularly relevant in areas where a vehicle needs to brake or maneuver. Furthermore, diesel spillages are a particular road safety concern for motorcyclist (Lambourn and Viner, 2006).

Another important aspect is the environmental impact of a diesel spill. Diesel is a harmful substance and can cause seriously harm to humans and the environment. Diesel from a spill can also enter the water system through the drainage of the pavement endangering wildlife

DOI: 10.1201/9781003222897-12

and vegetation (Highways England, 2019a). Diesel spillage incidents can lead to large clean-up costs and lengthy delays with the associated economic costs to users and road owners. They are also responsible for both structural and surface degradation of the pavement which could lead to large resurfacing costs for the road operator (Baldwin et al., 2005).

Diesel spills are caused by many factors including road traffic accidents, mechanical failures and rupture fuel tanks. Most large spills, however, result from traffic collisions of Heavy Good Vehicles (HGVs). In 2018, Highways England recorded 314 diesel spillages involving HGVs (Highways England, 2019a).

The current process followed by Highways England (HE) for dealing with diesel spillages in the Strategic Road Network (SRN) is based on a step-by-step approach to carrying out correctional works involved in the clean-up of the diesel spillage. However, HE operational team including, Traffic Officers and Maintenance Service Providers (MSPs) have to make decisions on whether or not to traffic the damaged surface based on experience but with no objective measure available. Furthermore, although there are a number of clean-up procedures and products available to arrest any damage, there are no objective means, other than through trial and error, in which to assess the effectiveness of these treatments (Meitei et al., 2010).

The purpose of the project was to provide Traffic Officers or Maintenance Providers with an objective means of measuring the magnitude of the structural damage of an asphalt surface course following a diesel spillage. With this intelligence it was anticipated that more informed decisions will be able to be made on site with regard to earlier trafficking of the road and thus reducing the frequency of unnecessary resurfacing with its consequential cost and further traffic delay. Furthermore, establishing a performance measure will potentially enable the various spillage absorbents on the market to be evaluated objectively in terms of their performance.

The proposed laboratory study to evaluate the impact of diesel spillage on an asphalt surface assessed the road surface hardness device as a potential tool to monitor on-site surface and structural damage. Furthermore, the laboratory wheel tracking machine was also selected to provide deformation data of the asphalt surface under laboratory conditions. Limited number of skid resistance measurements were also carried out using the pendulum tester.

2 MATERIALS

A standard SMA 10 surf 40/60 mixture complying with BS EN 13108-5 was used in the study. The mixture was manufactured using 4/10 mm, 2/6.3 mm and 0/4 mm aggregates from Bardon Hill Quarry. Reclaimed filler, cellulose fibres and a standard 40/60 penetration grade binder were also used. Design binder content was 6.3 %.

Asphalt specimens for testing were prepared in the laboratory as follows. Aggregates and bitumen were pre-heated in an oven at the same temperature i.e. 170 °C. Heated aggregates were mixed for 30 seconds in a laboratory mixer. Hot bitumen was then added to the aggregate blend and mixed for a further 2 ½ minutes. The mixtures were then compacted to 300 mm x 300 mm slabs using a laboratory roller compactor. Slab thickness was 40 mm. Typical compaction temperature was 150 °C. A total of 16 asphalt slabs were manufactured.

Bulk density by dimensions and air voids of the slabs were determined in accordance with BS EN 12697-6 Procedure D and BS EN 12697-8, respectively. Prior to this, the maximum density of the mixture was determined in accordance with BS EN 12697-5. Average bulk density and voids of the asphalt slabs were 2.236 Mg/m^3 and 11.0 %, respectively. It should be noted that higher bulk density values and therefore lower air voids would be expected on cylindrical specimens cored from these slabs and determined using the saturated surface dry method (BS EN 12697-6 Procedure B) instead of the dimensions method (BS EN 12697-6 Procedure D). Furthermore, in UK trunk roads, in-situ air voids of SMA surface courses are specified between 2 % and 6 % air voids (SHW, 2021).

3 EXPERIMENTAL METHODS

3.1 *Road surface hardness test*

The road surface hardness test as described in BS 598-112: 2004 was selected in the study. The standard describes a method to determine the penetration of a standard probe into the road surface. In this test a steel rod with a rounded shaped tip of 4.0 mm diameter is force into the road surface under a constant load of (340 ± 10) N for a constant time of (10 ± 1) s. The depth of penetration of the probe is then measured with a ruler to the nearest whole millimetre. Typically, 10 probe measurement are carried out to determine the road hardness. Measurements are carried out when the surface temperature is between 15 °C and 35 °C.

Road hardness is usually determined prior the application of a surface dressing as part of the design process to select the correct size of chippings (Bateman, 2016). It is a property that represents the resistance of an existing road surface in a particular location to the embedment of chippings. It is influenced by both the type of surfacing material and the temperature.

In this work surface hardness measurements were first carried out on asphalt specimens conditioned at different temperatures from 10 °C to 60 °C. The road hardness probe was then used to determine the surface hardness of laboratory prepared asphalt specimens after diesel was poured on to the surface of the specimen.

The procedure for preparing in the laboratory asphalt specimens following a diesel spill was as follows. First, the side and bottom of the asphalt slabs were sealed using cling film and aluminium foil. Then, a 200 mm diameter circle was marked on the surface of the asphalt slabs. Blue tack was then used to contain the diesel spill in the marked area. Asphalt slabs were then put on a metal tray. Diesel was then poured on to the marked area using a calibrated beaker. Three different volumes of diesel were poured on to the asphalt surface, 126 ml, 188 ml and 251 ml. These corresponded to spillage levels of 4, 6 and 8 l/m^2. Surface hardness measurements were carried out before and after the diesel was poured on the asphalt surface. The first measurement after pouring the diesel was taken after 10 minutes and then continued for 25 days. A minimum of 5 measurements were taken each time. Furthermore, the locations for the measurements were selected randomly but care was taken to avoid testing on the same location. Figure 1 shows a technical operative taking surface hardness measurements.

Figure 1. Surface hardness testing of asphalt specimens.

3.2 *Wheel tracking test*

Deformation resistance was evaluated using the wheel tracking test in accordance with BS EN 12697-22 small size device, Procedure B, conditioning in air. Asphalt slabs prepared

using a laboratory roller compactor were used for testing. Tests were performed at 45 °C and the number of load cycles applied was 10,000.

The procedure for preparing the asphalt specimens following a diesel spillage was explained before. Four different volumes of diesel were poured on to the asphalt surface: 63 ml, 126 ml, 188 ml and 251 ml. These corresponded to spillage levels of 2, 4, 6 and 8 l/m^2. Wheel tracking tests started 2 h and 24 h after the diesel was poured on to the asphalt surface. The duration of the test was 6 ½ h (10000 cycles).

3.3 *Pendulum tester*

Skid resistance measurements were carried out using the pendulum tester. Measurements were carried following BS EN 13036-4 as a guide. Asphalt slabs were used for testing. Skid resistance measurements were taken when the surface of the asphalt specimen was dry, after wetting the asphalt specimen with water and after pouring diesel on to the asphalt surface. The volume of diesel poured on to the asphalt surface was 63 ml which corresponded to a spill level of 2 l/m^2. Furthermore, pendulum test measurements of asphalt specimens with diesel were taken at various time intervals.

4 RESULTS

4.1 *Surface hardness*

Figure 2 shows the penetration of the surface hardness probe into the SMA 10 surf 40/60 asphalt specimens conditioned at different temperatures. It can be seen that, as expected, the penetration increased as the temperature increased, indicating softening of the asphalt mixture.

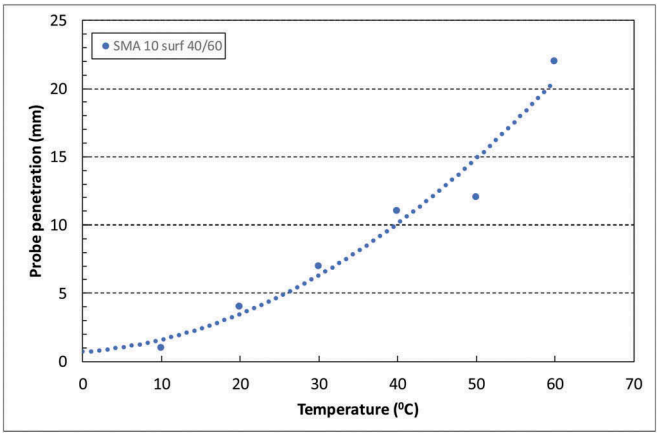

Figure 2. Change in surface hardness (probe penetration) with temperature.

The effect of different diesel spill levels on surface harness is presented in Figure 3. It can be seen that probe penetration increased during the first 2 ½ h (150 min) and that this increase was more pronounce for medium (6 l/m^2) and high (8 l/m^2) diesel spill levels (see Figure 3a). This indicated some form of damage (softening) of the asphalt surface, particularly, at high diesel spill levels.

A further limited increase in surface penetration was observed after 1 day, suggesting some further damage caused by the diesel (see Figure 3b). Surface hardness, however, did not appreciably change after that. Moreover, surface penetration after 25 days was 7 and 8 mm depending on the spill level.

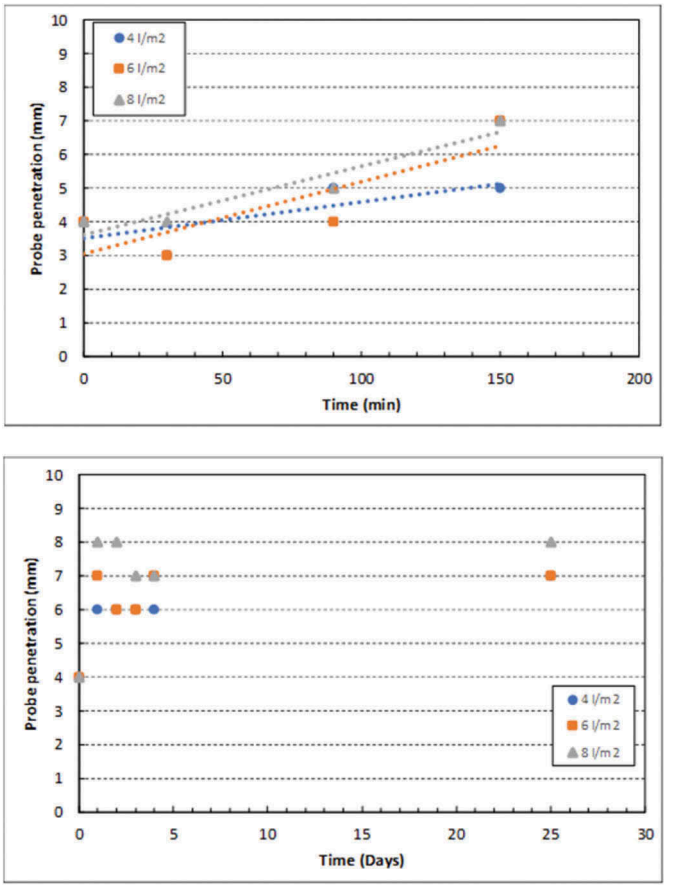

Figure 3. Evolution of surface hardness with time for different diesel spill levels: a) Short-term and b) Long-term.

4.2 *Surface deformation*

Wheel tracking curves showing the evolution of the rut depth with number of loading cycles are presented in Figure 4. These curves correspond to asphalt specimens tested 2 and 24 h after diesel was poured on to the surface. Volume of diesel added was 63 ml, 126 ml, 188 ml and 251 ml, giving spillage levels of 2, 4, 6 and 8 l/m^2. Furthermore, maximum rut depth (RD_{AIR}) and wheel tracking slope (WTS_{AIR}) were also determined and are presented in Table 1.

Results show that higher levels of diesel lead to higher surface deformation (rutting). Furthermore, for the specimen with 8 l/m^2 tested after 24 hours the deformation limit (i.e. 15 mm) was reached before the completion of the test (see Table 1). It can also be seen that, in general, rut depth increased when the specimens were tested after 24 h conditioning compared to 2 h. This suggest that the longer the diesel spill is left untreated on the higher the damage in terms of deformation.

Maximum rut depth (RD_{AIR}) and wheel tracking slope (WTS_{AIR}) values been compared against the specification limits for SMA surfaces for Class 1 site description where a maximum WTS_{AIR} of 1.0 is specified (PD 6691 Table D.2). It should be note that Class 1 corresponds to moderate to highly stress sites requiring high rut resistance. It can be seen that for a spill level of 6 l/m^2 the mixture would fail to meet the requirement if the diesel spill was untreated for 24 h. Also, for a spill level of 8 l/m^2, the mixture would fail to meet the requirement after only 2 h after the spill. Mixtures with no diesel, and 2 and 4 l/m^2 diesel spill level would meet the specification.

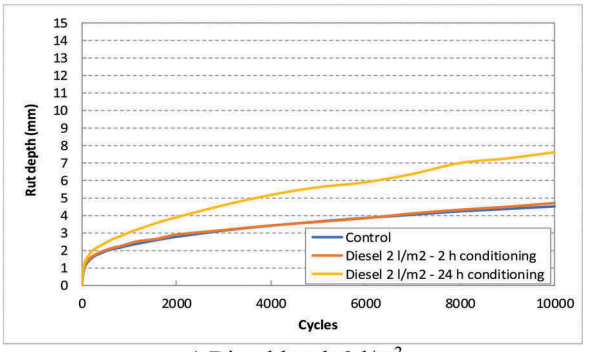

a) Diesel level: 2 l/m^2

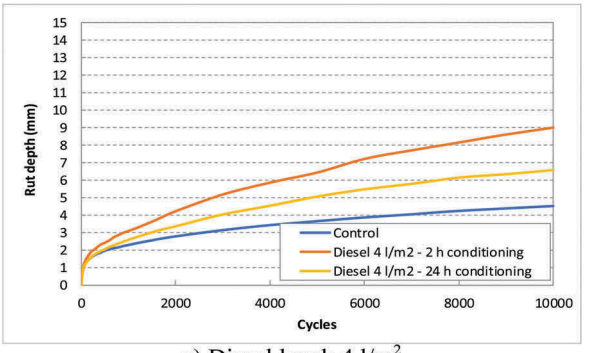

a) Diesel level: 4 l/m^2

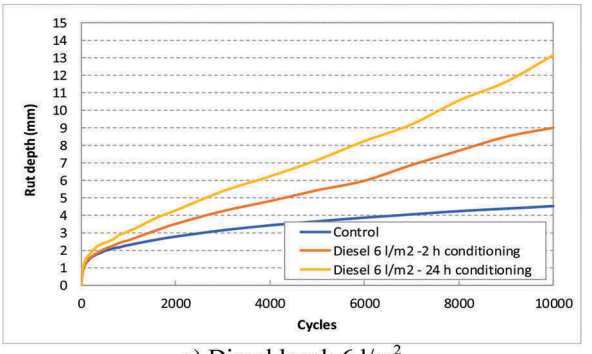

a) Diesel level: 6 l/m^2

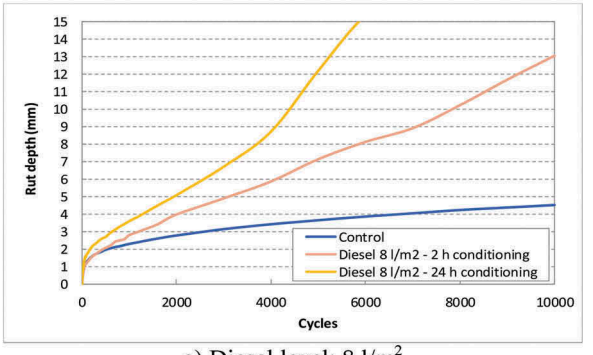

a) Diesel level: 8 l/m^2

Figure 4. Rut depth with number of cycles.

Table 1. Wheel tracking test results.

Diesel level (L/m^2)	Conditioning time (h)	RD_{AIR} (mm)	WTS_{AIR} ($mm/10^3$ cycles)
0	0	4.5	0.17
2	2	4.7	0.21
	24	7.6	0.40
4	2	9.0	0.51
	24	6.6	0.30
6	2	9.0	0.71
	24	13.1	1.20
8	2	13.1	1.18
	24	15.0 mm@ 6000 cycles	

4.3 *Skid resistance*

Skid resistance values determined with the pendulum tester are presented in Table 2. Results showed that, as expected, the skid resistance value dropped when the surface of the specimen was wet compared to dry. Furthermore, the skid resistance value dropped even further when diesel was spilled on the surface of the specimen. Results also indicated that the skid resistance after the diesel spill remained low for at least 2 days after the spill and increase thereafter probably as some of the diesel on the surface evaporated and penetrated into the mixture.

Table 2. Pendulum test results.

Surface Condition	SRV
Dry	98
Wet	70
5 min after diesel spill	40
1 h after diesel spill	42
2 h after diesel spill	40
1 day after diesel spill	42
2 days after diesel spill	43
10 days after diesel spill	63

Skid resistance values have been compared against the recommended values given in Road Note 27 (RRL, 1969). It can be seen that the material used in the study (SMA 10) would be suitable for all site categories as the wet skid resistance value, 70, is above that given in Road Note 27 for difficult sizes (e.g. roundabouts) which is 65. Skid resistance values after a diesel spill are, however, below the suggested values for difficult sizes. It should be noted that these results corresponded a to a relatively low diesel spill level (2 l/m^2). For higher levels, low skid resistance values might be expected as more diesel will be retained on the surface for a longer period of time. It should be also noted that skid resistance measurements were carried out on fresh asphalt specimens. It is known that skid resistance values of road surfaces that have been subjected to traffic and therefore surface wear and polishing are lower than those for new surfaces. Thus, the effect of a diesel spill on an old polished road might differ from that on a new road.

5 DISCUSSIONS

Diesel is known to dissolve bitumen which is the main component of asphalt. It is believed that when diesel is spilled on an asphalt surface the damage on the asphalt will depend on its

surface texture and on its porosity. For low porosity surfacing materials with relatively high texture (e.g. HRA) diesel might concentrated on the surface. In this case, damage might result from the liquification of the binder coating the aggregate resulting in loss of aggregate-binder adhesion. Under traffic, this could lead to surface fretting or loss of aggregate particles.

For semi-porous materials, on the other hand, the time the diesel is retained on the surface will decrease and its effect on surface damage (surface softening, fretting and reduction in friction) might be limited. In this case, the diesel that has penetrated the material will start to dissolve the binder resulting in loss of binder cohesion. This, in turn, will cause loss of material structural integrity leading to a rapid increase in permanent deformation under the action of traffic.

For thin surfacing materials including SMA, a combination of both loss of adhesion resulting in surface fretting and loss of binder cohesion leading to a reduction in material structural integrity and premature deformation of the road are the main surface and structural effects of a diesel spill.

Moreover, the damage caused by the diesel on the surface of the material is initially concentrated of the surface of the material in contact with the vehicle tyres. This localised damage might nor result on a reduction on surface hardness as measured by the surface hardness probe. Results from this work has shown that although the surface hardness probe was able to depict some softening of the asphalt surface as a result of diesel damage, it was not able to provide a clear indication of the evolution of these changes with time. Furthermore, although this tool was able to quantify the effect of temperature on surface hardness it was not able to clearly quantify the effects of diesel spill level.

Tests conducted in this project have shown that the wheel tracking device is a suitable laboratory tool to investigate the effect of diesel spillages in asphalt. Wheel tracking data has clearly shown the damage caused by diesel in terms of deformation. Furthermore, the data indicated that the extent of damage (deformation) depended on the volume of diesel spill on the surface. The results also indicated that the longer a diesel spill was left untreated the higher the damage in terms of deformation. Data provide in this study could provide the basis to estimate in which cases resurfacing might be required, for instance, when the level of the spill is larger than 6 l/m^2. Data could be also used to estimate when the resurfacing works need to be carried out depending on the level of diesel.

Data provided in this project has also shown that although the effect of a small diesel spill might be relatively small in terms of surface hardness and deformation, the reduction in skid resistance is a major problem. Skid resistance measurements have shown that even for a small diesel spill, skid resistance values were below the recommended values for motorways and trunk roads. Thus, the main considerations when dealing with diesel spillages and clean-up procedures should be focused on restoring the skid resistance of the road.

6 CONSLUSIONS

Based on this laboratory work the following conclusions can be drawn:

- The surface hardness probe assessed in this study was able to provide some measure of the softening of the asphalt surface as a result of diesel damage. The probe, however, could not provide a clear indication of the evolution of these changes with time nor the effect of different spill levels on surface degradation.
- The wheel tracking device is a suitable laboratory tool to investigate the effect of diesel spillages in asphalt. Wheel tracking data has shown the damage caused by diesel in terms of deformation depended on the level of the diesel spill on the surface and on the time the spill was left untreated.
- Skid resistance measurements using the pendulum tester showed a dramatic loss of skid resistance of the asphalt surface after a diesel spill. Thus, the main considerations when dealing with diesel spillages and clean-up procedures should be focussed on restoring the skid resistance of the road.

REFERENCES

Balwin, B., Carmody, O. and Collins, T., 2005. *Degradation of asphalt due to diesel spills on roads*, Skid resistance: district implications and applications, Road System and Engineering Technology Forum, Brisbane, Queensland, Australia.

Bateman, D., 2016. *Design Guide for road surface dressing, Road Note 39 (7th Ed.)*, TRL Transport Research Laboratory.

BS 598-112: 2004. Sampling and examination of bituminous mixtures for road and other areas. Method for the use of road surface hardness probe.

BS EN 12697-5: 2018. Bituminous mixtures. Test methods. Determination of the maximum density

BS EN 12697-6: 2020. Bituminous mixtures. Test methods. Determination of bulk density of bituminous specimens

BS EN 12697-8: 2018. Bituminous mixtures. Test methods. Determination of void characteristics of bituminous specimens

BS EN 12697-22: 2020. Bituminous mixtures. Test methods. Wheel tracking.

BS EN 13036-4: 2011. Road and airfield surface characteristics. Test methods. Method for measurement of slip/skid resistance of a surface: The pendulum test.

BS EN 13108-5: 2016. Bituminous mixtures. Material specifications. Stone Mastic Asphalt.

Highways England, 2019a. *Diesel spillage. Best Practice Guide*.

Highways England, 2019b. *What is the impact and cost of a diesel spillage*.

Lambourn, R., F. and Vine, H. E., 2006. *Friction test on contaminated road surfaces*, Published Project Report PPR073, TRL, Transport Research Laboratory.

Meitei, B., Keigan, M., Chislett, W., Carswell, I. and Harper, J., 2010. *Review of diesel spillage clean-up procedures*, Published Project Report PPR509, TRL Transport Research Laboratory.

PD 6691: 2015+A1:2016. Guidance on the use of BS EN 13108, Bituminous mixtures. Material specifications.

Road Research Laboratory, 1969. *Instructions for using the portable skid resistance tester*, Road Note 27 (2nd Ed.). Ministry of Transport.

Specification for Highways Works, 2021. *Cl 942 Thin Surface course system*, *Series 900 Road Pavements – Bituminous Bound Material*, Manual of Contracts Documents for Highways Works, Vol. 1 Specification for Highways Works.

Effects of climate changes

Eleventh International Conference on the Bearing Capacity of Roads, Railways and Airfields, Volume 2 – Hoff, Mork & Saba (eds)

Bio-mediated soil stabilisation using biopolymers for enhancing performance of transport infrastructure

A. Heitor
School of Civil Engineering, Leeds University, Leeds, UK

M. Grady
Eslers Land Consulting, Albury, Australia, Formerly University of Wollongong, Wollongong, Australia

R. Russel & J. Vongsvivut
ANSTO, Australian Synchrotron, Australia

ABSTRACT: Cost efficient and robust transport systems are of critical importance to future economic prosperity as well as for the society's social and environmental well-being. However, current performance shortcomings in the transport infrastructure formations induced by extreme climatic events associated with climate change cause excessive maintenance requirements with increased costs and disruptions to commuters and loss of productivity in the freight services.

Bio-mediated soil stabilisation is an innovative technology that improves the physical characteristics of soil using biological systems (e.g. microorganisms). This technique has substantial advantages compared to traditional chemical stabilizers (e.g. cement, lime) in terms of environmental sustainability while showing comparable performance.

In this paper, particular attention is given to the use of biopolymers and its potential application to subgrade soil. Biopolymers have high specific surfaces with electrical charges, which enable direct interactions between the finer soil particles, thereby providing biopolymer-soil matrices with higher strength. A series of unconfined compression tests were conducted to assess the potential use for subgrade stabilisation. Results indicate that small amounts of biopolymer in the order of 1% by weight are sufficient to obtain comparable strength to more established chemical stabilisers.

Keywords: Compacted soil, microorganisms, biopolymers, soil stabilisation

1 INTRODUCTION

The need and demand for safe, durable, and reliable transport infrastructure to accommodate faster and heavier traffic has been increasing steadily in the past decades. However, current performance shortcomings in the transport infrastructure formations (Figure 1) induced by extreme climatic events cause excessive maintenance requirements with increased costs and disruptions to commuters and loss of productivity in the freight services. For instance, in the rail sector these costs can amount to 30% of the total operation costs, corresponding to approximately €33 billion/year in Europe alone (European Commission, 2015).

DOI: 10.1201/9781003222897-13

1.1 *Role of unsaturation in the transport formations*

Most transport infrastructure formations are essentially compacted, hence remain unsaturated under capillarity stresses or matric suction, which influences their hydro-geomechanical response (e.g. Romero et al., 1999, Gens, 2010, Alonso et al., 2010 and Heitor et al, 2015). Sun et al. (2007), Kodikara (2012) and Heitor et al. (2013) showed that the behaviour of such materials is governed by the initial compacted state. This is particularly important in the areas where local conditions can be unfavourable due to the existence of compressible and/or expansive soils. In these locations, the assessment of the in-service performance of the subgrade soils and compacted fills (i.e. sub-base and capping or sub-ballast, structural fills) under cyclic stresses and notable variations in subsurface moisture caused by climate change; i.e. intense periods of rainfall and droughts (e.g. wetting and drying) becomes critical in design (Figure 1). For instance, a sudden reduction of matric suction associated with intense rainfall periods may initiate sudden wetting collapse causing excessive settlements and unstable conditions (e.g. rail derailments).

Soil stabilisation can be employed to enhance compacted fills performance, mitigate wetting collapse and control of volume changes that the soil undergoes during the cyclic wetting-drying processes. Bio-mediated soil stabilisation is an innovative technology that improves the physical characteristics of soil using biological systems (e.g. microorganisms). This technique has substantial advantages compared to traditional stabilizers (e.g. cement, lime) in terms of environmental sustainability (CO_2 emissions and alkaline leaching) while showing comparable performance and contributing to the net carbon zero targets.

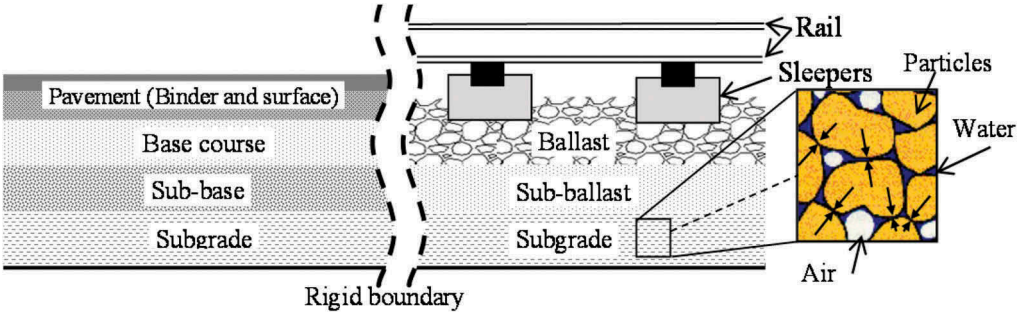

Figure 1. Profile of typical transport systems.

1.2 *Role of climate change on transport infrastructure performance*

Resilient construction design and maintenance operations of transport infrastructures are vital to ensure their serviceability requirements in a changing climate. For instance, in road transport infrastructures in Europe, in 2012 it was estimated that 30% to 50% of road maintenance costs were caused by weather stresses (approximately 8 to 13 billon €/yr,). Of those, only 10% (approximately 0.9 billion €/yr) were reported to be associated with extreme weather events, e.g. extreme heavy rainfalls accompanied by floods events (Nemry and Demirel, 2012). However, as climate patterns continued to change over the last decade, frequent rainfall periods with larger intensity resulted in excessive precipitation, flooding and had dramatic consequences for infrastructure recently, e.g., 2021 summer floods in western Germany, Netherlands and Belgium (The Guardian, 2021). The increasingly larger frequency of flash flooding in river banks and urban spaces is particularly noteworthy as it can results in an extra cost for road transport infrastructures. This is because the stability of an embankment supporting a transport infrastructure asset is strongly related the increase in water content or reduction of matric suction in the subgrade soil and embankment fill materials (Figure 2). The magnitude of the changes in moisture content are in turn related to the weather conditions (e.g., rainfall, temperature, humidity, infiltration/evaporation potential), and their impact is directly associated with the soil properties (e.g., plasticity, water retention and thermal properties).

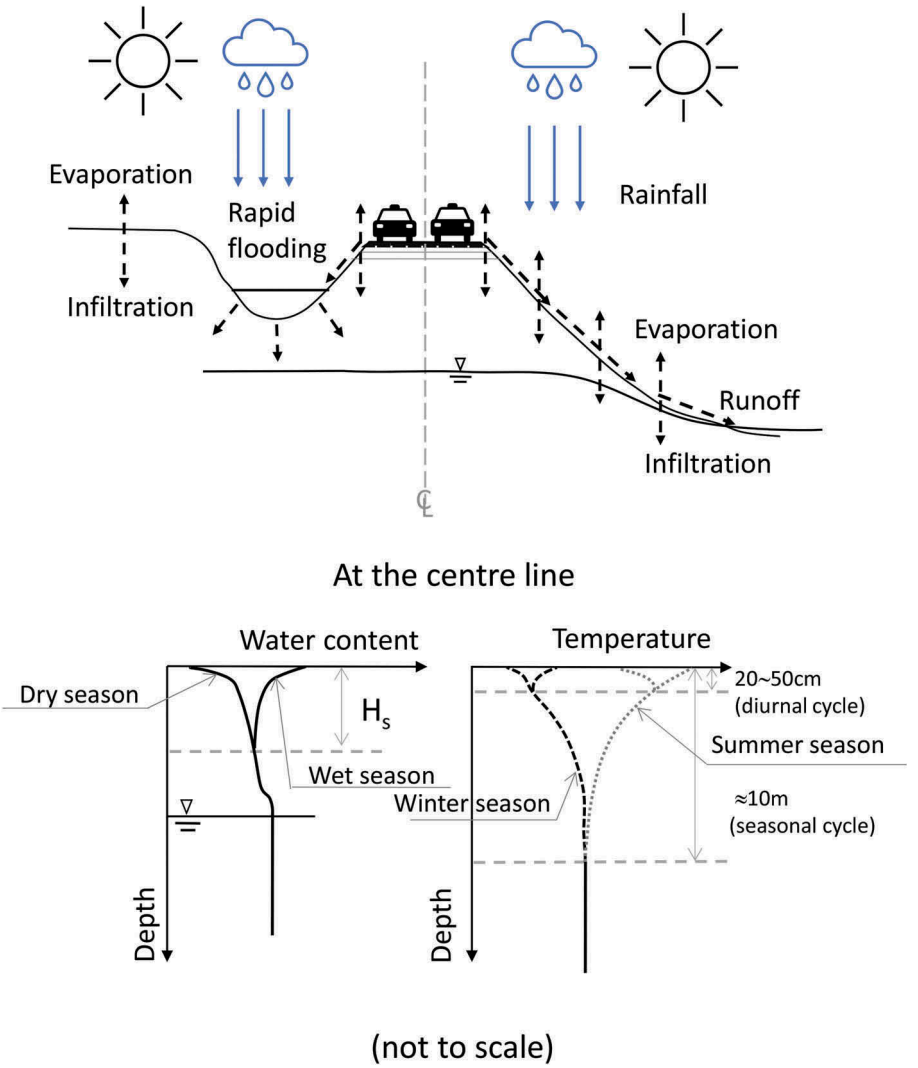

Figure 2. Diagram of a roadway embankment subjected to seasonal climatic variations (after Heitor et al, 2021, reproduced under the Creative commons Attribution license, CC BY 4.0, http://creativecommons.org/licenses/by/4.0/).

The impact climate change in stability of infrastructure can be twofold, i.e.:

a) increase in temperature and extensive periods of droughts and
b) different rainfall patterns, e.g. few and far between but having a high intensity leading to rapid flooding

This means that during dry summer periods water would be removed from the ground by evaporation processes, whereas prolonged and intense rainfall events could cause saturation of the group and contribute to an increase in pore water pressures. Figure 2 illustrates the effects of seasonal climatic variation on a typical roadway embankment. As it can be observed, the increase in temperature caused by atmospheric conditions will cause evaporation to take place and hence a reduction in water content (dry season). This may cause a change in the soil properties as well as the onset of cracking caused by desiccation and soil shrinkage which can propagate through the pavement layers. This is particularly important in

locations with soils that have potential for volume changes (e.g., swelling and shrinkage), especially because repeated shrink-swell cycles can lead to accumulation of shear strains resulting in strain softening and progressive failure (Take and Bolton, 2011).

Considering these performance shortfalls, it is critical to enhance the shear strength behavior transport infrastructure substructures, at subgrade level and compacted fills. To address this challenge, in this paper, a low carbon technique is investigated, i.e., soil stabilisation using biopolymer xanthan gum.

2 SOIL STABILISATION USING BIOPOLYMERS

Numerous soil treatment methods are already in practice, among these the most used chemical admixtures are Portland cement and lime (e.g. quicklime and hydrated lime). However, their use has several shortcomings, especially from an environmental perspective, e.g., carbon emissions and energy expended in their production associated with the calcination processes. As an alternative to traditional soil treatment and improvement techniques, bio-mediated approaches are now being actively investigated in the field of geotechnical engineering (Chang et al. 2016). Biopolymers have high specific surfaces with electrical charges, which enable direct interactions between the finer soil particles, thereby providing biopolymer-soil matrices with higher strength. Typically, the biopolymer directly bonds with clay particles, producing accumulated face-to-face clay layers, while in sand it coats the particles with biofilm linked through threads resembling a web (Figure 3).

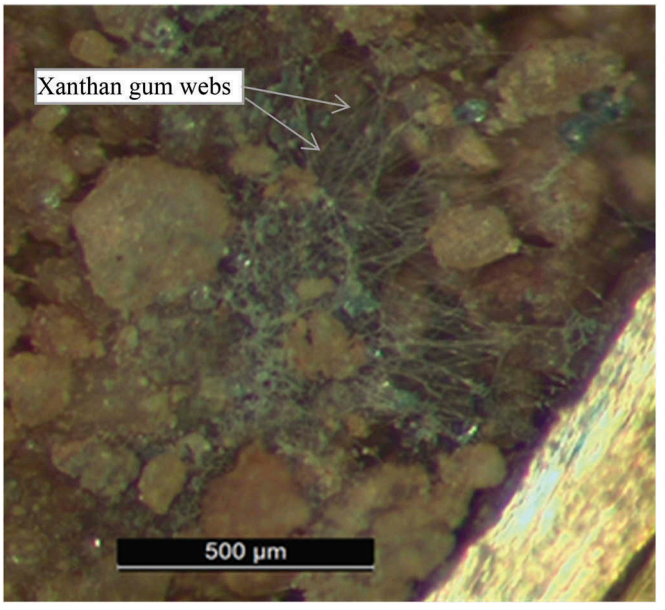

Figure 3. Micrograph of a compacted silty sand with biopolymer xanthan gum showing web structures.

This paper focus on the biopolymer xantham gum, which is a polysaccharide with a cellulose backbone and pendant sugars secreted by the bacterium *Xanthomonas campestris*. It is soluble in water and it is mainly used in the food and drilling industry for its ability to increase the viscosity of fluids due to its hydrocolloid rheology. Xanthan gum has been selected for this study because it can contribute to a substantial increase in shear strength while maintaining ductile behaviour. Furthermore, past studies indicated that soil treated with 3.0% of the commercial biopolymer has comparable performance to 10% cement-treated soil

(Chang et al., 2015; Qureshi et al., 2017). In addition, the cellulose backbone is likely to provide a greater durability against biodegradation and permanence in post-compacted hydraulic loading cycles (e.g. wetting and drying, Muguda et al., 2020) while showing high stability under a wide range of temperatures and pH values (Zohuriaan and Shokrolahi, 2004 & Sun and Gunasekaran, 2009). Recent research efforts in the application of commercial biopolymers in the stabilisation of soil and mine tailings also support these observations (Bouazza, 2009, Cabalar and Canakci, 2011, Cabalar et al., 2017, Chen et al., 2014, Guo, 2014 and Chang et al., 2016, Musuga et al, 2017).

3 MATERIALS AND TESTING PROGRAM

3.1 *Materials*

The soil used in this study was silty sand classified as SP-SM (Unified Soil Classification System, USCS). The soil is a by-product of cobble quarrying activities that has been widely used to fill low areas in Penrith. The soil consists of particles ranging in size from silt to sand. While the soils present on site are quite variable, for this study only a single grading was used. The particle size distribution was composed of 89% sand and 11% fines, of which 7% is silt and the remaining 4% is clay size particles. It has a liquid limit of 25.5%, a plasticity index of 10, a specific gravity of 2.7 and an optimum moisture content of 12% for standard Proctor compaction level (Heitor et al., 2013). In this study xanthan gum was produced by the bacterium *Xanthomonas campestris* adopting standard culturing protocols, however as the bacterial biopolymer precipitation yield was relatively small, and the amounts required for preparing the specimens tested were much larger, the xanthan gum used in the study was food grade and obtained commercially. The Portland cement and hydrated lime procured for comparison were also obtained commercially.

3.2 *Testing program*

The material was first air dried and then any clumps were carefully disaggregated using a mortar and pestle so that the particles could meet a nominal size of 2mm. The required amount of powdered chemical admixture was added and thoroughly mixed. Thereafter, a given amount of water was then added to the sample (12% for optimum moisture content) and the mixture was thoroughly mixed with a masonry trowel and then left under constant temperature and humidity conditions for 24h to ensure a uniform distribution of moisture. The specimens were subsequently dynamically compacted in a 38mm diameter mold and compacted in three layers. The number of blows per layers was adjusted such that a comparable dry unit weight to that of standard Proctor compaction could be attained.

Unconfined Compressive Strength (UCS) testing was carried out in accordance with AS-5101-2008 (Standards Australia, 2008). A total of 12 samples were prepared with XG concentrations from 0% (un-stabilized) to 1.5% XG. Two specimens were prepared for each of the concentration considered. The primary reason for this was to confirm repeatability. Additional specimens were also prepared with cement and lime for comparison. The samples were tested at a curing time of 21 days. It should be noted that a 28 day curing period would have been desirable, so that the results could be directly compared to standardized cement testing procedures however scheduling issues meant that this was not possible, a shorter curing period was adopted. For the UCS testing, an Instron testing apparatus was used and shearing was undertaken at a rate of 1.0mm per minute until the specimen reached failure. A datalogger system was used to continuously record the displacement and load readings during shearing. At the end of the UCS shearing a portion of the specimens was used to determine moisture content.

4 RESULTS AND DISCUSSION

A series of unconfined compression tests results for different percentages of biopolymer xanthan gum (XG) show a continuous increase in shear strength with increasing XG concentration (Figure 4). However, it should be noted that the rate of increase is not linear, and it tends to be smaller for larger percentages of XG addition. The lowest concentration tested at 0.5% showed a dramatic increase in axial strength with a peak stress of 62 kPa, an increase of 248% compared to the baseline un-stabilized specimen which achieved a peak stress of 25 kPa. This illustrates that a substantial increase in performance is achieved at a very small quantity of XG. For larger concentration of XG, the peak axial stress continues to increase but by a smaller amount. For instance, at 1% XG the specimen has a peak stress of 76 kPa, an increase of 304% compared to the unstabilized specimen, but this represents only an 8% increase compared to the 0.5% XG specimen that achieved a peak stress of 62 kPa. This rate of increase is further reduced for the 1.25% and 1.5% stabilized samples which achieved only a 4% and 5% relative increase in performance compared to the previous results. It should also be note that the UCS results seem to indicate that as the percentage of XG is increased, the soil stress strain response changes from strain softening to strain hardening. However, a more comprehensive stress-strain behavior evaluation would be required to assess whether this change is caused by the addition of xanthan gum.

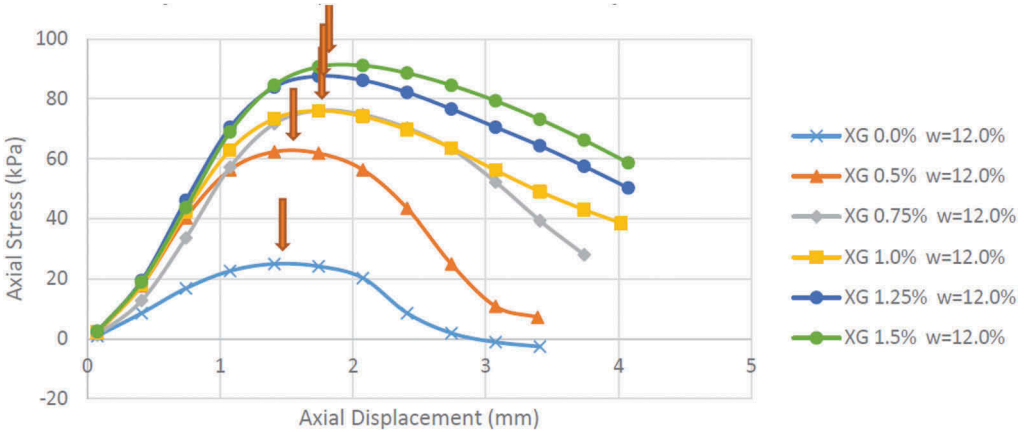

Figure 4. Unconfined compressive strength results for different percentages by weight of xanthan gum addition (arrows indicated peak stress).

To better illustrate this trend the peak axial stress results indicated in Figure 4 with arrows are plotted in terms of percentage addition of XG in Figure 5. It can be observed that once a percentage of 1% is exceeded the performance returns for using more stabilizer are minor. This seems to indicate that for the silty sand tested, an optimal percentage of XG addition is 1%. This was not surprising and is consistent with the proposed 1.0 – 1.5% optimum range indicated previously by Chang et al. (2015). Once the optimal percentage was determined additional specimens were prepared with Portland cement and hydrated lime at the same dry weight percentage. The results are shown in Figure 6. It can be observed that for the same dry weight addition, the xanthan gum performance in terms of peak stress is the best for the soil tested. This is not surprising and similar trends have been observed for other low plasticity soils stabilized with other biopolymer gums (Chang et al., 2016). In fact, in the latter study the performance returns in terms of compressive strength of 1% XG addition was comparable to 10% Portland cement addition for kaolin. However, the study also reported smaller performance returns of compressive strength, friction angle and cohesion intersect for clayey soils.

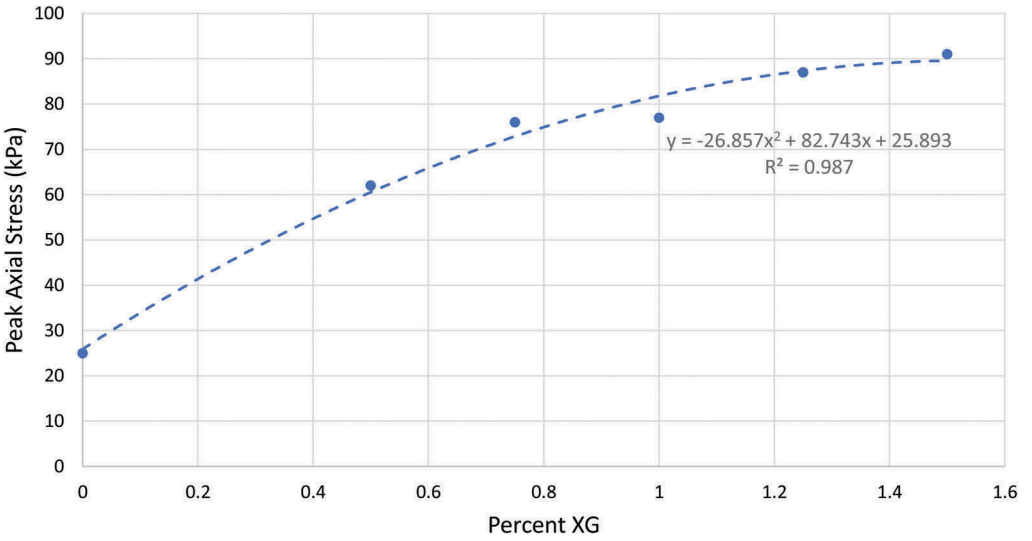

Figure 5. Unconfined compressive tests peak axial stress values for different percentage of XG (the goodness-of-fit measure for linear regression value, R^2 is also included).

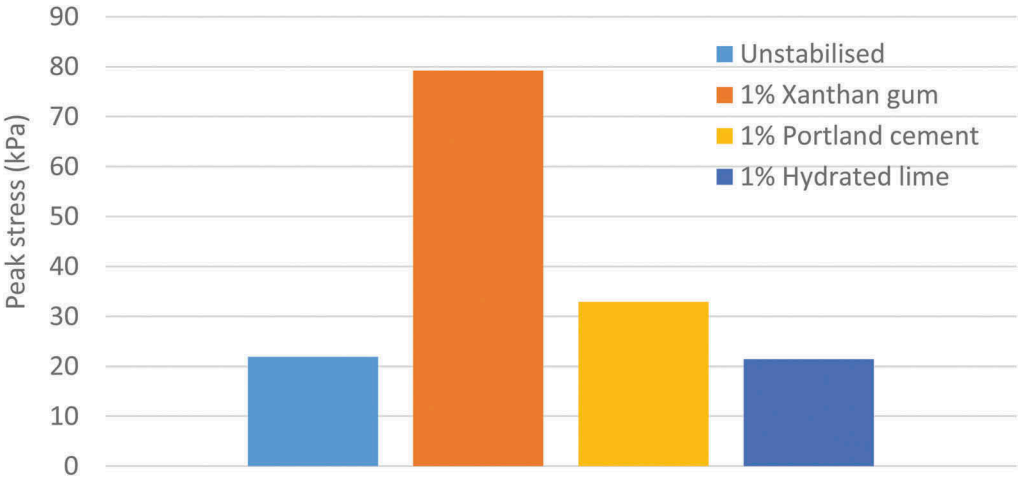

Figure 6. Unconfined peak stress for different stabilizers at the dry weight percentage of 1% addition.

5 CONCLUSIONS

To evaluate the potential of bio-mediated soil stabilisation for enhancing performance of transport infrastructure, a series of unconfined compression strength tests were conducted with a typical subgrade soil stabilized with several percentages of the biopolymer xanthan gum (XG). The results shows considerable increased in peak stress and Young modulus for the specimens prepared with XG. However, after about 1% XG addition the performance returns for additional XG were marginal. In fact, the best performance returns were found to be between 0 – 0.75% XG additions. This indicates that even small dry weight percentage addition can have a dramatic effect on the performance of the compacted soil. However, it should be noted that the same trend may not be as evident in soil of intermediate to high plasticity having a greater percentage of clay size particles. While the production of biopolymer using

the bacterium *Xanthomonas campestris* was attempted, this proved to be challenge as the biopolymer precipitation yield was very small. Therefore a food grade commercial product was used instead.

Past studies have clearly highlighted the advantage of XG in terms of carbon. For instance, the production of xanthan gum is known to consume approximately 4.97 kg of CO_2 for 1 kg of biopolymer whereas cement production emits 1.25 tons of CO_2 per 1 ton of cement during the calcination process (Chang et al., 2016). However, in situ production of XG from the bacterium *Xanthomonas campestris* still remains a challenge, as biopolymer precipitation yield is small. While the commercial production is well established, the product cost is still not as competitive as cement is and its application would involve transport that in turn generate emissions. Thus, in-situ precipitation would be preferable.

Finally, the dry material requirement for a desired shear strength increase is much smaller for XG compared to Portland cement. This indicates that smaller quantities can be used for equivalent performance returns. Thus, it can be concluded that the use of XG is not only cost effective due to the smaller quantities being used but it is also is an attractive and more sustainable alternative that could take an important place in soil stabilisation in a low carbon future. It should be noted that while an application to transport infrastructure was explored in this paper, other soil stabilization applications, for instance near the main gas pipelines (Yavorskyi et al, 2017) could also be considered.

ACKNOWLEDGMENTS

This work was supported by a seed grant funded under ANSTO-UOW collaboration scheme. Their financial contribution is gratefully acknowledged. The laboratory assistance provided by Richard Berndt from the University of Wollongong is appreciated. This work was conducted while the first author was in the University of Wollongong; the facilities and support provided by the Centre for Geomechanics and Railway Engineering are gratefully acknowledged.

REFERENCES

Alonso, E.E., Pereira, J. M.; Vaunat, J., Olivella S. (2010) A microstructurally based effective stress for unsaturated soils. Géotechnique, 60 (12), 913–925.

Bouazza, Gates, & Ranjith (2009). Hydraulic conductivity of biopolymer-treated silty sand Géotechnique 59(1): 71–72.

Cabalar & Canakci (2011) Direct shear tests on sand treated with xanthan gum ICE - Ground Improvement, 164(2), 57–64

Cabalar, A. F., M. Wiszniewski and Z. Skutnik (2017). Effects of Xanthan Gum Biopolymer on the Permeability, Odometer, Unconfined Compressive and Triaxial Shear Behavior of a Sand. 54: 356–361.

Chang, I. and G.-C. Cho (2012). "Strengthening of Korean residual soil with β-1,3/1,6-glucan biopolymer." Construction and Building Materials 30: 30–35.

Chang, I., J. Im and G.-C. Cho (2016). Introduction of Microbial Biopolymers in Soil Treatment for Future Environmentally-Friendly and Sustainable Geotechnical Engineering. Sustainability, 8 (3), 251; https://doi.org/10.3390/su8030251

Chang, I., J. Im, A. K. Prasidhi and G.-C. Cho (2015). "Effects of Xanthan gum biopolymer on soil strengthening." Construction and Building Materials 74: 65–72.

Chang, I., A. K. Prasidhi, J. Im, H.-D. Shin and G.-C. Cho (2015). "Soil treatment using microbial biopolymers for anti-desertification purposes." Geoderma 253-254: 39–47.

Chen, R., I. Lee and L. Zhang (2015). Biopolymer Stabilisation of Mine Tailings for Dust Control. 141.

European commission (2015) Study on the Cost and Contribution of the Rail Sector, European Commission Directorate General for Mobility and Transport, accessed on 10/10/2021 https://ec.europa.eu/transport/sites/default/files/modes/rail/studies/doc/2015-09-study-on-the-cost-and-contribution-of-the-rail-sector.pdf

Gens, A. (2010) Soil–environment interactions in geotechnical engineering. Géotechnique, 60 (1), 3–74.

Guo (2014) Investigation of soil stabilisation using biopolymers, Graduate Theses and Dissertations. 13909 Iowa State University.

Heitor, A., Indraratna, B. and Rujikiatkamjorn, C. (2013) Laboratory study of small-strain behavior of a compacted silty sand. Canadian Geotechnical Journal, 50(2): 179–188.
Heitor, A., Indraratna, B. and Rujikiatkamjorn, C. The role of compaction energy on the small strain properties of a compacted silty sand subjected to drying-wetting cycles Géotechnique, 2015, Volume 65, Issue no. 9, pp. 717–727.
Heitor, A., Parkinson, J., and Kotzur, T. (2021) The Role of Soil Stabilisation in Mitigating the Impact of Climate Change in Transport Infrastructure with Reference to Wetting Processes, Applied Sciences, 11(3), 1080; https://doi.org/10.3390/app11031080
Kodikara, J.K. (2012). New framework for volumetric constitutive behaviour of compacted unsaturated soils, Canadian Geotechnical Journal 1227–1243.
Muguda, Booth, Hughes, Augarde, Perlot, Bruno, Gallipoli (2017), Géotechnique Letters, 7 309–314
Muguda, Lucas, Hughes, Auguarde, Perlot, Bruno, Gallipoli (2020) Construction & Building Materials 259, 119725
Nemry, F. and Demirel, H. (2012) *Impacts of Climate Change on Transport: A focus on road and rail transport infrastructures*, JRC Scientific and Policy reports, Luxembourg: Publications Office of the European Union, doi:10.2791/15504
Qureshi, Chang & Al-Sadarani (2017). Strength and durability characteristics of biopolymer-treated desert sand, Geomechanics and Engineering 12, No. 5, 785–801.
Romero, E., Gens, A. and Lloret, A. 1999. Water permeability, water retention and microstructure of unsaturated compacted Boom clay. Engineering Geology 54(1-2): 117–127.
Sun DA, Sheng D, Xu XF (2007). Collapse behaviour of unsaturated compacted soil. Canadian Geotechnical Journal, 44, 673–686.
Sun and Gunasekaran (2009). The Viscosity of Xanthan Gum Grout with Different pH and Ionic Strength, Food Hydrocolloids: 23(1):165–74.
Standards Australia (2008) Methods for preparation and testing of stabilized materials, Method 4: Unconfined compressive strength of compacted materials, AS-5101-2008.
The Guardian (2021) At least 58 dead in Germany as heavy rains bring catastrophic flooding, accessed on 14/10/2021 https://www.theguardian.com/world/2021/jul/14/firefighter-drowns-and-army-deployed-amid-severe-flooding-in-germany
Take, W.A. and Bolton, M.D. Seasonal ratcheting and softening in clay slopes, leading to first-time failure. Géotechnique. 2011, 61(9), pp.757–769.
Yavorskyi, A. V., M. O. Karpash, L. Y. Zhovtulia, L. Y. Poberezhny and P. O. Maruschak (2017). "Safe operation of engineering structures in the oil and gas industry." Journal of Natural Gas Science and Engineering 46: 289–295.
Zohuriaan & Shokrolahi (2004) Thermal studies on natural and modified gums, Polymer Testing 23(5):575–9.

Eleventh International Conference on the Bearing Capacity of Roads, Railways and Airfields, Volume 2 – Hoff, Mork & Saba (eds)

Determining the impact of climate change on road infrastructure in Germany

Markus Clauß
Institute of Urban and Pavement Engineering, Technische Universität Dresden, Germany

Sebastian Pinnau
Institute of Power Engineering, Chair of Technical Thermodynamics, Technische Universität Dresden, Germany

ABSTRACT: Current Mechanistic-Empirical asphalt pavement design methodologies are based on the evaluation of the mechanical stresses caused by traffic loads and temperature effects. The material characteristics of asphalt strongly depend on temperature and, therefore, it is important to describe the thermal conditions of asphalt pavements during the life span in an accurate way.

In recent years, the influence of climate change on local climatic conditions has grown. Especially, droughts and heat waves in summer have caused significant damage to nature. This is indicative that the changes resulting due to climate change will have a pronounced impact on the temperature conditions of asphalt pavements in the future.

To determine the influences of climate change, numerical simulations were carried out and an extended analysis method for the determination of relevant temperature conditions was developed. With the help of a cluster method, significant profiles (mean temperature profiles) were derived from the hourly temperature states. These profiles take into account the characteristics of the road construction.

Using the method of mean temperature profiles and the design method according to the German ME asphalt pavement design methodology, a detailed analysis of the vulnerability of the transportation infrastructure in Germany was performed. Due to the large variance of local climatic conditions, strongly differing regional effects were determined. A clear north-south gradient was observed for fatigue cracking and development of ruts. Furthermore, it has been identified that climate change has a significant influence on the life span of asphalt pavements in particular regions.

1 INTRODUCTION

The mechanical durability of asphalt road pavements and their expected service life are highly dependent on environmental effects due to the temperature dependency of the material properties and the traffic loads.

Observations of the atmospheric temperature conditions over the past century have shown that a continuous increase in surface temperature could be detected within the period under consideration. The influence of Climate change is already affecting all regions on earth (Intergovernmental Panel on Climate Change 2021). Especially hot extremes and heavy precipitation have increased.

DOI: 10.1201/9781003222897-14

The results of regional climate simulations for Germany have shown a general trend of increasing temperatures as well as a simultaneous intensification of climate variance (Fischer and Schär 2010). The combination of these two effects results in little changes to the frequency of cold weather extremes, but causes increases in the intensity and frequency of warm weather extremes (Hartmann *et al.* 2013).

However, indications of these developments can already be identified at the present time. In the media, there have been reports all over the world about the consequences of high temperatures for the transportation infrastructure. A particularly extreme event was documented during the 2015 heat wave in India. Due to persistent high temperatures in New Delhi, extremely large plastic deformations occurred in certain areas as a result of the induced traffic loads. In the press, an increased probability of the occurrence of potholes - the article spoke of heat blisters on the upper side of the road surface - was noted for Germany (Neubauer 2015). However, railway infrastructure or concrete pavements were also affected. The mentioned damage pattern are still very rare at the moment, but can already be identified as an important factor when looking in detail at the sources of the damage. Considering the projected anomaly of the earth's surface temperature, it must be assumed that damage will occur more frequently and with a potentially higher level of damage.

In order to detect the influence of climate change on asphalt road pavements, detailed simulations were carried out. Based on a climate projection, the temperature conditions within the road pavement were calculated by using thermal simulations. Based on these simulations, the decisive temperature conditions and the corresponding profiles (mean temperature profiles) were determined by applying a clustering method. Finally, an analysis of the damage potential of the projected changes due to climate change has been carried out for Germany and recommendations derived from these simulations.

2 METHOD OF ANALYSIS

2.1 *Input data and thermal simulations*

In order to carry out thermal simulations, the boundary conditions within the analysis period must be available. For the calculation of the temperature conditions within road pavements, long-term climate simulations can be used as boundary conditions. In this analysis, the climate model REMO-UBA with the emission scenario A1B was used (Jacob 2005). This regional model was developed specifically for Germany and offers an extremely high spatial and temporal resolution of the data. This is absolutely necessary for realistic and meaningful simulations.

Emission scenarios describe the boundary conditions of the climate projections. The scenario used assumes that the development of the future world is accompanied by very strong economic growth. The world population will increase until the middle of the century and then decline. The use of new technologies will increase, with emphasis on the development of efficient systems. This will cause regions to converge economically, resulting in a homogenization of incomes. The A1 scenario family can be divided into three groups that describe atalternative paths of technological change in the energy systems. The group is divided into three further sub-groups (A1FI, A1T, A1B). For scenario A1B, it is assumed that a balanced use of fossil and non-fossil energy sources takes place.

Based on the results of climate simulations, characteristic input data for the thermal simulation were determined for each district in Germany (smallest territorial unit). For this purpose, area-averaged data sets were calculated from the node data of the climate model. The input data generated synthetically are representative for the respective district, whereby local extremes could possibly not be taken into account sufficiently well due to area-averaging.

The climatic parameters have a direct effect on the temperature conditions in road constructions. For the following calculations of the service life, these conditions must be known during the time of use. For this reason, a thermal model was developed to simulate the temperature

conditions in the depth of the road construction using climatic data. The focus of the model is to achieve a very high spatial and temporal resolution of the simulation results.

The structures for asphalt road constructions in Germany usually consist of an asphalt pavement package with several functional layers, an unbound frost protection layer and the subgrade. The basic design of the thermal model is shown schematically in Figure 1. To calculate the temperature distribution within the road structure, the energy balance for the road construction must be formulated, that describes the heat conduction in the road layers down to the subsurface, the irradiation from the sun and the sky, and the convective heat transfer between the road surface and the ambient air.

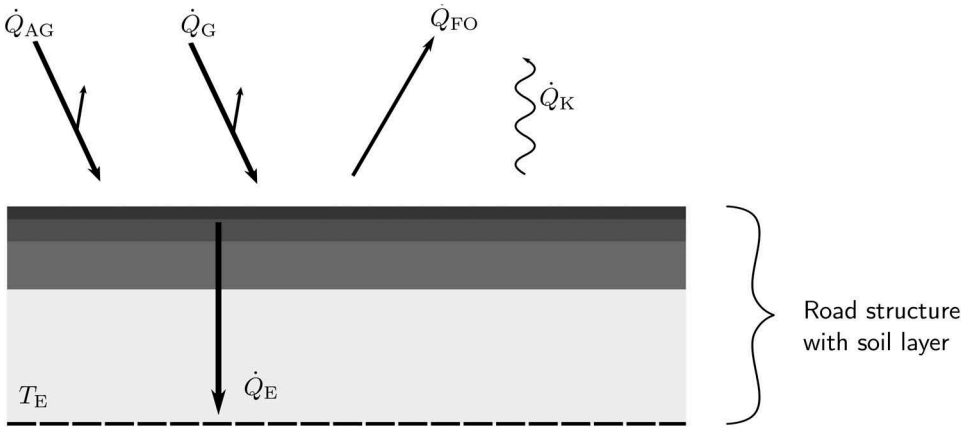

Figure 1. Radiation balance of a road construction.

The short-wave global radiation $\dot{Q}_G$ emitted by the sun and the long-wave atmospheric counter radiation $\dot{Q}_{AG}$ form the incoming radiant heat flux and are partially absorbed by the road surface. A portion of these heat fluxes is reflected by the road structure. Due to the temperature of the road surface, the radiant heat flux $\dot{Q}_{FO}$ is emitted. In addition, a convective heat flux $\dot{Q}_K$ is transferred by the air movement between the surroundings and the road surface. The remaining absorbed energy is dissipated as a heat flow $\dot{Q}_E$ conductive into the ground (Clauß *et al.* 2019).

Heat transport occurs between the individual layers of the road pavement as a result of thermal conduction. The implementation within the 1D layer model is realized by the Finite Volume Method (FVM). It is assumed that the temperature distribution in the depth direction is subject to continuous change, but that constant temperatures T_E (Figure 1) occur within a plane of the respective layers. This assumption is possible due to the large width and length in relation to the depth, so that boundary influences can be neglected. The consideration of time-varying boundary conditions in transient simulations requires the consideration of the heat storage capacity of all layers and the associated specific materials.

Using the hourly values of the simulation results of the climate model, the average annual near-surface air temperature were calculated and the deviation from the long-term mean value for the period 1960 to 2020 is shown in Figure 2. The results of this analysis reveal that moderate temperatures have been simulated for the past. From 2020 onwards, the influence of climate change increases significantly and there is a continuous rise in mean annual near-surface air temperature until the end of the century. The trend shows that a significantly higher thermal load will be expected on the transport infrastructure in the future.

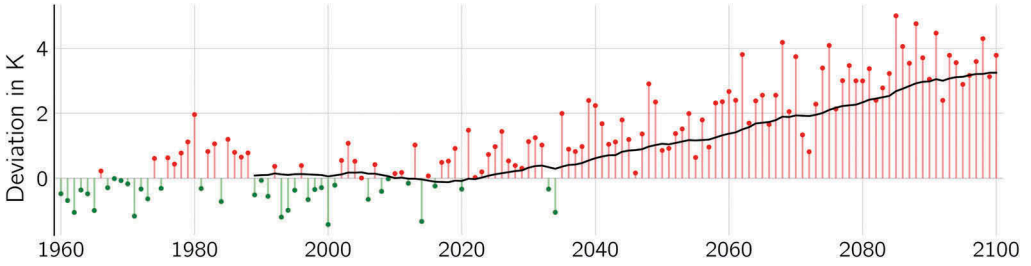

Figure 2. Annual near-surface air temperature of the city of Dresden, Germany; data from Jacob (2005).

2.2 *Mean temperature profiles*

The thermal simulations provide hourly temperature conditions in the road construction within the period under consideration. Within the computational design procedure, a limited number of characteristic temperature states are considered in order to reduce the computational effort. For this purpose, the temperature conditions of the road surface are currently divided into 13 (RDO Asphalt 2009) or up to 156 (Kayser 2007) classes and for each class a representative temperature curve is defined in depth. The resulting frequency distributions of the temperature classes are only related to the surface temperatures of the road structure. The shape of the standardized temperature profiles in the depth of the road construction are independent from the simulated data and are defined as defaults in the standard.

For this reason, a method was developed that can be used to extract relevant temperature conditions from the data and can therefore be used to determine specific temperature profiles for the design process. This method uses the cluster analysis algorithm k-means to determine relevant temperature conditions. The method is well scalable and offers an excellent separation of the temperature conditions. At the beginning of the analysis, so-called features are derived from the raw data of the thermal simulation. These characterize each hourly value of the data set. Among other things, the average temperature and the temperature gradient per layer were used as input parameters for the cluster analysis. Based on the cluster analysis, the characteristic temperature curves in depth (mean temperature profiles, Figure 3) are formed in a further step using the temperature profiles selected for each cluster. Finally, the maximum deviation between the cluster mean and the data is determined. If the deviation was very large, the number of clusters was increased and the analysis was carried out again.

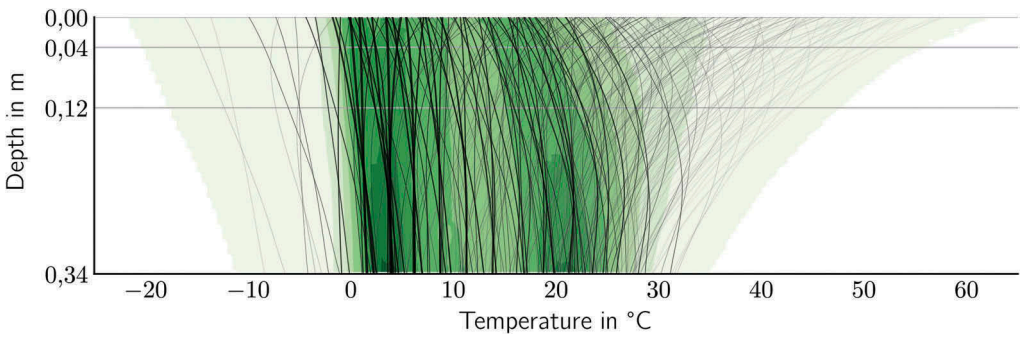

Figure 3. Mean temperature profiles; the green background shows the range of temperatures within a road construction.

Figure 4a shows the comparison of the deviations between the standardized profiles based on the normalized characteristic temperature profiles (Kayser 2007) and the corresponding

temperatures. The method shows that in a number of profiles strong differences of more than 14.0 were detected. This mainly affects the lower layers, with the largest errors in the asphalt base layer. The application of the method for determining the mean temperature profiles reduces the differences considerably. In all cases, a temperature difference of less than 8.0 could be achieved (Figure 4b). In a significant proportion, the difference even sinks below 4.0. With the method, a significant reduction of the calculation effort for determining the fatigue behavior or the rutting prediction can be achieved, with only minimal losses in the quality of the prediction.

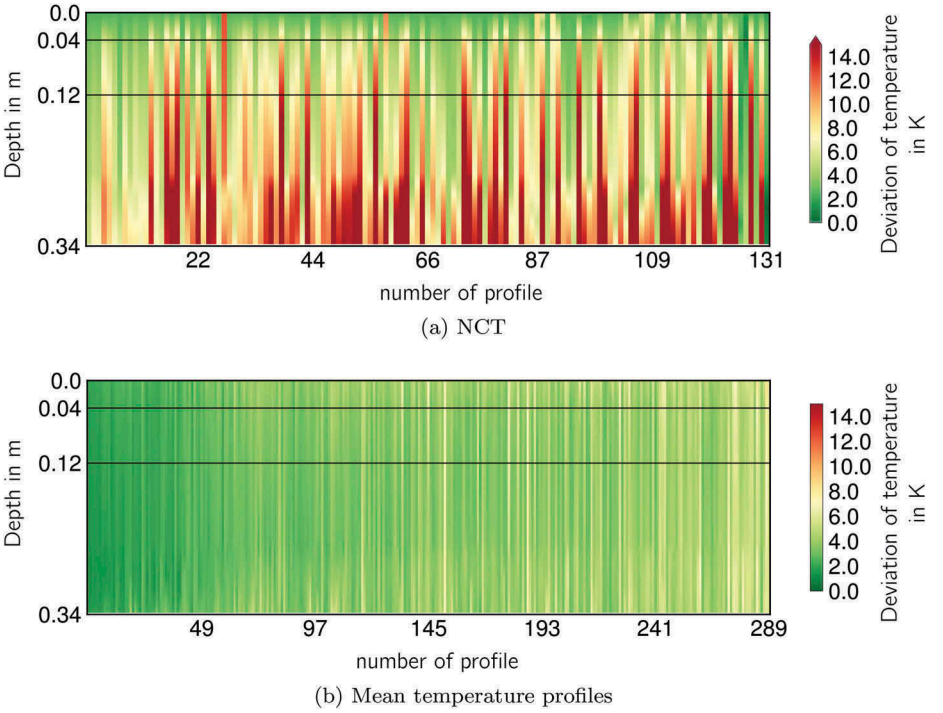

Figure 4. Comparison of the differences between the temperature profiles used for design to the respective temperature conditions; period 2020 to 2049; Dresden area.

In contrast to the procedure of the guideline, this method offers several advantages. On the one hand, material-specific influences on the thermal conductivity of the building materials are taken into account. Furthermore, the thickness of the road construction and the local climatic conditions are also taken into consideration. The use of the mean temperature profiles has a considerable effect on the increase of the quality of the design or prognosis analysis of asphalt road constructions.

2.3 *Pavement service life analysis*

In this part, the Mechanistic-Empirical asphalt pavement design methodology (RDO Asphalt 2009) is presented. Using this approach, the service life of a pavement structure with asphalt layers can be calculated depending on the locale climatic conditions, the traffic load and the material properties. In the following, the term service life is only used for verification at the beginning of fatigue cracking.

The different locale climatic conditions within Germany have an influence on the thermal conditions of the pavement structure. The design guide specifies, that a statistical analysis of

the surface temperature of the pavement structure has to be carried out. The individual surface temperatures were categorized into different temperature classes and the relative frequency of each class was determined. The variation of the temperature within the construction is described by a specific function and the course of the function depends on the surface temperature of the pavement structure. As described above, this approach was modified so that material-specific input data and the influence of local conditions on the relevant temperature profiles can be described. The following analyses were carried out on the basis of the mean temperature profiles.

Within the design process, mechanical material properties of each layer of the pavement structure can be taken into account. Figure 5 shows the material properties of the asphalt mixes used for this study. The characteristics of the materials have been determined within the project Clauß *et al.* (2019) by using the Cyclic Indirect Tensile Test (CIT-test) following the German guidelines (Asphalt-StB Part 26 2018). The master curves describe temperature and frequency dependency of the Young modulus (Figure 5a). Furthermore, long-term CIT tests were untertaken in order to determine the fatigue curves of the asphalt mixtures (Figure 5b). The laboratory tests were realized here at a temperature of 20.0 °C in accordance with Asphalt-StB Part 24 (2018).

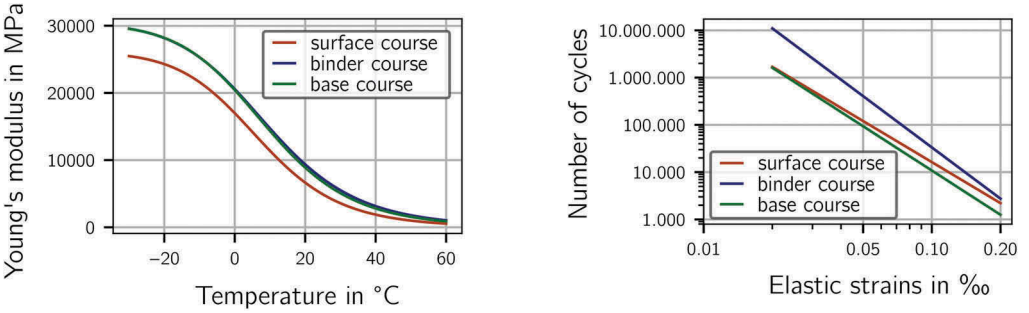

(a) Master curves

(b) Fatigue functions

Figure 5. Material parameters of the asphalt mixtures used at a load frequency of 10 Hz.

The rollovers by vehicles causes loads within he pavement structure. Below the tire footprint, compressive stresses (contact stress) are applied, which are distributed by the individual layers of the construction. The distribution of the load in depth depends, among other things, on the stiffness of the material. Since the material properties of asphalts are highly dependent on temperature, the load distribution is different at each point in time during the period of use. Furthermore, between the layers of asphalt there is usually a tight bonding. This means that the asphalt package functions as a kind of laminated plate. The deformations caused by the loading lead to tensile strains or compressive strains in the material. These strains lead to fatigue cracks in the asphalt pavements. With the numerical design methodology based on the RDO Asphalt (2009) this can be calculated and a service life analysis can be carried out based on the numerical results.

The evaluation of the individual conditions is made according to the Miner's linear damage hypothesis (Eq. 1). The different damage portions of a pavement structure are accumulated linearly and the total damage of the asphalt can be determined. The sum gives the remaining service life of the road structure. Each change of load consumes a small fraction of the service life. According to the Miner's linear damage hypothesis (Miner 1945), the magnitude of damage consumption is independent of the chronological order in which the damage occurs. In the field of pavement structure, this hypothesis is used to prove the individual damages against fatigue cracking.

$$\sum_{i=0}^{n} \frac{N_{ex,i}}{N_{per,i}} \leq 1 \tag{1}$$

The resulting principal strains in a pavement structure vary depending on the axle loads and the temperature distribution. The maximum permissible number of load cycles (Eq. 2) under defined condition is determined using the fatigue function (Figure 5b), taking a safety factor into account. The total amount of traffic within the period of usage of the pavement structure is divided according to the frequency of occurrence of defined temperature conditions and axle load classes (Eq. 2).

$$\text{(a) } N_{per,i} = \frac{SF}{F} \cdot a \cdot \varepsilon^{b} \quad \text{(b) } N_{ex,i} = N \cdot H_{climate} \cdot H_{loads} \tag{2}$$

where:

SF, F safety and adaption factor
a, b material parameters of the fatigue function
ε elastic strains
N total number of rollovers
Hclimate, Hloads frequency distributions of the axle loads and the temperature profiles

Because of the extremely high calculation effort and the fact that the material behaviour of asphalts cannot be fully described by the material examinations that are used, some simplifications were made in the procedure. The fatigue functions for the asphalts and the layer bonding between the asphalt layers were defined as temperature-independent. Furthermore, a uniform contact area and lane guidance were defined for the traffic loads. These assumptions have allowed the necessary batch simulations for the calculation of the service life as a result of fatigue to be calculated.

3 RESULTS

The results of the thermal calculations show that, analogous to the increase in the near-surface air temperature, there is also a rise in the temperatures in the asphalt surface course. Figure 6 shows the changes for a hypothetical road pavement at the city of Dresden. The average temperature in the asphalt surface layer in the period from 1960 to 2020 was simulated to be 12.8 °C. In the years 1960 to around 2030, the temperature level was roughly equal, with fluctuations of up to 1.0 °C in the long-term average. Like the near-surface air temperature, there is a continuous increase in the core temperatures in the asphalt surface course from around 2030. At the end of the century, a deviation of more than 4.0 °C in the long-term mean could be projected.

Further analyses of the simulation results have shown that thermal stresses are not uniform in Germany. The effects of climate change are locally specific and also lead to regional influences on the temperature conditions in road pavements. However, the areas have in common that temperatures within road structures will continuously increase in the coming decades. This means that low temperatures will not occur as often and it is assumed that there will be an intensification of freeze-thaw cycles as a result.

The simulation results continue to show that high temperatures and extreme values will increase significantly. The development of very warm temperatures (0.99 quantile value) presented in Figure 7 shows that a continuous increase in extreme values must be expected from the 2020s onwards. Based on the assumptions of the climate simulations, there is an extreme rise of high temperatures in asphalt pavements in the middle of the 21st century. The increase in high temperatures will continue to lead to a longer exposure of the road structure.

The calculated service life of the asphalt base layer using the simulation results on the basis of the Mean Temperature Profiles is shown in Figurefig:map. The service life of the asphalt base layer is normalized to the area average value for the period 2020 to 2059. For comparison,

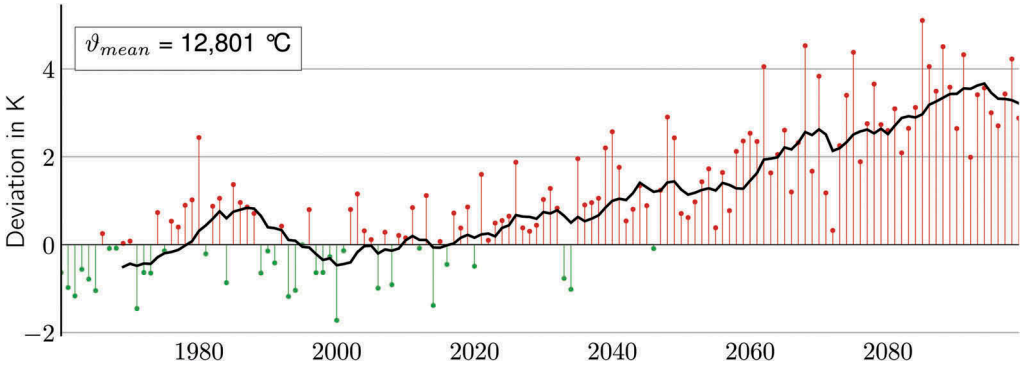

Figure 6. Annual mean temperature of the asphalt surface course in Dresden, Germany.

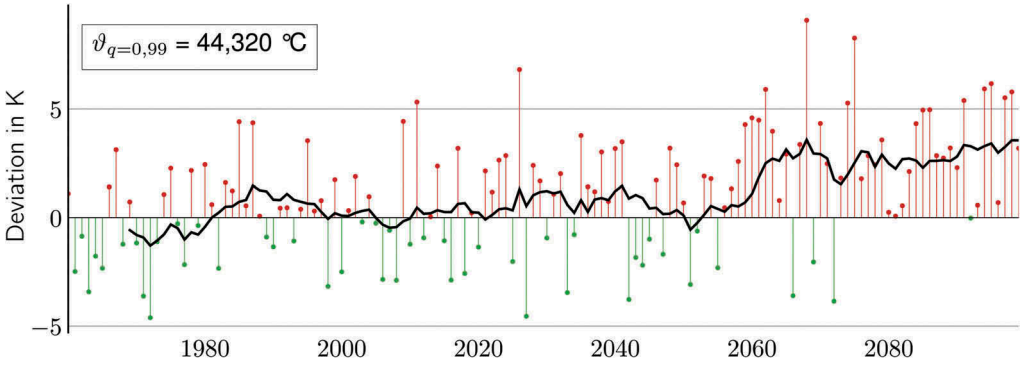

Figure 7. Annual 0.99 percentile temperature of the asphalt surface course in Dresden, Germany.

the service lives were normalized to the normed value. The results with the traffic opening from 2020 show that throughout Germany there is a relatively low potential for damage as a result of the climatic changes. In the southern region, there are slightly higher values, which are currently being taken into account through suitable adaptation strategies such as material optimization. As the effects of climate change progress, there will be a significant reduction in service life for all parts of Germany. Areas in southern Germany and central Germany will be particularly affected. The extent of these changes is remarkable, because in some areas a halving of the damage-free service life in the asphalt base course was calculated.

In Clauß (2021), the influence of climate change on the development of permanent deformations was also calculated. Due to the complexity, a detailed description of the procedure and the effects was not included here. However, the results of the investigations show a clear increase in the damage potential as a result of climate change, analogous to the effects described in this paper.

4 SUMMARY

There is a wide scientific community agreement that projected climate change will have consequences for people and societies. In Germany, in the field of climate impact research for transportation systems made of asphalt, there are only limited studies on the spatial impact of climate change. However, in Clauß (2021) it could be proven that the influence of climatic changes will lead to a significant impact on the transport infrastructure in Germany.

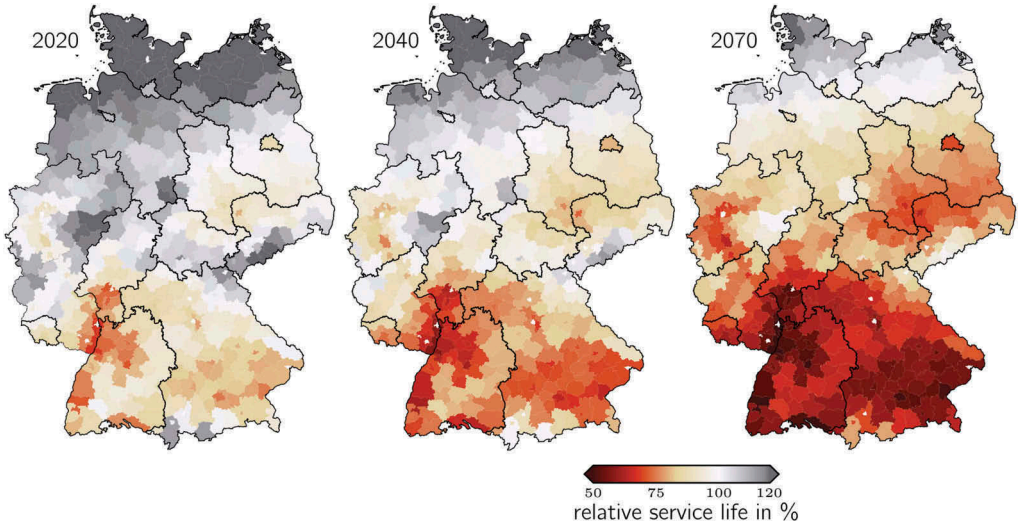

Figure 8. Comparison of calculated service life for the asphalt base layer for constructions completed in the years 2020, 2040 and 2070.

For the analyses, high-resolution climate data were processed and the thermal conditions in fictitious transportation systems within Germany were calculated on the basis of the synthetically generated data sets. The climatic changes in the period from 1960 to 2100 were evaluated using the extended approach for determining relevant temperature conditions according to the method of the Mean temperature profiles (Clauß 2021) and the resulting service life was calculated for different time periods. To detect the influence of the climate, the boundary conditions of the calculations were defined as constant in the analyses, so that the deviations can be derived from the climatic conditions alone.

The results show that a considerable influence could be determined throughout Germany. Areas in the south are particularly affected, but central Germany also suffers from a considerable reduction in the damage-free service life of asphalt road pavements.

From the findings of this study, it can be concluded that it is essential to develop adaptation strategies for asphalt transportation infrastructure. It is conceivable that the materials used and the construction structure will be adapted to the local traffic loads and climatic conditions. It is important that the input data used for service life predictions are not based on historical data, but are derived from forecasts and climate projections. The safety level to be achieved can be selected via the boundary parameters used, such as the choice of a suitable emission scenario. Furthermore, computational design procedures must be adapted for climate change.

REFERENCES

Asphalt-StB Part 24, 2018. Technische Prüfvorschriften für Asphalt (TP Asphalt-StB) - Teil 24 Spaltzug-Schwellversuch – Beständigkeit gegen Ermüdung.

Asphalt-StB Part 26, 2018. Technische Prüfvorschriften für Asphalt (TP Asphalt-StB) - Teil 26 Spaltzug-Schwellversuch – Bestimmung der Steifigkeit.

Clauß, M., 2021. *Erweiterte Analyse der thermischen Zustände in Straßenbefestigungen unter besonderer Berücksichtigung klimatischer Einflüsse und stoffspezifischer Materialparameter*. Dissertation. Technische Universität Dresden, Dresden.

Clauß, M., *et al*., 2019. *Untersuchung multifunktionaler Straßenbaumaterialien und Verbundwerkstoffe zur Nutzung solarer Energie und Verbesserung der Dauerhaftigkeit*. Dresden: Techische Universität Dresden, April.

Fischer, E.M. and Schär, C., 2010. Consistent geographical patterns of changes in high-impact European heatwaves. *Nature Geoscience*.

Hartmann, D., *et al*., 2013. *Observations: Atmosphere and surface*, vol. 9781107057999. Cambridge University Press, 159–254.

Intergovernmental Panel on Climate Change, 2021. *harvid|IPCC AR6 WG1 Summary for Policymakers|2021*.

Jacob, D., 2005. REMO A1B SCENARIO RUN, UBA PROJECT, 0.088 DEGREE RESOLUTION, RUN NO. 006211, 1H DATA. Available from: http://cera-www.dkrz.de/WDCC/ui/Compact.jsp?acronym=REMO_UBA_A1B_1_R006211_1H.

Kayser, S., 2007. *Grundlagen zur Erfassung klimatischer Einflüsse für Dimensionierungsrechnungen von Asphaltbefestigungen*. Dissertation. Technische Universität Dresden.

Miner, M., 1945. Cummulative damage in fatigue. *Journal of Applied Mechanics*, 12 (3).

Neubauer, D., 2015. Düsseldorf schmilzt dahin: Asphalt so weich wie pudding – sperrungen auf gruner- und spichernstraße. www.report-d.de.

RDO Asphalt, 2009. Richtlinien für die rechnerische Dimensionierung des Oberbaus von Verkehrsflächen mit Asphaltdeckschicht.

Full scale testing; HVS, LTPP, etc.

Eleventh International Conference on the Bearing Capacity of Roads, Railways and Airfields, Volume 2 – Hoff, Mork & Saba (eds)

Laboratory and full scale pavement evaluation of cracking potential of mixtures containing RAP

F. Leiva
National Center for Asphalt Technology, Auburn University, Alabama, USA

G. Sholar
Florida DOT, State Materials Office, Florida, USA

ABSTRACT: The objective of this experiment was to evaluate cracking potential of asphalt mixtures containing RAP in the laboratory and in the field. A secondary objective of this work was to characterize the mixtures' properties in the laboratory to determine which cracking tests might most successfully predict cracking resistance in the field. Four mixtures were placed in 100-foot test strips at the NCAT Test Track in the 2015 test cycle. The mixtures varied in terms of binder type (PG grades: 64-28 and 76-22) and recycled material content (20, 25 and 30% RAP). The mixtures were evaluated for cracking potential using five different tests: Illinois flexibility index test (I-FIT), Energy ratio from Florida, Cantabro test, Overlay test (OT) – NCAT modified and dynamic modulus test. 20 million ESALs of traffic have been applied to all sections. Laboratory results did not completely exhibit expected trends in terms of cracking potential. The mixture with the highest content of RAP and highest critical performance temperature (30% RAP, PG 76-22) was not the worst cracking performer. However, the mixture with the softest binder was the top performer. With regards to field performance, all four sections have shown no significant differences in rutting, ride quality and texture. On the other hand, after 15 million ESALs, there is significant cracking in all sections (from 6% to 19% per lane). All sections followed the expected cracking trend but the section with the highest RAP content. At 15 million ESALs, Energy Ratio and Cantabro test results have shown good correlations with field cracking performance with R^2 values over 0.7.

Keywords: Cracking, accelerated testing, RAP, energy ratio, IFIT, Cantabro, overlay

1 INTRODUCTION

As many state agencies have successfully mitigated rutting as a primary cause of pavement deterioration, more emphasis has been placed on identifying properties of mixtures that may influence the overall durability of the pavement structure. One such distress that affects durability is top-down cracking, which has been documented worldwide. The Florida DOT and the University of Florida were some of the first to recognize the widespread nature of this distress with over 90% of cracking in the state of Florida categorized as top-down (Wang et al. 2007).

As the name implies, these cracks form at the top of the pavement structure and are load-related, as they tend to originate in the wheel path. However, Roque et al. note the complex interaction of load, thermal, and aging effects as contributing to top-down cracking. They further explain that after reviewing a wide variety of material characteristics, there is not one single mixture property that could reliably discern between acceptable and poor cracking performance (Roque et al. 2004).

DOI: 10.1201/9781003222897-15

1.1 *Objective and scope*

The objective of this experiment was to determine which asphalt mixtures were more prone to surface cracking. A secondary objective of this work was to characterize the mixtures' properties in the laboratory to determine which cracking tests might most successfully predict cracking resistance. To complete this research, four mixtures were placed in 100-foot test strips in sections E7 and E8 during the reconstruction of the 2015 test cycle. The mixtures varied in terms of binder type (PG grade) and recycled material content. Only one lift per section was replaced with an average thickness of 1.5 inches

1.2 *Mix design and construction*

Four mixtures were designed at the NCAT laboratories for this experiment. All mixtures utilized asphalt binder modified with styrene-butadiene-styrene (SBS) and used a similar aggregate skeleton. The change in the RAP content appears to have influenced the combined gradation, by a magnitude of 10% in some cases (i.e. %passing #8 sieve Table 1). The main difference among all four mixtures is the amount of reclaimed asphalt pavement (RAP), which varies from 20% to 30%. Mixture gradations, base binder grades, volumetrics, and construction data for all four mixtures are provided in Table 1. The performance grade (PG) of the binder for section E8B was originally intended to be a polymer modified PG 58-28 binder. However, the final product was a PG 64-28 after the polymer modification.

Mixtures E8-1A and E8-1B had the same aggregate structure with a different binder. In this study, volumetric design was performed on E8-1A using the PG 76-22 only and no verifications were made on the mixture with the polymer PG 58-28 modified binder because it was not available to NCAT prior to construction. The Cantabro test (ASTM D 7064) was performed on design samples at three binder contents (5.0, 5.5 and 6.0%) and quality control samples. Table 1 shows calculated Cantabro percent of weight loss by interpolation at optimum binder content for design samples.

Table 1. Florida DOT mixture characteristics.

Mix Design Parameters	E7-1A	E7-1B	E8-1A	E8-1B	E7-1A	E7-1B	E8-1A	E8-1B
Design Method Compactive Effort	Superpave 100 Gyrations							
Results	Design Data				Quality Control Data			
Binder Grade	76-22	76-22	76-22	58-28	76-22	76-22	76-22	64-28
Modifier Type	SBS							
Total Binder Content, %	5.2	5.2	5.1	5.1	4.8	5.0	5.0	5.0
Effective Binder Content, %	4.6	4.5	4.4	4.4	4.2	4.4	4.3	4.3
% RAP	20.9	26.4	31.8	31.8	20.0*	23.9*	28.9*	28.8*
Air Voids, %	4.0	4.0	4.0	4.0	4.3	4.0	3.5	4.5
Voids in Mineral Aggreg., %	14.6	14.5	14.4	14.4	14.0	14.0	14.0	14.0
Voids Filled with Asphalt, %	73	72	72	72	69	72	74	69
Cantabro % Loss	5.89	6.59	6.30	NA	5.41	5.45	4.55	3.49
Tensile Strength Ratio, %	96.3	97.8	92.4	NA				
Construction Data								
Lift Thickness, in	1.5				1.8	1.9	1.8	1.7
Temperature at Plant, °F					340	340	340	340
Average Mat Compaction, %					93.9	91.6	92.5	93.5

* Plant Settings

2 LABORATORY TESTING

While the field experiment was being conducted, materials (plant-produced loose mix and asphalt binder) that had been sampled during construction were taken back to the NCAT laboratory for evaluation. The binders were characterized under the Superpave Performance Grading system. The mixtures were evaluated for cracking potential using five different tests: Illinois flexibility index test (I-FIT), Energy ratio from Florida, Cantabro test, Overlay test (OT) – NCAT modified and dynamic modulus test.

2.1 *Binder characterization*

The virgin binders for the asphalt mixtures were sampled from the tank at the plant and tested in the NCAT binder laboratory to determine the PG grade in accordance with AASHTO M 320. The blended asphalt binders were extracted and recovered using AASHTO T 164 Method A (using Trichloroethylene - TCE) and ASTM D 5404 before AASHTO M 320 was conducted. The test results for these two procedures are shown in Tables 2 and 3. Table 4 provides the test requirements from AASHTO M332, non-recoverable creep compliance. In addition to testing the virgin binders and extracted binders, the PG properties of the RAP binder were determined.

The results indicated a significant increase in the stiffness of both binders when RAP was added to the mix. Both critical high and low temperatures of the PG 76-22 binder were increased to 94°C and -16°C, respectively. Although the same trend was observed for the PG 64-28 binder, the critical low temperature was more affected with an increase in temperature from -28°C to -16°C.

Table 2. Florida DOT cracking study performance grades.

			T_{crit}, °C							
Mix/ Material	Extracted	% RAP	High Original	High RTFO	Interm.	Low S	Low m	True High PG	True Low PG	PG
76-22	No	NA	80.2	80.9	21.2	-29.4	-26.4	80.2	-26.4	76-22
64-28	No	NA	67.5	67.5	11.0	-35.6	-33.2	67.5	-33.2	64-28
E7-1A	Yes	20	97.1	94.0	24.1	-26.7	-19.5	94.0	-19.5	94-16
E7-1B	Yes	25	100.7	97.6	23.1	-28.5	-19.3	97.6	-19.3	94-16
E8-1A	Yes	30	99.6	96.2	22.7	-25.8	-19.1	96.2	-19.1	94-16
E8-1B	Yes	30	92.0	89.1	21.1	-30.2	-18.5	89.1	-18.5	88-16
RAP	Yes	100	115.4	112.0	30.5	-22.9	-13.8	112.0	-13.8	112-10

2.2 *Dynamic modulus (AASHTO TP 79)*

Dynamic modulus (E*) testing was conducted in accordance with AASHTO TP 79 on the four previously described mixtures. This testing was performed using an Asphalt Mixture Performance Tester (AMPT). Specimens were produced in accordance with AASHTO PP 60. The air voids of the prepared specimens were 7 ± 0.5%.

To provide the necessary information for mechanistic-empirical (M-E) pavement analyses, the three samples of the four completed mix designs were tested using three temperatures (4, 20, and 45oC) and three frequencies (10, 1, and 0.1 Hz) in an unconfined state. The mixes were also tested at the 0.01 Hz frequency at the high test temperature. This testing produced a data set for generating master curves for all four mixtures using the procedure outlined in AASHTO PP 61.

While the master curves are not direct indicators of performance, they are used in mechanistic pavement design and can give an indication of relative mixture stiffness. This is particularly useful for mixtures containing RAP where the degree of binder blending is unknown. For the four master curves (Figure 1), the mixture with the PG 64-28 binder was the "softest" at all

temperatures and frequencies. On the other hand, the mixture with PG 76-22 and 25% RAP showed higher dynamic moduli at almost all temperatures and frequencies. Table 3 shows the master curve coefficients and regression parameters for all mixtures.

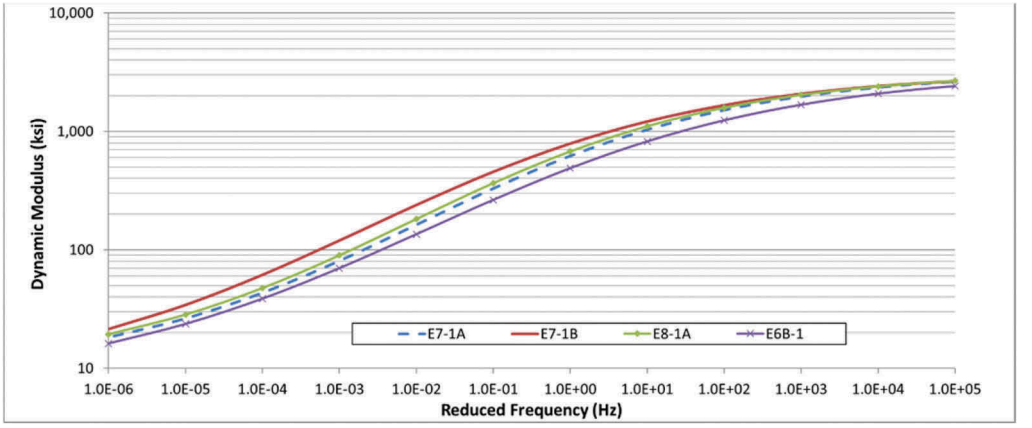

Figure 1. Florida DOT cracking study master curves.

Table 3. Master curve coefficient and regression parameters.

Mix	Max E*, Ksi (MPa)	Min E*, Ksi (MPa)	Beta	Gamma	EA	R^2	Se/Sy
E7-1A	3211 (22137)	8.9 (61.4)	-0.950	-0.488	199954	0.998	0.031
E7-1B	3190 (21992)	7.2 (49.5)	-1.215	-0.456	204156	0.998	0.028
E8-1A	3185 (21956)	9.1 (62.7)	-1.025	-0.490	202090	0.998	0.034
E8-1B	3212 (22145)	6.8 (47.0)	-0.819	-0.439	206247	0.998	0.033

The results of statistical analyses conducted at 20°C (intermediate temperature related to cracking) and frequencies are shown in Table 4. The Tukey-Kramer test ($\alpha = 0.05$) was used to determine where these statistical differences occurred and how the mixtures grouped within each section. For each temperature-frequency combination, mixtures with the same letter were not statistically different. At 20°C, E* values for the 25% RAP, PG 76-22 mixture were statistically higher (potentially more susceptible to cracking) and the E* values for the 30% RAP, PG 64-28 mixture tended to be statistically lower ((potentially less susceptible to cracking).

Table 4. E* statistical grouping (Tukey-Kramer Test at $\alpha = 0.05$).

Mix ID	20°C - 10 Hz			20°C - 1 Hz			20°C - 0.1 Hz		
E7-1B - FL 25% RAP, PG 76-22	A			A			A		
E8-1A - FL 30% RAP, PG 76-22	A	B			B			B	
E7-1A - FL 20% RAP, PG 76-22		B			B			B	C
E8-1B - FL 30% RAP, PG 64-28			C			C			C

2.3 *Overlay test*

The overlay test was performed in accordance with Tex-248-F using the OT kit designed for the IPC Global AMPT. Four replicates with air voids between 6 and 8% were tested at 25°C in controlled displacement mode. Tex-248-F specifies a maximum opening displacement of 0.025 inches. There is no definitive pass/fail criterion for the OT, with minimum recommended cycles to failure at the above parameters ranging between 150 and 700 depending on the type

of mixture tested (Sheehy E., 2013; Chen D., 2008; Zhou et al. 2001). An NCAT modified method of this test was also performed with a higher frequency (1 Hz), and modified failure criteria where the peak value of the normalized load multiplied by number of cycles (NL x Cy) indicates the point of failure.

Figure 2 provides the OT results for the four mixtures. None of the mixtures performed well in this test, highlighting the need for state-specific parameters in performance tests to match field performance. Statistical analyses indicated that all mixtures were not statistically different from each other when following the Texas OT standard practice. However, when the modified NCAT method was used, the 25% RAP PG 76-22 (E7-1B) mixture was the only statistically different mixture and had the lowest number of cycles to failure. Figure 2 also suggest that the lack of statistical significance is largely due to the relatively high variability noted with mixture E8-1B compared to the others.

The Critical Fracture Energy (crack initiation parameter) and Crack Resistance Index (crack propagation parameter) were determined from the OT test results according to Tex-248-F-2017 test procedure. These results are shown and compared against the number of cycles to failure in Table 5. Both cracking parameters were able to identify mix E7-1B as the only statistically different mixture with the highest initiation and propagation parameters. This indicates that mix E7-1B would not permit easily the initiation of a crack but it would not attenuate the rate of the propagation of the crack after it is initiated as well as the other mixtures. The overall variability of the results when computing these parameters was significantly decreased as observed with the coefficient of variability (COV), especially for the crack initiation parameters with COV values below 11%.

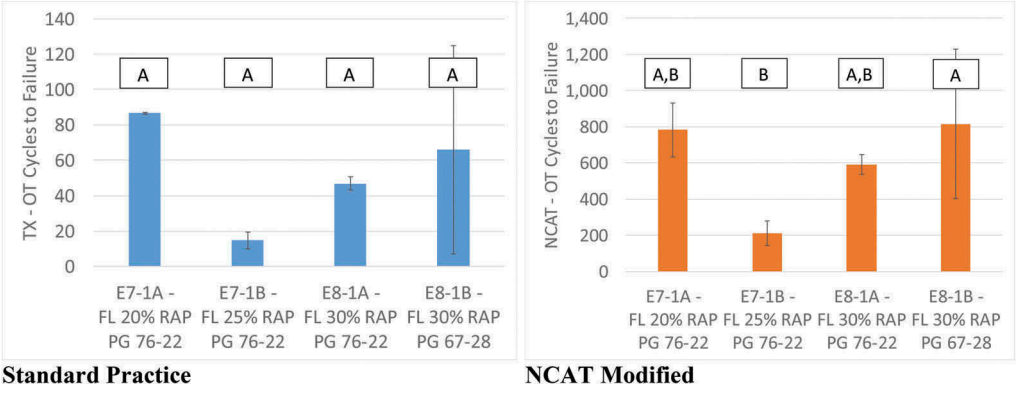

Figure 2. Texas overlay tester results.

2.4 *Energy ratio*

The energy ratio test procedure was developed to assess an asphalt mixture's resistance to top-down or surface cracking (Roque et al. 2004). This testing procedure has been used in past research cycles at the NCAT Test Track as a predictor of whether a mixture might be susceptible to top-down cracking (Timm et al. 2009). Energy ratio is determined using a combination of three tests: resilient modulus (M_r), creep compliance, and indirect tensile strength.

The creep compliance test was performed as described in AASHTO T 322-07; however, the temperature of the test was 10°C with a test duration of 1000 seconds. Finally, the tensile strength and dissipated creep strain energy at failure ($DCSE_f$) were determined from the stress-strain curve of the given mixture during the indirect tensile strength test. Detailed testing procedures and data interpretation methods for the three testing protocols are described elsewhere (Roque et al. 2004; Timm et al. 2009; Roque et al. 1997). The target air voids for the specimens was 7 ± 0.5%.

Table 5. OT cracking parameters.

	N_f (93%)				Crack Propagation Parameter				Crack Initiation Parameter			
Mix	Ave	Std Dev	COV	Group	Ave	Std Dev	COV	Group	Ave	Std Dev	COV	Group
E7-1A	87	0.6	1%	A	0.49	0.03	7%	A	2.77	0.14	4.9%	A
E7-1B	15	4.6	31%	A	0.99	0.23	23%	B	3.48	0.26	7.5%	B
E8-1A	47	3.8	8%	A	0.53	0.05	10%	A	2.89	0.31	10.7%	A
E8-1B	66	59	89%	A	0.61	0.22	36%	A B	2.59	0.12	4.7%	A

Data analysis was performed using a software package developed at the University of Florida. The details of the software operation are documented elsewhere (Roque et al. 1997). Recommended thresholds for the energy ratio as a function of rate of traffic are also documented elsewhere (Roque et al. 2004), with a minimum energy ratio of 1.95 for high traffic conditions such as the ones used at the NCAT Test Track. A higher energy ratio provides more resistance to surface cracking. Additionally, a DSCE at failure of less than 0.75 kJ/m3 has been used to identify excessively brittle mixes in the field (Roque et al. 2004).

Table 6 shows the energy ratio results for the four mixtures in the cracking study. When comparing these data, all mixtures except the 25% RAP, PG 76-22 mixture had energy ratios above 1.95 and DSCEf values higher than 0.75 kJ/m3. Therefore, three mixtures are expected to sustain over one million equivalent single axle loads (ESALs) per year and one mixture could resist between 250,000 and 500,000 ESALs per year, although it may be too brittle and negatively affect cracking performance. One of the objectives of this study was to examine the potential impact of using a softer polymer modified grade on resistance to cracking, and several of the results shown in Table 8 suggest this to be the case. For instance, mixture E8-1B with a PG 64-28 virgin binder, had the highest DSCEf value and it showed higher ductility compared to the other mixtures (highest failure strain).

Table 6. Florida DOT cracking study energy ratio results.

Mix	Tensile Strength (MPa)	M_r (GPa)	Fracture Energy (kJ/m^3)	$DCSE_f$ (kJ/m^3)	Failure Strain	Creep Compliance Rate	ER
E7-1A	2.57	10.06	4.2	3.87	2,152	4.092E-09	5.09
E7-1B	2.05	12.41	0.8	0.63	648	2.354E-09	1.30
E8-1A	2.49	13.66	3.1	2.87	1,522	2.279E-09	6.12
E8-1B	2.16	9.02	5.8	5.54	3,301	4.929E-09	5.26

2.5 *Fracture energy and flexibility index test*

The development of flexibility index (FI) threshold values is ongoing, but research conducted for the Illinois Center for Transportation by the University of Illinois at Urbana-Champaign has made some lab to field comparisons between FI and field cracking performance (Al-Qadi et al. 2015). Currently, a very aggressive preliminary recommendation of 8 has been given for minimum flexibility index.

The Illinois flexibility index test (I-FIT) was performed at NCAT for this project using an I-FIT device. Semi-circular asphalt specimens were prepared to an air void level of 7.0 ± 0.5% after trimming. The test results from all mixtures are given in Table 7. All mixtures had FI values below the preliminary criterion, but significant differences were observed. The 30% RAP, PG 64-28 mixture (section E8B) was statistically the top performer, followed by the 20% RAP, PG 76-22 mixture (section E7A), followed by the two remaining sections at the same level.

Finally, Table 8 shows a ranking analysis to organize all four mixtures from one to four with one performing best based on several laboratory cracking related parameters. Most parameters put the 30% RAP, PG 64-28 mixture (section E8B) as the most resistant to cracking and the mixture with 25% RAP, PG 76-22 (section E7B) as the least resistant. Fitting

Table 7. I-FIT test results.

Mix	Average of Fracture Energy (J/m2)	Std. Dev. of Fracture Energy (J/m2)	Average of Flexibility Index (FI)	Std. Dev. of Flexibility Index (FI)	Statistical Group
E7-1A	1,688	73	3.54	0.37	B
E7-1B	1,344	83	1.82	0.34	C
E8-1A	1,434	159	1.86	0.55	C
E8-1B	1,399	119	5.59	0.80	A

parameters used to describe the shape of the mastercurve sigmoidal function and the E* value obtained at 20°C and 10 Hz were also incorporated in this analysis. The inflection point frequency parameter -β/γ is being studied as a potential cracking susceptibility indicator (Rastegar R., 2016, Leiva et al. 2016). The lower this parameter, the more susceptible the mixture could be to fatigue cracking. The stiffness of the mixture at intermediate temperatures could also be used as a cracking indicator (E* at 20°C and 10 Hz). Finally, the Cantabro test has provided strong relationships to fatigue cracking in the field and seems to be able to detect differences among common mixture variables (West et al. 2017). In this case, Cantabro percentage loss was able to identify the top performer and the bottom performer similarly to other laboratory performance tests.

Table 8. Laboratory test results ranking analysis.

Mix ID	PG Grade	ER	OT-NCAT	FI	Cantabro %Loss	-β/γ (Inflection Point)	E* 20C, 10 Hz (ksi)	
E7-1A	94-16	5.1	782	3.5	5.41	-1.95	986	
E7-1B	94-16	1.3	212	1.8	5.45	-2.66	1154	
E8-1A	94-16	6.1	591	1.9	4.55	-2.09	1042	
E8-1B	88-16	5.3	816	5.6	3.49	-1.87	795	
Mix ID	%RAP	Individual Ranking						Combined Ranking
E7-1A	20	3	2	2	3	2	2	2
E7-1B	25	4	4	4	4	4	4	4
E8-1A	30	1	3	3	2	3	3	3
E8-1B	30	2	1	1	1	1	1	1

3 FIELD PERFORMANCE

The final phase of the evaluation was to correlate the laboratory performance of these mixtures to their performance at the Test Track. Figure 3 shows cracking (express as percentage of the lane) for all sections from 0 to 20 million ESALs of traffic. The 25% RAP, PG 76-22 mixture was the first to crack in the field (E7B). However, cracking after 10 million ESALs was the highest for the 20% RAP, PG 76-22 mixture (E7A) and the lowest cracking was reported for the 30% RAP, PG 76-22 mixture (E8A), which also was the last mix to crack. At the end of the study, Section E7A showed 19.3% cracking followed by Section E7B with 19.2% cracking. Cracking severity stayed low until the end of the study for all the sections. It was observed that after 5 million ESALs, cracks did not change much in length but increased in width (from approximately 3 to 5 mm) for Sections E7A and E7B. It was also determined that most cracks were reflective cracks, based on the cracking map created prior to the placement of these mixtures. Figure 4 shows pictures of representative cores from each section. The same cracking pattern was observed on all the cores, where the cracks were found throughout the entire thickness of the core which includes the 1.5 in lift built for this experiment and about 8 to 10 inches from the previous cycles.

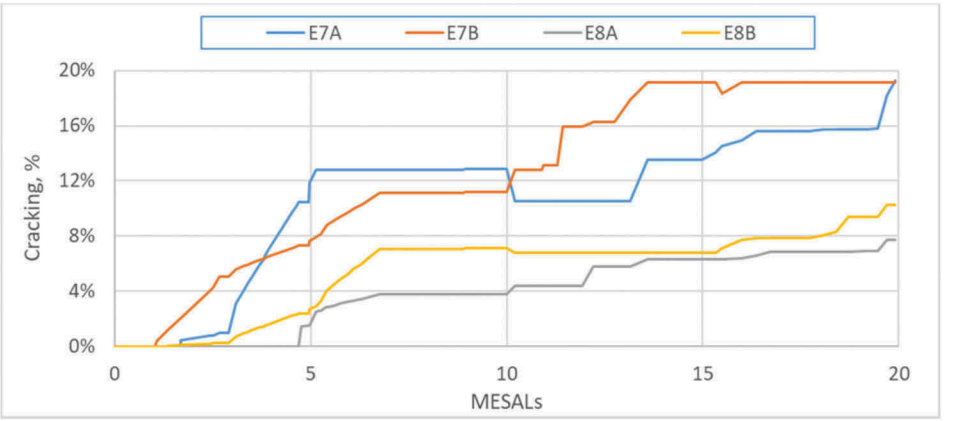

Figure 3. Measured cracking.

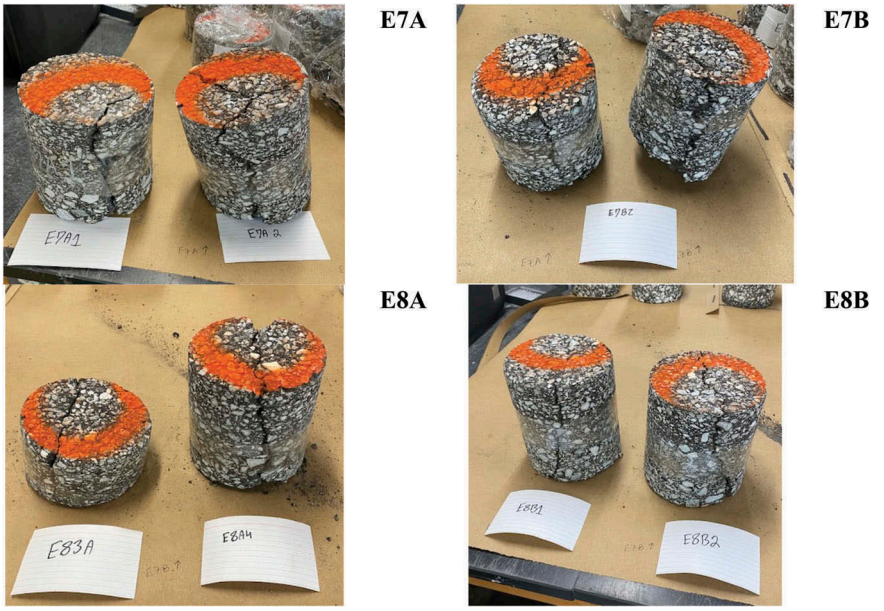

Figure 4. Extracted samples for cracking origin evaluation.

Pearson correlations were also developed between the average laboratory mixture properties/results and the percent cracking in the field at 10 and 20 million ESALs with results provided in Table 8. Despite some good correlations among laboratory parameters, percent field cracking showed a good correlation with Cantabro mass loss (percent) only. The Energy Ratio, and the crack initiation parameter from the OT-TX showed fair correlation (tan highlighted fields) with field cracking, as shown in Table 11. These correlations correspond to linear relationships between variables. Other best fit trend lines were analyzed (exponential and polynomial), but no improvement in the correlation coefficient was observed.

In addition to field measurements, core samples were obtained from every section after two years of trafficking to evaluate the change in binder grade due to aging. The whole core/layer thickness was used to extract and recover binder. Table 9 shows the performance grade of all binders after two years of trafficking. High critical temperature was little affected by aging. The true high PG value increased 3% on average. On the other hand, the low critical temperature was increased by two PG grade levels going from -16°C to -10°C; therefore, aging

Table 9. Pearson correlation analysis of laboratory vs. field results.

Cracking, % Lane	10 Million ESALs	20 Million ESALs
Mr (GPa)	-0.40	-0.19
DCSEf (kJ/m3)	-0.23	-0.44
ER	-0.55	-0.68
FI	0.01	-0.20
OT-TX-PRO	0.29	0.44
OT-TX-INI	0.30	0.50
E* 20C, 10 Hz (ksi)	0.24	0.45
Cantabro %Loss	0.66	0.79

produced a significant effect on low temperature susceptibility to cracking. The true low PG increased 39% on average. Moreover, as shown in Table 10 all mixtures became more susceptible to block cracking as suggested by the decrease in the Delta Tc parameter. On average, this parameter decreased 46%. Delta Tc is defined as the numerical difference between the low continuous grade temperature determined from the Bending Beam Rheometer (BBR) stiffness criteria (the temperature where stiffness, S, equals 300 MPa) and the low continuous grade temperature determined from the BBR m-value (the temperature where m equals 0.300).

Table 10. Florida DOT cracking study performance grades after two years.

	True PG					Delta T_c	
Test Section	Time Zero High	Time Zero Low	Two-year High	Two-year Low	PG After two years	Time Zero	Two-year Sample
E7-1A	94.0	-19.5	97.6	-10.0	94-10	-7.1	-10.9
E7-1B	97.6	-19.3	99.9	-11.5	94-10	-9.1	-13.4
E8-1A	96.2	-19.1	96.9	-13.1	94-10	-6.7	-9.7
E8-1B	89.1	-18.5	92.4	-11.7	88-10	-11.7	-16.6

4 CONCLUSIONS

The results of this study support the following conclusions.

- Laboratory results did not exhibit expected trends in terms of cracking potential. The mixture with the highest content of RAP and highest critical performance temperature (30% RAP, PG 76-22) was expected to be more susceptible to cracking. However, laboratory testing showed mixed results. On the other hand, the mixture with the softest binder did exhibit less susceptibility to cracking based on laboratory results. In addition, the use of a softer modified binder did not show significant differences in field performance (Section E8B with a softer binder compared to E8A).
- After 20 million ESALs of traffic, percent field cracking showed good correlation with Cantabro loss and fair correlation with Energy Ratio.
- After 20 million ESALs of traffic, cracking in the test sections was classified as low severity and the overall field performance was fair with cracking less than 20% and two cases with less than 8%.
- After inspection of cracking maps and extracted samples, the majority of measured cracks for these sections can be characterized as reflective.
- After two years of trafficking, the low critical temperature and Delta Tc parameter were the most affected by aging, thus increasing cracking susceptibility. These parameters seemed also to identify the mixture of section E8-1A as the least susceptible to cracking.

- Field aging compared to the laboratory aging level may potentially influence the lack of correlation between the measured field cracking and laboratory parameters.

REFERENCES

Al-Qadi, I., H. Ozer, J. Lambros, A. El Khatib, P. Singhvi, T. Khan, J. Rivera Pérez, and B. Doll. *Testing Protocols to Ensure Performance of High Asphalt Binder Replacement Mixes using RAP and RAS*. Illinois Center for Transportation Series No. 15-017, Illinois Center for Transportation, University of Illinois at Urbana-Champaign, 2015.

Chen, D. *Field Experiences with RDD and Overlay Tester for Concrete Pavement Rehabilitation*. ASCE Journal of Transportation Engineering, 2008, pp. 24–33.

Leiva-Villacorta F., A. Taylor, and J. Fort. *Analysis of High-Modulus Asphalt Concrete (HMAC) Mixtures Design Methodology Containing Recycle Material*. Presented at Transportation Research Board 2018 Annual Meeting, Washington D.C., 2016.

Rastegar, R. *Plant versus Laboratory Production: Impact on Measure Properties of Mixtures with RAP and RAS*. Presented at Transportation Research Board 2016 Annual Meeting, Washington D.C., 2016.

Roque, R., B. Birgisson, C. Drakos, and B. Dietrich. *Development and Field Evaluation of Energy-Based Criteria for Top-Down Cracking Performance of Hot Mix Asphalt*. Journal of the Association of Asphalt Paving Technologists, Vol. 73, 2004, pp. 229–260.

Roque, R., W. G. Buttlar, B. E. Ruth, M. Tia, S. W. Dickison, and B. Reid. Evaluation of SHRP *Indirect Tension Tester to Mitigate Cracking in Asphalt Concrete Pavements and Overlays*. Final Report FDOT B-9885. University of Florida, Gainesville, Fla., 1997.

Sheehy, E. *Case Study: High RAP Pilot Project*. Presented at New Jersey Asphalt Paving Conference, March 6, 2013.

Timm D. H., G. A. Sholar, J. Kim, and J. R. Willis. *Forensic Investigation and Validation of Energy Ratio Concept*. In Transportation Research Record: Journal of the Transportation Research Board, No. 2127, Transportation Research Board of the National Academies, Washington, D.C., 2009, pp. 43–51.

Wang, J., B. Birgisson, and R. Roque. *Windows-Based Top-Down Cracking Design Tool for Florida Using Energy Ratio Concept*. In Transportation Research Record: Journal of the Transportation Research Board, No. 2037, Transportation Research Board of the National Academies, Washington, D.C., 2007, pp. 86–96.

West R., C. Van Winkle, S. Maghsoodloo, and S. Dixon. *Relationships between Simple Asphalt Mixture Cracking Tests Using N design Specimens and Fatigue Cracking at FHWA's Accelerated Loading Facility*. Road Materials and Pavement Design, 18(sup4), 2017, pp. 1–19.

Zhou, F., S. Hu, D. Chen, and T. Scullion. *Overlay Tester: Simple Performance Test for Fatigue Cracking*. In Transportation Research Record: Journal of the Transportation Research Board, No. 2001, Transportation Research Board of the National Academies, Washington, D.C., 2007, pp. 1–8.

Eleventh International Conference on the Bearing Capacity of Roads, Railways and Airfields, Volume 2 – Hoff, Mork & Saba (eds)

The impact of tracked farm vehicles upon small rural roads

S. Baltzer, H.H. Thustrup, H. Clemmensen & M.F. Mortensen
Danish Road Directorate, Hedehusene, Denmark

ABSTRACT: As part of the increased use of heavy vehicles, the agricultural industry in Denmark has for several years expressed a desire for a general facilitation of the rules regarding weights and mass per axle. With less restrictive rules, heavy farm vehicles can drive themselves to the fields on the road system, instead of having to be transported on oversize-trailers, which is the alternative today. There has in Denmark been many years of discussion on how to calculate the effects from the farm vehicles, that do not have standard road tyre configurations but are fitted with rubber tracks and wide low-pressure tyres. It was decided that maybe a simple practical test could bring knowledge and assumptions a step forward. Therefore, the Danish Road Directorate, in broad cooperation with KL (the National Association of Danish Municipalities), the agricultural industry, the asphalt industry, and the Danish Road Safety and Transport Agency, has carried out a series of practical tests by driving certain heavy farm vehicles on the road system. The purpose of these tests was to explore the deterioration of the roads as well as the impact from "legal" alternatives (Heavy goods vehicles, HGV's) on a typical rural road, where such vehicles would typically drive. The tests were conducted in the days of 1-5 of May 2018, and they included three sub-tests respectively focusing on:

- Fatigue test – any deterioration of the road surface and edges with attention to crack propagation and rutting
- Measurements of the pressure in the depth of the road
- Measurements of axle loads and contact pressures

The paper will present the test set-up, the measurements obtained and the final conclusions.

Keywords: Full-scale testing, flexible pavement, field-test, farming vehicles, tracks

1 BACKGROUND

The general development in the society of larger farms and increasing productivity demands, has had the effect, that the agricultural industry seeks to use larger agricultural machinery. In combination with a general increase of precipitation, this has prompted the use of rubber tracks, instead of wheels, on some of the large machines, to protect the soil from soil compaction.

Some of the agricultural machinery in use do not however comply with Danish legislation for vehicles travelling on public roads, and these must therefore be transported on oversize-trailers between fields. This is both costly and inflexible for the agricultural industry.

In recent years, two types of tracked harvesters have obtained a dispensation to be allowed to drive on the national road system. However, on the local roads, where these vehicles primarily drive, the agricultural industry needs to ask the authorities for dispensation every year.

DOI: 10.1201/9781003222897-16

The municipality then must balance the desire to support local business against the risk of increased expenditures for maintenance of weaker municipal roads and bridges. For this, knowledge on road wear imposed by heavy tracked harvesters is in demand. Also, it is a relevant question whether tracked vehicles are more or less friendly to the roads than the alternative - transport on an oversize-trailer?

The Danish Road Directorate and the agricultural industry have had different consultancies calculate how severe the tracked machinery impacts the road, compared to legal vehicles. However, results have been contradictory, as different presumptions have been used. Therefore, the Danish Road Directorate, in broad cooperation with KL (the National Association of Danish Municipalities), the agricultural industry, the asphalt industry, and the Danish Road Safety and Transport Agency, decided to carry out a series of practical tests, by driving certain heavy farm vehicles on the road system. The purpose of these tests was to explore the attrition effects on the roads, as well as the impact from "legal" alternatives on a typical rural road, where such vehicles would typically drive. This paper focusses on tracked farm vehicles, but the tests also included tractors with slurry tankers. The trials are described in detail in the report from the Danish Road Directorate, 2020.

2 TEST INTENTIONS

The aim of the conducted practical tests has been to explore any road wear from tracked farm vehicles, and relate to road wear from legal vehicles, on a typical municipal road, where farm vehicles mainly drive.

The tests included three sub-tests focussing respectively on:

- Measurements of the axle loads and contact pressures
- Fatigue test – any distress to the road surface with particular attention to crack propagation and rutting
- Measurements of pressure in the subgrade

Heavy vehicles on narrow roads are tough on the edges, that easily break if not well supported. Farm vehicles with rib tyres and tracks are more likely to pull over to the shoulder, as they do not get stuck in the soil. The practical tests also investigated how well the different wheels or tracks distribute the load between the edge and the shoulder being at a lower level. For these results, the reader is referred to [Danish Road Directorate, 2020].

3 VEHICLES

The vehicles included in the test are presented below, as well as shown in Figure 1:

- The beet harvester, Grimme Maxtron, currently an unlimited dispensation in some municipalities, but is one of the heaviest tracked vehicles.
- The Ploeger pea harvester has over the last couple of years had a time limited dispensation (given one year at a time), but it is lighter than the beet harvester.
- 7-axle 56 tonnes HGV semi-trailer vehicle combination. This combination is the "worst" legal vehicle.
- Low-loader (block truck tractor with a block semi-trailer carrying a tracked vehicle). This would be the kind of low-loader that would transport the tracked vehicle, with a special transport permission, if this vehicle would not have a dispensation to drive on the roads by itself.

To gain basic knowledge on the vehicles and their tyres/tracks, measurements of axle load and contact pressure were performed. Axle loads were measured by the Danish company Autoconsult, with portable static axle load scales of the type the Police often uses. Table 1 shows measured axle loads and gross vehicle weights.

The tank on the 7-axle lorry was filled with water with the intent of loading it to the maximum allowable gross weight of 56 tons. However, measurements show that "only" 54 tons

Beet harvester, Grimme Maxtron

Pea harvester, Ploeger

Standard 7-axle lorry

Low-loader

Figure 1. Photos of the vehicles included in the test.

was reached, and therefore the tested lorry is slightly more gentle to the road, than what is legally allowed. Measurements also showed the low-loader to have overload on the 1st axle. The fifth-wheel coupling should have been moved, taking some load from the 1st axle, and mowing it to the 3-axle bogie on the trailer. The tested low-loader therefore stresses the road a little more than it would have done in a correctly loaded condition.

Table 1. Measured axle loads in tons.

Axle number	Beet harvester	Pea harvester	7-axle lorry	Low-loader
1	24.5 (track)	20.1 (track)	9.2	10.4
2	8.3	9.5	8.7 (dual tyre)	12.4 (dual tyre)
3			8.7 (dual tyre)	12.7 (dual tyre)
4			5.2	10.8 (dual tyre)
5			7.3	10.8 (dual tyre)
6			7.1	11.4 (dual tyre)
7			7.7	
Gross vehicle weight	32.8	29.6	53.9	68.5

Not only axle load, but also the actual contact pressure under rib tyres or tracks has been of concern. Based on the measurements of mass per axle, the heaviest loaded wheel or axle for each vehicle were selected for contact pressure measurements. The measurements were conducted by the Swedish measuring company CA Mätsystem, using the Tekscan I-Scan system. Example plot of the measurements for the beet harvester and the low-loader is shown in Figure 2. Measurements on the tracks show that it is primarily the ribs under the rollers that are stressed. The pressure is very low or non-existent between the rollers. The measurements also showed that tracks do not give higher discrete values of contact pressure than wheels.

The contact pressure measurements show in addition to pressure, the actual contact area. These measurements are listed in Table 2, where also the mean contact pressure is calculated. The low-loader and the 7-axle lorry give the highest mean pressure across the contact area. The tracked vehicles give the lowest mean pressure.

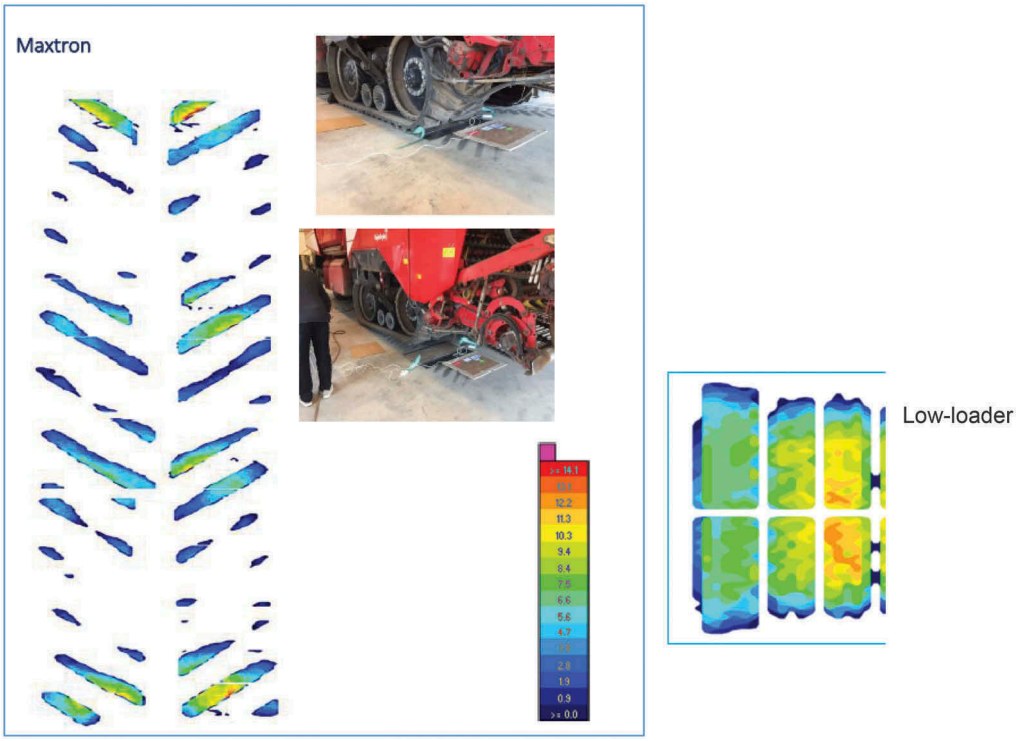

Figure 2. Left: Contact pressure under track of beet harvester. The contact area was found to be 233,000 mm^2. Right: Contact pressure under axle 1, left wheel of low-loader.

Table 2. Measurements of contact area, and mean contact pressure.

Vehicle	Axle and wheel/track	Contact area [mm^2]	Weight [kg]	Mean contact pressure [MPa]
Beet harvester	Track, right side	233,000	12,700	0.54
Pea harvester	Track, left side	180,000	8,950	0.49
7-axle lorry	Axle 1, left wheel	50,000	4,600	0.90
Low-loader	Axle 1, left wheel	56,000	5,320	0.93

4 FATIGUE TEST

The setup for the fatigue test was to put each of the vehicles on each their short test section and drive forth and back for a maximum of 1 day. The development of cracks and rutting were to be measured, after an agreed number of passes, by Dynatest using their MFV (Multi-Functional Vehicle).

A typical weak rural road was found for this test. It has an asphalt layer of 110 mm, with a surface dressing on top. Below is 330 mm gravel and a subgrade of boulder clay. Seven 10 m test fields with similar bearing capacity (centre deflection of approximately 1000 microns) were identified and marked. Each test field is marked with a start and stop line across the entire width of the road, as well as a driving line, that was used to ensure that the vehicles followed exact same line on all passes, as shown in Figure 3.

After 50 runs, signs of bitumen bleeding under the two tracked vehicles began to show. Figure 3 shows the impression marks in field 3 (beet harvester) between 50 and 150 runs had

been made. This development continued and lead to impression marks from the rib patterns of the tracks.

After 200 runs with the beet harvester and the pea harvester, the surface dressing was bleeding severely, with clearly visible impression marks. It was therefore decided to stop the runs with the two tracked vehicles at 200 runs. The test was performed on a sunny day in early May, with temperatures ranging from 10 to 16°C over the day. Had it been a warm day in the summer, bleeding had occurred faster.

A short supplementary test was performed by driving the pea harvester to a road section with hot mix asphalt as wearing course and repeating the test. This extra test was stopped after 67 runs backwards and forwards, as there were no signs that bleeding would occur. Crack width and length were measured before and after the supplementary test, showing that crack length was unchanged, but the width had increased. The cracks were not visible for the eye.

Figure 3. Impression marks in field 3 in between 50 and 150 runs.

The municipality, shortly after the test, remedied the bleeding of the surface dressing by applying a layer of small aggregates followed by a roller. This remedy is an effective method of restoring friction. Friction measurements, 6 months after the test, showed no difference in friction between the test sections that were subjected to rib tyres or normal tyres. Also, the even surface had been restored, as the subsequent traffic during the summer months, had evened out the impression marks.

Cracks and rutting were impossible to measure in a reliable manner under the tracked vehicles, due to the bleeding and impression marks. However, the lorries continued to run for another 200 runs. Figure 4 shows that some rutting developed: approximately 3,5 mm under the low-loader and 1 mm under the 7-axle lorry.

5 PRESSURE IN DEPTH

5.1 *Test section and instrumentation*

The purpose was to measure the stresses imposed by the vehicles, on a typical rural road. The project had no budget for construction of a test site with instrumented sensors, so equipment that could be installed in an existing road, without too much disturbance, was looked for. It was found that the University of Aarhus, Institute of Agroecology and Soil Physics, had previously used so-called "Bolling probes" to measure soil pressure under farm vehicles when operating in the fields. The probes are described in [Keller et al., 2016].

The Bolling probe is a long tube having a section of silicon rubber membrane (balloon) at the end, as shown in Figure 5. On the other end is a plastic syringe, which is used to increase the pressure in the tube thereby expanding the balloon, so it fits tightly to the surrounding

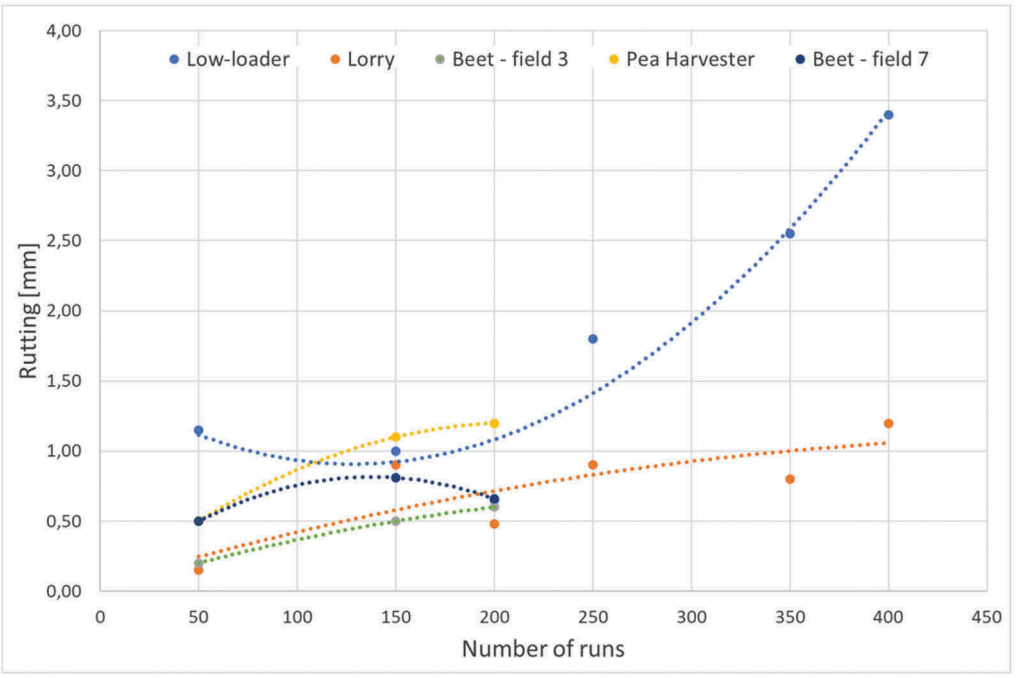

Figure 4. Rutting measured during fatigue test. Tendency lines have been drawn between the individual measurements.

soil. The pressure in the tube is kept at about 1 bar in tests. The equipment senses the mean radial stress experienced by the probe.

Figure 5. Bolling probe.

The test section chosen for this sub-test was also a typically weak rural road, which had a slope as shoulder, making it easier to dig a trench for inserting the probes. It has an asphalt layer of 130 mm, 330 mm of gravel layer and a subgrade of boulder clay. The centre deflection is approximately 1000 microns.

The project borrowed five probes from the University of Aarhus. These were inserted vertically into the subgrade in premade drill holes, in depths varying from 56 to 75 cm from the road surface. The vehicles were to pass the sensors with a constant speed of 5 and 20 km/h, following driving lines, where line 1, the one nearest the edge, is directly above the sensor (balloon). Figure 6 shows the test setup.

Figure 6. Tractor with slurry tanker following line 1.

5.2 *Measured pressure under farm vehicles*

Figure 7 shows examples of the measured time-series, when passing the sensors at 20 km/h. The red curve shows the 7-axle lorry; first a single axle, then a dual axle and last a bogie of four axles. The green curve shows the track of the beet harvester, followed by the rear tyre. The figure also gives an impression of the sensitivity of the measurements. A Skoda Fabia drove over the test field and the measurement is shown with the blue curve. The figure clearly shows the insignificance of a car, as compared to heavy vehicles, when it comes to road wear.

In Figure 8, the tracked vehicles are compared to the 7-axle lorry, as well as the low-loader. Measurements are taken when the vehicles were driving with a speed of 20 km/h. The measurements are presented in box plots displaying all the registered measurements for the individual vehicle. The mean value is shown as "X", the median as a line in the box, quartiles as "box limits" and the variance is shown as tails. Any outliers are shown in dots outside the box.

The box diagram indicates that there is quite a spread in values of the measurements. This variation is due to differences in how precisely the driving line was followed, small differences in speed, difference in depth and measurement uncertainties in the equipment. Pressures measured in different depths were not significantly different, and therefore all included in the box diagram.

Based on the mean values for the test sequences with 20 km/h on line 1, Figure 8 shows that the rear axle on the tractor of the low-loader (being a 2-axle bogie) has the highest peak pressure in the depth. The pressure under the Grimme beet harvester and the 7-axle lorry show fairly similar pressures, both slightly lower than the pressures under the low-loader. Judging from the peak stresses in the subgrade, it is worse to transport the beet harvester on a low-loader, than letting it drive on its own.

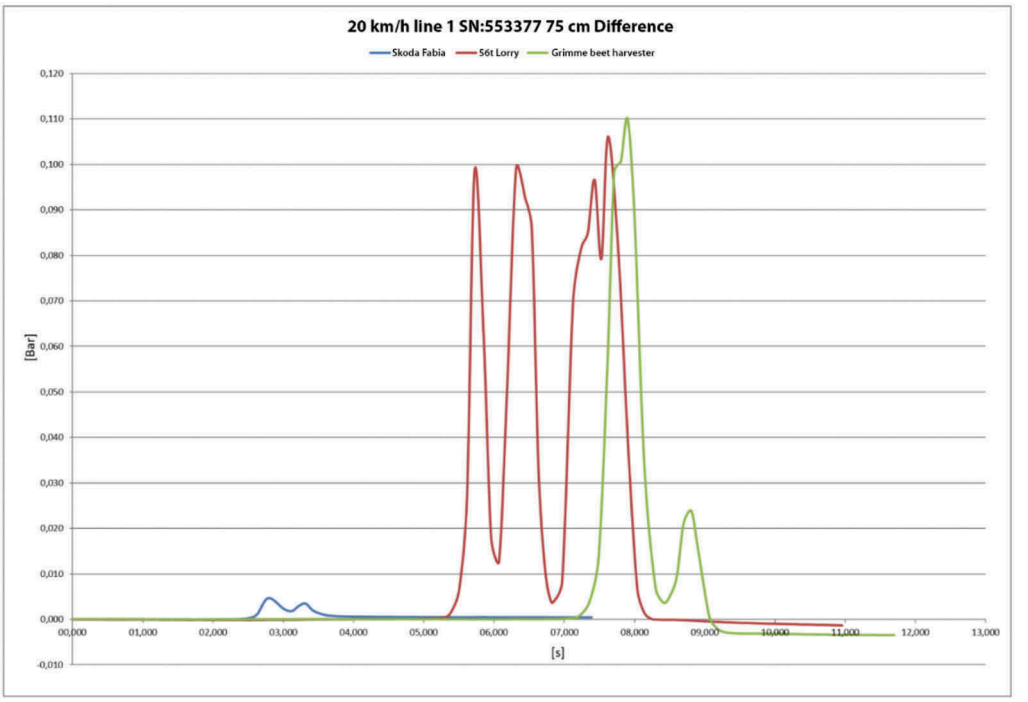

Figure 7. Comparison between the measured pressure when driving across with a car (blue), the 7-axle lorry (red) and the beet harvester (green).

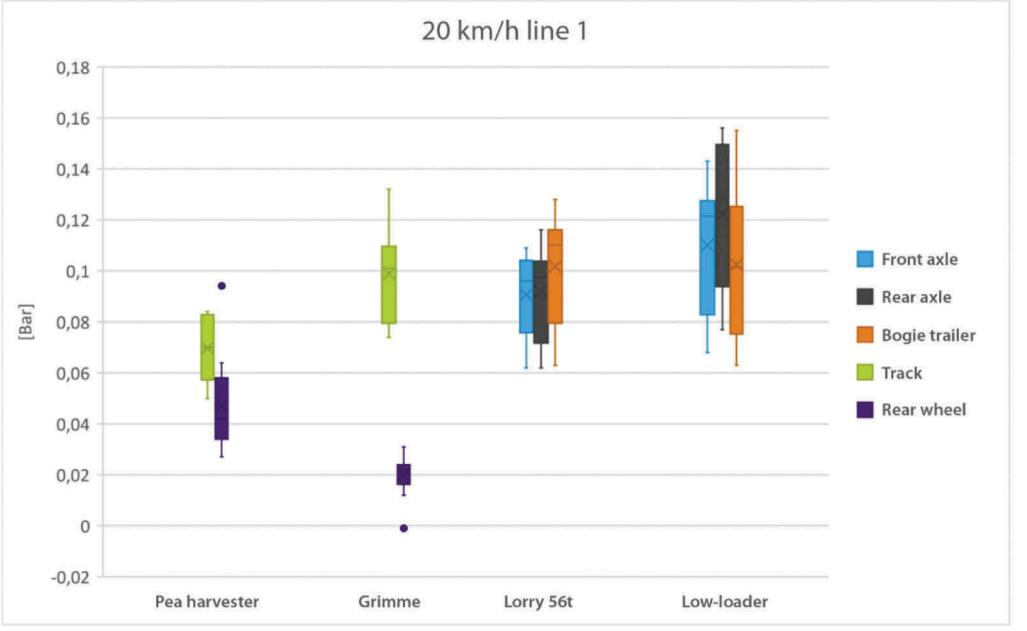

Figure 8. Box diagram displaying measurements at 20 km/h for tracked vehicles, low-loader, and 7-axle lorry.

The low mean pressure of the beet harvester rear wheel is due to the fact, that the rear wheel is positioned centrally under the machine, and consequently it is further from the line (and thereby the measuring equipment), which the track is driving on. This is also the case with the pea harvester, however, to a lesser degree, as its rear wheel is located not so far from the track in the transverse direction.

The test was conducted at both 20 km/h and 5 km/h. Results are not consistent. The two trucks do not show speed dependency, whereas the pressure measured under the tracked vehicles are approximately 35-65% higher at 5 km/h as compared to 20 km/h. It is believed that the trucks had difficulties driving as slow as 5 km/h, and therefore the measurements at 20 km/h are considered more trustworthy.

In this project only the peak stresses are evaluated. The area under the pressure curve in Figure 7 could also have influence on the deterioration effects. This is not investigated further in this analysis.

6 CONCLUSIONS

The practical tests are first step on the way to increase our knowledge of the impact of tracked vehicles on rural roads. They showed that:

- The contact area of tyres or tracks with ribs is small, compared to the size of the belt or tractor wheel. Even so, the mean contact pressure is markedly lower than the mean contact pressure under traditional wheels. Also, for the vehicles in this test, tracked vehicles do not impose higher discrete values of contact pressure than wheels.
- Measuring rutting and fatigue cracks partially failed, as the test section, with a wearing course of surface dressing, showed severe bleeding, making it impossible to continue measurements for tracked vehicles. It would most likely have been possible if the test section had a wearing course of hot mix asphalt.
- Rib tyres and ribs on tracks cause impression marks and bleeding on roads with surface dressing. However, the driving pattern in the test was unusually severe. Typically tracked vehicles only pass once or twice on the road. Any impression marks may be evened out by subsequent traffic, so it is only the bleeding and a potential slippery surface that remains. Bleeding and impression marks were not found to occur on hot mix asphalt.
- Maximum pressure measured in the road construction at depth 56-75 cm was not significantly higher under the tracked vehicles than under legal trucks.
- Loading the tracked vehicle on a low-loader, creates a greater peak pressure in the subgrade than letting it drive by itself.

In this project the pressure under the vehicles is compared at same speed. The impact is speed dependent, and therefore it should be considered that farming equipment typically drives with a maximum of 40 km/h, while the speed limit for trucks is 80 km/h.

The stresses measured in this test cannot be used to verify calculations. To verify calculations of stresses and strains under rib tyres and tracks, it is recommended to install a test section with strain gauges and pressure cells.

ACKNOWLEDGEMENTS

The Danish Road Directorate wishes to acknowledge Mathieu Lamandé from University of Aarhus for letting us borrow the Bollinger probes, DM Contractor for providing the vehicles, and the Municipality of Guldborgsund for letting us use their roads as test sites. Also sincere thanks to KL (the National Association of Danish Municipalities), the agricultural industry, the asphalt industry, and the Danish Road Safety and Transport Agency for a fruitful cooperation, good advice, and recommendations.

REFERENCES

Danish Road Directorate (Vejdirektoratet), 2020. *The impact of selected farm vehicles upon small rural roads, Report on practical tests*, Report published at www.Vejdirektoratet.dk

Keller, T., S. Ruiz, M. Stettler and M. Berli. 2016. *Determining Soil Stress beneath a Tire: Measurements and Simulations*, Soil Science Society of America Journal.

Eleventh International Conference on the Bearing Capacity of Roads, Railways and Airfields, Volume 2 – Hoff, Mork & Saba (eds)

Encapsulated bitumen rejuvenators for reflective cracking and ravelling mitigation

N. Ruiz-Riancho
Nottingham Transportation Engineering Centre, Faculty of Engineering, The University of Nottingham, Nottingham, UK
AECOM Ltd, Nottingham, UK

L. Traseira Piñeiro, M. Abedraba Abdalla & A. Garcia
Nottingham Transportation Engineering Centre, Faculty of Engineering, The University of Nottingham, Nottingham, UK

ABSTRACT: Reflective cracking is usually caused by discontinuities, such as joints, in the layers under the asphalt surface. Ravelling is the result of aggregate course material loss in the surface and rutting is linked to surface bowls located in the wheel path. This paper assesses the capability of the encapsulated bitumen rejuvenators addition to stone mastic asphalt mixtures to mitigate the reflective cracking, particle loss and rutting performance. Capsules containing asphalt resulted in 23% increase in the healing index, 1.5% reduction in mass loss, and negligible ruth depths.

Keywords: Self-healing asphalt, encapsulated rejuvenators, reflective cracking, ravelling, rutting

1 INTRODUCTION

The development of materials able to self-repair makes a positive impact on our society and, especially, when the material is as widely used as asphalt is. It is the most used material for pavements construction. It is mainly formed by bitumen and aggregates.

Usually, the loss of asphalt properties, and therefore, the crack formation are due to the bitumen oxidation and loss of volatiles (Airey, 2003). However, reflective cracking can appear after a short period (Dhakal et al., 2016) without that type of bitumen deterioration. The reflective cracks are mainly induced because of two phenomena: thermal changes or traffic loads (Lytton, 1989).

The loss of bond between aggregates is a common distress of asphalt when the voids content is higher than 20% (You et al., 2018). It contributes to the 90% of the surface damage in porous asphalt (Huurman et al., 2015). Ravelling, also known as particle loss, is mainly caused by either the cohesive failure of the bituminous mastic or adhesive failure in the adhesive zone of the asphalt (Mo et al., 2008).

In order to mitigate or delay reflective cracking in asphaltic overlays, researchers have proposed different treatments: The use of geo-synthetics, which consist of polymeric materials added to pavements to reinforce them or release the stresses caused by traffic (Button & Lytton, 2007). The placement of the fibreglass grid (Lee, 2008) or steel-reinforcing nettings (Baek & Al-Qadi, 2006) as reinforcement techniques. The application of compo-site systems

DOI: 10.1201/9781003222897-17

(Dempsey, 2002) and stress absorbing membrane interlayers (Ogundipe et al., 2013) which work relieving the stresses.

"Rubblization" is another treatment that consists of transforming the concrete layer into an aggregate base to avoid the movement of the concrete layer (Thompson, 1998). "Strata" treatment consists of placing a polymer-rich dense fine aggregate mixture layer on top the damaged pavement followed by an asphalt layer (Bischoff, 2007). Garcia et al., 2019 presented the electromagnetic induction as a way to increase the self-healing properties of a hot mix asphalt showing good results for healing of the reflective cracks.

Another way to increase the natural self-healing capability (Hager et al., 2010) of asphalts is the addition of encapsulated bitumen rejuvenators (Al-Mansoori et al., 2018a,b; Micaelo et al., 2016). It has been proven that encapsulated rejuvenators for self-healing asphalts can sig-nificantly prolong the lifespan of the material. Besides being a sustainable and resilient alternative, it does not require human action to activate the healing process. It is triggered automatically when the mate-rial is deformed and compressed by the traffic loads (Norambuena-Contreras et al., 2019a,b).

This paper delves into the evaluation of encapsulated bitumen rejuvenators as a solution to mitigate the reflective cracking induced by traffic loads, ravelling and rutting in Stone Mastic Asphalt (SMA) mixtures. In order to reproduce the joints or discontinuities in underlying layers, which cause the reflective cracks (Hu et al., 2010), cyclical loads were applied over the samples by a laboratory wheel tracker. Furthermore, self-healing properties were evaluated as the prolongation of the asphalt's lifespan. Computed tomography scanning technology was used to analyse the in-ternal structure of asphalt changes when the cyclical loads were applied, and the reflective cracking appeared. Finally, standard testing methods were used to evaluate ravelling and rutting.

2 MATERIALS AND METHODS

2.1 *Materials*

Stone mastic asphalt with 5% of air voids was prepared in order to analyze the capability of encapsulated bitumen rejuvenators to mitigate reflective cracking. Table 1 shows the percentages used:

Table 1. Asphalt mixture with capsules.

Item	Percentage % by mass	Description
Bitumen	5.6	40/60 Penetration
Aggregates	93.9	Limestone Max. size of 10mm
Encapsulated rejuvenators	0.5	Calcium alginate - Sunflower oil

In this paper, the term rejuvenator refers to the liquid contained in the capsules. The authors have kept this name along the paper, although the liquid in the capsules does not work restoring the original properties of aged bitumen in the traditional sense of the word. The liquid in the capsules, the rejuvenator, improve asphalt self-healing when it is mixed inside a capsule.

The capsules are mixed in the asphalt as another aggregate. As a rule of thumb, 5 kgs of capsules are mixed per ton of asphalt. In asphalt plants, the capsules are added into the mixture in melting bags. See an example in Figure 1.

Figure 1. Melting bag containing 5 kgs of capsules.

2.2 *Encapsulation procedure*

The encapsulation procedure is described thoroughly in (Norambuena-contreras et al., 2018). Capsules were prepared at 20°C by ionic gelation of sodium alginate in the presence of a calcium ions source. First, the sodium alginate emulsion is prepared with water and the bitumen rejuvenator (sunflower oil). At the same time, a calcium chloride solution is prepared in another recipient. Dropping the emulsion into the calcium chloride solution the ions exchange is promoted and the encapsulation takes place. Finally, the capsules are dried and stored. The capsules used in this work were composed of a 75% vol. of sunflower oil and a 25% vol. of calcium-alginate with an average diameter of 2.5 mm.

2.3 *Reflective cracking generation*

The reflective cracking was generated by using a wheel tracker machine. It consists of a wheel passing and applying a determined load over the asphalt beam. This test counts the number of cycles needed for the complete fracture of the asphalt beam.

The asphalt beams were placed over two concrete plates, which create a gap of 4 cm. In order to ease the crack detection, the asphalt beams were painted in white. Additionally, to avoid the production of permanent deformations during the fatigue test, a flexible pad was placed under the sample. Each cycle lasted 2.4 seconds and the force applied over the sample was 930 N. The tests were carried out at 20 C. This process was carried out for 16 asphalt samples (8 with capsules and 8 without capsules) to obtain the N0.5 number through a Weibull distribution. This number represents the number of cycles needed to provide a 50% probability of the asphalt specimens cracking.

2.4 *Crack self-healing measurement*

The reflective crack self-healing of asphalt mixture with capsules was determined by testing the samples until a determined number of wheel tracker loading cycles that corresponded to 25%, 30%, 35%, 40% and 50% of N0.5. After that, the test samples were placed to rest for 24 h at 30 °C. Finally, the test samples were tested until the complete fracture and the total number of cycles quantified (Nt). The self-healing was quantified according to the following equation (1):

$$CHI = \frac{N_t - N_{0.5}}{N_{0.5}} \tag{1}$$

Where CHI = the crack healing index, Nt = the total number of cycles quantified and N0.5 = the number of cycles where the probability of fracture is a 50%.

2.5 *Assessment of ravelling resistance*

The Cantabro test was performed in order to determine if the addition of capsules affects asphalt mixture resistance to ravelling. Cylindric samples were introduced in Los Angeles machine (without the steel balls) and were subjected to 300 cycles at 33 rpm. This process stopped at cycles 30, 90, 150, 210, 270 and 300 in order to weight the samples and calculate the mass loss according to the following equation (2):

$$ML = \frac{M_i - M_t}{M_i} \tag{2}$$

Where ML = the mass loss (%), Mi = the initial mass and MT = the mass after t cycles. This process was carried out for 10 asphalt samples (5 with capsules and 5 without capsules) to obtain the average values of mass loss on asphalt mixtures with and without capsules at the specified cycles.

2.6 *Assessment of rutting resistance*

The resistance to rutting development of asphalt mixtures with and without capsules was determined by testing asphalt slabs fully submerged in water in the Hamburg wheel tracker for 10000 cycles. Prior to start tracking, samples were preconditioned for 4 hours at the test temperature (45°C). Samples were tested by pairs (2 slabs with capsules and 2 slabs without capsules), and then the rut depth for each cycle was calculated as the average value registered in the center of the wheel path, in mm.

2.7 *Computer tomography scanning*

The reflective crack generation was visualized by applying X-ray scanning technology. In order to analyze how the cyclic loading and the self-healing influence in the internal structure of the asphalt specimens, the changes in the percentage of air voids content were quantified for 9 specimens with capsules and 9 specimens without capsules in three different stages (pre-loading, after-loading and after-healing).

After the loading, the samples were stored at 5 °C until the tomography was taken to avoid healing of cracks. The tomography took 40 minutes for each sample. The resting time needed for the healing process (24 h at 30 °C) was applied in nine different moments (6, 15, 22, 30, 32, 35, 37, 50 and 60% of the N0.5 calculated previously), one per sample. A GE Sensing and Inspection Technologies GMBH VTomeX M X-ray scan was used for the images generation (Norambuena-contreras et al., 2018). The dimensions of the damaged part scanned were (60x48x35 mm). The 2D image slices were reconstructed into 3D images by ImageJ where the percentage of air voids was calculated for the three different stages mentioned.

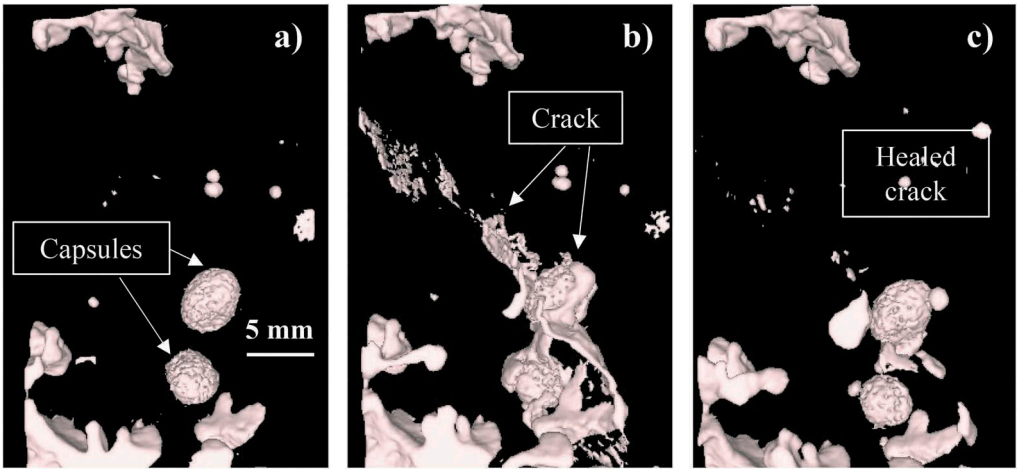

Figure 2. 3D reconstruction of an asphalt sample internal structure for a) pre-loading, b) after 37% N0.5 cyclical loading and c) after self-healing stages.

3 RESULTS AND DISCUSSION

3.1 *Evolution of the internal structure of asphalt mixtures with and without capsules*

As it can be observed in Figure 3 a), the cyclical loading applied over the stone mastic asphalt specimens causes a decrease in the air voids content. This effect took place for the specimens with and without capsules. It is important to remark that the reduction of air voids was more pronounced for the specimens with capsules than the specimens without capsules. This result could be related to the sunflower oil released due to the loading applied which reduces the bitumen's viscosity providing densification of the material. Additionally, it can be noticed that when the number of cycles applied over the samples is higher, the decrease in the air voids content until the 37% of the N0.5 is less pronounced. For the highest numbers of cycles applied (50 and 60% N0.5), the air voids content has a significant increment related to bigger reflective cracks generated by loading.

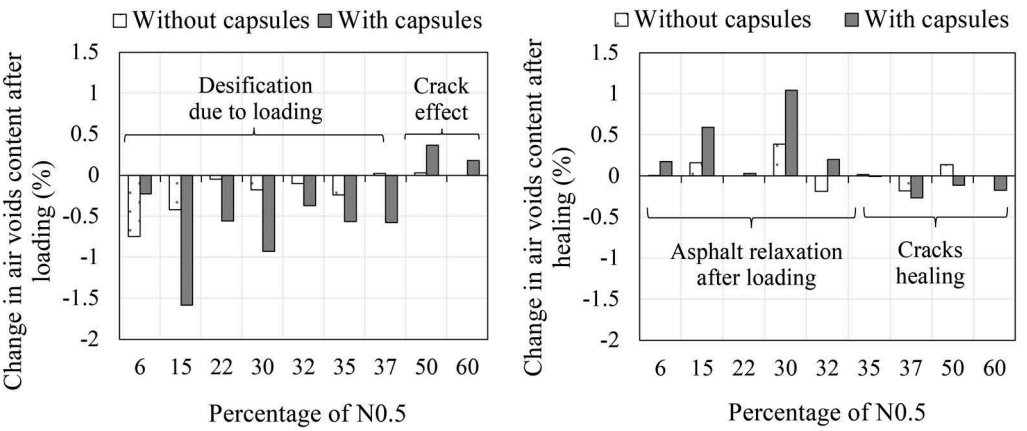

Figure 3. Changes in the percentage of air voids of asphalt mixtures a) after loading; and b) after healing.

Furthermore, Figure 3 b) shows the change in the percentage of air voids of asphalt mixtures with and without capsules after healing for 24 hours at 30 °C. When the number of cycles applied is low, the air voids content after the healing resting period was recovered slightly in the asphalt samples in which the air voids content was reduced during the cyclical loading. The resting period has the maximum healing effect reducing the air voids content when the number of cycles applied is higher than approximately 35% of N0.5.

3.2 *Reflective cracking self- healing properties of asphalt mixtures with and without capsules*

As it can be observed in the 3D reconstruction of a reflective crack in Figure 2, stone mastic asphalt mixtures with capsules can heal reflective cracking damage. Figure 4 shows a comparison between the healing properties of stone mastic asphalt with and without capsules. Furthermore, different resting moments were analyzed to find the optimum number of cycles to apply the healing resting period. In the case of the asphalt without capsules, the healing index was maximum when the number of cycles applied was 35% N0.5 reaching a value of 19%. Regarding the asphalt with capsules, the optimum number of cycles to apply the resting period was 30% N0.5 reaching a healing index around 53%.

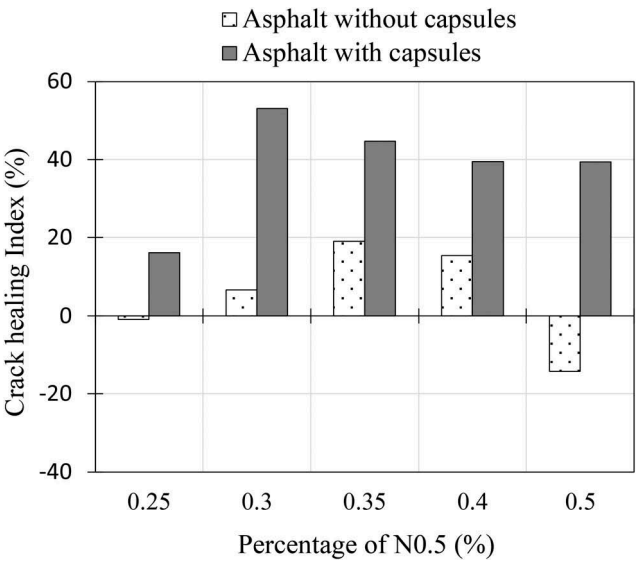

Figure 4. Crack healing index for asphalt mixtures.

3.3 *Effect of capsules on particle loss*

The effect of the capsules on ravelling resistance was tested in the Cantabro. The mass loss results of asphalt mastic samples with and without capsules is shown in Figure 5. It can be observed that the particle loss in asphalt samples without capsules was greater than samples containing 0.5% of capsules. In addition, particle loss was markedly consistant in both samples, and specimens with capsules have approximately 25% lower mass loss. As a result, lower levels of particle loss may indicate that capsules have a significant influence on ravelling resistance (Micaelo et al., 2016). Also, it is interesting to observe that the number of cycles had no influence on the effectiveness of the capsules, which provides considerable insight into the application of encapsulated rejuvenators to mitigate ravelling (Al-Mansoori et al., 2018).

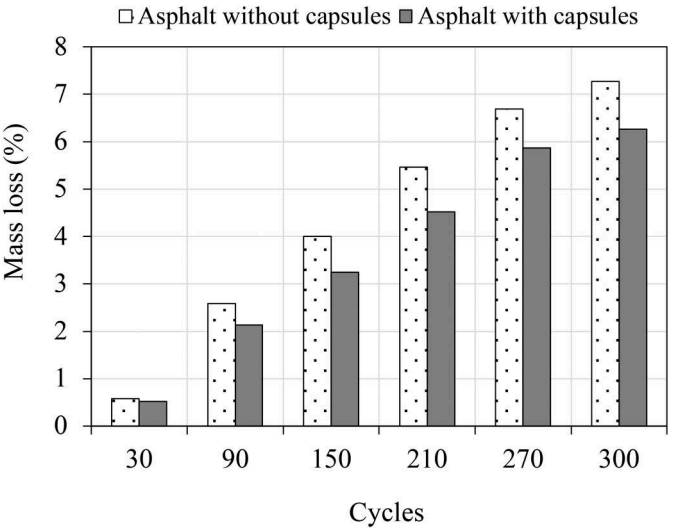

Figure 5. Mass loss values from the Cantabro test.

3.4 *Effect of capsules on rutting development*

Figure 6 shows the average rutting depth results of asphalt mastic samples with and without capsules in the Hamburg wheel tracker. It can be noticed that samples containing capsules registered approximately 0.25mm higher ruth depths. However, this increase was not significant and did not show any accelerated increase in deformation. As a hypothesis, and comparing Figures 4 and 5, it can be thus deducted that the minor variations in rut depth may be linked to the improvement in particle loss. This correlates favorably with previous findings and further support the idea that capsules are softer than aggregate and bitumen, and when a load is applied, the capsules break, releasing oil, which might improve the compatibility of the asphalt (Al-Mansoori et al., 2017)

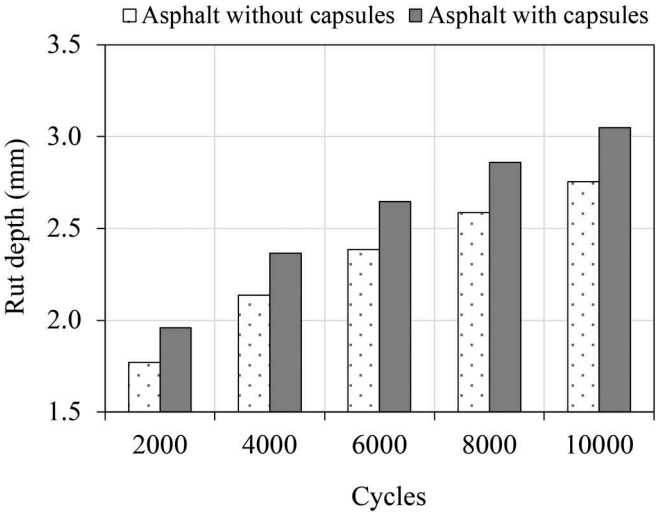

Figure 6. Results from rutting resistance testing using the hamburg wheel tracker.

4 CONCLUSIONS

This paper has assessed the addition of encapsulated bitumen rejuvenators in the stone mastic asphalt mixtures as a mitigation technique for reflective cracking, ravelling and rutting. Additionally, an optimum level of damage was found for reflective cracking before applying the resting time to maximize the self-healing properties. The following conclusions were obtained based on the obatined results:

- The reduction in the air voids content after loading shows densification of the material caused by the cyclical loading. This reduction was more pronounced if the capsules were added due to the action of the encapsulated rejuvenator in comparison to the asphalt samples without capsules.
- Regarding the optimum number of cycles before applying the resting period, the change in the air voids after healing showed a key point in the 37% N0.5 where the reduction of air voids was maximum.
- The healing index was higher when the resting period was applied after the 30% N0.5. In addition to that, the X-ray scans after loading showed a critical point after the 37% N0.5 where the air voids content started to increase, which might be related to bigger reflective cracks generated.
- It can be concluded that the optimum number of cycles before applying the healing resting period is between 30% and 37% N0.5.
- The addition of capsules showed a 23% increment of the healing index in comparison to the asphalt without capsules. This concludes that the addition of encapsulated bitumen rejuvenators can delay the reflective cracking in stone mastic asphalt mixtures.
- Asphalt with capsules presented 25% lower mass loss compared to samples without capsules. Also, the particle loss was not affected by the increase in number of cycles. This evidence suggest that the encapsulated rejuvenators can enhance the ravelling resistance in stone mastic asphalt mixtures.
- Asphalt containing capsules had not significant effect on rutting. Moreover, the number of cycles did not accelerate the rut depth. These results points towards the idea that lower particle loss could be correlated to minor variations in rutting depths.

REFERENCES

Airey, G. D. (2003). *State of the Art Report on Ageing Test Methods for Bituminous Pavement State of the Art Report on Ageing Test Methods for Bituminous Pavement Materials*. International Journal of Pavement Engineering, (4:3), 165–176.

Al-Mansoori, T., Micaelo, R., Artamendi, I., Norambuena-Contreras, J., & Garcia, A. (2017). *Microcapsules for self-healing of asphalt mixture without compromising mechanical performance*. Construction and Building Materials, 155, 1091–1100.

Al-Mansoori, T., Norambuena-Contreras, J., & Garcia, A. (2018). *Effect of capsule addition and healing temperature on the self-healing potential of asphalt mixtures*. Materials and Structures/Materiaux et Constructions, 51(2),1–12.

Al-Mansoori, T., Norambuena-Contreras, J., Micaelo, R., & Garcia, A. (2018). *Self-healing of asphalt mastic by the action of polymeric capsules containing rejuvenators*. Construction and Building Materials, 161, 330–339.

Baek, J., & Al-Qadi, I. L. (2006). *Effectiveness of Steel Reinforcing Interlayer Systems on Delaying Reflective Cracking*. Airfield and Highway Pavements, 486–497.

Bischoff, D. (2007). Evaluation of Strata ® *Reflective Crack Relief System Final Report*, Report.

Button, J. W., & Lytton, R. L. (2007). *Guidelines for using geosynthetics with hot-mix asphalt overlays to reduce reflective cracking*. Transportation Research Record, (2004), 111–119.

Dempsey, B. J. (2002). *Development and performance of interlayer stress-absorbing composite in asphalt concrete overlays*. Transportation Research Record, (1809), 175.

Dhakal, N., Elseifi, M. A., & Zhang, Z. (2016). *Mitigation strategies for reflection cracking in rehabilitated pavements – A synthesis*. International Journal of Pavement Research and Technology, 9(3), 228–239.

Hager, B. M. D., Greil, P., Leyens, C., Zwaag, S. Van Der, & Schubert, U. S. (2010). *Self-Healing Materials*, 5424–5430.

Hu, S., Zhou, F., & Scullion, T. (2010). *Reflection cracking-based asphalt overlay thickness design and analysis tool*. Transportation Research Record, (2155), 12–23.

Huurman, M., Mo, L. T., & Woldekidan, M. F. (2010). *Porous Asphalt Ravelling in Cold Weather Conditions*. International Journal of Pavement Research & Technology, 3 (3).

Lee, S. J. (2008). *Mechanical performance and crack retardation study of a fiberglass-grid-reinforced asphalt concrete system*. Canadian Journal of Civil Engineering, 35(10), 1042–1049.

Lytton, R. L. (1989). *Use of geotextiles for reinforcement and strain relief in asphalt concrete*. Geotextiles and Geomembranes, 8(3), 217–237.

Micaelo, R., Al-Mansoori, T., & Garcia, A. (2016). *Study of the mechanical properties and self-healing ability of asphalt mixture containing calcium-alginate capsules*. Construction and Building Materials, 123, 734–744.

Mo, L. T., Huurman, M., Wu, S. P., & Molenaar, A. A. A. (2008). *2D and 3D meso-scale finite element models for ravelling analysis of porous asphalt concrete*. Finite elements in analysis and design, 44(4), 186–196.

Morea, F., Agnusdei, J. O., & Zerbino, R. (2011). *The use of asphalt low shear viscosity to predict permanent deformation performance of asphalt concrete*. Materials and structures, 44(7),1241–1248.

Norambuena-Contreras, J., Liu, Q., Zhang, L., Wu, S., Yalcin, E., & Garcia, A. (2019). *Influence of encapsulated sunflower oil on the mechanical and self-healing properties of dense-graded asphalt mixtures*. Materials and Structures/Materiaux et Constructions, 52(4), 1–13.

Norambuena-contreras, J., Yalcin, E., Garcia, A., Al-mansoori, T., Yilmaz, M., & Hudson-griffiths, R. (2018). *Effect of mixing and ageing on the mechanical and self-healing properties of asphalt mixtures containing polymeric capsules*. Construction and Building Materials, 175, 254–266.

Norambuena-Contreras, J., Yalcin, E., Hudson-Griffiths, R., & García, A. (2019). *Mechanical and Self-Healing Properties of Stone Mastic Asphalt Containing Encapsulated Rejuvenators*. Journal of Materials in Civil Engineering, 31(5),1–10.

Ogundipe, O. M., Thom, N., & Collop, A. (2013). *Investigation of crack resistance potential of stress absorbing membrane interlayers (SAMIs) under traffic loading*. Construction and Building Materials, 38, 658–666.

Thompson, M. R. (1998). *Hot-Mix Asphalt Overlay Design Concepts for Rubblized Portland Cement Concrete Pavements*. Transport

You, Q., Zheng, N., & Ma, J. (2018). *Study of ravelling failure on dense graded asphalt pavement*. In Proceedings of the Institution of Civil Engineers–Transport (Vol. 171, No. 3, pp. 146–155). Thomas Telford Ltd.

In-situ measurements and condition surveys

Eleventh International Conference on the Bearing Capacity of Roads, Railways and Airfields, Volume 2 – Hoff, Mork & Saba (eds)

Reducing the rut depth of a thin-paved road by controlling the driving lines of heavy trucks

N. Vuorimies & P. Kolisoja
Research Centre Terra, Tampere University, Tampere, Finland

P. Varin
Roadscanners Oy, Tampere, Finland

ABSTRACT: Deepening of ruts due to heavy trucks driving constantly the same driving line on thin-paved roads is a significant problem to road maintenance. The problem is worsening as truck weights and truck traffic volumes are increasing. Especially rapidly ruts can develop during the thawing period of seasonal frost. As rut depth increases, longitudinal cracks may develop and the bearing capacity of road deteriorate also outside of the thawing period, since ruts are gathering rainwater and cracks allow it infiltrate into the road structure. There are plenty of this kind of thin-paved low-volume roads, which may be occasionally exposed to intensive heavy truck loading, when for instance timber is harvested on the region.

In an earlier study funded by the Finnish Transport Infrastructure Agency it was noticed that a heavy truck can uplift road surface even at distance of 1.5 to 2.0 m from the driving line. Therefore, it was decided to test if it is possible to reduce rut depth by controlling the driving lines of heavy trucks. Loading tests were carried out using seven-axle log trucks weighing 64 tons instantly after the frost thawing. The vertical movements of road surface were measured using two displacement transducers, one located at the wheel path and the other one 0.5 m apart from it, while the development of rut depths on a longer road section was monitored using a laser scanner.

The results clearly indicated that by controlled variation of driving lines it was possible to restore a major part of rutting developed by the preceding heavy truck overruns. This observation has great practical significance regarding autonomous traffic when in the worst scenario all heavy vehicles are guided to the same driving line.

Keywords: rutting recovery, thin-paved road, driving line, autonomous driving, case study

1 INTRODUCTION

Deepening of ruts due to heavy trucks driving constantly the same driving line on thin-paved roads is a remarkable problem to road maintenance. The problem is worsening as truck weights and truck traffic volumes are increasing. In different parts of the world there are plenty of this kind of thin-paved low-volume roads, which may be occasionally exposed to intensive heavy truck traffic, when for instance timber is harvested on the region. Finland is an example of countries located on climatic region where pronounced seasonal variation prevail and seasonal frost occur. Especially rapidly ruts can develop during the thawing period of seasonal frost. As rut depth increases, longitudinal cracks may develop and the bearing

DOI: 10.1201/9781003222897-18

capacity of road deteriorate also outside of the thawing period, since ruts are gathering rainwater and cracks allow it infiltrate into the road structure.

In an earlier study funded by the Finnish Transport Infrastructure Agency it was noticed that a heavy truck can uplift road surface even at distance of 1.5 to 2.0 m from the driving line. (Vuorimies et al. 2018) As a part of larger research, it was decided to test if it is possible to reduce rut depth of a thin-paved low-volume road by controlling the driving lines of heavy trucks.

Width of a road or a lane are known to have an effect on focusing of vehicle on driving lines. Blab and Lizka (1995) have found that vehicle speed and rut depth have a significant impact on the focusing of vehicle driving lines as well. Hjort et al. (2008) observed that the variation of driving lines spreads load and pavement wear over a wider area, thus economic benefit from the variation of driving lines increases with decreasing pavement thickness. Wu and Harvey (2008) modelled Heavy Vehicle Simulator (HVS) test results when driving line was not changed and when it was varied at even intervals from edge to edge and they found that modelling results were near the results of HVS tests. According to some modellings carried out, controlled variation of the lateral position of autonomous vehicles can delay damages and reduce life cycle cost (Chen et al. 2019, Gungor and Al-Qadi 2020).

2 MEASURING METHODS AND SITES

Loading tests were carried out at a low volume road site in Kyyjärvi, in the middle part of Finland. ADT on that site is only about 50. The width of the road is 5.8-6.0 m. Figure 1 shows the layers of road structure. A Soft asphalt layer (SA) is about 30-40 mm thick and the subsoil is peat according to a soil map. The installed transducers were after a gentle curve when normal driving direction was used. On the road there were two visible ruts and longitudinal cracks. The test loadings were carried out in the spring when the frost was assumed to have thawed. Before the loading tests weather had been warm and rainless for more than two weeks. Temperature had varied between 21 and 3°C while average temperature had been 13 ° C. However, on May 22nd and 23rd 2018 average temperature was slightly lower. (Finnish Meteorological Institute, 2019).

At the test site, two displacement transducers were installed to measure the vertical deflection of the road surface. The transducers were located 1.0 m and 1.5 m from the edge of SA layer so that one was at a driving line called here as primary driving line (PDL) and the other

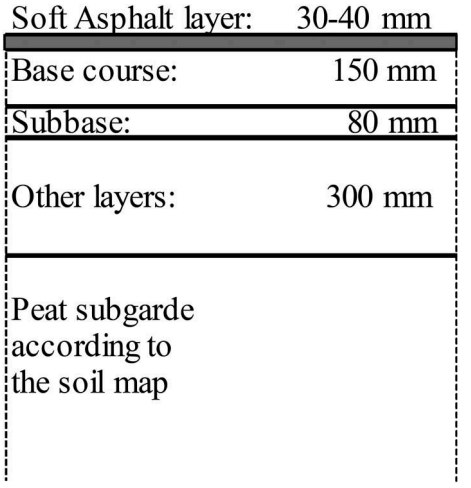

Figure 1. Layers of road structure at the test site in Kyyjärvi.

one 0.5 m towards centre line, called here as secondary driving line (SDL) (Figure 2). Both transducers were attached between a steel bar, which was installed into stiff subsoil, and underside of the SA layer.

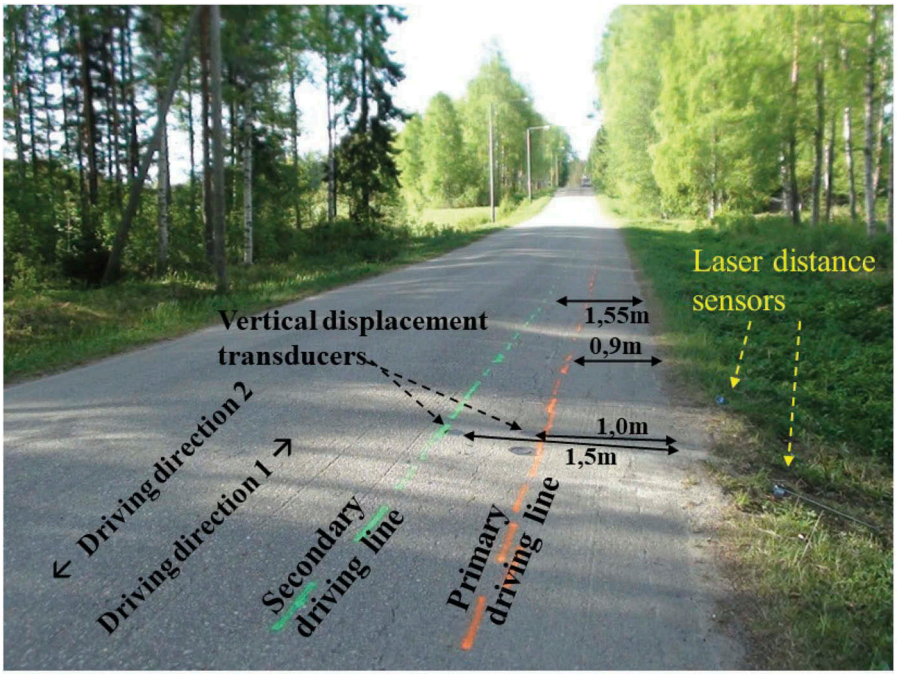

Figure 2. Driving lines and directions and transducers at the test site.

Two laser distance sensors with a measuring range of 400 to 5000 mm were installed at the edge of the road. One was in the cross section of the displacement transducers and the other one was at 1.8 m distance after that in the driving direction 1. The laser distance sensor was set to measure the profile of a passing vehicle at a height of approximately 0.35 m from the road surface at wheel path. Passes of the loading vehicles (LV) were also recorded by a video camera.

Roadscanners Oy used a laser scanner of a Road Doctor Survey Van (RDSV) to measure rut depths of the road at the site and their changes after every LV overpass. The principle to determine maximum rut depth is shown in Figure 3. The maximum rut depth was calculated for every meter. An average change in maximum depth of rut was determined on a "short" distance of 10 m around the installed displacement transducers and on a longer distance of about 60 m. The 60 m was assumed to be the length which the LVs drove along the intended driving lines.

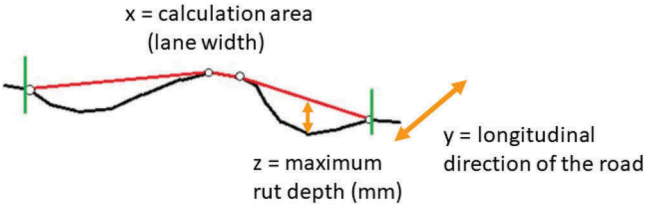

Figure 3. Principle of maximum rut depth calculation method in laser scanning.

The LVs were seven-axle trucks weighing 64 tons and their driving speed was about 50 km/h. The steering axle had single tires, while the other axles had dual tires. In addition to the LVs, some other vehicles (cars, trucks, tractors), whose driving lines on the lane could not be influenced, overpassed the measuring area during the monitoring session. The road structure was loaded during two consecutive days. Figure 2 indicated driving lines and directions as well as transducer locations at the test site. In the mornings the LVs were driving along the PDL, which was indicated by painted red line on road surface. In the afternoons the LVs were driving along the green line called SDL, which was 0.65 m towards the centre line of road from the red line. During the first day, one LV overpassed the site about every 20 minutes. On the next day, two LVs were running as close as possible to each other, simulating as closely as possible a 14-axle vehicle combination. Two consecutive LVs overpassed the site at intervals of about 40 min. After the morning loading session there was about one and half hours pause so that the road had time to rest before altering the driving line. The loadings were done in both driving directions. One difference between the two loading test days was that the actual distribution of driving lines was wider on May 23rd than on May 22nd.

3 RESULTS

3.1 *Maximum vertical displacements at the test site*

Maximum vertical displacement (deflection) of road surface at the test site, when LVs were driving over the transducers was almost 4 mm. Table 1 shows the highest and lowest values of maximum vertical deflection during every loading session at PDL and SDL. On May 22nd maximum axle mass was 10 tons while on May 23rd it was one ton bigger.

3.2 *Accumulation of permanent displacements*

Figure 4 shows the permanent vertical displacements measured by transducers at PDL (TaPDL) and SDL (TaSDL) about 30 seconds after each vehicle overpass on May 22nd. As the LV drove along the PDL the surface of the road at TaPDL deflected permanently downwards but stayed at about the initial level at TaSDL. The figure indicates also that a tractor with full sand cargo on a 1-axle trailer made a significant permanent deformation at the TaPDL during the pause in between 13:30 and 15:00. The driving line of the LV was changed after the pause. As the LV drove along the SDL the road surface at the TaSDL deflected permanently downwards. At the same time the road surface lifted up at the TaPDL during the first two LV overpasses and stayed at that level after two more LV overpasses.

Two loaded gravel trucks and a tractor with full of sand on 1-axle trailer drove to the direction 1 during the morning loading session. The trucks and the tractor caused the road surface to settle at TaPDL, but the effect was ambiguous at TaSDL. A loaded 8-axle log truck which drove along the other lane to direction 2 caused the road surface to rise at the measuring points. However, it seems that the other trucks did not have significant effect to the trend of measured values during the morning loading session. On the contrary, during the afternoon

Table 1. The highest and lowest maximum deflections during each loading session, δ_{max} and δ_{min}, as the LVs were driven along PDL or SDL.

	Primary driving line		Secondary driving line	
	δ_{max}, mm	δ_{min}, mm	δ_{max}, mm	δ_{min}, mm
22.5.2018 morning PDL, 7-axle LV	3.5	3.0	1.9	1.5
22.5.2018 afternoon SPL, 7-axle LV	1.45	1.0	3.1	2.3
23.5.2018 morning PDL, "14-axle" LV	3.9	3.0	1.85	1.65
23.5.2018 afternoon SPL, "14-axle" LV	1.55	0.7	3.05	2.2

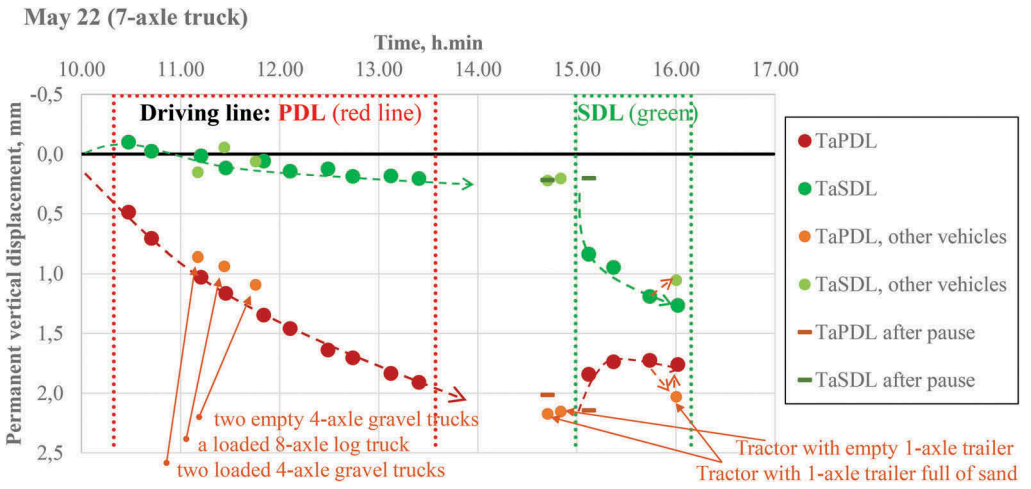

Figure 4. Permanent vertical displacements at TaPDL and TaSDL about 30 seconds after vehicle overpasses on May 22nd, 2018. LVs were driving along PDL in the morning and four passes along SDL in the afternoon.

loading session the tractor with full sand cargo likely did have an effect to the recorded permanent deflections at the measuring points.

Figure 5 presents differences between the permanent vertical displacements of TaPDL and TaSDL about 30 seconds after each measured vehicle overpass on May 22nd. As the LV drove along the PDL the difference between TaPDL and TaSDL increased denoting that the rut depth also increased. It seems that during the morning loading session other passing vehicles had little or no effect to the difference between the two transducers. The difference was about 1.7 mm after the morning loading session. The figure shows also that a tractor with sand loaded 1-axle trailer caused about 0.2 mm increase of the rut depth slightly before the 1.5 hours pause ends. As the LV was driving along the SDL after the pause the height difference of the road surface between TaPDL and TaSDL decreased significantly. The decrease was about 1 mm after the first LV overpass and 1.5 mm after three LV overpasses. During the

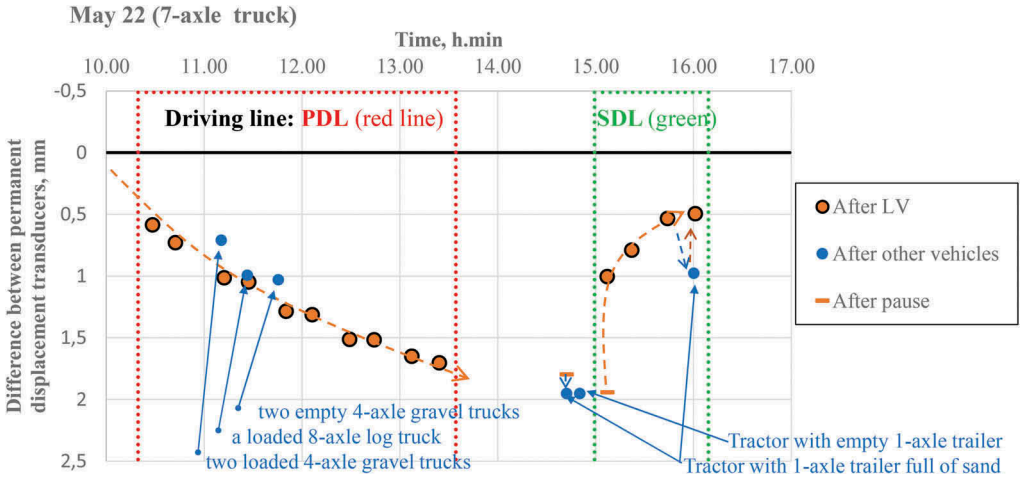

Figure 5. The difference of permanent displacements between TaPDL and TaSDL on May 22nd, 2018. LV was driving ten times along PDL in the morning and four times along SDL in the afternoon.

afternoon loading session the same tractor with the trailer increased the difference about 0.5 mm, but the next pass of LV returned the difference back to the earlier value.

The above results indicate clearly that the position of driving lines have great effect to development of rut depth and presumably to the shape of ruts on low-volume roads. Figures 4 and 5 indicate also that the first loadings on a new driving line caused the greatest changes to the road surface level at the measuring points.

Figure 6 shows permanent vertical displacements of TaPDL and TaSDL about 30 seconds after each measured vehicle overpass on May 23rd. The LV consisted of two 7-axle log trucks running as close as possible to each other. As the LV drove along the PDL the surface of the road at TaPDL deflected permanently downwards and at TaSDL stayed at first at the initial level and then settled a little bit downwards. The figure indicates also that a 9-axle log truck going to the direction 2 uplifted the road surface at the TaPDL. It was the only other heavy vehicle in addition to LV during the day. The driving line of the LV was altered after the pause. As LV was driving along the SDL the surface of the road at the TaSDL deflected downwards. At the same time the first loading caused rising of the road surface at the TaPDL, but the next loadings did not change that level further.

Figure 7 shows difference between the permanent vertical displacements of TaPDL and TaSDL about 30 seconds after each measured vehicle overpass on May 23rd. As the LV drove along the PDL the difference between TaPDL and TaSDL increased denoting that the rut depth also increased. It seems that during the morning a 9-axle log truck had a small effect to the difference between the two transducers. The difference between transducer readings during morning loading session increased about 1.2 mm. As the LV drove along the SDL after the pause the height difference of road surface between PDL and SDL decreased significantly. The decrease was about 1.4 mm after the two LV overpasses thus indicating diminishing of rut depth.

As the road and subsoil had thawed shortly before the loading sessions, the LV overpasses also compacted road structure and subsoil, which have been loosened by frost heave. During the two loading test days the road surface settled about 3.5 mm at TaPDL and 2.5 mm at TaSDL. During the night level of road surface settled about 0.5 mm at both measuring points. This might indicate that all of the densification did not happen at once and the loadings might have restarted consolidation of peat under the road.

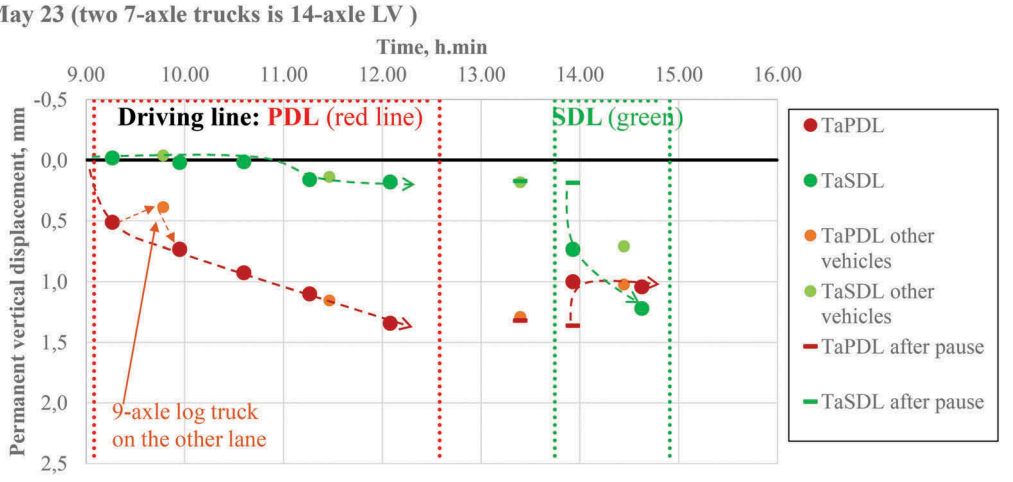

Figure 6. Permanent vertical displacements at TaPDL and TaSDL about 30 seconds after vehicles overpasses on May 23rd, 2018. LV was driving along PDL five times in the morning and twice along SDL in the afternoon.

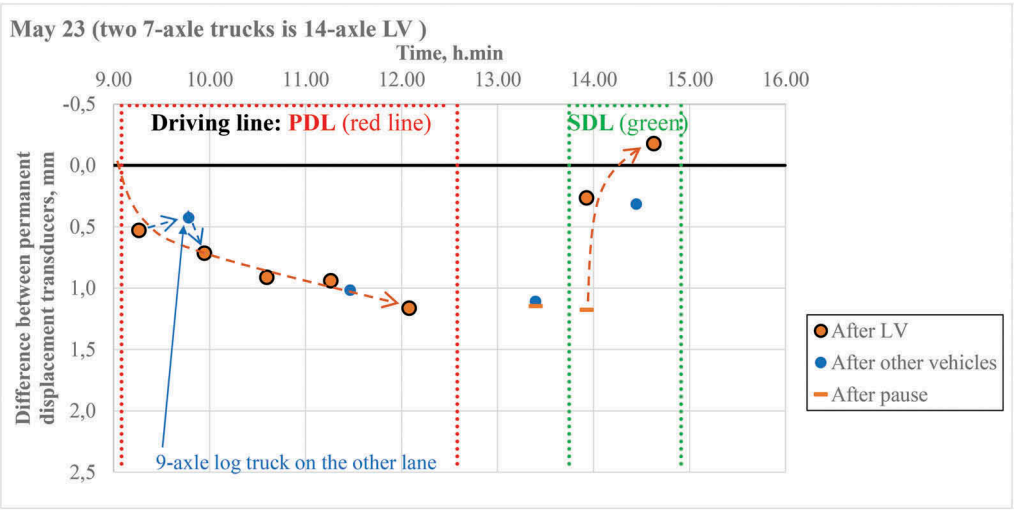

Figure 7. The difference of permanent displacements between TaPDL and TaSDL on May 23rd, 2018. LV was driving five times along PDL in the morning and twice along SDL in the afternoon.

3.3 *Maximum rut depths measured by laser scanning*

The Figure 8 shows measured maximum rut depths by laser scanner. The red vertical line shows the place of the vertical displacement transducers and white dotted lines show the 60 m distance for studying maximum rut depths. On the studied distance maximum rut depths were about 10-20 mm. Unfortunately, the measurements on morning of May 22nd failed due

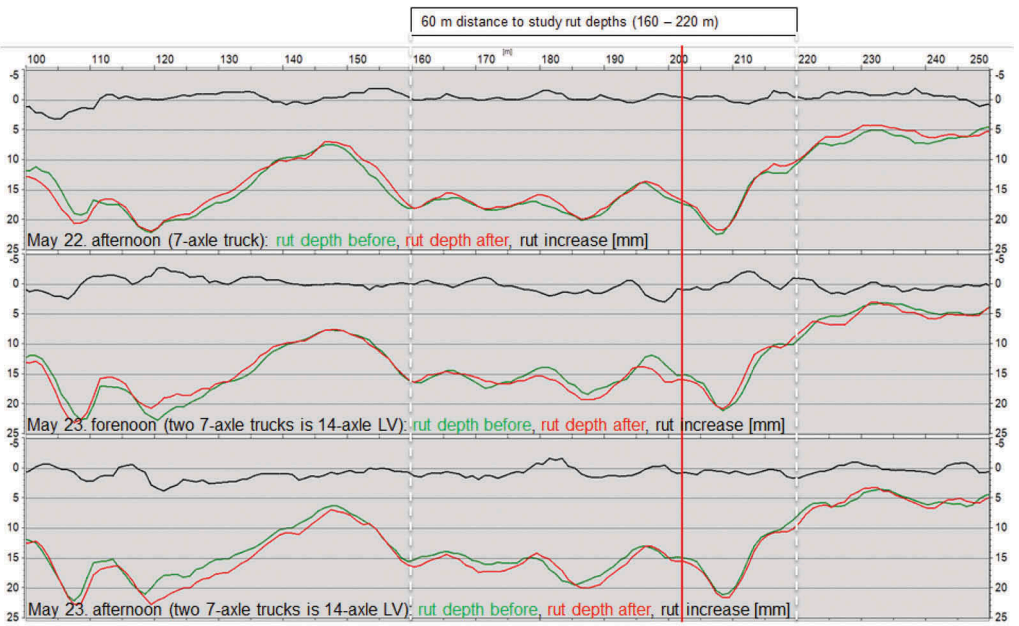

Figure 8. Measured maximum rut depths and changes of them during the morning and afternoon loading sessions of May 22nd and 23rd. Vertical red line shows the measuring points of vertical displacement transducers. Note the location of 0-level on the vertical axis.

to technical problems. Figure 8 indicates that the maximum rut depths mostly decreased in the afternoon of May 22nd while the maximum rut depths mostly increased on May 23rd.

3.4 *Changes in maximum rut depths and in permanent displacements between the transducers*

Figure 9 shows average changes of maximum rut depths determined from the two distances and the respective change in permanent displacements between TaPDL and TaSDL on May - 22nd. As the maximum rut depths were not available from the morning loading session the initial values for the afternoon session were chosen to be the same as the values of transducers in the beginning of the afternoon. The average change of maximum rut depths determined on a distance of ±5 m from the transducers corresponds well to the change of road surface positions measured using displacement transducers when the LV was driving along the SDL. Also, the average change in maximum rut depths between poles 160 and 220 shows reasonably good compatibility.

Figure 10 indicates average changes of maximum rut depths determined on the distances of 10 and 60 meters and the change of permanent displacements between TaPDL and TaSDL on May 23rd. The average change of maximum rut depths on a distance of ±5 m from the transducers is about the same as the change in the height difference of road surface determined using displacement transducers when the LV was driving along the PDL. However, the average change in maximum rut depths determined between poles 160 and 220 doesn't indicate that good compatibility. It seemed also that during the loading pause the average maximum rut depths decreased but the height difference between displacement transducers remained at the same level. As the LV was driving for the first time after the loading pause, average maximum rut depths on the distance of ±5 m from the transducers decreased clearly but between the poles 160 and 220 corresponding decrease was small. The next LV increased average maximum rut depths on both distances. Interestingly, at the same time the height difference between displacement transducers decreased.

4 DISCUSSION

Figures 9 and 10 show that driving line of a heavy truck can have a significant effect on rut depth on a thin-paved low-volume road. Driving along the same wheel path will likely deepen

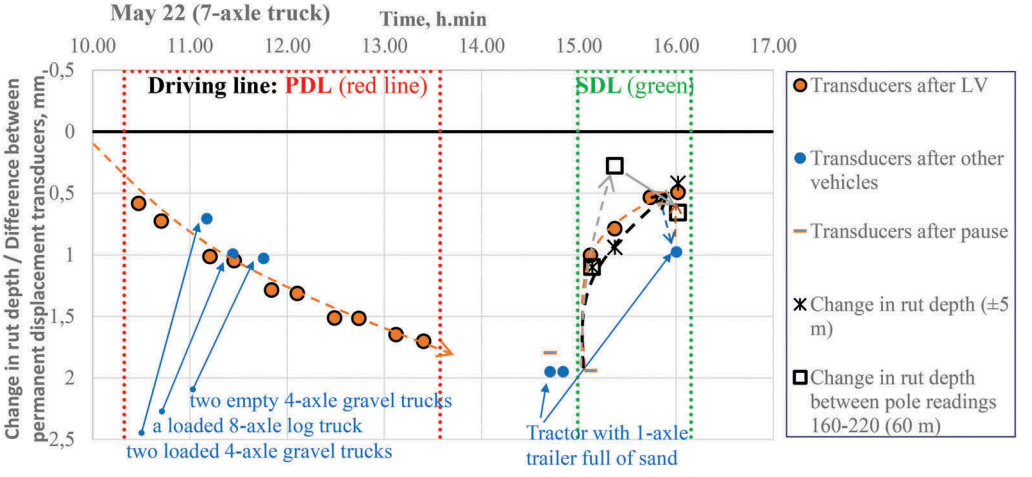

Figure 9. The change of permanent displacements between TaPDL and TaSDL and average changes in maximum rut depths for the distances of 10 and 60 meters on May 22nd, 2018. Laser scanner measurement failed on morning. LV was driving along PDL in the morning and four times along SDL in the afternoon.

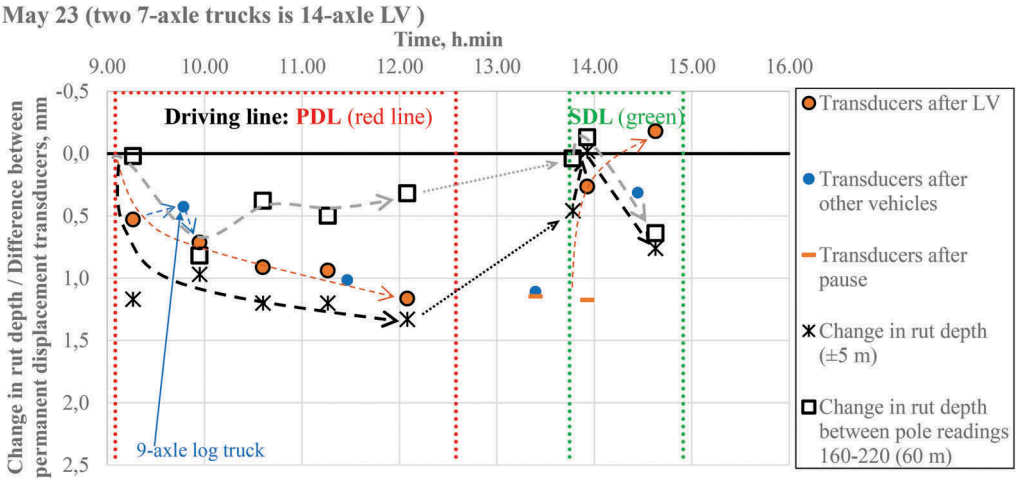

Figure 10. The chance of permanent displacements between TaPDL and TaSDL and changes in maximum rut depths determined on the distances of 10 and 60 meters on May 23rd. LV was driving along PDL in the morning and two passes along SDL in the afternoon.

rut depth the fastest, while altering of driving lines wisely can even decrease rut depths. As SA layer is very thin, almost all deformation occurs in unbound layers and subsoil. When tires of a truck compacts certain areas of a road, other areas might become looser. Driving over the loosened areas of road might restore the earlier situation very quickly. Altering of driving lines also means that grains move continuously against each other, which will smoothen their contact surfaces and thus reduce their resistance against deformations over a long period of time. Optimal minimizing or even decreasing of rut depths on a very thin-paved road, needs in addition to altering of driving lines, also thinking of correct timing to do it. That will be very challenging task and needs more examination.

As the above results clearly indicated, controlled variation of driving lines makes it possible to restore a major part of rutting developed by the preceding heavy truck overruns. Even if the observations presented here were made at a thin-paved low-volume road site, they can give ideas regarding the performance of other roads too, where measurable observations need lots of overruns. When these observations are considered, guiding all the vehicles to drive along the same driving line will have an additional damaging effect on roads. Therefore research theme for the best practises for altering the driving lines of heavy vehicles to minimize the damages of roads will be needed. However, it is not sure, if the best practises are the same if asphalt or unbound layers have a dominant effect on bearing capacity of road? Naturally the width of road and road safety will also set their own restrictions for the possible solutions.

5 CONCLUSION

The loading tests carried out showed that the driving line of a heavy truck can have a significant effect on rut depth on a thin-paved low-volume road. The results indicated also clearly that by controlled variation of driving lines it was possible to restore a major part of rutting developed by the preceding heavy truck overruns. Sometimes altering driving line can even decrease earlier rut depth. Results also showed that the first overrun along a new driving line will have greatest effect on rut depth. Planning of driving lines will have a significant role on the life cycle costs of roads especially when autonomous driving becomes more common.

ACKNOWLEDGEMENTS

The authors want to acknowledge the financial support provided by the Finnish Transport Infrastructure Agency that has enabled the instrumentation and the research

REFERENCES

Blab R. and Litzka J., 1995. *Measurements of the lateral distribution of heavy vehicles and its effects on the design of road pavements*. Road transport technology.

Chen F., Song M., Ma X., Zhu X., 2019. *Assess the impacts of different autonomous trucks' lateral control modes on asphalt pavement performance*. Transportation Research Part C.

Finnish Meteorological Institute. 2019. Download observations -website: https://en.ilmatieteenlaitos.fi/download-observations, last accessed 2020/01/15

Gungor O., and Al-Qadi I., 2020. *All for one: Centralized optimization of truck platoons to improve roadway infrastructure sustainability*. Transportation Research Part C.

Hjort M., Haraldsson M. and Jansen JM., 2008. *Road Wear from Heavy Vehicles – an overview*. Report nr. 08/2008. NVF committee Vehicles and Transports. Vägverket.

Vuorimies, N., Kalliainen, A., Rossi, J., Kolisoja, P., Varin, P. and Saarenketo, T. 2018. *Road Structure Strain on Test Loads of More than 76 tons HCT combinations in 2015–2017*. Research Reports of Finnish Transport Agency 63/2018. (In Finnish)

Wu R., and Harvey JT., 2008. *Evaluation of the Effect of Wander on Rutting Performance in HVS Tests*. Proceedings of the third International Conference on Accelerated Pavement Testing.

Eleventh International Conference on the Bearing Capacity of Roads, Railways and Airfields, Volume 2 – Hoff, Mork & Saba (eds)

Flexible strain sensing plate for determination subgrade elastic modulus

A. Skar
Technical University of Denmark, Nordvej, Lyngby, Denmark

ABSTRACT: The purpose of this study was to contribute to the development of portable measurement devices for characterization and compaction control of unbound pavement layers. The paper presented a proof-of-concept study utilizing a prototype flexible strain sensing plate and a straightforward data interpretation scheme to determine subgrade elastic modulus utilizing recent advances in fiber-optic technology. The approach involved tracking the location of distinct points of zero and minimum strain along fiber-optic cables glued to the flexible plate and relating their shift in location to the changes in the subgrade elastic modulus. For initial validation, the methodology was successfully demonstrated on a simple laboratory-scale setup, utilizing a Plexiglas plate and Polystyrene block to represent the plate and support material, respectively. It was shown that the approach proposed is direct, load-independent, and allows for accurate determination of the elastic modulus, assuming that the plate characteristics are known.

Keywords: Plate Load Test, Distributed Fiber-Optic Strain Sensing, Compaction Control, Soil-Structure Interaction, Non-Destructive Testing

1 INTRODUCTION

Accurate prediction of unbound material properties, such as subgrade and unbound granular material elastic modulus, are essential to ensure appropriate pavement design. Moreover, compaction control is a topic of significant importance in pavement construction, e.g., control of the layer-wise built-in materials. Proper compaction is critical to ensure uniformity of the support, reduce settlements and enhance the overall robustness of the pavement system.

Several field tests have been developed for characterization and quality control and assurance (QC/QA) of unbound pavement layers. Traditionally, the large-scale static plate load test has been used. This test involves the application of a load having known dimensions and intensity and measurement of the resulting mechanical responses (Setiadji, B.H. and Fwa, T. F., 2009). The procedure is, by very nature, expensive and service-disruptive; it is essentially relevant for sparse time intervals.

Due to these shortcomings, the Light Weight Deflectometer (LWD) is increasingly used to assess unbound material properties (Fleming et al., 2007). The LWD is a small-scale field test device that applies an impact-like load to a load plate. The device is practical and has proven to be a suitable control and acceptance testing tool. However, several issues need to be considered for the interpretation of LWD data. Significant factors that influence the analysis include (Vennapusa 2009): (i) size of the loading plate, (ii) plate contact stress, (iii) type and location of deformation sensor, (iv) plate rigidity, (v) loading rate, (vi) buffer stiffness and (vii) load measurement method. Thus, LWD data should be treated carefully. Detailed

DOI: 10.1201/9781003222897-19

knowledge regarding the specific device and test setup is required to get valuable results. Moreover, the device provides a dynamic response, calling for complex analysis (Adam et al., 2009, Ryden and Mooney, 2009) seldom used by practitioners.

In recent years, new sensing technologies have been developed to transform traditional civil engineering structures into intelligent infrastructure (see e.g., Klar et al. 2016, Nielsen et al. 2020, Skar et al. 2020). One leading technology in this connection is distributed fiber-optic strain sensing (DFOS). This technology enables measurement of spatial strain profiles along the sensing cable. It has led to a reevaluation of how strains can be used in civil engineering. Recently, Skar et al. (2019) and Levenberg et al. (2020) proposed a new method to characterize plate foundation support using high-resolution DFOS. The interpretation method proposed was based on the idea that the plate support characteristics can be inferred by tracking the location of Distinct Points (DPs) of zero and maximum strains and relating their shift in location to changes in soil reaction.

This study aims to contribute to the development of portable devices for characterization and QC/QA of unbound pavement layers. It is hypothesized that the methodology proposed in Skar et al. 2019 and Levenberg et al. 2020 is generic, i.e., applies to any representative modelled plate-support system, and thus can be utilized to support these efforts. Specifically, this paper presents a prototype strain sensing plate and straightforward data interpretation scheme for direct and load-independent determination of subgrade elastic modulus. Initially presented are the methodology – theoretical background, data interpretation method, and modeling framework. Next presented is the design of a flexible strain sensing plate – description of prototype and validation of data interpretation scheme. Finally, an experimental investigation is carried out to demonstrate the methodology on a simple laboratory-scale setup.

2 METHODOLOGY

2.1 *Theoretical background*

The idealized Winkler model and the elastic half-space continuum model are typically utilized to represent the subgrade support in the rigid and flexible pavements systems analysis, respectively. In the Winkler model, the subgrade properties are idealized as independent springs on a rigid base, neglecting the effect of shear deformation. It is common experience that, in the case of soil media, surface deflections will occur not only immediately under the loaded region but also within certain limited zones outside the loaded region. In attempts to account for this continuous behavior, soil media have often been idealized as three-dimensional or axisymmetric continuous elastic isotropic solids.

The mechanical behavior of plates typically follows the classical Germain-Kirchhoff plate formulation (Timoshenko and Woinowsky-Krieger, 1959). The infinite plate is characterized by thickness h_p, elastic modulus E_p, Poisson's ratio v_p, and therefore flexural rigidity D. The plate is loaded by a uniform vertical stress with intensity q distributed over a circular area with radius a. For this axisymmetric situation, the vertical displacement field, u_z, depends only on the radial coordinate r with the origin located directly under the load centroid. The plate moments (per unit length) in the radial (M_r) and tangential (M_θ) are obtained from the expressions

$$M_r = -D\left(\frac{d^2u_z}{dr^2} + \frac{\nu}{r}\frac{du_z}{dr}\right) \tag{1}$$

$$M_\theta = -D\left(\frac{1}{r}\frac{du_z}{dr} + \nu\frac{d^2u_z}{dr^2}\right) \tag{2}$$

The corresponding radial and tangential bending stresses are $\sigma_r = 12zM_r/h^3$ and $\sigma_\theta = 12zM_\theta/h^3$, respectively, where z is measured from the plate's mid-surface or neutral plane (positive = up). The extremal bending stresses are obtained at the bottom of the plate where $z = -h/2$ and at the

surface where $z=h/2$. Note that this notation is opposite of normal practice, i.e., such that a positive moment is associated with compressive bending stress at the plate top under the loaded area. Finally, radial strain (ε_r) at a given z are obtained from

$$\varepsilon_r = \frac{\sigma_r - \nu\sigma_\theta}{E} \tag{3}$$

In the case of the elastic half-space continuum model, relevant theoretical expressions such as the vertical displacement field (u_z) and plate bending moments (M_r) are given in Skar et al. (2019).

2.2 *Interpretation method*

This sub-section describes a method for determining subgrade elastic modulus based on distributed fiber-optic strain measurements of the radial strain (ε_r) at the top of a flexible plate ($z=h/2$). The strains can be detected by fiber-optic cables attached to the plate. The methodology is composed of three elements: (i) a mechanical plate-subgrade support model, (ii) distributed fiber-optic strain measurements, and (iii) an interpretation scheme.

The interpretation method is based on the idea that the subgrade elastic modulus can be inferred by tracking the location of Distinct Points (DPs) of zero and maximum strains first proposed in Skar et al. (2019) and Levenberg et al. (2020). Although this method was tailored towards the characterization of large-scale structures such as slab-on-grade construction and plate foundation systems, it is hypothesized herein that the same principles apply to any representative modelled system, e.g., plates suitable for portable measurement devices. Since the strain response of the plate is insensitive to changes in the Poisson's ratio of the soil, the subgrade elastic modulus, E_s, can be inferred directly. Specifically, the method proposed herein deals with tracking the location DPs of zero strain DP_0 (i.e., ε_0), and second maximum absolute strain DP_m (i.e., ε_m), and relating their ratio (i.e., $\delta=DP_0/DP_m$) to the changes in the subgrade elastic modulus.

To exemplify the overall strain response of a standard slab-on-grade construction, the radial strain is plotted versus the radial distance, shown in Figure 1a for three different load radii (i.e., a=100-400 mm) and a constant load of 50 kN. Moreover, the slab is composed of concrete having an elastic modulus E_p=30,000 MPa and a Poisson's ratio ν_p=0.25. Its thickness is h_p =150 mm, leading to a flexural rigidity of $D=9\cdot10^9$ Nmm. In the Figure, it was assumed that slabs are constructed on a subgrade support with varying stiffness (i.e., 30, 120, 240 and 480 MPa), leading to characteristic lengths of l_e=320-807 mm. The solid, dashed, dash-dotted and dotted lines represent the different subgrade modulus utilized.

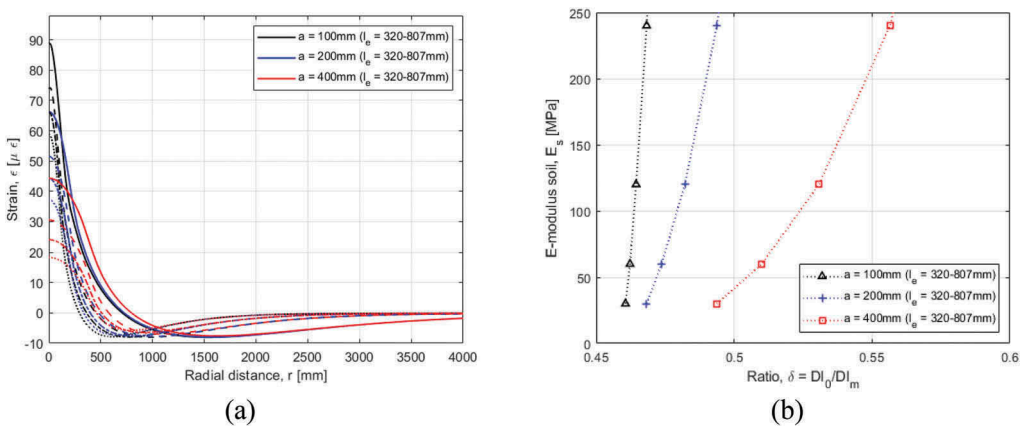

Figure 1. Strain response of typical slab-on-grade structure for three different load configurations showing (a) radial distance versus radial strain, (b) ratio between distinct points (DPs), and E-modulus of soil (E_s).

It is observed from Figure 1a, that the strain curves coincide for the same subgrade modulus. From Figure 1b, it is found that the ratio between DPs increases with increasing subgrade elastic modulus. In order to further assess the results, some normalizations are introduced. In Figure 2a the radial strain is plotted versus the normalized radial distance ($\rho=r/l_e$).

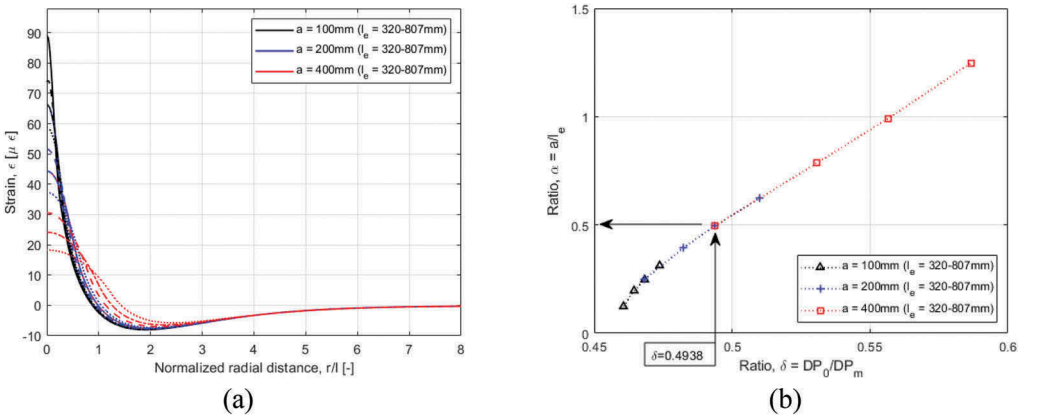

Figure 2. Strain response of typical slab-on-grade structure for three different load configurations showing (a) radial strain versus the normalized radial distance and (b) ratio between DPs (δ) versus ratio between load radius and characteristic length (α).

From Figure 2a it is observed that all the post-peak curves coincide after normalization. Moreover, a significant shift DPs is observed for a load radius of 400 mm. The effect increases with increasing subgrade elastic modulus. Thus, both Figure 1b and Figure 2a indicate that the strain response is affected by the load radius.

Based on these observations, and to enable a load-independent analysis, the results are normalized w.r.t. the load radius. The proposed interpretation scheme is shown in Figure 2b. In the Figure, the ratio between the DPs (i.e., $\delta=DP_0/DP_m$) is plotted versus the ratio between the load radius and the characteristic length (i.e., $\alpha=a/l_e$). The Figure shows that the DPs for all the curves in Figure 2a compose a near-linear line. Thus, determining the elastic modulus of the subgrade can be done directly (or graphically). This process is shown with black arrows in Figure 2b for $\delta=0.4938$, i.e., first plotting the ratio δ on the abscissa axis and then finding the corresponding ratio α on the ordinate axis. The elastic modulus can then be calculated from the expression for l_e, i.e., $E_s=(2D(1-\mu_s^2))/\alpha^3$.

2.3 *Modelling framework*

In order to both demonstrate the methodology and to enable further development of the concept proposed, the Finite Element (FE) method is chosen as a numerical tool to simulate the plate-subgrade support system. First, a simple axisymmetric linear elastic FE model is prepared in ABAQUS. This model consists of a finite plate, supported by an elastic half-space continuum, and is a FE representation of the analytical model. Moreover, this model enables analysis of various slab sizes, thicknesses, layer interfaces and is, therefore, more suitable for interpretation of measurements collected in the field. Next, the FE model is modified to represent a laboratory-scale mechanical setup (i.e., supported by a finite medium).

Thus, the modelling framework is composed of three models as visualized in Figure 3, i.e.: (i) the analytical elastic half-space continuum model (Figure 3a), (ii) the FE elastic half-space continuum model (see Figure 3b), and (iii) the FE laboratory-scale elastic half-space continuum model (see Figure 3c).

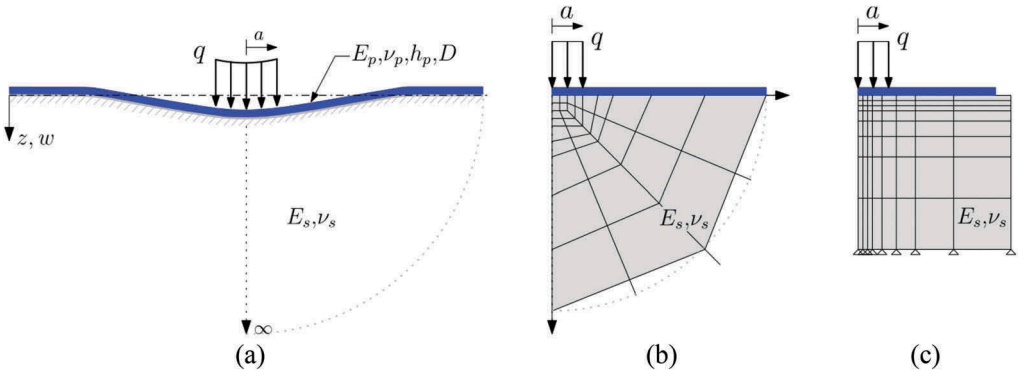

Figure 3. Proposed modelling concept for the design of a prototype flexible strain sensing plate, showing (a) the analytical elastic half-space continuum model, (b) the FE elastic half-space continuum model, and (c) the FE laboratory-scale elastic half-space continuum model. The plate and subgrade support material are shown in blue and gray color, respectively.

The plates were meshed with 17,760 linear 4-node axisymmetric elements of type CAX4. The FE half-space (see Figure 3b) was meshed with 48,285 linear axisymmetric 4-node elements of type CAX4 and 26 linear 4-node continuum infinite elements of type CINAX4. The latter was attached to the outer edges of the supporting medium. The finite support (see Figure 3c) was meshed with 30,000 linear 4-node axisymmetric elements of type CAX4 and rigidly supported at the bottom. The plate-subgrade support interfaces were characterized by full contact with no friction.

3 DESIGN OF FLEXIBLE STRAIN SENSING PLATE

This section presents the design of a prototype flexible strain sensing to determine subgrade elastic modulus. The design represents a first-order development focusing on the demonstration of the proposed concept. Practical aspects, w.r.t. the mechanical design and robustness, e.g., for routine field measurements, were not considered.

Based on a separate analysis and tests in the laboratory, Plexiglas and Polystyrene were selected for the plate and subgrade support material, respectively. Further, a plate size of a=500 mm, hereafter referred to as the 'large plate', and a=250 mm, hereafter referred to as the 'small plate', were selected.

The large plate was designed to validate the proposed concept, i.e., ensure that the physical laboratory-scale model complies with the theory presented in Section 2 (i.e., acting as an infinite plate). The small plate was designed to demonstrate that the concept proposed is generic, i.e., applies to any representative modelled plate-support system, and therefore can be used to develop plates more suitable for portable devices. In order to provide a sufficient stiffness variation of the subgrade support, four different Polystyrene blocks (of type 'EPS60', 'EPS80', 'EPS150' and 'EPS250'), with an elastic modulus of E_s=2.0-7.5 MPa were selected. The elastic modulus of Plexiglas is 2,800 MPa.

The proposed design is validated numerically by plotting the radial strain versus the normalized radial distance for all model types (see Figure 3), shown in Figure 4a. In the example, the plate was loaded with a load intensity of q=0.025 MPa (i.e., a load of 49 N), supported by an expected lower limit subgrade elastic modulus of E_s=1 MPa. The location of DP_0 and DP_m is shown as a black dotted and black dashed line, respectively.

It is observed from Figure 4a that both FE models resemble the strain response of the analytical model for the large plate. For the small plate, the location of the DPs and shape of the post-peak curve changes since the strain at plate ends must be zero (i.e., acts as a finite plate for low elastic modulus of the subgrade).

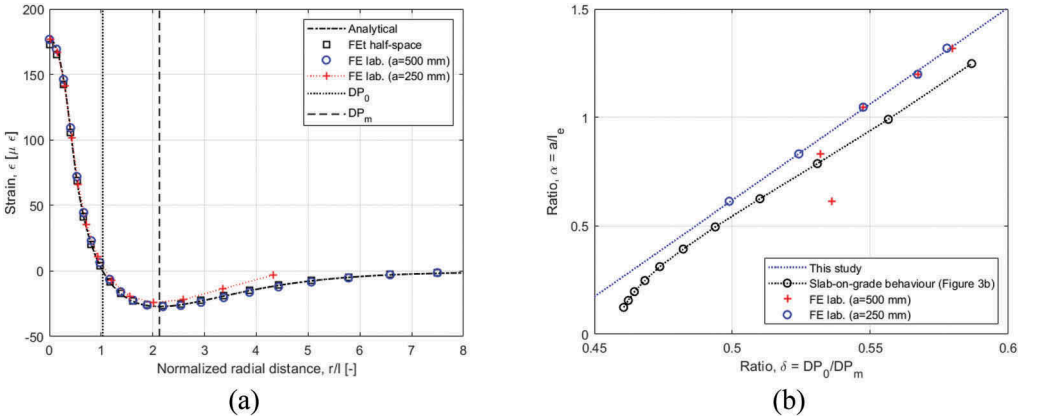

Figure 4. Validation of the proposed design showing (a) strain response for all model types in Figure 3 and (b) revised interpretation scheme for the laboratory scale model. Typical slab-on-grade response is shown as a black dotted line.

This behavior is also exemplified in Figure 4b, showing a revised interpretation scheme (blue dotted line) based on the FE laboratory-scale model. In order to generate the plot, an elastic modulus of the subgrade of E_s=1-10 MPa was assumed. The results for the small and large plate are shown as red crosses and blue circles, respectively. The original scheme from Figure 2b is shown as a dotted black line. It is observed from the Figure that the strain response for the large plate complies with the infinite plate theory. The curve is slightly shifted compared to Figure 2b due to differences in modelling technique.

The small plate behaves similarly for E_s>2 MPa. For E_s<2 MPa, the strain response shows a pronounced finite plate behavior, i.e., the response is influenced by plate ends. The transition in behavior occurs around a normalized plate size of 6 (i.e., plate size/l_e≈6). Interpretation of measurements with small plates on low modulus support material may therefore require further modification of the interpretation scheme.

4 EXPERIMENTAL INVESTIGATION

4.1 *Experimental setup*

As described in the previous section, the experimental setup consisted of circular Plexiglas plates and square Polystyrene blocks. The Polystyrene blocks were resting on a concrete floor, as shown in Figure 5a. The Plexiglas plates were instrumented with a fiber-optic cable, glued to the top of the plate, and connected to the measurement device in one end. Moreover, dead-load was applied using weights to ensure contact between the plate and the support material. The Plexiglas plate was loaded at the center with hand-held weights, placed on a small stiff load plate. A rubber sheet was glued to the bottom of the load plate to ensure a uniform stress distribution.

Strain measurements were then recorded with an Optical Backscatter Reflectometer (OBR) devise depicted in Figure 5b. Strain values were recorded in intervals of 1 mm with a gauge length of 20 mm. Moreover, measurements were performed at four load levels, unloading the plate from 5 kg to 1 kg. In total eight measurements were recorded for each support type.

4.2 *Experimental results*

Fiber-optic measurements for the small and large plate are presented in Figures 6a and b, respectively. The Figure shows strain measurements recorded at the four different load levels for high and low modulus support depicted as black and colored lines, respectively. The measurements at load levels 1-3 were scaled to load level 4 for clarity.

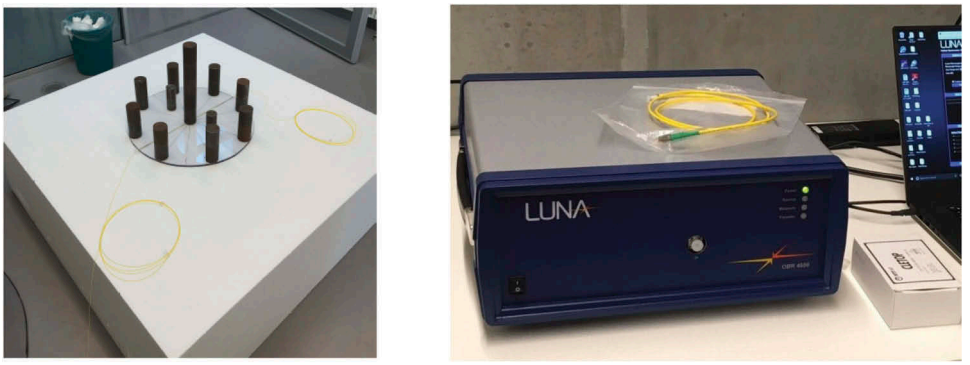

Figure 5. Experimental setup showing (a) Plexiglas plate instrumented with a fiber-optic cable and supported by a 400 mm thick Polystyrene block on a concrete floor (b) the LUNA Optical Backscatter Reflectometer 4600 utilized in the experiment.

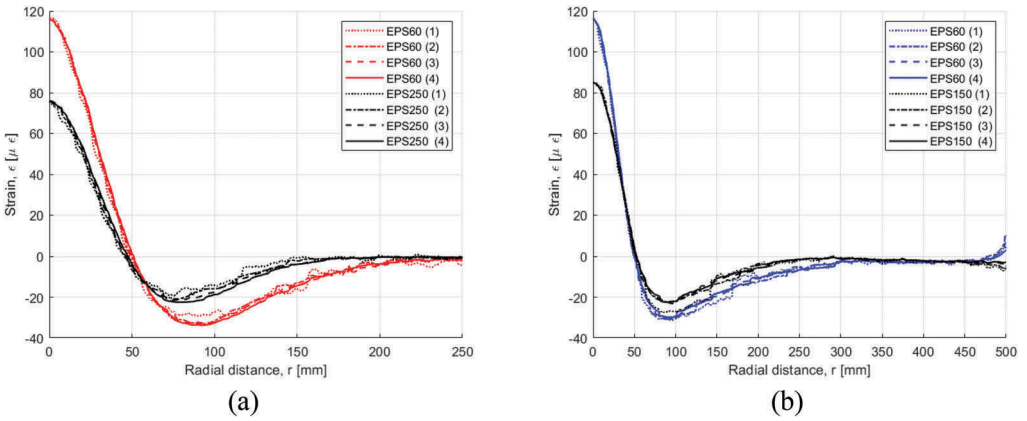

Figure 6. Experimental results for (a) small plate and Polystyrene support type EPS 60 (red) and EPS250 (black) and (b) large plate and Polystyrene support type EPS 60 (blue) and EPS150 (black).

It is observed from both Figure 6a and b that the high modulus support result in a shift of DPs closer to the center of the plate and a shorter post-peak curve. The opposite is the case for the low modulus support. Moreover, the strain response for the high modulus support in Figure 6a resembles infinite plate behavior, whereas the curve for low modulus support approaches finite plate behavior, as expected. It is also seen from the curves how the signal-to-noise ratio improves for increasing load levels, i.e., the curves are smoothened from the lowest load level (dotted lines) to the highest load level (full lines).

The results were interpreted by first identifying the location of the DPs in each test and calculating the ratio δ. Then, the averaged δ were utilized to infer the subgrade elastic modulus for each support type from the scheme in Figure 4b (i.e., predict the ratio α). The results of the analysis are summarized in Table 1.

From Table 1, it is observed that the inferred subgrade elastic modulus is in the same order of magnitude as the specified elastic modulus. Moreover, all tests show that the flexible strain sensing plate capture the variation in stiffness between the different support types. For the small plate, the EPS60 (low modulus) and EPS250 (high modulus) support were inferred with an error of 9.5% and -1.3% compared to the specified properties, respectively. For the EPS80 support, the error was 55.3%. Experiments with the small plate and the EPS150 support were

Table 1. E-modulus inferred from laboratory scale mechanical setup.

Specification	Plate size 250 mm			Plate size 500 mm		
E-modulus [MPa]	E-modulus [MPa]	Difference [%]	Coefficient of Variation [-]	E-modulus [MPa]	Difference [%]	Coefficient of Variation [-]
2	2.2	9.5	0.086	3.4	71.6	0.013
3	4.7	55.3	0.049	3.8	25.9	0.050
5.3	#N/A	#N/A	#N/A	5.9	11.2	0.065
7.5	7.4	-1.3	0.040	8.4	12.2	0.051

unsuccessful, as the strain measurements recorded indicated non-linear behavior of the system, probably due to lack of contact between plate and support. For the large plate all inferred modulus were above the specified properties, with an error of 71.6%, 25.9%, 11.2% and 12.2% for the EPS60, EPS80, EPS150 and EPS250 support, respectively. However, considering the relatively low modulus of the support material selected, the natural variation in material properties, and other sources of possible errors such as minor damages (e.g., local pressure marks), the results obtained match well with the specified material properties.

5 CONCLUSIONS

This study focused on developing a new flexible strain sensing plate and interpretation method to determine subgrade elastic modulus. The proposed methodology was based on tracking of distinct points of first zero and second absolute maximum strain and relating their ratio to the changes in the subgrade elastic modulus. This approach has the advantage that it is direct (i.e., no computational modelling or processing of data required) and load-independent.

The first prototype of a portable strain sensing plate consisted of a Plexiglas plate instrumented with a fiber-optic cable. In order to demonstrate the functionality of the device and validate the proposed interpretation method, a small-scale experiment was carried out by loading the plate while resting on thick Polystyrene blocks with varying elastic modulus.

In general, the proposed method demonstrated good performance. In summary, the work presented showed that: (i) the experimental strain curves resemble that of the elastic half-space continuum model with (i.e., only one zero-crossing), (ii) the location of the distinct points are consistent across all load levels (i.e., elastic behavior and load-independent), (iii) the inferred subgrade elastic modulus are in the same order of magnitude as the specified elastic modulus for Polystyrene material, (iv) the flexible strain sensing plate constructed are capable of capturing the variation in stiffness between the different support types spanning from approx. 2-7.5 MPa, (v) the inferred subgrade elastic modulus resulted in an error of -1.3 to 71.6% compared to the specified elastic modulus for Polystyrene material, and (vi) the discrepancy between FE model response and experimental curves is likely due to the effect of friction and/or lack of contact between the plate and support.

There are many challenges in line before the proposed idea can be implemented into practice. These mainly involve practical aspects w.r.t. the mechanical design, e.g.: (i) improvement of the robustness and protection of fiber-optic cables, (ii) improvement/control of the contact between sensing plate and support (e.g., by increasing plate weight and include additional sensors), (iii) improvement of loading device (e.g., considering LWD for loading). Moreover, the next development phase should focus on the application of the proposed method for real subgrade soils and the development of interpretation schemes based on more realistic FE models. Future efforts should also be expended on improving the technology, enabling analysis of dynamic loads.

REFERENCES

Adam, C., Adam, D., Kopf, F., & Paulmichl, I., 2009. *Computational validation of static and dynamic plate load testing*. Acta Geotechnica, 4(1), 35–55.

Fleming, P. R., Frost, M. W. and Lambert, J. P., 2007. *Review of lightweight deflectometer for routine in situ assessment of pavement material stiffness*. Transportation Research Record, 2004(1), 80–87.

Klar A, Levenberg E, Tur M. and Zadok A., 2016. *Sensing for smart infrastructure: prospective engineering applications*. In: Transforming the future of infrastructure through smarter information - proceedings of the international conference on smart infrastructure and construction, ICSIC 2016, pp 89–295

Levenberg, E., Klar, A. A. and Skar, A., 2020. *Soil Support Characterization in Slab-on-Grade Constructions with Fiber-Optic Distributed Strain Sensing*. In Geo-Congress 2020: Foundations, Soil Improvement, and Erosion (pp. 370–378). Reston, VA: American Society of Civil Engineers.

Nielsen, J., Levenberg, E. and Skar, A, 2020. *Inference of Pavement Properties with Roadside Accelerometers*. In Proceedings of the 9th International Conference on Maintenance and Rehabilitation of Pavements—Mairepav9 (pp. 719–728). Springer, Cham.

Ryden, N. and Mooney, A.M., 2009. *Analysis of Surface Waves from the Light Weight Deflectometer*," Soil Dynamics and Earthquake Engineering, 29(7), 1134–1142.

Setiadji, B.H. and Fwa, T.F., 2009. *Examining k-E relationship of pavement subgrade based on load-deflection consideration*. Journal of Transportation Engineering, 135, 140–148, doi:10.1061/(ASCE)0733-947X(2009)135:3(140).

Skar, A., Klar, A., and Levenberg, E., 2019. *Load-independent characterization of plate foundation support using high-resolution distributed fiber-optic sensing*. Sensors,19(16), 3518.

Skar, A., Nielsen, J., and Levenberg, E., 2020. *Pavement instrumentation with near surface LVDTs*. In Advances in Materials and Pavement Performance Prediction II (pp. 232–235). CRC Press.

Timoshenko, S.P. and Woinowsky-Krieger, S., 1959. *Theory of Plates and Shells*; McGraw-Hill Book Company, Inc., New York, NY, USA.

Vennapusa, P. K., and White, D. J., 2009. *Comparison of light weight deflectometer measurements for pavement foundation materials*. Geotechnical Testing Journal, 32(3), 1–13.

Eleventh International Conference on the Bearing Capacity of Roads, Railways and Airfields, Volume 2 – Hoff, Mork & Saba (eds)

Use of field and laboratory measurements for estimating pavement layer coefficients

Jian-Shiuh Chen & Chin Hung Yang
Department of Civil Engineering, National Cheng Kung University, Tainan, Taiwan

Chia-Hung Lai
CECI Nova Technology Co., Ltd., Taipei, Taiwan

ABSTRACT: There is no question that every country around the world is currently confronted with the enormous task of identifying priorities for the allocation of funds and resources as required to rehabilitate and upgrade existing highways. In giving consideration to future needs for improvements, these rehabilitations are justified to the extent that they contribute to an increased effectiveness of the highway system. To perform this task effectively, data must be available on the relative condition of pavements within the system so that priorities may be established on the basis of their ability and serviceability of carrying traffic loading. This research focused on developing guidelines for implementing structural condition index (SCI), and determining the layer coefficients for asphalt pavements including open-graded friction course (OGFC), dense-graded asphalt concrete (DGAC), stone mastic asphalt (SMA), and bitumen-treated base (BTB). The falling weight deflectometer (FWD) and laboratory tests were conducted to evaluate the load carrying capacity of existing pavements. The SCI score was established to distinguish pavements that required maintenance and rehabilitation (M&R), and was shown to be useful to apply M&R treatments to pavements that were structurally inadequate. Deflection data from FWD testing were used to find the layer coefficients for OGFC, SMA, DGAC, and BTB equal to be 0.150, 0.429, 0.371, and 0.270, respectively.

Keywords: Guidelines, abstract, title, text, figures

1 INTRODUCTION

The current funding for highway infrastructure is becoming increasingly limited due to factors such as construction cost inflation, reduced fuel tax revenue, and insufficient budget. The available funding will not be able to address all the pavement needs, resulting in an impact at both economic and serviceability levels. There is no question that every country around the world is currently confronted with the enormous task of identifying priorities for the allocation of limited funds and resources as required to rehabilitate and upgrade existing highways. In giving consideration to future needs for improvements, these rehabilitations are justified to the extent that they contribute to an increased effectiveness of the highway system. To perform this task effectively, data must be available on the relative condition of pavements within the system so that priorities may be established on the basis of their ability and serviceability of carrying traffic loading.

DOI: 10.1201/9781003222897-20

The Taiwan Freeway Bureau (TFB) uses a pavement management system to store, retrieve, and analyze pavement data, and to prepare reports that summarize information needed to support pavement-related decisions. However, a direct measure of the pavement structural condition is currently not in use. A network-level index that can distinguish pavements requiring pavement maintenance from those requiring pavement rehabilitation is necessary, given that applying maintenance treatments to pavements that are structurally inadequate is not cost-effective. Thus, the need to improve the pavement treatment selection process under budget constraints has motivated this research.

The structural condition of a pavement section can be assessed through non-destructive methods such as the falling weight deflectometer (FWD) or the ground penetrating radar (GPR) (Rohde 1994, Chen et al. 2000, Alavi et al. 2008, Joshaghani 2019). Since the FWD and the GPR provide different types of information, the back-calculation of the subgrade and the pavement layer moduli is one of the procedures commonly used to characterize the structural condition of a pavement using the FWD data. Most of highway agencies adopt either the FWD or the GPR or in some cases, both pieces of equipment for the structural evaluation of pavements at the network level. However, certain challenges are associated with using GPR and FWD at the network level. Evaluating pavement structural conditions with GPR and/or FWD data at the network level requires personnel, traffic control, and other resources, resulting in high data collection costs. Moreover, TFB does not have an automated GPR data analysis software system, making GPR data interpretation completely dependent on human experts.

Using FWD data, the structural condition index (SCI) can be obtained (Zhang et al. 2003, Nam et al. 2016, Saleh 2016). The SCI is the ratio of the "existing/effective" AASHTO (American Association of State Highway Transportation Officials) Structural Number (SNeff) determined from both the FWD measurements and the total pavement thickness (AASHTO 1986), the "required" AASHTO Structural Number (SNreq) based on the estimated 20-year Equivalent Single Axle Loads (ESALs) for the route, and the subgrade modulus (MR) (AASHTO 1993, Guo et al. 2021). The objectives of this research are to: (1) develop guidelines about pavement treatments based on the representative SCI value of a pavement section; and (2) determine pavement layer coefficients for adequately characterizing the pavement structural condition using SCI.

2 DATA COLLECTION

The data collection activities undertaken for this study include discussions on the collected data and supporting documents from TFB. More specifically, the following data were collected from TFB: deflection data along with reference markers, maintenance and rehabilitation construction plan sheets showing both the project location and typical sections, photographs of pavement conditions taken during data collection (if available), core data with laboratory thickness measurement records (if available), pavement design documents (if available), and project-level traffic data.

TFB provided the project-level FWD data for 350 pavement sections. All FWD data were collected using the Carl Bro Primax 1500 for flexible pavement testing. The layer thickness information and other supporting data for all the sections were obtained for this research. The researchers reviewed the obtained data and requested any additional data needed for the SCI analysis. In this research, the pavement layers consisting of a bituminous surface (single or multiple layers), stabilized base, aggregate base, and compacted subgrade were considered to be part of the total pavement thickness.

The actual bedrock depth measurements, made using an auger or similar device, were not available in this research. Hence, the bedrock depth measurement was obtained from the calculated rigid layer depth estimate provided as a part of the MODULUS program output (Rohde 1994). The average bedrock depth was thus based on an assessment of the calculated rigid layer depth values associated with each FWD test point. The data preparation also included pavement subgrade modulus and traffic loading.

2.1 *Subgrade modulus*

Subgrade modulus is a major factor in determining the performance of pavements. The resilient modulus (NMR) values were assigned to following five categories: very poor (0–6,000 psi), poor (6,400–10,000 psi), fair (10,000–14,000 psi), good (14,000–18,000 psi) and very good (18,000–100,000 psi).

2.2 *Traffic loading*

The estimated 20-year equivalent single-axle load (ESAL) is one of the inputs in the SCI analysis. For this research, the estimated 20-year ESAL stratification included five major categories as shown as follows: low (0–1,000,000 ESALs), standard (1,000,000–3,000,000 ESALs), high (3,000,000–10,000,000 ESALs), very high (10,000,000–30,000,000 ESALs), and extremely high (> 30,000,000 ESALs). The very high categories include very high volume routes with high truck traffic that usually exceeds 750 heavy trucks per day.

2.3 *FWD deflections*

Most of the FWD data was collected between 2007 and 2017 during any given month of the year. The interval at which the FWD data was collected varied from section to section depending on the purpose of testing. For some projects, FWD measurements were recorded every 50 m, whereas others were taken at 0.5-km intervals. FWD deflections (mm) along with the corresponding, actual applied loads (pounds) were recorded in the spreadsheet for each test station. In addition to the FWD data, the visual distress comments were also recorded based on the observations of the FWD crew during the data collection. Following the AASHTO Guide (1993), the measured deflection at a test temperature was corrected to a deflection value at a representative temperature of 20°C under a standard 80 kN load, which was used for subsequent calculations. Since the temperature correction factor is equal to 1 at the reference temperature of 20°C, the following equation represents the relationship (Kim et al.1995):

$$D_{20} = 10^{\alpha(20-T)} \times D_T \tag{1}$$

where,

D_{20} = adjusted deflection to the reference temperature of 20°C (mm)
D_T = deflection measured at temperature T (mm)
α = $5.807 \times 10^{-6} \times t^{1.4635}$ for wheelpath and
= $6.560 \times 10^{-6} \times t^{1.4241}$ for lane center,
t = thickness of asphalt layer (mm)
T = the asphalt layer mid-depth temperature at the time of FWD testing (°C).

2.4 *Pavement thickness*

The pavement thickness or material type information was usually obtained from the construction plan sheet, typical section details, pavement maintenance and rehabilitation reports, or pavement designs. On a few sections, GPR or core log information was used to obtain the pavement thickness information. Figure 1 summarizes the asphalt concrete (AC) layer thickness information for each of the route types in the 180 sections. Open-graded friction course (OGFC) is commonly used as a surface layer for freeways in Taiwan. An OGFC layer, relatively thin, is placed on top of dense-graded asphalt concrete (DGAC) over a bitumen-treated base course (BTB). The total AC thicknesses ranging from 26.5 cm to 38.5 cm are designed to carry heavy traffic loading.

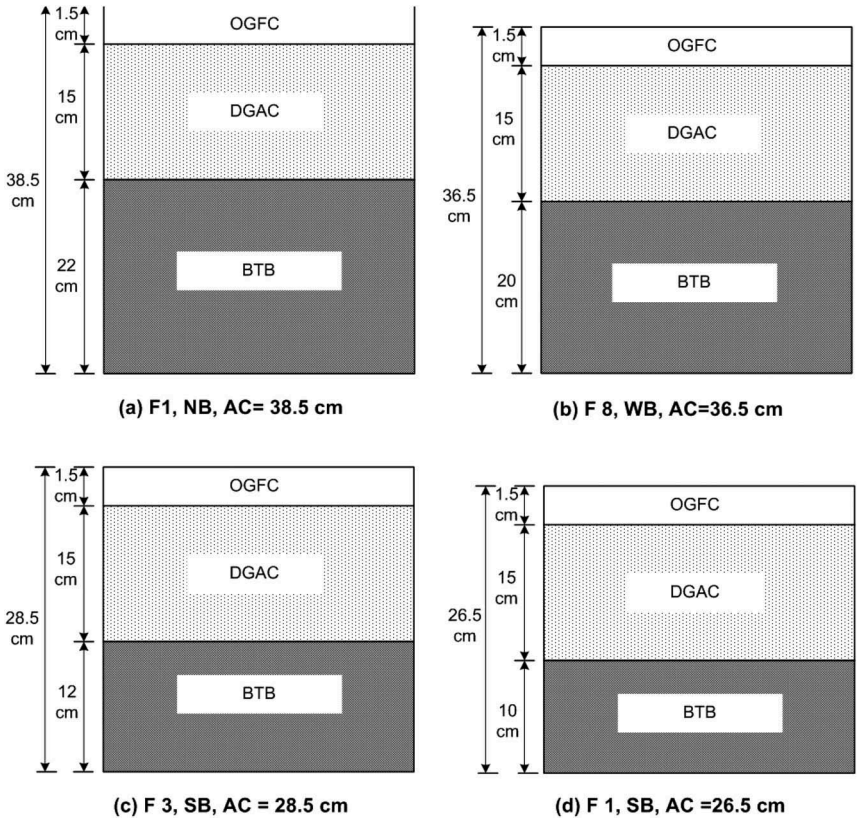

Figure 1. Asphalt concrete (AC) thickness for each route type.

3 EVALUATION OF STRUCTURAL CONDITION INDEX (SCI)

3.1 *Structural Number (SN) of flexible pavements*

The FWD deflections are related to the performance of flexible pavement structures, expressed by the structural number (SN) in this study. The SN expresses the capacity of pavements to carry loads for a given combination of subgrade support, estimated traffic, terminal serviceability, and environment. It is an abstract number defined by the 1993 AASHTO Guide as follows:

$$\mathrm{SN} = \sum_{i=1} a_i D_i m_i \tag{2}$$

where,

a_i = structural coefficient of layer i,
D_i = thickness of layer i (in.), and
m_i = drainage coefficient.

The layer coefficients (a_i), which describe the contribution of each material to the performance of the pavement structure, were derived from stress and strain calculations in a multilayered pavement system and correlated with performance on the basis of the AASHO Road Test conducted in the late 1950s (AASHTO 1993). The SN is the most widely accepted concept because of its applicability and adaptability to various material types and environmental conditions.

3.2 *Structural Condition Index (SCI)*

The SCI is a ratio of the effective AASHTO Structural Number (SNeff) and the required AASHTO Structural Number (SNreq), and is expressed as follows:

$$\mathrm{SCI} = \mathrm{SN}_{eff}/\mathrm{SN}_{req} \tag{3}$$

In order to assess the value of the SCI, the FWD data along with the supporting data for pavement sections was analyzed with an Excel workbook. The SNeff for each of the sections was calculated following the procedures defined by Romanoschi and Metcalf (1999):

$$\mathrm{SN}_{eff} = 6.96 - 0.196 \times [(AREA) - 450 \times (D_{1200})]^{0.5} \tag{4}$$

$$\mathrm{AREA} = 25.4 \times [4 \times D_0 + 6 \times D_{200} + 5 \times D_{300} + 3 \times D_{450}] \tag{5}$$

where D_0, D_{200}, D_{300}, D_{450} and D_{1200} are the normalized deflection at 0, 200, 300, 450, and 1200 mm offset, respectively.

The deflections measured are affected by pavement thickness; therefore, the SNeff depends on the pavement thickness information. An SNreq check-up table, as shown in Table 1, was used in this research (Nam et al. 2016). This check-up table has five categories for both of the subgrade modulus and the 20-year ESALs. The analysis results were summarized for each pavement section and presented with plots of the SCI values over the length of the pavement section, along with the cumulative frequency distributions of the SCI values.

Table 1. SNreq check-up table for varying traffic and subgrade modulus (Nam et al. 2016).

			20-Year accumulated traffic in ESALs ($x10^6$)				
			Low	Standard	High	Very High	Extremely High
SNreq		Category Range	0 - 1	1 - 3	3 - 10	10 - 30	> 30
Subgrade Modulus (psi)	Very Poor	0 – 6000	4.4	4.9	5.9	5.9	7.5
	Poor	6000 - 10,000	3	3.5	4.4	5.1	5.6
	Fair	10,000 - 14,000	2.5	3	3.8	4.5	5
	Good	14,000 - 18,000	2.3	2.7	3.4	4	4.5
	Very Good	18,000 - 100,000	2	2.3	3	3.5	4

3.3 *Representative SNeff, SNreq, and SCI values*

In general, the SNeff and SNreq values may not be uniform along a pavement section due to variability in material composition or moisture content. The variations of freeways in both the pavement structure and the subgrade soil condition are found to be limited because of careful quality control and quality assurance during pavement construction, maintenance and rehabilitation. An average SNeff or SNreq for a one-kilometer long pavement section based on individual SNeff and SNreq values obtained at multiple stations can properly capture the condition variability within the section. The pavement thickness listed in Figure (d) is used as an example. An adequate assessment of the structural capacity of the pavement is shown Figure 2. The mean value of SNeff for this test section is 4.21 with the standard deviation of 0.47.

Pavement sections were analyzed to compare the SCI values in different routes as listed in Table 2. The main principle of a SCI technique is to identify a homogeneous segment by analyzing changes in the mean or deviation of the data series, and thus the sections were chosen in such a way that different ranges of SCI average and standard deviation were included. This selection helped to monitor if the test sections would perform well under all possible scenarios.

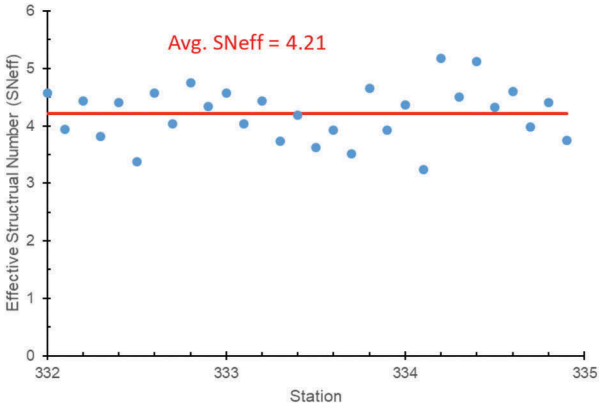

Figure 2. Typical changes in SNeff values in a pavement section.

Table 2. Mean values and standard deviations for SCI.

Route	Subgrade	20-year ESALs	Total Pavement Thickness (cm)	SCI	
				Mean	Standard Deviation
F 1 NB	Good	83,500,000	73.5	0.81	0.18
F 8 EB	Good	52,438,000	71.5	0.86	0.12
F 3 SB	Very Good	61,082,000	63.5	0.84	0.13
F 1 SB	Very Good	71,404,000	61.5	0.82	0.16

3.4 *SCI threshold and treatment*

To develop guidance for the maintenance and rehabilitation (M&R) treatment, it should be based on the corresponding SCI threshold values. The SCI values and other types of project-related data were evaluated by six TFB pavement experts to determine which M&R treatment option should be selected. These experts are knowledgeable and experienced in choosing M&R treatments based on an assessment of various types of project-level data. The M&R treatment options include minor surfacing (MS), light rehabilitation (LR), medium rehabilitation (MR) and heavy rehabilitation (HR). The experts selected M&R treatments given an unlimited budget in order to assess the type of treatment that was actually needed rather than the treatment that might be selected due to inadequate funding.

For the same homogenous segment, the selection of M&R treatment categories might slightly vary from expert to expert. Sometimes the same M&R treatment option could be described for different M&R treatment categories. To assist the analysis process, M&R treatment categories (MS, LR, MR and HR) were converted from linguistic terms to numerical scores as shown in Table 3, so that the average of all expert opinions could be used to determine the average M&R treatment category for a homogeneous segment. The SCI thresholds can be established as follows: 90–100 as "Do Nothing," 80–89 as "MS," 60–79 as "LR," 50–59 as "MR," and 49 or

Table 3. SCI threshold values and treatments.

SCI Score (SCI*100)	M&R Category	Activities
90–100	Do Nothing	None
80–89	Minor Surfacing, MS	1.5-cm OGFC
60–79	Light Rehabilitation, LR	1.5-cm OGFC, and 5-cm DGAC
50–59	Medium Rehabilitation, MR	1.5-cm OGFC, and 10-cm DGAC
0–49	Heavy Rehabilitation, HR	1.5-cm OGFC, and 15-cm DGAC

lower as "HR." Applying this categorization, an SCI score of 72 is assigned LR treatment level, which includes milling of 6.5 cm of old asphalt pavements and replaces with 1.5-cm OGFC over 5-cm DGAC. This treatment is reasonable from an engineering point of view.

4 PAVEMENT LAYER COEFFICIENT

One of the major issues in the pavement management is the estimation of layer coefficients based on FWD data collection for determining the structural condition of stone mastic asphalt (SMA) pavements. The SMA is a coarse mix with gap-graded aggregates. SMA has its origins in Europe and is used commonly because it exhibits high resistance to permanent deformation. The Taiwan Freeway Bureau (TFB) uses the AASHTO Guide for Design of Pavement Structures 1993 to determine the minimum pavement stiffness that ensures pavement longevity. During design, this stiffness is first determined using an iterative design process. The engineer selects materials and layer thicknesses that provide the required stiffness by summing the contributions of individual layers. The contribution from any given layer is calculated by the product of that layer's thickness and a structural layer coefficient that captures the overall quality and structural benefit of the material. However, there is a gap between the existing procedure and the SMA layer coefficient that should be filled to achieve optimal pavement structural designs.

Cores were taken from fields to measure the resilient modulus of samples in the laboratory. The results of the study show that laboratory and field measurements are consistent with the materials tested. The resilient modulus values measured show that different layer coefficients should be given to the different materials depending on the nature of the components. For newly designed pavements, the structural layer coefficient of dense-graded asphalt concrete (DGAC) is in the range of 0.30 to 0.60 (used as surface, intermediate mixtures), or 0.20 to 0.50 (used as bitumen-treated base mixtures, BTB) (AASHTO 1993, Dave et al. 2019). Other material types are lower, e.g., the structural layer coefficient for crushed aggregate base (CAB) is between 0.10 and 0.20 (George 1984, AASHTO 1993, Alvarez et al. 2006). The inclusion of open-graded friction course (OGFC) in pavement thickness design has varied across highway agencies (Chent et al. 2005, Cooley et al. 2009, Timm and Vargas-Nordcbeck 2012). Although some agencies give no structural value, the structural contribution of OGFC to total thicknesses is taken account for economical pavement cross sections in this study.

While the TFB has had success with these structural layer coefficient values, SMA selection and design have resulted in substantial changes in asphalt mixtures. These improvements have likely resulted in different structural contributions from traditonal materials, which means the structural layer coefficients should be reviewed. Proper characterization of SMA layer coefficient could result in substantial cost savings to the TFB by reducing the required pavement thickness and/or leading to pavements that require less frequent maintenance and rehabilitation.

4.1 *Approach for determining SMA layer coefficient*

This section is to present an approach to find the SMA layer coefficient using paired sections where the only difference between sections is one particular SMA layer as shown in Figure 3. This approach that uses the effective structural number (SNeff) relies on having two nearly identical pavement sections, i.e., SMA and traditional sections. Only SMA layer differs between the two sections, and the structural coefficient of other materials is estimated from the traditional section illustrated in Figure 3(b). The effective structural number can be computed according to Equation (4) based on deflections from FWD testing (Rohde 1994, Pologruto 2001). The SNeff represents the structural integrity of the pavement as a function of the thickness of the pavement and the pavement modulus. The computed SNeff value of the traditional section is equated to the other parameters by using Equation (6). The structural and drainage coefficients of the layers in this section can be obtained.

$$\text{SNeff, traditional} = a_{OGFC}{*}D_{OGFC} + a_{DGAC}{*}D_{DGAC} + a_{BTB}{*}D_{BTB} + a_{CAB}{*}D_{CAB}{*}m_{CAB} \quad (6)$$

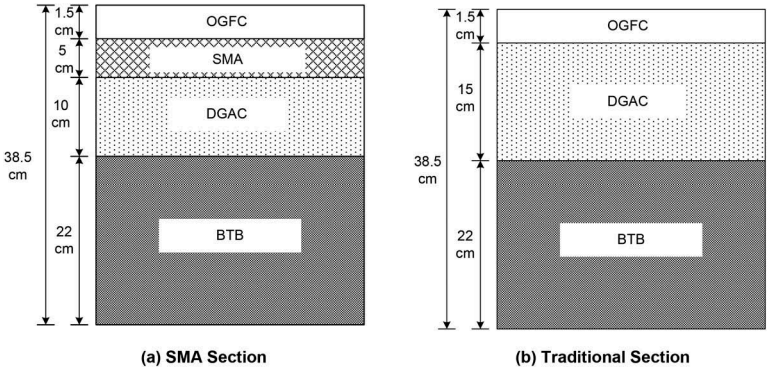

Figure 3. Paired test sections for determining SMA layer coefficient.

The paired test sections shown in Figure 3 differ only in the SMA layer while the underlying materials are nearly identical with only slight differences due to inevitable construction variation. This approach, depicted in Figure 4, assumes that, since every parameter in Equation (6) is obtained except for a_{SMA}, the SMA layer coefficient may be simply calculated as follows:

$$a_{SMA} = \frac{[\text{SNeff, SMA} - (a_{OGFC} * D_{OGFC} + a_{DGAC} * D_{DGAC} + a_{BTB} * D_{BTB} + a_{CAB} * D_{CAB} * m_{CAB})]}{D_{SMA}} \tag{7}$$

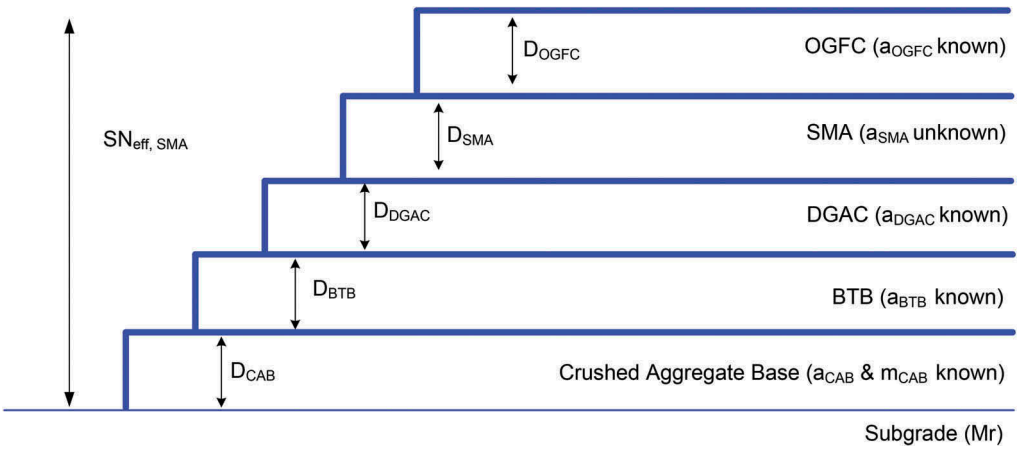

Figure 4. Estimate of layer coefficient for SMA.

4.2 *SMA layer coefficient*

The estimation of stone mastic asphalt layer coefficient (a_{SMA}) begins with a determination of the SNeff associated with each pavement section, which is, in turn, dependent on the value of thickness and modulus (i.e., layer coefficient). The FWD data for each section were analyzed through the MODULUS back-calculation program to estimate layer moduli for each layer and the subgrade. The SNeff is established to be 5.789 and 5.902 for the traditional and SMA test sections, respectively. The change in SNeff for any two adjacent material interfaces represents the SN contribution for the material bounded by these adjacent layers.

Table 4 lists the pavement thickness and the layer coefficient for the traditional section. The structural number is the product of the layer coefficient and thickness of that material layer. The layer coefficient for OGFC, DGAC, BTB, CAB is found to be 0.150, 0.371, 0270, and 0.085, respectively. The resulting structure number is 5.789, which is the summation of the SN contribution for all materials and their thickness.

Table 4. Estimate of layer coefficients for traditional section.

Layer	Thickness (cm)	Thickness (in.)	Layer Coefficient	SN_i
OGFC	1.5	0.591	0.150	0.088
DGAC	15	5.906	0.371	2.192
BTB	22	8.661	0.270	2.339
CAB	35	13.780	0.085	1.170
Sum (SNeff, traditional)				5.789

Table 5 shows the result from the paired test sections where two sections differed only in the stone mastic asphalt layer. In this particular case, the objective was to establish a layer coefficient of the SMA layer. Since the traditional pavement has known structural coefficients, and have measured the SNeff and thickness of both pavement test sections, the structural coefficient of the SMA layer may be computed by solving Equation (7) for a_{SMA}:

$$a_{SMA} = \frac{[5.902 - (0.150*0.591 + 0.371*3.937 + 0.270*8.661 + 0.085*13.780*1)]}{1.968} = 0.429 \quad (8)$$

Table 5. Estimate of SMA layer coefficient.

Layer	Thickness (cm)	Thickness (in.)	Layer Coefficient	SN_i
OGFC	1.5	0.591	0.150	0.088
SMA	5	1.968	0.429	0.844
DGAC	10	3.937	0.371	1.461
BTB	22	8.661	0.270	2.339
CAB	35	13.780	0.085	1.170
Sum (SNeff, SMA)				5.902

5 CONCLUSIONS AND RECOMMENDATIONS

The goal of this research is to develop guidelines for implementing structural condition index (SCI) at the network level, and to establish the structural layer coefficients based on the deflections of service pavements. The scope of the research covered only flexible pavements in freeways in Taiwan. Following conclusions were drawn from this research and the recommendations were made for future work. The recommended SCI threshold values for maintenance and rehabilitation treatments were recommended as follows: SCI scores between 0.9–1.0 as "Do Nothing," 0.80–0.89 as "minor surfacing (MS)," 0.60–0.79 as "light rehabilitation (LR)," 0.50–0.59 as "medium rehabilitation (MR)," and 0.49 or lower as "heavy rehabilitation (HR)." With measured pavement deflection, a difference in effective structural number was found between the SMA and control cross sections. The difference was directly attributed to the presence of the SMA, from which a layer coefficient of 0.429 was determined. The layer coefficients for OGFC, DGAC, BTB, and CAB were found to be 0.150, 0.371, 0270, and 0.085, respectively.

REFERENCES

Alavi, S., J.F. Lecates and M.P. Tavares, 2008. *Falling Weight Deflectometer Usage*. NCHRP Synthesis 318, Transportation Research Board, Washington D. C.

American Association of State Highway and Transportation Officials (AASHTO), 1986. *AASHTO Guide for Design of Pavement Structures*, Washington, D.C.

American Association of State Highway and Transportation Officials (AASHTO), 1993. *AASHTO Guide for Design of Pavement Structures*, Washington, D.C.

Alvarez, A.E., A. Epps Martin, C.K. Estakhri, J.W. Button, G.J. Glover and S.H. Jung, 2006. *Synthesis of Current Practice on the Design, Construction, and Maintenance of Porous Friction Courses*. FHWA TX-06/0-5262-1. Texas Transportation Institute, Texas.

Chen, D.H., J. Bilyeu, H.H. Lin, and M. Murphy, 2000. Temperature Correction on Falling Weight Deflectometer Measurements. *Transportation Research Record 1716*, pp.30–39.

Chen, J.S., K.Y. Lin, and S.Y. Wong, 2005. Quantification of Movements of Flat and Elongated Particles in Hot Mix Asphalt Subject to Wheel Load Test. *Materials and Structures*, Vol.38(3), pp.395–402.

Cooley, L. A., J. W. Brumfield, R. B. Mallick, W. S. Mogawer, M. Partl, L. Poulikakos and G. Hicks, 2009. *Construction and Maintenance Practices for Permeable Friction Courses*. NCHRP Report 640, Washington, D.C., 2009.

Dave, E.V., J.E. Sias and R. Nemati, 2019. *Layer Coefficients for New Hampshire Department of Transportation Pavement Design*. FHWA-NH-RD-26962N, New Hampshire Department of Transportation.

George, K.P., 1984. Structural Layer Coefficient for Flexible Pavement. *Journal of Transportation Engineering*, Vol. 110(2), pp.251–267.

Guo, L., H. Wang and J. Gagnon, 2021. Comparison Analysis of Airfield Pavement Life Estimated from Different Pavement Condition Indexes. *Journal of Transportation Engineering, Part B: Pavements*, Vol.147(2), 04021002.

Joshaghani, A. 2019. Identifying the Problematic Areas with Structural Deficiencies of Pavements Using Non-Destructive Tests (NDT). *International Journal of Pavement Engineering*, Vol.20(11), pp.1359–1369.

Kim, Y.R., B.O. Hibbs and Y.C. Lee, 1995. Temperature Correction of Deflections and Backcalculated Asphalt Concrete Moduli. *Transportation Research Record 1473*, pp.55–62.

Nam, B.H., J. An, M. Kim, M.R. Murphy and Z. Zhang, 2016. Improvement to the Structural Condition Index (SCI) for Pavement Structural Evaluation at Network Level. *International Journal of Pavement Engineering*, Vol.17(8), pp.680–697.

Pologruto, M. 2001. Procedure for Use of Falling Weight Deflectometer to Determine AASHTO Layer Coefficients. *Transportation Research Record 1764*, pp.11–19.

Rohde, G.T. 1994. Determining Pavement Structural Number from FWD Testing. *Transportation Research Record 1448*, pp.61–68.

Romanoschi, S., and J.B. Metcalf, 1999. Simple Approach to Estimation of Pavement Structural Capacity. *Transportation Research Record 1652*, pp.198–205.

Saleh, M. 2016. Utilisation of the Deflectograph Data to Evaluate Pavement Structural Condition of the Highway Network. *Road Materials and Pavement Design*, Vol.17(1), pp.136–152.

Timm, D.H. and A. Vargas-Nordcbeck, 2012. Structural Coefficient of Open-Graded Friction Course. *Transportation Research Record 2305*, pp.102–110.

Zhang, Z., M. Lance, I. Damnjanovic and Z. Li, 2003. *Development of a New Methodology for Characterizing Pavement Structural Condition for Network-Level Applications*. Research Report Number 0-4322-1, Center for Transportation Research, University of Texas, Austin.

Eleventh International Conference on the Bearing Capacity of Roads, Railways and Airfields, Volume 2 – Hoff, Mork & Saba (eds)

Intelligent pavement assessment vehicle for structural and functional evaluation of road pavements

B. Schmidt
ARRB Systems AB, Hyllie, Sweden

S. Tetley
ARRB Systems Africa (Pty) Ltd, KwaZulu-Natal, South Africa

J. Daleiden
ARRB Group Inc., Pennsylvania, USA

ABSTRACT: Roads are generally designed and built based on strength characteristics or bearing capacity, but generally managed according to their functional condition, as strength has historically been difficult and expensive to measure on a routine basis. Until now, overall pavement condition has been largely determined using evenness, or IRI, which assumes that if a road is smooth, the pavement is not in a state of structural distress and has not exceeded its bearing capacity. However, experience shows that the inverse can also be true.

Having a complete dataset, incorporating information of the pavement below and at the surface, enables the road asset manager to better understand its condition. This dramatically improves decision making in managing the road network. Road agencies in North America, Europe, South Africa, China, Australia and New Zealand are now using Intelligent Pavement Assessment Vehicle (iPAVe) TSDD as a tool to collect pavement stiffness properties, at traffic speed, on a yearly basis, along with associated synchronized and simultaneous collected surface condition data.

Combining pavement structural and surface data, enables the identification and cause of pavement failure much easier, providing a powerful tool, in managing pavement condition and providing a solid background for robust infrastructure maintenance strategies. The unique capability of continuous high accuracy and high-resolution data enables infrastructure managers to pinpoint areas where pavement structure is deficient and subject to failure.

The collection of structural and surface condition data simultaneously, at traffic speed, provides a comprehensive assessment of infrastructure condition, enabling an effective and intelligent management of road infrastructure assets.
The paper presents:

- The ability and benefit of collecting structural (pavement strength) and functional (surface condition) in a single pass.
- How integrated structural and functional pavement characteristics can be presented in a user- friendly application.
- How structural and functional data sets can be filtered to enable the identification of critical areas in road infrastructures.

Keywords: infrastructure, condition, bearing capacity, functional characteristic, management, performance

DOI: 10.1201/9781003222897-21

1 THE CHALLENED ROAD INFRASTRUCTURE

A well-functioning road infrastructure is fundamental for societal growth, supporting the increasing population, urbanization, and development. It is of outmost importance that not only the development of the road infrastructure keeps pace with societal evolution, but also that of maintaining existing infrastructure at optimal cost levels. The capacity and quality of the road infrastructure is constantly challenged by increasing traffic, higher axel loading and demand for mobility. New scenarios for traffic patterns, truck platooning and autonomous vehicles requires add to the need for a paradigm shift in creating and maintaining the future road infrastructure. Furthermore, climate changes with higher temperatures, increasing storm-water incidents and rising ground water tables challenge the durability and structural life of the infrastructure and will require additional funding for maintenance and rehabilitation. (OECD ENVIRONMENT POLICY PAPER NO. 14 2018; Mollerup and Rohde 2016)

To overcome these challenges and providing an efficient road network infrastructure, often with stringent budget constraints, needs carefully planned and optimized maintenance strategies and solutions. Optimizing the maintenance strategies with limited budgets requires detailed and reliable condition data of the road infrastructure, i.e. data that reflects the road condition in relation to the functional surface and structure of the road both of which are constantly changing. With a significant increase in traffic and user expectations, the cost of temporary road closures is significant both financially and socially, so the need of performing road condition inventory surveys without interfering with the traffic flow is vital. Collecting road condition data under traffic is not new, although the discrete measuring of road surface characteristic and bearing capacity has been the tradition for decades.

Introducing a simultaneous and comprehensive structural and functional pavement survey methodology, provides comparable information on surface condition and bearing capacity. Integrated measurements also reduce the required time and resources for data collection and associated data analysis.

2 THE BENEFIT OF COLLECTING CONCURRENT STRUCTURAL (PAVEMENT STRENGTH) AND FUNCTIONAL (SURFACE CONDITION) DATA

Combining pavement structural and surface data, enables road engineers to carry out holistic analysis of distress mechanisms leading to the identification of cause and detection of possible pavement failure at an earlier stage than would be possible using separate data collection methods. This is thereby an essential and powerful tool, in managing the road infrastructure by providing a solid background for determination of a robust and cost beneficial maintenance strategy using correct maintenance solutions.

A comprehensive pavement assessment vehicle iPAVe TSDD is a fully integrated survey vehicle capable of collecting both structural and functional pavement condition data simultaneously and at traffic speed. It collects the following information:

- pavement strength through deflection measurement
- cracking
- longitudinal and transverse road profile
- pavement macro texture
- road geometry
- geospatial position
- digital imaging
- asset inventory and condition

The iPAVe TSDD can collect bearing capacity information of a road network at traffic speeds, and thus minimize the use of traditional stationary or slow-moving equipment such as Falling Weight Deflectometer (FWD) or Deflectograph. With a typical operating speed of up to 80 km/h, bearing capacity measurements can be performed without disturbing the traffic, as often seen when using stationary devices.

Depending on network characteristics, the iPAVe TSDD can collect approximately 70 000 lane kilometers of surface and structural condition data during a typical work year of 10 months. This compares very favorably to around 10 000 lane kilometers using an FWD and network survey vehicle combination that would otherwise be used. Furthermore, network level FWD testing is typically spaced at 200 m intervals, while the iPAVe TSDD provides continuous measurement, which can be delimited at intervals from 25 mm and upward. At 5 m spacing, the iPAVe TSDD could measure 14 million deflection points per annum, compared to around 50 000 for the FWD. For the FWD to generate the same coverage of testing, it would take around 280 years!

2.1 *Deflection measurements*

The sensors used to derive the deflection measurements are 11 Doppler lasers positioned in front and behind the loading wheel to record the deflection basin in the longitudinal direction of the road. These lasers measure the instantaneous deflection velocity of the pavement, as the load (50 KN) is applied by the rolling trailer tyres on the rear axle.

2.2 *Riding quality*

Continuous riding quality data, in the form of the International Roughness Index (IRI) standard, is derived from the digital laser profiler (DLP) which uses lasers and an accelerometer located above each wheel path to measure the roughness of the pavement.

2.3 *Rut depth measurements*

Continuous rut depth measurements are generated from the DLP equipment which establishes the transverse road profile to determine both the rut depth and the shape characteristics. The processing software allows for differentiation between general lane and wheel path rutting.

2.4 *Texture measurements*

The surface macro texture is continuously measured using three (3) lasers i.e. one (1) in each wheel path and a third in between the wheel path for comparison purposes. The macro texture is reported in standardized terms of mean profile depth (MPD).

2.5 *High definition road surface and spatial imaging*

The iPAVe TSDD is fitted with five digital imaging cameras to record high resolution images of the pavement and other road assets. The cameras are orientated to ensure that a wide field of view is recorded and are all calibrated for scale measurement and geospatial referencing.

Road surface information is used for the post rating of the road condition, whilst the spatial images provide essential information on roadside furniture, structures, signage, drainage, safety assets and road prism details.

2.6 *Road geometry*

A Global Positioning Satellite (GPS) system provides accurate and synchronized coordinated spatial data of the vertical and horizontal road alignment.

2.7 *Automated crack detection*

Automatic Crack Detection (ACD) using two (2) Laser Crack Management System (LCMS) is an integral component of the iPAVe TSDD. The laser units project a 4m wide laser line across the pavement with the laser image being captured by two 3D cameras mounted off-axis

to the laser light source. The cameras interpret the distortions and each frame is analysed to determine the presence and type of cracking on the pavement surface.

3 COMPARING STATIONARY (FWD) AND TRAFFIC SPEED DEFLECTION MEASUREMENTS (TSD)

Over the years, many comparisons around the world have been made between FWD and TSD measurements, the comparison study methodologies were all different but all aimed to answer the same question i.e., "is the same structural information obtained by the two devices?"

First of all, it is important to look at the differences between the two principles:

The FWD test, Figure 1, is done stationary with intervals tailored to either project or network level, typically between 50 to 200meter intervals. FWD is currently the device with the longest history for structural evaluation and, therefore, the most commonly used device for deflection surveys, this despite the obvious drawbacks, particularly for network level assessment.

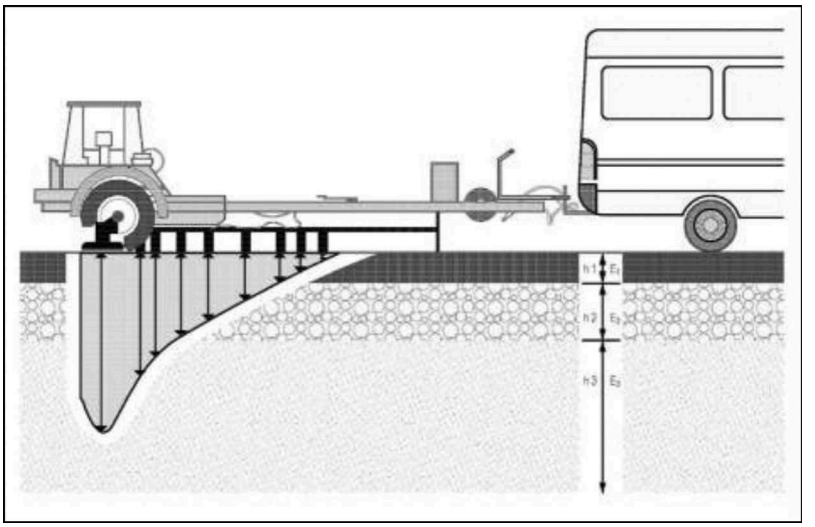

Figure 1. Falling Weight Deflectometer (FGSV, 2004).

The TSD, being an integral part of the iPAVe TSDD, shown in Figure 2, is a significant improvement for measuring structural conditions at traffic speeds of up to 80 km/h. It uses a patented Doppler laser technology beam, also shown in Figure 2, to measure the vertical displacement velocity at various offsets from the loaded wheel. The area under curve method (Muller and Roberts. 2013) is used to convert deflection slopes to a deflection bowl which represents the pavement's response to the wheel load of the iPAVe TSDD.

The main difference between the FWD and the iPAVe TSDD is the loading mechanism of a static impulse type load and a rolling wheel, respectively. Because of the dynamic loading, iPAVe TSDD measured deflections can be influenced by surface irregularities such as surface distress and roughness (Flintsch et al, 2013). However, as dynamic forces induced by unevenness causes heavier loading on the pavement structure, resulting in lower structural serviceability, the influence of unevenness on the iPAVe TSDD measurements are seen as a true representation of actual conditions.

The deflection bowl of the FWD is produced from the physical measured deflection by geophones located at different distances from the load center and represents the magnitude of

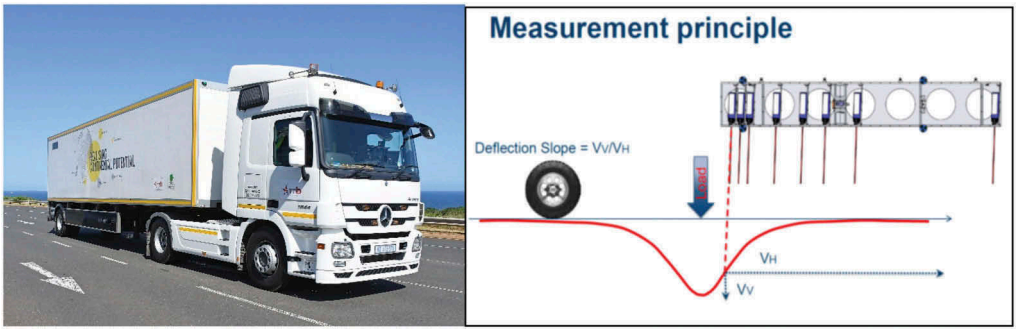

Figure 2. iPAVe TSDD (left) and Doppler laser beam (right).

displacement caused by the impulse load of the FWD. load (typically 50 kN – European standard).

The iPAVe TSDD measures the horizontal traveling speed of the iPAVe TSDD and the vertical deflection velocity of the pavement surface in response to the iPAVe TSDD wheel load. The vertical pavement deflection velocity is divided by the horizontal velocity to derive the deflection slope or tangent at each laser. The combination of deflection slopes at each laser forms the deflection bowl as shown on the bottom right of Figure 3. The slope of the deflection is thus a derivative of the pavement displacement (Ferne et al, 2009). This allows indices such as maximum deflection (D0), base layer index (BLI), middle layer index (MLI) and lower layer index (LLI) to be derived from the deflections.

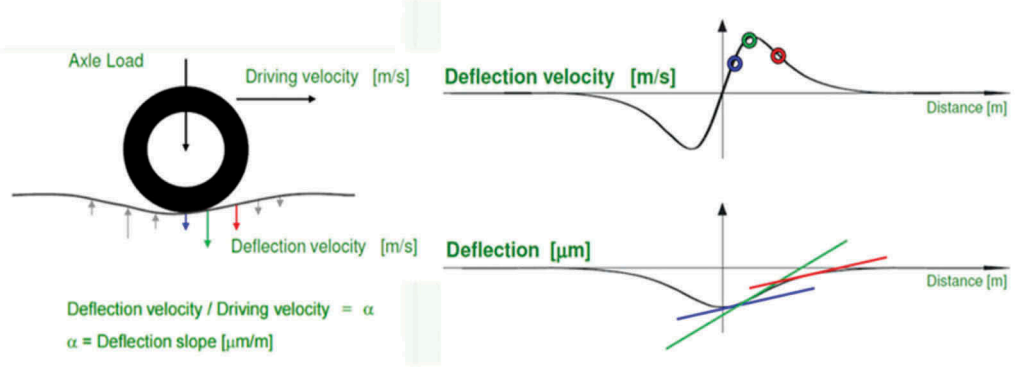

Figure 3. Concept of deflection slope.

3.1 *Pavement layer stiffness*

The measured deflection bowl whether it is from an FWD or an iPAVe TSDD represents the pavement's ability to distribute the load from the traffic applied by the loading plate of the FWD and the dual wheel configuration on the iPAVe TSDD. The shape and the magnitude of the deflection bowl provides information of the pavement stiffness. However, to perform capacity and remedial analysis of a pavement, the characteristics of the individual layers needs to be determined, requiring knowledge of the individual layer thicknesses and to a lesser extent, the layer type. Traditionally the structural capacity of each layer is calculated using a "back-calculation" processes.

3.2 *Are the same results obtained with the FWD compared to iPAVe TSDD?*

Often, existing, and traditionally used equipment's are used as references for validating new methodologies, this although there are often fundamental differences between the old and new equipment. If we compare the traditional method of measuring pavement bearing capacity i.e., the FWD with the new approach, namely iPAVe TSDD, we need to look at the differences of the two methods. And in this case, there are some significant differences. Not only in the recording of the pavement deflections, where geophones are used with the FWD and Doppler sensors are used with the iPAVe TSDD, going from deflection recordings to recording vertical pavement surface speed, during loading. Also, the loading and the footprint of the loading is different, having a single circular loading plate for the FWD and a dual wheel configuration as used in reality on trucks, on the iPAVe TSDD. These differences cause different loadings, stress and strains and thereby different deflections of the pavement. Even though these differences are accepted, comparison of the two principles are done, and often with the FWD as reference.

The first question to be raised is how comparable are the actual deflections when measured? More importantly, what is the end result, i.e.

1) does the measurement inform the road engineer that the road is structural sound? and
2) how much capacity does it have? and
3) when will strengthening be required to extend its structural lifetime?

A study performed in South Africa (Visser and Tetley 2020), highlighted the comparisons between the FWD and the iPAVe TSDD by doing structural evaluation, as it would be carried out in a "real life" project level design on several test sections in South Africa. The back and forward calculations were undertaken using commercial software compiled for the analysis of FWD generated deflections.

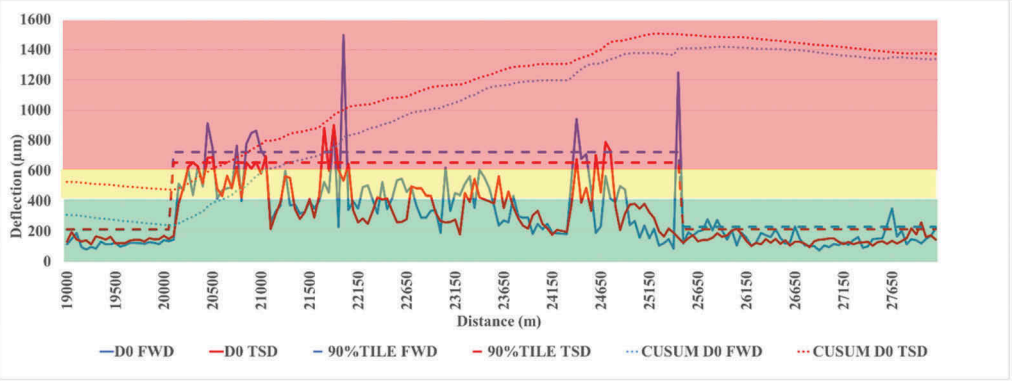

Figure 4. Comparison of FWD and iPAVe TSDD, max deflection and structural condition benchmarking (SAPEM ch. 10).

Figure 4, presents the actual and 90th percentile D0 values from the FWD and iPAVe TSDD, together with uniform section demarcation (cusum method) and benchmarking against deflection bowl parameter structural condition rating criteria as per South African Pavement Engineering Manual Chapter 10: Pavement Design. From the above, it can be clearly seen that the D0 values generated by the FWD and iPAVe TSDD are not identical but are comparable, with 90 percentile values for each method falling into the same condition limits with the uniform section turn points also coinciding.

In order to assess the comparative back calculated layer moduli and subsequent bearing capacity evaluation, the deflections obtained from FWD and iPAVe TSDD were analysed using the Rubicon Toolbox computer software package – this program having been compiled for the analysis of FWD deflection measurements.

Table 1. Comparison of iPAVe TSDD and FWD derived layer stiffness moduli and estimated structural capacity.

Test	Uniform Section	Back calculated Stiffness's (MPa)					Capacity (MESA)
		Layer 1	Layer 2	Layer 3	Upper Subgrade	Substratum	
FWD	Section 1	6000	960	70	120	210	8,5
iPAVe TSDD	Section 1	5900	980	80	120	160	8,6
FWD	Section 2	750	160	40	100	120	0,1
iPAVe TSDD	Section 2	700	140	140	100	90	0,1
FWD	Section 3	6900	990	80	100	130	9,1
iPAVe TSDD	Section 3	6500	980	120	110	150	9,7

As showed in Table 1, despite using a design package intended for use with FWD data, there is very little difference between the mechanistic empirical analysis results that were derived from iPAVe TSDD and FWD measurements. This holds true for distressed and sound condition pavements. It is therefore evident that iPAVe TSDD technology could, in fact, be utilised for project level investigations as well as in network level surveys.

4 HOW CAN SIMULTANEOUS MEASUREMENTS OF STRUCTURAL AND FUNCTIONAL CONDITIONS STRENGTHEN THE EVALUATION OF PAVEMENT LIFE?

The need for actual bearing capacity measurements, particularly in network level assessment, is a subject of interest for many. Unfortunately, it has been a common belief that lack of structural capacity will always result in surface deterioration. This is not always the case as discussed below and, when it is, by the time structural inadequacy has manifested as surface distress, the structural condition is generally so poor that maintenance and rehabilitation is no longer possible and the road will require resource demanding rehabilitation. Seen from a financial and optimization perspective, the earlier the need for maintenance is detected, the more possibilities are available for remedial interventions and, therefore, structural assessments should be conducted to confirm the presence of structural deterioration before treatments are planned for such extensive deterioration. It is not uncommon for some administrations to delay treatments on some roads when such extensive work is required. Either way, the need for confirmation is an important part of appropriate treatment selection.

Not surprisingly, continuous structural capacity assessment, can reveal isolated/discrete portions of highways that may appear acceptable from the surface, but (for a multitude of potential reasons) are not able to provide the same structural support as adjacent portions of the same highway, as shown in the example in Figure 5.

When the opposite occurs, where the pavement section exhibits extensive surface deterioration, as shown in Figure 6, but provides a sufficient structural support, it can lead the administration to believe that substantial maintenance and repairs are required.

Pavement sections that exhibit extensive surface deterioration, may lead to the following, if corresponding structural assessment is not carried out:

a) Treatments may be delayed as a result of the perceived deterioration being caused by structural inadequacy. If the surface continues to decline the result could be a rapid structural

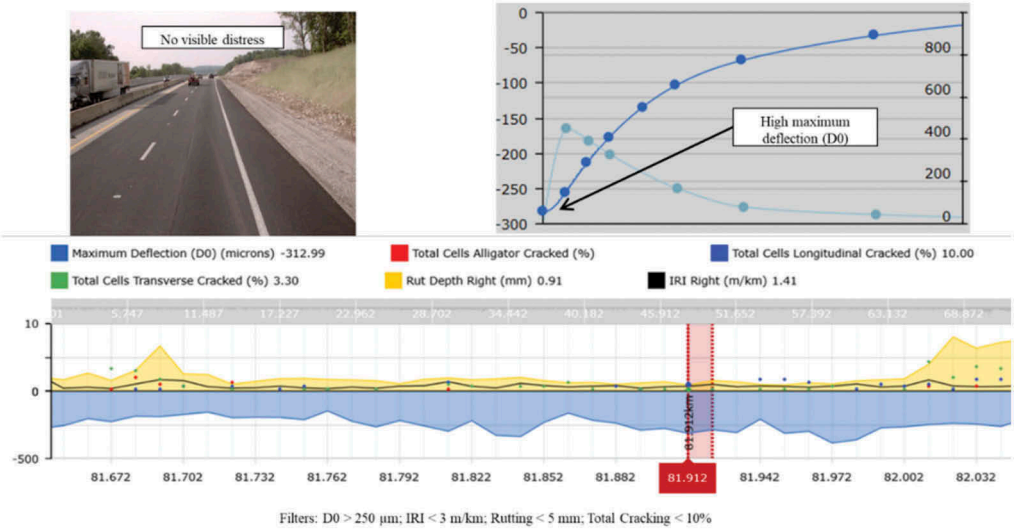

Figure 5. High deflection and a smooth, even road surface.

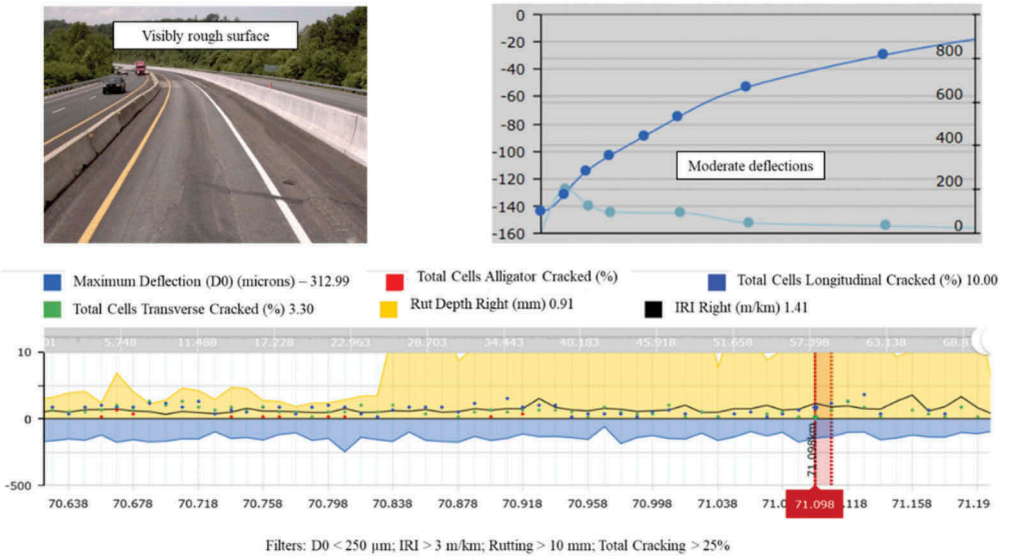

Figure 6. Low deflection and a rough, uneven road surface.

deterioration and ultimately structural collapse (by allowing water to infiltrate the pavement). This will likely lead to accelerated deterioration, regardless of whether structural issues existed initially or not.

b) If an extensive treatment plan is decided (based on the surface deterioration) unnecessary expenditure would result, taking resources away from other road sections where it may likely be more appropriate to spend the maintenance effort.

When the surface is heavily deteriorated as shown in the example in Figure 6, and the assessment reveals a road pavement with a sound structural capacity, the administration can optimize their maintenance budget by e.g.:

c) Remove and replace the problematic surface layer and avoid more extensive unnecessary costly remedial measures.
d) Use saved resources to investigate true cause(s) of surface anomalies.

The above examples clearly show that, regardless which case applies, continuous synchronized structural and surface data provides for a more detailed assessment within a project and/or network level scenario. Rather than assigning some "average" condition for treatment selection and design, discrete sections can be identified with greater confidence and accuracy. This ability offers the potential for isolating and treating areas of greater need. Project level decisions can now be made with 'network level' data thereby negating additional specialist procurement and providing road authority engineers with requisite information on which to base remedial design options. Such work can also be performed in advance of larger rehabilitation projects to produce a more 'homogeneous' structure for more cost-effective designs. Potentially, isolated repairs of this nature may even be performed (on their own) to proactively "buy some time" before additional work is needed.

5 CONCLUSION AND FURTHER INITIATIVES

Using comprehensive measurements (recording both surface characteristics and bearing capacity simultaneously) analysis provides the administrations the ability to detect present and forthcoming conditions at an earlier stage than has been traditionally possible. This provides a unique possibility for the administration to:

a) Proactively conduct spot repairs at precisely defined locations in advance of surfacing treatments, to improve treatment performance and optimize required thicknesses.
b) Proactively alter treatment forecasts and strategies to mitigate more extensive areas of structural concern, that currently are not identifiable e from the surface condition.

A newly published report by Samer W. K et al. 2020, shows the immediate benefit of using traffic speed deflection measurements but also the need for conducting comprehensive measurements for the decision making process, and that measurements and observations of pavement surface characteristics cannot stand alone. Implementing comprehensive and simultaneous pavement measurement data into road infrastructure asset management will greatly assist in overcoming the challenges of providing and efficient and safe road infrastructure that meets modern and future social expectations.

REFERENCES

OECD Environment Policy Paper No 14, 2018 *Climate-resilient Infrastructure*

Mikkel Mollerup og Thomas Rohde 2016. *Grundvandsstigningers påvirkning af vejes bæreevne*

Research Society for Roads and Traffic, FGSV Working Paper draft Feb. 2004 *"Load Capacity", Part C2 "FWD, Evaluation and Evaluation"*,

Wayne B. Muller & Jon Roberts. 2013. *Revised approach to assessing traffic speed deflectometer data and field validation of deflection bowl predictions*, International Journal of Pavement Engineering, 14:4,388–402,

Flintsch G., Katicha, S., Bryce, J., Ferne, B., Nell, S., and Diefenderfer, B. 2013. *Assessment of Continuous Pavement Deflection Measuring Technologies*. SHRP 2 Report S2-R06F55 RW-1.

Visser, H.J., Tetley, S. 2020 *Comparative evaluation of the structural capacity of cracked and uncracked flexible pavements using mechanistic empirical methods based on deflection measurements by the Falling Weight Deflectometer (FWD) and A Traffic Speed Deflectometer Device (TSDD)*

Samer W. K., Shivesh S., Flintsch G., Via C. E., Diefenderfer B., 2020. *Network Level Pavement Structural Testing with the Traffic Speed Deflectometer*

Eleventh International Conference on the Bearing Capacity of Roads, Railways and Airfields, Volume 2 – Hoff, Mork & Saba (eds)

Systematic use of transport infrastructure non-destructive assessment and remote sensing

Andrea Benedetto
Department of Engineering, Roma Tre University, Rome, Italy

Imad L. Al-Qadi
Illinois Center for Transportation, Department of Civil and Environmental Engineering, University of Illinois at Urbana-Champaign, Urbana

Amir M. Alani
School of Computing and Engineering, University of West London (UWL) Ealing, London, UK

Luca Bianchini Ciampoli
Department of Engineering, Roma Tre University, Rome, Italy

Andreas Loizos
Laboratory of Pavement Engineering, National Technical University of Athens (NTUA), Zografou Campus, Zografou, Athens, Greece

Fabio Tosti*
School of Computing and Engineering, University of West London (UWL) Ealing, London, UK

ABSTRACT: For decades, remote sensing technologies and the non-destructive testing (NDT) methods have been used for the assessment of transport infrastructure, highways, railways and airfields. The existence of provisions of multi-source, multi-scale and multi-temporal based information on infrastructure conditions on one hand and the developments of hardware and software technologies in the other, have provided opportunities for the growth of the applications of NDT techniques. The outcome lends itself to be incorporated into existing infrastructure management models. This paper presents an overview of the latest developments in ground-based (Ground Penetrating Radar (GPR) and interferometric radar systems) and satellite (space-borne Synthetic Aperture Radar (SAR) interferometry) remote sensing that applied to transport infrastructures. The applications of GPR to pavements, e.g. multi-layered pavement structure and asphalt concrete (AC) density, and rail-tracks, e.g. ballast assessment are discussed. In addition, the applicability of ground-based radar interferometry and SAR for the bridge structural health monitoring and horizontal transport infrastructure is presented. A novel integrated approach is introduced to form the base of a novel intelligent transport infrastructure management system. The approach is aimed utilizing the structure condition assessment-based information collected using SAR and NDT techniques to prioritize maintenance/rehabilitation activities of transportation assets. For example, analyses of multi-temporal SAR data are used to identify areas of concern at the network level (e.g. differential settlements at bridge approaches or rail track-beds, and excessive deformation rate of pavement surface). The identified locations would be further assessed using ground-based techniques to collect more accurate data. This approach would provide an effective, efficient, and sustainable state of good repair over the life cycle of the transportation infrastructure system.

*Corresponding author
DOI: 10.1201/9781003222897-22

Keywords: Non-destructive assessment, remote sensing technologies, interferometric synthetic aperture radar (InSAR), intelligent infrastructure management systems

1 INTRODUCTION

Non-destructive testing (NDT) methods have been widely used for the assessment of transport infrastructure in the last decades. Several indirect non-invasive technologies have been successfully applied ad proved to enhance effectiveness and productivity of monitoring transportation infrastructural asset. This includes applications to superstructure (Joshaghani, 2019, Plati et al. 2020), subgrade (Nabizadeh et al. 2019, Xu et al. 2013) and concrete elements (Capozzoli and Rizzo 2017, Tosti and Ferrante 2020), highways (Plati and Loizos 2012, Goktepe et al. 2006), railways (Artagan et al. 2020, Al-Qadi et al. 2016) and airfields (McQueen et al. 2001, Gopalakrishnan and Thompson, 2007).

The advancements of hardware and software technologies have generated new opportunities for the growth of the NDT techniques applications to transportation infrastructure; allowing collection of multi-source, multi-scale and multi-temporal based information on its condition. Such information can be readily available for incorporation into existing transportation infrastructure management models (AASHTO 2019, Nasimifar et al. 2019, Tosti et al. 2018, FAA 2016). To further advance current continuous and rapid measurements and enhance measurement resolution, new NDT technologies have been introduced (Artagan et al. 2020, Nasimifar et al. 2019).

Ground penetrating radar (GPR) technique has proven versatile for pavement application due to its relatively surveying flexibility, rapidity of data collection, and accuracy (Ciampoli et al. 2019, Al-Qadi and Lahouar 2005). Hence, GPR could be integrated with a deflection-based non-destructive testing (e.g., Falling Weight Deflectometer (FWD)) for the evaluation of layer structural capacity (Elbagalati et al. 2017, Crook et al. 2012). The calculated layer thicknesses from GPR measurements are used in the backcalculation of FWD data analysis to predict layer moduli. This would affect the remaining pavement service life prediction (Tosti et al. 2018, Elbagalati et al. 2017). GPR has been also successfully used in asphalt concrete (AC) pavement density estimation and part of the paving quality control (QC) and quality assurance (QA). An accurate density measurement during compaction allows for a near real-time correction to better control the compaction process (Plati et al. 2020, Zhao and Al-Qadi 2019, Killingsworth 2004).

The proper non-destructive evaluation (NDE) application mainly relies on existing inventory data and the provision of routine inspection carried out at the network level of the transportation infrastructure asset, considering a prioritization criterion. The outcome of the NDE network monitoring allows producing a dynamic priority list of critical sections that require action utilizing an optimization approach. However, such management models may be hindered by NDT resources and expertise required and available to inspect the asset network periodically, which is crucial to optimize maintenance/rehabilitation strategies.

To overcome the above limitations, remote sensing could be utilized. Remote sensing is defined as the measurement or the acquisition of information on specific properties of a target by a recording device, which is not in physical contact with the object itself (Colwell 1997). These techniques can be passive (e.g., infrared thermography) or active (e.g., RADAR, LiDAR), depending on the source of the received energy. Amongst the active remote sensing tools, satellite Synthetic Aperture Radar (SAR) can benefit from the forward motion of the orbiting satellite, resulting in an equivalent 'synthesized' large aperture to obtain adequate measurement resolution from high altitudes (Hoppe et al. 2016).

A dense array of information could be collected on the overall structural stability of the asset and the surrounding environment, using multi-scale and multi-temporal SAR images. The coverage of every image collected by SAR sensors, allows the evaluation of large infrastructures at the network level in a single data processing flow. Hence, interferometric approaches based on the comparison between multiple SAR images have proven effective in assessing transport infrastructure conditions (Tosti et al. 2021). However, individual outcome

may be inevitably incomplete under different perspectives. To achieve a faster and accurate information on the transportation infrastructure asset, the integration between multi-source, multi-scale and multi-temporal datasets allows to fill individual technology gaps. Despite of the high potential for the application of this technology to transport infrastructures (Bianchini Ciampoli et al. 2020, Monserrat et al. 2014), the use of remote sensing techniques is still not implemented as a routine inspection method.

This paper presents an overview of the latest developments in GPR and interferometric radar systems, and satellite (space-borne SAR interferometry) remote sensing that applied to transport infrastructure. Successful applications of GPR are presented for pavements and railtracks, including the evaluation of multi-layered pavement structure, AC density, and railway ballast assessment. In addition, the paper discusses the applicability of ground-based radar interferometry and SAR for bridge structural health monitoring and horizontal transport infrastructure, respectively.

2 EMERGING TRANSPORT INFRASTRUCTURE NON-DESTRUCTIVE ASSESSMENT AND REMOTE SENSING

Major damage in transport infrastructure could occur due to reduced load bearing of pavement layers. Hence, laboratory and on-site assessment of the structural layer bearing capacity can be performed by measuring pavement progressive deformation due to applied loading (ASTM 2009a,b). Although electromagnetic properties of the material may not be related to its strength characteristics, various NDT methods may be used to indirectly relate material properties to potential damage (e.g., relating the change in the dielectric properties of a pavement layer to its potential distress). The term dielectric in the study refers to relative dielectric constant or relative permittivity.

2.1 *Ground-based NDTs*

Amongst the available non-destructive NDT methods, GPR has been extensively used for the assessment and health monitoring of transport infrastructure. The GPR technology relies on the transmission of electromagnetic (EM) waves through a target/medium. In case an inhomogeneity is encountered, the energy radiated by a transmitting antenna is partly reflected to the receiver and partly transmitted through the medium. However, as its propagation (amplitude, velocity, attenuation) is ruled by the dielectric properties of the illuminated medium (Jol 2009). The change in the dielectric constant due to subsurface conditions is returned in the form of EM reflection. Post-processing algorithms are usually applied to predict the dielectric constant of the medium and then to calculate the medium dimensions (2 dimensions unless 3D GPR is used).

Research on GPR has resulted in new emerging trends, including the following:

- *High-accurate AC pavement density assessment*. AC pavement density estimation from GPR measurements is based on predicting the dielectric properties of the AC material, which is obtained by applying Fresnel's law. Based on the mixing theory, the Al-Qadi, Lahouar and Leng (ALL) model (Leng et al. 2012, Leng et al. 2011) relates the AC mixture component dielectrics to the bulk density of the AC. In addition, the effect of signal noise and surface moisture are accounted for in the pre-processing of the GPR signals to ensure the model accuracy in AC prediction (Wang et al. 2020, Wang et al. 2019).
- *Railway ballast health assessment.* Railway ballast is referred to as a homogeneously graded hard-rock-derived material providing adequate support to the loads passing onto the rails and proper drainage capacity (Selig and Waters 1994). During the infrastructure life cycle, this material is likely to be polluted by different sources of ballast fouling. Fragmentation of aggregates under cyclic loading and the uprising of fine particles from the subgrade have been reported amongst the main causes that can trigger severe deformations to railways, undermining safety and operability of the infrastructure (Solomon 2001). In the last decades, GPR has been increasingly used as a fast

and reliable tool for the assessment of critical railway ballast conditions (Artagan et al. 2020). It is also observed that the research focus in this area has been progressively moved from time-domain analyses (e.g., layering and reconstruction of structural elements (Benedetto et al. 2017a, Sussmann et al. 2003, Gallagher et al. 1999)) to frequency and time-frequency analyses of the GPR signal (e.g., the evaluation of changes in the as-built ballast aggregates' arrangement) (Al-Qadi et al. 2010, Al-Qadi et al. 2008a). In this context, the spectral analyses of clay-related fouling and grading changes caused by aggregates friction are worthy of mention (Benedetto et al. 2017b, Bianchini Ciampoli et al. 2017, Al-Qadi et al. 2008a). In addition, time-frequency analyses and wavelet approaches have proven successful at relating signal scattering effects to ballast voids at different rates of fouling (Bianchini Ciampoli et al. 2020, Al-Qadi et al. 2016, Shangguan and Al-Qadi 2014, Shangguan et al. 2012, Al-Qadi et al. 2008b).

- *Health monitoring of masonry arch bridges*. Arch bridge structures are very common and historical types of asset vital to the economy, mobility and development of communities. No doubt an effective assessment and routine monitoring of bridge structures are nowadays crucial for maintenance, regardless of their historical value and mobility function. Health of bridges can be assessed using several monitoring methods and sensors (Zhou and Yi 2013, Moschas and Stiros 2011), including GPR (Solla et al. 2012, Lubowiecka et al. 2009). Due to the structural complexity of the target, stand-alone GPR applications on masonry bridges has been mostly employed for initial mapping and subsurface target locations, as opposed to a more comprehensive structural health monitoring (Saarenketo 2009). However, promising research has been recently published with a focus on the integration between GPR and other NDT method for comprehensive assessment and health monitoring (Alani et al. 2020, Biscarini et al. 2020, Solla et al. 2011).

The ground-based synthetic aperture interferometry (GB-SAR) is another emerging technology in transport infrastructure monitoring. The GB-SAR is a radar-based terrestrial remote sensing imaging system (Tarchi et al. 1997) based on a radar sensor that emits and receives a field of microwaves while moving along a rail track (Bernardini et al. 2007). The imaging capability is achieved by exploiting the SAR technique (Lin et al. 1992). The GB-SAR technique is acknowledged as a reliable tool for landslide and slope monitoring (Pipia et al. 2013), although it has proven effective for structural monitoring applications (Tapete et al. 2013). This is due to the possibility to acquire both temporal and spatial samplings as well as to a high sensitivity of this technique in detecting small displacements. In this context, the joint application of the GB-SAR and other NDT techniques can be regarded as a future prospective approach to collect information for inclusion in infrastructure management systems.

2.2 *Satellite remote sensing*

Various processing techniques have been proposed for displacement mapping from SAR imaging and, amongst these, the Permanent Scatterers InSAR (PSI) method (Ferretti et al. 2000, Ferretti et al. 2001) is one of the most acknowledged. This technique is based on a statistical analysis of the signals back-scattered from a network of phase-coherent targets, named as Permanent Scatterers (PSs). These are defined as points on the ground returning stable signals back to the satellite receiver.

In the last decade, the PSI technique has proven effective in land monitoring applications, such as landslide surveillance (Squarzoni et al. 2020, Frattini et al. 2013), pre- and post-seismic evaluations (Duan et al. 2020) and urban subsidence detection (Khorrami et al. 2020). Regarding the monitoring of transport infrastructures, recent research on emerging applications of the PSI technique is summarized below:

- *Pavement distress assessment.* Linear infrastructures in rural environment contexts are among the most reflective target in terms of SAR transmissions, triggering the generation of a high number of PSs in a PSI analysis. This implies a good potential of the PSI

technique in the monitoring of major pavement distresses (e.g., rutting, deformations and settlements) in both highways (Ozden et al. 2017) and airport runways (Gagliardi et al. 2021, Marshall et al. 2018).

- *Railway track subsidence monitoring.* Similar to roads, railways are excellent scatterers for InSAR analyses. Millimetre-scale displacements can be monitored and accurately located across rail track sections using high-resolution (X-band) satellite data (Bianchini Ciampoli et al. 2020, Tosti et al. 2020), including differential displacements at the rail-abutment sections in railway bridges (D'Amico et al. 2020).
- *Bridge monitoring*. It is known that vertical and horizontal displacements at the piers of bridges may seriously compromise their structural stability. This occurrence is generally related to geodynamic (e.g., the sliding of the slope) or geotechnical aspects (e.g., oedometric subsidence of the piles). The SAR-based processing technique was successful applied for the evaluation of three major bridge features. The linear deformation trend, the height of the structure over terrain, and the thermal expansion were proven to create variations in the SAR phase (D'Amico et al. 2020, Lazecky et al. 2017, Zhao et al. 2017).
- *Assessment of tunnelling-induced subsidence*. In general, formation of vertical settlements is first observed at the tunnel construction stage, followed by an increased instability of the concerning area compared to the surrounding, once the structure is built. An accurate assessment of these two major stages is crucial for predicting any potential future subsidence expected on nearby buildings and infrastructures. Multi-temporal SAR analyses have allowed to monitor the entire construction process, and verify the future stability to ground settlements of the investigated area (Milillo et al. 2018, Perissin et al. 2012).

3 THE INTEGRATED APPROACH

Based on the potential integration of remote sensing technologies and NDT methods, an intelligent transport infrastructure management system is introduced (Figure 1). The proposed approach is developed based on the provision of inventory data, identified network elements, and as-built information. It is characterized by two concurrent routine monitoring stages at low- and high-frequency monitoring rates applied at local and network levels, respectively.

Remote sensing technologies can be used to assess the entire infrastructure network in terms of ongoing geotechnical/geodynamic processes, with a high time resolution (~10 days) permitted by the scale of analysis. In case critical spots are identified, targeted inspections can be carried out with dedicated NDT techniques to build a more comprehensive information system on the type and scale of the developing distress at the identified infrastructure sections. The information obtained at this stage and processes in distress prediction models, could assist in the maintenance/rehabilitation requirement and priority decision.

Parallel to remote sensing, ground-based NDTs would be applied to the network, but at a lower frequency rate. The testing frequency is controlled by cost, productivity, and resource availability. The main scope of this stage is to assess any potential distress in terms of severity level and extent, causes, and effects, which may not be detected by satellite remote sensing.

The outcome is a scale of priority of the maintenance and rehabilitation (M&R) activities for individual assets of the network. In case the need for an intervention is ascertained, the provision of M&R alternatives is assessed based on the compliance to safety requirements and economic constraints.

For each of the alternatives, a cost-benefit analysis is performed, leading to the selection of the optimal strategy of M&R intervention. This approach is updated periodically to continuously upgrade the prioritization list that can be dynamically used to allocate funding.

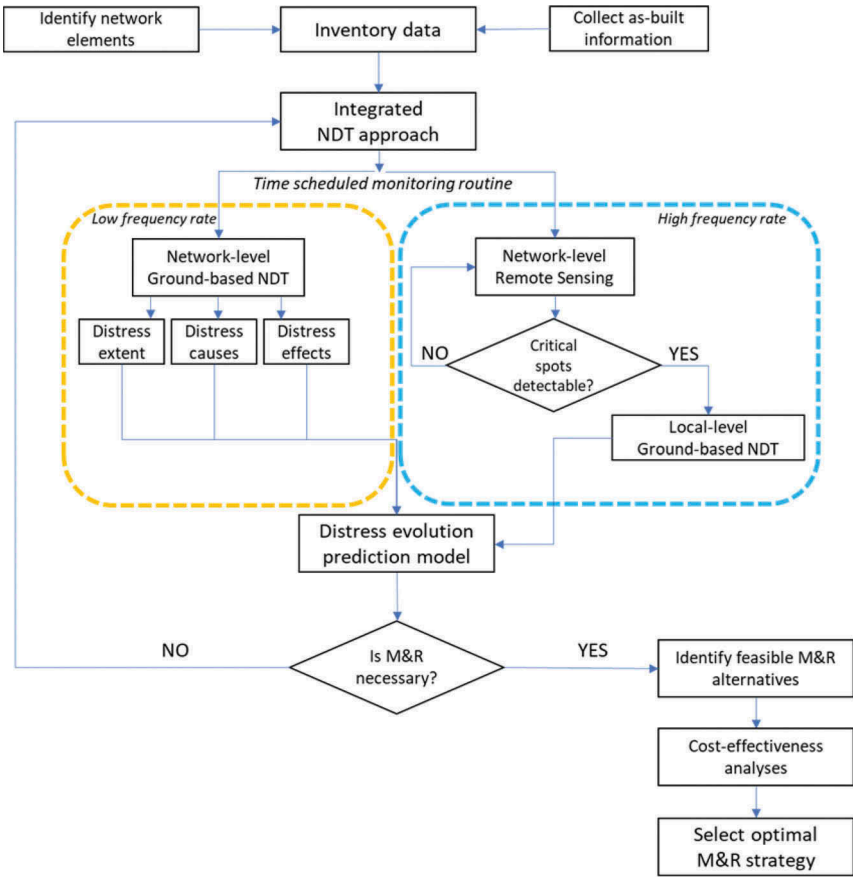

Figure 1. Proposed intelligent transport infrastructure management system.

4 CONCLUSIONS

This paper presents an overview of the emerging developments in ground-based non-destructive testing (NDT) and remote sensing technologies that applied to transport infrastructure. Ground penetrating radar (GPR) and ground-based synthetic aperture radar (GB-SAR) interferometry are presented. In addition, applications of the space-borne SAR interferometry (InSAR) for infrastructure network surveillance are discussed. The use of multi-source, multi-scale and multi-temporal information is required to achieving a comprehensive knowledge of distresses and build more reliable prediction models.

An integrated approach for transport network surveillance is proposed for application to transportation infrastructure. The approach considers inventory data as input, identifies network elements and as-built information. Surveys with remote sensing technologies and NDT techniques are envisaged to be carried out at different scales and times to monitor the genesis and the evolution of the damage progression. Based on the relevant outcome, distress evolution prediction models could be developed – compared to traditional infrastructure management systems (e.g., Pavement Management Systems (PMSs)) – to define a priority scale of intervention that can be updated with a higher temporal frequency. This allows proposing alternative M&R approaches and compares then using cost-benefit analyses for optimal intervention strategy.

REFERENCES

Al-Qadi, I.L. and Lahouar, S., 2005. *Measuring Layer Thicknesses with GPR–Theory to Practice*. Construction and Building Materials, 19(10), 763–72.

Al-Qadi, I.L., Xie, W. and Roberts, R., 2008a. *Time-Frequency Approach for Ground Penetrating Radar Data Analysis to Assess Railroad Ballast Condition*. Research in Nondestructive Evaluation;19, 219–37.

Al-Qadi, I.L., Xie, W. and Roberts, R., 2008b. *Scattering Analysis of Ground-Penetrating Radar Data to Quantify Railroad Ballast Contamination*. NDT &E International, 41, 441–7.

Al-Qadi, I.L., Xie, W., Jones, D.L. and Roberts, R., 2010. *Development of a Time–Frequency Approach to Quantify Railroad Ballast Fouling Condition Using Ultra-Wide Band Ground-Penetrating Radar Data*. International Journal of Pavement Engineering, 11(4), 269–279.

Al-Qadi, I.L., Zhao, S. and Shangguan, P., 2016. *Railway Ballast Fouling Detection Using GPR Data: Introducing a Combined Time-Frequency and Discrete Wavelet Techniques*. Near Surface Geophysics, 14(2), 145–153.

Alani, A.M., Tosti, F., Ciampoli, L.B., Gagliardi, V. and Benedetto, A., 2020. *An Integrated Investigative Approach in Health Monitoring of Masonry Arch Bridges Using GPR and InSAR Technologies*. NDT & E International, 115,102288.

American Association of State Highway and Transportation Officials (AASHTO), 2019. *Guidelines for Geometric Design of Low-Volume Road*. Ed. AASHTO, Washington, USA.

Artagan, S.S., Bianchini Ciampoli, L., D'Amico, F., Calvi, A. and Tosti, F., 2020. *Non-destructive Assessment and Health Monitoring of Railway Infrastructures*. Surveys in Geophysics, 41(3), 447–483.

ASTM D1195/D1195M-09, 2009. *Standard Test Method for Repetitive Static Plate Load Tests of Soils and Flexible Pavement Components, for Use in Evaluation and Design of Airport and Highway Pavements*. ASTM International, West Conshohocken, PA.

ASTM D4429-09a, 2009. *Standard Test Method for CBR (California Bearing Ratio) of Soils in Place*. ASTM International, West Conshohocken, PA.

Benedetto, A., Tosti, F., Bianchini Ciampoli, L., Calvi, A., Brancadoro, M.G. and Alani, A.M., 2017a. *Railway Ballast Condition Assessment Using Ground-Penetrating Radar – an Experimental, Numerical Simulation and Modelling Development*. Construction and Building Material; 140, 508–20.

Benedetto, F., Tosti, F. and Alani, A.M., 2017b. *An Entropy-Based Analysis of GPR Data for the Assessment of Railway Ballast Conditions*, IEEE Transactions on Geosciences and Remote Sensing, 55, 3900–8.

Bernardini, G., Ricci, P. and Coppi, F., 2007. *A Ground Based Microwave Interferometer with Imaging Capabilities for Remote Measurements of Displacements*. Proceedings of GALAHAD Workshop 3rd International Geotelematics Fair (GlobalGeo), Barcelona, Spain.

Bianchini Ciampoli, L., Calvi, A. and D'Amico, F., 2020. *Railway Ballast Monitoring by GPR: A Test-Site Investigation*. Remote Sensing, 11(20), 2381.

Bianchini Ciampoli, L., Gagliardi, V., Clementini, C., Latini, D., Del Frate, F. and Benedetto A., 2020. *Transport Infrastructure Monitoring by InSAR and GPR Data Fusion*. Surveys in Geophysics, 41(3), 371–394.

Bianchini Ciampoli, L., Tosti, F., Brancadoro, M.G., D'Amico, F., Alani, A.M. and Benedetto, A., 2017. *A Spectral Analysis of Ground-Penetrating Radar Data for the Assessment of the Railway Ballast Geometric Properties*. NDT & E International, 90, 39–47.

Biscarini, C., Catapano, I., Cavalagli, N., Ludeno, G., Pepe, F.A. and Ubertini, F., 2020. UAV *Photogrammetry, Infrared Thermography and GPR for Enhancing Structural and Material Degradation Evaluation of the Roman Masonry Bridge of Ponte Lucano in Italy*. NDT and E International, 115, 102287.

Capozzoli, L. and Rizzo, E., 2017. *Combined NDT Techniques in Civil Engineering Applications: Laboratory and Real Test*. Construction and Building Materials, 154(15), 1139–1150.

Ciampoli, L.B., Tosti, F., Economou, N. and Benedetto, F., 2019. *Signal Processing of GPR Data for Road Surveys*. Geosciences, 9(2), 96.

Colwell, R.N., 1997. *History and Place of Photographic Interpretation, Manual of Photographic Interpretation*. W.R. Philipson (Ed.) 2nd Ed., Bethesda: American Society for Photogrammetry & Remote Sensing, 33–48.

Crook, A.L., Montgomery, S.R. and Guthrie, W.S., 2012. *Use of Falling Weight Deflectometer Data for Network-Level Flexible Pavement Management*. Transportation Research Records: Journal of Transportation Research Board 2304, 75–85.

D'Amico, F., Gagliardi, V., Bianchini Ciampoli, L. and Tosti, F., 2020. *Integration of InSAR and GPR Techniques for Monitoring Transition Areas in Railway Bridges*. NDT and E International, 115, 102291.

Duan, H., Wu, S., Kang, M., Xie, L. and Chen, L., 2020. *Fault Slip Distribution of the 2015 Mw7.8 Gorkha (Nepal) Earthquake Estimated from InSAR and GPS Measurements*. Journal of Geodynamics, 139, 101767.

Elbagalati, O., Elseifi, M.A., Gaspard, K. and Zhang, Z., 2017. *Implementation of the Structural Condition Index into the Louisiana Pavement Management System based on Rolling Wheel Deflectometer Testing*. Transportation Research Records: Journal of Transportation Research Board, 2641, 1, 39–47.

Ferretti A., Prati C. and Rocca F., 2000. *Nonlinear Subsidence Rate Estimation Using Permanent Scatterers in Differential SAR Interferometry*. IEEE Transactions on Geoscience and Remote Sensing, 38 (5), 2202–12.

Ferretti A., Prati C. and Rocca F., 2001. *Permanent Scatterers in SAR Interferometry*. IEEE Transactions on Geoscience and Remote Sensing, 39(1), 8–20.

Frattini, P., Crosta, G.B. and Allievi, J., 2013. *Damage to Buildings in Large Slope Rock Instabilities Monitored with the PSinSAR™ Technique*. Remote Sensing, 5(10), 4753–4773.

Gagliardi, V., Bianchini Ciampoli, L., Trevisani, S., D'Amico, F., Alani, A.M., Benedetto, A.; and Tosti, F. 2021. *Testing Sentinel-1 SAR Interferometry Data for Airport Runway Monitoring: A Geostatistical Analysis*. Sensors, 21, 5769.

Gallagher, G.P., Leiper, Q., Williamson, R., Clark, M.R. and Forde, M.C., 1999. *The Application of Time Domain Ground Penetrating Radar to Evaluate Railway Track Ballast*. NDT & E International, 32, 463–8.

Goktepe, A.B., Agar, E. and Lav, A.H., 2006. *Advances in Backcalculating the Mechanical Properties of Flexible Pavements*, Advances in Engineering Software, 37(7), 421–431.

Gopalakrishnan, K. and Thompson, M.R., 2007. *Use of Nondestructive Test Deflection Data for Predicting Airport Pavement Performance*. J. Transp. Engin., 133(6), 389–395.

Hoppe, E., Bruckno, B., Campbell, E., Acton, S., Vaccari, A., Stuecheli, M., Bohane, A., Falorni, G. and Morgan, J., 2016. *Transportation Infrastructure Monitoring Using Satellite Remote Sensing*. Materials and Infrastructures, 1, 5, 185–198.

Jol H. (Ed.), 2009. *Ground Penetrating Radar*, Elsevier.

Joshaghani, A., 2019. *Identifying the Problematic Areas with Structural Deficiencies of Pavements Using Non-Destructive Tests (NDT*). International Journal of Pavement Engineering, 20 (11), 1359–1369.

Khorrami, M., Abrishami, S., Maghsoudi, Y., Alizadeh, B. and Perissin, D., 2020. *Extreme Subsidence in a Populated City (Mashhad) Detected by PSInSAR Considering Groundwater Withdrawal and Geotechnical Properties*. Scientific Reports, 10(1), 11357.

Killingsworth B.M., 2004. *Quality Characteristics for Use with Performance Related Specifications for Hot Mix Asphalt*. 291. Research Results Digest.

Lazecky, M., Hlavacova, I., Bakon, M., Sousa, J. J., Perissin, D. and Patricio, G., 2017. *Bridge Displacements Monitoring Using Space-Borne X-Band SAR Interferometry*. IEEE Journal of Selected Topics in Applied Earth Observations and Remote Sensing, 10, 1, 205–210.

Leng, Z., Al-Qadi, I.L. and Lahouar, S., 2011. *Development and Validation for In Situ Asphalt Mixture Density Prediction Models*. NDT & E International, 44(4), 369–375.

Leng, Z., Al-Qadi, I.L., Shangguan, P. and Son, S., 2012. *Field Application of Ground-Penetrating Radar for Measurement of Asphalt Mixture Density*. Transportation Research Record, 2304, 133–141.

Lin, Q., Vesecky, J.F. and Zebker, H.A., 1992. *New Approaches in Interferometric SAR Data Processing*. IEEE Transactions on Geoscience and Remote Sensing, 30, 3.

Lubowiecka, I., Armesto, J., Arias, P. and Lorenzo, H., 2009. *Historic Bridge Modelling Using Laser Scanning, Ground Penetrating Radar and Finite Element Methods in the Context of Structural Dynamics*. Engineering Structures, 31(11), 2667–2676.

Marshall, C., Large, D.J., Athab, A., Evers, S.L., Sowter, A., Marsh, S. and Sjögersten, S., 2018. *Monitoring Tropical Peat Related Settlement Using ISBAS InSAR, Kuala Lumpur International Airport (KLIA*). Engineering Geology, 244, 3, 57–65.

McQueen, R.D., Marsey, W. and Arze, J.M., 2001. *Analysis of Nondestructive Test Data on Flexible Pavements Acquired at the National Airport Pavement Test Facility*. Proceedings of the International Air Transportation Conference, 267–278. Atlantic City, NJ, USA.

Milillo, P., Giardina, G., DeJong, M.J., Perissin, D. and Milillo, G., 2018. *Multi-temporal InSAR Structural Damage Assessment: The London Crossrail Case Study*. Remote Sensing, 10, 2, 287.

Monserrat, O., Crosetto, M. and Luzi, G., 2014. *A Review of Ground-Based SAR Interferometry for Deformation Measurement*. ISPRS J Photogrammetry and Remote Sensing, 93, 40–48.

Moschas, F. and Stiros, S., 2011. *Measurement of the Dynamic Displacements and of the Modal Frequencies of a Short-Span Pedestrian Bridge Using GPS and an Accelerometer*. Engineering Structures, 33, 10–7.
Nabizadeh, H., Siddharthan, R.V., Hajj, E.Y., Nimeri, M. and Elfass, S., 2019. *Validation of the subgrade Shear Strength Parameters Estimation Methodology Using Light Weight Deflectometer: Numerical Simulation and Measured Testing Data*. Transportation Geotechnics, 21, 100259.
Nasimifar, M., Thyagarajan, S., Chaudhari, S. and Sivaneswaran, N., 2019. *Pavement Structural Capacity from Traffic Speed Deflectometer for Network Level Pavement Management System Application*. Transportation Research Record, 2673(2), 456–465.
Ozden, A., Faghri, A., Li, M. and Tabrizi, K., 2017. *Evaluation of Synthetic Aperture Radar Satellite Remote Sensing for Pavement and Infrastructure Monitoring*. Procedia Engineering, 145, 752–759.
Perissin, D., Wang, Z. and Lin, H., 2012. *Shanghai Subway Tunnels and Highways Monitoring Through Cosmo-SkyMed Persistent Scatterers*. ISPRS J Photogrammetry and Remote Sensing, 73, 58–67.
Pipia, L., Fabregas, X., Aguasca, A. and Lopez-Martinez, C., 2013. *Polarimetric Temporal Analysis of Urban Environments with a Ground-Based SAR*. IEEE Transactions on Geoscience and Remote Sensing, 51, 4.
Plati, C. and Loizos, A., 2012. *Using Ground-Penetrating Radar for Assessing the Structural Needs of Asphalt Pavements*. NDT & E International, 27(3), 273–284.
Plati, C., Loizos, A. and Gkyrtis, K., 2020. *Integration of Non-Destructive Testing Methods to Assess Asphalt Pavement Thickness*. NDT & E International, 115,102292.
Saarenketo, T., 2009. *NDT transportation*, In: Jol HM, editor. Elsevier.
Selig, E.T. and Waters, J.M., 1994. *Track Geotechnology and Substructure Management*. London: Thomas Telford.
Shangguan, P. and Al-Qadi, I.L. 2014. *Content-Based Image Retrieval Approaches to Interpret Ground Penetrating Radar Data*, Construction and Building Materials, 69, 10–17.
Shangguan, P., Al-Qadi, I.L. and Leng, Z. 2012. *Development of Wavelet Technique to Interpret Ground-Penetrating Radar Data for Quantifying Railroad Ballast Conditions*, Transportation Research Record, no. 2289, 95–102.
Solomon, B., 2001. *Railway Maintenance: the Men and Machines that Keep the Railroads Running*. Wisconsin: MBI Publishing Company.
Solla, M., Lorenzo, H., Rial, F.I. and Novo, A., 2012. *Ground-Penetrating Radar for the Structural Evaluation of Masonry Bridges: Results and Interpretational Tools*. Construction and Building Materials, 29, 458–465.
Solla, M., Lorenzo, H., Riveiro, B. and Rial, F.I., 2011. *Non-Destructive Methodologies in the Assessment of the Masonry Arch Bridge of Traba, Spain*. Eng Failure Analy, 18(3), 828–835.
Squarzoni, G., Bayer, B., Franceschini, S. and Simoni, A., 2020. *Pre- and Post-Failure Dynamics of Landslides in the Northern Apennines Revealed by Space-Borne Synthetic Aperture Radar Interferometry (InSAR*). Remote Sensing of Environment, 249, 111983.
Sussmann T.R. and Selig E.T., Hyslip J.P., 2003. *Railway Track Condition Indicators from Ground Penetrating Radar*. NDT & E International, 36, 157–67.
Tapete, D., Casagli, N., Luzi, G., Fanti, R., Gigli, G. and Leva, D., 2013. *Integrating Radar and Laser-Based Remote Sensing Techniques for Monitoring Structural Deformation of Archaeological Monuments*. Journal of Archaeological Science, 40, 1, 176–189.
Tarchi, D., Ohlmer, E. and Sieber, A., 1997. *Monitoring of Structural Changes by Radar Interferometry*. Research in Nondestructive Evaluation, 9, 4, 213–255.
Tosti, F., Bianchini Ciampoli, L., D'Amico, F., Alani, A.M. and Benedetto, A., 2018. *An Experimental-Based Model for the Assessment of the Mechanical Properties of Road Pavements Using Ground-Penetrating Radar*. Constr Build Mater, 165, 966–974.
Tosti, F. and Ferrante, C., 2020. *Using Ground Penetrating Radar Methods to Investigate Reinforced Concrete Structures*. Surveys in Geophysics, 41(3), 485–530.
Tosti F., Gagliardi V., Bianchini Ciampoli L., Benedetto A., Threader S. and Alani A.M., 2021. *Integration of Remote Sensing and Ground-Based Non-Destructive Methods in Transport Infrastructure Monitoring: Advances, Challenges and Perspectives*. Proceedings - 2021 IEEE AGERS 2021, Virtual Event.
Tosti F., Gagliardi V., D'Amico F. and Alani A.M., 2020. *Transport Infrastructure Monitoring by Data Fusion of GPR and SAR Imagery Information*. Transp Res Proc; 45 771–778. 721.
U.S. Department of Transportation Federal Aviation Administration (FAA), 2016. *Advisory Circular 150/5320-6F*, Airport Pavement Design and Evaluation.
Wang, S., Al-Qadi, I.L. and Cao, Q., 2020. *Factors Impacting Monitoring Asphalt Pavement Density by Ground Penetrating Radar*. NDT & E International, 115, 102296.
Wang, S., Zhao, S. and Al-Qadi, I.L., 2019. *Real-Time Density and Thickness Estimation of Thin Asphalt Pavement Overlay During Compaction Using Ground Penetrating Radar Data*. Surveys in Geophysics, 1–15.

Xu, P., Wang, F.M., Li, X.L. and Cai, Y.C., 2013. *Comparisons Between New and Traditional NDT Devices and Control Methods for Construction Quality of Highway Subgrade*. Geotechnical Special Publication, (215 GSP), 83–91.

Zhao, S. and Al-Qadi, I.L., 2019. *Algorithm Development for Real-Time Thin Asphalt Concrete Overlay Compaction Monitoring Using Ground-Penetrating Radar*. NDT & E International, 104, 114–23.

Zhou, G.-D. and Yi, T.-H., 2013. *Recent Developments on Wireless Sensor Networks Technology for Bridge Health Monitoring*. Mathematical Problems in Engineering, 947867.

Zhao, J., Wu, J., Ding, X. and Wang, M., 2017. *Elevation Extraction and Deformation Monitoring by Multitemporal InSAR of Lupu Bridge in Shanghai*. Remote Sensing, 9, 9, 897.

Eleventh International Conference on the Bearing Capacity of Roads, Railways and Airfields, Volume 2 – Hoff, Mork & Saba (eds)

Evaluation of interface bonding condition on mechanical responses of full-scale asphalt pavements with and without grid reinforcement

X-Q. Le
MAST-LAMES, Gustave Eiffel University, Nantes Campus, Bouguenais, France
University of Transport and Communications, Hanoi, Vietnam

M-L. Nguyen & P. Hornych
MAST-LAMES, Gustave Eiffel University, Nantes Campus, Bouguenais, France

Q-T. Nguyen
University of Transport and Communications, Hanoi, Vietnam

E. Godard, Y. Legal & L. Brissaud
COLAS SA, France

D. Doligez
6D Solutions, France

C. Chazallon
ICUBE, CNRS, INSA Strasbourg, Université de Strasbourg, Strasbourg, France

ABSTRACT: The construction and maintenance of road infrastructure with a view to sustainable development must nowadays integrate the problems of a future scarcity of raw materials such as petroleum products. Glass fiber grids are an efficient and economical solution for reinforcing asphalt pavements in order to increase their service life and reduce crack propagation. In this context, the French National Research Agency-funded SolDuGri project aims to develop more rational and more mechanical approaches for the evaluation of grids, and for the design of reinforced pavements. An accelerated full-scale test (APT) of experimental pavement structures without and with reinforcement using glass fiber grids was carried out on the fatigue carrousel at Nantes Campus of Gustave Eiffel University. During the test, the mechanical behavior of the pavements was monitored using sensors installed in the pavement layers and surface measurements. This paper focuses on analyzing the influence of interface bonding condition between the asphalt layers on the pavements behavior in non-damaged condition. Horizontal strains measured at the bottom of the asphalt layers and surface deflections showed clearly that the reinforced pavement has lower interface bond level than the reference section. Moreover, inverse analysis using FWD measurements and a horizontal shear stiffness parameter allows quantifying field conditions of the asphalt layer interface bonding in both unreinforced and reinforced structures. Associated laboratory interface bonding tests made on specimens extracted from the full-scale pavements and fabricated in laboratory attest the aforementioned impact of the presence of glass fiber grids.

Keywords: Asphalt pavement, glass fiber grid, interface bond, structural behavior, APT

DOI: 10.1201/9781003222897-23

1 INTRODUCTION

Road networks play a crucial role in guaranteeing the mobility of goods and people. As a result, evaluating the structural condition of these networks is essential for optimizing their design life. In many countries, generally more than 90 % of the network consists of asphalt pavements, which are multi-layer structures. When there is more than one asphalt layer, one of the key elements for ensuring a good performance of the pavement is the bond between the asphalt layers. Evaluating and improving the bond between pavement layers is among the principal objectives in many national and international studies (Raab et al. 2009, Canestrari et al. 2013, Zofka et al. 2015, Petit et al. 2018, DVDC, RILEM TC272-PIM, among others). However, these studies are mainly focused on laboratory evaluations. Until now, few studies have investigated this issue at structural level on real-scale pavement (Chun et al. 2015, Nguyen et al. 2016, Grellet 2018). One of the difficulties, at structural level, is the variability of different parameters, such as material properties, loading conditions, environmental factors. In that case, appropriate monitoring methods need to be employed.

Furthermore, for pavements reinforced with glass fiber grid to increase their service life and reduce crack propagation, the presence of such interlayer system will have a significant effect on the pavement behavior. This is due not only to the reinforcing characteristics of the grid (high Young's modulus and high tensile strength), but also to the bonding condition at the pavement layers interface where it is placed, generally between the asphalt layers. While the first aspect is measurable directly from the grid, the second one still needs further investigations, for a better understanding of its impacts. For the last one, several recent studies have been conducted by testing on reinforced material specimens in laboratory (Gharbi et al. 2017, Freire et al. 2018, Canestrari et al. 2018) and on actual full-scale pavement structures as well (Nguyen et al. 2013, Graziani et al. 2014). However, the aforementioned difficulties of the above studies at structural level were effectively revealed.

The objective of the present study is to evaluate the influence of the interface bonding condition between the asphalt layers on the mechanical responses of full-scale pavements with and without glass fiber grid reinforcement (Figure 1). It is based on the analysis of strain measurements in the asphalt layers with well-characterized material properties under well-controlled load characteristics (level, position and speed) and of falling weight deflectometer (FWD) deflection measurements on the pavement surface, in non-damaged condition of the evaluated pavements. It is noteworthy that the fatigue behavior and design of glass grid reinforced pavements are discussed in another recent work (Nguyen et al. 2021).

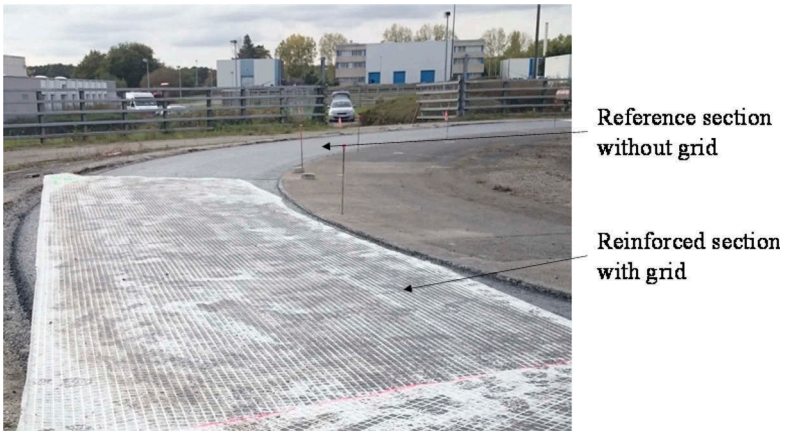

Figure 1. Full-scale pavement sections with and without glass fiber grid reinforcement before application of the overlay during the construction.

The paper first presents the tested pavement structures and materials tested in the APT experiment as well as test methods. A synthetic theoretical background of a mechanical indicator for consideration of the layers interface bonding condition and its implementation in the multi-layer elastic pavement design program Alizé are then introduced. Main results of horizontal strains and FWD deflections measured in the asphalt layers and on the pavements surface respectively and their numerical simulations using Alizé with the special implementation option for interface bond condition are presented and discussed. An associated laboratory test campaign of interface bond strength measurements on specimens extracted from the full-scale pavements and fabricated in laboratory provides additional results in accordance with the observed structural responses.

2 GENERAL CHARACTERISTICS OF PAVEMENT STRUCTURES AND TEST METHODS

2.1 *Presentation of pavement structures, asphalt material and experimental program*

The two experimental pavement sections (Figure 1 and Figure 2) were constructed from 25th to 29th September 2017 on the carrousel test track in Nantes Campus, Gustave Eiffel University (UGE). Those sections, noted S1 and S2, were placed at the radius of 19 m, corresponding to a track of 120 m length and 3 m width, and were instrumented with strain gauges and temperature probes. Section S1 was considered as the reference section with conventional pavement structure, which was designed by the French pavement design method (NF P98-086 standard), including two asphalt (AC) layers of targeted thickness of 6 cm and 5 cm for surface and base layers respectively, over an unbound granular (UGM) subbase of 30 cm and a 260 cm-thick sandy subgrade. The asphalt material was a hot mix asphalt (HMA) with the formulation of a standard semi-coarse asphalt concrete (SCAC-10 Class-3 based on EN 13108-1 standard). Its complex modulus was determined according to EN 12697-26 standard. Section S2 had the same structure and materials as section S1 but was reinforced with a glass fiber grid (associated with a thin non-woven polyester layer of no more than 20 g/m²) of 100 kN/m in tensile strength at the interface between the two asphalt layers (see Figure 2). A tack coat layer of classical cationic rapid setting bitumen emulsion (according to EN 13808-2013 standard) with rates of application of 350 g/m^2 and 700 g/m^2 respectively (in residual bitumen) was used for reference and reinforced sections. These applications rates have been chosen because they led to the best performance according to the results from an associated laboratory study where tests at different application rates have been performed (Nguyen et al. 2021).

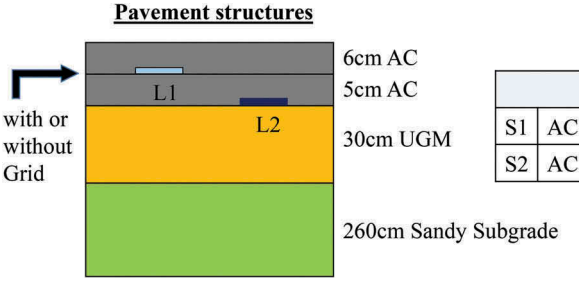

Sections		Tack coat
S1	AC Reference	350 g/m^2 (residual binder)
S2	AC + grid 100 kN/m	700 g/m^2 (residual binder)

Figure 2. Design of the evaluated pavement structures.

The full-scale experiment, presented in this study, was carried out on the carrousel test track from 28th May 2018 to 8th February 2019. A traffic simulator with four loading arms was operated to produce real traffic with dual-wheel configurations. The test program was as follows: the

first 2 000 cycles was performed with 45 kN loads, the 3 000 following cycles were performed at 55 kN load level, and then loads of 65 kN were applied. At the end of the experiment, a total of 1 850 000 cycles were applied. In this paper, the study only focuses on data obtained during the first 10 000 cycles where it is assumed that no damage happened to the pavement structure.

2.2 *Monitoring methods*

Pavement instrumentation

To follow pavement responses during the full-scale experiment, each section was instrumented with asphalt strain gauges (L1, L2), model TML-100HAS, placed at the bottom of the asphalt layers and a temperature probe (TP) placed at a depth of 6 cm in the asphalt layers (see Figure 2). Temperature data was recorded every 10 minutes.

FWD measurements

The FWD measurements were performed on 5th April 2018, before the start of loading, with a spacing of 2 m between the measurement points on the test track. The equipment used is a Super Heavy Weight trailer mounted Deflectormeter (SHWD) inducing a load of 65 kN on a circular load plate (30 cm in diameter). A series of geophones located at positions of 0; 0.3; 0.4; 0.6; 0.9; 1.2; 1.5; 1.8; 2.1m from the center of the plate, recorded deflection responses to the load. The average temperature during the tests was 15°C at a depth of 6 cm in the asphalt layers.

3 THEORETICAL BACKGROUND AND IMPLEMENTATION IN NUMERICAL SIMULATIONS

In order to evaluate the bonding level of the interface between layers, Goodman (Goodman 1986) has introduced a parameter K_s (equation (1)), which is the shear or bonding stiffness of the interface, to describe the interfacial response to pavement loading.

$$K_s = \frac{\tau}{\Delta u} \tag{1}$$

where, τ is the shear stress and Δu is the relative horizontal displacement at the interface between layers induced by the pavement loading.

This formula has been implemented in the Alizé pavement design software (based on the multi-layer linear elastic model of Burmister (1943)), in considering the above linear relationship between the relative horizontal displacement of the two asphalt layers on either side of the interface and the shear stress, to simulate the bonding conditions. For these numerical simulations, the value of the elastic modulus of the asphalt layer was determined from results of laboratory complex modulus tests on asphalt material extracted from the pavement. The asphalt temperature was the one recorded in the pavement and the loading frequency was determined from the loading time of the measured strain signal according to (Barksdale 1971).

4 EVALUATION OF INTERFACE BONDING CONDITIONS IN THE FULL-SCALE PAVEMENTS

4.1 *Evidence from strain measurements*

In this section, the longitudinal strain responses measured from the full-scale test and modelled with two interfacial bonding conditions (bonded and debonded) in the multi-layer linear elastic model (Alizé) are compared to evaluate in-place bonding level between asphalt layers.

Figure 3 and Figure 4 present the measured and modelled strain signals at the respective bottom of the surface and base asphalt layers, for the two pavement sections. The experimental signals were collected at around 5 600 cycles under the 65 kN load, a traffic speed of

57 km/h and asphalt temperature of 20°C. These loading conditions were also used for the simulations. The figures show a strong influence of the level of bonding on the strain signals at the bottom of the surface and base asphalt layers. On section S1 (without grid), the strain signals calculated with a bonded condition are in good agreement with the experimental measurements. On section S2 (with grid), however, high tensile strains are measured at the bottom of the surface layer, and the values are close to the predictions obtained with the model with debonded interface. This indicates a poor interlayer bond on section S2, leading to tension at the bottom of the surface asphalt layer, and potentially to fatigue of the surface layer.

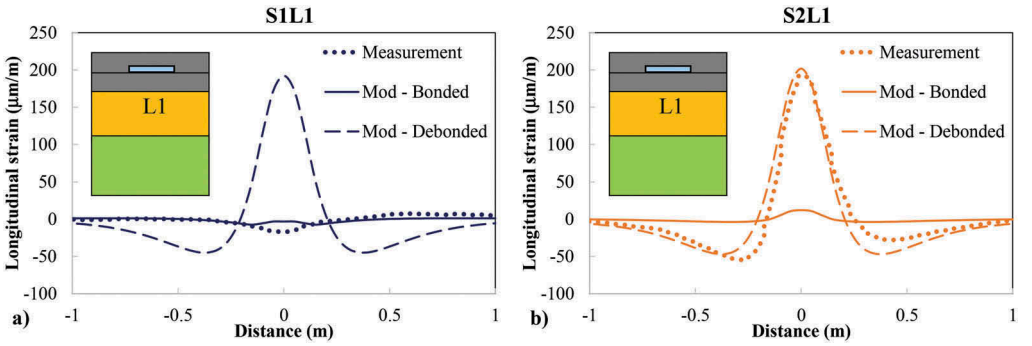

Figure 3. Comparison of measured longitudinal strain signals at the bottom of the surface asphalt layer with Alizé simulations (with bonded and debonded interfaces) in a) Section S1 and b) Section S2, after 5 600 cycles (Load level of 65 kN, traffic speed of 57 km/h, asphalt temperature of 20°C).

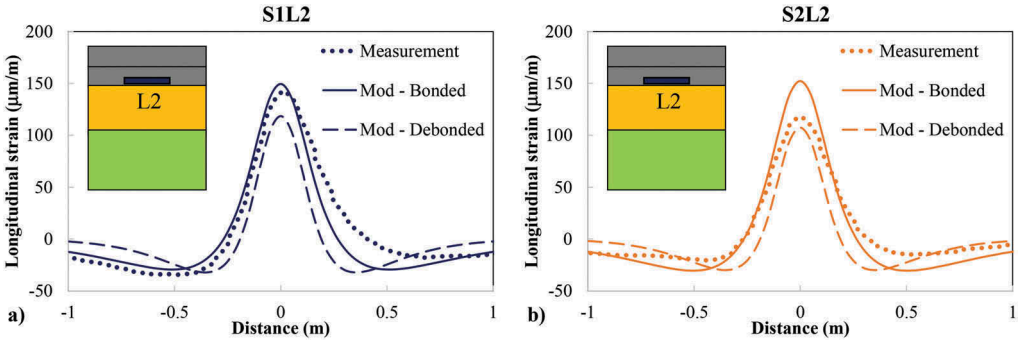

Figure 4. Comparison of measured longitudinal strain signals at the bottom of the base asphalt layer with Alizé simulations (with bonded and debonded interfaces) in a) Section S1 and b) Section S2, after 5 600 cycles (Load level of 65 kN, traffic speed of 57 km/h, asphalt temperature of 20°C).

To observe the evolution of the bonding condition with temperature, the maximum longitudinal strains obtained during the first 10 000 load applications were compared with the simulations with two interface bonding conditions (bonded and debonded) with average measured thicknesses of the two asphalt layers of the two sections (6.4 cm and 4.8 cm respectively for the surface and base layers), for a range of asphalt temperatures, for a 65 kN dual-wheel load. As mentioned in section 2.1, the load level was increased at the beginning of the full-scale experiment: the first 2 000 cycles were performed at 45 kN, the following 3 000 cycles at 55 kN load level, and then the remaining cycles at 65 kN. For that reason, the strain values were

normalized with respect to the load level, according to equation (2), assuming a linear elastic response of the pavement.

$$\varepsilon_t^{normalized} = \varepsilon_t \frac{F_{ref}}{F_{exp}} \tag{2}$$

where, $\varepsilon_t^{normalized}$ can be obtained from the experimental strains ε_t, the reference load (F_{ref} = 65 kN), and the applied load (F_{exp} = 45, 55, or 65 kN).

The normalized strain data was then plotted in Figure 5. As can be seen from that figure, for section S1, the measured strains correspond well with the modelling results with a bonded interface condition, both for the surface layer and for the base layer, up to a temperature of about 25°C. For temperatures higher than 25°C, the strains in the base layer decrease and get closer to the curve corresponding to the debonded condition, indicating a change of bonding level. This evolution is probably due to the sensitivity of the interlayer (bitumen) to temperature. For section S2, the measured strains are close to the curve corresponding to a debonded interface, for both layers and for all temperature levels, confirming a poor bonding of the interface with grid.

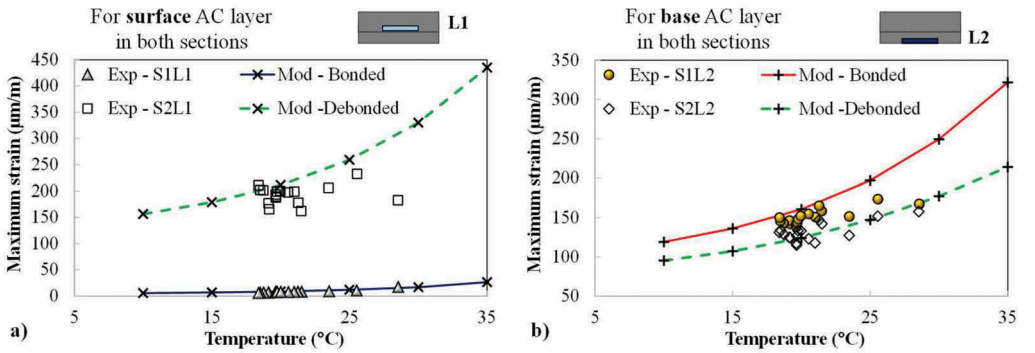

Figure 5. Comparison of measured and calculated maximum longitudinal strains at the bottom of the a) surface and b) base asphalt layers with bonded and debonded interfaces, for different temperatures.

4.2 *Quantitative evaluation based on the analysis of FWD measurements*

In this section, both back-calculation and forward-calculation procedures were employed to verify the bonding condition of the asphalt layer interface, using the multi-layer linear elastic model of the Alizé software. In the back-calculation procedure, the two asphalt layers, in both reinforced and unreinforced sections, were assumed as a single and homogenous layer characterized by an equivalent modulus.

As mentioned in section 2.2, the FWD measurements were carried out every 2 meters along the test track. Figure 6a shows all the deflection basins measured in each section and their corresponding characteristic basins (defined as the real basin which are closest to the average basin of the section). The actual layer thicknesses (obtained during the construction by leveling measurements) were taken into account in the backcalculation process, to improve the accuracy of the calculations. The average values of backcalculated layer moduli, and corresponding asphalt layer thicknesses are presented in Table 1. It can clearly be seen that, with the same pavement structure and materials, the "equivalent" modulus of the two asphalt layers is about 38% lower on the reinforced section (S2), mostly due to the asphalt interlayer system. In other words, the lower bonding level on section S2 leads to a decrease of the "equivalent" asphalt layer modulus.

Table 1. Average backcalculated layer moduli and average layer thickness.

Section		1	2
Asphalt layer	Modulus (MPa)	11 784	7 299
	Thickness (cm)	11.3	11.1
UGM layer	Modulus (MPa)	176.8	176.3
	Thickness (cm)	30	30
Soil layer	Modulus (MPa)	169.5	170.3
	Thickness (cm)	260	260

To precise the bonding level of the asphalt layer interface, forward-calculations were performed using the Alizé software. The calculations were performed with average actual thicknesses of the two asphalt layers (6.4 cm and 4.8 cm respectively for the surface and base layers) in both sections. The asphalt layer moduli were determined from laboratory test results, while the moduli of the granular layer and of the subgrade were respectively 177 MPa and 170 MPa (corresponding to average backcalculated values). In Figure 6b, the deflection basins modelled for two bonding conditions (bonded and debonded) are compared with the experimental characteristic basins. These figures indicate that deflection basins in section S1 correspond to a well bonded interface, whereas those in section S2 correspond to a poor bonding condition. These findings confirm the observations made in section 4.1.

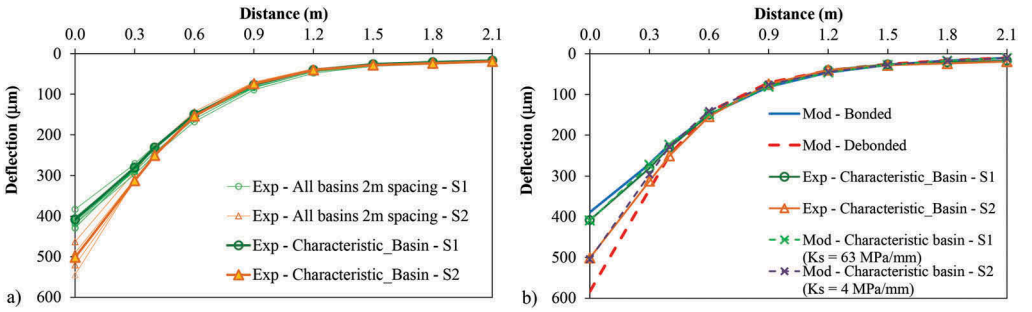

Figure 6. FWD deflections at the asphalt temperature of 15°C: a) All measurements in sections S1 and S2 and their corresponding characteristic basins; b) Characteristic basins measured in S1 and S2 and their modellings (with experimentally fitted K_s values) and fully bonded and debonded conditions.

To quantify the asphalt interfacial bonding level, the bonding stiffness K_s, as mentioned in section 3, was introduced in the calculations with Alizé. The calculations were performed with average measured thicknesses of the two asphalt layers (6.4 cm and 4.8 cm respectively for the surface and base layers). The asphalt layer moduli were determined from laboratory test results, while the moduli of the granular layer and of the subgrade were respectively 177 MPa and 170 MPa (corresponding to average backcalculated values). A trial-and-error procedure was then applied to match the modelled basins to the experimental characteristic basins in sections S1 and S2 as displayed in Figure 6b. In this figure, bonding stiffness values K_s of 63 MPa/mm and 4 MPa/mm were obtained for section S1 and section S2, respectively. These values also indicate a much better interlayer bonding condition on section S1. The K_s value on section S2 is less than 10 MPa/mm, indicating poor bonding according to the criterion proposed in several previous studies (Bachar et al. 1999, Tu et al. 2020, Roussel et al. 2020).

With the same values of K_s, good predictions were also obtained for the longitudinal strain signals in the two experimental sections. Due to the limited length of the paper, the details of these result are not presented.

5 ASSOCIATED LABORATORY TEST OF INTERFACE BOND STRENGTH

Additional results of laboratory tests, performed to evaluate the interface bond strength on double-layered specimens, are presented in this section. For this study, the direct tension bonding (DTB) test (Figure 7) developed at the research center of Colas was used. The initial double-layered specimen (rectangular or cylindrical) had sufficient dimensions to drill a 100mm diameter core. A core drill was used to make a circular grove, going 5 mm deeper than the layer interface. A fixing cap was glued to the top of the created cylindrical specimen. A monotonic tensile loading, at a rate of 200 N/s, was then applied to the cylindrical specimen, at a constant temperature (20°C in this study), until the specimen failed.

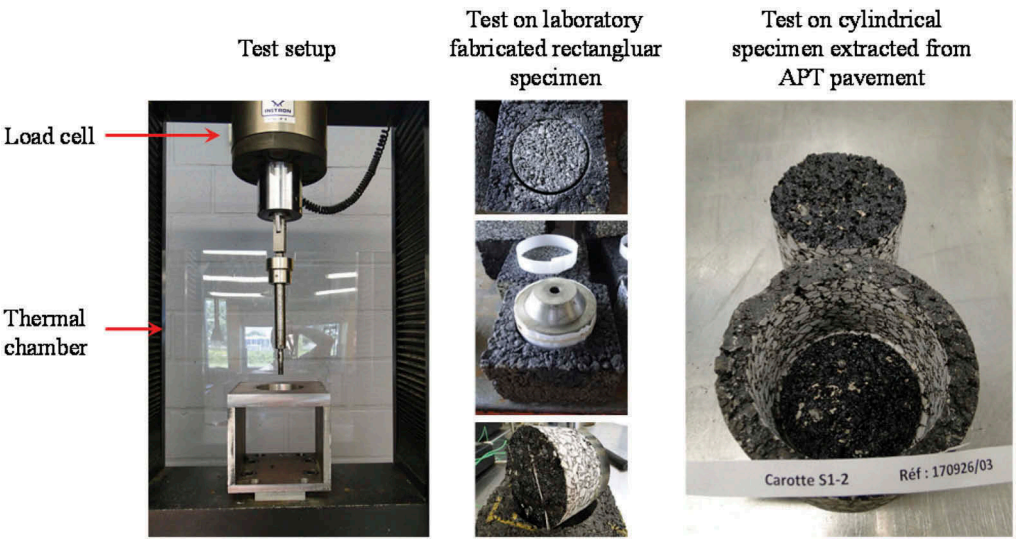

Figure 7. Direct tension bonding (DTB) test setup and tested specimens.

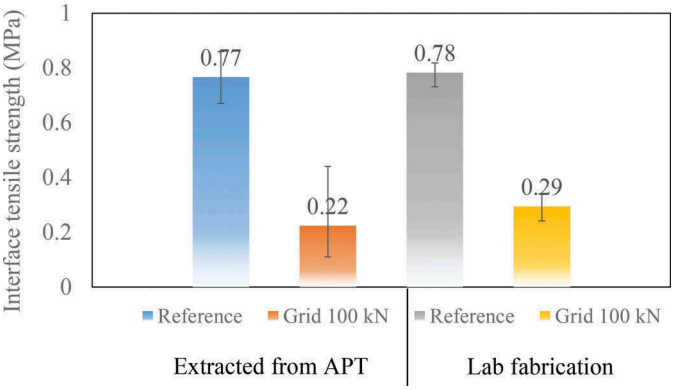

Figure 8. Laboratory test results of the interface tensile strength at 20°C.

Tests were conducted on double-layered cylindrical specimen extracted from the two full-scale pavement sections and on specimens fabricated in the laboratory. The results of the tests are presented in Figure 8. For both types of specimens, extracted from the APT pavement sections and fabricated in the laboratory, the average tensile strengths of the specimens with a grid at the interface (0.22 and 0.29 MPa respectively) are about three times lower than those

of the specimens without grid (0.77 and 0.78 MPa respectively). This result confirms again that the presence of a glass fiber grid at the interface between the asphalt layers reduces the interface bond strength.

6 CONCLUSIONS AND PERSPECTIVES

The results of the present study lead to the following conclusions and perspectives:

- The distribution of horizontal strains is modified when the bonding condition at the asphalt layers interface changes due to the presence of the glass fiber grid. Measured and simulated horizontal strains at the bottom of each asphalt layer on both sides of the interface showed a less bonding condition in case of pavement with a grid than without a grid. This phenomenon is similar to the effect of a stress absorbing membrane interlayer (SAMI) which could contribute to a delay of the offset of reflective cracking.
- Similar observations were obtained for deflection basins measured under FWD tests, on sections with and without grid at the interface.
- Using the notion of a pseudo dynamic interface stiffness modulus implemented in the multilayer pavement design software Alizé, it is possible to determine by inverse analysis a corresponding value of interface stiffness that fits the experimental measurements in terms of strain signals and of FWD deflection, for each interface bonding condition.
- Associated laboratory studies, using a direct tension bonding test, on material specimens extracted from the APT pavements and fabricated in the laboratory confirmed the influence of the interface conditions with and without grid on the measured bond strength.
- More complete experimental results, with different testing conditions, will be analyzed in the next steps of the work.
- A first numerical parametric analysis of the structural behavior shows that the reduced bond strength, associated with the high horizontal tensile strength of glass fiber grids, can lead in some cases to a reduction of the maximum tensile stresses in the asphalt layers (due to strain redistribution), leading to a better performance of the reinforced pavement. This study is not presented in this paper, due to its limited length, and will be developed in the next steps of the work.
- Additional numerical parametric analyses of structural behavior will be carried out, to evaluate the influence of the interface bonding condition, of the grid tensile strength, and of the grid position, on pavement performance.

REFERENCES

Bachar, A. H., Lam, W. C., Robert, J. A., 1999. *Use of FWD Data for Prediction of Bonding Between Pavement Layers*. International Journal of Pavement Engineering, 1:1, 49–59.

Barksdale, R. G., 1971. *Compressive Stress Pulse Times in Flexible Pavements for Use in Dynamic Testing*. Highway Research Record 345, 1971, pp. 32–44.

Brown, S., Brunton, J., 1984. *The influence of bonding between bituminous layers*. Highw. Transp. 31 (5),16–17.

Burmister, D. M., 1943. *The theory of stress and displacements in layered systems and applications of the design of airport runways*. In: Proceedings of the Highway Research Board, 23.

Canestrari, F. et al., 2013. *Mechanical testing of interlayer bonding in asphalt pavements*. In: Advances in Interlaboratory Testing and Evaluation of Bituminous Materials, pp. 303–360. Springer, Dordrecht.

Canestrari, F. et al., 2018. *Advanced interface testing of grids in asphalt pavements*. In: RILEM state-of-the-art reports: Vol. 24. Testing and characterization of sustainable innovative bituminous materials and systems, 127–202.

Freire, R., et al., 2018. *Linear Viscoelastic Behaviour of Geogrids Interface within Bituminous Mixtures*. KSCE J. Civ. Eng., 22, 2082–2088.

Gharbi, M., Nguyen, M. L., Chabot, A. and Trichet, S., 2017. *Characterisation of the bond between an asphalt layer and glass grid layers with help of a Wedge Splitting Test*. BCRRA, Athenes.

Goodman, R. E., Taylor, R. L., Brekke, T. L., 1968. *A model for the Mechanics of Jointed Rocks*. J. Soil Mech. Found. Div. 1968, 94, 637–659.

Graziani, A. et al., 2014. *Structural response of grid-reinforced bituminous pavements*. Materials and Structures 47, 1391–1408.

Grellet, D., Doré, G., Chupin, O., and Piau, J.-M., 2018. *Highlighting of the viscoelastic behaviour of interfaces in asphalt pavements – a possible origin to top-down cracking*. Road Mater. Pavement Des. 19, 581–590.

Leutner, R. *Untersuchung des Schichtenverbundes beim bituminösen Oberbau*. Bitumen 1979, 41, 84–91.

Le, M. T., Nguyen, Q. H., Nguyen, M. L., 2020. *Numerical and Experimental Investigations of Asphalt Pavement Behaviour, Taking into Account Interface Bonding Conditions*. Infrastructures, 5, 21.

Nguyen, M. L., Blanc, J., Kerzrho, J. P. and Hornych, P., 2013. *Review of glass fibre grid use for pavement reinforcement and APT experiments at IFSTTAR*. Road Mater. Pavement Des., 14:sup1, 287–308.

Nguyen, N. L., Dao, V. D., Nguyen, M. L. and Pham, D. H., 2016. *Investigation of Bond Between Asphalt Layers in Flexible Pavement*. 8th RILEM International Conference on Mechanisms of Cracking and Debonding in Pavements, Springer Netherlands, 519–525.

Nguyen, M. L., Hornych, P., Le, X. Q., Dauvergne, M., Lumière, L., Chazallon, C., Sahli, M., Mouhoubi, S., Doligez, D. and Godard, E., 2021. *Development of a rational design procedure based on fatigue characterisation and environmental evaluations of asphalt pavement reinforced with glass fibre grid*. Road Mater. Pavement Des., 22(sup1), S672–S689.

Petit, C., Chabot, A., Destree, A., Raab, C., 2018. *Recommendation of RILEM TC 241-MCD on Interface Debonding Testing in Pavements*. Mater. Struct., 51, 96.

Raab, C., Partl, M. N., Abd El Halim, A. O., 2009. *Evaluation of interlayer shear bond devices for asphalt pavements*. Balt. J. Road Bridge Eng., 4, 176–195.

Roussel, J. M., Di Benedetto, H., Sauzéat, C., Broutin, M., 2020. *Spectral Element Simulation of Heavy Weight Deflectometer Test Including Layer Interface Conditions and Linear Viscoelastic Behaviour of Bituminous Materials*. Accelerated Pavement Testing to Transport Infrastructure Innovation (Vol. 96, pp. 658–665) Springer, Cham.

Zofka, A., Maliszewski, M., Bernier, A., Josen, R., Vaitkus, A., Kleizien˙ e, R., 2015. *Advanced shear tester for evaluation of asphalt concrete under constant normal stiffness conditions*. Road Mater. Pavement Des., 16 (Suppl. 1), 187–210.

Eleventh International Conference on the Bearing Capacity of Roads, Railways and Airfields, Volume 2 – Hoff, Mork & Saba (eds)

Black boxes data for road pavement conditions monitoring: A case study in Florence

M. Meocci & V. Branzi
Department of Civil and Environmental Engineering, University of Florence, Florence, Italy

ABSTRACT: The Road Pavement Condition (RPC) represents one of the most important aspects of a country's development. Maintaining an appropriate road service level and evaluating an effective road pavement maintenance programme is a major current challenge for Road Authorities (RAs). The road pavement damage represents the first risk element for most road users while travelling. In this context, road pavement conditions monitoring plays an important role in the entire process. However, the most efficient monitoring methodologies are sometimes prohibitively expensive for RAs. To detect road pavement anomalies, high-performance and low-cost methodologies are needed, in order to allow the reinvestment of the RA's budget directly on the maintenance and conservation of the existing pavement. This research presents an innovative and proactive concept of road pavement management process, based on an efficient monitoring method that gives technicians knowledge of RPC before it poses a safety concern, especially for PTW drivers. The paper focuses on the description of operating procedures that aim to perform a screening network based on the most deteriorated sections, using the "floating car data" deriving from black boxes placed inside vehicles that routinely pass through the road network. A case study conducted in the Municipality of Florence has been described.

The main purpose of the case study is to demonstrate that the vertical acceleration data obtained by black boxes allow us to identify the road sections that need urgent maintenance. At the same time, the simple processing of the recorded data makes it possible to classify the RPC in the entire network.

Keywords: Road pavement distress, Inertial device, Acceleration, Monitoring, Low-cost

1 INTRODUCTION

Well-maintained roads are mandatory for efficient and safe transportation. Ageing and distress due to traffic load and environmental factors are physical phenomena that inevitably deteriorate the road surface and consequently the driving comfort, safety and operating costs (Qiao et. al., 2020). Therefore, to guarantee a high-quality standard for the road network, preventive monitoring and appropriate maintenance are indispensable. Pavement condition monitoring represents the most important preventive step to maintain the road pavement quality because it supports Road Authorities (RAs) both in defining maintenance programmes and in obtaining critical information regarding pavement performance (Lekshmipathy et al., 2020). It also helps both the definition of the distress evolution over time and the best maintenance strategy.

The Pavement Management System (PMS) represents one of the most widespread sustainable approaches in the planning and decision-making process. However, to be effective, it

DOI: 10.1201/9781003222897-24

requires the availability of road pavement distress data and the ability to update and maintain the data. To this end, monitoring systems are considered a significant step of the entire maintenance programme.

Over time, further efforts have been made to implement advanced and effective monitoring systems at increasingly low costs, moving from impractical manual and destructive methods through on-board automated equipment to the latest technologies (e.g. image processing) (Di Graziano et al., 2020).

Currently, the monitoring processes for the identification of road surface anomalies and their severity can be divided into two categories: low-performance and high-performance methodologies. The first is characterized by high time consumption, tends to the subjectivity of inspectors and shows a lack of precision and no correlation between the different indices derived. The second, which offers an automated or semi-automated detection solution, is instead time-consuming and improves productivity, but currently involves high implementation costs.

The most commonly used automated technologies, such as Road Surface Profiler, Ground Penetrating Radar, Laser Road Imaging system or video or image processing methodology, provide excellent results and accuracy but are very expensive. Moreover, these systems are designed to monitor non-urban roads, where speeds are generally above 50 km/h.

Frequently, however, the RAs' budgets are limited and, the road pavement monitoring and maintenance may become increasingly costly (both in terms of money and time) as the pavement ageing. In this context, each RA needs to have a sustainable approach to the problem.

In fact, despite the costs for adequate maintenance that cannot be reduced, those for effective monitoring can. It is therefore essential to equip RAs with a tool that allows them to obtain a reliable screening of the road pavement condition of the entire road network, characterized by high performance, low-cost, user friendly and readable for the operators involved.

Alternative methods based on the use of an accelerometer installed in a moving vehicle can be a potentially useful tool for pavement condition assessment conducted in an economically advantageous way (Loprencipe et al., 2021). In this context, smartphones have recently been proposed to evaluate road pavement conditions using different approaches and algorithms.

Some smartphone applications are based on the IRI procedure (Road Lab Pro). Other applications proposed new indices or given the pavement evaluation based on the acceleration peaks (Forslof and Jones, 2015; Alessandroni et al., 2014; Lima et al., 2019). Already in 2008, the Pothole Patrol system proposed the use of the smartphones' accelerometer to detect potholes (Eriksson et al., 2008). Bus Net and Nericell are systems that instead utilized the smartphone combined with the monitoring system within the smartphones (such as GPS; accelerometer, etc.) to analyse pollution, traffic and road surface conditions (Zoysa et al., 2007; Mohan et al., 2008). A few years later Kyriakou et al. (2016; 2019) evaluated the results recorded by pitch and roll sensors within smartphones for the detection and the classification of road pavement anomalies. Li and Goldberg (2018) developed a low-budget system based on built-in sensors of low-cost smartphones using two descriptive indices, IRI-proxy and the number of transient events recorded. Lekshmipathy et al. (2020) showed that the best method to collect routine pavement conditions is represented by the smartphone process versus monitoring the image process.

Although the smartphone represents the most used device, different apps and algorithms have been used which lead to a different result (Tutor Drive). Therefore, the use of smartphones could provide different results, also in terms of accuracy, due to the different positions used for the smartphone (e.g. dashboard, floorboard, drivers' pockets). In addition, several studies showed that the smartphone accelerometer offers a limited accuracy in acceleration value measurements compared to the road profiling equipment or the black boxes devices (Souza et al., 2018; Staniek 2021).

One of the best approaches to road pavement condition assessment seems to be a solution able to detect the main road distress using real-time data crowdsourcing from inertial devices (black-boxes inside the car) also taking into account the type of distress (Martinelli et al., 2021) obtained with statistical analysis or machine learning approaches.

This document shows the first results obtained with the proactive approaches provided in the analysed case study located in an urban area of Florence (Italy). As mentioned above, numerous researches and efforts have been directed towards the sustainability of pavements to contribute to the improvement of the economic and social aspects of road pavement. However, these researches apply the concept of pavement management activities on highways and major roads; only a few studies have been applied to the management and monitoring of urban areas (Cottrel et al., 2009; Loprencipe et al., 2017) which, too often, are the most deteriorated.

The main objective of this paper is therefore to highlight the experience conducted, the time consumption and the reliability of the results obtained. Some cost-benefit considerations can be made to explain the advantages of the monitoring procedure offered that, at the same time, allows the collection and post-processing of the pavement surface data along with the road network.

2 CASE STUDY IN FLORENCE URBAN ROAD

2.1 *Study area*

Firenze is a small city in the centre of Italy. The road network of the Florence Municipality extends for over 1,000 km. The test road is located in the middle of the urban context (Figure 1: Location) and it represents the main arterial in Firenze. The definition of the study area considered the choice of homogeneous sections and similar characteristics in terms of traffic, cross-section and pavement distress.

Figure 1. Location of the case study analysis.

The road section analysed serves all types of movement inside the city, both those of crossing and those of final displacement. A high level of traffic affects the area during the day.

The chosen extension is about 2 km long (Figure 1). Two separate carriageways serve the movement from the suburb to the city centre and vice versa. Each carriageway is composed of three lanes. Parking, cycle path and sidewalk complete the road space. Figure 2 shows a typical cross-section configuration.

Figure 2. Cross section of the study area.

The road axis is composed of two long straights connected by a bend (R = 250 m). For each direction, the road cross-section includes three traffic lanes approximately 3.00 m wide, two lateral spaces of variable width and two sidewalks. The selected section starts from the traffic-light intersection inside Piazza Beccaria and ends at the traffic-light intersection inside Piazza Libertà (see the white path in Figure 1). Along with this section, numerous intersections (with different characteristics: signalized or not signalized) interrupt the vehicular flow along the 2 km selected. The posted speed limit is uniform and is equal to 50 km/h.

All types of light vehicles (PTW, car, motorcycle, etc.) and heavy vehicles (trucks, bus, etc.) are admitted on this road. This is the first reason that affects the selection of the test road within the city road network. In fact, the pavement of the three lanes of the carriageway is characterized by very different distress levels.

2.2 *Critical issue and main road pavement distress*

The whole study area is characterized by flexible pavement. The properties of the different layers (thickness, material performances, etc.) are unknown.

A preliminary visual inspection is carried out along the three-lane which compose each carriageway. According to the ASTM appendix instructions, the main distresses are identified, localized and classified in terms of type and severity (ASTM, 2018).

The main findings of the visual inspection are summarized below:

- the road pavement distress is greater in each right lane because usually, the two right lanes are those where the HGVs passage is greater (i.e. buses, trucks, etc.). In free-flowing traffic conditions only light vehicles pass through in the overtaking lanes (two per direction);
- the road pavement is affected by two types of cracking: transversal and alligator. The two types of distress are present within the lanes with different severity. In the right lane, transversal and alligator crackings are classified with high severity levels;
- the road pavement is also affected by potholes and patches. The severity of this type of distresses range from low to high (classified according to the ASTM appendix catalogue (ASTM, 2018));
- the rutting affected the two right lanes with medium or high severity levels. The presence along the path of rutting is not uniform.

All the distresses summarized qualitatively have been compared with the results obtained by the Pave Box Methodology to verify the outcome obtained with the proposed automatic process.

3 METHODOLOGY

3.1 *Experimental setup*

The hardware components selected for the case study described in this paper are one very common Black-Boxes, with no specific performances.

The selected technology allowed to make the monitoring process independent of the characteristics of the devices inside the vehicle that routinely pass through on the road network. Thus, according to the main goals of the proposed monitoring procedure and the crowdsourcing objectives (Meocci et al., 2021).

The black box used is equipped by:

- one inertial sensor which recording accelerations in the three-axis X, Y and Z;
- one 3-axis gyroscope, able to record the rolling, pitching and yawing movements of the car, and
- one GPS device.

The acceleration data generated by the inertial sensor are acquired at a frequency of 100 Hz according to the most valuable research (Aleadelat et al., 2018; Mednis et al., 2011; Strazdins et al., 2011). Black boxes with a sampling rate less than 20 Hz are not recommended due to the limitation of the procedure in detecting small anomalies.

The maximum recorded acceleration value is 16 g (for each direction).

To carry out the experiment, the black box was rigidly fixed to the car floorboard, between pedals and the gearbox, as close as possible to the car's centre of gravity.

The position described allows to have a minimal impact on the data recorded by any curvilinear trajectories of the vehicle, also generating centripetal and/or centrifugal accelerations on the measurement. In these terms, the best position would be on the tunnel of the car, but, in most vehicles, this component is not horizontal, therefore its configuration could direct the value of the vertical acceleration recorded.

The black boxes used in the experiment do not require any installation procedure or other requirements to start the monitoring. It is only required that 5 seconds before starting the monitoring, the black box is switched on to stabilize the GPS connection. All tests are conducted with the black box in the same position. Data acquired by the black box are finally downloaded by micro-USB to the computer for the post-processing procedure.

3.2 *Procedure*

The procedure performed was conducted according to the process defined in (Meocci, 2021), which can be summarized by steps shown in Figure 3.

The test was carried out by the same vehicle, a Fiat Panda 4x4. Before starting the test, each tire was checked and adjusted to the recommended tire pressure for the car used (2.4 bars).

3.3 *Data collection and analysis*

According to the pavement condition procedure proposed by the Pave Box methodology (Meocci et al., 2021), the data resulting from the monitoring were used for the evaluation of the **Global Pave Box Index**. The index offers a comprehensive damage assessment of the entire road segment. The index can be useful both for screening the entire road network and for comparing the different road sections within the network, which is characterized by different road damages.

In equation (1), the global index is shown.

$$GPB = \left(\int_0^L \widehat{\sigma(l)}^2 dl \right) \times \frac{100}{L} \tag{1}$$

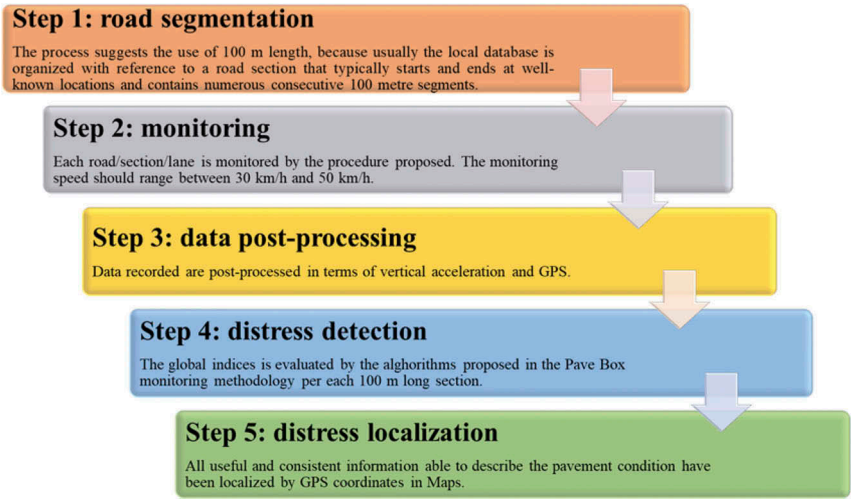

Figure 3. Procedure.

where $\widehat{\sigma(l)}^2$ represents the moving variance of the signal measured by black box (a_v), L represent the total length of the homogeneous road segment. The moving variance $\widehat{\sigma^2}$ is given by the equation (2).

$$\widehat{\sigma^2} = \frac{\sum_{i=1}^{n} \left(a_{v,i} - \overline{a_v}\right)^2}{n} \tag{2}$$

where $a_{v,i}$ represent the i^{th} vertical acceleration value and $\overline{a_v}$ represents the centred moving average across a range of 20 values (0.2 s) evaluated as in equation (3).

$$\overline{a_v} = \frac{\sum_{i-9}^{i+10} a_v}{n = 20} \tag{3}$$

As a function of the value obtained, the road section can be classified into four different classes corresponding to the different distress severity: low, fair, high and need to repair. The first three classes must be considered in the priority algorithm, while the last one needs immediate repair (Table 1). The rating scale and thresholds were defined by a large campaign of PCI surveys carried out along with a test road section also monitored by the new methodology. The correspondence between PCI and GPB was defined and detailed in Meocci et al. (2021).

Table 1. GPB index rating scale.

GPB rating scale	Severity levels		PCI
GPB<0.40	good		100-70
0.40<GPB<0.65	fair		70-55
0.65<GPB<1.45	high		55-25
GPB>1.45	need to repair		≤25

Each lane was monitored several times at speeds ranging from 30 km/h to 50 km/h. The car's transversal position is assumed in the middle of the lane (as far as possible).

4 RESULT AND DISCUSSION

4.1 *Segmentation*

The study area is segmented following the previously defined criteria. Specifically, 7 sections are defined for both directions. The sections are simply defined with reference to the division of the entire road based on the signalized intersections (light position/STOP marking). This represents the main reason because, often, each section differs from the others in terms of length and start-end points. In Table 2 the sections' information are summarized.

Table 2. Segmentation of the study area.

Direction 1			Direction 2		
Section ID	Length [m]	Number of subsection	Section ID	Length [m]	Number of subsection
1	180	2	1	180	2
2	270	3	2	135	1
3	240	2	3	300	3
4	250	2	4	200	2
5	290	3	5	225	2
6	150	3	6	275	3
7	150	2	7	205	2

4.2 *GPB evaluation*

The recorded measurements (a_v) constitute the dataset to be processed both for the identification and the classification of the pavement surface distresses severity through the GPB index. Table 3 and Table 4 summarize the GPB indices evaluated in the data post-processing. The table shows the GPB indices obtained section by section, their standard deviation and the average speed that characterize the overall survey carried out. The colour of the GPB index (red, yellow or green) represents the distress severity defined in Table 1.

Table 3. GPB index values – direction to the city centre.

		Lane 1 (right)			Lane 2 (central)			Lane 3 (left)		
Section ID	Length [m]	GPB [m/s^2]	Std. Dev. [km/h]	Vm [km/h]	GPB [m/s^2]	Std. Dev. [km/h]	Vm [km/h]	GPB [m/s^2]	Std. Dev. [km/h]	Vm [km/h]
1	180	**0.97**	**0.615**	33	**0.18**	0.015	33	**0.25**	0.002	35
2	270	**2.25**	0.640	33	**0.64**	0.155	33	**0.37**	0.065	35
3	240	**0.43**	0.010	33	**0.13**	0.035	35	**0.23**	**0.150**	38
4	250	**0.71**	**0.245**	39	**0.81**	0.195	35	**0.57**	0.085	38
5	290	**0.43**	0.110	39	**0.23**	0.225	35	**0.39**	0.030	38
6	150	**0.36**	0.105	30	**0.19**	**0.065**	35	**0.18**	0.010	34
7	150	**0.37**	0.035	30	**0.19**	**0.155**	34	**0.54**	0.125	34

High standard deviation values (> 30% of the index value) are shown in grey. These represent the road sections that need to improve the monitoring process to stabilize the GPB index and therefore, to improve the quality of the distress characterization.

Tables show that the carriageway leading to the suburb has better road pavement conditions than the opposite direction. In fact, within the carriageway leading to the city centre, there are two sections on the right lane, that need immediate restoration. Figure 4, Figure 5 and Figure 6 show the moving variance of the acceleration signal (the right lane-section 1, the central lane-section 5 and the left-lane section 1, respectively). Figures also show some distresses (or absence of distresses) that characterize each lane, coupled with their ASTM severity level.

Table 4. GPB index values – direction to the suburb.

Section ID	Length [m]	Lane 1 (right) GPB [m/s^2]	Lane 1 (right) Std. Dev. [km/h]	Lane 1 (right) Vm [km/h]	Lane 2 (central) GPB [m/s^2]	Lane 2 (central) Std. Dev. [km/h]	Lane 2 (central) Vm [km/h]	Lane 3 (left) GPB [m/s^2]	Lane 3 (left) Std. Dev. [km/h]	Lane 3 (left) Vm [km/h]
1	180	**0.25**	0.00	32	**0.18**	0.050	31	**0.23**	0.015	37
2	135	**0.24**	0.015	32	**0.12**	**0.035**	31	**0.14**	0.025	37
3	300	**0.15**	0.02	34	**0.14**	0.040	34	**0.15**	0.015	37
4	200	**0.25**	0.05	34	**0.54**	0.095	34	**0.40**	0.118	37
5	225	**0.65**	0.02	37	**0.55**	0.005	34	**0.19**	0.055	37
6	275	**1.15**	**0.45**	37	**0.31**	**0.200**	34	**0.15**	**0.146**	34
7	205	**0.92**	0.18	37	**0.35**	0.000	36	**0.34**	**0.165**	34

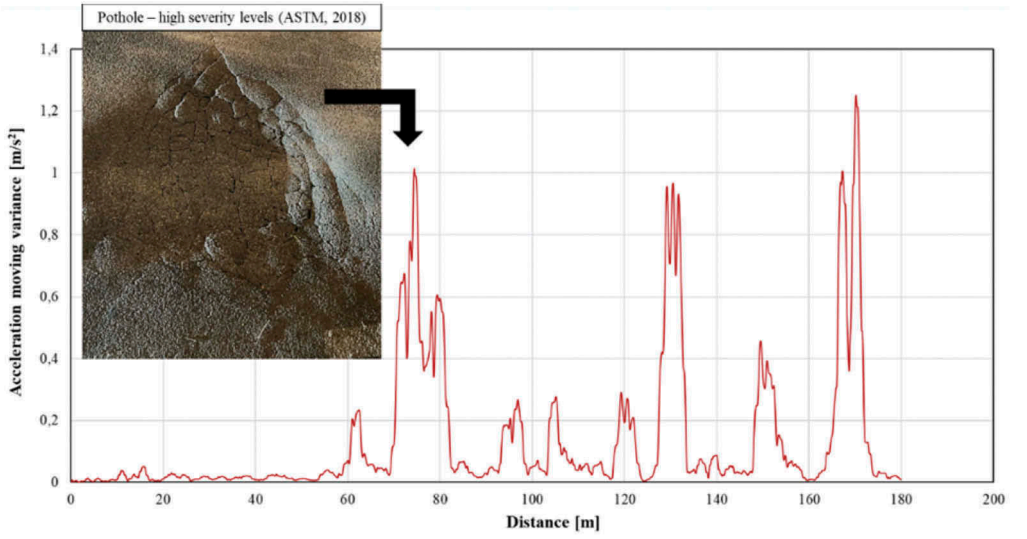

Figure 4. Section 1, right lane – direction: City-Centre.

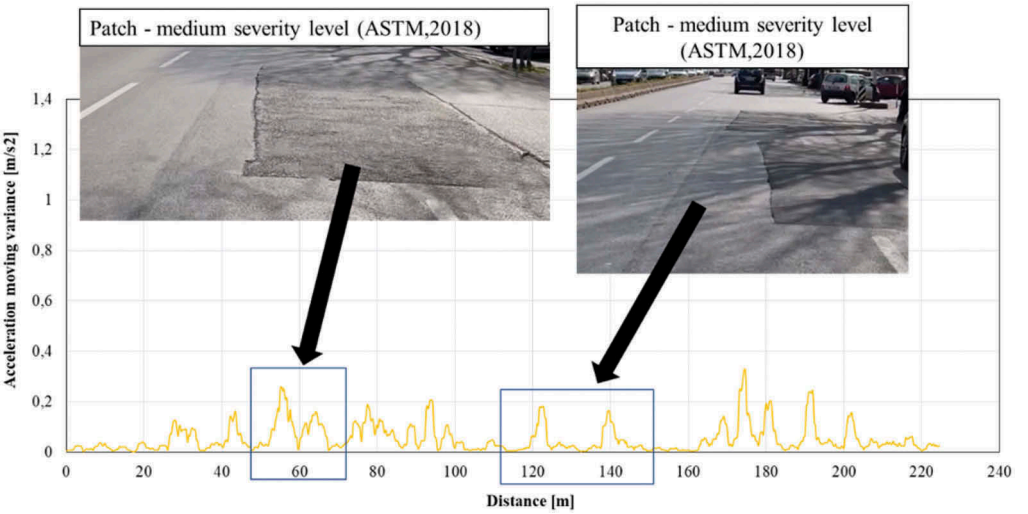

Figure 5. Section 5, central lane – direction: suburb.

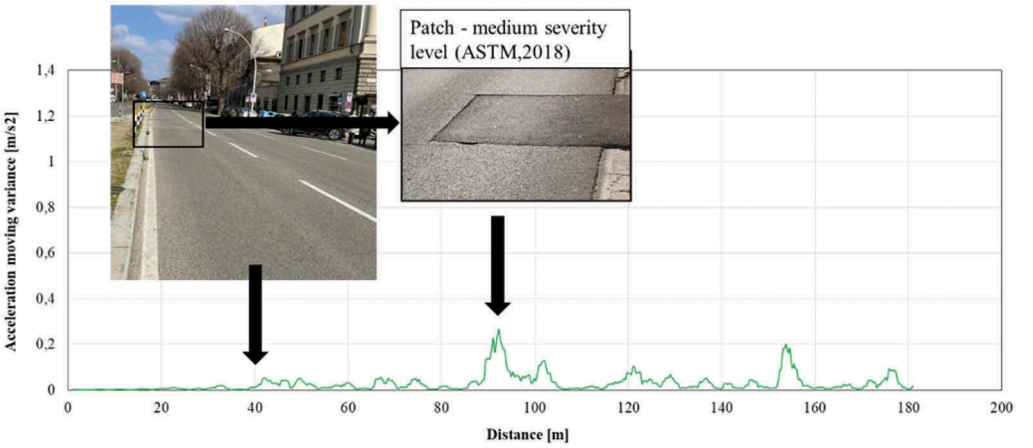

Figure 6. Section 1, left lane – direction: City-Centre.

In the direction of the city centre, only two sections can be classified as "good condition" in the right lane. The result obtained is consistent with the high number of HGVs passing through this lane. The other lanes, on the other hand, show good or fair road pavement conditions and they are the lanes travelled mostly by light vehicles (cars and PTWs).

Generally, the two sections near Piazza Beccaria (in both directions) are those with the worst paving conditions.

5 CONCLUSION

Despite the numerous technologies available for monitoring road pavements, too often the RAs cannot use them because of their high costs, especially in urban areas. Therefore, the proposed distress-detection process is designed to satisfy the needs of RAs, using a data collection based on crowdsourcing.

This paper aims to show a case study carried out in the Municipality of Firenze, along the main arterial street using the Pave Box Methodology.

The methodology consists of the post-processing of the vertical acceleration and GPS data recorded by an inertial device within a car (black box) to evaluate the presence and severity of road pavement distress. The approach aims to quickly screen (in real-time) the road pavement condition within the road network and defines the priority list to prevent and/or quickly repair the road anomalies according to their severity.

The illustrated survey is generally conducted with a short time, less than 3 hours. The total length of the monitored road is approximately 12 km (6 lanes per 2 km each).

In conclusion, the presented case study demonstrates to the RAs the power of the proposed low-cost and easy-to-use process.

REFERENCES

Aleadelat, W., Ksaibati, K., Wright, C. and Saha, P., 2018. *Evaluation of pavement roughness using an android-based smartphone*. Journal of Transportation Engineering-Part B, Pavements, vol.144(3).

Alessandroni, G., Klopfenstein, L.C., Delpriori, S., Dromedari, M., Luchetti, G., Paolini, B.D., Seraghiti, A., Lattanzi, E., Freschi, V., Carini, A., and al., 2014. *SmartRoadSense: Collaborative road surface condition monitoring*. In Proceedings of the UBICOMM 2014-8th International Conference on Mobile Ubiquitous Computing, Systems, Services and Technologies, Rome, Italy, 24-28 August 2014; pp. 210–215.

ASTM International, 2018. *Standard practice for road and parking lots pavement condition index surveys*, D6433–18.

Cottrell, W.D., Bryan, S., Chilukuri, B.R., Kalyani, V., Stevanovic, A. and Wu, J., 2009. *Transportation Infrastructure Maintenance Management: Case Study of a Small Urban City*. Journal of Infrastructure System, vol. 15 (2).

Di Graziano, A. Marchetta, V. and Cafiso, S., 2020. *Structural health monitoring of asphalt pavements using smart sensor networks: A comprehensive review*, Journal of Traffic and Transportation Engineering (English Edition), vol. 7(5), pp. 639–651.

Eriksson, J., Girod, L., Hull, B., Newton, R., Madden, S. and Balakrishnan, H., 2008. *The pothole patrol: using a mobile sensor network for road surface monitoring*, in Proceeding of the 6th international conference on Mobile system, applications and service, ser. MobySys'08, New York, NY, USA, pp.29–39.

Forslöf, L. and Jones, H., 2015. *Roadroid: Continuous Road Condition Monitoring with Smart Phones*. Journal of Civil Engineering and Architecture, vol. 9, pp. 485–496.

Kyriakou, C., Christodoulou, S.E. and Dimitriou, L., 2016. *Roadway pavement anomaly classification utilizing smartphones and artificial intelligence*. In Proceeding of *18th Mediterranean Electrotechnical Conference (MELECON)*, pp. 1–6.

Kyriakou, C., Christodoulou, S.E., and Dimitriou, L. (2019). *Smartphone-Based Pothole Detection Utilizing Artificial Neural Networks*. Journal of Infrastructure System, vol.15(3),

Lekshmipathy, J., Samuel, N.M. and Velayudhan, S., 2020. *Vibration vs. vision: based approach for automated pavement distress detection*, International Journal of Pavement Research and Technology, vol. 13, pp. 402–410.

Li, X. and Goldberg., D.W., 2018. *Toward a mobile crowdsensing system for road surface assessment, Computers, Environment and Urban Systems*, vol.69, pp.51–62.

Lima, L.C., Amorim, V.J.P., Pereira, I.M., Ribeiro, F.N. and Oliveira, R.A.R., 2016. *Using crowdsourcing techniques and mobile devices for asphaltic pavement quality recognition*. In Proceedings of the Brazilian Symposium on Computing System Engineering, SBESC, João Pessoa, Brazil, 1–4 November 2016; pp. 144–149.

Loprencipe, G., Pantuso, A. and Di Mascio, P., 2017. Sustainable pavement management system in urban areas considering the vehicle operating costs. Sustainability, vol.9, p. 453.

Loprencipe, G., Vaz De Almeida Filho, F.G., Oliveira, R.E. and Bruno, S., 2021. *Validation of a Low-Cost Pavement Monitoring Inertial-Based System for Urban Road Networks*. Sensors, vol. 2, p. 3127.

Mednis, A., Strazdin, G., Zviedris, R., Kanonirs, G. and Selavo, L., 2011. *Real time photole detection using android smartphone with accelerometers*. In: International Conference on Distributed Computing in Sensor Systems and Workshops (DCOSS). IEEE.

Meocci, M., Branzi, V. and Sangiovanni, A., 2021. *An innovative approach for high-performance road pavement monitoring using black box*, Journal of Civil Structural Health Monitoring, vol 11, pp. 485–506. https://doi.org/10.1007/s13349-020-00463-8.

Martinelli, A., Meocci, M., Dolfi, M., Branzi, V., Morosi, S., Argenti, F., Berzi, L. and Consumi T., 2021. *Road Surface Anomaly Assessment Using Low-Cost Accelerometers: A Machine Learning Approach*. Submitted to IEEE Access, August 2021.

Mohan, P., Padmanabhan, V.N. and Ramjee, R., 2008. *Nericell: Rich monitoring of road and trafc conditions using mobile smartphones*. In Procedeeng of 6th ACM Conf. Embedded Netw. Sensor Syst (SenSys), pp. 323–336.

Qiao, Y., Santos, J., Stoner, A.M. and Flinstch, G., 2020. *Climate change impacts on asphalt road pavement construction and maintenance: an economic life cycle cost assessment of adaptation measures in the State of Virginia*, Unites States, Journal of Industrial Ecology, vol 24(2), pp. 342–355.

Souza, V.M.A., Giusti, R. and Batista, A.J.L., 2018. *Asfault: a low-cost system to evaluate pavement condition in real-time using smartphones and machine learning*. Pervasive and Mobile Computing, vol. 51, pp. 121–137.

Staniek, M., 2021. *Road pavement condition diagnostics using smartphone-based data crowdsourcing in smart cities*. Journal of Traffic and Transportation Engineering, vol.8, pp. 554–567.

Strazdins, G., Mednis, A., Kanonirs, G., Zviedris, R. and Selavo, L., 2011. *Towards vehicular sensor networks with android smartphones for road surface monitoring*. In: Proc., Second Int. Workshop on Networks of Cooperating Objects (CONET'11): Electronic Proc., CPSWeek'11, 1–4. Chicago.

Tutor Drive, available at: TutorDrive.AlteVista.org

World Bank, Road Lab Pro, app available at: https://play.google.com/store/apps/details?id=com.softteco.roadlabpro&hl=it&gl=US.

Zoysa, K.D., Keppitiyagama, C., Seneviratne, G.P. and Shihan, W.W.A.T., 2007. *A public transport system based sensor network for road surface condition monitoring*. In: Proceedings of the Workshop on Networked Systems for Developing Regions, 27 August 2007, Kyoto, Japan, pp. 1–6.

Eleventh International Conference on the Bearing Capacity of Roads, Railways and Airfields, Volume 2 – Hoff, Mork & Saba (eds)

The performance of different frost protection materials for road design

K. Rieksts, B. Loranger & I. Hoff
Department of Civil and Environmental Engineering, Norwegian University of Science and Technology, Trondheim, Norway

J. Aksnes & K.A. Skoglund
Norwegian Public Roads Administration, Trondheim, Norway

ABSTRACT: Transportation infrastructures built in cold regions with underlaying frost susceptible subgrade soils may require a frost protection layer. The national guidelines for road construction in Norway provide three distinct design concepts for frost protection layers. The layer can consist of granular stone material (natural or crushed rock), lightweight aggregates (foam glass or expanded clay) or extruded polystyrene (XPS). To better investigate the performance of different frost protection materials, Norwegian Public Roads Administration constructed a series of test sections within a newly reconstructed highway. The test site is located outside Trondheim and is a part of the national level road E6. The test site consists of seven test sections, each 50 m long. All sections have the same thickness of asphalt layers, base layer, and subbase layers. The variation of the test section is within different materials used for frost protection. One section included XPS, two sections were built with lightweight aggregate materials and four sections were built with granular stone material with different gradations. The test site was constructed during the fall of 2018. The winter of 2020/2021 had a freezing index of 9938°C·hours. The results show that sections constructed with lightweight aggregates and XPS provides very similar effect and are overall most efficient to limit the frost penetration. All granular stone materials, except 22/180 mm crushed rock provides moderate frost protection. Crushed rock with 22/180 mm is the least effective and in this section the frost front reached the subsoil. Measured values of frost depth in sections with granular materials agrees well with predicted values from N200 handbook. Values of frost depth from sections with lightweight aggregates and XPS are difficult to compare to the predicted values. However, these sections are substantially overdesigned based on the current guidelines and could be constructed using less material for frost protection layer.

Keywords: Frost penetration, frost protection

1 INTRODUCTION

In cold regions where roads are constructed on frost susceptible soils it is typical to design them with consideration of winter severity and resulting frost penetration. Appropriate materials, mainly based on their thermal properties, have to be selected to limit the frost depth that could eventually cause some structural damage (Andersland & Ladanyi, 2004; Doré & Zubeck, 2009). Under the current guidelines in Norway defined by the Norwegian Public Road Administration (NPRA), for roads with average annual daily traffic of over 8000 the

DOI: 10.1201/9781003222897-25

frost front should be contained within the road structure. These roads should have sufficient thickness of frost protection so no frost heave would occur. These guidelines are specified in the handbook N200 (Håndbok N200, 2018). Although, the desired outcome is to limit the frost from penetrating into the subsoil, the N200 also specifies the maximum thickness of roads. For high volume roads the total thickness should not exceed 2.4 m. When designing the road for its frost protection, the severity of winters is characterized by freezing index. The freezing index considered in the N200 for road design uses the statistical concept of period of return. Freezing indexes for period of return of 5, 10 and 100 years, noted F_5, F_{10} and F_{100}, are typically used for local, main, and national roads respectively.

Based on the N200 handbook, three different types of frost protection materials can be used in roads. These are granular stone material, both natural and crushed, lightweight aggregates and XPS. Granular materials are further subdivided mainly based on their coarseness and the amount of fines.

Previous similar test site were built along the years for frost protection layer performance analysis, the latest being the Røros test site, which been analyzed in 2019 (Loranger et al., 2019; Rieksts et al., 2019). However, The Røros test site was built off-traffic. The NPRA wished to implement a test site on a high-volume road in service, which brought choosing the E6, already in reconstruction near Trondheim, for implementation.

This paper first gives the description of the test site and materials used for construction. Measurements of air temperature, freezing index and frost penetration of all sections are then presented. Measured values of maximum frost penetration are then compared with the predicted values form the N200 handbook.

2 TEST SITE DESCRIPTION

The test site is located outside Trondheim, Norway. The test site is incorporated into a major highway (E6) during its reconstruction process. The test site was constructed during the fall of 2018. However, continuous measurements of temperature distribution were not started before spring of 2019. The mean annual temperature in the region is 5°C and the F_{10} and F_{100} freezing index is 11000°C·hours (458°C·days) and 19000°C·hours (792°C·days) respectively.

The test site consists of seven test sections, each 50 m long. Each section is constructed with a different frost protection material. The total thickness of frost protection layer is 1.1 m. Although different frost protection material requires different thickness to achieve the same insulating effect, the thickness of each section has been equalized to fit with the rest of the constructed road for logistic purposes. The frost protection materials used were unsorted gravel (section F1), expanded polystyrene (XPS) (section F2), 0/180 mm crushed rock (section F3), foam glass (section F4), 0/32 mm crushed rock (section F5), expanded clay (section F6), and 22/180 mm crushed rock (section F7). The top part of the road consists of 0.09 m of asphalt layer (wearing and binder course) followed by 0.16 m of bound base layer. The subbase is constructed of 20/120 mm crushed rock material with a thickness of 0.8 m.

To monitor the temperature distribution, each section is instrumented with series of T-type thermocouples with accuracy of ±1°C. Exact location of all thermocouples is shown in Figure 1. For the majority of layers, a thermocouple is placed on the interface and middle of a layer. Thermocouples are placed also in the subsoil down to 0.5 m below the superstructure. To better monitor the ground temperature two sections (F1 and F7) has extra thermocouples placed at a depth of 3.15 and 3.85 m.

The three types of frost protection materials are very different in terms of their thermal properties. XPS has the lowest thermal conductivity of 0.025 W/m°C which is the lowest from all frost protection materials (Heiersted, 1976). The two lightweight aggregates (foam glass and expanded clay) are very similar to each other in terms of their density and overall thermal properties. Thermal conductivity under dry state is around 0.1 W/m°C while under field conditions with some water content is around 0.18 W/m°C (Hoff et al., 2002). Thermal conductivity for natural materials can vary a lot. As it has been observed in a different test site where

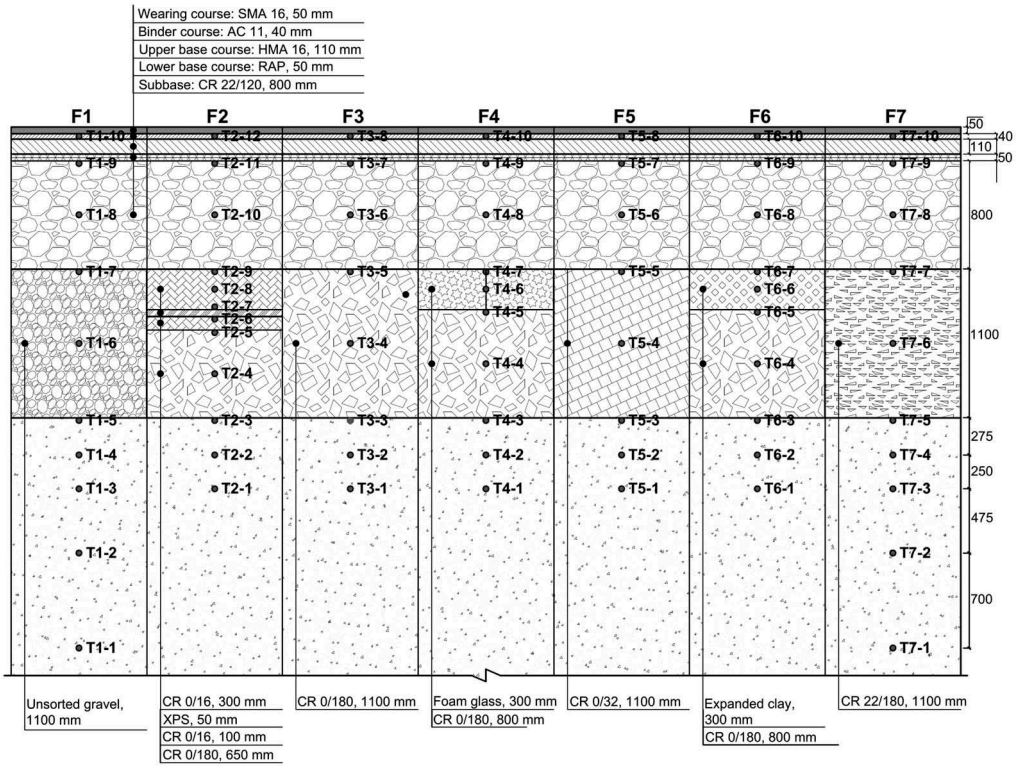

Figure 1. Cross-section of all test section and locations of temperature sensors.

different gradation of crushed rock materials was used, unfrozen thermal conductivities varied between 0.4 to 1.9 W/m°C (Heiersted, 1976; Loranger et al., 2019).

3 FROST DEPTH OBSERVATIONS

The winter of 2020/2021 was relatively cold, and the freezing index reached 9938°C·hours (414°C·days) which corresponds to a F_{10} freezing index in the area. Figure 2 shows the air temperature during the winter season along with the freezing index progression. The main freezing season lasted for 48 days starting 31st of December and lasted until 16th of February. This is the period for which the freezing index has been summed up. However, several frost-thaw cycles occurred before. This kind of temperature fluctuations is typical for the region which could make the estimation of FI complicated. A short thaw period was also in the middle of the freezing season. This warmer period accounts for 192°C·hours (8°C·days). The minimum temperature observed during the winter was -18.8 °C.

Figures 3a to 3g shows the frost progression and air temperature in all seven test sections. In the section with unsorted gravel, the frost front reached a maximum depth of 1.54 m (Figure 3a). In section with a layer of XPS the frost front stopped at the bottom of the insulation layer reaching a maximum frost depth of 1.39 m (Figure 3b). Sections with foam glass and expanded clay had a very similar frost penetration reaching a maximum depth of 1.29 and 1.31 respectively (Figure 3d and 3f). Test sections with well graded crushed rock materials (0/180 and 0/32 mm) had also quite similar frost penetration. Section with 0/180 mm crushed rock reached a maximum frost depth of 1.66 m (Figure 3c) while the section with 0/32 mm material had frost depth of 1.53 m (Figure 3e). Finally, the section with open-graded frost protection material had the largest

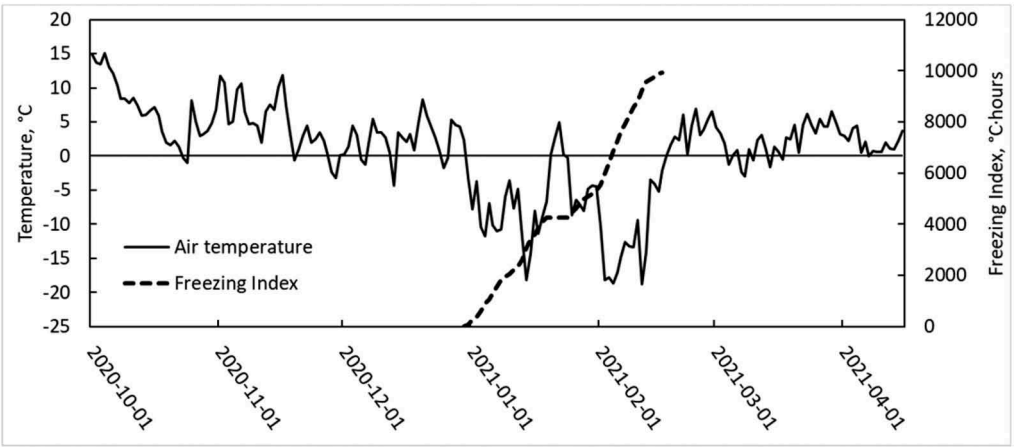

Figure 2. Air temperature and freezing index of winter 2020/2021.

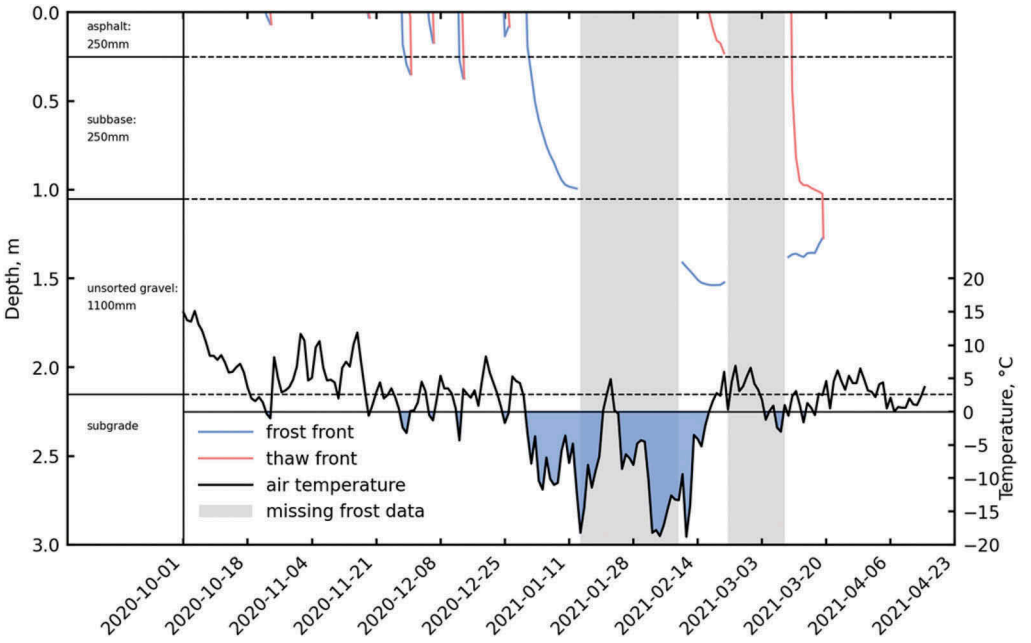

Figure 3a. Frost penetration in section F1: unsorted gravel.

frost penetration. This is the only section where the frost front slightly penetrated the subsoil. The maximum frost depth was 2.16 m (Figure 3g).

4 DISCUSSION

Figure 4 shows temperature profiles of all section on 15th of February. This date corresponds to the largest frost depth observed for section F7 with open-graded frost protection layer. All temperature gradients largely fall into three groups based on the maximum frost depth and temperature on the subsoil interface.

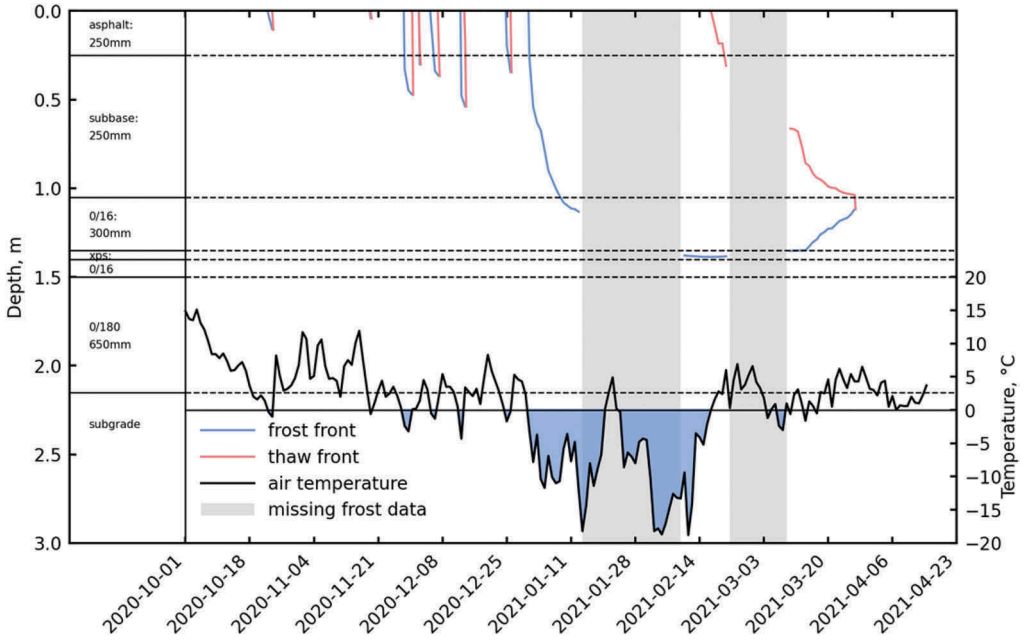

Figure 3b. Frost penetration in section F2: xps.

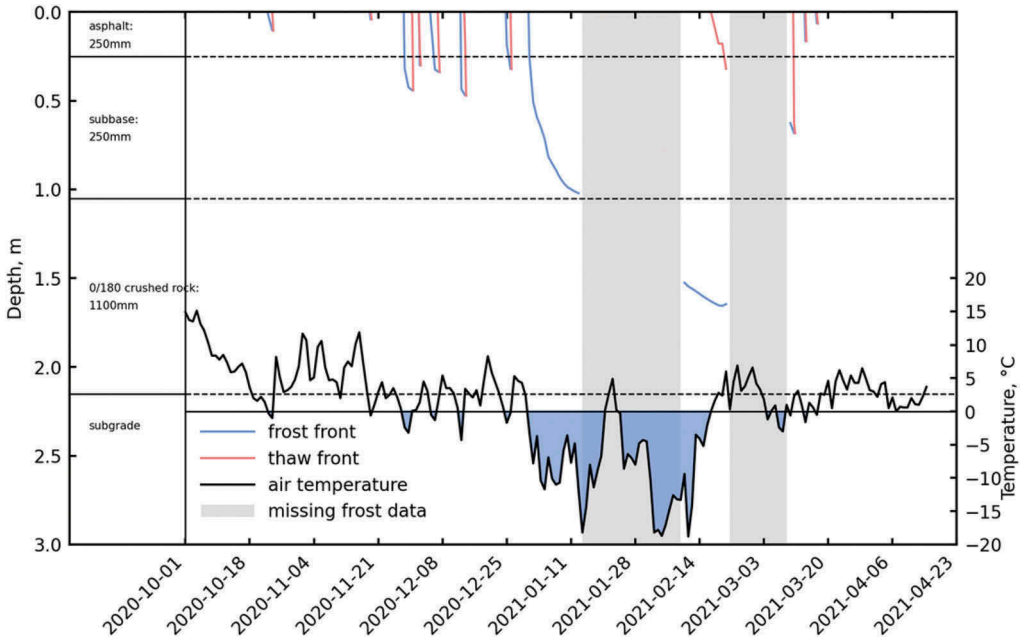

Figure 3c. Frost protection in section F3: 0/180mm crushed rock.

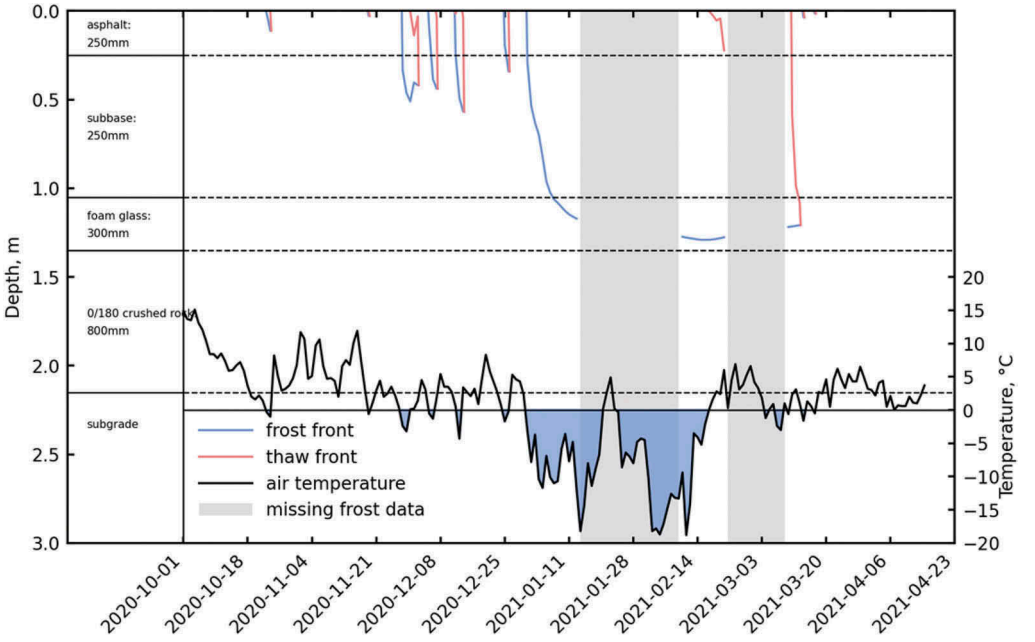

Figure 3d. Frost protection in section F4: foam glass.

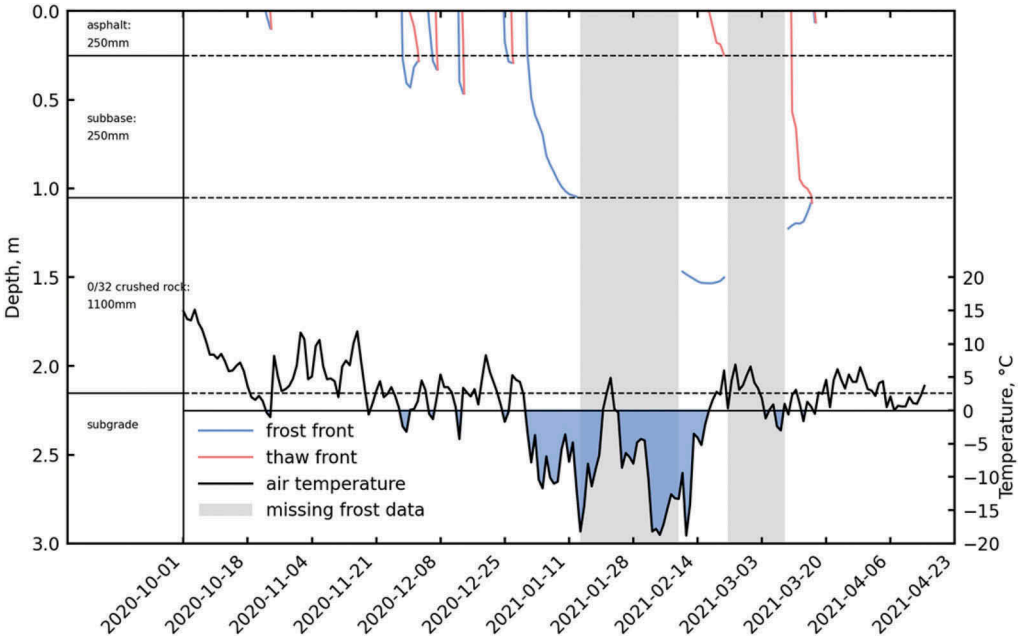

Figure 3e. Frost protection in section F5: 0/32 crushed rock.

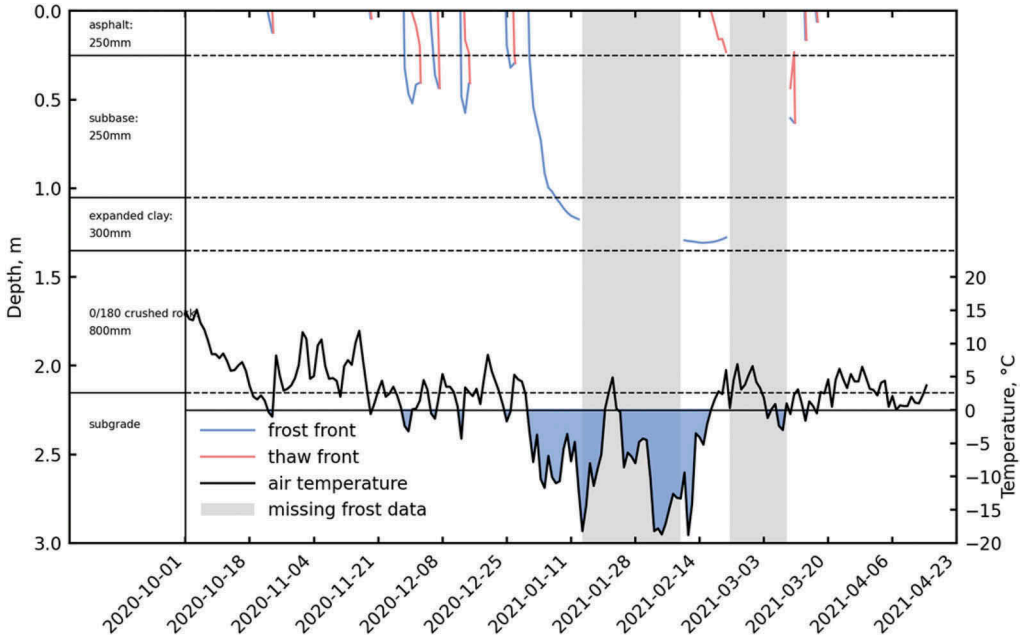

Figure 3f. Frost protection in section F6: expanded clay.

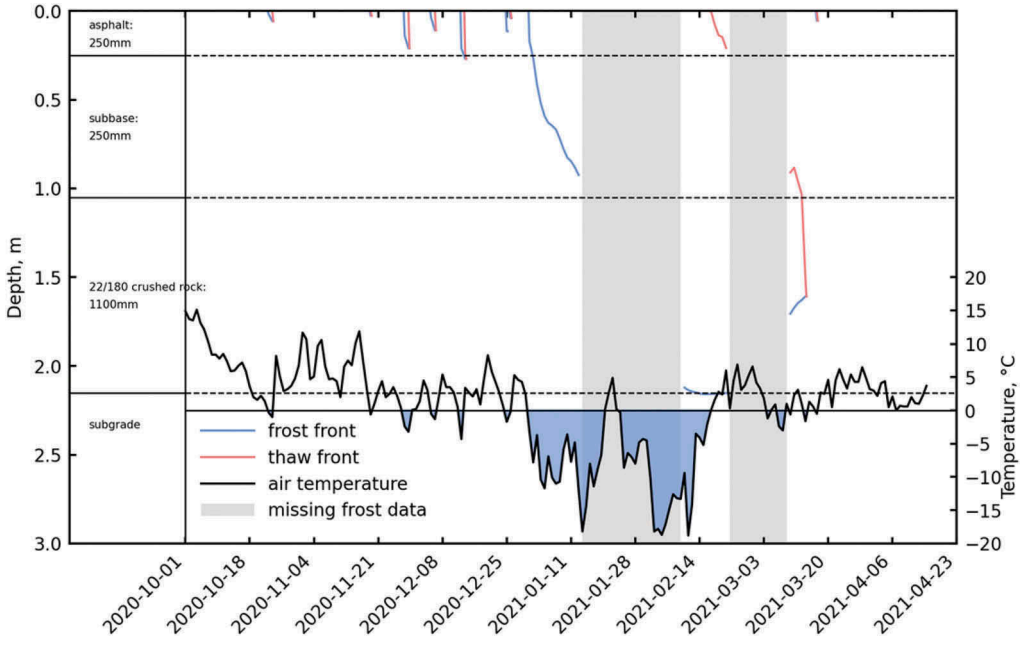

Figure 3g. Frost protection in section F7: 22/180 crushed rock.

As expected, all three sections with a layer of insulation (XPS, foam glass and expanded clay) provided the highest resistance to frost penetration. The maximum observed frost penetration in section F2 (XPS), F4 (foam glass) and F6 (expanded clay) was 1.39, 1.29 and 1.31 m respectively. The depth of lower interface for XPS is 5cm lower compared to the other two sections. Hence the overall frost penetration is almost the same for all three sections. Sections with insulation materials also maintained the highest temperature at the top of the subsoil. The average temperature maintained at around 4.2°C.

Three of the granular stone materials (unsorted gravel, 0/180 mm and 0/32 mm crushed rock) have roughly the same frost protection effect. The maximum frost penetration varied from 1.53 to 1.66 m. The temperature at the subsoil interface was around 2°C.

As expected, the 22/180 mm crushed rock material has substantially weaker performance than any other material. The frost penetrates this material very fast due to its low water content. However, the thermal conductivity of this material is lower compared to other granular materials. This can be seen by a less steep temperature gradient through the frost protection layer. This means that while the frost front propagates very fast through the frost protection layer, the subsequent progression of the frost front is rather slow due to relatively high thermal resistance.

These observations from test site can be compared to the predicted frost penetration based on the N200 handbook. For the sections with granular materials (F1, F3, F5, F7) the comparison is straight forward since the handbook provides a chart for frost protection as a function of frost index. The handbook distinguishes between five different types of granular materials. These mostly vary based on their gradation and fines content. However, the factor that affects the predicted frost penetration is the water content of these materials. The five materials defined in N200 handbook have a water content of 1%, 2%, 4%, 6% and 8%. Based on the approximate water content, materials used in the test site can be classified as follows: unsorted gravel – 4% water content; 0/180 mm crushed rock – 2% water content; 0/32 mm crushed rock – 6% water content; 22/180 mm crushed rock – 1% water content. These water

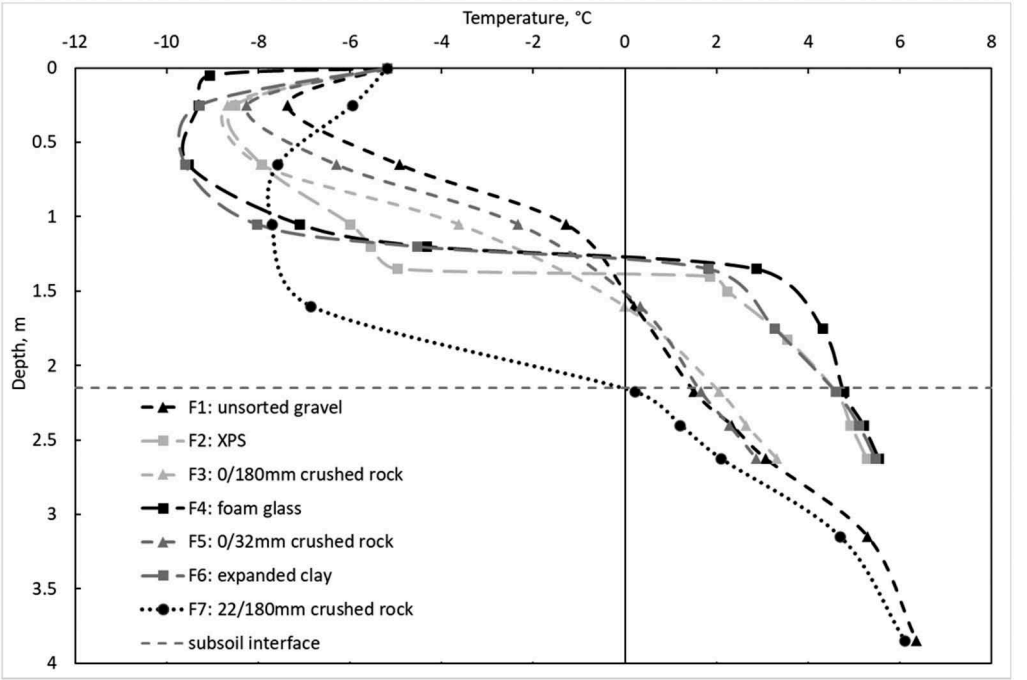

Figure 4. Temperature profiles of all sections on 15th of February.

contents were taken from previous studies with similar materials (Loranger et al., 2019). Table 1 summarizes maximum observed frost depth in comparison to the predicted value from the N200 handbook. The predicted values correspond to a FI of 10000°C·hours (417° C·days). Only the section with unsorted gravel has a good match between measured and predicted values. For the other three sections there is some variations when comparing the two values. However, it does not seem that the predicted value is consistently overpredicted or underpredicted. There are limited data available to characterize materials in terms of their water content. Hence some inconsistency between measured and predicted values are only reasonable. In addition, the N200 handbook is limited to only a certain number of materials. Nevertheless, the difference between measured and predicted values is no more than 10%.

Table 1. Comparison between measured and predicted frost depth values.

Material	Test section	Water content	Measured frost depth	Predicted frost depth
Unsorted gravel	F1	4%	1.54 m	1.54 m
0/180 crushed rock	F3	2%	1.66 m	1.75 m
0/32 crushed rock	F5	6%	1.54 m	1.39 m
22/180 crushed rock	F7	1%	2.16 m	1.95 m

Comparing the measured values of lightweight aggregates and XPS with predicted values from N200 is more complicated. The construction of frost protection layer with these materials includes a combination of the actual insulation material (XPS or lightweight aggregates) and additional layer of granular material below it. The design procedure is selecting the FI and mean annual temperature and then choosing the thickness of the lower granular layer. The output of the design chart is the necessary thickness of the insulation layer. The combination of the two layers should then be sufficient so that the frost front would remain at the bottom of the lower granular layer at the given freezing index. Hence, the design charts do not provide a means of comparing a measured frost depth with the predicted value unless the measured frost depth is at the bottom of the frost protection layer. However, from design perspective it can be clearly seen that the sections with XPS and lightweight aggregates are substantially overdesigned. The constructed layers of lightweight aggregates based on design charts could withstand around 49000°C·hours (2042°C·days) while the section with XPS could withstand a winter with freezing index of 38000°C·days (1583°C·days). The F_{100} winter at the given region is 19000°C·days (792°C·days). This means that if road with this type of frost protection materials would be constructed separately, the total thickness of the road could be substantially decreased. As mentioned earlier, the sections had to constructed with equal height due to the constraints of the rest of the road construction.

5 CONCLUSION

To observe better the frost protection of various materials, a test site was constructed while reconstructing a major highway in Trondheim, Norway. The test site consists of seven test sections, each 50 m long. The frost protection layer was constructed with four types of granular materials (1.1 m), two types of lightweight aggregates (0.3 m) and XPS (0.05 m). This paper presents frost penetration data from winter 2020/2021. The winter was cold with a freezing index (FI) of 9938°C·hours (414°C·days). This roughly corresponds to a 10-year period of return freezing index (F_{10}). The highway however is design to withstand a F_{100} freezing index that corresponds to 19000°C·hours (792°C·days). Although the main freezing season was only 48 days, multiple freeze-thaw cycles occurred before. This is quite typical for the region and sometimes might make the calculation of an overall freezing index complicated.

Results show that sections constructed with XPS, foam glass and expanded clay have very similar effectiveness. Comparing the measured values to predicted ones from handbook is complicated due to the design procedure that does not provide frost depth as a function of freezing index. Nevertheless, these sections are overdesigned and could potentially with stand double the amount of the freezing index that is expected in the area.

Section constructed with unsorted gravel, 0/180 mm crushed rock and 0/32 mm crushed rock provide a moderate frost protection. The section constructed with the open-graded 22/180 mm materials was the only one where the frost front reached the subsoil. These measured values were compared with predicted ones form the N200 handbook. Overall, there is a good agreement between the two values and the difference does not exceed more than 10%.

REFERENCES

Andersland, O., & Ladanyi, B. (2004). *Frozen ground engineering*, *2nd edition.* John Wiley & Sons.

Doré, G., & Zubeck, H. K. (2009). *Cold regions pavement engineering*.

Håndbok N200. (2018). *Vegbygging (Road construction). Statens vegvesens håndbokserie. Norway*.

Heiersted, R. S. (1976). *Sikring mot teleskader*. Norges teknisk-naturvitenskapelige forskningsråd og Statens vegvesens utvalg for frost i jord.

Hoff, I., Watn, A., Øiseth, E., Emdal, A., & Amundsgård, K. (2002). *Light weight aggregate (LWA) used in road pavements*. In Bearing Capacity of Roads, Railways and Airfields (pp. 1013–1022). CRC Press.

Loranger, B., Rieksts, K., Hoff, I., & Scibila, E. (2019). *Frost Depth and Frost Protection Capacity of Crushed Rock Aggregates Based on Particle Size Distribution*. In Cold Regions Engineering 2019 (pp. 169–176). American Society of Civil Engineers Reston, VA.

Rieksts, K., Loranger, B., Hoff, I., & Scibilia, E. (2019). *In Situ Thermal Performance of Lightweight Aggregates Expanded Clay and Foam Glass in Road Structures*. In Cold Regions Engineering 2019 (pp. 440–446). American Society of Civil Engineers Reston, VA.

Eleventh International Conference on the Bearing Capacity of Roads, Railways and Airfields, Volume 2 – Hoff, Mork & Saba (eds)

Too late snow wall removal as an enabler of rapid edge deformations - results from Aurora instrumented road sections on road E8 in Finland

P. Kolisoja, N. Vuorimies & A. Kurki
Research Centre Terra, Tampere University, Tampere, Finland

T. Saarenketo
Roadscanners Oy, Rovaniemi, Finland

ABSTRACT: Since early spring 2018 Tampere University and Roadscanners Oy have conducted long term structural and functional monitoring of two road sections on road E8 in Muonio, Finnish Lapland. This monitoring has been part of the Aurora project, an open testing ecosystem of intelligent transport and infrastructure solutions launched by the Finnish Transport Infrastructure Agency (FTIA). One of the unique observations made based on monitoring the vertical strains of base course layer and the vertical displacement of road surface concerns abrupt frost heave that takes place in the upper part of pavement structure in late spring before the start of thawing period. The phenomenon coincides with the melting of snow next to road edge, which indicates that the source of water enabling this late spring frost heave is from the side of road, not through the deeply frozen structural layers below. The conclusion was verified by means of periodic GPR measurements applied in monitoring the water content of road structure. The above observation emphasizes the importance of early enough removal of snow walls from road shoulders as a means of limiting the edge deformation and rutting of road structures during the thawing phase of seasonal frost.

Keywords: Edge deformation, spring thaw, frost heave, snow wall, Aurora

1 INTRODUCTION

The effects of seasonal frost have for long time been acknowledged as one of the dominant reasons for road deterioration in the Northern regions (e.g. Kestler 2003). Especially harmful are the consequences of thaw weakening of road structure during the early phase of thawing when the melting ice lenses are increasing the water content of road structure, but there is still frozen and thus almost impermeable subgrade soil below (Saarenketo & Aho 2005). From road structure's point of view typical consequences of this bearing capacity loss are rapid rut development in unbound structural layers and accelerated fatigue in bound layers.

A less acknowledged phenomenon related to the very beginning of thawing period concerns frost heaves that take place near to the edge of road just before the actual thawing of road structure starts. According to the authors' understanding it is due to the melting water of snow infiltrating into the road structure via road shoulders due to cryo-suction in the unbound structural layers of road. As this results in an increase in the moisture content of base course layer during the critical time of early spring thaw, it is potentially a marked contributor to rut

DOI: 10.1201/9781003222897-26

development in the upper part of road structure. Consequently, on areas with high snowfall a very critical issue is thus early enough removal of snow walls next to the road edge, since this is the most efficient action that can be taken to limit the amount of infiltrating water.

In connection with Aurora project, an open testing ecosystem of intelligent transport and infrastructure solutions launched by the Finnish Transport Infrastructure Agency (FTIA), Tampere University and Roadscanners Oy have jointly been monitoring the structural and functional condition of two extensively instrumented road sections on road E8 in Muonio, Finnish Lapland since late autumn 2017 (Kolisoja et al. 2019). The results of long-term monitoring have clearly indicated, to the knowledge of authors for the very first time in the world, this phenomenon of thawing time frost heave to take place in a measurable quantity. Furthermore, the monitoring results indicate an abrupt increase in base course rutting when this short-term frost heave settles. The actual monitoring results from Aurora instrumented road sections concerning this issue are presented in more detail in the following chapters.

2 MATERIALS AND METHODS

2.1 *Long-term structural monitoring of Aurora sites*

The Aurora monitoring sites are located on road E8, a couple of kilometers South from the village of Muonio, in Western Finnish Lapland. On the Aurora 1 site, located on a curve to the right in a place where nearby threes are providing some shadow when the sun is not shining very high, the thickness of structural layers is about 1.1 meters. The substructure of the Aurora 1 site consists of dense moraine with stones and boulders. Before the structural instrumentations were installed, existing asphalt concrete (AC) layer was removed from the site on an area of about 3 * 5 m^2. After the instrumentation the Aurora 1 site was overlain by about 120 mm of new AC that was installed in two layers. On the Aurora 2 site, located on a straight road section open for sunshine, the overall thickness of unbound structural layers resting on top of a sandy embankment is about 1.5 meters. In connection with the renovation works carried out on the Aurora 2 area in 2017 the old AC layer that was about 70 mm thick, was mix-milled with some added coarse grained aggregate and the existing unbound base course layer made of crushed rock. Finally, the road was overlain by 90 mm of new AC installed in two layers. Corresponding to the alignment of both sites the slope of road surface at Aurora 1 is one sided towards the installed instruments while at Aurora 2 it is two-sided as is typical for straight road sections.

Both the Aurora 1 and 2 sites are furnished with almost identical structural instrumentation setups, a sematic picture of which is shown in Figure 1. The instrumentations consist of the following instrument types and the numbers of installed transducers given in parentheses for the Aurora 1 and Aurora 2 sites, respectively:

- Displacement transducers monitoring the road surface deflection, RSDEF (0 + 3)
- Acceleration transducers monitoring the road surface deflection, RSACC (20 + 20)
- Horizontal strain transducers at the base of lower AC layer, ACSTR (5 + 6)
- Vertical pressure cells at two levels in unbound base course layer, BCPRE (8 + 8)
- Vertical strain transducers in the unbound base course layer, BCSTR (4 + 4)
- Percostation probes for monitoring dielectric value, electrical conductivity and temperature, PERCO (10 + 10)

A bit more detailed description of the instrumentations has been given earlier by Kolisoja et al. (2019). Regarding frost heaves taking place during early spring thaw the most interesting instruments are those measuring the vertical movements of road surface and the vertical strain of base course layer. Locations of these transducers in relation to the inner side of edge line have been summarized in Figure 2. At Aurora 1 site the typical driving lines of vehicles are somewhat closer to the road shoulder due to the right turning alignment of road.

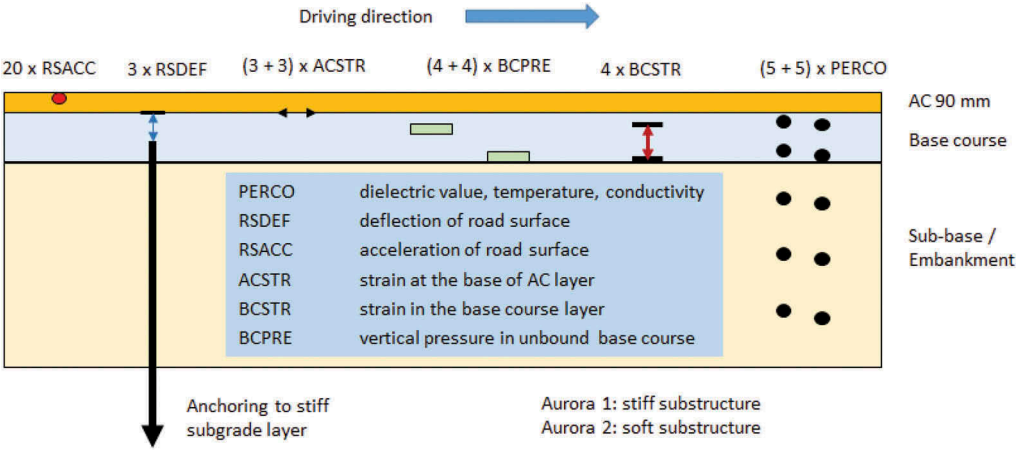

Figure 1. Sematic picture of structural instrumentations at Aurora 1 and 2 sites.

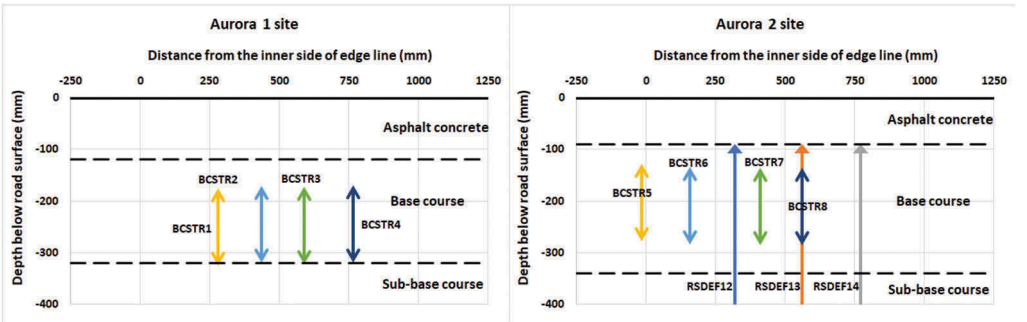

Figure 2. Distances of road surface deflection transducers and base course strain transducers from the inner side of edge line at Aurora 1 and 2 sites.

2.2 *Periodic on-surface monitoring of Aurora sites*

In 2018 and 2019 Aurora test sites were monitored using RDSV (Road Doctor Survey Van) equipped with Ground Penetrating Radar (GPR), laser scanner (lidar), 3D accelerometer technique and recording of digital videos from the road (Saarenketo 2017). In addition, GPR cross section surveys were conducted on both Aurora 1 and 2 sites. In 2018 both Aurora site road cross sections were monitored eight times starting from early February when road was frozen until June 18 when it had completely thawed. In 2019 surveys were conducted a few times during spring and summer. From the GPR data a special Moisture Damage Index (MDI), developed by Roadscanners Oy, was calculated (Arnold et al. 2017). In wintertime MDI indicates the amount of unfrozen water in frozen structure while in late spring high MDI values indicate high saturation degree in the material. In addition, laser scanner data was used to measure the exact shape of road surface, based on which rut depth maps and rut growth maps were derived. Figure 3 presents an example of the analyzed MDI values as well as rut depth and rut growth data at Aurora 1 site in 2018 and 2019. It indicates that moisture content was higher in late April 2019 than it was at the same time in 2018. It also shows fast rut growth, even more than 5 mm, in outer wheel paths especially in Southbound lane that loaded trucks are more often using.

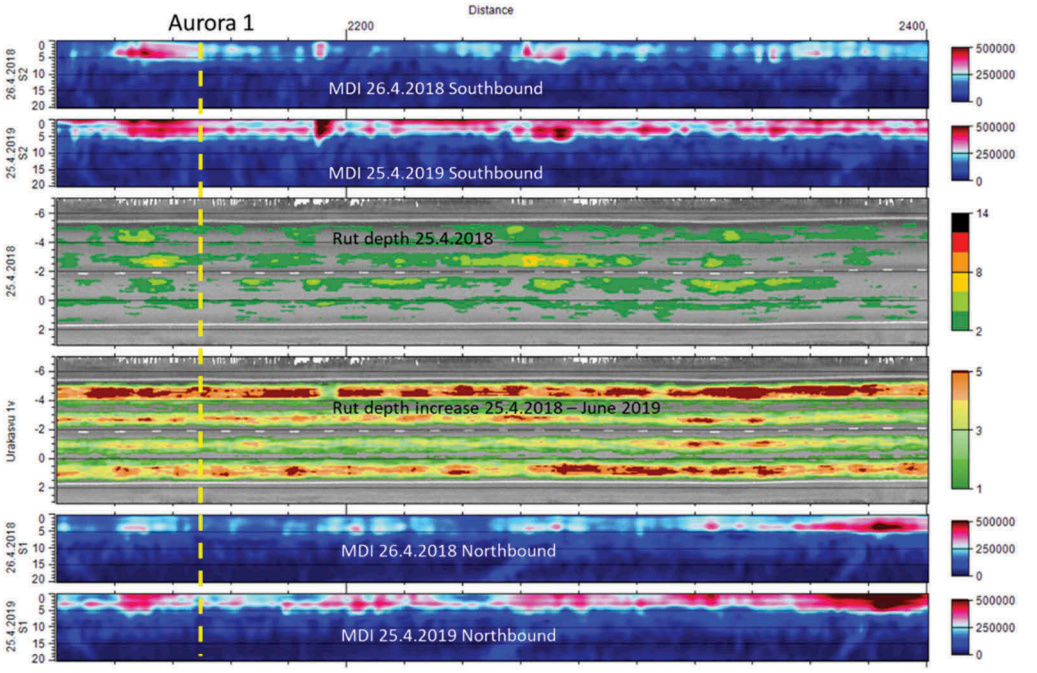

Figure 3. MDI values in April 2018 and 2019, rut depths in April 2018 and rut depth increase in between April 2018 and June 2019 at and around Aurora 1 site in Muonio.

3 MONITORING RESULTS

3.1 *Vertical displacements of road surface*

Long-term monitoring results regarding the vertical displacement of road surface are only available from Aurora 2 site since the installation of anchoring rods for displacement transducers was not successful at Aurora 1 site due to boulders in subgrade soil. At Aurora 2 site three displacement transducers were installed at distances from 0.32 to 0.77 m from the edge line and the respective changes in transducer readings in between the beginning of year 2018 to the late summer of 2019 have been shown Figure 4.

The results shown in Figure 4 indicate clearly that just before the thawing period of seasonal frost there has been a sudden heave of road surface of up to more than 5 mm. Correspondingly, in the very beginning of thawing period the road surface has settled from 7 to 9 mm in about one week, which means that most part of the overall frost heave on this site has taken place in the upper part of road structure also during the freezing period in the autumn (Figure 4).

In Figure 5 the thawing time road surface displacements at Aurora 2 site are show in cross sectional view for the first weeks of April 2018 and 2019. It seems obvious that at this site the thawing time frost heaves have been more pronounced towards the edge of road.

3.2 *Vertical deformations of base course layer*

3.2.1 *Aurora 1 site*

The vertical deformations of base course layer were monitored using four parallel displacements transducers on both Aurora sites. At Aurora 1 site transducers were located 0.28 m to 0.77 m from the edge line, while at Aurora 2 site the corresponding range was from -0.02 to 0.56 m (Figure 2). Right after installation the measurement range of base course strain

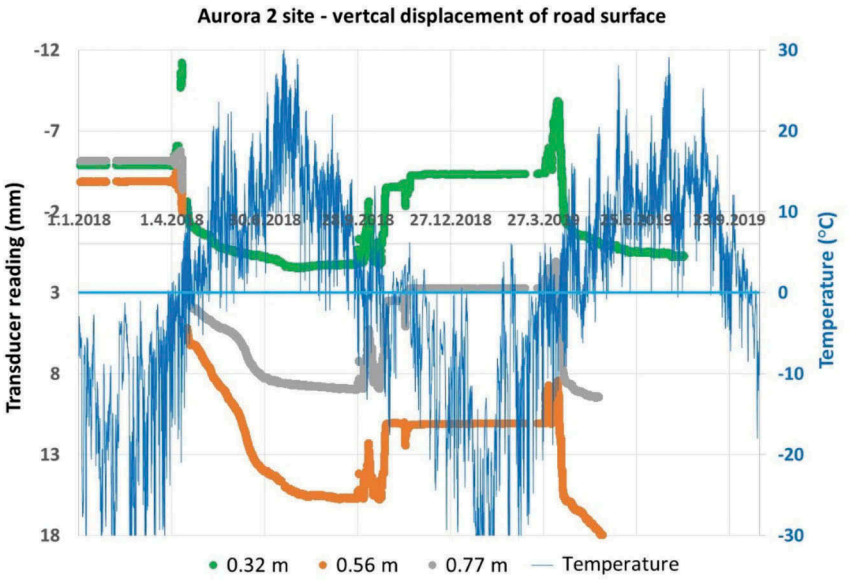

Figure 4. Vertical displacements of road surface at Aurora 2 site in between 1.1.2018 and summer 2019 and the respective air temperatures at Muonio weather station.

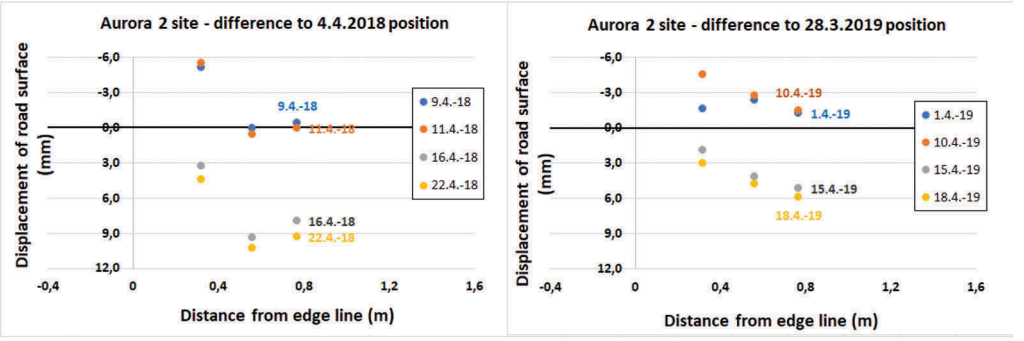

Figure 5. Vertical displacements of road surface in cross sectional view at Aurora 2 site in April 2018 and 2019.

transducers was adjusted to 150 mm, but due to permanent deformations that have taken place in the base course layer since then, the actual measurement range has slightly decreased. In Figures 6 to 9 all the transducer readings have been given directly in millimeters i.e. no conversion to strain values has been made.

Figure 6 indicates long-term vertical deformations that have taken place in the base course layer of Aurora 1 site in between 1.1.2018 and August 2019. Basically all the phenomena already seen in Figure 4 regarding the vertical displacement of road surface are reproduced here. An abrupt lengthening of measurement range similar to the very beginning of freezing period in the autumn 2018 is observed just preceding the start of thawing period both in early April 2018 and 2019. As thawing starts, both components of frost heave settle within in a few days.

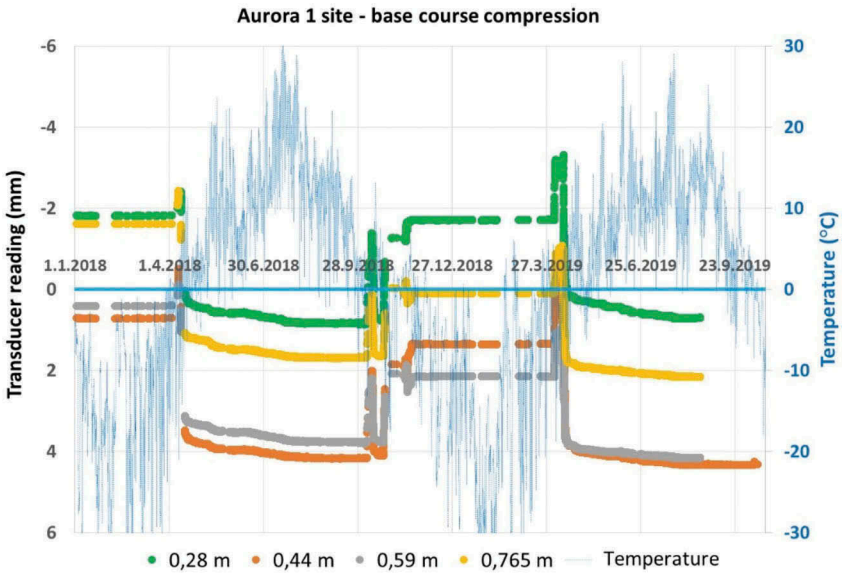

Figure 6. Vertical deformations of base course layer at Aurora 1 site in between 1.1.2018 and August 2019 and the respective air temperatures at Muonio weather station.

In Figure 7 the respective base course deformations taking place at Aurora 1 site during the first weeks of April are shown in cross sectional view. In comparison to the corresponding results from Aurora 2 (Figure 9) site as well as the vertical displacements measured from Aurora 2 site (Figure 5), the main difference is that the measured thawing time frost heaves are smaller in magnitude and also more evenly distributed in cross sectional direction. A possible explanation for this is that Aurora 1 site is located in a place less exposed to early springtime sunshine due to nearby trees than Aurora 2 site.

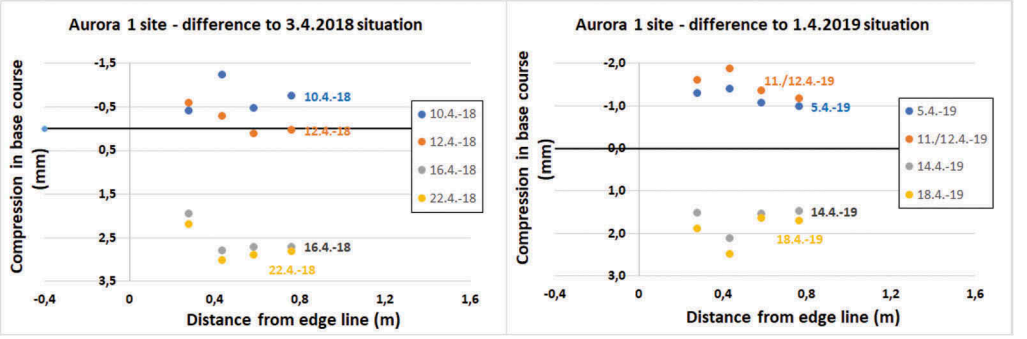

Figure 7. Vertical deformations of base course layer in cross sectional view at Aurora 1 site in April 2018 and 2019.

3.2.2 *Aurora 2 site*

Figure 8 presents the development of long-term vertical deformations in the base course layer of Aurora 2 site in between 1.1.2018 and September 2019. Again, an abrupt lengthening of the measurement range is preceding the start of thawing period both in April 2018 and 2019. Especially in April 2019 the magnitude of frost heave in base course layer is also clearly larger than that happening during the actual freezing of base course layer in autumn 2018.

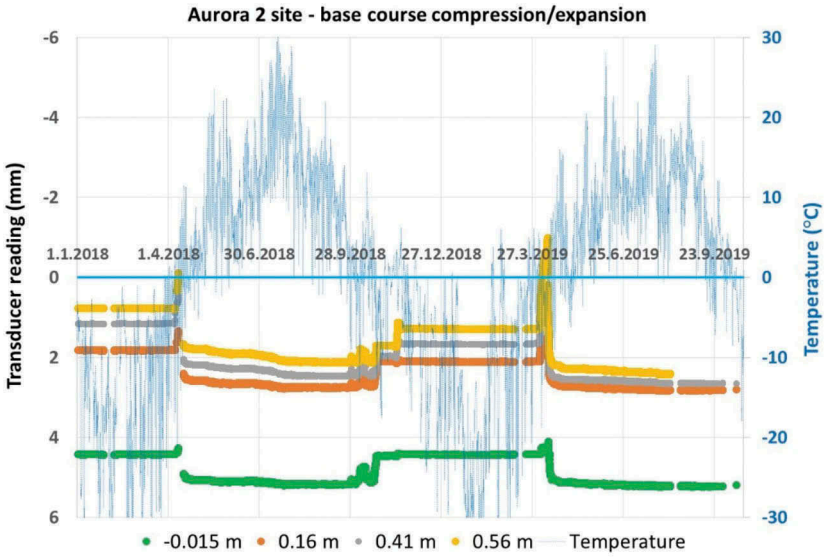

Figure 8. Vertical deformation of base course layer at Aurora 2 site in between 1.1.2018 and September 2019 and the respective air temperatures at Muonio weather station.

The cross-sectional distribution of frost heaves during the first weeks of April 2018 and 2019 corresponding to the results of Figure 8 are shown in Figure 9. It is noteworthy that the range of locations covered by base course strain transducers is now closer to the edge of AC layer than that of the displacement transducers measuring the road surface deflection (Figure 2), but still the result is somewhat contradictory to that of Figure 5. The frost heaves in base course seem to be the highest at a distance of about half a meter from the edge line, while at the edge line base course heave is hardly measurable. The reason for that has not been figured out by the time of writing this article.

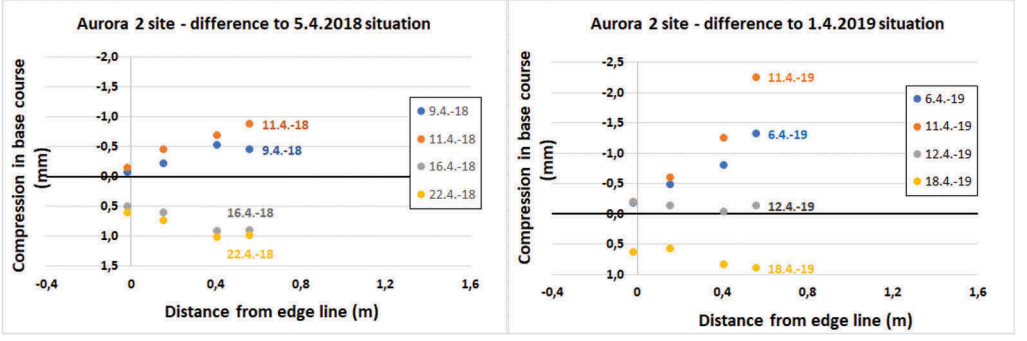

Figure 9. Vertical deformations of base course layer in cross sectional view at Aurora 2 site in April 2018 and 2019.

3.3 *GPR measurements*

The MDI values derived based on GPR measurements carried out at both road cross sections of the Aurora sites several times in 2018 are summarized in Figure 10 for the Aurora 1 site and in Figure 11 for the Aurora 2 site. As stated already above, in a frozen layer, i.e.

measurements made in February and March, red and black colours indicate high amount of unfrozen water while in an unfrozen layer they indicate high saturation ratio, respectively.

At the Aurora 1 site the highest MDI values both before and after the thawing of road structure are observed near to the edge of Southbound lane (Figure 10). This implies the existence of high cryo-suction values that would give a logical explanation for the movement of additional water into the base course layer and the appearance of consequent frost heave (Figures 6 and 7) as soon as melting water is available from snow walls next to the edge of road. After thawing, this additional water is keeping the moisture content of base course layer high until summer and making it thus susceptible to permanent deformations. As Figure 3 indicates permanent deformations determined using lidar measurements were observed to be most pronounced below the outer wheel path of Southbound lane where MDI values are also the highest.

At the Aurora 2 site MDI values are in general lower and also more evenly distributed (Figure 11) than at Aurora 1 site. A plausible reason for the lower MDI values and somewhat lower frost heaves at the Aurora 2 site is that the base course layer of the Aurora 2 site is more coarse grained and also contains some amount of bitumen as the result of aggregate addition and consequent mix-milling of the existing base course with the old AC layer during the rehabilitation works carried out on the site in 2017. In fact it seems that the highest MDI values after thawing of Aurora 2 site have been determined towards the center of road, which could imply to an unperfect AC layer joint in the middle of road, but this assumption has not been confirmed.

4 DISCUSSION

Long-term monitoring results both concerning road surface displacements and vertical deformations of base course layer at the Aurora 1 and 2 sites indicate undeniably that abrupt frost heaves take place just before the thawing of seasonal frost starts, in Western Lapland typically in early April. According to the presented monitoring results the magnitude of these

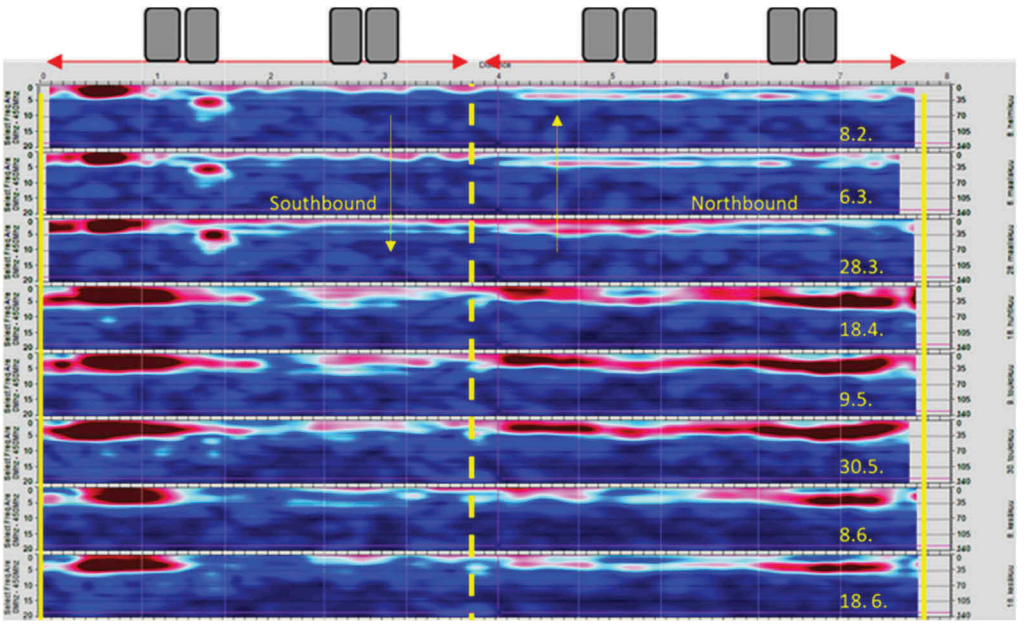

Figure 10. MDI values at the Aurora 1 site cross section in 2018. Red and black colors indicate high values of moisture content.

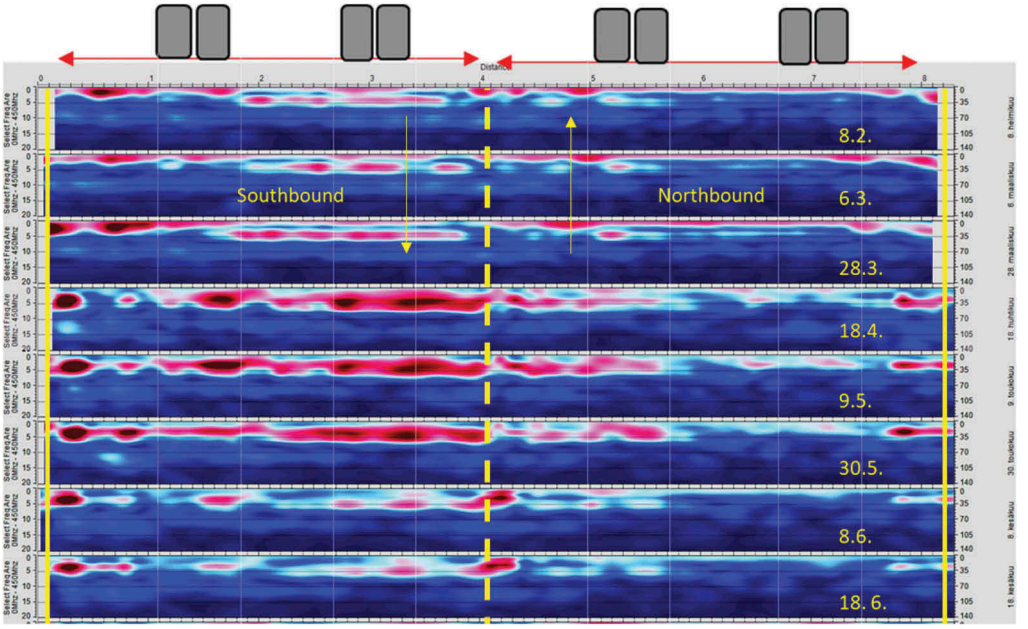

Figure 11. MDI values at the Aurora 2 site cross section in 2018. Red and black colors indicate high values of moisture content.

springtime frost heaves has been even exceeding frost heaves developing in the autumn when the monitoring sections have been freezing originally. The explanation for this phenomenon is believed to be so called tertiary frost heave, a concept originally suggested by Tommy Edeskär (2018) in a frost symposium held in Luleå. According to the concept, available water from the edge of road, typically originating from the melting of snow walls next to the road, moves inside to road structure driven by cryo-suction prevailing in the structural layers of frozen road.

The most important practical consequence of the observed phenomenon is that moisture content in the upper part of road structure increases markedly during the critical time when the thawing of frost starts from the top of road. This makes road structure susceptible to the rapid development of permanent deformations that is exactly what has happened especially at the Aurora 1 site (Figure 3) in a time period of only one and a half years after the installation of a new AC overlay. Correspondingly, the most efficient – but at the same time very inexpensive - countermeasure to avoid this detrimental process is early enough removal of the snow walls from the edges of road.

5 SUMMARY

In this paper monitoring results from two comprehensively instrumented road sites located at E8 in Muonio, Western Finnish Lapland, were presented. Based on those results the following conclusions could be drawn:

- Vertical displacements of road surface at one of the sites and vertical deformations at both of the sites have been monitored during two thawing periods from the beginning of 2018 to the summer of 2019.
- Marked frost heaves have been observed to take place in the upper part of road structure at the very beginning of thawing period. This phenomenon, also called as tertiary frost

heave, is assumed to be caused by the melting water of snow walls that is drawn into the base course layer of road by cryo-suction effect.
- The MDI values derived based on GPR measurements strongly support this assumption.
- Rapid rut development has been recorded at the points were this tertiary frost heave phenomenon has been observed to take place.
- Early enough removal of snow walls next to road shoulders is evidently the most important measure to counteract rapid rut development caused by thawing time frost heave.

ACKNOWLEDGEMENTS

The authors want to acknowledge the financial support provided by the Finnish Transport Infrastructure Agency that has enabled the instrumentation of Aurora test sites and thus also the accumulation of results presented in this paper.

REFERENCES

Arnold, G., Sing, P.F., Saarenketo, T. and Saarenpää, T., 2017. *Pavement moisture measurement to indicate risk to pavement lifetime*. New Zealand Transport Agency Research Report 611. 160 pp.

Edeskär, T., 2018. *Review of current heave and thaw theories/approaches. Frost research workshop*. Luleå University of Technology, Sweden.

Kestler, M. A., 2003. *Techniques for Extending the Life of Low-Volume Roads in Seasonal Frost Areas*. Transportation Research Record Journal of the Transportation Research Board 1819(1): 275–284 Paper No. LVR8-1150. https://doi.org/10.3141/1819b-35.

Saarenketo, T., 2017. *What New Technologies can Provide to Intelligent Road Asset Management*. Proceedings of the 29th International Baltic Road Conference, 28-30 August 2017, Tallin.

Saarenketo, T. and Aho, S., 2005. *Manging Spring Thaw Weakening of Low-Volume Roads*. ROADEX II Report. 130 pp. Available at: https://www.roadex.org/services/knowledge-center/publications/permanent-deformation/

Eleventh International Conference on the Bearing Capacity of Roads, Railways and Airfields, Volume 2 – Hoff, Mork & Saba (eds)

InSAR analysis of C-band data for transport infrastructure monitoring

L. Bianchini Ciampoli, V. Gagliardi & A. Benedetto
Department of Engineering, Roma Tre University, Rome, Italy

A.M. Alani & F. Tosti
School of Computing and Engineering, University of West London (UWL), London, UK

ABSTRACT: In recent years, successful applications of the Synthetic Aperture Radar Interferometry (InSAR) have been reported for the monitoring of subsidence and deformation in transport infrastructures. Compared to other non-destructive surveying methodologies, this technique can perform network-level analyses more rapidly and it can provide time-series of ground displacements by multi-temporal data acquisition. However, processing of satellite images by high-resolution sensors (i.e., X-band radars) is demanding in terms of computational resources and specialist skills. This aspect has contributed to partially hinder this technique to become a strategic infrastructure asset management tool. Parallel to this, it is important to emphasise that the use of middle-range frequency SAR sensors (i.e., C-band) allows for the acquisition of lighter datasets and, hence, more computationally affordable analyses. However, due to a lower system resolution and the challenges in identifying features of scattering objects with size below the resolution cell, the C-band imagery is usually not employed for infrastructure monitoring. This limitation could be compensated in rural environment areas, where transport infrastructures are usually the most stable scatterers.

This study aims to demonstrate the viability of the medium-range resolution SAR imagery in transport asset monitoring for the preliminary identification of sections affected by subsidence in rural areas. InSAR analyses of high (COSMO-SkyMed) and medium-resolution (Sentinel-1A) datasets are performed on a dual-carriageway rural motorway. A comparison between the Persistent Scatterers Interferometry (PSI) outcomes from data processed with the two resolutions demonstrates the viability of using Sentinel-1A images for multi-temporal subsidence monitoring in highway infrastructure.

Keywords: Remote Sensing, transport infrastructure monitoring, InSAR, Sentinel 1, COSMO- SkyMed

1 INTRODUCTION

Monitoring the structural integrity of transport infrastructure, such as railways, roads and bridges, is a priority for asset owners to ensure the operation and prevent damage and deterioration prior to rehabilitation or failures (Chang et al. 2003, Hosseini Nourzad et al. 2016).

Public awareness has been raised in many countries, where new guidelines and standards of practice were released in this area. This is the case of Italy, where guidelines on classification and risk management, and the safety assessment and monitoring of infrastructure and bridges have been published by the Italian Higher Council for Public Works and Ministry of

DOI: 10.1201/9781003222897-27

Infrastructure and Transport (Italian Higher Council for Public Works et. al 2020). Currently, several on-site non-destructive testing (NDT) technologies and sensors are available for subsidence monitoring and displacement mapping. Amongst others, accelerometers (Kongyang et. al 2011), strain gauges (Olund et al. 2017), wireless network systems (Chae et al. 2012), Global Position System (GPS) and levelling (Mossop A et al. 1997, Sato et al.2003), Ground Penetrating Radar (GPR) (Alani et al. 2013, Benedetto et al. 2016) and the Ground-based Interferometer (Stabile et al. 2013), have been recognised as viable technologies to support ordinary and extraordinary asset management. However, these equipment can be expensive to acquire and they may be not fully proficient for use at the network level.

To overcome this limitation, various innovative satellite-based remote sensing technologies, i.e. the Interferometric Synthetic Aperture Radar (InSAR), Persistent Scatterers Interferometry (PSI) (Colesanti et al. 2003, Ferretti et al. 2000, 2001, 2011), and the Small Baseline Subsets (SBAS) techniques (Berardino et al. 2003, Lanari et al. 2004), have gained momentum in the last few years in the monitoring of transport assets. This is due to relatively affordable and high-frequently updated datasets that allow to reconstruct the historical time-series of displacements for vast territories, including infrastructure assets.

Despite the high-resolution of X-Band data allows for an accurate and dense detection of PS points, it is worthy of note that a minimum of 20 SAR images are required to reach a sufficient level of statistical significance of data. This can impact costs for image acquisition and can still be a factor that limits their application for routine structural monitoring. Furthermore, the time required for data processing of large areas increases drastically and requires important computational efforts. On the other hand, the use of C-Band data allows inherently to analyse vast areas in shorter time. However, there might be data resolution constraints that are not compatible with the level of detail required for infrastructure monitoring. New research has been developed that identify critical infrastructure areas at the network level by the processing of C-band data, and then uses high-resolution (X-band) data to make more detailed analyses (Wang et al., 2021). In this context, the use of C-band data is still to be explored, especially for application to roads and transport infrastructure.

This research aims to demonstrate the viability of using C-band SAR imagery for effective monitoring of linear transport infrastructure in rural environments. To this purpose, a C-band dataset, collected in the framework of the Sentinel 1 mission, provided by the European Space Agency (ESA), was processed for the monitoring of a section of a dual-carriageway rural motorway and one major exit ramp located in an area affected by known subsidence. The outcomes from the PSI analysis were compared to the Permanent Scatterers (PSs) obtained from the processing of high-resolution SAR datasets, acquired by the COSMO-SkyMed mission.

2 MULTI-TEMPORAL INSAR: WORKING FRAMEWORK AND MAIN APPLICATIONS IN TRANSPORT INFRASTRUCTURE MONITORING

The working framework of the multi-temporal Interferometric Synthetic Aperture Radar (MT- InSAR) technique relies on a statistical analysis of the signals emitted by the on-satellite sensor and back-scattered by a network of coherent targets on the ground, i.e., the PSs. This approach allows to estimate the displacements occurred between different acquisitions by a separation between the phase shift from the ground motions and the phase component related to atmosphere, topography and signal noise contributions (Berardino et al. 2003, Colesanti et al. 2003, Ferretti et al. 2000,2001, Lanari et al. 2004).

A main advantage of these techniques is the relatively lighter data-processing required for the assessment of displacements and the detection of critical areas, as opposed to the higher computational load needed in other approaches (Ferretti et al. 2000,2001). Therefore, the multi- temporal InSAR approach has proven ideal in monitoring transport infrastructure, as the high density of radar stable targets allows for more comprehensive measurements.

Several multi-temporal InSAR techniques were developed in the last few years for the detection of PS point targets, such as the PS- InSAR (Ferretti et al. 2000,2001), the SqueeSAR

(Ferretti et al. 2011), and the SBAS (Berardino et al. 2003, Lanari et al. 2004) techniques, all of which are based on different approaches.

To this effect, many works can be found in the literature that relate to the use of PS-InSAR techniques in transport infrastructure monitoring, such as railway networks (Bianchini Ciampoli et al. 2019 a, Chang et al. 2017, Qin et al. 2017, Tosti et al. 2020, Yang et al. 2014), highways and tunnels, (Barla et al. 2016, Koudogbo et al. 2018, Perissin et al. 2012), bridges (Alani et al. 2020, Bianchini Ciampoli et al. 2019 b, D'Amico et al. 2020, Gagliardi et al. 2020a, 2021a,, Jung et al. 2019, Milillo et al. 2019) and airport runways (Gagliardi et al. 2021 b,c, Bianchini Ciampoli et al. 2020, Gao et al. 2016, Jiang et al. 2010). This evidence confirms the effectiveness of satellite-based remote sensing techniques to these specific areas of application, and their potential to become strategic infrastructure asset management tools.

3 EXPERIMENTAL FRAMEWORK

3.1 *The case study*

To pursue the above-set objectives, datasets of SAR images from both the Sentinel 1A and COSMO- SkyMed missions in the time interval 2015–2019 were collected and processed by means of the PSI technique. A comparison between results from the PS analysis for both the operating frequencies was performed to assess the viability of the C-band data in the monitoring of highways.

In detail, the present study focuses on the monitoring of a road intersection connecting the A91 and the A12 motorways, located nearby Rome, Italy (Figure 1). This section has been selected due to a well-known subsidence affecting the whole area. The process has been monitored in the past (Delgado Blasco et al., 2019; Orellana et al., 2020), as it affects a strategic area connecting the "Leonardo Da Vinci" International Airport and other major industrial areas to the municipality of Rome.

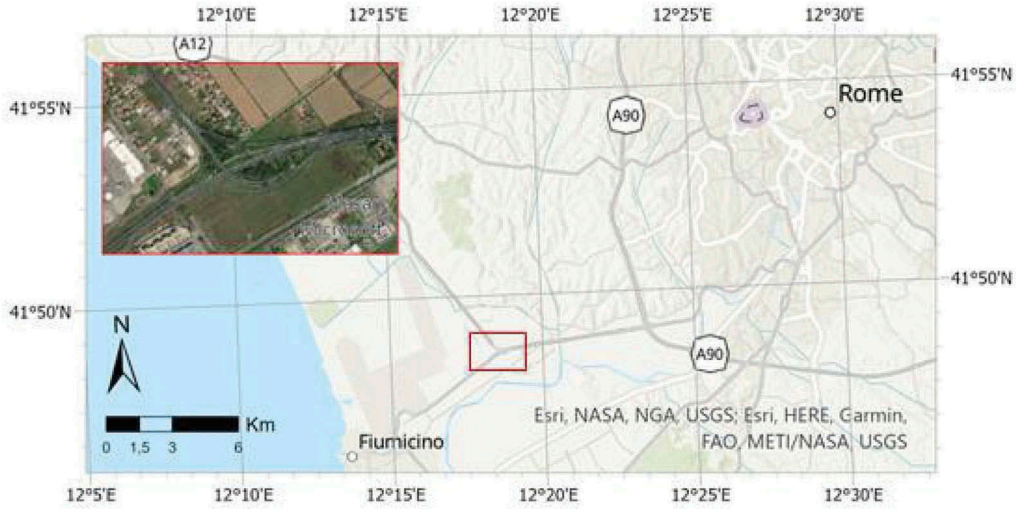

Figure 1. The road intersection investigated in this study.

3.2 *SAR datasets*

Multi-frequency SAR datasets (C-band and X-band) were collected and processed by the PSI technique to assess displacements associated with the investigated infrastructure. The C-Band SAR products were acquired by the European Space Agency (ESA) in the framework of the

Sentinel-1 mission which is the European Radar Observatory for the Copernicus joint initiative of the European Commission (EC) and the European Space Agency (ESA). The Sentinel-1 satellite, operates at a frequency of 5.4 GHz, which allows to detect displacements with a centimetre accuracy. A number of 23 Single Look Complex (SLC) SAR products collected in the time period from 2017 to 2019, were processed. Furthermore, 35 images of X-Band SAR data were collected by the COSMO- SkyMed mission (COSMO-SkyMed Product - ©ASI: Italian Space Agency, 2015-2019, All Rights Reserved), and delivered under the license to use. The Cosmo-SkyMed system operates at a frequency of 9.6 GHz corresponding to a wavelength of 3.1 cm. This allows to achieve a 3 m ground-resolution cell and, under ideal conditions, to reach a millimetre accuracy of measurements.

3.3 *PSI processing*

The SAR datasets were processed following the PSI method (Colesanti et al. 2003, Ferretti et al. 2000,2001) by means of the Interferometric Stacking Module of the Software SARscape (Sarmap, 2012) integrated in the Software ENVI, licensed within the framework of the ESA approved project "STRAIN2: Sensing Transport Infrastructures 2" (EOhops proposal ID 53071). More specifically, the PSI technique operates by the application of the following sequential stages (Colesanti et al. 2003, Ferretti et al. 2000,2001):

i. A statistical analysis of the amplitudes of the electromagnetic returns is developed on a pixel-by- pixel base to compute the Amplitude Dispersion Index (Da), reported in Eq.1, where μ and σ are the mean and the standard deviation of the amplitude values, respectively. This index is a measure of the phase stability over time for each pixel at least for high Signal-to-Noise Ratio (SNR) values.

$$\mathrm{Da} = \mu/\sigma \tag{1}$$

ii. Persistent Scatterer Candidates (PSCs) were selected by computing the dispersion index of the amplitude values relative to each pixel. These are pixels with a value of stability index that exceeds a fixed threshold of typically 0.25.;

iii. the interferometric phase $\Delta\phi i$ is computed for any PSC, at any i^{th} interferogram;

iv. the atmospheric phase contributions, the orbital and noise-related effects were identified and removed from the interferometric phase to identify the phase-shift related to the range variation only.

As a result of the above steps, the stable reflectors, i.e., the PSs, can be recognized over the inspected area. At the end of the processing stages, historical displacement trends can be produced for every pixel identified as the PS, providing an indication of the average ground motion over the time-period investigated. These steps were successfully completed using the two different SAR band datasets acquired in in this study (i.e., C-band, X-band).

However, SAR satellites can only detect displacements in the Line-of-Sight (LoS), with reference to the specific orbit-related incident angle. Consequently, the displacement detected is a component of the real displacement on the ground. Several research proposed different approaches, i.e., the vector- based approach, to overcame these occurrences and calculate the actual displacement-velocity-vector from datasets acquired in different acquisition geometries (i.e. Ascending and Descending). (Dalla Via et al. 2012, Gagliardi et al. 2020a, Wright et al. 2000).

For the area of interest investigated in this study, different SAR images in the ascending acquisition geometry have been collected and analysed for the same investigated period for the Sentinel 1A and the COSMO-SkyMed missions. Hence, in this work we refer only to displacements detected in THE LoS direction of the SAR sensors.

4 RESULTS AND SHORT DISCUSSION

To demonstrate the effectiveness of using C-Band imagery processed by the PSI technique for subsidence monitoring in transport infrastructure, results were compared to the data obtained by the processing of the high-resolution COSMO-SkyMed products.

Several PSs from the processing of both the datasets were identified in the investigated road intersection (Figure 2). The processing of C-Band dataset (Figure 2b) was effective in highlighting the deformation trends compared to the processing carried out on X-Band data (Figure 2a). To quantitatively assess the goodness of fit between the two datasets, data from a critical area (marked in yellow in Figure 2) were extrapolated and the corresponding time series of displacements were analyzed for any given PS in this area.

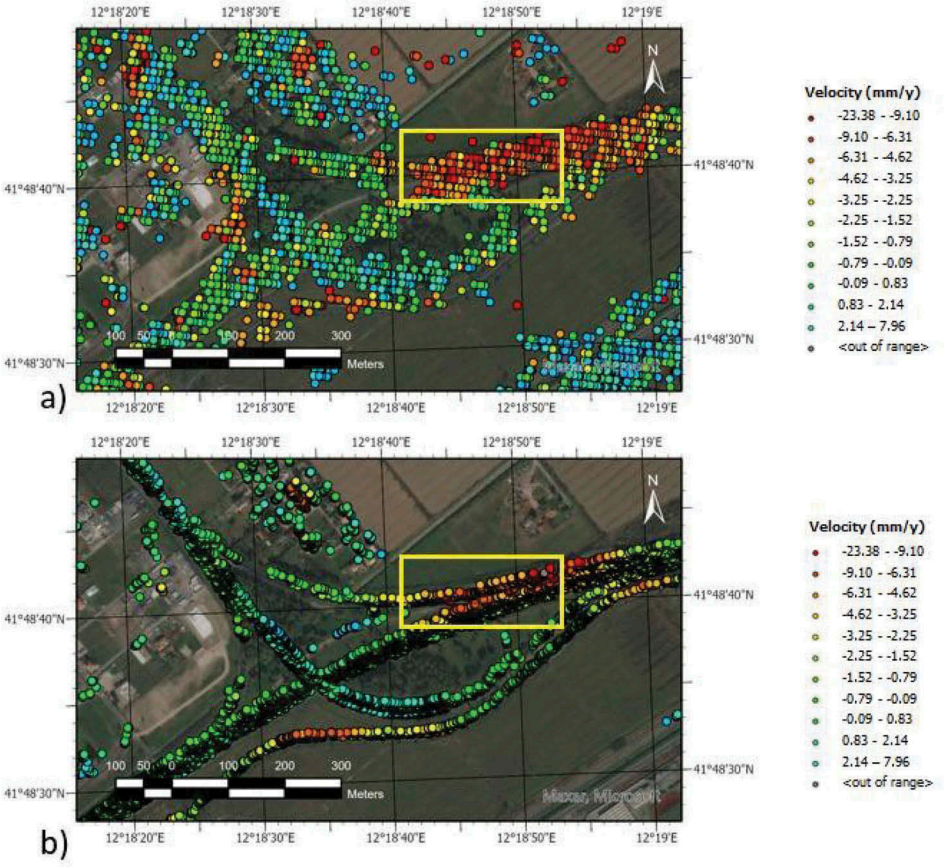

Figure 2. Comparison between the displacement velocity of PSs for a) COSMO-SkyMed and b) Sentinel-1 missions.

To elaborate, 753 PSs and 235 PSs were extracted from the processing of the COSMO-SkyMed and the Sentinel-1 datasets, respectively. The time series of displacements for individual PSs were then plotted against the acquisition time (Figure 3). As the Sentinel-1 dataset relates to a shorter period of observation time, this was related to the COSMO-SkyMed observation time by matching the zero time at the first acquisition (i.e., October 2017) with the value of displacement measured by the processing of COSMO-SkyMed data at the same period. The trend of the average displacements for COSMO-SkyMed and Sentinel-1clearly proves a good matching between the two datasets.

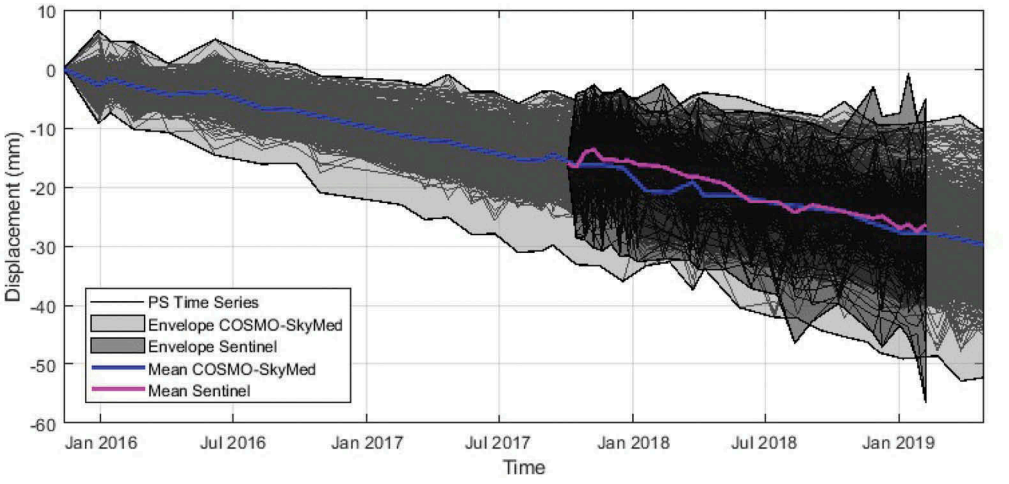

Figure 3. Comparison between displacement time series of PSs within the investigated area (i.e., the yellow rectangular area in Figure 2) for both Sentinel and COSMO-SkyMed data. The envelopes represent areas of maximum and minimum variations of each averaged displacement value across the period analysed.

Considering a linear regression fitting of the average deformation points for the two datasets, very close slopes of the fitting lines are observed. These indicate velocities of deformation equal to –8.43 mm/y and –9.78 mm/y for the COSMO-SkyMed and the Sentinel-1 data, respectively (Figure 4). The quality of the fitting is proven by very high values of R2, i.e., 0.96 (COSMO-SkyMed) and 0.88 (Sentinel-1).

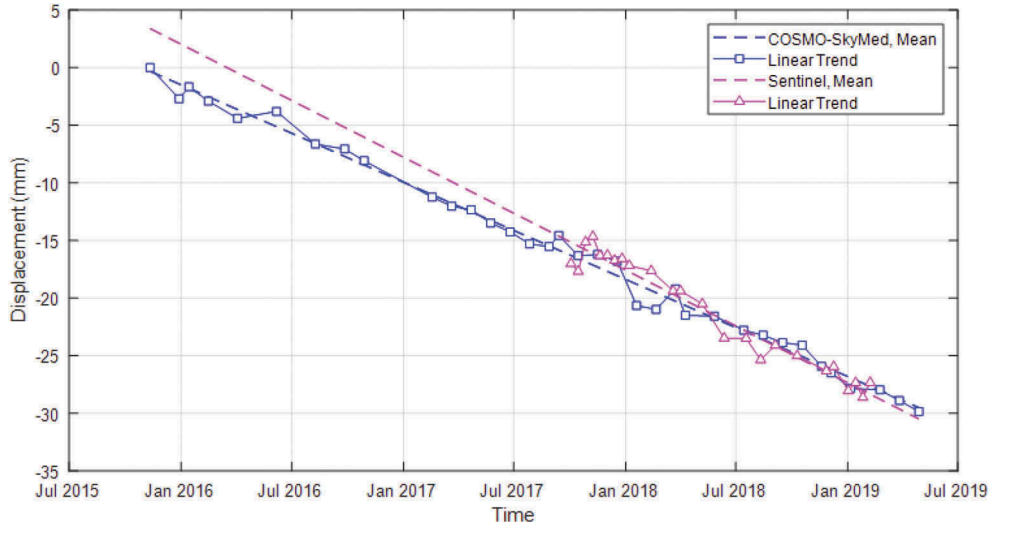

Figure 4. Linear fitting of average displacement time series for COSMO-SkyMed and Sentinel-1 datasets.

The analysis of the statistical distribution of the two populations of displacement velocities confirms a good agreement between COSMO-SkyMed and Sentinel-1 datasets (Figure 5), with COSMO-SkyMed being more centred around the mean value (i.e., a lower standard deviation). This is expected considering the lower resolution associated with Sentinel-1 images.

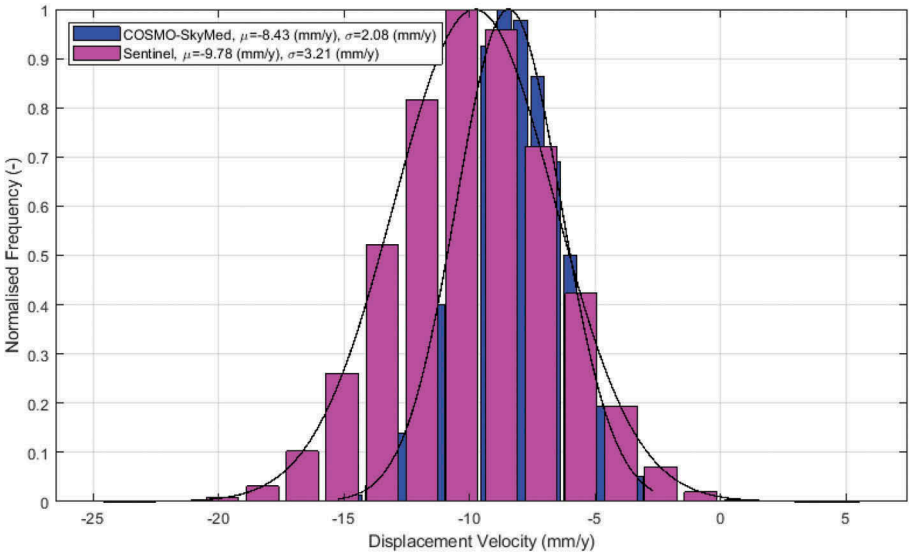

Figure 5. Normal probability density functions of displacement velocity for COSMO-SkyMed and Sentinel-1 PSs.

5 CONCLUSIONS AND FUTURE DEVELOPMENTS

This work aims to demonstrate the viability of the medium-range resolution SAR datasets in transport asset monitoring for effective detection of subsidence. To this effect, InSAR analysis of high (COSMO-SkyMed) and medium-resolution (Sentinel-1A) datasets is performed on a dual- carriageway rural motorway and one major exit ramp located in an area affected by known subsidence. A comparison between the outcomes of the Persistent Scatterers Interferometry (PSI) processing with the two resolutions demonstrates the viability of using Sentinel-1A images for the monitoring of subsidence.

This information is crucial for integration into Pavement Management Systems (PMSs) to predict critical displacements and optimize maintenance prior to pavement degradation and failure. Results have proven that medium-resolution data could be used effectively to preliminarily identify areas of concern, where in depth analyses (e.g., using X-band data or ground-based non-destructive testing methods) could be carried out at a later stage. However, an integration with other specialist techniques must be mandatory for areas affected by natural hazards, such as subsidence or landslides.

ACKNOWLEDGEMENTS

The Sentinel 1a SAR products are © of the ESA (European Space Agency) delivered under the license to use. the COSMO-SkyMed products - ©ASI: Italian Space Agency, 2017-2019, are © of the ASI (Italian Space Agency), delivered under the license to use. The license for using the software Sarscape ® integrated in the software Envi® is granted by the ESA-approved project "STRAIN2", EOhopS proposal (ID 53071). This paper reports research supported by the Italian Ministry of Education, University and Research under the national project "EXTRA TN", Prin 2017, Prot. 20179bp4sm.

REFERENCES

Alani A. M., Tosti F., Bianchini Ciampoli L., Gagliardi V., Benedetto A., 2020. *Integration of GPR and InSAR methods for the health monitoring of masonry arch bridges*. NDT&E International. https://doi.org/10.1016/j.ndteint.2020.102288

Alani, A.M., Aboutalebi, M., Kilic, G., 2013. *Applications of ground penetrating radar (GPR) in bridge deck monitoring and assessment, J*. Appl. Geo., 97, 45–54

Barla G. et al., 2016. *InSAR monitoring of tunnel induced ground movements*. Geomechanik und Tunnelbau 9(1):15–22. https://doi.org/10.1002/geot.201500052

Benedetto A., Tosti F., Bianchini Ciampoli L. and D'Amico F., 2016. *An overview of ground- penetrating radar signal processing techniques for road inspections*, Signal Processing, http://dx.doi.org/10.1016/j.sigpro.2016.05.016

Berardino P., Fornaro G., Lanari R., Sansosti E., 2003. *A new algorithm for surface deformation monitoring based on small baseline differential SAR interferograms*. IEEE Trans. Geosci. Remote Sens. 40, 2375–2383

Bianchini Ciampoli L., Gagliardi V., Clementini C., Latini D., Del Frate F., Benedetto A., 2019a. *Transport Infrastructure Monitoring by InSAR and GPR Data Fusion*, Surveys in Geophysics, 1–24, 2019. https://doi.org/10.1007/s10712-019-09563-7

Bianchini Ciampoli L., Gagliardi V., Calvi A., D'Amico F., Tosti F., 2019 b. *Automatic network- level bridge monitoring by integration of InSAR and GIS catalogues*. Proceedings of SPIE - The International Society for Optical Engineering, 11059. DOI: 10.1117/12.2527299

Bianchini Ciampoli L., Gagliardi V., Ferrante C., Calvi A., D'Amico F. and Tosti F., 2020. *Displacement monitoring in Airport Runways by Persistent Scatterers SAR Interferomet*ry. Remote Sensing. (In press).

Chae, M. J., Yoo, H. S., Kim, J. Y., & Cho, M. Y., 2012. *Development of a wireless sensor network system for suspension bridge health monitoring*. Automation in Construction, 21, 237–252. doi:10.1016/j.autcon.2011.06.008

Chang L., Dollevoet R. P. B. J., & Hanssen R. F., 2017. *Nationwide Railway Monitoring Using Satellite SAR Interferometry*. IEEE Journalof Selected Topics in Applied Earth Observations and Remote Sensing, 10(2), 596–604. doi:10.1109/jstars.2016.2584783

Chang, P. C., Flatau, A., & Liu, S. C. 2003. Review Paper: *Health Monitoring of Civil Infrastructure. Structural Health Monitoring*, 2(3),257–267. https://doi.org/10.1177/1475921703036169

Colesanti C., Ferretti A., Prati C. et al., 2003. *Monitoring landslides and tectonic motions with the Permanent Scatterers Technique*. Eng Geol 68(1–2):3–14. https://doi.org/10.1016/S0013-7952(02)00195-3

D'Amico F., Gagliardi V., Bianchini Ciampoli L., Tosti F., 2020. *Integration of InSAR and GPR Techniques for Monitoring Transition Areas in Railway Bridges*. NDT&E International. https://doi.org/10.1016/j.ndteint.2020.102291

Dalla Via G., Crosetto M., and Crippa B., 2012. *Resolving vertical and east-west horizontal motion from differential interferometric synthetic aperture radar: The L'Aquila earthquake*. Journal of geophysical research: solid earth 117, no. B2

Delgado Blasco, J.M.; Foumelis, M.; Stewart, C.; Hooper, A. Measuring Urban Subsidence in the Rome Metropolitan Area (Italy) with Sentinel-1 SNAP-StaMPS Persistent Scatterer Interferometry. Remote Sens. 2019, 11, 129. https://doi.org/10.3390/rs11020129

Ferretti A., Fumagalli A., Novali F., Prati C., Rocca F., Rucci A., 2011.. *A new algorithm for processing interferometric data-stacks: SqueeSARTM*. IEEE Trans. Geosci. Remote Sens.

Ferretti A., Prati C., Rocca F., 2000. *Nonlinear subsidence rate estimation using permanent scatterers in differential SAR interferometry*. IEEE Trans Geosci Remote Sens 38(5):2202–2212, https://doi.org/10.1109/36.86887 8

Ferretti A., Prati C., Rocca F., 2001. *Permanent scatters in SAR interferometry*. IEEE Trans Geosci Remote Sens 39(1):8–20. https://doi.org/10.1109/36.898661

Gagliardi V., Benedetto A., Bianchini Ciampoli L., D'Amico F., Alani A., Tosti F. (2020 a). *Health monitoring approach for transport infrastructure and bridges by satellite remote sensing Persistent Scatterer Interferometry (PSI)*. Proceedings of SPIE -11534, Earth Resources and Environmental Remote Sensing/GIS Applications XI, 115340K. doi:10.1117/12.2572395

Gagliardi V., Bianchini Ciampoli L., D'Amico F., Tosti F., Alani A and Benedetto A. (2020 b). *A Novel Geo-Statistical Approach for Transport Infrastructure Network Monitoring by Persistent Scatterer Interferometry (PSI)*. In: IEEE Radar Conference 2020, Florence, Italy.

Gagliardi V., Bianchini Ciampoli L., D'Amico F., Alani A. M., Tosti F., Benedetto A. (2021a), *Multi-Temporal SAR Interferometry for Structural Assessment of Bridges: The Rochester Bridge Case Study*. International Airfield and Highway Pavements Conference 2021. https://ascelibrary.org/doi/abs/10.1061/9780784483510.028

Gagliardi, V.; Bianchini Ciampoli, L.; D'Amico, F.; Alani, A.M.; Tosti, F.; Battagliere, M.L.; Benedetto, A. (2021b). *Novel perspectives in the monitoring of transport infrastructures by Sentinel-1 and COSMO-SkyMed Multi-Temporal SAR Interferometry*. In Proceedings of the 2021 International Geoscience and Remote Sensing Symposium, IGARSS, Brussels, Belgium, 12–16 July 2021.

Gagliardi, V.; Bianchini Ciampoli, L.; Trevisani, S.; D'Amico, F.; Alani, A.M.; Benedetto, A.; Tosti, F. (2021c). *Testing Sentinel-1 SAR Interferometry Data for Airport Runway Monitoring: A Geostatistical Analysis*. Sensors 2021, 21, 5769. https://doi.org/10.3390/s21175769

Gao M., Gong H., Chen B., Zhou C., Chen W., Liang Y., Shi M., Si Y., 2016. InSAR time-series investigation of long-term ground displacement at Beijing Capital International Airport, China. Tectonophysics, 691, 271–281. doi:10.1016/j.tecto.2016.10.016

Hosseini Nourzad, S. H. and Pradhan, A. 2016. *Vulnerability of Infrastructure Systems: Macroscopic Analysis of Critical Disruptions on Road Networks*. Journal of Infrastructure Systems, 22(1), 04015014. doi:10.1061/(asce)is.1943-555x.0000266

Italian Ministry of the Environment and the Superior Council of Public Works., *2020. Guideilines for the classification and management of the risk, the evaluation of the safety and the monitoring of the existing bridges*, Online resource accessed, 21/ 09/2020 at (http://www.mit.gov.it/sites/default/files/media/notizia/2020-05/1_Testo_Linee_Guida_ponti.pdf)

Jiang L., & Lin H., 2010. *Integrated analysis of SAR interferometric and geological data for investigating long-term reclamation settlement of Chek Lap Kok Airport, Hong Kong*. Engineering Geology, 110 (3-4), 77–92. doi:10.1016/j.enggeo.2009.11.005

Jung J., Kim D-J, Palanisamy Vadivel SK, Yun S-H., 2019. *Long-term deflection monitoring for bridges using X and C-band time-series SAR interferometry*. Remote Sens 2019;11(11):1258.715. https://doi.org/10.3390/rs11111258

Kongyang Chen, Mingming Lu, Xiaopeng Fan, Mingming Wei and Jinwu Wu., 2011. *Road condition monitoring using on-board Three-axis Accelerometer and GPS Sensor*, 6th International ICST Conference on Communications and Networking in China, Harbin, 2011, pp. 1032–1037, doi: 10.1109/ChinaCom.2011.6158308.

Koudogbo F., Urdiroz A., Robles JG., Chapron G., Lebon G., Fluteaux V., Priol G., 2018. *Radar interferometry as an innovative solution for monitoring the construction of the Grand Paris Express metro network—first results*. In: World tunnel conference, 2–25 April, Dubai

Lanari R., Mora O., Manunta M., Mallorqui J.J., Berardino P., Sansosti E., 2004. *A small baseline approach for investigating deformation on full resolution differential SAR interferograms*. IEEE Trans. Geosci. Remote Sens. 42, 1377–1386,

Milillo P., Giardina G., Perissin D., Milillo G., Coletta A., Terranova C., 2019. *Pre-collapse space geodetic observations of critical infrastructure: the Morandi Bridge*, Genoa, Italy. Remote Sensing;11 (12):1403. https://doi.org/10.3390/rs11121403

Mossop A., Segall P., 1997. *Subsidence at The Geysers Geothermal Field*, *N. California from a comparison of GPS and leveling surveys*. Geophys. Res. Lett., 24, 1839–1842,

Olund J., & DeWolf J. 2007. *Passive Structural Health Monitoring of Connecticut's Bridge Infrastructure. Journal of Infrastructure Systems*, 13(4),330–339. doi:10.1061/(asce)1076-0342(2007)13:4(330).

Orellana, F.; Delgado Blasco, J.M.; Foumelis, M.; D'Aranno, P.J.V.; Marsella, M.A.; Di Mascio, P. DInSAR for Road Infrastructure Monitoring: Case Study Highway Network of Rome Metropolitan (Italy). Remote Sens. 2020, 12, 3697. https://doi.org/10.3390/rs12223697

Perissin D., Wang Z., & Lin H., 2012. *Shanghai subway tunnels and highways monitoring through Cosmo-SkyMed Persistent Scatterers*. ISPRS Journal of Photogrammetry and Remote Sensing, 73, 58–67. doi:10.1016/j.isprsjprs.2012.07.002

Qin X., Liao M., Zhang L., & Yang M., 2017. *Structural Health and Stability Assessment of High- Speed Railways via Thermal Dilation Mapping With Time-Series InSAR Analysis*. IEEE Journal of Selected Topics in Applied Earth Observations and Remote Sensing, 10(6),2999–3010. doi:10.1109/jstars.2017.2719025

Sarmap. 2012. *SARscape technical description*, 2012. Internet resource accessed 2020-03-05at: http://www.sarmap.ch/pdf/SARscapeTechnical.pdf

Sato H.P., Abe K., Ootaki O., 2003. *GPS-measured land subsidence in Ojiya City*, Niigata Prefecture, Japan. Eng. Geol., 67, 379–390,

Stabile T. A., Perrone A., Gallipoli M. R., Ditommaso R. and Ponzo F. C., 2013. *Dynamic Survey of the Musmeci Bridge by Joint Application of Ground-Based Microwave Radar Interferometry and Ambient Noise Standard Spectral Ratio Techniques*, in IEEE Geoscience and Remote Sensing Letters, vol. 10, no. 4, pp. 870–874, doi: 10.1109/LGRS.2012.2226428.

Tosti F., Gagliardi V., D'Amico F., Alani A.M., 2020. *Transport infrastructure monitoring by data fusion of GPR and SAR imagery information*. Transp Res Proc 2020; 45:771–778. 721 https://doi.org/10.1016/j.trpro.2020.02.097

Wang Y., Bai, Z., Zhang, Y., Qin, Y., Lin, Y., Li, Y. and Shen, W., *Using TerraSAR X-Band and Sentinel-1 C-Band SAR Interferometry for Deformation Along Beijing-Tianjin Intercity Railway*

Analysis, in IEEE Journal of Selected Topics in Applied Earth Observations and Remote Sensing, vol. 14, pp. 4832–4841, 2021, doi: 10.1109/JSTARS.2021.3076244.

Wright T. J., Parsons B. E., & Lu Z., *Toward mapping surface deformation in three dimensions using InSAR*. Geophysical ResearchLetters, 31, L01607. https://doi.org/10.1029/2003GL018827 (2004).

Yang Z., Schmid F., Roberts C., 2014. *Assessment of railway performance by monitoring land subsidence*. In: 6th IET conference on railway condition monitoring (RCM 2014), pp 1–6. https://doi.org/10.1049/cp.2014.1000

Eleventh International Conference on the Bearing Capacity of Roads, Railways and Airfields, Volume 2 – Hoff, Mork & Saba (eds)

In situ measurements of deflections on an instrumented pavement section using geophones

Natasha Bahrani, Juliette Blanc, Pierre Hornych & Fabien Menant
Materials and Structures Department, LAMES, University Gustave Eiffel, Nantes, France

ABSTRACT: Deflection information can be used as a global parameter to define the overall performance of a pavement. In this paper, deflection data from an instrumented section on a French motorway is analysed. A method for the measurement of deflections using geophones, embedded in pavement layers, is presented. Geophones measure the vertical velocity, and by treating and integrating their signals, the pavement deflection can be determined. This work focuses on the multiple applications of geophones, using the deflection to gather information on the pavement structure and the traffic on the motorway. It highlights the importance of continuous monitoring of roads, and different possibilities of interpretation of the acquired data from an instrumented road.

Keywords: Pavement continuous monitoring, Geophones, Deflection basin

1 INTRODUCTION

Deflection is a widely used parameter for evaluating the structural performance of pavements, and back-calculating pavement layer properties. Usually, deflection is measured using mobile loading devices such as FWD, or Traffic speed deflectometer (Hadidi & Gucunski, 2010). With such devices, deflection measurements can only be performed infrequently, typically every one or two years. Continuous measurement of deflections using sensors, installed in the pavement, under vehicle traffic, can provide much more detailed information on the evolution of pavement response with traffic loads and climatic variations.

In recent research, innovative methods have been developed to measure deflections using different sensor technologies. In particular, geophones and accelerometers are small and economical sensors, which seem well suited to this type of measurements. These sensors measure respectively the vertical speed and acceleration, and their measurements can be integrated to obtain pavement deflections (vertical displacements), and back-calculate pavement layer properties. In (Levenberg, 2012) accelerometers are used to measure the mechanical response and back-calculate layer moduli. (Arraigada et al., 2009) also uses accelerometer to measure the deflection and focuses on the issues of the conversion of the acceleration into deflection and treatment of the noise related to the signal received from the sensors. Similarly in the work of (Liu et al., 2017), geophones were used to monitor pavement deteriorations. This approach used an array of sensors and performed predictive analysis of the pavement response using neural network algorithms.

At Université Gustave Eiffel, in order to evaluate the possibility of using geophones for the monitoring of pavement deflections, a laboratory study was first carried out. The tests consisted of submitting two types of geophones to simulated deflection signals, using a vibrating table. A suitable signal treatment procedure, to integrate the signals and obtain accurate

DOI: 10.1201/9781003222897-28

deflection measurements was proposed (Bahrani et al., 2019). Then, tests were also carried out on the accelerated pavement testing facility of Université Gustave Eiffel, in which the 2 types of geophones were placed in the top layer of the pavement. This study was carried out to test the response of the sensors under real axle loads, and different loading conditions (speeds, load levels and transversal wheel positions). The data was processed using the same data treatment process and showed favourable outputs, when compared with deflections measured with a reference displacement sensor (Bahrani et al., 2020). The deflection basins measured in the APT tests were also used to back-calculate the moduli of the pavement layers (Bahrani et al., 2020). This study confirmed the interests of using geophones for the continuous monitoring of pavement performance over time.

The work described in this paper presents an application of the measurement method with geophone, to the instrumentation of a real motorway section, under continuous traffic. The motorway, named as Ax (for confidentiality reasons) was instrumented with geophones and temperature probes connected to a remote data acquisition system. A detailed description of the section, and a first analysis of the results, have been presented by (Duong et al., 2018). The aim of this study is to re-analyse the geophone measurements; using the newly developed signal treatment procedure, and to explore different possibilities of interpretation of the deflection measurements. More precisely, the objectives of the work are:

- To evaluate the sensor's ability to measure the vertical deflections, in real field conditions;
- To measure the deflection, and its evolution with time;
- To analyse the evolution of pavement layer moduli with temperature and traffic;
- To characterise the heavy vehicle traffic.

2 AX MOTORWAY INSTRUMENTATION

A section on the Ax motorway, located between Bayonne and Bordeaux, was instrumented with 4 geophones and 8 temperature probes. During the rehabilitation of the pavement 3 new layers were constructed, on the existing pavement base. The characteristics of the pavement layers are defined below:

- 2.5 cm thick very thin asphalt concrete, (VTAC);
- 6 cm thick binder course, high modulus bituminous concrete, (HMBC);
- 7 cm thick base course, high modulus Asphalt concrete (HMAC) (EME, or "enrobé à module élevé");
- 8 cm thick cracked layer of Gravel stabilized with bitumen (GB)
- About 30 cm thick sand-cement treated layer;
- Natural sandy subgrade.

The geophones used are of type Geospace GS11D with a sensitivity of 89.2V/m/s and a natural frequency of 4.5 Hz. The temperature sensors used are PT100. The sensors were installed in the wheel path of the slow lane, close to the emergency lane and the temperature sensors were installed at the edge of the lane. Figure 1 shows the installation of the sensors in the pavement structure. The 4 geophones are placed in the HMAC layer and the 8 temperature probes are located in pairs at the base of each bituminous layer. These geophones were attached to a data acquisition system, based on Pegase (Cam, 2011; Cam & Bourquin, 2008) data acquisition boards that stored the data and transferred it using the 3G/4G technology. The data acquisition system was set up to record the deflections corresponding to heavy vehicles only, with a minimum deflection threshold of 5mm/100. For every vehicle passage, a trigger with an adjustable acquisition duration, is used to record the signal. In this application the signals of all the sensors were recorded in total for 10 seconds. The temperature measurements on the other hand were recorded at a rate of one measurement every 15 minutes. The continuous recording started in October 2014 and ended in december 2016. There were two periods of interruption of the acquisition, from january to Febuary 2015 and from January 2016 to march 2016, due to technical failures.

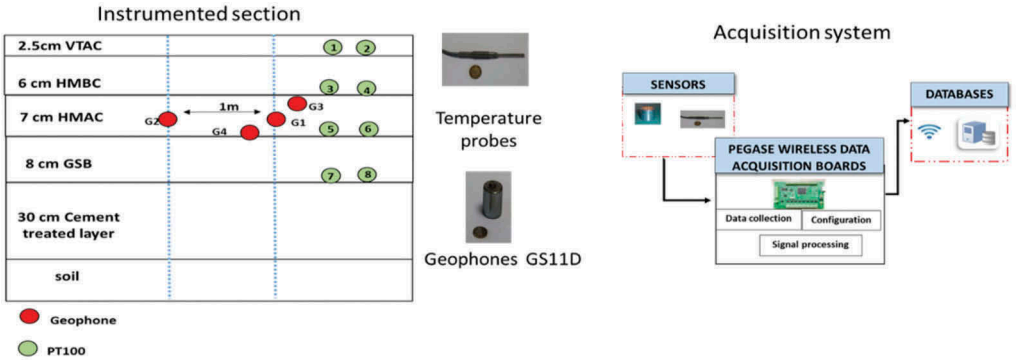

Figure 1. Instrumentation scheme on the Ax motorway.

2.1 *Calculation of deflection signals and processing*

Under the passage of each vehicle, the geophones deliver a voltage signal which is proportional to the vertical displacement velocity. In order to get the pavement vertical displacement (deflection), their signal needs to be integrated. However, it was found from the previous laboratory performance tests on the geophones that a simple integration of the velocity signal is not sufficient to obtain an accurate deflection value. Therefore, an improved signal processing procedure has been developed and used to obtain realistic displacement signals (N. Bahrani et al., 2019). This procedure consists of filtering, amplification, integration and applying the Hilbert transform. It was observed in the experimental tests that the filtering needs to be adjusted to the speed of the vehicle. The cut off frequency of the filter was set to 8.5 Hz assuming a mean heavy traffic speed of 90 km/h (corresponding to a loading frequency around 13 Hz, based on the results of (Chupin et al. 2010), who established that 10 Hz is equivalent to a speed of 70km/h). An amplification factor of 3 was used, to compensate the amplitude loss after filtering. The signal treatment procedure was validated in the laboratory and in the APT tests, by comparing the deflections obtained from the geophones with reference displacement sensor measurements. Figure 2 illustrates the procedure applied for the processing of the geophone signals. The example corresponds to geophone G1, installed in the motorway; on this figure, negative values correspond to downward displacements and velocities. This signal processing technique was applied to all the signal corresponding to the geophones in order to evaluate the pavement deflection signals.

Figure 3 Presents a comparison between the geophone signal and the theoretical signal calculated with the Alize pavement modelling software (LCPC-SETRA. 1994), based on a linear elastic model. This figure shows that after a simple integration, the geophone signal does not give an adequate deflection signal. However, the final signal, after processing, is very close to the theoretical deflection signal . The deflection basin produced by the passage of the vehicle depends on the type of silhouette of the vehicle. For example, the 5 downwards peaks in Figure 3 correspond to the passage of a 5-axle semi-trailer vehicle. (N. Bahrani et al., 2020).

2.2 *Identifying vehicle silhouettes and speeds*

The first proposed application of the geophones is the detection and counting of the heavy vehicle silhouettes.. On the geophone deflection signal (Figure 3), each downward displacement peak corresponds to the passage of one axle, and thus the type of vehicle can easily be identified. A procedure to automate the detection of the vehicle silhouettes was proposed, based on the calculation of the derivative of the displacement. A derivative of the signal is calculated by successive intervals of 20 data acquisition points (A_i,. . .A_{i+20}), in order to eliminate the noise, according to equation (1). The peaks of the signal are detected by the change of sign of the derivative. This procedure to identify the vehicle silhouette was programmed using

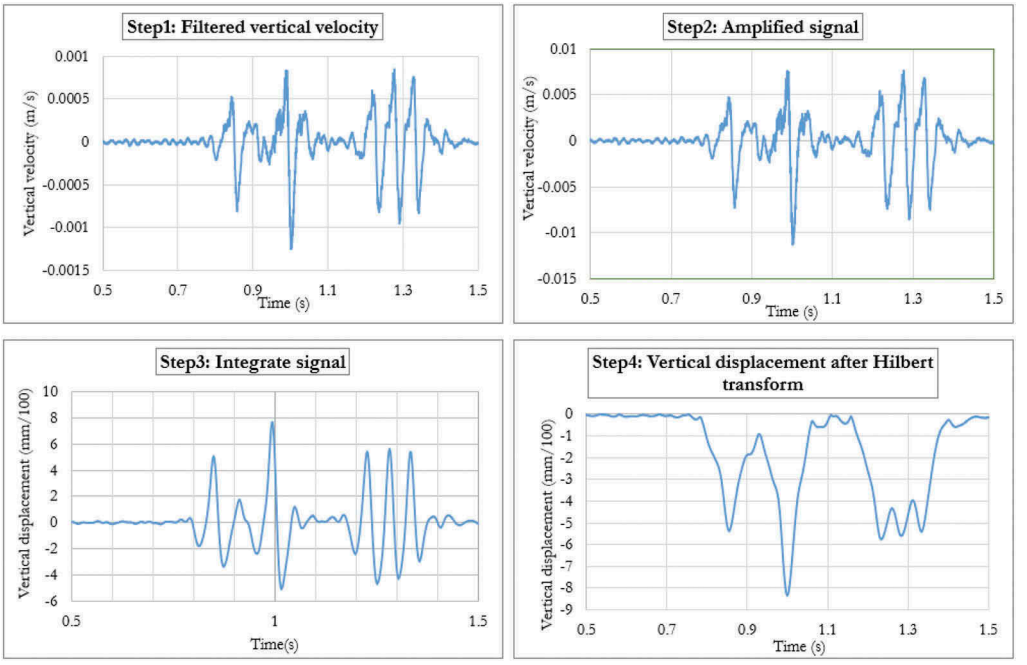

Figure 2. Signal treatment method (example with geophone G1).

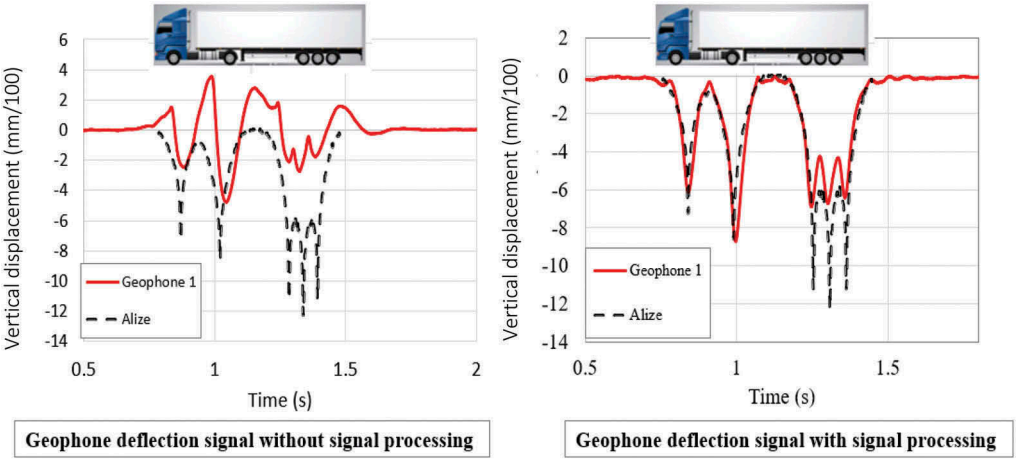

Figure 3. Example of comparison of the geophone G1 signal with the Alize theoretical signal, at the speed of 24m/s.

the Scilab software, and the criteria used to identify different heavy vehicle types are defined in Figure 4. Figure 4 also represents 2 examples of heavy vehicle silhouettes, and the corresponding recorded signals, characterised by the number of downward peaks and the axle spacings.

$$f'(A_i) = \frac{f(t_{i+20}) - f(t_i)}{t_{i+20} - t_i} \quad (1)$$

The detection procedure for vehicle silhouettes was applied to all the signals recorded over the period of two years between October 2014 and December 2016. Therefore, it was possible to determine the composition of the heavy truck traffic and establish statistics,which showed that the five axle semi-trailers (called here T2S3 trucks) are most frequent on the Ax motorway, representing 80% of the total heavy traffic. For this reason, it was decided, in the rest of this study, to focus the analysis on the deflection signals of the T2S3 trucks only.

Heavy vehicle type	Number of downward peaks
2- axles truck	2
3-axles truck	3
4-axles truck	4
5-axles truck	5 peaks, time btw the 3nd and 4th peak > (time btw 4th and 5th peak) ×1.2
5-axles T2S3 truck (semi-trailer, with 2 axles on the tractor)	5 peaks, time btw the 3nd and 4th peak < (time btw 4th and 5th peak) ×1.2

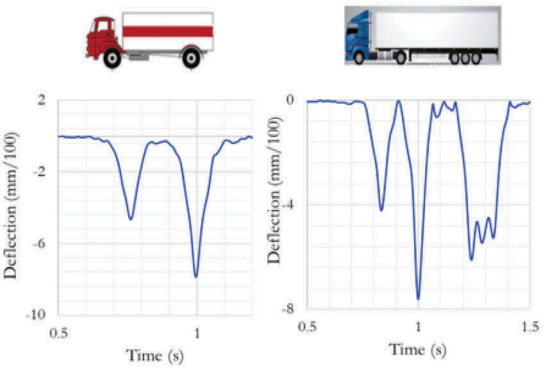

Figure 4. Identification of heavy vehicle silhouettes based on the number of deflection peaks.

To calculate the vehicle speed two geophones G1 and G2 were installed at the same lateral position but at a longitudinal distance D=1 meter from each other as shown in Figure 1. The speed is calculated using the distance between them "D" and the time difference between the two sensor signals. The speeds of the heavy vehicles passing over the instrumented section could thus be calculated. The results indicated an average speed of the heavy vehicles of 96km/h, with a standard deviation of 8 km/h, over the whole monitoring period.

2.3 *Evolution of the deflection*

In order to understand the evolution of the performance of the pavement with traffic, and with climatic variations, it is important to analyse the evolution of the deflection over a long continuous period of time.

On the experimental section, 3 geophones G1, G3 and G4 were positioned at different lateral positions in the wheel path, to detect the different lateral positions of the passing vehicles. For each vehicle, it was assumed that the position of the vehicle wheels is closest to the geophone giving the maximum amplitude, and the signal of this geophone was used for the analysis of deflection basins. The analysis of the data indicated that the maximum deflection amplitude was obtained most frequently for geophone G3 (placed on the right of the wheel path), less frequently for geophone G1 (the central geophone) and rarely for geophone G4 (placed on the left). This indicates that most heavy vehicles drive with their wheels close to the emergency lane, which is close to G3 geophone.

To analyse the evolution of the pavement deflection with time, the following approach was used, for each recorded vehicle signal (corresponding only to T2S3 trucks): (1) first, the geophone giving the maximum deflection was determined. (2) Then, for this geophone, the peak deflection under the first axle of the truck was determined. (3) Then, the monthly average of these values was calculated for each geophone, G1, G3 and G4, and the evolution of these monthly average values with time was plotted. As these monthly average values were calculated for a large number of vehicles (several hundred), it was considered that the statistical distribution of the loads is very similar each month, and thus that this "average" deflection

can be considered as representative of the average stiffness of the pavement during the considered month. Figure 5 shows the monthly average deflection values obtained for the two-year monitoring period for geophone G1. The results indicate that the monthly average deflection values present seasonal variations, due to the variations of temperature (and also possibly of subgrade moisture). The deflections increase during the summer, when the pavement temperature increases, and decrease in the winter, due to the high sensitivity to temperature of the bituminous materials. Apart from these seasonal variations, no long term evolution of the deflection is observed, indicating no sign of damage of the pavement.

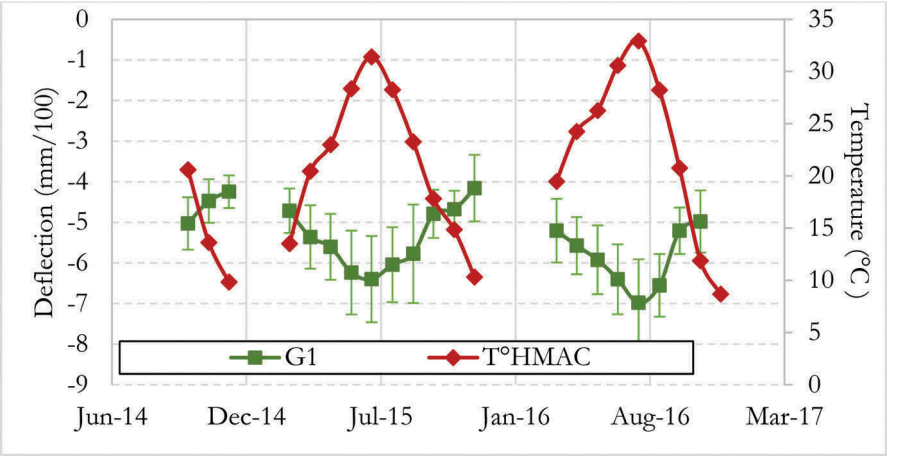

Figure 5. Evolution of the average deflections measured by geophone G1, for the two-year monitoring period .

3 PAVEMENT RESPONSE MODELLING AND COMPARISON WITH THE MEASURED DEFLECTIONS

As the instrumented section on the motorway has no reference sensor to compare the geophone measurements with, it seemed important to make a comparison with calculated theoretical signals. In this section, the measured deflections are compared with deflections obtained with the linear elastic pavement modelling software ALIZE.

On the instrumented section the data acquisition system records large numbers of deflection signals (several hundred heavy vehicles per day). Therefore, it was decided to choose a limited number of representative signals for the comparison with the Alize calculations. The signals obtained with geophone G1, which has a central position in the wheel path, where chosen for this analysis. To select "representative" signals of geophone G1, a method defined by (BROUTIN 2014) was used, for each month. The "representative" signal is defined as the recorded signal which maximum deflection is closest to the monthly average deflection value calculated previously. It is defined by the minimal difference between the peak deflection values and the monthly average values, which corresponds to the equation:

$$ei = \frac{\sqrt{\left(d_{max,1stpeak} - d_{mean,1stpeak}\right)^2 + \left(d_{max,2ndpeak} - d_{mean,2ndpeak}\right)^2 + \ldots \left(d_{max,(5thpeak} - d_{mean,5thpeak}\right)^2}}{5}$$

Where : $d_{max,i^{th}peak}$ is the measured deflection corresponding to the i^{th} peak of the signal

$d_{mean,\ ith\ peak}$ is the monthly average deflection, for the i^{th} peak of the signal.

n is the number of peaks of the deflection signal (n=5 for T2S3 trucks).

In order to compare the representative measured signals with the theoretical signals calculated using ALIZE, it was necessary to define an initial pavement model. The initial pavement layer moduli were determined using results of Falling Weight Deflectometer (FWD) tests performed on the experimental section in October 2013. These tests were used mainly to back calculate the moduli of the cement treated layer and of the soil. The moduli of the asphalt pavement layers were determined from complex modulus laboratory tests, performed on samples taken in situ, except for the very thin surface layer, for which a standard modulus value, obtained from the ALIZE database was used. The moduli of the bituminous layers (VTAC, HMBC and HMAC layer, GB layer) were adjusted to the temperature and frequency of the selected deflection signals. In the calculations, all layer interfaces were considered bonded, and values of Poisson ratio of 0.35 were used for all layers.

Figure 6(a) shows an example of pavement model obtained for the month of June 2016, for a frequency of 13 Hz and temperature of 26°C of the HMAC layer. It corresponds to a vehicle speed of 27m/s, using the speed/frequency equivalency proposed by Chupin et al., (2010). Figure 6 (b) shows the coordinates and the weight of the axles of the T2S3 "reference truck" used in the calculations, with a total load of 44 tons (maximum legal load in France).

	Thickness (m)	Modulus (MPa)	Nu	Material type
Bonded	0.025	1826	0.35	VTAC
Bonded	0.06	6726	0.35	HMBC
Bonded	0.07	9158	0.35	HMAC
Bonded	0.08	2427	0.35	GSB
Bonded	0.3	3964	0.35	TREATED LAYER
Bonded	1	180	0.35	SOIL
Bonded	INFINTE	10000	0.35	OTHER

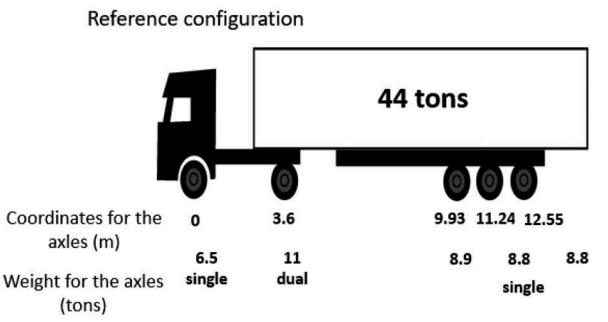

Figure 6. (a) Pavement structure defined for the simulation of the deflection basins (month: June 2016, temperature: 26°C, frequency 13 Hz) –(b) Reference T2S3 Truck dimensions and weights.

The first step consisted in comparing the "representative" measured deflection signal with the response calculated with the initial pavement layer moduli, and the reference 44 ton T2S3 truck loading. From previous studies (Blanc et al., 2019), it was found that the load of the first axle of T2S3 trucks depends mainly on the weight of the tractor and is little influenced by the weight of the cargo of the trailer. In average, for different tractors, the weight of the first axle is equal to 6.5 tons (Schmidt et al., 2016). This information was used for the modelling, and the modulus of the subgrade was adjusted until a good fit with the measured deflection was obtained for the first axle of the truck, supposed loaded at 6.5 tons. Figure 7(a) shows the comparison between the "representative" deflection measured with geophone G1, and calculated with ALIZE, for the month of June 2016, after adjustment of the soil modulus. As expected, the measured and calculated deflections are very similar in amplitude for the first axle, (and also relatively close for the second axle, supposed loaded at 11 tons). For the 3 rear axles, however the measured deflections are lower than the calculated values. This is explained by the difference between the real load of the truck, which is not known, and the load used for the modelling (44 tons). The modulus of the subgrade was adjusted using the same methodology for each month of the 2-year period of monitoring. Figure 7(b) presents the adjusted modulus values, and shows that the subgrade modulus presents seasonal variations during the two-year monitoring period. The subgrade modulus varies between 180 to 200 MPa in the summer and 90 to 140 MPa in the winter, probably due to moisture content variations.

This experiment represents a first feasibility study of the use of geophones for monitoring of a real motorway section, and only a limited number of sensors were installed in the pavement. Therefore, no reference sensors were available for validating the measured deflections or for

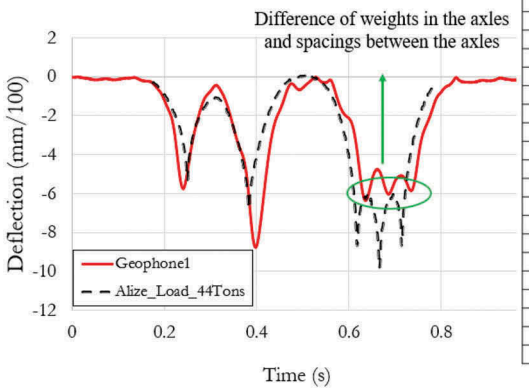

March-2015	150
April-2015	150
May-2015	160
June-2015	200
July-2015	200
August-2015	200
September-2015	140
October-2015	110
November-2015	120
December-2015	140
January-2016	
Febuary-2016	
March-2016	
April-2016	150
May-2016	160
June-2016	180
July-2016	180
August-2016	190
September-2016	170
October -2016	90
November-2016	140
December-2016	N/A

Figure 7. a) Comparison of the deflection obtained with the representative signal of June 2016 (26/06/2016, 23h 37min 23s, 27m/s and 26°C and the simulation with Alize, with a truck loaded at 44 tons b) Estimated monthly variations of the subgrade modulus during the monitoring period.

measuring the vehicle loads. Therefore, comparisons between the measured and calculated deflections could be made only for the first axle, for which a load of 6.5 tons was assumed. In the future, another instrumented site, with more geophones, and with a reference weight in motion system is planned, to study the repeatability of the measurements, and measure the real vehicle loads, in order to make more precise comparisons with modelling results. After calibration of the model with known loads, the geophone measurements could also be used to estimate truck loads, by adjusting the axle loads in ALIZE, to match the measured deflections.

4 CONCLUSION AND PERSPECTIVES

This paper presents a first application of geophones for long term monitoring of deflections on a motorway section. An original procedure, for processing the geophone signals, validated by laboratory and accelerated pavement tests, has been used for converting the velocity measurements into pavement deflections. Pavement deflections under real heavy vehicle traffic, along with pavement temperatures, were recorded during a two year period, from 2014 to 2016, leading to a large database of results.

Different procedures for analysing the measurements have been developed to characterise the evolution of the pavement response, and to characterise the traffic (vehicle silhouettes and vehicle speeds). By selecting only deflections under the first axe of T2S3 trucks, average monthly values of deflection were determined and the evolution of deflections over the two years of monitoring was analysed. In a second phase, deflection signals were modelled using the pavement design software ALIZE. A model of the pavement was defined, using FWD measurements. Then, reference signals (one per month), corresponding to T2S3 trucks, were modelled. The calculations were performed considering a "reference "T2S3 truck, loaded at 44 tons. The deflections measured and calculated under the first axle (which load is known to be close to 6.5 tons for T2S3 trucks) were compared, and then the subgrade modulus was adjusted, until a good fit with the measurements was obtained. By this procedure, monthly values and seasonal variations of the subgrade modulus, could be estimated.

As future perspectives, it is planned to combine the geophone instrumentation with a weight in motion system, in order to evaluate the deflections obtained under known axle loads, and thus calibrate the pavement model. After calibration, the deflection measurements could be used for estimating vehicle loads, by comparing the calculated and measured

response, and adjusting the levels of load of each axle in the model, until a good fit with the measurements is obtained. Another perspective is to automate the processing described in the paper, by implementing the different processing algorithms in the data acquisition system. This will allow to obtain directly, in real time, information on the composition of the traffic, heavy vehicle speeds, deflections and possibly vehicle loads, without additional post-processing.

REFERENCES

Arraigada, M., Partl, M. N., Angelone, S. M., & Martinez, F. (2009). Evaluation of accelerometers to determine pavement deflections under traffic loads. *Materials and Structures/Materiaux et Constructions*, *42*(6), 779–790. https://doi.org/10.1617/s11527-008-9423-5

Bahrani, N., Blanc, J., Hornych, P., & Menant, F. (2019). Pavement instrumentation for condition assessment using efficient sensing solutions. *International Conference on Smart Infrastructure and Construction 2019, ICSIC 2019: Driving Data-Informed Decision-Making*, 471–480.

Bahrani, N., Blanc, J., Hornych, P., & Menant, F. (2020). Alternate method of pavement assessment using geophones and accelerometers for measuring the pavement response. *Infrastructures*, *5*(3). https://doi.org/10.3390/infrastructures5030025

Bahrani, Natasha., Levenberg, E., Blanc, J., & Hornych, P. (2020). Inverse Analysis of Pavement Layer Moduli Based on Data Collected by Buried Accelerometers and Geophones. In *Accelerated Pavement Testing to Transport Infrastructure Innovation 2020*. Springer.

Blanc, J., Hornych, P., Duong, N. S., Blanchard, J. Y., & Nicollet, P. (2019). Monitoring of an experimental motorway section. *Road Materials and Pavement Design*, *20*(1), 74–89. https://doi.org/10.1080/14680629.2017.1374997

Cam, V. Le (2011). *Journées techniques Ouvrages d' Art Utilisation de la carte d ' instrumentation PEGASE de l ' IFSTTAR dans plusieurs applications*.

Cam, V. Le, & Bourquin, F. (2008). *Design of a generic smart and wireless sensors network – Benefits of emerging technologies*.

Chupin, O., Chabot, A., Piau, J. M., & Duhamel, D. (2010). Influence of sliding interfaces on the response of a layered viscoelastic medium under a moving load. *International Journal of Solids and Structures*, *47*(25–26), 3435–3446. https://doi.org/10.1016/j.ijsolstr.2010.08.020

Duong, N. S., Blanc, J., Hornych, P., Menant, F., Lefeuvre, Y., & Bouveret, B. (2018). Monitoring of pavement deflections using geophones. *International Journal of Pavement Engineering*, *21*(9), 1103–1113. https://doi.org/10.1080/10298436.2018.1520994

Hadidi, R., & Gucunski, N. (2010). Comparative study of static and dynamic falling weight deflectometer back-calculations using probabilistic approach. *Journal of Transportation Engineering*, *136*(3), 196–204. https://doi.org/10.1061/(ASCE)0733-947X(2010)136:3(196)

LCPC-SETRA. (1994). *Conception et dimensionnement des structures de chaussées: Guide technique national. citation*.

Levenberg, E. (2012). Inferring Pavement Properties using an Embedded Accelerometer. *International Journal of Transportation Science and Technology*, *1*(3), 229–246. https://doi.org/10.1260/2046-0430.1.3.229

Liu, P., Otto, F., Wang, D., Oeser, M., & Balck, H. (2017). Measurement and evaluation on deterioration of asphalt pavements by geophones. *Measurement: Journal of the International Measurement Confederation*, *109*, 223–232. https://doi.org/10.1016/j.measurement.2017.05.066

Michael BROUTIN. (2014). *Auscultation des chaussées souples aéronautiques au HWDGuide technique*.

Schmidt, F. J., Jacob, B., & Domprobst, F. (2016). Investigation of truck weights and dimensions using WIM data. *Transportation Research Procedia*, *14*, 811–819.

Eleventh International Conference on the Bearing Capacity of Roads, Railways and Airfields, Volume 2 – Hoff, Mork & Saba (eds)

Correlation between LWD and FWD deflections for asphalt pavement

A. Sawangsuriya
Bureau of Road Research and Development, Department of Highways, Bangkok, Thailand

ABSTRACT: This study presents the correlation between deflections from the falling weight deflectometer (FWD) and those from the light weight deflectometer (LWD) over twenty asphalt pavement sections, which were selected as part of twelve major highways in Thailand. Each section had approximately 250-m long. The deflection measurements were taken at every 25 m interval along the trial section. Both FWD and LWD tests were performed at the same testing points. The results indicated that the correlation between deflections from the FWD and those from the LWD exhibited a linear relationship with R^2 of 0.7. The FWD deflections were respectively ten times and six times the LWD deflections based on the field measurement and the elastic solution. Although a single combination of contact stresses was used, the difference in the measured and calculated deflections might be explained due to the pavement layer material characteristics, temperatures, testing constraints etc.

Keywords: FWD, LWD, deflection, asphalt, pavement

1 INTRODUCTION

Falling Weight Deflectometer (FWD) is a non-destructive test (NDT) adopted worldwide by several highway agencies for pavement structural integrity and capacity evaluation. However, the FWD testing usually involves high initial and maintenance costs. In Thailand, the number of FWD equipment owned by highway authorities, e.g. the Department of Highways (DOH), was very limited and obsolete, resulting in insufficient testing opportunities for road maintenance and rehabilitation in the network levels (Sawatparnich and Sawangsuriya 2019). Light weight deflectometer (LWD) is an emerging non-destructive test (NDT) based on the same testing principle as the FWD. Typically, the LWD is an alternative quality control (QC) test for in-place assessment of stiffness for compacted earthwork. It has gained acceptance over years in Thailand highway construction QC (Sawangsuriya 2017). Both FWD and LWD measure the pavement surface deflections under an impulse load. The LWD is a portable, rugged, and inexpensive version of the FWD, which can be rapidly operated by only one person. The possible adoption of LWD for the structural and performance evaluation of existing pavements has not yet been reported in Thailand. In addition, the correlation studies between FWD and LWD were very limited for this topic. Most investigations were performed either in the laboratory or for the earthwork construction control of base course and embankments (Abu-Farsakh et al. 2004, White et al. 2007, 2013). The objective of this study is therefore to investigate the correlation between deflections as measured by the FWD and those as measured by the LWD over twenty asphalt pavement sections, which were selected as part of twelve major highways in Thailand.

DOI: 10.1201/9781003222897-29

2 BACKGROUND

2.1 *Falling Weight Deflectometer (FWD)*

One of the non-destructive testing methods for pavement structural performance evaluation known as the FWD is increasing and widely adopted worldwide in the pavement engineering society. Since its introduction to Thailand DOH in 2000, the FWD has become an invaluable NDT for pavement structural condition evaluation of road pavements e.g. determination of overlay thickness, selection of suitable maintenance and rehabilitation strategies, long-term assessment of structural capacity etc.

For over 20 years, the Bureau of Road Research and Development (BRRD), DOH, has been using the Dynatest Model 8000 FWD from Denmark as shown Figure 1 (Sawangsuriya et al. 2020). The FWD applies an impulse load into the pavement system through a 300-mm diameter loading plate. The magnitude of load is measured by a load cell. The corresponding surface deflections are measured by a series of velocity sensors (geophones) installed at various radial distances from the applied load on the pavement surface. Typically, nine sensors were located at 0, 200, 300, 450, 600, 900, 1200, 1500, and 1800 mm distance from the center of the loading plate. A deflection basin generated by the impulse load was measured by these sensors e.g. the central sensor (d_o) measured maximum deflection, the first sensor (d_1) offset 200 mm away from central sensor and the remaining sensors measured deflections at different points. The corresponding elastic moduli of pavement layers were back-calculated from the measured deflection basin.

Figure 1. Falling Weight Deflectometer (FWD).

2.2 *Light Weight Deflectometer (LWD)*

LWD (Fleming et al. 2007) is a portable NDT device used to measure the in situ elastic modulus of pavement layers and earth fill embankment. The LWD is primarily used for construction QC/QA of the entire earthwork, subgrade evaluation prior to pavement design (mechanistic approach), as well as design verification of pavement construction (Sawangsuriya et al. 2017). The LWD used in this study was modeled Prima 100 manufactured by SWECO. It consists of a 10-kg (22 lbs) standard drop mass with an adjustable drop height ranging from 0.1 to 0.9 m as shown in Figure 2. The impact force imparted by the drop mass is buffered by elastomeric pads, which produces a pulse load up to 15 kN. The applied force is measured by a built-in load cell while the surface deflection is measured by an integrated center geophone

in direct contact with the ground through varied loading plates of 100 mm (4 inches), 200 mm (8 inches), and 300 mm (12 inches) in diameter. Additional geophones can be also used for spectrum response. The LWD interfaces with a handheld PDA device outputting the time history of layer response to applied impulse load in term of deflection (d). The Prima LWD software uses the stress distribution factor (f) of 2.0, which implies a uniform plate-ground contact stress distribution (e.g. flexible plate) and Poisson's ratio (v) of soil to estimate elastic modulus of compacted materials based on the elastic solution as follows:

$$E_{LWD} = \frac{f\sigma_o r(1-\nu^2)}{d_o} \tag{1}$$

where E_{LWD} = elastic modulus of pavement from the LWD (MPa); σ_o = maximum contact stress (MPa); d_o = maximum surface deflection at center of loading plate (mm); and r = radius of loading plate (mm). The LWD tests are performed in accordance with ASTM E2583.

Figure 2. Light Weight Deflectometer (LWD).

3 TEST METHODOLOGY

Twenty asphalt pavement sections as part of twelve major national highways in Thailand were selected in this study. Every trial section was located near the stationary weight station. For the sake of simplicity, these sections were classified into four major groups according to their cross-sections and layer materials. Typical cross-section for each group was described as follows: group 1 (e.g. conventional flexible pavement), group 2 (e.g. semi-rigid pavement), group 3 (e.g. composite pavement), and group 4 (e.g. cold in-place pavement recycling). Typical cross-sections of groups 1-4 are graphically illustrated in Figure 3.

The FWD was performed in companion with the LWD at the exact test location. The FWD was performed first, followed by the LWD. The surface deflections at center of loading plate

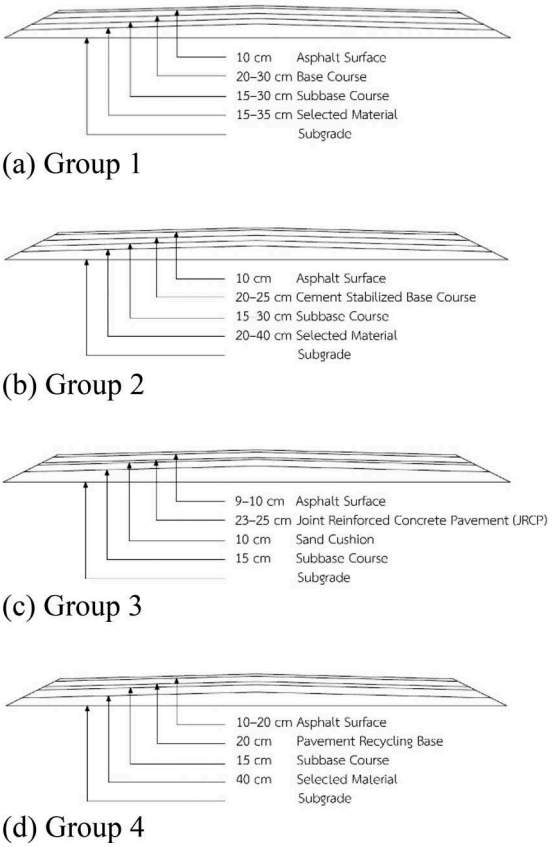

Figure 3. Typical cross-sections of groups 1-4.

(d_o) were measured at every 25 m interval with the total length of 250 m in each section. The measurements were made along the outermost lane (e.g. design lane). It should be also noted that six drops of LWD deflection measurement were taken and the average value of last three drops were reported. The average pavement temperatures during the test ranged between 37 and 42 °C.

In this study, the contact stress (σ_o) of 750 kPa and 180 kPa were respectively applied for the FWD and the LWD tests. These stresses were practically adopted in accordance with the experimental studies (Jitareekul et al. 2017, Sawangsuriya et al. 2020). The radius of loading plate (r) was 150 mm for the FWD and 100 mm for the LWD. By assuming that E and v of the pavement layer are uniquely given, the relationship between the FWD surface deflection ($d_{o,\ FWD}$) and the LWD surface deflection ($d_{o,\ LWD}$) can be determined using the elastic solution in Equation (1). The calculation indicated that $d_{o,FWD}$ was approximately six times $d_{o,\ LWD}$.

4 RESULTS

Figures 4 – 7 illustrate examples of measured surface deflections obtained from the FWD and the LWD on the trial sections for groups 1 – 4, respectively. Both FWD and LWD deflections were consistently varied along the test location. The FWD deflections were significantly higher than the LWD deflections due to the different stress regimes. In general, the correlations between the FWD deflections ($d_{o,\ FWD}$) and the LWD deflections ($d_{o,\ LWD}$) exhibited

linear with R^2 ranging from 0.6 to 0.8. Figures 8 – 11 depict the FWD and LWD deflection correlations for groups 1 – 4, respectively. A correlation for all deflection data combined was shown in Figure 12. The linear regression between $d_{o,\ FWD}$ and $d_{o,\ LWD}$ was determined with R^2 of 0.7.

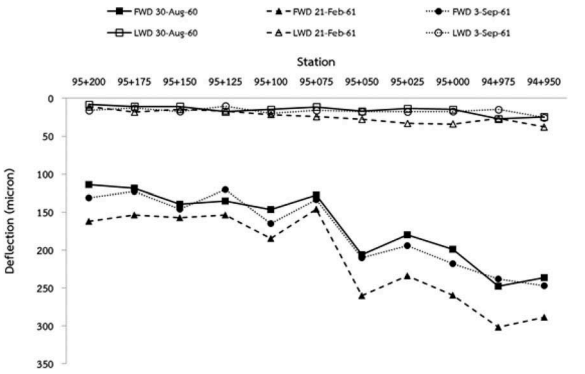

Figure 4. Examples of measured surface deflections on the trial sections for group 1.

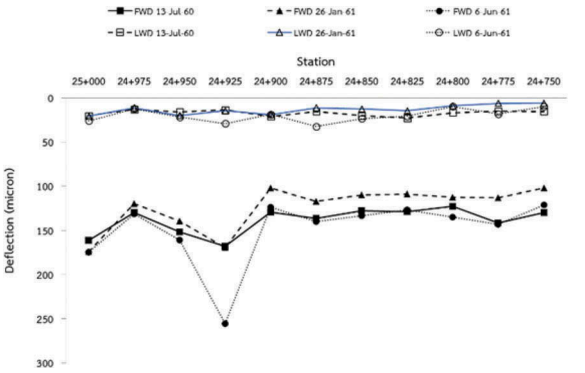

Figure 5. Examples of measured surface deflections on the trial sections for group 2.

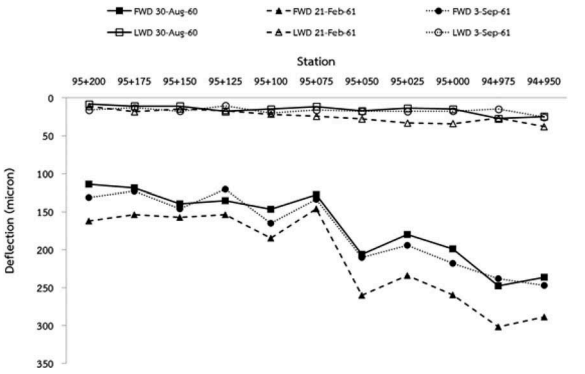

Figure 6. Examples of measured surface deflections on the trial sections for group 3.

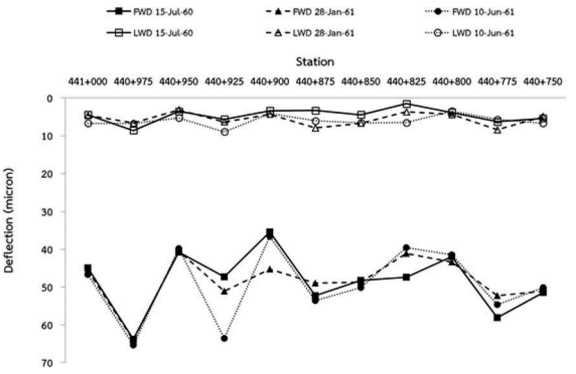

Figure 7. Examples of measured surface deflections on the trial sections for group 4.

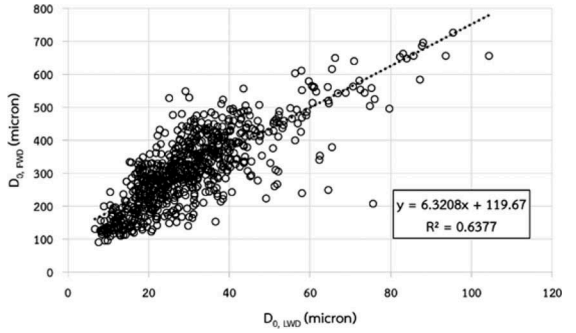

Figure 8. FWD and LWD deflection correlations for group 1.

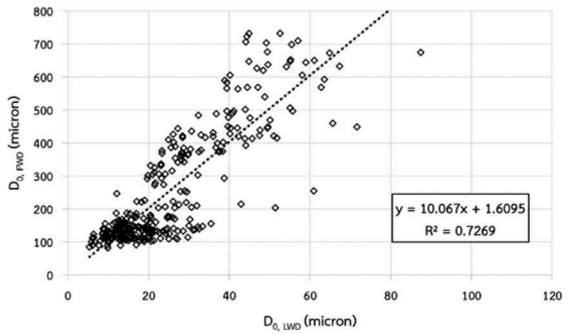

Figure 9. FWD and LWD deflection correlations for group 2.

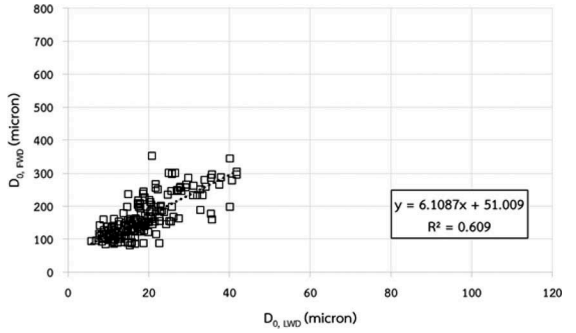

Figure 10. FWD and LWD deflection correlations for group 3.

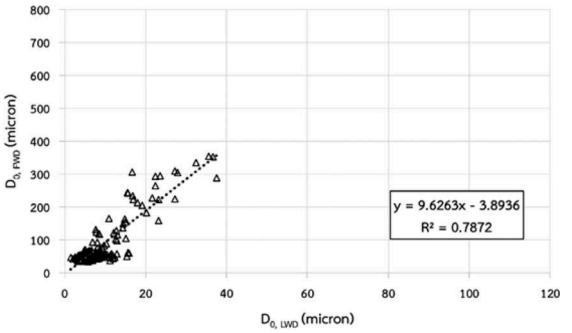

Figure 11. FWD and LWD deflection correlations for group 4.

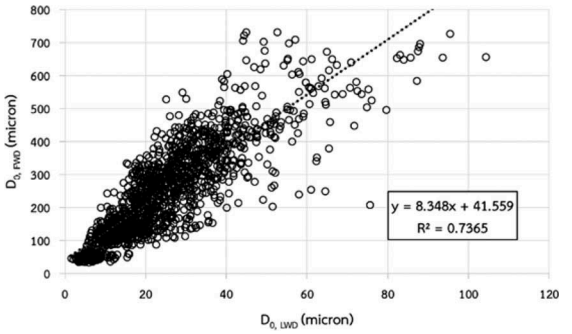

Figure 12. FWD and LWD deflection correlations for all data combined.

In addition, a linear regression in Figure 12 indicated that $d_{o,\ FWD}$ was approximately ten times $d_{o,\ LWD}$ (e.g. $d_{o,\ FWD}/d_{o,\ LWD} \sim 10$). It is noteworthy that the measured deflections obtained from the trial sections were larger than the calculated deflections based on the elastic solution. The difference was estimated to be approximately 35 percent. A summary of the statistical data, e.g. maximum (Max.), minimum (Min.), average (Avg.), number of samples (n), and standard deviation (SD), from the FWD and LWD deflection measurements are also presented in Table 1.

Table 1. A summary of statistical data.

	Mn	Ag	Max	n	SD
FWD	595	754	763	167600	17.06
LWD	123	181	201	154500	444

5 CONCLUSION

Correlations between LWD and FWD deflections for asphalt pavement sections in Thailand were investigated. The deflection relationship exhibited linear with R^2 of 0.7. Based on the measured data from twenty asphalt pavement sections as part of twelve major national highways in Thailand, the FWD deflections were approximately ten times the LWD deflections. While according to the elastic solution, the FWD deflections were approximately six times the

LWD deflections. Although a single combination of contact stresses was used, the difference in the measured and calculated deflections might be explained due to the pavement layer material characteristics, temperatures, testing constraints etc.

REFERENCES

Abu-Farsakh, M., Alshibli, K., Nazzal, M., and Seyman, E., 2004. *Assessment of in situ test technology for construction control of base course and embankments*. Final Report No. FHWA/LA 04/385, Louisiana Transportation Research Center, Baton Rouge, LA.

Fleming, P.R., Frost, M.W. and Lambert, J.P., 2007. *A review of the lightweight deflectometer (LWD) for routine in situ assessment of pavement material stiffness*. Transportation Research Record 2004, Washington, DC, pp. 80–87.

Jitareekul, P., Sawangsuriya, A. and Singhatiraj, P., 2017. *Integration of pavement layer evaluation using LWD for road safety control*. Transportation Geotechnics and Geoecology, TGG 2017, Saint Petersburg, Russia.

Sawangsuriya, A., 2017. *Performance-based in situ tests for compaction quality control of pavement layers*. Proceedings of 2017 MAIREINFRA, Seoul, South Korea.

Sawangsuriya, A., Jitareekul, P., Taesiri, Y., Sirisak, S. and Lawanwisut, W., 2017. *Implementation of modulus-based quality control testing for pavement construction in Thailand*. Proceedings of the Tenth International Conference on the Bearing Capacity of Roads, Railways and Airfields, Athens, Greece.

Sawangsuriya, A., Sirirattanachat, T., Taworn, D. and Yuayong, S., 2020. *Application of falling weight deflectometer to assess road structural condition for Thailand pavement management system*. Engineering Journal of Research and Development, Vol. 31, No. 3, pp. 49–61.

Sawatparnich, A. and Sawangsuriya, A., 2019. *Deflection measurements for pavement structural condition evaluation*. IRF Global R2T Conference and Exhibition, Las Vegas, Nevada, USA., pp. 116–124.

White, D., Thompson, M.R., and Vennapusa, P.K.R., 2007. *Field validation of intelligent compaction monitoring technology for unbound materials*. Center for Transportation Research and Education, Minnesota Department of Transportation, MN.

White, D., Vennapusa, P.K.R., Becker, P., White, C., 2013. *Stiffness-based QC/QA testing*, Center for Earthworks Engineering Research, Institute for Transportation, Iowa State University, IA.

Eleventh International Conference on the Bearing Capacity of Roads, Railways and Airfields, Volume 2 – Hoff, Mork & Saba (eds)

Mitigating excavation-induced surface settlement and building tilting: A case study

C.H. Ho & D. Zhang
Department of Civil Engineering, Construction Management and Environmental Engineering, Northern Arizona University, Flagstaff, USA

A. Abdelaziz
Department of Civil and Environmental Engineering, Texas A&M University, College Station, USA

P. Zhao
Department of Civil Engineering, Construction Management and Environmental Engineering, Northern Arizona University, Flagstaff, USA

ABSTRACT: This paper presents a case study using chemical churning pile (CCP) grouting and micropiles to mitigate surface settlement and building tilting due to nearby deep foundation excavation. The CCP grouting method is a process of injecting liquid cement material into soil or rock to change its physical properties. Micropiles are then installed beneath the tilted building in an attempt to lift the building up to its original position. For this case study, ten control points along the edge of the tilted building were installed, so that construction crews could closely monitor, better understand, and control the mitigation process. After completion of CCP grouting, a series of standard penetration tests (SPT) were performed to evaluate the effectiveness of CCP grouting in the improvement of soil strength. Based on soil test results and surveying records, it was concluded that the construction method of using CCP grouting and micropiles were successful in mitigating surface settlement and building inclination.

Keywords: Deep foundation excavation, Surface settlement, Building tilting, Cement grouting, Micropiles

1 INTRODUCTION

Deep foundation excavation has been widely used in the construction of high-rise buildings and underground facilities such as tunnels, metro stations, and bridge piers. During deep foundation excavation, surface settlement is a potentially serious issue that could jeopardize the safety of construction, damage adjacent buildings, and interrupt daily life of the occupants (Son and Cording, 2005). Highly populated metropolitan areas are particularly vulnerable to surface settlement complications due to their densely built structures. When facing a surface settlement and adjacent building tilting problem, an immediate construction method must be implemented to mitigate the issue. However, having a contractor choose construction methods within the very short period of available time is challenging. Various methods can be found in technical reports, papers, and references, but since there is no "one-size fits all" method, the selection is highly dependent on the experienced persons' engineering judgement. Therefore,

DOI: 10.1201/9781003222897-30

this paper presents (i) an excavation project as a case study where an adjacent 10-story building was tilting due to foundation excavation-induced surface settlement, and (ii) the construction methods used to mitigate surface settlement and the building tilting. The purpose of the paper is to provide a state-of-the-practice experience for contractors to use in a similar case. Note that due to information sensitivity, the location of the project must remain anonymous.

Please adhere to the Ethics and malpractice statement found at the conference web-page.

2 EXCAVATION BACKGROUND

A highway overpass construction project was scheduled to be built along a corridor. Based on a site map, a 10-story existing building was only 7.5 meters away from the construction site for proposed bridge piers. The piers were supported by a crossbeam with nine deep piles (60 cm in diameter and 60 m in length) to be installed beneath the surface. A braced-cut excavation was planned for deep foundation constriction. To fulfil the requirement of structural analysis, diaphragm walls (60 cm thick and 21m deep) were designed as a soil shoring structure to resist lateral earth pressure as well as high water pressure. Five levels of a strut-and-wale system were installed between two diaphragm walls. The excavation finish surface was set at a depth of 11.4 m below the ground surface. According to the soil boring report and soil logs (see Table 1), the groundwater table was detected between -2.0 m to -3.0 m below the ground surface. Because the excavation finish surface had to be maintained in a dry condition, dewatering was used such that the existing ground water table was able to be kept at least 1 meter below the excavation finish surface (i.e., -12.5 m below the ground surface). A well-point dewatering system with multiple wells was used. The dewatering wells were connected to a pipe surrounding the excavation site. The pipe then carried the water out of the job site to the nearby creeks. Based on Schroeder et al. (2004), lowering the ground water table by 3 m is approximately equivalent to imposing a surface load on the soil of 30 MPa. Thus, it was obvious that significant surface settlement could be expected.

Table 1. Soil Properties and Boring report.

Boring Data				Test Results								
				Gradation distribution (%)								
No.	SPT N	Depth (m)	Soil Classification	Gravel	Sand	silt/ clay	Water content, %	Unit weight, t/m3	void ratio	LL, %	PL, %	Gs
S1	9	1.55-2.0	CL	0	6.9	93.1	30.1	2.01	0.82	35.6	22.7	2.74
S2	8	2.55-4.0	CL	0	7.2	92.8	30	2	0.82	34.6	22.1	2.74
S3	10	5.55-6.0	SM	0	66.6	33.4	21.9	2.04	0.59	-	NP	2.7
S4	11	7.55-8.0	SM	0	69.2	30.8	23	2.07	0.62	-	NP	2.71
S5	34	9.55-10.5	SM	0	69.5	30.5	22.2	2.07	0.6	-	NP	2.71
S6	9	11.55-12.0	CL	0	7.5	92.5	29.8	2.02	0.81	34.9	23	2.73
S7	6	13.55-14.0	CL	0	6.5	93.5	33.4	1.98	0.92	34.5	21.7	2.74
S8	9	15.55-16.0	CL	0	7.1	92.9	31.2	2.01	0.85	35.1	22.5	2.72

3 EXCAVATION-INDUCED SURFACE SETTLEMENT

As soon as the completion of excavation, groundwater flooding was observed on the excavation finish surface as shown in Figure 1. On the following day, the adjacent existing 10-story building (7.5 meters away from the excavation site) was reported to be tilting and a horizontal crack, perpendicular to the settling direction on the wall of the basement of the building, was noticed. After the building started leaning, the contractor installed a tiltmeter mounted on the basement wall of the tilting building to monitor the deformation of the damaged structure due to excavation-induced surface settlement. The angular distortion of tiltmeter was first recorded at a radian of 1/480 that exceeded the tolerable settlement of buildings (1/500, the safe limit for no cracking of buildings) as recommended by Bjerrum (1963). This measure indicated that the existing building has leaned towards the excavation site and the surface settlement could have an impact on the integrity of the entire building structure. To prevent the further inclination of the tilting building, the contractor immediately informed the jurisdictional government staff of the excavation failure event and then called design consulting firm, consultants, and local government engineers for an urgent meeting

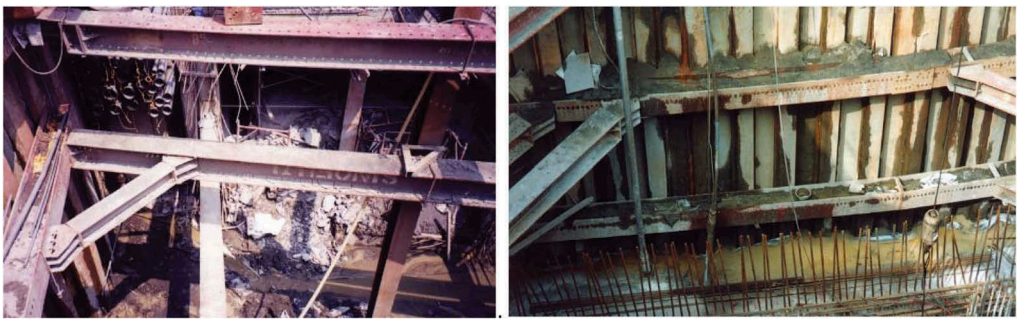

Figure 1. Groundwater flooding on excavation finish surface.

4 UPLIFTING ANALYSIS

As shown in the soil report (see Table 1), there are two layers of the soil located between -5.5 m and -16 m. Their soil properties are expressed as follows:

- The layer of soil between 5.5 m and 10.0 m below the ground surface was classified as silty sand (SM). The standard penetration test (SPT) N value was tested at 10, indicating the soil was in a loose state.
- The layer of soil located between 10.0 m and 16.0 m below the surface was classified as sandy clay (CL). The water content (w) was tested at 34.9% and the liquid limit (LL) was tested at 34.5%, suggesting that the soil was nearly in a liquid state.

Because an impermeable soil (i.e. sandy clay) is located below the excavation finish surface, a potential uplifting event might have caused the bottom of the excavation finish surface to move upward (heaving). Thus, a hydrostatic uplift analysis was performed to determine if the factor of safety is below the generally accepted value of 1.5:

Hydrostatic uplift analysis (Factor of Safety, FS) can be expressed in Eq. 1:

$$FS = \frac{\gamma_{L*H_L}}{\gamma_w * H_P} 1.5 \tag{1}$$

where γ_L is field density of clay, γ_w is density of water, H_L is thickness of clay, H_p is piezometric level (head)

A mathematical relationship between a depth of excavation and a FS is shown in Figure 2. It can be seen in Figure 2 that a critical excavation depth for foundation operation is found at 8 meters below the ground surface. According to the soil logs in conjunction with geotechnical engineering analysis, when the foundation is excavated at a depth of 11.57 m, FS is equal 0.34 which is significantly less than 1.5. The uplifting analysis, along with the FEM modeling results, confirmed that soil uplifting within the excavation site was likely to occur during excavation, and it could be the primary reason in causing the adjacent building to tilt.

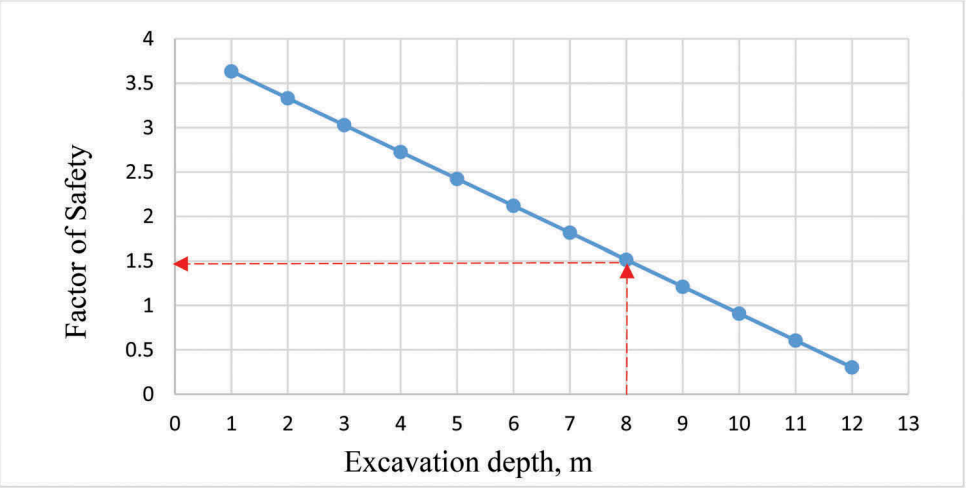

Figure 2. Mathematical relationship between FS and excavation depth.

5 MITIGATION OF EXCAVATION INDUCED SURFACE SETTLEMENT

5.1 *Use of chemical churning pile grouting and micropile installation*

During the urgent meeting, some mitigating strategies were proposed by attendees to remedy the building tilting and surface settlement. Among the proposed methods, the consensus was to use low pressure cement grouting (chemical churning piles, known as CCP) along with micropiles which would be installed beneath the building foundation (see Figures 8 & 9). This decision was based on the soil properties, foundation type, as well as the surrounding environment. CCP grouting is a process of injecting liquid cement material (slurry) mixed with water, sand and sodium silicate into soil or rock to increase its strength. It is used to fill pores or voids in soil or rock with mixed grouts. The injecting pressure varies depending on a construction plan, soil properties, and site locations. In this case study, the CCP grouting (2.5 m in radius with 4 m spacing) was set to a pressure of 5-10 kg/cm^2 and a rate of 30 liter/min. The low grouting pressure was decided based on the concern that a higher pressure could have undermined the confining area formed by soil, diaphragm walls, and the existing foundation. The target improvement areas were determined to be a layer of silty sand and a part of clay ranging from -5 m to -12 m. The mix design of slurry grouting was determined at a ratio of 1:1:0.6 (cement: water: sand) with a designed unconfined compressive strength (q_u) of 30-40 kg/cm^2. The CCP grouting was injected at an interval of 4 meters along the sidewalks in front of the damaged building (see Figure 3)

5.2 *Literature review of cement grouting and CCPs*

More recent studies of cement grouting have been done concerning the mitigation of building tiling and settlements due to (a) the tunneling process through existing foundations of structures (Mohammed et al. 2013) (Xu et al. 2013), (b) liquidation (Huang et al. 2008), and (c) foundation excavation (Chepurnova 2014). To deal with surface settlements, a number of

studies have been implemented using numerical analyses to predict surface settlements, lateral displacement, and strain and strength of the soil during deep foundation excavation (Ou et al. 1993, Wu, et al. 2013, Liu et al. 2011, Tan and Li, 2011, Wang et al. 2012, Heiseh et al. 2003). A research work done by Heieh et al (2013) indicated that cement grouting beneath adjacent buildings during the excavation is advanced to compensate for ground loss. However, its operation is tedious and risky in nature since the effectiveness of grouting under adjacent buildings is uncertain (S. Coulter 2006). Heieh et al. (2003) also urged that any future design must be implemented in a case-by-case manner as the local soil properties vary and would in turn change the prediction of ground settlement. Coulter (2006) studied the effect of CCP grouting on surface settlement for the Aeschertunnel in Switzerland. The CCP grouting umbrella for the Aeschertunnel was formed with the installation of 39 columns along the crown of the top of the tunnel with a diameter of 600 mm and a spacing of 450 mm between the boreholes at the tunnel face to ensure overlapping columns. S. Coulter also indicated that the installation of CCP grout columns as primary excavation support resulted in very low volume losses in the range of 0.35% and a very narrow settlement trough. From the above research works, it is clear foundation excavation could cause an inclination of buildings as well as surface settlements. CCP or cement grouting methods could be adopted by a contractor in a case-by-case manner to mitigate foundation failures.

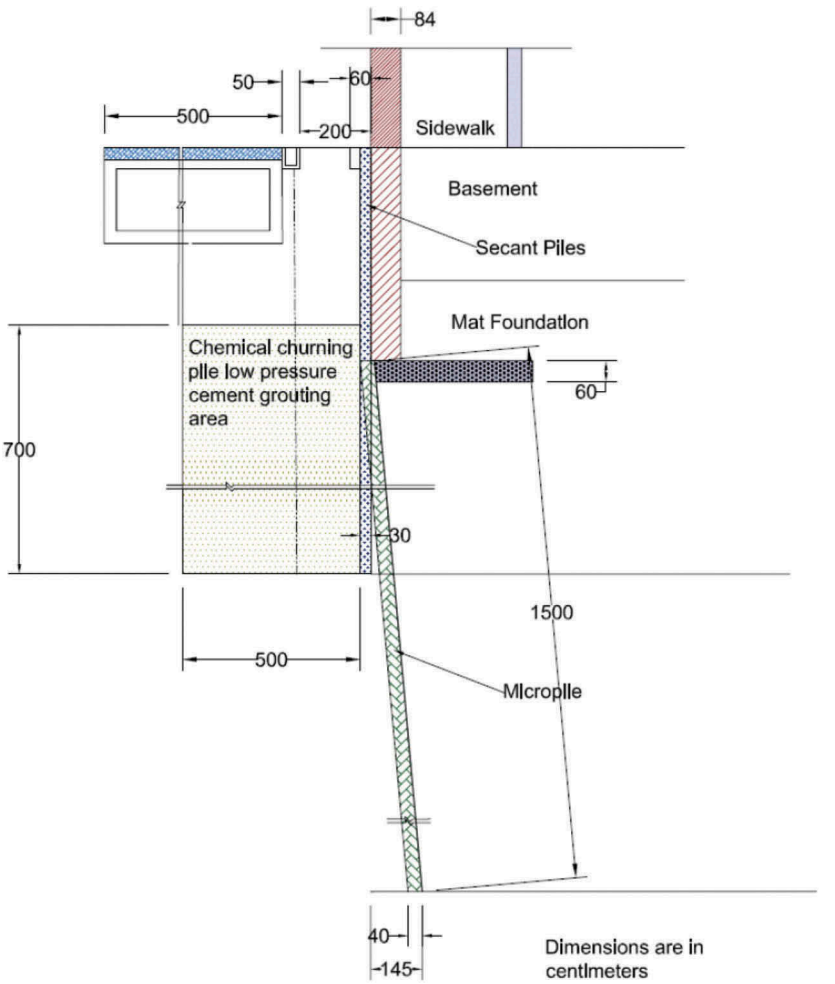

Figure 3. Arrangements of cement grouting and micropile installation.

5.3 *Installation of micropiles*

As indicated in the mitigating construction drawing set, secant piles were designed as a shoring facility. The depth of the existing adjacent building's mat foundation was calculated to be 5.6 m below the ground surface. As previously mentioned, soil uplifting caused an inclination of the nearby building. The purpose of micropiles (40 cm in diameter, 100 cm apart on center) installed beneath the existing adjacent building was to reinforce the integrity of the soil to prevent further surface settlement. Hopefully, the building could be lifted up to its original position. The installation criterion is described below:

a. As illustrated in Figure 4, there is an existing confined soil area in front of the tilted building. Further disturbance to the confined area would create secondary settlement that could worsen the tilted building. The beginning installation point must keep away from the confined soil area.
b. There is a potential sliding plane (see Figure 4) which has the potential to cause further tilting. Thus, the length of micropiles must be designed in such a way that the micropile should penetrate through the potential sliding plane.
c. Micropiles should be designed with sufficient bearing capacity to resist building deformation and hopefully lift the tilted building up back to its original position.

Based on the above three design criteria, the contractor and engineers decided that the micropiles should be installed from the bottom of the building's mat foundation down to a depth of 21 m (where soil was classified as stiff sand with SPT values from 20-24).

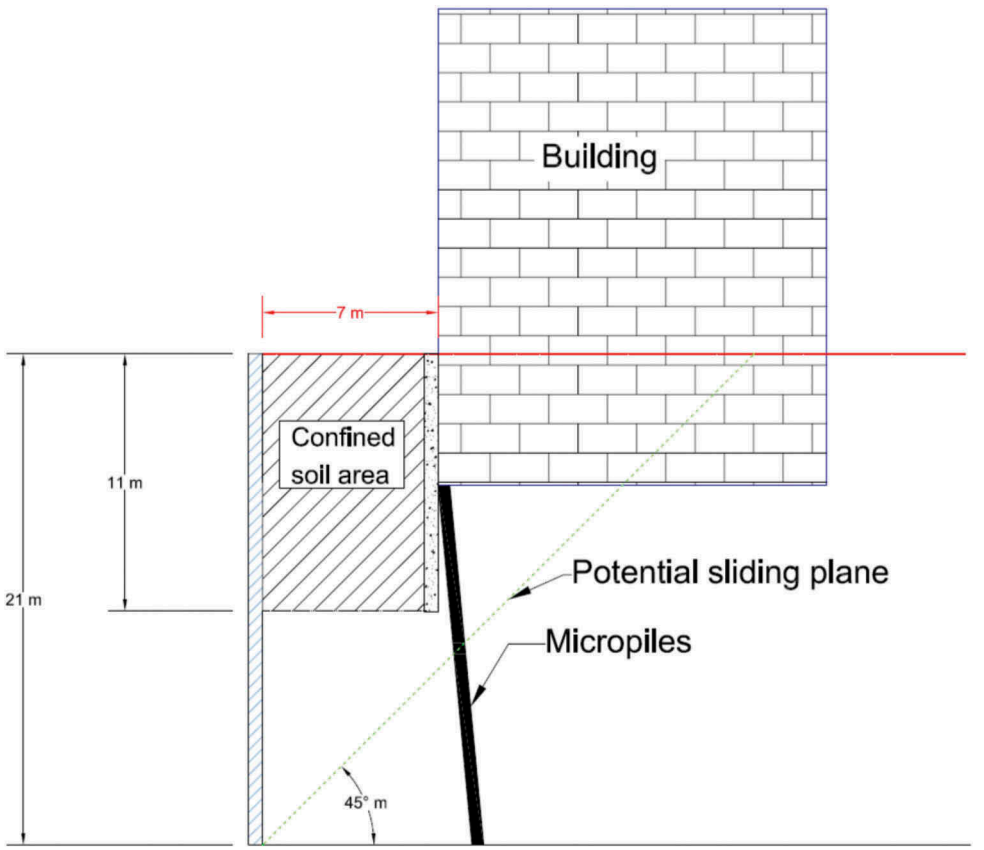

Figure 4. Schematic and mechanism of micropile installation.

5.4 *Arrangement of survey control points*

After the mitigation strategy of CCP grouting and micropile installation was determined, survey control points were set up along the edges of the building to help construction crews closely monitor the surface settlement. The arrangements of CCP grouting, micropiles, and 10 survey control points (S1 through S10) were displayed in Figure 5. On-site surveying work was scheduled on a daily basis and readings on the ten points were recorded in the morning and afternoon. As soon as readings and settlements were calculated, the contractor, along with field engineers, thoroughlycompared any changes with readings from the previous day, and adjusted CCP grouting speed and micropile installation as needed. The entire duration of the mitigation construction lasted 34 days.

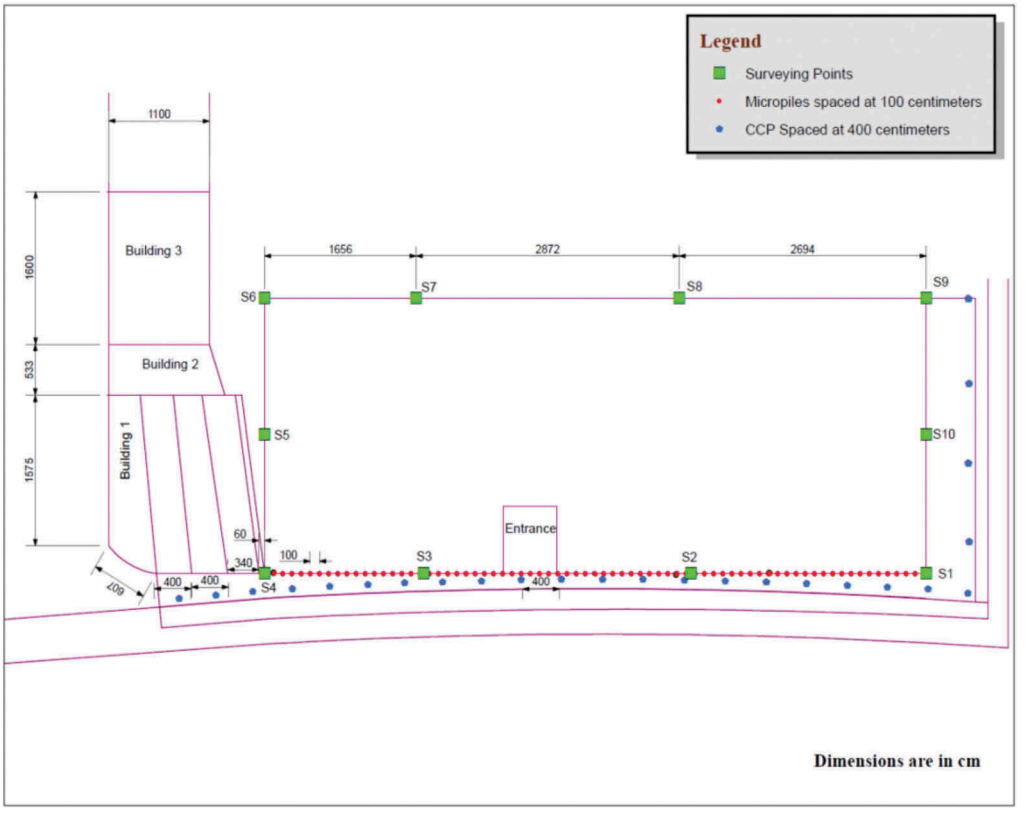

Figure 5. Arrangement of survey control points, CCPs, and micropiles.

5.5 *Effectiveness of cement grouting and micropiling*

To evaluate the effectiveness of CCP grouting in mitigating excavation-induced surface settlement and building tilting, a series of standard penetration test (SPT) were performed. SPT samples were collected from the range of -2 m to -22 m. Based on boring data, depths between -8 to -12 m were specifically monitored as this range was identified as the critical area for uplifting event. Figure 6 shows the comparison result and improvement of soil properties before and after CCP grouting. It is noticed that SPT N values increased from 11 to 22 at a depth of 8 m, and from 9 to 27 at a depth of 12 m. The increase in SPT N value was less substantial at a depth of 10 m. However, the soil properties between 9-10 meters show the SPT N value was 33 and 34 before and after grouting meaning that the soil was stiff and consolidated at this range. Apparently, the use of CCPs had effectively improved the shear strength of the soil between depths of 2 m to 22 m.

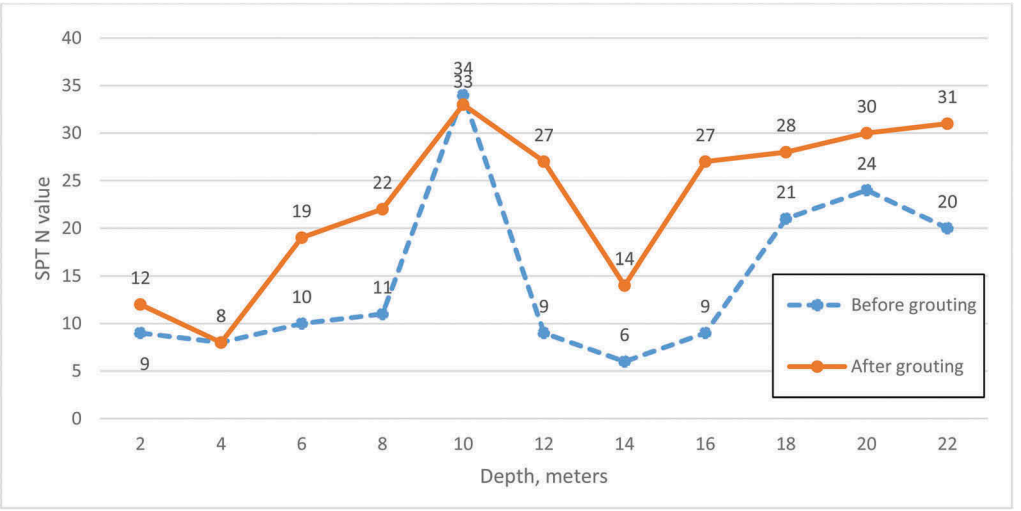

Figure 6. Effectiveness of cement grouting in improving soil strength.

Table 2 depicts the surveying results and settlement calculations. The total settlement calculations from the four points at the front (S1 to S4) were positive indicating the front surface of tilted building was successfully lifted up 2 mm while the four points at the back were settled down about 4mm. The tilting situation of the building seemed to be under control and did not show any further significant surface settlement. Table 2 shows the improvement of CCP grouting and micropile installation in mitigating excavation-induced settlement. Field observations were implemented during CCP grouting and micropile installation to closely monitor the inclination of the tilted building. Until the completion of both mitigating works, no further settlement was observed and the tilting of the building had been terminated. CCP grouting and micropiles worked well in reinforcing the soil. The effectiveness of mitigation construction strategies was substantial.

Lessons learned from this case study are intended to be shared with contractors so that they can better prepare for deep foundation excavation and prevent surface settlements and building tilting, particularly in sites near existing adjacent buildings.

Table 2. Surface settlement before and after cement grouting.

Survey control points	Initial reading in mm (first day)	End reading in mm (34th day)	Total settlement in mm
S1	-355	-353	2
S2	-285	-285	0
S3	-304	-303	1
S4	-409	-407	2
S5	-834	-837	-3
S6	-110	-109.5	0.5
S7	29	25	-4
S8	9	5	-4
S9	179	179.5	0.5
S10	-444	-438	6

Note: positive values in the total settlement column indicate points were lifted up and

6 CONCLUSIONS

This paper provides the following conclusions:

(1) Based on soil properties and the surrounding environment, CCP grouting and micropiles successfully demonstrated their effectiveness in mitigating surface settlement and building deformation due to nearby deep excavation.
(2) When a layer of impermeable soil is located beneath the excavation finish surface, contractors must evaluate the potential risk of uplifting.
(3) Whenever underground water flooding is noticed on excavation finish surface, immediate review must be done to find out where the underground water comes from and what might cause the flooding.
(4) The pressure of CCP grouting has to be determined carefully based on existing soil conditions prior to construction. Due to in-place confined soil area identified from the soil report and mitigation construction drawings, the grouting pressure was set at 5 kg/cm^2 to slowly inject slurry paste into soil. This is to avoid further disturbance in the confined soil area and prevent secondary settlement.
(5) The micropiles have to be installed on top of stiff soil and penetrate through assumed potential sliding planes in order to reinforce soil and provide sufficient bearing capacity to resist foundation deformation/settlement.
(6) Survey control points should be set along the edges of the tilted building so that all soil responses from CCP grouting and micropile installation could be reflected in surveying notes. Readings must be closely monitored by contractors.

REFERENCES

Bjerrum, L., 1963. *Discussion Section IV*, Proceeding of European Conference on Soil Mechanics and Foundation Engineering, Wiesbaden, 2, 135–137.

Chepurnova, A., *Assessing the influence of jet-grouting underpinning on the nearby buildings*. Journal of Rock Mechanics and Geotechnical Engineering, 6(2), 2014, pp.105–112.

Heiseh, H.S, Wang, C.C., and Ou, C.Y., 2003. Use of jet grouting to limit diaphragm wall displacement of a deep excavation. Journal of geotechnical and geoenvironmental engineering. 129(2), 2003, pp.146–157.

Huang, Y., Zhang, F., Yashima, A., and Ye, W., 2008. *Numerical simulation of mitigation for liquefaction-induced soil deformations in a sandy ground improved by cement grouting*. Environmental Geology, 55(6),pp.1247–1252.

Liu, G.B., Jiang, R.J., Ng, W.W., and Hong, Y.C., 2011. *Deformation characteristics of a 38 m deep excavation in soft clay*. Canadian Geotechnical Journal, 48(10),pp.817–1828.

Mohammed, M.H., Pusch, R., Knutsson, S., 2013. *Study of cement-grout penetration into fractures under static and oscillatory conditions*. Tunneling and Underground Space Technology, 45, pp.10–19

Ou, CY. Hsieh, P.G., Chiou, D.C., 1993. *Characteristics of ground surface settlement during excavation.* Canadian Geotechnical Journal, 30(5),pp.758–767.

S. Coulter, 2006. *Effect of jet-grouting on surface settlements above the Aeschertunnel, Switzerland.* Journal of Tunnelling and Underground Space Technology. Vol. 21, pp.542–553.

Sayed, S. M., 1987.*Geotechnical Modeling and Applications*, Gulf Publishing Co., Houston, Texas, USA.

Schroeder, W. L., Dickenson, S.E., and Warrington, D. C., 2004. *Soils in Construction*. 5th edition, Prentice Hall, Upper Saddle River, New Jersey.

Son, M. and Cording, E.J., 2005. *Estimation of building damage due to excavation-induced ground movements*. Journal of geotechnical and geoenvironmental engineering, 131(2),pp.162–177.

Tan, Y., and Li, M, 2011. *Measured performance of a 26 m deep top-down excavation in downtown Shanghai*. Canadian Geotechnical Journal, 48(5): 704–719.

Wang, Z.W., Ng, W.W., and Liu, G.B., 2005. *Characteristics of wall deflections and ground surface settlements in Shanghai*. Canadian Geotechnical Journal, 42(5), 2005, pp.1243–1254.

Hsieh, P.G., Ou, C.Y., Shih, C., 2012. *A simplified plane strain analysis of lateral wall deflection for excavations with cross walls*. Canadian Geotechnical Journal, 49(10),pp.1134–1146.

Wu, Y.D., Liu, J. Ng, W.W. *Effects of pile extraction and refilling with cement slurry on ground settlements*. Canadian Geotechnical Journal, 50(3), 2013, pp.343–349.

Xu, Q., Zhu, H., Ma, X., Ma, Z, Li, X., Tang, Z., and Zhou, K., 2013. *A case history of shield tunnel crossing through group pile foundation of a road bridge with pile underpinning technologies in Shanghai*. Tunneling and Underground Space Technology, Vol.45, 2013, pp.20–33.

Eleventh International Conference on the Bearing Capacity of Roads, Railways and Airfields, Volume 2 – Hoff, Mork & Saba (eds)

Monitoring of a timber pile-supported road embankment

Per Gunnvard, Nelson Garcia, Hans Mattsson, Jan Laue & Qi Jia
Department of Civil, Environmental and Natural Resources Engineering, Luleå University of Technology, Luleå, Sweden

ABSTRACT: Timber piling allows for a solution with lower carbon footprint than concrete or steel piling, yet there exist few well-documented cases of modern timber piled embankments. In this paper, field measurements on a geosynthetic-reinforced timber pile-supported road embankment are reported and evaluated. The monitored road embankment is a section of a newly reconstructed semi-motorway in northern Sweden. The embankment was constructed on 8 m long untreated timber piles with 1.1 m spacing in a triangular pattern, without pile caps. On top of that, a 1.7 m high embankment was constructed, reinforced by two layers of biaxial geogrids. A long-term monitoring program is being carried out from when the semi-motorway was reconstructed. This study presents results from the first year of monitoring. The measurements include the load on the pile heads and subsoil, geogrid strain, pore water pressures, and settlements. The measurements show the development of arching over time, the interlocking of geogrid and embankment material, the subsoil consolidation, etc. The results of the monitoring are compared with results of analytical models from recommendations and codes.

Keywords: Piled embankment, timber piles, monitoring, soft soil, geosynthetic reinforcement, arching

1 INTRODUCTION

Geosynthetic-reinforced pile-supported embankment (GRPSE) is a common foundation method across the world for both road and railway on soft subsoils. GRPSE has a short construction time and reduces settlements and horizontal displacements of the embankment. One or more layers of geosynthetic reinforcement (GR) are placed in the base of the embankment to increase the tensile strength of the fill. The philosophy of pile-supported embankments is to transfer as much of the embankment weight and traffic load onto the piles as possible, to minimise the settlement of the embankment. The mechanism behind the load transfer is primarily arching in the embankment fill. The arches being shear bands generated by differential settlement as the subsoil settles, due to consolidation and creep, whilst the piles remain stationary. As illustrated in Figure 1, the overburden pressure reduces beneath the arch. These arches are not permanent and will collapse to substantial differential settlement. Presence of GR affects the arching as the layer(s) limits the settlement of the embankment fill between the piles, supporting the formed arches. Additionally, the tensile load in the GR is transferred to the piles at each end of the span by what is known as the membrane effect. The membrane effect is the ability of the GR to support (or absorb) forces that act perpendicular to its surface through tension from deformation (Gourc and Villard, 2000).

DOI: 10.1201/9781003222897-31

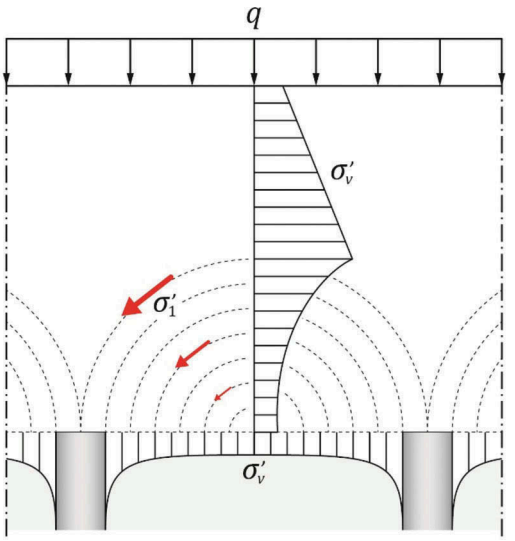

Figure 1. Illustration of a semi-circular arch formation and stress distribution in the embankment above two adjacent piles. Surcharge load q, effective overburden pressure σ'_v and major principal effective stress σ'_1. Based on Zaeske (2001) and Van Eekelen et al. (2013).

Reduced impact is a constant strive in the world today. Even the foundation engineering business is searching for more sustainable solutions to reduce resource usage and pollutions directly or indirectly. Often the solution lies in reapplying old foundation methods. One such method is timber piling, which humans has been using for thousands of years. Cities such as Venice, Rotterdam, Louisiana, and Stockholm are to a great extent founded on timber piles. Since the introduction of mass-produced reinforced concrete and steel piles, timber piling has been left aside. Fortunately, timber piling has started to make a comeback in the last few decades as a competitive and more sustainable deep foundation method. Geosynthetic-reinforced timber pile-supported embankments, also known as lightly piled embankments (Gunnvard, 2020), is a low-cost alternative to GRPSE with steel or concrete piles, as the material and transport cost of timber often is far less. More importantly, timber piling allows for a solution with lower carbon footprint than concrete or steel piling. Timber is highly suitable as a pile material due to its high strength-to-weight ratio. The piles can be easily handled and trimmed to a preferred length. To avoid fracturing or brooming (splitting at the toe), timber piles are pushed down to a firmer soil layer or bedrock with a low practical refusal blow count limit. If driven below the lowest groundwater level in fully saturated silt or clay, timber piles are virtually immune to biological degradation. The piles can be extended to the surface if needed using concrete sections.

Notable GRPSE projects with timber piles include the Kyoto Road in Giessenburg, the Netherlands (Van Eekelen et al. 2007) and the Port Mann Highway 1 Improvement project in Vancouver British Columbia, Canada (Logheed 2017). Although timber piles are widely used in the United States, Canada, Australia, and the Netherlands, Sweden is the only country with an explicit standard or recommendation for GRPSE with untreated timber piles. Figure 2 shows a vertical cross section of the embankment according to the Swedish design criterion in TK Geo 13 (STA, 2016a). No pile caps are used, to further lower the carbon footprint. However, the piles should have a centre-to-centre spacing of 0.8–1.2 m, requiring a lot of timber. The load distribution layer is reinforced with two layers of GR. It is assumed that the two layers interlock the soil particles. Horizontal stresses are built in during the compaction of the soil particles, causing the load distribution layer to act like a beam resting on top of the timber piles. Since it is believed that the Swedish method of GRPSE with untreated timber

piles (Gunnvard, 2020) is too conservative, a project was funded to monitor a timber pile-supported motorway. The results of the first year of monitoring is presented in this paper. The purpose of the monitoring is to collect data as a basis for physical and numerical modelling, to optimise the design criterion of geosynthetic-reinforced timber pile-supported embankments in terms of resource efficiency. More specifically in terms of the amount of GR and number of piles. In practice, the case specific designs come down to prediction with analytical models. Thus, it is also of interest to compare the monitored results with the results of suitable analytical models.

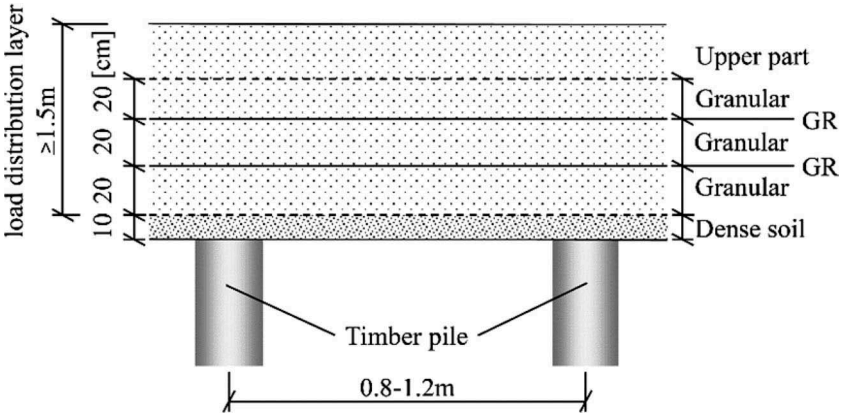

Figure 2. The design criteria by TK Geo 13 (STA 2016a) for geosynthetic-reinforced timber pile-supported embankments.

2 SITE CONDITIONS

The monitored road embankment is a reconstructed 400 m long section of a three lane (2+1) motorway at the coastline in northern Sweden, outside the city of Luleå. Due to large settlements, the old road was under risk of flooding from high sea levels or rapid snowmelt runoff. The monitoring project was initiated parallel to the reconstruction of the road with timber pile support and geosynthetic reinforcement.

The old road embankment was 1.8 m tall, consisting of crushed rock on top of granulated blast furnace slag and a brushwood mattress (corduroy) basal reinforcement. The embankment sat on a thin layer of peat, a 5-12 m thick layer of lightly overconsolidated sulphide silt and sulphide-bearing clay, and a bottom layer of glacial till. The sulphide soil is a soft subsoil with 1070 kPa compression modulus, 20° friction angle, 7 kPa cohesion and 95% water content, on average.

Figure 3 shows a cross section of the new road embankment. Construction spanned from July to September 2020. The sulphide soil is approximately 7.5 m deep at the monitored part of the road. Untreated timber piles were driven down to the glacial till with a centre-to-centre spacing of 1.1 m in a triangular arrangement. The sulphide soil was soft enough to use an excavator with a vibrating grip claw as pile driver, shown in Figure 4. The bottom 20-30 cm part of the embankment (including the brushwood mattress) was left in place as a working platform for the heavy machinery. The pile cut-off level of the new embankment is situated about 60 cm above the old foundation level. A mixture of the furnace slag and excavated sulphide silt was used as a filling material up to the pile cut-off level. The pile heads were covered with a 10 cm thick layer of silty sand to keep the pile heads in a fully saturated and anaerobic zone by capillary action, to avoid rotting should the lowest groundwater level be below the pile heads. The groundwater level was on average 0.2 m above the pile cut-off level for the

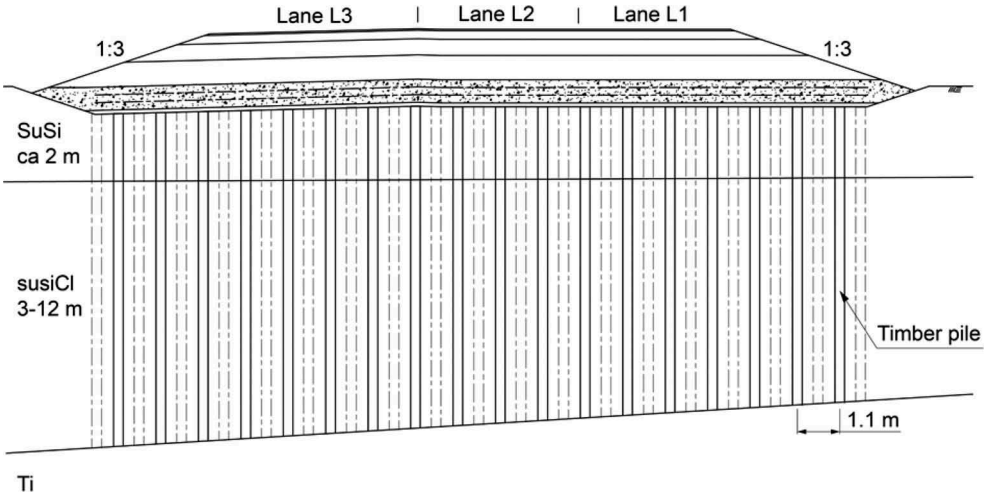

Figure 3. Cross section of the monitored geosynthetic-reinforced timber pile-supported road embankment and soil profile.

Figure 4. Pile driving using an excavator with a grip claw. The piles in the foreground have been trimmed down to the pile cut-off level. Photo: Hjalmar Törnqvist, AFRY.

duration of the monitoring presented in this paper. The final pile length along the monitored part of the road was approximately 8.0 m. The structural bearing capacity of the piles is 90 kN, based on strength class C14 (SIS, 2016) and 125 mm pile end diameter.

The load distribution layer was constructed according to the design criteria shown in Figure 2, with a layer of crushed rock (fraction size 0-90 mm) reinforced with two geogrids (Enkagrid MAX 60). Both geogrids are uniaxial grids (stronger in the machine direction, see Figure 5) of extruded polyester bars with 64 kN/m characteristic tensile strength and 1070 kN/m characteristic stiffness in the machine direction. The lower geogrid was placed with its machine direction in the transversal road direction, and the upper geogrid was placed with its machine direction in the longitudinal road direction. The final embankment height is 1.7 to 2.1 m from pile cut-off level to top surface. The monitored part of the road embankment is 1.7 m high.

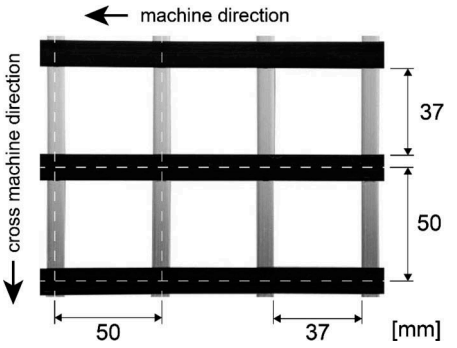

Figure 5. Dimensions of the installed uniaxial geogrid.

2.1 *Instrumentation*

The part of the test area considered in this paper is shown in Figure 6. The instruments are located below the two northbound traffic lanes (L1 and L2) along a 12 m long section, spread out evenly between the two lanes. The choice of instruments and their layout was primarily inspired by the full-scale tests by Van Eekelen et al. (2010), Briançon and Simon (2012) and Zhang et al. (2016). One of the four reinforcement cases tested by Briançon and Simon (2012) had a load-distribution layer geometry with two geogrids, similar to Figure 2.

Settlements are measured using a hydrostatic profiler gauge system and levelling of several settlement plates. Pore pressures are measured by piezometers located in the pile group.

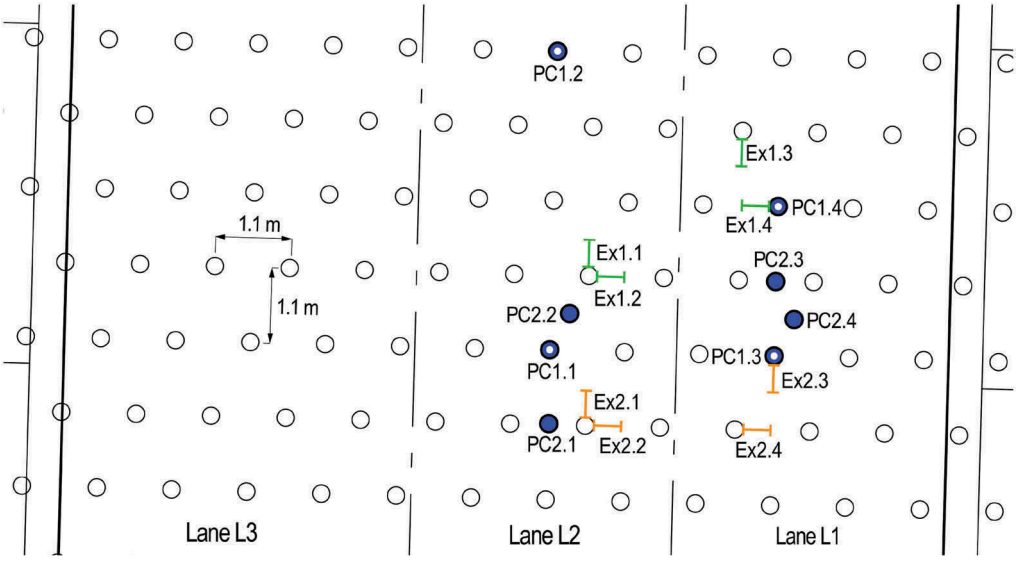

Figure 6. Layout of the part of the monitored road under consideration.

The load distribution in the embankment is measured with a total of eight earth pressure cells. Four earth pressure cells were placed in the pile cut-off level in between the piles; two pressure cells (PC2.2 and PC2.4) were placed in between two adjacent piles and two pressure cells (PC2.1 and PC2.3) were placed in between four adjacent piles. Four earth pressure cells (PC1.1 to 1.4) were installed in the piles as shown in Figure 7. Placing the pressure cell directly on top of the pile head would result in an over- or underestimated soil-pile load transfer as the

diameter of the eight pile heads differed to that of the pressure cells. The average pile head diameter was 24 cm, compared to the earth pressure cell diameter of 23.0 cm. Thus, the cells were installed inside the piles, 20 cm from the pile head (Figure 7). All eight pressure cells are total earth pressure cells with a vibrating wire pressure transducer (Geokon model 4815). PC1.1–1.4 have 0-2 MPa range, 0.5 kPa resolution and ±0.6 kPa accuracy. PC2.1–2.4 have 0-350 kPa range, 0.09 kPa resolution and ±0.18 kPa accuracy. The pore water pressure is measured near the pile cut-off level to determine the effective earth pressure in each total earth pressure cell.

Figure 7. To the left: view of pressure cell installed inside a timber pile. To the right: view of protective aluminium sheet around the pressure cell inside the pile.

Geogrid strain is being measured in both geogrid layers with extensometers to assess the tensile force. A total of eight extensometers were installed in the geogrid layers as shown Figure 8; four extensometers in both the lower (Ex1.1–1.4) and upper geogrid (Ex2.1–2.4). Half of the extensometers were placed in parallel to the geogrid machine direction and the other half were placed in parallel to the geogrid cross-machine direction.

Figure 8. View of the geogrid with extensometer to measure geogrid strain. To the right: extensometer covered with a protective metal pipe.

The extensometers are vibrating wire crackmeters (Geokon model 4420-50MM) with 0-50 mm range, 0.0125 mm resolution and ±0.015 mm accuracy. The anchor spacing distances of the eight anchors were 340–344 mm. All the extensometers were placed with one anchor point above the edge of a pile head, where the GR strain will be at its maximum (Zaeske, 2001; Briançon and Simon, 2012; Van Eekelen, 2012; Zhang et al., 2019).

The output data from the earth pressure cells and extensometers is corrected for temperature influence. Each of the instruments are equipped with a high temperature thermistor that has a range of -80 to +200 °C and an accuracy of ±0.5 °C.

3 MONITORING DATA ANALYSIS

The monitoring results are from 3 September 2020 to 3 September 2021. The road opened for traffic on September 28. Based on the settlement monitoring, the road embankment had settled on average 6.5 cm in early September 2021. The subsoil had at the pile cut-off level settled 2–4 cm relative to the pile heads. The excess pore pressure in the subsoil, from the pile driving and embankment construction, dissipated in only a month's time. The settlements are expected to continue to increase over time as the sulphide soil is prone to creep strain.

3.1 *Load transfer*

The total vertical load W_{tot} of embankment self-weight γH (soil unit weight γ, embankment height H) and surcharge load q on a unit cell (including a pile) is the sum of load parts A, B and C (Van Eekelen and Han, 2020):

$$W_{tot} = (\gamma H + q) \cdot s^2 = A + B + C \tag{1}$$

where s is the centre-to-centre pile spacing, A is the part of W_{tot} that is transferred directly onto the piles via the arching effect, B is the part of W_{tot} that is transferred onto the piles through the GR, and C is the part of W_{tot} that is carried by the subsoil.

Van Eekelen and Han (2020) discussed different ways of quantifying soil arching. In this paper, the level of arching is quantified as pile efficacy E and soil arching ratio ρ (sometimes referred to as stress reduction ratio). Pile efficacy is the ratio of load part $A+B$ and W_{tot}:

$$E = \frac{A+B}{W_{tot}} = \frac{\sigma'_{p1} \cdot A_p}{(\gamma H + q) \cdot s^2} = \frac{\sigma'_{p1} \cdot A_p}{\sigma'_{v0} \cdot s^2} \tag{2}$$

where σ'_{p1} is the measured effective earth pressure on PC1.1–1.4, σ'_{v0} is the initial overburden pressure (γH+ q) and A_p is the pile head cross-section area. When there is no arching $\sigma'_{p1} = \sigma'_{v0}$ and $E = A_p/s^2 = 0.037$, in this case. Soil arching ratio is the pressure on the subsoil of load part C in relation to σ'_{v0}:

$$\rho = \frac{C}{(\gamma H + q) \cdot (s^2 - A_p)} = \frac{\sigma'_{p2}}{\gamma H + q} = \frac{\sigma'_{p2}}{\sigma'_{v0}} \tag{3}$$

where σ'_{p2} is the measured effective earth pressure in PC2.1–2.4, assuming uniform stress distribution on the subsoil. If there is no arching, $\rho = 1.0$.

The unit weight of the embankment is assumed as 22 kN/m^3 and the traffic load is set to an equivalent static surcharge load of 19 kPa. Thus, $\sigma'_{v0} = 56.4$ kPa and $W_{tot} = 68.2$ kN for the final height of the embankment.

Figures 9 and 10 show E, ρ and temperature in the load distribution layer over time.

The gaps in the curves in Figure 9 and 10 are due to loss of battery power supply to the monitoring system. The spikes in the E and ρ curves are due to heavy vehicles passing at the precise time of data logging.

Overall, the load on and in between the piles in lane L1 were naturally greater than the piles in L2, on average 27% greater load part A+B and 62% greater load part C. L1 is busier than L2, and the preferred lane for trucks, which can be seen in the greater number of spikes in the curves for those pressure cells. The significantly lower pressure on PC2.1 is most likely due to lack of soil compaction around that pressure cell.

From the time the road was completed in mid-September, the pile efficacy (Figure 9) remained relatively constant at 0.29–0.48 most of the monitored period. This is much lower than $E = 0.74$ in the full-scale test by Briançon and Simon (2012), but in-line with $E = 0.32$ evaluated from the field test by King et al. (2017) in which the subsoil settlements were minor.

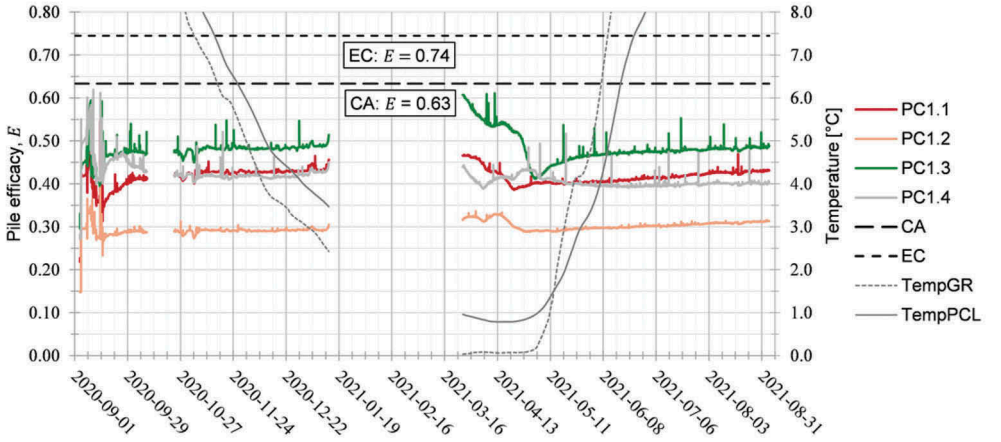

Figure 9. Pile efficacy over time and temperature in the lower geogrid (TempGR) and pile cut-off level (TempPCL). Measured pile efficacy and derived efficacy with the CA model and the EC model.

The soil arching ratio (Figure 10) remained at 0.31–0.48 from October up until mid-January, if excluding PC2.1. After a peak value around the time the road was completed, the values of ρ decreased and recovered slightly later that autumn. Similarly, the results by Briançon and Simon (2012) showed 0.31–0.41 soil arching ratio after embankment construction and 0.47–0.60 after 100 days. An initial peak, followed by a low point and recovering were also observed by Van Eekelen et al. (2010) and King et al. (2017) for subsoil settlements of similar magnitude. The results by King et al. (2017) gives $\rho = 0.54$.

The measured results of E, ρ were compared with predicted results using two analytical GRPSE models used in business practice: the Extended Carlsson (EC) model (Rogbeck et al. 1998) in the Swedish recommendations TR Geo 13 (STA, 2013b) and the Concentric Arches (CA) model (Van Eekelen et al. 2013) in the Dutch standards CUR226 (SBCURnet, 2016). The EC model is the primarily used model for timber piled embankment design in Sweden. It is a simple rigid triangular arch model in which it is assumed that all the load is transferred onto the piles, i.e. $C = 0$ kN/pile. The CA model is a relatively advanced limit equilibrium model that has received a lot of attention. In contrast to the EC model, the CA model takes the subsoil support into consideration, i.e. $C \geq 0$ kN/pile. The subsoil support is based on a subgrade reaction modulus, estimated as 1900 kN/m^3 for the present case. As seen in Figure 9 and 10, both models overestimated the measured pile efficacy. The EC model underestimated the soil arching ratio since C is assumed as zero. Excluding PC2.1, the CA model gave a good fit to the average measured soil arching ratio. The results of the comparison are consistent with the comparison in Gunnvard (2020) of numerical results and predictions with the EC and CA model.

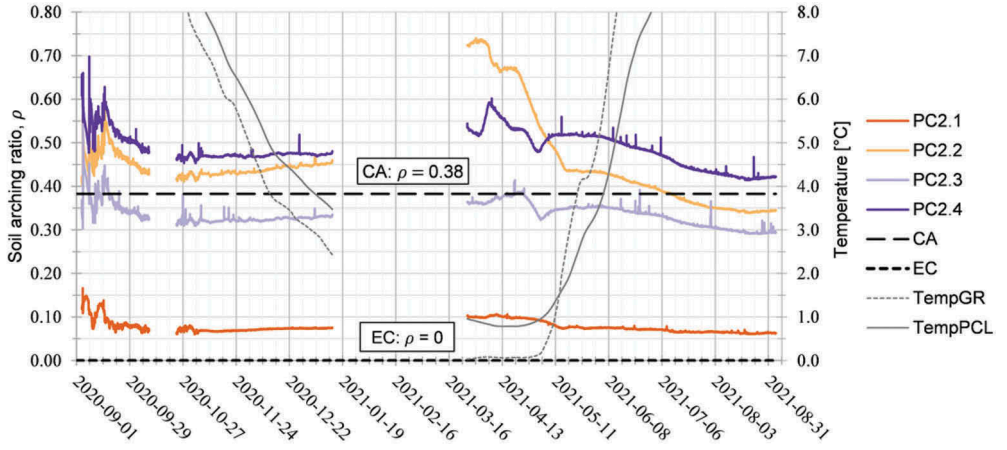

Figure 10. Soil arching ratio over time and temperature in the lower geogrid (TempGR) and pile cut-off level (TempPCL). Measured soil arching ratio and derived arching ratio with the CA model and the EC model.

3.2 *Geosynthetic-reinforcement strain*

Figure 11 and 12 show the strain over time in the lower and upper geogrid. The strains are calculated based on the measured displacement in each of the extensometers, relative to the spacing between their two anchor points. 1% absolute strain equals ~3.4 mm displacement. The results shown are the geogrid strains after road construction. Most of the extensometers compressed up to 0.6% during embankment construction. Ex2.3 compressed almost 1.5%. Ex1.3 extended roughly 0.3%. As the protective pipes (Figure 8) are open-ended, the crushed material could likely have pushed on the extensometer during compaction, causing the compression.

No detailed analysis can be made of the monitored strains after construction. Both the tensile strain in the lower (Figure 11) and upper geogrid (Figure 12) were ≤0.03%, which is estimated as small. Nonetheless, the lower geogrid is overall in tension, whilst the upper geogrid is partly in tension and partly in compression. The high frequent strain fluctuations in the upper geogrid are due to traffic. The lower geogrid showed the same fluctuation, but only in its stiffer direction.

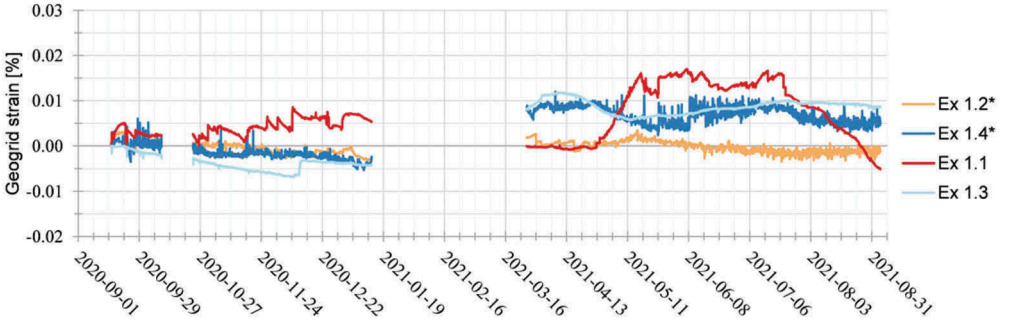

Figure 11. Strain in the lower geogrid over time measured with extensometers (Ex). Geogrid machine direction marked with *.

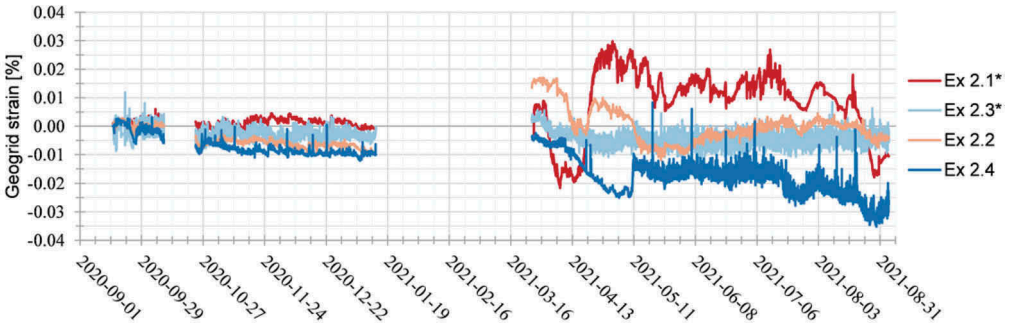

Figure 12. Strain in the upper geogrid over time measured with extensometers (Ex). Geogrid machine direction marked with *.

Though the measurements with hydrostatic profiler showed 2–4 cm subsoil settlement, settlement plates in the load distribution layer suggest only a few millimetres of geogrid deflection. Thus, the geogrids can be regarded as only partially mobilized.

Small tensile strains of ≤0.15% were detected in the GRPSE field tests by King et al. (2017), which they attributed to small subsoil settlements. In comparison, Briançon and Simon (2012) measured after embankment construction ≤0.7% tensile strain and almost 4 cm differential settlement between pile and subsoil. Calculation of the geogrid strain with the CA model gave a predicted strain of 0.1%, which can be considered as reasonable given the simplification of a linear-elastic subgrade stiffness. The strain is not calculated in the EC model but assumed based on maximum allowable strain.

4 CONCLUSIONS

The effects of arch formation over a one-year period were observed and analysed for a geosynthetic-reinforced timber pile-supported embankment outside Luleå, Sweden.

The embankment was reinforced with two layers of geogrid, placed 0.3 and 0.5 m above the pile cut-off level, in accordance with the design criteria in TK Geo 13 (STA, 2016a). Small geogrid strains were generated, due to minor geogrid deflection. Subsequently, load distribution analysis showed partial arch formation. Placement of the geogrids resulted in support from not only the subsoil, but also embankment fill and the mixture of sulphide soil and granulated furnace slag. It is possible that the two layers of geogrid have interlocked the crushed rock to the extent that no greater geogrid deflection will occur. It can be concluded that the geogrid placement criteria in TK Geo 13 is sub-optimal, as discussed in Gunnvard et al. (2020).

Increased load was detected on the pile group and subsoil due to the frost front almost reaching down to the pile cut-off level. Though the maximum observed load did not exceed the timber piles' structural bearing capacity, local settlements could occur that exceed the serviceability limit state. The embankment height should be increased, and possibly the frost susceptible dense soil layer excluded, to reduce the risk of local settlements.

Of the two analytical models, the Concentric Arches model gave a good prediction of the stress on the subsoil, whilst the Extended Carlsson model erroneously overlooks the subsoil support. Both models overestimated the amount of load transfer to the piles due to partial arching.

ACKNOWLEDGEMENTS

Setup of the monitoring was done in collaboration with the consultant company AFRY. The research has been supported financially by the Swedish Transport Administration (STA) and Branschsamverkan i grunden (BIG).

REFERENCES

Briançon, L. and Simon, B., 2012. *Performance of Pile-Supported Embankment over Soft Soil: Full-Scale Experiment*. Journal of Geotechnical and Geoenvironmental Engineering 138(4): 551–561.

Gourc, J.P. and Villard, P., 2000. *Reinforcement by membrane effect: application to embankments on soil liable to subsidence*. In Proceedings of the 2nd Asian Geosynthetics Conference, Kuala Lumpur, 29–31 May 2000. International Geosynthetics Society, volume 1, pp. 55–72.

King, D.J., Bouazza, A., Gniel, J.R., Rowe, R.K. and Bui, H.H., 2017. *Load-transfer platform behaviour in embankments supported on semi-rigid columns: implications of the ground reaction curve*. Canadian Geotechnical Journal 54(8): 1158–1175. doi:10.1139/cgj-2016-0406

Logheed, A., 2017. *The Use of Geosynthetic Reinforced Pile-Supported Embankments on Port Mann Highway 1 Improvement Project*. In Proceedings of the 6th International Young Geotechnical Engineers Conference, Seoul, Republic of Korea, 16-17 September 2017. International Society for Soil Mechanics and Geotechnical Engineering, London, pp. 92–93.

Gunnvard, P., 2020. *Optimal design av träpålar: Optimal design of timber piles*. Department of Civil, Environmental and Natural Resources Engineering, Luleå University of Technology, Luleå.

Gunnvard, P., Laue, J. and Jia, Q., 2020. *Geosynthetic reinforcement in lightly piled embankments: Laboratory model development*. In Proceedings of the 4th European Conference on Physical Modelling in Geotechnics, Luleå, Sweden, 7-8 September 2020. pp. 301–302

Rogbeck, Y., Gustavsson, S., Södergren, I. and Lindquist, D., 1998. *Reinforced Piled Embankments in Sweden – Design Aspects*. In Proceedings of the 6th International Conference on Geosynthetics, Atlanta, Georgia, 25-29 March 1998. International Geosynthetics Society, Jupiter, Florida, pp. 755–762.

SBRCURnet, 2016. *CUR226 Design Guideline Basal Reinforced Piled Embankments*. SBRCURnet, Delft. Publ. CUR226: 2016.

SIS, 2016. *Structural timber – Strength classes, SS-EN 338:2016*. Swedish Standards Institute (SIS), Stockholm.

STA, 2016a. *Trafikverkets tekniska krav för geokonstruktioner-TK Geo 13*. The Swedish Transport Administration (STA), Borlänge. Publ. 2013:0667, version 2.0 (in Swedish).

STA, 2016b. *Trafikverkets tekniska råd för geokonstruktioner-TR Geo 13*. The Swedish Transport Administration (STA), Borlänge. Publ. 2013:0668, version 2.0 (in Swedish).

Van Eekelen, S.J.M., Bezuijen, A., and Alexiew, D., 2010. *The Kyoto road piled embankment: 3.5 years of measurements*. In Proceedings of the 9th International Conference on Geosynthetics, Guaruja, Brazil, 23–27 May 2010. pp. 1941–1944.

Van Eekelen, S.J.M, Bezuijen, A., Lodder, H.J. and Van Tol, A.F., 2012. *Model experiments on piled embankments. Part I*. Geotextiles and Geomembranes 32: 69–81. doi:10.1016/j.geotexmem.2011.11.002

Van Eekelen, S.J.M., Bezuijen, A. and Van Tol, A.F., 2013. *An analytical model for arching in piled embankments*. Geotextiles and Geomembranes 39. 78–102. doi: 10.1016/j.geotexmem.2013.07.005

Van Eekelen, S.J.M. and Han, J., 2020. *Geosynthetic-reinforced pile-supported embankments: state of the art*. Geosynthetics International 27(2): 112–141. doi:10.1680/jgein.20.00005

Zaeske, D. 2001. *Zur Wirkungsweise von unbewehrten und bewehrten mineralischen Tragschichten über pfahlartigen Gründungselementen*. University of Kassel, Kassel, Schriftenreihe Geotechnik Heft 10 (in German).

Zhang, C., Jiang, G., Liu, X. and Buzzi, O., 2016. *Arching in geogrid-reinforced pile-supported embankments over silty clay of medium compressibility: Field data and analytical solution*. Computers and geotechnics 72: 11–25. doi:10.1016/j.compgeo.2016.03.007

Zhang, Z., Wang, M., Ye, G.-B. and Han, J., 2019. *A novel 2D-3D conversion method for calculating maximum strain of geosynthetic reinforcement in pile-supported embankments*. Geotextiles and Geomembranes 47: 336–351. doi:10.1016/j.geotexmem.2019.01.011

Measurement of traffic loading

Eleventh International Conference on the Bearing Capacity of Roads, Railways and Airfields, Volume 2 – Hoff, Mork & Saba (eds)

Advanced WIM system incl. measuring vehicle dimensions module – Metrological regulation

Emil Doupal & Jiří Novotný
Transport Research Centre, Czech Republic

ABSTRACT: The advance weigh-in-motion (WIM) system uses additional measuring modules to gain precise data on the traffic stream. The purpose of the project is to determine the correct procedure for measuring the dimensions of vehicles which move in normal operation as a separate module for WIM systems. This is to define the method of demonstrating metrological continuity and to determine the evaluation procedure for data measured. This article describes the test data acquired using temporary measuring devices and evaluates the data collected.

Keywords: Weigh-in-Motion, WIM, vehicle dimensions, metrological prescriptions

1 INTRODUCTION

The Road and Motorway Directorate of the Czech Republic (RSD), the State Fund for Transport Infrastructure (SFDI), the research institute "Transport Research Centre v.v.i" (CDV), the Czech Metrology Institute (CMI) and a variety of commercial companies have the goal of extending the existing Weigh-in-Motion (WIM) systems to allow for direct enforcement by additional modules as an approved system for the automatic measurement of vehicle dimensions.

The vehicle weight (WIM) and dimension (scanner) monitoring system consists of a measuring system that records both the vehicle weight as well as the vehicle dimensions in 3D. This system consists of a camera system that records and identifies individual measured vehicles and switchboards where power supplies, a data switch, an evaluation unit with metering and documentation software, and a communication interface to connect the system to the user.

The measuring system records the 3D contours of vehicles passing under the portal, which is used to calculate the dimensions of the vehicle. The measured data is processed using artificial intelligence algorithms in the computing unit. The system is also equipped with algorithms for classifying vehicles into predefined categories. This function specifies whether the vehicle has exceeded permitted dimensional limits.

Due to the nature, principle and use of the Free Flow Profiling System for the purposes of the automatic determination of vehicle heights in normal road traffic, it is necessary to divide the measurement, or metrological continuity, into two parts. The first part deals with measuring the dimensions of static objects and determining the standard deviation of the resulting variables (i.e. height, width and length of the object). The second part examines the accuracy of measurements of dynamically moving objects and determines the dependency of the standard deviations and dimensions of the object on the object's speed.

DOI: 10.1201/9781003222897-32

1.1 *Static test (measurement)*

The main objective is to verify the accuracy of the system measurement according to technical parameters. Due to the precision of the equipment declared under technical conditions (in [cm]), we can assume the using based on geodetic methods (spatial polar methods, intersections, laser scanning, etc.) using the total Leica MS50 instrumentation equipment (hereinafter MS50, instrument accuracy in [mm]) or a very precise device, such as the Leica Absolute tracker AT401 (hereinafter AT401, instrument accuracy in the order of tenths of [mm]). As a control method to meet the dual focusing criterion by another method and other technology, the measuring band (measurement accuracy in the order of several [mm]) can be used.

1.2 *Dynamic test (measurement)*

The objective is to verify the suitability of using the system in normal road traffic, i.e., to determine the accuracy of data gathered on the dimensions of moving objects and to determine the dependency on the standard deviations of object dimensions on object speed. This determination is made based on different types of objects, including not only geometric and dimensional aspects, but also the material of the object (material - solid, movable - sail, colour, etc.).

Several sets of measurements have been performed at different speeds in relation to the structure on which the measuring device where mounted (assumed to be 10 km/h, 25 km/h, 50 km/h, 75 km/h and 100 km/h). Similar measurements have also been made at these speeds with an object with a non-solid structure, such as a tilt truck. As the tarpaulin on truck on the vehicle will vibrate due to its speed, the ideal solution is to determine the magnitude of this vibration and incorporate this uncertainty into the accuracy calculation of the measurement.

According to the results of the static test, it is possible to test the system measurement on various materials which are used in practice (e.g., metal, plastic or fabric painted surfaces, treated surfaces, etc.) and which result in diminished accuracy of measurements (e.g., significant noise in readings) or exhibit non-standard behaviour when measured (e.g. double reflection of laser beams).

2 TECHNICAL SOLUTION

The systems were installed on the toll portal 2458 - E 52 KM 6,5 – Brno, Czech Republic in one traffic direction. The following components where installed:

- 3x SICK scanner with cabling 20 m;
- 1x PC;
- 1x SWITCH;
- 1x switchboard;
- 1x power cabling from the new SICK switchgear to the WIM switchgear;
- 2x holder for SICK – perpendicular to the communication axis;
- 1x holder for SICK – longitudinally with the communication axis;
- 1x rack mount for the rear gate of the toll gate; and
- 2x overview camera.

All components were mechanically fastened in a manner which avoided mechanical damage to the existing structures and their surfaces. A 3G/LTE data modem has been supplied to the WIM switchgear. The switchboard is linked to the existing WIM station.

The scanner used is a non-contact laser measurement sensor that scans the surrounding perimeter radially on a single plane using light pulses. The scanner takes measurements in two-dimensional radial coordinates. If a laser beam emitted is reflected from a target object, then the position of the object is given in the form of distance and angle. Scanning takes place in a sector of 190°. The scanning range of the LMS5xx is maximum 80m on light, natural surfaces with an object remission > 100 % (e.g., a white house wall). [5]

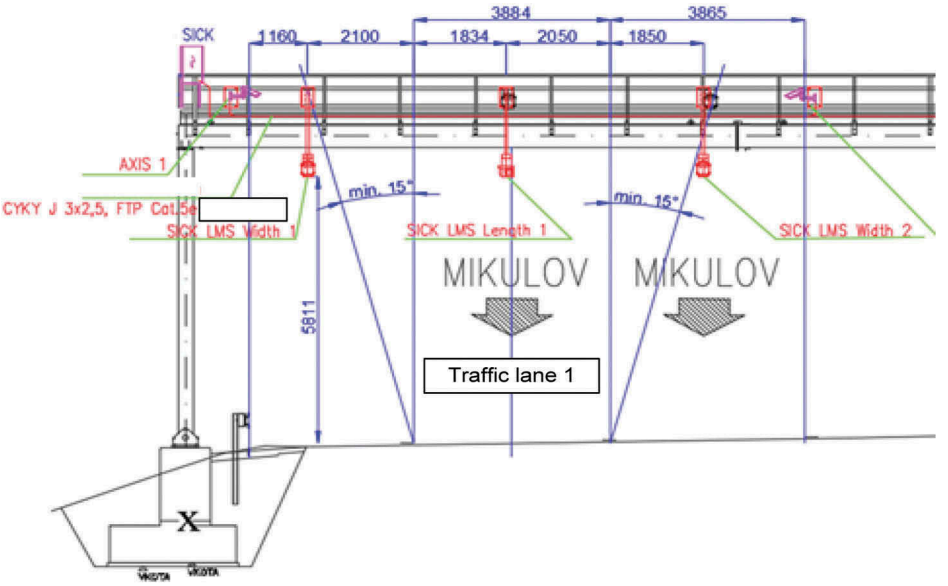

Figure 1. Schematic of layout in the road profile [4].

2.1 *System calibration*

In the first phase, the system was calibrated statically using a standard. After the calibration factors were inserted into the system, they were verified by measuring vehicles passing. The measured vehicle complied with the verification requirements with respect to its "variable profile" (i.e., roof air conditioning and orange warning beacon) - see Figure 2. The first series of measurements started immediately following the system calibration.

2.2 *Static measurements of test vehicles*

The static measurement of vehicles was carried out in the CDV laboratory according to standard ČSN 30 0521.

The measuring equipment comprise of:

– Measuring tape (calibration sheet: KL – P01572/2014);

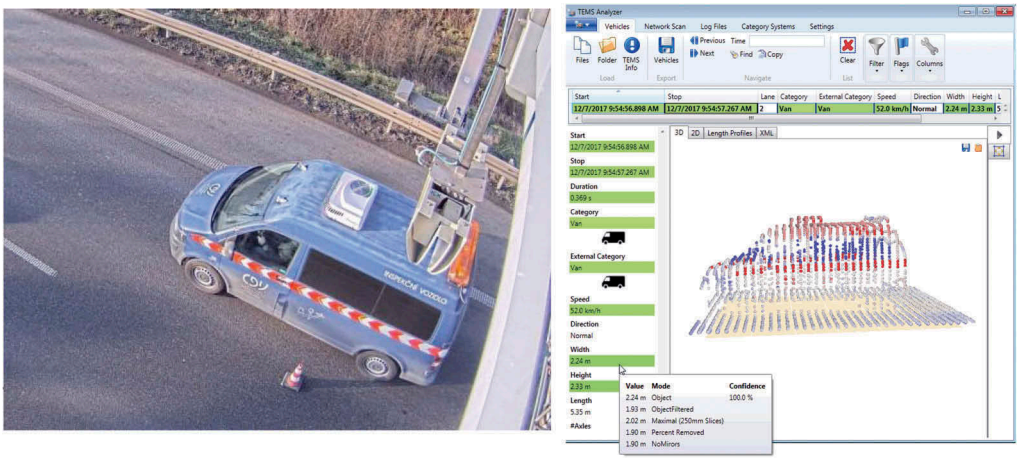

Figure 2. Calibration and system output [4].

– Inclinometer (calibration sheet: SKL003/2014);
– Measuring bar;
– Lead;
– Pressure gauge; and
– Thermometer.

Measuring the ground plan dimensions of the vehicle (i.e. length and width. The vehicle, the length and width of which have been previously measured, was brought to the control point and locked against movement. The two most distant points on the four corners of the roof of the vehicle were projected on the control plane and highlighted. In case of doubt about the most distant points, several points were considered at the control level. After marking the points, the vehicle was removed from the checkpoint and the distances of the distances of the distant points were verified using the measuring tape.

3 METROLOGICAL RULE FOR "MEASUREMENT OF VEHICLE DIMENSIONS"

The purpose of this article is to: (i) establish the correct procedure for measuring the dimensions of vehicles moving in normal operation, (ii) define the method of proving the metrological continuity, and (iii) determine the procedure for the evaluation of the measured data. This is done based on test measurements performed using temporary measuring devices and the evaluation of collected data.

3.1 *Definition of reference vehicles*

The reference vehicle serves as a standard for determining the metrological characteristics of the measuring device. It is therefore necessary to properly select reference vehicles to detect any deficiencies of the measuring equipment.

Selected reference vehicles should include protrusions from the smooth surface of the bodywork (e.g., warning beacons, air conditioning units, hydraulic loading arm, etc.) to demonstrate the ability of the measuring device to detect and measure these elements.

Another requirement for the choice of reference vehicles is dimensional diversity. This means selecting vehicles which best reflect the dimensional spectrum of conventional vehicles in use on the roads. The choice must therefore include for example, vans, lorries, trailers with a semi-trailer, etc. The minimum number of reference vehicles is three.

3.2 *Measurement description*

Measurement of the dimensions of vehicles moving in normal operation consists of a static measurement (as detailed in section 2.2), which is used to determine the initial dimensions of reference vehicles. Another element is the dynamic measurement, which is carried out by means of the measured measuring device (e.g. measuring scanner, optical barriers, etc.)

Static measurements of selected vehicle types follow the recommendations of the ČSN 30 0521 standard and must include the maximum dimensions of the vehicle. This means considering the protruding parts of the vehicle from the smooth body contour. The measured dimensions are identified in the standard as:

A vehicle length [mm]
B vehicle width [mm]
C vehicle height [mm]

Work metrics used for static measurement must be met by metrological traceability. This continuity is met by the calibration sheet measurements from the accredited calibration laboratory to all the gauges used before performing the static measurement.

Based on the correct static measurements, vehicles can be declared as reference vehicles for subsequent dynamic measurement. Below is presented an example for extended measurement uncertainty:

U_A = 4 mm; U_B = 4 mm; U_{C1} = 2 mm; U_{C2} = 2 mm; U_{C3} = 3 mm

The index refers to the appropriate measurement designation.

This expanded measurement uncertainty is the product of the standard uncertainty of measurement and the coverage coefficient k = 2, which for the normal distribution corresponds to the coverage probability of about 95%.

3.3 *Evaluation method of static measurement*

The aim of static measurement is to obtain the dimensions (i.e. height, width, length) of reference vehicles with the assigned combined measurement uncertainty. The data obtained from the static measurement serves to calculate the standard measurement uncertainty.

The standard measurement uncertainty can be divided into two parts.

Standard uncertainty u_a: The calculation of the standard uncertainty u_a is based on the statistical analysis of the repeated series of measurements. If there are (***n***) independent equally accurate measurements (***n*** > 10), then the estimate of the resulting value is represented by the value of the sample arithmetic mean.

$$\bar{x} = \frac{1}{n}\sum_{i=1}^{n} x_i \tag{1}$$

Determination of the uncertainty of type A where s_***x*** is the standard deviation of the arithmetic mean and ***n*** is the number of measurements in this case calculated:

$$u_a = s_{\bar{x}} = \frac{s_x}{\sqrt{n}} = \sqrt{\frac{1}{n(n-1)}\sum_{i=1}^{n}(x_i - \bar{x})^2} \tag{2}$$

Standard uncertainty u_b:

The calculation of the standard uncertainty u_b is based on non-statistical approaches to analyse the series of observations. For evaluation, for example, available information, values obtained from calibration sheets, or measurement experience are used.

The uncertainty of type B is determined by the geometric sum of uncertainties caused by individual influences, e.g.:

uncertainty of the standard (e.g. from the calibration certificate) u_{b1}

bandwidth uncertainty u_{b2}

uncertainty due to temperature u_{b3}

other influences u_{bn}

$$u_b = \sqrt{u_{b1}^2 + u_{b2}^2} \tag{3}$$

Each component (u_{b1}, u_{b2}, u_{b3}, ... u_{bn}) is assigned the appropriate probability distribution. Uncertainties of types A and B must be combined to obtain combined standard uncertainty. Combined standard measurement uncertainty: determined from uncertainty type A and B

$$u = k\sqrt{u_A^2 + u_B^2} \tag{4}$$

The calculated uncertainty u was determined from probabilities P = 68%, is k = 1. For another probability, the uncertainty is recalculated by multiplying by the coefficient ***k***.

In the calibration sheets the uncertainty of the measurement result is given by the coefficient k = 2, is for the probability P = 95%. The measurement result is in the form:

$$X \pm U \tag{5}$$

where U is the expanded combined uncertainty of the measurement results. [2]

3.4 *Dynamic measurement*

The dynamic measurement is performed by passing the reference vehicles through the measuring device. The measuring device must be installed and then calibrated in accordance with the manufacturer's technical specifications. For statistical evaluation, it is necessary to perform at least ten repeated measurements for each vehicle at a given speed (Table 1). Measurements must be made for three different vehicle speeds in such a way that the measurement range given by the technical specification of the gauge is evenly covered.

To demonstrate the ability of the measuring device to detect vehicles exceeding the permitted speed, measurement is also required at a speed higher than the permitted speed at a given measuring point. To verify the accuracy of the measuring system function, it is necessary to perform dynamic measurements under various meteorological conditions (e.g. snow, rain, fog, frost, etc.), and these data must also be recorded including changes during measurement (e.g. temperature, pressure, humidity).

Table 1. Requirements for dynamic measurements [4].

	Speed [km/h]	Number of passes
Vehicle 1	20, 50, 80 (100, 120)*	10 (3)**
Vehicle 2	20, 50, 80 (100, 120)*	10 (3)**
Vehicle 3	20, 50, 80 (100, 120)*	10 (3)**

)* recommended speeds - higher than allowed
)** number of passages for higher speeds than allowed

Method of evaluating dynamic measurement

The dynamic measurement is coupled to the static measurement, as shown in Figure 2. The procedure for calculating the uncertainty of the dynamic measurement is analogous to the determination of the uncertainty of the static measurement. They differ only in uncertainty types B (uncertainty effect u_b). The size and types of uncertainty contributions depend on the measurement principle of the selected measurement system. Dynamic measurement results (measured data) must not be filtered, i.e., no measurements can be excluded. Extreme values in the measured data file may not be a measurement error, but a correct response of the measuring device to protrusions of the reference vehicle body. If filtered, this data could be erroneously excluded from the dataset.

Based on the measurement result with assigned combined measurement uncertainty, the measuring system shall be judged whether it is in conformity or not. The method of the conformity decision is described in ILAC-G8: 03/2009.

4 TEST AND EVALUATION

The static measurements were performed in the CDV laboratory in accordance with ČSN 30 0521. Dynamic measurements were performed using two different scanning systems devices installed at toll gate 2458.

Based on the selection of reference vehicles and the subsequent characterization of conditions, dynamic measurements of these vehicles were carried out. Dynamic measurement refers to the determination of the reference vehicle's dimensions when passing through the measuring device. The result is a set of data, such as a set of lengths, widths, hights from one pass. Only datasets of individual vehicle dimensions were processed separately. For each vehicle, each dimension (height, width, length), an experimental evaluation was performed for each individual velocity and extended combined uncertainty was calculated (Table 2).

However, this calculation is only a guideline to serve as a proposal for a procedure for assessing partial impacts mainly on type B uncertainty.

Table 2. Accuracy expression of measuring systems [mm], [4].

	Hight [mm]	Width [mm]	Length [mm]
System 1	-311	-568	-833
System 2	-312	-568	-1084

Table 3. Expression of accuracy of measuring systems [%], [4].

	Hight [%]	Width [%]	Length [%]
System 1	15,2	23,5	5,3
System 2	15,2	23,5	7,0

4.1 *Conclusion - findings from practical measurements*

Minimum dimensions of the vehicle element when measuring dimensions:

For systems that work with scanners, measurement resolution is limited by the following factors: *Frequency of sweep, Angular sweep step, Geometry of installation.*

For an optical method, the surface properties of the vehicle (reflectance and absorption of light at the used wavelength) are also affected.

Example:

The system works with scanners at the margins of the lanes. The maximum installation height is 8 m. The measurement is limited so that the sharpest angle between the scanner and the vehicle point is limited to at least 15 °. The system works with the following parameters:

Sweep frequency 75 Hz, Angular sweep of 0.5 °, Height above the road 8000 mm, Maximum horizontal distance of vehicle points 8000 mm, Maximum vehicle speed is 100 km/h

Using these example parameters: The beam at the furthest point of the vehicle proceeds in vertical steps of approximately 270 mm:

$$\left(1 - \frac{\tan 74,5^{\circ}}{\tan 75,0^{\circ}}\right) 8000 = 270\ mm$$

Since the angles and distances in the example are chosen in the same way, this value also applies to the horizontal steps on the horizontal roof of the vehicle. There is a 1/75 second time interval between the samples, the vehicle moves at a speed of 27.78 m/s. Thus, between the two scans, the pitch is approximately 370 mm. At lower speeds and less sharp angles the step size decreases.

4.2 *Summary of the example*

An object with a vertical height or a horizontal length less than 270 mm may not be recorded by the beam. At a maximum speed, an object with a length of less than 370 mm may not be recorded. The system may be equipped with algorithms for filtering measured data. In this case, the values may be even worse, because a separate point may not be accepted as a valid measure.

This is just a simple example. The actual values will vary with respect to scanning parameters, beam size and position, shape, and dimensions of the vehicle. The number of installed scanners and the geometry of their installation are also affected. These effects are not included in the example for purposes of clarity.

The consequences of this problem were observed during the tests carried out on 27 February 2018 with the Renault D18. The hook of the loading area was measured at various altitudes (heights) at different elevations, depending on whether at what point the scanner caught the hook. In some cases, the roof of the vehicle was measured, and the hook was not measured at all.

Figure 3. Example of the problem, with the hook encircled in red.

Similarly, the Air Conditioning Unit and Vehicle Beacon CDV (VW Transporter) caused problems with measurements.

4.3 *Critical notes - Additional effects on the experiment*

Based on the analysis of measured data in dynamic mode, several steps can be recommended for further development of the improvement of scanning results. The first step was to increase the sampling frequency of the scanners. The methodology for both calibration of reference vehicles and scanners should be based on interlaboratory comparisons in the future. The supplier may also consider increasing uncertainty by introducing a safety factor, thereby reducing risks.

Verification of measurement quality, especially when introducing new technology, would make it convenient to perform interlaboratory comparisons. Interlaboratory comparisons organized by CMI are evaluated using the criteria E_n.

$$E_n = \frac{X_{lab} - X_{ref}}{\sqrt{U_{lab}{}^2 + U_{ref}{}^2}} \leq 1$$

X_{lab} is the value of the participating laboratory

X_{ref} is a reference value, not known for the laboratory at the time of measurement

U_{lab} measurement uncertainty of the participating laboratory

U_{ref} the uncertainty of the pilot laboratory is not known for the laboratory at the time of measurement [2]

Risk reduction

In some industries, for example in the automotive industry, a “safety factor” is introduced. This is an increase in the uncertainty band, whereby for example, a coefficient of 5 has been chosen in the automotive industry in certain sectors. This means that the uncertainty based on

the measurement is extended fivefold. A further reduction in the risk would be to supplement the measurement by scanning the optical gate.

5 CONSEQUENCES AND RECOMMENDATIONS

In addition to errors in maximum vehicle dimension measurements, the minimum vehicle element dimension (i.e., minimum resolution) that the system can reliably include in dimension measurement is also considered. This element should be determined by the minimum height, width and length when considering the worst possible case (i.e., maximum distance, sharpest angle and maximum work speed).

This minimum object size should be determined by the system manufacturer with respect to the parameters of the scanners used and the recommended installation method specified by the manufacturer. The value should be based on a description of the calculation by which the manufacturer has reached the value.

The system can be used to measure vehicle dimensions while driving, considering the uncertainty of measurement and the minimum size of the elements, which the system may not record reliably.

The minimum size of the vehicle element and the measurement tolerances must be clearly communicated to the system end user to prevent its misuse. For example, the system is not suitable for use in protecting the gangway profile. There may be a situation where the vehicle does not comply with the clearance profile, but this condition will not be signalled.

The main objective of the project was to develop, in co-operation of CMI and CDV, a metrological regulation for the certification and type verification of vehicle dimensioning systems as a complement to existing WIM systems. This metrological regulation is now available for road administration.

„This article was produced with the financial support of the Ministry of Transport within the programme of long-term conceptual development of research institutions. “

REFERENCES

[1] TNI 01 0115. International metrological vocabulary, Prague, 2009.
[2] Document EA-4/02 M:2013. Expression of Measurement Uncertainty in Calibration.
[3] Český institut pro akreditaci, o.p.s. Dokument ILAC-G8:03/2009. Instructions to indicate compliance with the specifications.
[4] Doupal E., Novotny J., Centrum dopravního výzkumu, v. v. i. Project SFDI „Vehicle dimension inspection systems“SICK Modular Profiling system
[5] Technical documentation SICK, 8020775_BA_Modulares_Profiling_System_en, & Dimension Measuring with FPS V2.6.1.0

Eleventh International Conference on the Bearing Capacity of Roads, Railways and Airfields, Volume 2 – Hoff, Mork & Saba (eds)

Tire footprint analysis of agricultural vehicles for rural pavements

L.S. Salles, Z. Wan & L. Khazanovich
Department of Civil and Environmental Engineering, University of Pittsburgh, Pittsburgh, USA

ABSTRACT: Construction and maintenance of roads in rural communities have significant economic impacts as these routes play a major role in agricultural production worldwide. Even though rural roads experience much less traffic than highways, they are subjected to heavy and unconventional vehicles that are usually ignored in traditional design and rehabilitation of new and existing pavements. This paper presents an analysis of different tire footprints from a set of agricultural vehicles and how to consider these unique loads into pavement design and analysis. Tire footprints were obtained from measurements performed with a Tekscan device with different load levels and then simulated in a thin pavement structure. Tire footprint pressure was determined considering the gross area where the entire footprint region is represented by a single area, and the multi circle approach where each individual footprint is considered as an individual load. Results point out that both methods show similar pavement responses. This is helpful for pavement design and analysisgo considering that most design methods are based on traditional vehicle tire footprint (single load) and as seen in this research, agricultural vehicles present quite unconventional tire footprints.

Keywords: rural pavements, agricultural vehicles, tire footprint, gross area, multi circle approach

1 INTRODUCTION

Agriculture production has increased constantly over the last decades worldwide. With that, innovations in agricultural equipment developed novel and heavier types of agricultural vehicles with diverse axle types and tires that greatly differ from conventional trucks used for pavement design and analysis.

Several projects aimed to study the effect of agricultural vehicles in pavements. A 1999 study by the Iowa Department of Transportation on both flexible and rigid pavements resulted in legislation restricting the maximum loads on agricultural vehicles (Fanous et al., 1999). Regulation changes were also recommended in South Dakota as Sebaaly et al. (2002) observed that some agricultural vehicles, when overloaded, are potentially more harmful to the pavement than the conventional 80kN single axle truck. The Minnesota Department of Transportation (MnDOT) developed two studies in 2001 and 2005 investigating the impact of such vehicles in low volume roads, general roads, and bridges (Oman et al., 2001; Phares et al, 2005). Both studies concluded that agricultural vehicles could cause substantial damage to pavements and therefore should be considered in pavement design. A broader pool study lead by MnDOT was concluded in 2011 with full scale testing of pavement sections subjected to agricultural vehicles. The study provided many important recommendations regarding loading of shoulders by agricultural vehicles, potential for one-time failures by different vehicles types and axle load distribution (Lim et al., 2011).

DOI: 10.1201/9781003222897-33

One of the difficulties in including agricultural vehicles in pavement design and evaluation is the load analysis due to the unique tires of these vehicles. To analyze pavement responses, these unconventional tires must be processed in a way that is possible to simulate the loads in a pavement analysis software. Research has advanced greatly in the analysis of tire contact area (footprints) of conventional trucks (Hernandez et al, 2013; Hernandez et al, 2014). For agricultural vehicles, Lim et al. (2011) scanned agricultural vehicles tires and compared different modes of processing tire footprints. The authors recommended the use of multiple circles in which each footprint for a single tire was considered as a load. However, this method requires a great level of detail from the scanned footprint. In addition, computing each individual footprint is time consuming and prone to errors.

The objective of this paper is to determine if the tire load as delineated by the entire tire footprint can be represented using the gross footprint area in comparison with the multiple circle footprint approach which considers the area of each individual footprint. For that, the gross and multiple circle footprint areas and correspondent pressures were determined. The data accuracy was evaluated by comparing equal tires subjected to slightly different loads in different load levels. Finally, pavement responses using both methods were compared.

2 AGRICULTURAL VEHICLES FOOTPRINT ANALYSIS

Tire footprints from six different tires were obtained from measurements performed with a Tekscan device along with axle weight estimated with scales. The Tekscan device is composed of sensorial mats (Figure 1a) and data handles with attached cables (Figure 1b). The sensorial mats are approximately 0.6 m by 0.9 m. with a sensing area of 0.57 m by 0.88 m. As the truck passes over the sensorial mats with constant speed the Teckscan software records information from the pass to create the tire footprints. A detailed process of these measurements can be found in Lim et al. (2011). The data was corresponded to different load levels: 0%, 50% and 80% of tank capacity as detailed in Table 1.

Figure 2 shows tire footprints from an agricultural vehicle under different load levels and a footprint from a semi-truck rear dual axle. Both footprints were obtained using a sensorial pressure mat Tekscan under the TPF-5(148) study (Azari 2012). The footprint significantly increases in size with the increase of the wheel load. However, the AASHTO-ME procedure for flexible pavements assumes that an increase in the wheel load leads to a proportional increase in contact pressure between the wheel and the pavement surface unaffecting the footprint radius.

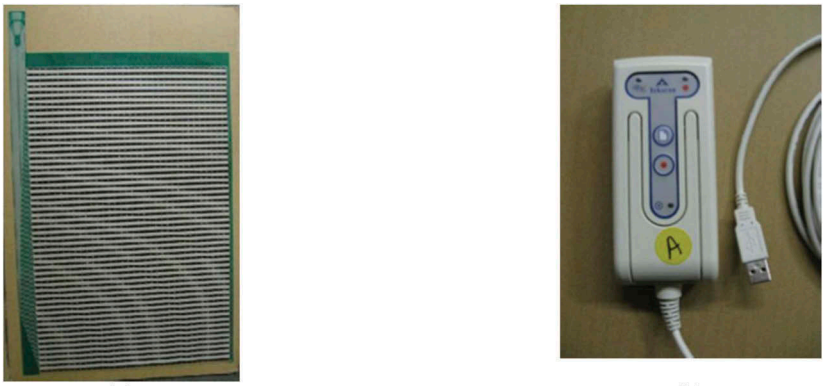

Figure 1. Examples of tire footprints from an (a) agricultural vehicle and (b) commercial truck (Lim et al 2011).

Table 1. Tire types and load levels.

Vehicle Type	Axle	Tire Name	Load Level	Tire Load (kN)
A (S1-S5*)	2	Alliance Flotation (29× 47)	0%	18.50
			50%	35.01
			80%	43.95
	3		0%	15.75
			50%	33.70
			80%	44.26
B (S2-S4*)	2	315/80r 22.5	0%	17.13
			50%	33.50
			80%	42.97
	3		0%	15.17
			50%	34.56
			80%	45.02
C (T3-T6*)	3	Firestone Bias/30.5Lx32	0%	17.35
			50%	41.37
			80%	46.71
	4		0%	17.59
			50%	41.37
			80%	48.49
D (T1*)	3	Galaxy/725/65x26	0%	13.97
			50%	37.28
			80%	46.71
	4		0%	17.75
			50%	43.48
			80%	54.89
E (T2*)	3	Alliance Bias 28Lx26 Flotation	0%	10.05
			50%	26.91
			80%	37.63
	4		0%	9.96
			50%	25.44
			80%	34.74
F (T4-T7*)	3	Galaxy/725/65x26	0%	14.19
			50%	32.07
			80%	43.10
	5		0%	14.50
			50%	35.36
			80%	46.97

* Vehicle type as classified by Lim et al. (2011). More information on vehicle type and axle configuration can be found in Lim et al. (2011).

As illustrated in Figure 3, tire footprints were classified in three types: type 1 with a single or double footprint in a roughly square shape; type 2 with multiple scattered footprints; and type 3 with multiple elongated and clustered footprints.

The area of the footprint can be represented by a gross area encompassing all the footprints or by using the multiple circle approach in which the total area is the sum of areas of each individual footprint of a single tire. Depending on the chosen approach, load area, and consequently, load pressure can be significantly different, especially for tire types 2 and 3. Type 1 footprints are the typical footprints used for conventional trucks in pavement design and therefore will not be used in this analysis.

2.1 *Gross tire contact area*

To analyze the effect of various tires on pavement structural responses, the tire footprints (Figure 4a) captured by the Tekscan device were processed to determine a gross tire contact

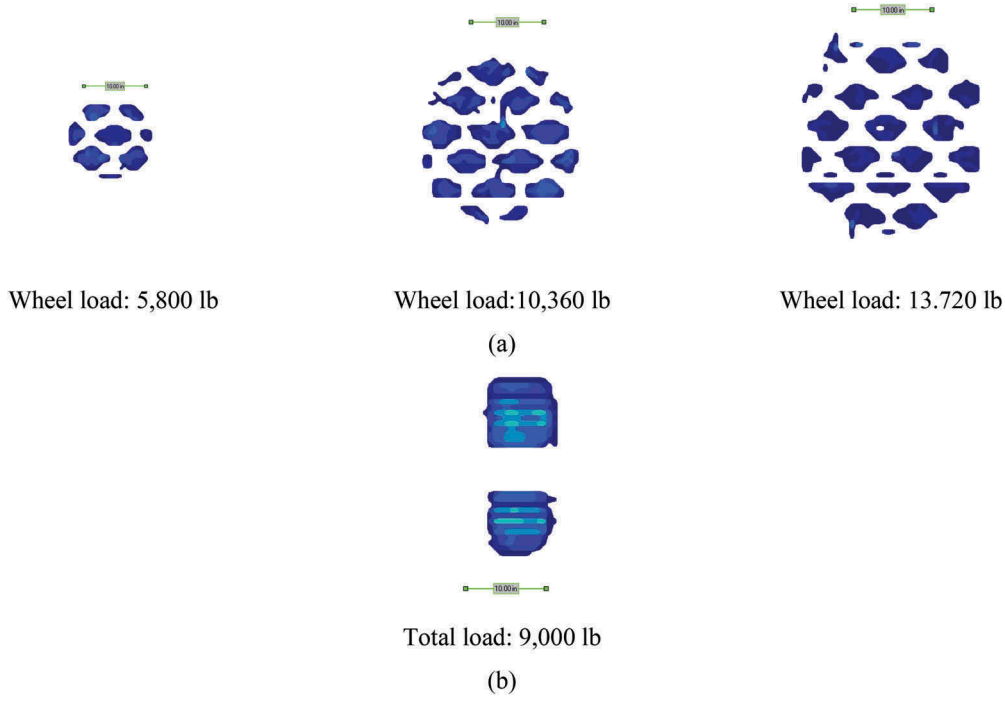

Figure 2. Examples of tire footprints from an (a) agricultural vehicle and (b) commercial truck (Adapted from Azari 2012).

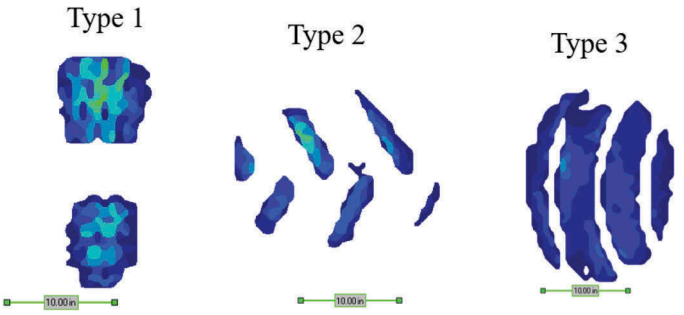

Figure 3. Typical tire footprints for agricultural vehicles.

area. The gross area includes the entire footprint area with high contact stresses (including the gaps between high contact pressure areas). The tire footprints captured by the Tekscan device were processed to determine the gross tire contact area as illustrated in Figure 4 for an Alliance flotation tire. The process involves determining the pentagon shape external boundary of the Tekscan-measured footprint and subdividing it into triangles to compute the area.

2.2 *Gross tire pressure*

Assuming that the tire contact pressure is uniformly distributed over the estimated gross contact area, the gross tire pressure can be calculated as:

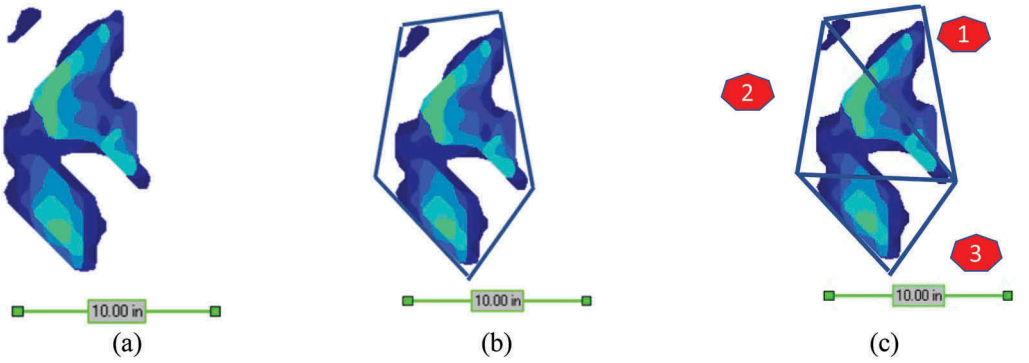

Figure 4. Gross tire contact area estimation from tire footprint.

$$Gross\ Tire\ Pressure\ (psi) = \frac{Wheel\ Load(lbs)}{Gross\ contact\ Area(in^2)} \tag{1}$$

To evaluate the repeatability of this procedure, the gross tire pressures were computed for six tire types of manure tanks subjected to three load levels corresponding to 0%, 50% and 80% of tank capacity as detailed in Table 1. For each tire type, two tires from different axles were analyzed. Figure 5 presents the comparisons of the computed gross pressures for the same tire type and similar load levels from different axles. A very good agreement is observed. Although wheel loads varied significantly (up to 4 times) between the load levels, the computed gross pressures differ by less than 10% and were approximately equal to the cold inflation pressure.

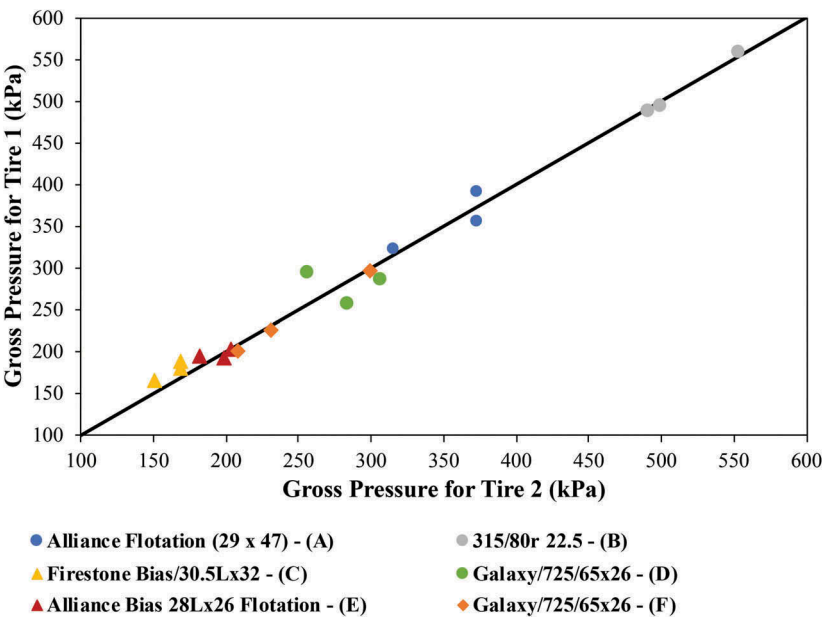

Figure 5. Comparison of gross pressure for identical tires on different axles subjected to the same load level.

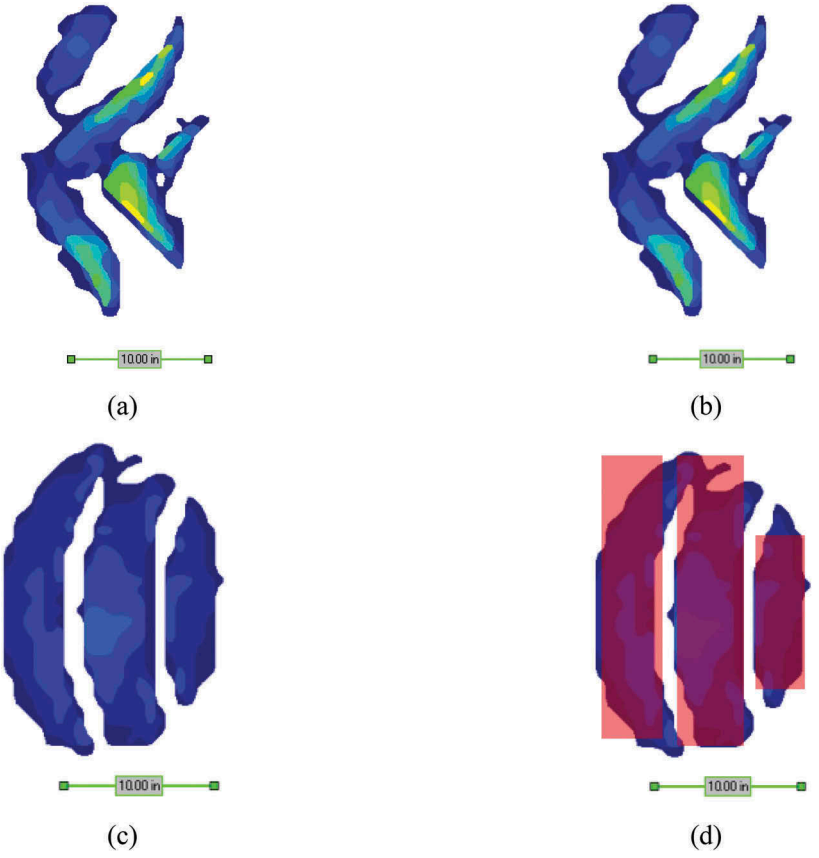

Figure 6. Tire footprints and equivalent rectangles for tires (a) and (b) Alliance Flotation (29 x 47) (A vehicle) and (c) and (d) Galaxy/725/65x26 (D vehicle).

2.3 *Multiple circle tire area*

Figure 6a and Figure 6c presents two examples of tire footprints used to compute the total area considering the multiple circle approach. Primarily, each individual footprint area was assigned with an equivalent rectangle to estimate the area of each individual footprint (Figure 6b and Figure 6d). The height and width of each pre-determined rectangle was recorded along with the scale of each scan. The total area is the sum of the areas of each individual footprint for the same tire. This process was conducted with a basic drawing computer application. For future studies, a more efficient and automated process should be considered.

2.4 *Multiple circle tire pressure*

Multiple circle tire pressure was computed using a similar process for gross tire pressure but considering the total sum of all individual footprint areas.

$$Multiple\ Circle\ Tire\ Pressure\ (psi) = \frac{Wheel\ Load(lbs)}{\sum Individual\ footprint\ Area(in^2)} \tag{2}$$

3 PAVEMENT RESPONSES UNDER GROSS AND MULTIPLE CIRCLE TIRES

A flexible pavement was analyzed to compare pavement responses when using the gross or multiple circle tire approaches. Table 2 shows the pavement parameters inputs for the simulation using the pavement analysis software MnLayer (Khazanovich and Wan, 2007). A thin – 76 mm hot mix asphalt surface layer – pavement was selected since the effect of load geometry is more pronounced for thinner structures.

Pavement responses were recorded at the bottom of the asphalt layer (longitudinal strain) and at the top of the subgrade (vertical strain).

3.1 *Tire load processing for pavement simulation*

The pavement was subjected to vehicle loading considering two models: the single load model in which the gross radii based on the gross area and the gross pressure were used; and the multiple load model in which the multiple circle approach was used.

For the single load model simulation, the total gross area as an equivalent circle area was used to compute the gross load radii. The gross radius and pressure were used as input in MnLayer.

Regarding the multiple load simulation, for each tire, a rectangle footprint center was chosen as the center of the load. Transversal and longitudinal coordinates for each individual footprint (rectangle) were obtained regarding the load center. Actual footprint rectangle dimensions and coordinates were computed based on scale.

Each individual footprint in a same tire was considered as a circle with equivalent area regarding the footprint rectangle (Figure 7). Radius was calculated for each footprint. Tire load was computed regarding total axle load and number of tires in one axle. Assuming that tire load was proportionally distributed for each footprint based on footprint area, pressure was equal to each footprint in a same tire.

Table 2. Thin flexible pavement input parameters.

	Asphalt Surface Layer			Base Layer			Subgrade	
Pavement Structure	Elastic Modulus (MPa)	Poisson's Ratio	Thickness (mm)	Elastic Modulus (MPa)	Poisson's Ratio	Thickness (mm)	Elastic Modulus (MPa)	Poisson's Ratio
Thin	5,861	0.33	76.2	294	0.41	152.4	98	0.49

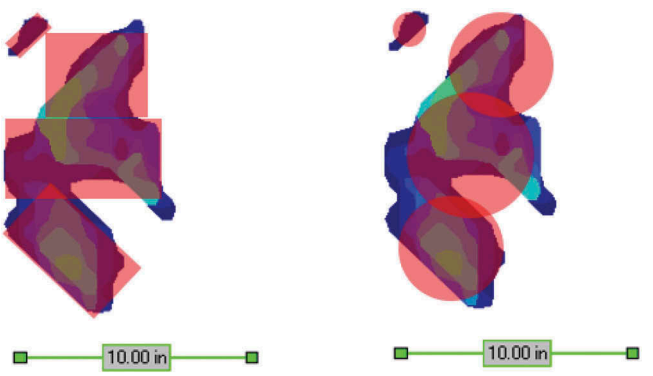

Figure 7. Tire footprint equivalent area from rectangle to circle for tire Alliance Flotation (29 x 47), vehicle A, axle 2 at 0% load level.

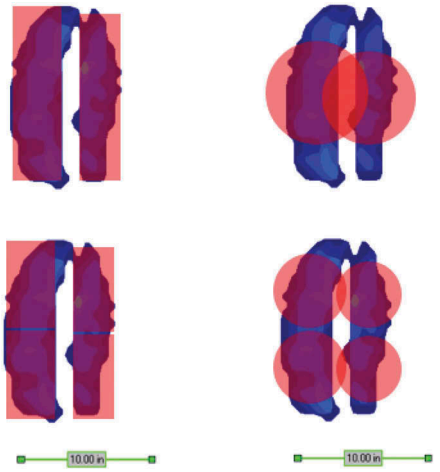

Figure 8. Tire footprint division to minimize load overlapping in tire Galaxy/725/65x26, vehicle D, axle 4 at 0% load level.

Table 3. Tire load input for pavement simulation.

#	Vehicle	Axle	Tire	Tire Load (kN)	Gross Area (m^2)	Gross Pressure (kPa)	Multiple Circle Total Area (m^2)	Multiple Circle Total Pressure (kPa)
1	A	3	Alliance Flotation (29 × 47)	44.26	0.1248	354.57	0.0979	451.99
2	E	3	Alliance Bias 28L×26 Flotation	10.05	0.0551	182.55	0.0415	242.52
3	F	5	Galaxy/725/65×26	46.97	0.2094	224.28	0.1372	342.34
4	D	3	Galaxy/725/65×26	46.71	0.1522	306.97	0.1337	349.26

Tire footprints that presented a ratio between width and height smaller then 1.5, i.e., elongated footprints, were divided in height to create more square shaped footprints. This was performed to avoid load overlapping in tires with multiple footprints. Figure 8 illustrates this process. After that these rectangles are replaced with circles with the same areas and centers of gravity.

The load parameters that were simulated using MnLayer considering the single load model (gross area and pressure) and the multiple circle load model are displayed in Table 3.

3.2 *Comparison of pavement responses*

For the single load model, pavement responses were obtained under the center of the load. For the multiple circle load model, pavement responses were obtained in using two methods:

1) The response under each individual load (footprint) was computed. The maximum response between each individual load was selected.

2) The response at the center of gravity of the loaded area was computed. The coordinates of the center of gravity were obtained by summation of the transversal and longitudinal

Table 4. Longitudinal strain at the bottom of the asphalt layer for different load models.

	Single Load	Multiple Circle Load (Method 1)		Multiple Circle Load (Method 2)	
#	yy Strain	yy Strain	Δ%	yy Strain	Δ%
1	1.87E-04	1.81E-04	3%	1.49E-04	25%
2	7.37E-05	7.44E-05	-1%	7.53E-05	-2%
3	1.29E-04	1.43E-04	-9%	1.35E-04	-4%
4	1.69E-04	1.86E-04	-9%	1.09E-04	55%

Table 5. Vertical strains at the top of the subgrade for different load models.

	Single Load	Multiple Circle Load (Method 1)		Multiple Circle Load (Method 2)	
#	zz Strain	zz. Strain	Δ%	zz Strain	Δ%
1	-7.66E-04	-7.29E-04	5%	-7.52E-04	2%
2	-2.14E-04	-2.20E-04	-3%	-2.21E-04	-3%
3	-6.63E-04	-6.40E-04	4%	-6.66E-04	-1%
4	-7.53E-04	-7.65E-04	-1%	-7.94E-04	-5%

coordinates of the centers of the circular footprints multiplied by the footprint areas and dividing the sum by the total area of all footprints.

Table 4 and Table 5 show the results for longitudinal strains at the bottom of the asphalt layer and vertical strains at the top of the subgrade, respectively. Both tables present comparative results indicating the percent difference (Δ%) in each response when using the single load model instead of the multiple circle load model.

Results indicate that using the gross area to represent the tire footprint and estimate tire pressure produces equivalent pavement responses to using the net load area for vertical strains at the top of the subgrade regardless of the method used to compute the net load responses.

Both loading models resulted in similar vertical subgrade strains for all tires. A larger difference was observed for the computed asphalt strains. The asphalt strains computed using the multiple circles model with Method 2, i.e., at the center of gravity of the loading area, can be significantly lower than the strains obtained with Method 1 or with the single load model. This happens when the center of gravity is located between the individual circles meaning that no pressure is applied at this location as illustrated in Figure 8.

The asphalt strains computed using the multiple circles model with Method 1 might be up to 9% higher than the strains computed using the single load model. It should be noted that for Method 1 strains are very sensitive to the choice of circles sizes and locations. Considering any potential inaccuracies with the footprint measurements with the Tekscan device, we might conclude that the single load model based on the gross area determination yields reasonable estimates of the maximum asphalt and subgrade strains.

4 CONCLUSIONS

Tire footprints from six different agricultural vehicles were processed using two approaches to compute tire contact area and pressure. Pavement simulations indicate that using a single load based on the gross area which encompasses the whole tire footprint region produces equivalent pavement responses than using the multiple circle load model where each individual footprint is considered as a load. Since the former involves a much simpler processing than the latter, this prelaminar result can be beneficial for the inclusion of agricultural vehicles for pavement design and analysis.

The consideration of agricultural vehicles in pavement design and analysis of rural roads can have a significant impact on the roads' structural and functional integrity. This research proposed an efficient method to compute agricultural vehicles loads for pavement analysis. Future studies can be focused on developing comprehensive databases for agricultural vehicles' footprints and their effect on the responses of typical rural road pavements.

REFERENCES

Azary, A., 2012. *Quantification of the Effects of Heavy Agricultural Vehicle Loading on Pavement Performance*. Master of Science Thesis. University of Minnesota.

Fanous, F., Coree, B., Wood, D., 1999. *Response of Iowa Pavements to Heavy Agricultural Loads*. Ames, IA: Center for Transportation Research and Education at Iowa State University.

Hernandez, J., Al-Qadi, I., De Beer, M. 2013. *Impact of Tire Loading and Tire Pressure on Measured 3D Contact Stresses*. 2013 Airfield & Highway Pavement Conference

Hernandez, J., Games, A., Al-Qadi, I., De Beer, M. 2014. *Analytical Approach for Predicting Three-Dimensional Tire-Pavement Contact Load*. Transportation Research Record 2456(-1):75–84

Khazanovich L., Wang Q. 2007. MnLayer: High-Performance Layered Elastic Analysis Program. Transportation Research Record. 2037(1):63–75. doi: 10.3141/2037-06

Lim, J., Azary, A., Khazanovich, L., Wang, S., Kim, S., Ceylan, H., Gopalakrishnan, K., 2011. *Effects of Implements of Husbandry (Farm Equipment) on Pavement Performance*. MN/RC 2012–08. St. Paul, MN: Minnesota Department of Transportation.

Oman, M., Deusen, D. V., Olson, R., 2001. *Scoping Study: Impact of Agricultural Equipment on Minnesota's Low Volume Roads*. St. Paul, MN: Minnesota Department of Transportation.

Phares, B. M, Wipf, T., Ceylan, H., 2005. I*mpacts of Overweight Implements of Husbandry on Minnesota Roads and Bridges*. Synthesis Report MN/RC-2005-05. St. Paul, MN: Minnesota Department of Transportation.

Sebaaly, P. E., Siddharthan, R. V., El-Desouky, M., Pirathapan, Y., Hitti, E., Vivekanathan, Y., 2002. *Effects of Off-Road Tires on Flexible and Granular Pavements*. Final Report SD1999-15-F. Pierre, SD: South Dakota Department of Transportation.

Eleventh International Conference on the Bearing Capacity of Roads, Railways and Airfields, Volume 2 – Hoff, Mork & Saba (eds)

Characterizations of super heavy loading configuration for flexible pavement analysis

Yongsung Koh
Graduate Research Assistant, Department of Civil, Construction and Environmental Engineering (CCEE), Iowa State University, Ames, Iowa, USA

Halil Ceylan
Ph.D., Pitt-Des Moines, Inc. Department of Civil, Construction and Environmental Engineering (CCEE), Iowa State University, Ames, Iowa, USA
Director of Program for Sustainable Pavement Engineering and Research (PROSPER)

Sunghwan Kim
Ph.D., P.E., Associate Director of PROSPER, Institute of Transportation, Iowa State University, Ames, Iowa, USA

In Ho Cho
Ph.D., Associate Professor of Department of Civil, Construction and Environmental Engineering (CCEE), Structural Engineering and Intelligent Infrastructure Engineering, Iowa State University, Ames, Iowa, USA

ABSTRACT: Super-heavy loading vehicles, also called superloads, have weight, size, and loading configurations different from those of traditional vehicle classes found in Federal Highway Administration (FHWA) classifications. In general, superloads include Implements of Husbandry (IoH), non-divisible vehicles, and other non-standardized industrial vehicles. Although oversize/overweight load permit regulations differ somewhat among State Highway Agencies, superloads can potentially exceed regulated load limits and cause unexpected distress and damage to pavement systems. Accordingly, to satisfactorily and more accurately determine the impact of superloads on pavement systems with less time-consuming pavement analysis, it is important to characterize superload loading configurations. This study will focus on a method of identifying the number of tire loadings (i.e., nucleus segment) required in analyzing the impact of IoHs on flexible pavement systems. Layered Elastic Theory (LET)-based analysis using MnLayer has been performed to determine the nucleus segments of IoHs, followed by determining critical flexible-pavement responses such as horizontal tensile strain at the bottom of an asphalt surface layer for assessing fatigue-cracking potential, and determining vertical compressive strain at the top of the subgrade for assessing rutting potential induced by applying a nucleus segment of IoH as a loading input. Using the superposition method, the critical flexible-pavement responses induced by the nucleus segments of IoHs can be compared to those induced by only one row of tire loadings within the nucleus segment to confirm its applicability to performing analysis of pavement under IoHs with reduced computational effort.

Keywords: Super-heavy loading vehicle, Implement of husbandry, Flexible pavements, Nucleus segment, Superposition method

DOI: 10.1201/9781003222897-34

1 BACKGROUND

Unlike traditional vehicle types included in Federal Highway Administration (FHWA) vehicle classifications, super-heavy loading vehicles, also called superloads, have significant potential for damaging pavement systems by carrying heavy cargo, e.g., agricultural products, livestock product, excavators, or wind towers, in addition to their own intrinsic weights. Weights, including heavy cargo, are distributed through each tire of a superload, so that each tire load impacts the pavement system directly through tire-pavement contact (Siddharthan et al. 2005). To accurately identify the impact of superloads on a pavement system, up-to-date development of tire or axle loading by each superload must be found to help engineers perform pavement analysis under superloads while fully considering loading conditions for establishment of dimensional and weight regulations of transportation vehicles. The critical load factors of a superload that would affect resulting pavement distresses vary not only with the number of tires and axles, but also with other factors such as tire-pressure variation, use of wide-base rather than dual tires, vehicular-tire types (e.g., radial tire, bias tire, etc.), and suspension types (Kim et al. 2005). Because of the current trucking-industry trend of pursuing high-efficiency and large-scale transportation vehicles to transport agricultural commodities or industrial products, the number of tires and axle configurations along with their loading magnitudes are still considered major factors in predicting pavement damage resulting from heavy transportation vehicles. This has led U.S. states to restrict axle loadings and Gross Vehicle Weights (GVWs) to protect road infrastructures and to secure driver safety, either by adopting federal weight and size limits for trucks or establishing their own limit regulations in different states.

Superloads can be distinguished from general vehicle types not only by high GVWs and axle loadings that may exceed the allowed dimensions of a state's permit limit, but also by their non-standardized configurations of tires and axles representing a wide range of dimensions with respect to number, spacings, and loading magnitudes. An Implement of Husbandry (IoH) is a representative type of superload known to be a major type of transport vehicle whose use has resulted in unexpected damages on pavement systems, especially in the Midwestern region of the U.S. (Ceylan et al. 2015, Lim et al. 2012, Phares et al. 2004). The main feature of an IoH is that it consists of a tractor and trailer, or even just a tractor by itself, whose highest loading portion tends to be allocated mostly over the rear axle group due to placement of the cargo load. Even though IoHs tend to reflect non-standardized tire and axle configurations, most of them can be satisfactorily analyzed by mainly considering only their rear axle group, allowing engineers to efficiently analyze pavement systems subjected to IoHs with relatively low computational effort. However, to catch up with the rapidly-evolving mechanical equipment, particularly the transportation vehicles, a mechanistic analysis methodology to determine proper loading configurations of IoHs on pavements is needed.

In this paper, an innovative method of identifying the number of influencing tires introduced in a previous FHWA study (Nimeri et al. 2018), a so-called nucleus segment, has been used to represent the entire IoH loading applied to the flexible pavement analysis as a loading input. To determine the nucleus segments of IoHs, mechanistic analysis was performed using the Layered Elastic Theory (LET)-based program MnLayer (developed by Khazanovich and Wang 2007) to obtain critical flexible pavement responses such as vertical compressive strain at the top of the subgrade induced by incremental tire loadings. Moreover, to reduce computational effort, a superposition method has been introduced as a post-processing step and applied to analysis of flexible pavement under IoHs.

2 OVERVIEW OF CHARACTERIZATION METHODS

Since configurations of tire or axle loadings vary greatly over the spectrum of IoH types, it is impossible to classify all IoHs using traditional classification methods based on the number of axles (i.e., single, tandem, tridem, and quad axle) within the critical-loading portion. Instead,

a newly-developed characterization method for identifying the influencing tires, i.e., the nucleus segment, a group of critical tire loadings representing the entire IoH loading as a loading input, has been applied. To perform mechanistic analysis for determining the nucleus segment of each type of IoH, an LET-based analysis program, MnLayer, has been used.

Furthermore, application of the superposition method in post-processing has been introduced to demonstrate how it can reduce the total volume of analysis by obtaining critical-pavement responses under single-axle loading only, eliminating the need to apply all axle loadings within a given nucleus segment.

2.1 *Identification of loading inputs: Nucleus segment*

Recent study had developed a new approach for identifying the nucleus segment, particularly for Superheavy Loads (SHL) comprised of specialized large and heavy trailers with larger numbers of axles than general truck types (Nimeri et al. 2018). The same approach was also applied to another recent flexible-pavement study of SHLs, constructing data-driven surrogate models to provide high performance in predicting critical-pavement responses under nucleus segment loadings (Koh et al. 2022).

To begin identification of nucleus segments of an IoHs, a specific type of critical pavement response, e.g., vertical strain or vertical stress at the subgrade top, under an incremental number of tire loadings at a particular depth beneath the flexible-pavement surface should be determined. The critical pavement response from one tire-loading only immediately below the first tire-loading point will be increased when two or more tire loadings are added, as shown in Figure 1. In our case, to determine fully-overlapping impact when multiple tire loadings have been applied, we chose vertical strain at the top of subgrade ($\varepsilon_{v,sg}$) as a specific type of pavement response. The number of tire loadings should be increased from one up to the specific number where the last-added tire-loading influences by less than 5% the magnitude of critical pavement response resulting from the first tire-loading determined immediately below the first tire-loading point (Figure 2). This specific number of tire loadings will be defined as the influencing number of tires, and the tire group comprised of influencing tires in both X and Y directions will be defined as the nucleus segment.

As shown in Figure 2, the critical pavement response determined immediately below the first loading point is significantly influenced by the tire spacing. If an IoH has a tire spacing more than 1500 mm from the previous tire loading and would not influence the critical pavement response at the first loading point, additional tire loading need not be considered as influencing tires (Luo et al. 2017, Rada et al. 2016).

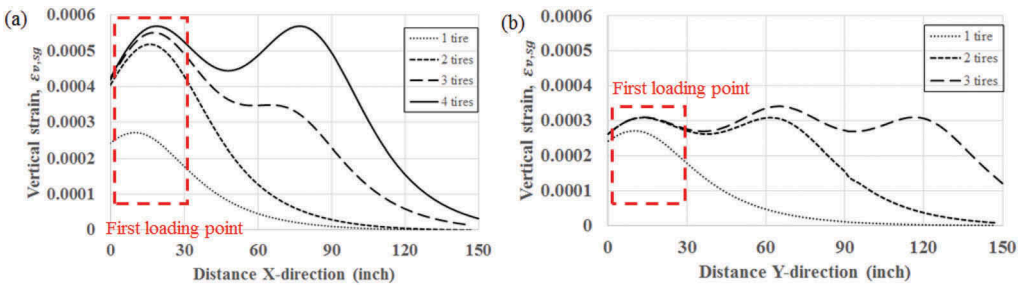

Figure 1. Distribution of vertical strain at the top of subgrade ($\varepsilon_{v,sg}$) under one to four tire loadings for X-direction (lane-width direction) (a), and under one to three tire loadings for Y-direction (traffic direction) (b).

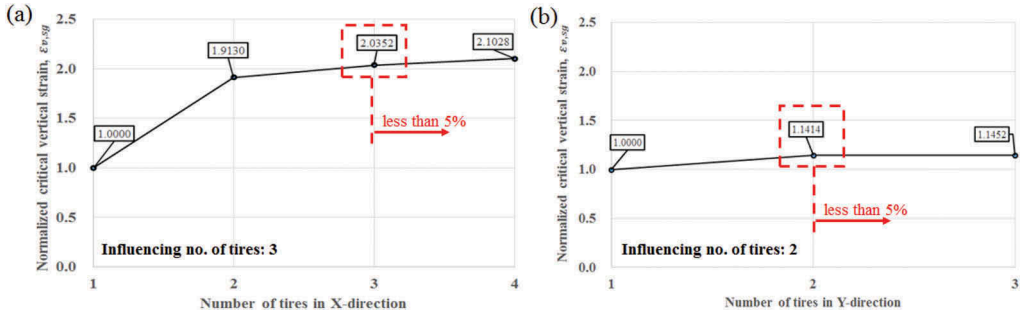

Figure 2. Normalized critical vertical strain at the top of subgrade ($\varepsilon_{v,sg}$) immediately below the first loading point variation with the number of tire loadings in the X-direction (lane-width direction) (a), and in the Y-direction (traffic direction) (b).

2.2 *Post-processing: Superposition method*

After determining the nucleus segment of each IoH as a loading input, critical pavement responses can be obtained by mechanistic flexible-pavement analysis empirically transferred into pavement distresses. To reduce the required computational effort from all analysis cases, pavement responses generated by a single-axle loading of IoH can be determined, followed by expanding the analysis results from the single-axle loading case to tandem, tridem, and quad-axle cases through application of the superposition method during post-processing. According to the Guide for Mechanistic-Empirical Design, at least 70 response points distributed in both the lane-width direction (X-direction) and the traffic direction (Y-direction) are needed to linearly calculate locations and magnitudes of critical pavement responses under single, tandem, tridem, and quad axle loadings, as shown in Figure 3 (Witczak and El-Basyouny 2004).

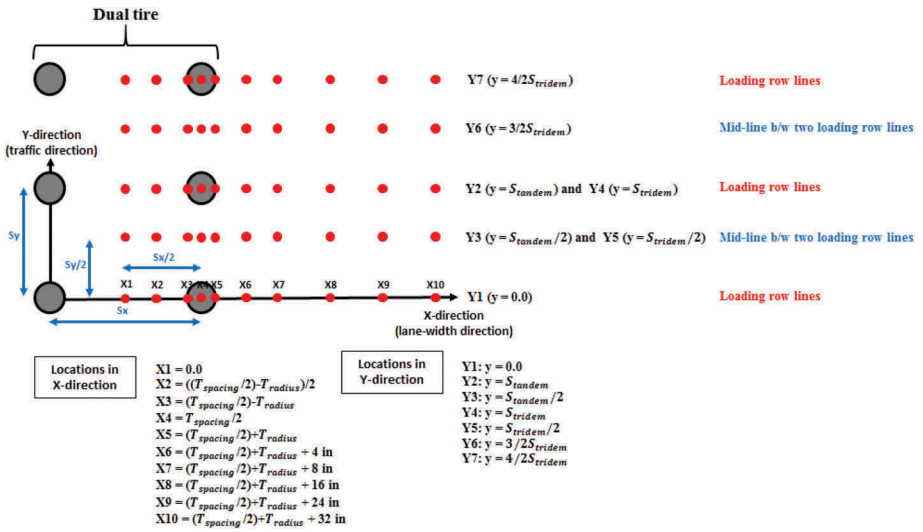

Figure 3. Schematic drawing of the superposition method.

Since the superposition method calculates the critical pavement responses under single, tandem, tridem, and quad axle loadings by combining pavement responses at specific locations under single-axle loading using a linearly-elastic approach, it can be assumed that the

critical pavement response will only occur exactly either at the loading row lines (Y1, Y2, Y4, and Y7 in Figure 3) or at the mid-line between two loading row lines (Y3, Y5, and Y6 in Figure 3) with respect to the Y-axis, as shown in Table 1. By comparing all the pavement responses about the X-axis (X1 to X10 in Figure 3), the critical pavement response among 70 response points can eventually be determined.

Table 1. Equations to calculate critical pavement responses using the superposition method.

Location of critical responses	Single axle	Tandem axle	Tridem axle	Quad axle
Critical response at the loading row lines	$Y1$	$Y1 + Y2$	$Y1 + 2 \times Y4$	$Y1 + 2 \times Y4 + Y7$
Critical response at the mid-line	-	$2 \times Y3$	$2 \times Y5 + Y6$	$2 \times Y5 + 2 \times Y6$

3 MECHANISTIC ANALYSIS FOR LOADING CHARACTERIZATION

The nucleus segments of IoHs were determined as loading inputs, followed by use of the superposition method to calculate the critical pavement responses under each nucleus segment.

3.1 *Precedent classification of Implements of Husbandry (IoH)*

Since a previous study had performed research related to analysis of bridges under various types of IoH, encompassing most farm equipment found on secondary roadway bridges in the U.S. (Freeseman et al. 2017), 120 types of IoH were adapted from that study for identifying nucleus segments. Among those 120 types, only 4 types of IoH consisted solely of tractors, while the others represented tractor-trailer combinations. As mentioned previously, since trailers most often weigh more than tractors because of their additional loading from heavy cargo, it seemed reasonable to reduce the 120 types of IoH into 18 types by classifying some IoHs into groups with identical trailers, as shown in Table 2.

Table 2. List of trailers from original list of IoHs (Freeseman et al. 2017).

No.	Name of trailer	Trailer type	No.	Name of trailer	Trailer type
1	Kinze 1050 ROW	Grain Cart	10	Kinze 1050 SOF	Grain Cart
2	Houle 3-axle Tank	Manure Tanker	11	Balzer 1250	Grain Cart
3	Houle 2-axle Tank	Manure Tanker	12	Balzer 1500	Grain Cart
4	Half Full Houle 7300 Tank	Agricultural Truck	13	J&M 1075-22	Grain Cart
5	Balzer 6350 Narrow	Manure Tanker	14	Empty NUHN QT Quad Tanks	Agricultural Truck
6	Brent 1082 Grain Wagon	Agricultural Truck	15	Terragator 8400	Agricultural Truck
7	Better-Bilt 3400	Manure Tanker	16	Terragator 7300	Agricultural Truck
8	Better-Bilt 4950	Manure Tanker	17	Terragator 2505	Agricultural Truck
9	Better-Bilt 6600	Manure Tanker	18	Case 340B	Agricultural Truck

3.2 *Identification of nucleus segments*

As a preliminary step, entire sets of tires within each trailer could be grouped separately if there was more than a 1500-mm spacing between tires or axles. Detailed properties of each trailer, including GVWs, number of tires and axles, and tire and axle spacings are shown in Table 3.

Table 3. Properties of trailers of IoHs.

Name of trailer	GVW (kg)	Tire			Axle		
		Type	Number in 1 axle	Spacing (mm)	Pressure (MPa)	Number	Spacing (mm)
Kinze 1050 ROW	33,285	Dual	4	762, 1,593, 762	0.192	1	-
Houle 3-axle Tank	36,197	Single	2	2,134	0.080	3	1,737
Houle 2-axle Tank	28,386	Single	2	2,134	0.094	2	1,737
Half Full Houle 7300 Tank	22,136	Single	2	2,438	0.049	3	1,768
Balzer 6350 Narrow	32,825	Single	2	2,225	0.092	2	1,769
Brent 1082 Grain Wagon	7,103	Single	2	2,377	0.030	1	-
Better-Bilt 3400	16,711	Single	2	2,408	0.082	2	1,250
Better-Bilt 4950	24,723	Single	2	2,438	0.121	2	1,341
Better-Bilt 6600	33,783	Single	2	2,560	0.110	3	1,585
Kinze 1050 SOF	32,704	Single	2	2,438	0.072	1	-
Balzer 1250	39,473	Single	2	3,048	0.114	2	1,981
Balzer 1500	46,869	Single	2	3,048	0.102	3	1,981
J&M 1075-22	31,162	Single	2	3,719	0.129	1	-
Empty NUHN QT Quad Tanks	8,301	Single	2	2,896	0.023	2	1,920
Terragator 8400	9,115	Single	2	2,286	0.014	2	5,121
Terragator 7300	9,115	Single	2	2,438	0.016	2	6,949
Terragator 2505	19,713	Single	2	2,438	0.024	3	1,951
Case 340B	29,000	Single	2	2,591	0.046	3	2,073

IoH trailers exhibit non-standardized tire and axle configurations, as can be seen in Table 3, and most trailers have axle and tire spacings greater than 1500 mm, except for three types: Kinze 1050 ROW for tire spacing, Better-Bilt 3400 for axle spacing, and Better-Bilt 4950 for axle spacing; for these nucleus segments were sought using a mechanistic approach using a LET-based program, MnLayer. To determine the specific number of tire loadings that would influence by not more than 5% the critical pavement response of the first tire loading point in both the X-direction and the Y-direction, vertical strains at the top of subgrade ($\varepsilon_{v,sg}$) induced by the three IoH trailers were determined. The flexible-pavement properties used for this analysis are given in Table 4. To obtain the highest number of influencing tires in the worst case, each layer was assumed to be relatively thick to secure sufficient depth from the loadings and fully overlap the influence of each loading. The seasonal modulus of elasticity was also varied to reflect seasonal effects in determining the nucleus segment.

Table 4. Structure and properties of flexible pavement for LET analysis.

Layers	Thickness (mm)	Modulus of elasticity (MPa)				Poisson's ratio
		Spring	Fall	Summer	Winter	
AC layer	380	3,447	3,447	689	13790	0.35
Base layer	305	172	241	241	345	0.35
Subbase layer	230	138	207	207	276	0.35
Subgrade	∞	34	69	69	117	0.35

The normalized $\varepsilon_{v,sg}$ under the incremental number of tire loadings based on only one tire loading was calculated for all three trailers, as shown in Figure 4. From these results, the nucleus segments of all trailers could be determined as shown in Table 5. Note that, according to Table 3, only two tires required consideration as influencing tires for the Kinze 1050 ROW (X-direction), the Better-Bilt 3400 (Y-direction), and the Better-Bilt 4950 (Y-direction). Other directions required consideration of only one tire as an influencing tire due to presence of a gap of at least 1500mm between axles or tires.

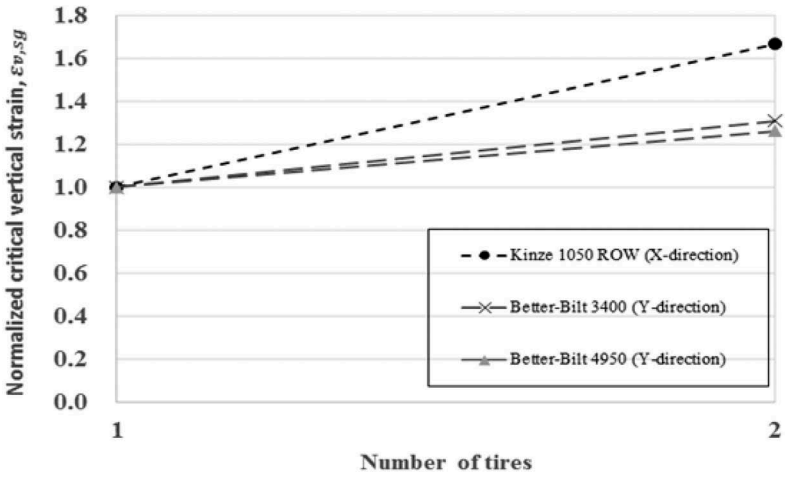

Figure 4. Normalized critical vertical strains for three types of trailer (spring season).

Table 5. Nucleus segments for all types of trailer.

Types	Kinze 1050 ROW	Better-Bilt 3400	Better-Bilt 4950	Others
Nucleus segment (X,Y)	(2,1) for all seasons	(1,2) for all seasons	(1,2) for all seasons	(1,1) for all seasons

3.3 *Determination of critical pavement responses to verify superposition method*

To confirm the applicability of the superposition method to analysis of flexible pavement subjected to IoHs loading, three types of trailers, a Kinze 1050 ROW, a Better-Bilt 3400, and a Better-Bilt 4950, were analyzed to obtain representative types of critical pavement response, e.g. vertical strain at the top of subgrade ($\varepsilon_{v,sg}$) and tensile strain at the bottom of the AC layer ($\varepsilon_{t,ac}$). By comparing the critical pavement responses determined directly from LET-based analysis under the whole nucleus segment with those obtained using the superposition method that included only one row of tire loadings within the nucleus segment, the applicability of the superposition method to flexible pavement under IoHs was verified by demonstrating that the results from two approaches were the same, as indicated in Table 6, Table 7, and Figure 5.

Table 6. Critical vertical strain at the top of subgrade from LET-based analysis applying the whole nucleus segment and superposition method using one row of tire loadings.

Types	Critical vertical strain at the top of subgrade (whole nucleus segment) ($\mu\varepsilon$)				Critical vertical strain at the top of subgrade (superposition method) ($\mu\varepsilon$)			
	Spring	Fall	Summer	Winter	Spring	Fall	Summer	Winter
Kinze 1050 Row	469	312	475	133	469	312	475	133
Better-Bilt 3400	193	123	173	56	193	123	173	56
Better-Bilt 4950	274	173	250	79	274	173	250	79

Table 7. Critical tensile strain at the bottom of AC layer from LET-based analysis applying the whole nucleus segment and superposition method using one row of tire loadings.

Types	Critical tensile strain at the bottom of AC layer (whole nucleus segment) ($\mu\varepsilon$)				Critical tensile strain at the bottom of AC layer (superposition method) ($\mu\varepsilon$)			
	Spring	Fall	Summer	Winter	Spring	Fall	Summer	Winter
Kinze 1050 Row	130	105	176	39	130	105	176	39
Better-Bilt 3400	49	38	61	15	49	38	61	15
Better-Bilt 4950	70	55	88	22	70	55	88	22

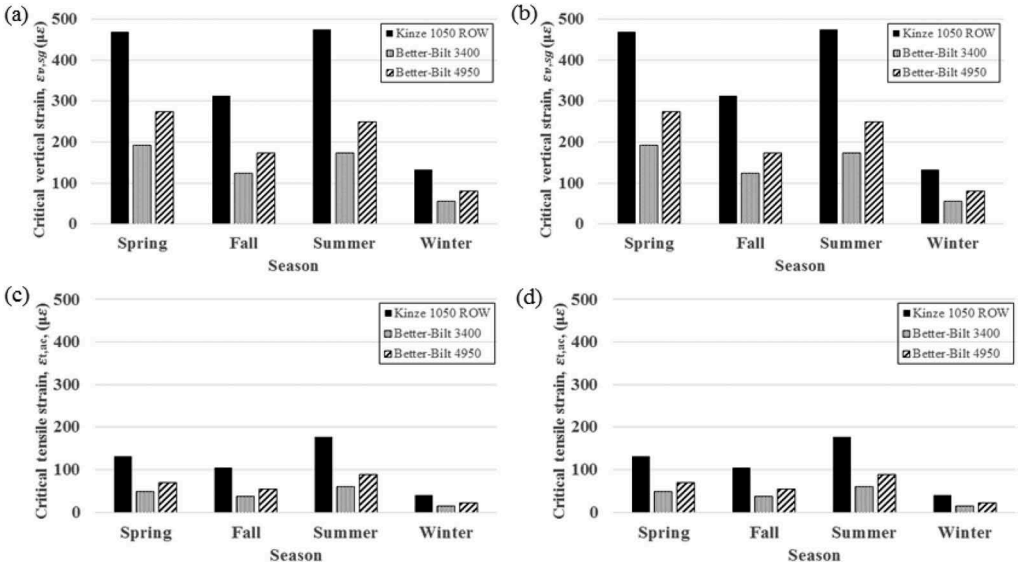

Figure 5. Critical vertical strain at the top of subgrade ($\varepsilon_{v,sg}$) applying whole nucleus segment (a) and superposition method (b); Critical tensile strain at the bottom of AC layer ($\varepsilon_{t,ac}$) applying whole nucleus segment (c) and superposition method (d).

4 CONCLUSIONS

The main features of superloads not only include their high GVWs and axle loadings, but also their non-standardized tire and axle configurations whose dimensions can widely vary. This is especially true for so-called Implements of Husbandry (IoH), a kind of superloads.

To determine reasonable loading configurations of IoHs as a loading input, mechanistic analysis using a LET-based program, MnLayer, was performed to determine a nucleus segment that could represent the entire IoH loading. To reduce computational effort, a superposition method was then introduced and applied as post-processing to the LET-based analysis of flexible pavement under IoHs. The results can be summarized as follows:

- Nucleus segments for 18 trailer types of IoH were determined as loading inputs for further LET-based pavement analysis;
- Critical pavement responses were calculated using the superposition method that applied only one row of tire loading within the nucleus segment as post-processing, and results were compared with those obtained when applying the whole nucleus segment. The identical results obtained from the two approaches reflect the excellent applicability of the superposition method to analyzing flexible pavements under IoHs.

ACKNOWLEDGEMENTS

The authors gratefully acknowledge the Iowa Highway Research Board and the Iowa Department of Transportation for supporting this study. The project technical advisory committee (TAC) members from Iowa county engineers, including Lee Bjerke, Zach Gunsolley, Todd Kinney, Brian Moore, Mark Nahra, John Riherd, Brad Skinner, Jacob Thorius, and Danny Waid, are gratefully acknowledged for their guidance, support, and direction throughout the research. The authors would also like to express their sincere gratitude to other research team members from Iowa State University's Program for Sustainable Pavement Engineering and Research (PROSPER) at the Institute for Transportation (InTrans) for their assistance. The contents of this paper reflect the views of the authors who are responsible for the facts and accuracy of the data presented within. The contents do not necessarily reflect the official views and policies of the Iowa Highway Research Board, the Iowa Department of Transportation, or Iowa State University. This paper does not constitute a standard, specification, or regulation.

FUNDING

The research (TR-781) is supported by the Iowa Highway Research Board and the Iowa Department of Transportation (Grants IHRB-187).

REFERENCES

Ceylan, H., Wang, S., Kim, S., Gopalakrishnan, K., Khazanovich, L., and Dai, S., 2015. *Impact of farm equipment loading on low-volume concrete road structural response and performance*. The Baltic Journal of Road and Bridge Engineering, 10(4), 325–332.

Freeseman, K., Phares, B., Greimann, L., and Kilaru, C.T., 2017. *Study of the Impacts of Implements of Husbandry on Bridges Volume III: Appendices* (No. IHRB Project TR–613).

Kim, D., Salgado, R., and Altschaeffl, A.G., 2005. *Effects of supersingle tire loadings on pavements*. Journal of Transportation Engineering, 131(10), 732–743.

Khazanovich, L., and Wang, Q. *MnLayer: High-Performance Layered Elastic Analysis Program*. Transportation Research Record, 2007. 2037(1), pp.63–75.

Lim, J., Azary, A., Khazanovich, L., Wang, S., Kim, S., Ceylan, H., and Gopalakrishnan, K., 2012. *Effects of Implements of Husbandry (Farm Equipment) on Pavement Performance*.

Luo, R., Gu, F., Luo, X., Lytton, R., Hajj, E.Y., Siddharthan, R.V., Elfass, S., Piratheepan, M., and Pournoman, S., 2017. *Quantifying the influence of geosynthetics on pavement performance* (No. NCHRP Project 01–50).

Nimeri, M., Nabizadeh, H., Hajj, E., Siddharthan, R.V., and Elfass, S., 2018. *Analysis Procedures for Evaluating Superheavy Load Movement on Flexible Pavements, Volume III: Appendix B, Superheavy Load Configurations and Nucleus of Analysis Vehicle* (No. FHWA-HRT-18-051). United States. Federal Highway Administration. Office of Infrastructure Research and Development.

Phares, B.M., Wipf, T.J., and Ceylan, H., 2004. *Impacts of overweight implements of husbandry on Minnesota roads and bridges*.

Rada, G.R., Nazarian, S., Visintine, B.A., Siddharthan, R.V., and Thyagarajan, S., 2016. *Pavement structural evaluation at the network level* (No. FHWA-HRT-15-074). United States. Federal Highway Administration. Office of Infrastructure Research and Development.

Siddharthan, R.V., Sebaaly, P.E., El-Desouky, M., Strand, D., and Huft, D., 2005. *Heavy off-road vehicle tire-pavement interactions and response*. Journal of Transportation Engineering, 131(3), 239–247.

Witczak, M.W., and El-Basyouny, M.M., 2004. *Calibration of Fatigue Cracking Models for Flexible Pavements. Guide for Mechanistic-Empirical Design, Appendix IT-1*. National Cooperative Highway Research Program, Washington, D. C.

Koh, Y., Ceylan, H., Kim, S., and Cho, I.H., 2022. *Critical Responses of Flexible Pavements Under Superheavy Loads and Data-Driven Surrogate Model*. International Journal of Pavement Research and Technology, 1–31.

Eleventh International Conference on the Bearing Capacity of Roads, Railways and Airfields, Volume 2 – Hoff, Mork & Saba (eds)

Contribution of dynamic vehicle loads to pavement failure

D. Rys
Faculty of Civil and Environmental Engineering, Gdansk University of Technology, Gdansk, Poland

ABSTRACT: Pavement surfaces are not ideally even, which causes dynamic loads of vehicle axles. Distribution of dynamic loads of a given axle is similar to normal distribution and can be described by static load and dynamic load coefficient. The dynamic load coefficient depends on road profile, vehicle speed, properties of suspensions and static load of axle. While for a given road section road profile remains constant, vehicle speed and suspension properties are subject to limited variations, the static loads of particular axle vary significantly. The weigh-in-motion systems are the source of data on static loads, which are characterized by axle load spectra. The axle load spectra are the key data input for pavement design. The article presents a new approach to inclusion of the dynamic loads in axle load spectra. The theoretical explanation is supported by sample calculations. A one-kilometer road section was selected for calculations and its profile was measured using laser road surface profilograph. The dynamic loads were then calculated using the quarter car model and parameters appropriate for heavy vehicle suspensions. This part of calculations proved that dynamic loads significantly increase for less loaded axles. Dynamic axle load spectra were calculated based on static axle load spectra and function of dynamic load coefficient. The load equivalency factors and truck factors were calculated using the fourth power equation and considering both static and dynamic axle load spectra. Contribution of dynamic loads to pavement failure equals up to 19% for the considered example of road profile, which is characterized by IRI = 1.54 m/km.

Keywords: axle load spectra, dynamic loads, International Rough Index, dynamic load coefficient, load equivalency factor

1 INTRODUCTION

Axle load spectra (ALS) are input data for advanced methods of pavement design according to the principles of mechanistic-empirical pavement design (M-EPDG). In M-EPDG, the number of equivalent standard axle loads (ESAL) was replaced with ALS, containing both the total number of vehicles and vehicle class distribution. However, in design methods that use ESALs to express traffic loads (including AASHTO 1993 method and catalogs of typical structures, which are used in many European countries), ALS are also used to determine load equivalency factors or truck factors, which are further used to transform number of trucks into the number of ESALs. Pavement life is commonly expressed by the number of ESALs resulting in pavement failure. Due to this fact, accurate determination of ALS result in more reliable design of pavement structure, regardless of the approach used to characterize the traffic loads.

ALS are determined on the basis of Weigh-in-Motion (WIM) data. Inaccuracy of axle load measurements may have impact on the ALS. The problem was solved using several methods, which enable identification and removal of incorrect data, as well as appropriate correction of ALS due to random or systematic error (Dawid Rys & Burnos, 2021). Despite the fact that

DOI: 10.1201/9781003222897-35

vehicles are weighed in motion, the data on axle loads are processed to represent static loads. ALS determined directly on the basis of WIM data represent static loads of vehicles as well. Due to surface roughness, pavements are loaded by vehicles dynamically. The article presents a new approach to include the dynamic loads from vehicles in ALS. The method is explained using an example case of road profile and a sample set of WIM data. Finally, the contribution of dynamic loads to pavement failures is calculated.

2 DYNAMIC LOAD COEFICIENT

Gillespie et al. (1992) performed measurements of dynamic loads of a wheel in motion. Distribution of dynamic loads is similar to normal distribution and can be described by the static load, which corresponds to their mean value, and the Dynamic Load Coefficient (DLC), which corresponds to coefficient of variation. DLC is a measure that characterizes the probability distribution of dynamic axle loads. It is defined as follows:

$$DLC = \frac{\sigma}{\overline{F}} \tag{1}$$

where:

σ – standard deviation of axle loading force,

$\overline{F}$ – mean value of axle loading force, approximately equal to static loading.

An increase in DLC is correlated with an increase in the maximum dynamic pavement loading from the vehicle. The values of DLC are affected by suspension characteristics, vehicle speed and pavement evenness.

Sweatman (1983) researched the impact of pavement evenness and vehicle speed on DLC coefficient for various vehicle suspension systems. The results imply that DLC increases with vehicle speed. This conclusion is supported by studies by many other researchers, including (Bilodeau, Gagnon, & Doré, 2017; Cebon, 1999; Kakara, Chintada, & Chowdary, 2020; Misaghi, Nazarian, & C. J. Carrasco, 2010; Shi & Cai, 2009). They also show that the DLC increases with a decrease in evenness, expressed by an increase in International Roughness Index (IRI). Higher value of DLC means that dynamic loads reach greater extreme values. The assessment of relationship between IRI and DLC were performed in the following works (Bilodeau et al., 2017; Hassan & McManus, 2001; Misaghi et al., 2010; Moran & Sullivan, 1995; Park, Papagiannakis, & Kim, 2014). The methodology of IRI calculation and the length of sequence of integration (Múčka, 2017; Šroubek, Šorel, & Žák, 2021) has some impact on DLC as well. However, previous works do not include the effect of freight load on DLC. While suspension parameters are subject to lesser variations, the freight weight and the consequent gross vehicle weight may vary significantly.

A sample computer simulation was performed by the author in order to present how the axle load, resulting from carried freight loads, affects dynamic loads. It is discussed below. The dynamic loads and DLC parameter were used in further parts of the analysis as well. The following assumptions were made:

- Profile measured by RSP laser profilograph for a 1-km-long section of main national road located in Pomerania district in Poland (National road No. DK20, section from km 296 +000 to km 297+000, right lane, right wheel path). The section was selected to represent highly varied roughness (from fairly even to very rough).
- The quarter car model was used to calculate IRI and dynamic loads.
- Calculations of IRI were performed with standard parameters of a "golden car":
  - Sprung mass (car body): $m_s = 300\text{kg}$,
  - Unsprung mass (car wheel): $m_u = 45\text{kg}$,
  - Suspension stiffness: $k_s = 1890\text{N/m}$,
  - Suspension damping: $c_b = 1800\text{N} \cdot \text{s/m}$,
  - Tire stiffness: $k_s = 195900\text{N/m}$,
  - Quarter car velocity: $v = 80\text{km/h}$.

- Calculations of dynamic loads of commercial vehicles were performed for modified parameters of suspension, which were assumed after studies of Belay, OBrien, & Kroese (2008):
  - Sprung mass, various, for standard axle load: $m_s = 4677\text{kg}$,
  - Unsprung mass, constant: $m_u = 420\text{kg}$,
  - Suspension stiffness, constant: $k_s = 50000\text{N/m}$,
  - Suspension damping, constant: $c_b = 2100\text{N} \cdot \text{s/m}$,
  - Tire stiffness, constant: $k_s = 150000\text{N/m}$,
  - Velocity, constant: $v = 80\text{km/h}$.

The sprung mass in a model of commercial vehicle was assumed to vary due to the fact that vehicles carry various loads. The remaining parameters of suspension depend on the type of suspension (e.g. leaf or pneumatic) and are related with the load of vehicle to a minor extent. Therefore, they were assumed to be constant in the considered analysis. To simplify the analysis, the velocity (vehicle speed) was assumed to be constant as well. The road profile was measured with RSP device and it is presented in Figure 1 as deviations from the road profile elevations at 0.1 m intervals. The International Roughness Index (IRI) was calculated for this profile. It is presented in Figure 1 as well. IRI was calculated for 1.0 m sequences. It is visible that pavement is fairly even along the most of its length. The average IRI for the whole length of section equals 1.52 mm/m. However, in a short part of section near 600 m, high unevenness occurs and IRI reaches extremely high value IRI = 14 mm/m at this point.

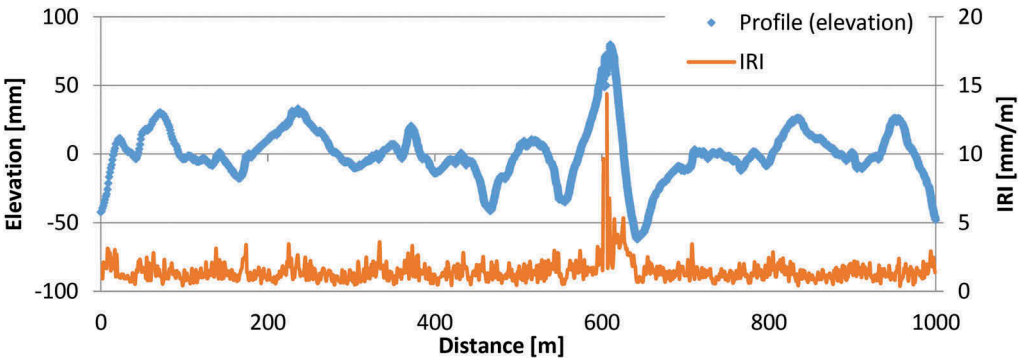

Figure 1. Longitudinal profile elevation adopted for sample analysis of dynamic loads and International Roughness Index (IRI) calculated for the "golden car" suspension parameters.

The standard wheel load was assumed as 50 kN, which corresponds to standard axle load Q_s = 100 kN. Dynamic loads caused by the standard wheel moving along the assumed road profile with the speed of 80 km/h were calculated with the use of quarter car model and they are presented in Figure 2. It is visible that dynamic loads are mostly within the range from 47 kN to 53 kN, apart from the short section near 600 m, where loads reach extreme values of up to 64 kN, due to very high unevenness at this point (local IRI = 14 mm/m).

Variations in dynamic loads are described by DLC. For the moving standard wheel, the DLC calculated on the basis of dynamic loads given in Figure 2 equals DLC = 0.169. In the case of commercial vehicles, such parameters of suspension as suspension stiffness, damping coefficient, tire stiffness and unsprung mass are less subject to variations than the sprung mass, which may vary considerably. The reasons of its variations include different mass of carried freight, uneven load distribution and varying extent of use of vehicle capacity. The calculations of DLC for various sprung masses, with all other parameters remaining constant, are given in Figure 3. It have to be noticed that DLC as a function of axle loads (Figure 3) was obtained with the use of theoretical dynamic axle loads (Figure 2) calculated with the use of quarter car model and real (measured) road profile (Figure 1).

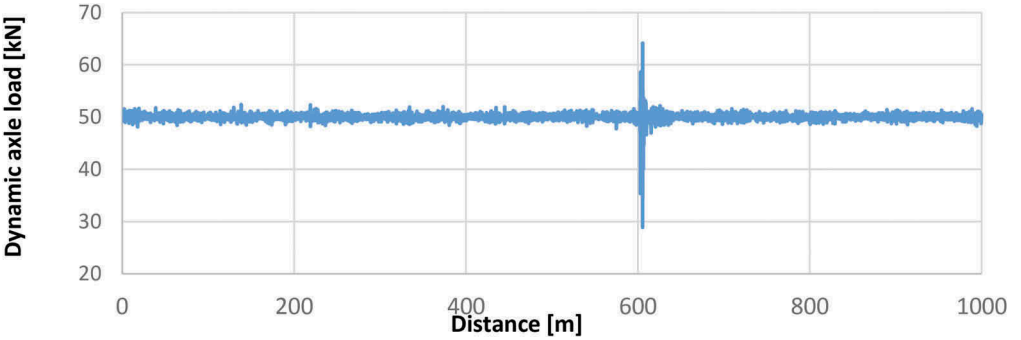

Figure 2. Example of dynamic loads of heavy vehicle wheel obtained for the adopted road profile and m_s = 4677 kg.

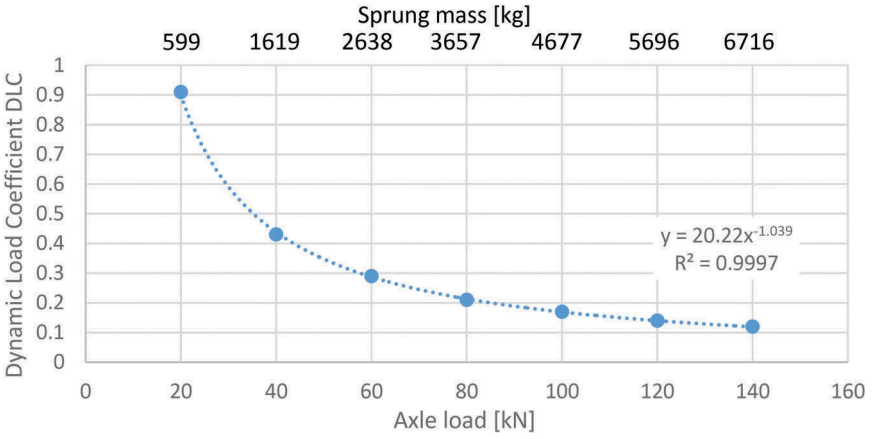

Figure 3. Relationship between DLC and axle load obtained for the sample road profile.

Figure 3 implies that deviations from static loads are greater in the case of lighter axles for the same road profile and suspension properties. DLC significantly depends on ratios between wheel load (sprung mass) and the remaining parameters of suspensions, which may explain high differences in DLC reported in the literature. The fact that DLC increases with a decrease in axle load does not mean that the dynamic impact of the lighter axles on pavement structure will be greater than that of the heavier ones. The issue is more complex; in order to analyze it, axle load spectra including dynamic loads should be determined first.

3 EFFECT OF DYNAMIC LOADS ON AXLE LOAD SPECTRA

In the studies of the author (Dawid Rys, 2019) the method of determination of ALS including dynamic loads from vehicles has been developed. The discrete distribution of axle loads is characterized by percentage of axle passes falling into a set of axle load intervals. Static Axle Load Spectrum (further abbreviated to SALS) is visible as column series in Figure 4 and the percentage of axle observations in particular load interval i is marked as s_i. The Dynamic Axle Loads Spectrum (further abbreviated to DALS) includes both SALS and distributions of dynamic loads coming from particular axle load intervals. In DALS the number of observations in a given axle load interval j is a sum of observations of dynamic loads being close to the static load Q_j (differing from the load Q_j so slightly that they fall into the range of the same load interval) as well as

observations of dynamic loads resulting from all other intervals (coming from any other given SALS interval k, but, due to the distribution of its dynamic loads, falling within the range of the interval j). Formula (2), which is the probability density function of a normal distribution, is used to calculate the percentage of recorded loads in the interval j coming from axles with real loads Q_k, but classified into interval j due to dynamic loads

$$d_{j,k} = s_k \frac{1}{\sigma_k \sqrt{2\pi}} \cdot exp\left(-\frac{(Q_k - Q_j)^2}{2{\sigma_k}^2}\right) = s_k \frac{1}{DLC_k Q_k \sqrt{2\pi}} \cdot exp\left(-\frac{(Q_k - Q_j)^2}{2{DLC_k}^2 Q_k^2}\right) \tag{2}$$

where:

$d_{j,k}$ – percentage of observations of dynamic loads Q_j caused by axles with static load Q_k,
s_k – percentage of axles with static load Q_k determined from SALS,
DLC – dynamic load coefficient,
j, k – designations of load intervals.

For the entire considered range of axle loads, the values of $d_{j,k}$ create a matrix with n rows and columns. The matrix will be designated as D (after *Dynamic loads*). The discrete spectrum of static axle loads can be also expressed by a vector SALS, within which the values s_k express percentages of observations in particular load intervals Q_k, in other words – express the actual spectrum of static loads obtained from weigh-in-motion system. The vector DALS defines the real axle load spectrum, which includes dynamic effects of vehicle loading. For the spectrum (vector) DALS, the total percentage d_j, reflecting all axle loads falling into a given load interval j, is calculated as a sum of loads coming from all the static load spectrum intervals k (k from 1 to n, including $k = j$). The percentage of loads δ_j in the interval j in the spectrum including all dynamic loads is calculated according to:

$$\delta_j = \sum_{k=1}^{n} s_k d_{k,j} \tag{3}$$

The formula (3) for the whole range of axle load intervals n is the same as formula for matrix multiplication. Therefore, the spectrum DALS is delivered from multiplication of the matrix of dynamic loads D by the spectrum of static axle loads SALS:

$$DALS = D \cdot SALS \tag{4}$$

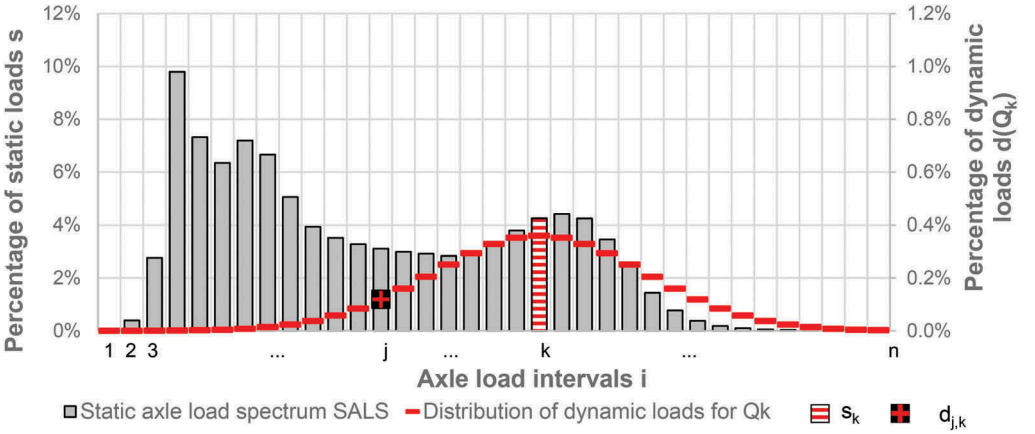

Figure 4. Example scheme of static load spectrum and distribution of dynamic loads obtained for mean load Q_k.

To perform sample calculations of DALS, the data from weigh-in-motion were used. The WIM station is located on national road DK 22 (GPS coordinates 53.68499N, 17.42860E). The measurements were conducted from 1 January to 14 October 2014 (286 days). Data delivered from 141 448 commercial vehicles were used. Data were verified in order to filter invalid records and were processed to minimize the effect of systematic and random error (D. Rys, 2019; Dawid Rys & Burnos, 2021). Figure 5 presents Static Axle Load Spectra SALS, which were obtained on the basis of WIM data, as well as Dynamic Axle Load Spectra DALS, which were calculated according to equation (4). SALS were determined for six groups of axles: 1) front single axle(steering axle of the vehicle), 2) second single axle (which is a drive axle), 3) all remaining single axles in trailers, 4) tandem axles in trucks (both steering and drive), 5) tandem axles in trailers, and 6) tridem axles, which are found only in semi-trailers. In order to further simplify the analysis, ALS were determined without distinguishing between particular vehicle classes. Due to this fact, the shape of ALS of single axles includes several "peaks". The first peaks correspond to the group of lighter commercial vehicles (e.g. 2-axle single-truck units), peaks shifted towards heavier loads correspond to articulated trucks with trailer or semi-trailer. Triple axles occur only in the group of heavy articulated trucks with semi-trailer. Two peaks which are observed in ALS of triple axles correspond to empty and optimally loaded vehicles, respectively.

Incorporation of dynamic loads results in "flattening" of the shape of ALS and less peaks are observed. It means that local modes in the static axle load spectra disappear when dynamic effects are included. The effect is especially visible in the case of lighter axles, because DLC is higher in those intervals of axle loads (cf. Figure 3). The DALS have significantly higher percentages of the heaviest loads than SALS.

Dynamic axle load spectra presented in Figure 5 were calculated theoretically. The tendency of "flattening" of ALS due to dynamic loads is in accordance with the observations of random error, which occur on WIM stations. The phenomenon was described by D. Rys (2019) and Dawid Rys & P. Burnos (2021). Dynamic loads of vehicles are one of the main component of random error. WIM systems with high random error provides more "flattened" ALS, similarly as observed in Figure 5. Nevertheless in further works it would be advisable to perform full-scale measurements to ultimately validate the theoretical calculations.

4 CONTRIBUTION OF DYNAMIC LOADS TO A DECREASE IN PAVEMENT LIFE

Pavement life is commonly expressed by a number of equivalent standard axle loads (ESALs) resulting in pavement failure. The moment of pavement failure depends on the assumed fatigue criteria; in the case of flexible pavements fatigue cracking and permanent deformation are predominantly considered. Equation (5) is valid for calculations of ESAL for both criteria.

$$ESAL = NV \cdot TF \tag{5}$$

where:

NV – total number of vehicles to pavement failure (also referred to simply as "traffic"),

TF – truck factor, which expresses the number of equivalent standard axle loads per one vehicle. TF can be calculated according to Equation (6):

$$TF = \sum_{i=1}^{6} LEF_i \cdot a_i \tag{6}$$

where:

LEF_i – load equivalency factor for a given type of axle i,

a_i – average number of i-axles per one vehicle,

i – type of considered axle (e.g. single steering, tandem in trucks etc.). In the presented study 6 types of axles were assumed, according to distinction given in Figure 5.

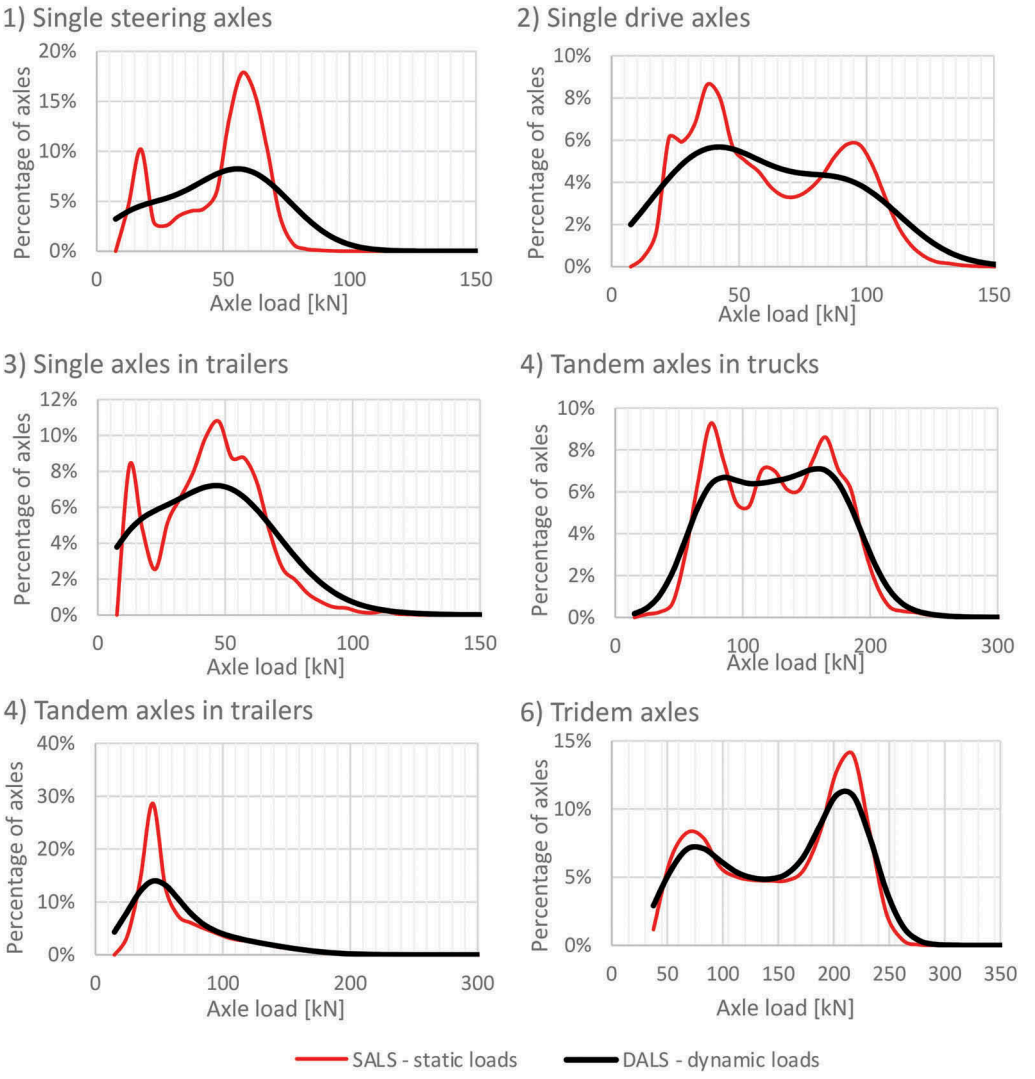

Figure 5. Static Axle Load Spectra obtained for a sample set of WIM data and Dynamic Axle Load Spectra, according to axle type.

Load equivalency factor is calculated as the sum of multiplications of axle load spectrum (ALS) by the function of equivalent axle load factor in the range of axle loads. It is expressed by the following formula:

$$LEF = \sum_{j=1}^{l} F_j m_j \tag{7}$$

where:

F_j – equivalent axle load factor for axle load Q_j,

m_j – percentage of loads in the interval j obtained from ALS, the m_j can be equal to s_k when static loads and SALS are considered, or can be equal to δ_j when dynamic loads and DALS are considered.

l – total number of load intervals.

There are numerous methods of determination of equivalent standard axle load factors F_j, and the following works include a wide summary of those methods (Atkinson, Merrill, & Thom, 2005; Hjort, Mattias, & Jansen, 2008; Judycki, 2010; Kawa, Zhang, & Hudson, 1998). For the purpose of this work, the fourth power equation was adopted. The effect of tandem and tridem axles was included according to the studies of (Judycki, 2006). The method presented by Judycki (2006) yields results very close to the AASHTO 1993 equations for structural number SN = 5.15 and terminal serviceability index $p_t = 2.5$.

The real service life of pavement structure includes dynamic loads from vehicles and it can be expressed by $ESAL_{dynamic}$. The hypothetic number of equivalent axle loads caused by the same number of vehicles NV on a perfectly even pavement, where dynamic effects would not occur, can be expressed by $ESAL_{static}$. The contribution of dynamic effects to the decrease in pavement life can be expressed by a dynamic factor DF, according to the following formula:

$$DF = \frac{ESAL_{dynamic} - ESAL_{static}}{ESAL_{dynamic}} \tag{8}$$

After substituting equation (5) into equation (8), the following formula is obtained:

$$DF = 1 - \frac{TF_{static}}{TF_{dynamic}} \tag{9}$$

where:

DF – dynamic factor, i.e. contribution of vehicle dynamic effects to change in pavement service life. DF also expresses the contribution of dynamic loads to pavement failures.

TF_{static} – truck factor calculated from equation (6) for static axle load spectra SALS,

$TF_{dynamic}$ – truck factor calculated from equation (6) for dynamic axle load spectra DALS.

Calculations performed for the example road profile and WIM data considered in this study are summarized in Table 1.

Table 1. Summary of calculations of dynamic factor for the considered example.

ID and type of axle	Average number of axles per vehicle a_i	Load equivalency factor LEF_i	Truck factor TF		Dynamic factor DF	
		Static	Dynamic	Static		Dynamic
1 Single steering	0.99	0.10	0.15	0.579	0.714	0.19
2 Single drive	0.93	0.37	0.45			
3 Single in trailers	0.04	0.09	0.13			
4 Tandem in trucks	0.08	0.40	0.42			
5 Tandem in trailers	0.19	0.06	0.07			
6 Tridem in trailers	0.40	0.23	0.24			

The presented methodology of calculation of dynamic load contribution to change in pavement life is universal and can be applied to any road profile or WIM data. The presented case shows that despite the relatively favorable average IRI calculated for a one-kilometer-long section (IRI = 1.52 m/km) the contribution of dynamic loads to pavement failure equals up to 19%. The high unevenness near the 600 m mark of the 1-km-long section had a significant impact on the obtained values of DLC and the resultant DF. This finding suggests that appropriate maintenance of pavement and improvement of its evenness may reduce the contribution of dynamic effects from vehicles to pavement failures.

5 CONCLUSIONS

The new approach to calculation of contribution of dynamic loads to failure of road pavement structures was proposed. The methodology was explained using an example case. The following conclusions can be drawn from the performed analysis:

1) According to calculations of Dynamic Load Coefficient (DLC), which were performed with the use of quarter car model and real (measured) road profile it can be stated that DLC significantly depends on the axle load. With all the other properties of suspension in a quarter car model remaining constant, a decrease in sprung mass, which corresponds to freight load, results in an increase in DLC.
2) The dynamic effects can be included in axle load spectra. The shape of dynamic axle load spectra is "flattened" in comparison to static axle load spectra, which means that local modes observed in the static axle load spectra disappear when dynamic effects are included. It also means that the percentage of the heaviest loads is greater.
3) The presented case of calculation, which was performed for a 1-km-long road profile with average IRI = 1.52 m/km, implies that the contribution of dynamic loads to pavement failure equals up to 19%. It shows that even for a fairly even road, the contribution of dynamic loads is relatively high.
4) According to previous studies, the dynamic load coefficient DLC increases with the deterioration of pavement evenness (increase in IRI). In consequence, the contribution of dynamic loads to pavement failure increase as well. It means that appropriate pavement maintenance and ensuring the highest possible evenness may significantly extend pavement service life.

REFERENCES

Atkinson, V. M., Merrill, D., & Thom, N. (2005). *Pavement wear factors, TRL Published Project Report PPR 066*.

Belay, A., OBrien, E., & Kroese, D. (2008). Truck fleet model for design and assessment of flexible pavements. *Journal of Sound and Vibration*, *311* (3–5),1161–1174. https://doi.org/10.1016/j.jsv.2007.10.019

Bilodeau, J. P., Gagnon, L., & Doré, G. (2017). Assessment of the relationship between the international roughness index and dynamic loading of heavy vehicles. *International Journal of Pavement Engineering*, *18*(8), 693–701. https://doi.org/10.1080/10298436.2015.1121780

Cebon, D. (1999). *Handbook of Vehicle-Road Interaction*. Swets & Zeitlinger.

Gillespie, T. D., Karamihas, S. M., Sayers, M., Nasim, M. A., Hansen, W., Ehsan, N., & Cebon, D. (1992). *Effects of heavy vehicles characteristic on pavement response and performance*.

Hassan, R., & McManus, K. (2001). Estimating dynamic load of pavements from surface profile properties. *Road And Transport Research*, *10*(3).

Hjort, M., Mattias, H., & Jansen, J. M. (2008). Road wear from Heavy Vehicles, (08), 47.

Judycki, J. (2006). Podstawy określania współczynników równoważności obciążenia osi do projektowania nawierzchni drogowych. *Drogi i Mosty*, (2), 55–92.

Judycki, J. (2010). Determination of equivalent axle load factors on the basis of fatigue criteria for flexible and semi-rigid pavements. *Road Materials and Pavement Design*, *11*(1), 187–202. https://doi.org/10.3166/rmpd.11.187-202

Kakara, S., Chintada, C., & Chowdary, V. (2020). Influence of Commercial Vehicle Characteristics on the Magnitude of Dynamic Wheel Loads Over Asphalt Pavement Profiles with Different Roughness. *Journal of The Institution of Engineers (India): Series A*, *101*(4), 723–734. https://doi.org/10.1007/s40030-020-00467-z

Kawa, I., Zhang, Z., & Hudson, W. R. (1998). Evaluation of the AASHTO 18-Kip Load Equivalency Concept, *7*.

Misaghi, S., Nazarian, S., & C. J. Carrasco. (2010). Impact of Truck Suspension and Road Roughness on Loads Exerted to Pavements. *Fhwa-Rd-07-1008-02*, *79968* (November).

Moran, T., & Sullivan, M. (1995). Replication of Heavy Truck Dynamic Wheel Loads Using a Road Simulator. *Road Transport Technology*, *4*, 309–316. Retrieved from http://road-transport-technology.org/Proceedings/4-ISHVWD/Replication Of Heavy Truck Dynamic Wheel Loads Using A Road Simulator-Moran.pdf

Múčka, P. (2017). International Roughness Index specifications around the world. *Road Materials and Pavement Design*, *18*(4), 929–965. https://doi.org/10.1080/14680629.2016.1197144

Park, D. W., Papagiannakis, A. T., & Kim, I. T. (2014). Analysis of dynamic vehicle loads using vehicle pavement interaction model. *KSCE Journal of Civil Engineering*, *18*(7), 2085–2092. https://doi.org/10.1007/s12205-014-0602-3

Rys, D. (2019). Investigation of Weigh-in-Motion Measurement Accuracy on the Basis of Steering Axle Load Spectra. *Sensors, 19(15)*(3272), 20–22. https://doi.org/10.3390/s19153272

Rys, Dawid. (2019). Consideration of dynamic loads in the determination of axle load spectra for pavement design. *Road Materials and Pavement Design*, *0*(0), 1–20. https://doi.org/10.1080/14680629.2019.1687006

Rys, Dawid, & Burnos, P. (2021). Study on the accuracy of axle load spectra used for pavement design. *International Journal of Pavement Engineering*, *0*(0), 1–10. https://doi.org/10.1080/10298436.2021.1915492

Shi, X. M., & Cai, C. S. (2009). Simulation of Dynamic Effects of Vehicles on Pavement Using a 3D Interaction Model. *Journal of Transportation Engineering*, *135*(10), 736–744. https://doi.org/10.1061/(ASCE)TE.1943-5436.0000045

Šroubek, F., Šorel, M., & Žák, J. (2021). Precise International Roughness Index Calculation. *International Journal of Pavement Research and Technology*, (September). https://doi.org/10.1007/s42947-021-00097-z

Sweatman, P. F. (1983). *A study of dynamic wheel forces in axle group suspensions of heavy vehicles. Australian Road Research* Board, *Research Report SR27*.

Eleventh International Conference on the Bearing Capacity of Roads, Railways and Airfields, Volume 2 – Hoff, Mork & Saba (eds)

The impact of platooning action on asphalt pavement: Monitoring on site

P. Leiva-Padilla & F. Hammoum
MAST-MIT, University Gustave Eiffel, IFSTTAR, Campus de Nantes, Bouguenais, France

J. Blanc, S. Trichet, Y. Baudru, M.L. Nguyen, T. Gouy & P. Hornych
MAST-LAMES, University Gustave Eiffel, IFSTTAR, Campus de Nantes, Bouguenais, France

A. Salgado
Applus IDIADA Group, L'Albornar Santa Oliva, Tarragona, Spain

ABSTRACT: The concept of truck platooning is to take advantage of the connectivity technologies and automated driving support systems to link trucks in close formation (convoy) to increase transport efficiency, reduce fuel consumption and gas emissions while improving road safety. However, closely following guided trucks could have a different impact on road structures than the usual truck traffic. In this context, the study reported in this paper addresses the multi-loading effects of truck platoons on road structures. For this purpose, an experimental test track located in Spain was instrumented with longitudinal and transverse strain gauges. The strain gauges were used to collect the strains obtained in the pavement under the following conditions: (1) trucks in individual and platoon configuration, (2) a time gap of 0.8 s between trucks in the platoon configuration, and (3) four speeds (40 km/h, 60 km/h, 70 km/h and 80 km/h). The viscoelastic response of the pavement structure (strain field) under the test conditions applied on-site was computed using software Viscoroute 2.0 and was compared with the results measured with the strain gauges. Finally, the effect of individual and platoon truck configurations was compared.

Keywords: autonomous truck platoon, pavement performance, full scale test

1 INTRODUCTION

The automotive sector in the last decade has demonstrated the following benefits from partially/fully self-driven truck platooning: (1) better braking/acceleration abilities of the vehicles, (2) reduction of fuel consumption and operating costs of the vehicles, (3) enhancement of road safety for less traffic accidents and better traffic control, among others (Gungor & Al-Qadi, 2020; Hoque et al., 2021; Konstantinopoulou et al., 2019; Ladino et al., 2021; Thunberg et al., 2019).

Despite all the already mentioned benefits, a truck platoon deployment without precaution can accelerate pavement damage due to (Chen et al., 2019; Gungor & Al-Qadi, 2020; Noorvand et al., 2017): (1) the channelization of truck loading, which reduces the scattering in the lateral position of human-driven trucks, and (2) the reduction in the inter-truck distances, which may hinder the self-healing capacity of asphalt concrete materials.

DOI: 10.1201/9781003222897-36

In this context, since 2018, the European Union has been developing the research project called ENSEMBLE, which main objective is to pave the way for the adoption of multi-brand truck platooning in Europe, to improve fuel economy, traffic safety, and throughput (Ladino et al., 2021; Mascalchi et al., 2020).

This paper presents part of the research efforts done by ENSEMBLE to evaluate the effect of platooning trucks on pavement structures. For this purpose, a test section of a full-scale pavement was instrumented and subjected to the passage of trucks in individual and platoon configurations. The experimental results were simulated with a viscoelastic model, using the software Viscoroute 2.0 (Chabot et al., 2010).

2 MATERIALS AND METHODS

2.1 *Pavement structure and instrumentation*

The test section corresponding to this research is located in the test track facilities of the automotive company IDIADA Applus in Tarragona, Spain. As shown in Figure 1, the pavement structure of the test section is composed of a zahorra foundation (Spanish term for a granular material with continuous grading) and three asphalt layers in the top: 15 cm of a subbase layer, 6 cm of a base layer and 4 cm of a wearing layer. According to the UNE-EN 13108-1 asphalt mixture classification, the types of asphalt mixtures are respectively: AC 22 G (G-20), AC 22 S (S-20), and AC11 surf (D12). The mixtures were manufactured with a polymer-modified binder type PMB 45-80/65 according to the UNE-EN 14023, reaching densities of 2.38 to 2.39 g/cm^3 and air voids of 4.7% to 6.8%.

As Figure 1 shows, the instrumentation installed to measure the fatigue performance of the test section consists of an array of 24 strain gauges. Half of the strain gauges were used to measure the transverse strains (12 strain gauges) and the remaining half the longitudinal strains (12 strain gauges) at both the bottom of the base layer (six strain gauges) and the bottom of the subbase layer (six strain gauges). The strain gauges were installed under the right path of the truck, with a spacing of 20 cm in the transversal direction. Thermocouples were also installed at the bottom of each asphalt layer at two different locations, with a total of six thermocouples used to monitor the pavement temperature at different pavement depths during testing.

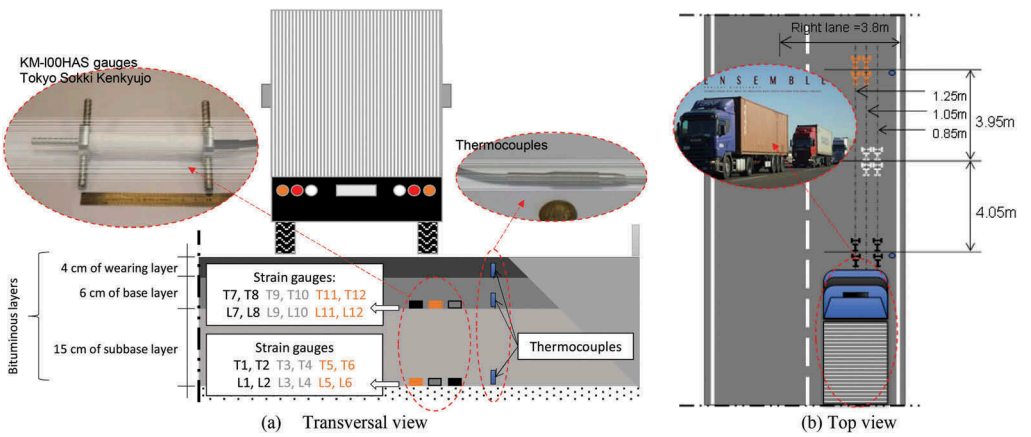

Figure 1. Pavement structure and instrumentation (the images are not to scale).

2.2 *Test protocol*

To evaluate the platooning effect of semi-autonomous/autonomous trucks, the test protocol defined in this experiment was based on using 3 semitrailer trucks (5-axle), with the loads and geometry shown in Figure 2. To simulate more easily different positions and speeds, the trucks were driven by human drivers. The platooning configuration defined for the test considered the following characteristics: (1) trucks in individual and platoon configuration with three trucks; (2) 0.8 s time gap for inter-truck separation; (3) lateral deviation of Axle 1 to each strain gauge is approximately zero (i.e. wandering ≅ 0 cm, measured by using a laser installed in the guard line and a reflective disc placed in the right wheel of the steer axle of each truck); (4) variation of temperature conditions through two test campaigns, one carried out in winter and the other one in summer; (5) four different test speeds, 40 km/h, 60 km/h, 70 km/h and 80 km/h.

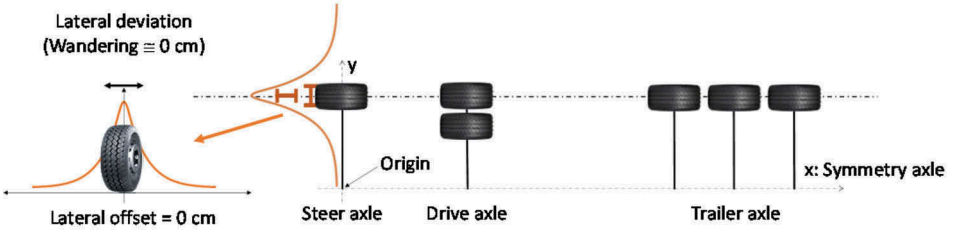

No. Truck	Axle	Axle type	Tire designation	No. Tire	y (m)	x (m)	Winter campaign		Summer campaign	
							Load (kN)	Pressure (kPa)*	Load (kN)	Pressure (kPa)*
1	Steer	Standard single tire	315/80 R = 22.5	1	1,073	0,0	34	757	34	737
	Drive	Standard dual tires	315/80 R = 22.5	1	1,073	3,7	31	727	25	565
				2	0,721		31	727	25	565
	Trailer	Tridem with single tires	385/65 R = 22.5	1	1,057	9,4	43	862	40	790
				2	1,057	16,5	40	786	36	690
				3	1,057	24,9	31	565	34	639
2	Steer	Standard single tire	315/80 R = 22.5	1	1,073	0,0	34	741	40	908
	Drive	Standard dual tires	315/80 R = 22.5	1	1,073	3,7	29	685	29	682
				2	0,721		29	685	29	682
	Trailer	Tridem with single tires	385/65 R = 22.5	1	1,057	9,45	39	759	42	848
				2	1,057	10,75	39	761	32	573
				3	1,057	12,08	40	806	41	828
3	Steer	Standard single tire	315/80 R = 22.5	1	1,073	0,0	35	768	38	840
	Drive	Standard dual tires	315/80 R = 22.5	1	1,073	3,7	32	764	29	689
				2	0,721		32	764	29	689
	Trailer	Tridem with single tires	385/65 R = 22.5	1	1,057	9,25	35	656	25	397
				2	1,057	10,55	35	667	37	717
				3	1,057	11,85	36	690	46	946

Figure 2. Loads and geometries corresponding to the right axles of each truck.

Note Figure 2: * Pressure values estimated from (Bridgestone, 2020; European Commission Directorate General Transport, 2001).

2.3 *Pavement modeling*

2.3.1 *Material properties and geometry*

As shown in Table 1, the pavement structure used in the model is composed of seven layers, considering a foundation layer and three asphalt layers, with three thin interlayers at the interfaces. Table 1 shows each layer thickness, Poisson ratio, modulus, and material behavior, as well as the corresponding pavement temperature used for each test campaign and load configuration. The modeling was done using the software Viscoroute 2.0 (Chabot et al., 2010). It is a semi-analytical software, developed to model pavement response under moving wheel loads, considering elastic or visco-elastic pavement materials. The viscoelastic behavior of the asphalt layers was simulated using the Huet-Sayegh model, which equation and parameters are shown in Table 2.

Table 1. Material properties used in the model.

					Pavement temperature (°C) ***			
					Winter		Summer	
Layer	Thickness (m)	Poisson ratio	Modulus (MPa)	Material behavior	Indiv.	Pl-at.	Indiv.	Plat.
Wearing course	0.040	0.35	Master curve *	Viscoelastic	12.8	4.5	24.9	34.1
Thin interlayer	0.002				12.8	4.5	24.9	34.1
Base layer	0.060				11.3	6.1	25.9	27.0
Thin interlayer	0.002				11.3	6.1	25.9	27.0
Subbase layer	0.150				10.3	8.3	27.5	27.7
Thin interlayer	0.002				10.3	8.3	27.5	27.7
Foundation	-	0.40	180 **	Elastic	-	-	-	-

Notes Table 1:
*Tack coat, typical values for a bitumen emulsion: Huet-Sayegh parameters (Table 2).
**Common value for a zahorra (Spanish nomitation for a granular material with discontinuous grading) and a heavy traffic, NTL-357/98.
***Temperature values measured with the temperature probes installed on the test section.

Table 2. Huet-Sayegh parameters at 15°C for viscoelastic characterization of the asphalt layers.

Huet Sayegh*:	$E^*(\omega,\tau) = E_0 + \frac{E_\infty - E_0}{1+\delta(i\omega\tau(\theta))^{-k}+(i\omega\tau(\theta))^{-h}}$								
Adjustment factor*:	$\tau(\theta) = \exp(A_0 + A_1\theta + A_2\theta^2$								
Layer	Material type	E_∞ (MPa)	E_0 (MPa)	δ	k	h	A_0	A_1	A_2
Wearing	AC11 surf (D12) **	19644	19	2,535	0,213	0,628	3,072	-0,382	0,002
Base	AC22 S (S-20) ***	27320	511	5,387	0,194	0,556	8,395	-0,389	0,001
Subbase	AC22 G (G-20) ***	22114	328	6,400	0,190	0,566	9,058	-0,387	0,001
Interlayer	Tack coat ****	1968	0	9,048	0,272	0,883	-1,629	-0,391	0,002

Notes Table 2:
*E_∞: instantaneous modulus, E_0: long term modulus, k and h: parabolic elements ($1 > h > k > 0$), δ: dimensionless coefficient managing the contribution of the first spring to the overall behavior of the bituminous material, ω: loading time (frequency), $\tau(\theta)$: adjustment factor, θ: test temperature, A_0, A_1, A_2: adjustment factors.
**Very thin asphalt concrete (VTAC) layer (Duong et al., 2018).
***Calculated with data obtained from the study (Mateos & Soares, 2015).
****Typical values obtained for a bitumen emulsion (Duong et al., 2018).

2.3.2 *Boundary conditions*

As Figure 3 shows, the load contact area used for modeling is composed of five rectangles distributed along the traffic line according to each axle position. The five rectangles represent the right half of the five axles that compose the semitrailer trucks used during testing. Each rectangle geometry was determined by fixing the width to 25.5 cm and 28.3 cm depending on the type of tires used, 315/80 R = 22.5 and 385/65 R = 22.5 respectively, as well as the tire loads and pressures already shown in Figure 2.

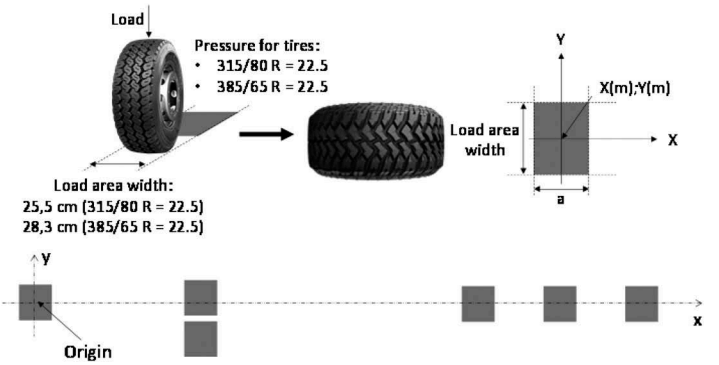

Figure 3. Load areas used during modeling (the images are not to scale).

3 DISCUSSION OF RESULTS

3.1 *Transverse strains*

The transverse strain signals obtained at the bottom of the subbase layer were selected in this paper, to evaluate bottom-up fatigue cracking of the asphalt layers. Figure 4 and Figure 5 show a comparison between the values measured with the transverse strain gauges installed in the test section, for truck speeds of 40 km/h and 80 km/h, during the winter and summer campaigns respectively, and obtained by the modeling process with Viscoroute 2.0. Figure 6 shows the inter-truck distances correspondingly applied for each speed tested. Truck passages with zero-wandering values for each truck in both individual and platoon truck configurations were selected for the analysis. The following observations can be made on these transverse strain signals:

- The transverse strain signals predicted with Viscoroute 2.0 are in good agreement with the real measured signals.
- The transverse strain values present a slow return to zero after loading, indicating a delayed strain response (and possibly some permanent deformations) in the material. This strain accumulation is more important for the summer campaign and for the platoon configuration (Figure 5). In terms of modeling, three interface configurations were probed to analyze the way to simulate this delayed response: (a) fully bonded layers, (b) sliding layers and (3) viscoelastic thin interlayer. From the results obtained, it was found that to reproduce the sliding effect occurring at the interfaces, thin viscoelastic tack coat interlayers should be included (Duong et al., 2018).
- The transverse strain values obtained under the passage of the trucks are only in tension. Once the vehicle passes, the values tend to return to the original condition with a delay caused by the viscoelastic performance of the material in the asphalt layers.
- In general terms, the strain values obtained in summer, with pavement temperatures ranging from 25.0°C to 29.5°C, are much higher (1.32 to 3.50 times and 1.62 to 4.93 times in the individual and platoon configuration respectively) than the strains measured in the winter, when the temperatures range from 6.1°C to 11.3°C.

- For the winter campaign, truck platoon configurations seem to have a negligible effect on the maximum transverse strain values obtained compared to the ones obtained in individual configurations. In contrast, for the summer campaign, the values obtained under platoon truck configurations are 0.76 to 2.0 times higher (depending on the speed, the type of axle and the truck) than individual ones.
- Using a constant time gap to represent platoon truck configurations based on vehicle reaction times means an increase in the inter-truck distances when truck speeds increase.

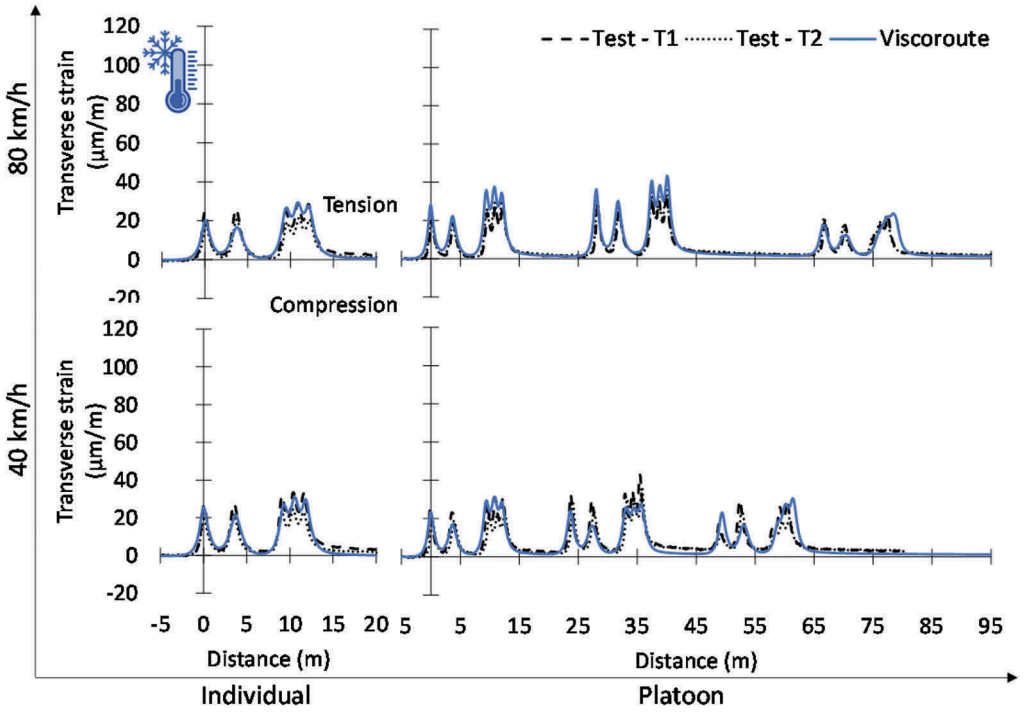

Figure 4. Measured and calculated transverse strains at the bottom of the subbase asphalt layer (winter campaign).

3.2 *Longitudinal strains*

Considering the longitudinal strain gauges at the bottom of the subbase layers, Figure 7 and Figure 8 show the comparison between the values measured and the values obtained by modeling for truck speeds of 40 km/h and 80 km/h. In addition, Figure 9 shows a comparison between the maximum longitudinal and transversal values obtained under the passage of each axle. In this case, the following observations can be made:

- Like transverse strain signals, the longitudinal strain signals predicted with Viscoroute 2.0 follow closely the real measured longitudinal strain signals.
- For all the cases, the shape of the longitudinal strain signals is significantly different from the shape of the transverse strain signals. The longitudinal signals are first in compression (when the load approaches) then in tension (under the center of the load), and finally in compression again after loading.
- Similar to the transverse strains, the longitudinal strains are much higher (ranging from 1.58 to 2.58 times higher in the individual configuration and from 1.90 to 4.86 times higher in the platoon configuration) in the summer, when the measured pavement temperatures

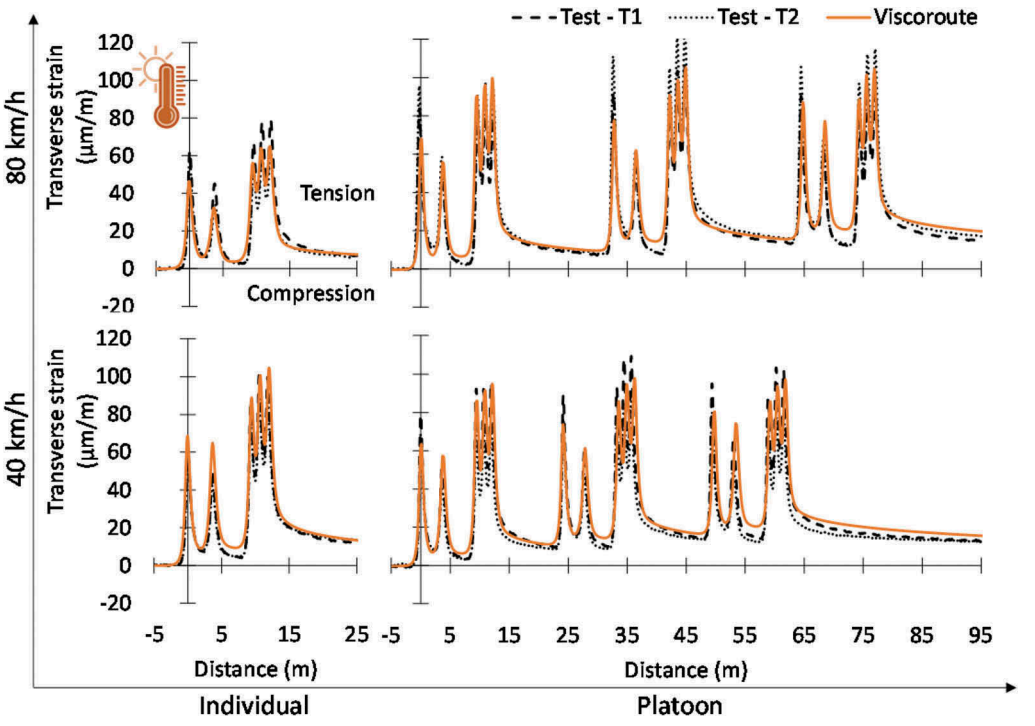

Figure 5. Measured and calculated transverse strains at the bottom of the subbase asphalt layer (summer campaign).

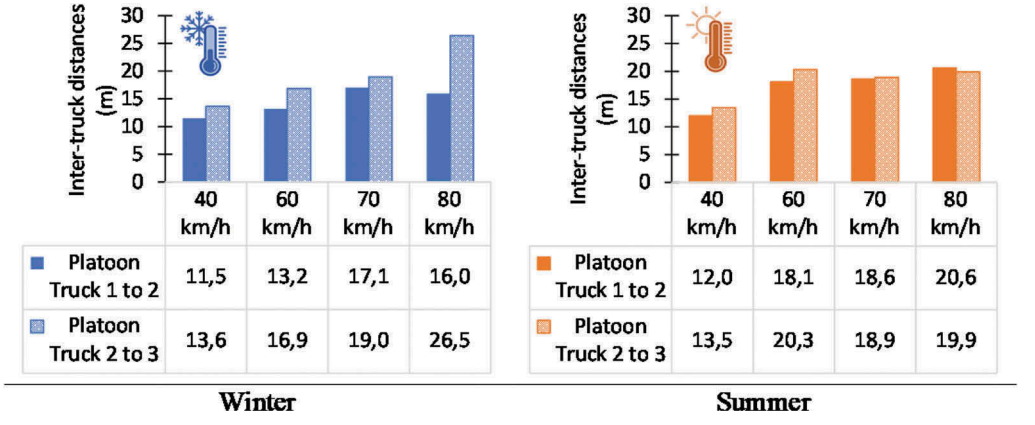

Winter	40 km/h	60 km/h	70 km/h	80 km/h
Platoon Truck 1 to 2	11,5	13,2	17,1	16,0
Platoon Truck 2 to 3	13,6	16,9	19,0	26,5

Summer	40 km/h	60 km/h	70 km/h	80 km/h
Platoon Truck 1 to 2	12,0	18,1	18,6	20,6
Platoon Truck 2 to 3	13,5	20,3	18,9	19,9

Figure 6. Inter-truck distances in the platoon configuration.

range from 25.0°C to 29.5°C, in comparison to the ones obtained in the winter, when the temperatures range from 6.1°C to 11.3°C.

- Like the transverse strains, truck platoon configurations seem to have a negligible effect on the maximum longitudinal strain values obtained for the winter campaign. In contrast, the values obtained under platoon truck configurations for the summer campaign are 0.65 to 1.27 times higher than individual ones.

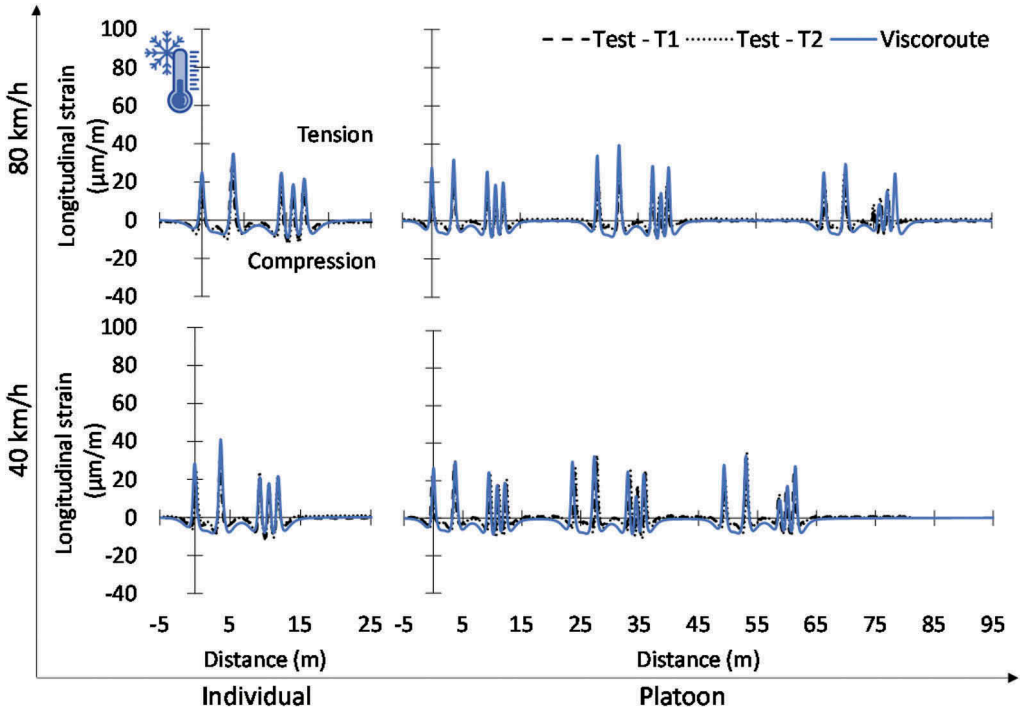

Figure 7. Measured and calculated longitudinal strains at the bottom of the subbase asphalt layer (winter campaign).

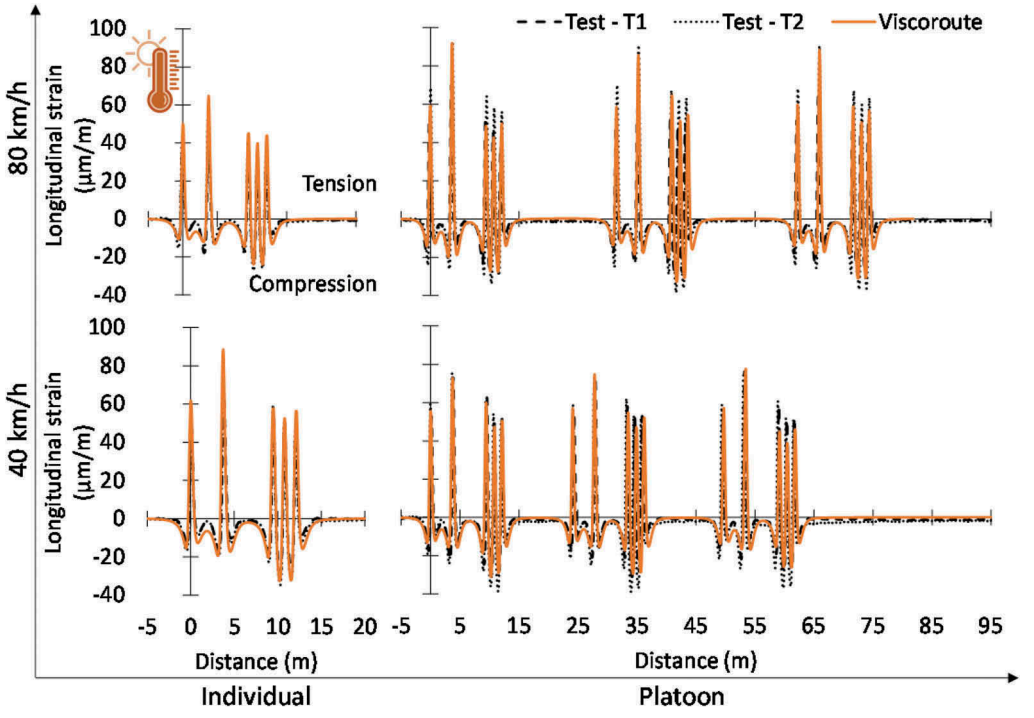

Figure 8. Measured and calculated longitudinal strains at the bottom of the subbase asphalt layer (summer campaign).

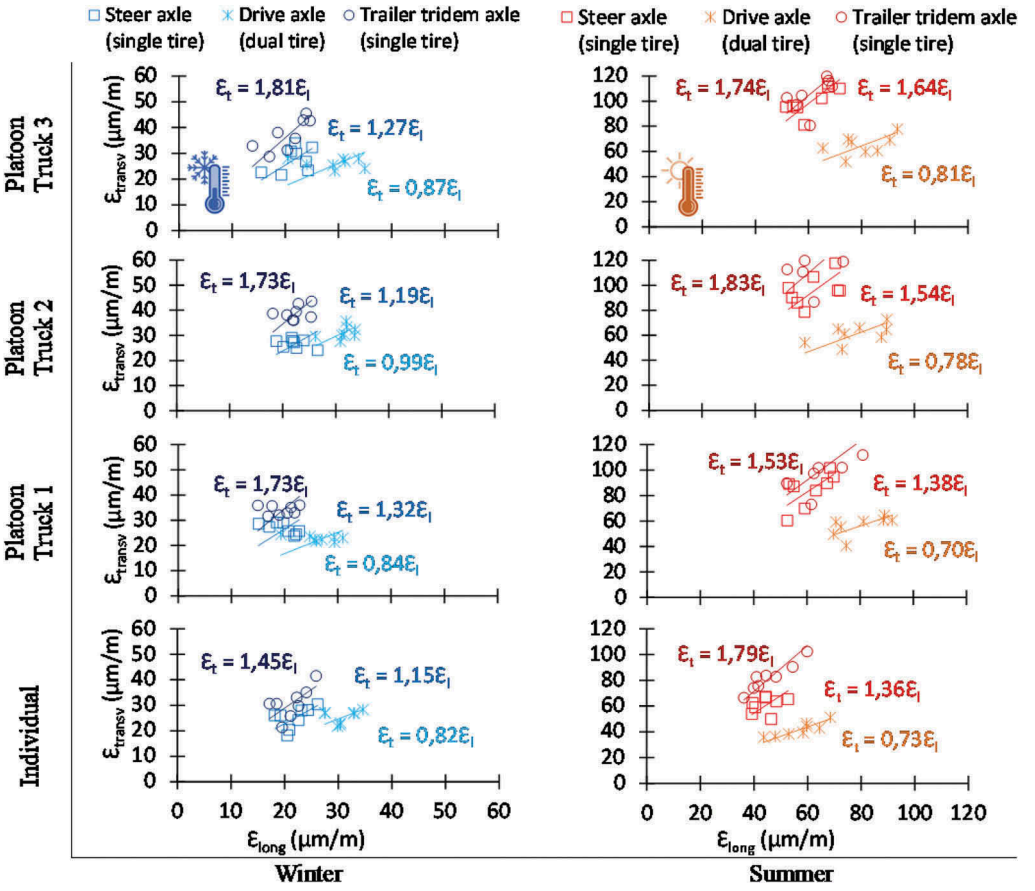

Figure 9. Comparison of the maximum transverse/longitudinal strains.

- For the conditions tested, individual/platoon truck configurations, and winter/summer test campaigns, by the analysis of the slopes of the linear equations relating longitudinal and transverse strains (Figure 9), the maximum strain values obtained are higher in the transversal direction for the single wheel axles (steer and trailer), the highest values being obtained for the trailer (from 1.45 to 1.83 times higher). In this sense, it can be expected that fatigue cracking will develop in the longitudinal direction along the vehicle's passage.

4 CONCLUSIONS

This paper presents some of the results obtained from a full-scale test performed on a pavement test section subjected to individual and platoon truck loadings. Three non-autonomous semi-trailer trucks were driven by different drivers to configured platoon truck configurations with 0.8 s time gaps and testing speeds of 40 km/h, 60 km/h, 70 km/h and 80 km/h, during two test campaigns, carried out in winter and summer conditions. The viscoelastic responses of the pavement structure (strain fields) were modelled using the software Viscoroute 2.0, for different speed and temperature conditions, and compared with the experimental measurements.

The study has led to the following conclusions: (1) the model with viscoelastic interfaces was able to reproduce correctly the experimental strain values; this confirms the capacity of Viscoroute to predict pavement response under complex multiple load

conditions, and the possibility to use it as a predictive tool to evaluate the effect of other platoon configurations; (2) both transversal and longitudinal strains were considerably higher for the higher temperatures of summer, due to the thermoviscoelastic behavior of the asphalt layers; (3) the highest level of strains were obtained for the trailer tridem axle and the transversal direction, in the summer campaign; (4) transverse strains also showed important strain accumulation after the passage of the vehicles, especially in the platoon configuration; (5) only for the case of the summer campaign, platoon truck configurations showed higher maximum transversal/longitudinal values than the individual truck configurations. These results suggest that pavement fatigue damage induced by platooning could be mitigated by controlling parameters like traffic times (to avoid hot temperatures), inter-vehicle distances and lateral wandering.

As a continuation of the experimental measurements presented in this paper, it is planned, in the ENSEMBLE project, to perform laboratory fatigue tests, reproducing the same multiple axle strain signals, to study the influence of multiple axles, and platoon configurations, on the fatigue performance of the bituminous layers. Additionally, recognising that platooning trucks can also have important impacts in terms of rutting, especially at reduced wandering patterns, further research studies will also be oriented to investigate the effect of platoons on vertical strains and therefore permanent deformation of asphalt pavements.

ACKNOWLEDGEMENTS

The research presented in this paper is part of the ENSEMBLE project, co-funded by the European Union under the Horizon2020 Research and Innovation Program, grant agreement No 769115.

REFERENCES

Bridgestone. (2020). *Truck Tire Data Book. Version 20.1*.

Chabot, A., Chupin, O., Deloffre, L., & Duhamel, D. (2010). ViscoRoute 2.0 A: Tool for the Simulation of Moving Load Effects on Asphalt Pavement. *Road Materials and Pavement Design*. https://doi.org/10.1080/14680629.2010.9690274

Chen, F., Song, M., Ma, X., & Zhu, X. (2019). Assess the impacts of different autonomous trucks' lateral control modes on asphalt pavement performance. *Transportation Research Part C: Emerging Technologies*. https://doi.org/10.1016/j.trc.2019.04.001

Duong, N. S., Blanc, J., Hornych, P., Bouveret, B., Carroget, J., & Le feuvre, Y. (2018). Continuous strain monitoring of an instrumented pavement section. *International Journal of Pavement Engineering*, *8436*, 1–16. https://doi.org/10.1080/10298436.2018.1432859

European Commission Directorate General Transport. (2001). *Cost 334 Effects of Wide Single Tyres and Dual Tyres. Final Report of the Action* (Issue November).

Gungor, O. E., & Al-Qadi, I. L. (2020). All for one: Centralized optimization of truck platoons to improve roadway infrastructure sustainability. *Transportation Research Part C: Emerging Technologies*. https://doi.org/10.1016/j.trc.2020.02.002

Hoque, M. M., Lu, Q., Ghiasi, A., & Xin, C. (2021). Highway Cost Analysis for Platooning of Connected and Autonomous Trucks. *Journal of Transportation Engineering Part A: Systems*, *147*(1). https://doi.org/10.1061/JTEPBS.0000474

Konstantinopoulou, L., Coda, A., & Schmidt, F. (2019). Specifications for Multi-Brand Truck Platooning. *ICWIM 8, 8th International Conference on Weigh-In-Motion, May 2019*, 8.

Ladino, A., Xiao, L., Adjenugwhure, K., Deschle, N., & Klunder, G. (2021). Cross-Platform Simulation Architecture with application to truck platooning impact assessment. *27th ITS World Congress, 11-15 October*.

Mascalchi, E., Coda, A., & Willemsen, D. (2020). Specifications for multi-brand truck platooning. *8th Transport Research Arena TRA 2020, April 27- 30*.

Mateos, A., & Soares, J. B. (2015). Validation of a dynamic modulus predictive equation on the basis of Spanish asphalt concrete mixtures. *Materiales de Construccion*, *65*(317). https://doi.org/10.3989/mc.2015.01114

Noorvand, H., Karnati, G., & Underwood, B. S. (2017). Autonomous vehicles: Assessment of the implications of truck positioning on flexible pavement performance and design. In *Transportation Research Record* (Vol. 2640). https://doi.org/10.3141/2640-03

Thunberg, J., Lyamin, N., Sjoberg, K., & Vinel, A. (2019). Vehicle-to-Vehicle Communications for Platooning: Safety Analysis. *IEEE Networking Letters*, *1*(4). https://doi.org/10.1109/lnet.2019.2929026

Modelling and methods of functional testing

Eleventh International Conference on the Bearing Capacity of Roads, Railways and Airfields, Volume 2 – Hoff, Mork & Saba (eds)

Effects of patching on the cracking performance of asphalt pavements based on a macrostructure-based heterogeneous finite element method

Cong Du, Quan Liu, Chonghui Wang, Zeyu Zhang, Pengfei Liu & Markus Oeser
Institute of Highway Engineering, RWTH Aachen University, Aachen, Germany

ABSTRACT: This paper presents a finite element (FE) method to investigate the effects of asphalt patching mixture on the cracking performance of asphalt pavements. A heterogeneous model, which combines the asphalt patching mixture and asphalt pavement into a macroscale system, was established using the ABAQUS finite element software. Based on a pre-defined initial crack, the extended finite element method (XFEM) was employed to characterize the crack propagations in the pavement. In addition, the temperature stress produced by the patching construction process was taken into consideration. The results showed that the developed FE model provided an insight into the cracking behavior of asphalt pavement with respect to various asphalt patching mixture types, patching locations and loading conditions. In light of these benefits, the presented approach can be expected to be utilized as a mechanistic tool for predicting and evaluating the asphalt pavement performance after the patching maintenance.

Keywords: Asphalt mixture patching shape, Finite element method, Extended finite element method, Crack propagation, Temperature stress

1 INTRODUCTION

In recent years, asphalt pavements often subject to various kinds of pavement distresses including fatigue cracking, rutting and pothole due to the increase of the traffic loading. Asphalt mixture patching, as a remedy, is widely employed to repair the asphalt pavements in the locations where distresses occur. Asphalt mixture patching is regarded as an economical method by replacing the distressed asphalt pavement with new asphalt mixture. However, due to the different mechanical properties between original and patched asphalt mixture, significant stress concentration would occur in the interface and further induce the crack propagation.

To this end, many researches have been made to improve the mechanical performance of the patched asphaltic materials. For example, Kwon et al. [1] investigated the performance of spray injection patching materials for pothole repair that utilize 100 percent RAP and compared the results to the performance of patching materials made with virgin aggregate. The results show that the performance depended on the type of aggregate and emulsion in the mixtures, and the mixtures that contained RAP had good stability and adhesion properties compared to the mixtures made with virgin aggregate. Yang et al. [2] evaluated the fatigue performance of the patched asphalt pavement structure by conducting the three-point bending fatigue test, and the results showed that the fatigue test performed well on exposing the vulnerable parts of patched structures. In addition, the cold patched asphalt material is developed

DOI: 10.1201/9781003222897-37

due to its high performance and is less possibly effected by seasons [3]. Liu et al. provided detailed description on the material composition, the compaction process and repair procedure of the cold patched asphalt mixture. Yuan et al. [4] proposed a new method to improve the moisture stability of the cold patched asphalt mixture by incorporating cement, and the performance of the cold patched asphalt mixture with difference cement content is tested by Marshall tests and freeze thaw indirect tensile test.

However, except for the mechanical properties of the patched asphalt material, the shape of the asphalt mixture patching in the repairing procedure can cause significant stress variation and crack propagation within asphalt pavement under traffic loadings. The effects of the shape of the asphalt mixture patching are seldom reported due to the difficulty of deeply investigating the stress and crack behavior in asphalt pavement.

To address this issue, the finite element (FE) method is widely accepted as effective tool to simulate the stress-strain responses in structures without exhausted labor work and high cost. In this study, the four asphalt pavement model, including unpatched, rectangular shape patched, stair shape patched and trapezoid shape patched pavements, respectively, were established and simulated in the ABAQUS finite element software. Incorporating with the extended finite element method (XFEM), a pre-defined initial crack was inserted in the surface layer, and the crack evolution behavior was exhibited. In addition, the stress distribution of the asphalt mixture patching during the cooling process was simulated to investigate the temperature stress responses in the repair construction.

2 METHODOLOGY

2.1 *XFEM theory*

According to [5–10], the enrichment function is employed in the XFEM simulation to investigate the fracture behavior of materials. The approximation for a displacement vector function u with the partition of unity enrichment can be formulated as,

$$u(x)=\sum_{i=1}^{N} N_i(x)\left[u_i+H(x)a_i+\sum_{\alpha=1}^{4} F_\alpha(x)b_i^\alpha\right] \tag{1}$$

where $N_i(x)$ is the usual nodal shape function; u_i is the usual nodal displacement vector associated with the continuous part of the finite element solution; a_i is the product of the nodal enriched degree of freedom vector that associated with the discontinuous jump function $H(x)$ across the crack surface; $b_\alpha{}^i$ is the product of the nodal enriched degree of freedom vector that associated with the elastic asymptotic crack tip function $F_\alpha(x)$. The discontinuous jump function $H(x)$ across the crack surface can be expressed as,

$$H(x)=\begin{cases} 1(\boldsymbol{x}-\boldsymbol{x}^*)\cdot\boldsymbol{n}0 \\ -1(\boldsymbol{x}-\boldsymbol{x}^*)\cdot\boldsymbol{n}<0 \end{cases} \tag{2}$$

In addition, the asymptotic crack tip function F_α(x) can be formulated as,

$$F_\alpha(x)=\left[\sqrt{r}\sin\frac{\theta}{2},\sqrt{r}\cos\frac{\theta}{2},\sqrt{r}\sin\theta\sin\frac{\theta}{2},\sqrt{r}\sin\theta\cos\frac{\theta}{2}\right] \tag{3}$$

where (r, θ) is the polar coordinate system. The enrich nodes of the XFEM simulation and crack path is illustrated in Figure 1,

To define the fracture initiation and propagation, the maximum stress criterion was used, and the fracture will occur when the following equation is satisfied,

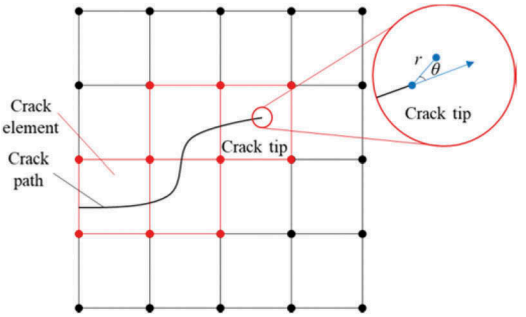

Figure 1. Enrich nodes in the XFEM.

$$\left\{\frac{\langle t_{\max}\rangle}{t^0_{\max}}\right\} = 1 \tag{4}$$

where $t°_{\max}$ is the fracture strength of the XFEM elements; the symbol $\langle\rangle$ is the e Macaulay bracket.

Once the criterion is reached, the scalar damage variable D will increase from 0 to 1, which represents the fracture behavior of the elements.

$$D = \frac{\delta_{\mathrm{m}}(\delta^{\max}_{\mathrm{m}} - \delta^0_{\mathrm{m}})}{\delta^{\max}_{\mathrm{m}}(\delta_{\mathrm{m}} - \delta^0_{\mathrm{m}})} \tag{5}$$

where $\delta^{\max}_{\mathrm{m}}$ refers to the maximum value of the effective separation attained during the loading history; δ_{m} is the effective separation at complete failure; δ^0_{m} is a tabular function of the mode mix, temperature, and field variables.

Meanwhile, the stress components in the fracture surface are expressed as,

$$t_n = \begin{cases} (1-D)\bar{t}_n, & \bar{t}_n 0 \\ \bar{t}_n, & \bar{t}_n < 0 \end{cases} \tag{6}$$

$$t_t = (1-D)\bar{t}_t \tag{7}$$

where $\bar{t}_{\mathrm{n}}$ and $\bar{t}_{\mathrm{t}}$ are the normal and shear stress components predicted by the elastic traction–separation behavior for the current separations without damage.

2.2 *Model development*

The two-dimensional asphalt pavement model was established using the commercial FE software ABAQUS, and the pavement layer structure is specified according to German specification [11], as shown in Figure 2. In this study, three types of patching shape were defined, which are rectangular shape, stair shape and trapezoid shape, respectively. The size of the patch area was defined as 30 cm width and 10 cm depth, which is presented in Figure 3. In addition, by simulating on the unpatched asphalt pavement, a pre-defined initial crack was inserted in the asphalt mixture layer.

According to [12–14], the stiffness of the asphalt mixture increases while the fracture strength decreases during the service of asphalt pavement. Therefore, it is assumed that the stiffness and strength of the asphalt mixture patching were respectively 50% higher and 75% lower than the original asphalt mixture in the surface layer. In addition, the parameters for

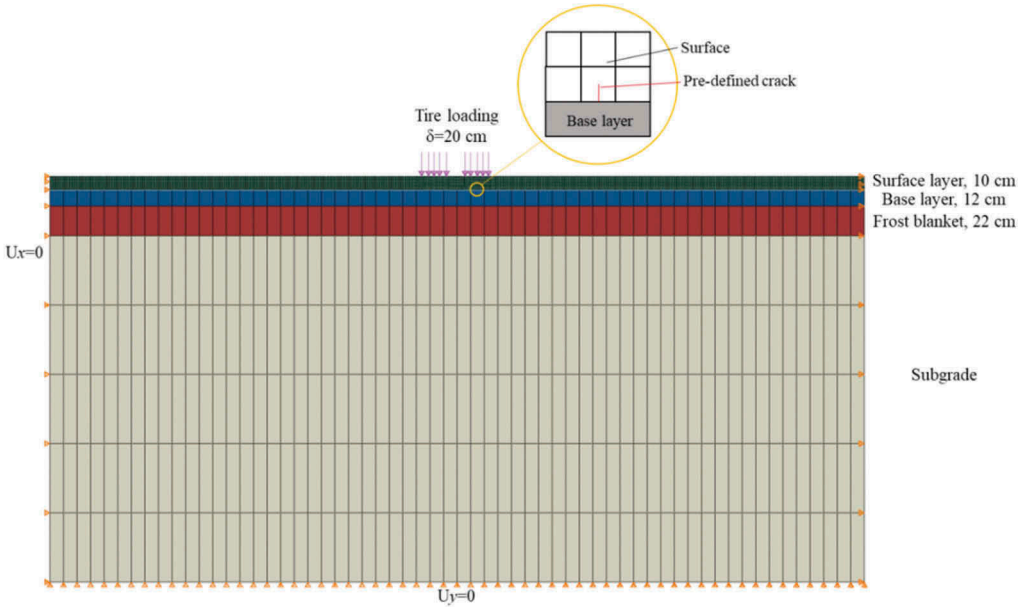

Figure 2. Model of asphalt pavement.

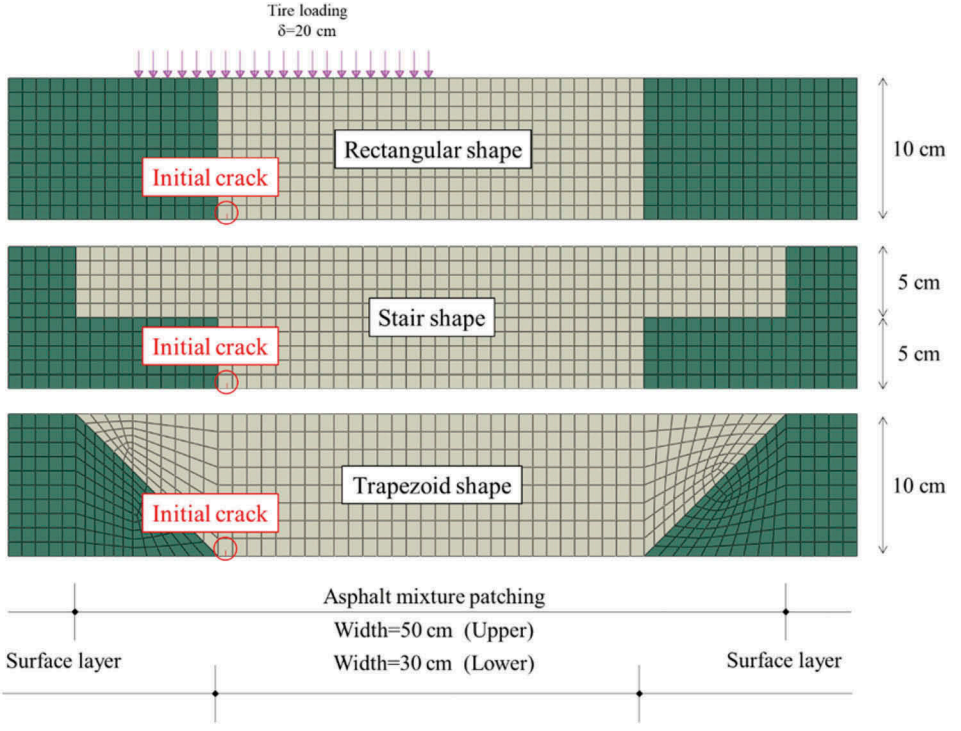

Figure 3. Shapes of the asphalt mixture patching.

the strength of the surface layer were determined according to [15], and the model parameters for the rest layers in the asphalt pavement were determined according to [16]. All the model parameters are listed in Table 1.

Table 1. Model parameters.

	Modulus (MPa)	Poisson's ratio (-)	Strength (MPa)
Surface layer	4535	0.35	0.2
Asphalt mixture patching	2902	0.35	0.35
Base layer	5219	0.25	-
Frost blanket	101	0.45	-
Subgrade	45	0.45	-

In this study, the static tire loadings were applied on the patched and unpatched asphalt pavements with the pre-defined initial cracks. To deeply investigate the patched asphalt mixture on the fracture performance of asphalt pavements, the initial cracks were inserted near the interface between surface layer and patched asphalt mixture, as shown in In addition, the temperature declining process of the patched asphalt mixture was simulated. According to the engineering practice, the temperature in the production of the asphalt mixtures is about 150 ºC, and the environmental temperature near the asphalt pavement surface is about 30 ºC. Therefore, the cooling process in the temperature stress simulation is defined from 150 ºC to 30 ºC, and the horizontal and shear stress distributions are exhibited.

3 RESULTS AND DISCUSSION

3.1 *Traffic loading simulation*

The scalar damage variables and shear stress distribution were extracted to exhibit the crack propagation and mechanical behavior of asphalt pavements, as shown in Figure 4 and Figure 5. In addition, the unpatched asphalt pavement was simulated for the comparison consideration.

It can be seen from Figure 4 that the crack propagation behaviors in the four different surface layers shown remarkable differences. Due to the insertion of the patched asphalt mixture, the crack propagation behaviors in the patched asphalt pavements are more serious than that in the unpatched asphalt pavement, which can be ascribed to the lower stiffness of the asphalt mixture patching. The asphalt mixture patching position in the asphalt pavement is "softer" than other position, which can cause higher stress responses in the surface layer, especially in the initial crack tips. Therefore, the patched asphalt pavements are more vulnerable to the crack propagations. In addition, it should be noted that the crack in the rectangular shape propagates longer than that in the other two patched asphalt pavements. According to the asphalt mixture patching shapes, it can be deduced that the crack in the stair and trapezoid patched asphalt pavements evolved entirely in the asphalt mixture patching, while in the rectangular patched pavement, half of the crack propagation occurs in the original asphalt surface layer. According to the common practice, the aged asphalt mixture has lower strength, and therefore, the rectangular patched asphalt pavement shows more crack propagation. On the contrary, the other two patched asphalt pavements show shorter crack length. Further, the crack in the stair patched asphalt pavement shows the shortest length amongst the three patched asphalt pavements, which is caused by the direction of the interfaces between patched and original asphalt mixture. The interface in the trapezoid patched asphalt pavement is a slope, and hence higher stress will distribute in the pavement.

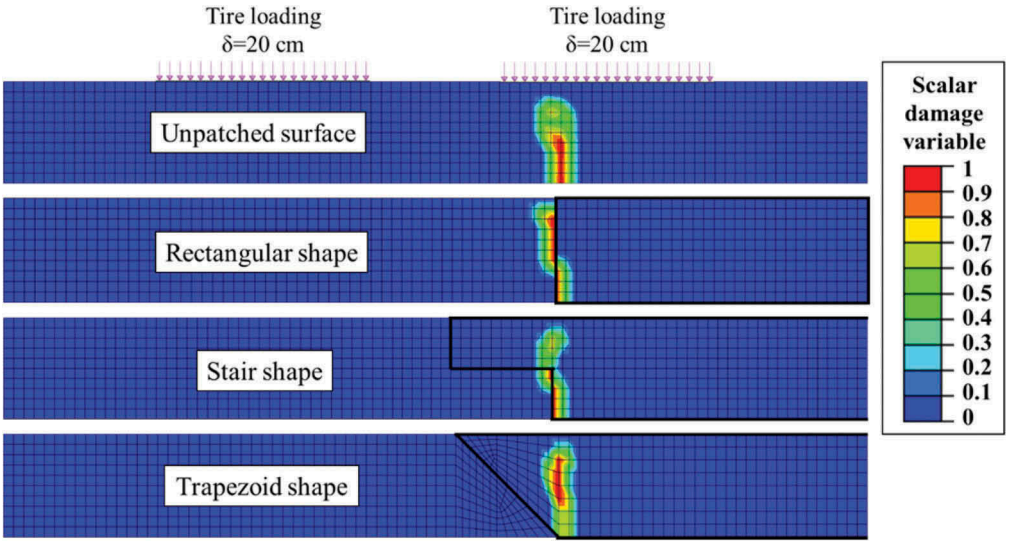

Figure 4. Scalar damage variable distributions under traffic loading.

To further investigate the stress responses in the pavements with consideration of the crack behaviors, the shear stress distributions are extracted and analyzed. Figure 5 presents the shear stress distribution in the unpatched pavement and three patched pavements. It can be seen that the shear stress in the three patched shows higher values in the interface between patched and original asphalt mixture. Comparing the three patched asphalt pavement, the shear stress distributions in the rectangular and stair patched pavements are close to each other; whilst higher shear stress distributes in the trapezoid patched pavement, which is consistent with the crack propagation behavior. Therefore, it can be concluded that the slope interface in the patched asphalt pavement will cause higher stress responses in the pavement.

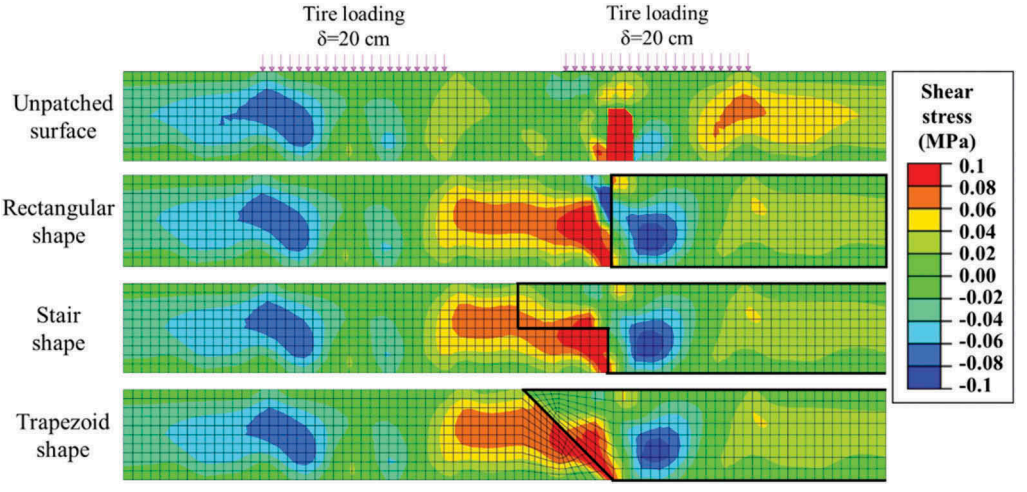

Figure 5. Shear stress distribution under traffic loading.

To evaluate the further crack evolution in the four pavement types, the horizontal stress at the crack tips was extracted and exhibited in Figure 6. It can be seen from the figure that the horizontal stress at crack tips in the stair and trapezoid patched pavements are relatively

lower, which can be ascribed to the patched asphalt mixture. In the stair and trapezoid patched asphalt pavements, the crack mainly propagates in the patched asphalt mixture. However, the stiffness and strength of the patched asphalt mixture are relatively lower and higher than the original asphalt mixture, and therefore, the horizontal stress at the crack tips in these two patched pavements are reduced. On the other hand, the horizontal stress at the crack tip in the cube patched asphalt pavement is the highest amongst the four pavements. These phenomena can be explained that the crack mostly propagates in the original asphalt mixture in this pavement type, and the high difference between the stiffness in the original and patched asphalt mixtures causes higher stress concentration in the crack tip.

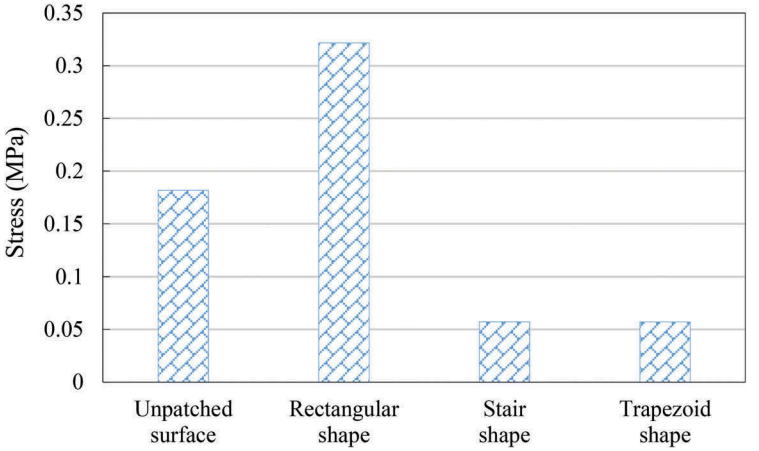

Figure 6. Horizontal stress at crack tips.

3.2 *Temperature stress*

The horizontal and shear stress distributions in the patched asphalt pavements in the temperature cooling process from 150 ºC to 30 ºC are exhibited in Figure 7 and Figure 8, respectively. The stress in the rectangular patched pavement is lower than that in the other two patched pavements, which might be caused by that the volume of the rectangular patching is the smallest amongst the three patched shapes. Therefore, lower stress will be generated in the

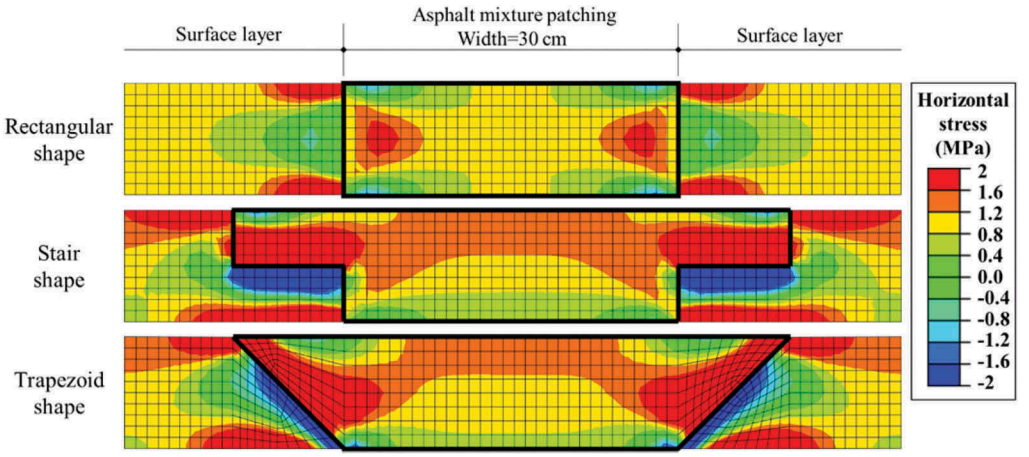

Figure 7. Horizontal stress distribution under temperature cooling process.

rectangular patched pavement during the cooling down process. For the other two patched pavements, the horizontal stress distributions are close to each other in the stair and trapezoid patched asphalt pavements; however, the shear stress in the trapezoid patched pavement is much higher than that in the stair patched asphalt pavement.

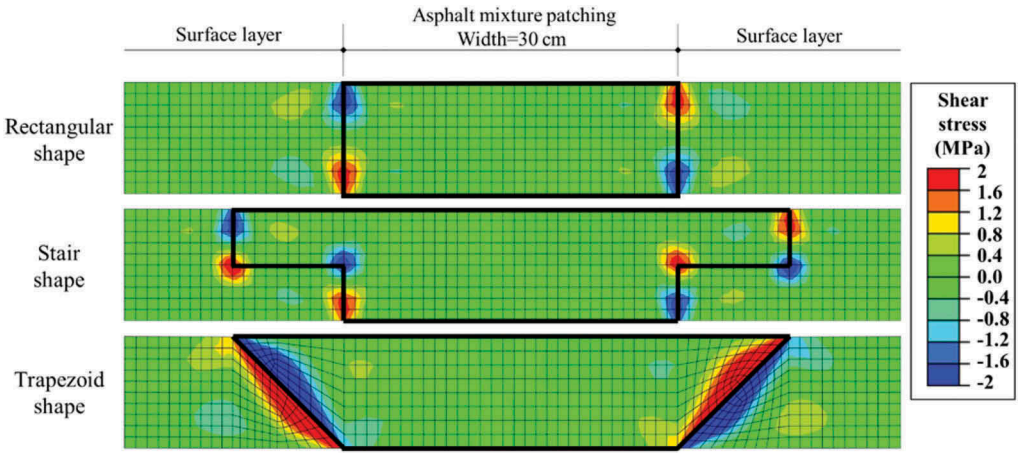

Figure 8. Horizontal stress distribution under temperature cooling process.

The maximum horizontal and shear stress with their locations caused by the temperature contraction are extracted and presented in Figure 9. It can be observed that the trapezoid patched asphalt pavement has the highest horizontal and shear stress during the cooling process, followed by stair and rectangular patched pavements. This phenomenon can be explained that the temperature stress is closely related to the volume of the patched asphalt mixture. The rectangular patched pavement requires the least patched asphalt mixture and hence causes the lowest stresses amongst the three pavements. According to the location of the maximum stress, the maximum horizontal and shear stress in the rectangular patched pavement occur in the surface of the asphalt mixture layer. In the trapezoid patched asphalt

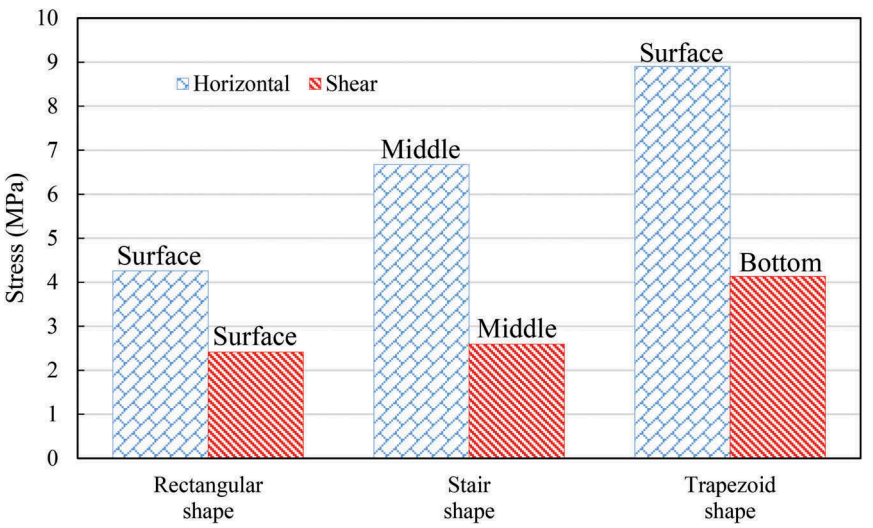

Figure 9. Maximum horizontal and shear stress in the three patched asphalt pavements.

pavement, the maximum horizontal and shear stress respectively exist in the surface and bottom of the asphalt mixture layer. Thus, it can be deduced that cracks can easily occur in the surface of the rectangular and trapezoid patched pavements. However, in the stair patched pavement, both the maximum horizontal and shear stress occur in the middle of the asphalt mixture layer. Therefore, the stair shape is recommended for asphalt pavement patching to reduce the effects of the temperature stresses in the construction process.

4 CONCLUSION

To investigate the mechanical and crack performance of the patched asphalt pavements under traffic tire loading and temperature cooling stress, three types of patched asphalt mixture, including rectangular shape, stair shape and trapezoid shape, were established and simulated using the ABAQUS finite element method. To simulate the crack propagate in the asphalt pavement, the extended finite element (XFEM) was employed. A pre-defined crack initiation was inserted in the bottom of the asphalt mixture layer, and a static tire load was applied on the surface of the asphalt pavement. The crack evolution behavior was also simulated in the unpatched pavement. In addition, the temperature cooling process during the construction of the patched asphalt mixture was simulated, and the horizontal and shear stress distributions were analyzed. The main conclusions are as the following.

(1) The patched asphalt pavements are more vulnerable to the crack propagation than the unpatched asphalt pavement especially the rectangular patched pavement, which is caused by the higher strength and lower stiffness of the unpatched asphalt mixture.
(2) The higher shear stress during the traffic loading distributes in the trapezoid patched asphalt pavement mostly because the slope interface between original and patched asphalt mixture.
(3) In the crack tip, the highest horizontal stress occurs in the rectangular patched asphalt pavement, which indicates that the rectangular shaped pavement are the most vulnerable to the further crack evolution amongst the four pavement types. In addition, the horizontal stress in the stair and trapezoid patched pavement are both lower than that in the unpatched asphalt pavement.
(4) In the temperature cooling simulation of the three patched asphalt pavements, the temperature stress distribution is related to the volume of the patched asphalt mixture. Therefore, the least horizontal and shear stress distribute in the rectangular patched asphalt pavement.
(5) The locations of maximum horizontal stress and shear stress exist in the middle of the stair patched asphalt mixture layer, which indicates that the crack initiation is less possible to occur in this pavement type during the construction process.

ACKNOWLEDGMENT

This research is funded by German Research Foundation (Grant Project No. FOR 2089/2, OE 514/1-2) and Excellence Strategy of the German Federal and State Governments (Grant Project No. StUpPD373-20). The authors gratefully acknowledge their financial support.

REFERENCES

[1] Kwon, B.J., Kim, D., Rhee, S.K., Kim, Y.R., Spray injection patching for pothole repair using 100 percent reclaimed asphalt pavement, Construction and Building Materials 166 (2018) 445–451.
[2] Yang, Y.M., Qian, Z.D., Song, X., A pothole patching material for epoxy asphalt pavement on steel bridges: Fatigue test and numerical analysis, Construction and Building Materials 94 (2015) 299–305.

[3] Zhao, L.D., Tan, Y.Q., A Summary of Cold Patch Material for Asphalt Pavements, in: L.J. Li (Ed.), Advances in Building Materials, Pts 1-3, Trans Tech Publications Ltd, Stafa-Zurich, 2011, pp. 864–869.
[4] Yuan, J.W., Dong, Q., Zhang, T.J., Gu, X.Y., Design and Performance Evaluation of Cement Enhanced Cold Patch Asphalt Mixture, Springer-Verlag Singapore Pte Ltd, Singapore, 2018.
[5] Belytschko, T., Black, T., Elastic crack growth in finite elements with minimal remeshing, Int. J. Numer. Methods Eng. 45(5) (1999) 601–620.
[6] Elguedj, T., Gravouil, A., Combescure, A., Appropriate extended functions for X-FEM simulation of plastic fracture mechanics, Comput. Meth. Appl. Mech. Eng. 195(7-8) (2006) 501–515.
[7] Sukumar, N., Huang, Z.Y., Prevost, J.H., Suo, Z., Partition of unity enrichment for bimaterial interface cracks, Int. J. Numer. Methods Eng. 59(8) (2004) 1075–1102.
[8] Sukumar, N., Prevost, J.H., Modeling quasi-static crack growth with the extended finite element method Part I: Computer implementation, International Journal of Solids and Structures 40(26) (2003) 7513–7537.
[9] Huang, R., Sukumar, N., Prevost, J.H., Modeling quasi-static crack growth with the extended finite element method Part II: Numerical applications, International Journal of Solids and Structures 40(26) (2003) 7539–7552.
[10] Cox, J.V.,, An extended finite element method with analytical enrichment for cohesive crack modeling, Int. J. Numer. Methods Eng. 78(1) (2009) 48–83.
[11] Association, G.R.a.T.R., Guidelines for the standardisation of pavement structures of traffic areas, RStO 12, Cologne, Germany, 2012.
[12] Wang, P.E.Y., Wen, Y., Zhao, K.C., Chong, D., Wong, A.S.T., Evolution and locational variation of asphalt binder aging in long-life hot-mix asphalt pavements, Construction and Building Materials 68 (2014) 172-182.
[13] Li, P.L., Ding, Z., Zhang, Z.Q., Analysis of Performance Decay Behavior for Asphalt Pavement Based on Aging, in: J.R. Chang, S.R. Yang (Eds.), Innovation and Sustainable Technology in Road and Airfield Pavement, Trans Tech Publications Ltd, Durnten-Zurich, 2013, pp. 22-+.
[14] Baek, C., Underwood, B.S., Kim, Y.R., Effects of Oxidative Aging on Asphalt Mixture Properties, Transp. Res. Record (2296) (2012) 77–85.
[15] Sun, Y.R., Du, C., Zhou, C.H., Zhu, X.X., Chen, J.Y., Analysis of load-induced top-down cracking initiation in asphalt pavements using a two-dimensional microstructure-based multiscale finite element method, Engineering Fracture Mechanics 216 (2019) 21.
[16] Liu, P., Wang, D., Hu, J., Oeser, M., SAFEM – Software With Graphical User Interface for Fast and Accurate Finite Element Analysis of Asphalt Pavements, Journal of Testing and Evaluation 45 (4) (2017) 1301–1315.

Eleventh International Conference on the Bearing Capacity of Roads, Railways and Airfields, Volume 2 – Hoff, Mork & Saba (eds)

IFC development for BIM application to railway projects

S. Fontul
Transportation Department, LNEC, Lisbon, Portugal

M.J. Falcão Silva & P. Couto
Buildings Department, LNEC, Lisbon, Portugal

ABSTRACT: Transport infrastructures such as roads, railways and runways are under increased traffic loading and their rehabilitation has to be performed in an efficient way, structurally and financially. In this process, monitoring of structural and functional capacity of transport infrastructures using nondestructive tests is performed in a systematic way. It is important to take advantages of these measurements to plan a future rehabilitation.

Using the Building Information Modelling (BIM) methodology, it is possible to obtain a model that, besides containing the three-dimensional graphic representation of the pavement or rail track and its physical and mechanical characteristics, also has information regarding the structural condition resulting from the continuous inspections.

The authors developed case studies of BIM applied to roads, runways and railways for the integration of structural capacity in the modelling, the study of transition zones and their behavior and the modelling of rehabilitation solutions for existing infrastructures.

To minimize compatibility problems between the various software based on this methodology, a standard format called Industry Foundation Classes (IFC) has been developed. This allows the user to have access to all the information without being limited to the source software of the model.

In this paper, the application of IFC to railways projects was evaluated. Therefore, basic criteria that allow IFC to store all the essential information for the railway design were presented in this study. Their implementation in a case study of a railway structural assessment is still under development. The main troubleshooting and consideration reached so far are presented herein, identifying the advantages of BIM approach.

Keywords: BIM, IFC, Structural elements, Railways

1 INTRODUCTION

The Architecture, Engineering, Construction and Operation (AECO) sector still requires efficiency improvement, due to the occurrence of tasks repetition, as well as the costs increase or the deadlines extension for the conclusion of projects.

Building Information Modelling (BIM) is seen as an innovative methodology, which allows for complete collaboration and compatibility, being pointed out as the solution for increasing the competitiveness and sustainability needed by the construction sector (CEN/TC 442, 2020). BIM is a construction approach methodology, created with the aim of facilitating integration and interoperability in the construction industry. For the verification of the above motivations, it is essential for the coordination to be precise and coherent, so as not to jeopardize

DOI: 10.1201/9781003222897-38

the project's viability or the productivity of those involved. In recent years, BIM has had a dizzying development, with an increasing need to interact with this methodology on a daily basis, thus demanding a re-education of designers.

Transport infrastructures are critical for society. The authors developed case studies of BIM applied to roads, runways and railways. In the road and airport pavements cases, the integration of structural capacity in the modelling was studied (Manico, 2018) (Lopes, 2017). Regarding the railway's cases, a construction of a transition zone was addressed and its behavior during the first three years after entering in service was modelled (Carmali, 2018). For both roads and railways, rehabilitation of existing infrastructures was modelled using BIM (Manico, 2018) (Pereirinha, 2018).

Mainly, in case of railways a rigorous interaction between several stakeholders is required. There are various areas that are crucial to railway user's safety, such as signaling, electricity supply, communications and, one of the most important, the infrastructure condition. The railway presents increased complexity in terms of maintenance due to the interdictions needed for maintenance actions. Therefore, it is important to monitor the rail track condition in a systematic way (Solla et al, 2021) and to follow its deterioration in time to be able to plan maintenance actions efficiently. BIM represent an essential tool to reflect track condition evolution in time (Fontul et al, 2021).

It is common knowledge that the various stakeholders in the AECO sector, both at the project level and in the different phases of work and exploration, sometimes do not use compatible applications in carrying out their work, others often need inputs from different specialties, which are not always available with the necessary quality and brevity, or still have different levels of knowledge and mastery in relation to the BIM methodology. In this sense, the study of interoperability is a topic of the greatest relevance and timeliness, considering several types: i) interoperability between applications; ii) interoperability between different stakeholders and specialties; iii) interoperability between people with very different levels of education and/or knowledge in the area. The issue of interoperability is inseparable from buildingSMART, which has as main objective to contribute to the effective interconnection between the different stakeholders in the construction industry, throughout its life cycle, and contribute to the creation and dissemination of protocols for information exchange.

Throughout this work, the way of sharing information based on standardized data of the Industry Foundation Classes (IFC) type for railways will be presented, which were created and developed to enhance the interoperability between different applications and BIM software, being a format of open file with free access, which allows to describe the different components of a construction.

2 BASIC CONCEPTS

2.1 *Level of Development (LOD)*

Level of Development (LOD) defines the minimum requirements at a dimensional, spatial, quantitative, qualitative level, among others, that are necessary and authorized. There are 5 LODs: LOD100, LOD200, LOD300, LOD400, LOD500, and LOD350 was later added. The higher the LOD, the greater the associated requirements. In LOD100, the element can be graphically represented in the model through a symbol or other generic representation, but it does not satisfy the requirements that make it a LOD200. Information related to the element can be obtained through other elements of the model. In LOD200 the element is graphically represented in the model as a generic system, object or assembly with approximate quantities, dimension, shape, location and orientation. Non-graphical information may also be associated with the modelled element. In LOD300 the element is graphically represented in the model as a specific system, object or assembly in terms of quantity, dimension, shape, location and orientation. Non-graphical information may also be associated with the modelled element. In LOD350 the element is graphically represented in the model as a specific system, object or assembly in terms of quantity, dimension, shape, location, orientation and encounter with

other systems. Non-graphical information may also be associated with the modelled element. In LOD400 the element is graphically represented in the model as a specific system, object or assembly in terms of quantity, dimension, shape, location and orientation with information on detailing, fabrication, assembly and installation. Non-graphical information may also be associated with the modelled element. Finally, in LOD500 the modelled element is a representation verified on the ground in terms of dimension, shape, location, quantity and orientation. Non-graphical information may also be associated with the modelled element. The information required in each IFC is a function of the required LOD (Eastman et. al, 2008) (BIM Forum, 2020).

2.2 *OmniClass CICS*

The OmniClass Construction Information Classification System (CICS) was developed by the association of the International Alliance for Interoperability (IAI) with companies in the AECO sector, to respond to the need of organizing databases in an electronic way. This classification system is based on ISO 12006-2:2015 and two other classifications, UniFormat and MasterFormat (ISO 12006-2, 2015). The OmniClass can cluster, unify and update several existing CICS, making it easier to use for everyone involved. Even so, the CICS knowledge is necessary to use the most appropriate table, which is not an easy task for people outside the process (Secretariat, 2006).

OmniClass is a CICS that consists on the combination of tables. The purpose of a table system is to facilitate communication between the stakeholders, assigning a clear and simple code to each element, with all elements having an associated code that is detailed throughout the levels. Its main use is in the initial phase of the project before there is a concern with the type of material or construction method to be used. Like so many other classification systems, it has advantages, including: i) Attribution of detailed information about the project, cost data and specifications information; ii) Allow exchange of information between stakeholders; iii) Compatible with standard systems: Masterformat and Uniformat. However, OmniClass has some associated inconveniences, which should be remembered, namely: i) Number of levels of variable analysis; ii) Independent numbering system between different tables; iii) No direct correspondence with the tables proposed in ISO12006-2:2015.

OmniClass tables can be grouped into three main categories: i) Organization of construction results; ii) Classification of construction processes; iii) Organization of building resources. According to Weygant (2011), the most relevant for BIM are Elements, Work Results, Products and Properties Tables. The Properties Table is difficult to be elaborated and updated, as it concerns manufacturer-specific information, which is generally not defined, nor is there a standardization system (Secretariat, 2006).

3 INTEROPERABILITY

3.1 *Industry Foundation Classes (IFC)*

BuildingSMART defines Industry Foundation Classes (IFC) as a data schema that makes possible to contain data and exchange information between different BIM software. The IFC is currently recognized, in its version 4 (IFC4.3) dated 2020 through the ISO 16739:2020 standard, for Data Sharing in the Construction and Building Management Industries, which defines the concept of data structure, as well as the format of the exchange file to be used in BIM (ISO 16739, 2020).

The IFC schema is a standardized data model that codifies, in a logical way: i) Identity and semantics (name, machine-readable unique identifier, object type or function); ii) Characteristics or attributes (such as material, colour and thermal properties); iii) Relationships (including locations, connections and ownership); iv) Objects (like columns or slabs); v) Abstract concepts (performance, costing); vi) Processes (installation, operations); vii) People (owners, designers, contractors, suppliers, etc.). The schema specification can describe how a facility or

installation is used, how it is constructed and operated. IFC can define physical components of buildings, manufactured products, mechanical/electrical systems, as well as structural analysis models, energy analysis models, cost breakdowns, work schedules, and much more.

The IFC scheme have information about an asset life cycle (conception, design, construction, operation and demolition phases). The need to adopt this type of formats is a consequence of the large number of software that intervene throughout the lifecycle and in which the model will be used. The organization of the IFC data structure includes four levels (Figure 1): Resources, Core, Interoperability and Domain.

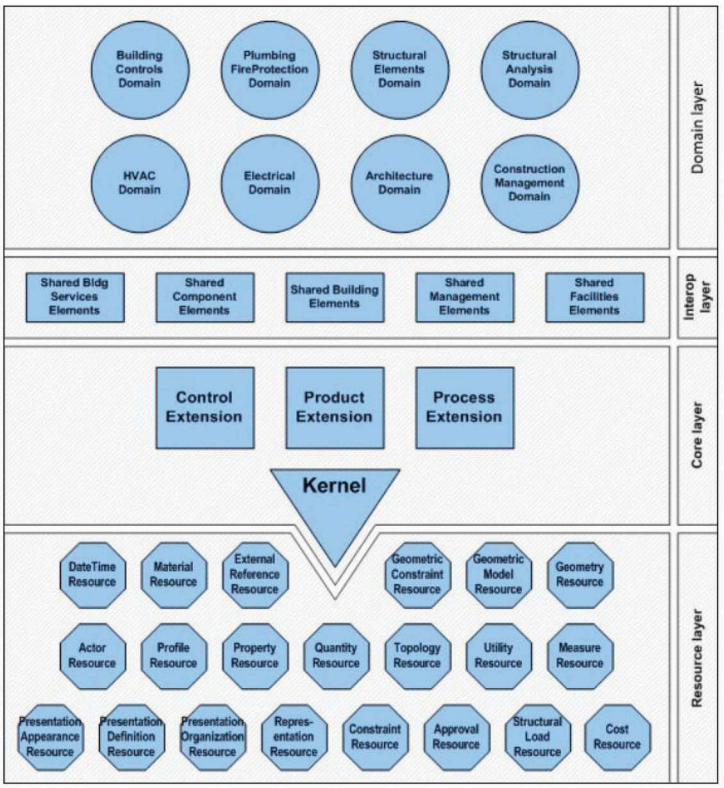

Figure 1. Schematic IFC4 Structure, adapted from buildingSMART (2021a).

According to Oliveira (2016), buildingSMART's ambition to make the IFC a complete and comprehensive format is conditioned, given that the defined variables are insufficient to accommodate all the properties necessary for the building elements.

The lowest level, the Resources level, includes all structures that contain definitions relating to resources, does not have a globally unique identifier and should not be used separately from the definition established at the top level. Regarding the Core level, this covers the most generic definitions of entities, which are defined at this level or higher, comprise a unique global identification, and may contain information relating to the owner. The Interoperability level gathers the entities definition structures that are specific to a generic product, process or resource, used in various specialties; these definitions are normally used in the exchange and sharing of construction information between different domains, and within the scope of this work, a particular focus is given to this level. The highest level, the Domain level, encompasses all structures and definitions of entities that are not specializations of a specific product,

process or resource inherent in a particular specialty. These definitions are commonly used in exchanging and sharing the construct within the domain itself. In general, these levels can describe geometric and non-geometric elements, properties, performance, processes, among other elements (buildingSMART, 2021a).

IFC files use the STEP structure, in which each object described has a unique identifier that ensures compatibility between the IFC files and the possibility of completing the object's information. There is currently a lot of information on IFC transport infrastructures, developed by buildingSMART, including reports with the codes, with some information still to be developed and published (Figure 2).

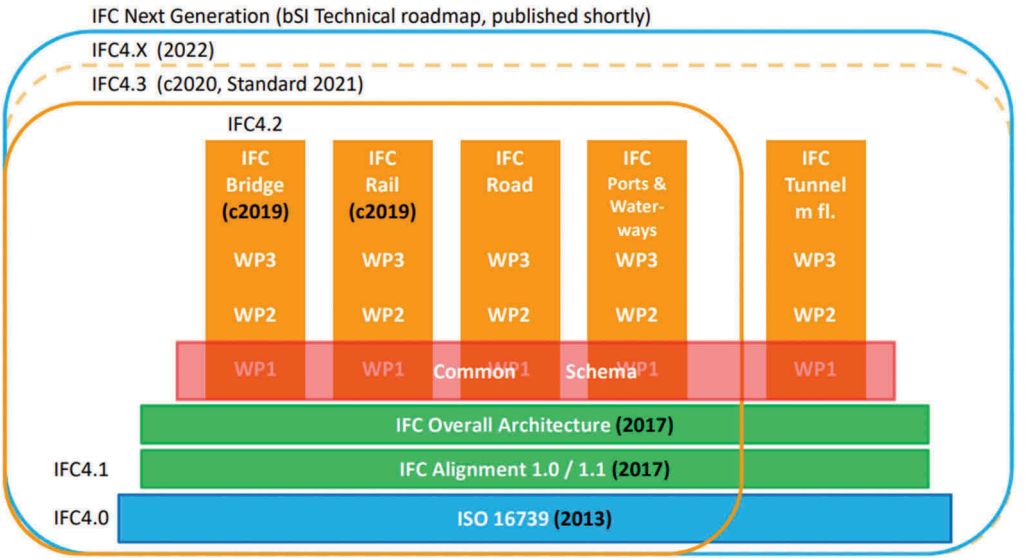

Figure 2. IFC developed and to be developed, *copyright of IFC Road,* (buildingSMART, 2021a).

3.2 *NATSPEC element matrix*

NATSPEC BIM, a division responsible for the Standardization of Practices for the Exchange of Digital Building Information in Australia, has created several written documents that define how BIM should be implemented in a project, the so-called National BIM Guides, among which stand out, as it is of particular interest for the elaboration of this work, the BIM Element Matrix (BIM Object/Element Matrix). This matrix consists of a set of tables developed with the intention of being used in the identification and chaining of BIM information, throughout the life cycle of the work (NATSPEC, 2011b). The information listing is referenced according to the OmniClass CICS and according to the LOD for the different phases of the life cycle.

The matrix organization (Figure 3) includes a logical sequence of columns, from left to right: i) Definition of development levels (5LODs); ii) Categorization of information, with colour code in which information is grouped according to the level of development required and the objectives defined in the project. The corresponding OmniClass CICS tables are also referenced: iii) Properties of the element or construction system; iv) Responsibility matrix for each item related to the element; v) Information of the data required by the customer; vi) Relation of the information in the second column with the corresponding IFC variable. An illustrative image and a general description of the element are also requested. According to Oliveira (2016), NATSPEC's BIM Object/Element Matrix presents greater development in associated information, to the detriment of the element's geometric characteristics.

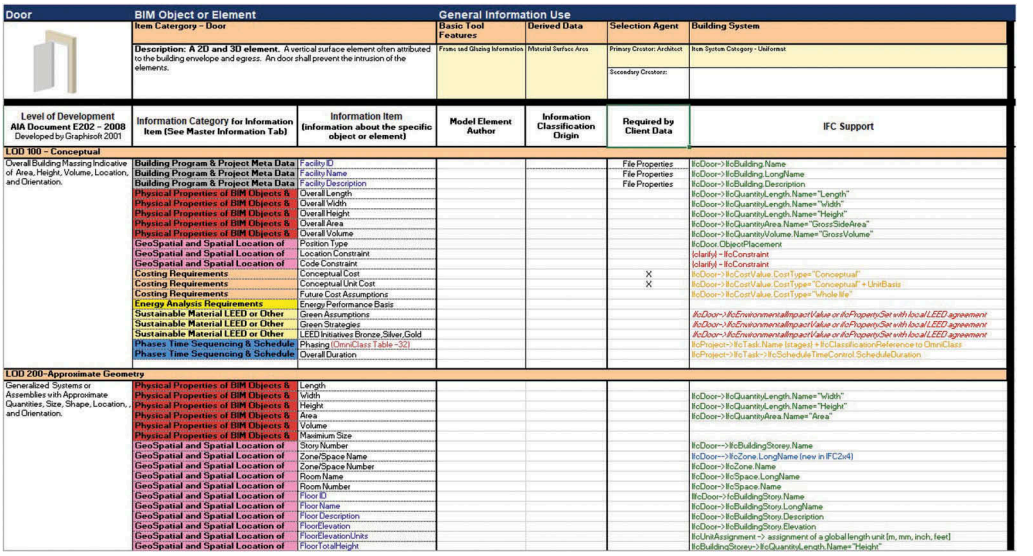

Door	BIM Object or Element		General Information Use			
	Item Catergory – Door		Basic Tool Features	Derived Data	Selection Agent	Building System
	Description: A 2D and 3D element. A vertical surface element often attributed to the building envelope and egress. An door shall prevent the intrusion of the elements.		Frame and Glazing Information	Material Surface Area	Primary Creator: Architect Secondary Creators:	Item System Category - Uniformat
Level of Development AIA Document E202 – 2008 Developed by Graphisoft 2001	Information Category for Information Item (See Master Information Tab)	Information Item (Information about the specific object or element)	Model Element Author	Information Classification Origin	Required by Client Data	IFC Support
LOD 100 – Conceptual						
Overall Building Massing Indicative of Area, Height, Volume, Location, and Orientation.	Building Program & Project Meta Data	Facility ID			File Properties	IfcDoor->IfcBuilding.Name
	Building Program & Project Meta Data	Facility Name			File Properties	IfcDoor->IfcBuilding.LongName
	Building Program & Project Meta Data	Facility Description			File Properties	IfcDoor->IfcBuilding.Description
	Physical Properties of BIM Objects &	Overall Length				IfcDoor->IfcQuantityLength.Name="Length"
	Physical Properties of BIM Objects &	Overall Width				IfcDoor->IfcQuantityLength.Name="Width"
	Physical Properties of BIM Objects &	Overall Height				IfcDoor->IfcQuantityLength.Name="Height"
	Physical Properties of BIM Objects &	Overall Area				IfcDoor->IfcQuantityArea.Name="GrossSideArea"
	Physical Properties of BIM Objects &	Overall Volume				IfcDoor->IfcQuantityVolume.Name="GrossVolume"
	GeoSpatial and Spatial Location of	Position Type				IfcDoor.ObjectPlacement
	GeoSpatial and Spatial Location of	Location Constraint				(clarify) – IfcConstraint
	GeoSpatial and Spatial Location of	Code Constraint				(clarify) – IfcConstraint
	Costing Requirements	Conceptual Cost			X	IfcDoor->IfcCostValue.CostType="Conceptual"
	Costing Requirements	Conceptual Unit Cost			X	IfcDoor->IfcCostValue.CostType="Conceptual" + UnitBasis
	Costing Requirements	Future Cost Assumptions				IfcDoor->IfcCostValue.CostType="Whole life"
	Energy Analysis Requirements	Energy Performance Basis				
	Sustainable Material LEED or Other	Green Assumptions				*IfcDoor->IfcEnvironmentalImpactValue or IfcPropertySet with local LEED agreement*
	Sustainable Material LEED or Other	Green Strategies				*IfcDoor->IfcEnvironmentalImpactValue or IfcPropertySet with local LEED agreement*
	Sustainable Material LEED or Other	LEED Initiatives Bronze,Silver,Gold				*IfcDoor->IfcEnvironmentalImpactValue or IfcPropertySet with local LEED agreement*
	Phases Time Sequencing & Schedule	Phasing (OmniClass Table -32)				IfcProject->IfcTask.Name [stages] + IfcClassificationReference to OmniClass
	Phases Time Sequencing & Schedule	Overall Duration				IfcProject->IfcTask->IfcScheduleTimeControl.ScheduleDuration
LOD 200–Approximate Geometry						
Generalized Systems or Assemblies with Approximate Quantities, Size, Shape, Location, and Orientation.	Physical Properties of BIM Objects &	Length				
	Physical Properties of BIM Objects &	Width				IfcDoor->IfcQuantityLength.Name="Width"
	Physical Properties of BIM Objects &	Height				IfcDoor->IfcQuantityLength.Name="Height"
	Physical Properties of BIM Objects &	Area				IfcDoor->IfcQuantityArea.Name="Area"
	Physical Properties of BIM Objects &	Volume				
	Physical Properties of BIM Objects &	Maximum Size				
	GeoSpatial and Spatial Location of	Story Number				IfcDoor<-->IfcBuildingStorey.Name
	GeoSpatial and Spatial Location of	Zone/Space Name				IfcDoor<-->IfcZone.LongName (new in IFC2x4)
	GeoSpatial and Spatial Location of	Zone/Space Number				IfcDoor->IfcZone.Name
	GeoSpatial and Spatial Location of	Room Name				IfcDoor->IfcSpace.LongName
	GeoSpatial and Spatial Location of	Room Number				IfcDoor->IfcSpace.Name
	GeoSpatial and Spatial Location of	Floor ID				IfcDoor->IfcBuildingStory.Name
	GeoSpatial and Spatial Location of	Floor Name				IfcDoor->IfcBuildingStory.LongName
	GeoSpatial and Spatial Location of	Floor Description				IfcDoor->IfcBuildingStory.Description
	GeoSpatial and Spatial Location of	FloorElevation				IfcDoor->IfcBuildingStory.Elevation
	GeoSpatial and Spatial Location of	FloorElevationUnits				IfcUnitAssignment -> assignment of a global length unit [m, mm, inch, feet]
	GeoSpatial and Spatial Location of	FloorTotalHeight				IfcBuildingStorey->IfcQuantityLength.Name="Height"

Figure 3. NATSPEC Element Matrix – Door element (NATSPEC, 2011a).

4 IFC FOR RAILWAY PROJECTS

4.1 *IFC RAIL strategy*

The necessity to implement digitalization in all construction sectors, combined with the low productivity in the railway sector and the need to improve the structure throughout the life cycle of these infrastructures, led to the urgent need for digitization in this field, and there seems to be a growing interest in the implementation of the BIM methodology to railway infrastructures. Rail projects are a good example of a multidisciplinary project, in which different specialties use different software and the need for interoperability between them is even more important.

According to buildingSMART (2021b), in 2017 China Railway BIM (CRBIM) and the 7 European Rail Infrastructure Managers joined together and formed IFC RAIL, with the objective of drawing up a plan for the digitization of railway infrastructures, for the better design, build, operate and maintain (Figure 4). BuildingSMART was involved throughout the project to ensure that all BIM modelling processes were respected.

The IFC RAIL team focuses on advancing standardization for railway infrastructures. At the end of 2019, the work that developed the IFC files for the railways was delivered. After completion of the first phase of work, in March 2020, the team started the second phase of work in April of the same year. The second phase of the IFC RAIL project has as main objective to implement and validate the IFC 4.3 version, making it a standard for use. After completion, and subsequent validation, the standard is expected to be published in an international ISO standard. Leading to advantages for promoting the digitization of the railway infrastructures sector. These infrastructures are part of the "class" of linear infrastructures, as their length (extent) is considerably larger than the others dimensions. The way to design and budget these infrastructures is to divide the entire railway line into smaller alignments with homogeneous characteristics.

In the following item, as an example of IFC structure elements that constitute the railroad, obtained based on the NATSPEC Element Matrix, the IFC for the object type Rail (rails) is exposed.

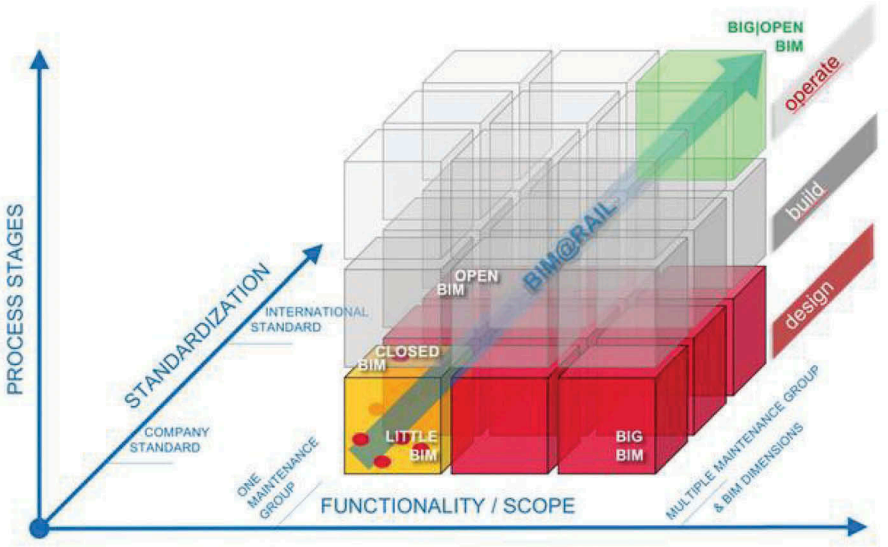

Figure 4. Summary of the strategy applied by IFC RAIL, *copyright of IFC Rail* (buildingSMART, 2021b).

4.2 *IFC RAIL existing proposal*

Rail's function is to support and transfer the concentrated loads from the train wheels to the sleepers, impose the steering on the vehicle's wheels and distribute the forces resulting from the start-up and from the adhesion braking. Generally, just for the sake of designation, the rail is divided into three parts: Head, Web and Foot. In the following, IFC proposal for rails elements are identified (considering the example of UIC60E type). The 28 IFC sources considered for rail correspond to the lower level, the Resources level (buildingSMART, 2019), as identified in Figure 1, considering that include the structures that contain resource-related definitions and can be fixed in the corresponding NATSPEC Element Matrix, in alignment with what is shown in Figure 3:

i) Space. *Designates the space in which the element fits. In this case the railway infrastructure* (rail type UIC60E). Data type – *Text*. IFC system - *IfcRail.ObjectPlacement*;
ii) Element Name. *Designates the name of the element*. Data type – *Text*. IFC system - *IfcRail->IfcTrackElement.Name;*
iii) Element Type. *Corresponds to the rail type*. Data type – Text. IFC system - *IfcRail->IfcTrackElement.type;*
iv) Element Number. *Corresponds to the identification of the rail number*. Data type – Integer. IFC system - *IfcRail->IfcTrackElement.Number;*
v) Track Gauge. *Corresponds to the rail gauge*. Data type – *Number*. IFC system - *IfcRail->IfcTrack.TrackGauge;*
vi) Elementary rail length. *Corresponds to rail unit length*. Data type – *Number*. IFC system - *IfcRail->IfcQuantityLength.Name="Length";*
vii) Dimension C. *Corresponds to the rail head width*. Data type - *Number.* IFC system - *IfcRail- >IfcQuantityLength.Name="DimensionC";*
viii) Dimension D. *Corresponds to the rail head height*. Data type - *Number.* IFC system - *IfcRail- >IfcQuantityLength.Name="DimensionD";*
ix) Dimension E. *Corresponds to the rail soul thickness*. Data type - *Number.* IFC system - *IfcRail- >IfcQuantityLength.Name="DimensionE";*
x) Relative Position. *Corresponds to the relative position of the rail in relation to the horizontal alignment*. Data type - *Text.* IFC system - *IfcRail->IfcQuantityLength.Name="Relative Position";*

xi) Vertical Moment of Inertia. *Corresponds to the vertical moment of inertia of the rail section.* Data type – *Number*. IFC system - *IfcRail->IfcQuantityLength.Name= "VerticalMomentofInertia";*
xii) Horizontal Moment of Inertia. *Corresponds to the horizontal moment of inertia of the rail section.* Data type – *Number*. IFC system - *IfcRail->IfcQuantityLength.Name= "HorizontalMomentofInertia";*
xiii) Gaps between Rails. *Corresponds to the Type of joints in rail bar joints.* Data type – *Text*. IFC system - *IfcRail->IfcObjects.Rail="GapsBetweenRails";*
xiv) Steel type. *Corresponds to the steel type used in the model*. Data type – Integer. IFC systems - *IfcRailType->IfcMaterial.Type*;
xv) Stainless. *Corresponds to the situation in which it's stainless steel (yes or no)*. Data type – *Boolean. IFC* systems - *IfcRailType->IfcMaterial.Stainless (yes/no)*;
xvi) Technical standard. *Identifies the existing standard to be applied relating to railways*. Data type – Integer. IFC systems - IfcRail->Pset_ManufacturerOccurrence->Property="Technical Standard";
xvii) Modulus of Elasticity. *Corresponds to the elasticity module of the steel that makes up the rail*. Data type – Number. IFC systems - IfcRail->IfcProperty. ModulusofElasticity;
xviii) Density. *Corresponds to the density or specific mass of the steel that makes up the rail*. Data type – Number. IFC systems - IfcRail->IfcProperty.Density;
xix) Tenacity. *Corresponds to the toughness associated with the steel that makes up the rail*. Data type – Number. IFC system - IfcRail->IfcProperty.Tenacity;
xx) Minimum Tensile Strength. *Corresponds to the minimum tensile strength value of the steel that makes up the rail*. Data type – Number. IFC system - IfcRail->IfcProperty. MinimumTensileStrength;
xxi) Flexural. *Corresponds to the flexural strength of the steel that makes up the rail*. Data type – Number. IFC system - IfcRail->IfcProperty.FlexuralStrength;
xxii) Wear. *Corresponds to the wear resistance of the steel that makes up the rail*. Data type – Number. IFC system - IfcRail->IfcProperty.WearResistance;
xxiii) Environmental Corrosion. *Corresponds to the corrosion susceptibility*. Data type – Number. IFC system - IfcRail->IfcProperty.EnvironmentalCorrosion;
xxiv) Electric Conductivity. *Corresponds to the electrical conductivity of the steel that makes up the rail*. Data type – Number. IFC system - IfcRail->IfcProperty.ElectricCondutivity;
xxv) Reused rail. *Considers if the rail is new or not*. Data type – Number. IFC system – Boolean. IFC system - IfcRail->IfcProperty.ReusedRail;
xxvi) Space Usable length. *Corresponds to the extension occupied by the rails*. Data type – Number. IFC system - IfcRail->IfcRelSpaceBoundary->IfcSpace: space quantity length;
xxvii) Space Usable length. *Corresponds to the unit to which extent is measured*. Data type – Text. IFC system - IfcUnitAssignment -> assignment of a global length unit [m, mm, inch, feet] - given consistently to all elements;
xxviii) Manufacturing date. *Corresponds to the date on which the production of the rail is expected*. Data type – Number. IFC system - IfcRail->IfcRelAssignsToProcess->IfcTask->IfcScheduleTimeControl.ActualManufacturing.

5 FINAL REMARKS

It is notorious the growing recognition by the construction industry of the predominant role of BIM and the necessity for the digitization of the sector (Industry 4.0). This is justified by the huge investment, both public and private, that exists around the world in this sector. To ensure the success of projects, resulting from the increased use of these methodologies, it is necessary to guarantee complete interoperability between all entities involved in the project. It

is necessary to create instruments that allow the definition of the requirements needed for the model.

In a project environment, the application of new work methodologies, such as BIM, requires time for analysis, which is not an easy task nowadays. However, competitiveness requires companies to keep up with the evolution of the construction digitalization. In the field of transport infrastructures, it is possible to state that the IFC variables are still insufficient to define the construction elements, making the application of the BIM methodology difficult. However, numerous advantages are foreseen in its application, either in the design and construction phase, or during the follow-up of the work.

Despite the issue of interoperability being a wide-ranging issue, there is still a long way to go, particularly in the case of railway infrastructures. The standardization of these infrastructures is still just an application proposed by buildingSMART (IFC RAIL) and, therefore, the validity of the correspondence of the IFC variables is not known, nor are these available for the software.

In the specific case of Portugal, there are already some studies carried out for transport infrastructures, and considerable effort is still required, both financially and personally.

ACKNOWLEDGEMENTS

The authors acknowledge the contributions of Eng.ª Patrícia Vieira to the development of this research work.

REFERENCES

BIMForum, 2020 - LOD - Mentions of the LOD Specification. BIMForum, 2020. <https://bimforum.org/lod/>.

BuildingSMART, 2019 – IFC Rail Project – WP2 Data Requirements Report.

BuildingSMART, 2021a – IFC Road Project. <https://www.buildingsmart.org/standards/calls-for-participation/ifcroad/>

BuildingSMART, 2021b – IFC Rail Project. <https://www.buildingsmart.org/standards/rooms/railway/ifc-rail-project>.

Carmali, S., 2018. BIM application to railway infrastructures. Quality control during construction. MsC dissertation. Nova University of Lisbon, Portugal.

CEN/TC 442 - Business Plan. CEN/TC 442 Building Information Modelling, 2020. Disponível em WWW: <http://standards.cen.eu/BP/1991542.pdf>.

Eastman, C. et al., 2008 - Eastman, Chuck; Teicholz, Paul; Sacks, Rafael; Liston, Kathleen - BIM Handbook: A Guide to Building Information Modeling for Owners, Managers, Designers, Engineers and Contractors. Wiley Publishing, 2008.

Fontul S., Couto P., Silva M.J.F. (2021) BIM Applications to Pavements and Railways. Integration of Numerical Parameters. In: Rodrigues H., Gaspar F., Fernandes P., Mateus A. (eds) Sustainability and Automation in Smart Constructions. Advances in Science, Technology & Innovation (IEREK Interdisciplinary Series for Sustainable Development). Springer, Cham. https://doi.org/10.1007/978-3-030-35533-3_10

ISO 12006-2:2015 - Standardization, International Organization for - ISO 12006-2:2015 Building Construction - Organization of Information about Construction Works. Geneva: International.

ISO 16739:2020 –Standardization, International Organization for - ISO 16739:2020 Industry Foundation Classes (IFC) for data sharing in the construction and facility management industries. Geneva: International.

Lopes, J., 2017. Evaluation of airport infrastructures. Proposal for data integration in BIM. MsC dissertation. Nova University of Lisbon, Portugal.

Manico, H., 2018. Flexible road pavements in Angola. Characterization and application of BIM methodologies. MsC dissertation. Nova University of Lisbon, Portugal.

NATSPEC, 2011a - BIM Object/Element Matrix. NATSPEC, 2011. Disponível em WWW:<https://www.bim.natspec.org/documents/natspec-national-bim-guide/NATSPEC_BIM_Object-Element_Matrix_v1.0_Sep_2011.xls>.

NATSPEC, 2011b - NATSPEC National BIM Guide. Australia: Construction Information Systems Limited, 2011b.

Oliveira J., 2016. BIM Standardization - Level of Development Specification and Modeling by Objectives. MsC dissertation, Civil Engineering Department, FEUP, Oporto University, Portugal.
Pereirinha, A., 2018. Application of BIM methodology in monitoring and rehabilitation of railway infrastructures. MsC dissertation. Nova University of Lisbon, Portugal.
Secretariat, O., 2006, - Secretariat, OmniClass - OmniClass - Introduction and User's Guide. USA: Construction Specifications Institute, 2006.
Solla, M., Pérez-Gracia, V., Fontul, S., 2021. A Review of GPR Application on Transport Infrastructures: Troubleshooting and Best Practices. Remote Sens. 2021, 13(4), 672; https://doi.org/10.3390/rs13040672
Weygant, R. S. (2011). BIM content development: standards, strategies, and best practices. John Wiley & Sons.

Eleventh International Conference on the Bearing Capacity of Roads, Railways and Airfields, Volume 2 – Hoff, Mork & Saba (eds)

Construction of asphalt mixture master curves for a Norwegian mechanistic-empirical pavement design system

Hao Chen, Diego Maria Barbieri, Inge Hoff & Helge Mork
Department of Civil and Environmental Engineering, Norwegian University of Science and Technology, Trondheim, Norway

Pål Wathne
Norconsult AS, Trondheim, Norway

Gang Liu
School of Materials Science and Technology, Wuhan University of Technology, Wuhan, China

ABSTRACT: As part of the development of a mechanistic-empirical pavement design system for Norwegian conditions, this paper presents the results of a laboratory study assessing asphalt mixture master curves based on Cyclic Indirect Tensile Tests (CITT). Specimens were prepared by means of a gyratory Intensive Compactor Tester (ICT), as well as by means of a roller compactor. The four asphalt mixtures of AC (asphalt concrete) 11, AC 16, SMA (stone mastic asphalt) 11, and SMA 16 with bitumen 70/100 commonly used as the surface layer in Norway were investigated. The dynamic modulus of the asphalt mixture samples was determined by frequency-sweep CITT at different temperatures. Based on the time-temperature superposition principle, the master curves were constructed and they are an important input for the mechanistic-empirical pavement design system to be implemented in the country. The voids characteristics, shift factor, and dynamic modulus of the four types of asphalt mixtures were compared. Besides, the effect of different compaction methods in the laboratory was investigated and recommendations regarding the specimen preparation were given.

Keywords: Asphalt mixture, cyclic indirect tensile test, dynamic modulus, master curve

1 INTRODUCTION

The Norwegian Public Roads Administration (NPRA) in cooperation with Swedish Transport Administration (TV), Swedish National Road and Transport Research Institute (VTI) and Norwegian University of Science and Technology (NTNU) is developing and implementing a new mechanistic design system for Norwegian roads adopting the mechanistic-empirical approach, which is based on the mechanics of materials for evaluating the pavement response (Huang, 1993). The characterization of asphalt mixtures is a central task to achieve this. The asphalt materials have viscoelastic behavior with distinctive temperature- and frequency-dependent properties (Lesueur et al. 1996). The dynamic modulus at different temperatures and frequencies characterizes the mechanical properties of asphalt mixtures, and can be evaluated in the laboratory by performing the uniaxial compression test (NCHRP, 2004) and the Cyclic Indirect Tensile Test (CITT) (Kim et al. 2004). The dynamic modulus master curve can then be constructed according to the time-temperature superposition principle within the Linear ViscoElastic (LVE) range by

DOI: 10.1201/9781003222897-39

horizontally shifting the test results measured based on a selected reference temperature (Chehab et al. 2002, Schwartz et al. 2002). A dynamic modulus master curve is constructed by fitting a sigmoidal function to the data, by using a time-temperature shift factor based on the Mechanistic-Empirical Pavement Design Guide (MEPD Guide) (NCHRP, 2004). The shift factor for asphalt materials can be accurately described by using the Williams, Landel and Ferry (WLF) equation at temperatures above the glass transition temperature (Williams et al. 1955). The dynamic modulus master curve can be used to predict the mechanical properties of the asphalt material for a wider frequency and temperature range than included in the actual test conditions.

The compaction of the asphalt pavement is an important factor affecting the overall performance of the material (Hunter et al. 2009). The roller compression method and gyroscopic compression method are two most commonly preparation methods of asphalt mixtures in the laboratory. Therefore, many studies have compared the influence of two laboratory compression methods on the asphalt mixture performance. Consuegra et al. (Consuegra et al. 1988) compared the engineering properties (resilient moduli, indirect tensile strengths and strains at failure, and tensile creep data) of laboratory-compacted samples prepared by roller compactor and gyratory compactor. The results related to the resilient modulus of laboratory specimens created with roller compactor were closer to the performance of field core samples than those created with gyratory compactor. Later, Button et al. (Button et al. 1994) investigated the physical properties of laboratory samples created by different compaction methods, and compared the results to the ones pertaining to pavement cores. The specimens prepared by both gyratory compactor and roller compactor were more similar to the pavement cores than the specimens prepared by the Marshall method. Besides, the roller compactor exhibited better air-void distribution than the gyratory compactor. Other researchers also indicate that the selected compaction methods exert different responses in terms of void characteristics and mechanical properties of asphalt mixtures (Sarsam and Jumaah 2016, Renken, 2000). However, the effect of the compaction methods on the dynamic modulus of asphalt mixtures has been studied less: ie. a comparison of the influence of the roller compactor method and the gyratory compactor method on the dynamic modulus of asphalt mixtures can provide recommendations regarding the specimen preparation procedures to be used in the development of the new Norwegian pavement design system.

In this research study, four asphalt mixtures were selected; AC 11, AC 16 (asphalt concrete), SMA 11 and SMA 16 (stone mastic asphalt), being the most commonly used surface layers of Norwegian asphalt pavements. The roller compactor and the gyratory Intensive Compactor Tester (ICT) were used to prepare the asphalt mixture specimens. The dynamic modulus was measured by the CITT employing the Nottingham Asphalt Tester (NAT). The sigmoidal function based on the MEPD Guide and the WLF equation were used to construct the dynamic modulus master curves, and the influence of the different types of asphalt mixtures and the different compaction methods on the dynamic modulus master curve was evaluated. Hence, the objective of this study is to provide data support for the development of the mechanistic-empirical design system for Norwegian conditions, and to recommend a proper compaction approach.

2 MATERIALS AND METHODS

2.1 *Materials*

A 70/100 bitumen supplied by the Veidekke company (Trondheim, Norway) was used and its main physical properties are given in Table 1.

Table 1. Physical properties of bitumen 70/100.

Physical properties	Unit	Value	Test standard
Penetration at 25 °C	0.1 mm	91.6	EN 1426 (CEN, 2015)
Softening point (Ring and Ball)	°C	46.0	EN 1427 (CEN, 2015)

The crushed rocks and limestone filler supplied by the Franzefoss company (Heimdal, Norway) were adopted, and their resistance to wear and fragmentation is specified in Table 2. The aggregates used in this study fulfil the requirements for AC and SMA mixtures considering an Annual Average Daily Traffic (AADT) bigger than 15000 (NPRA, 2018).

Table 2. Resistance to wear and fragmentation of crushed rock aggregates.

Test	Value	Requirements for AADT > 15000	Test standard
Los Angeles value	18.2	≤ 20	EN 1097-2 (CEN, 2020)
Micro-Deval coefficient	14.2	≤ 15	EN 1097-1 (CEN, 2011)

2.2 *Specimen preparation*

The asphalt mixture specimens were prepared in the laboratory based on the gradation curves of AC 11, AC 16, SMA 11, and SMA 16 shown in Figure 1 (NPRA, 2019), and the Optimum Binder Content (OBC) was determined by the Marshall mixture design and specific requirements of the Air Voids Content (V_a) and the Voids Filled with Binder (VFB) (NPRA, 2005).

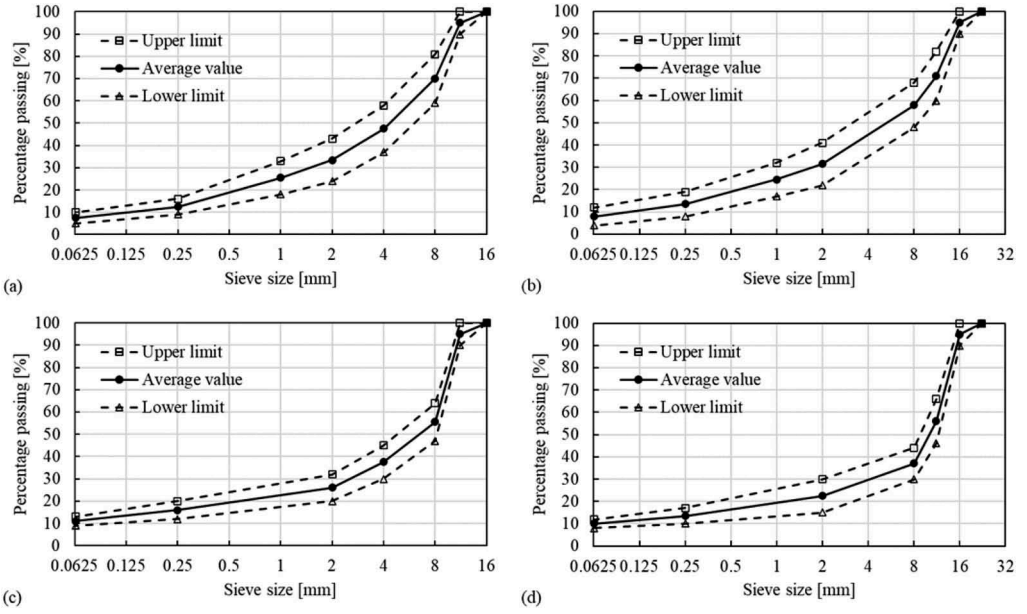

Figure 1. Gradation curves of (a) AC 11, (b) AC 16, (c) SMA 11, and (d) SMA 16.

The void characteristics of the Marshall specimens impacted by 50 blows per side were verified to meet the requirements of the design criteria (NPRA, 2019). The OBCs were 5.1%, 4.9%, 5.3%, and 5.1% for AC 11, AC 16, SMA 11, and SMA 16, respectively.

The specimens were prepared by both a roller compactor (manufactured by Cooper Technology, Ripley, UK) and a gyratory compactor (ICT-150RB produced by Invelop oy, Semolina, Finland). Referring to the former one (CEN, 2019), the space inside a mold correspond to a rectangular parallelepiped with dimensions 305 mm × 305 mm × 57 mm. The compaction process was divided into four stages further subdivided into four passes. The pressure in the first, second stage, and the third stage is 2 bar, 4 bar and 6 bar, respectively.

No pressure was provided during the fourth stage, only the weight of the roller was applied to the specimen; meanwhile, the vibration was applied at the last two passes of the fourth stage for sufficient and effective compaction.

For the gyratory compactor, the cylindrical asphalt mixture specimens had a diameter of 150 mm and a height of 180 mm. The compaction pressure was 620 kPa, and the gyratory angle was set to 17 mrad (0.97°) (CEN, 2019). To ensure sufficient compaction, 100 and 115 gyrations were applied for the AC mixtures and SMA mixtures, respectively.

Afterwards, cylindrical specimens with a diameter of 100 mm and a height of 40 mm were drilled and cut from the asphalt slabs and gyratory specimens to be tested by the CITT. The eight mixture types designated in Table 3 were investigated in this study and four parallel specimens were prepared for each type, ie. a total of 32 specimens was tested. The preparation process of specimens is shown in Figure 2. The void characteristics of NAT test specimens were also recorded (CEN, 2018).

Table 3. Designation of the tested specimens according to selected mixture type and compaction method.

Mixture type	Compaction method	Designation
AC 11	Roller compaction	AC 11-R
	Gyratory compaction	AC 11-G
AC 16	Roller compaction	AC 16-R
	Gyratory compaction	AC 16-G
SMA 11	Roller compaction	SMA 11-R
	Gyratory compaction	SMA 11-G
SMA 16	Roller compaction	SMA 16-R
	Gyratory compaction	SMA 16-G

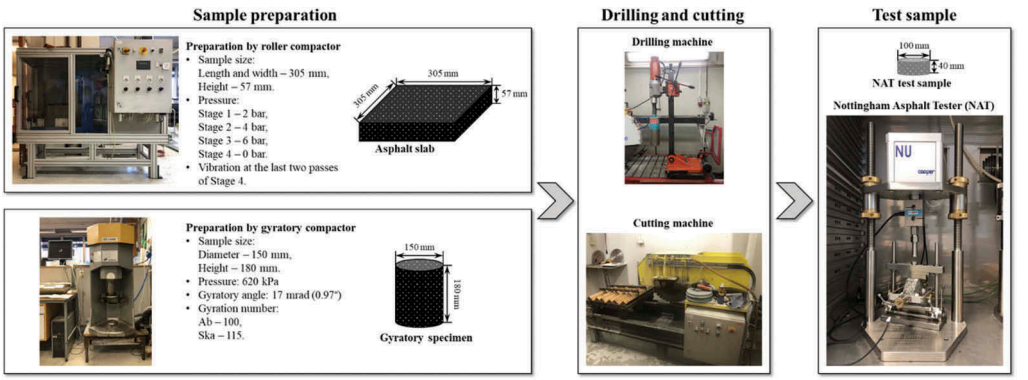

Figure 2. Preparation process of specimens.

2.3 *Cyclic indirect tensile test*

The cyclic indirect tensile test was performed by a servo-pneumatic universal testing machine produced by Cooper Technology exerting a controlled harmonic sinusoidal load without rest periods according to the relevant standard (CEN, 2018). The applied load ensured that the sample was in the LVE range as the initial horizontal strain was in a range between 50 με to 100 με for each test temperature and frequency. This research study presents the mean results corresponding to the CITT testing of four parallel specimens for each asphalt mixture.

The CITT was performed at temperatures of -15 °C, 0 °C, 15 °C and 30 °C and at frequencies of 10 Hz, 5 Hz, 3 Hz, 1 Hz, 0.3 Hz and 0.1 Hz for each specimen.

The dynamic modulus was determined for each load pulse in the CITT using the following equation:

$$|E^*| = \frac{F \cdot (\nu + 0.27)}{z \cdot h} \tag{1}$$

where $|E^*|$ is the dynamic modulus, in megapascal (MPa), v is the Poisson's ratio, F is the maximum load, in Newton (N), z is the sample thickness, in millimeter (mm), and h is the horizontal deformation, in millimeter (mm).

2.4 *Master curve construction*

The sigmoidal function described in MEPD Guide (NCHRP, 2004) and the WLF equation as the shift factor (Williams, 1955) were referred to in this study. The sigmoidal function is given by equation (2):

$$\log(|E^*|) = \delta + \frac{\alpha}{1 + e^{\beta - \gamma(\log f_r)}} \tag{2}$$

where $|E^*|$ is the dynamic modulus, in megapascal (MPa), f_r is the frequency at the reference temperature, in hertz (Hz), δ, α, β and γ are the fitting parameters, where δ represents the minimum value of $|E^*|$. $\delta + \alpha$ represents the maximum values of $|E^*|$, β and γ describe the shape of the sigmoidal function as shown in Figure 3 (Pellinen et al. 2004).

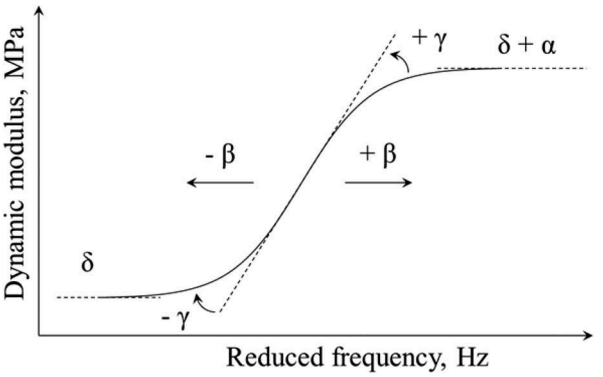

Figure 3. Shape description of dynamic modulus considering the parameters of sigmoidal function.

The shift factor, α_T, describes the temperature dependency of the dynamic modulus and Equation (3) provides the general form.

$$\alpha_T = \frac{f_r}{f} \tag{3a}$$

$$\log(f_r) = \log(f) + \log(\alpha_T) \tag{3b}$$

where f_r is the reduced frequency at the reference temperature, in hertz (Hz), f is the frequency at the test temperature, in hertz (Hz), and T is the test temperature, in degrees Celsius (°C).

The Williams-Landel-Ferry (WLF) equation is widely used to describe the relationship between the shift factor and the temperature and thereby assess the shift factor of asphalt mixtures:

$$\log[\alpha(T)] = \frac{-C_1(T - T_r)}{C_2 + (T - T_r)} \tag{4}$$

where T is the temperature, in degrees Celsius (°C), T_r is the reference temperature chosen to construct the compliance master curve, in degrees Celsius (°C), C_1 and C_2 are two empirical constants adjusted to fit the values of the shift factor.

The fitting procedure to construct the dynamic modulus master curve was conducted by using the Microsoft Excel Solver tool, in which optimization of the data with non-linear least squares regression techniques was performed. The Sum of Square Error (SSE) between measured values after shifting, $|E^*|_{measured}$, and predicted values, $|E^*|_{predicted}$, as shown in Equation (5) was used to optimize the fitting procedure. To define the optimum results of the master curves, the values of δ, α, β, γ, C_1 and C_2 were fitted to minimize SSE.

$$SSE = \sum \frac{(|E^*|_{measured} - |E^*|_{predicted})^2}{(|E^*|_{measured})^2} \tag{5}$$

3 RESULTS AND DISCUSSION

3.1 *Void characteristics*

The void characteristics reflect how well a specimen is compacted, and the results for the four asphalt mixture types prepared by both roller compactor and gyratory compactor are shown in Figure 4. The void characteristics of an asphalt mixture depend on many factors including compaction mode and effort, binder content, aggregate type, mixture type, etc. As indicated in Figure 4, the V_a of AC 11-G, AC 16-G, SMA 11-G and SMA 16-G were 0.6%, 0.7%, 1.7% and 0.8% lower than for the corresponding specimens prepared by roller compactor, respectively. The Void in Mineral Aggregate (VMA) of AC 11-G, AC 16-G, SMA 11-G and SMA 16-G were 0.5%, 0.6%, 1.5% and 0.6% lower than for the corresponding specimens prepared by roller compactor, respectively. The VFB of AC 11-G, AC 16-G, SMA 11-G and SMA 16-G were 3.0%, 3.9%, 8.0% and 3.8% higher than for the corresponding specimens prepared by roller compactor, respectively. These findings indicate that gyratory compaction applied a higher degree of compaction when compared to roller compaction. Based on the Marshall mix design performed in this study, the AC mixtures had lower V_a and VMA, and higher VFB than the SMA mixtures. Meanwhile, the specimens with larger particle size had lower V_a and VMA, and higher VFB than the specimens with smaller maximum grain size.

3.2 *Shift factors*

Figure 5 shows the WLF shift factor curves of the different mixtures. It was found that the logarithm of the shift factor linearly decreased with the increase in temperature. The linear regression results are calculated according to an equation of the form $y = ax + b$, where x is the temperature, y is the predicted shift factor, a is the slope of the line, and b is the intercept (Table 4). The coefficients of determination (R^2) of AC 11 and AC 16 were higher than those of SMA 11 and SMA 16, this shows that the logarithm of the shift factor of the AC mixtures tends to be more prone to follow a linear trend than that of the SMA mixtures; furthermore, it also shows that the shifted distances of the dynamic moduli of the AC mixtures per unit temperature were more even than those of the SMA mixtures when the master curves were constructed.

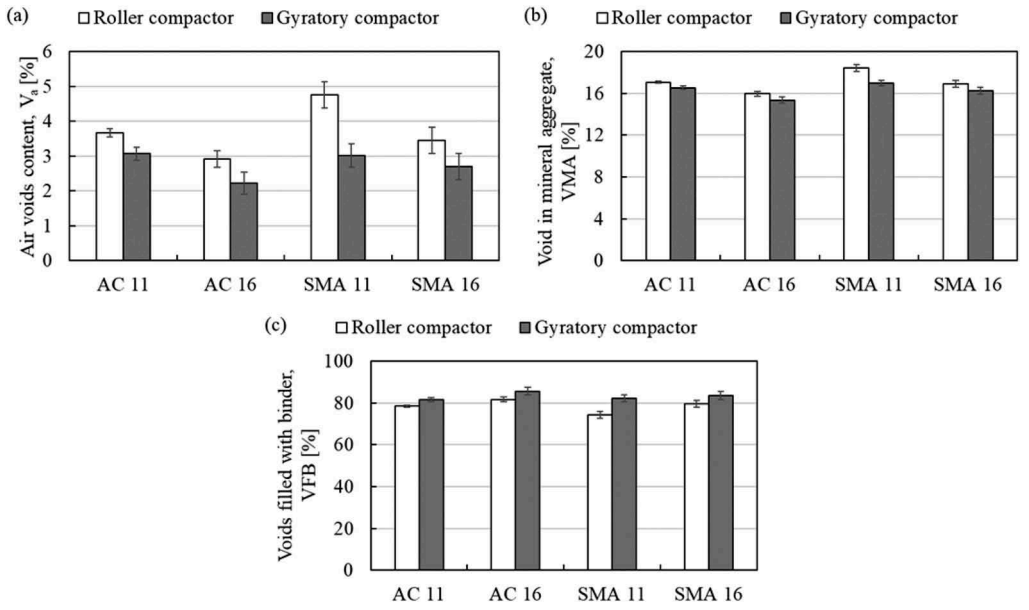

Figure 4. Void characteristics of specimens: (a) V_a, (b) WMA, and (c) VFB.

Table 4. Linear regression of shift factors.

Mixture	Linear regression		
	a	b	R^2
AC 11-R	-0.159	2.602	0.990
AC 11-G	-0.182	3.002	0.988
AC 16-R	-0.161	2.721	0.980
AC 16-G	-0.176	2.957	0.981
SMA 11-R	-0.166	2.952	0.946
SMA 11-G	-0.184	3.291	0.942
SMA 16-R	-0.169	2.948	0.963
SMA 16-G	-0.183	3.177	0.963

Figure (b) shows that the shift factor of AC 11 prepared by roller compactor is different from the one related to gyratory compaction. At -10 °C, the shift factors of AC 11-G, AC 16-G, SMA 11-G and SMA 16-G were 15.8%, 8.5%, 11.9% and 7.7% higher than for the corresponding specimens prepared by roller compactor, respectively. At 30 °C, the shift factors of AC 11-G, AC 16-G, SMA 11-G and SMA 16-G were 11.4%, 10.2%, 8.8%, and 8.4% lower than for the corresponding specimens prepared by roller compactor, respectively. These results indicate that the shift amplitude of the dynamic modulus curve of the specimens prepared by the gyratory compactor at each temperature is larger than the corresponding values related to roller compaction.

Figure (c) indicates that SMA 11-R has higher shift factors at both low temperatures and high temperatures than that of AC 11-R. The shift factors of SMA 11-R, SMA 11-G, SMA 16-R, and SMA 16-G were 19.6%, 15.5%, 10.5%, and 9.7% higher than that of AC 11-R, AC 11-G, AC 16-R, and AC 16-G, respectively, at -10 °C, and 25.2%, 27.0%, 7.2%, and 8.7% higher at 30 °C. These results indicate that the dynamic modulus curves of the SMA mixtures shifted more at the low temperature (high frequency) and less at the high temperature (low frequency) than that of the AC mixtures.

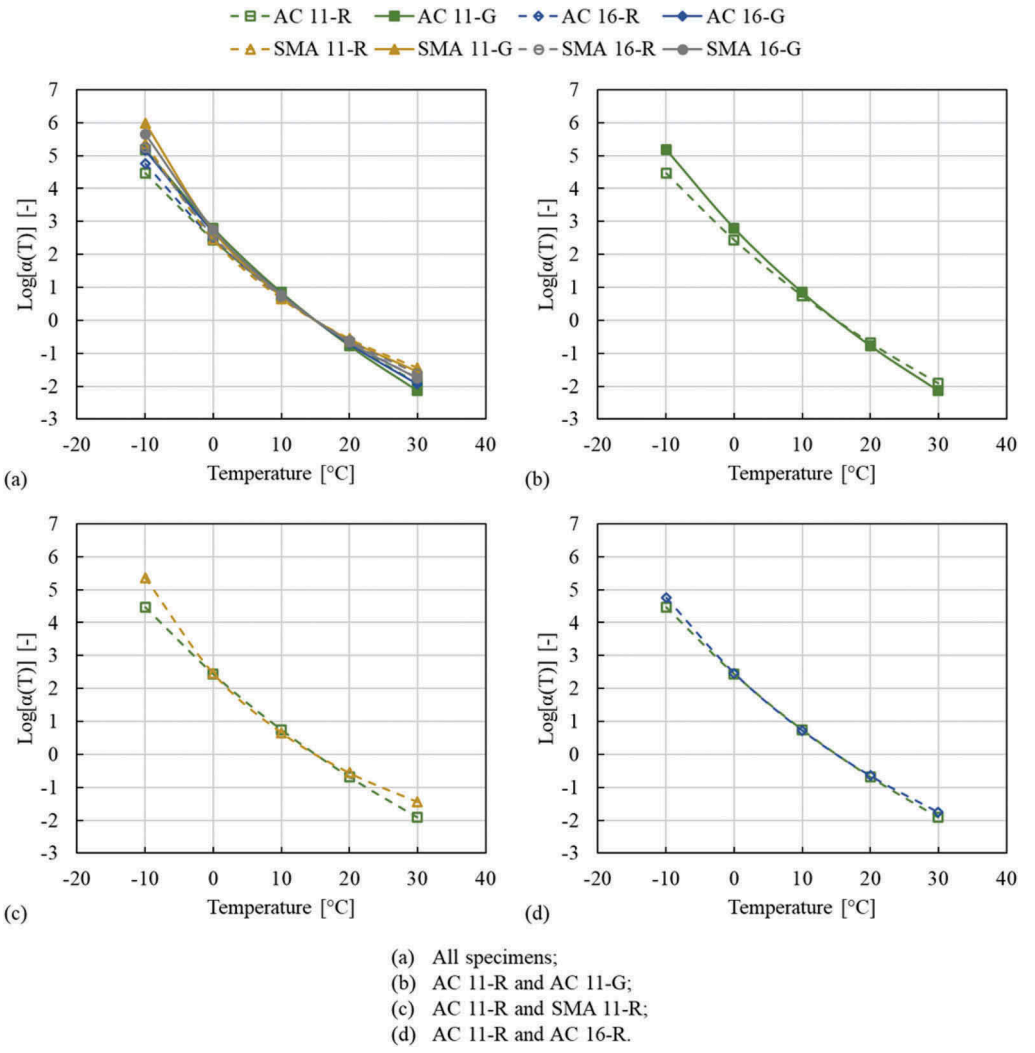

Figure 5. WLF shift factor curves for tested mixtures.

Figure (d) illustrate that there are just slight differences in the shift factors between AC 11-R and AC 16-R. The shift factor did not change much with the maximum grain size of the asphalt mixture, thus indicating the minor role played by the particle size of the aggregates.

3.3 *Master curves*

The fitting parameters, R^2 and SSE, are reported in Table 5. The R^2 of all asphalt mixtures ranged from 0.9927 to 0.9997, and the SSE values were comprised between 0.0331 and 0.1947, to be concluded that all the experimental values were then satisfactorily fitted.

As shown in Table 4, the compaction method, asphalt mixture type, and maximum grain size all exerted clear effects on the fitting parameters. The compaction method had a major influence on the fitting parameters of δ and α for AC mixtures. However, there was a smaller difference of δ and α between the two compaction methods for SMA mixtures. This shows that the compaction methods exerted a greater impact on the AC mixtures than the SMA mixtures. The AC and SMA mixtures have different structures causing this result. The AC mixture is composed of a dense gradation. The structural strength of the AC mixture is mainly based on the cohesive

Table 5. Fitting parameters, SSE and R^2 for mixtures.

Mixture	Sigmoidal function				WLF equation		R^2	SSE
	δ	α	β	γ	C_1	C_2		
AC 11-R	0.406	4.300	-1.070	0.364	17.93	125.21	0.9997	0.0710
AC 11-G	0.830	3.854	-1.097	0.391	18.22	112.91	0.9984	0.0836
AC 16-R	0.529	4.159	-1.070	0.413	12.11	88.71	0.9976	0.1352
AC 16-G	0.313	4.391	-1.254	0.396	13.69	91.34	0.9986	0.0780
SMA 11-R	0.777	3.766	-1.037	0.497	6.91	57.31	0.9962	0.0331
SMA 11-G	0.749	3.776	-1.177	0.469	7.36	55.72	0.9946	0.0413
SMA 16-R	1.562	3.026	-0.589	0.515	8.96	67.63	0.9927	0.1947
SMA 16-G	1.436	3.138	-0.851	0.464	9.78	68.21	0.9973	0.1375

force between the mineral aggregate and the binder. The SMA mixture is a semi-dense and semi-inlaid structure. The structural strength of the SMA mixture is composed of the squeezing force, internal friction between the mineral aggregates, and the cohesive force between the mineral aggregate and the binder (Jiang et al. 2020). The compaction method has a more important influence on the dense structure.

The range of the dynamic modulus reflects the temperature sensitivity of asphalt mixtures. The δ values for AC mixtures were generally lower than those for SMA mixtures while the δ + α values for AC mixtures tended to be higher than those for SMA mixtures. These results indicate that the AC mixtures were more sensitive to temperature than the SMA mixtures. This phenomenon can be explained by considering their structures: for AC mixtures, the cohesiveness of the binder exerts more influence on the structural strength; therefore, their temperature sensitivity is stronger than for SMA mixtures.

The fitting parameters also varied for each considered aggregate grading curve. As the coarse grains constitute the three-dimensional matrix structure of the asphalt mixture and are directly related to the stiffness, the different aggregate sizes form a skeleton structure of various qualities resulting in different values and trends of the dynamic modulus.

The master curves are portrayed in Figure 6. The dynamic modulus values are then compared at the condition of -10 °C and 10 Hz (low-temperature condition) and at the condition of 40 °C and 0.1 Hz (high-temperature condition) based on the modeling of the dynamic modulus, as shown in Figure 7.

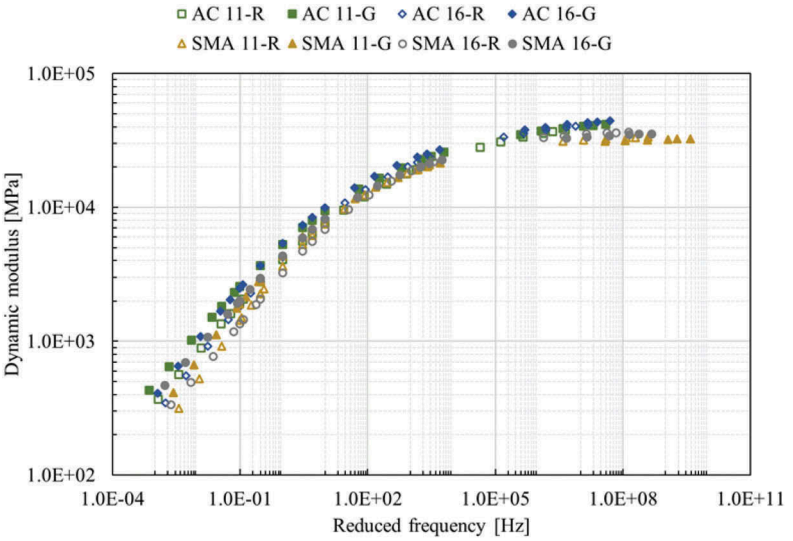

Figure 6. Master curves for tested mixtures.

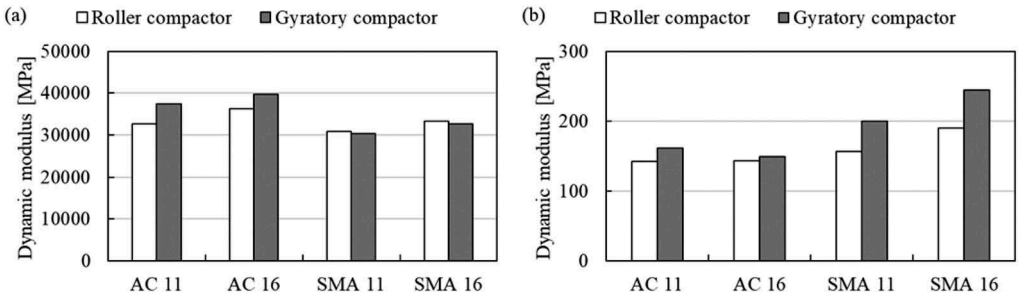

Figure 7. Dynamic modulus at (a) the low-temperature condition -10 °C and 10 Hz and (b) the high-temperature condition 40 °C and 0.1 Hz.

As shown in Figure 7 (a), the dynamic moduli of AC 11-G and AC 16-G were 14.6% and 9.4% higher than those of AC 11-R and AC 16-R at the low-temperature condition. The AC mixtures prepared by the gyratory compactor were denser, leading to a higher dynamic modulus. However, even though the gyratory compaction also made the SMA mixtures denser, the dynamic moduli at the low-temperature condition for SMA mixtures prepared by the gyratory compactor were slightly lower than the corresponding ones attained by the roller compactor. This indicate that the combined effect of the embedded and dense structures caused the dynamic modulus of the SMA mixture at low temperature to be less affected by the compaction method.

As shown in Figure 7 (b), the dynamic moduli of AC 11-G, AC 16-G, SMA 11-G, and SMA 16-G were 13.4%, 4.3%, 27.7%, and 28.3%, respectively, higher than those of AC 11-R, AC 16-R, SMA 11-R, and SMA 16-R at the high-temperature condition. Considering the findings related to high temperatures, the dynamic moduli of AC mixtures and SMA mixtures were affected the least and the most by the compaction mode, respectively. As the bitumen attains a viscous flow state at high temperatures, the cohesive force between the binder and the aggregate is greatly reduced. Therefore, the dynamic modulus of the AC mixtures was less affected by the compaction method. The structure of the SMA mixture was also improved by the gyratory compactor, which then caused less affected by the temperature at high temperatures.

The dynamic modulus of SMA 16-G decreased by 17.7% at the low-temperature condition and increased by 63.6% at the high-temperature condition compared to that of AC 16-G. The lower dynamic modulus at low temperatures can prevent thermal cracking of an asphalt pavement, while a higher dynamic modulus at high temperatures is beneficial for protecting an asphalt pavement from permanent deformations (Zhang et al, 2012). This outcome documents that the SMA mixture has a better performance than the AC mixtures at both high and low temperatures.

At high temperatures, the dynamic moduli of AC 16-R and SMA 16-R were 11.0% and 8.4% higher than those of AC 11-R and SMA 11-R, respectively. As thoroughly documented in other studies, the scaling effect of the aggregates including particle shape and particle size has a significant impact on its strength (Thuro et al. 2001) and thereby on the modulus of the asphalt mixture. In this study, as the particle shapes were the same for all asphalt mixtures, the large-sized mineral aggregates improved the quality of the skeleton structure showing a higher dynamic modulus.

4 CONCLUSIONS

In this laboratory study, the asphalt mixtures that are most commonly employed in Norway were prepared using two different compaction methods, namely gyratory compaction and roller compaction. The corresponding dynamic moduli at different temperatures and frequencies were obtained using the Cyclic Indirect Tensile Test (CITT). The dynamic modulus master curves for these mixtures were constructed by the Sigmoidal function and the Williams, Landel and Ferry (WLF) equation. Based on the results attained, the conclusions are as follows:

- Gyratory compaction made both AC and SMA mixtures denser compared to the case of roller compaction, resulting in lower Air voids content (V_a), lower Void in Mineral Aggregate (VMA), and higher Voids Filled with Binder (VFB), as well as leading to a higher dynamic modulus of AC mixtures at low temperatures and of SMA mixtures at high temperatures. The shift factors of specimens prepared by the gyratory compactor were higher at low temperatures and lower at high temperatures than those related to the samples prepared by the roller compactor.
- The SMA mixtures were characterized by a lower dynamic modulus at low temperature and higher dynamic modulus at high temperature when compared to the AC mixtures, thus showing better performance than the AC mixture. The shift factors of SMA mixtures were significant higher at both high and low temperatures than those of AC mixtures.
- The asphalt mixtures with a larger maximum grain size displayed better compact ability, resulting in lower V_a, lower VMA, and higher VFB, as well as higher dynamic modulus than the asphalt mixtures with a smaller maximum grain size. The grain size had little effect on the shift factor.

According to these key-findings, the SMA mixture can be recommended for asphalt pavements carrying a high traffic volume because of its better mechanical properties at both high and low temperatures from the perspective of asphalt stiffness. Besides, the volumetric properties and dynamic modulus of specimens prepared by roller compactor and gyratory compactor were different. Considering that the roller compactor method is closer to on-site paving, the roller compaction is thus recommended to develop the new Norwegian pavement design system and for modeling the dynamic modulus of asphalt pavements.

ACKNOWLEDGMENTS

This research work was supported by the VegDim project of the Norwegian Public Roads Administration. The financial support provided by China Scholarship Council (No. 201806950077) and Department of Civil and Environmental Engineering, Norwegian University of Science and Technology (No. K-649105) is highly acknowledged. The support kindly provided by the laboratory technicians Bent Lervik and Jan Erik Molde is greatly acknowledged.

REFERENCES

Button, J. et al., 1994. *Correlation of Selected Laboratory Compaction Methods with Field Compaction*. Transportation Research Record, 1454.

CEN, 2011. *NS-EN 1097-1 Tests for Mechanical and Physical Properties of Aggregates - Part 1: Determination of the Resistance to Wear (Micro-Deval)*. European Standard, Brussels, Belgium.

CEN, 2015. *NS-EN 1426 Bitumen and Bituminous Binders - Determination of Needle Penetration*. European Standard, Brussels, Belgium.

CEN, 2015. *NS-EN 1427 Bitumen and Bituminous Binders - Determination of Softening Point - Ring and Ball Method*. European Standard, Brussels, Belgium.

CEN, 2018. *NS-EN 12697-8 Bituminous Mixtures - Test methods - Part 8: Determination of Void Characteristics of Bituminous Specimens*. European Standard, Brussels, Belgium.

CEN, 2018. *NS-EN 12697-26 Bituminous Mixtures - Test Methods - Part 26: Stiffness*. European Standard, Brussels, Belgium.

CEN, 2019. *NS-EN 12697-31 Bituminous Mixtures - Test methods - Part 31: Specimen Prepared by Gyratory Compactor*. European Standard, Brussels, Belgium.

CEN, 2019. *NS-EN 12697-33 Bituminous Mixtures - Test method - Part 33: Specimen Prepared by Roller Compactor*. European Standard, Brussels, Belgium.

CEN, 2020. *NS-EN 1097-2 Tests for Mechanical and Physical Properties of Aggregates - Part 2: Methods for the Determining of Resistance to Fragmentation*. European Standard, Brussels, Belgium.

Chehab, G. R. et al., 2002. *Time-Temperature Superposition Principle for Asphalt Concrete with Growing Damage in Tension State*. Journal of the Association of Asphalt Paving Technologists, 71.

Consuegra, A. et al., 1988. *Comparative Evaluation of Laboratory Compaction Devices Based on Their Ability to Produce Mixtures with Engineering Properties Similar to Those Produced in the Field*. Master's thesis, Texas A&M University.

Huang, Y., 1993. *Pavement Analysis and Design*.
Hunter, A. et al., 2009. *Effect of Compaction Mode on the Mechanical Performance and Variability of Asphalt Mixtures*. Journal of Transportation Engineering, 135(11), 839–851.
Jiang, Y. et al., 2020. *Performance of Stone Mastic Asphalt Mixtures Fabricated by Different Compaction Methods*. Applied Sciences, 10(7), 2523.
Kim, Y. et al., 2004. *Dynamic Modulus Testing of Asphalt Concrete in Indirect Tension Mode*. The 83rd Transportation Research Board, Washington, DC, United States.
Lesueur, D. et al., 1996. *A Structure-Related Model to Describe Asphalt Linear Viscoelasticity*. Journal of Rheology, 40(5), 813–836.
NCHRP, 2004. *Guide for Mechanistic-Empirical Design of New and Rehabilitated Pavement Structures*. National Cooperative Highway Research Program, Washington, DC, United States.
NPRA, 2005. *Håndbok 018 Vegbygging*. Vegdirektoratet, Norway.
NPRA, 2018. *Håndbok N200 vegbygging*. Vegdirektoratet, Norway.
NPRA, 2019. *STATENS VEGVESENS RAPPORTER Nr. 670 Retningslinjer asfalt 2019*. Vegdirektoratet, Norway.
Pellinen, T. et al., 2004. *Asphalt Mix Master Curve Construction Using Sigmoidal Fitting Function with Non-Linear Least Squares Optimization*.Recent Advances in Materials Characterization and Modeling of Pavement Systems, 83–101.
Renken, P., 2000. *Influence of Specimen Preparation onto the Mechanical Behaviour of Asphalt Aggregate Mixtures*. The 2nd Eurasphalt and Eurobitume Congress, Barcelona, Spain.
Sarsam, S. and Jumaah, M., 2016. *Modeling of Comparative Performance of Asphalt Concrete under Hammer, Gyratory, and Roller Compaction*. Journal of Engineering, 22(11), 1–15.
Schwartz, C. W. et al., 2002. *Time-Temperature Superposition for Asphalt Concrete at Large Compressive Strains*. Transportation Research Record, 1789(1), 101–112.
Thuro, K. et al., 2001. *Scale Effects in Rock Strength* Properties. *Part 1: Unconfined Compressive Test and Brazilian Test*. ISRM Regional Symposium, EUROCK, 169–174.
Williams, M. L. et al., 1955. *The Temperature Dependence of Relaxation Mechanisms in Amorphous Polymers and Other Glass-Forming Liquids*. Journal of the American Chemical society, 77(14), 3701–3707.
Zhang, Y. et al., 2012. *Characterizing Permanent Deformation and Fracture of Asphalt Mixtures by Using Compressive Dynamic Modulus Tests*. Journal of Materials in Civil Engineering, 24(7), 898–906.

Eleventh International Conference on the Bearing Capacity of Roads, Railways and Airfields, Volume 2 – Hoff, Mork & Saba (eds)

Effective experimental characterization of the non-linear elastic deformation behavior of unbound granular materials

S. Leischner, T. Spanier & G. Canon Falla
Institute of Transportation Engineering, TU Dresden, Dresden, Germany

ABSTRACT: Aggregates are a necessary and important resource for the construction of pavements worldwide. In order to reduce the risk of early pavement failure, it is required to use aggregates with high resistance against plastic deformation in both - wet and dry conditions, especially for high trafficked pavements.

The use of high quality UGMs significantly improve the rutting performance of the base course and hence, that of the whole pavement. Repeated Load Triaxial (RLT) tests results could give detailed information as to which UGMs should be selected in order to provide sufficient performance. However, these RLT tests are expensive and time consuming. In addition, this testing are quite complicated and only a few testing devises are available in Germany. Therefore, there is a need of simple and economical test methods to characterize the mechanical behaviour of UGMs under the action of high traffic loads. The paper shows the principle of operation and methodology of a simplified test (Repeated Load CBR (RLCBR) test) used to characterize the elastic and plastic response of UGMs to harmonic loads using a uniaxial testing machine. Different UGMs commonly used in the base course of Federal roads in Germany were tested at two different moisture contents. The results of the tests were analysed regarding the elastic deformation response showed a strong dependency of bearing capacity on the stress level. The RLCBR tests results were compared to the RLT test results and it was found that it is possible to determine the parameter of a non-linear elastic model for UGMs (Modified Universal Model) with a relatively high accuracy. The testing regime used and test results are discussed in this paper.

Keywords: Unbound granular materials, repeated load, RLT tests, RLCBR tests

1 INTRODUCTION

In Germany, pavements have so far been designed on the basis of empirical approaches according to the RStO 12 [RStO 12]. Unbound Granular Layers (UGL) commonly used in pavements in Germany consist of gravel or crushed aggregates. These UGL play an important role in the structural performance especially for pavement structures with a thin asphalt layer. According to the German guidelines (e.g. RStO 12), a sufficient bearing capacity is required for the UGL. At the moment, the bearing capacity in-situ is described by a specific E_{v2}-value determined by the results of the plate bearing tests. However, this value does not reflect the in-situ performance/bearing capacity of the UGL. In addition these tests con not provide input parameter for an analytical design.

UGM show a stress dependent elasto-plastic behavior under cyclic loading. Thus, the realistic characterization of the elastic and plastic deformation is essential in order to have effective usage on the materials in pavements.

DOI: 10.1201/9781003222897-40

With the guidelines for the analytical design of the asphalt (RDO Asphalt 09), a procedure has been available in Germany since 2009 for the first time, with which, among other things, the realistic material behavior of the materials, the behavior of the UGL is currently implemented in a simplified manner, is taken into account in the design process. Analytical methods are also useful for the design of pavements, where the stress-deformation behavior of the UGL plays a particularly important role. Particularly in analytical design, it is important to describe the behavior of the UGL more realistically, so that pavement structures deviating from the RStO structures can also be designed economically. For this purpose, the approaches used in the RDO Asphalt (linear-elastic deformation behavior of the UGM) must be further developed, especially with regard to the analysis of the elasto-plastic behavior of the UGM under cyclic loading. Therefore, efficient laboratory testing methods must be developed to provide the realistic performance parameters for UGM within an analytical pavement design process.

2 AIM OF THE RESEARCH

The publication shows that it is possible to realistically consider the nonlinear-elastic deformation behaviour of UGM by means of laboratory tests. For this purpose, experimental test methods on a laboratory scale were further developed and optimized. In addition to the RLT test, RLCBR tests were carried out under the same conditions as for the RLT test. The aim was, to investigate whether a simplified testing method of UGM is possible to investigate the elastic deformation properties of UGM and to rank the materials based on their bearing capacity in a similar manner compared to the RLT tests.

3 LABORATORY TESTS

3.1 *Materials tested*

The laboratory tests were carried out using different UGMs. Six unbound granular materials (UGM) with a similar grading were tested (Figure 1).

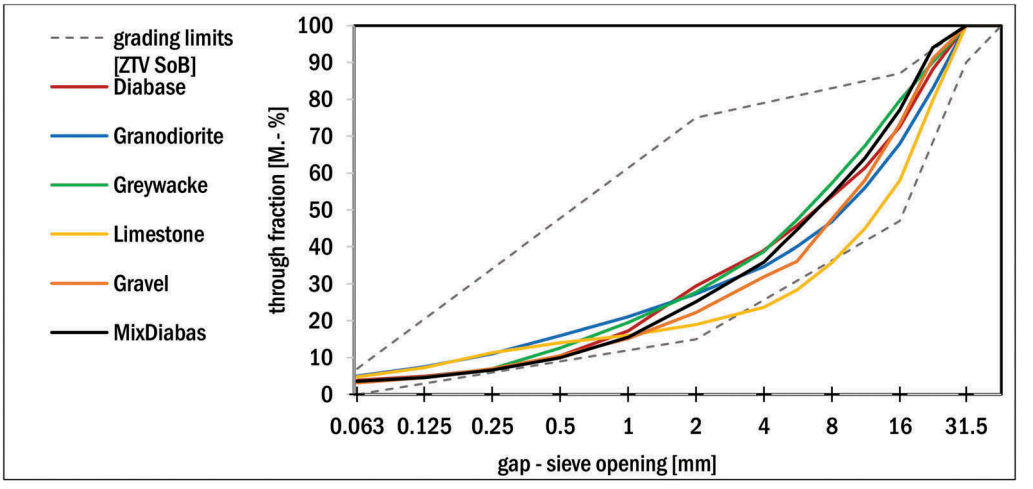

Figure 1. Grading of the materials tested [Spanier et.al. 2017].

Table 1 presents the results of the Proctor tests in terms of the optimum moisture content (OMC) and the maximum dry density (MDD) for all materials.

Table 1. Results of the Proctor Tests and fine content.

	OMC (%)	MDD (g/cm^3)	Fine Content < 0.063 mm (%)
Diabase	4.8	2.199	3.9
Granodiorite	4.9	2.153	5.0
Greywacke	5.2	2.048	3.6
Limestone	5.8	2.155	4.8
Gravel	4.9	1.971	3.1
Mix Diabase	4.7	2.235	3.5

3.2 *RLT tests*

The RLT testing machine at the Laboratory of Pavement Engineering at TU Dresden was used to determine the elastic deformation behavior of the UGM (Figure 2). The samples were tested at 70% and 85% of OMC and 97% of MDD (Table 1). The test specimens were produced using a special compaction mold. The UGM was then placed in 5 to 6 layers and compacted layer by layer with a vibratory hammer. The sample size was 300 mm x 150 mm (height x diameter).

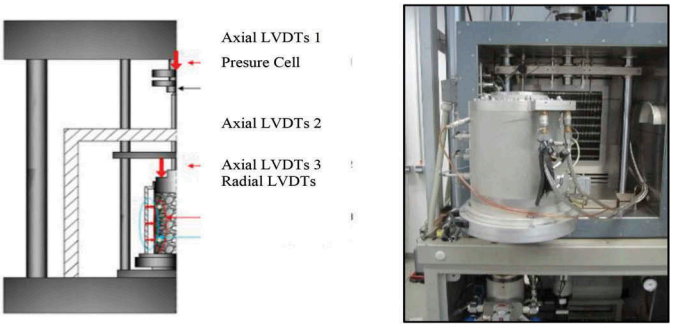

Figure 2. RLT testing device.

The deviatoric, sinusoidal vertical load was applied in all experiments with a frequency of 1 Hz while the horizontal stress was kept constant. In the RLT tests, both strain components (deviatoric and hydrostatic strains) were recorded. Before carrying out the tests to determine the elastic deformation behavior, it was necessary to apply a preload (20,000 load cycles at 10 Hz, $\sigma_1 = 450$ kPa. $\sigma_3 = 150$ kPa) to stabilize the sample. Figure 3 shows the stress ratios applied to investigate the elastic deformation behavior.

3.3 *RLCBR tests*

In addition to the RLT tests, RLCBR tests were carried out under drained conditions with the same sample conditions as for the RLT tests. The RLCBR tests have the advantage of a relatively simple test setup compared to the RLT tests. The effort required for specimen fabrication is also significantly lower than for the RLT tests. The disadvantage of these tests is that the stress ratios that can be realized only be transferred to the in-situ conditions to a limited extent. With RLT tests, these in-situ conditions can be reproduced much better. A uniaxial servo-hydraulic testing machine was used for the tests (see Figure 4).

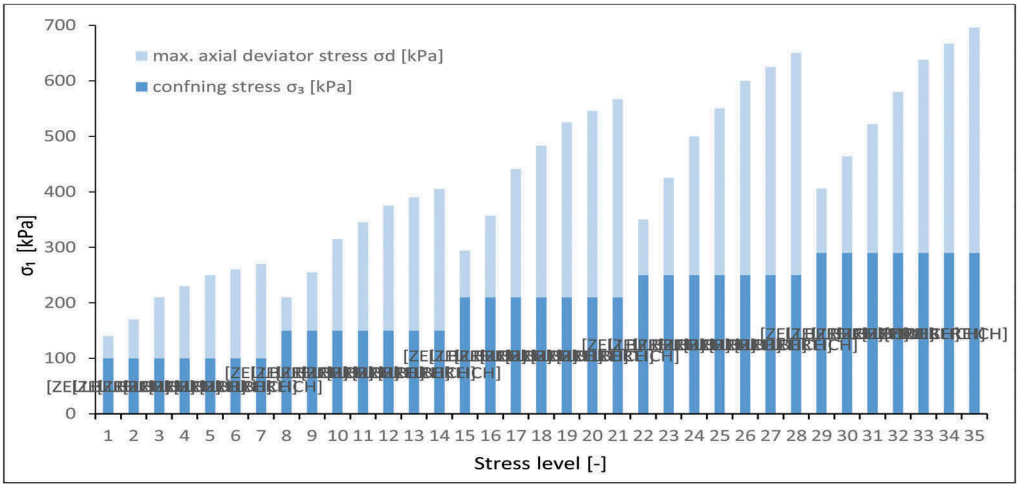

Figure 3. Stress levels for investigating the elastic deformation performance of UGMs by RLT tests [Spanier et.al. 2017].

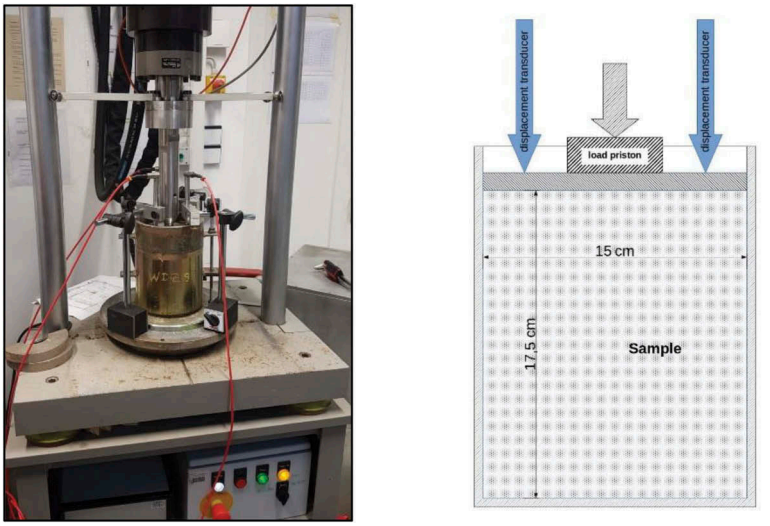

Figure 4. RLCBR test configuration.

The cylindrical specimens. Ø = 150 mm, height = 175 mm were manufactured in a test mold and then tested. The load was applied over the entire specimen surface. To ensure uniform load distribution of the test load. A round steel plate (load distribution plate with Ø = 150 mm and h = 10 mm) was placed on the finished specimen. The load was applied to the steel plate with the aid of a punch (Ø = 56.42 mm, h = 20 mm). In this test arrangement, the three inductive displacement transducers were positioned on the loading plate of the specimen, each offset by 120° (Figure 4). In the RLCBR test, no radial strain ($\varepsilon_3 = 0$) is possible. Due to the rigid horizontal limitation of the specimen.

First of all, a conditioning test was used to stabilize the permanent strains of the specimen to attain nearly elastic behavior. The samples were conditioned for 20,000 load cycles at 10 Hz with a reference stress level of a constant confining pressure of 150 kPa and cyclic deviator stress of 300 kPa. At the end of the test the behavior of the material was nearly elastic.

After conditioning, a resilient test was performed to characterize the material resilient modulus for varying stress and moisture combinations. The stress states in this laboratory test are thus only comparable to those of the RLT test to a limited extent. The results of the RLCBR tests to investigate the elastic deformation behavior should allow to determine the parameters of a non-linear elastic model. The vertical load was applied sinusoidal in all tests. The test program is presented in Table 4.

Table 4. RLCBR test program.

Load level	min [kPa]	max [kPa]	f [Hz]	Load cycles [-]
1	35	100	1	100
2	35	200	1	100
3	35	300	1	100
4	35	400	1	100
5	35	500	1	100

4 TEST RESULTS

4.1 *RLT tests*

To determine the elastic modulus, the last 5 load cycles of each load cycle group were evaluated for an applied stress ratio. In Figure 5 the E-Moduli are shown as a function of the deviator stress and the cell pressure. The elastic moduli are graded as a function of the applied cell stress. These results confirm the previous knowledge about the deformation behavior of UGM. A higher cell stress causes an increase in stiffness due to the stronger compression of the individual grains and thus an increase in the deformation resistance to an applied load. The influence of the deviator stress on the resilient modulus is discernible, however, this is less pronounced compared to the influence of the cell pressure on the resilient modulus, especially at low deviator stresses.

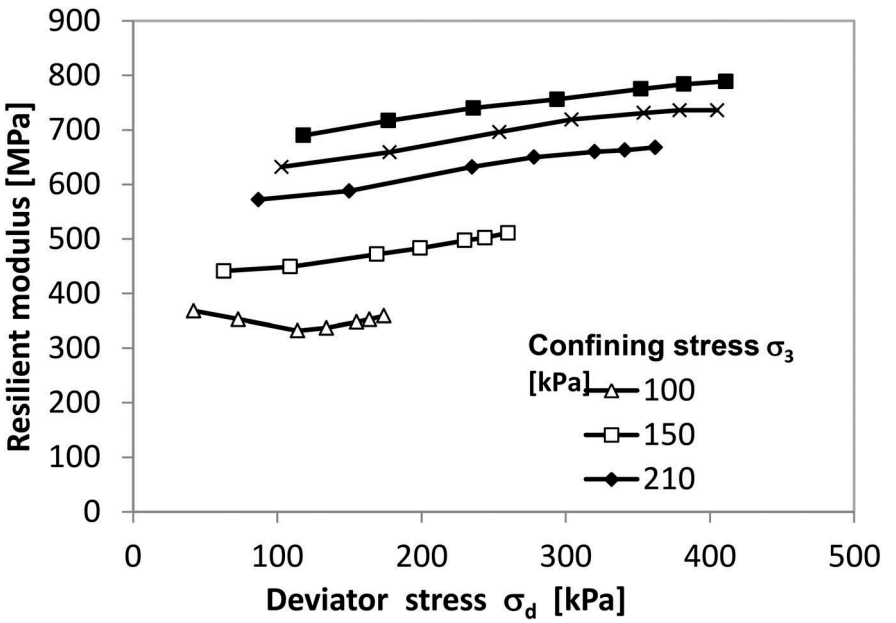

Figure 5. Resilient modulus versus deviator stress, Diabas; 70 % of OMC, ϱ = 97 % of OMC.

Equation 1 presents the non-linear model developed by Witczak and Uzan [Witczak & Uzan 1988] [UZAN 1985] (Modified Universal Model) which describes well the resilient behaviour of UGM under constant confining pressure. The model captures the effect of the average bearing resistance of the material (parameter k_1), the stiffening effect due to bulk stress (parameter k_2) and the softening effect due to shear stress (parameter k_3). According to previous experience, this model has a good approximation quality for a simple structure [COURAGE 1999].

$$M_r = k_1 \left(\frac{\theta}{p_a}\right)^{k_2} \left(\frac{\tau_{oct}}{p_a} + 1\right)^{k_3} \tag{1}$$

where M_r is the resilient modulus, θ is the bulk stress, τ_{oct} is the octahedral shear stress, p_a is a constant stress of 100 kPa and k_1, k_2, $k_{3\ are}$ material parameter. The model parameters k_1, k_2 and k_3 were determined by a non-linear least square technique that minimize the error between the experimental and numerical data. The parameter k_2 always assumes positive values, which is due to the fact that an increase in the hydrostatic compressive stress always results in an increase in the resilient modulus. This effect would only reverse when the hydrostatic compressive stresses are so high that grain breakage occurs. However, the model does not apply to such high stress conditions. The parameter for all materials tested are shown in Table 4.

Table 4. Model parameter for Eq. 1 (RLT tests) material_% of OMC.

Load level	k_1 [kPa]	k_2 [-]	k_3 [-]	R^2 [%]
*Diabas_70	114.26	0.8497	-0.2131	98.3%
Diabas_85	108.65	0.8657	-0.2662	98.3%
Grano_70	70.42	0.8308	-0.1401	98.2%
Grano_85	68.32	0.8541	-0.1614	95.7%
Greywacke_70	92.65	0.8436	-0.2563	94.0%
Greywacke _85	93.75	0.8296	-0.2539	96.6%
Lime_70	116.33	0.8737	-0.2252	98.0%
Lime_85	115.47	0.8469	-0.1936	97.3%
Gravel_70	69.38	0.8812	-0.1776	97.3%
Gravel_85	70.88	0.8938	-0.1784	97.4%
MixDia_70	130.26	0.8542	-0.2235	98.7%
MixDia_85	130.2	0.8245	-0.2125	97.4%

* Material_% of OMC

The impact of the moisture content on the resilient modulus can be identified by close examination of the parameter k_1 (Figure 6). Previous RLT test results at TU Dresden [Canon Falla et. al.2017] were included into the analysis. It is observed that the stiffness of most of the UGM is almost not affected by the increase of moisture content. On the other hand, a loss of bearing capacity expressed by a decreasing k_1 value was observed on Gravel tested by Canon Falla [Canon Falla et al. 2017], Diabase and Andesite with increasing moisture.

4.2 *RLCBR tests*

Investigations have shown that preloading in the form of a preliminary test is also advisable for the RLCBR test in order to anticipate the initial high plastic deformations. This ensures that the plastic deformations are negligible in the tests to record the elastic deformations. This preloading was realized by a preliminary test with a stress of 500 kPa and 50,000 load cycles at 5 Hz. The material parameters of the UGM for the Modified Universal Model (Equation 1) were determined analogously to the procedure for evaluating the RLT tests on the basis of the measurement results of the tests for determining the elastic deformation behavior. The model parameters k_1 and k_2 were defined by means of regression calculation (least squares method).

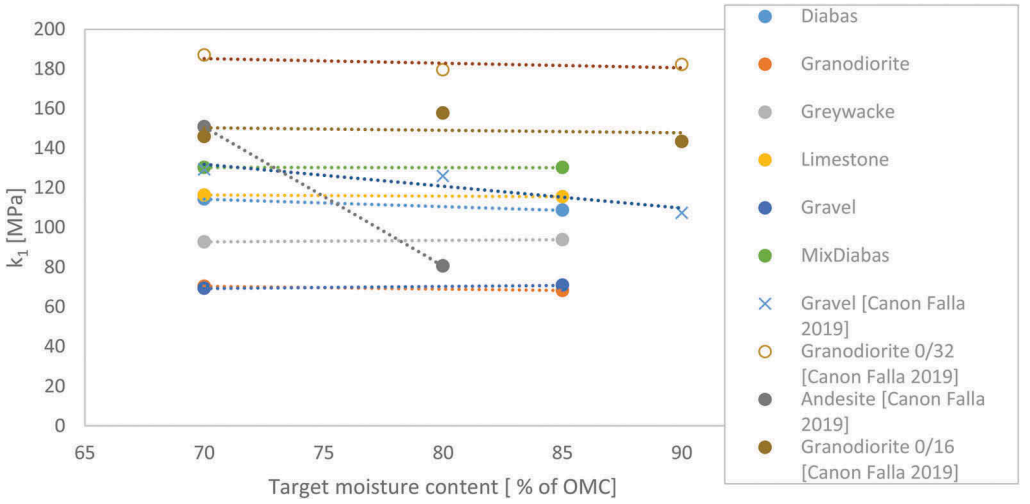

Figure 6. Material parameter k_1 for the Modified Universal Model.

In contrast to the evaluation of the RLT tests, a full regression with the RLCBR test data provided, i. e. all three model parameters k_1, k_2 and k_3 are undetermined. In these calculations, positive values were determined for model parameter k_3. The reason for this can be seen in the mathematical structure of the Modified Universal Model and the lack of isolation of the influence of the deviator stress in the RLCBR test. The data obtained in the RLCBR test do not provide the necessary information to be able to determine all parameters for the Modified Universal Model. Therefore, the value for the parameter k_3 was determined based on the result of the associated RLT tests. Hence, the model parameters k_1 and k_2 were determined by means of partial regression, i.e. with a given value of the model parameter k_3. In addition to the partial regression, the model parameters k_1 and k_2 were determined iteratively for the Modified Universal Model by specifying initial values. Compared to the regression calculation, this resulted in slightly better fit between the model and the test result. The results of the calculations are shown in Table 5. The model parameters determined are only valid for the investigated UGMs and moisture contents (70% and 85% of OMC). For the UGM, the R^2 which is used for assessing the goodness of fit, was at least 83.9 %.

Table 5. Model parameter for Eq. 1 for the materials tested (RLCBR test).

	k_1 [kPa]	k_2 [kPa]	k_3 [kPa]	R^2 [%]
*Diabas_70	158.54	0.737	-0.213	91.0 %
Diabas_85	146.84	0.737	-0.266	94.5 %
Grano_70	99.62	0.685	-0.140	97.5 %
Grano_85	125.19	0.608	-0.171	93.5 %
Greywacke_70	101.85	0.758	-0.256	92.3 %
Greywacke _85	92.68	0.745	-0.254	93.6 %
Lime_70	229.01	0.612	-0.225	83.9 %
Lime_85	169.27	0.756	-0.191	96.1 %
Gravel_70	127.15	0.704	-0.178	97.9 %
Gravel_85	129.19	0.690	-0.178	96.6 %
MixDia_70	151.93	0.876	-0.224	98.9 %
MixDia_85	208.10	0.759	-0.213	83.9 %

* material_% of OMC

4.3 *A new model for the RLCBR test*

The existing Modified Universal Model was developed primarily to predict the non-linear deformation behavior from RLT test results but cannot be used directly for RLCBR tests. Hence, an adapted model was proposed in this research to describe the RLCBR test results and to determine the Modified Universal Model parameters (k_1, k_2 and k_3). The new model was developed based on the Modified Universal Model. Two constant parameters were introduced in this model. The parameter k1 which captures the bearing resistance of the material was corrected with a factor of a = 0.72 via multiplying it with the model parameter. In addition, a factor of b = 1, 17 was introduced to regularize the model parameter k2 in this study. The parameter k3 = -0.2085 was chosen, because it provided the best fitting to RLCBR test results for the materials tested.

$$M_r = ak_1\left(\frac{\theta}{p_a}\right)^{bk_2}\left(\frac{\tau_{oct}}{p_a}+1\right)^{k_3} \tag{2}$$

$$\theta = \sigma_1 + 2\frac{\nu\sigma_1}{(1-\nu)} \tag{3}$$

$$\tau_{oct} = \frac{\sqrt{2}}{3}\left(\sigma_1 - \frac{\nu\sigma_1}{(1-\nu)}\right) \tag{4}$$

where σ_1 is the vertical stress applied by the plunger. The Poisson ratio can be assumed to 0.35. Figure 7 presents the initial and the corrected k_1 and k_2 values.

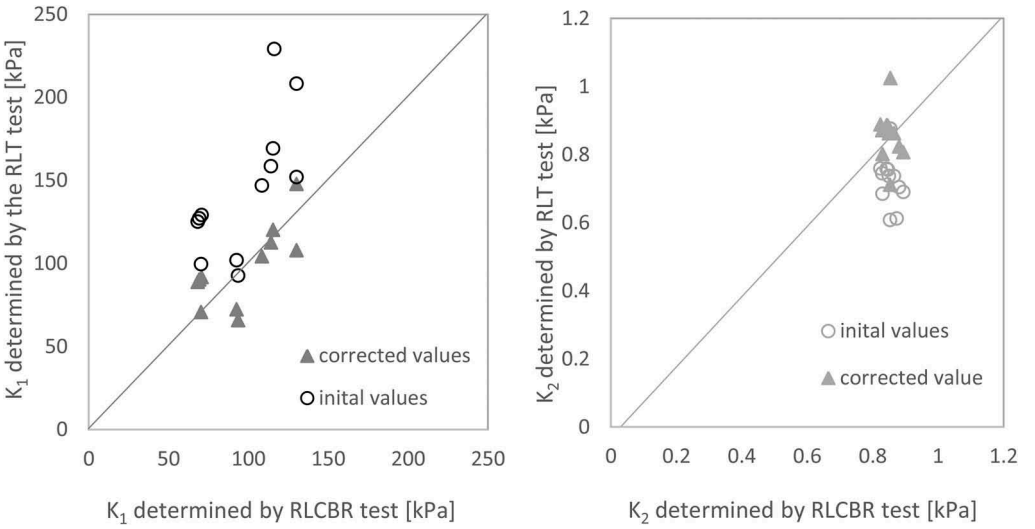

Figure 7. Comparison of the k_1 and k_2 values determined by the results of RLT tests and RLCBR tests.

4.4 *Classification for base course granular materials based on a characteristic resilient modulus value*

The conditioning tests and the resilient test can be used to perform a macromechanical classification for UGM intended to rank/classify base course materials for pavements [Canon Falla et al 2019]. As already explained in [Canon Falla et al. 2017], the classification uses beside the plastic deformation rate a characteristic elastic modulus (E_c), determined with Eq. (1) at a hydrostatic stress of 250 kPa and a deviator stress of 500 kPa.

Table 6. Characteristic resilient modulus, Ec.

Material Quality	Characteristic resilient modulus, Ec [MPa]
Good	Ec > 500
Moderate	500 < Ec < 250
Poor	250 < Ec

Figure 8 presents the resilient modulus values for the materials tested using the results of RLT tests and RLCBR tests. In general the ranking of the materials using either the RLT test results or the RLCBR test results is almost the same. Table 7 shows that only in one case of Greywacke and Gravel the order is reversed. This preludes that the results of RLCBR tests can be used to rank/classify the materials as well with s sufficient accuracy.

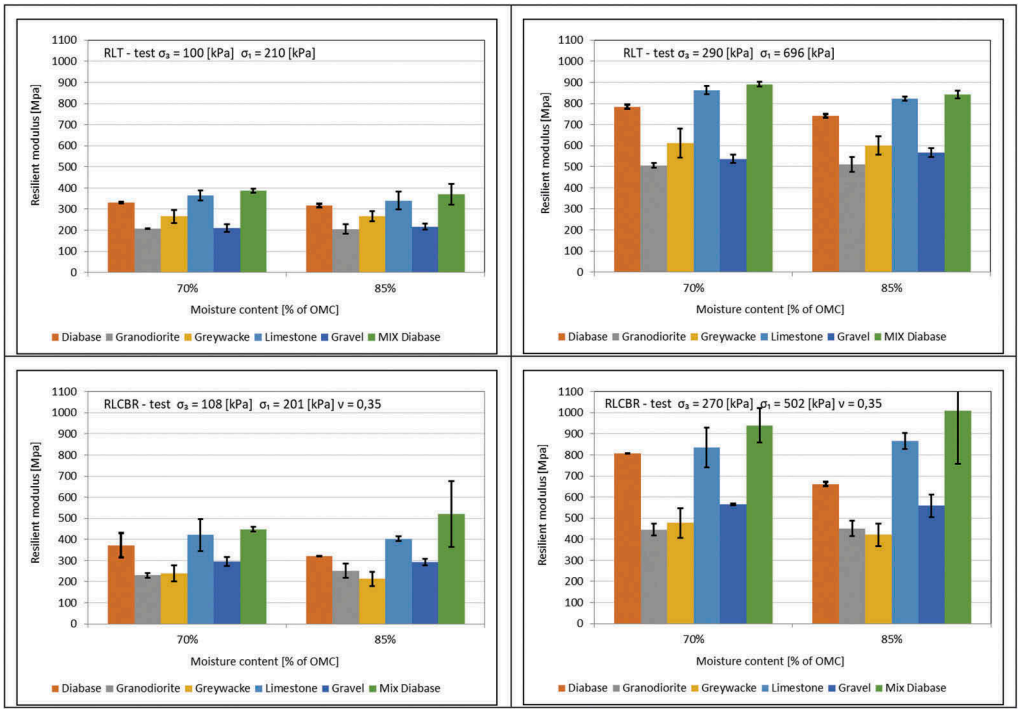

Figure 8. Resilient modulus values for the materials tested, RLT tests and RLCBR tests [Spanier et al. 2017].

Table 7. Ranking of the materials tested [Spanier et. al. 2017].

Material	Ranking	
	RLT test	RLCBR test
Diabase	3	3
Granodiorite	6	6
Greywacke	4	5
Limestone	2	2
Gravel	5	4
MIX Diabase	1	1

5 SUMMARY

This paper shows the principle of operation of the RLCBR test to determine the elastic response of UGMs to harmonic loads. Different materials commonly used in the base course of German roads were tested at different moisture contents. The results of the tests showed only for selected materials a clear dependency of the stiffness on the amount of moisture. All the materials showed a clear dependency of the stiffness on the stress level. Based on the RLCBR test results it is possible to determine the model parameters k_1 and k_2 for the Modified Universal Model with a good accuracy. Furthermore the classification method for UGMs intended to be used as criterion for base courses in pavements is applicable for the UGMs using the results of RLCBR tests. The proposed elastic material selection criteria seems to be able to rank and differentiate the quality of materials based on the stiffness using the RLCBR tests. In order to validate the defined quality limits, more tests should be carried out with different grading, moisture contents and material types.

ACKNOWLEDGEMENTS

The authors gratefully acknowledge the financial support of the BASt within the research project FE 04.0294/2015/OGB.

REFERENCES

Canon Falla G, Leischner S, Blasl A, Erlingsson S (2017). *Characterization of unbound granular materials within a mechanistic design framework for low volume roads*, Transportation Geotechnics 13 pp. 2–21

COURAGE 1999. *Final report of the 5th framework European research project*. Technical report.

TL SoB-StB, 2004. *Technische Lieferbedingungen für Baustoffgemische und Böden zur Herstellung von Schichten ohne Bindemittel im Straßenbau* [in German].

EN 13286-7 (2004) *Unbound and hydraulically bound mixtures – Part 7: cyclic load triaxial test for unbound mixtures*. European committee for standardization, Brussels.

RStO 12 (2012) *Richtlinien für die Standardisierung des Oberbaus von Verkehrsflächen*, Ausgabe 2012, Forschungsgesellschaft für Straßen- und Verkehrswesen, Köln (in German)

RDO Asphalt 09 (2009) *Richtlinien für die rechnerische Dimensionierung des Oberbaus von Verkehrsflächen mit Asphaltdeckschicht*, Ausgabe 2009, Forschungsgesellschaft für Straßen- und Verkehrswesen, Köln (in German)

Spanier T, Leischner S, Wellner F (2017) Verbesserung der Erfassung des Verhaltens von Tragschichten ohne Bindemittel (ToB) zur Berücksichtigung in den RStO, RDO und den RSO. Research Report FE 04.0294/2015/OGB (in German)

TL SoB-StB (2004) *Technische Lieferbedingungen für Baustoffgemische und Böden zur Herstellung von Schichten ohne Bindemittel im Straßenbau* (in German)

Uzan J. (1985) *Characterization of granular materials. Transportation research record 1022*. Transportation research board.

Witczak M, Uzan J. (1988) *The universal airport pavement design system report: Granular material characterization*. Technical report, University of Maryland, Department of Civil Engineering.

Eleventh International Conference on the Bearing Capacity of Roads, Railways and Airfields, Volume 2 – Hoff, Mork & Saba (eds)

Proposed a practical and reliable test method for direct adhesion bond between asphalt binder and aggregate surfaces

Y. Hadi Abed
PhD in Highway and Transportation Engineering, Ministry of Health, Environment Directorate of Operations and Emergency Medical Services, Baghdad, Iraq

A. Hadi Abedali AL-Haddad
Professor, Department of Highway and Transportation, University of Mustansiriyah, Engineering College, Baghdad, Iraq

ABSTRACT: The tensile behaviour of asphalt films confined between aggregates particles as an adhesive was inspected to appraise the direct adhesion bond between asphalt binder and the surface of aggregate using a set of laboratory experiments including the direct tension test. The effects of test type, asphalt cement type, modifier type, and mixing proportions on the practical work of fracture were investigated. The results revealed that all the included variables have great impact on the practical work of fracture required to failure. Specifically, the practical work of fracture required to produce failure decreased with the increase in testing temperature and the decrease in asphalt binder film thickness. The greatest reduction in practical work of fracture was due to the presence of water; especially for asphalt binder modified by SBS with higher reduction ratio of 61%. In contrast, the smallest value of reduction ratio, 13%, was in the case of anti-stripping agent BG plus-modified asphalt binder.

Keywords: Asphalt binder, fracture work, direct tension test, moisture damage, film thickness

1 INTRODUCTION

Weakening in asphalt pavement mixture is mainly due to the deterioration in asphalt binder films that work as a glue between the mixture's components, due to the lost in adhesion between the asphalt and the aggregates, or due to the lost in cohesion within the asphalt binder or both of them. In addition, it happens due to moisture that can lead to loss strength and durability and finally causing raveling and stripping deformation (Huurman et al., 2010). The ability of asphalt binder to resist stripping can be evaluated by using adhesive bond strength as an essential parameter. Adhesion at asphalt binder-aggregate interface is determined by using the adhesive bond energy (Moraes et al., 2011). Consequently, any test method conducted directly on an asphalt binder-aggregate system can evaluate both adhesive and cohesive failure types effectively and provide better understanding of the sensitivity of asphalt mixtures to moisture.

The main cause for moisture damage is the adhesive failure between asphalt binder and aggregates that principally occurs due to the ability of water in removing the asphalt binder that coats the aggregate surfaces in a phenomenon called stripping, which became apparent in asphalt mixtures. Water infiltrates between the films of asphalt binder and aggregates surface

DOI: 10.1201/9781003222897-41

and strips the binder from aggregate surfaces and breaks the bond between them. This is usually due to the strong affinity of aggregates to moist than to asphalt binder (Fromm,1974).

A number of studies were performed to assess the adhesion property between asphalt binder and aggregate surfaces. The basic method used to measure the adhesion performance of the asphalt binder-aggregate system is the peeling method. The pull-out device and similar tools were used in the mechanical method to test adhesion bond strength. Moreover, the surface free energy theory was used to analyze the adhesion condition (Cheng et al., 2002; Cheng, 2002; and Wei, 2008). Also, the method of simulating molecular dynamics was used to study the cohesion and adhesion properties of asphalt concrete pavement (Xu and Wang, 2016). Another method that used to illustrate the mechanism of adhesion bonding of asphalt binder-aggregate combination is the chemical reaction theory (Chen and Huang, 2006).

In 2003, Kanitpong and Bahia pointed out that the bond strength between asphalt binder and aggregate is related to asphalt binder film thickness, and the samples with thicker asphalt binder film expected to experience cohesively failure after moisture conditioning whereas samples with thinner asphalt film tend to fail adhesively.

Bahia et al. (2010) proposed a practical and reliable method for verifying the cohesion of asphalt binder and the adhesion properties of asphalt binder–aggregate systems using the modified version of the PATTI. They used eight cuts on the edge of the stub to help the excess asphalt cement to flux when the stub pressed on the aggregate plate surface and improving the head of pull-stub with a 200 μm thick parametrical.

Till now, there are no specific testing techniques or procedures that can be used to quantify the direct adhesive bond between asphalt cement and aggregates. Previous studies carried out by Marek and Herrin (1967), Kanitpong and Bahia (2003,2004,2005), Copeland (2007), and Masad et al. (2010) only dealt with the mechanical tests of adhesion in different techniques mainly the methods or devices that were used in other industries to determine the adhesive bond strength such as Pneumatic Adhesion Tensile Testing Instrument (PATTI) that is used in the coatings and adhesive industry. The PATTI test was utilized in pavement engineering to evaluate the adhesion bond performance of asphalt binder-aggregate systems in both wet and dry conditions (Copeland, 2007 and Abed, 2011).

2 RESEARCH OBJECTS

The main objectives in this research are:

1. To develop criteria and procedures for laboratory adhesion test method in terms of the test setup, apparatus and specimen preparation that can be used to measure the adhesive bond strength between asphalt cement and aggregates directly.
2. To evaluate the effect of various parameters like asphalt binder film thickness, testing temperature, modifier types, modifier percentage and water conditions on the practical work of fracture required to failure.

3 MATERIALS AND EXPEREMENTAL TESTS

3.1 *Materials*

One type of aggregate with twenty different base and modified asphalt binder were collected to perform direct tension test on asphalt binder and aggregate combinations.

One of the limestone aggregates types was brought from Dukan regions in the north of Iraq. The group of asphalt binders that were utilized in the experimental work included two AC 40-50 base asphalt binder samples provided from Al-Durah and Al-Basrah refineries, one is radial styrene–butadiene styrene (SBS)-modified asphalt cement containing 3.5 and 7% (by weight of asphalt cement) mixing at temperature 180 C^{o} for 2 hours. In addition to asphalt binder modified with Butyl rubber (BR) with 6.9 and 12% (by weight of asphalt binder)

mixing for one hour at 165 Cº and modified asphalt cement with liquid anti-stripping agent called (BG plus) with 0.05, 0.075 and 0.1% (by weight of asphalt binder) mixed for 30 minutes at 150 Cº.

The properties of BG plus and SBS are presented in Tables 2 and 3 respectively.

Table 1. The physical and rheological properties of base asphalt binder.

Property	Asphalt binder	
	Durah	Basrah
Penetration	43	41
Rotational viscosity (c.P)	479.01	527.4
Softening point (˚C)	51.3	52
Penetration Index (PI)	-1.219	1.156
Complex modulus G*(Pa) at 40°C and 10 Hz	$5.43*10^5$	$5.5*10^5$
Phase angle (δ°)	61.13	60.79

Table 2. The properties of anti-stripping agent BG plus.

Property	Unit	Requirement
Density	Kg\ m³	1240
Specific gravity	- - - - - -	0.95
Tensile Strength (σt)	MPa	min.32
Melting point	Cº	170-190
Elongation	%	880
Molecular structure	- - - - - -	Radial

Table 3. The properties of the SBS modifier.

Property	Requirement
Chemical Base	Nanotechnology, Silane based
Form	Liquid
Appearance	Pale yellow
Density	1.0 Approximately @ 27º C
pH Value	Approx. 9.00
Dosage	0.02% to 0.1%. By weight of Binder

3.2 *Experimental tests*

3.2.1 *Direct tension test*

A universal testing machine (UTM) has been used in this study to measure the applied forces and displacements of asphalt binder-aggregate samples with different asphalt binder film thicknesses and loading rates, more details about this test are presented in Abed (2020).

The force was recorded using the servo-hydraulic frame at static while the displacement of the thin asphalt binder film was directly measured using IPC's world-class IMACS digital controller system and UTS software in addition to digital high-speed camera with image correlation software. Testing conditions involve testing temperature of 20˚C for 24 hours as a conditioning period before performing the tests, deformation rate of loading 60 mm/min (1mm/sec) and different asphalt binder film thickness in dry conditioning.

3.2.1.1 SUGGESTED METHOD FOR PREPARING TEST SAMPLES

Each test sample consisted of two fingers of aggregate with a height of 15 mm that were adhered together by asphalt binder. The modified asphalt binder has been prepared (details are listed in Abed (2020)) and used in the test with different film thicknesses (0.01 mm, 0.05 mm and 0.1 mm). The cylindrical aggregate samples (finger sample) used in the direct tension test were prepared with a total height around 30 mm and a diameter of 14 mm.

The aggregate finger samples can be prepared with the following steps:

1. Rock cores (aggregate stubs) were prepared by cutting the rocks into plates with a uniform thickness of around (15-18 mm) by an electrical saw. Each plate was polished and sand-blasted to obtain a uniform surface roughness of the aggregate surface in order to increase the surface area per unit mass, providing a stronger adhesive bonding between the binder and the surface of aggregate (Lent et al., 2008).
2. To have a cylindrical core of aggregate with an inner diameter of 14 mm, the plates of rocks were cored using a bench drill press (inc-co model). The reason for chosen a small contact area with (14 mm) diameter for coring the plate is to reduce the probability of cavitation development, since the chance of forming cavitation increases with the increase of contact area. In general, rock particles contain cavitation, cracks, or inclusions that can impact the integrity of rock structure, the texture of rock surface, and roughness, respectively. The presence of micro-cracks in rock structure can cause a tension failure in the substrate before the failure of the interface or the adhesive.
3. The rock or aggregate cores were then cleaned using distilled water to remove the impurities such as the dust from the sawing, drilling process and polishing powder off the surface of the aggregate by immersion in distilled water, boiled for 15 min, and then drying it with hot air.
4. The final aggregate cores were placed in an oven for one hour at 160°C to remove any remaining moisture.
5. The aggregate cores were marked by numbering both parts of pairs and stored in small plastic containers.

After preparing the modified asphalt binder samples and keeping them in small cans for performing the experimental tests. The samples' containers of base and modified asphalt binder are heated in the oven from 30 to 60 minutes at asphalt binder mixing temperature 165 °C and mixing with a spatula because the modifier can be float or settle at the bottom, so it is necessary to mix before using it. The purpose of heating the asphalt binder in this stage (preparation process) was to reach it to the liquid state, mutating its properties (physical and rheological) as slightly as possible and at the same time making the adhesion process between the two fingers of aggregate smoother as much as possible.

3.2.1.2 ASPHALT BINDER-AGGREGATE SANDWICH PREPARATION

The sandwich sample can be prepared according to the following steps:

1. The cleaning process for the surface of the aggregate sample was done using distilled water and acetone because preparing the aggregate surface properly is an essential step for proper bonding process. Care was taken by using gloves to avoid any contaminating in the cleaned surface after preparation and then heating aggregate fingers in the oven shortly for less than three minutes at a temperature of 165 °C to achieve the adhesion of the binder in preparing binder-aggregate sandwiches.
2. Asphalt binder-aggregate sandwich samples were prepared with (10, 50 and 100 μm) as thin-film thickness; a prototype assembly mold was designed to identify the desired film thickness. The two fingers of aggregate were placed in the holders at first then the screw in each holder was locked to fix the fingers. Then, the two holders were placed in the farm of prototype and were fixed with two butterfly bolts to determine the micrometer reading which represents a zero-binder film thickness position with a micrometer. After heating the two fingers of aggregate for a while in the oven, a small drop of hot asphalt cement is put on the surface of the first finger by using a thin stick that was prepared for this purpose in order to ensure that only a small amount of asphalt is placed on the surface of the rock finger's sample. The second finger is then properly and quickly placed over it and the whole sample is immediately placed in the holders of the assembly prototype before locking the screw in each holder. Thereafter, the distance was adjusted using the micrometer shown in Figure (1-A) to the required thickness of asphalt binder film

and left the sample in holders with an assembly prototype system for one minute to stabilize. The sample and the holders were then removed from the frame of the prototype and the excess asphalt binder was trimmed using a heated knife after leaving the sample to cool down for at least 20 minutes as illustrated in Figure (1-B). The assembly sample was left to sit for 24 hours, even though less than one hour is more than enough for the sample to cure. All the assembly process steps took a maximum of five minutes. The precise of protocol for sample fabrication proved to be essential for sample's quality and repeatability.

3. An aluminum mold, that has been specially designed and manufactured for this experiment, consists of four grips, two holders with cylindrical holes at their center with a diameter of (14.5 mm) and (2mm) depth, and four circular columns distributed around the surface of the lower to fix the asphalt binder-aggregate sandwich at the middle of mold. The reason is to prevent any unnecessary movement during the installation of the mold in the UTM device. Another four grips were manufactured as shown in Figure (1-C) to install the asphalt, binder-aggregate sandwich holders, within the UTM machine and to avoid any prospect of misalignments between the upper and lower sample's holders as depicted in Figure (1-D). To ensure the cleanliness of the surface holes in fixing holders, a chemical solution was used to clean the dust and preliminary gluing of samples from the previous testing.
4. The asphalt-aggregate sandwiches glued into the aluminum holders using a fast-drying epoxy. The epoxy gluing cured period lasted for about 1-3 minutes according to the product's specifications to get a full connection. The prepared sandwiches of asphalt binder-aggregate were conditioned for one day in the refrigerator at a test temperature of 10 C° and 20 C° as shown in Figure (1-E) to achieve a full adhesive bond. To evaluate the impact of water on the mechanical properties of the samples, the samples were conditioned by immersion in the water for 24 hours at testing temperatures of 10 C° and 20 C°. Water conditioning time (24 hr) allowed the samples to be tested rapidly after fabrication, and the change in mechanical properties was observed. After conditioning, samples were moved to the testing chamber, which was kept at a constant testing temperature at 10 C° and 20 C°. To reduce the creep within asphalt binder's film produced by the weight of the upper aluminum holder, the aggregate-binder sandwiches should be rest horizontally by using a developed fixing device (v-plate manufacture plastic), as described in Figure (1-E), while maintaining perfect alignment.

The real challenge in performing the direct tension test is in achieving the test without any lose or failure in the samples. Even if the preparation procedure used for all samples was similar, same level of quality cannot be guaranteed. In some cases, it was apparent during the experiment that the sample was not valid. For example, the failure would occur at the glue or in aggregate as shown in Figure (1-F).

3.2.1.3 TEST PROCEDURE

The testing of asphalt binder-aggregate sandwich samples was performed by using a servo-hydraulic frame. As can be seen in Figure (1-G), the software-controlled operation system of the testing machine records the loading rate, displacement and force history. The whole testing apparatus was placed into an environmental chamber that controlled the testing temperatures at 10 C° and 20 C°. The grip system was specially designed for this experiment. Aluminum grips were designed to hold the sample holders. The upper one was connected directly to the load cell, while the lower grip was connected to the floor of the testing chamber through a locking big screw as stated in Figure (1-D).

The whole experiment was carried out in a climate chamber. The sample was placed in the holders using the alignment pin, the four pins removed before the test starting; the chamber door closed and then the conditioning at testing temperatures was started; this takes 10 minutes for reaching the chamber subjected temperature.

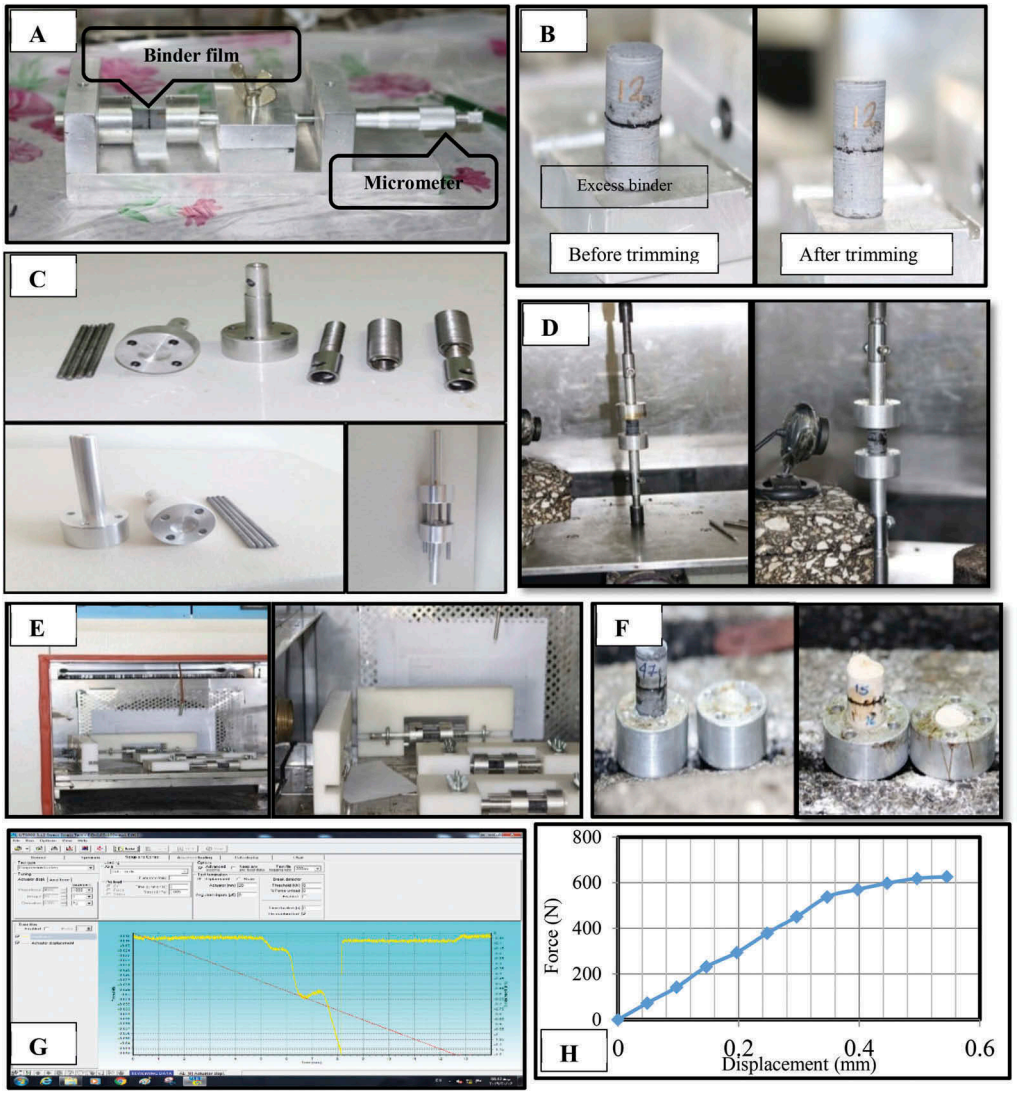

Figure 1. The steps of sample preparation and test procedures.

The entire testing apparatus was contained inside an environmental chamber that controlled the test temperature at 10 C° and 20 C°. The stainless steel grips were specially designed to hold the sample holders. The upper grip was attached directly into the load cell, and the lower grip was attached to the floor of the testing chamber using a locking silicone-stainless steel joint. The locking silicone-stainless steel joint served the purpose of aligning the top and lower grips. A prepared aggregate-bitumen sample was inserted into the bottom grip, Figure 3, and locked in using a compression joint. The inside of the bottom grip was textured to provide a better hold and to prevent the sample from moving during testing. The upper grip was lowered and attached to the sample through bearing force on a screw.

The practical work of fracture required to produce failure (per unit area) was measured using Microsoft Excel to calculate the area under the curve of tensile load versus displacement graph and to calculate the total practical work of fracture divided by the unit area of the adhesive layer of asphalt cement as can be noticed in Figure (1-H).

4 RESULTS AND DISCUSSION

The direct tension test data at dry and wet conditions were analyzed to measure the practical work of fracture which represents the amount of external work required to remove thin film asphalt binder from the aggregate surfaces by determining the maximum tensile loads and the amount of deformation that occurred in the samples at failure. The practical work of fracture was measured as the area under the tensile load-displacement curve until failure and comprised all stored and dissipated energy components such as elastic, viscoelastic, and plastic that are related to the deformation process. Test conditions included Dukan aggregate type, different asphalt binder types, test temperature (10 C° and 20 C°), 0.01, 0.05 and 0.1mm film thickness, deformation rate of 1mm/sec and finally wet and dry conditions.

4.1 *Effect of film thickness*

Based on the results that presented in Figures 2 – 4, for all types of asphalt binder (base and modified), the practical work of fracture increased due to the increment in the asphalt binder film thickness. As asphalt cement layer thickness increases, the dissipated energy in the bulk of the viscoelastic asphalt binder prior to failure (viscose deformation) increases and thus the practical work of fracture increases.

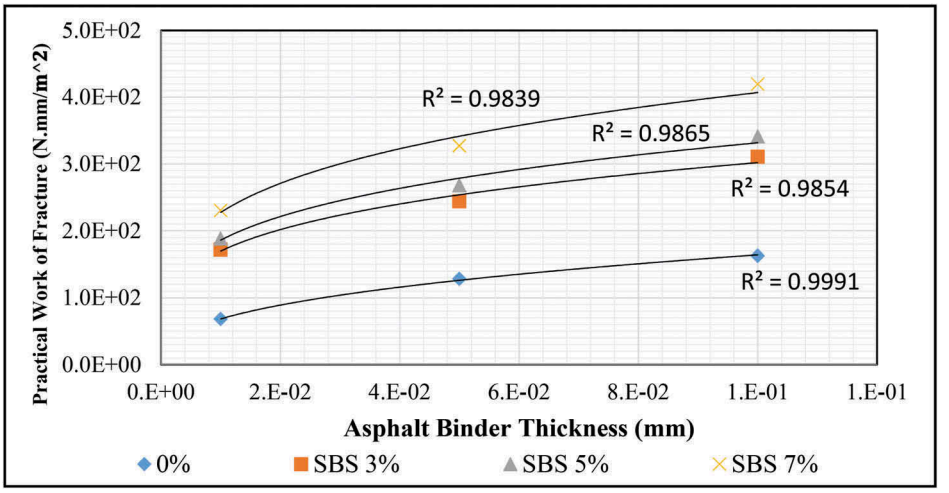

Figure 2. Effect of film thickness on practical work of fracture of asphalt binder modified with different percent of SBS.

The figures above revealed the following:

1) The practical work of fracture increases when adding SBS modifier for the same asphalt binder thin film thickness, and also increases with the increase of modifier content.
2) The same behavior occurs when adding BR until 9% and then the behavior is reversed as same as when adding BG+ until 0.07%
3) The addition of SBS has enhanced the practical work required to failure more than BR and BG Plus.

4.2 *Effect of moisture condition*

The moisture conditioning has a great impact on reducing the practical work of fracture due to the decrease in tensile load at failure as shown in Table 4. The samples were tested after

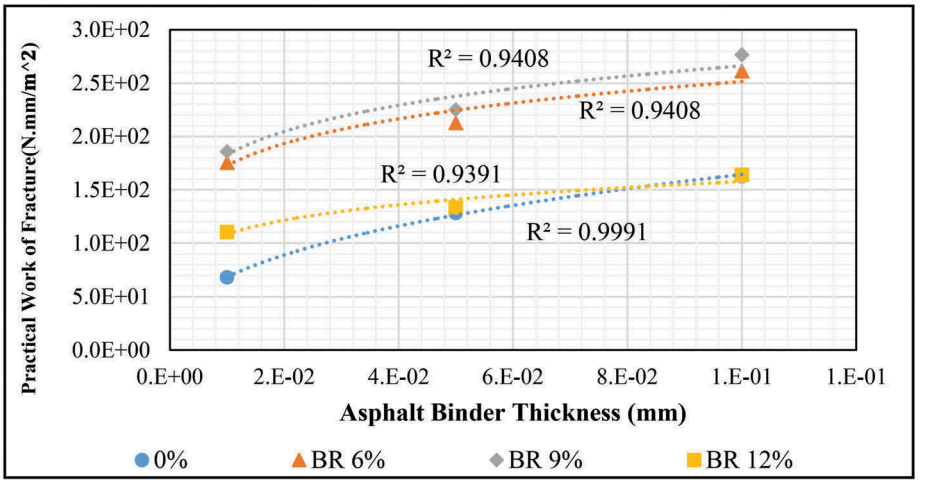

Figure 3. Effect of film thickness on practical work of fracture of asphalt binder modified with different percent of BR.

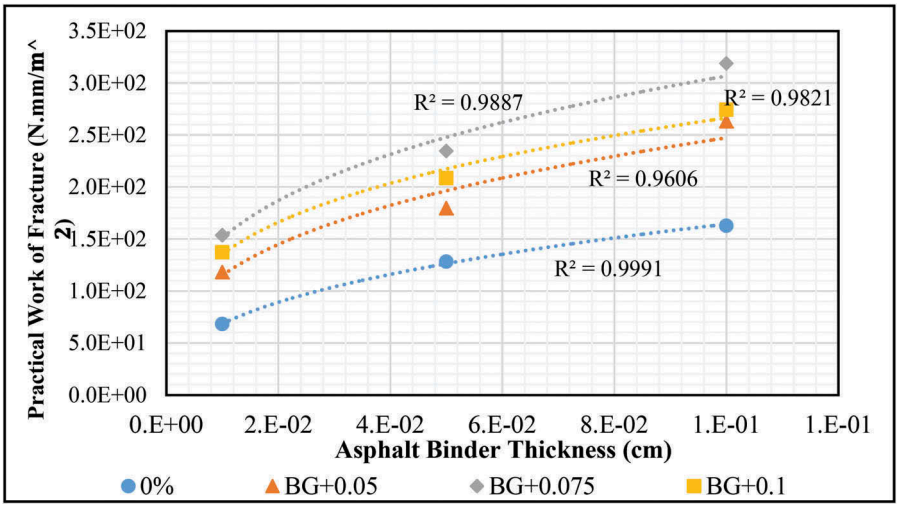

Figure 4. Effect of film thickness on practical work of fracture of asphalt binder modified with different percent of BG Plus.

being submerged in water for 24 hrs. The results of the tested samples are tabulated in Table 4 and depicted in Figure 5. Based on these results, the values of fracture work required to produce failure in dry condition is high comparing with those in wet condition. In case of moisture condition, when asphalt binder-aggregate combination exposed to water, the water runs on penetrating the aggregate and reducing the adhesion between asphalt cement and aggregate and thus causing a reduction in the tensile load needed to failure and eventually minimizing the practical work required to failure.

The greatest reduction ratio in practical work of fracture due to the presence of water occurs in the case of 7% SBS-modified asphalt binder and it is about (61%), comparing with base asphalt binder (25%), reduction ratio, while the smallest value of reduction ratio was for the case of anti-stripping agent BG plus-modified asphalt binder which is about (13%).

Table 4. The effect of moisture condition on the practical work of fracture (N.mm/$\mathbf{m}^2$) different types of Durah binder with Dukan aggregate.

Film thickness (mm)	The average value of Practical Work of Fracture (N.mm/$\mathbf{m}^2$) for 3 specimens in Dry Condition									
	Base	SBS			BR			PG Plus		
	0%	3%	5%	7%	6%	9%	12%	0.05	0.075	0.1
0.01	68.1	171.6	188.1	230.3	175.4	185.8	110.2	118.1	153.5	137.1
0.05	128.2	243.7	267.9	327.1	212.6	225.13	133.3	179.5	234.4	208.4
0.1	162.6	310.6	340.9	419.3	261.1	276.5	163.9	263.2	318.7	274.2
The average value of Practical Work of Fracture (N.mm/$\mathbf{m}^2$) for 3 specimens in Wet Condition										
0.01	51.3	118.6	124.6	89.3	111.2	107.7	80.6	102.8	130	118.7
0.05	96.2	168.4	177.2	147.3	136.3	117.9	97.5	156.3	199.4	181.4
0.1	122.1	214.6	225.3	188.9	167.2	116.2	119.9	229	271.1	238.6

Test conditions: Dukan aggregate type, Durah asphalt binder, testing temperature 20°C and deformation rate1mm/sec

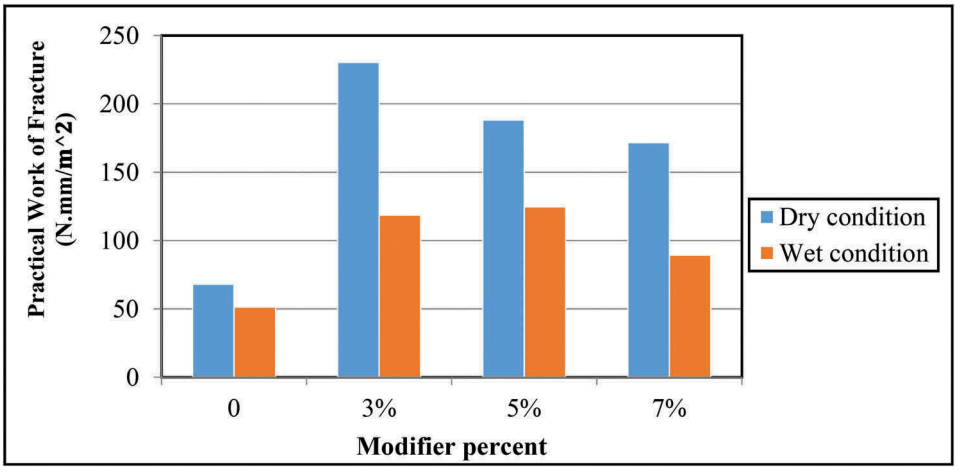

Figure 5. Effect of moisture condition on the practical work of fracture of modified asphalt binder with different percent of SBS.

4.3 *Effect of modifiers*

According to Table 4, the modification of asphalt binder with different kinds of modifiers has a great impact on the practical work required to failure. In general, the addition of modifiers can increase the practical work of fracture. The increment of the practical work of fracture was stemmed from the increase of maximum tensile load and the displacement at failure. At a given type of asphalts binder, the practical work of fracture increased with increasing the SBS content as shown in Figure 6. The addition of SBS modifier to base asphalt cement improved its viscosity and increased connection between its particles and also increased the maximum tensile load required to failure. The maximum incremental ratio of practical work of fracture was due to the addition of a 7% SBS modifier as presented in Figure 6. In contrast, the addition of BR and liquid anti-stripping agent (BG plus) to the asphalt binder has increased the practical work of fracture gradually to the maximum value at (9%BR and 0.075 BG plus) and then decreased with increasing the modifier content. The incremental ratio in practical work of fracture due to the addition of these modifiers in Durah asphalt binder is higher than the Basrah asphalt binder.

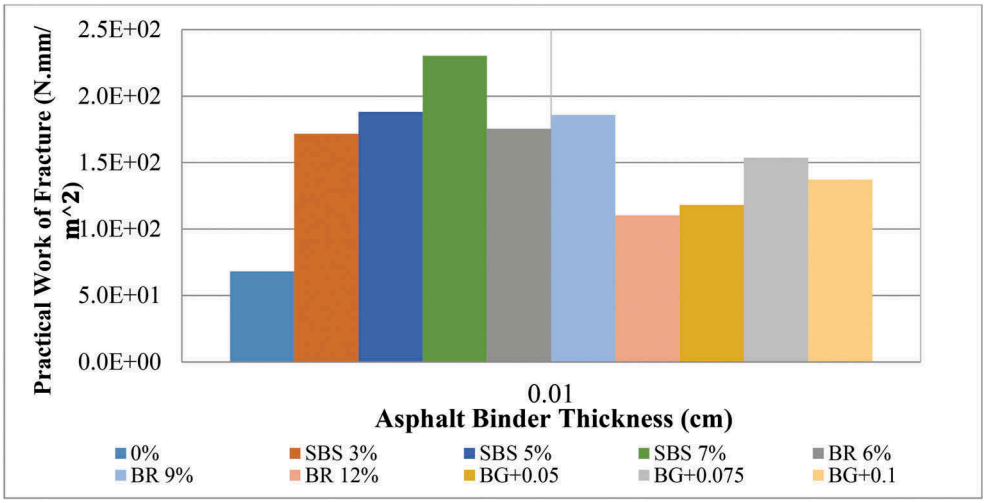

Figure 6. The effect of modifier type and percentage on the practical work of fracture.

4.4 *Effect of temperature*

Temperature is an important measurement that affects the behavior of asphalt binder. According to the results in and Figure 7, at a given type of asphalt binder and keeping the deformation rate constant at (1 mm/sec), the work of fracture decreased with increasing test temperature from 10C° to 20 C°. The reduction in the practical work of fracture was stemmed a decrease in the tensile load or an increase in the displacement at failure. Decreasing tensile load at failure with increasing testing temperature due to losing the asphalt binder to its stiffness and viscosity and begins to flow. This will justify the reduction in the practical work required to failure.

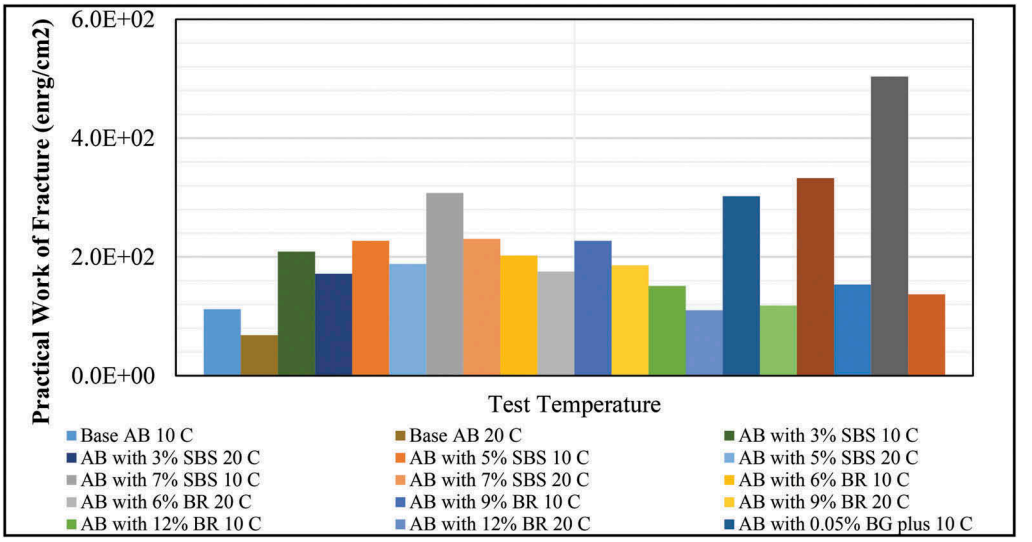

Figure 7. The effect of testing temperature on the practical work of fracture.

4.5 *Effect of asphalt binder type*

Results in Table 5 illustrate the effect of asphalt binder type on the practical work of fracture required to failure. The samples were tested at a constant deformation rate of 1-mm/s with 20° C testing temperature and in dry condition. In general, the practical work of fracture of Durah asphalt cement (base and modified) was higher than Basrah asphalt cement (base and modified). This might be related to the difference in chemical composition between them.

Table 5. Effect of asphalt binder type on practical work of fracture (N.mm/**m**^{2}) for different types of Durah and Basrah asphalt binder with Dukan aggregate.

	Practical Work of Fracture (N.mm/m^2)	
Asphalt Binder (AB) Type	Durah Binder	Basrah Binder
Base	68.16	67.34
3% SBS	171.65	89.45
5% SBS	188.11	197.31
7% SBS	230.39	280.15
6% BR	175.49	103.6
9% BR	185.8	144.71
12% BR	110.22	111.34
0.05% BG plus	118.12	132
0.075% BG plus	153.58	149.85
0.1% BG plus	137.13	124.22

Test conditions: test temperature 20°C 0.01mm film thickness and deformation rate1mm/sec

5 CONCLUSIONS

The results from the experimental work present the following:

1. This paper worked on developing and updating the proposed mechanism to calculate the amount of the direct adhesion bond between the asphalt binder and aggregate surfaces in order to increase the data accuracy resulting from showing the orientation of the sample during the examination or its junction. The experimental results of the proposed mechanism to calculate the direct tensile strength are more accurate and reliable.
2. Asphalt binder film thickness has agreat influence on the measured tensile load and displacement, and thus on the practical work of fracture which increased with the increasing in the film thickness of asphalt binder from 0.01 to 0.1mm.
3. The modification of asphalt binder using different kinds of modifiers (SBS, BR and BG Plus) with different percentages has agreat impact on the practical work required to failure.
4. Practical work required to failure in wet condition is low compared with the samples tested in dry condition.
5. The highest reduction ratio in the practical work to fracture caused by moisture conditioning was for the case of 7% SBS-modified asphalt binder-Dukan aggregate and is about 61% comparing with base asphalt binder with about 25%. The smallest value of reduction ratio was for the case of anti-stripping agent BG plus-modified asphalt binder and is about 13%.
6. The testing temperatures can influence the practical work required to failure. Increasing testing temperature from 10C$^\circ$ to 20 C$^\circ$ can lead to decrease the practical work required to failure for all types of asphalt binder. This is as a result of losing the asphalt binder to its stiffness and viscosity and beginning to flow.
7. The chemical composition of asphalt binder can greatly affect the practical work of fractures at failure under various conditions. Durah asphalt cement (base and modified) has a higher practical work of fractures at failure comparing with Basrah asphalt binder.

ACKNOWLEDGMENTS

The authors acknowledge the Technical & Soil Mechanics Laboratory in the Amirkabir University of Technology and the Civil Dept. in Tehran for the direct tension and DSR tests on the different asphalt binders used in this research, and would like to thank the Mustansiriyah University, Engineering College, Highway and Transportation Dept. for supporting this research.

REFERENCES

Abed, A. H., 2011. *Enhanced aggregate-asphalt adhesion and stability of local hot mix asphalt*. Engineering and Technical Journal, vol. 29, no. 10, pp. 2044–2059.

Abed, Y., 2020. *The Deformation Strength Characterization of a Thin Film Bitumen Material*. Ph.D. Dissertation, Mustansiriayah University, Baghdad, Iraq.

Abed, Y., Khudhair, Y. and Alhaddad, A., 2020. *Discrepancies in Rheological Properties of Modified Asphalt Cement*. IOP Conf. Series: Materials Science and Engineering. doi:10.1088/1757-899X/870/1/012029.

ASTM (D7175 – 08), 2015. *Determining the Rheological Properties of Asphalt Binder Using a Dynamic Shear Rheometer*.

Bahia, H.U., Canestrari, F., Cardone, F., Graziani, A. and Santagata, F.A., 2010. *Adhesive and Cohesive Properties of Asphalt- Aggregate Systems Subjected to Moisture Damage*. Road Materials and Pavement Design, vol. 11, p.p.11–32.

Chen, J. S. and Huang, C. C.,2006. *Fundamental Characterization of SBS-Modified Asphalt Mixed with Sulfur*. Journal of applied polymer science, vol. 103, p.p. 2817–2825.

Cheng, D., Little, D.N., Lytton, R.L. and Holste, J.C., 2002. *Use of surface free energy properties of the asphalt-aggregate system to predict moisture damage potential*, J. Assoc. Asphalt Paving Technol., vol. 71, p.p 59–88.

Cheng, D., 2002. *Surface Free Energy of Asphalt-aggregate System and Performance Analysis of Asphalt Concrete Based on Surface Free Energy*. Ph. D. Thesis, Texas A&M University, College Station.

Copeland, A. R., 2007. *Influence of moisture on bond strength of asphalt-aggregate systems*, Ph.D. Thesis, Vanderbilt University, Nashville, Tennessee.

Fromm, H.J., 1974. *The mechanisms of asphalt stripping from aggregate surfaces*. Proceedings of the Association of Asphalt Paving Technologists, vol. 43, p.p. 191–2.

Huurman, M., Mo, L.T., Woldekidan, M.F., Wub, S.P.and Molenaar, A.A.A. 2010. *Investigation into material development and optimization of improved raveling resistant porous asphalt concrete*. Materials and Design, vol. 31 (7),p.p. 3194–3206.

Kanitpong, K. and Bahia, H., 2003. *Role of Adhesion and Thin Film Tackiness of Asphalt Binders in Moisture Damage of HMA*. Journal of the Association of Asphalt Paving Technologists, vol. 72, pp. 611–642.

Kanitpong, K. and Bahia, H., 2004. *Evaluation of the Roles of Adhesion and Cohesion Properties of Asphalt Binders in Moisture Damage of HMA*. Dissertation, University of Wisconsin – Madison Department of Civil and Environmental Engineering.

Kanitpong, K. and Bahia, H., 2005. *Relating adhesion and cohesion of asphalt to the effect of moisture on laboratory performance of asphalt mixtures*. Journal of the Transportation Research Board, vol. 1901, pp.33–34.

Marek, C.R. and Herrin, M., 1967. *Tensile behavior and failure characteristics of asphalt cement in thin film*. Journal of the Association of Asphalt Paving Technologists, vol. 37, pp. 386–421.

Moraes, R., Velasquez, R., and Bahia, H.U., 2011. *Measuring the Effect of Moisture on Asphalt-Aggregate Bond with the Bitumen Bond Strength Test*. Transportation Research Record: Journal of the Transportation Research Board, vol. 2209, pp. 70–81.

Wei, J. and Dong Ying, 2008. *Study on Surface Free Energy of Asphalt Aggregate and Moisture Diffusion in Asphalt*. Ph.D. Thesis, China University of Petroleum.

Xu, G. and Wang, H., 2016. *Study of cohesion and adhesion properties of asphalt concrete with molecular dynamics simulation*, Comput. Mater. Sci., vol. 112, pp. 161–169.

Eleventh International Conference on the Bearing Capacity of Roads, Railways and Airfields, Volume 2 – Hoff, Mork & Saba (eds)

Modelling the resilient modulus of cement-stabilized quarry fines using element-wise calculation

D. Castillo, Y. Zhang, A. Cannone Falchetto & L. Korkiala-Tanttu
Department of Civil Engineering, Aalto University, Espoo, Finland

ABSTRACT: This paper demonstrates the use of a simple approach to model the mechanical response of cement-stabilized quarry fines (CQF) as bounded base layer material in pavement structures. Quarry fines are secondary materials, i.e. by-products of industrial processes. Quarry fines can be stabilized with chemical agents like cement to improve their strength and stiffness as part of a pavement structure. Using a finite element model of a pavement structure, the response of CQF material was first approximated as fully elastic under static traffic loading. This preliminary result was followed by an iterative process to calculate the resilient modulus of the material, adjusting its response element by element to the individual three-dimensional stress conditions experienced at every spatial coordinate (i.e. principal stresses of the individual finite elements). After 3-5 iterations, the stresses on the CQF and other layers in the pavement structure were found to stabilize and converge.

Keywords: Cemented quarry fines, model, pavement structure, stabilized, finite elements

1 INTRODUCTION

1.1 *Background*

The maintenance and rehabilitation of a road network generally constitute a significant component of the overall budget devoted to transportation. Low-volume roads can represent a considerable portion of the network; consequently, significant resources may be dedicated to the remediation of such paved and gravel roads. With sparse traffic and often remote locations, low volume roads may be most susceptible to distresses related to weather conditions, such as low temperatures and moisture damage. However, the traffic cannot be completely neglected as an important source of distress.

Among other challenges, road infrastructure worldwide is facing increasing truck weights and more demanding tire configurations (Kolisoja et al., 2019). These circumstances are reflected in regulations that allow tougher conditions for the roads; for example, the allowable axle weight limits were increased in Finland in 2013 (Kolisoja et al., 2015). While such measures can make the transportation of freight more efficient and thus have positive impacts on trade, it is crucial to give proportional importance to the associated drawbacks affecting infrastructure, including the potential increase in damage to the roads and the ensuing need for maintenance. In this context, it is critical to expand research efforts on *sustainable* construction materials, *timely* maintenance techniques, and *appropriate* modelling tools, to better study, characterize, and address the current challenges.

From the point of view of sustainability, it is beneficial to promote maintenance and rehabilitation alternatives that consider different types of recycling. Such techniques have been gaining

DOI: 10.1201/9781003222897-42

acceptance, and as they fulfil engineering design objectives, they are finding their way into regulations. Alternatives that consider recycling include, for example, partially or entirely replacing aggregates in the granular layers with waste materials from industrial processes. Recycling brings economic as well as environmental advantages, mainly that the usage of recycled material implies a reduction in the demand for other virgin materials (i.e. aggregates that were replaced). Additionally, the waste material usually has a low economic value before recycling; however, recycling can lead it to regain value after reconstruction, regardless of the material.

1.2 *Quarry fines and cement stabilization*

One of such sources of potentially recyclable materials is quarry by-products, or quarry fines (QF). Quarry fines are *secondary* materials, that is, not a primary outcome but a by-product of an industrial process; in this case, the crushing and processing of stones in a quarry. A picture of the quarry fines taken in Finland is presented in Figure 1. Using quarry fines as an alternative material for infrastructure construction brings associated benefits: it alleviates the issue of aggregate resource depletion, at the same time offering a solution to the extensive piling of unused quarry fines (Zhang, Korkiala-Tanttu, Gustavsson, et al., 2019), which can have a high environmental impact. Due to its accumulation, the material may be obtained essentially for free.

Figure 1. Quarry fines stockpiled in a quarry (Koskenkylä, Finland). Credit: Yinning Zhang.

Like with other by-products, a possible application for quarry fines is to reuse them as part of layers in a pavement structure. The overall conditions of the structure of a road can be upgraded by improving the mechanical properties of the lower granular layers during maintenance. These layers support a substantial amount of stress, especially in thin, flexible pavement structures; additionally, they act as a 'buffer' for weather effects between the natural soil and the pavement structure (Doré & Zubeck, 2009). Among other applications, quarry wastes have been used recently to improve applications of recycled asphalt (Edeh et al., 2020), and they can also be used as stabilizers to clay (Xiong, 2019).

It is relevant to remark that a common trade-off when using recycled materials is that their economic and environmental benefits may come at the cost of relatively poor mechanical quality. Zhang, Korkiala-Tanttu, Gustavsson, et al. (2019) presented a summary of structural uses of quarry waste, where they concluded that it is more common to use quarry fines as a replacement and/or as an additive (usually in a proportion lower than 30%) than as a construction material by itself. This is because the mechanical properties of untreated quarry fines are modest when compared to the high requirements of infrastructure construction. Moreover, quarry fines have large amounts of fines; wet sieving tests have indicated fine contents as high as 12.5 %, making them especially vulnerable to frost heaving, a critical distress in the Nordic region. An example of a gradation of QF is presented in Figure 2. The material thus needs to be stabilized for its use in pavement construction and to counter potential frost susceptibility (Zhang, Korkiala-Tanttu, Gustavsson, et al., 2019).

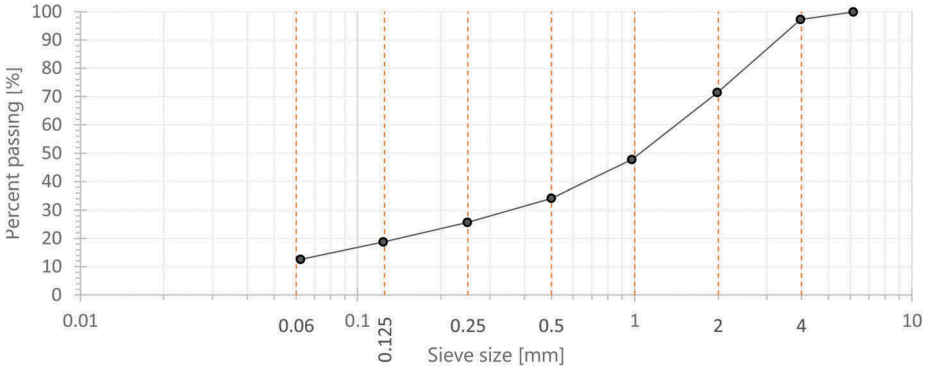

Figure 2. Gradation of quarry fines (wet sieving). Data from Zhang, Korkiala-Tanttu, Gustavsson, et al. (2019).

To improve the mechanical properties and the frost susceptibility of quarry fines, the material can be stabilized with cement. Cement treatment of the quarry fines is considered a chemical stabilization. Cement stabilization is a common practice in road construction, and there is extensive experience in stabilizing granular soils. This method has been in use, for example, for soil stabilization and to improve the mechanical properties of granular materials (Haichert et al., 2012; Prusinski & Bhattacharja, 1999). Cement-stabilized quarry fines (CQF) were used in base layers as part of two full-scale test sections, as reported by Qamhia et al. (2019). The authors reported beneficial effects on stress distribution in the subgrade and satisfactory rut performance. In their work, the CQF materials were tested under low to medium load volumes. Quarry fines in the form of stone powder and muck have also been stabilized with quick lime (Manandhar et al., 2014).

Zhang, Korkiala-Tanttu, and Borén (2019) conducted unconfined compressive tests on specimens of quarry fines stabilized with cement. The specimens had cement contents of 2.5% and 4.5%, and water-cement ratios 0.4 and 0.6. According to the authors, quarry fines that have been stabilized are suitable for use as filter, subbase, and base layers in pavement structures. However, more experience is needed to optimise cement content selection (Zhang, Korkiala-Tanttu, & Borén, 2019). A picture of some of the cylindrical samples of cement-stabilized quarry fines after the unconfined compression tests is presented in Figure 3. Several specimens presented a combination of tensile and shear cracks, indicating that these are the main failure modes of interest in this material.

The recent research on quarry fines conducted at Aalto University is part of a more comprehensive research effort directed towards materials with recycling potential. Other materials include fly ash, blast furnace slag, bio ashes, and municipal solid waste incineration (bottom ash).

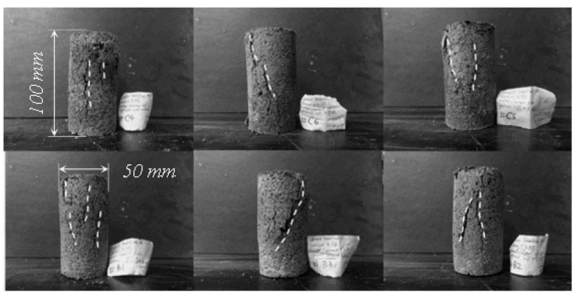

Figure 3. Cylindrical specimens of cement-stabilized quarry fines after unconfined compression tests. Modified from (Zhang, Korkiala-Tanttu, & Borén, 2019).

An additional material of particular interest is Ecolan, a cement-based sustainable binder with coal ash, wood biomass, and lime. Considering that the cement industry has a heavy environmental impact on CO_2 production, globally, alternative binders can and should be explored by researchers.

1.3 *Computational modelling*

As presented previously, cemented quarry fines have been characterized experimentally in the laboratory at the meso-scale, and also in the field at larger scales (Qamhia et al., 2019; Zhang, Korkiala-Tanttu, & Borén, 2019). Both of these approaches can produce highly relevant data under specific conditions of specimen or structure geometry, weather conditions, and mechanical loads. Nevertheless, experimental research can be costly and time-consuming, especially full-scale tests, making data scarce. In the interest of making the best possible use of this data, modelling is a powerful alternative to gain better knowledge of the CQF material.

Computational models can reproduce simplified versions of laboratory or field conditions. Experimental results can be complemented with suitable models to enable decision-making even in contexts different from those where the full-scale test took place. Modelling approaches can be helpful, for example, to 'extend' hypothetical scenarios towards different configurations, environmental conditions, and solicitations, as well as for selecting appropriate testing methods.

An additional point to consider is that recycled materials are highly heterogeneous. For example, moderate to high variability was evidenced in behaviours such as the capillary rise and unconfined compressive strength of the quarry fines among laboratory-prepared specimens (Zhang, Korkiala-Tanttu, & Borén, 2019; Zhang, Korkiala-Tanttu, Gustavsson, et al., 2019), and the natural variability of quarry fines has been noted in particular (Qamhia et al., 2019). Computational approaches are particularly well-suited to deal with heterogeneous conditions.

1.4 *Overview*

Regarding the quarry fines as an alternative material for road construction, there is a growing availability of laboratory test data. At the same time, however, the availability of field tests is relatively scarce, save for the exception of a recent and comprehensive accelerated pavement testing plan (Qamhia et al., 2019). From the modelling perspective, however, there seem to be relatively few results available. The only study found with a modelling phase for CQF materials reports the instrumentation of a road built in Arlington, Texas, where this material was used as a base (Puppala et al., 2012). We intend to complement this lacking by offering a versatile modelling alternative for this material.

In this study, we developed a code that automates the modelling of pavement structures with CQF layers. We use it to model a two-dimensional axisymmetric pavement structure with a base layer composed of cement-stabilized quarry fines. The model offers a simple computational approximation that enables bringing together available laboratory data with the possibility to generalize, adapt, and improve applicability to new geometries and materials.

The present modelling effort is at the macro scale. The authors are simultaneously advancing efforts at the micro scale, where the particles of quarry fines are characterized explicitly.

2 MODELLING STAGE

2.1 *Computational approach to model CQF material*

Current finite element software packages have some limitations when modelling road structures and materials like the cemented quarry fines. For example, characteristics like a maximum (limited) number of layers, and the availability of limited behaviour models can be challenging. Particularly, stress-dependent material behaviours may not be supported by default.

A code was created to address these limitations. The code is composed of a set of scripts, and it is run using Python and ABAQUS. MATLAB code is also used for visualization of the

resulting stresses and moduli. This software are efficient and well-established computational platforms for finite element and mathematical analyses in engineering.

The model performs *element-wise assignment* of material properties for the CQF layer, and it applies an iterative process to calculate the stress-dependent resilient modulus of the elements of this layer. Using the code, we can model pavement structures with an arbitrary number of layers, thicknesses, and materials. More importantly, cement-stabilized layers are modelled including their stress-dependent response. The model is axisymmetric, so it extends an apparent two-dimensional geometry into a more representative three-dimensional state.

2.2 *Iterative calculation of the resilient modulus of the cement-stabilized quarry fines*

Similarly to granular materials, cement-stabilized quarry fines exhibit stress-dependency. Models of varying degrees of complexity have been used to characterize such behaviour in two and three dimensions (Araya, 2011; Li & Hao, 2020; Saevarsdottir & Erlingsson, 2015; Sidess et al., 2021). In any case, most of the references available in the literature make use of one of several versions of the *K-θ* model. This model expresses the resilient modulus of a material as a function of its stress state. To find the resilient modulus of the cement-stabilized material, we first obtain the principal stresses (σ_1, σ_2, σ_3) at every location in the CQF layer, and then compute the resilient modulus as follows:

$$M_R = k_1 \cdot p_a \cdot \left(\frac{\theta}{p_a}\right)^{k_2} \left(\frac{\tau_{oct}}{p_a} + 1\right)^{k_3}$$

where M_R is the resilient modulus, k_1, k_2 and k_3 are characteristic constants of the material, p_a is a reference pressure used to ensure units consistency (herein the atmospheric pressure, 101.3 kPa), θ is the bulk modulus (sum of principal stresses, $\sigma_1+\sigma_2+\sigma_3$), and τ_{oct} is the octahedral shear stress, calculated here as (Caicedo, 2019):

$$\tau_{oct} = \frac{1}{3}\sqrt{(\sigma_1 - \sigma_2)^2 + (\sigma_2 - \sigma_3)^2 + (\sigma_3 - \sigma_1)^2}$$

Puppala et al. (2012) provide the results of triaxial tests of CQF material at varying stress states and their associated resilient modulus at the point where the deviator stress equalled the confining stress. This data was used to calibrate the model and to attempt to replicate the results. The following values were calculated:

$$k_1 = 2258.8433$$

$$k_2 = 0.9680347$$

$$k_3 = -2.352713067$$

This model (*K-θ* with octahedral stresses) was selected as it offered a good fit for the reported CQF resilient modulus data, as well as for data measured independently in the laboratory at Aalto University. Figure 4 presents a comparison between the data presented by Puppala et al. (2012) and the data fitted with the established values of k.

The computational model starts with an initial (high) resilient modulus of 369 MPa assigned to the whole CQF layer for the first iteration. This value is reported in the numerical analyses from Puppala et al. (2012). The load is then applied, and element-wise principal stress data is extracted from the layer of cement-stabilized quarry fines. New element-wise moduli are calculated for the CQF layer, and iterative calculations are performed to converge to a stable value of resilient modulus and associated stress, strain, and deformation response.

In the code, different values of k can be adjusted to represent different materials. Also, the code is flexible enough to allow the rapid adaptation to other *K-θ* models for the calculation of resilient modulus, and the use of added randomness for the values of k.

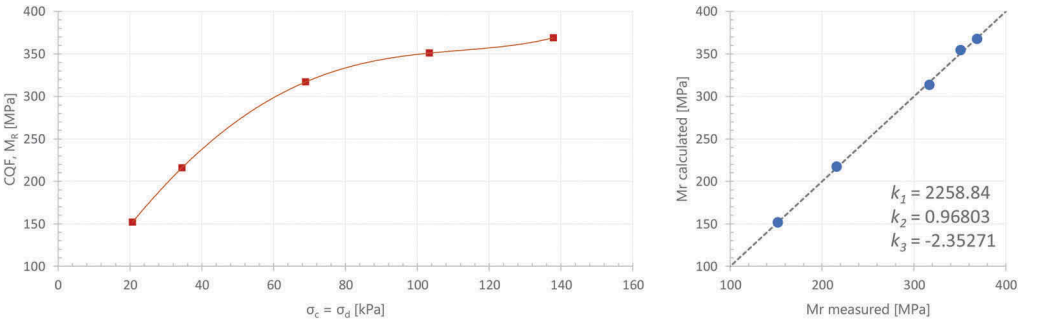

Figure 4. Stress relationship and *k*-values calculated from data reported by Puppala et al. (2012).

2.3 *Attempt to replicate experimental and computational reported values*

This modelling effort started as an attempted approximation to the only application found in the literature including modelling for cement-stabilized quarry fines (Puppala et al., 2012). Having calibrated the resilient modulus, the next step was to attempt to replicate the results. The structure instrumented by Puppala et al. (2012) is the "north-bound section" consisting of four pavement layers over the natural subgrade. The layers are (1) continuously reinforced concrete (CRC, 280 mm), (2) hot-mix asphalt (HMA, 100 mm), (3) the cement-stabilized quarry fines base (CQF, 840 mm), and (4) a lime-treated subgrade (LSG, 460mm).

In their analysis, as in ours, the load was simplified as a circular load of 276 kPa with a radius 15 cm. The geometry and characteristics of the FE model were approximated as best as possible from the figures and data of the original paper, including the thickness of layers, the width of the computational model, the size and number of elements and divisions per layer in horizontal and vertical directions. The results of the first approximation are presented next.

Figure 5 presents the vertical stresses calculated for the computational structure after five iterations, compared with the profile and experimental data presented by Puppala et al. (2012). The data profile is obtained from the left-most edge of the axisymmetric model; that is, it represents the stresses below the centre of the load and into the pavement structure. The boundary conditions of the axisymmetric model, including the load and the displacement restrictions on the outer edges, can also be observed in Figure 5.

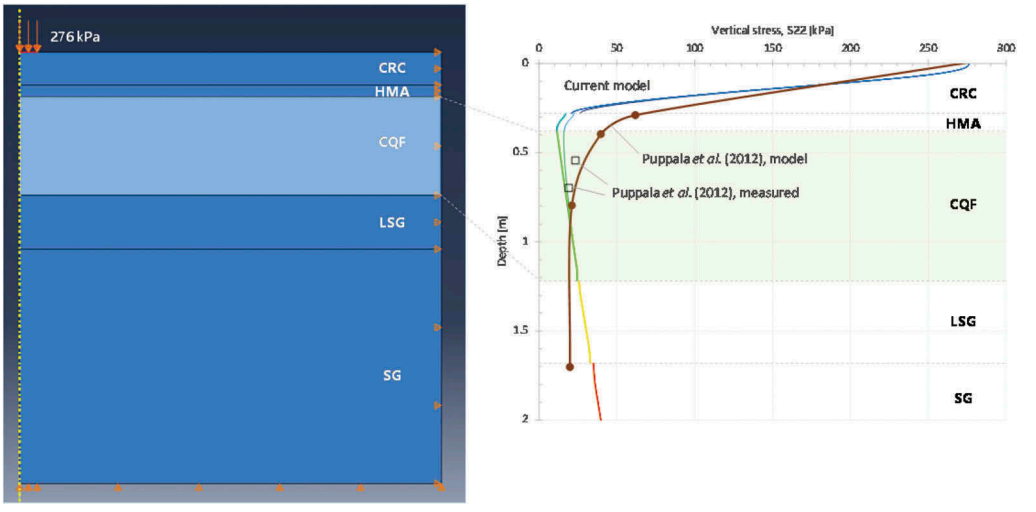

Figure 5. Vertical stress profile below a load for the whole structure. Bold profile and experimental data points from Puppala et al. (2012).

It is apparent that there are important discrepancies, and the stresses reported and modelled previously do not match the values produced by the current model. Most noticeable are the stresses that are expected inside the upper layer (CRC, reinforced concrete); these will be explored in the next section. Notice that the iterations change only very slightly and almost cannot be discerned at this scale. There are in fact five iterations plotted in the figure, but the change in stresses is quite low; therefore at the scale of the structure the changes in stress inside the CQF layer seem negligible at first.

The associated field of modulus for the CQF layer has low values. Given that the stresses expected from this prediction are small (between 10-25 kPa at most, and larger at the bottom of the layer), the modulus below the load varies between 40 and 80 MPa and even lower values appear away from the centre of the load. Some comments can be raised from the comparison:

- Importantly, there may be a possible mismatch in the description of the load. Puppala et al. (2012) mention a 40-kN (9-kip) half-single axle wheel load over a circular area of radius 0.15 m, and a pressure of 276 kPa. However, this configuration actually produces a larger pressure (~566 kPa). The 276 kPa pressure was kept for consistency.
- The discrepancies may be explained by an extended discussion of the models that were used to characterize the layers in Puppala et al. (2012), including possible affectations by saturation, which are not described in the source text.

2.4 *Adjustment without upper layers ('topped-off' model)*

To pinpoint the cause for potential differences in the previous comparison, a model of the pavement structure was created using KENPAVE. In this model, the dimensions and parameters are the same as those provided by Puppala et al. (2012) and as presented before. Figure 6 contrasts the vertical stress profile obtained from the KENPAVE model (no self-weight) with the profile and experimental data reported by Puppala et al. (2012). Mainly, it can be observed that the stress transferred to the CQF layer is considerably different from their computational prediction. The value calculated by KENPAVE is closer to the values currently being obtained from the element-wise model. Fundamental differences may exist in the manner of calculating stresses transferred trough the concrete layer and perhaps in the actual values of stress measured and reported by the source. These may partly explain the discrepancies.

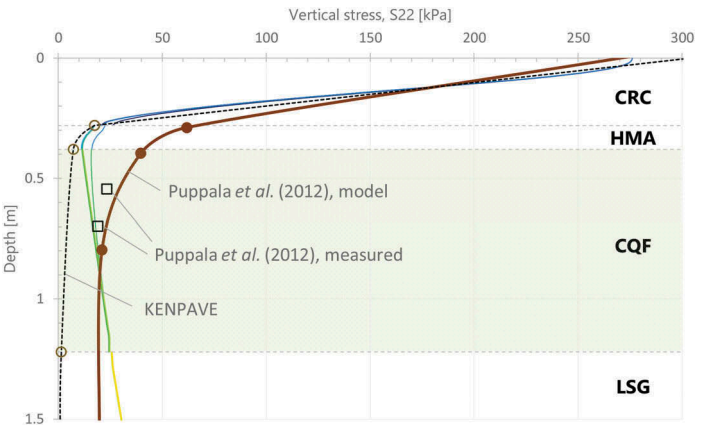

Figure 6. Stress results compared with KENPAVE (dotted curve). Profile below the load. Bold profile and experimental data points from Puppala et al. (2012).

After this comparison, it was decided that the best way forward would be to concentrate the modelling efforts on the CQF layer. Therefore it was decided to create one last model, equal in all regards to the previous structure, with two key differences: the upper two layers (concrete and asphalt mixture) above the CQF layer were removed, and the surface load was replaced with the value obtained from the stress profile modelled by the authors (bold in previous figures, ~40 kPa). The results of this modified ('topped-off') model are presented next.

Figure 7 presents the stress profile from the toped-off model. In contrast with the previous results, a greater agreement is now seen in the vertical stresses expected and measured inside the CQF layer. The results suggests that, once the discrepancy in the load transferred to the CQF has been removed, the model is a good representation not only of the data reported by Puppala et al. (2012) but also of their field measurements. At the same time, this modified model is perhaps more representative of a gravel and/or unpaved road, as the traffic loads are directly transferred to the upper layers. A detail of the vertical stress profiles inside the CQF layer is presented in Figure 8. The profiles were calculated in successive iterations of the model. Based on the stresses reported along the CQF layer, it can be observed that the iterations seem to converge and to offer a reasonably good representation of the measurements.

The "map" of modulus in the CQF layer after the last iteration is presented as well in Figure 9. Likewise, element-to-element stress, strain, and displacement maps are available for the whole layers of the pavement structure. In this new model, due to the higher stresses, the modulus ranges between 60 and 160 MPa directly below the layer, consistent with the ranges reported in the experiments that were conducted by Puppala et al. (2012). Such values may be contrasted with experimental data from Zhang, Korkiala-Tanttu, and Borén (2019), where the secant modulus (modulus of deformation E_{50}) was between 70 and 170 MPa (average 120 MPa).

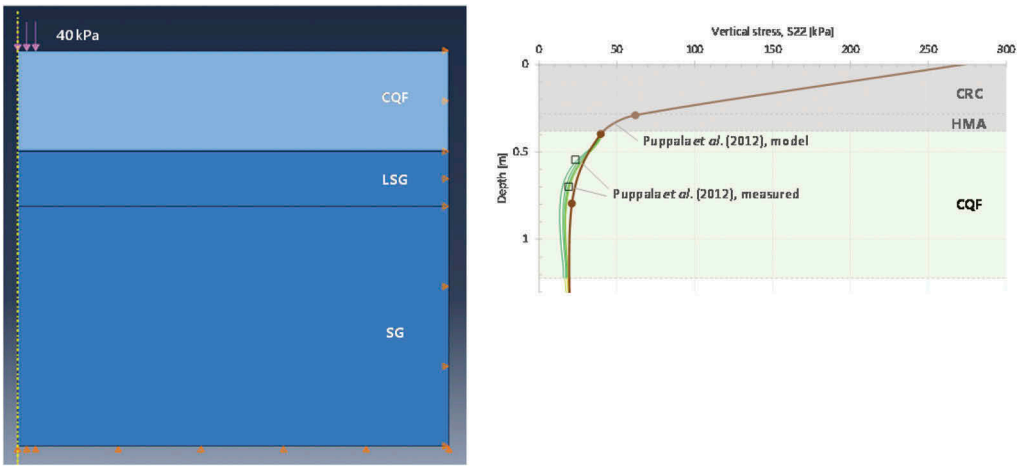

Figure 7. Stress results of the topped-off model. Profile below the load. Bold profile and experimental data points from Puppala et al. (2012).

3 CONCLUDING REMARKS

Quarry fines are by-products of the quarry industry. When unmodified, their mechanical properties may be relatively poor, sometimes even prone to frost susceptibility. To improve these conditions for use as support layers in road infrastructure, the material is stabilized with cement. Much like other granular materials, the mechanical behaviour of cement-stabilized quarry fines (CQF) exhibits stress-dependency.

This paper presents a model to represent a pavement structure with a layer of cement-stabilized quarry fines. The code uses scripting in Python for the construction and iterations of

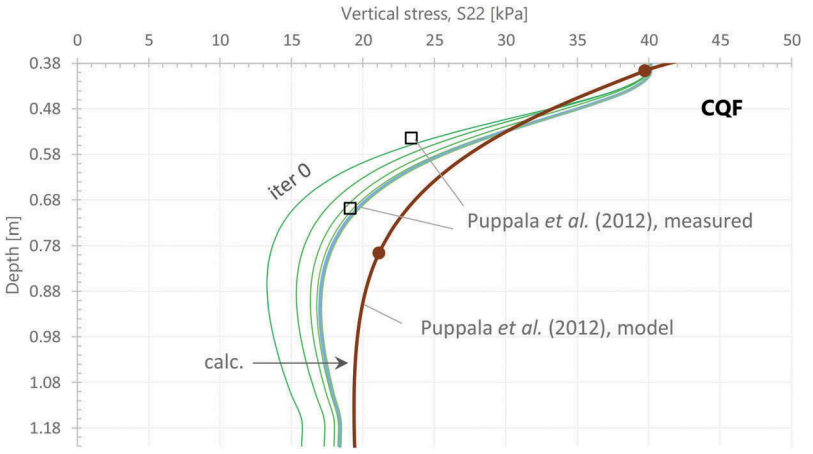

Figure 8. Vertical stress profile inside the CQF layer for the iterations. Topped-off model, profile below the load. Bold profile and experimental data points from Puppala et al. (2012).

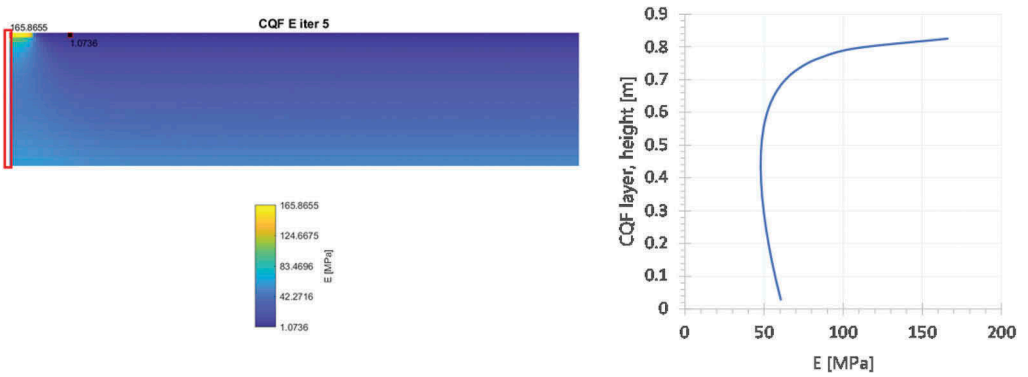

Figure 9. Modulus of the CQF layer. Last iteration, topped-off model. The profile below the load is presented to the right.

the model and commercial software ABAQUS for finite element modelling. The model performs an element-wise iterative calculation to calculate the resilient modulus of CQF layers under traffic loads and the self-weight of the structure. The model is calibrated with experimental data reported in the literature. A validation of the model is attempted based on data reported for a pavement structure with a CQF layer (Puppala et al., 2012). Some issues with this comparison are highlighted, and a set of boundary conditions are proposed that produce a better approximation to experimental results.

The characteristics of cemented quarry fines may be favourable to the structural and functional requirements particular to granular layers of low-volume roads. Although this material still has no applications to roads in Finland, it has an important potential for its application in the Nordic region and Europe. The model as it exists in the code is versatile and can be adapted to a variety of pavement structure geometries, traffic loads, material types and properties for the different layers. Validation and development of the model can continue based on reported and independently measured data in the Aalto University laboratories. Future applications may include the modelling of a random seeding of modulus and other mechanical properties in the CQF layer.

REFERENCES

Araya, A. A. (2011). *Characterization of Unbound Granular Materials for Pavements*. (Ph.D. Thesis), TU Delft, Delft, the Netherlands.

Caicedo, B. (2019). *Geotechnics of Roads: Fundamentals*. Leiden, The Netherlands: CRC Press/Balkema.

Doré, G., & Zubeck, H. K. (2009). *Cold regions pavement engineering*. Reston VA: McGraw-Hill.

Edeh, J. E., Ugama, T., & Okpe, S. A. (2020). The use of cement treated reclaimed asphalt pavement-quarry waste blends as highway material. *International Journal of Pavement Engineering*, *21* (10), 1191–1198.

Haichert, R., Kelln, R., Wandzura, C., Berthelot, C., & Guenther, D. (2012). Cement Stabilization of Conventional Granular Base and Recycled Crushed Portland Cement Concrete. *Transportation Research Record (Journal of the Transportation Research Board)*, *2310*, 121–126.

Kolisoja, P., Kalliainen, A., & Haakana, V. (2015). Effect of Tire Configuration on the Performance of a Low-Volume Road Exposed to Heavy Axle Loads. *Transportation Research Record (Journal of the Transportation Research Board)*, *2474*, 166–173.

Kolisoja, P., Vuorimies, N., Kurki, A., & Saarenketo, T. (2019). *Open structural monitoring data from two extensively instrumented road sections–case Aurora*. Paper presented at the XVII European Conference on Soil Mechanics and Geotechnical Engineering, Reykjavik, Iceland.

Li, S., & Hao, P. (2020). Stress dependent and redistribution behaviour of unbound granular material. *International Journal of Pavement Engineering*, *21*(3), 347–356.

Manandhar, S., Suetsugu, D., Hara, H., & Hayashi, H. (2014). *Performance of waste quarry by-products as a supplementary recycled subgrade material*. Paper presented at the 9th International Symposium on Lowland Technology, Saga, Japan.

Prusinski, J. R., & Bhattacharja, S. (1999). Effectiveness of Portland cement and lime in stabilizing clay soils. *Transportation Research Record*, *1652*(1), 215–227.

Puppala, A. J., Saride, S., & Williammee, R. (2012). Sustainable reuse of limestone quarry fines and RAP in pavement base/subbase layers. *Journal of Materials in Civil Engineering*, *24*(4), 418–429.

Qamhia, I. I. A., Tutumluer, E., Ozer, H., Shoup, H., Beshears, S., & Trepanier, J. (2019). Evaluation of Chemically Stabilized Quarry Byproduct Applications in Base and Subbase Layers through Accelerated Pavement Testing. *Transportation Research Record: Journal of the Transportation Research Board*, *2673*(3), 259–270.

Saevarsdottir, T., & Erlingsson, S. (2015). Modelling of responses and rutting profile of a flexible pavement structure in a heavy vehicle simulator test. *Road Materials and Pavement Design*, *16*(1), 1–18.

Sidess, A., Uzan, J., & Nigem, P. (2021). Fundamental characterisation of the anisotropic resilient behaviour of unbound granular materials. *International Journal of Pavement Engineering*, *22*(3), 283–293.

Xiong, T. (2019). *The use of recycled materials as binders to stabilize soft clay in laboratory*. (M.Sc. Thesis), Aalto University, Espoo, Finland.

Zhang, Y., Korkiala-Tanttu, L., & Borén, M. (2019). Assessment for Sustainable Use of Quarry Fines as Pavement Construction Materials: Part II - Stabilization and Characterization of Quarry Fine Materials. *Materials*, *12*(15), 2450.

Zhang, Y., Korkiala-Tanttu, L., Gustavsson, H., & Miksic, A. (2019). Assessment for Sustainable Use of Quarry Fines as Pavement Construction Materials: Part I - Description of Basic Quarry Fine Properties. *Materials*, *12*(8), 1209.

Eleventh International Conference on the Bearing Capacity of Roads, Railways and Airfields, Volume 2 – Hoff, Mork & Saba (eds)

Modeling of asphalt mixture based on aggregate morphology distribution using the contact dynamics method

Haitao Ge, Juan Carlos Quezada & Cyrille Chazallon
Université de Strasbourg, INSA de Strasbourg, CNRS, ICube, UMR, Strasbourg France

Vincent Le Houerou
Université de Strasbourg, CNRS, ICube, UMR, Strasbourg, France

ABSTRACT: Asphalt mixture performance depends highly on the particle shape. Discrete element method (DEM) has become a highly prevalent approach for testing and reconfiguring particles in asphalt mixtures in recent decades. Nevertheless, most simulation studies simplify particle shapes and ignore irregular morphology features. In this study, morphological characteristics for a large number of particles were analyzed statistically using three-dimensional laser scanning technology. Combining morphology statistics and particle size distribution, numerical samples of asphalt mixtures were generated using Voronoi tessellations. Finally, the model reliability is validated by conducting experiments and simulations for the complex modulus test based on the Contact Dynamics (CD) method. Using this procedure, the aggregate morphology and size distribution can be incorporated in numerical simulations of asphalt mixtures. The modeling method provides a basis for the high-precision simulation of asphalt mixes comprising polyhedral particles, which can be seen as an enriching improvement of the classical procedures.

Keywords: Morphology characterization, Contact dynamics Method, 3D laser scanning, Particle tessellation, Complex modulus

1 INTRODUCTION

Asphalt mixture is an integral component of pavement materials. It includes aggregate particles enclosed by a viscoelastic matrix made up of bitumen, filler, and air. Hence, the mechanical behavior of this multiphase material is highly dependent upon the properties of the interacting components.

In the last few decades, discrete element method (DEM) has proven effective for simulating granular materials at the particle-scale. As the morphology of aggregate particles has an essential influence on the mixture performance (Chen et al., 2013; Souza et al., 2012; Castillo et al., 2018; Zhou et al., 2019; Quezada-Guajardo & Chazallon, 2021), establishing a numerical model closer to real particle assembly is an issue that deserves much attention. Many studies are currently being conducted on the simulation of irregular particles using computer-assisted algorithms (Lu & McDowell, 2007; Ma et al., 2018; Zhou et al., 2018) and image scanning devices (Tutumluer et al., 2012; Liu et al., 2017; Li et al., 2020). Despite this, most studies modeled particles as clumps of spheres, entirely ignoring important particle properties like angularity. As a result, granular fabric properties are more or less impacted, including porosity, contact anisotropy, and force chains (Alonso-Marroquin & Herrmann, 2002; Azéma

DOI: 10.1201/9781003222897-43

et al., 2009). Although high-resolution particle clumps can capture the characteristics of real particles, their enormous computation costs are unaffordable. Moreover, current numerical models only treat the aggregate size distribution explicitly, particle shapes used in the current research are usually created or selected randomly in the simulation and do not consider the aggregate morphology distribution in the real assembly. Selecting limited particle templates is not representative of real samples due to the wide variation of particle shapes in nature. Additionally, preparing numerical samples consisting of polyhedral particles is a very time-consuming process. During the preparation stages, such as gravity deposition, compaction, and stabilization of numerical samples, complex algorithms are required for contact detection and repulsive force computation.

In this study, the morphological characteristics of a significant number of particles were analyzed statistically based on the acquisition of three-dimensional (3D) aggregate shapes from laser scanning. The contact dynamics (CD) method is introduced to simulate irregular particles, and numerical specimens of asphalt mixtures were generated by a tessellation method based on aggregate size distribution and morphology data. Numerical and experimental tests were conducted on the complex modulus to verify model reliability at different temperatures and loading frequencies. The modeling method presented in this study is founded to provide a basis for establishing high-precision asphalt mixture models and optimal pavement design.

2 AGGREGATE SHAPE STATISTICS

2.1 *Statistical distribution of particle aspect ratio*

During this study, aggregate particles with sieving sizes ranging from 4 mm to 31.5 mm were selected from the stockyard. A portable three-dimensional laser scanner (FARO Edge ScanArm HD) was adopted to obtain real geometrical data of the selected 500 aggregates. After scanning and acquiring data from all specimens, the point cloud data obtained by the laser scanner was imported into MATLAB for further processing, as illustrated in Figure 1. Particle dimension characteristics are described by the ratio of their three linear dimensions, length (L), width (I), and thickness (S). Depending on whether a particle resembles a column or a plate, the Elongation ratio (LI) and Flatness ratio (IS) are determined. If the value of LI and IS is closer to 1, the aggregate is nearer to a cube. Otherwise, particles are more elongated or flatted. The minimum bounding box algorithm (Ge et al., 2018) was used to calculate the dimension values of L, I, and S of a particle.

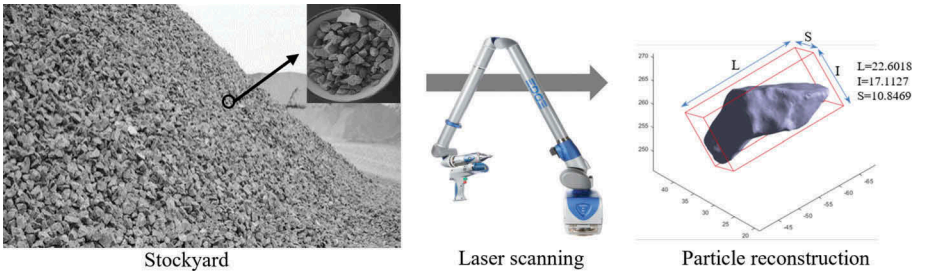

Figure 1. Materials preparation and laser scanning of particles.

Statistical features of LI and IS of all particles were analyzed. Figure 2 and Figure 3 show the Cumulative distribution histogram (CDF) and normal P-P plot of the LI and IS, respectively. The normal P–P plot is used to test if the data follows the normal distribution. As shown in the figures, the LI and IS of aggregate particles both obey the normal distribution.

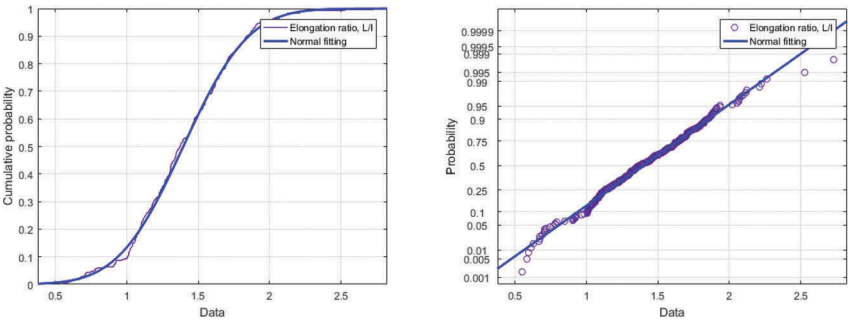

(a) LI-CDF (b) LI-PP

Figure 2. LI statistics.

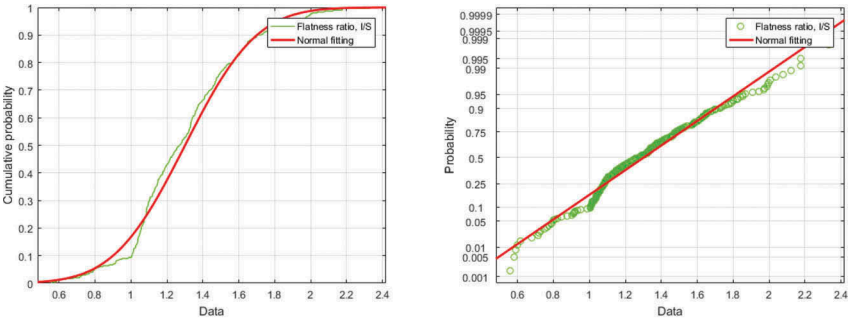

(a) IS-CDF (b) IS-PP

Figure 3. IS statistics.

2.2 *Statistical distribution of particle angularity*

Angularity belongs to mesoscopic shape characteristics. If particles are closer to cubes and their edges are sharper, it will be more favorable to the mixture interlocking. If aggregates are rounded, the overall mixture strength will be significantly reduced, even with better gradation. The Sphericity value ($Sp = \sqrt[3]{36\pi V^2}/A$) was used to characterize the angularity of aggregate particles, here, V and A represent particle volume and surface area, respectively. The closer this value to 1, the more spherical a particle.

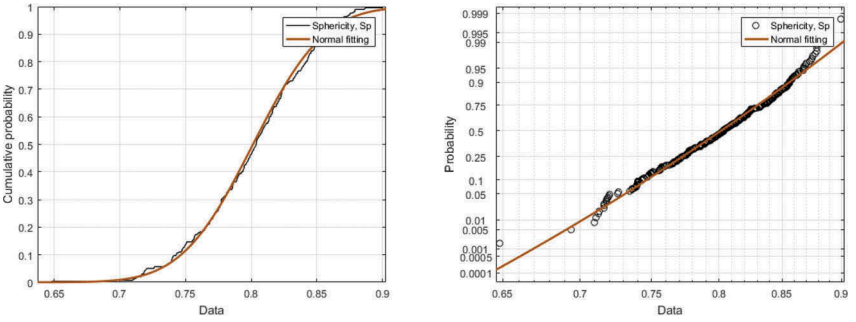

(a) Sphericity-CDF (b) Sphericity-PP

Figure 4. Sphericity statistics.

The statistics of Sp were analyzed using the same method above, as Figure 4 displays. The results show that the Sp obeys the normal distribution approximately. The average aspect ratio (L: I: S) for aggregates is about 1.815: 1.301: 1, the mean and standard deviation of the Sp are 0.8013 and 0.0428 respectively.

3 MODELING PREPARATION

3.1 *Contact dynamics method*

Discrete element method (DEM) is an approach dedicated to analyzing the assembly behavior of interacting particles. In the contact dynamics (CD) method, the contacting laws are non-differential steep laws defining the relation between relative velocities $\mathcal{V}$ and impulses I. A significant advantage of the CD method is that particle dynamics determine the characteristic system time, so a larger time step than that in the explicit DEM method can be used. The CD method was adopted as our simulation strategy for modeling asphalt mixture consisting of polyhedral aggregate particles because of its advantages. The open-source software LMGC90 (https://git-xen.lmgc.univ-montp2.fr/lmgc90/lmgc90_user/-/wikis/home) is adopted in which CD method is completely implemented.

3.2 *Numerical modeling of irregular aggregates*

Asphalt mixture is composited by two main types of material: aggregates and asphalt mastic, where aggregates occupy almost 95% mass in the mix. Consequently, asphalt mixture can be seen as a system of irregular particle tessellations from a geometrical point of view, and particles interact with each other through asphalt mastic between them. Therefore, the open-source software NEPER (Quey et al., 2011; Quey & Renversade, 2018) is adopted to generate particle tessellation samples.

The viscoelastic behavior of an asphalt mixture under cyclic loading can be assessed by the dynamic modulus $|E^*|$ and the phase angle Φ. To identify the mechanical properties of asphalt mixtures, complex modulus tests were conducted in a two-point bending (2PB) configuration according to the EN 12697-26:2012 specifications (EN et al., 2012).

Table 1. Particle size distribution (PSD) of asphalt mixture.

Diameter (mm)	12.5	10	8	6.3	4	2	1	0.5	0.25	0.125	0.063
PSD (%)	100	90	75	58	44	31	20	15	12	9	6.5

Two main parameters need to be input before generating a trapezoidal numerical specimen for the 2PB test. For particle size, aggregate size from the PSD results (Table 1) was inputted to simulate aggregate gradation. For particle morphology, the aspect ratio, sphericity, and distribution of the aggregate shape parameters from the previous statistics were inputted into the NEPER software. In this way, aggregate morphology and aggregate size can be incorporated into numerical simulations of asphalt mixtures.

After the generation, about 5,680 tessellations were created following the experimental gradation cut at 2 mm to reduce the total quantity of elements in the sample, in which finer aggregates are included in the asphalt mastic. Then, the vertices of each tessellation were imported in LMGC90 to build numerical models. In this stage, particles were generated based on the convex hull of vertices from the tessellation. As rigid particles interact with each other through viscoelastic asphalt mastic between them, the particle size is decreased by multiplying a correction factor (Gaillard et al., 2020) to create gaps among particles to model the mastic, Figure 5 displays the snapshot of the numerical sample reconstructed in LMGC90 software.

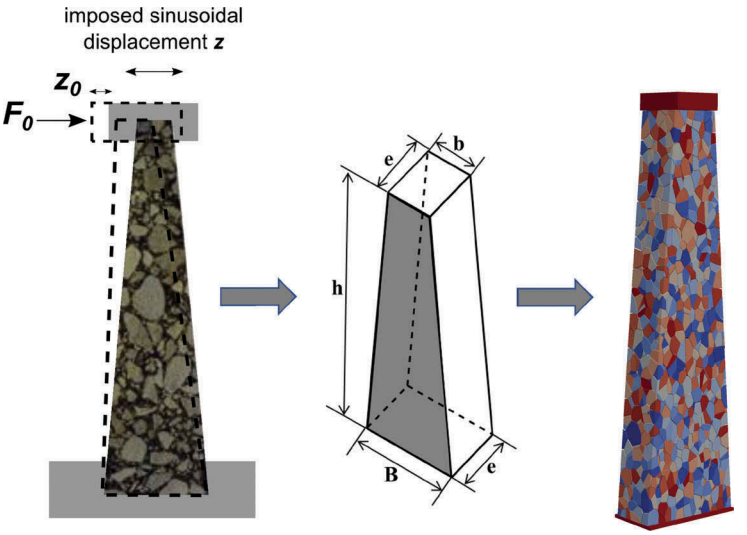

Figure 5. Test set-up and numerical modeling of test sample.

4 NUMERICAL MODELING VALIDATION

4.1 *Calibration of the Burgers model*

Asphalt mixture is a complex composite material showing a viscoelastic behavior, thus a viscoelastic contact model based on the Burgers model is adopted in the simulation. This model comprises a Maxwell model putting in series with a Kelvin-Voigt model (Figure 6), the stiffness and the viscosities for the Maxwell and the Kelvin-Voigt parts correspond to K_m, C_m, K_k, and C_k, respectively. More details about the numerical implementation of this contact model can be found in (Quezada & Chazallon, 2020).

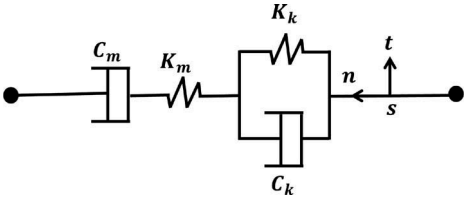

Figure 6. Burgers contact model between particles.

For a viscoelastic material under cyclic loading, it is possible to determine the complex compliance from the resulting strain and stress as following:

$$|D^*| = \sqrt{D'(\omega)^2 + D''(\omega)^2} \tag{1}$$

$$D'(\omega) = \frac{1}{K_m} + \frac{K_k}{{K_k}^2 + \omega^2 {C_k}^2} \tag{2}$$

$$D''(\omega) = \frac{1}{\omega C_m} + \frac{\omega C_k}{{K_k}^2 + \omega^2 {C_k}^2} \tag{3}$$

Where:

• K_m,C_m, K_k and C_k correspond to the Maxwell and Kelvin-Voigt stiffness and viscosities respectively.

• $|D^*|$ is the complex compliance, D' and D'' are the real and the imaginary parts of the complex compliance, and ω is the pulsation.

4.2 *Macro mechanical behavior*

The master curve describing the loading time dependency of asphalt mixtures can be generated according to the time-temperature superposition principle. To build the corresponding master curve, a reference temperature T_{ref} was chosen, then the translation of all isotherm values was performed by calculating the reduced frequency as $f_r = a_T \times f$, where f corresponds to each frequency value in each curve and a_T is the shift factor. These values are obtained from the temperature fit using the Williams-Landel-Ferry (WLF) equation (Eq. 9):

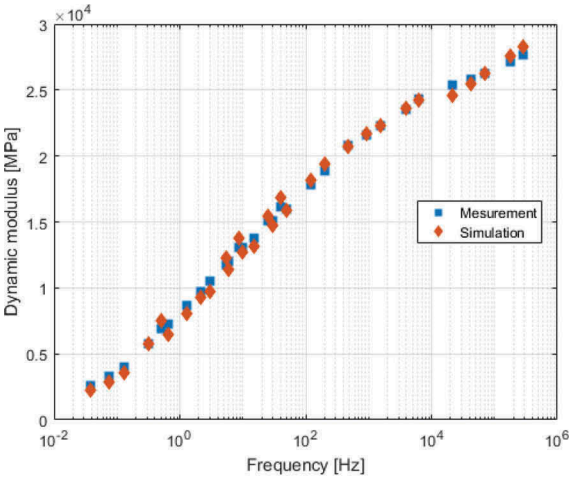

(a) Dynamic modulus

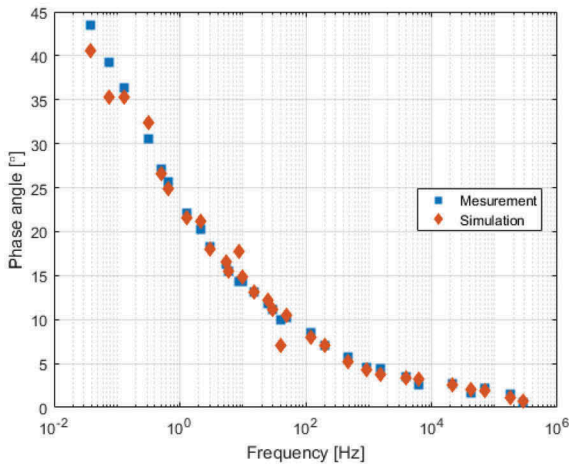

(b) Phase angle

Figure 7. Experimental and numerical master curve at $T_{ref} = 15$ °C.

$$\log a_T = \frac{-C_1(T - T_{ref})}{C_2 + (T - T_{ref})} \tag{4}$$

Where:

• C1 and C2 are 28 and 206.8 $^\circ C$ respectively, and T is the test temperature.

Figure 7 Displays the experimental and numerical results for the master curve at the reference temperature of 15 °C, which is a referenced value in French pavement design (EN et al., 2012).

The numerical values from simulations are in good agreement with experimental values for $|E^*|$ and Φ for all the tested frequencies, despite some fluctuations around the average values. The best fitting parameters for the Burgers contact model are listed in Table 2.

Table 2. Burgers model parameters used in numerical simulations.

T ($^\circ C$)	K_m (Pa)	C_m (Pa.s)	K_k (Pa)	C_k (Pa.s)
-10	1.34×10^8	1.79×10^8	2.55×10^9	3.26×10^7
0	1.18×10^8	6.86×10^7	9.36×10^8	1.03×10^7
10	1.02×10^8	1.93×10^7	2.80×10^8	3.05×10^6
15	9.48×10^7	1.02×10^7	1.70×10^8	1.79×10^6
20	8.64×10^8	4.81×10^6	1.02×10^8	1.05×10^6
30	7.18×10^7	8.84×10^5	3.39×10^7	2.80×10^5

4.3 *Particle movement characteristics*

During the 2PB test, a trapezoidal sample is fixed between two plates, and a sinusoidal displacement is applied to the top of the sample, while the bottom base remains fixed. Empirically, the macroscopic fracture usually occurs at 1/3 sample height from the bottom, as figure 8 (left) shows. To conduct the microanalysis at the particle level, a particle is selected at the critical position (side center of the 1/3 sample height) and its displacement during one loading cycle is recorded and shown in figure 8 (right). As can be seen, the displacement is mainly a result of horizontal particle movement. Besides, similar results have been found for the particle located at the left part of the sample. The peak value of particle displacement magnitude was chosen and its changing trend was further analyzed under different temperatures and frequencies. Figure 9a shows that particle displacement increases with the temperature, and the displacement increases especially dramatically above the temperature exceeds 20 °C.

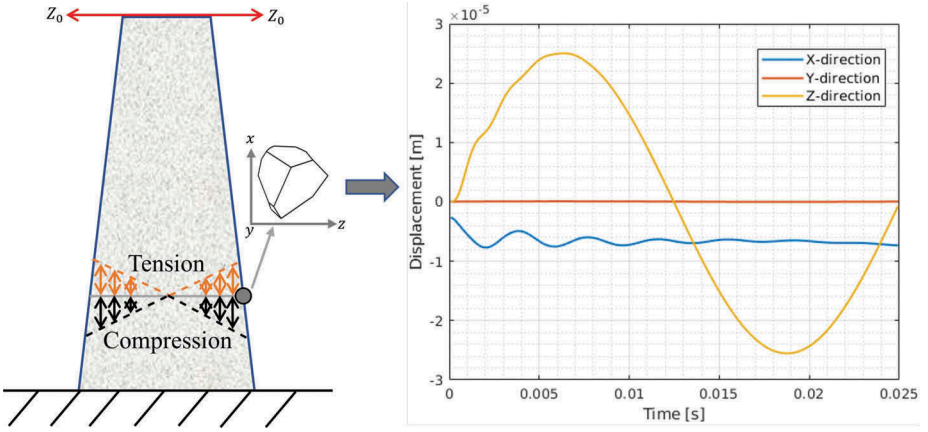

Figure 8. Macro-mechanical behavior and displacement distribution for the particle located at the third height (right) of the sample.

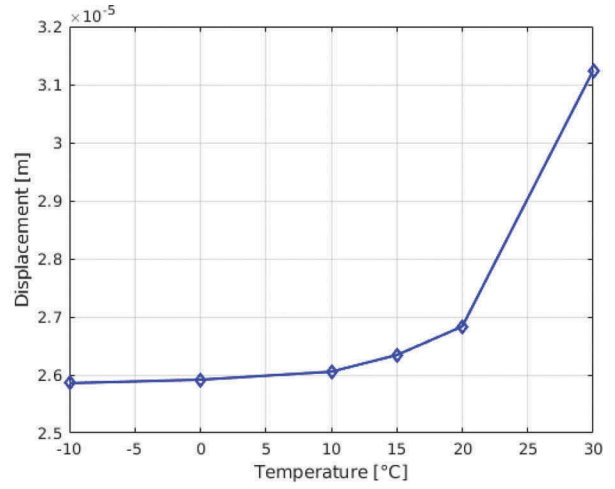

(a)

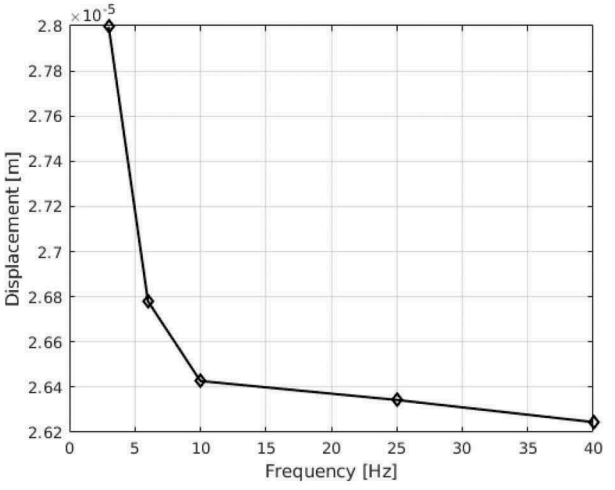

(b)

Figure 9. Maximum particle displacement under different (a) temperatures (b) frequencies.

According to Figure 9b, particle displacement decreases with increasing frequency, and its decrease becomes dramatic as frequency exceeds 3 Hz. The above results indicate that asphalt mixtures are sensitive to temperature and loading frequency due to their viscoelastic nature, especially at low frequencies and high temperatures. Furthermore, it also reveals that a test sample at high temperatures or low loading frequencies tends to produce significant particle movements, which could cause large bending deformations at the macroscopic level. Additionally, the results confirm the frequency–temperature superposition where the large displacement corresponds to high-temperature and low-frequency.

5 CONCLUSION

In this study, laser scanning technique was combined with image processing to statistically analyze the morphology features of aggregates. Aggregate flatness ratio, elongation ratio, and

Sphericity value all obey normal distribution approximately. The obtained statistical parameters were then used as input particle shape parameters in the numerical simulation. The 2PB specimens of asphalt mixtures were created using a tessellation method based on particle morphology statistics and then simulated in the discrete element framework based on the CD theory. With regard to the master curves, these simulations were in good agreement with experimental findings. The modeling method presented in this study incorporates aggregate morphology and size distribution in the numerical simulation, which provides a basis for the high-precision simulation of asphalt mixtures. Additionally, the micro-mechanism of mixture damage can be revealed at the particle level by using the proposed method.

ACKNOWLEDGEMENTS

The work presented in this article was supported by the French institution Agence Nationale de la Recherche (ANR, eng: National Agency for Research) (ANR-Binary project, ref. ANR-19-CE22-0001). The first author gratefully acknowledge financial support from China Scholarship Council (No. 201806560055).

REFERENCES

Alonso-Marroquin, F., & Herrmann, H. J. (2002). Calculation of the incremental stress-strain relation of a polygonal packing . *Phys. Rev. E*, *66*, 021301 . https://link.aps.org/doi/10.1103/PhysRevE.66.021301 . doi: 10.1103/PhysRevE.66.021301.

Azéma, E., Radjai, F., & Saussine, G. (2009). Quasistatic rheology, force transmission and fabric properties of a packing of irregular polyhedral particles . *Mechanics of Materials*, *41*, 729–741.

Castillo, D., Caro, S., Darabi, M., & Masad, E. (2018). Influence of aggregate morphology on the mechanical performance of asphalt mixtures . *Road Materials and Pavement Design*, *19*, 972–991.

Chen, J.-S., Hsieh, W., & Liao, M.-C. (2013). Effect of coarse aggregate shape on engineering properties stone mastic asphalt applied to airport pavements . *International Journal of Pavement Research and Technology*, *6*, 595.

EN, C. et al. (2012). Bituminous mixtures–test methods for hot mix asphalt–part 26: Stiffness.

Gaillard, L., Quezada, J. C., Chazallon, C., & Hornych, P. (2020). Resilient modulus prediction of rap using the contact dynamics method . *Transportation Geotechnics*, *24*, 100371.

Ge, H., Sha, A., Han, Z., & Xiong, X. (2018). Three-dimensional characterization of morphology and abrasion decay laws for coarse aggregates. *Construction and Building Materials*, *188* . doi: 10.1016/j.conbuildmat.2018.08.110.

Li, N., Ma, B., Wang, H., Zhao, J., Wang, H., & Wang, X. (2020). Numerical simulation of dynamic repetitive load test of unbound aggregate using precision unbound material analyzer . *Road Materials and Pavement Design*, *21*, 1675–1693.

Liu, Y., Zhou, X., You, Z., Yao, S., Gong, F., & Wang, H. (2017). Discrete element modeling of realistic particle shapes in stone-based mixtures through MATLAB-based imaging process . *Construction and Building Materials*, *143*, 169–178.

Lu, M., & McDowell, G. R. (2007). The importance of modelling ballast particle shape in the discrete element method . *Granular matter*, *9*, 69.

Ma, T., Zhang, D., Zhang, Y., Wang, S., & Huang, X. (2018). Simulation of wheel tracking test for asphalt mixture using discrete element modelling . *Road Materials and Pavement Design*, *19*, 367–384.

Quey, R., Dawson, P., & Barbe, F. (2011). Large-scale 3d random polycrystals for the finite element method: Generation, meshing and remeshing . *Computer Methods in Applied Mechanics and Engineering*, *200*, 1729–1745.

Quey, R., & Renversade, L. (2018). Optimal polyhedral description of 3d polycrystals: method and application to statistical and synchrotron x-ray diffraction data . *Computer Methods in Applied Mechanics and Engineering*, *330*, 308–333.

Quezada, J. C., & Chazallon, C. (2020). Complex modulus modeling of asphalt concrete mixes using the non-smooth contact dynamics method . *Computers and Geotechnics*, *117*, 103255.

Quezada-Guajardo, J.-C., & Chazallon, C. (2021). Discrete element modeling of hot asphalt mix complex modulus using realistic aggregate shapes . *Road Materials and Pavement Design*.

Souza, L. T., Kim, Y.-R., Souza, F. V., & Castro, L. S. (2012). Experimental testing and finite-element modeling to evaluate the effects of aggregate angularity on bituminous mixture performance . *Journal of Materials in Civil Engineering*, *24*, 249–258.

Tutumluer, E., Huang, H., & Bian, X. (2012). Geogrid-aggregate interlock mechanism investigated through aggregate imaging-based discrete element modeling approach . *International Journal of Geomechanics*, *12*, 391–398.

Zhou, C., Liu, X., Apostolidis, P., Scarpas, A. T., & He, L. (2018). Induction heating-assisted compaction in Porous Asphalt Pavements: A computational study . *Applied sciences*, *8*, 2308.

Zhou, C., Zhang, M., Li, Y., Lu, J., & Chen, J. (2019). Influence of particle shape on aggregate mixture's performance: Dem results . *Road Materials and Pavement Design*, *20*, 399–413.

Eleventh International Conference on the Bearing Capacity of Roads, Railways and Airfields, Volume 2 – Hoff, Mork & Saba (eds)

Characterization of interface between bituminous layers under shear loading cycles using 2T3C apparatus

T. Nhan Tran, S. Mangiafico, C. Sauzéat & H. Di Benedetto
University of Lyon/ ENTPE, LTDS (CNRS), France

ABSTRACT: In most of the design methods for pavement structures, bituminous layers are considered either fully unbonded or perfectly bonded. However, the actual bonding between interfaces is likely to decrease progressively during service life of pavements. As for bituminous mixtures this results from several factors (traffic, climate, aging of materials, etc……). The design of sustainable pavements requires characterization of the behavior of interfaces both in undamaged conditions (Linear Viscoelasticity) and in the fatigue domain. A specially conceived testing apparatus was developed at University of Lyon/ENTPE in order to study the thermomechanical behaviour of interfaces between bituminous layers. The device can apply quasi-homogenous axial and shear (torsion) stresses on hollow cylindrical samples, under cyclic or monotonic loading. In this study, samples composed of two layers of different bituminous materials are tested by applying a sinusoidal torsion load. Digital Image Correlation (DIC) technology is used to obtain the strain field in the sample and to determine locally the relative displacements at the interface. Tests are conducted in strain control, by applying a small number of loading cycles in a wide range of temperatures and frequencies. The combinations of temperature, loading frequency, strain amplitude and number of loading cycles were adapted in order to investigate the behavior of the interface in its undamaged condition.

Keywords: Pavement, interface, shear loading, Linear Viscoelasticity, DIC

1 INTRODUCTION

Pavement is a multi-layer structure consisting of asphalt concrete layers or/and cement concrete ones. Each layer plays its own roles in the pavement including friction, drainage, noise reduction,… for the wearing course and mainly load transfer for the base course. To make sure bituminous layers working all together in a structure, a thin bituminous coat is applied in order to bind two superposed layers. This coat is made of emulsified bitumen. In French design method (NF P98-86 2019), the tack coat is considered either perfectly bonded or fully unbonded which means no matter the quality of the material and construction condition, the coat works at its perfection during the service life. This may be correct for a new pavement at the beginning of its service life for an ideal tack coat application (at an ideal quantity everywhere on a clean surface during good weather conditions). For an older pavement, this is certainly not correct, as the tack coat is expected to degrade gradually during its service life. When two layers are not well bonded, they tend to work independently under traffic and climate solicitations leading to the overbearing capacity of asphalt concrete layers (Petit et al. 2009, Diakhaté et al. 2011). The degradation of tack coat, therefore, reduces the durability of whole pavement structure.

DOI: 10.1201/9781003222897-44

A better knowledge and the characterization of mechanical properties of interface between bituminous layers should be considered as a key issue. Recently, varieties of apparatus have been developed to address this topic, such as direct shear test (Leutner test) and Accroca shear testing research and analysis device (ASTRA) at Politechnic University of Marche (Canestrari et al. 2013; Canestrari, Ferrotti, and Graziani 2016; Graziani et al. 2017), the double shear test and the shear-torque fatigue testing device at University of Limoges (Diakhaté et al. 2011; Ktari et al. 2017; Ragni et al. 2020, 2021), the direct shear test at Technische Universität Braunschweig (Isailović, Falchetto, and Wistuba 2017; Isailović and Wistuba 2018) and other tests (Raab, Partl, and El Halim 2009). These tests can apply monotonic or cyclic shear load on samples in order to study the behaviour of interface under different conditions (different temperatures, and/or with normal loading). However, the shear stress applied in samples by those tests are heterogeneous, which makes the observed behaviour difficult to generalize and does not enable to determine intrinsic thermomechanical properties of the interface.

A new testing device was developed at University of Lyon/ENTPE called 2T3C (abbreviation in French of "Torsion, Traction/Compression sur Cylindre Creux", in English: Torsion, Tension/Compression on Hollow Cylinder) which can apply quasi-homogeneous torsion and tension/compression on hollow cylinder samples of bituminous bilayer (Attia et al. 2017, 2018, 2020, n.d.).

The objective of this study is to use 2T3C to investigate the thermomechanical properties of the interface between two bituminous layers under small amplitude shear loading cycles. Torsional shear load is applied sinusoidally in a wide range of frequencies and temperatures. A system of 4 cameras is used to determine the displacement locally at the interface and in the layers.

2 THE TESTING METHOD FOR 2T3C APPARATUS

2.1 *2T3C apparatus*

The testing system 2T3C (Figure 1) uses a servohydraulic press that can apply maximal sinusoidal/ monotonic load of ±100 kN in the vertical direction and maximal torque of ±2kN.m. For cyclic loading, the maximal frequency at which the press can work is 10 Hz in controlled stress or strain. A climate chamber with the interior dimensions of 600x500x500 mm^3 is used to regulate the temperature within the range of -20°C to 60°C. It was designed with two windows so that cameras could films specimens from outside.

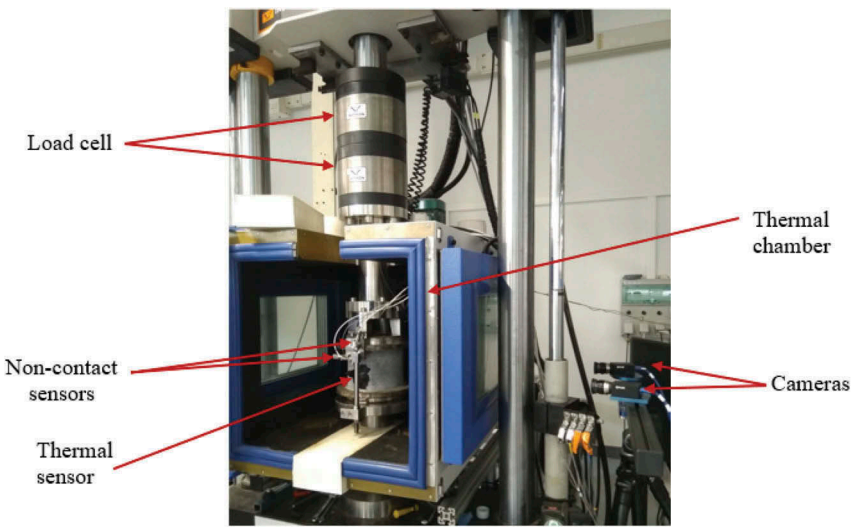

Figure 1. 2T3C apparatus used to study the interface between 2 bituminous layers.

The tested sample for 2T3C apparatus is a hollow cylinder with the internal diameter of 61 mm and the external diameter of 86 mm, as shown in Figure 2. The sample is composed of two bituminous mixture layers, with an interface between them. The total sample height is around 125 mm separated at the middle, so approximate 60 mm height for each layer. By applying torque on a hollow cylinder whose thickness is sufficiently thin, the shear stress can be assumed quasi-homogenous (Sayao and Vaid 1991). The assumption allows having less complicated and more correct experimental analysis.

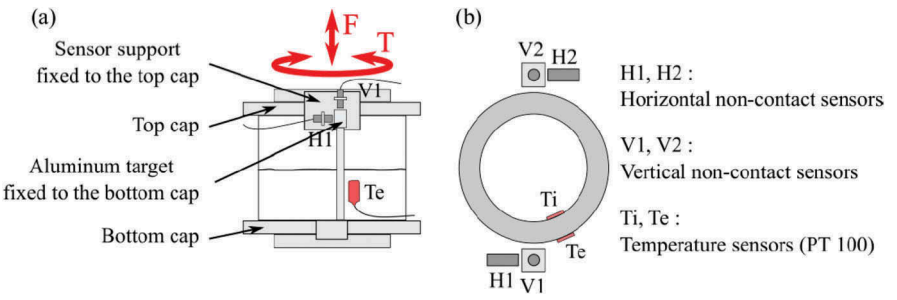

Figure 2. Hollow cylinder sample for 2T3C test and the placement of sensors: (a) front side view and (b) top side view (Attia et al. 2020).

There are two thermal sensors placed in the outer and inner surfaces of the sample to check temperature homogeneity in the sample. Four contactless sensors are attached to the top cap as illustrated in Figure 2, to measure the global displacements of the sample. The metallic targets are fixed to the lower cap. Two of these sensors are used for the axial displacement measurements and the other two are employed for measuring the torsional displacements. Pairs of sensors are placed in the opposite direction, and the data averaged in both sides are used by the press to precisely control the global displacement of the sample. The contactless sensors can measure displacements up to 1000 μm with the accuracy of 0.1 μm.

For each side of the sample, a pair of cameras takes images with the greatest acquisition frequency of 10 Hz. The cameras are placed outside of the thermal chamber, at a distance of 600 mm of the sample surface. They aim at the same area of interest through transparent windows at the two sides of the thermal chamber. Two pictures are taken at a side, to represent the deformation state of the area of interest at an instant time. The first two images are taken and considered as a reference state which will be used to deduce the displacement for following images. Algorithms of 3D Digital Image Correlation (DIC) are employed to construct a 3D image from each pair of images taken by two cameras, and to calculate displacement in deformed states. It is worth mentioning that the surface of interest on sample has to be contrasted. For that reason, a random speckle pattern is applied on the surface as described in the next section. 50 pictures are taken by each camera during a loading cycle, or less if the highest camera speed of 10 Hz is reached (e.g., at the loading frequency of 0.3 Hz, only 33 pictures are taken).

A data acquisition device, connected to camera system is used to acquire the loading information whenever an image is captured. Shear stress is calculated from acquired torque and shear displacement is measured with DIC technology. This information is important for later complex modulus and stiffness calculation, which will be described in the 2.4.

2.2 *Experiment procedure*

The complex shear modulus tests are performed by applying sinusoidal rotation in the small strain domain. Four different temperatures from 10°C to 40°C with the step of 10°C and four frequencies (0.01, 0.03, 0.1 and 0.3 Hz) are chosen for testing the viscoelastic property of

materials and interface. The procedure is shown in Figure 3. Before testing at a temperature, the sample is kept in the isolated chamber at that temperature for at least 4 hours to ensure thermal homogeneity inside the sample. During the test, axial stress is maintained at 0 MPa.

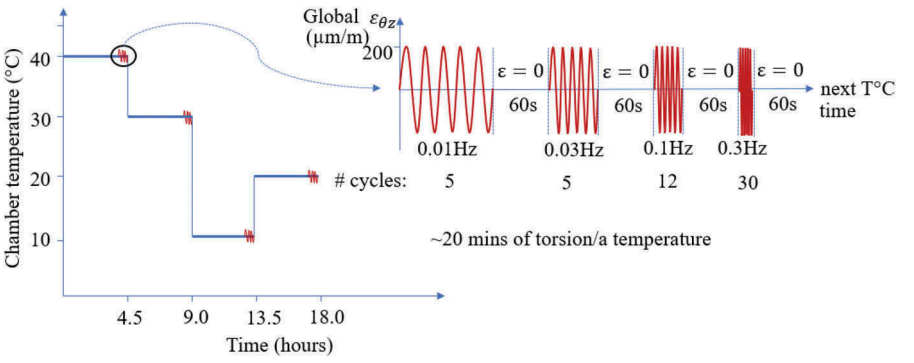

Figure 3. Shear complex modulus test performed with the 2T3C apparatus at 4 temperatures (10 – 40° C) and 4 frequencies (0.01 – 0.3Hz).

The amplitude of sinusoidal rotation cycles was fixed. It corresponds to a shear strain amplitude of 200μm/m on the global specimen (if it was composed of a single material).

2.3 *Image analysis method*

The 3D DIC is made with the software Vic-3D® developed by Correlation Solution for displacement measurements. The displacement of a point in the area of interest is deduced by correlating the subset around that point in the reference state and the deformed state. The area of interest in this study is 100x100mm², and each subset has the dimension of 25x25 pixels². The distance between the centers of 2 subsets is 6 pixels. The cylindrical coordinates system (r, θ, z) is employed to convey the displacements in 3D of points on the outer surface of hollow cylinder. A method has been developed at University of Lyon/ENTPE to calculate strain tensor component $\varepsilon_{\theta\theta}$, ε_{zz} and $\varepsilon_{\theta z}$ in each bituminous layer. In this paper, the method to compute $\varepsilon_{\theta z}$ is illustrated in Figure 4. Horizontal strips are drawn in both layers, and the number of strips chosen for each layer is 12. A strip is 100 mm long and 3 mm high. The displacements u_θ are averaged in

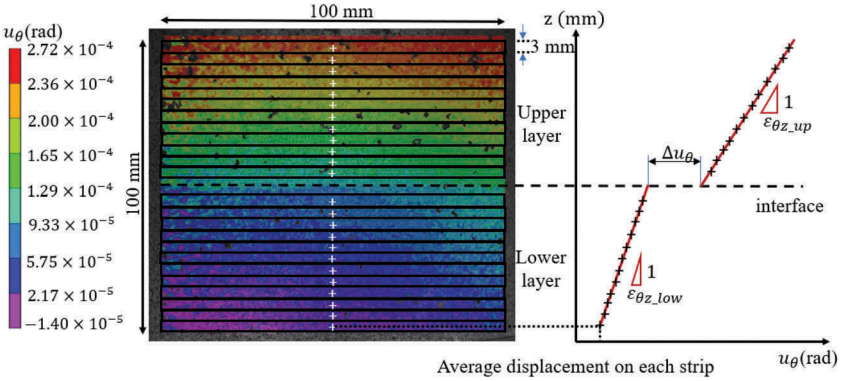

Figure 4. Rotational displacement u_θ obtained by 3D DIC and developed calculation method to measure $\varepsilon_{\theta z}$ strain in the two bituminous layers and the displacement gap Δu_θ at the interface.

strips. These averaged values are plotted against their corresponding coordinate Z at the center of each strip. In the diagram Z-u_θ, two linear regression lines for both layers are calculated. The slopes of these two linear regression lines give $\varepsilon_{\theta z}$ strain in the two layers, and the distance between two lines at the interface gives the shear displacement gap Δu_θ of that interface.

2.4 *Shear complex modulus in layers and shear complex interface stiffness calculations*

As the homogeneity of shear stress field is assumed, the shear stress $\tau_{\theta z}$ can be calculated from the torque (T) obtained from the load cell, the external radius (R_{ext}) and internal radius (R_{int}) of the sample. Equation (1) for shear stress calculation is

$$\tau_{\theta z} = \frac{3T}{2\pi\left(R_{ext}^3 - R_{int}^3\right)} \tag{1}$$

When a small strain amplitude is applied within a small number of loading cycles, bituminous mixture behaves as a linear viscoelastic material. Since the shear strain loading is sinusoidal (Equation 2), the shear stress response is also sinusoidal (Equation 3) with a phase lag (phase angle φ_G) (Figure 5).

$$\varepsilon_{\theta z} = \varepsilon_{\theta z\_0}\sin(\omega t) \tag{2}$$

$$\tau_{\theta z} = \tau_{\theta z\_0}\sin(\omega t + \varphi_G) \tag{3}$$

Where $\varepsilon_{\theta z\_0}$ and $\tau_{\theta z\_0}$ are respectively the applied shear strain amplitude and the responding shear stress amplitude.

Shear complex moduli in layers are calculated as in Equation (4):

$$G_{\theta z}^* = \frac{\tau_{\theta z\_0}}{2\varepsilon_{\theta z\_0}} e^{i\varphi_G} = \left|G_{\theta z}^*\right| e^{i\varphi_G} \tag{4}$$

The displacement gap at the interface appears also to be a sinusoidal signal. Therefore, the complex shear interface stiffness is computed in Equation (5) with Δu_{θ_0} the amplitude of horizontal displacement gap.

$$K_{\theta z}^* = \frac{\tau_{\theta z\_0}}{\Delta u_{\theta\_0}} e^{i\varphi_K} = \left|K_{\theta z}^*\right| e^{i\varphi_K} \tag{5}$$

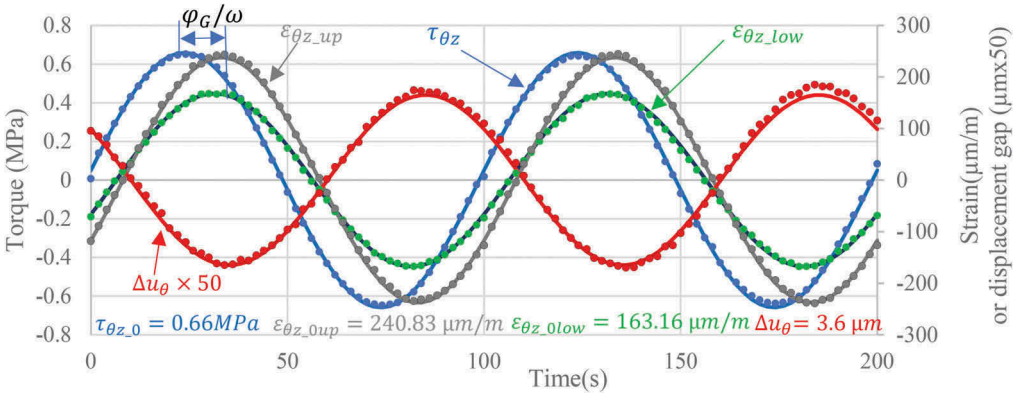

Figure 5. An example of shear stress, strains in the two layers and displacement gap at the interface, measured at 8.5°C and 0.01Hz (continuous lines are approximated from experimental data points using the least squared method).

3 MATERIALS AND SAMPLE PREPARATION

3.1 *Materials*

A double-layer sample comprising two different bituminous mixtures is tested. The upper layer is made of a classical French BBSG3 0/10 mixture (NF EN 13108-1), working as the wearing course in a pavement structure. The lower layer, which represents the base course in that structure, is a French high modulus EME2 0/14 mixture (NF EN 13108-1). The two layers have roughly similar height and are bonded by a tack coat. This tack coat has its bitumen 160/220 modified by latex, and the residual bitumen content is 350 g/m^2.

3.2 *Sample preparation*

The sample used in the test can be prepared in laboratories or cored in situ. The sample analyzed in the present paper was laboratory-fabricated. There are 3 main stages of fabrication of a doubled-layer asphalt slab with an interface: (1) the lower layer is compacted with a French wheel compactor in order to obtained the dimension of 600x400x75 mm^3, then left for cooling down 24 hours; (2) the tack coat is applied on the top of the first layer until emulsion brakes; (3) the upper layer is compacted on top of the lower layer to reach the final height of 150 mm.

The slab is left at least 24 hours before the sample preparation. Firstly, the sample is cored with the smaller drill to have 122 mm of diameter for the inner surface of hollow cylinder. Then, the second core leaves the diameter of 172 mm for the external surface. Both edges of the hollow cylinder are sawed to get smooth parallel surface. The final height is 125 mm.

For the DIC analysis, a speckle pattern is used on the lateral surface of the hollow cylinder as can be seen in Figure 6. The pattern is created by spraying random black dots over a thin white coat painted. The sample is then glued into two caps by using epoxy resin.

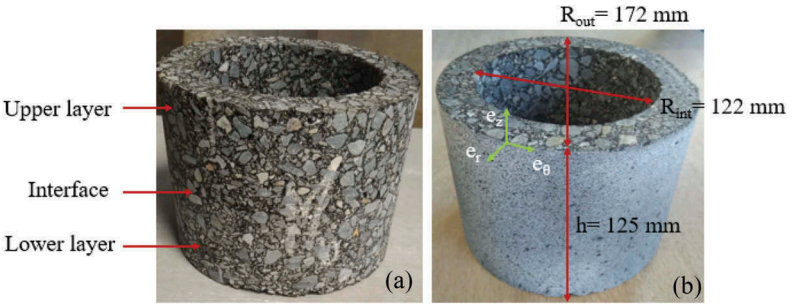

Figure 6. Bi-layered hollow cylinder sample: (a) before the speckle pattern application and (b) after the speckle pattern application.

4 RESULTS AND DISCUSSION

Since different materials are used for upper and lower layers, the strains are distinct in both layers at all testing frequencies and temperatures. The amplitude of shear strain $\varepsilon_{\theta z_0}$varies in the range of 205 to 330 μm/m in upper layer and 110 to 165 μm/m in lower layer. The shear displacement gaps amplitude at the interface Δu_{θ_0} are recorded between 2 to 5 μm. At the same loading condition, the two materials show their different shear complex moduli at all combinations of temperatures and frequencies. Master curves for the norms of shear complex

modulus, shear complex interface stiffness as well as phase angle of complex modulus and phase angle of shear complex interface stiffness are built with the shift factors (a_T) shown in Figure 7. The reference temperature chosen in this paper is 18.8°C.

Names in legends of the following figures are written in the order: (1) Name of the layer – (2) temperature recorded on sample's surface – (3) camera sides from which plotting data is analyzed. Table 1 shows coding method of the legends:

Table 1. Coding method of names in legends used in following figures.

Coding method: (1)-(2)-(3), for example: BBSG-8.5°C-R		
(1) Name of the layer	(2) Temperature	(3) Camera side
BBSG: Upper layer EME: Lower layer Inter: Interface	8.5°C, 18.8°C, 29.0°C, 39.1°C	R: right L: left

The results calculated in both camera systems (left and right) are perfectly superimposed. That proves the accuracy of the camera systems and the measuring as well as calculating method developed at ENTPE/University of Lyon.

Figure 8 shows master curves for the amplitude of shear complex moduli in both layers and shear complex stiffness at the interface. These norms form three unique corresponding master curves for the two layers and the interface. The lower layer has higher norm of complex shear modulus with respect to the lower layer, as expected for such bituminous materials.

By using the shift factors a_T, three master curves for phase angle of complex shear moduli of two layers and complex shear stiffness at the interface are uniquely formed (Figure 9). As we can see, the material in lower layer shows lower phase angle at low temperatures/high frequencies with respect to that in the upper layer.

Unique curves are observed in the Black space (Figure 10) and Cole-Cole space (Figure 11 and Figure 12). Therefore, under a small shear strain amplitude application, as for the bituminous mixtures, the interface shows a linear viscoelastic behaviour and follows the Time-Temperature superposition principle (TTSP) (Di Benedetto, Delaporte, and Sauzéat 2007).

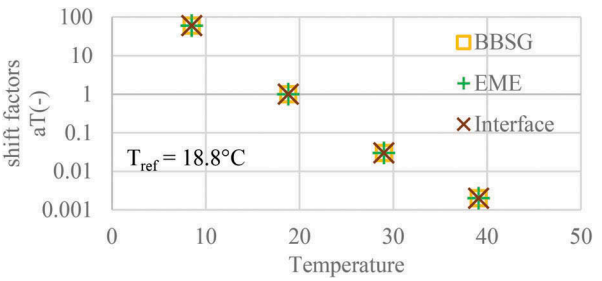

Figure 7. Shift factors a_T used to build master curves of complex shear moduli in two layers, complex shear stiffness at the interface, and phase angles.

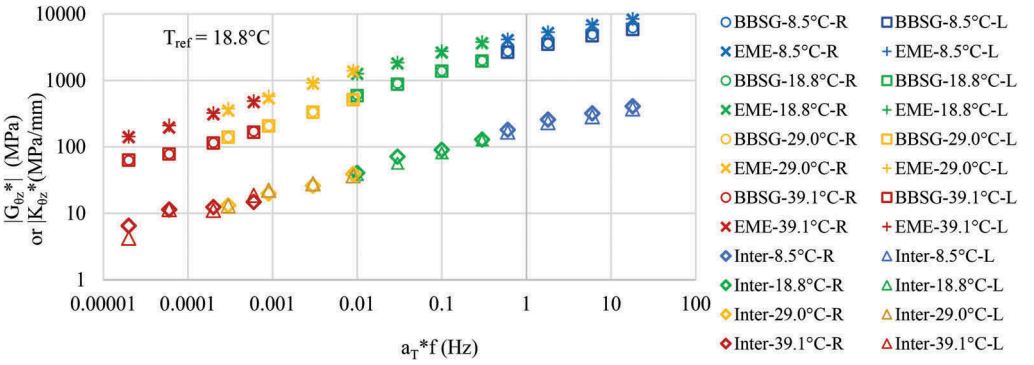

Figure 8. Master curves for norm of complex shear modulus for bituminous mixtures in upper layer, lower layer and shear stiffness at the interface.

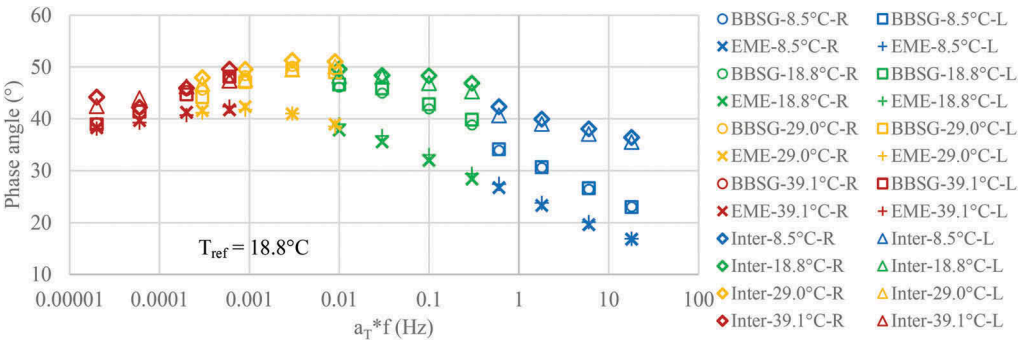

Figure 9. Master curves of phase angle of complex modulus for bituminous material in upper layer, lower layer, and shear stiffness at the interface.

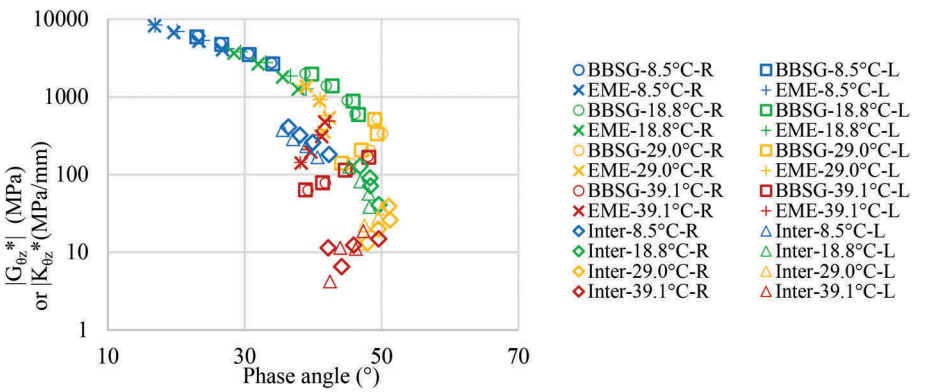

Figure 10. Black space of complex shear modulus for bituminous materials in upper and lower layers, and interface shear stiffness.

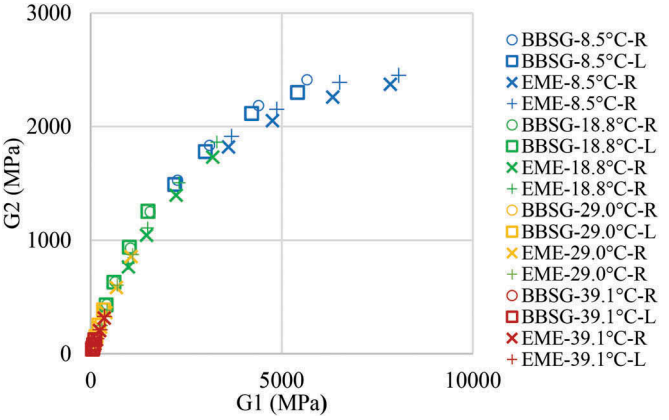

Figure 11. Cole-Cole plane of complex shear modulus for bituminous mixtures in upper layer and lower layer.

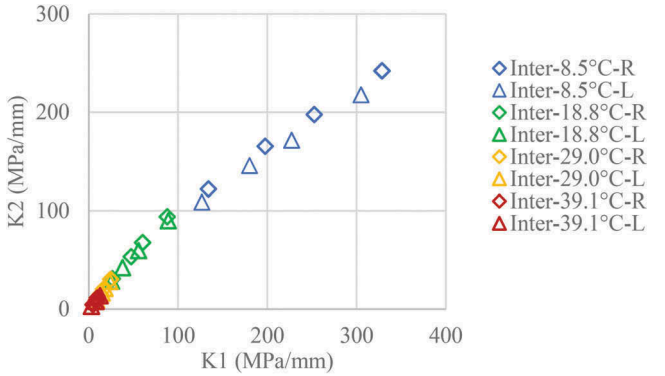

Figure 12. Complex shear interface stiffness in Cole-Cole plane.

5 CONCLUSIONS

2T3C is an outstanding apparatus that can apply sinusoidal tension/compression or torsional loading on a hollow cylinder. The quasi-homogeneity of axial and torsional loading applied on a sample allows straightforwardly characterizing the thermomechanical properties of an interface as well as bituminous mixtures. In this paper, we have shown the capacity of the apparatus in shear loading mode. The tests were performed at four temperatures (10°C, 20°C, 30°C and 40°C) and four frequencies (0.01 Hz, 0.03Hz, 0.1Hz, 0.3Hz). Some conclusions are withdrawn:

- Cameras system and DIC technology allows measuring the displacement at the interface in few micrometers (in this study is 2-5 µm). The method developed at ENTPE was used to calculate precisely strains in bi-layered sample. Results obtained from both side of the specimen by the two pairs of cameras are superimposed for all testing temperatures and frequencies.
- TTSP is validated for both mixtures composing the layers and also for the interface. The bituminous mixtures and the interface show viscoelastic behaviour when small shear strain or displacement gap are applied.
- The lower layer considered as the base course is stiffer compared to the upper layer (wearing course). This is compatible with the materials in these layers, and designing methods.

The future work will aim assessing the fatigue behaviour of the interface between two asphalt layers with the innovative presented apparatus and the analysis method developed at University of Lyon/ENTPE.

REFERENCES

Attia, T., H. Di Benedetto, C. Sauzéat, F. Olard and S. Pouget. 2017. *Hollow Cylinder Apparatus to Characterize Interfaces between Pavement Layers*. International Conference on Advances in Construction Materials and Systems Proceedings (1): vol. 4, 401–410.

Attia, T., H. Di Benedetto, C. Sauzéat, and S. Pouget. 2020. *2T3C HCA, a New Hollow Cylinder Device Using Digital Image Correlation to Measure Properties of Interfaces between Asphalt Layers*. Construction and Building Materials 247: 118499.

Attia, T., Hervé Di Benedetto, Cédric Sauzéat, and Simon Pouget. 2018. *Experimental Investigation of the Mechanical Behaviour of Interfaces Between Pavement Layers*. Proceedings of GeoShanghai 2018 International Conference: Transportation Geotechnics and Pavement Engineering 1: 344–52.

Attia, T, H Di Benedetto, C Sauzéat, and S Pouget. 2021. *Behaviour of an Interface between Pavement Layers Obtained Using Digital Image Correlation*. Materials and structures: 1–14.

Canestrari, Francesco et al. 2013. 9 RILEM State-of-the-Art Reports Mechanical Testing of Interlayer Bonding in Asphalt Pavements.

Canestrari, Francesco, Gilda Ferrotti, and Andrea Graziani. 2016. *Shear Failure Characterization of Time–Temperature Sensitive Interfaces*. Mechanics of Time-Dependent Materials 20(3): 405–19.

Di Benedetto, Hervé, Brice Delaporte, and Cédric Sauzéat. 2007. *Three-Dimensional Linear Behavior of Bituminous Materials: Experiments and Modeling*. International Journal of Geomechanics 7(2): 149–57.

Diakhaté, M. et al. 2011. *Experimental Investigation of Tack Coat Fatigue Performance: Towards an Improved Lifetime Assessment of Pavement Structure Interfaces. Construction and Building Materials* 25(2): 1123–33.

Graziani, Andrea, Francesco Canestrari, Fabrizio Cardone, and Gilda Ferrotti. 2017. *Time–Temperature Superposition Principle for Interlayer Shear Strength of Bituminous Pavements*. Road Materials and Pavement Design 18 (March): 12–25.

Isailović, Ivan, Augusto Cannone Falchetto, and Michael Wistuba. 2017. *Fatigue Investigation on Asphalt Mixture Layers' Interface*. Road Materials and Pavement Design 18: 514–34.

Isailović, Ivan, and Michael P. Wistuba. 2018. *Asphalt Mixture Layers' Interface Bonding Properties under Monotonic and Cyclic Loading*. Construction and Building Materials 168: 590–97.

Ktari, Rahma, Fazia Fouchal, Anne Millien, and Christophe Petit. 2017. *Surface Roughness: A Key Parameter in Pavement Interface Design*. European Journal of Environmental and Civil Engineering 21 (March): s27–42.

Petit, Christophe et al. 2009. *Pavement Design for Curved Road Sections: Fatigue Performance of Interfaces and Longitudinal Top-down Cracking in Multilayered Pavements*. Road Materials and Pavement Design 10(3): 609–24.

Raab, Christiane, Manfred Norbert Partl, and Abd El Halim Omar Abd El Halim. 2009. *Evaluation of Interlayer Shear Bond Devices for Asphalt Pavements*. Baltic Journal of Road and Bridge Engineering 4(4): 186–95.

Ragni, Davide, Gilda Ferrotti, Christophe Petit, and Francesco Canestrari. 2020. *Analysis of Shear-Torque Fatigue Test for Bituminous Pavement Interlayers*. Construction and Building Materials 254: 119309.

Ragni, Davide, Nithin Sudarsanan, Francesco Canestrari, and Y. Richard Kim. 2021. *Investigation into Fatigue Life of Interface Bond between Asphalt Concrete Layers*. International Journal of Pavement Engineering 0(0): 1–15.

Sayao, A., and Y. P. Vaid. 1991. *Critical Assessment of Stress Nonuniformities in Hollow Cylinder Test Specimens*. Soils and Foundations 31(1): 60–72.

NF P98-086. 2019. Road pavement structural design - Application to new pavement. AFNOR

NF EN 13108-1. 2007. Bituminous mixtures - Material specifications - Part 1: asphalt concrete. AFNOR

Eleventh International Conference on the Bearing Capacity of Roads, Railways and Airfields, Volume 2 – Hoff, Mork & Saba (eds)

Manufacture of asphalt concrete virtually by physics engine and algorithm generation

L. Wan & A. Garcia-Hernandez
Nottingham Transportation Engineering Centre, Department of Civil Engineering, University of Nottingham, Nottingham, UK

ABSTRACT: Precise and fast simulations of asphalt concrete are essential to obtain asphalt's properties quickly and precisely, instead of doing several laboratory experiments. This kind of simulation is what we propose in this paper. The first step to achieve this method is to create realistic virtual aggregates. Using procedural generation algorithms, we generated virtual aggregates with convexities and concavities, using original aggregate morphologies as inputs. After inputting the gradations of asphalt concretes, hundreds of virtual aggregates were generated and compacted in a physics engine to create realistic asphalt concrete skeletons. We found that the most influential factors influencing asphalt concrete compaction are the number of aggregate particles and volume of mastic (aggregates smaller than 2mm, bitumen and filler). An equation was deduced based on the Weibull distribution function, which used the volume of mastic and the number of aggregates as inputs. This Equation was used to control the compaction level of aggregates in the physics engine.

Keywords: Virtual asphalt concrete, physics engine, air voids contents, skeleton

1 INTRODUCTION

Asphalt concrete is the most commonly used material to build roads. Aggregate and bitumen are two main components. As the primary bearing structure in asphalt concrete, aggregates form the solid skeleton to provide stability. Moreover, the properties of aggregates play an important role in the skid resistance of roads (Bessa et al. 2015), surface stresses and permanent deformations (Pan et al. 2006). Usually, three shape properties of aggregates are considered, form, texture and angularity (Barrett, 1980). Feret diameter, aspect ratio, area, perimeter and chord length can also describe the shape of aggregates. Bitumen coheres and fill gaps in the solid skeleton. Also, its viscosity partly determines the compactability of asphalt concrete (Stimilli er al. 2017).

Since asphalt is a heterogeneous material, it is difficult to control its variability and distinguish it from experimental errors. In addition, manufacturing and testing asphalt are time-consuming activities. Therefore, computational simulations, specifically the Discrete Element Method (DEM), have been tested to design asphalt. Cundall et al. used DEM to simulate aggregates in asphalt concrete (Cundall and Strack 1979). Khattak et al. also simulated asphalt binder using DEM (Khattak and Roussel 2009). Chen et al. used DEM to analyse characteristics of asphalt concrete skeletons (Chen et al. 2015). DEM uses very small time steps to complete the simulations, making them last very long, which prevents the asphalt industry from using DEM in their everyday activities.

DOI: 10.1201/9781003222897-45

The impulse-based Discrete Element Method (iDEM) is commonly used in computer games because of its ability to create real-time simulations, however, at the cost of lower precision. It can also be used to simulate granular materials. For example, Pytlos et al. researched the compaction of polygonal particles (Pytlos et al. 2015). Unlike DEM, impulse-based physics engines do not allow the penetration between objects (Mirtich, 1996). However, penetration can be difficult to avoid, especially when particles are moving at high speed (Hahn, 1988), and sometimes simulations may not be strictly forbidden to improve computational times (Guendelman et al. 2003). In iDEM when the particles come very close to each other, an impulse is generated that separates them and, if the particles are penetrated, the impulse losses precision. Penetration is impossible to avoid if particles of different sizes, such as those in an asphalt gradation, are simulated; however, inaccuracies can be corrected by combining iDEM simulations with experimental results, as shown in Garcia et al., 2021.

In order to produce precise simulations of asphalts, the geometries of aggregates must also be measured. This can be done by using imaging techniques, which capture the projection of aggregates to measure their shapes (Czajkowska et al. 2015). After, virtual geometries with shapes equivalent to rocks must be created (Garcia et al. 2020, Garcia et al. 2021). Then, the rocks need to be compacted; see Garcia et al. 2021 and the results compared to experiments, such as values from X-Ray Computed Tomography Scans (Yin et al. 2015, Yang et al. 2016).

This paper depicts a method to create asphalt concrete simulations using iDEM, implemented in a physics engine. In this paper, we measure the shape properties of aggregates experimentally, create virtual particles computationally and compact them to form solid virtual skeletons. Moreover, we prove that we can use this method to predict the air voids contents of asphalts.

2 METHODOLOGY

2.1 *Measurement and creation of aggregates*

The shape parameters of aggregates were measured using a Camsizer machine (from Retsch), including Maximum Feret diameter (Max Feret), Minimum Feret diameter (Min Feret), Aspect Ratio (AR), Area (A), and Perimeter (P) of aggregate's projection. The diameter of one circle (x_{area}) which has the same area of that measured aggregate was also introduced to help describe aggregate's height (H_v). More details can be found in Garcia et al. 2020.

After acquiring these parameters, we used Weibull distribution functions to depict Min Feret and AR. To start creating virtual aggregates, we start with a prism with Min Feret and AR equivalent to these of the aggregates, and the height (H_v). Then, the prisms are deformed until their perimeter and area match those measured experimentally. The creation process is described clearly in (Garcia et al. 2020). Figure 1 shows an example of virtual granite aggregates with a size of 14 mm.

2.2 *Materials and manufacture of asphalt concrete*

Aggregates in our research are granite, with sizes ranging from dust (0-4 mm) to 20 mm, named from G1 to G5, and Limestone from dust (0-4mm) to 20mm, named L1 to L5. All aggregates' properties are listed in Table 1, where WSc Min Feret means the scale factor of the Weibull distribution of Min Feret, WSh Min Feret means the shape factor of Min Feret, A_{50} means the median area, % mass < 2 mm means the mass percentage smaller than 2 mm. In our simulation, we only considered aggregates with size (Min Feret) bigger than and equal to 2 mm, which means aggregates smaller than 2 mm are regarded as mastic. We do this to reduce the computing times.

Besides, we used bitumen with penetration 40/50, limestone filler and cellulose fibers. The density of bitumen is 1.040 g/cm^3, fiber's density is 1.500 g/cm^3.

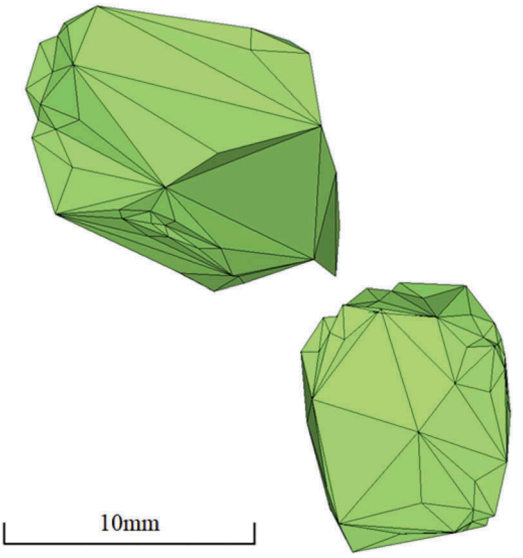

Figure 1. Virtual Granite aggregates in 14 mm.

Twelve asphalt mixtures were manufactured in the laboratory, following the British Standards (British Standards Institution, 2016, British Standards Institution, 2018). All gradations, compaction temperatures and air voids contents are shown in Table 2. Air voids contents were measured based on (British Standards Institution, 2018). More details are shown in (Garcia et al. 2021).

Table 1. Shape parameters of aggregates. Table extracted from (Garcia et al. 2020, and Garcia et al. 2021).

Type of rock	Code	WSc Min Feret (mm)	WSh Min Feret (mm)	WSc *AR*	WSh *AR*	A_{50} (cm^2)	P_{50} (cm)	H_v	% mass < 2 mm	Density (g/cm^3)
Granite, Dust	G1	3.47	4.06	0.87	18.46	0.08	1.09	0.87	81.88	2.70
Granite, 6mm	G2	4.87	3.13	0.66	4.21	0.22	1.79	0.86	3.58	2.70
Granite, 10mm	G3	6.88	2.66	0.66	3.92	0.42	2.49	0.80	1.46	2.70
Granite, 14mm	G4	11.45	4.03	0.68	3.87	1.25	4.24	0.78	1.42	2.70
Granite, 20mm	G5	12.02	4.35	0.61	4.73	1.55	4.71	0.94	0.78	2.70
Limestone, Dust	L1	2.92	6.43	0.75	5.97	0.08	1.05	0.67	82.61	2.70
Limestone, 6mm	L2	5.43	3.84	0.70	4.56	0.27	1.97	0.91	3.48	2.70
Limestone, 10mm	L3	7.53	3.34	0.70	4.69	0.52	2.69	0.88	2.38	2.70
Limestone, 14mm	L4	10.85	4.99	0.70	5.53	1.12	4.00	0.76	0.49	2.70
Limestone, 20mm	L5	13.31	3.88	0.74	5.93	1.61	4.69	0.84	1.10	2.70

Table 2. Gradations of asphalt concrete.

Mixture number	Type of aggregates, L: Lime-stone, G: Granite	20 mm (%)	14 mm (%)	10 mm (%)	6 mm (%)	Dust (%)	Filler (%)	Bitumen (%)	Fiber (%)	Compaction temperature (°C)	Air voids content (%)
1	G	0.00	0.00	55.00	22.00	15.00	8.00	6.60	0.30	145-155	9.56
2	G	0.00	0.00	67.00	20.00	8.00	5.00	5.50	0.00	145-155	19.19
3	G	0.00	0.00	61.00	15.00	20.00	4.00	5.70	0.00	145-155	13.44
4	G	0.00	0.00	63.00	8.00	20.00	9.00	6.50	0.00	150-160	5.56
5	L	20.00	20.00	15.00	15.00	30.00	0.00	6.00	0.00	145-155	6.81
6	L	0.00	0.00	75.00	7.00	18.00	0.00	4.00	0.00	145-155	17.49
7	L	0.00	0.00	0.00	70.00	30.00	0.00	6.00	0.00	145-155	13.24
8	L	0.00	0.00	0.00	68.60	29.40	2.00	6.00	0.00	145-155	11.70
9	L	0.00	0.00	0.00	67.20	28.80	4.00	7.00	0.00	145-155	7.12
10	G	0.00	0.00	66.40	7.00	17.70	8.90	6.50	0.30	150-160	7.62
11	G	0.00	0.00	57.70	14.80	23.60	3.90	5.50	0.00	145-155	16.49
12	G	0.00	0.00	54.50	16.20	21.50	7.80	6.60	0.30	145-155	7.43

2.3 *Virtual compaction of asphalt concrete*

All virtual aggregates were generated in a cylinder with a diameter of 65 mm and a height of 500 mm, as shown in Figure 2. Two pistons with the same diameter compacted the virtual aggregates. We used 250 g of virtual materials to reduce computational costs.

The virtual compaction process of virtual asphalt was divided in two phases. In Phase I, virtual aggregates were generated. Then, the pistons compacted the aggregates until the air voids content (defined as the total volume between the cylinders, minus the volume of aggregates and mastic) was 50 %. In Phase II, ramps of Virtual Force (*VF*) were applied on the pistons, starting from 0 N, at 0.12 N/s increments. Additional details can be found in (Garcia et al. 2020, Garcia et al. 2021).

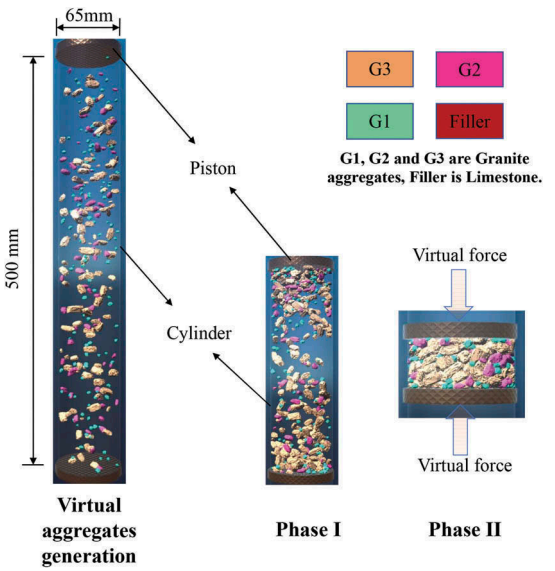

Figure 2. Virtual compaction process.

2.4 *iDEM properties, particle's collision, and penetration*

The timestep that we chose was 0.007 seconds. The smallest distance between particles to consider they had collided was 0.01 micron. If the distance between particles was smaller than 0.01 micron, an impulse separated the particles.

The timestep was chosen by trial and error; however, this was high enough for particles to penetrate each other within one timestep, which may cause instabilities of the simulations.

2.5 *Predictive model of VF*

In (Garcia et al. 2021), we used a Weibull Equation to deduce an equation that predicts virtual force as a function of the number of aggregates (NA) and the volume of mastic (M). See Equation (1):

$$VF = \frac{A \times NA + Q \times M + P}{NA + Q \times M + C} \tag{1}$$

Where A, Q, P and C are all constants.

2.6 *X-ray CT scans*

Samples 1 and 6 from Table 2, were scanned using X-ray Computer Tomography. The scanner properties are described in (Garcia et al. 2021). ImageJ was used to process CT images and obtain the air voids content and distribution.

3 RESULTS AND DISCUSSION

3.1 *Penetrations between aggregates*

Due to the high time step (0.007 s) in our simulation, penetration between aggregates may occur, as shown in Figure 3 (a). We also measured the average penetration values in the last

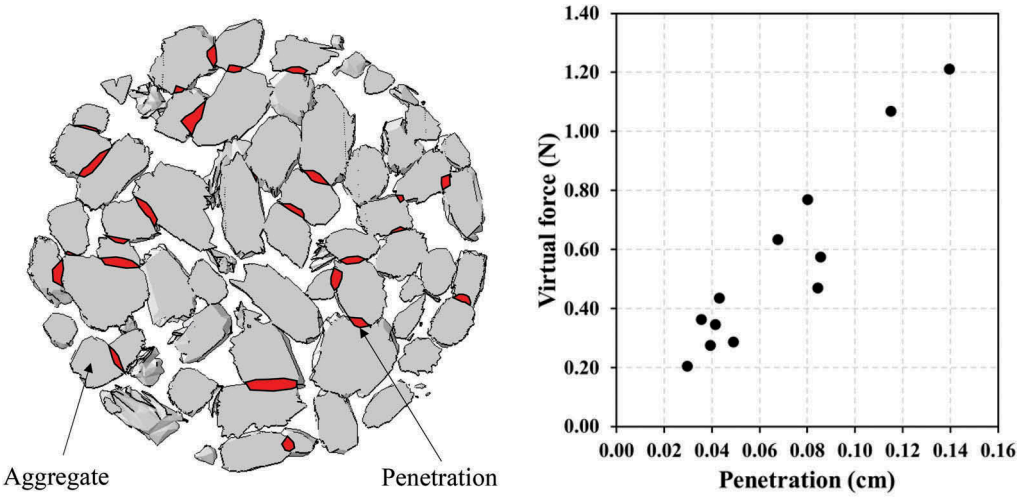

(c) (b)

Figure 3. (a) Aggregates penetrations in virtual skeletons of Sample 2. (b) Penetration versus virtual compaction force.

five time steps between aggregates (see Table 3) for each asphalt concrete in Table 2, and found that the higher the penetration, the higher the virtual force (VF), please see Figure 3 (b). Asphalt concretes with different gradations will have different penetrations because of different aggregate numbers and mastic's volume. Therefore, VF is related to the penetration and the number of aggregates (NA) and volume of mastic (M).

3.2 *Virtual compaction force*

Table 3 shows the number of aggregates and mastic volume obtained from simulating the 12 asphalt concretes. This Table also shows the virtual force required to compact the aggregates to the air voids content measured experimentally. Based on these data, we got the fitting parameters for Equation (1), as seen in Equation (2). Figure 4 (a) shows this relationship:

$$VF = \frac{0.23 \times NA - 3.58 \times M + 50.36}{NA - 0.13 \times M - 413.50} \tag{2}$$

The virtual force decreases with the increase of the number of aggregates and volume of mastic. The penetration is higher when aggregates are big; in other words, the number of aggregates is small. Also, when we fix the type or size of aggregates, the higher the mastic's volume, the lower the aggregate's number, which means that the total penetration is reduced and the virtual force is also small.

Figure 4(b) shows the required virtual force from the simulation versus the predicted virtual force from Equation (2). The R-square is 0.92, Sum of Squares of Error (SSE) is 0.0861 and Root Mean Square Error (RMSE) is 0.0847, which means Equation (2) is well fitted. However, there are only twelve asphalt concrete. So, the accuracy of predictions may change when we consider additional types of asphalt.

Table 3. Data from the simulation.

Number	Number of aggregates	Volume of mastic (cm^3)	VF from the software (N)	Predicted VF (N)	Penetration (cm)	Predicted air voids content (%)
1	505	35.24	0.5744	0.4914	0.0856	22.3992
2	501	24.81	1.0684	0.9387	0.1152	22.3948
3	516	32.74	0.4696	0.5521	0.0844	22.4001
4	445	38.64	0.6329	0.6210	0.0677	22.4055
5	471	37.08	0.3458	0.5340	0.0417	22.4122
6	475	24.64	1.2107	1.2624	0.1397	22.3908
7	719	38.17	0.2753	0.2744	0.0395	22.4104
8	732	39.44	0.2871	0.2584	0.0491	22.4075
9	685	42.83	0.2047	0.2174	0.0298	22.4127
10	446	37.68	0.7681	0.7284	0.0803	22.4029
11	545	34.74	0.3623	0.4244	0.0357	22.4129
12	494	39.47	0.4359	0.3314	0.0432	22.4099

3.3 *Predicted air voids contents*

Air voids contents for each asphalt concrete is also predicted. Results are shown in Figure 5. Here the air voids contents in real are them measured in the laboratory. The prediction of air voids contents also has a high R-square (0.90) with the 45-degree line.

3.4 *Air voids distribution*

Figure 6 (a) and (b) depict the virtual skeletons of Sample 1 and Sample 4 in Table 2, with air voids contents of 9.56 % and 5.56 %, respectively.

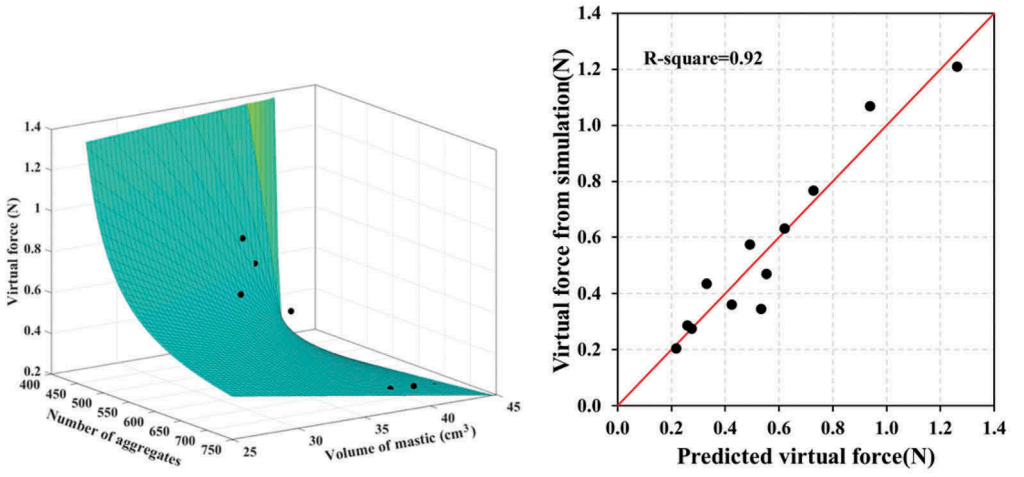

Figure 4. (a) Relationship of *VF* with *NA* and *M*. (b) Virtual force from simulation versus prediction.

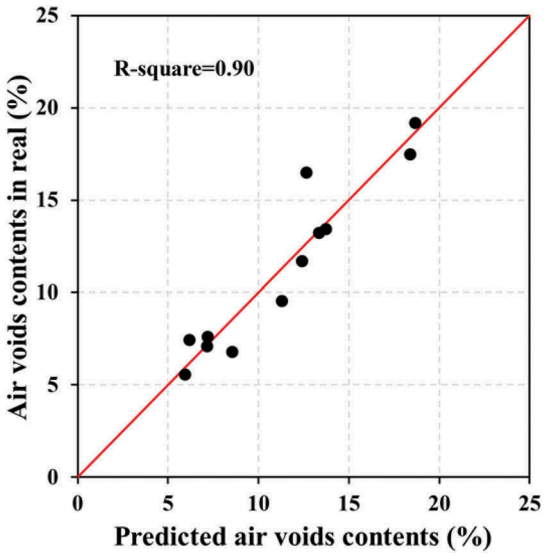

Figure 5. Air voids contents in real versus predicted air voids contents.

Since the simulations cannot show mastic by now, we only compared Voids in Mineral Aggregate (VMA) from CT images and the simulation shown in Figure 6 (a) and (d). VMA of Sample 1 and Sample 4 in real obtained from X-ray CT images analysis are 46.69 % and 44.62 %, respectively. And, the VMA values of Sample 1 and 4 obtained from virtual skeletons analysis from our simulation are 43.47 % and 42.93 %, which have 93.12 % and 96.21 % reliability, respectively.

However, the wavelength of VMA in real and virtual do not fit well on each slice. We believe that this may result from the different sample sizes. For Marshall core in the laboratory, its

diameter is 102 mm, and height is 65 mm. But its diameter is 65 mm for the virtual skeletons, and its height is only around 33 mm. In the future, we may change the cylinder's diameter and simulated mass. Moreover, mastic also needs to be painted.

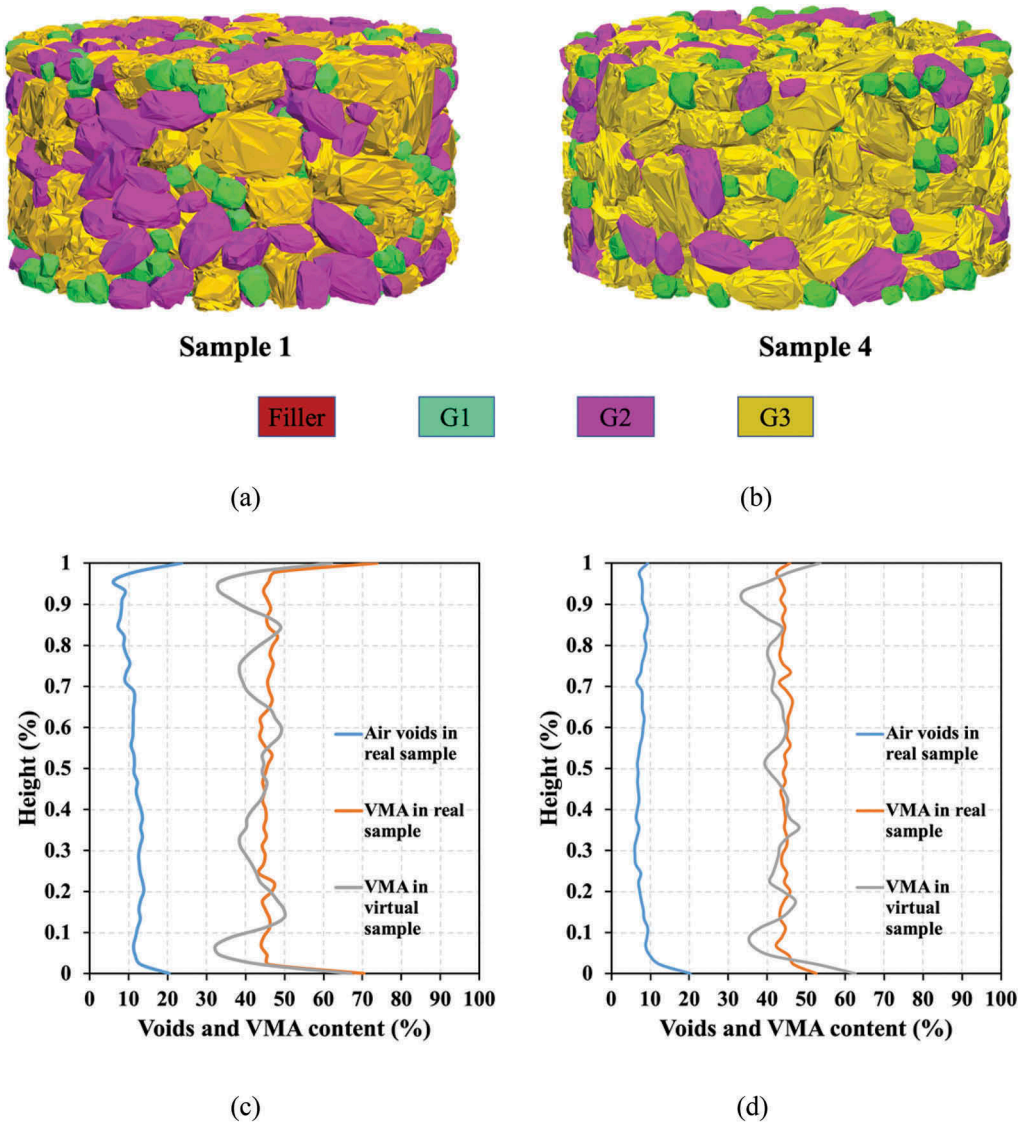

Figure 6. (a) and (b) Virtual skeleton of Sample 1 and Sample 4. (c) and (d) Vertical distribution of air voids and VMA of Sample 1 and Sample 4.

4 CONCLUSIONS

This paper depicts a method to simulate asphalt concrete by the impulse-based Discrete Element Method. Ten types of Granite and Limestone aggregates were measured using imaging techniques and re-created virtually. Twelve gradations of asphalt concrete were re-created virtually. The following specific conclusions can be obtained:

Realistic virtual aggregates and asphalt solid skeletons can be reproduced using an impulse-based numerical method. Virtual force controls the virtual compaction.

The compaction force required to produce virtual asphalts compacted to a level equivalent to that of a Marshall test in the lab is influenced by the penetration between aggregates. This implies that errors caused by the nature of iDEM are systematic. Hence, a fitting equation of virtual force can be produced based on the number of aggregates and volume of mastic.

These simulations can be used to predict the air voids contents of asphalt concrete. The voids distribution in mineral aggregate were compared in real and virtual samples.

While this iDEM approach has been useful to digitally build asphalt mixtures, there is still a lot of progress needed to create asphalt samples to the resolution required to include mastic and filler minerals.

REFERENCES

Bessa, I.S., Branco, V.T.C., Soares, J.B. and Neto, J.A.N., 2015. *Aggregate shape properties and their influence on the behavior of hot-mix asphalt*. Journal of Materials in Civil Engineering, 27(7), p.04014212.

Barrett, P.J., 1980. *The shape of rock particles, a critical review*. Sedimentology, 27(3),pp.291–303.

British Standards Institution, 2016. *Bituminous mixtures — Test methods, Part 35: Laboratory mixing (BS EN 12697-35:2016)*. Retrieved from https://bsol.bsigroup.com/.

British Standards Institution, 2018. *Bituminous mixtures – Test methods, Part 30: Specimen preparation by impact compactor (BS EN 12697-30:2018)*. Retrieved from https://bsol.bsigroup.com/.

British Standards Institution, 2018. *Bituminous mixtures — Test methods, Part 8: Determination of void characteristics of bituminous specimens (BS EN 12697-8:2018)*. Retrieved from https://bsol.bsigroup.com/.

Cundall, P.A. and Strack, O.D., 1979. *A discrete numerical model for granular assemblies*. geotechnique, 29(1),pp.47–65.

Chen, J., Li, H., Wang, L., Wu, J., and Huang, X., 2015. *Micromechanical characteristics of aggregate particles in asphalt mixtures*. Construction and Building Materials, 91, pp. 80–85.

Cao, P., Jin, F., Feng, D., Zhou, C. and Hu, W., 2016. *Prediction on dynamic modulus of asphalt concrete with random aggregate modeling methods and virtual physics engine*. Construction and Building Materials, 125, pp.987–997.

Czajkowska, M., Sznitowska, M. and Kleinebudde, P., 2015. *Determination of coating thickness of mini-tablets and pellets by dynamic image analysis*. International journal of pharmaceutics, 495(1), pp.347–353.

Guendelman, E., Bridson, R. and Fedkiw, R., 2003. *Nonconvex rigid bodies with stacking*. ACM transactions on graphics (TOG), 22(3),pp.871–878.

Garcia, A., Wan, L. and Dopazo-Hilario, S., 2021. *In-silico manufacturing of asphalt concrete*. Powder Technology, 386, pp.399–410.

Garcia, A., Michot-Roberto, S., Dopazo-Hilario, S., Chiarelli, A. and Dawson, A., 2020. *Creation of realistic virtual aggregate avatars*. Powder Technol.

Garcia-Hernandez, A., Wan, L., Dopazo-Hilario, S., Chiarelli, A. and Dawson, A., 2021. *Generation of virtual asphalt concrete in a physics engine*. Construction and Building Materials, 286, p.122972.

Hahn, J.K., 1988. *Realistic animation of rigid bodies*. ACM Siggraph computer graphics, 22(4), pp.299–308.

Khattak, M.J. and Roussel, C., 2009. *Micromechanical modeling of hot-mix asphalt mixtures by imaging and discrete element methods*. Transportation research record, 2127(1),pp.98–106.

Mirtich, B.V., 1996. *Impulse-based dynamic simulation of rigid body systems*. University of California, Berkeley.

Pan, T., Tutumluer, E. and Carpenter, S.H., 2006. *Effect of coarse aggregate morphology on permanent deformation behavior of hot mix asphalt*. Journal of transportation engineering, 132(7), pp.580–589.

Pytlos, M., Gilbert, M. and Smith, C.C., 2015. *Modelling granular soil behaviour using a physics engine*. Géotechnique Letters, 5(4),pp.243–249.

Stimilli, A., Virgili, A. and Canestrari, F., 2017. *Warm recycling of flexible pavements: Effectiveness of Warm Mix Asphalt additives on modified bitumen and mixture performance*. Journal of Cleaner Production, 156, pp.911–922.

Yin, A., Yang, X., Zhang, C., Zeng, G. and Yang, Z., 2015. *Three-dimensional heterogeneous fracture simulation of asphalt mixture under uniaxial tension with cohesive crack model*. Construction and Building Materials, 76, pp.103–117.

Yang, X., You, Z., Wang, Z. and Dai, Q., 2016. *Review on heterogeneous model reconstruction of stone-based composites in numerical simulation*. Construction and Building Materials, 117, pp.229–243.

Eleventh International Conference on the Bearing Capacity of Roads, Railways and Airfields, Volume 2 – Hoff, Mork & Saba (eds)

Finite element modelling of permanent deformation of hot mix asphalt tested in the Modified Wheel Tracker (MWT)

A.B. Roy-Chowdhury & M.F. Saleh
Department of Civil Engineering, University of Canterbury, Christchurch, New Zealand

M. Moyers-Gonzalez
School of Mathematics and Statistics, University of Canterbury, Christchurch, New Zealand

ABSTRACT: Permanent deformation in the form of rutting is one of the most common and critical modes of failures in flexible pavements in the wheel path under the repeated axle loads. Rutting occurs mostly in the asphalt layer and/or all other pavement layers. The Wheel Tracking Test (WTT) is a very common device for laboratory study and characterisation of rutting in Hot Mix Asphalt (HMA). However, the conventional setup of the device is fully confined and has drawback in the sense that it is unable to capture the shear deformation characteristics of the asphalt mixtures. This makes it difficult to analyse the permanent deformation resistance behaviour of HMA. Hence, a modified setup of the wheel tracker with controlled confining pressure was utilised in this study, which is standardised under ASTM D8292. In this study, three different confinement conditions: unconfined, partially confined with 1.35 kPa lateral pressure and fully confined were simulated. In addition, solid rubber wheel versus pneumatic rubber wheels were investigated. The plastic creep parameters derived from the uniaxial static creep test were used to develop a finite element model in Abaqus, and the validation of the experimental data was investigated. A good match was observed between the experimental and the predicted rut depths at different cycles. Strong correlations were observed between the experimental and the predicted rut depths at different cycles for individual wheel type and confinement.

Keywords: Permanent deformation, wheel tracker, creep, finite element modelling, abaqus

1 INTRODUCTION

Rutting is a form of permanent deformation, and a critical failure in asphalt concrete pavements. Saleh (2018), and Roy-Chowdhury et al. (2020) suggest that the composition of asphalt mixture along with the degree of compaction, temperature and loading rate are the contributory factors for rutting resistance and stiffness of asphalt concrete pavements. Saleh (2018) concluded that the combination of densification and shear deformation causes rutting, and that, the latter causes the severe form of the distress. Therefore, the characterisation of rutting must consider the asphalt mixture susceptibility to shear deformation. To study the rutting behaviour of the asphalt mixtures, the Flow Time (FT) or Flow Number (FN) tests, collectively called the Simple Performance Test (SPT) are recommended (Witczack et al. 2002, Witczack 2006, Irfan et al. 2018). However, one drawback of the SPT methods is that, these are not simple and need relatively sophisticated setup.

DOI: 10.1201/9781003222897-46

The Wheel Tracking Test is a common and simple test method for rutting characterisation of asphalt mixtures in laboratory. However, Saleh (2018) concluded that the fully confined assembly or the conventional wheel tracker creates unrealistic boundary conditions around the asphalt specimen, thereby immobilising the shear deformation. The research showed that despite using vastly different mixes, the fully confined test data revealed no significant difference in rut depth in the samples as also discussed by Shami et al. (1997), and Yildirim et al. (2007). Additionally, Azari (2014), Saleh (2018), and Roy-Chowdhury et al. (2020) concluded that the conventional or the fully confined system of the wheel tracker is unlikely to capture the shear deformation characteristics of the asphalt mixtures. This indicates that only densification occurs in the mixes tested in the conventional setup of the device. Although the rutting curves of the asphalt mixes studied by Al-Khateeb and Basheer (2009) did reveal three zones when tested in the fully confined setup, it was also noted by the authors that most of the models developed to predict rutting in asphalt mixes are for characterising the primary phase. While Chaturabong and Bahia (2017) concluded that the dry Hamburg Wheel Tracker (HWT) could be used as an alternative to the wet HWT test, the asphalt mixes tested in the dry HWT did not result in an inflection point. The authors further reported that rutting curves of the mixes tested even in wet HWT do not always tend to reveal the tertiary zone. This indicates that a vast majority of researchers are still able to record only the primary and at most a fraction of the secondary phase of the rutting curve using the fully confined setup of the wheel tracker. Romero and Stuart (1998) investigated on the accuracy of various confined wheel trackers in predicting rutting resistance of asphalt pavements. It was concluded that while the devices distinguished the poor and well-performing mixtures made with the same aggregate and different binders, no device was able to do distinguish the mixtures made with different aggregate gradations. It would also be interesting to note that despite utilising a high temperature of 60°C and a high cycle number of 75000, Ebrahimi (2015) observed considerably smaller permanent deformation in the confined setup of the wheel tracker than what a realistic confinement would cause. Hence, Saleh (2018) proposed a modified wheel tracker, which was subsequently standardised as ASTM D8292-20. In the new setup, the lateral sides along the wheel tracking direction are unconfined or can be under full lateral pressure control, while the remaining two sides are fixed. Roy-Chowdhury et al. (2020) and Roy-Chowdhury et al. (2021) experimented with this new setup of the wheel tracker, and successfully concluded that it is capable of capturing the shear deformation that occurs in compacted asphalt mixture slabs, tested in dry condition.

The study by Rahmani et al. (2013) indicated that the level of confinement has a significant effect on the nonlinear viscoelastic characteristics of asphaltic materials. It can be noted that NCHRP reports suggest the option of altering confinement only for the SPTs, such as the dynamic modulus and dynamic creep tests. However, no study until now addressed or analysed the effect of confinement in a simulative test such as the wheel tracker. The current study addresses this point, for which the modified assembly of the wheel tracker was utilised.

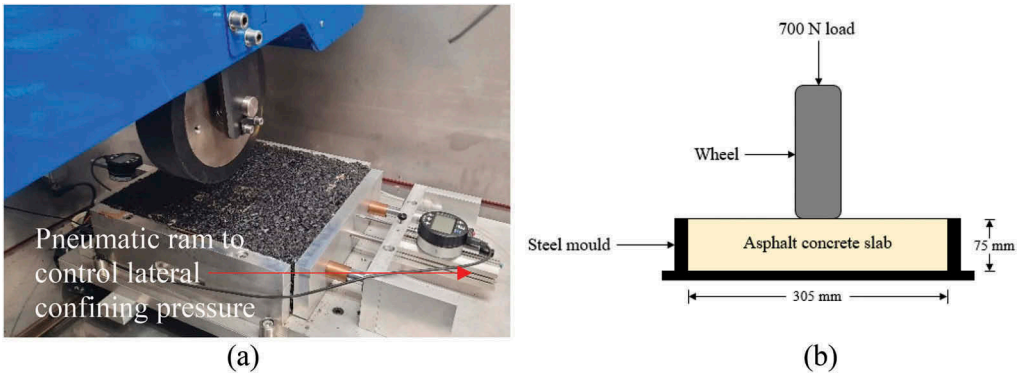

Figure 1. Modified wheel tracker assembly.

Figure 1a shows a photograph of the modified wheel tracker (MWT) setup and Figure 1b shows a simplified representation of the same.

2 RESEARCH OBJECTIVES

The aim of this paper is to simulate the permanent deformation (rutting) behaviour of asphalt mixtures in the modified wheel tracker (MWT) utilising the Finite Element (FE) modelling in Abaqus. Additionally, the differences between the laboratory rutting characteristics of HMA using pneumatic and solid wheel tyre in the wheel tracker is explored. At the time being, very limited studies have investigated the difference in the test results when pneumatic wheel is used instead of the conventional solid rubber tyre wheel. Hence, the study focuses on the investigation of the effect of the pneumatic wheel on the permanent deformation characteristics of asphalt concrete mixtures. This could help in accurate measurements and thereby, help verify the performance of asphalt mix rutting performance. The viscoelastic parameters were determined based on the data from the uniaxial static creep test at a deviatoric stress of 240 kPa. The aim of developing these models under realistic boundary conditions is to use them in the Mechanistic Empirical (M-E) procedure to predict rutting in flexible pavements more accurately. Figure 2a through 2d depict the solid and pneumatic wheels used in this study and their respective footprints. As can be seen, there exists a considerable difference in the footprint dimensions between the two, and that, the pneumatic wheel has a larger surface area than the solid wheel. The footprint of the solid wheel tyre has a dimension of 22.5 mm×50 mm, while that of the pneumatic wheel is 80 mm×35 mm. The contact stress on the asphalt slab surface for the solid wheel tyre translates to 620 kPa, and that for the pneumatic wheel tyre to about 320 kPa. The pneumatic wheel was inflated to 310 kPa, which corresponds to the maximum air pressure in modern domestic vehicles. Although this is less than the truck tyre pressure which is in excess of 700 kPa, this research aims to provide some bases of comparison between the solid and pneumatic tyre.

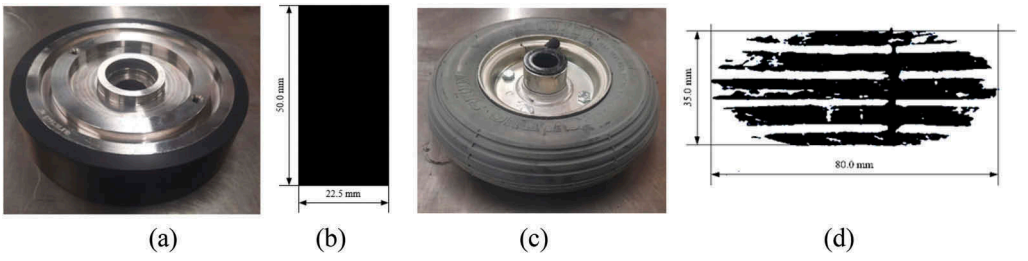

Figure 2. (a) Solid rubber wheel tyre, (b) footprint of the solid wheel tyre, (c) pneumatic wheel tyre, and (d) footprint of the pneumatic wheel tyre.

3 MATERIALS AND METHODS

This study utilised New Zealand dense-graded AC20 asphalt mixture with 20 mm maximum nominal aggregate size (NMAS). The gradation curve of the mixture is shown in Figure 3.

The mixing temperature was chosen as 150°C according to AS/NZS2891.2.1:2014. After mixing, the loose asphalt mix was short-term aged at 150°C for one hour before compaction, according to Austroads standard AG: PT/T220 (2005). A gyratory compactor with 240 kPa ram pressure and 3° gyration angle was used to compact the cylindrical samples for static creep test and the compaction was done as per AS/NZS AS/NZS 2891.2.2:2014. The slab specimens for MWT were compacted using a roller compactor. Both the asphalt concrete cylindrical samples and the slab samples were compacted at 5.5% air voids content, and were tested at 50°C.

x

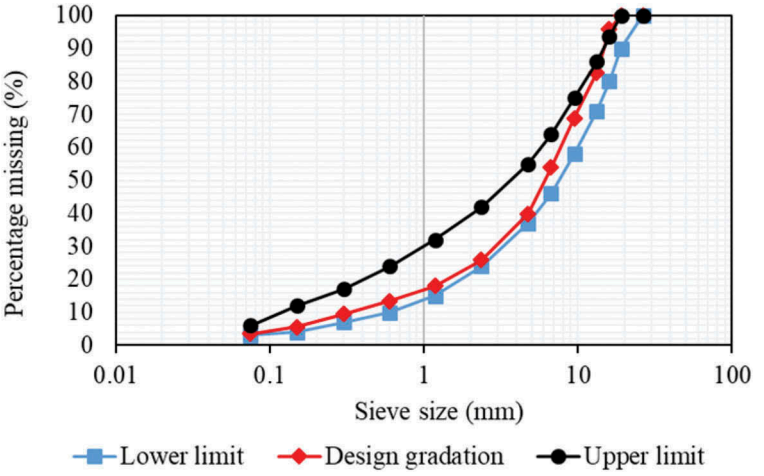

Figure 3. Gradation curve of AC 20 asphalt mixture.

4 DETERMINATION OF VISCOELASTIC PARAMETERS

Asphalt mixture is a viscoelastic material and it is well-accepted that rutting in asphalt concrete can be simulated by creep models (He and Wong, 2007, and Al-Qadi et al., 2009). Abaqus uses two kinds of creep models, which are the power-law model and the hyperbolic-sine model. The power-law model, which includes the time-hardening and the strain-hardening versions, is a relatively simple model but can be used for appropriately describing creep behaviour of asphalt mixtures (White et al., 2002, and Arabani et al. 2014). The gradual increase of material deformation with time under certain temperature and constant stress is called creep deformation. Asphalt mixture can exert significant creep under normal temperature. For describing the creep behaviour of the asphalt material, its total strain $\varepsilon(t)$is decomposed into elastic strain ε_e and non-elastic strain ε_{in}, that is,

$$\varepsilon(t) = \varepsilon_e + \varepsilon_{in} \tag{1}$$

Where, ε_{in} includes plastic strain ε_p and creep strainε_c, such that,

$$\varepsilon_{in} = \varepsilon_p + \varepsilon_c \tag{2}$$

Assuming that the pavement has not entered its plastic deformation phase under the wheel load effect, then $\varepsilon_p = 0$and $\varepsilon(t)$ can be expressed as follows:

$$\varepsilon(t) = \varepsilon_e + \varepsilon_c \tag{3}$$

Where, $\varepsilon_e$is time-independent. ε_c is a function of time t, temperature T, and stress σ, that is,

$$\varepsilon_c = f(t, T, \sigma) = f_1(t) f_2(T) f_3(\sigma) \tag{4}$$

The time-hardening version of the creep power-law model is appropriate to use when the stress remains essentially constant during the creep process. The differential expression of this is given by Equation (5)

$$\frac{d\varepsilon_c}{dt} = A\sigma^n t^m \tag{5}$$

Where, $\frac{d\varepsilon_c}{dt}$is defined as the equivalent creep strain rate, σ is the uniaxial equivalent deviatoric stress, t is the time, and A, n, m are the creep parameters (with $A>0$, $n>0$, $-1<m\leq 0$).
The direct integral expression of Equation (5) is given by Equation (6)

$$\varepsilon_c = \frac{A}{m+1}\sigma^n t^{m+1} \tag{6}$$

The elastic parameters were determined by conducting the dynamic modulus test and fitting a master curve for the asphalt mix. In this approach, the dynamic modulus value associated with the frequency of 0.44 Hz (equivalent to that of wheel tracker loading) is read from the master curve, as shown in Figure 4a. To determine the creep parameters of the asphalt concrete mixes, a uniaxial static creep test was conducted at 50°C and 240 kPa stress. The materials and mix design for the samples used in the creep test are the same as those used in the MWT. The static creep test was performed on 150mm high and 100 mm diameter cylindrical samples according to NCHRP report 465. The creep power-law model was fitted to the experimental data to obtain the necessary creep parameters, as shown in Figure 4b.

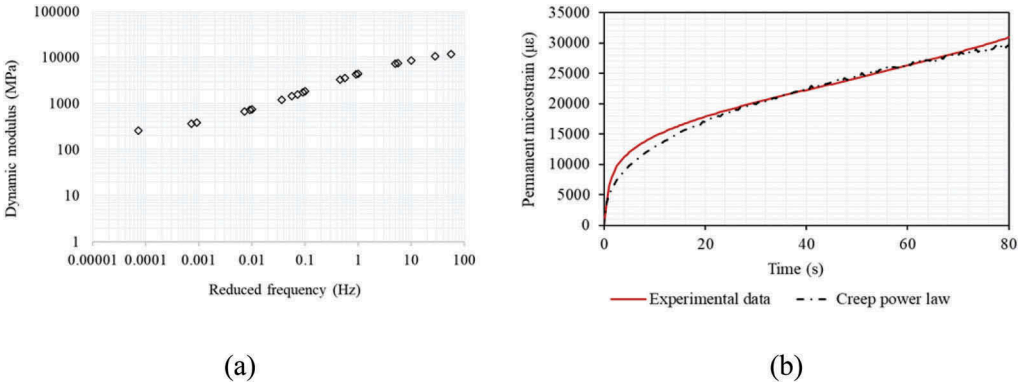

Figure 4. (a) Dynamic modulus master curve, and (b) Creep power-law fitted to static creep test data.

The elastic and creep parameters of the asphalt material utilised in this study are tabulated in Table 1.

Table 1. Elastic and creep material parameters for Abaqus modelling.

Elastic		Creep		
Modulus (Instantaneous) (MPa)	Poisson's ratio	A	n	m
293	0.4	0.009	1.348	-0.784

5 THE FINITE ELEMENT MODEL AND THE OPTIMAL MESH DENSITY

The determination of the optimal mesh density in the FE model is a crucial step for the accurate simulations. Generally, the mesh used in the modelling should be fine enough to ensure convergence, however, it must also ensure a reasonable computational effort. For this purpose, four mesh densities were tried to obtain the optimum mesh density. Figure 5a illustrates the effect of mesh density and the computational effort in reaching a rut depth of 10 mm. Each time, the simulation was run for an equivalent time required for 75000 cycles in the wheel tracker to capture the effect of different mesh density over a moderately long period of time. Figure 5a shows that the improvement in prediction could be observed only when the mesh was refined from

medium to fine, after that, there is barely a marginal change in the result, while a significantly greater computational effort was observed. Therefore, the 'fine mesh' was finally considered for the FE model, which includes 86,152 elements as shown in Figure 5b. To ensure an accurate prediction, a significantly denser mesh was chosen for the wheel-loaded area, where the displacement response (rutting) is required, as shown in Figure 5b. A 3D 8 node-brick element with reduced integration (C3D8R) was used in the modelling.

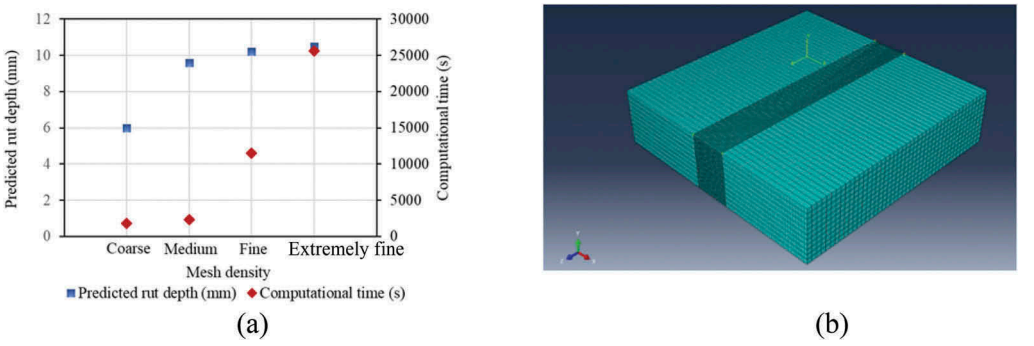

Figure 5. (a) Comparison of mesh and computational time, and (b) Meshing of the model.

6 APPLICATION OF WHEEL LOAD

The time of loading in one pass is about 0.08 s for the average wheel footprint length of 22.5 mm, which is that of the solid wheel tyre. This study utilised the time of loading conversion described by Hua (2000), and Saleh and Ebrahimi (2017). The load is immediately and statically applied to the model in this modelling scheme. Subsequently, the calculation of the required time for the wheel to pass the path, is based on wheel speed and the footprint length of the corresponding wheel tyre. The required time (T) can then be calculated by:

$$T = d/v \tag{7}$$

Where, d is the tyre footprint length and v is the wheel speed.

7 RESULTS, COMPARISON, AND DISCUSSION

The boundary conditions and loading conditions for the unconfined and with lateral pressure of 1.35 kPa were kept at par with the experimental conditions. As can be seen, the lateral sides along the wheel direction were kept unrestrained, representing the boundary conditions in the

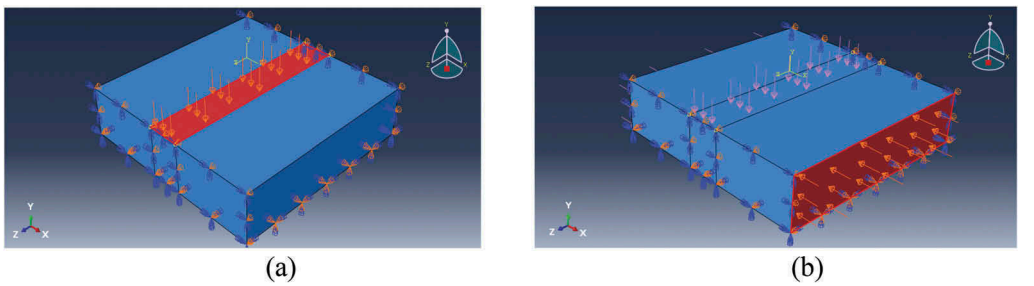

Figure 6. Boundary conditions and loading for (a) unconfined, and (b) with 1.35 kPa lateral pressure modelling.

unconfined MWT setup (Figure 6a). For the condition where lateral pressure was used, two opposite sides along the wheel-tracking direction were kept unrestrained and a pressure of 1.35 kPa was applied on those faces of the model (Figure 6b).

Figure 7 shows the experimental rut depth data from the wheel tracker test with solid and pneumatic wheel with different confinement conditions and the predicted rut depths from the FE modelling in Abaqus. The measured and the predicted rut depths are reasonably close with minor deviations, which could be attributed to the fact that the states of stresses in the static creep test is not similar to that in the wheel tracker. Additionally, it can also be said that the static modelling is not expected to yield identical match with the true dynamic scenario. Therefore, it can be said that the viscoelastic parameters determined from the uniaxial static creep test are not expected to perfectly match with the wheel tracker test, as also concluded by Saleh and Ebrahimi (2017). However, the results confirm the ability of the plastic creep power-law model to reasonably predict rutting in asphalt concrete mixtures tested in the MWT. It can also be noted that the vertical permanent deformation that resulted from the test and prediction with lateral pressure is smaller than that resulted from the totally unconfined test. The fully confined or the conventional setup was also utilised in this study for experimental run and the numerical modelling of the same was conducted. The results show that the fully confined or the conventional setup of the wheel tracker produced lower vertical deformation than that with 1.35 kPa lateral pressure. This indicates that the fully confined condition results in increased stiffness of the asphalt mix and therefore less permanent deformation. This subsequently reaffirms the conclusion made by Saleh (2018) that the fully confined setup of the wheel tracker prevents the lateral flow of the asphalt slab by imposing high confinement. While in practice there exists variable lateral pressure from the nearby lanes and/or shoulders (for which the lateral pressure can be estimated as per ASTM D8292), the fully confined wheel tracker is still not representative of the actual in-situ conditions. Therefore, the utilisation of the modified wheel tracker gives full control of the confining pressure, thereby providing more realistic match to the actual field conditions.

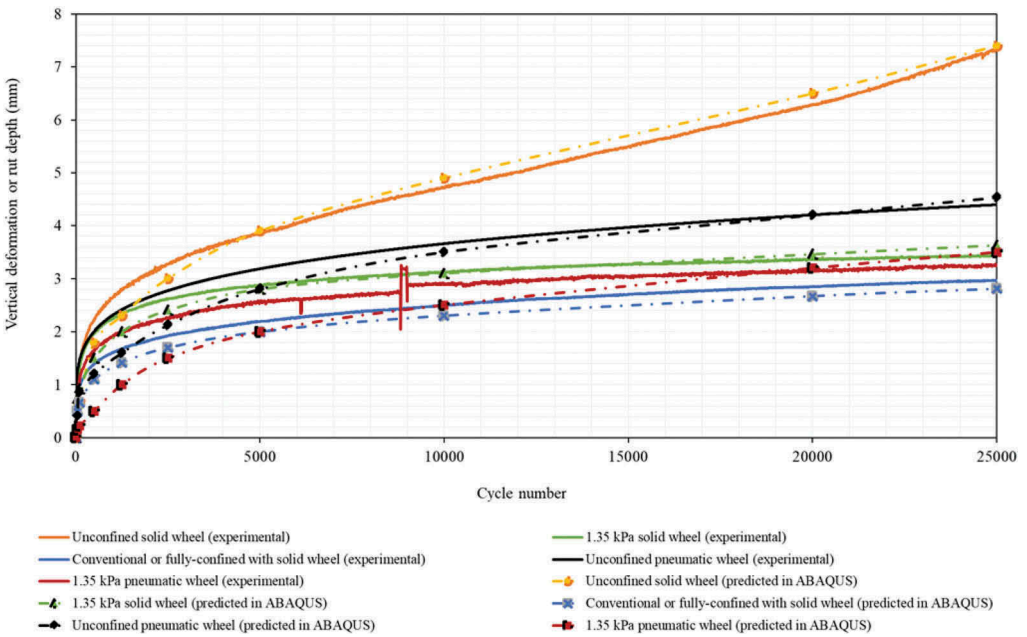

Figure 7. Comparison of experimental and predicted vertical deformation for different confinement conditions and wheel tyre type.

It can also be observed from Figure 7 that the corresponding experimental and predicted values for the pneumatic wheel are lower than the values obtained from the experimental and prediction for the solid wheel. This difference is attributed to the difference in the footprint of the solid and pneumatic wheel, and therefore, the resulting difference in the contact stress distribution. The pneumatic wheel evidently exerted lower contact pressure due to its larger contact area, thereby producing lesser deformation than solid wheel. This can be further supported by the findings of Casey et al. (2018), which indicated that an increased accumulation of damage in the form of rutting occurs when the wheel load is transmitted into the pavement over a smaller area with higher contact pressure, as is the case with the solid rubber wheel tyre. Nonetheless, Figure 8a and 8b indicate that strong correlations exist for the experimental rut depth at specific cycles between solid and pneumatic wheel for unconfined setup and with lateral pressure. This agreement and the linear regressions should in turn help estimate in-situ rutting in road pavements, where, generally pneumatic wheel tyre is used in the vehicles.

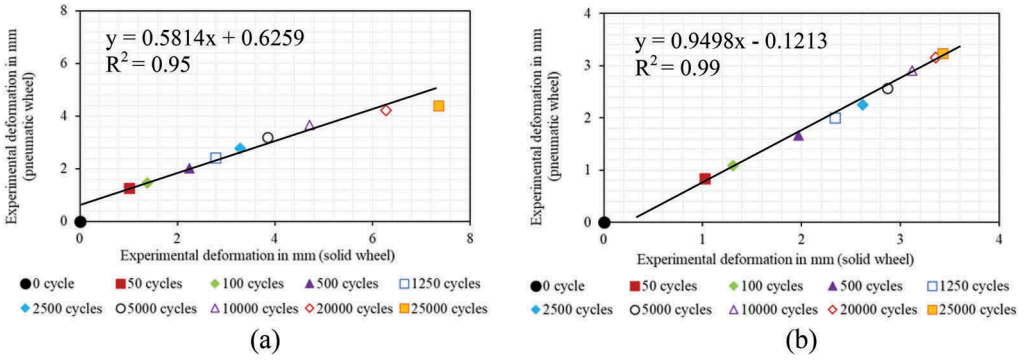

Figure 8. Correlations for experimental rut depth between solid and pneumatic wheel for (a) unconfined setup, and (b) with lateral pressure of 1.35 kPa.

The experimental and predicted rut depth at specific cycles for the unconfined and with lateral pressure setup are presented in Table 2 for pneumatic and solid tyre wheels. As can be observed, the general trend is that, the creep plastic model underestimated the vertical deformation initially, however, gradual improvements in prediction is evident after the post-compaction phase (500 cycles or 1000 wheel passes, according to Yildirim et al. 2007). The percentage difference method was used in background to study the agreement between the experimental and predicted values, which reconfirms that the match between the experimental and predicted deformations increased with the increase in cycle number. The predicted final rut depth values were found to be within ±10% of the experimental final rut depth values for every confinement and wheel type.

Table 2. Experimental and predicted rut depth with and without confinement.

Solid wheel									
Unconfined (0 kPa lateral pressure)									
Cycles	50	100	500	1250	2500	5000	10000	20000	25000
Experimental rut depth (mm)	1.01	1.38	2.24	2.78	3.28	3.85	4.71	6.28	7.36
Predicted rut depth (mm)	0.60	0.70	1.80	2.30	3.00	3.90	4.90	6.50	7.40

(*Continued*)

Table 2. (*Continued*)

Semi-unconfined (1.35 kPa lateral pressure)									
Cycles	50	100	500	1250	2500	5000	10000	20000	25000
Experimental rut depth (mm)	1.02	1.31	1.97	2.34	2.62	2.87	3.12	3.36	3.43
Predicted rut depth (mm)	0.73	0.93	1.50	2.00	2.40	2.80	3.10	3.46	3.63
Fully confined									
Cycles	50	100	500	1250	2500	5000	10000	20000	25000
Experimental rut depth (mm)	0.77	0.95	1.39	1.67	1.92	2.18	2.49	2.86	2.96
Predicted rut depth (mm)	0.50	0.66	1.10	1.42	1.70	2.00	2.30	2.67	2.81
Pneumatic wheel									
Unconfined (0 kPa lateral pressure)									
Cycles	50	100	500	1250	2500	5000	10000	20000	25000
Experimental rut depth (mm)	1.27	1.46	2.01	2.41	2.77	3.19	3.66	4.20	4.40
Predicted rut depth (mm)	0.40	0.85	1.20	1.60	2.12	2.80	3.50	4.20	4.53
Semi-unconfined (1.35 kPa lateral pressure)									
Cycles	50	100	500	1250	2500	5000	10000	20000	25000
Experimental rut depth (mm)	0.84	1.09	1.66	2.00	2.25	2.57	2.91	3.16	3.24
Predicted rut depth (mm)	0.15	0.22	0.50	1.00	1.50	2.00	2.50	3.20	3.50

Strong correlations were also observed between the experimental and the predicted rut depths at different cycles for individual wheel type and confinement, as can be seen in Figure 9. The highest correlation was found for unconfined setup with solid wheel, followed by lateral pressure with solid wheel, unconfined with pneumatic wheel, and lateral pressure with pneumatic wheel. In general it can be noted that the creep plastic model underestimated the rut depths at most cycle numbers when pneumatic wheel was used, which may be attributed to the complex effect of the wheel treads in the pneumatic wheel in the experimental condition, which caused non-uniform pressure distribution. This complexity and sophistication in the analysis was not incorporated in the FE modelling in this study. Therefore, future studies should investigate the effect of wheel treads in the FE prediction of asphalt rutting in the MWT.

8 SUMMARY AND CONCLUSIONS

The finite element modelling of rut depth of a dense-graded asphalt mixture was investigated in this study. A modified setup of the wheel tracker was utilised and the boundary conditions for the FE modelling were kept consistent with the modified wheel tracker (MWT). This assembly can be used to account for the permanent deformation (rutting) under the application of a variety of lateral pressure, which is more realistic and is representative of the actual field conditions. For the modelling, three different confinement conditions and two types of wheels were considered. The uniaxial static creep test was performed to determine the viscoelastic parameters, and the plastic creep power-law model was utilised for the modelling. Comparing the experimental data with the predicted data confirms the suitability of the plastic creep power-law model for this simulation. The difference in the contact stress distribution between the solid and pneumatic wheel tyre played a significant role in the difference in the rut depth values. The results show that the fully confined or the conventional setup of the wheel tracker produced lower vertical deformation than that with the unconfined condition and 1.35 kPa lateral pressure, indicating an increased stiffness of the asphalt mix and therefore less permanent

x

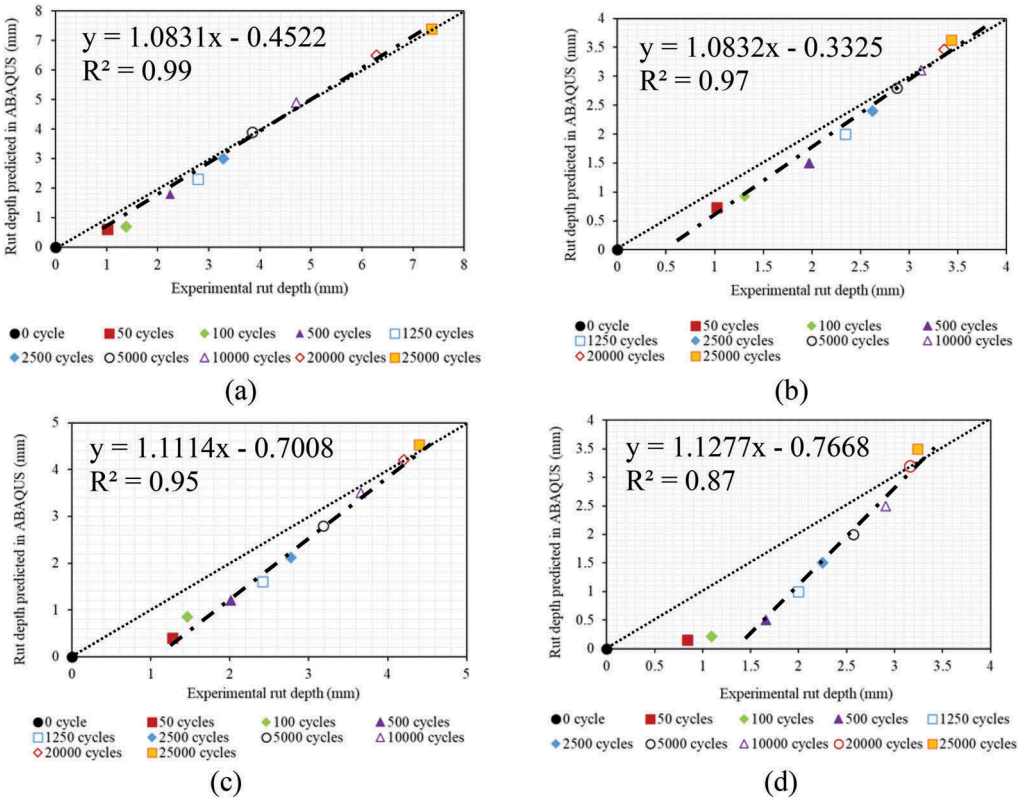

Figure 9. Correlation of experimental and predicted rut depth for (a) unconfined with solid wheel, (b) 1.35 kPa lateral pressure with solid wheel, (c) unconfined with pneumatic wheel, and (d) 1.35 kPa lateral pressure with pneumatic wheel.

deformation. It was observed that strong correlations exist for the experimental rut depth at specific cycles between solid and pneumatic wheel for unconfined setup and with lateral pressure. This agreement and the linear regressions should in turn help estimate in-situ rutting in road pavements, where, generally pneumatic wheel tyre is used in the vehicles. Strong correlations were also observed between the experimental and the predicted rut depths at different cycles for individual wheel type and confinement.

REFERENCES

Al-Khateeb, G., and Basheer, I., 2009. *A three-stage rutting model utilising rutting performance data from the Hamburg Wheel-Tracking Device (WTD)*. Road & Transport Research: A Journal of Australian and New Zealand Research and Practice, 18(3), 12–25.

Al-Qadi I.L., Yoo, P.J., Elseifi, M.A., and Neslon, S., 2009. *Creep Behavior of Hot-Mix Asphalt due to Heavy Vehicular Tire Loading*. Journal of Engineering Mechanics. 135(11): 1265–1273.

Arabani M, Jamshidi R, and Sadeghnejad M. 2014. *Using of 2D finite element modeling to predict the glasphalt mixture rutting behaviour*. Construction and Building Materials. 68(0): 183–191.

AS/NZS 2891.2.1, 2014. *Methods of sampling and testing asphalt. Part 2.1: Sample preparation – Mixing, quartering and conditioning of asphalt in the laboratory*.

AS/NZS 2891.2.2, 2014. *Methods of sampling and testing asphalt. Part 2.2: Sample preparation-Compaction of asphalt test specimens using a gyratory compactor*.

ASTM D8292, 2020. *Standard Test Method for Permanent Deformation Behavior and Rutting Resistance of Compacted Asphalt Mix in the Modified Loaded Wheel Tracker Test Utilizing Controlled Confining Pressure*. ASTM International.

Azari, H., 2014. *Precision Estimates of AASHTO T 324, Hamburg Wheel-Track Testing of Compacted Hot Mix Asphalt (HMA)*. Washington, DC: The National Academies Press. https://doi.org/10.17226/22242

Casey, D.B., Grenfell, G.R., Airey, G.D., Millar, P., and Woodward, D., 2018. *Contact pressure measurement of a small-scale wheel tracking device for different surface types*. Proceedings of 7th Transport Research Arena TRA 2018, Vienna, Austria.

Chaturabong, P., and Bahia, H.U., 2017. *Mechanisms of asphalt mixture rutting in the dry Hamburg Wheel Tracking test and the potential to be alternative test in measuring rutting resistance*. Construction and Building Materials, 146(2017): 175–182. doi:10.1016/j.conbuildmat.2017.04.080.

Ebrahimi, M.G., 2015. *Investigation of viscoelastic behaviour and permanent deformation modelling for New Zealand hot mix asphalts*. Ph.D. Thesis, University of Canterbury, Christchurch, New Zealand.

He, G., and Wong W., 2007. *Laboratory study on permanent deformation of foamed asphalt mix incorporating reclaimed asphalt pavement materials*. Construction and Building Materials. 21(8): 1809–1819.

Hua, J., 2000. *Finite Element Modeling and Analysis of Accelerated Pavement Testing Devices and Rutting Phenomenon*. Ph.D. Thesis, Purdue University.

Irfan, M., Ali, Y., Iqbal, S., Ahmed, S., and Hafeez, I., 2018. *Rutting Evaluation of Asphalt Mixtures Using Static, Dynamic, and Repeated Creep Load Tests*. Arabian Journal for Science and Engineering. 43:5143–5155.

Rahmani, E., Darabi, M.K., Al-Rub, R.K.A., Kassem, E., Masad, E.A., and Little, D.N., 2013. *Effect of confinement pressure on the nonlinear-viscoelastic response of asphalt concrete at high temperatures*. Construction and Building Materials 47 (2013) 779–788. http://dx.doi.org/10.1016/j.conbuildmat.2013.05.090

Romero, P., and Stuart, K., 1998. *Evaluating accelerated rut testers*. Public Roads, 62(1): 50–54.

Shami, H.I., Lai, J.S., D'Angelo, J.A., and Harman, T.P., 1997. *Development of temperature-effect model for predicting rutting of asphalt mixtures using Georgia loaded wheel tester*. Transportation Research Record: Journal of the Transportation Research Board, 1590: 17–22. doi:10.3141/1590-03.

Roy-Chowdhury, A. B., Saleh, M., and Moyers-Gonzalez, M., 2020. *Precision Assessment of the Modified Wheel Tracking Device Based on Small-Scale Testing of New Zealand Hot Mix Asphalt*. Proceedings of the 9th International Conference on Maintenance and Rehabilitation of Pavements — Mairepav9. https://doi.org/10.1007/978-3-030-48679-2_64

Roy-Chowdhury, A. B., Saleh, M., and Moyers-Gonzalez, M., 2021. *Empirical correlation of the Modified Wheel Tracker (MWT) and the dynamic creep test for evaluating the permanent deformation of HMA*. Canadian Journal of Civil Engineering. https://doi.org/10.1139/cjce-2020-0599

Saleh, M., 2018. *Modified Wheel Tracker as a Potential Replacement for the Current Conventional Wheel Trackers*. International Journal of Pavement Engineering, 2018. doi: https://doi.org/10.1080/10298436.2018.1435880

Saleh, M., and Ebrahimi, M.G. 2017. *Finite Element Modeling of Permanent Deformation in the Loaded Wheel Tracker Test*. Transportation Research Record: Journal of the Transportation Research Board, No. 2641. pp. 94–102. http://dx.doi.org/10.3141/2641-12

White, T.D., Haddock, J.E., Hand, A.J.T., and Fang, H., 2002. *Contributions of pavement structural layers to rutting of hot mix asphalt pavements*. Transportation research board, NCHRP Report 468, Washington, D.C.

Witczack, M.W., Kaloush, K., Pellimen, T., and El-Basyouny, M., 2002. *NCHRP Report 465: Simple Performance Test for Superpave Mix Design*. Transportation Research Board, Washington, DC.

Witczack, M.W. 2006. *NCHRP Report 547: Simple Performance Tests: Summary of Recommended Methods and Database*. Transportation Research Board, Washington, DC.

Yildirim, Y., Jayawickrama, P.W., Hossain, M.S., Alhabshi, A., Yildirim, C., Smit, A.F., and Little, D., 2007. *Hamburg wheel-tracking database analysis. Report FHWA/TX-05/0-1707-7, Project 0-1707-7*. Texas Department of Transportation.

Eleventh International Conference on the Bearing Capacity of Roads, Railways and Airfields, Volume 2 – Hoff, Mork & Saba (eds)

Analysis of low temperature relaxation properties of asphalt binder and asphalt mastic using a dynamic shear Rheometer

J. Büchner & M. Wistuba
Braunschweig Pavement Engineering Centre (ISBS), Technische Universität Braunschweig, Germany

ABSTRACT: One predominant type of failure in under-designed asphalt pavements in cold regions is cracking due to low-temperature induced stress. The asphalt binder is the key factor that drives cracking resistance of the asphalt layer. Due to its visco-elastic behavior, the asphalt binder is basically able to relax induced stress, however relaxation capacity is limited at low temperatures. In the frame of performance prediction of asphalt mixtures at low temperature conditions, laboratory relaxation tests are performed to analyze the resistance of a binder sample to thermal cracking. Today's most common low temperature binder test is a bending test using a Bending Beam Rheometer (BBR). However, BBR testing demands for relatively large amount of binder material. For this reason, in this paper, use of the Dynamic Shear Rheometer (DSR) is proposed to analyze low-temperature relaxation properties. By using a 4-mm parallel-plate geometry, a novel DSR relaxation test procedure is presented for studying low-temperature properties of asphalt binders and corresponding asphalt mastics (combination of asphalt binder and fine aggregates <0.063 mm). The test series includes a set of 10 different asphalt binders and 18 corresponding asphalt mastics. The results of the DSR relaxation tests are also compared to relaxation tests (i. e. Thermal Stress Restrained Specimen Test, TSRST) performed on samples of asphalt mixtures, which were produced of the corresponding material. Finally, the relaxation properties of the asphalt binder, asphalt mastic and asphalt mixture tests are correlated, and the interrelation between these three material scales is determined in terms of a regression analysis.

Keywords: Dynamic Shear Rheometer, relaxation, low temperature properties, asphalt mastic

1 INTRODUCTION AND BACKGROUND

When temperatures change due to weather conditions, asphalt shrinks when cooled and expands when heated. In asphalt pavements, these changes are hindered by geometric constraints due to jointless paving, resulting in thermal stresses (see, e.g., Golalipour, 2020). The occurring low-temperature induced stress is usually relieved naturally in the asphalt by relaxation (time-dependent stress decrease at constant elongation). This relaxation takes place through internal rearrangements of the viscously reacting mortar phase (Arand, 1983). The lower the temperature, the more the self-reduction of stresses by relaxation is constrained, and cryogenic (tensile) stresses develop in the asphalt pavement (Bouldin et al., 2000; Wistuba et al., 2009; Wistuba, 2019). The progressive buildup of cryogenic tensile stresses leads to cold cracking when the temperature-dependent tensile strength of the asphalt is reached. In practice, cold cracks usually appear as a group of parallel transverse cracks at approximately

DOI: 10.1201/9781003222897-47

equal intervals (Arand et al., 1986; Jung & Vinson, 1994; Marasteanu et al., 2007; Behnia et al., 2018; Golalipour, 2020).

Different studies demonstrated that the low temperature cracking of asphalt pavements is significantly influenced by the asphalt binder (Arand et al., 1986; Anderson et al., 1992; Golalipour, 2020). At the same time also mineral components and their interaction with the asphalt binder seem to influence the cracking behavior (Jung & Vinson, 1994; Spiegl et al., 2005; Marasteanu et al., 2007). To avoid cold cracking, cryogenic stresses should always be kept as low as possible by using sufficiently relaxing binder properties, e. g. by using soft bitumen (Arand et al., 1986; Jung & Vinson, 1994). The cold cracking of asphalt is thus mainly influenced by its relaxation behavior. An asphalt pavement with a high resistance to low-temperature cracking must therefore exhibit good relaxation behavior.

The ability of a bituminous binder to quickly relieve occurring stresses by relaxation is a crucial factor for the cold-cracking resistance of the asphalt pavement (Coufalík et al., 2015). For this reason, relaxation tests are particularly recommended to check the low-temperature behavior (Bouldin et al., 2000; Spiegl et al., 2005; Laukkanen, 2018). On binder level relaxation behavior is usually indirectly determined by flexural tests using the Bending Beam Rheometer (BBR) according to EN 14471 (2012). However, relaxation behavior of bituminous binder can directly be measured using the Dynamic Shear Rheometer (DSR) by applying a constant shear strain on the specimen and measuring the resulting shear stress. During a pre-defined testing time the stress will decrease due to relaxation. There are some studies available applying relaxation tests in the DSR (Sui et al., 2011; Coufalík et al., 2015; Gehrke, 2017; Gražulytė, 2019; Radenberg & Staschkiewicz, 2020; Xing et al., 2020) but there is no consensus regarding the selected test temperature, test geometry, loading time and applied deformation. So far, either -10, 0 or +10 °C was selected as the test temperature in combination with a test geometry of 8 mm or 4 mm.

In the range of the complex shear modulus between 10 MPa and 1000 MPa a testing geometry with 4 mm diameter is most suitable for DSR testing, which corresponds to an approximate temperature range between -40 bis +10 °C (Büchner, 2021). The applicability of the 4 mm geometry for low-temperature testing of asphalt binders was recently demonstrated as part of a European interlaboratory study (Büchner et al., 2020). Accordingly, the 4 mm geometry also offers a possibility for material evaluation in terms of relaxation tests at low temperatures below -10 °C. The use of this geometry is particularly advantageous for mastic tests due to the higher material stiffness in the low service temperature range (Büchner, 2021).

2 OBJECTIVE

The objective of this study is to analyze the applicability and suitability of relaxation tests in the DSR for asphalt binder and asphalt mastic using 4 mm parallel-plate geometry in the low-temperature range. For this purpose conclusive evaluation parameters are defined in order to allow a distinct differentiation of materials. Additionally, a correlation of relaxation behavior of asphalt binder and of asphalt mastic with cryogenic stress of corresponding asphalt mixtures is investigated. Finally, the impact of asphalt binder and filler on the low-temperature performance of asphalt mixtures is determined.

3 MATERIALS AND TESTING

In this study, 18 different asphalt mixture compositions are used, following the specifications of an asphalt concrete of the type AC 11, with a nominal maximum grain size of 11 mm. The asphalt mixture compositions are distinguished through variation of the asphalt binder (two plain and two modified binders are considered, i. e. 50/70, 70/100, 25/55-55, and 45/80-65), of four asphalt binder manufacturers (A to D), and of three types of aggregate (gabbro, porphyry, silicate), as summarized in Table 1. The composition of any asphalt mixture variant is

always adjusted as such, that volumetric mix properties of all variants are more or less in the same range (with regard to void content, binder content, and grain size distribution).

Table 1. Asphalt binders and aggregates considered in this study to compose 18 different variants of asphalt mixture.

Asphalt mixture AC 11 variants	Asphalt binder type (plain and polymer modified)		Aggregate type (gabbro, porphyry, silicate)
1	50/70	manufacturer A	coarse aggregate: gabbro
2		manufacturer B	added filler: limestone
3		manufacturer C	provenience: Germany
4		manufacturer D	
5	25/55-55	manufacturer A	
6		manufacturer B	
7		manufacturer C	
8		manufacturer D	
9	70/100	manufacturer B	
10	45/80-65		
11	50/70		coarse aggregate: porphyry
12	25/55-55		added filler: limestone
13	70/100		provenience: Austria
14	45/80-65		
15	50/70		coarse aggregate: silicate
16	25/55-55		added filler: limestone
17	70/100		provenience: Switzerland
18	45/80-65		

The 18 asphalt mixtures described above were produced in the laboratory at a mixing temperature of 160 °C. Afterwards, the asphalt mixtures were compacted to asphalt slabs using a segmented steel roller compactor (see Wistuba, 2016), and prismatic specimen with the dimensions 40 x 40 x 160 mm were prepared for performing Thermal Stress Restrained Specimen Test (TSRST).

For all the variants of asphalt mixture specified in Table 1, the individual fractions of filler was determined and used to produce asphalt mastic test samples. In this context, filler is understood as the aggregate fraction of grain size smaller than 0.063 mm. Hence, for each asphalt mixture variant, the corresponding asphalt mastic was determined, and composed in the laboratory from the relevant asphalt binder and filler (reclaimed filler, and new filler). The so-obtained asphalt mastic test samples together with the asphalt binder itself were used for the DSR relaxation tests.

3.1 *Asphalt binder and asphalt mastic relaxation test*

The relaxation test of asphalt binder and asphalt mastic were both performed in a regular DSR equipped with 4 mm parallel-plate geometry capable to measure down to temperatures of -40 °C. Specimen preparation for asphalt binder as well as asphalt mastic was carried out according to the typical procedure in EN 14770 (2012) with silicone molds having a cavity with a diameter of 4 mm and a depth of 2.5 mm. The specimen installation was done by radial trimming following the procedure presented by Büchner et al. (2021) applying a testing gap between the plates of 2 mm.

For the relaxation test a constant shear strain of 0.1 % was applied to the specimen for a duration of 60 minutes (as proposed earlier by Büchner & Wistuba (2020) and Büchner (2021)). After loading, the relaxation of the shear stress was monitored (Figure 1).

The relaxation test was carried out for all 10 asphalt binders at constant test temperatures of -15 and -20 °C with two repetitions at each temperature. As to asphalt mastic, three

different test temperatures were used, i. e. -25 °C, -20 °C and an equi-shear modulus temperature of the respective binder T(G^*_{binder} = 400 MPa). This specific temperature was proposed by Büchner (2021) to compare different materials in the same rheological state (same stiffness). The temperature T(G^*_{binder} = 400 MPa) for most asphalt binders is in the range of -5 to-25 °C. At each of the three temperatures, two repetitions were tested for all 18 asphalt mastic variants.

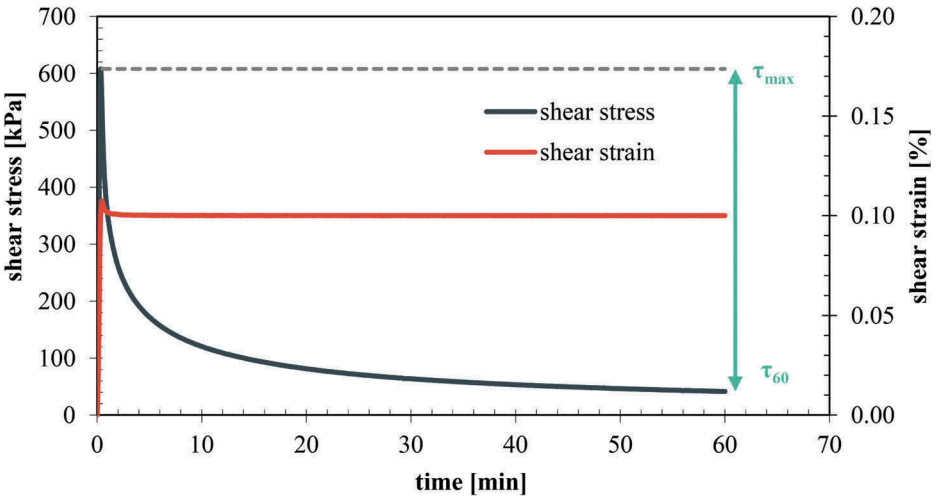

Figure 1. Exemplary progressions of shear stress and shear strain over time during DSR relaxation test.

From the curve of the shear stress, the maximum value (τ_{max}) and the value at the end of the test (τ_{60}) were derived (Figure 1). Both values were then used to calculate the percent of stress relaxation by dividing the amount of relaxed stress (τ_{max}-τ_{60}) by the maximum value.

The percentual stress relaxation after 60 min is proposed as an indicator of the low-temperature performance of the tested material. A high stress relaxation represents a material with high resistance to low-temperature cracking because developing stresses within the material are decreased by relaxation.

3.2 *Asphalt mixture TSRST test*

The low temperature behavior of asphalt mixtures was analyzed through the Thermal Stress Restrained Specimen Test (TSCRT) according to European Standard EN 12697-46 (2012). According to the standard, prismatic specimens (40 x 40 x 160 mm) are vertically mounted in a universal testing machine with a climate chamber. Starting with a temperature of 20 °C the temperature within the climate chamber is constantly reduced with a temperature rate of -10 ° C/h while the length of the specimen is held constant. Due to this constraint, the thermal shrinkage of the specimen is impeded and thermal (cryogenic) stresses evolve. In Figure 2 the development of cryogenic stress is exemplarily displayed for three specimens. With decreasing temperature the cryogenic stress is exponentially increasing until reaching the maximum tensile strength where the specimen breaks.

Usually, failure stress and failure temperature are determined as the results of the TSRST. However, this study is focusing on the relaxation capability of the material at different temperatures. Consequently, cryogenic stresses at distinct temperatures were identified to evaluate the temperature dependent relaxation behavior, as exemplarily displayed with black arrows in Figure 2. The respective temperatures were chosen based on binder and mastic tests to be -25, -20, -15 °C and T(G^*_{binder} = 400 MPa). For each of the 18 asphalt mixture variants three

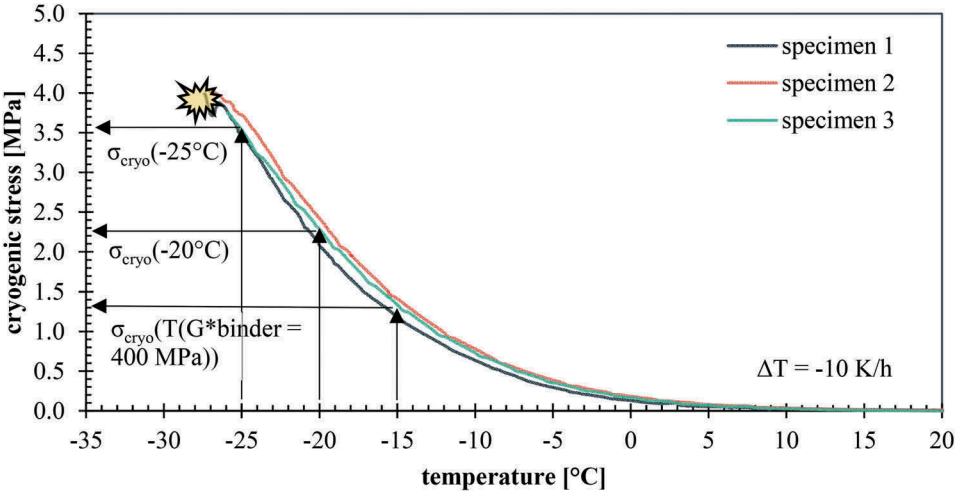

Figure 2. Exemplary development of cryogenic stress with decreasing temperature during Thermal Stress Restrained Specimen Test (TSRST) of asphalt mixture.

individual specimen were analyzed separately. In this context, a high cryogenic stress indicates unfavorable material property linked with low relaxation capability and therefore more prone to low-temperature cracking.

4 RESULTS

From the tests described above, significant material parameters were obtained for asphalt binder, asphalt mastic and asphalt mixture to evaluate their low-temperature behavior. Therefore, the test results are presented in form of a correlation analysis, directly comparing the percentual stress relaxation after 60 min from relaxation tests and the cryogenic stress from TSRST.

In Figure 3 the cryogenic stress of the asphalt mixture scale are plotted over the stress relaxation of the asphalt binder scale. The corresponding mean values for each parameter are displayed in color and with different symbols. The total number of underlying results for asphalt mixture and binder (n [-]) is indicated, as well as the test temperatures (T [°C]). For a total number of 145 individual test results, a reasonable linear correlation with a coefficient of determination of 0.88 is obtained (Figure 3). Asphalt binders with high relaxation capability show low cryogenic stress in the corresponding asphalt mixture, while the relaxation capability is much higher at -15 °C compared to -20 °C. It can be observed that soft binders (70/100) have much higher relaxation capability, thus lower cryogenic stress, compared to harder binders (25/55-55).

Using the same type of diagram, the results of asphalt mastic and asphalt mixture for the three temperatures considered are presented in Figure 4. For a total number of 275 individual test results, a reasonable linear correlation with a coefficient of determination of 0.93 is obtained between the stress relaxation of mastic and cryogenic stress of mixture. Consequently, asphalt mastic with high relaxation capability shows low cryogenic stress in the corresponding asphalt mixture, while the relaxation capability decreases with decreasing temperatures. Compared to the asphalt binder with stress relaxation between 91 and 98 %, the asphalt mastic demonstrates a much larger range of material behavior from 75 to 96 %. Therefore, mastic testing at various temperatures allows for clear differentiation while soft materials demonstrate favorable material behavior, as previously noticed in Figure 3.

Overall, the percentual stress relaxation of asphalt binder and asphalt mastic obtained from DSR relaxation tests appears as a suitable and conclusive parameter to evaluate low-

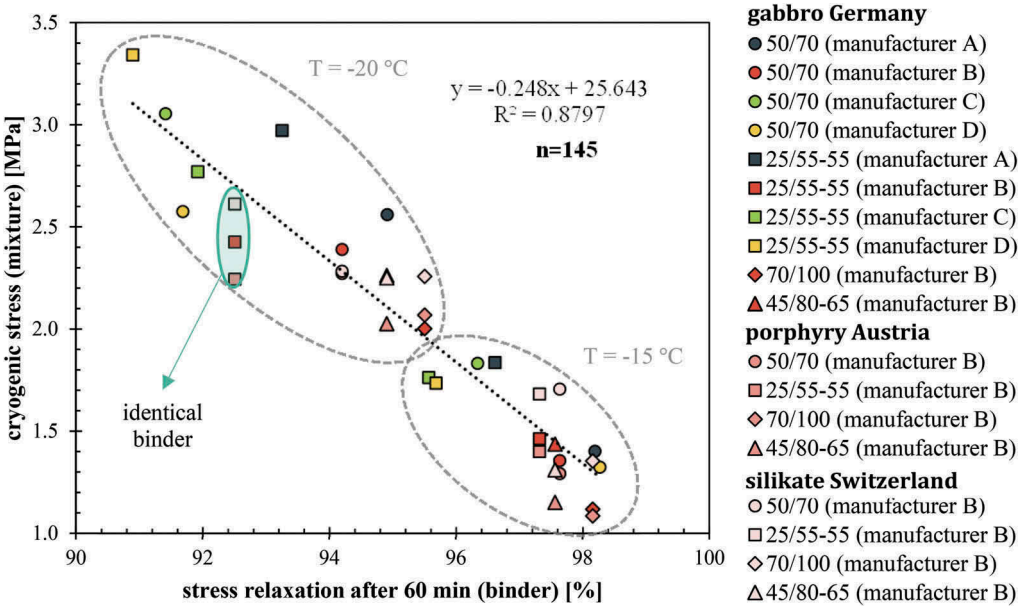

Figure 3. Correlating cryogenic stress of asphalt mixtures and stress relaxation of asphalt binders obtained from DSR relaxation tests and TSRST.

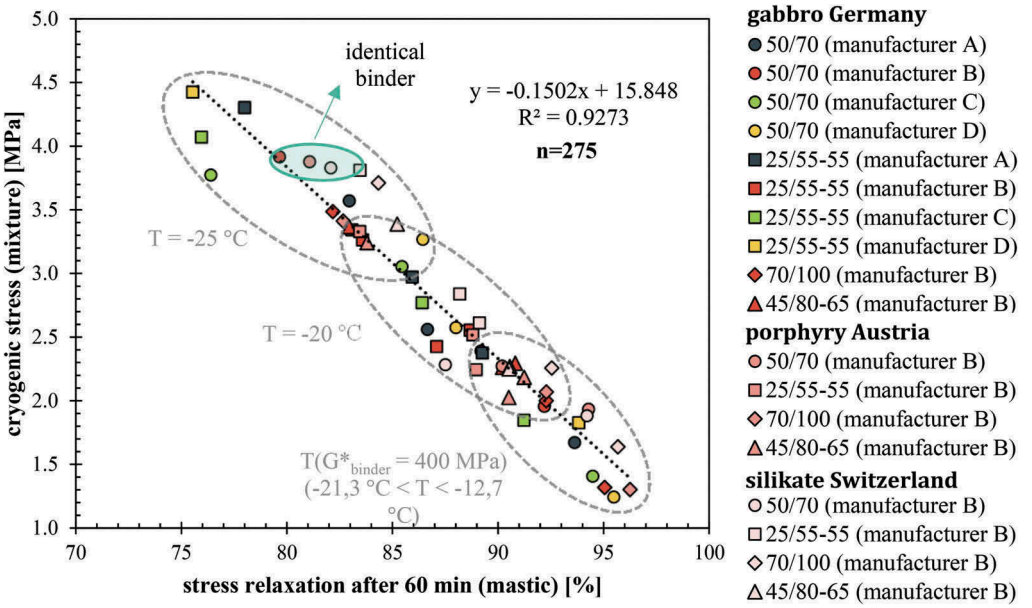

Figure 4. Correlating cryogenic stress of asphalt mixture and stress relaxation of asphalt mastic obtained from DSR relaxation test and TSTRST (Büchner, 2021).

temperature behavior. It can be observed that the relaxation capability of asphalt binder, respectively asphalt mastic, significantly influences initiation and progression of cryogenic stresses in the corresponding asphalt mixture. While asphalt mastic testing seems more suitable for differentiation, it appears that the asphalt binder and not the filler is the governing factor and there is no obvious difference between plain and polymer modified asphalt binder.

However, it needs to be noted that this study only included proficient fillers with a long experience background and very similar filler-to-binder-ratios.

5 SUMMARY AND CONCLUSIONS

In this study, a novel relaxation test is proposed for low-temperature evaluation of asphalt binder and asphalt mastic using a Dynamic Shear Rheometer (DSR) with 4 mm parallel-plate geometry. Relaxation tests at different temperatures were carried out on a set of 10 asphalt binders and 18 asphalt mastics consisting of the same binders but with varying fillers. Test results of asphalt binder and asphalt mastic relaxation tests were compared with the low-temperature performance of corresponding asphalt mixtures from Thermal Stress Restrained Specimen Tests (TSRST). The following conclusions can be made from this study:

- The percentual stress relaxation after 60 min appears as a suitable and conclusive material parameter to evaluate low-temperature behavior of asphalt binders and asphalt mastics based on a simple and fast DSR test. Different asphalt binders and asphalt mastics can be characterized based on their temperature dependent relaxation capability.
- Reasonable correlations were identified between the cryogenic stress of asphalt mixtures and the stress relaxation of corresponding asphalt binders and asphalt mastics. The low-temperature performance of asphalt mixtures seems to be significantly affected by the included asphalt binder and asphalt mastic, respectively.
- The type and quality of asphalt binder seem to have the most significant influence on low temperature performance of asphalt mixtures. Softer binders are more favorable to prevent low-temperature cracking due to their superior relaxation capability. In this context, no advantages were found for polymer-modified asphalt binders compared to plain binders.

The scope of this study is limited to one laboratory-mixed asphalt mixture type (AC 11). The results need to be validated for other mixture types with varying compositions in terms of asphalt binder and filler. Especially the effect of the type and the quantity of different fillers should be analyzed. The relaxation behavior should also be investigated in combination with aging and recycling.

ACKNOWLEDGEMENT

The authors would like to acknowledge NETZSCH-Gerätebau GmbH for providing parts of the instruments used to determine rheological material properties.

REFERENCES

Anderson, D. A., Bahia, H. U. & Dongre, R. N. 1992. *Rheological Properties of Mineral Filler-Asphalt Mastics and Its Importance to Pavement Performance*. In: Effects of Aggregates and Mineral Fillers on Asphalt Mixture Performance (Ed.: R. C. Meininger), STP/ ASTM, Vol. 1147, ASTM International, Philadelphia, Pennsylvania.

Arand, W. 1983. *Zum Einfluss tiefer Temperaturen auf das Ermüdungsverhalten von Asphalten*. Straße und Autobahn, Jahrgang 34, Heft 10, 424–431, Kirschbaum Verlag, Bonn.

Arand, W., Steinhoff, G., Eulitz, H.-J. & Milbradt, H. 1986. *Verhalten von Asphalt bei tiefen Temperaturen*, *Schlussbericht zum AIF-Forschungsvorhaben Nr. 5699*. Technische Universität Braunschweig, Institut für Straßenwesen, Fraunhofer IRB Verlag, Stuttgart.

Behnia, B., Buttlar, W. & Reis, H. 2018. *Evaluation of Low-Temperature Cracking Performance of Asphalt Pavements Using Acoustic Emission: A Review*. Applied Sciences, Vol. 8, Issue 2, Article 306. DOI: 10.3390/app8020306.

Bouldin, M. G., Dongre, R. N., Rowe, G. M., Sharrock, M. J. & Anderson, D. A. 2000. *Predicting Thermal Cracking of Pavements from Binder Properties - Theoretical Basis and Field Validation*. Journal of

the Association of Asphalt Paving Technologists, Vol. 69, 455–496, Association of Asphalt Paving Technologists (AAPT).

Büchner, J. 2021. *Prüfung von Asphaltmastix im Dynamischen Scherrheometer*. Dissertation, Technische Universität Braunschweig, Institut für Straßenwesen, Schriftenreihe Straßenwesen, Heft 38, Braunschweig. DOI: 10.24355/dbbs.084-202107151007-0.

Büchner, J., Sigwarth, T. & Wistuba, M. P. 2021. *Testing Conditions for Asphalt Binder Testing Using Dynamic Shear Rheometer with 4 mm Diameter Parallel Plate Geometry*. Braunschweig Pavement Engineering Centre (ISBS), Braunschweig. DOI: 10.24355/dbbs.084-202103181558-0.

Büchner, J. & Wistuba, M. P. 2020. *Relating Asphalt Mixture Performance to Asphalt Mastic Rheology*. Proc., 8th International Conference on Maintenance and Rehabilitation of Pavements and Technological Control (MAIREPAV9), Swiss Federal Laboratories for Material Science and Technology (Empa), July 1-3, 2020, Zurich. In: Proceedings of the 9th International Conference on Maintenance and Rehabilitation of Pavements - Mairepav9 (Ed.: C. Raab), Lecture Notes in Civil Engineering, Vol. 76, 639–649, Springer.

Büchner, J., Wistuba, M. P., Dasek, O., Staschkiewicz, M., Soenen, H., Zofka, A. & Remmler, T. 2020. Interlaboratory Study on Low Temperature Asphalt Binder Testing Using Dynamic Shear Rheometer with 4 mm Diameter Parallel Plate Geometry. Road Materials and Pavement Design, Taylor & Francis. DOI: 10.1080/14680629.2020.1851291.

Coufalík, P., Dašek, O., Kachtík, J., Kudrna, J. & Stoklásek, S. 2015. *The Stress Relaxation Of Modified Bitumens*. International Journal on Pavement Engineering & Asphalt Technology, Vol. 16, Issue 1, 66–81. DOI: 10.1515/ijpeat-2015-0004.

EN 12697-46, 2012. Bituminous mixtures - Test methods for hot mix asphalt - Part 46: Low temperature cracking and properties by uniaxial tension tests. European Committee for Standardization (CEN), Brussels.

EN 14770, 2012. Bitumen und Bitumenhaltige Bindemittel - Bestimmung des komplexen Schermoduls und des Phasenwinkels - Dynamisches Scherrheometer (DSR). Europäisches Komitee für Normung (CEN), Beuth Verlag, Berlin.

EN 14771, 2012. Bitumen and bituminous binders – Determination of the flexural creep stiffness – Bending Beam Rheometer (BBR). European Committee for Standardization (CEN), Brussels.

Gehrke, M. 2017. *Komplexe Charakterisierung bitumenhaltiger Bindemittel anhand temperatur-, frequenz- und belastungsabhängiger Kennwerte*. Dissertation, Ruhr-Universität Bochum, Lehrstuhl für Verkehrswegebau, Schriftenreihe Lehrstuhl für Verkehrswegebau, 27, Bochum.

Golalipour, A. 2020. *Asphalt Material Creep Behavior*. In: Creep Characteristics of Engineering Materials (Ed.: T. Tański), IntechOpen, London.

Gražulytė, J. 2019. Bitumen stress relaxation modulus as an indicator of asphalt pavements resistance to low temperature cracking. Dissertation, Vilniaus Gedimino technikos universiteto, Vilnius, Lithuania.

Jung, D. H. & Vinson, T. S. 1994. *Low-Temperature Cracking: Test Selection*, *SHRP-A-400*. National Research Council, Washington, D.C.

Laukkanen, O.-V. 2018. *Rheology of complex glass-forming liquids*. Aalto University pulication series, doctoral dissertations, 198, Aalto University, Helsinki.

Marasteanu, M. O., Zofka, A., Turos, M. I., Li, X., Velasquez, R., Li, X., Buttlar, W. G., Paulino, G., Braham, A., Dave, E. V., Ojo, J., Bahia, H. U., Williams, R. C., Bausano, J., Gallistel, A. & McGraw, J. 2007. *Investigation of Low Temperature Cracking in Asphalt Pavements*, *National Pooled Fund Study 776, Report No. MN/RC 2007-43*. Minnesota Department of Transportation, St. Paul, Minnesota.

Radenberg, M. & Staschkiewicz, M. 2020. Rheologische Untersuchungen zur Charakterisierung des Kälteverhaltens von bitumenhaltigen Bindemitteln mit dem Scher-Relaxationsversuch. Straße und Autobahn, Jahrgang 71, Heft 6, 479–485, Kirschbaum Verlag, Bonn.

Spiegl, M., Wistuba, M. P., Lackner, R. & Blab, R. 2005. *Risk Assessment of Low-Temperature Cracking of Asphalt - An Experimental Study*. Proc., 11th International Conference on Fracture (ICF11), Politecnico di Torino, 20-25 March, 2005, Turin, Italy.

Sui, C., Farrar, M. J., Harnsberger, P. M., Tuminello, W. H. & Turner, T. F. 2011. *New Low-Temperature Performance-Grading Method*. Transportation Research Record: Journal of the Transportation Research Board, Vol. 2207, Issue 1, 43–48, Transportation Research Board (TRB), Washington D.C. DOI: 10.3141/2207-06.

Wistuba, M. P. 2016. *The German segmented steel roller compaction method – state-of-the-art report*. International Journal of Pavement Engineering, Vol. 17, Issue 1, 81–86, Taylor & Francis. DOI: 10.1080/10298436.2014.925555.

Wistuba, M. P. 2019. *Straßenbaustoff Asphalt*. Erste Auflage, Technische Universität Braunschweig, Institut für Straßenwesen, Braunschweig, ISBN 978-3-932164-16-3.

Wistuba, M. P., Metzker, K. & Mollenhauer, K. 2009. *Assessing low temperature properties of asphalt materials by means of static testing techniques*. Proc., 8th International Conference on the Bearing Capacity of Roads, Railways and Airfields, University of Illinois at Urbana-Champaign, June 29 - July 2, 2009, Champaign, Illinois (Eds.: E. Tutumluer, I. L. Al-Qadi), 327–337.

Xing, B., Fan, W., Lyu, Y., Che, J. & Zhuang, C. 2020. *Influences of ball-milled limestone particle sizes and shapes on asphalt mastic stress relaxation behavior*. Construction and Building Materials, Vol. 255, Paper 119396, Elsevier. DOI: 10.1016/j.conbuildmat.2020.119396.

Eleventh International Conference on the Bearing Capacity of Roads, Railways and Airfields, Volume 2 – Hoff, Mork & Saba (eds)

Modeling the loading behavior of railway structure under static load using a verified 3D finite element model

M. Peltomäki, P. Kolisoja & H. Luomala
Research Centre Terra, Tampere University, Tampere, Finland

ABSTRACT: When trying to optimize the life-cycle behavior of railway structures it is important to identify the main deformation factors of the structure and to understand the influence mechanisms behind these. Due to the complex behavior of railway structures, powerful numerical tools are needed to get realistic simulation results. Therefore, the focus of this study has been to create a three-dimensional finite element model to simulate the loading behavior of railway structures under static load using non-linear material models. The model is verified using measured field data from heavily instrumented test structures. The calculations mainly focus on the behavior of railway embankments of different subgrade stiffness and axel load levels. It is shown that subgrade stiffness seems to have a major role on the behavior of railway structures, whereas the influence of the axel load seems to be fairly linear.

Keywords: FEM, railway, verification, modeling

1 INTRODUCTION

To optimize the technical performance of a track structure, it is important to recognize the factors influencing the loading behavior of the structure and to understand the underlying mechanics behind these. The use of numerical simulation tools makes it possible not only to study arbitrary structures, but also to analyze the behavior of different structures at a detailed level. However, to ensure the validity of the calculated results, the importance of model verification is emphasized when a theoretical approach is used.

Historically, Winkler's classical BOEF theory (Beam on Elastic Foundation) presented in 1867, can be considered as a starting point for modeling the loading behavior of a track structure. Based on Winkler's work, Hetényi created one of the earliest mathematical models of a ballasted railway track in 1946 to describe the deflection behavior of a rail on an elastic foundation. Later in the 1970s, various structural modeling software based on multilayer theory (e.g., GEOTRACK, ILLITRACK) started to become more common (Selig & Waters 1994; Robnett et al. 1975).

With the increase in the computing power of computers and the number of suitable modeling software, the element method has now become one of the key numerical tools in railway structure research and various 3D element method-based calculation models have been presented by different researchers. For example, Gallego et al. (2011) found that subgrade stiffness plays a key role in the overall stiffness of the structure - a similar observation has been made by Sowmiya et al. (2010) and Ganesh Babu & Sujatha (2010). In turn, Kalliainen et al. (2016) conducted a parametric study using nonlinear material models and found that the subgrade stiffness, structural layers thickness, and material properties, are the most significant factors affecting the load carrying capacity of a railway track. Also, detailed 3D FE-models

DOI: 10.1201/9781003222897-48

have been used to analyze the internal stress distribution in the structure (e.g., Powrie et al. (2007), Varadas et al. (2016)). Alongside static models, some researchers have also used dynamic models to estimate the loading effects of high-speed trains (e.g., Shahraki et al. 2014, Sayeed (2016)).

However, most existing models are based on simple linear elastic theory, in which the stress-dependency of strength and stiffness characteristic of granular materials is not considered. Also, the verification of the models could be considered deficient in some respects. Therefore, the aim of this study has been to create and verify a non-linear 3D FEM model to describe the stress-strain response of a railway structure. The model has been created using Plaxis 3D software (version 2017) and the verification uses versatile field measurement data from two heavily instrumented test structures.

2 MATERIAL MODELS AND CALCULATION PHASES

In the modeling method used, the calculation includes two phases; in the first phase, the model calculates the displacement and stress field due to its own weight for the structure. Then, in the second and actual calculation phase, the external load is activated, and the final results are calculated. The basic idea is that the model is parameterized in such a way that its primary static loading behavior corresponds to the resilient behavior of the real structure, which is hardened under several thousands of load cycles. However, mathematically the behavior of the model is plastic, so such an approach is valid only to describe the stress-strain response caused by a single load cycle. In the model, the isotopically hardening Hardening Soil material model (HS-model) has been used for the granular structural layers – The HS-model has also been used in many previous ballasted track-related studies (e.g. Indraratna & Nimbaikar 2013, Shahraki et al. 2014). In the HS-model, material stiffness depends on the minor principal stress σ_3 and in primary loading stiffness corresponds to the secant modulus E_{50} (Plaxis 2017):

$$E_{50} = E_{50\,ref.}\left(\frac{c' \cdot \coth\varphi + \sigma_3}{c' \cdot \coth\varphi + \sigma_0}\right)^m \tag{1}$$

where $E_{50\,ref.}$ is the reference modulus, m is the stiffness exponent, σ_0 is the reference pressure used in the calculation (= 100 kPa), φ is the friction angle and c' is the cohesion (Plaxis 2017). In practice, the secant modulus determines the secant line slope that intersects the stress-strain curve through a point corresponding to 50% of the failure stress. The basic idea of the formulation of the HS-model is the hyperbolic relationship between primary strain and deviatoric stress in primary triaxial loading Hence, in a standard drained triaxial test, the relationship between primary strain ε_1 and stress state can be described by using the equation 2:

$$\varepsilon_1 = -\frac{2 - R_f}{2E_{50}}\frac{q}{1 - R_f q/q_f} \tag{2}$$

where q_f is the deviator stress corresponding to the failure state. In its original application, parameter R_f determines the shape of the yield curve at the plastic state and it can have values between 0 and 1. For natural sands, R_f has been found to be about 0.9 during virgin loading. However, in this study R_f describes the shape of the loading side of the hysteresis loop of already hardened soil material, and therefore the used values are slightly smaller than usual.

For the subsoil and superstructure components a linear elastic material model has been used, in which case the relationship between the stress and strains can be directly described by the elastic modulus E and Poisson's ration v of the material (Plaxis 2017). The material model of subsoil layers has been deliberately kept as simple as possible, allowing an unambiguous assessment of the effects of subsoil conditions in terms of the stress-strain behavior of the upper railway structure.

3 CALCULATION PARAMETERS

3.1 *Rails, sleepers, and interfaces*

In the created calculation model, the rails are modelled using one-dimensional beam elements and the calculation parameters used correspond to the 60E1 rail profile (SFS-EN 13674-1:2011); therefore value 210 GPa has been used as the modulus of elasticity of the rail steel, the rail cross section area is 0,00767 m^2 and the second moments of cross section area are $3.055 \cdot 10^{-5}$ m^4 for the vertical bending and $5.120 \cdot 10^{-6}$ m^4 for the horizontal bending.

The geometry of the modeled sleeper is based on the geometry of the B97 concrete sleeper with certain simplifications. The sleeper is modeled as a linear elastic material with an elastic modulus of 40 GPa and a Poisson's ratio of 0.15. In order for the sleeper to be able to move freely, all sides are separated from the surrounding ballast layer by interface elements. A contact factor of 0.01 has been used for the interface elements of the sleeper sides, whereby the shear strength and stiffness between sleeper and ballast is only one percent of the strength and stiffness of the surrounding ballast material - a more detailed mathematical description of the interface elements can be found in Plaxis (2017 b).

On flexible subsoils, the sleeper distributes most of its load through its ends when the underlying structure bends under the stiff sleeper. However, in this case, the deformation caused by the number of load cycles is mainly concentrated in the ends of the sleeper, causing a change in the sleeper support. To consider changing the support situation under train traffic, the interface elements between the sleeper and the underlying ballast layer are divided into several parts, in which case uneven support can be taken into account by changing the interface contact factors. Based on calculations, the contact factor distribution 0.33, 0.5 and 0.65 at the bottom of the sleeper (direction from the end of the sleeper to the center) proved to be a very good option. In this case, most of the load is transmitted directly through the contact area below the rail, without the discontinuous interface distribution causing unrealistically large node-specific load concentrations at the edges of the different interface areas.

3.2 *Ballast-layer and substructure*

As mentioned above, the ballast layer and substructure have been modeled using the Hardening Soil material model. The HS-model uses a linear Morh Coulumb yield criterion, in which the maximum shear stress of the material can be described by using the friction angle φ and the cohesion c. However, the ballast shear strength has been found to be a nonlinear stress-dependent quantity (Indraratna et al. 2011) and therefore the determination of the constant friction angle and cohesion term is not entirely unambiguous. The calculation parameters used for the ballast are based on the sources of Skoglund (2002), Suiker et al. (2005) Nurmikolu & Kolisoja (2010) Indraratna et al. (2011) and Kolos et al. (2017). Thus, it has been

Table 1. Material parameters used in FE modelling.

	y	E	E_oed	E_ur	v_ur	m	c'	ϕ	φ	R_f	K_0
	[kN/m^3]	*[MPa]*	*[MPa]*	*[MPa]*	*[-]*	*[-]*	*[kPa]*	*[°]*	*[°]*	*[-]*	*[-]*
Koria-Kouvola-model											
New ballast	17	420	420	840	0,2	0,65	5	53	18	0,5	0,35
Old ballast	18	400	365	800	0,2	0,7	4	50	17	0,5	0,35
Coarse sand	20	270	270	540	0,2	0,35	4	44,5	13	0,6	0,37
Gravel	19,5	475	475	950	0,2	0,5	3	51	17	0,55	0,35
Pori-Mäntyluoto-model											
Ballast layer	17	380	380	760	0,2	0,6	6	52	18	0,5	0,35
Fine sand	19,5	240	240	480	0,2	0,5	1	37	6	0,6	0,40

decided to use a friction angle of 50–53 ° and cohesion values of 4–6 kPa as the ballast layer strength parameters - other ballast parameters are listed in Table 1. The substructure calculation parameters of the Koria-Kouvola verification model are based on the laboratory test results reported by Kolisoja et al. (2000). In other respects, references Kolisoja (1997), Suiker et al. (2005) and Duncan et al. (2014) have been used to determine other parameters for the substructure layers. All calculation parameters are listed in Table 1.

4 TEST STRUCTURES AND VERIFICATION MODELS

Measurement data from two different test structures have been used to verify the calculation model. The first verification structure is in Eastern Finland on the double-track Koria-Kouvola line section. This test structure is characterized by a thick ballast layer with a total thickness of 1.2 meters, consisting of an upper 0.6-meter-thick new ballast layer and a lower 0.6-meter-thick old ballast layer. The total thickness of the test structure is 2.4 m, and the 1.2 m thick substructure consists of a 0.8 m thick layer of coarse-grained sand and a 0.4 m thick layer of gravel located on the surface of the subsoil. Sensors measuring vertical stress and strain are placed in the structure at different distances from the elevation line (el); el-0.7 m, el-1.3 m and el-2.0 m. Also, sensors measuring horizontal strains have been installed at heights el-0.7 m and el-1.3 m. The vertical displacements of the structure have been measured at three different points from the sleeper: at both ends and in the middle.

The second test structure is located in western Finland on the Pori-Mäntyluoto line section, a single-track section with a total thickness of 1.1 meters. The ballast layer of the structure is 0.5 meters thick, and the substructure consists of a 0.6-meter-thick fine-grained sand layer. Vertical, longitudinal, and transverse earth pressures have been measured below the sleeper from two different depths: from the upper part of the substructure layer (0.4 meters from the bottom of the sleeper) and from the lower part of the substructure layer (0.7 meters from the bottom of the sleeper) - a total of six different pressure sensors are installed in the substructure. Also, the vertical displacements of the structure have been measured from three different depths: from the top of the sleeper, elevation line -1.0 m and elevation line -1.5 m.

The geometry of the verification models is shown in Figure 1. The total length of the Koria-Kouvola calculation model is 36.8 meters, whereas the Pori-Mäntyluoto model is 48.8 meters long. The total width of both models is 30 meters, and the external load consists of three wagons. The thickness of the subsoil of the Koria-Kouvola verification model is 5 meters and its modulus of elasticity has a constant value of 56 MPa, while subsoil-layer Poisson's ration is 0.2. In the Pori-Mäntyluoto verification model, the subsoil is divided into two layers based on the Swedish weight sounding results; For a 2.2 m thick clay layer with an initial modulus of 50 MPa and a lower 3-meter-thick sand layer with an initial modulus of 100 MPa. The stiffness of the upper subsoil is assumed to increase linearly with respect to depth by 5 MPa per meter and the stiffness of the lower layer by 10 MPa per meter. A constant Poisson's ratio of 0.2 has been used for both subsoil layers.

Due to the lack of more accurate information, the loading diagram used in the Koria-Kouvola verification model used a bogie wheelbase spacing of 1.8 meters and a bogie spacing of 5.4 meters. The length of one train carriage in the calculation model is 10.8 meters, while the distance of the bogies of successive carriages is 1.8 meters. In turn, the test train at the Pori-Mäntyluoto site consisted of VOK-wagons with an axle weight of 20–22 tones (total wagon length 13.92 meters, bogie spacing 8.55 meters and bogie wheelbase 1.8 meters). A dense element mesh has been used in both models; the total number of elements in the Koria-Kouvola model is about 500,000 and, in the Pori-Mäntyluoto model about 350,000. A three-nobe beam elements have been used in the modeling of the rails and 10-nobe tetrahedral elements to modeling of the volume elements (more detailed mathematical description of the elements can be found in source Plaxis 2017 c).

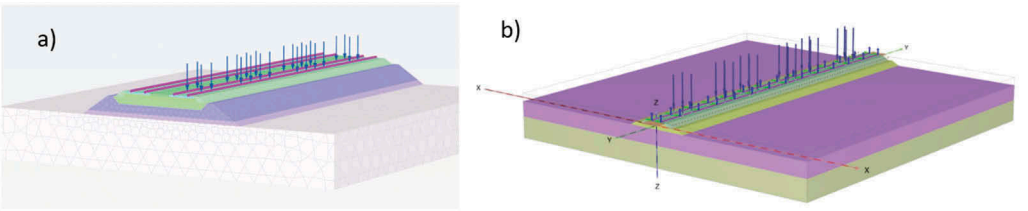

Figure 1. Koria-Kouvola FE-model (a) and Pori-Mäntyluoto FE-model (b).

5 VERIFICATION CALCULATIONS

5.1 *Koria-Kouvola*

Figure 2 shows the calculated and measured values of vertical stress increase, vertical and transverse strains, and vertical displacements of the sleeper under an axle load of 250 kN. According to the results, the modeling results seem to correspond to the behavior of the test structure very well. Only the calculated vertical stress level increase at a depth of 1.1 meters from the bottom of the sleeper is about 20% higher than the measured value. Correspondingly the model slightly underestimates the horizontal compression of the embankment material.

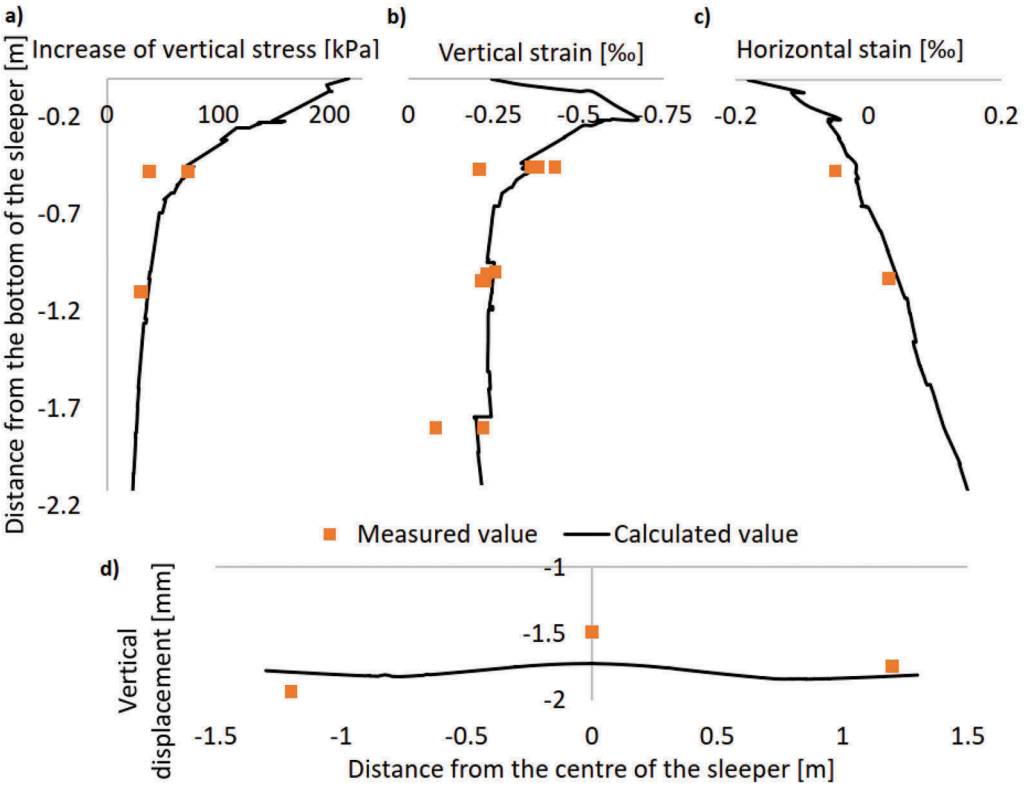

Figure 2. Measured and calculated vertical stress increments (a), vertical strains (b), horizontal strains (c) and vertical displacements of the sleeper (d).

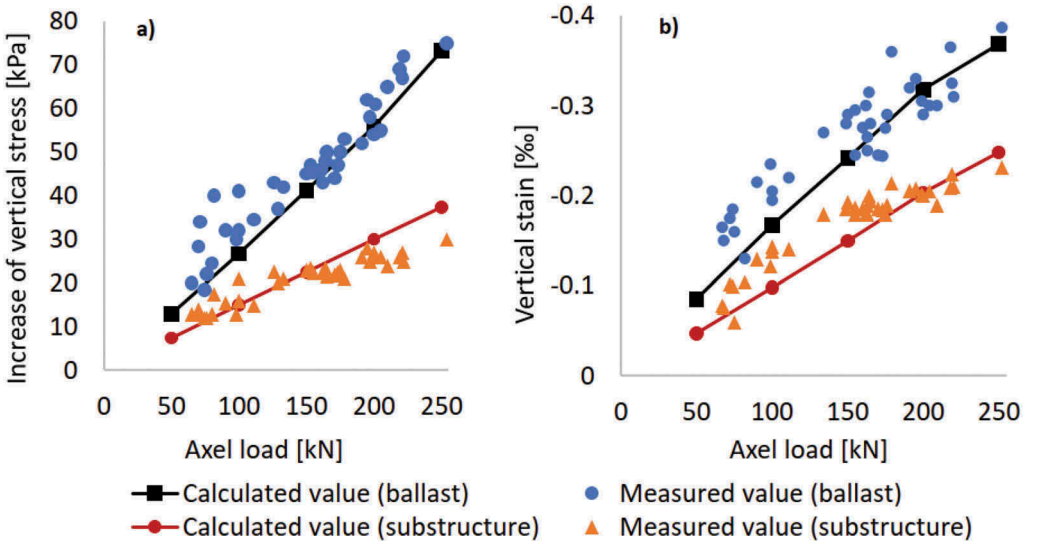

Figure 3. Measured and calculated vertical stress increases (a) and vertical strains (b) at different axel load levels.

Figure 3 shows the measured and calculated vertical stress and vertical strain levels at different axle loads at two different depths (el-0.7 m and el-1.3 m). At low load levels, the calculation model slightly underestimates the compression of the material, but in general the calculated values can be considered to correspond very well to the measured values - especially given the differences in load diagrams for vehicles with different axle loads.

As shown in Figure 3, the effect of axle load on the stress-strain response of the structure appears to be quite linear. For example, in the case of the Koria-Kouvola verification model, the vertical stress increase due to external axel load as a function of depth, can be described very accurately using the four-parameter approximation equation:

$$\sigma_{ZZ} = \frac{Q}{250}\left[\frac{180}{e^{\frac{z}{0,33}}} + \frac{43}{1+\frac{z}{2,29}}\right] \tag{3}$$

where Q is the axle load to be used (unit kN) and z is distance from the bottom of the sleeper (as meters). Equation 3 produces an excellent 0.9948 correlation with the modeling results (five different axle weight levels, 645 observation points). However, it should be noted that Equation 3 is intended to be used primarily on medium-rigid subgrades (E = 40 - 80 MPa) - on stiffer substrates it may underestimate the stress level of the structure. Also, if the load diagram significantly differs from the one used in the Koria-Kouvola model, the shape of the load distribution may slightly differ from the prediction of Equation 3.

5.2 *Pori-Mäntyluoto*

Figure 4 shows the measured and calculated vertical stress increments under the overrun of a test train with an axle weight of 208 kN. For the vertical stress increase in the upper substructure layer, the calculated and measured stress profiles are quite similar, but in the deeper structure, the calculation model slightly overestimates the stress increase under the bogie overrun. However, the measured and modeled longitudinal and transverse stress increment profiles in the lower substructure are very closely matched (Figure 5).

Figure 6 shows the measured and calculated vertical displacement profiles under the test train overrun. In general, the model corresponds very well to measured values of vertical displacements, especially the vertical displacements of the sleeper. Compared to the vertical displacement profile measured in the deeper structure, the calculation model slightly overestimates the structure displacement levels between the axles and the bogies, however, the magnitude of the maximum displacements under the axles is correct. In general, the calculated values can be found to correspond very well to the measurement results.

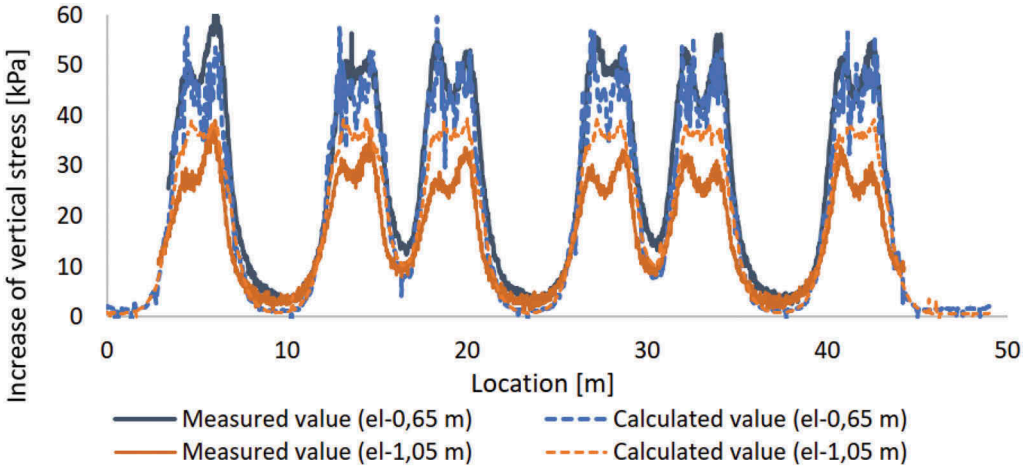

Figure 4. Calculated and measured vertical stress changes at two different depths (el-0.65 m and el-1.05 m).

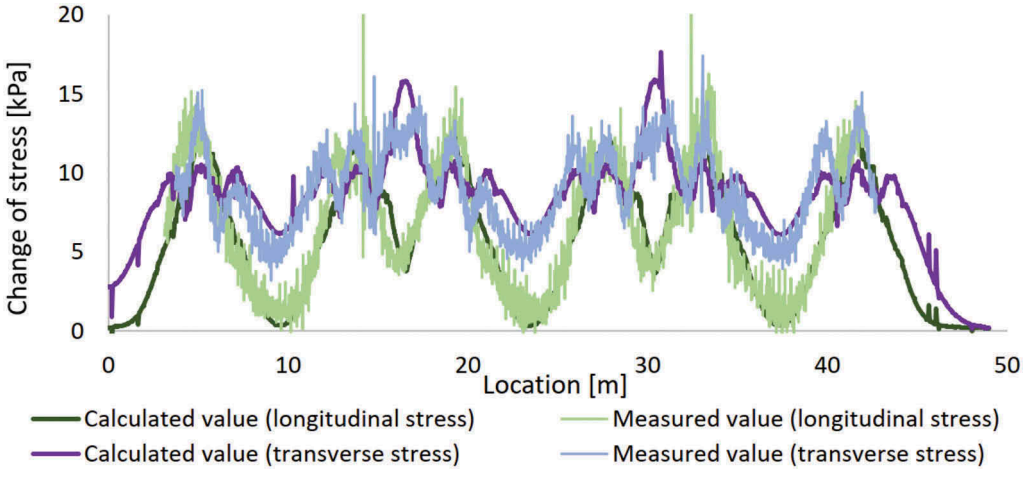

Figure 5. Calculated and measured longitudinal and transverse stress changes (at depth el-1.05 m).

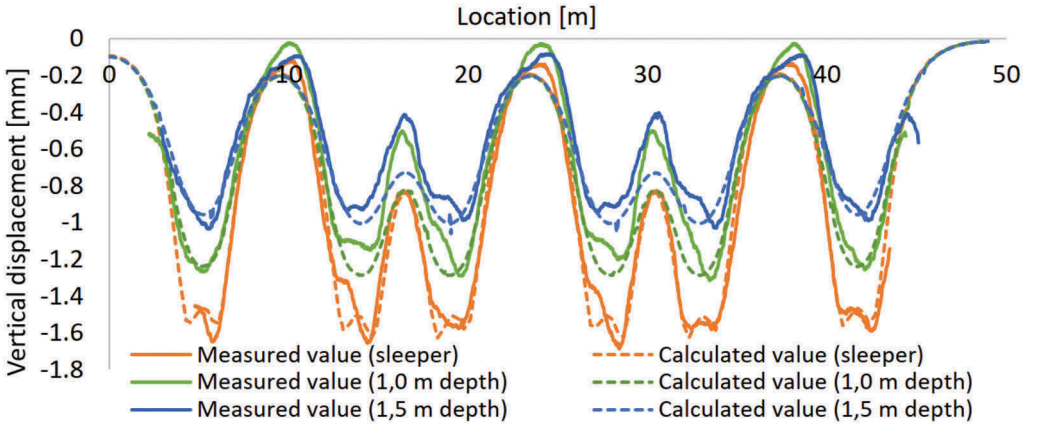

Figure 6. Measured and calculated vertical displacements at three different depths.

6 THE EFFECT OF SUBGRADE STIFFNESS

To illustrate the significance of subsoil conditions, a simulation series of six calculations was performed in which the modulus of subgrade stiffness was varied while its Poisson's ratio remained ration at 0.2. The two-meter substructure thickness and the material parameters of the Pori-Mäntyluoto verification model were used in the calculation. The subgrade consists of a single 5 m thick linear elastic layer with a constant modulus of elasticity. An axle load of 250 kN has been used in all calculations and the loading diagram is similar as in the Koria-Kouvola verification model.

Based on their miniature embankment experiments, carried out in laboratory conditions, Kalliainen & Kolisoja (2013) found that subgrade stiffness plays a key role in terms of the deterioration rate of the embankment geometry; when the deformations are large enough, the individual grains will no longer be able to return to their original position after the external loading has been removed. Figure 7a shows results on the computational effect of subgrade stiffness on the deformation level of the structure. When moving to flexible subgrades, the deformation level increases rapidly - especially in the upper part of the substructure. If the deviatoric strains are presented as a function of the vertical displacement of the sleeper, the trend is almost linear (Figure 7b). In flexible subgrades, deformations are typically large throughout the structure; when the subsoil deflects, the structure above must follow.

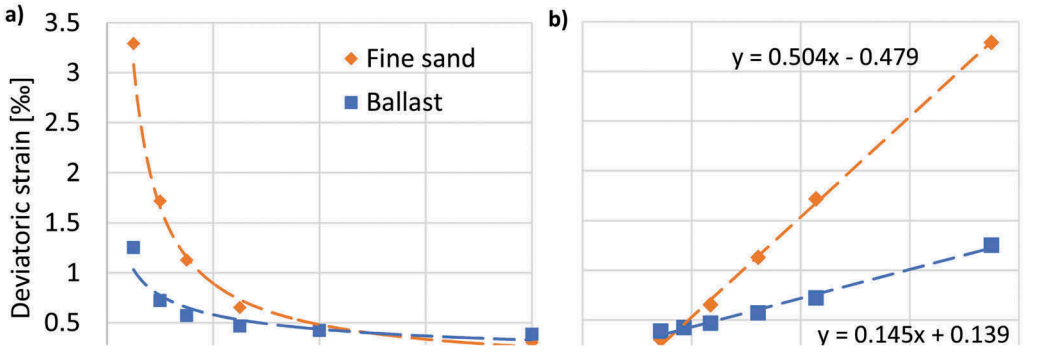

Figure 7. Deviator strains of the ballast layer and the upper part of the substructure as a function of subgrade stiffness (a) and as a function of vertical displacement of the sleeper (b).

7 CONCLUSIONS

1. In this study, a full-scale 3D computational model was created to examine the static stress-strain response of a railway structure using the finite element method. Comprehensive measurement data from two different test sites were used to verify the model, and data available from laboratory experiments were extensively utilized in the model parameterization. Based on the verification calculations performed, the calculation model corresponds very well in overall to the test structures in its behavior.
2. Based on calculations and field measurements, the effect of axle weight on the behavior of the structure appears to be quite linear. Based on the calculation results, a simple fitting model (Equation 3) was developed for estimating the stress level of the structure at different depths, producing an excellent correlation with the modeling results.
3. The subgrade stiffness seems to be the single most important factor in terms of the deviatoric strain levels of the structure - with flexible subgrades, the deformations are typically large throughout the structure. In practice, the strain levels of railway structure increase almost linearly as a function of subsoil deflection, which partly explains the relationship between the measured track stiffness and the rate of geometry deterioration.

ACKNOWLEDGMENTS

The authors gratefully acknowledge the Finnish Transport Infrastructure Agency for funding the study.

REFERENCES

Duncan J. M., Wriqht S. G., Brandon T. L. (2014). Soil strength and slope stability. John Wiley & Sons, Inc., Hoboken, New Jersey.

Gallego I., Muñoz J., Rivas A., Sánchez-Cambronero S. (2011). Vertical Track Stiffness as a New Parameter Involved in Designing High-Speed Railway Infrastructure. J. Transp. Eng., 2011, 137(12): 971–979.

Ganesh Babu K, Sujatha C (2010) Track modulus analysis of railway track system using finite element model. J Vib Control 16(10):1559–1574.

Hetényi, M. (1946). Beams on elastic foundation. Theory with applications in the fields of civil and mechanical engineering, The University of Michigan Press, Ann Arbor, 1946

Indraratna B., Nimbaikar S. (2013). Stress-strain degradation response of railway ballast stabilized with geosynthetics. J. Geotech. Geoenviron. Eng. 2013.139:684–700.

Indraratna B., Salim W., Rujikiatkamjorn C. (2011). Advanced Rail Geotechnology – Ballasted Track.

Kalliainen A & Kolisoja P. (2013). Modelling of the effect of embankment dimensions on the mechanical behaviour of railway track. (In Finnish) Finnish Transport Agency, Infrastructure and the Environment. Helsinki 2013. Research reports of the Finnish Transport Agency 33/2013. 85 pages and 2 appendices.

Kalliainen A, Kolisoja P, Nurmikolu A (2016) 3D finite element model as a tool for analysing the structural behaviour of a railway track. Procedia Eng 143:820–827

Kolisoja P. (1997). Resilient Deformation Characteristics of Granular Materials. Tampere University of Technology, Tampere.

Kolisoja P., Järvenpää I., Mäkelä E., Levomäki M. (2000) Instrumentation and Modelling of Track Structure, 250 kN and 300 kN axel loads. (In Finnish) Publications of Finnish Rail Administration. A5/2000. Finnish Rail Administration, Technical Unit. Helsinki 2000. 137 pp. + 15 app.

Kolos A., Konon A., Chistyakov P. (2017). Change of ballast strength properties during particles abrasive wear. Transportation Geotechnics and Geoecology, TGG 2017, 17-19 May 2017, Saint Petersburg, Russia.

Nurmikolu A. & Kolisoja P. (2010). Effects of ballast cleaning on the properties of railway ballast. (In Finnish) Finnish Transport Agency, Railway Department. Helsinki 2010. Research reports of the Finnish Transport Agency 11/2010. 64 pages and 3 appendices.

Plaxis. (2017). Plaxis Material Models Manual.

Plaxis (2017 b). Plaxis 3D Reference Manual.

Plaxis (2017 c). Plaxis Scientific Manual.
Powrie W, Yang L, Clayton CR (2007) Stress changes in the ground below ballasted railway track during train passage. Proc Inst Mech Eng Part F J Rail Rapid Transit 221(2):247–262.
Robnett, Q.L., Thompsom, M.R., Knutson, R.M. & Tayabji, S.D. (1975). Development of a structural model and materials evaluation procedures. Ballast and Foundation Materials Research Program, University of Illinois, report to FRA of US/DOT, Report No. DOT-FR.30038, May.
Sayeed A. (2016). Design of Ballasted Railway Track Foundations using Numerical Modelling with Special Reference to High Speed Trains. PhD thesis of Curtin University, Department of Civil Engineering.
Selig, E. T. & Waters, J. M. (1994). Track geotechnology and substructure management. London, Thomas Telford Publications. 407 p.
SFS-EN 13674-1:2011 + A1:2017 (2017). Railway applications. Track. Rail. Part 1: Vignole railway rails 46 kg/m and above.
Shahraki M., Salehi M., Witt K. J., Meier T. (2014). 3D Modelling of Train Induced Moving Loads on an Embankment. Plaxis Bulletin, Autumn issue 2014.
Skoglund K. A. (2002). A Study of Some Factors in Mechanistic Railway Track Design. Phd-thesis. Department of Road and Railway Engineering, Norwegian University of Science and Technology NTNU, Trondheim.
Sowmiya, L.S. Shahu, J.T. Gupta, K.K. (2010). Three-Dimensional Finite Element Analysis of Railway Track. Indian Geotechnical Conference – 2010, GEOtrendz December 16 –18, 2010.
Suiker, A. S. J., Selig, E. T., and Frenkel, R. (2005). "Static and cyclic triaxial testing of ballast and subballast." J. Geotech. Geoenviron. Engng., 131(6),771–782.
Varandas J. N., Paixão A., Fortunato E., Hölscher P. (2016). A Numerical Study on the Stress Changes in the Ballast due to Train Passages. Advances in Transportation Geotechnics 3. The 3rd International Conference on Transportation Geotechnics (ICTG 2016). 143: 1169–1176.
Winkler, e. (1867). Die lehere vonder Elastizität und Festikeit: Verlag H.Dominicus 1867.

Eleventh International Conference on the Bearing Capacity of Roads, Railways and Airfields, Volume 2 – Hoff, Mork & Saba (eds)

Performance evaluation of composite pavements on Mississippi highways via machine learning

R. Barros, H. Yasarer & Y.M. Najjar
Department of Civil Engineering, University of Mississippi, Oxford, Mississippi, USA

ABSTRACT: Local, state, and federal highway agencies run some form of maintenance and rehabilitation program during the design life of highways. Due to budgetary restrictions, maintenance and rehabilitation actions must be prioritized based on the future condition of the highway section. There are important factors that affect the performance of highways. To properly assess the condition of the pavement and operate maintenance, prediction models with significant condition variables are essential. Mississippi Department of Transportation (MDOT) utilizes probability-based prediction models to determine which sections of the highway and when they need rehabilitation. The current probability models predict the performance without the section-specific parameters. The goal of this study is to develop a new set of performance prediction models for the composite Pavements in Mississippi by using machine learning. The best-performing model can be used as a simple and user-friendly tool to allow the user to visualize the future projections of the pavement section. MDOT personnel can employ this application to predict the condition of the composite pavement section and prioritize the maintenance and rehabilitation schedule.

Keywords: Artificial Neural Network (ANN), machine learning, Mississippi Department of Transportation (MDOT), pavement performance, composite pavement

1 INTRODUCTION

Road networks are one of the largest public infrastructure assets of a country, they provide public mobility and freight transport to secure the nation's economy and prosperity (Sultana et al. 2021). Annually, transportation agencies spend billions of dollars for the maintenance and rehabilitation (M&R) of their road networks. One of the most difficult tasks for state transportation agencies, such as the Mississippi Department of Transportation (MDOT), is to maintain roads and highways in acceptable conditions to meet the public's needs and safety concerns (Tennant Duckworth 2020). If timely M&R is not performed, it may lead the pavement to poor conditions, causing an uncomfortable ride experience for road users (Barros et al. 2021a). To assess pavement surface condition and ride quality, Performance Condition Rating (PCR) and International Roughness Index (IRI) are the two widely used measures worldwide. Pavement performance models assist agencies to predict how a pavement deteriorates over time due to traffic, environmental conditions, and M&R history, being an important part of the pavement management system (PMS). The use of prediction models allows decision-makers to develop a better budget allocation plan and M&R schedule (Barros et al. 2022).

Flexible and rigid pavements are the main concern of most studies in the literature. However, a portion of the paved surfaces is comprised of composite pavements, which are made of an asphalt overlay on concrete pavements (Barros et al. 2021b). When concrete pavements

DOI: 10.1201/9781003222897-49

start to fail, they are overlaid with a layer of a hot mix of asphalt (HMA) to provide better levels of performance being a more cost-effective alternative (Chen et al. 2015). Although a PMS includes all types of pavements, the study of composite pavements has not been well investigated in the literature, which is the focus of this paper.

A growing body of studies has been exploring several modeling techniques and variables to reach accurate predictions. The use of an Artificial Neural Network (ANNs) technique has shown significant improvements over traditional methods, such as regression, by processing large volumes of data with a higher degree of accuracy. However, present pavement performance prediction models did not account for the influence of some essential parameters such as pavement design, rehabilitation interventions, and traffic in the model development, which affects the accuracy of the predictions (Barros et al. 2021b).

In this study, composite pavement performance models were developed for the Mississippi road network using the ANN approach to predict the future condition of pavement sections incorporating the influence of pavement structure and design, traffic, and M&R interventions. The data used for this project was provided by the MDOT, and only data collected between 2010 and 2020 were analyzed. Several models were created to predict PCR and IRI. Over time, this model can be improved further in the future for the prediction of pavement conditions as more data is accurately measured and added to the existing database.

1.1 *Objectives*

The major objectives of this paper are to:

(1) Analyze data for composite pavement sections in the MDOT database.
(2) Use the ANN technique to develop performance models for composite pavements in the MDOT database using different independent variables.
(3) Evaluate the accuracy of the developed models using statistical measurements to identify the most accurate model.

2 LITERATURE REVIEW

There has been an increased interest in the use of machine learning approaches in different fields of engineering. Several types of machine learning algorithms have been developed and used to process large volumes of data with high degrees of accuracy, handle noisy and complex data, solve non-linear problems, and once trained, make predictions and generalizations at any time. The machine learning techniques hold significant potential for building a modern and robust pavement system management due to the excellence in automation and pattern recognition (Bashar and Torres-Machi 2021; Darko et al. 2020). The literature review shows that ANN is not only one of the first machine learning techniques to be used, but also the most used technique in civil and pavement engineering (Adeli 2001; Ceylan et al. 2014). The ANN method attempts to emulate the structure and/or functional aspects of biological neural networks (Yasarer 2010). Complex relationships that are difficult to reproduce using traditional sequential, logic-based modeling and computation technics can be successfully represented by neural networks. However, the accuracy of ANN models depends on the accuracy of the database used to train the neural network.

Several studies have used ANN to predict pavement performance. Prediction of IRI values for flexible pavements in the wet freeze region and rigid pavements in the wet non-freeze region of the Long-Term Pavement Performance (LTPP) database achieved reasonable accuracy for both short-term and long-term predictions(Hossain et al. 2020, 2019). Models for Jointed Plain Concrete Pavement (JPCP), Jointed Reinforced Concrete Pavement (JRCP), and Continuously Reinforced Concrete Pavement (CRCP) were developed with a high degree of accuracy presenting better accuracy compared to models that currently use mechanistic-empirical pavement design or multiple regression (Sultana 2021). ANNs were also used to predict pavement performance of flexible and rigid roads in Mississippi achieving satisfactory

results (Duckworth et al. 2022; Yasarer and Andrews 2021). Because machine learning has a data-driven approach, PCR and IRI appear as suitable indicators for modeling, as they are widely available in pavement databases and known as one of the most common indicators for pavement performance evaluation.

3 MODEL DEVELOPMENT

3.1 *Methodology*

The database for the ANN model development is obtained after cleansing and reorganizing the raw data files. Due to new data acquisition methods, materials, and tools used by the MDOT, only data collected from 2010 to 2020 are included in the model development. Sections with missing or illogical data have been excluded as the ANN model development process needs a complete dataset. Each section is comprised of five different datasets based on PCR, IRI, and rehabilitation actions. In Mississippi, the distress data is collected every even year. To develop prediction models that are applicable for a 1-year increment, the odd year data was needed to be generated by averaging consecutive years from 2010 to 2020 (Tennant Duckworth 2020; Yasarer et al. 2020). The sections of the roads with JCP varied in length from 0.04 miles to 15.9 miles and includes variables such as beginning and ending latitudes and longitudes, the thickness of pavement layer, initial PCR, initial IRI, minor and major rehabilitation, and traffic. The pavement age was included in the model development.

MDOT conducts a survey to monitor the actual condition of Mississippi roads every two years. A database was generated with all data collected over the years and combined to develop the performance prediction model for composite pavements. Additional information regarding maintenance and rehabilitation history were also incorporated into the model's database. An independent variable is added to indicate that an M&R was performed on a particular section so it can be utilized in the performance model. By doing this, the ANN can learn the effect of a maintenance and rehabilitation intervention in the pavement section and provide more accurate PCR and IRI predictions. However, the MDOT did not keep track of all rehabilitation actions and for this reason, they were assigned based on a few criteria. Improvement of PCR and IRI values without any rehabilitation action was considered irrational. Some uncertainty due to the calibration of the profilometer, systematic errors, and the environmental conditions on the day of the survey may have resulted in some of the irrational condition measures. To incorporate the effect of the rehabilitation on PCR and IRI, artificial rehabilitation actions based on the significant changes in PCR and IRI have been assigned to the database (Yasarer et al. 2020). Threshold values for PCR and IRI were assigned based on the evaluation of data history. If PCR increased 8% to 12% and IRI decreased 5% to 16% in a year compared to the previous measurement, a minor rehabilitation was assumed to take place in that year. If PCR increased above 12% and IRI decreased more than 16%, a major rehabilitation was assumed. If none of these situations occurred, it was assumed no rehabilitation.

3.2 *ANN development*

This study uses a feedforward neural network with a back-propagation training algorithm for the development of the performance prediction model. A one hidden layer network was considered in the model development, as the use of more than one hidden layer may cause the network to memorize the data in the training phase (Yasarer 2010). For the development of the composite performance models 10,305 data points from 1,145 pavement sections throughout the state of Mississippi were used. In this study, the TR-SEQ1 computer program (Najjar 1999) was used to develop the ANN models. A total of three different models have been developed by changing selected variables to identify the optimum model. For each of the three models that were created for this study, one network was chosen to be the best performing using three statistical measures.

3.3 *ANN model architecture*

For this paper, three models were developed using different independent variables and PCR and IRI as dependent variables. Table 1 shows the variables used for each ANN model.

Table 1. Independent and dependent variables configuration for three ANN models.

Models	Model 1	Model 2	Model 3
Independent Variables	Begin Lat.	Begin Lat.	Begin Lat.
	Begin Long.	Begin Long.	Begin Long.
	End Lat.	End Lat.	End Lat.
	End Long.	End Long.	End Long.
	Thickness	Thickness	Thickness
	Length	Length	Length
	Age in 2010	Age in 2010	Age in 2010
	PCR in 2010	PCR in 2010	PCR in 2010
	IRI in 2010	IRI in 2010	IRI in 2010
	Time (t)	Time (t)	Time (t)
	Drainage	Drainage	Drainage
		Minor Rehabilitation	Minor Rehabilitation
		Major Rehabilitation	Major Rehabilitation
			ESAL
	PRE PCR	PRE PCR	PRE PCR
	PRE IRI	PRE IRI	PRE IRI
Dependent Variables	Complementary PCR	Complementary PCR	Complementary PCR
	IRI	IRI	IRI

The three models created in this study have the same core of inputs: beginning latitude and longitude, ending latitude and longitude, the thickness of the top layer of pavement, length of pavement, pavement age at the year 2010, PCR at the year 2010, IRI at the year 2010, time counted from 2010, drainage, pre-PCR, and pre-IRI. Minor and major rehabilitations and a traffic variable were utilized in different models to study the significance of each variable. The time ranges from 1 to 9 because there are only 9 years of past data available for this study.

Model 1 utilized 13 independent variables and did not utilize any M&R history and traffic variables in its development. Model 2 included 15 independent variables, incorporating M&R history, but not using a traffic variable. Model 3 included 16 independent variables incorporating the effects of minor and major rehabilitation and traffic in the model. A two-output model with IRI and complementary PCR was utilized for all developed models. The two outputs (i.e., PCR and IRI) were modified to be used with the complementary PCR (i.e., 100-PCR), as the outputs need to be directly proportional in the ANN modeling. Because PCR and IRI usually change inversely over time, it was necessary to utilize the complementary PCR and IRI, as both change proportionally over time. Therefore, the use of complementary PCR assisted the network to optimize the model with better accuracy and to establish a superior correlation between actual and predicted outputs. The use of variables that are not related to distress data makes the models more accessible for transportation agencies, as most of these variables are easily available in their databases. Therefore, this model brings a valuable tool for the MDOT's pavement management system.

4 RESULTS AND DISCUSSION

4.1 *ANN model selection*

The best model was chosen based on how close the prediction of the model is with the existing data. The three best-performing models were selected based on the lowest average square error (ASE), lowest mean absolute relative error (MARE), and highest coefficient of determination (R^2). Table 2 shows the statistical measures of each ANN model development stage (i.e., training, testing, validation, and all data) for the complementary PCR output.

Table 2. ANN model results for complementary PCR output.

		Model 1	Model 2	Model 3
Complementary PCR		9-12-20000	16-19-20000	8-18-16000
Training	MARE	20.84	8.13	7.66
	R^2	0.672	0.819	0.838
	ASE	0.0029880	0.0008506	0.0007635
Testing	MARE	21.89	8.22	8.35
	R^2	0.575	0.805	0.785
	ASE	0.0035952	0.0009134	0.0010196
Validation	MARE	19.19	8.55	8.34
	R^2	0.693	0.779	0.739
	ASE	0.0026957	0.0010106	0.0011974
All data	MARE	21.971	7.566	7.926
	R^2	0.654	0.833	0.827
	ASE	0.0034965	0.0007808	0.0008096

For the complementary PCR output, the training stage showed that Model 3 indicated better accuracy measures in terms of ASE, MARE, and R^2. In the testing stage, Model 2 had the lowest ASE and MARE values and the highest R^2. In the validation stage, Model 2 had the lowest ASE and highest R^2 while Model 3 showed the lowest MARE. In the all data stage, the 1,930 data points were used to retrain the network at its optimal structure and iteration to obtain the generalized response throughout the complete database. The all data stage results show that Model 2 and Model 3 had good accuracy with low ASE and MARE values and an R^2 around 0.83. However, Model 1, the only model that did not use any variable related to M&R actions demonstrated lower accuracy compared to the other models that incorporated the effects of rehabilitation interventions. Statistical measures of Model 2 trained with all data showed to be the best model for the complementary PCR with an ASE of 0.0007808, a MARE of 7.566, and an R^2 of 0.833. Table 3 shows the comparison of each model for the IRI output.

For the IRI output, the training stage showed that Model 3 demonstrated better accuracy measures in terms of ASE, MARE, and R^2. In the testing and validation stages, Model 2 had the lowest ASE and highest R^2, while Model 3 had the lowest MARE. The all data stage results show that all models had good accuracy with really low ASE values and high R^2 values that vary from 0.781 to 0.819. It is important to notice that the least accurate model (Model 1) was the only one that did not incorporate M&R history in its development. Model 2 and

Table 3. ANN model results for IRI output.

		Model 1	Model 2	Model 3
IRI		9-12-20000	16-19-20000	8-18-16000
Training	MARE	23.84	12.85	12.11
	R^2	0.805	0.825	0.836
	ASE	0.0000171	0.0000092	0.0000084
Testing	MARE	25.97	13.96	13.89
	R^2	0.715	0.763	0.757
	ASE	0.0000249	0.0000110	0.0000113
Validation	MARE	21.80	14.03	13.25
	R^2	0.763	0.747	0.726
	ASE	0.0000183	0.0000112	0.0000123
All data	MARE	19.823	12.147	12.333
	R^2	0.781	0.819	0.816
	ASE	0.0000157	0.0000088	0.0000090

Model 3 demonstrated better accuracy when using minor and major rehabilitation variables. Statistical measures of Model 2 trained with all data showed to be the best model for IRI with an ASE of 0.0000088, a MARE of 12.147, and an R^2 of 0.819.

Therefore, Model 2 was chosen as the best performing ANN model for composite pavements in the MDOT database. The network structure of Model 2 includes 15 input variables, 1 hidden layer with 19 hidden nodes, 20,000 iterations, and 2 outputs. Figure 1 shows the observed PCR values collected from the MDOT database versus the predicted values using all developed models.

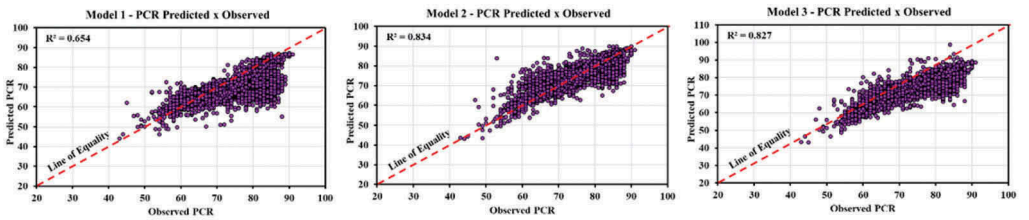

Figure 1. Observed versus predicted PCR for all developed models.

PCR predictions clustered around the line of equality and showed that the PCR behavior was captured by all the prediction models. However, some prediction values for Model 1 did not follow closely the line of equality, which explains the lower R^2 value compared to other models. Model 2 and Model 3 showed a high R^2 of 0.834 and 0.827, respectively, but it is possible to observe that Model 2 prediction values were closer to the line of equality. Figure 2 shows the observed IRI values collected from the MDOT database versus the predicted values using all developed models.

IRI predictions followed the line of equality and showed reliable results for all developed models. However, Model 1 demonstrated that several predicted values were overpredicted, showing higher IRI values, which reduced the model accuracy. Model 2 and Model 3 showed similar results where the models could capture the IRI behavior, but Model 2 showed a better

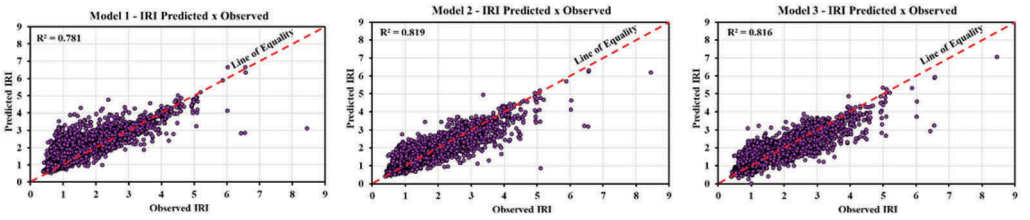

Figure 2. Observed versus predicted IRI for all developed models.

trend for predicted values and was chosen as the best performance model for composite pavements in the MDOT database.

Therefore, all developed models were able to imitate the pavement deterioration behavior. However, the model that did not use variables that incorporate the effect of M&R actions showed lower accuracy compared to other models. The results show the importance of considering maintenance and rehabilitation history when developing performance models, especially for composite pavements, which is the focus of this study.

5 CONCLUSIONS

In this study, an artificial neural network approach was used to develop performance prediction models for composite pavements in Mississippi from the MDOT database. Three different models were developed using different input variables and a two-output structure. All models had satisfactory results and could be used for generating reliable predictions for pavement performance. However, the only model that did not consider the effects of maintenance and rehabilitation history (Model 1) showed to be the least accurate. Models that considered M&R (Model 2 and Model 3) showed better predictions. The best-performing model was selected based on three accuracy measures shown in Table 2 and Table 3. Model 2 outperformed all other models in the all-data stage with lower ASE, MARE, and higher R^2 for IRI and PCR outputs. The final ANN model includes 15 input variables, one hidden layer with 19 hidden nodes, 20,000 iterations, and two outputs. Figure 1 and Figure 2 show predicted versus observed values for PCR and IRI for all developed models. It is possible to observe that the developed ANN models were able to capture the pavement deterioration behavior over time, but Model 2 and Model 3 had better accuracy than Model 1. Predicted values clustered around the line of equality, showing good agreement between observed and predicted values. Therefore, the development of performance models that include maintenance and rehabilitation variables provided a more accurate, inclusive, reliable, and realistic model for transportation agencies. The developed model can support objective decisions regarding maintenance and rehabilitation interventions and budget plans permitting state agencies to prioritize the resources for critical pavement sections. Furthermore, the best-performing model can be used as a simple and user-friendly tool to allow the user to visualize the future projections of the pavement section. MDOT personnel can employ this application to predict the condition of the composite pavement section and prioritize the maintenance and rehabilitation schedule.

REFERENCES

Adeli, H. 2001. "Neural networks in civil engineering: 1989-2000." *Computer-Aided Civil and Infrastructure Engineering*, 16 (2): 126–142. https://doi.org/10.1111/0885-9507.00219.

Barros, R., H. Yasarer, and S. Sultana. 2022. "International Roughness Index Model for Composite Pavements in the LTPP Wet Non-Freeze Climate Region: Machine Learning and Regression Approaches." *101st Annual Meeting of the Transportation Research Board (TRB) 2022*.

Barros, R., H. Yasarer, W. Uddin, and S. Sultana. 2021a. "Roughness Modeling for Asphalt Overlay on Concrete Pavements Using Neural Networks." *Transportation Research Board*.

Barros, R., H. Yasarer, W. Uddin, and S. Sultana. 2021b. "Roughness Modeling for Composite Pavements using Machine Learning." *IOP Conference Series: Materials Science and Engineering*, 1203 (3): 032035. https://doi.org/10.1088/1757-899X/1203/3/032035.

Bashar, M. Z., and C. Torres-Machi. 2021. "Performance of Machine Learning Algorithms in Predicting the Pavement International Roughness Index." *Transportation Research Record: Journal of the Transportation Research Board*, 036119812098617. https://doi.org/10.1177/0361198120986171.

Ceylan, H., M. B. Bayrak, and K. Gopalakrishnan. 2014. "Neural networks applications in pavement engineering: A recent survey." *International Journal of Pavement Research and Technology*, 7 (6): 434–444. https://doi.org/10.6135/ijprt.org.tw/2014.

Chen, C., R. C. Williams, M. G. Marasinghe, J. C. Ashlock, O. Smadi, S. Schram, and A. Buss. 2015. "Assessment of composite pavement performance by survival analysis." *Journal of Transportation Engineering*, 141 (9): 1–9. https://doi.org/10.1061/(ASCE)TE.1943-5436.0000784.

Darko, A., A. P. C. Chan, M. A. Adabre, D. J. Edwards, M. R. Hosseini, and E. E. Ameyaw. 2020. "Artificial intelligence in the AEC industry: Scientometric analysis and visualization of research activities." *Automation in Construction*. Elsevier B.V.

Duckworth, P., H. Yasarer, and Y. Najjar. 2022. "Evaluation of Flexible Pavement Performance Models in Mississippi: A Neural Network Approach." *Lecture Notes in Civil Engineering*, 179–190. Springer International Publishing.

Hossain, M., L. S. P. Gopisetti, and M. S. Miah. 2020. "Artificial neural network modelling to predict international roughness index of rigid pavements." *International Journal of Pavement Research and Technology*, 13 (3): 229–239. https://doi.org/10.1007/s42947-020-0178-x.

Hossain, M. I., L. S. P. Gopisetti, and M. S. Miah. 2019. "International roughness index prediction of flexible pavements using neural networks." *Journal of Stomatology*, 145 (1): 1–10. https://doi.org/10.1061/JPEODX.0000088.

Najjar, Y. 1999. *Quick Manual for the Use of ANN program TRSEQ1*. Manhattan, Kansas.

Sultana, S. 2021. "Computational Modeling of Climate Attributes and Condition Deterioration of Concrete Highway Pavements."

Sultana, S., H. I. Yasarer, W. Uddin, and R. Barros. 2021. "International Roughness Index Model for Jointed Plain Concrete Highway Pavements: An Artificial Neural Network Application." *Transportation Research Board*.

Tennant Duckworth, P. 2020. "Evaluation of Flexible Pavement Performance Models in Mississippi: A Neural Network Approach." *Master Thesis*.

Yasarer, H. 2010. "Characterizing the Permeability of Concrete Mixes Used in." *Master Thesis*. Kansas State University.

Yasarer, H., and W. Andrews. 2021. "Performance Evaluation of Jointed Concrete Pavements on Mississippi Highways via Artificial Neural Network." *Tran-SET 2021*, 86–92. Reston, VA: American Society of Civil Engineers.

Yasarer, H., M. N. S. Oyan, and Y. Najjar. 2020. "A Performance Prediction Model for Continuously Reinforced Concrete Pavement Using Artificial Neural Network." *Proceedings of the 9th International Conference on Maintenance and Rehabilitation of Pavements—Mairepav9*, 771–782.

Eleventh International Conference on the Bearing Capacity of Roads, Railways and Airfields, Volume 2 – Hoff, Mork & Saba (eds)

Modelling the permanent strains measured by in-situ cyclic light weight deflectometer for silty sand subgrade soil

Dina Kuttah
Senior researcher at the Swedish National Road and Transport Research Institute, Linköping, Sweden

ABSTRACT: It is well known that limiting rutting in pavements should consider the actual load-associated plastic (permanent) strains. Therefore, the Swedish transport administration have paid a particular attention to find a simple in-situ time saving technique that can be used to predict the permanent strains for unbound road materials to provide a powerful material assessment and pavement design tool. Such a design tool can be utilized to establish the risk level of permanent strains in the unbound road layer during the design and construction stages something which may result in an increase in pavement service life. To fulfill the objective of the study, cyclic (repeated) light weight deflectometer tests have been conducted at a test pit located at the backyard of VTI in Linköping. A silty sand subgrade soil has been chosen for testing. Initially, the selected subgrade soil was placed in the test pit and thoroughly compacted using a small vibrator, then, series of in-situ cyclic LWD were conducted at different ranges of water contents (namely 8%, 10% and 15%) and various applied stress levels (namely, 50 kPa, 100 kPa and 200 kPa).

Prediction models for accumulated permanent strains based on the cyclic LWD measurements are suggested in this study. These models correlate the measured accumulated permanent strains using the new developed LWD to the number of loading cycles, stress levels and water contents. It is expected that the suggested models will provide supporting data for an increased understanding of future pavements ruts. For the tested subgrade soil, the suggested models have showed good matching to the accumulated permanent strain (εp) data measured by the cyclic LWD tests except for the cases of p=100 kPa and 200 kPa at 15% water content due to the excessive accumulated permanent deformations reported for these cases.

Keywords: Repeated light weight deflectometer test, Modeling, Permanent strains, Silty sand subgrade, Stress levels, Water content

1 INTRODUCTION

Over the past decades, researchers have been concerned about the deformation characteristics of materials used for roads construction and they continually search for the most accurate methods and models that will measure and predict reasonably all types of soil and unbound material deformations (Monismith 1975; Ullidtz, 1993; Lekarp and Dawson, 1998; Lekarp et al., 2000, Puppala et al., 2009; Razouki et al., 2011; Rahman and Erlingsson, 2015; Xiao et al., 2015; Mohammadinia et al., 2019; Lima et al., 2019; Kuttah, 2020, Silva et al., 2021; Bilodeau et al.; 2021; Lu et al., 2021 and Kuttah, 2021), among others. These methods have often been used to determine shear stress–strain behaviour of geomaterials considering reversible and irreversible deformation under cyclic loads (Gomes Correia, 2004). The behaviour of geomaterials under cyclic loads can be characterized by either using complex elastoplastic

DOI: 10.1201/9781003222897-50

models (recoverable and permanent deformation are both considered) or by shakedown theory and mechanistic-empirical models (Hornych et al., 2004).

As far as the author know, no study has been conducted yet to predict the accumulated permanent deformations of compacted road material based on data collected by simple in-situ tests, except those carried out by Kuttah (2020) and Kuttah (2021). Therefore, the current study has been undertaken to deal with measuring and modelling the in-situ accumulated permanent strains of compacted subgrade soil using an accurate and simple field test, namely the cyclic light weight deflectometer (LWD) test. Correspondingly, the current VTI's LWD has been developed further to fulfill the purpose of this study. The research is based on finding a permanent strain computational methodology to be used in Mechanistic-Empirical Pavement Design Guide (MEPDG).

Mechanistic-empirical models can be divided into single-stage models and multi-stage models. A single-stage implies that the repetitive load tests are carried out at one stress level in one test; in this instance, multiple specimens are tested at different stress levels. Multistage models can test multiple levels of stress in one test on one specimen. This approach enables the effects that the stress level and stress history have on permanent deformation to be considered (Gregoire et al, 2011). These models can correctly simulate the response of materials; they are easy to implement, and they depend on fewer parameters than conventional elasto-plastic models (Ramosa et al., 2020).

Mechanistic-empirical models often describe a relationship between the number of load cycles (N) and the accumulated permanent deformation. In fact, those models that only consider the value of N should not be used to predict permanent deformation because they are too simple and lacks accuracy (Ramosa et al., 2020).

One of the first simple models proposed, which relates plastic strains to the number of load applications and other factors, was the model of Monismith et al. (1975), as shown in Equation (1) below:

$$\varepsilon_p = a.N^b \tag{1}$$

where:
ε_p= Accumulated plastic strain (%)
N= Number of load applications
a, and b= Parameters that represent the influence of other factors.

A more developed permanent strain model which includes directly the influence of the axial applied stress level is the one developed by Ullidtz (1993) as given in Equation (2).

$$\varepsilon_p = a.\ N^b.\ (\sigma_z/p_a)^c \tag{2}$$

where ε_p is the accumulated permanent strain, N is the total number of load cycles, a, b and c are model parameters, σ_z is the axial effective stress; and p_a is the atmospheric pressure, p_a = 101.3kPa.

Puppala et al. (1999) performed dynamic triaxial tests adopting three types of soils. Then, it was found that the effect of force on deformation can be more fully reflected by mean normal bulk stress and an improved model based on the model in Equation (2), as shown in Equation (3)

$$\varepsilon_p = a.\ N^b.(p_m/p_a)^c \tag{3}$$

where p_m is the mean normal bulk stress, and a, b and c are regression coefficients.

More recent models depend on the mean (p) and deviatoric (q) stresses have been developed, as does the model developed by Rahman and Erlingsson (2015), see Equation (4).

$$\varepsilon_p = a.\ S_f.\ N^{bS_f} \tag{4}$$

where ε_p is the accumulated permanent strain, N is the total number of load cycles, a and b are model parameters associated with the material and the term S_f considers the effect of stress state in permanent deformation accumulation given as:

$$S_f = \frac{\left\{\frac{q}{p_a}\right\}}{\left\{\frac{p_m}{p_a}\right\}^{\alpha}} \tag{5}$$

where p_m is the hydrostatic stress (one third of the sum of the principal stresses, θ), q is the deviator stress, p_a is the reference stress, here taken equal to the atmospheric pressure of about 100 kPa, and α is a parameter obtained from regression analysis.

2 CHARACTERISTICS OF THE TESTED SOIL

As illustrated previously, a silty sand subgrade soil has been selected to be tested in this study. Series of laboratory tests were carried out on the selected soil to determine its physical properties, namely, the particle size distribution, clay fraction, soil classification, specific gravity, liquid and plastic limits, and compaction characteristics.

The particle size distribution test on the selected soil has been carried out in accordance with SS-EN 933-1 (2004) and the result of the test is shown in Figure 1 below. The result of the test has showed that about 40% of the tested soil is passing 0.063 mm sieve. The clay content in the soil was tested according to VTI method for grain size distribution analysis with laser diffraction [10 nm - 2 mm] and has found to be 5%. The specific gravity of the selected soil has been tested according to SS-EN 1097-6 (2013), annex G, and it has found to be 2.64.

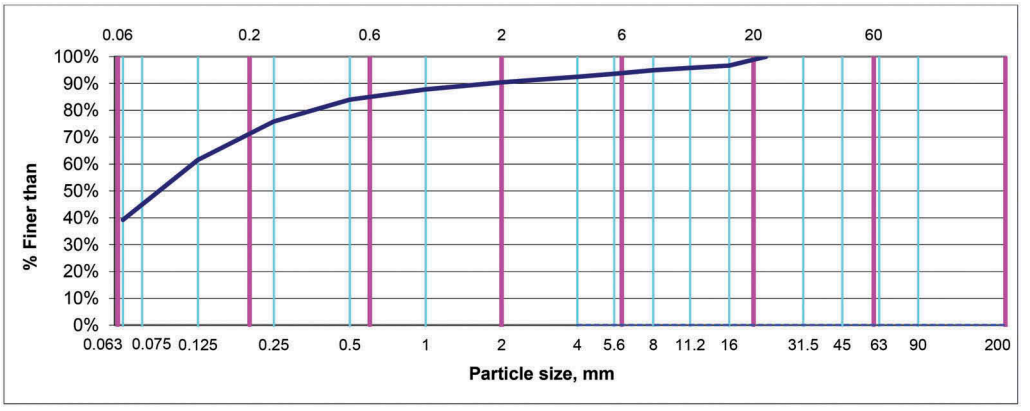

Figure 1. Particle size distribution of the tested soil.

The liquid and plastic limits have been determined at SGI according to SS-EN ISO 17892-12 (2018). The tests results revealed a liquid limit (LL) of 18% and a plastic limit of (PL) 14.3% resulting in 3.7% plasticity index for the tested soil.

In this study, the compaction properties were determined by modified Proctor test as per ASTM D1557 (2012). The test has been performed by compacting several soil samples using a cylindrical mold of 152.4 mm diameter. The soil samples were compacted at different molding water contents ranging between 0 to 16% to determine the water-density relationship. The results of the compaction tests revealed that the tested soil has a maximum dry density of 2.03 g/cm^3 at about 8.2% optimum moisture content.

3 TESTING METHODOLOGY

A test pit of about 9.5 m long x 5.7 m width x 1.5 m depth was constructed at the backyard of the Swedish Road and Transport Research Institute (VTI) and instrumented with an electric drive motor roof panel. The roof panel can be opened and closed with the help of an electric motor to control as much as possible the testing conditions in the test pit. The test pit was also equipped with a concrete well with a water discharging motor that was used to control the ground water level during testing.

Initially, the selected silty sand subgrade soil was placed and thoroughly compacted using a small vibrator. When the compaction completed, the final subgrade surface was marked with circles representing the selected positions of the points to be tested.

The in-situ cyclic LWD tests were divided into three groups. For each testing group, the cyclic LWD tests have been carried out at three different applied stresses namely 50 kPa, 100 kPa and 200 kPa for a set of testing points. These stress levels have been chosen to simulate the real ranges of applied stresses on the subgrade soil by moving vehicles for subgrade soil used for paved and unpaved roads of thin superstructure. During all the in-situ cyclic LWD tests, the LWD plate diameter was 200 cm. The applied stresses have been varied to achieve the target stresses by changing the drop height of 10 kg drop weight,

Directly after completing the compaction, series of NDG tests were carried out indicating an average water content of about 10%on the tested subgrade surface. Afterward, series of LWD tests were carried out at the three chosen applied stresses, namely, 50 kPa, 100 kPa and 200 kPa when the testing water contents were still around 10%. To carry out LWD tests at a water content drier than the compaction water content of 10%, the steel cover of the test pit was left open for several hours in order to dry the soil under sunshine and then the LWD tests were carried out at a water content of about 8% under the similar chosen applied stresses. Later on, in order to carry out LWD tests at a water content wetter than the latest water content of 8% and even wetter than the compaction water content of 10%, the soil in the test pit was watered. Before carrying out the last LWD tests series, the research team waited for few hours, to ensure consistence water content penetration and distribution through the soil layer. Then, the cyclic LWD tests were performed at about 15% water content.

The current VTI's LWD has been developed further to measure simply and accurately the permanent and recoverable deformations induced by impact loading, see Figure 2.

During the test, a falling mass (a basic of 10 kg) impacts the plate, producing a load pulses that may be adjusted in magnitudes depending on the dropping heights and dropping masses. The center deflection of the tested material surface is measured through a hole in the loading plate by a highly accurate, seismic transducer (geophone). The diameter of the loading plate used in this study was 200 mm. The drop height can be easily and quickly adjusted by a movable release handle and the peak value of the impact force is based on actual measurements from the load cell.

The new developed LWD has been supplied with a new control beam linked to a central LVDT to register the plastic deformations during testing at the centerline of loading. The central geophone (used to measure the total deformation) and a LVDT (used to measure the plastic deformation), both placed along the center of the dropping weight to measure the total and plastic deformation on the soil surface directly through a hole on the center of the steel plate. The LVDT was coupled to a control beam to measure the absolute plastic deformation. The measurement of plastic deformations by a mounted LVDT is important because the plastic deformations cannot be conducted from the central geophone due to the general integration errors usually encountered. This evolution enables a continuous monitoring and displaying of load versus accumulated soil deformation loops similar to the stress-stain loops usually collected during RLT tests.

The data collection software is installed in a PC coupled to the LWD control panel. In combination with in-situ LWD measurements, the Nuclear Density Gauge (NDG) has

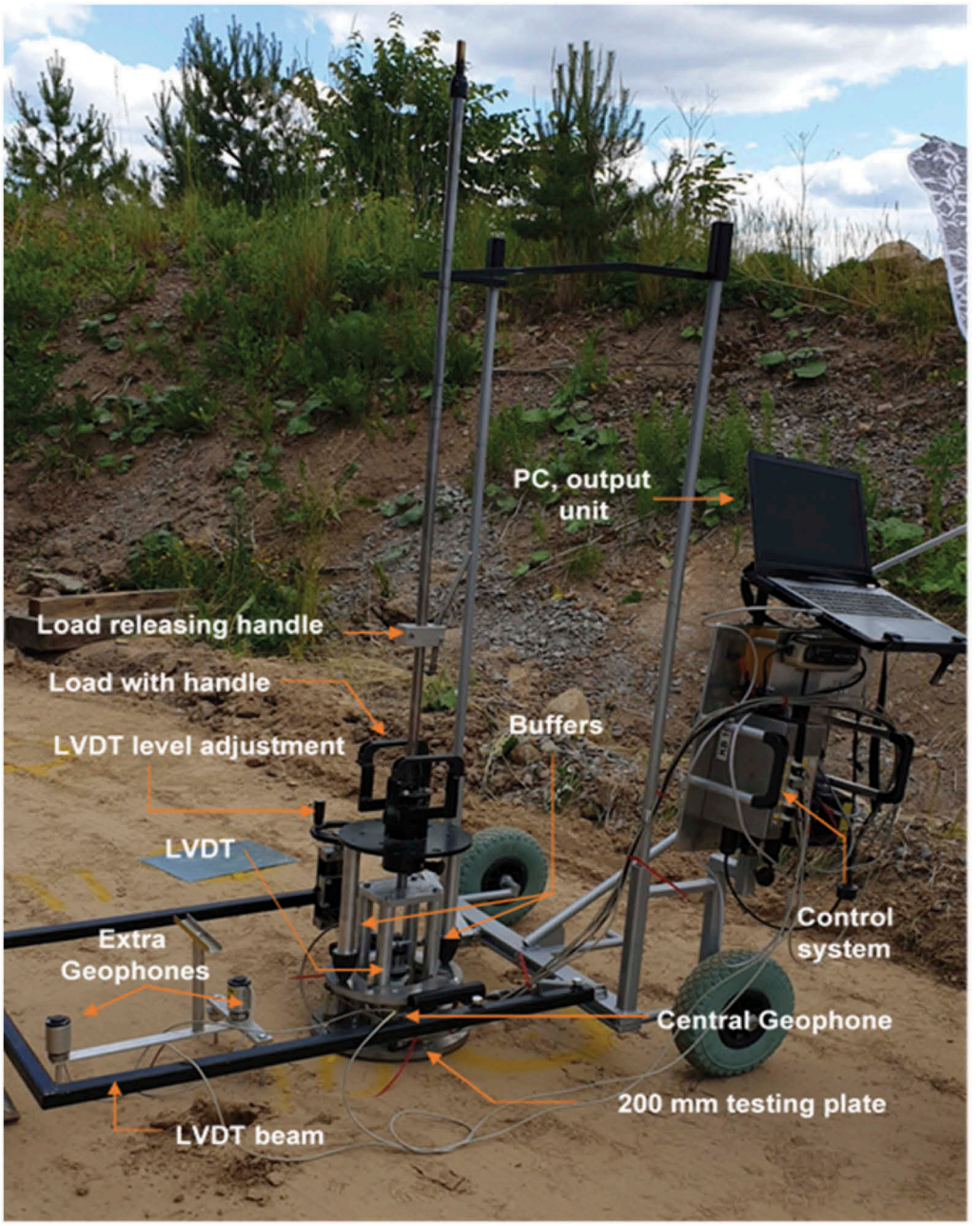

Figure 2. The VTI's light weight deflectometer which can measure the permanent (plastic) deformations of the tested soil separately and accurately.

been used to determine the in-situ density and moisture content of the tested soil in the test pit.

4 RESULTS AND DISCUSSION

As mentioned previously, the models shown in Equations (1) to (5) require the permanent strains while in the developed cyclic LWD test, the permanent deformations can be measured. Therefore, in order to convert the measured permanent, the LWD's zone of influence should be estimated.

Nazzal (2003) and Tompai (2008) found that the zone of influence of the LWD to vary between 1 and 2 times the plate diameter something which goes well with Elhakim et al. (2014) findings. Correspondingly, the zone of influence of the LWD was assumed to be 1.5-fold of the plate diameter of 20 cm (i.e. the zone of influence of the LWD was assumed to be 30 cm) in this study. Correspondingly all the measured plastic deformations by in-situ LWD test have been converted to plastic strains by making use of the LWD suggested depth of influence of 30 cm.

Figure 3 shows the effect of repeated loading on the permanent soil strains during cyclic LWD testing at different water contents and stresses levels. The missing data in Figure 3 for some of the LWD tests are because of termination of the tests due to excessive deformations that goes beyond the measurement limits of the used sensors.

It was found that the accumulated permanent strains increase with increasing the loading cycles, applied stress levels and water content during testing. It can be deduced that the increase in permanent strains does not behave in the same way under all load and water contents conditions. One can notice that most of the permanent strains have been developed at the first few cycles and then the accumulation of permanent strains has continued its slow but steady decline during the last cycles of LWD loading for the points tested at the lowest stress levels and under 8% and 10% water contents. The material in the wettest water content tested in this study was more prone to the accumulation of permanent strain when subjected to larger stress levels, see Figure 3.

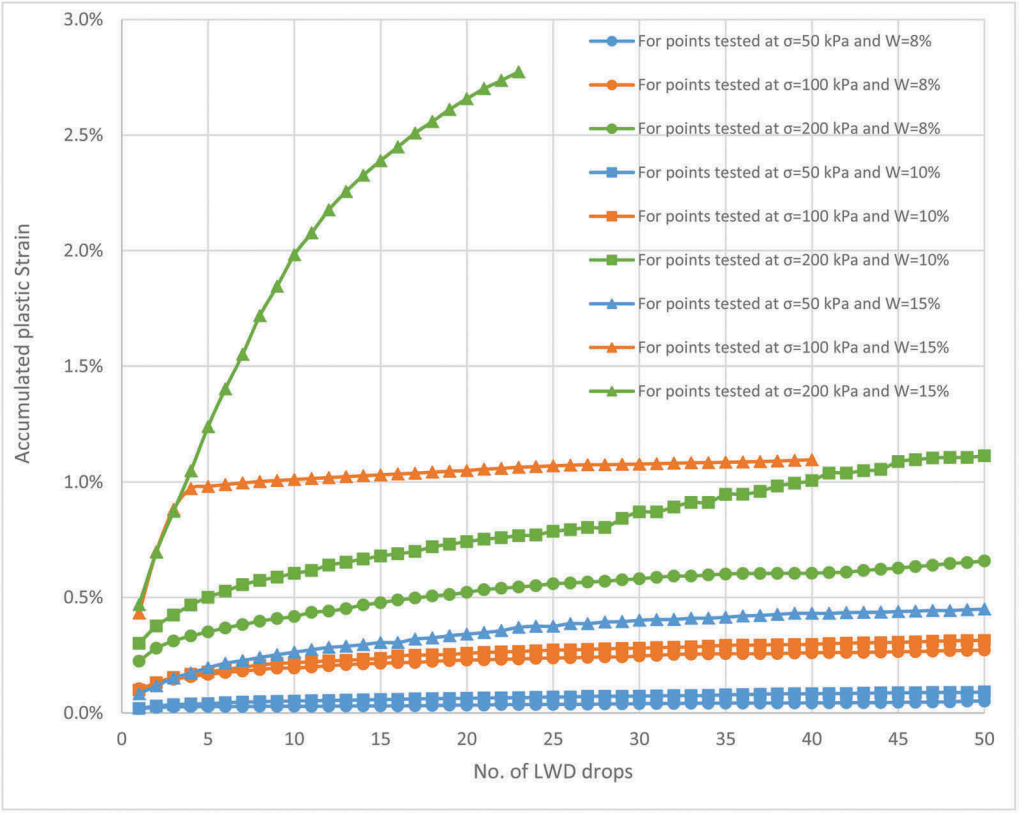

Figure 3. Effect of repeated loading on the permanent deformations during LWD testing at different water contents and applied stress levels.

It is well known that many researchers have developed models to describe the stress and moisture dependency of the measured permanent deformation during RLT testing as described previously. However, the models given in Equations (1) to (5) have been developed to predict the accumulated plastic (permanent) strains measured by repeated load triaxial (RLT) testing and not by cyclic LWD tests. Therefore, in order to consider the effect of loading frequency, water content and the applied stresses on the prediction of the accumulated permanent strain measured by cyclic in-situ LWD tests, the model given in Equation (6) has been developed accordingly, as shown below:

$$\varepsilon_p = a \,.\, W \,.\, S.\; N^{bS} \tag{6}$$

where ε_p is the accumulated permanent strain, N is the total number of load cycles, a and b are regression parameters associated with the material, W is the water content measured during LWD testing by NDG in (%), and S is the normalized applied stress level as given as:

$$S = p/p_a \tag{7}$$

where p is the applied stress level during LWD testing in (kPa) which is equal to the applied load /area of LWD plate. Note that the diameter of the used plate in this study was 20 cm.

p_a= a reference pressure =100 kPa

In order to adapt further the model given in Equation (6) to match better the measured in-situ LWD accumulative plastic strains, a power water content (W) variable has been used as given in Equation (8) below.

$$\varepsilon_p = a \,.\, W^c.\; S.\; N^{b\,S} \tag{8}$$

where ε_p is the accumulated permanent strain, N is the total number of load cycles, a and b *and* c are regression parameters associated with the material, W is the water content measured during LWD testing by NDG in (%), and S is as defined in Equation (7).

Based on the discussion above, a set of nonlinear parameters namely a, b and c that would provide a reasonable fit for a given model were determined, see Table 1.

The optimization of the model's parameters given in Equations (6) and (8) was carried out so that the sum of squares for error from the test data and the model predictions is minimized.

Table 1. The model parameters that provide best fit for ε_p given in Equations (6) and (8).

Model	a	b	c
Equation (6)	*0.0191*	0.1115	. . ..
Equation (8)	0.00045	0.1435	2.5803

Figure 4 shows the accumulated permanent strain (ε_p) as a function of loading cycles for the data measured by in-situ cyclic LWD and the developed models given in Equations (6) and (8).

From the results of the accumulated permanent strains measured by cyclic light weight deflectometer tests, it can be deduced that the increase in permanent strains does not behave in the same way under all load and water contents conditions. In general, ε_p increased with increasing water content and applied stress levels. It can be noticed that most of the ε_p accumulation occurred in the initial phase of the tests.

Some results presented excessive ε_p in some testing conditions, such as the cases of the largest stress levels in the wettest testing conditions.

The missing data showing N < 50 LWD drops for two test groups are because of termination of the tests due to excessive deformations that goes beyond the measurement limits of the used sensors, as described previously.

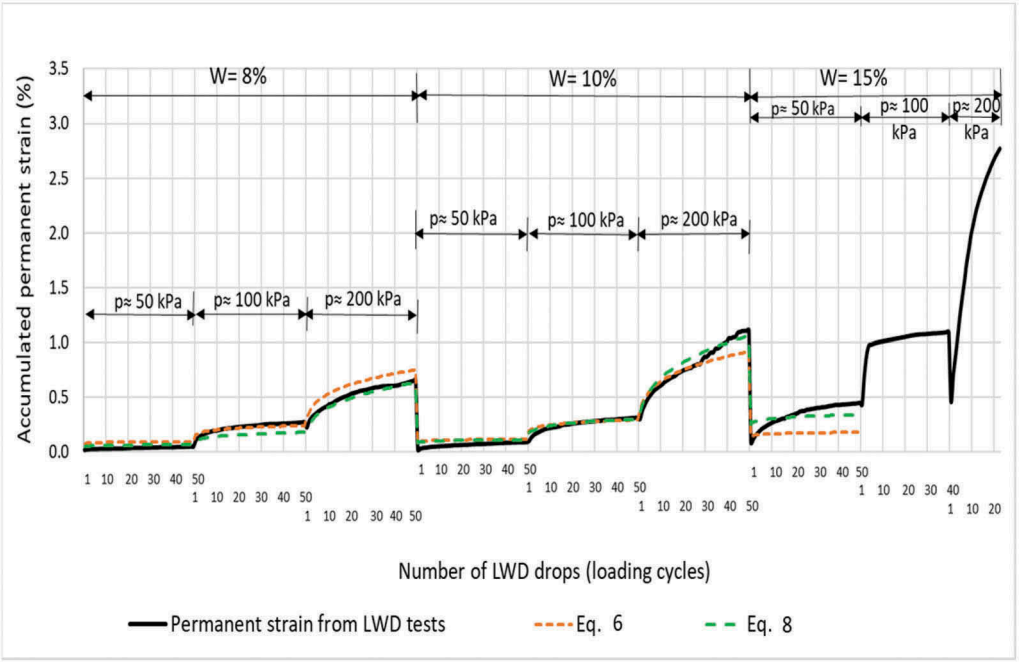

Figure 4. The accumulated permanent strain as a function of loading cycles for the data measured by in-situ cyclic LWD and the developed models given in Equations (6) and (8).

For the εp curve of the points tested at 8% and 10% water contents under 50 kPa and 100 kPa, a slow increase in εp with increasing the number of loading cycles is produced. For the curve of points tested at 15% water contents under 50 kPa, the increase in εp is more accentuated. Regarding the curves of points tested at 8% and 10% water contents under 200 kPa, the increase in εp is even more accentuated.

On the other hand, for the curves of points tested at 15% water contents under 100kPa and 200 kPa, the increase in εp (%) is much more accentuated and the stabilization of the material is not observed.

Furthermore, it can be seen from Figure 3 that the model given in Equation (8) with power water content variable (with c=2.56) gives better matching to the permanent deformations measured by in-situ cyclic LWD tests, as compared to the model given in Equation (6). This observation emphasis the importance and influence of water content on the permanent deformations of the tested soil.

5 CONCLUSIONS AND RECOMMENDATIONS

Geomaterials exhibit elastoplastic behaviour during dynamic and repeated loading conditions. Modelling this behaviour is still a challenge for geotechnical engineers as it implies the understanding of the complex deformation mechanism.

This work is part of a broader research at VTI to provide input data to pavement design guides using simple in-situ technology. Correspondingly, selected mechanistic-empirical models used to predict the permanent strains of unbound materials were examined and

modified to match better the permanent strains conducted in this study using in-situ cyclic LWD tests.

From the results of this research the following conclusions may be withdrawn:

- It has been shown from this study that the cyclic LWD testing could provide a powerful and quick material assessment tool for accumulated permanent strain which could simplify the flexible pavement design by predicting the rutting behaviour. Information about the sum of plastic strains provided by the cyclic LWD tests could be adopted to determine the proper usage of construction materials and their performance.
- For the tested subgrade soil, prediction models for accumulated permanent strains based on the cyclic LWD measurements are suggested in this study. The models given in Equations (6) and (8) have showed very good matching to the accumulated permanent strain (εp) for the data measured by in-situ cyclic LWD tests as a function of loading cycles, stress levels and water content during testing. The model given in Equation (8) with power water content variable (of c=2.58) gave better matching to the permanent deformations measured by in-situ cyclic LWD tests, as compared to the model given in Equation (6). This observation emphasis the importance and influence of water content on the permanent deformations of the tested soil.

Nevertheless, it is important to mention that all the models developed in this study to fit cyclic LWD test data are recommended to be used keeping in mind that they have been developed for specific materials and testing conditions (i.e. tested water contents, and stress levels). When using these equations for different testing materials and conditions as that they developed for, a combination of previous experience and engineering judgement should be considered. It is also recommended to carry out similar studies on other types of road materials to measure and model the accumulated permanent strains using in-situ cyclic LWD.

ACKNOWLEDGEMENT

The author would like to acknowledge the financial support from the Swedish Transport Administration via the industry program BVFF (Bana Väg För Framtiden). Thanks also to KUAB AB for developing further the VTI's lightweight deflectometer in cooperation with the author.

REFERENCES

ASTM D1557, 2012. *Standard test methods for laboratory compaction characteristics of soil using modified effort (56,000 ft-lbf/ft3-2,700 kN-m/m3)*. ASTM International, West Conshohocken, PA, United States.

Bilodeau J.; Leandro, E. and Gonzalez P., 2021. *Permanent deformation analysis of base layers with recycled material: Effect of density and stress level*. Transportation Geotechnics, ISSN: 2214-3912, Vol: 27, https://doi.org/10.1016/j.trgeo.2020.100466

Elhakim, A. F.; Elbaz, K.; and Amer, M. I., 2014. *The use of light weight deflectometer for in situ evaluation of sand degree of compaction*. Housing and Building National Research Center HBRC Journal, 10, 298–307, http://ees.elsevier.com/hbrcj.

Gomes Correia, A., 2004. *Evaluation of mechanical properties of unbound granular materials for pavements and rail tracks*. Gomes Correia and Loizos (Editors), Geotechnics in Pavement and Railway Design and Construction, MillPress

Gregoire C, Correia AG, De Bel R, Dethy B., 2011. *Mechanical behavior of natural and recycled granular materials for roads*. J Test Evaluat.;39.

Hornych P, Chazallon C, Allou F, El Abd A., 2004. *Selection and evaluation of models for prediction of permanent deformations of unbound granular materials in road pavements*. Work Package 5, Performance-based specifications. SAMARIS. https://doi.org/10.1016/j.trgeo.2020.100326.

Kuttah, D., 2021. *Determining the resilient modulus of sandy subgrade using cyclic light weight deflectometer test*. Transportation Geotechnics, Volume 27,100482, ISSN 2214-3912, https://doi.org/10.1016/j.trgeo.2020.100482.

Kuttah, D., 2020. *Simple and quick evaluation of unbound materials bearing capacities that could be used as input data in Mechanistic-Empirical Pavement Design*. VTI report 1054, ISSN 0347-6030, in Swedish, VTI rapport 1054 (diva-portal.org).

Lekarp F, and Dawson A., 1998. *Modelling permanent deformation behaviour of unbound granular materials*. Constr Build Mater.;12:9–18.

Lekarp F, Isacsson U, and Dawson A., 2000. *State of the art. II: Permanent strain response of unbound aggregates*. J Transp Eng 126(1):76–83. https://doi.org/10.1061/(ASCE)0733-947X(2000)126:1(76)

Lima, C.; Motta, L., and Aragão, F., 2019. *Effects of Compaction Moisture Content on Permanent Deformation of Soils Subjected to Repeated Triaxial Load Tests*. Transportation Research Record, Vol. 2673(2) 466–476. https://doi.org/10.1177/0361198118825124

Lu, C.; Chen, J.; Chuan, G.; Wang, J.; Yuanqiang, C. Zhangd, T. and Lin, G., 2021. *Resilient and permanent deformation behaviors of construction and demolition wastes in unbound pavement base and subbase applications*. Transportation Geotechnics, in press, https://doi.org/10.1016/j.trgeo.2021.100541.

Mohammadinia A.; Arulrajah A.; Disfani M. and Darmawan S., 2019. *Small-Strain Behavior of Cement-Stabilized Recycled Concrete Aggregate in Pavement Base Layers*. J. Mater. Civ. Eng., 31(5): 04019044.

Monismith CL, Ogawa N, Freeme CR., 1975. *Permanent deformation characteristics of subgrade soils due to repeated loading*. Transp Res Rec;537: 1–17.

Nazzal, D. M., 2003. *Field evaluation of in-situ test technology for QC/QA during construction of pavement layers and embankments*. Master's thesis, Louisiana State University, Baton Rouge.

Puppala AJ, Saride S, Chomtid S.,2009. *Experimental and modeling studies of permanent strains of subgrade soils*. Geotech Geoenviron Eng,135:1379–89.

Puppala, A.J., Mohammad, L. and Allen, A., 1999. *Permanent deformation characterization of subgrade soils from RLT test*. Journal of Materials in Civil Engineering, 11 (4), 274–282. https://doi.org/10.1061/(ASCE)0899-1561(1999)11:4(274)

Rahman, M. S. and Erlingsson, S., 2015. *A model for predicting permanent deformation of unbound granular materials*. Road Mater Pavement Des; 16:653–73. https://doi.org/10.1080/14680629.2015.1026382

Ramosa, A.; Correiaa, A. G.;Indraratnab, B.; Ngob, T.; Calcadac, R. and Costac, P., 2020. *Mechanistic-empirical permanent deformation models: Laboratory testing, modelling and ranking*. Transportation Geotechnics Volume 23, 100326.

Razouki, S. S., Kuttah, D. K. and Abood, M., 2011. *Compaction and Design of Gypsiferous Fill for Hot Desert Road Pavements*. proceedings of ICE, Construction Materials Journal, London, Vol. 164, 1, pp. 3–11.

Silva, M., Ribeiroa, M., Furlana, A.; Fabbria, G., 2021. *Effect of compaction water content and stress ratio on permanent deformation of a subgrade lateritic soil*. Transportation Geotechnics 26 (2021) 100443. https://doi.org/10.1016/j.trgeo.2020.100443.

SS-EN 1097-6, 2013. *Tests for mechanical and physical properties of aggregates*. Part 6 "Determination of particle density and water absorption", SIS, Swedish Standards Institute, Stockholm, Sweden.

SS-EN 933-1, 2004. *Tests for geometrical properties of aggregates*. Part 1 "Determination of particle size distribution – sieving method", SIS, Swedish Standards Institute, Stockholm, Sweden.

SS-EN ISO 17892-12, 2018. *Geotechnical investigation and testing — Laboratory testing of soil — Part 12: Determination of liquid and plastic limits*. ISO, the International Organization for Standardization.

Tompai, Z., 2008. *Conversion between static and dynamic load bearing capacity moduli and introduction of dynamic target values*. Periodica Polytechnica, Civil Engineering, Hungary, 52–2: pp. 97–102.

Ullidtz P.,1993. *Mathematical model of pavement performance under moving wheel load*. J. of Trans. Res. Rec., Washington, D.C.;1384:94–9.

Xiao Y., Tutumluer E., and Mishra D., 2015. *Performance evaluation of unbound aggregate permanent deformation models for different aggregate physical properties*. Transport Res Record J Transport Res Board; 2525:20–30.

Eleventh International Conference on the Bearing Capacity of Roads, Railways and Airfields, Volume 2 – Hoff, Mork & Saba (eds)

Author Index